Recent Progress in Steel and Composite Structures

Editors
Marian A. Giżejowski
Aleksander Kozłowski
Jakub Marcinowski
Jerzy Ziółko

CRC Press
Taylor & Francis Group
A BALKEMA BOOK

This page intentionally left blank

PROCEEDINGS OF THE XIII INTERNATIONAL CONFERENCE ON METAL STRUCTURES (ICMS2016), ZIELONA GÓRA, POLAND, 15–17 JUNE 2016

Recent Progress in Steel and Composite Structures

Editors

Marian A. Giżejowski
Department of Metal Structures, Warsaw University of Technology, Poland

Aleksander Kozłowski
Department of Building Structures, Rzeszów University of Technology, Poland

Jakub Marcinowski
Institute of Civil Engineering, University of Zielona Góra, Poland

Jerzy Ziółko
Chair of Building Structures, Bydgoszcz University of Science and Technology, Poland

CRC Press
Taylor & Francis Group
Boca Raton London New York Leiden

CRC Press is an imprint of the
Taylor & Francis Group, an **informa** business

A BALKEMA BOOK

Cover design by Dorota Marcinowska

CRC Press/Balkema is an imprint of the Taylor & Francis Group, an informa business

© 2016 Taylor & Francis Group, London, UK

Typeset by V Publishing Solutions Pvt Ltd., Chennai, India
Printed and bound in Great Britain by CPI Group (UK) Ltd, Croydon, CR0 4YY

All rights reserved. No part of this publication or the information contained herein may be reproduced, stored in a retrieval system, or transmitted in any form or by any means, electronic, mechanical, by photocopying, recording or otherwise, without written prior permission from the publisher.

Although all care is taken to ensure integrity and the quality of this publication and the information herein, no responsibility is assumed by the publishers nor the author for any damage to the property or persons as a result of operation or use of this publication and/or the information contained herein.

Published by: CRC Press/Balkema
P.O. Box 11320, 2301 EH Leiden, The Netherlands
e-mail: Pub.NL@taylorandfrancis.com
www.crcpress.com – www.taylorandfrancis.com

ISBN: 978-1-138-02946-0 (Hbk + CD-ROM)
ISBN: 978-1-315-62319-1 (eBook PDF)

Recent Progress in Steel and Composite Structures – Giżejowski et al. (Eds)
© 2016 Taylor & Francis Group, London, ISBN 978-1-138-02946-0

Table of contents

Foreword ix

Preface xi

Organisation and committees xiii

Keynote papers

Advances in understanding shell buckling phenomena and their characterisation for practical design 3
J.M. Rotter

Advances in seismic assessment of steel-concrete composite high-rise buildings and engineering practices 17
J. Qian, Z. Zhou & X.H. Wu

Harmonization of structural standards on the reliability basis of design 29
J.V. Retief

Recent steel structures in Poland—the selected projects 41
K. Żółtowski & T.W. Siwowski

Land-based supporting structures for wind energy converters 55
M. Veljkovic, C. Rebelo & M. Pavlovic

Cold-formed sections and profiled sheeting

Shear strength of trapezoidal and sinusoidal corrugated steel webs 69
M. Gajdzicki & W. Perlinski

Curved cold formed steel roofing: Numerical and experimental analysis 75
L.C. Prola, T.F.R. Lopes, J.R. Baptista & P.A.L. Fernandes

Flexural elastic buckling stress of light gauge built-up member 83
K. Mitsui, A. Sato, H. Okada & T. Ono

FEM model of the steel building roof includes stressed skin diaphragm action effects 93
M. Gryniewicz & J.K. Szlendak

Experimental investigation of the stabilization of the C-section purlins by sandwich panels 101
R. Studziński & K. Ciesielczyk

Innovative cold-formed GEB section under compression 107
A. Łukowicz, P. Deniziak, W. Migda, M. Gordziej-Zagórowska & M. Szczepański

Steel-concrete composite structures

Concrete confinement estimation in composite steel-concrete columns 117
E. Szmigiera, B. Grzeszykowski & M. Szadkowska

AAEM method against Volterra integral analysis of composite beam 125
D. Partov & V. Kantchev

Tests of shear connectors used in aluminium-concrete composite structures 133
Ł. Polus & M. Szumigała

Innovative solution of transition zone in steel-concrete hybrid beam 137
P. Kozioł, M. Kożuch, W. Lorenc & S. Rowiński

Composite structural electric transmission tower 143
J. Chen, W.L. Jin & W. Xue

Prestressing of simply supported composite bridges: A cost-benefit analysis 149
G. Bertagnoli, D. Gino & E. Martinelli

Buckling and effect of bracings

Diagonal bracing members of lattice towers—analytical versus experimental studies 161
J. Szafran & K. Rykaluk

A unified resistance verification of beam-columns not susceptible to LT-buckling 169
M.A. Gizejowski, R.B. Szczerba & M.D. Gajewski

Lateral-torsional buckling of steel beams with simultaneously tapered flanges and web 179
J. Kuś

Global geometrical imperfections for refined analysis of lateral roof bracing systems 187
A. Biegus & D. Czepiżak

A new method of buckling resistance evaluation of laterally restrained beam-columns 197
M.A. Gizejowski, Z. Stachura, M.D. Gajewski & R.B. Szczerba

Distortional lateral torsional buckling of open and closed steel cross-sections 207
R. Studziński & M. Czaja

Dynamics, fatigue and seismic analyses

Experimental and numerical study on polymer element used for reduction of temporary steel grandstand vibrations 215
N. Lasowicz & R. Jankowski

The effect of steel properties on deformation capacity of HSS columns 223
A. Sato & K. Mitsui

Shakedown seismic analysis of composite steel-concrete frame systems 231
P. Alawdin & G.V. Bulanov

Comparison between behavior of steel and composite Eccentrically Braced Frames with long links 237
M. Şenilă, A. Şigăuan & I. Petran

Collapse behaviour of steel box columns under seismic effect of the combined earthquakes 245
S. Shimizu

Determination reserve of bearing capacity for steel, with influence of long-term fatigue load, used in structures in case of a fire 253
K. Pawłowski, R. Świerzko & A. Włóka

Bridges

Atmospheric corrosion tests on weathering steel bridges in the Czech Republic 263
V. Krivy, V. Urban & K. Kreislova

The history of the first orthotropic bridge in Bulgaria 271
D. Partov, R. Ivanov & D. Dinev

Finite element analysis of metal-soil bridge under static loads 279
D. Beben

Effect of endogenous deformations in composite bridges 287
G. Bertagnoli, D. Gino & G. Mancini

Quality of butt welds in bridges and fatigue classes according to European codes and testing 299
B. Wichtowski & J. Hołowaty

Fatigue of structural elements in steel bridges—theory and practice 305
A. Wysokowski

Structural steel, metallurgy and behaviour in fire

Redistribution of internal forces generated in a steel frame structure with flexible joints when exposed to a fire 315
M. Maslak, M. Pazdanowski & M. Snela

Fire resistance evaluation of a steel sway frame load-bearing structure using the linear programming 323
M. Maslak, M. Pazdanowski & A. Tkaczyk

Recent developments in heavy plate production for modern steel bridges 331
T. Lehnert & F. Schröter

Modelling for the effect of welding process on buckling of built-up high strength steel box column 337
J. Jiang, C.K. Lee & S.P. Chiew

Application of Barkhausen method to determine internal stresses in cold-rolled and hot-rolled sheets 345
A. Łukowicz & D. Kowalski

Application of Barkhausen effect in the impact assessment of welding to internal stress distribution in steel 353
D. Kowalski

Strength, stability and postbuckling behaviour

Experimental investigations on non-uniform torsion of the two-chord members laced at a single plane 363
P. Lorkowski & B. Gosowski

Computer FVM-FEM analysis of the large span grid shell roof 371
J. Szafran, K. Juszczyk & M. Kamiński

Buckling strength of a steel multi-storey framework according to Eurocode's general method 381
M.A. Gizejowski & Z. Stachura

Shakedown optimization of the Thin-Wall Metal structures under strength and stiffness constrains 393
P. Alawdin & L. Liepa

Buckling capacity curves for pressurized spherical shells 401
P. Błażejewski & J. Marcinowski

An integrated approach for fatigue prevention in Movable Scaffolding System 407
H. Coelho, A. Torres, C. Moreira, R. Silva, J.M. Soares, D. Pinto & P. Pacheco

Stability of a truss under upward wind loading 417
M. Krajewski & P. Iwicki

Preliminary experimental research on stability of truss' joint with positive eccentricity 425
M. Gordziej-Zagórowska, E. Urbańska-Galewska, Ł. Pyrzowski, P. Deniziak & A. Łukowicz

Joints and connections

Durability assessment of connections between sandwich panels and purlins 435
M. Górski & A. Kozłowski

FEM analysis of the extended end-plate splice of welded I-girders with multiple bolt rows and bolts per row 443
P. Kawecki, J. Łaguna & A. Kozłowski

Equivalent model of semi-rigid supporting node in the calculations of steel frames 451
P. Krystosik

Component-based modelling of beam-to-column joints subjected to variable actions 457
L. Ślęczka

Steel column-base solutions for over-roofing of existing buildings: A numerical study 463
A. Floricel, S. Benzar, V. Ungureanu & G. Zagari

Numerical analysis of stainless steel bolted lap joints 471
A. Silveira, W. Barbosa, P. Vellasco, A. Silva & L. Lima

FEM based assessment of the rotation capacity of bolted joints 479
K. Ostrowski & A. Kozłowski

Truss design with one-membered elements and N-joints 489
J. Bródka & M. Broniewicz

Silos, tanks and vessels

Experimental investigations on the resistance of vertical stiffeners of steel silos shells made of corrugated sheets 499
E. Hotała, Ł. Skotny, M. Kuśnierek & J. Boniecka

Load-bearing capacity of discretely supported steel silos shells with skirts 507
Ł. Skotny, E. Hotała & J. Boniecka

Postbuckling behaviour of open thin-walled shells made of stainless steel 515
N. Stranghöner & S. Stehr

Simplified stability analysis of steel cylindrical silos with corrugated walls and vertical columns 525
K. Rejowski & P. Iwicki

Problems of designing tubular shell galleries 533
J. Dudkiewicz & R. Ignatowicz

Reliability, masts and towers

Searching for significant basic variables of experimentally tested steel, cylindrical shells 543
J. Kaliszuk, J. Marcinowski & Z. Waszczyszyn

Reliability level of the buried Main Pipelines Linear Part 551
S. Pichugin, O. Zyma & P. Vynnykov

Influence of the bearing capacity and reliability of connections and nodes on the bearing capacity and reliability of complex bar structures 559
Z. Kowal

Deformation of steel lattice towers for overhead lines—case study 565
M. Just

Influence of the initial guy forces on the static computations of mast taking into account the mast shaft buckling form 571
M. Matuszkiewicz

Recent Progress in Steel and Composite Structures – Giżejowski et al. (Eds)
© 2016 Taylor & Francis Group, London, ISBN 978-1-138-02946-0

Foreword

The University of Zielona Góra is one of the youngest and the most developing institution of the Polish higher education system . 2016 is the year in which we celebrate the 15th anniversary of founding the university. The academic and research traditions in Zielona Góra date back to the 1960s when the first higher education institution was established. Our University founded in 2001 was established as a merger of the Zielona Góra Technical University and the Pedagogical University. The new university integrated in its structure extremely varying academic disciplines and fields of study. They included science, engineering, humanities, education, law, and since 2015 also medical studies.

Currently the University is composed of 12 faculties employing more than 700 researchers. The University offers more than 60 courses, for more than 13 thousand students, leading towards the degrees of Bachelor of Arts, Bachelor of Science, Engineer, Master of Arts, Master of Science, Doctor of Philosophy.

The University is the biggest tertiary education institution in the region of Lubuskie and many of its graduates have found the employment in the local businesses, companies, offices and institutions. I can safely say that the graduates of our University are present in every economic and social field. The research conducted to satisfy the needs of the local and regional companies and state administration provides proof of the great significance of the University for the Lubuskie region. The new possibilities of close cooperation and collaboration between the researchers and entrepreneurs have been generated due to the creation of the Science and Technology Park in 2015.

A very prominent position in the university structure is occupied by the Faculty of Civil Engineering, Architecture and Environmental Engineering which for almost 50 years has been conducting the research and educating the engineers—specialists in civil engineering, architecture and environmental engineering. The faculty has the *new*, purpose-built *premises* supplied with modern lecture halls and specialised laboratories.

The academic magnitude of the faculty is represented by the fact that it was assigned the task of organising such a crucial and significant conference on metal structures.

As the Rector of the University I am extremely honoured that in the year in which we celebrate the 15th anniversary I have the pleasure to host the international company of the most distinguished scholars. I do hope that your visit to the University and Zielona Góra would be a perfect occasion for mutual recognition and better understanding and appreciation of our University.

Professor Tadeusz Kuczyński, PhD, Eng.
The Rector of the University of Zielona Góra

This page intentionally left blank

Recent Progress in Steel and Composite Structures – Giżejowski et al. (Eds)
© 2016 Taylor & Francis Group, London, ISBN 978-1-138-02946-0

Preface

The International Conference on Metal Structures 2016 (ICMS 2016) is yet another conference held periodically at different universities in Poland, this time organized by the University of Zielona Góra and held from June 15 to June 17, 2016. The Conference has a long tradition. The first one took place in the year 1958 at the initiative of the Committee of Civil Engineering of the Polish Academy of Sciences and organized under the auspices of its Metal Structures Division and the Committee of Metal Structures of the Polish Association of Civil Engineers and Technicians. At the beginning, the conferences were organized at a four year interval and recently every five years. The aim of the conferences remains the same over the years, namely bringing together academics, researchers and practicing engineers, professionally engaged in solving different problems related to the behavior, design, fabrication, and execution of steel, aluminum and composite structures. In particular, the conferences have focused on summarizing the progress in theoretical, numerical and experimental research, with special attention given to new concepts and algorithmic procedures, and to the background knowledge as well as the development and implementation of rules and recommendations for codification worldwide.

Over the past decade, after joining the European Union, Poland started to intensively develop its infrastructure of roads, bridges and airports. This development was particularly rapid during the preparation for the EURO 2012 Soccer Cup, co-hosted with Ukraine. At this time, the demand for innovative solutions in design and construction technologies associated with sporting infrastructure reached a level unseen in the past. The last two Conferences held in Rzeszów in 2006 and in Wrocław in 2011 provided an ideal opportunity for the exchange of professional experience in this regard between local and international participants. The current Conference creates yet another chance to continue the exchange of such views and opinions.

Five keynote lectures were prepared for presentation at the Conference plenary sessions. From all the submissions from several continents, sixty-two peer reviewed papers were accepted for publication and presentation at the Conference. The first part of the Conference book contains the keynote lectures in full length and the following part includes two-page extended abstracts of individual contributions. The diverse topics covered reflect the broad spectrum of civil engineering problems the ICMS is focused on.

The opening keynote contribution from J. Michael Rotter (University of Edinburgh, UK) is devoted to advances in the shell buckling phenomenon, which is of particular importance for industrial metal structures such as silos, tanks and vessels. The author gives an authoritative perspective for the design provisions in present and future European recommendations. The paper by Milan Veljkovic (Lulea University, Sweden) deals with conceptual and design aspects of supporting structures for wind energy generation. This topic is related to the intense worldwide discussion about the benefits of wind power in light of high vulnerability of modern economies to changes in fuel prices and the imminent shortage of fossil resources. Advances in seismic assessment and control of steel-concrete composite high-rise buildings are highlighted in the paper of Jiang Qian (Tongji Univeresity, China). The keynote contribution of Johan V. Rietief (University of Stellenbosch, South Africa) is related to international efforts to harmonize and unify reliability-based codification within the area of civil engineering structures. The infrastructure development in Poland, mentioned earlier, is summarized in the last of the keynote papers by Tomasz Siwowski (Rzeszów University of Technology, Poland) and Krzysztof Żółtowski (Gdańsk University of Technology, Poland). Advances in modern structural shaping, material engineering and technology, as well as in computation and design, are described using examples of recent, spectacular bridges and sporting venues in Poland.

The CD attached to the Conference book contains all keynote and individual papers in full length, sorted according to ten Conference theme sessions:

1. Cold-formed sections and profiled sheeting.
2. Steel-concrete composite structures.
3. Buckling and effect of bracings.
4. Dynamics, fatigue and seismic analyses.
5. Bridges.
6. Structural steel, metallurgy and behaviour in fire.
7. Strength, stability and postbuckling behaviour.
8. Joints and connections.
9. Silos, tanks and vessels.
10. Reliability, masts and towers.

Profound gratitude goes to those who carried out the numerous organizational demands of the Conference that arose during the two years preceding this event. The dedication of these individuals and institutional sponsors has been vital to the Conference's success. The authors of keynote lectures and individual contributions are greatly appreciated for presenting the results of their recent research and progress in their areas of expertise. Last but not least, the editors extend special thanks to the members of the Organizing Committee for preparing the Conference and the Scientific Committee for extensive work to review submissions. The scientific standard of this series of conferences has been maintained as the result of their efforts.

M.A. Giżejowski, A. Kozłowski,
J. Marcinowski & J. Ziółko
Editors

Recent Progress in Steel and Composite Structures – Giżejowski et al. (Eds)
© 2016 Taylor & Francis Group, London, ISBN 978-1-138-02946-0

Organisation and committees

ORGANIZED BY

Polish Academy of Sciences, Committee for Civil Engineering, Section of Metal Structures
University of Zielona Góra, Faculty of Civil Engineering, Architecture and Environmental Engineering, Institute of Civil Engineering

HONORARY COMMITTEE

Prof. Kazimierz Furtak, *Chairman of Committee for Civil Engineering, Polish Academy of Sciences, Poland*
Prof. Tadeusz Kuczyński, *The Rector of the University of Zielona Góra, Poland*
Karol Heidrich, *President of Polish Chamber of Steelworks, Poland*
Andrzej Roch Dobrucki, *President of Polish Chamber of Civil Engineers, Poland*
Ryszard Trykosko, *President of Polish Association of Civil Engineers and Technicians, Poland*

and

Tadeusz Biliński, Jan Bródka, Roman Jankowiak, Zbigniew Kowal, Witold Kucharczuk, Ernest Kubica, Stanisław Kuś, Antoni Matysiak, Zbigniew Mendera, Janusz Murzewski, Kazimierz Rykaluk, Bernard Wichtowski, Wojciech Włodarczyk, Wojciech Żółtowski

INTERNATIONAL SCIENTIFIC COMMITTEE

Jerzy Ziółko, *Honorary Chairman, Honorary Chairman of SMS CCE PAS*
Marian Giżejowski, *Chairman*
Aleksander Kozłowski, *Vice-chairman*
Jakub Marcinowski, *Vice-chairman*

C.C. Baniotopoulos (UK)
A. Biegus (Poland)
F. Bijlaard (Holland)
A.H. Bouchair (France)
M. Bradford (Australia)
L. Braganca (Portugal)
D. Camotim (Portugal)
S.L. Chan (HongKong)
D. Dubina (Romania)
L. Dunai (Hungary)
R. Folic (Serbia)
B. Gosowski (Poland)
D. Grecea (Romania)
W. Guggenberger (Austria)
M. Gwóźdź (Poland)
M. Holicky (Czech Republic)
E. Hotała (Poland)
P. Iwicki (Poland)
J. Jankowska-Sandberg (Poland)
K. Jarmai (Hungary)
J.-P. Jaspart (Belgium)
S.A. Karamanos (Greece)
J. Kawecki (Poland)
P. Konderla (Poland)
U. Kuhlmann (Germany)
K.E. Kurrer (Germany)
V. Kvocak (Slovakia)
L. Kwaśniewski (Poland)
R. Liew (Singapore)
A. Limam (France)
W. Lorenc (Poland)
X. Lu (China)
M. Łagoda (Poland)
Cz. Machelski (Poland)

D. Markulak (Croatia)
M. Maślak (Poland)
G. de Matteis (Italy)
F. Mazzolani (Italy)
G.R. Miller (USA)
R. Nascimbene (Italy)
D. Nethercot (UK)
A.S. Nowak (USA)
I. Ovchinnikov (Russia)
Sz. Pałkowski (Poland)
J. Papangelis (Australia)
D. Partov (Bulgaria)
H. Pasternak (Germany)
M. Piekarczyk (Poland)
J. Qian (China)
P.M. Vila Real (Portugal)
A. Reichhart (Poland)
J. Retief (South Africa)
M. Rotter (UK)
A. Sapalas (Lithuania)
B. Schafer (USA)
S. Shimizu (Japan)
L. da Silva (Portugal)
T. Siwowski (Poland)
W. Skowroński (Poland)
B. Snijder (Holland)
L. Sokół (France)
N. Stranghoener (Germany)
A. Shymanovsky (Ukraine)
J. Szlendak (Poland)
E. Szmigiera (Poland)
M. Szumigała (Poland)
L. Ślęczka (Poland)
J.G. Teng (Hong Kong)
R. Tremblay (Canada)
T. Ummenhoffer (Germany)
E. Urbańska-Galewska (Poland)
P. Vellasco (Brazil)
I. Vedjakov (Russia)
M. Veljkovic (Sweden)
F. Wald (Czech Republic)
K. Wilde (Poland)
W. Wuwer (Poland)
A. Wysokowski (Poland)
N. Yardimci (Turkey)
R. Zandonini (Italy)
A. Zingoni (South Africa)
H. Zobel (Poland)
J. Żmuda (Poland)
K. Żółtowski

ORGANIZING COMMITTEE

Jakub Marcinowski, *Chairman*
Adam Wysokowski, *Vice chairman*
Elżbieta Grochowska, *Secretary*
Joanna Kaliszuk, *Secretary*
Grażyna Marcinowska, Jolanta Mazgajczyk, *Secretary's Office*
Paweł Błażejewski, Artur Juszczyk, Paweł Kasza, Anna Kucharczyk, Maria Mrówczyńska, Anna Staszczuk, Marta Świrydziuk

Keynote papers

This page intentionally left blank

Recent Progress in Steel and Composite Structures – Giżejowski et al. (Eds)
© 2016 Taylor & Francis Group, London, ISBN 978-1-138-02946-0

Advances in understanding shell buckling phenomena and their characterisation for practical design

J. Michael Rotter
Institute for Infrastructure and Environment, University of Edinburgh, Edinburgh, Scotland, UK

ABSTRACT: The design of thin shell structures against buckling has a long and tricky history. The sensitivity of elastic buckling loads to geometric imperfections and the challenges in relating research findings to practical construction have required extensive research work over many decades. The wide range of geometries, construction forms and loading conditions has also led to many distinct solutions to individual situations. But recent innovations have enabled a new all-embracing perspective to be developed, which gives great potential for addressing new problems in a systematic manner. The new method of Reference Resistance Design provides a hand calculation process that can address all shell buckling and collapse situations, with particular attention to unsymmetrical and local loading conditions, including imperfections, geometric nonlinearity, plasticity and strain hardening all within a consistent framework.

1 INTRODUCTION

1.1 *Background*

Thin metal shell structures give both designers and analysts some of the greatest challenges in structural engineering. Every practical design must guarantee the safety of the structure under the most deleterious conditions that may occur in its lifetime, and a thin shell structure is susceptible to a wide range of alternative modes of failure. Understanding the behavior of the shell under different loading conditions requires considerable experience, which both analysts and designers must take time to acquire.

There is a huge rather mathematically oriented literature on the analysis of shell structures, relating to linear elastic, stability, imperfection sensitivity, geometric nonlinearity, plastic and collapse analyses. Some of these analyses may be used directly to make a strength evaluation of some kind, but most give only a first estimate of the real strength based on criteria of failure that are specific to the individual analysis: the outcomes do not easily lead to designs that are both safe and cost-effective. The difficulties in interpreting these analyses, and their complexity, have led to a divergence between the rules of regulatory standards and advanced analyses for shells.

Most designers of practical shell structures have never read a book on shell theory, and most shell theoreticians have never tried to use a design standard. The dichotomy between these two perspectives has led, on the one hand, to excessive conservatism, whilst on the other, disastrous failures continue to be common (Fig. 1). Such a situation indicates a lack of sufficient understanding on both sides: this is to be expected considering the complexity of shell buckling phenomena and the history of the concepts used in design verifications.

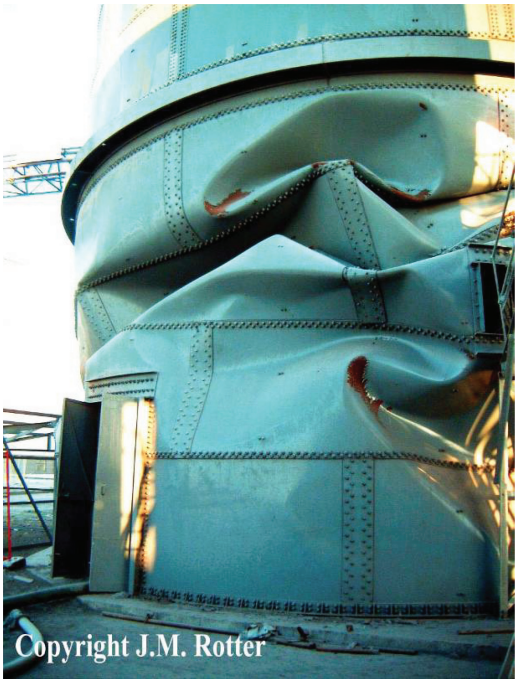

Figure 1. Typical shell buckling failure in service.

1.2 *Safe structural design and traditional standards*

The safe design of a structure must normally be undertaken following the requirements of a design standard. The standard may be a national or international document. But the above divergence between designers and analysts means that, historically, there has been a large gap between the design rules of the standards (e.g. NASA SP8007 1968, ECCS EDR4 1988, DIN 18800 1990, DASt 1994, API 650 1998, API 620 2002) and the sophisticated analyses found in the research literature. Because standards historically used empirical rules, it has always been difficult to determine how to use more sophisticated modern analyses in design (Rotter, 2011). This difficulty is exacerbated by the prevalence of cylindrical shells as the basis for the rules in these standards.

1.3 *Practical design and simplifications*

Most practical thin shells are designed using hand calculations, exploiting algebraic expressions that define the expected buckling resistance. Hand calculation rules for the elastic buckling resistance were mostly devised empirically as a lower bound on relevant test results. But since few shell buckling geometries and load cases had been comprehensively tested, the majority on cylindrical shells, these empirical rules are far from many practical conditions.

The easiest shell buckling conditions to test are the three conditions that lead to uniform membrane stresses in a thin isotropic elastic cylindrical shell: uniform axial compression, uniform external pressure, and uniform torsion (Fig. 2), termed here the Primary Load Cases. Because these simple cases have been used as the basis of most design, the critical aspects of sensitivity to geometric nonlinearity and to imperfections are, by implication, transferred to other conditions. The outcome is a set of quite complicated rules for practical application, coupled with criteria of failure that are not necessarily appropriate. The details are discussed below.

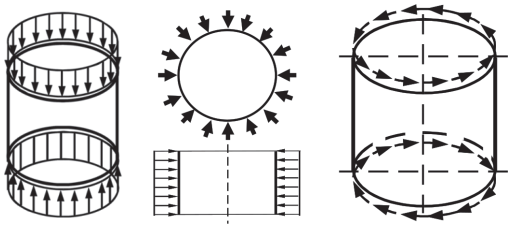

Figure 2. Primary load cases with uniform membrane stresses.

This paper presents a critique of traditional hand calculation design, followed by an outline of the Eurocode standard developments to address the shortcomings, a discussion of the remaining difficulties, and a presentation of the new Reference Resistance Design method, which it is hoped will provide a more satisfactory basis for much future work. A range of shell design challenges is then outlined.

2 TRADITIONAL HAND CALCULATIONS AND THE EUROCODE TREATMENT

2.1 *Introduction*

As noted above, both experiments and algebraic analyses are easier to perform on shell structures subject to a loading that produces a uniform membrane stress state in the shell. The easiest form is the right circular cylinder, both to fabricate and to analyse, so the literature on them is very extensive.

The test results on such cylindrical shells have formed the basis of most empirical rules in the past. But a critical feature of thin shells is the sensitivity of the buckling resistance to tiny geometric imperfections (Koiter 1945, Yamaki 1984). The form and amplitude of these imperfections is critically important. Relatively few measurements of geometric imperfections in field-fabricated large shells have been made (Ding et al. 1996, Teng et al. 2005), and the methods of fabrication are very different from those in laboratory specimens (e.g. Michel et al. 2000, Mathon & Limam 2006). The different fabrication leads to different imperfection forms and amplitudes, so that the test results may not be relevant to full scale construction. Thus the use of these laboratory tests as a basis for empirical design rules is seriously questionable.

2.2 *Hand calculation rules in EN 1993-1-6 (2007)*

The following outlines the hand calculation rules of the Eurocode on steel shells, EN 1993-1-6 (2007). The assessments are based on the evaluation of the membrane stress at a point as the instigation of a buckle. The following applies to each of the three membrane stresses in turn at any point in a shell.

For each membrane stress state in an ideal elastic-plastic material, there are two limiting conditions: elastic buckling and full yield. The characteristic stress at buckling is determined as a proportion of the yield stress, $\sigma_{Rk} = \chi f_y$ (amended where shear is involved). The proportion χ depends on the slenderness ratio, which is defined as

$$\overline{\lambda} = \sqrt{f_y / \sigma_{Rcr}} \tag{1}$$

in which σ_{Rcr} is the elastic linear bifurcation stress.

The characteristic buckling value of the membrane stress σ_{Rk} is determined by $\chi = \sigma_{Rk}/f_y$ as

$$\begin{aligned} \chi &= \chi_h - \left(\bar{\lambda}/\bar{\lambda}_o\right)\left(\chi_h - 1\right) \quad \text{when } \bar{\lambda} \le \bar{\lambda}_o \\ \chi &= 1 - \beta\left(\frac{\bar{\lambda} - \bar{\lambda}_o}{\bar{\lambda}_p - \bar{\lambda}_o}\right)^{\eta} \quad \text{when } \bar{\lambda}_o < \bar{\lambda} < \bar{\lambda}_p \\ \chi &= \alpha/\bar{\lambda}^2 \quad \text{when } \bar{\lambda}_p \le \bar{\lambda} \end{aligned} \tag{2}$$

with $\bar{\lambda}_p = \sqrt{\alpha/(1-\beta)}$ as illustrated in Fig. 3.

The effects of geometric imperfections and geometric nonlinearity are included by reducing the elastic buckling stress from σ_{Rcr} to $\alpha\sigma_{Rcr}$, and the effects of yielding and partial plasticity through the parameters β and η. The characteristic buckling stress σ_{Rk} is deemed to reach the yield stress at the slenderness $\bar{\lambda}_o$: strain hardening is included if $\chi_h > 1$.

The same curve is used for each of the three cases (Fig. 2): axial σ_x, circumferential σ_θ and shear $\tau_{x\theta}$, with each parameter α, β etc. separately defined as α_x, α_θ and $\alpha_{x\theta}$ etc. These separate definitions permit each stress condition to have different imperfection sensitivity and yielding parameters to capture the different behaviour under each Primary Load Case.

2.3 *Stress combinations in EN 1993-1-6 (2007)*

In developing the Eurocode on the buckling of steel shells (EN 1993-1-6 2007), the drafters sought to make the hand calculation procedure more systematic and comprehensive. The procedure is termed Stress Design (Schmidt et al. 2013). It addresses all shell buckling conditions as a combination of three primary load cases in cylindrical shells (Fig. 4).

The three Primary Load Cases (Fig. 2) correspond to uniform axial stress, uniform circumferential stress and uniform shear stress throughout the cylinder. Most practical load cases and load combinations produce a location of highest stress that potentially contains components of all three stresses, so EN 1993-1-6 (2007) has a procedure to address this situation. The resistance to a uniform stress in each direction is evaluated, and these three resistances are then combined to provide an estimate of the local buckling resistance. A description and commentary on this method is given in Schmidt et al. (2013).

The combination process is based on studies of cylindrical shells under uniform states of combined stresses (Winterstetter & Schmidt 2002). Because stress state at all points in the cylinder is the same, buckles of any size may develop. The test for buckling is applied at any location in a shell, and the peak stress state may not extend over a large area (Fig. 4). But a buckle always has a finite size and the buckling resistance so assessed can only be valid if the stress is relatively uniform over the buckle zone.

Unfortunately the buckling modes for the three Primary Load Cases have quite different shapes and sizes. Uniform external pressure usually induces large buckles, uniform shear moderate sized ones and axial compression very short buckles (Fig. 5). If the stresses have a rapid spatial variation, the buckle cannot be large: an axial compression buckle

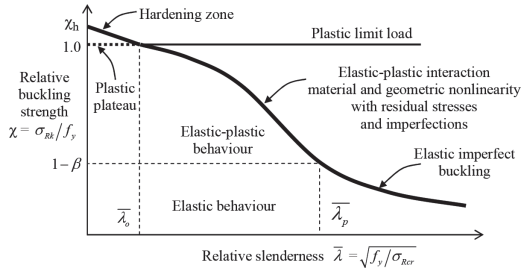

Figure 3. Capacity curve for stress design.

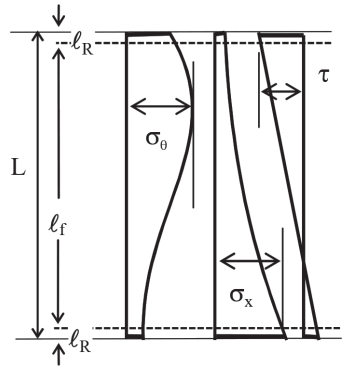

Figure 4. Potential distributions of the three membrane stresses with peaks at different locations (EN 1993-1-6 2007).

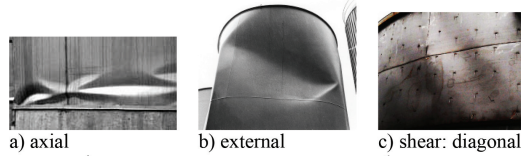

a) axial compression

b) external pressure

c) shear: diagonal shapes

Figure 5. Different shapes of buckles under uniform stress.

may then not differ much in size from its uniform stress form, so where axial stresses dominate, the use of a local peak stress may be relevant: but if either circumferential or shear stresses dominate, a much higher local stress may be needed to cause buckling (Yamaki 1984, Jumikis & Rotter 1986).

Under a uniform stress state, changes of geometry (geometric nonlinearity) before buckling in a thin shell play only a small role: around 15% for axial compression, but very little for the other cases (Yamaki 1984). By contrast, under unsymmetrical loading, changes in geometry have a serious effect (e.g. Houliara & Karamanos 2006, Sadowski & Rotter 2010). Conclusions drawn from uniform stress tests are quite misleading.

Because Stress Design relies on the Primary Load Cases, the effects of geometric nonlinearity and imperfections are simply agglomerated into a single "knock-down factor" in the parameter α. Since an improved quality of fabrication can certainly reduce imperfection amplitudes and thus increase the buckling resistance, the value of α is defined differently for three fabrication quality classes (FQC) in EN 1993-1-6 (2007). A natural inference from this is that a really super quality of fabrication could lead to $\alpha = 1$. Unfortunately in many structures, such as domes, the change of geometry of the perfect structure in the pre-buckling phase causes a substantial reduction in strength. This makes the Primary Load Cases once more misleading.

Under uniform pre-buckling stresses, many different buckling modes of different shapes and sizes may have almost the same buckling stress (Calladine 1983, Khamlichi et al. 2004). These many modes relate to the concept that the interaction between rival modes leads to a high sensitivity to geometric imperfections (Koiter 1945). However, when the loading produces a stress state that is far from uniform, the potential for different modes to have similar buckling resistances declines considerably, so the uniform membrane stress condition is again a misleading model and the imperfection sensitivity is much reduced (Song et al. 2004, Rotter et al. 2011).

A final troublesome feature of the uniform stress states as a basis for all others occurs when the buckling stress is high, as in thick cylinders. Almost the entire shell reaches the yield stress simultaneously, so tests then suggest that a small correction of the elastic buckling stress can account for yield. This useful simplification in early design rules for uniform stress states turns out to be rather unfortunate in many practical shell buckling conditions (Greiner & Guggenberger 1998, Doerich & Rotter 2008).

2.4 *Special load cases in EN 1993-1-6 (2007)*

Although EN 1993-1-6 (2007) offers a considerable advance on older standards for hand calculation, the authors recognised that some special cases of unsymmetrical loads had been studied sufficiently to permit more accurate assessments than the above general method offers. For these, *ad hoc* design procedures were included for wind loading on tanks and silos and for stepped walls, but these were not well integrated into the general procedure. Common cases of this kind are discussed below.

3 NUMERICAL ANALYSIS IN EUROCODE

3.1 *Alternative computational analyses*

To avoid the many difficulties associated with hand calculations, the drafters of EN 1993-1-6 (2007) devised two distinct procedures to permit finite element computations to be used in design. Whilst both have some disadvantages, these innovations present considerable advances on earlier standards.

Computational analyses must address all the key aspects of sensitivity to imperfection of different forms and amplitudes, tolerances in construction, plasticity, geometric nonlinearity and strain hardening. These must be done within the framework of a reliability assessment using partial safety factors on both loading and structural strength: much understanding is needed to use a numerical assessment.

A fully geometrically and materially nonlinear analysis with explicitly defined imperfections (GMNIA) is permitted, but many precautions are needed to assure the analyst that the outcome is reliable, and these are codified as requirements.

A simpler treatment provides a means by which linear elastic computational analyses can be effectively used in a design verification, based on a linear bifurcation analysis and an estimate of the plastic collapse resistance (LBA/MNA). The GMNIA process is extremely onerous, but LBA/MNA also presents many challenges in estimating the vital key parameters α, β, η, $\overline{\lambda}_o$ and χ_h (Rotter 2011, Schmidt & Rotter 2013).

3.2 *The LBA-MNA design process*

Many practical shell structures and their load combinations are too complicated to be treated well using the simple hand design rules outlined above. Most designers will use a simple elastic finite element analysis to determine the stress state in the shell before assessing its resistance. The drafters of EN 1993-1-6 (2007) devised a new method to help.

Knowing that most commercial software can perform both a linear stress analysis and a linear bifurcation analysis, the LBA/MNA method was devised to exploit these two analyses to obtain a better estimate of resistance than that of a hand calculation.

In any computational treatment, the design values of the loads are applied to the model. To reach any defined criterion of failure, these loads must be increased by a factor, and this factor is the resistance R for that loading and that criterion. The criterion could be first yield, elastic buckling, full plasticity, attainment of a peak load, or elastic-plastic buckling of the imperfect shell.

The first step in making a realistic estimate of the characteristic resistance R_k is to determine the relative slenderness of the complete structure, since this controls the extent to which yielding will affect the result. The reference resistances for any load case are the linear elastic bifurcation critical resistance R_{cr} and the resistance when a full plastic mechanism has formed under small displacement theory R_{pl}. The slenderness of the whole structure is defined as

$$\bar{\lambda} = \sqrt{R_{pl} / R_{cr}} \tag{3}$$

The LBA/MNA method is based on these two reference resistances R_{cr} and R_{pl}, which can always be determined for a structure of any complexity. Where it is not possible to perform a plastic collapse analysis, a linear elastic stress analysis can be used to provide a lower bound to the true value of R_{pl}, but the conservatism of this bound is very problem-dependent (Doerich & Rotter 2011a) so that it is safe, but a poor predictor. If the structure is a true shell, the assessment may be made using only the membrane stresses, but where bending dominates, the surface stresses must be used for a safe estimate (Doerich & Rotter 2011a).

The characteristic resistance of the complete structure is then found using

$$\begin{aligned}
\frac{R_k}{R_{pl}} &= \chi_h - \left(\bar{\lambda}/\bar{\lambda}_o\right)\left(\chi_h - 1\right) && \text{when } \bar{\lambda} \le \bar{\lambda}_o \\
\frac{R_k}{R_{pl}} &= 1 - \beta\left(\frac{\bar{\lambda} - \bar{\lambda}_o}{\bar{\lambda}_p - \bar{\lambda}_o}\right)^{\eta} && \text{when } \bar{\lambda}_o < \bar{\lambda} < \bar{\lambda}_p \\
\frac{R_k}{R_{pl}} &= \alpha / \bar{\lambda}^2 && \text{when } \bar{\lambda}_p \le \bar{\lambda}
\end{aligned} \tag{4}$$

with $\bar{\lambda}_p = \sqrt{\alpha/(1-\beta)}$ as before. The plot in Fig. 3 still applies, but the structural resistances R_{pl} and R_{cr} now replace f_y and σ_{Rcr} respectively.

It should be noted that Geometric Nonlinearity (GN) can produce either hardening and softening effects (Rotter 2005), so the two analyses that define R_{pl} and R_{cr} cannot be undertaken using GN, since it is neither certain that these failure criteria will be reached, nor whether such a measure will be conservative or not. Furthermore, if imperfections are included, the buckling event may disappear at larger imperfection amplitudes (Fig. 6) (Doerich, 2007).

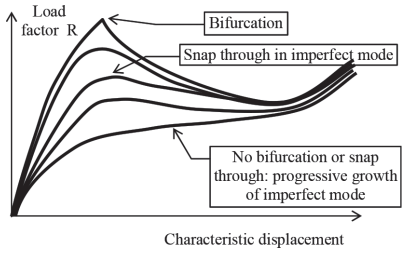

Figure 6. Changing load-deflection curve with imperfection amplitude.

The chief challenge for the LBA/MNA method is that the effects of geometric nonlinearity, geometric imperfections, partial yielding and strain hardening must be estimated by analogy with a comparable "known" case. At present, few cases can be classed as "known" and even the values of these parameters for the basic Primary Load Cases of external pressure and shear are not well established.

Nevertheless LBA/MNA is a powerful tool in providing much more insight into the buckling and yielding potential in the shell. It does have some other difficulties, notably when the buckling mode and plastic collapse mode are in very different locations and where the linear bifurcation location is in a zone that is not very imperfection sensitive but other zones are more so. These matters and a fuller description is given in Rotter (2011).

4 REFERENCE RESISTANCE DESIGN

4.1 *Introduction*

The calculation procedure of LBA/MNA holds considerable promise for complete structures, but its major disadvantage is the difficulty in determining appropriate values for the critically important parameters α, β, η, $\bar{\lambda}_o$ and χ_h. Further, although many problems in shell design are quite well identified, LBA/MNA is intended only for computational estimates of resistances R_{pl} and R_{cr}. This both restricts the usefulness of LBA/MNA and limits the potential for well-documented problems to be better defined.

The remedy for this situation is the invention of a new hand calculation method, termed Reference Resistance Design (RRD). As a hand calculation, it may be contrasted with Stress Design in that it uses a full plastic mechanism reference resistance, whilst retaining the benefit that it does not require estimates of quantities that are difficult to assess.

In devising RRD, advantage was taken of the fact that both R_{pl} and R_{cr} are commonly accurately represented with simple algebraic expressions,

provided that the geometry, boundary conditions and loading are well defined. The cause of this fortuitous situation is that these resistances are both based on small displacement theory analyses, leading to relatively simple mathematics. Sometimes an existing algebraic solution is available: on other occasions, the algebraic solution for a practical range of parameters can be deduced using strict LBA and MNA analyses.

The procedure for RRD is illustrated in Fig. 7.

4.2 *Implementation of RRD*

There are many well defined problems that are very well suited to RRD. In many cases, the two reference resistances R_{pl} and R_{cr} already exist as algebraic solutions in the literature.

Foremost amongst these is the global uniform bending of a thin cylindrical tube, for which the full plastic moment and the linear bifurcation moment are very well known. It is thus not necessary to use LBA and MNA computations to identify these quantities: what is needed instead is a full description of the parameters α, β, η, $\bar{\lambda}_o$ and χ_h for this condition.

An important feature of the RRD formulation is the division of the parameter α into two parts. As noted above, shells under uniform stresses are little affected by geometric nonlinearity, so this has always been put together with the sensitivity to geometric imperfections to give a single "knock-down" parameter α. However, in cases where significant change of geometry occurs before buckling, causing a reduction in resistance in the perfect structure, no improvement in strength can achieved by improved fabrication, and it is important to recognise the separate contributions of geometric nonlinearity α_G and geometric imperfections α_I. Thus the parameter α is now given by $\alpha = \alpha_G \alpha_I$. This also simplifies the formulation, since the two effects are often governed by quite different geometric quantities.

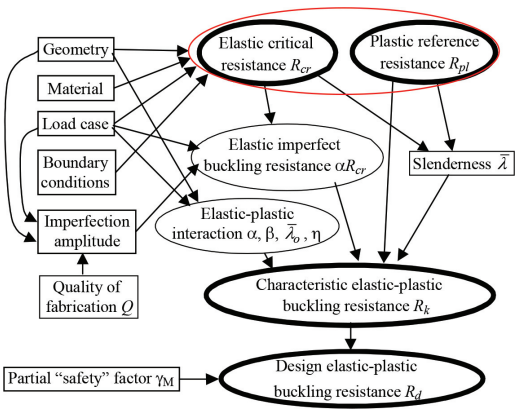

Figure 7. RRD design calculation procedure.

Whilst some experiments exist to assist in determining the quantities α, β, η, $\bar{\lambda}_o$ and χ_h, the database of tests for most practical shell buckling conditions is very sparse. Moreover such tests as exist are subject to the criticisms made above concerning the differences between laboratory fabrication and full scale structures. Computational assessments using GMNIA must therefore be used to find these parameters. The imperfection forms and amplitudes must be related to and verified by tolerance measures on full scale structures to guarantee their relevance. The variation of the parameters with factors such as the geometry, thickness and material.

Reference Resistance Design (RRD) (Rotter, 2013) has been approved as an amendment to EN 1993-1-6 (2007). As first applications, two geometries have been fully documented with algebraic expressions: cylinders under global bending and externally pressurised spherical shells.

The assumed imperfections for RRD should be established using the rules for GMNIA analysis in EN 1993-1-6 (2007): the corresponding tolerance measures for the full scale construction given in this standard are defined to match these assumed values.

4.3 *Application to specific situations*

Many practical situations arise in full scale structures that are not well treated by either Stress Design or LBA/MNA. The key features of good candidates that could be treated using RRD are:

- The structural form is well defined;
- Current rules in stress design are based on *ad-hoc* procedures special to that case;
- Significant yielding can occur well before a fully plastic mechanism develops;
- Only empirical rules derived from nonlinear finite element calculations are currently available;
- The loading is significantly unsymmetrical on an axisymmetric shell (this is not a requirement);
- The geometry includes details that make its behaviour significantly different from the Primary Load Cases on cylindrical shells.

Many structural situations meet these criteria, some of which have been quite thoroughly studied in the past. There is therefore considerable scope to transform available data on resistances into the format of RRD, so that all problems can be treated in a uniform manner.

One key advantage that comes from developing RRD in this manner is that a catalogue of values for the parameters α, β, η, $\bar{\lambda}_o$ and χ_h will be devel-

oped, and these will make the use of LBA/MNA more viable for a wide range of problems: it will then be easier to identify comparable cases to the one being studied, and thus to make confident choices of values for the buckling parameters.

5 CASES OF SHELL BUCKLING THAT DESERVE RRD TREATMENT

5.1 *Introduction*

Some practical situations that are worthy of RRD treatment are briefly reviewed here. This is only a small selection due to space limitations. These are classic problems for which researchers are encouraged to derive parameters for RRD.

5.2 *Global bending of cylinders*

Where a thin elastic cylinder is subjected to global bending, the matched compressive and tensile stresses that develop on opposite sides lead to ovalisation of the tubular section. Ovalisation is a severe case of geometric nonlinearity, and produces an elastic limit load: a condition of snap-through under elastic conditions (Brazier 1927). This snap-through is just pre-empted by elastic bifurcation (Houliara & Karamanos 2006), but both the reduced lever arm between the tensile and compressive stress peaks and the increased local radius of curvature in compression greatly reduce the buckling moment (~50%): both are geometrically nonlinear phenomena.

Thicker shells under bending present greater challenges because a significant yielded zone may develop before buckling (Limam et al. 2010): at full plasticity, a quasi-elastic calculation predicts the highest stress to be 27% above the yield stress. The concept that buckling is controlled by the stress at a point is clearly inappropriate and too conservative.

Although RRD has now been adopted for cylinders under uniform bending (Chen et al. 2008), many other practical situations occur that involve bending gradients (Schmidt & Winterstetter 2004), bending with shear and internal pressure (Antoine 2000) and bending with local loads (Fig. 8) that could be used to enhance the treatment for uniform bending.

5.3 *Stepped walls in tanks and silos*

In tanks and silos, the pressure on the inside surface increases with depth below the surface; in silos the axial compression in the wall grows even faster. Consequently the shell wall is designed to have an increased thickness with depth below the surface. Metal sheets of constant thickness produce a stepped wall: each uniform zone is termed a strake. The most critical location in each strake is at its base, where the formation of an axial compression buckle is restrained by the thicker strake below. The highest membrane stress thus occurs at a point where the resistance is significantly enhanced. Since the buckle lies in a steep stress gradient and has a finite size, the highest stress at one point is a poor choice. This situation is easily addressed by RRD where changes in R_{cr} and α are easily implemented.

Under external pressure, large buckles develop over a major part of the height (Fig. 9), but the circumferential stress varies with the strake thickness: a simple buckling criterion based on the stress concept is rather complicated (Fig. 9) since the relatively uniform membrane force must be transformed to produce a modified effective stress. A direct evaluation of R_{cr} for use in RRD is simpler (Chen et al. 2011) as it retains the specific loading condition.

5.4 *Tanks and silos under wind loading*

Wind loading on tanks and silos is a seriously unsymmetrical load case that has received considerable research attention. The definition of the wind pressure distribution is open to some discussion,

Figure 8. Example of cylindrical shell under bending, shear and local support loads.

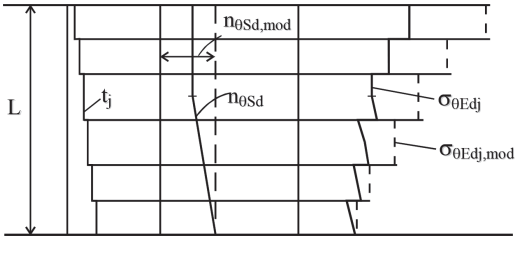

Figure 9. Transformation of step-changing stresses into equivalent stress for external pressure assessment.

and the differences between grouped and isolated tanks make for considerable complexity. Buckling is, nevertheless, generally elastic.

Whilst the situation casually appears to be one of circumferential compression (Fig. 10), significant axial stresses can develop in squatter geometries making the outcome dependent on the aspect ratio. This is another case where Stress Design leads to a complicated transformation of non-uniform loading into axisymmetric loading (EN 1993-1-6 2007) but a direct description of R_{cr} leads to a much simpler treatment (Chen & Rotter 2012). This is another good candidate for RRD.

5.5 *Lap-jointed construction*

It is often cost-effective in construction to eliminate site welding by using bolted construction, with overlapping plates at the vertical joints and strake boundaries (Fig. 11). This arrangement leads to a significant deviation of the thrust line as it passes through the joint, leading to local bending and increased membrane stresses at right angles to the line of thrust. Sometimes there is a change of plate thickness at the same location.

This problem is more complicated than it appears: the additional stresses reduce the resistance but the doubled plate at the overlap restrains a buckle (Rotter & Teng 1989). Further, the forms of imperfection that can develop adjacent to the lap joint are more limited. Finally, in thicker and pressurised shells, the local bending may lead to plasticity (Teng 1994). This is consequently another good case for an RRD treatment.

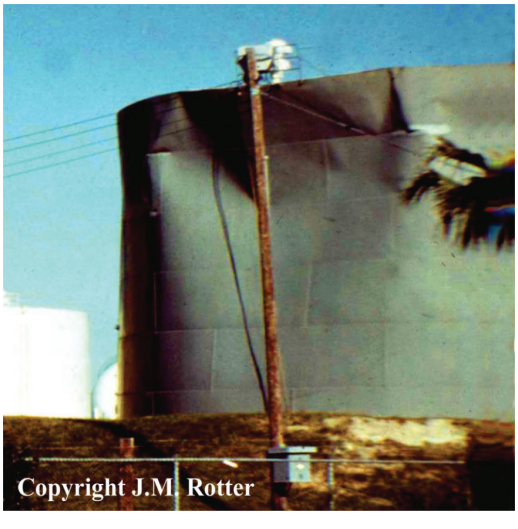

Figure 10. Buckling of a stepped wall tank under wind.

Figure 11. Typical lap-jointed bolted construction.

5.6 *Stiffened and unstiffened corrugated shells*

Silos used for agricultural storage are commonly constructed using corrugated sheets, usually with vertical stiffeners (Fig. 12). The corrugated wall provides stiffness against bending in the circumferential direction (useful to resist wind buckling) whilst the vertical stiffeners carry axial loads. The stiffeners are sometimes omitted (Fig. 12).

The resistance of these structures to axial compression from the stored solid involves a complex interaction between the sheeting and the stiffeners. The sheeting provides vital restraint against buckling of the stiffeners under axial load, permitting light sections to be used over great heights. Further the axial forces in the stiffeners derive from shear transmitted through the sheeting. The stiffeners also restrain some buckling modes in the sheeting under wind load pressure when the silo is empty. Under all loading conditions, it is the global resistance, rather than a local stress evaluation, that controls, and this is quite complex. These cases, which deserve further exploration, are best represented by RRD.

5.7 *Isotropic walls with vertical stiffeners*

Similar observations can be made concerning isotropic metal walls with vertical stiffeners: the interaction between the two components is critical to both. Internal pressure leads to different vertical stresses in the wall and the stiffeners, and any resistance assessment is best represented in terms of forces on the combined structure rather than the stress in any component. RRD offers this solution.

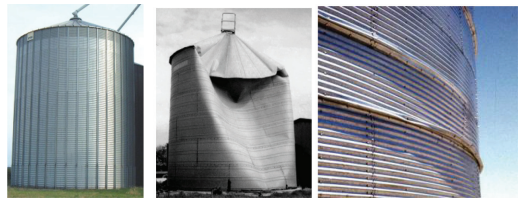

Figure 12. Corrugated silos and two failures.

Extensive research on this structural form has been undertaken in the context of missile structures (Singer 2004). The buckling resistance under axial compression is affected by many parameters of the shell and stiffener so that a comprehensive treatment is very difficult. However, the eccentricity of the stiffener to the shell surface plays a significant role, with internal stiffeners (Fig. 13) significantly less effective than external stiffeners. Further research is needed, but an RRD description would be useful.

5.8 *Local loads on a shell wall*

Local loads applied to shell structures can have a variety of different effects. A band or point load normal to a cylinder (Fig. 14) acting outwards induces a full plastic mechanism (Doerich & Rotter 2011b), but when acting inwards causes buckling. Both are poorly represented by a stress analysis, but can be treated well by algebraic expressions in RRD.

Local axial loads produce similar outcomes (Song et al. 2004, Rotter et al. 2011). Where the axial stress varies significantly within the shell, a treatment in terms of total forces is likely to be superior to an evaluation of an individual stress.

5.9 *Conical shells under external pressure*

A steep cone is similar to a cylinder, but a very flat cone behaves quite differently. In addition, whilst cylindrical shells fall into three simple length classes, the same does not apply to a cone: a cone cannot be really long unless the cone angle is small, but relative length involves the radius to thickness ratio too. Also, the boundary conditions used for cylindrical shells do not simply translate onto cones, making algebraic analyses less real. These aspects make it less easy to devise universal rules for cones.

In Stress Design (EN 1993-1-6 2007), a conical shell is transformed into equivalent cylindrical shell and the stress at buckling deduced. For medium length cones under a fixed axial compressive force, this is effective. But the varying radius produces high stresses on the thicker (in terms of r/t) small end and lower stresses on the thinner large end. The imperfection sensitivity at different shell slendernesses then determines where the buckle should form, leading to debates about which end is critical.

External pressure induces both axial circumferential stresses (Fig. 14), both non-uniform, and the transformation is much less secure (Greiner & Poggi 2013). If axial compression and external pressure are both present, both Stress Design and LBA/MNA become more tricky to apply (Schmidt et al. 2013). The end at which it is axially supported is also critical. A transformation of quality computational outcomes into RRD format would resolve these issues.

5.10 *Openings and cutouts in cylinders*

Openings are frequently needed in shells for access and functional reasons (Fig. 15). It is common practice to stiffen the boundaries of the opening with a comparable amount of metal to that removed, notionally to support the same load. However, local zones above and below any opening are subjected to much higher stresses, and the termination of a stiffener always causes a local stress increase.

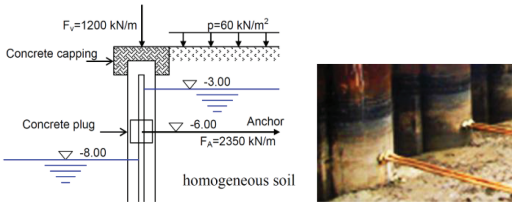

Figure 14. Local load introduced at a discrete location.

Figure 13. Internal cold-formed stiffeners.

Figure 15. Truck passage opening & buckle at stiffened cutout.

Several experimental and computational studies explored this condition (e.g. Jullien & Limam 1998), and a recent study has provided good data for the development of RRD proposals (Brunesi et al. 2016).

5.11 *Buckling above local supports and brackets*

Many shell structures must be locally supported to provide space for access beneath them. Local supports lead to high local stress concentrations, local plasticity and the potential for a local buckle in the adjacent part of the shell (Fig. 16).

This situation has received significant research attention in the past (Greiner & Guggenberger 1998, Guggenberger et al. 2000, 2004, Jansseune et al. 2013), but the problem is complicated by the many geometrical parameters and the variety of different ways in which the discrete forces can be transmitted into the shell. Since yielding begins at very low load levels but a full plastic mechanism requires extensive yielding, Stress Design cannot address this problem well. Significant data is available to begin the task of developing rules in the RRD format.

Bracket supports, attached to the side of a cylindrical shell, have been extensively studied and thoroughly characterised within the RRD framework (Doerich 2007). These are therefore ideally suited for transformation into rules in EN 1993-1-6.

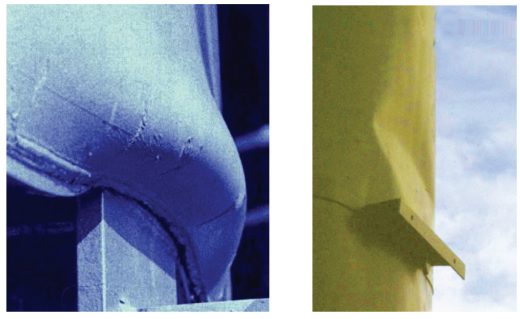

Figure 16. Buckle above a local support and above a bracket.

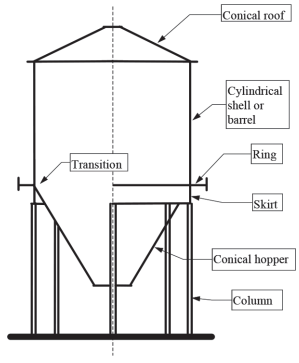

Figure 17. Silo geometry with transition junction.

5.12 *Elevated silos, junctions, ring beams and ring girders*

Where a hopper is used to discharge stored solids from a silo, the junction between the cylindrical vessel and the conical hopper is termed the transition (Fig. 17). Meridional hopper forces induce high circumferential compression at the transition: both bending and membrane stresses cause extensive plasticity: the local geometries can be complex.

Plastic collapse (Fig. 18) and elastic-plastic buckling failures of shell and ring under axisymmetric loading were studied some time ago (Rotter 1985, Teng & Rotter 1991). A good summary and further research is given by Teng (2004) and is suitable for direct adoption into RRD. The method now applies to all junctions between shell segments (Teng 2004).

The transition usually includes a ring, whose geometry may take many different forms: the annular plate, angle section and T section have been explored most. Early work can be found in Teng & Rotter (1991) and Teng (1997), with a good summary of buckling and collapse under axisymmetric loading in Teng & Zhao (2004).

But a junction supported on a few columns presents a more complex problem. The ring girder

Figure 18. Transition junction: uniform support with T section ring and axisymmetric plastic failure.

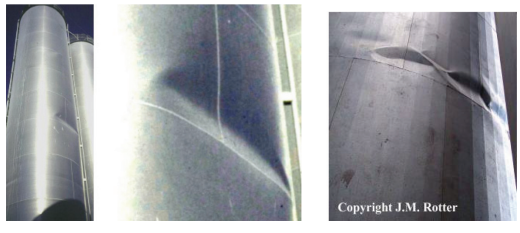

Figure 19. Buckles under eccentric discharge of stored solids.

is subject to varying bending and torsion around the circumference coupled with a strong interaction with the shell. Many parameters are involved in both the linear stress analysis (Rotter 1985, Topkaya & Rotter 2011) and the buckling of the shell above the ring girder (Sonat et al. 2015), making the problem challenging. Much further research is needed.

5.13 *Eccentric discharge of solids from silos*

When granular solids within a silo flow in a narrow channel adjacent to the wall, the pressure regime is particularly severe, unsymmetrical and varies in 3D. The variation in normal pressure leads to local axial compressive forces near the mid-height of the shell (Rotter 1986), and many buckling failures (Fig. 19) and complete collapses of silos have resulted.

Experimental studies of buckling under this condition (Rotter et al. 1989) show that complex interactions between the stored solid and shell occur, making prediction of the result very challenging. Nevertheless, considerable progress has been made in understanding this buckling condition in recent times (Sadowski & Rotter 2010, 2012).

5.14 *Spherical, tori-spherical and tori-conical shells*

Design rules for partial spherical domes, tori-spherical and tori-conical shells under external and internal pressure were established long ago using empirical approximations to computations (e.g. Blachut et al 1990). But since such results are not set out in a global context, it is difficult to generalise them. More recent research by Wunderlich (1995) and Wunderlich & Albertin (2000, 2002) has already been developed into RRD format and approved as an amendment to EN 1993-1-6. A constructed tank with a spherical dome roof has a supporting eaves ring, which is not yet covered. There are significant opportunities to extend the descriptions to deal with different geometries and load cases.

6 RECOMMENDATIONS IN THE DEVELOPMENT OF RRD EXPRESSIONS

6.1 *Introduction*

Researchers who seek to develop a description of a specific shell buckling problem that is characterised in the form of RRD may find the following suggestions and remarks useful.

1. RRD is based on accurate determinations of R_{cr} and R_{pl}. The resistance may be in terms of a pressure, a line load, a point load, a local value of pressure that characterises a complete load system, or a stress resultant within the structure.
2. The starting point should be to establish accurate algebraic expressions for R_{cr}. It may be necessary to restrict the dimensional range (just as cylindrical shells are often restricted to medium length) to produce simple expressions. The expression for R_{cr} is always linear in modulus E: so only the geometry needs to be varied.
3. The second task is to establish accurate algebraic expressions for R_{pl}. An elastic-perfectly plastic material model is required: if some hardening is used, it should be kept to less than 0.1% of the elastic modulus. It is very important that these algebraic expressions are accurate, because two different unsafe errors arise if R_{pl} is under- or over-estimated. The explanation is set out in Rotter (2011). The safest way to ensure that the plastic limit load is precisely extracted from in the nonlinear calculation is to use the CIP plot devised by Doerich & Rotter (2011b). The algebraic expression is always linear in yield stress f_y.
4. Use GNA bifurcation calculations to establish accurate values for the effect of geometric nonlinearity on the perfect structure. The parameter α_G is found as $\alpha_G = R_{GNA}/R_{cr}$. Find a simple expression for the variation of α_G with geometry.
5. Use GMNIA calculations to establish the values of $R_{GMNIA} = R_k$ for the full range of geometries. These must use geometric imperfections, following the rules of EN 1993-1-6 (2007) on the required forms and amplitudes. The three Fabrication Quality Classes give a clear indication of the range of imperfection amplitudes to be studied, but the effects of geometric imperfections are best explored as the variation of R_{GMNIA} with dimensionless imperfection δ_o/t. This permits the parameters β and η to be characterised generally.
6. A critical consideration is the effect of geometric nonlinearity. If the shell geometry is changed to reach different values of the dimensionless slenderness $\bar{\lambda}$, the effect of geometric nonlinearity may change, and it is more difficult to separate out α_I and α_G. A useful device is to change the dimensionless slenderness $\bar{\lambda}$ by retaining a fixed geometry and changing the yield stress f_y over a wide range (including completely impractical values) since this can be shown to produce the same outcome, but it ensures that the variation of α_I with geometry can also be determined.
7. The parameters α, β, η, $\bar{\lambda}_o$ and χ_h for each geometry, with varying slenderness at constant imperfection amplitude, are best extracted from

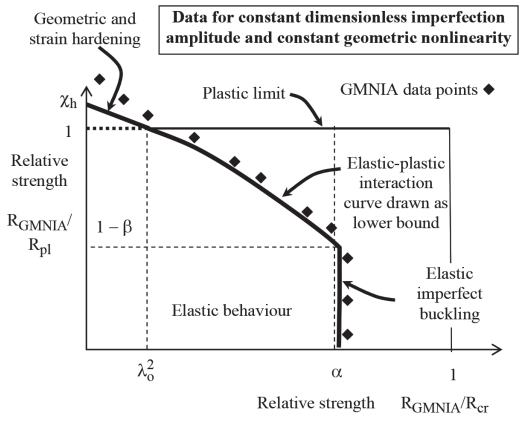

Figure 20. Modified capacity curve to extract parameters.

the modified capacity curve devised by Rotter (2005, 2011) (Fig. 20). The value of the imperfection sensitivity is found as $\alpha_I = \alpha/\alpha_G$ where α is the extracted value from Fig. 20.

8. When the variations of these parameters have been found, for the varying imperfection amplitudes and varying geometries, appropriate relationships can be easily developed to accurately model the full range of the discovered behaviour. There are some small limitations on the values that η can take, as described by Doerich & Rotter (2011b) and reproduced in Rotter (2011), but these are not very constraining.
9. This process, though it sounds onerous, leads to a consistent and very precise description of the elastic-plastic-hardening buckling and plastic behaviour of any shell structure under any loading. The results will be directly transferrable into the next edition of EN 1993-1-6, planned for 2019.

7 CONCLUSIONS

This paper has presented the background to shell buckling, its history in terms of a buckling stress and the adaptation of Stress Design to apply to general load cases. A critique of this methodology has been given, with a short description of the LBA/MNA computational method to improve assessments.

It has then presented the new Reference Resistance Design, whose aim is a hand calculation method that can accurately describe a wide range of shell buckling conditions without the contortions required to transform non-uniform stress states into equivalent uniform states, and without the constraint that the yield stress cannot be exceeded.

The paper has presented many different structural configurations and load cases that need the attention of shell buckling enthusiasts. Researchers are encouraged to produce suitable calculations to develop new RRD solutions or to transform current empirical and limited data into this universally applicable and practically useful methodology.

REFERENCES

Antoine, P.O. 2000. *Comportement des coques cylindriques minces sous chargements combinés*. PhD thesis, INSA de Lyon, France.

API 620 2002. *Design and Construction of Large Welded, Low-Pressure Storage Tanks*, 10th edn, Washington, D.C.: American Petroleum Institute.

API 650 1998. *Welded steel tanks for oil storage*, 10th Edn, Washington D.C.: American Petroleum Institute.

Blachut, J., Galletly, G.D. & Moreton, D.N. 1990. Buckling of Near-perfect Steel Torispherical and Hemispherical Shells subjected to external pressure. *Am Inst Aero & Astro J* 28(11): 1971–1975.

Brazier, L.G. 1927. On the flexure of thin cylindrical shells and other 'thin' sections. *Proc Roy Soc Series A* 116: 104–114.

Brunesi, E. Nascimbene, R. & Rotter, J.M. 2016. Influence of structural openings on buckling of shells under compression. Int Coll Stab & Duct Steel Structs, Timisoara: 8pp.

Calladine, C.R. 1983. *Theory of Shell Structures*. Cambridge: Camb Univ Press.

Chen, L. & Rotter, J.M. 2012. Buckling of Anchored Cylindrical Shells of Uniform Thickness under Wind Load. *Engrg Structs* 41: 199–208.

Chen, L. Doerich, C. & Rotter, J.M. 2008. A study of cylindrical shells under global bending in the elastic-plastic range. *Steel Construction—Design and Research Stahlbau* 1(1): 59–65.

Chen, L. Rotter, J.M. & Doerich, C. 2011. Buckling of cylindrical shells with stepwise variable wall thickness under uniform external pressure. *Engrg Structs* 33 (12): 3570–3578.

DASt 1994. *Beulsicherheitsnachweis fuer Schalen—spezielle Faelle*. DASt-Richtlinie 017. Köln: Deutscher Ausschuss für Stahlbau.

DIN 18800 1990. *Stahlbauten: stabilitätsfälle, schalenbeulen*. Part 4, Berlin: Deutsches Institüt für Normung.

Ding, X.L., Coleman, R.D. & Rotter, J.M. 1996. Surface profiling system for measurement of engineering structures. *J Surv Engrg ASCE* 122(1): 3–13.

Doerich, C. 2007. *Strength and stability of locally supported cylinders*, PhD thesis, Inst Infrastructure & Environ, Univ. Edinburgh.

Doerich, C. & Rotter, J.M. 2008. Behavior of cylindrical steel shells supported on local brackets. *J Struct Engrg ASCE* 134(8): 1269–1277.

Doerich, C. & Rotter, J.M. 2011a. Estimating the plastic collapse load of a shell using LA, MNA and GMNA finite element analyses. *Proc 6th Int Conf Thin-Walled Structs. Timisoara*: 889–896.

Doerich, C. & Rotter, J.M. 2011b. Accurate determination of plastic collapse loads from finite element analyses. *J Pres Ves Tech. 1*33(1): 011202-1 to 10.

ECCS EDR4 1988. *European Recommendations for Steel Construction: Buckling of Shells 4th edn*. Brussels: European Convention for Constructional Steelwork.

EN 1993-1-6 2003. *Eurocode 3, Part 1.6: Strength and Stability of Shell Structures*, Brussels: European Committee for Standardisation.

Greiner, R. & Guggenberger, W. 1998. Buckling Behaviour of Axially Loaded Steel Cylinders on Local Supports with and without Internal Pressure. *Thin-Walled Structs* 31(1–3): 159–167.

Greiner, R. & Poggi, C. 2013. Conical shells and truncated conical shells under general loading. In J.M. Rotter & H. Schmidt (eds), *Stability of Steel Shells: European Design Recommendations 5th Edn*: 265–286, Brussels: European Convention for Constructional Steelwork.

Guggenberger, W. Greiner, R. & Rotter, J.M. 2000. The Behaviour of Locally-Supported Cylindrical Shells: Unstiffened Shells. *J Constr Steel Res* 56(2): 175–197.

Guggenberger, W. Greiner, R. & Rotter, J.M. 2004. Cylindrical shells above local supports. In J.G. Teng & J.M.Rotter (eds), *Buckling of Thin Metal Shells:* 88–128. London: Spon.

Houliara, S. & Karamanos, S.A. 2006. Buckling and post-buckling of long pressurized elastic thin-walled tubes under in-plane bending. *Int J Non-Lin Mechs* 41(4): 491–511.

Jansseune, A. De Corte, W. & Van Impe, R. 2013. Column-supported silos: elasto-plastic failure. *Thin-Walled Structs* 73: 158–173.

Jullien, J.F. & Limam, A. 1998. Effect of openings on the buckling of cylindrical shells subjected to axial compression. *Thin-Walled Structs* 31(1): 187–202.

Jumikis P.T. & Rotter J.M. 1986. Buckling of Cylindrical Shells under Non-Uniform Torsion. *10th Austral Conf Mechs Structs & Matls*. 211–216.

Khamlichi A., Bezzazi M. & Limam A. 2004. Buckling of elastic cylindrical shells considering localized axisymmetric imperfections. *Thin-Walled Structs* 42(7): 1035–1047.

Koiter, W.T. 1945. *On the Stability of Elastic Equilibrium*. PhD Thesis (in Dutch), Delft Univ., Netherlands.

Limam, A., Lee, L.H., Corona, E. & Kyriakides, S. 2010. Inelastic wrinkling and collapse of tubes under combined bending and internal pressure. *Int J Mech Sci* 52(5): 637–647.

Mathon, C. & Limam, A. 2006. Experimental collapse of thin cylindrical shells submitted to internal pressure and pure bending. *Thin-Walled Structs* 44(1) 39–50.

Michel, G., Limam, A. & Jullien, J.F. 2000. Buckling of cylindrical shells under static and dynamic shear loading. *Engrg Structs* 22(5): 535–543.

NASA SP8007 1968. Buckling of Thin-Walled Circular Cylinders. Langley: NASA.

Rotter, J.M. 1985. Analysis and Design of Ringbeams. In J.M. Rotter (ed), *Design of Steel Bins for the Storage of Bulk Solids:* 164–183. Sydney: University of Sydney.

Rotter, J.M. 1986. The Analysis of Steel Bins Subject to Eccentric Discharge. *2nd Int Conf Bulk Matls Storage Handling & Transptn*, Wollongong: IEAust. 264–271.

Rotter, J.M. 2005. Stability and plasticity in structural analysis: a new conceptual framework. *Proc., 4th Int Conf Advances Steel Structs, Shanghai, July*: 1815–1826.

Rotter, J.M. 2011. Shell buckling design and assessment and the LBA-MNA methodology. *Stahlbau* 80(11): 791–803.

Rotter, J.M. 2013. Design of shells using reference resistances. *Amendment AM-1-6-2013-05 to EN 1993-1-6*, Approved by CEN TC250 SC3. Brussels: CEN.

Rotter, J.M. & Teng, J.G. 1989. Elastic Stability of Lap-Jointed Cylinders. *J Struct Engrg ASCE* 115(3): 683–697.

Rotter, J.M. Cai, M. & Holst, J.M.F.G. 2011. Buckling of thin cylindrical shells under locally elevated axial compression stresses. *J Pres Ves Tech* 133(1): 011204-1-11.

Rotter, J.M. Jumikis, P.T. Fleming, S.P. & Porter, S.J. 1989. Experiments on the Buckling of Thin-Walled Model Silo Structures. *J Constr Steel Res* 13(4): 271–299.

Sadowski, A.J. & Rotter, J.M. 2010. Study of buckling in steel silos under eccentric discharge flows of stored solids. *J Engrg Mechs ASCE* 136(6) 769–776.

Sadowski A.J. & Rotter J.M. 2012. The structural behaviour of thin-walled metal silos subject to different flow channel sizes under eccentric discharge pressures. *J Struct Engrg ASCE* 138(7): 922–931.

Schmidt, H. & Rotter, J.M. 2013. Rules for the buckling limit state assessment using global numerical analysis. In J.M. Rotter & H. Schmidt (eds), *Stability of Steel Shells: European Design Recommendations 5th Edn*: 89–143, Brussels: European Convention for Constructional Steelwork.

Schmidt, H. & Winterstetter, T.A. 2004. Cylindrical shells under torsion and transverse shear. In J.G. Teng & J.M. Rotter (eds), *Buckling of Thin Metal Shells.* 207–229. London: Spon.

Schmidt, H., Rotter, J.M. & Greiner, R. 2013. Rules for the buckling limit state assessment using stress design. In J.M. Rotter & H. Schmidt (eds), *Stability of Steel Shells: European Design Recommendations 5th Edn*: 145–165. Brussels: European Convention for Constructional Steelwork.

Singer, J. (2004) "Stiffened cylindrical shells", In J.G. Teng & J.M. Rotter (eds), *Buckling of Thin Metal Shells.* 286–343. London: Spon.

Sonat, C., Topkaya, C. & Rotter, J.M. 2015. Buckling of cylindrical metal shells on discretely supported ringbeams. *Thin Walled Structs* 93: 22–35.

Song, C.Y. Teng, J.G. & Rotter, J.M. 2004. Imperfection sensitivity of thin elastic cylindrical shells subject to partial axial compression. *Int J Solids & Structs* 41(24–25): 7155–7180.

Teng. J.G. 1994. Plastic Collapse at Lap-Joints in Pressurized Cylinders under Axial Load. *J Struct Engrg ASCE* 120(1): 23–45.

Teng, J.G. 1997. Plastic buckling approximations for transition ringbeams in steel silos. *J Struct Engrg ASCE* 123(12): 1822–1930.

Teng, J.G. 2004. Shell junctions. In J.G. Teng & J.M. Rotter (eds), *Buckling of Thin Metal Shells.* 369–408. London: Spon.

Teng, J.G. & Rotter, J.M. 1991. Plastic Buckling of Rings at Steel Silo Transition Junctions. *J Constr Steel Res* 19(1): 1–18.

Teng, J.G. & Zhao, Y. 2004. Rings at shell junctions. In J.G. Teng & J.M. Rotter (eds), *Buckling of Thin Metal Shells.* 409–454. London: Spon.

Teng, J.G., Lin, X. Rotter, J.M. & Ding, X.L. 2005. Analysis of geometric imperfections in full-scale welded steel silos. *Engrg Structs* 27(6): 938–950.

Topkaya, C. & Rotter, J.M. 2011. Ring Beam Stiffness Criterion for Column Supported Metal Silos. J Engrg Mechs ASCE 137(12): 846–853.

Winterstetter, T.A. & Schmidt, H. 2002. Stability of circular cylindrical steel shells under combined loading. *Thin-Walled Structs* 40: 893–909.

Wunderlich, W. 1995. Imperfection sensitivity of elastic-plastic torispherical pressure vessel heads. *Thin-Walled Structures* 23(1–4): 21–39.

Wunderlich, W. & Albertin, U. 2000. Analysis and load carrying behaviour of imperfection sensitive shells. *Int J Num Meths Engrg* 47: 255–273.

Wunderlich, W. & Albertin, U. 2002. Buckling behaviour of imperfect spherical shells. *Int J Nonlin Mechs* 37: 589–604.

Yamaki, N. 1984. *Elastic Stability of Circular Cylindrical Shells*. Amsterdam: Elsevier.

Recent Progress in Steel and Composite Structures – Giżejowski et al. (Eds)
© 2016 Taylor & Francis Group, London, ISBN 978-1-138-02946-0

Advances in seismic assessment of steel-concrete composite high-rise buildings and engineering practices

J. Qian, Z. Zhou & X.H. Wu
State Key Laboratory of Disaster Reduction in Civil Engineering, Tongji University, Shanghai, P.R. China

ABSTRACT: Steel-concrete composite structures that share the advantages of both steel and concrete are more efficient for high-rise buildings. The mega frame-core tube-outrigger system like Shanghai Tower is one of the most commonly adopted structural system in China and buildings of significant structural irregularities are also widely used in recent engineering practices. Their dynamic response behaviors and seismic performances are usually quite different from the conventional structural systems. This paper presents the progress on the recent developments of steel-concrete composite structures though a number of engineering examples. Attentions are mainly focused on the innovative structural system and its newly employed structural components. Numerical results of pushover analysis as well as elasto-plastic time-history analysis are also provided briefly to demonstrate their excellent performance to strong earthquakes.

1 INTRODUCTION

The rapid economic growth and urbanization which is inevitable in the development of human society have been one of the main causes that result in the centralized population in the urban area. As the environmental degradation and the limited availability of land are commonly acknowledged, the introduction of vertical urbanization, with its increased living area and green area, has a significant impact upon the future urban plans (Ali 2007).

In recent years, the whole world has witnessed a flourish in the construction of novel high-rise buildings. According to the global tall building database of the CTBUH, until September 2015, 123 buildings of height above 300 m have been completed and topped out architecturally or structurally, of which 56 are constructed in China. Meanwhile, 99 high-rise buildings above 300 m are under construction in the world and 55 of them are built in China. Buildings have been taller, and the configuration as well as structural systems has become more complex. The world tallest building is the Burj Khalifa Tower, with an architectural height of 828 meters. In China, the 632 m Shanghai Tower which has been architecturally topped out is temporarily the tallest, followed by Pang An Finance Center (599 m, architecturally topped out), Tianjin Goldin Finance 117 (597 m, structurally topped out) and Guangzhou CTF Finance Center (530 m, architecturally topped out). New structural materials, high-performance components and systems are employed for many of these super high-rise buildings, which bring new challenge to the design and analysis methodology.

Steel-concrete composite structures that share the advantages of both steel and concrete are more efficient for high-rise buildings. Typical steel-concrete composite high-rise buildings constructed in recent years in China Mainland are presented in this paper. Attentions are mainly focused on the innovative structural system and its newly employed structural components. Numerical results of pushover analysis as well as elasto-plastic time-history analysis are also provided briefly to demonstrate their excellent performance to strong earthquakes.

2 STEEL-CONCRETE COMPOSITE ENGINEERING PRACTICES

Steel-concrete composite structures have been widely used in high-rise buildings around the world. Different from the conventional steel structures and Reinforced Concrete (RC) structures, steel-concrete composite structures combine steel members, reinforced concrete members and steel-concrete composite members. Since the benefits of both steel and concrete, more efficient structural systems can be developed (Nie 2009).

According to the global tall building database of the CTBUH, 20 of the top 25 buildings completed or topped out are steel-concrete composite buildings. This structural system was recommended by the Chinese Ministry of Housing and Urban-rural Development, and has become more and more popular in China. Table 1 presents the top buildings that has been completed or topped out in China. As shown in the table, the composite mega

Table 1. Top buildings in China.

Official Name	Height*/m	Status	Structural System
Shanghai Tower	632/561	Topped Out	SRC mega frame-core tube-outrigger
Shenzhen Ping An Finance Center	599/555	Topped Out	SRC single braced mega frame-core tube-outrigger
Tianjin Goldin 117	597/584	Topped Out	CFST double braced mega frame-core tube
Guangzhou CTF Finance Centre	530/494	Topped Out	CFST mega frame-core tube-outrigger
Shanghai World Financial Center	492/474	Completed	SRC single braced mega frame- core tube-outrigger
Nanjing Zifeng Tower	450/317	Completed	SRC frame-core tube-outrigger
Shenzhen KK100 Development	442/427	Completed	CFST mega frame-core tube
Guangzhou International Finance Center	432/415	Completed	CFST diagrid tube-core tube

* The height includes architectural height and structural height separated by a slash.

frame-core tube-outrigger is the most commonly adopted composite structural system for high-rise buildings. Shaking table tests of this type of structure, such as Shanghai World Financial Center (Lu 2007) and Shanghai Tower (Jiang 2011), have been carried out to testify the seismic performance of this type of structure. Compared with steel frames and RC frames, mega frames which have larger lateral stiffness and clear load-carry path is more effective for super high-rise buildings (Shen 2001). Diagonal braces are commonly used to enhance the stiffness of frames and tubes. For diagrid structures which is utilized in Guangzhou International Finance Center, almost all the vertical columns are eliminated and the diagonal members carry gravity loads as well as lateral forces (Moon 2007). As many of the high-rise buildings are code-exceeding, conventional analysis methods developed for traditional structural systems need to be verified for their applicability to these new structural types. Performance-based seismic design as a promising method is under investigation (Jiang 2014).

The US-Japan Cooperative Earthquake Research Program on Composite and Hybrid Structures in 1993 carried out a series of representative researches on composite systems, revealing that three of them have attained a sufficient level of application for actual buildings: CFT column systems, RC column and Steel beam systems, and structural walls with encase steel braces or plates (Morino 1998, Geol 2004). Current studies of steel-concrete composite members are mainly focused on steel-composite columns such as Concrete-Filled Steel Tube (CFST) columns, Steel Reinforced Concrete (SRC) columns, and shear wall such as steel reinforced concrete shear wall and Steel Plate Reinforced Concrete (SPRC) shear wall. Steel-concrete composite members have their distinct structural advantages of less self-weigh, larger carrying capacity and ductility (Lu 2014). With the extensive engineering practices in China, many new types of steel-concrete composite components have been developed and tested to verify their performance. A composite shear wall with rectangular CFST columns at the wall boundaries was developed by Cao (2011). The cyclic loading tests on this new shear wall showed that its load carrying capacity as well as energy-dissipation capacity is very high. With the increase in cross-section of CFST columns for mega frames, the hexagonal cross-section with six cells and a total area of 45 m^2 were used in Tianjian Goldin Finance 117 (Peng 2012).

Tall buildings of various complex configuration are designed with new structural materials, components and structural systems. Typical composite high-rise buildings in China Mainland are introduced in detail.

2.1 *Shanghai tower*

Shanghai Tower, which has an architectural height of 632 m and 124 floors, is located by the side of 492 m Shanghai World Financial Center completed in 2008. It adopts an innovative steel-concrete composite mega frame-core tube-outrigger lateral structural system. The tower is divided into 9 main zones vertically, with a circular base plan of 83.6 m in diameter and 42 m on the 8th zone as shown in Figure 1. Figure 2 shows the standard floor and its typical strengthened story of Shanghai Tower.

The lateral resisting system of Shanghai Tower comprises an exterior composite mega frame and an interior reinforced concrete core tube. The exterior mega frame is composed of eight SRC mega-columns, four diagonal SRC mega-columns and eight 2-story-height belt trusses at each strengthened story. The mega frame can afford enough stiffness to work together with the core tube to resist the lateral force. The core tube is reinforced concrete above zone 2, while SPRC shear walls are used in zone 1~2 in order to improve the shear capacity and ductility of the shear wall. The out-

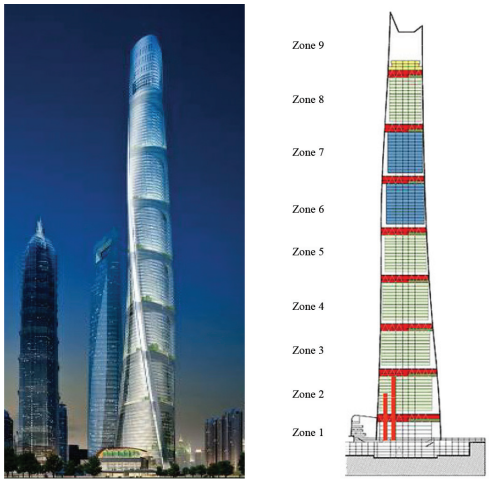

(a) Perspective view (b) vertical zones

Figure 1. Perspective view and vertical zones of Shanghai Tower.

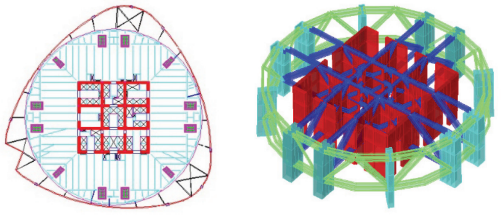

(a) Standard floor (b) Typical strengthened story

Figure 2. Structural plans of Shanghai Tower.

rigger trusses are designed to connect the mega frame and the core tube, which make them work together to resist the wind load and seismic load efficiently.

2.2 *Tianjin goldin finance 117*

Tianjin Goldin Finance 117 has an architectural height of 597 m with total 117 stories. The Tower has a quadrilateral plan with its first floor of 65 m × 65 m and degraded to 45 m × 45 m at the top. Figure 3 shows the global view of Goldin 117. A mega braced frame-core tube structure is adopted to Goldin 117. With an aspect ratio of about 9.5, a more efficient and stiffened structural system is required.

The lateral resisting systems consist an exterior mega frame and an interior core tube. The exterior mega frame is composed of CFST mega-columns, mega cross braces and transfer trusses. The hexagonal CFST column with six cells and the total cross-

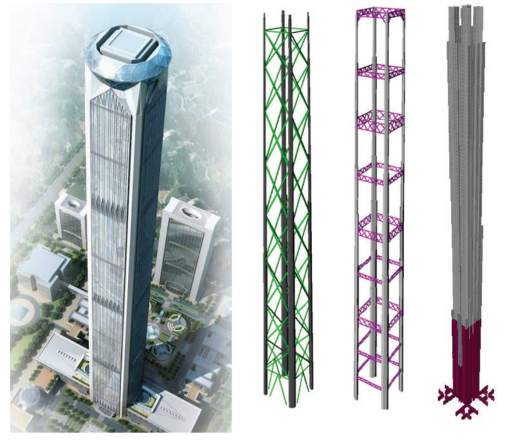

(a) Perspective view (b) Lateral resisting systems

Figure 3. Perspective view and lateral resisting systems of Tianjin Goldin Finance 117.

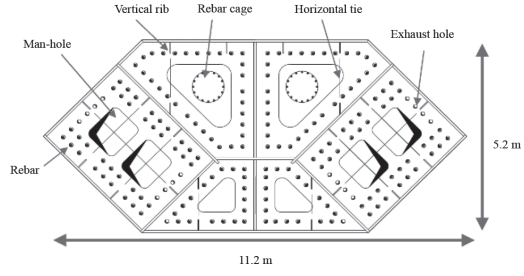

Figure 4. Section of the hexagonal mega CFST columns.

sectional area of 45 m^2 as shown in Fig.4 was used. Cyclic loading tests on the 1/25-scaled hexagonal mega CFST columns with six cells were carried out by Peng (2012). It is proved that the CFST columns has reliable seismic performance. Divided into nine zones as the belt trusses, the mega braces cross several floors and are separated from the gravity resisting system. They are directly connected to the mega columns and are constrained by the floor beam to avoid buckling. The mega cross braces play an important part in stiffening the mega frame. Since the length of the V-shaped braces at the elevation of −10~39 m is about 48 m, buckling restrained braces are used while cross braces in the other eight zones above are conventional braces (Bao 2014).

Since the stiffness of the exterior braced mega frame exceeds that of the core tube at most floors, the outrigger does not have much influence on the structural stiffness. The mega frame and the core are simply connected by the floor (enhanced at strengthened stories) and added floor braces at strengthened stories.

2.3 *Guangzhou international finance center*

Guangzhou International Finance Center has a total height of 432 m and 103 stories with a curved triangle plan. The structural system employed is a tube-in-tube structure, with an interior reinforced concrete tube in an exterior CFST diagrid tube. Figure 5 shows the perspective view and lateral resisting systems of the structure.

The standard floors of the interior hexagon core tube are presented in Figure 6. The exterior diagrid tube is composed of 30 CFST columns diagonally connected with each other, forming 16 joint layers. The lateral and torsional stiffness of the diagrid tube are larger than that of the traditional frame structure. Most loadings are transferred by the axial force which makes it more efficient than a moment type frame. Making the constraint of the joints stronger can improve its vertical stiffness and reduce the shear force and moment of the diagrid columns. External prestressing method are adopted in order to restraint the outward horizontal displacement of the joints, thus strengthening the constraint and the vertical stiffness of the exterior diagonal tube (Meng 2010).

(a) Perspective view (b) Lateral resisting systems

Figure 5. Perspective view and lateral resisting systems.

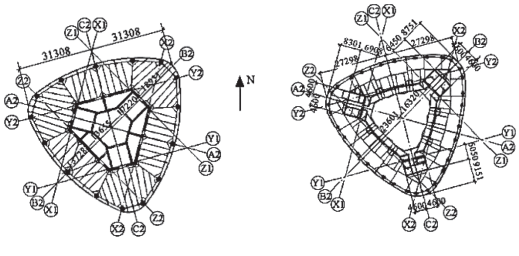

(a) Under 67 floor (b) Above 73 floor

Figure 6. Standard floors.

3 SEISMIC ANALYSIS OF TYPICAL STEEL-CONCRETE COMPOSITE STRUCTURES

3.1 *Shanghai tower*

As introduced in paragraph 2, Shanghai Tower is a typical steel-concrete composite mega frame-core tube-outrigger structure. According to the current Chinese code, the total structural height of 574.6 m and the elevation irregularity including strengthened and transfer stories are identified as code-exceeding.

3.1.1 *Numerical model*

A refined FE model for Shanghai Tower was established by using ANSYS including all 126 stories above the ground and the top steel trusses. SOLID elements were employed to simulate all the mega-columns, and BEAM elements were used for the beams, secondary columns and trusses. The shear walls, coupling beams and floors were modeled by SHELL elements. Beam-core wall connections were considered as rigid joints. The global view of the computational model and the typical strengthened story are shown in Figures 7–8.

3.1.2 *Dynamic properties*

The first 40 vibration modes of the structure are obtained by modal analysis. Table 2 presents the first 6 natural periods of the structure.

3.1.3 *Elasto-plastic time-history analysis*

To evaluate the seismic performance of the structure by nonlinear time-history analysis, three sets of earthquake records including Shanghai artifi-

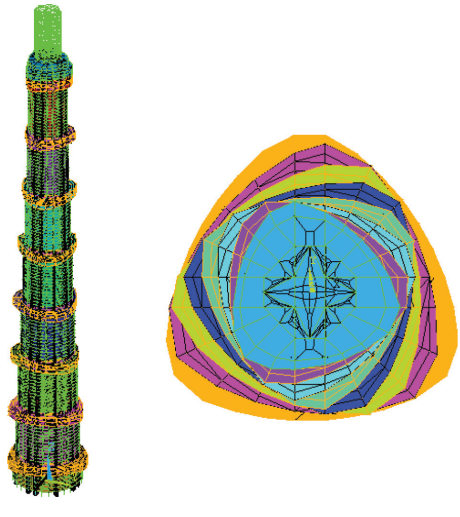

Figure 7. Perspective view and plan of the model.

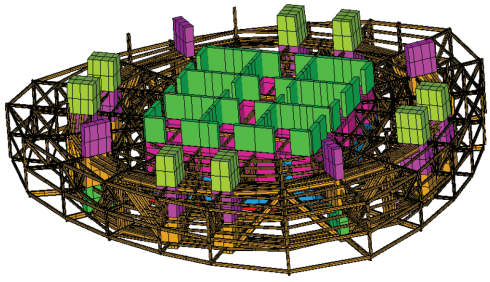

Figure 8. Strengthened story of 35th and 36th floor.

Table 2. Characteristics of the first 6 vibration modes.

Number of modes	Vibration periods(s)	Characteristic of vibration
1	8.8625	The 1st order translation in X direction
2	8.8105	The 1st order translation in Y direction
3	4.6537	The 1st order torsion
4	3.1481	The 2nd order translation in X direction
5	3.0868	The 2nd order translation in Y direction
6	2.2198	The 2nd order torsion

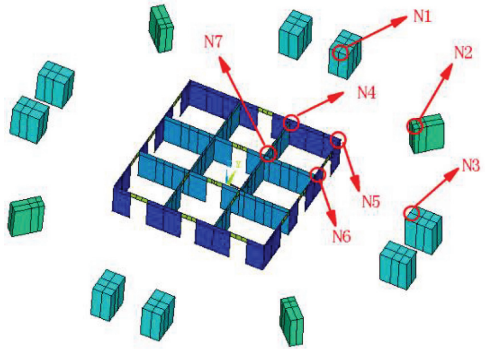

Figure 9. Typical nodes of the model.

cial wave-3 (SHW3), ATS000-090 (Kocaeli, Turkey 1999/08/17, Station: Ambarli), CHY004 (Chi-Chi, Taiwan 1999/09/20, Station: CHY004) are selected according the current Chinese seismic design code. Two levels of seismic hazard, minor or frequent earthquakes and strong or rare earthquakes are considered. The Peak Ground Acceleration (PGA) of frequent earthquakes and rare earthquakes with intensity 7 is 35 cm/s^2 and 220 cm/s^2 respectively. SHW3 is applied for the X-direction and Y-direction seismic excitation separately, while X-direction and Y-direction components scaled with the PGA ratio of 1:0.85 are considered in ATS000-090 and CHY004.

Typical nodes of the numerical model are selected as marked in Figure 9. Figures 10–13 show the floor displacements and inter-story drift ratios under three sets of frequent and rare seismic excitations. The inter-story drift ratios decrease significantly in the strengthened stories since the stiffness there is much larger than that of the adjacent two stories, thus producing weak floors.

It can be found that responses in two horizontal directions show only a minor difference. Response displacement of the structure to ATS000-090 seismic wave is nearly half of that to SHW3 or CHY004. The maximum displacement and inter-story drift ratio, which is 439.61 mm and 1/868 respectively, both occur when the structure is subjected to the SHW3 wave. A further non-linear analysis to rare earthquakes, shown in Table 3, has affirmed the reliability of its seismic performance.

3.2 *Teaching and Research Complex of Tongji University*

Teaching and Research Complex of Tongji University is a complex high-rise building with extreme plane and vertical irregularity. This 98 m high structure, which has 21 standard floors and 6 mechanical floors, is divided into 7 zones with a spiral layout of L-shape block unites (Figure 14) and a quadrilateral plan of 48.6 m × 48.6 m. Each zone includes three standard floors (floor height of 4 m) and is separated from the others by the mechanical floors (floor height of 2 m).

The structure adopts a CFST column-steel beam frame with viscous damper braces. In order to enhance the stiffness of the frame, belt steel trusses are placed around the structure at mechanical floors, and discontinuous spirally uprising cross braces are installed as shown in Figure 15.

56 viscous dampers are used, efficiently minimizing the seismic response of the structure. Since the spiral L-shape plan of the floors and the discontinuous braces, the resisting capacity especially the torsional resistance of the structure has to be investigated.

3.2.1 *Numerical model*

The FE computational model of Teaching and Research Complex of Tongji University has been established also by using ANSYS. The confined concrete theory was employed in calculation of the concrete-filled steel tube which suggests that the steel tube is considered as the equivalent longitudinal reinforcement. The confinement factor is taken into consideration in order to get the improved

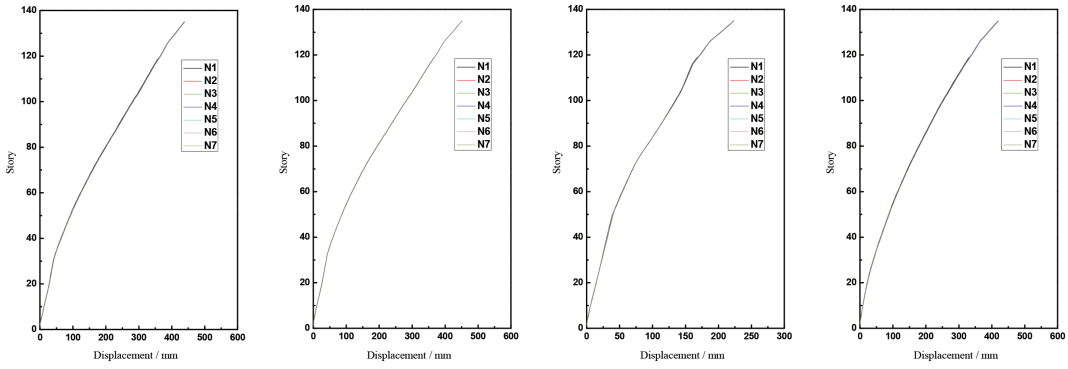

(a) SHW3 in X direction (b) SHW3 in Y direction (c) ATS000-090 (d) CHY004

Figure 10. Displacements of typical nodes under frequent earthquakes.

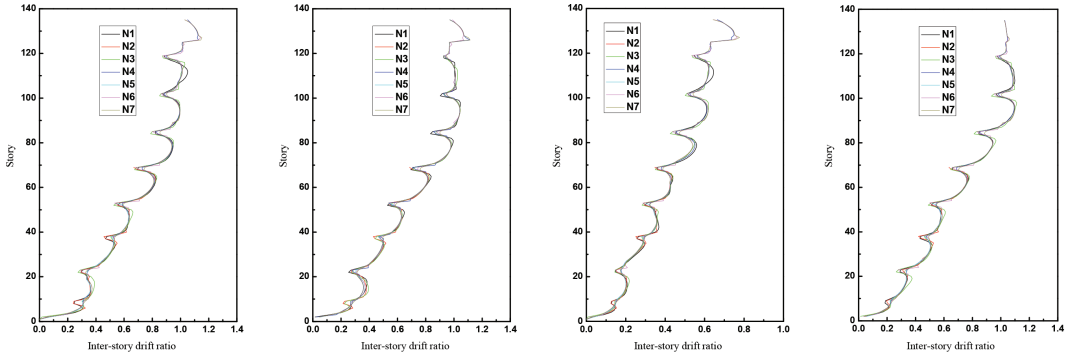

(a) SHW3 in X direction (b) SHW3 in Y direction (c) ATS000-090 (d) CHY004

Figure 11. Inter-story drift ratios under frequent earthquakes.

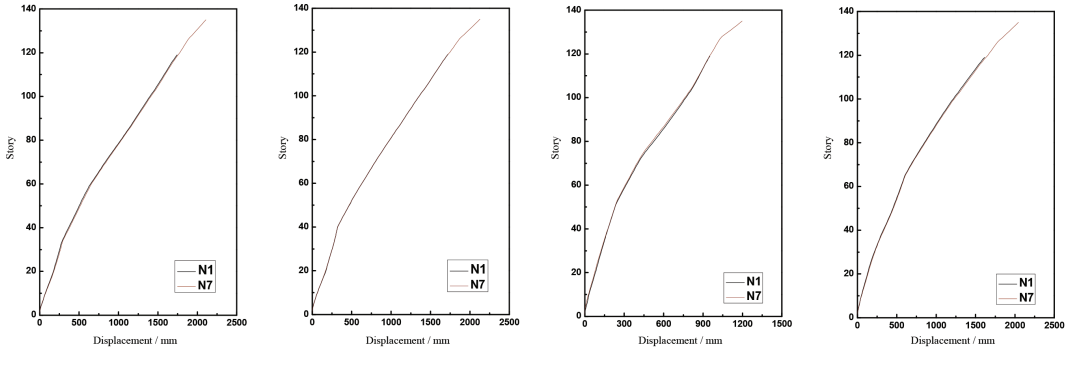

(a) SHW3 in X direction (b) SHW3 in Y direction (c) ATS000-090 (d) CHY004

Figure 12. Displacements of typical nodes under rare earthquakes.

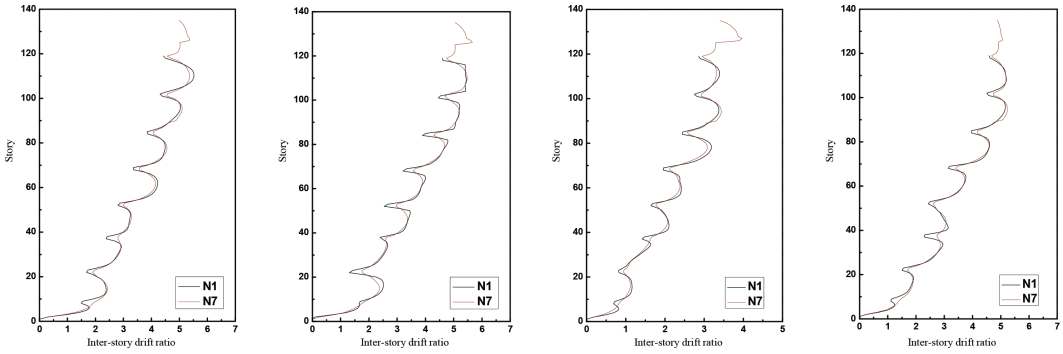

(a) SHW3 in X direction (b) SHW3 in Y direction (c) ATS000-090 (d) CHY004

Figure 13. Inter-story drift ratios under rare earthquakes.

Table 3. Maximum displacements and inter-story drift ratios.

Level of seismic hazard	Earthquake record	Maximum displacement (mm)	Maximum inter-story drift ratio	Location of maximum inter- story drift ratio (floor)
Frequent earthquakes	SHW3	439.61	1/868	127
	ATS000–090	223.81	1/1286	127
	CHY004	420.62	1/899	98
Rare earthquakes	SHW3	2127.36	1/177	125
	ATS000–090	1217.01	1/252	126
	CHY004	2043.74	1/191	108

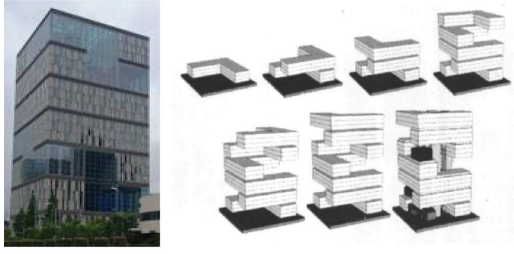

(a) Perspective view (b) Spiral layout of L-shape floors

Figure 14. Perspective view of the structure and the spiral layout of the L-shape floors.

yield strength of the core concrete. The Bilinear Kinematic Hardening Plasticity (BKIN) constitutive model has been used for steel.

3.2.2 *Dynamic properties*

The first 30 vibration modes of the structure are obtained by modal analysis. The first 6 natural periods of the structure are shown in Table 4. The torsional period ratio is 0.80 which is within the limitation of the Chinese code.

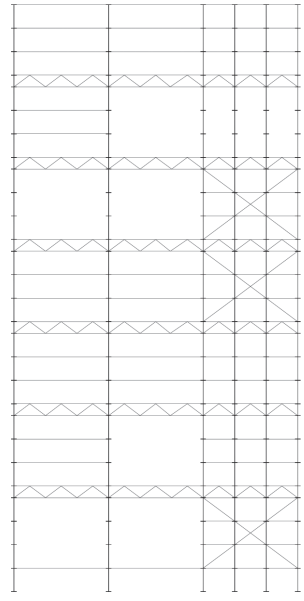

Figure 15. Layout of discontinuous brace of north elevation.

Table 4. Characteristics of the first 6 vibration modes.

Number of modes	Vibration periods(s)	Characteristic of vibration
1	3.2464	The 1th order translation in Y direction
2	3.2280	The 1th order translation in X direction
3	2.5884	The 1th order torsion
4	1.0981	The 2nd order diagonal translation
5	1.0650	The 2nd order diagonal translation
6	0.8324	The 2nd order torsion

3.2.3 *Pushover analysis*

Pushover analysis is a recommended method for performance-based design. To implement a pushover analysis, the relationship between base shear and roof displacement for the structure, which is referred as the capacity curve, should be obtained by non-linear static analysis of the structure. The structure is subjected to a monotonically increasing lateral forces with a certain lateral load pattern until a target displacement is reached. The target displacement is an estimated displacement that the design earthquake will produce. The selection of a reasonable lateral load pattern is particularly important in pushover analysis. FEMA356 suggests that at least two different patterns should be adopted.

Two lateral load patterns, the inverted triangle distribution and the fundamental mode distribution, are selected. Based on the mass distribution of the floor (Figure 16), the inverted triangle distribution of lateral force is presented in Figure 17. And Figure 18 shows the fundamental mode distribution.

Firstly, the ultimate target displacement is assumed to be 1/50 of the structural height. The capacity curves under different lateral load patterns are shown in Figures 19–20. When the structure is subjected to lateral load of the inverted triangle distribution, the yield displacement and the ultimate target displacement are 0.228 m and 1.921 m, respectively. For the fundamental mode distribution, they are 0.183 m and 1.971 m, respectively. Furthermore, the inter-story drift ratios are demonstrated in Figure 21.

Improved capacity spectrum method is used to assess the seismic performance of the structure. Inelastic demand spectrums are obtained by varied ductility factors (1.0, 1.5, 2.0, 3.0, 4.0). The maximum acceleration effect coefficient under rare earthquake is 0.5. The eigenperiod T_c is 0.90 s, and the damping ratio of the structure is 0.03. As shown in Figures 22–23, the target displacements of two lateral load pattern shows few differences. The target displacements of different ductility factors of 1, 1.5 and 2 are 50.3 cm, 34.5 cm and 28.2 cm respectively.

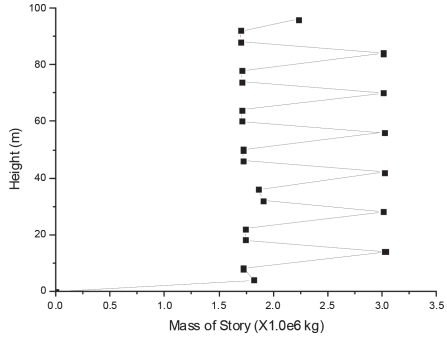

Figure 16. Mass distribution of the floors.

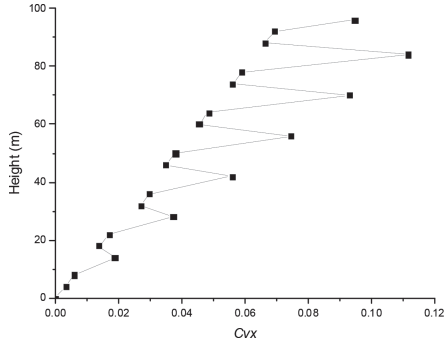

Figure 17. Inverted triangle distribution.

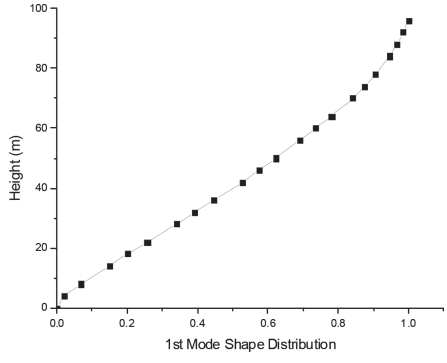

Figure 18. Fundamental mode distribution.

3.3 *China Pavilion for Shanghai Expo 2010*

China Pavilion for Shanghai Expo 2010 which is also called 'oriental crown', shown in Figures 24–25, is designed as a public building for exhibition, with a special shape of an inverted trapezoid in elevation and large non-column areas in the interior. China Pavilion has a total structural height of 68 m. The plan dimensions vary from 69.9 m × 69.9 m at the height of 33.3 m to 139.4 m × 139.4 m at the roof. The floors below the height of 33.3 m are hollow, while the upper floors are in a varying cantilever span up to about 33 m at the roof floor. Four RC tubes of the

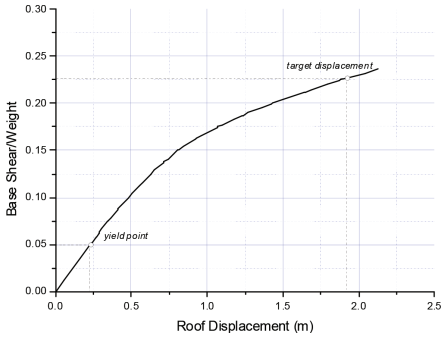

Figure 19. Capacity curve of inverted triangle load.

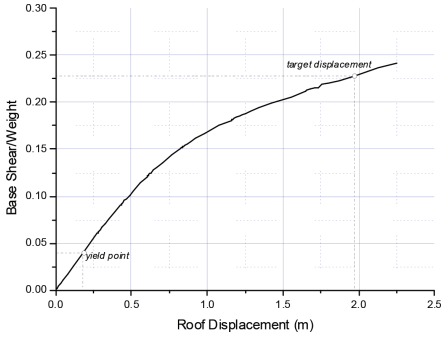

Figure 20. Capacity curve of fundamental mode load.

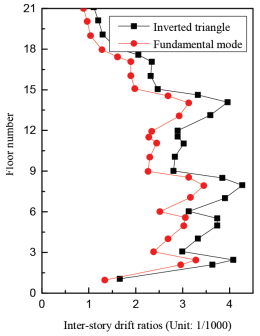

(a) Yield point

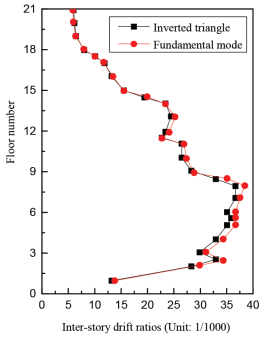

(b) Ultimate target point

Figure 21. Inter-story drift ratios under different lateral load.

same dimensions 18.6 m × 18.6 m, which stand at the corners stretching from the bottom to the top (7.7 m out of the roof), are designed to be the primary lateral resisting system as well as the vertical bearing system of China Pavilion. From the perimeter of the tubes of the height of 33.3 m to the edge of the cantilever roof floor, 20 inclined rectangular CFST columns are placed to support the big-span steel beams on the steel-concrete composite slabs.

The significant irregularity of the mass distribution of the structure weakens its torsional stiffness. the RC tubes which are the primary support of the structure are strengthened to control its torsional behavior. Steel tubes are placed at the corners of the tubes to improve its deformation capacity. Moreover, the connections between the inclined columns and the perimeter trusses of the structure are enhanced.

3.3.1 *Numerical model*

As shown in Figure 26, NosaCAD2005 is used to build the numerical model of China Pavilion. Beams and columns are combined with three different stiffness segments. For the beams mainly bearing moment, the bilinear and tri-linear moment curvature hysteretic model is employed to simulate the behavior of nonlinear segments, while fiber model is employed to simulate the

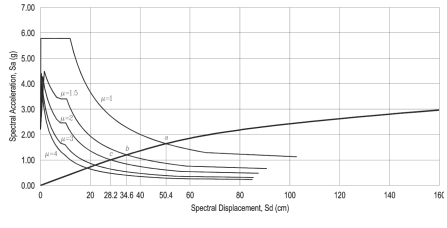

Figure 22. Capacity curve under inverted triangle distribution.

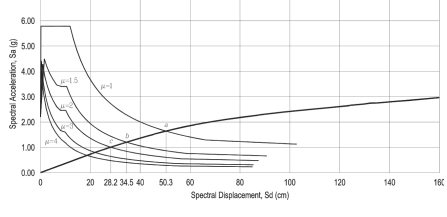

Figure 23. Capacity curve under fundamental mode distribution.

behavior of nonlinear segments of columns and trusses. Shear wall and tube are composed of shell elements, which nonlinear property in plane is described by Darwin-Pecknold model.

Figure 24. Perspective view of China Pavilion.

Table 5. Characteristics of the first 6 vibration modes.

Number of modes	Vibration periods(s)	Characteristic of vibration
1	1.36	The 1st order torsion
2	1.14	The 1st order translation in Y direction
3	1.13	The 1st order translation in X direction
4	0.47	The 2nd order translation in Y direction
5	0.46	The 2nd order translation in Z direction
6	0.45	Local deformation of the floors

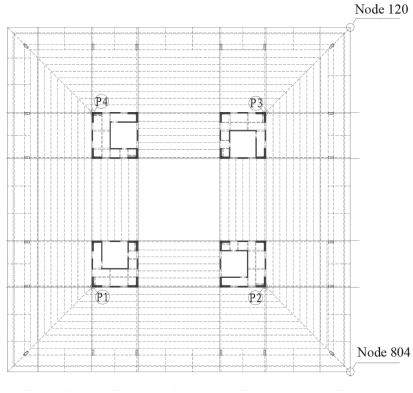

Figure 25. Plan of China Pavilion.

3.3.2 *Dynamic properties*

The first 6 natural periods of the structure are shown in Table 5. Due to the special shape of the structure, the fundamental vibration mode is the torsional mode, thereby resulting in the torsional period ratio exceeding the code limitation.

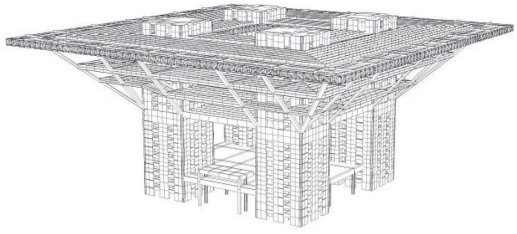

Figure 26. Global view of the numerical model by NosaCAD.

3.3.3 *Elasto-plastic time-history analysis*

Three sets of earthquake records including one artificial seismic wave (SHW3) and two natural waves (El Centro and Pasadema) are selected according the current Chinese seismic design code. Two levels of seismic hazard, frequent earthquakes and rare earthquakes are considered. The peak ground acceleration (PGA) of frequent earthquakes and rare earthquakes with intensity 7 is 35 cm/s^2 and 220 cm/s^2, respectively. SHW3 is applied for the X-direction only, while X-direction, Y-direction and Z-direction components scaled with the PGA ratio of 1:0.85:0.65 are considered in El Centro and Pasadena.

The time-history displacements of node 804 (the corner of the floor at the height of 60.9 m) under frequent earthquakes and rare earthquakes are presented in Figures 27–28. The displacement response under three earthquakes are obviously different. The maximum displacement under Pasadena wave is appropriate 30% smaller than that under El Centro and SHW2 wave. As exhibited in Table 6, the maximum displacement occurs when the structure is loaded under El Centro seismic wave, with a displacement of 316.7 mm in Z direction.

In order to evaluate the torsional behavior of the structure, the X-direction displacements of two point (shown in Figure 25) are presented in Figure 29. The displacements of these two nodes are similar, with a maximum difference of 52.21 mm. And the rotational angle of the roof in its plane is only 3.80×10^{-4} degree. Therefore, it can be concluded that the torsional mode is not activated under seismic load.

The inter-story drift ratios of four typical nodes from the tubes under El Centro wave are presented in Figure 30. The maximum inter-story drift ratio of the structure under frequent earthquake and rare earthquake are 1/813 and 1/137, fulfilling the re-quirements of the Chinese code. Figure 31 shows the damage pattern. The plastic hinges occur at the coupling beams at first, followed by the crush of the boundary concrete walls of the tubes. The inclined columns and the top floor show few plastic hinges.

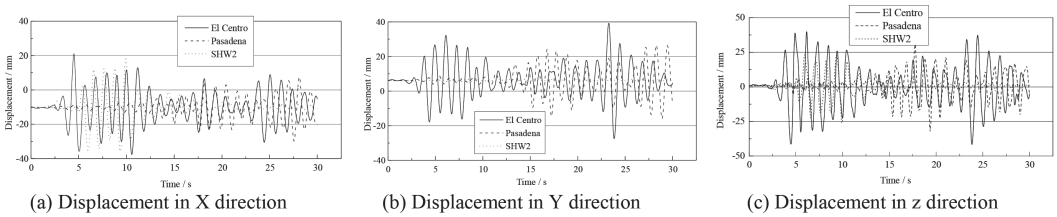

(a) Displacement in X direction (b) Displacement in Y direction (c) Displacement in z direction

Figure 27. Time-history displacement under frequent earthquakes.

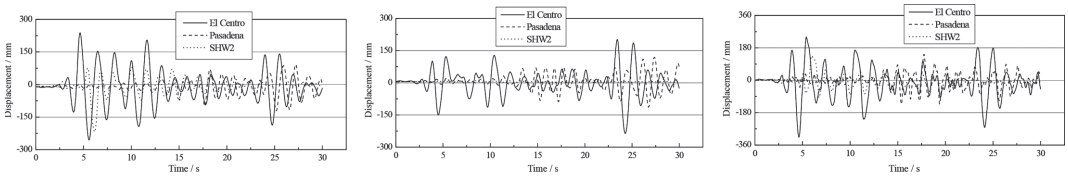

(a) Displacement in X direction (b) Displacement in Y direction (c) Displacement in z direction

Figure 28. Time-history displacement under rare earthquakes.

Table 6. Maximum displacements of node 804 in three directions (Unite: mm).

Level of seismic hazard	Earthquake record	X direction	Y direction	Z direction
Frequent earthquakes	El Centro	31.18	33.64	42.57
	Pasadena	19.63	22.06	33.21
	SHW2	28.27	0.99	26.91
Rare earthquakes	El Centro	248.37	241.76	316.70
	Pasadena	110.65	119.71	143.24
	SHW2	208.09	4.96	135.08

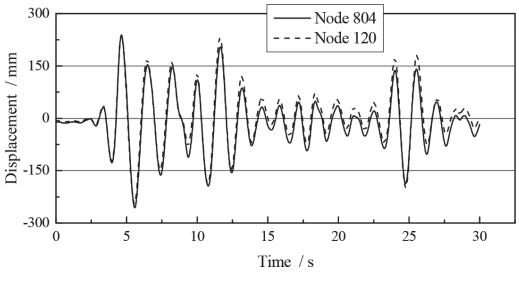

Figure 29. Time-history displacement under rare earthquakes.

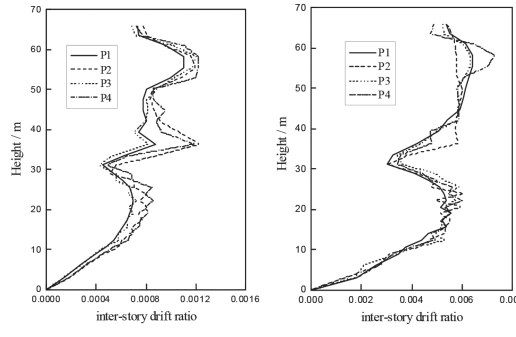

Figure 30. Inter-story drift to frequent and rare earthquake.

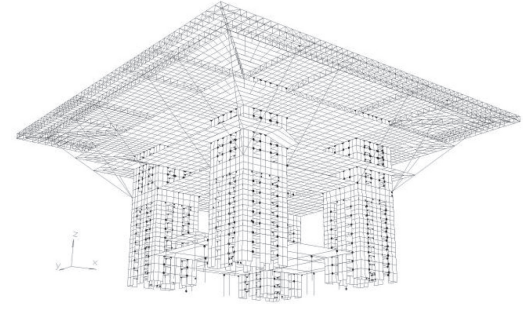

Figure 31. Damage patterns under El Centro of rare intensity.

4 CONCLUSIONS

A flourish in construction of novel high-rise buildings has been witnessed in China in the past decade. It is observed that, in most cases, steel-concrete composite structural system had been preferred for its superior performance in load carrying capacity and ductility. Three newly completed super high-rise buildings in China Mainland, namely Shanghai Tower, Tianjin Goldin Finance 117 and Guangzhou International Finance Center, are selected as examples for illustration. The double lateral resisting structural system with a core-tube has been adopted by all the three buildings. The main difference is their exterior mega-frame. For Shanghai Tower, the exterior mega frame is composed of 12 SRC mega-columns connected by eight 2-story-height belt trusses at strengthened story. That for Tianjin Goldin Finance 117, multi-celled CFST mega-columns have been used in conjunction with mega cross braces and transfer trusses. While that for Guangzhou International Finance Center, it is composed of 30 CFST columns diagonally interconnected with each other to form a exterior diagrid tube. All has been proved to be efficient and reliable in their seismic performance.

The commonly used analysis procedures, namely pushover analysis and non-linear time history analysis, have been applied to a number of composite high-rise buildings with extreme structural irregularity. It is satisfied to see that seismic assessment based on the calculation is well consistent with the conclusion of corresponding scaled model tests.

ACKNOWLEDGEMENT

The authors acknowledge with thanks support from (a) the Ministry of Science and Technology of China (grant No. SLDRCE15-B-06); (b) the National Natural Science Foundation of China (No. 91315301-4).

REFERENCES

Ali, M.M. & Moon, K.S. 2007. Structural developments in tall buildings: current trends and future prospects. *Architectural Science Review* 50(3): 205–223.

Bao, L. & Wang, D. 2014. Design and rethinking of mega brace in Tianjin 117 Tower. *Progress in Steel Building Structures (in Chinese)* 16(2): 43–48.

Cao W. & Zhang W. 2011. Seismic research and application on embedded steel plate concrete shear wall with concrete fille steel tube columns. *Journal of Civil Engineering and Management(in Chinese)* 28(3): 219–225, 253.

Goel, S.C. 2004. United States-Japan cooperative earthquake engineering research program on composite and hybrid structures. *Journal of Structural Engineering* 130(2): 157–158.

Jiang, H. & He, L. 2011. Analysis of seismic performance and shaking table tests of the Shanghai Tower. *Journal of Building Structures (in Chinese)* 32(11): 55–63.

Jiang, H. & Lu, X. 2014. Performance-based seismic design principles and structural analysis of Shanghai Tower. *Advances in Structural Engineering* 17(4): 513–528.

Johnson, R.P. 2008. Composite structures of steel and concrete: beams, slabs, columns, and frames for buildings. John Wiley & Sons.

Lu, X. & Zou, Y. 2007. Shaking table model test on shanghai world financial center tower. *Earthquake Engineering and Structural Dynamics* 36(4): 439–457.

Lu, X., & Jiang, H. 2014. Recent progress of seismic research on tall buildings in China Mainland. *Earthquake Engineering and Engineering Vibration* 13(1): 47–61.

Meng, H. & Huang, W. 2010. Application research on new hybrid structure systems in super-tall buildings. *Journal of Earthquake Engineering and Engineering Vibration (in Chinese)* 30(1): 69–76.

Moon, K.S. & Connor, J.J. & Fernandez, J.E. 2007. Diagrid structural systems for tall buildings: characteristics and methodology for preliminary design. *Structural Design of Tall and Special Buildings* 16(2): 205–230.

Morino, S. 1998. Recent developments in hybrid structures in Japan: research, design and construction. *Engineering Structures* 20(4): 336–346.

Ministry of Housing and Urban-Rural Development of China. 2010. *Code for Seismic Design of Buildings GB50011-2010 (in Chinese)*. Beijing: China Architecture and Building Press.

Nie, J. 1982. *Composite Structures of Steel and Concrete: Theory and Practice (in Chinese)*. Beijing: Science Press.

Peng, B. & Cao, W. 2012. Research on seismic behavior of multi-cell CFST mega-columns under horizontal forces in different directions. *World Earthquake Engineering (in Chinese)* 28(2): 90–97.

Poon, D.C. & Hsiao, L.E. 2011. Structural analysis and design challenges of the Ping An Tower under consideration of the upcoming China code. *Structures Congress* 2011 ASCE: 528–540.

Shen, Z. & Rongyi, C. 2001. Applications and developments of mega-structures. *Journal of Tongji University (in Chinese)* 29(3): 258–261.

Wang, H. & Ding, J. 2008. Study on column-and-brace system of Teaching and Research Complex of Tongji university. *Building Structure (in Chinese)* 38(10): 6–9.

Wu, X. & Qian, J. 2009. Elasto-plastic time history analysis of the structure of China Pavilion at the 2010 World EXPO. *Journal of Building Structures (in Chinese)* 30(5):112–118.

Yang, J. & Chen, Y. 2012. Shaking table tests on China pavilion for Expo 2010 Shanghai China. *The Structural Design of Tall and Special Buildings* 21(4): 265–282.

Recent Progress in Steel and Composite Structures – Giżejowski et al. (Eds)
© 2016 Taylor & Francis Group, London, ISBN 978-1-138-02946-0

Harmonization of structural standards on the reliability basis of design

J.V. Retief
Stellenbosch University, Stellenbosch, South Africa

ABSTRACT: Principles of structural reliability are integrally deployed in the semi-probabilistic design approach, as used in the in Eurocode partial factor limit states procedures. Characteristics of standards can be identified for assessment in terms of the functionality of the standard. The utilization of a common body of knowledge and experience can be closely associated with the harmonization of standards between various countries, regions or internationally as derived from a common reliability basis of design. Concepts for the characterization of standards for structural design and their development can be illustrated by reliability calibrations of Eurocode design models and procedures in accordance to South African needs and conditions. Generalization of these concepts may be useful even to Eurocode member states during the application of Eurocode in their country and to appreciate the differences of such application by other member countries. Structural reliability concepts could serve as useful vehicle and basis for the development of international standards.

1 INTRODUCTION AND OVERVIEW

Standards for the design of structures play a central role in ensuring the proper performance of load bearing structures for buildings and civil engineering infrastructure. Advances in the application of the theory and principles of structural reliability in the formulation of standardized design procedures, in turn, serve as basis for the enhancement of design standards.

This paper provides a review of the close interrelationship between the principles of structural reliability and the rational standardized basis of design. The emphasis is more on the concepts of reliability than on the structural mechanics modelling as used in design standards. However, under consideration is the *application* of reliability concepts, rather than a review of advanced models and their characteristics.

The principles of reliability can be applied at different levels: At the detailed level for example, the probabilistic representation of individual design parameters such as wind loading can be applied to the derivation of partial factors and characteristic values from which design values can be calculated. At the other end of the scale a common reliability basis can serve as basis for the unification of separate standards that may apply to individual projects, including alternative construction materials such as steel and concrete, composite construction or foundations. At an even higher level of generality the harmonization between standards from various countries and regions can serve as basis for sharing experience on a common basis. International standards for structural design are examples of the ultimate level of harmonization. However, concepts of reliability serve as basis for representing economic and societal interests in the performance of load bearing structures.

Full coverage of all aspects of structural reliability across all the levels of application is obviously beyond the scope of the paper. A flavor of the utility of specific applications, the various levels and the broad implications for standardized design can be obtained from examples provided in this review. These examples are mainly derived from the experience base of the author and colleagues.

The core of the examples of the application of reliability concepts derives from efforts to extract relevant material from Eurocode for application to South African conditions and practice. This process required not only the proper formulation of South African needs and conditions, but also a thorough assessment of Eurocode from the local perspective. Such an independent assessment might also be of interest to a country such as Poland when considering the national implementation of Eurocode.

The assessment of various reliability components provides an illustration of how the design representation of specific basic variables can be improved. Although some of these investigations do not strictly fall within the scope of this conference, generalization of the investigations are of interest: The important role of structural resistance is demonstrated, whereas the emphasis of reliability assessment is generally on the representation and treatment of actions on structures. Consideration of model uncertainty is another example of a topic of generic importance.

Recent advances on international standardization related to the reliability basis of structural design are addressed as the third general theme of the paper. This topic is of particular interest to "standards importer" countries, such as South Africa. The contribution of Eurocode towards harmonization is obviously a prime example of the benefits and a role model of what can be achieved internationally. The role of Poland in initiating the ISO Technical Committee on the basis of structural design (ISO TC98) and leading it since its inception should be noted with acclamation.

As a first step the conceptual basis of structural reliability is presented in terms of an elementary outline of the theory of reliability and its conversion into semi-probabilistic design procedures.

2 PRINCIPLES AND APPLICATION OF STRUCTURAL RELIABILITY

An outline of the relationship between the principles and theory of structural reliability and standardized semi-probabilistic partial factor limit states design is presented in this section. This exposition serves to define concepts that are central to the discussion of aspects of standards development presented in this paper.

2.1 *Elementary reliability theory*

2.1.1 *Basic expressions*

Fundamental concepts of reliability can be defined at an elementary level in terms of the probabilistic representation of the two concepts in the term "*load bearing*" defining the scope of structural engineering as considered in this paper, namely structural resistance (R) and actions, presented as action effects (E) in order to be directly comparable to resistance. As a first approximation the basic variables R and E are represented by a Gaussian or Normal distribution. When structural performance is expressed in reliability terms as a performance function (g) relating R&E, given by:

$$g = R - E \tag{1}$$

it is given by the probability of failure P_F:

$$P_F = P(g \le 0) = \Phi^{-1}(-\beta) \tag{2}$$

Where β is expressed in terms of the respective mean (μ_X) and standard deviation (σ_X) as:

$$\beta = \frac{\mu_R - \mu_E}{\sqrt{(\sigma_R)^2 + (\sigma_E)^2}} = \frac{\mu_R - \mu_E}{\sigma_g} \tag{3}$$

In the semi-probabilistic approach the design verification function (g_d) can be expressed in terms of the partial factor limit states design verification function, which is now a discreet and deterministic function:

$$g_d = \frac{\mu_R}{\gamma'_R} - \gamma'_E \mu_E \tag{4}$$

The partial factors γ'_X are expressed by:

$$\gamma'_R = 1/(1 - \alpha_R \beta V_R) \tag{5}$$

$$\gamma'_E = 1/(1 - \alpha_E \beta V_E) \tag{6}$$

where V_X is the coefficient of variation σ_X/μ_X and α_X the sensitivity factor of the basic variable X:

$$\alpha_X = \sigma_X / \sigma_g \tag{7}$$

Since the basic variables are specified in design practice as the characteristic values (X_k) the theoretical partial factors γ'_X need to be adjusted by the factor μ_X/X_k to obtain the design function:

$$g_d = \frac{R_k}{\gamma_R} - \gamma_E E_k \tag{8}$$

This expression, which effectively represents the Load and Resistance Factor Design (LRFD) format, can be expanded to provide for the basic variables of material strength and the combination of all relevant action effects. In addition, provision needs to be made for model uncertainties of the functions for resistance, actions and action effects.

2.1.2 *Resistance modelling*

The reliability model for resistance can be expressed in general terms as a function of resistance parameter(s) of material strength (X) geometry (a) and model uncertainty (θ) as:

$$R = \theta\, R(X; a) \tag{9}$$

The corresponding design function can be expressed in the following format in terms of the partial factors for material strength (γ_m) and model uncertainty (γ_θ) respectively:

$$R_d = \frac{1}{\gamma_\theta} R\left(\frac{X_k}{\gamma_m}; a_k\right) \tag{10}$$

The partial factors needs to be adjusted from the theoretical values similar to that provided by Equation (5) for the characteristic strength; for model

uncertainty the theoretical factor (γ_θ) any systematic bias (b) should be accounted for as:

$$\gamma_\theta = \gamma_\theta^{'} / b \tag{11}$$

This elementary representation of structural resistance obviously masks a multitude of complications, such as differences in structural materials ranging from steel to soil, failure modes ranging from strength to stability, static to dynamic, ductile and predictable to complex and composite behavior, to name but a few failure characteristics.

2.1.3 *Action representation*

Effectively structural reliability is dominated by the time variant nature of actions on structures, both on the basis of environmental actions and loads deriving from occupancy and use. Although the sensitivity of performance to permanent actions (G) can be significant, modelling of variable actions (Q) is decisive not only for its reliability representation, but also in defining appropriate design situations which are sufficiently representative over the design life of the structure. Furthermore due to the time variance, the combination of different variable actions (Q_i) needs to be considered.

The main consideration for the proper representation of Q is therefore given in terms of the specification of the characteristic value, ($Q_{k,i}$), a combination factor (ψ_i) and partial factor (γ_i); all based on appropriate probability models for the extreme value tails of the actions:

$$E_{d,Q} = \sum \left(\gamma_i \psi_i Q_{k,i} \right) \tag{12}$$

The conventional approach taken for the combination of variable actions is to apply the so-called Turkstra rule, taking each variable action in turn as 'leading' ($Q_{k,1}$) with $\psi_1 = 1{,}0$ and $\psi_i \leq 1{,}0$ for the 'accompanying actions' ($Q_{k,i}$).

The combination of permanent and variable actions also needs careful consideration, however: Alternative options include a single expression as given by Equation (13) for example (see EN 1990 Expression 6.10), a dual expression (EN 1990 Expression 6.10 a&b; SANS 10160:2011) and an additional check for permanent actions only (ASCE-7).

$$E_d = \sum \gamma_{Gi} \cdot G_{k,i} + \cdots \gamma_{Q1} \cdot Q_{k,1} + \cdots \sum \Psi_{Qi} \cdot \gamma_{Qi} \cdot Q_{k,i} \tag{13}$$

Accidental actions (A), which are not expected to occur but for which provision needs to be made, become increasingly more important to modern structures. The accidental design situation is therefore typically treated through the direct stipulation of the (unfactored) design action (A_d), such as an earthquake with a 10% probability of occurrence over the design life of the structure.

2.1.4 *Consequence representation*

The expression of all the basic variables into a single performance function (Equation (1)) as basis for the derivation of a semi-probabilistic partial factor limit states function (Equation (8)) can be considered as a reliability kernel representing one specific situation. Extension of the reliability kernel to provide for the full scope of a standard or suite of standards requires the setting up of a reliability framework for all classes of situations. Typically a specific limit state function needs to be stipulated for each case of element of the reliability framework.

Traditionally the reliability framework for design standards is based on advances in the identification of specific situations that need to be accounted for. The introduction of the limit states design approach requiring differentiation between the ultimate and serviceability limit states is a case in point (conceptually allowable stress design is based on a single case for design verification).

A more fundamental view is to base the reliability framework on a risk metric for structural performance, expressed in terms of the expected value of the consequences of failure:

$$Risk = \mathrm{P_F}\, \mathrm{C_F} \tag{14}$$

The probability of failure ($\mathrm{P_F}$) is represented by the reliability kernel, either to be calculated in accordance with Equation (1) or verified to comply with a target level of reliability through Equation (8). Such verification is therefore based on a set of stipulations for quantitative procedures.

The consequences of failure ($\mathrm{C_F}$) are treated by a system of classification to represent a specific set of consequences which are respectively sufficiently homogeneous to be served by a single performance function. The set of consequence classes $\{\mathrm{C_{F,i}}\}$ should correspond with the scope of application of the standard(s).

The representation of a risk based set of consequence classes can then be considered as a management scheme to complement the quantitative verification procedures. This complementary scheme provides a reliability framework, based on the standardized consequence classes, from which optimal target levels of reliability are derived. Additional requirements related to the reliability framework include structured schemes for levels of competence and experience for design and construction and the associated levels of quality management, even requirements for structural integrity or robustness.

The advantage of formulating the reliability framework is that both the scope of application of

the standard is considered from a reliability perspective, all possible situations are provided for and that the consequences of failure are critically evaluated.

The formal treatment of both elements of the risk metric given by Equation (14) contributes towards improving the rational basis of design for sufficient levels of structural performance.

3 STANDARDIZED RELIABILITY

The concepts of reliability given above serve as the basis for semi-probabilistic design procedures incorporated in recent limit states design standards such as Eurocode and the South African Loading Code SANS 10160:2011. The leading International Standard ISO 2394 *General principles on reliability for structures* not only provides the norm for the application of reliability concepts, but also reflects its evolution since the first publication as ISO 2394:1973. The main steps in the evolutionary process consist of the following:

- Edition 1 (1973): A minimal outline of the semi-probabilistic design verification that is based on the principles of reliability is specified, consisting of safety expressed as $R^* \geq S^*$; with design values of resistance (R^*) and load effects (S^*) each expressed in terms of characteristic values (X_k) and coefficients (γ_m). The standard is envisaged to be used by standards committees, with adaptation for each material. The appropriated degree of safety should be derived from cost optimization.
- Edition 2 (1986): Extensive elaboration of the basic concepts given by the 1st Edition is provided; limit states principles are extended to include design situations; extended treatment of basic variables include the classification of actions, material properties and geometry; consideration of analysis and testing; design format for action combinations and resistance, including partial coefficients; provision for structural integrity to limit the effects of local failure due to extreme conditions or human error and provision for quality control.
- Edition 3 (1998): Upgraded presentation of the normative standard is provided; extended to include provision for differentiated cause, mode and consequences of failure; definition of fundamental concepts include the formal representation of reliability in terms of probability; guiding annexes on reliability principles, actions and combinations, quality management.
- Edition 4 (2015): Completely revised version taking a fundamental approach derived from principles of risk optimization to derive a three tier decision making and design scheme of risk based, reliability based and semi-probabilistic design; enhanced logic from high level principles towards implementation format; extensive array of guiding annexes on quality management, lifetime integrity, testing, geotechnical structures, calibration, robustness, risk based life safety.

The 3rd Edition can be regarded as the basis for present standards, whilst the 4th Edition needs to be critically assessed for its implications for future development. Furthermore, ISO 2394 should be considered both in terms of peer standards and of operational standards which implement its principles.

3.1 *Present reliability practice*

ISO 2394:1998 can be regarded to standardize the principles of reliability from which present semi-probabilistic basis of design standards are derived. The Eurocode basis of design standard EN 1990:2002 is the primary example of design rules based on these principles. The close relationship between ISO 2394:1998 and EN 1990 is reviewed by Vrouwenvelder (1996). Conceptually the Probabilistic Model Code of the Joint Committee on Structural Safety (JCSS-PMC:2001) feeds into ISO 2394:1998 in spite of the inverse sequence of publication. The South African head standard to the loading code SANS 10160–1:2011 is derived directly from EN 1990, but adjusted to South African conditions and scaled down to the limited scope of buildings and similar structures.

Consistency in the value chain of the standards from the JCSS-PMC → ISO 2394 → EN 1990 → SANS 10160 can only be maintained on the common principles of reliability as outlined above. The chain can be characterized to consist of the pre-normative set of reliability principles and models from the JCSS-PMC; that can be fed into the structured set of reliability principles of ISO 2394; expressed in operational terms that can be applied directly in the design process across a wide range of conditions, structure classes, structural materials, even regulatory environments as given by EN 1990; scaled down to a specific set of conditions for a given country, with an associated improvement of operational suitability for day to day use as given by SANS 10160-1.

Various standards can be identified somewhere along the reliability value chain. The Canadian standard CSA S408:2011 falls somewhere between ISO 2394 and EN 1990, providing guidance to standards committees on the development of reliability based limit states design standards. Commentaries included in ASCE-7 on *Minimum Design Loads for buildings and Other Structures* and AIJ *Recommendations on Loads for Buildings*in Japan

are examples of the reliability basis for national standards.

3.2 *Risk basis for design standards*

Whilst concepts of structural reliability was sufficiently mature to be standardized effectively in ISO 2394:1998, this stage have only been reached more recently for the application of concepts of risk and risk based optimization (Faber 2015). Indications of such advances are given by the publication of JCSS *Risk Assessment in Engineering* (2008) and ISO 13824:2007 *Risk Assessment in Systems involving Structures*. Background on the revision of ISO 2394 to incorporate risk principles is summarized by Faber (2015). An overview of the completely revised standard is provided byPhoon and Retief (2015) as elaborated by Retief and Dithinde (2015), including an assessment of the implications for standardized semi-probabilistic design.

The fundamental principles of ISO 2394:2015 is that structural performance shall be based on optimized total risk which incorporates consideration of safety derived from marginal life-saving principles at societal level and economic optimization at facility level. Accordingly three levels of decision making and design are introduced, namely:

i. Direct application of a risk based approach; decision making based on optimal societal and economic risk.
ii. Reliability based approach base decisions on target reliability; it can be applied when the consequences of failure is understood sufficiently to be treated by categorization.
iii. Semi-probabilistic procedures for design may be followed if, in addition to failure consequences, uncertainty representation such as for failure modes and all basic variables are understood sufficiently well to ensure that reliability of structural performance can be achieved.

Due to the conditions set for the use of the more approximate procedures, the following cascade of applications can be identified:

a. Reliability based approach: Targetreliabilities need to be derived from risk optimization for given categories of failure consequences.
b. Semi-probabilistic approach: Reliability elements such as partial factors and the specification of characteristic values need to be calibrated, using the reliability approach for given categories of design situations and failure modes.

Central concepts of structural reliability based decision making and design that are treated both through normative stipulation and informative guidance, include the following: Based on the need to account for all uncertainties of relevance to structural performance, classes of uncertainties and the associated knowledge are identified; expressed in terms of Bayesian probability for the combination of information from various sources and for updating.

Decision making should be based on consideration of the service life of the structure, which is defined in terms of the need for the structure.

Quality management play a central role in the performance of structures and shall be completely integrated in the decision making process.

Requirements for robustness and damage insensitivity necessitate a structured approach ranging from risk-based assessment to standardized procedures, depending on consequence considerations.

Models for structural analysis as basis for design procedures and the associated model uncertainties are formally integrated in the reliability scheme.

The role of testing to complement or replace standardized design procedures are allowed, with the requirement that equivalent levels of reliability should be achieved.

Basic and alternative operational formats for semi-probabilistic design verification procedures are acknowledged. The most significant fundamental requirement for this approach is that full account must be taken of the consequences of failure, the associated design situations and the nature of failure when defining the basis of design for this approximate approach.

Effectively this inverts the traditional approach taken in the development of reliability based design which improves experience and judgment based procedures through an incremental introduction of reliability based modelling and calibration.

3.3 *International basis of design*

The more fundamental formulation of reliability principles in ISO 2394:2015 increased the need for a harmonized international standard to present a common basis of design that can be adopted nationally, or serve as direct reference for a national operational head standard, similar to the function of EN 1990.

Although ISO 22111:2007 *Basis of structural Design: General Requirements* nominally serve such a function, there is a need to update this standard firstly to account for the revised ISO 2394:2015 and secondly to strengthen its harmonization to similar standards internationally, such as EN 1990, ASCE-7, CSA S408, AIJ-R and AS/NZS 1170.

Accordingly ISO TC98 established a Working Group on the revision of ISO 22111 in 2014. The basis for the revision and working program was approved by the WG at a meeting in Vancouver BC, Canada in July 2015.

An important issue to settle is the balance or tradeoff between generality and operational use and

adoption of the standard. EN 1990 and ASCE-7 can be regarded as examples of the two extremes.

4 EXAMPLES OF RELIABILITY BASED STANDARDS DEVELOPMENT

4.1 *Eurocode based South African Loading Code*

The first formal consideration of Eurocode for use in South Africa was made by considering Eurocode 7 around 1993. By 1995 it was realized that the South African loading code SABS 0160:1989 would need to be revised to obtain compatibility with the Eurocode basis of design in order to proceed along this route. Accordingly, the South African National Conference on Loading held in 1998 served to initiate such a revision. This process is recorded by Day (2013).

Based on access that was given to Eurocode CEN TC250/SC1 by the chairman Prof Haig Gulvanessian in 2002, trial implementation of the action combinations schemes allowed by EN 1990 to a South African Loading Code could be investigated. Consistency that could be achieved between South African practice and EN 1990 resolved the issue of the potential implementation of Eurocode 7 in this country.

Additional trial implementations of Eurocode standards for imposed loads, wind and crane induced loading were made. This resulted in a decision to use appropriate Eurocode standards as reference for a completely revised and extended South African standard, published as the South African National Standard Series SANS 10160:2011. This standard is sufficiently compatible with Eurocode to be considered as a *concise version*, implemented outside Europe. Full account of the background to SANS 10160 is provided by Retief and Dunaiski (Eds. 2009) and Retief (2015).

4.1.1 *Basis of design—action combinations*

The action combination scheme used in the previous South African Loading Code SABS 0160:1989 was similar to the scheme used by ASCE-7 at that time, employing a load case consisting of permanent action only to provide for situations with dominant permanent actions. Allowance of the modified application of EN 1990 Expression 6.10a (6.10a-mod) bridged the gap between Eurocode and South African practice. Whilst the action combination scheme could be made consistent with Eurocode options, a smooth transition from existing practice was obtained. The revised scheme consisted of maintaining the 1989 primary action case (STR) as the equivalent to EN 1990 Expression 6.10b. Provision for the case where the permanent action is dominating (STR-P) is made by a simplification of Expression 6.10a to provide for only a single variable action.

Following an initial assessment of the reliability performance of the alternative Eurocode options and South African applications (Holický and Retief 2005), a systematic assessment of the {STR; STR-P} scheme was made (Retief and Dunaiski 2009). The assessment consisted of parametric investigations of the reliability performance of the scheme in comparison to Eurocode options; based on a target reliability $\beta = 3{,}0$; previous probability models for permanent and variable (imposed and wind) actions and generic resistance.

A convenient way in which to assess the reliability performance of alternative design functions is to compare the global safety factor GSF_k as the ratio of characteristic resistance R_k to total action (G_k+Q_k) to obtain the target reliability to the value provided by the design function.

GSF_k is shown graphically in Figure 1 for imposed loads as a function of the ratio (χ_k) of variable to total action $Q_k/(G_k+Q_k)$ for distribution parameters for the basic variables given in Table 1.

The alternative action combination schemes are shown as linear functions of GSF_k versus χ_k for the partial factors given in Table 2. Sufficient reliability is obtained where the GSF_k value of the design function exceeds that for the target reliability. This representation provides a convenient way in which to make a technical analysis of alternative action combination schemes and how they can be adjusted through the selection of partial factors.

The comparison shows that the combination of SABS'98 and STR would be similar in format to that of EN 1990 6.10a-modified and 6.10b; however, STR-P which is similar to 6.10a improves the representation of the reliability objective for operational values of χ_k, which are typically less than 0,66 (or $Q_k < 2G_k$).

Based on similar comparisons and reliability assessments, adjustments for the relevant target reliabilities for reliability classes and for resistance could be obtained. Reliability representation of wind actions is considered below.

4.1.2 *Wind actions*

Although it was accepted that EN 1991–1–4 on wind actions represented an advanced standard, adaptation to South African conditions and design practice nevertheless provided quite a challenge (Goliger 2005). From a reliability perspective, some of the issues included consideration of the scope of application, the target level of reliability, general reliability models for wind loading procedures, including the characteristics of the local climate and reasonable consistency with the previous standard.

In accordance with the scope of SANS 10160, provisions for wind loading was limited to buildings and similar industrial structures for which static equivalent procedures can be applied. Back-

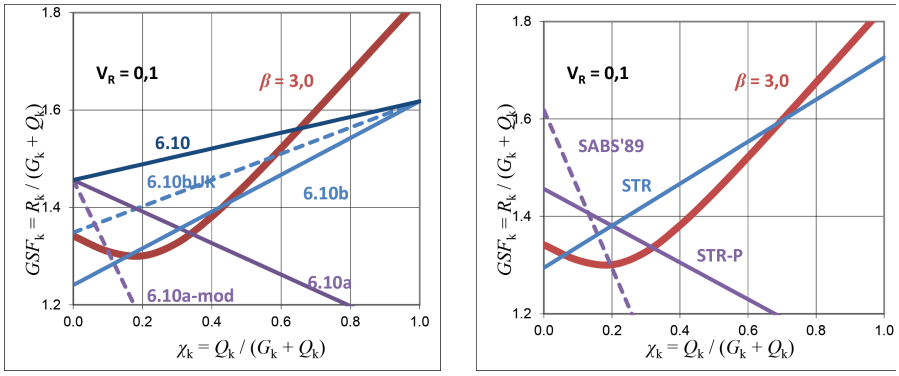

Figure 1. Comparison of action combination schemes for EN 1990 and SANS 10160.

Table 1. Reliability models for basic variables.

Basic variable		Distribution	μ_X/X_k	σ_X
SANS 10160:2010 Calibration				
G	Permanent	Normal	1.05	0.1
Q_I	Imposed	Gumbel	0.96	0.24
Q_W	Wind	Gumbel	0.5	0.35
R	Resistance R_k = EXP(−1,64V_k)	Log-Normal	1.18 1.39	0.1 0.2
Alternative models for wind				
Q_W	Eurocode (Holický)	Gumbel	0.7	0.35
	Revised (SA)	Gumbel	0.9	0.35

Table 2. Format and partial factors for action scheme.

Format	γ_G	γ_Q	γ_R		
EN 1990			EXP($\alpha_R\beta V_R$) / R_k		
6.10	1.35	1.5	β	$V_R = 0.1$	$V_R = 0.2$
6.10a	1.35	1.05			
6.10a-mod	1.35	0	3.0	1.08	1.16
6.10b	1.15	1.5			
6.10bUK	1.25	1.5			
SANS					
STR/wind	1.2	1.6/1.3	3.8	1.15	1.32
STR-P	1.35	1.0			
SABS'89	1.5	0			

ground investigations indicated that the new procedures will lead to significant increases in loading. The most significant increases result from changes in pressure coefficients, which were accepted as the representation of advancement of the procedures and were implemented accordingly.

Provisions for terrain roughness also resulted in some increase in wind loads, which were not implemented. A temporary fix was used to provide for thunderstorm strong winds, resolving to include provisions for gust representation together with an update of the South African strong wind climate and map (Kruger et al. 2012, 2013).

The investigation of the South African strong wind climate mainly focused on resolving the different wind generating mechanisms (Kruger et al. 2012), its implications on extreme value models, the compilation of geographically based probability models (Kruger et al. 2013; Retief et al. 2013) and the subsequent derivation of a design wind map. Based on these and additional investigations, an extensive comparison of the wind climate and damage characteristics of Poland and South Africa is reported by Goliger et al. (2013).

4.1.3 *Wind load reliability modelling*

The reliability assessment of provisions for wind loading given by SANS 10160 as adapted from EN 1991-1-4 provide an example of the nature of reliability based modelling and its application in standardized procedures that ranges from technical analysis to judgment based codification and decision making.

Figure 2 presents the comparison of the design functions {STR-P; STR; 6.10b} for two cases of structural resistance with a coefficient of variation of V_R (a) of 0.1 and (b) 0.2 respectively; with partial factors given in Table 2. The reliability model, labelled as $\beta = 3.0$ (0.7) is given by Holický (2009) as used for Eurocode calibration.

The relatively low value for the partial factor for wind loading $\gamma_{Q,W} = 1.3$ was originally derived from the wind load reliability model labelled $\beta = 3.0$ (0.5) as shown in Figure 2(a). It was nevertheless decided to maintain the value for $\gamma_{Q,W} = 1.3$ in the light of the general increase in wind loading based on the revised provisions. The design function Expression 6.10b is labelled accordingly in Figure 2, as calibrated to $\beta = 3.0$.

A series of investigations was launched to update probability models for wind loading that could be used for the recalibration of wind loading provisions

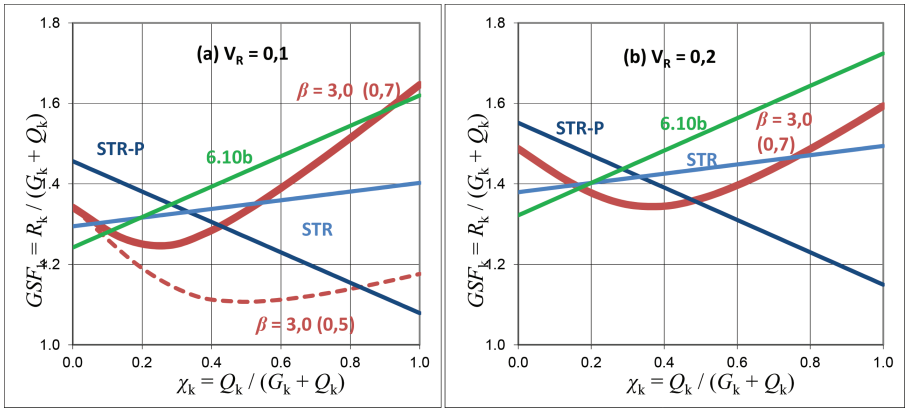

Figure 2. Reliability assessment for EN 1990 and SANS 10160 provisions for wind actions.

for SANS 10160. This investigation runs in parallel with a reassessment of models used for Eurocode. Initial results consideration the time variant component for wind loading and for the time-invariant components such as terrain effects and pressure coefficients are reported by Botha et al. (2015).

The results already indicate substantial changes to the design wind map and reliability models, based on the additional data, its analysis, subsequent reliability models and indicative calibration.

4.2 *Adaptation of Eurocode standards*

The first step in the adaptation of Eurocode to SANS 10160 for actions on buildings was the selection of appropriate standards. This included standards relevant to the scope of the 1989 standard, consisting of provision for imposed, wind, crane and seismic actions. The extended scope included the provision of a dedicated basis of design, geotechnical actions, thermal actions and actions during execution; the basis of design for the accidental design situation was incorporated in the head standard. A selection was therefore made of nine parts from EN 1990, EN 1991, EN 1997 & EN 1998.

Fundamental modifications in the transfer from Eurocode to SANS 10160 are recorded by Retief & Dunaiski (2009) and include:

- The scope of application was limited to building structures; design procedures were limited to non-specialist applications, for example by excluding dynamic response from wind loading procedures and limiting crane configurations to those generally used in the country.
- In addition to including provisions for local conditions, local design practice was also provided for.
- Sufficient information on local conditions was given for designers to be able to refer to advanced Eurocode procedures, but by requiring specialist input. Wind loading again provides examples of special consideration of local mixed climate conditions of thunderstorm meso-climate together with synoptic storms. Sufficient local information is provided to use Eurocode procedures for dynamic wind load effects.
- In the basis of design, all calibrations were done in accordance with established target levels of reliability, generally expressed by β_T = 3.0 (see Eq. 2 & 3).
- Action combination schemes were simplified to a more basic interpretation of the Turkstra rule. The limited range of variable actions to be considered, allowed for the simplification of the elaborate scheme of combination factors stipulated in EN 1990. The absence of snow loading and the treatment of seismic loading as an accidental design situationallowed for such a simplification. Accordingly only the case of irreversible serviceability was distinguished from other serviceability limit states.
- No separate part on the treatment of accidental actions was included in SANS 10160; however, the basis of design for the accidental design situation (presented in EN 1991–1–7) was incorporated in part 1 as the head standard. In this manner provision was made for robustness as the situation for unidentified accidental actions.
- An innovation introduced in SANS 10160 was the inclusion of a part on the geotechnical basis of design and actions related to buildings. In the absence of a South African geotechnical design standard, this part allows the use of Eurocode 7 under local conditions and requirements. It also includes a selected GEO & STR action combination scheme, in accordance with Design Approach 1stipulated by EN 1990.

– An effort was made to unify the various classification schemes used across SANS 10160, including reliability classes, consequence classes, quality management levels, seismic importance classes, geotechnical categories and crane classes. On the basis of the upper and lower consequence classes used by Eurocode, a four level scheme was used.

4.3 *Principles of standards development*

The function of standards for structural design is generally accepted as a statement of requirements, serving to fulfil its regulatory function. It also provides acceptable standardised procedures to assist practitioners to demonstrate compliance to the requirements.

The view of standards in terms of their technical formulation of verifiable requirements is however not sufficient to explain the process of standardisation of structural design. A more general perspective of the process is needed. An evident issue is the motivation for the development of standards, which subsequently provides the driving force of such development. Particularly the resources for such development and ownership of the standard become relevant. Related issues include the scope of a standard and its relationship with other standards; the level of advancement of the procedures; the degree to which provision is made for local conditions, design and construction practice.

Based on the experience with transferring parts of Eurocode to a South African standard led to the formulation of the principles of standards development that could be applied to initiate and manage such a process (Retief & Wium 2012). In the scheme the technical characteristics of standards are related to its meta-technical properties such as the function of a standard. Another technical characteristic is its function and relationship to the design process and to other standards that are typically used in the design of a given structure.

This includes standards on the basis of design, the various actions and multiple design standards for the various structural materials; notably geotechnical design to provide for foundations.

Attributes were identified that serve to provide the driving potential for their development, such as the interests of various stakeholders, the authorities and value added by the process of standardization, the technology base and its advancement caused by the development and various strategic and operational objectives.

These concepts were illustrated by an assessment of Eurocode and the South African standards development, from which guidelines were derived for establishing a South African approach (Wium et al. 2014).

5 MODEL UNCERTAINTY AND RELIABILITY

The significance of model uncertainty associated with the structural mechanics models on which design procedures are based, often serves as motivation for reliability investigations that are discussed here. Model uncertainty for both action and resistance models can rank in importance with that of the uncertainty (epistemic) and variability (aleatoric) probability dispersion of basic variables. The general practice followed presently of using nominal representation of model uncertainty in calibration of design procedures clearly is in need of being strengthened and improved by explicit treatment and use. Furthermore, model factor assessment provides an opportunity to fully utilize test results not only in reliability calibration, but also in the assessment and improvement of alternative structural mechanics design models.

5.1 *General methodology*

A general methodology for the treatment of model uncertainty for use in reliability assessment has been developed (Holický et al. 2015) based on a number of investigations on its role in wind and crane induced actions, pile foundations, concrete shear resistance and cracking.

The following steps should be considered when the model uncertainty for a specific theoretical model is investigated, as based on a dataset of test results for the model:

- Characterization of the assessment to determine the scope of investigation;
- Dataset of test results, either as a dedicated investigation or from a compilation of diverse tests;
- Compilation of a database of model uncertainty observations; statistical assessment of the dataset to derive a suitable probability model for the model factor θ;
- Application of the model considering its operational use;
- Further investigations including acquisition of new test data or use of a more advanced model, where warranted.

In addition to the quality assessment of the physical observations (meta-data in statistical terms), the set of model uncertainty observations $\{\theta_i\}$ shall be analysed using basic methods of mathematical statistics. This includes consideration of the following:

- Unbiased sampling of model factor observations, considering bias introduced by the specific objectives of test campaigns.
- Representativeness of the sample space of test results (Λ_O) in comparison to the design population space (Λ_d) in terms of both basic variables and design parameters.
- Correlation between model factor observations and variables indicate a lack of proper account being taken of the variable in the model, both in terms of trend and scatter around the trend.
- Outliers have a significant influence on the calculated model factor statistics; careful assessment should be made to differentiate between errors and true observation of extreme cases.
- Sample statistical moments serve as estimators of distribution parameters, including estimates of the mean which could represent bias of the model; dispersion representing uncertainty; skewness which may be important for extreme value models.
- Statistical uncertainty needs to be taken into account, particularly for a limited dataset and higher moment estimates.
- Although suitable probability distributions can be established by testing for goodness of fit, standardized distributions such as normal, lognormal or extreme value functions are often pre-selected.

5.2 *Classification scheme*

A classification scheme for the relative importance of model uncertainty provides a convenient framework for its assessment and application in reliability based procedures. The following classification scheme is provided by Holický et al. (2015) and Retief (2015):

5.2.1 *Nominal effect*

Partial factors for basic variables are adjusted to provide a nominal contribution of model uncertainty; for guidance, this approach could be followed when the FORM sensitivity factor (see ISO 2394:2015 and EN 1990:2002) for model uncertainty is less than $0.4 \times 0.8 = 0.32$.

This approach is typically taken across a general class of conditions, for example differentiating only between models for permanent and variable actions; or for the resistance of structural materials. Examples of investigative use are given by Dymond et al. (2009) for crane loading; McLeod et al. (2012, 2013) for concrete cracking.

5.2.2 *Significant contribution*

The contribution of model uncertainty is sufficiently significant to justify a separate partial factor, typically with a sensitivity factor between 0.32 and 0.8; considering importance of model uncertainty to be equivalent to the basic variables. Explicit provision for model uncertainty allows for differentiation between various failure modes, execution process, levels of approximation for the resistance of a specific material class or proneness to local instabilities.

Fields of application include bending or shear, rolled or welded steel sections, ordinary- or high-strength concrete and different classes of steel cross-sections. Investigations on the time-invariant component of wind load reliability models represent an example (Botha et al. 2015).

5.2.3 *Dominant role*

Limitations of functions to comprehensively predict structural resistance in operational terms result in model uncertainty to be the dominating factor, even for routine situations included in standardized design procedures. Special attention to the assessment of model uncertainty is then required to ensure the economic attainment of sufficient reliability.

Example investigations include design functions for pile foundation resistance (Dithinde et al. 2011, Dithinde & Retief 2013, 2014).

5.2.4 *Advanced investigations*

Model uncertainty investigations can be applied diagnostically to explore the effectiveness of deriving simplified design procedures and of the theoretical model as such. Alternative methodologies can be based on the three sets of information of

i. The test dataset;
ii. The prediction model;
iii. Reliability representation.

Conventional model assessment as described above consists of the combined set {(i) & (ii)}. Reliability calibration consists of combining {(ii) & (iii)}. Interrogation of {(i) & (iii)} reveals bias, trends and uncertainties. Ultimately the combined set {(i), (ii) & (iii)} can be used with model building.

Investigations on the shear resistance of reinforced concrete sections which required the implementation of alternative models provide a basic example of an advanced reliability based assessment of model uncertainty (Mensah et al. 2013a, 2013b).

6 OBSERVATIONS AND CONCLUSIONS

A number of investigations on the reliability performance of structures are presented in this paper, primarily with a view to illustrate the use of the reliability approach to advance standardized structural design. Although the individual investigations represent elements of an overall scheme of reliability based design, it also reflects progression not only in such application, but also in the conceptual basis from international standardization to the refine-

ment of specific models and basic variables. The review presented here is admittedly biased towards the author's involvement in the process, but nevertheless touches base with trends in general.

A summary of the various components of reliability based design is provided by way of conclusion, more or less ordered in a top down manner:

- The foundation of reliability based design has been advanced formally to being derived from optimal risk which fully account for the consequences of failure through the publication of ISO 2394:2015. The JCSS RAE (2008) serves as reference base for the risk concepts on which the new standard rests. Although concepts of risk assessment is provided by ISO 13824:2009, there is a potential for upgrading this standard to serve as the first in line of a series of international standards on the basis of structural design.
- The clear distinction between risk based, reliability based and semi-probabilistic design, strengthened partial factor limit states design as a practical and operational approach to be incorporated into design standards: Fundamental procedures are now stipulated as basis for target reliabilities for clearly defined classes of failure consequences, leading effectively to risk optimization. A distinction is made between societal and economic risk considerations. Reliability based calibration of all design parameters follows logically to serve as input to semi-probabilistic design procedures.
- There is a need to revise the present ISO 22111:2007 to serve as an international standard that implements the principles of ISO 2394:2015 in operational semi-probabilistic procedures that are internationally harmonized with Eurocode and equivalent national standards, primarily for use by countries that import standardization practice.
- Eurocode demonstrates the ability to achieve harmonization and unification across a wide range of countries and their conditions and practice, a comprehensive scope of standards for actions and materials based resistance, for the full scope of structures for buildings and civil engineering works through the head standard EN 1990.
- The reliability basis of design serves to adapt Eurocode to the needs of a country like South Africa, providing for scaling of scope, level of application, local conditions and practice, including safety levels.
- At the same time the extended reliability framework is transferred through the introduction of various classifications if limit states, reliability and consequence classes; the supporting role of quality management; access to background models that can be used and adapted for calibration purposes.
- The pragmatic scheme devised as basis for converting parts of Eurocode to the South African standard can be generalized to identify the attributes of design standards that serve as driver and motivation for campaigns of standards development and management.
- In addition to the recalibration of action combination schemes to improve the consistency of achieved reliability, probability models for actions were updated and improved, ultimately to be fed back into the calibration process. This was done for example for wind and crane induced loading.
- Similarly the reliability assessment of structural resistance not only improves the basis for the calibration of design models, but also enhances insight into design models and their limitations. Examples include pile foundation resistance models and calibration and the shear resistance of structural concrete.
- In addition to deriving specific and generic probability models for uncertainties of the design models, investigations demonstrate the utility of a reliability based approach to assess and improve structural mechanics functions and procedures, from which sound model building procedures can be devised.

In conclusion it can be claimed that on the one hand the risk and reliability basis for structural design has reached a level of maturity that contributes decisively to standardized design practice, but on the other hand there is still a wide scope for development and modelling that should close the gap between the high level principles and properly calibrated design procedures.

Although there is an extensive body of cases and examples for quantitative design elements such as partial factors, there is an emerging need for the rational representation of the consequences through the proper stipulation of the reliability framework, which is of the nature of a qualitative technical management scheme.

REFERENCES

AIJ-R (Undated). Recoomendations for loads on buildings.Architectural Institute of Japan.

AS/NZS 1170.0:2002. Structural design actions Part 0: General principles.Sydney: Standards Australia.

ASCE SEI 7-10 (2010) Minimum design loads for buildings and other structures. American Society of Civil Engineers.

Botha J, Retief JV, Viljoen C (2015). *Variability of time independent wind load components*. 12th International Conference on Applications of Statistics and Probability in Civil Engineering, ICASP12 Vancouver, Canada.

CSA S408:2011. Guidelines for the development of limit states design standards. Canadian Standards Organization.

Day, P.W. 2013.A contribution to the advancement of geotechnical engineering in South Africa.DEng dissertation, Stellenbosch University.

Dithinde M, Phoon KK, De Wet M, Retief JV (2011). Characterization of model uncertainty in the static pile design formula. *ASCE Journal of Geotechnical and Geoenvironmental Engineering*, Vol 137, No 1, pp 70–85.

Dithinde M, Retief JV (2013). Pile design practice in southern Africa: I Resistance statistics. *Journal of the South African Institute of Civil Engineering*, Vol 55, No 1, pp 60–71.

Dithinde M, Retief JV (2014). Resistance model uncertainty factors for ultimate limit state design of pile foundations. *Journal of the South African Institute of Civil Engineering.*Vol 56, No 2 pp 37–42.

Dymond JS, Retief JV, Dunaiski PE (2009). Reliability assessment of crane induced actions. In Retief & Dunaiski (Ed) *Background to SANS 10160* Sun Media, pp 297–306.

EN 1990:2002. Basis of structural design.CEN, Brussels.

EN 1991-1-7 (2006).Accidental actions. CEN, Brussels.

Faber, M.H. (2015). Codified risk informed decision making for structures. SRES 2015, Hangzhou, China.

Goliger, A, Zuranski, J., Gizejowski, M., Gaczek, M., Retief, J., Kruger, A., Dunaiski, P., Fiszer, S., Cwik, M. 2013. *Comparative study between Poland and South Africa: Wind climates, the related damage and implications of adopting the Eurocode for wind action on buildings.* Archives of Civil Engineering, LIX, 1, 2013, pp 51–95.

Goliger, A.M. 2005. *South African wind loading specifications: the Euro way?* Naprsteck J & Fischer C (Ed) 4th EACWE, Prague.

Holický M, Retief JV (2005). *Reliability Assessment of Alternative Load Combination Schemes for Structural Design.* Journal SAICE, Vol. 25, No 1, pp 15–20, 2005.

Holicky M, Retief JV, Sykora M, (2014). *General approach to model uncertainty.* Proceedings 12th International Probabilistic Workshop, Bauhaus University Weimar, pp 99–109.

Holicky M, Retief JV, Sykora M, (2015). *Assessment of model uncertainty for structural resistance.*Accepted by Probabilistic Engineering Mechanics Journal, Elsevier.

Holicky M, Sykora M, Barnardo-Viljoen C, Mensah KK, Retief JV (2013). *Model uncertainty in reliability analysis of reinforced concrete structures.*SEMC 2013. Cape Town.

Holický, Milan (2009). Reliability analysis for structural design. SUNMeDIA, Stellenbosch. ISBN 978-1-920338-11-4.

Huber UA, Retief JV, Wium JA (2004). *Structural concrete shear resistance*. Conference: Developing Concrete, Midrand, South Africa, pp 113–125.

ISO 13824:2009, *Bases for design of structures—General principles on risk assessment of systems involving structures.* ISO, Geneva, Switzerland.

ISO 22111:2007. Bases for design of structures—General requirements.ISO, Geneva, Switzerland.

ISO2394:1973/1986/1998/2015. General principles on reliability for structures.ISO, Geneva, Switzerland.

JCSS (2001).Probabilistic Model Code.http://www.jcss.byg.dtu.dk/Publications/Probabilistic_Model_Code.aspx.

JCSS RAE. 2008. Risk Assessment in Engineering, Joint Committee on Structural Safety. Faber, M.H. (Ed), http://www.jcss.byg.dtu.dk/Publications/Risk_Assessment_in_Engineering.aspx.

Kruger A.C., Retief, J.V., Goliger, A.M. 2013. Strong winds in South Africa. *Journal of the South African Institute of Civil Engineering.*Vol 55, No 2, pp 29–58.

Kruger, A.C., Goliger, A.M., Retief, J.V., Sekele, S. 2012. Clustering of extreme winds in the mixed climate of South Africa. *Wind and Structures Journal* 2012; 15(2): 87–109.

McLeod C, Wium JA, Retief JV (2012). Investigation of reliability model for cracking in South African reinforced concrete water retaining structures. 10th IPW Stuttgart, Germany, IGS 2012: 141–155.

McLeod CH, Retief JV, Wium JA (2013). *Reliability of EN 1992 crack model applied to South African water retaining structures.* SEMC 2013.2-4 September 2013, Cape Town.

Mensah KK, Retief JV, Barnardo-Viljoen C (2013a). *Eurocode 2's Variable Strut Inclination Method for shear, it's modelling uncertainty and reliability calibration.* fibSymposium. Tel Aviv, Israel.

Mensah KK, Retief JV, Barnardo-Viljoen C (2013b). *Reliability based application of Eurocode 2's Variable Strut Inclination Method for shear.* ICOSSAR 11. New York NY.

Phoon K.K., Retief J.V. (2015). ISO 2394:2015 Annex D. Georisk, Vol9, No3, 125–127.

Retief JV, Wium JA (2012). *Principles and application of structural design code development in South Africa*. Structural Engineering International 2012; 22(2): 182–189.

Retief, J.V. & Dithinde, M. 2015.General principles on reliability according to ISO 2394.Chapter 2 in Phoon & Retief (Eds) Reliability of Geotechnical Structures in ISO 2394.Taylor and Francis, in press.

Retief, J.V. & Dunaiski, P.E. (Editors) 2009.Background to SANS 10160.Sun Press. ISBN 978-1-920338-10-7.

Retief, J.V. & Dunaiski, P.E. 2009.The limit states basis of structural design for SANS 10160-1. Chapter 1–2 in Background to SANS 10160.Sun Press.

Retief, J.V. 2015.Contributions to the implementation of the principles of reliability to the standardized basis of structural design.DEng dissertation, Stellenbosch University.

Retief, J.V., Barnardo-Viljoen, C., Holicky, M. 2013.*Probabilistic models for the design of structures against wind loads.*SEMC 2013.2–4 September 2013, Cape Town.

SABS 0160:1989. Code of practice for the general procedures and loadings to be adopted in the design of buildings.SABS, Pretoria, South Africa.

SANS 10160–1:2011. Basis of structural design.South African National Standard, SABS, Pretoria, South Africa.

Vrouwenvelder, T., (1996). Revision of IS 2394 General principles on reliability for structures. IABSE Reports, 74(1966), 117–118.

Wium JA, Retief JV, Viljoen C (2014). *Lessons from Development of Design Standards in South Africa.* 37th IABSE Symposium, 2014, Madrid, Spain.

Recent Progress in Steel and Composite Structures – Giżejowski et al. (Eds)
© 2016 Taylor & Francis Group, London, ISBN 978-1-138-02946-0

Recent steel structures in Poland—the selected projects

K. Żółtowski
Gdansk University of Technology, Gdansk, Poland

T.W. Siwowski
Rzeszow University of Technology, Rzeszow, Poland

ABSTRACT: The paper presents selected examples of recently completed steel structures in Poland. These are roofs over sport stadiums, construction of public buildings and bridges. Described examples do not exhaust the acquis in the field of steel constructions in Poland. The authors, however, may hope that the presented constructions represents current achievements in Poland in the field of steel structures.

1 INTRODUCTION

The current decade in Poland is rich in construction activity in public space. EU financial programs have created a new area for the development of transport infrastructure mainly in roads and bridges. An important sport event for the construction industry was also Euro 2012. This one of Europe's biggest sporting events generated funds for the construction of new football stadiums and accompanying infrastructure. Improving the country's wealth also enabled the implementation of a number of construction projects in a public space.

The paper presents selected examples of steel structures completed recently in Poland. They were functionally divided into stadiums, sports arenas, railway stations or passenger terminals and bridges. Presented structures are always the result of a combination of steel and concrete, but steel plays there a key structural and architectural role.

2 LARGE ROOFINGS (WRITTEN BY K. ŻÓŁTOWSKI)

2.1 *PGE Arena in Gdansk*

The stadium which was built for UEFA EURO 2012 in Gdańsk is the biggest sport arena in the city. Its architecture refers symbolically to a piece of amber over seashore. As a result of a building process a complex structure composed of steel and concrete was built. According to UEFA standards, the stadium was planned to hold ~41000 people. The most spectacular part of the stadium is a steel roof and facade structure. Its characteristic shape and transparent cladding in tones of yellow shows the architect's vision mentioned before—a lump of amber (Fig. 1). The main structure of the roof is composed of 82 steel, sickle shape space truss girders connected together by a circumferential structure. Typical girder is made of tube profiles and stand on a 7 m high concrete ring. The steel roof (Fig. 2) is statically and structurally independent of the concrete part. The height of the construction is about 38 meters, measured from bearing to the roofing surface. The length of the cantilever over the tribune is about 48 meters, measured from bearing to the edge of the roof (centre ring).

The main radial girders (Fig. 3) are placed around the stadium at the distance of circa 8 meters. The framework of a single girder is made of welded steel tube profiles. The top and bottom chords are tubes of 355.6 mm in diameter and varying thickness. They are connected by horizontal tubes: top $-\phi$219.1 mm, bottom $-\phi$355.6 mm. Diagonal members of the truss are tubes of 219.1 mm in diameter and thickness of 8 mm. The girders are connected

Figure 1. PGE Arena (bieg 2012.pl, euro.gdansk.pl).

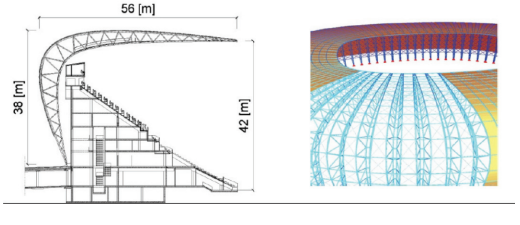

Figure 2. Roof construction. Static model (SOFiSTiK).

to each other by several horizontal rings made of circumferential tubes. Additional X bracings made of tension rods in the system X are implemented in every field between each girder. Thanks to the stiffening system, the roof works as an quasi-dome with the hole in the centre.

The roof elements were prefabricated as flat members in a workshop and assembled on site to space parts. The erection of the roof was divided into 6 phases (Fig. 4):

1. Installation of temporary supports,
2. Installation of a facade girder part,
3. Installation of a roof girder part,
4. Installation of circumference bracings,
5. Exemption from temporary support,
6. Installation of sheathing and peripherals.

The cladding of the roof, designed as a membrane made of polycarbonate, is supported by a special alu-minium sub construction. (Fig. 5) The roof is equipped with inspection platforms, rainwater drainage system, snow fences, lighting installation, four media screens, sound system and other equipment

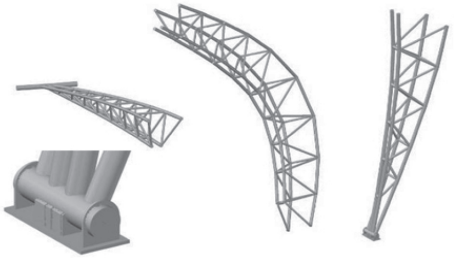

Figure 3. Main parts of a single girder.

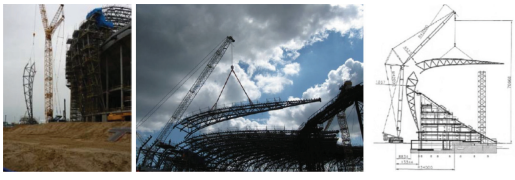

Figure 4. Installation of facade and roof parts of girder.

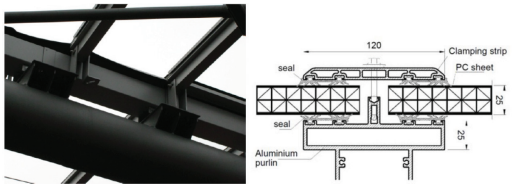

Figure 5. Aluminum sub construction.

Steel consumption was ~7200T.

Architect: Rhode—Kellermann—Wawrowsky, Düsseldorf. Structural consultant: KBP Żółtowski Gdańsk. Contractor: Hydrobudowa Polska, Alpine Bau.

2.2 *National stadium in warsaw*

Multifunctional sports arena with 58500 sits. Most spectacular and statically independent is steel elevation combined with suspended pre-stressed cable roof (Fig. 6).

The design of the facade symbolizes weaved wicker basket. Roof structure is referring to idea of a bicycle wheel and keeps the balance of forces between the outer steel structure and the inner tension ring and radial cables. Roof is composed of 72 quazi radial cable girders (Figs. 7, 8, 9, 10). Central, removable part of the roof membrane consists of a radial cables centered in the spectacular needle (Fig. 11). Needle is carrying overall ~190T of a retractable membrane storage system and broadcasting facilities. Roof covering is made of glass fiber–PTFE membrane.

Steel consumption~14000T.

Figure 6. Warsaw stadium (wikipedia.pl, popcorn.pl).

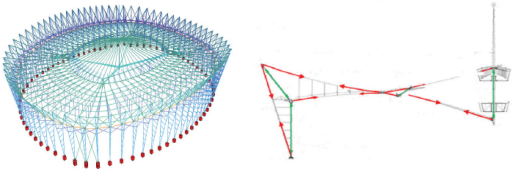

Figure 7. Static system and cross section with tension-compression schema.

Figure 8. Compression ring in workshop and during erection.

Figure 9. Steel roof supporting structure and facade.

Figure 10. Cable net and cast steel clamp.

Figure 11. Central needle node and retractable roof.

Architect: GMP International, JSK Architekci, Schlaich Bergermann und Partner.

Contractor: Alpine Bau, Hydrobudowa Polska SA.

2.3 *Silesian stadium in Chorzów*

Silesian Stadium in Chorzów is a multifunctional sports facility with a long history. Since 2009, the stadium is not used because of the ongoing modernization. One of the most spectacular elements of the new stadium is its roof (Fig. 12).

Silesian Stadium roof structure is based on the idea of a bicycle wheel. The main parts of the structure are two compression rings, one tension ring and forty radial cable girders placed all around. Cable girders consist of a prestressing cable (lower), suspension cable (upper) and hangers between them (see Fig. 13). Compression rings and connecting them columns are made of a steel box sections (Fig. 15), while the inner (tension) ring is composed of eight circumferential cables and connected with cable girders by custom designed steel clamps. The lower compression ring is based on forty reinforced concrete pillars by radial bearings. Roof covering is made of transparent polycarbonate panels which are laid on secondary steel girders.

The construction works were stopped due to the failure. During lifting of a cable structure two cast steel clamps were broken (Fig. 14). Official works related to the explanation of the causes of failure

Figure 12. Silesian Stadium. Architectural vision.

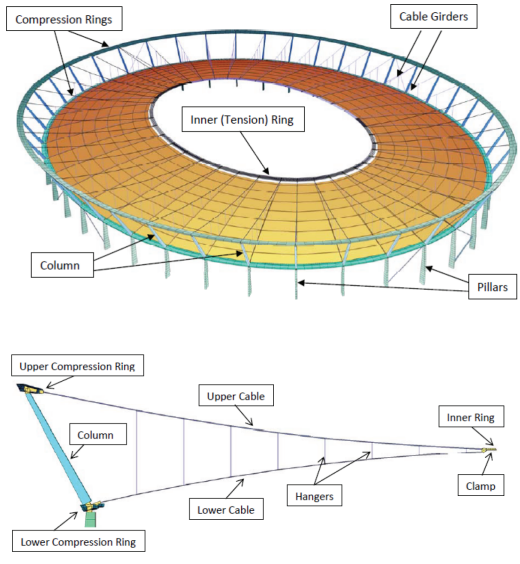

Figure 13. Visualization of FEM model and major elements of structure.

Figure 14. Broken cast steel clamps.

and global safety checking of construction halted construction process for more than two years.

Finally roof structure was completed in December 2015. Failed clamps were replaced by a new welded (Fig. 16). Lifting procedure and installation of substructure for polycarbonate cladding were finalized without further problems (Fig. 17).

Figure 15. Steel structure (stadiony.net).

Figure 16. New clamp on tension ring.

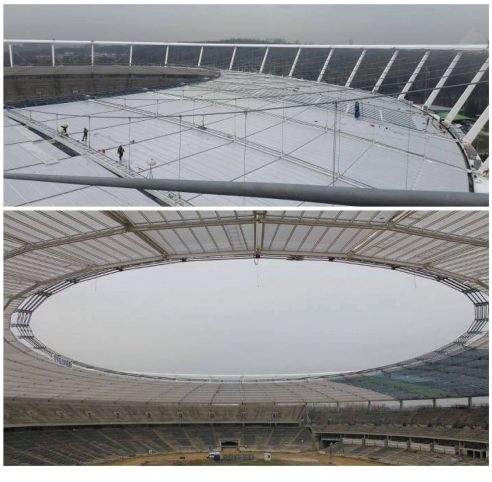

Figure 17. Roof surface. Top and bottom view (stadiony.net).

Steel consumption: ~10500T.

Roof surface: 43000 m^2.

Architect: GMP International, Schlaich Bergermann und Partner.

Contractor: HOCHTIEF, Mostostal Zabrze, Pfeifer.

2.4 *Roof over Tauron Area in Kraków*

Tauron Arena in Kraków is the biggest and the most modern enclosed entertainment and sport venue in Poland. Main building was constructed as a concrete. Elevation and roof structure were designed as steel structures (Fig. 18).

Most spectacular is a roof structure. Its idea is based on construction of bicycle wheel. Circular roof contains 20 radial girders composed of prestressed cables and truss elements. Span of the roof is 128,4 m, and the maximum structural height is 15,0 m (Fig. 19).

Figure 18. Tauron Arena in Kraków (wikipedia.pl).

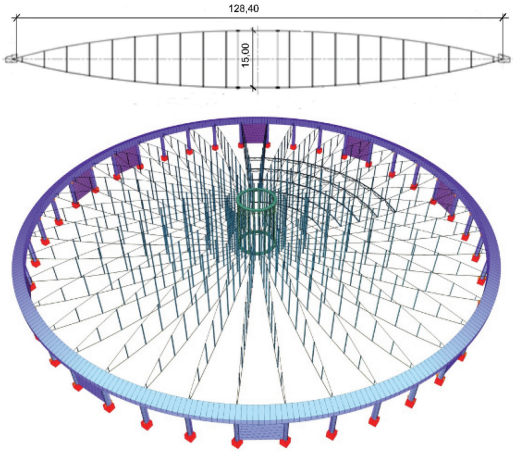

Figure 19. Arenas roof. Main dimensions and FEM model.

Cable structure of the roof is based on concrete compression ring. Radial cables are concentrated in the center of the roof by an internal ring structure (Fig. 20,21,22).

Architect: Perbo-Projekt Kraków, Modern Construction Systems Poznań.

Contractor: Mostostal Warszawa S.A., Acciona Infraestructuras S.A., Mostostal Puławy S.A. i Asseco Poland S.A.

Subcontractor for roof structure: B7, Mosty Gdansk.

2.5 *Roof over railway station Łódź Fabryczna*

The new three-storey building will be a key element of the New Centre of the city of Łódź. On the second level, placed 16.5 meters below ground, will be placed train station with four platforms and eight lanes (Fig. 23).

The main entrance to the building and internal passage is pleased at street level. Most characteristic features will be restored walls of the old railway station Łódź Fabryczna. Everything is covered by spectacular steel-glass roof. Recently steel structure with glass sheathing is ready but still final activities in construction are going on.

The overall dimensions of skylight is 40.7 m to 384 m. The cross section of the roof is a parabola with a span of max. 40.7 m and a variable height. Steel-glass structure is divided to three separated parts (Fig. 23). West part with global width of 86.4 m is reinforced by external prestressing and cable-stayed system (Fig. 24).

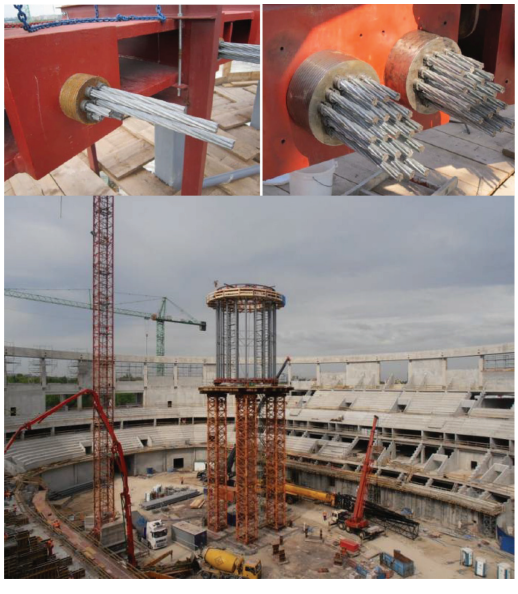

Figure 20. Anchor head of upper and lower radial cables and central ring structure (110 T weight).

Figure 21. Cable structure after lifting and prestressing and installation of the substructure of the roof.

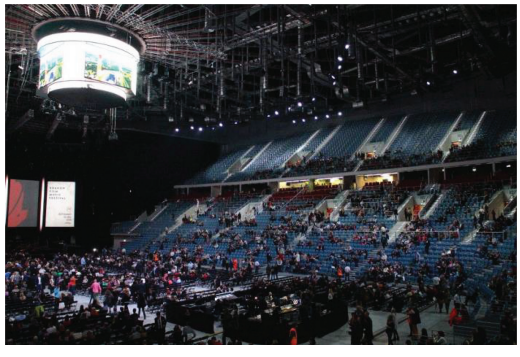

Figure 22. Tauron Arena inside (musictothepeople.pl).

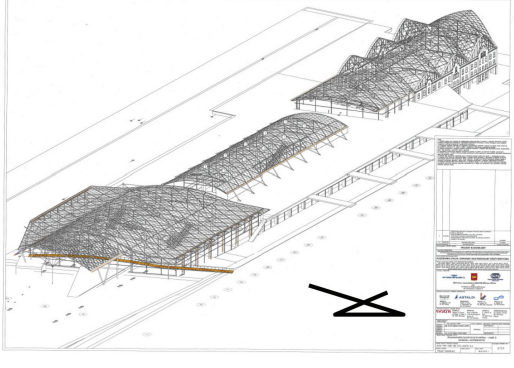

Figure 23. General layout of structure—axonometric view.

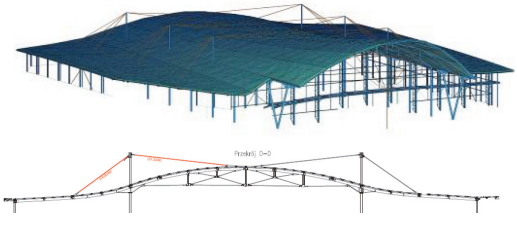

Figure 24. FEM model of west part and cross section.

The central part has constant shape with span of 40.7 m. In the eastern part, steel roof is composed with a replica of the facade of the old building of the station. Design corresponds with historic vault.

All structure was constructed from tube profiles. All joints are fully welded. Prestressing and cable-stayed system was designed as steel rod structure (Fig. 25).

Selected parts of final structures are presented bellow (Figs. 26, 27).

Steel consumption: ~1800 T. Designer: Systra S.A.

Figure 25. Steel welded join and prestressing.

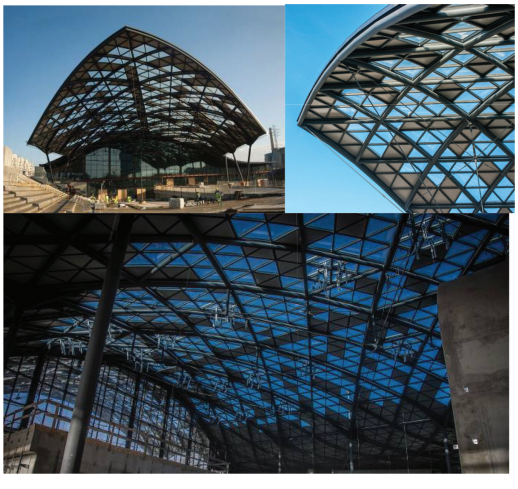

Figure 26. West building—December 2015 (face-book.com/KlubFotograficznyPL).

Figure 27. East building—December 2015 (face-book.com/KlubFotograficznyPL).

Contractor: Torpol-Astaldi-PBDiM-Intercor.

Subcontractor for steel works: Zeman HDF, M. Rabijasz.

2.6 *Terminal T2. Lech Walesa airport in Gdansk*

Terminal T2 (Fig. 28) is a key element of the development of the Airport in Gdańsk. The building is designed as a open space hall, which has three floors above ground and one underground. Building is constructed as a combination of concrete and steel structures. All space over terminal facilities is covered by steel roof based on structural columns. The outer walls of the building (facades) are designed too as steel structure.

Steel roof trusses were prefabricated in workshop, assembled onsite, erected to final level and placed on temporary supports. (Fig. 29). In second stage columns were assembled and connected witch trusses. After installation of purlins and bracings

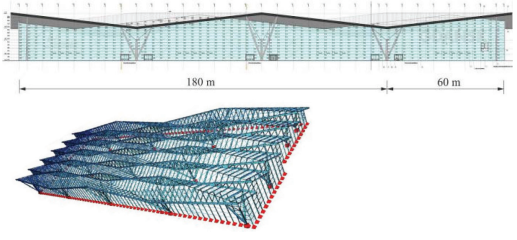

Figure 28. Terminal T2. Elevation and FEM model.

Figure 29. Terminal T2. Construction stage.

Figure 30. Terminal. Final stage (wyborcza.pl, naszemiasto.pl).

Figure 31. Terminal. Final stage (wyborcza.pl, naszemiasto.pl.

structure was freed (Figs. 30, 31). Building was designed by JSK Architekci and constructed by Budimex and NDI.

3 BRIDGES (WRITTEN BY T. SIWOWSKI)

3.1 *Beam and box girder bridges*

Due to the Polish topography and the medium size of main rivers and another obstacles to be crossed with bridges, most of these structures are designed as a beam and box girder bridges. In the range of small- and medium-span bridges, multi-beam steel–concrete composite decks consisting of high-strength hot-rolled girders have been recently introduced as an economical and interesting alternative to traditional pre-stressed concrete solutions. The use of reinforced concrete cross-beams at the supports allows for a further optimization because of the easy and simple construction. This deck typology is now becoming a common solution for many standard bridges in Poland.

One of the most recent example is the WD-7 viaduct on Sucharskiego Route in Gdańsk (Fig. 32), where high-strength steel HISTAR 460 rolled steel beams in a VFT technology was used, quite an innovative feature for medium-span bridges in Poland. The viaduct consists of two lanes corresponding to a deck width of 11.2 m. Its total length of 170 m is divided into five spans between 30 and 40 m. The sections delivered to the construction site were 41 m long, eliminating the need for any welding on site. After adding the pre-cambering, the finishing involving welding the necessary reinforcing plates to the lower flange in the support area, the end plates, shear studs and painting were also completed at the plant. Once the beams with the prefabricated slab forming a stay-in-place formwork are positioned correctly on the supports, the 0.25 m RC deck was poured on the slab. The pre-fabricated composite beams are joined at the intermediate piers through a transversal reinforced concrete beams. Designer: Europrojekt Gdańsk.

For longer spans the welded steel box girders are often used for creation the aesthetic and reliable bridge structures. Thanks to their slenderness, high torsion resistance and closed form of a girder, steel box bridges have been designed particularly in the cities. One of such examples is the Castle Bridge in Rzeszów (Fig. 33), the five-span continuous structure with lengths of $2 \times 44.0 + 3 \times 28.0 = 172.0$ m and with the box-girder composite superstructure. The total width of the deck is 21.0 m. The superstructure is made up of three steel box-girders with the depth of 1.5 m and axial spacing of 6.4 m, composite with RC deck slab 0.25 m thick. In the main span the superstructure is supported with three RC arches 50.0 m in length. The arches are founded on diaphragm walls creating together a rigid frame structure. The required street level, local terrain configuration as well as architectural requirements made the arches relatively flat (f/l = 1/5.8).

With the architectural constraints relating to the arch cross section, it caused a very dense reinforcement mesh which was the main reason for SCC application for arch construction. At those days (2002) it was one of the largest world structural applications of SCC for bridge structures. Moreover, anticorrosive concrete with migrating corrosion inhibitors was applied in the safety barriers. Designer: Promost Consulting, Rzeszow.

The longest steel box-girder bridge built recently in Poland is the Marie Curie Bridge over the Vistula River in Warsaw (Fig. 34). The 10-span bridge

Figure 32. Two VFT girders made of rolled beams (left) and the WD-7 viaduct (right).

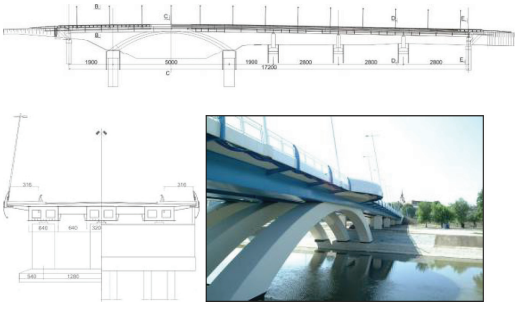

Figure 33. Longitudinal view (top), cross-section (bottom left) and general view (bottom right) of the Castle Bridge.

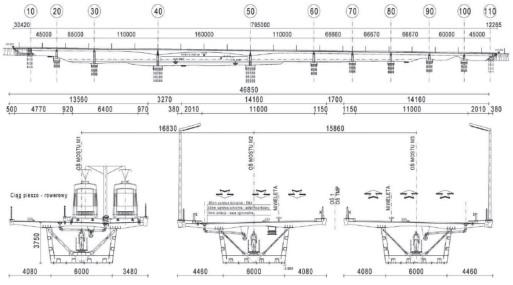

Figure 34. General view (top) and cross sections (bottom) of the Marie Curie Bridge.

with a total length of almost 800 m are designed as composite steel-concrete structure. The length of the bridge spans is 45 + 65 + 110 + 160 + 110 + 3 × 66.67 + 60 + 45 = 795 m. The structure actually consists of three parallel bridges, two for road vehicles and one for tram, bicycles and pedestrians. The total width of the road bridges is 2 × 14.2 m and of the third bridge – 13.6 m. The cross-section of the spans is haunched having the structural depth at the river piers 9.0 m and in the middle of the main span (and approaching spans) 3.75 m. The superstructure was made of S 355 J2 steel as a fully welded one chamber box-girder for each bridge. The steel boxes have inclined webs with the angle of 7.7° outwards and the distance of 6.80 at the top. The bridge deck was made of C 35/45 concrete without any technological or structural prestressing. Three various construction methods were used for steelwork erecting. Spans between supports 10 and 30 and were assembled by mobile cranes, between 30 and 60 with heavy lifting and finally between 60 and 110 with incremental launching method. Designer: Schuessler-Plan Inżynierzy, Warszawa.

Recently the same type of steel box-girder structure has been built over the Vistula River in Połaniec, where the project included bridge with the total length of 955 m and span lengths: 3 × 5 5 + 110 + 160 + 110 + 5 × 60 + 2 × 55 = 955 m. This structure is the two carriageways road bridge with the total deck width of 15 m. Incremental launching in approaching spans and heavy lifting in the central span over the river were used for bridge steelwork erection. Designer: Schuessler-Plan Inżynierzy, Warszawa (Fig.35).

3.2 *Truss bridges*

Steel truss bridges were the most popular structures for the Polish long bridges just after the Second World War, when the huge restoration of the Polish road and railway infrastructure was needed and performed. Most of the bridges over two Polish biggest rivers, i.e. Oder and Vistula were designed and constructed as a continuous steel truss or a series of simply supported truss spans. Between 1950s and 1970s more than 20 long truss bridges were built with the total length more than 500 m. Nowadays the steel truss bridges are very rare option for road administration, mainly because of economical and aesthetic reasons. Only from time to time the typical Warren trusses are used in the ongoing rehabilitation projects on the Polish railway network. Therefore in this sector of bridge engineering only one modern and innovative structure can be emphasized in the recent years. The road bridge over the Bug River in Brok (Fig. 36) is a six-span continuous structure consisting of two Warren type truss girders. The total length is 402.2 m, including 6 spans: 58 + 3 × 69 + 88 + 49 m. The total width of the bridge is 13.1 m. The superstructure consists of two fully welded truss girders with parabolic lower chord, operating in fully composite action with a reinforced concrete upper deck slab, post-tensioned with cables in piers areas. The truss steelwork was erected by assembling the steel elements on erection stays, enabling the additional slab prestressing with level adjustment during concreting. A very low steelwork consumption for a bridge of this class was achieved, only 210 kg/m^2. Designer: Pomost Warszawa.

3.3 *Arch bridges*

In contrary to truss bridges, arch bridges have become very popular structures in the recent years

Figure 35. The Marie Curie Bridge (left) and heavy-lifting of the central span of Połaniec bridge (right).

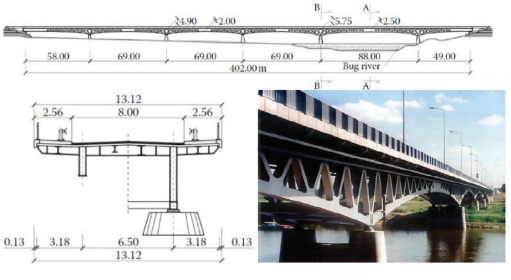

Figure 36. Longitudinal view (top), cross-section (bottom left) and general view (bottom right) of the bridge over the Bug.

in Poland. Hundreds of medium size arch viaducts have been built over the Polish motorways and expressways since 2000. Most of them are the steel tied arch bridges with post-tensioned concrete or composite deck slab to carry the thrust. These arch bridges are designed as a through arches mainly in *Langer* or *Nielsen* type (vertical or inclined hangers, respectively), but recently *the network arches* have been becoming more popular option. However, there are some of modern arch bridges with untypical shape of steelwork or with the considerable total length, which are worthy to mention in this review.

The Kotlarski Bridge over Vistula river in Kraków (Fig. 37) is a spatial, simply supported steel structure, composed of four (two internal and two external) "lens" arch girders and an orthotropic deck. Girders consist of upper parabolic arches and bottom circular arches, with different elevations for the internal and external ones. Effective distances between the arch centre lines are 18.0 m and 14.0 m, so with a span of 166 m that gives the slenderness ratio L/f equal to 9.2 and 11.8. The bridge is a very wide structure a total of 36.8 m.

The deck supporting the carriageways, tram and sidewalks was constructed as a steel orthotropic plate composed of 12 mm sheet plate, longitudinal channel ribs and transversal I beams, supported on longitudinal main beams placed at the girders' plane. Main beams are connected with upper arches by means of hangers and with bottom arches with I-shape pillars. Main steel arches were designed as closed boxes with overall dimensions of 950 × 2000 mm for the upper arches of the internal girders and 950 × 1600 mm for the remaining upper and bottom arches. The arch bracing for both upper and bottom arches, are *Vierendeel* type, with an extra strengthened portal (gantry) frame. Transversal upper bracings are in the form of an arch. The bridge erection process was divided into two stages. In the first stage, the bottom arches and deck were merged together and incrementally launched to its final position. In the second stage, the upper arches, bracing and hangers were erected. The bottom arches and deck were merged on the erection bed on the right river bank and then launched "stage by stage" onto temporary supports constructed in the midstream to the final position. Designer: Transprojekt Kraków.

The first Polish large network arch bridge was built over the Dziwna River at Wolin (Fig. 38). The total length of the structure is 1112 m. This multispan bridge consists of three types of structures divided into five parts connected with expansion joints. The main span over a river is a steel tied network arch 165 m long. The span consists of two inclined steel box arches with a rise of 24 m and a composite deck. The arches are box girders measuring 1.8 × 1.0 m connected by seven transverse piped braces. The deck grid binding the arches is formed of two outside beams, one central stringer, and traverse beams. The traverse beams have cantilevers beyond the outline of the bridge and the hangers are attached to them. The closed ropes constitute the suspension. The thrust of the arch

Figure 37. Longitudinal view (top), top view (bottom left) and deck view (bottom right) of the Kotlarski Bridge.

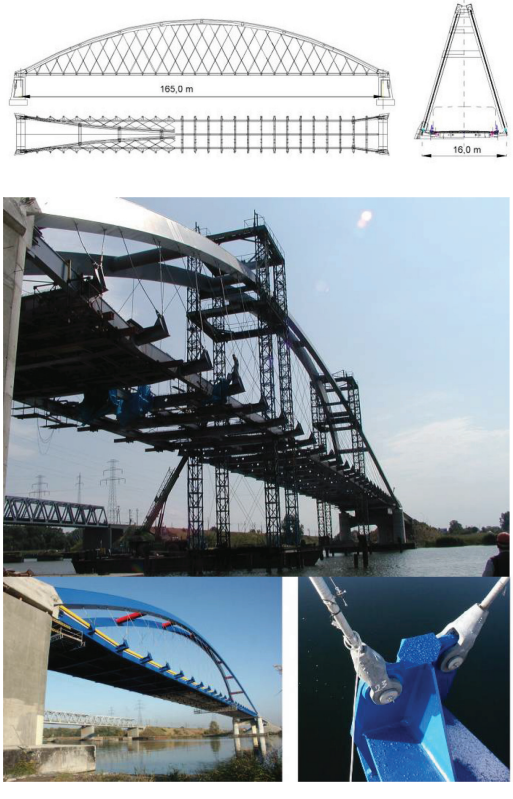

Figure 38. Arch bridge over the Dziwna River at Wolin.

is transferred by six external cables of size 37 L15. The prestressing force is greater than the thrust of the arch and causes prestressing of the reinforced concrete deck slab. The arch span was assembled using temporary supports. Designer: Transprojekt Gdański.

The bridge over the Vistula River in Puławy (Fig. 39) is the second longest arch bridge in Poland. The total length of the bridge is 1038 m. It is a continuous 14-span structure with spans of $44.0 + 3 \times 56.0 + 6 \times 64.0 + 80.0 + 212.0 + 80.0 + 44.0$ m, with the longest arch span crossing the riverbed. Rise of the arch over the roadway is 24.0 m. Two inclined toward the bridge axis arch girders have a rhomboidal box cross-section, varying from 2.5×3.0 m over the support to 2.5×2.0 m in the crown. The arches are braced by transverse box struts. Tie beam consists of four plate girders of a constant height of 3.0 m grouped in two tandems (two plate girders spaced at 2.5 m in each tandem) with spacing of 12.5 m. The girders are braced by crossbeams with regular spacing of 4.0 m. The deck is a steel-concrete composite structure. The reinforced concrete deck slab has a thickness of 0.25 m. The deck of the main tied through arch span is suspended by 28 vertical hangers. Each hanger consists of four tension bars with a diameter of 81 mm anchored in the crossbeam and in the webs of the arch using fork connectors. Spacing of the hangers is 12.0 m, their length varies from 3.5 to 24.0 m. Steel deck of the main span was constructed using two auxiliary supports situated in the river. Segments of the arches (each of them was divided into three units) were assembled on the riverside. Each segment was then launched on trolleys along the tie beam into the final position, lifted, supported by assembly towers and joined by welding. The reinforced concrete deck slab was cast after installation of hangers. Designer: Pomost Warszawa.

The longest Polish arch bridge was built two years ago over the Vistula River in Toruń (Fig.40). The bridge in Toruń consists of the following

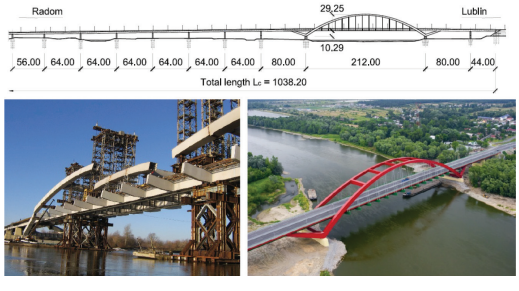

Figure 39. Longitudinal view (top), arch assembling (bottom left) and general top view (bottom right) of the bridge in Puławy.

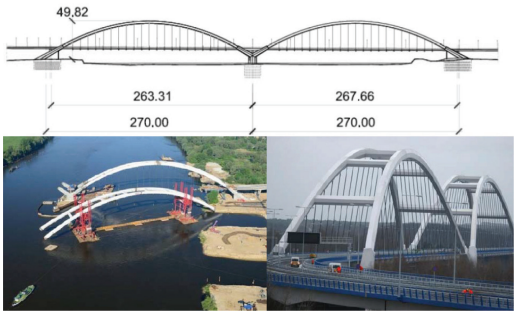

Figure 40. Longitudinal view (top), arch assembling (bottom left) and general view (bottom right) of the bridge in Toruń.

structures: right riverside flyovers with a length of 221.7 m + 279.5 m, two span arch bridge with a length of 540.0 m and left riverside flyovers with a length of 435.3 m + 394.9 m. The main bridge is a half-through fixed arch structure with two spans of 270.0 m. Central support is situated on an artificial island in the middle of the riverbed. Steel arch girders, designed as hexagonal box section with dimension of 2.5×3.0 m, are inclined to the axis of the bridge and braced by six transverse struts. The deck with a height of 3.0 m is a steel orthotropic plate consisting of closed ribs under the road pavement, open ribs under the sidewalks, longitudinal beams and transversal crossbeams suspended to the arches. Total width of the deck carrying two carriageways and sidewalks is 24 m. The arch spans were constructed in the following stages: construction of foundations including central support located on the artificial island, erection of concrete arch bases, assembly of arch segments on the construction site located on the river bank, water transport of assembled arches of weight of 3000 tons each, placing the arches on the concrete bases of supports and welding the joints (the arches are fixed in the supports) and finally assembly of 30 m long deck segments in the direction from the supports towards the center of the span. Designer: Pont-Projekt Gdańsk.

3.4 *Cable-stayed bridges*

The modern cable-stayed bridges have been started to be built in Poland since 1990s only after overthrowing a former communist regime. Since then more than 10 quite long cable-stayed bridges have been built in the biggest Polish cities. Two of them were built in Warszawa, two in Wrocław, its own landmark bridges have got also Gdańsk, Płock, Przemyśl, and most recently Rzeszów. One of the biggest bridge of this kind is now under construc-

tion in Kraków. Except for two bridges in Wrocław, the rest of them have got a steel or steel-concrete composite superstructure. The two most representative examples are presented below.

The John Paul II Bridge in Gdańsk is the first Polish modern cable-stayed bridge built after 1989 (Fig. 41). The bridge is a one-pylon structure with a main span of 230 m. The total length of the bridge is about 380 m. The composite bridge deck consists of two girders and a reinforced concrete deck slab with a thickness of 230 mm. The depth of the steel superstructure is 2.45 m. Each steel girder consists of two welded plate girders. Crosswise, the bridge deck is braced by steel crossbeam spaced every 4 m and 4.3 m. Total width of the bridge deck is 21.3 m. The width includes two two-lane carriageways each 7 m, a reserve lane (median strip) and service footways, each 0.75 m wide. The cable-stay system was designed as a semi-harp pattern of dense type with two-sided outside stays (two-planed). In the longer span, 15 stays were used, spaced every 12 m. In the back span 8 stays were used, spaced every 13 m. In the areas of the stays' anchorage in the pylon, additional strengthening was applied by means of steel frames, which enables the transfer of great tensile forces. The bridge erection on land was designed on scaffolding and on the river part, using the cantilever erection method. Assembly segments were subsequently lifted using the cantilever method and transported on barges on the waterway. They consist of a full composite section (steel girders and reinforced concrete deck slab). The assembly segment length was 12 m, and total weight of a single segment was about 2070 kN. Designer: BPBK Gdańsk.

The Solidarity Bridge over the Vistula River in Płock is so far the bridge structure with the longest span in Poland (Fig. 42). It was built as an alternative to the only existing rail-road bridge, built before the Second World War. The total length of the new bridge is 1200 m. It consists of two structures: main cable-stayed bridge over the riverbed with a length of 615 m and access flyover with a length of 585 m crossing left riverside flood plains. The cable-stayed bridge has the main span of 375 m and four back spans suspended by a single plane of stays (along the axis of the bridge) to two pylons. The fully welded steel superstructure of the main bridge is a three-cell box section with a constant depth of 3.6 m, a width of 27.3 m and inclined outer webs. Internal vertical webs form a central cell where the steel pylons are fixed and the anchor blocks are located. The deck is an orthotropic plate with closed longitudinal ribs under the roadway and open ribs under the sidewalks. Transverse bracing bars and sidewalk cantilevers are spaced every 3.75 m. Diaphragm plates are located above supports and in sections where the stays are anchored. Steel pylons with a height of 63.7 meters above the deck level are fixed in the superstructure. They have a rectangular cross-section varying from 3.75 × 2.25 m at the base to 3.1 × 2.2 m at the top. Anchorages are spaced every 6.25 m in the pylon and 22.5 m in the deck. The main span is

Figure 41. The John Paul II Bridge in Gdansk.

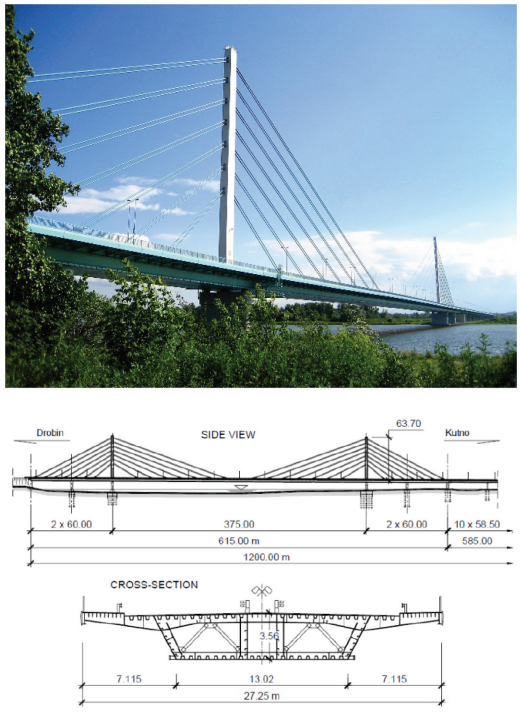

Figure 42. Solidarity Bridge over the Vistula River in Płock.

suspended to each pylon by seven pairs of harp-arranged cables. The number of backstays is the same. The length of the cables varies from 39 to 187 m. Superstructure of the main span was assembled with balanced cantilevering from both sides of the river. Preassembled segments with a length of 22.5 m and a weight of about 240 tons were transported on barges, heavy-lifted and welded to the previously erected steelwork. Designer: Budoplan Płock.

3.5 *Footbridges*

Steel is widely used in Poland for the construction of footbridges from the very large to the very small. It is a versatile and effective material that provides efficient and sustainable solutions. Modern steel footbridges taking advantage of the latest advances in automated fabrication and construction techniques are able to provide economic solutions to the demands of safety, rapid construction, aesthetics, shallow construction depth, minimal maintenance and flexibility in future use.

Due to specific requirements govern bridge design and construction in a city centers the urban footbridges often are to be quite unusual both structurally and technologically. Two such recent examples have been presented here (Fig. 43). The first example has shown how to solve the traffic problems in the city centre with the untypical steel structure. In order to separate pedestrian and vehicular traffic on one of the most crowded crossroads in the city and to enable the pedestrians to move in all directions, the circular form of the footbridge was proposed. The second example has presented the large arch steel footbridge which architectural shape, structural solutions and construction technology were strongly influenced by the location, i.e. a historical city centre. The most challenging part of the project was the footbridge assembly and erection using horizontal rotation method. Both examples proved to be sustainable for municipalities as well as attractive for city inhabitants, mainly due to very efficient use of steel.

The main function of the new footbridge in Rzeszów was to reorganize the traffic on the crossroad by separating pedestrians and vehicles. After a great number of functional, traffic and feasibility studies, the designers along with the municipality officers had decided, that the best form of the new footbridge was a ring, which enabled all existing and expected functions to fulfill and/or traffic flow directions to ensure. The circular footbridge is to serve as a specific pedestrian roundabout, raised 5.5 m above crossroad level. Its circular form makes possible to go upstairs from four sides of the crossroad, using stairs, ramps and elevators, located on the main existing pedestrian ways. It also enables to go downstairs in any point of the crossroad. The circular form also refers to *the agora* – the main city square—existing here in the past. The flat and lightweight structure is to give the impression of levitating ring, with no significant interference with a city centre panorama along the main avenue. Ramps and stairs create an elongation of existing footways—the type and color of their pavement materials are almost the same. The footbridge was built in the form of a ring with outer radius of about 40 m and service width of 4 m. The superstructure is made as a steel box girder with the depth of 0.65 m and the width of 4.0 m (Fig, 44). The box cross section is divided with 10 mm inner webs into four chambers and laterally stiffened with crossbeams (with 1.0 m spacing along the circle) and diaphragms (with 3.0 m spacing). The 12 mm upper deck plate is stiffened by the longitudinal (circular) T-ribs with the lateral spacing of 0.25 m. The bottom flange of the box girder is made of 12 mm plate without longitudinal ribs. Designer: Promost Consulting, Rzeszów.

The second footbridge spans two riverbanks of Vistula River in the historical city centre of Kraków. Designers were obliged to involve the remaining stone abutments and the system of historical embankments. Also one-span structure crossing the entire river bed without additional supports was required by the municipality. These limitations strongly influenced the architectural and structural form of new footbridge. The final proposal prepared by the architect presented key features, which had to be included in final design,

Figure 43. Two footbridge case studies: the circular footbridge in Rzeszów (left) and the arch footbridge in Kraków (right).

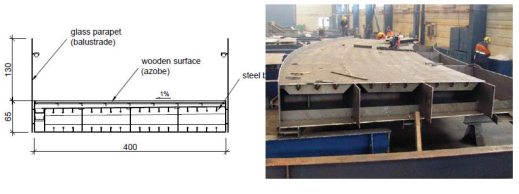

Figure 44. The superstructure: cross section (left) and steelwork in workshop (right).

f.e. low rise arch and split deck with leaf-like cross-beams/stringers skeleton and old stone masonry abutments incorporated into new footbridge. The footbridge is 148 m long tied arch steel structure with one main arch girder of circular cross section and twin suspended orthotropic steel deck covered with timber planks. With the arch radius of R = 170 m and the rise of 15.3 m, the structure is very slender with H/L = ~1/10 (Fig. 43,45). The arch girder is made of two steel tubes, the outer one with diameter of 2020 mm and the inner one with diameter of 1620 mm. Between both tubes the self-compacting concrete was poured. The twin steel deck with the total length of 137 m and the width of 2×3.0 m is suspended to arch girder by hangers with network arrangement. The network system for hangers along with horizontal bracing in deck level increased significantly the spatial stiffness of the span.

Two inclined hanger surfaces and the deck create very stiff triangular system, which enhanced the rigid body behavior of the superstructure. Additionally the steel deck is also fixed to RC abutments with 4.0 m tapered concrete brackets cast monolithically with the abutment bodies. The deck consists of the 508 mm diameter tubular cross beams, suspended directly to the arch with spacing every 5.0 m along the superstructure (Fig. 45). The 3.4 m wide steel orthotropic deck panels are supported on the cross beams and covered with exotic timber planks. The deck system is X-braced horizontally with 216 mm steel tubes. The external tie made of two 19×15.7 mm cables is situated under each deck part. The tie is anchored to the end cross beams and connected to RC abutment brackets.

The most challenging part of the project was the bridge assembly and erection. Vistula River had to remain open during construction because it serves as a navigation channel for tourist fleet and so conventional method on temporary supports founded in riverbed was questioned by the river navigation administration. Therefore it was decided to assemble the whole span on the right bank of Vistula River and to rotate it horizontally as a rigid body with help of floating support into its final position on the left bank abutment (Fig. 46). Designer: Consortium: Promost Consulting Rzeszów, KBP Żółtowski Gdańsk, Mosty Wrocław.

In recent years the trend toward innovative, exciting and adventurous steel footbridge design and construction has been clear in Europe. The both presented footbridges built recently in Poland seem to belong also to this group.

Moreover, dozens of steel footbridges have been built in Poland in recent years to serve on the new Polish motorway network. It seems that the main goal of making the motorways more attractive and promotion of the areas was achieved. These footbridges are recognizable from a distance by motorway users and serve as landmarks. Three of them are presented in (Fig. 47).

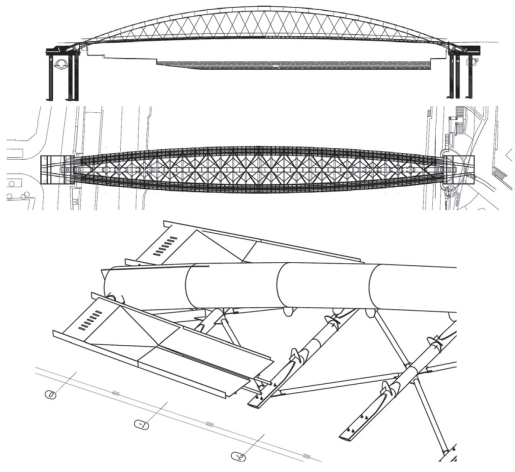

Figure 45. The footbridge structure: general layout and the twin steel deck scheme below.

Figure 46. The view of span rotation.

Figure 47. The Polish landmark steel footbridges—selected examples.

4 CONCLUSIONS

Design and production of steel structures has a big tradition in Poland. Great improvement in technology in steel structures comes from mining and shipbuilding industry. In XX century steel dominated in industrial and bridge building. Also spectacular other structures were built from steel.

Recently we observe a domination of reinforced and prestressed concrete but we are sure that steel will keep a good place in civil engineering in future. We hope that presented examples are a good proof of this thesis.

This page intentionally left blank

Recent Progress in Steel and Composite Structures – Giżejowski et al. (Eds)
© 2016 Taylor & Francis Group, London, ISBN 978-1-138-02946-0

Land-based supporting structures for wind energy converters

M. Veljkovic
Delft University of Technology, Delft, The Netherlands

C. Rebelo
ISISE, Department of Civil Engineering, University of Coimbra, Coimbra, Portugal

M. Pavlovic
Delft University of Technology, Delft, The Netherlands

ABSTRACT: A short state-of-the-art on design verification of supporting structures for wind energy converters is presented. On-going trend in building of land based wind farms is to install larger capacity wind energy convertors at the higher towers. Preliminary studies have indicated that use of higher strength steel (HSS) would be advantages in such applications. However, because of a rather low fatigue detail class of a ring flange connection which is traditionally used for in-situ assembling of segments to a tubular tower, the use of HSS is not justified. That was the main reason to search for an alternative in-situ connections. A possible solution is based on a single overlapping friction connection obtained by preloaded bolts and using open slotted holes. This connection is studied in RFCS research projects, HISTWIN and HISTWIN2, High-strenght tower in steel for wind turbines and Higher steel tubular towers for wind turbines (2012 and 2014), respectively. Parts of these results are presented here. Based on this research a new knowledge is gained to in order to optimize tower design and achieve economic benefits. A case study example of a real tubular tower is used to provide insight in real design values.

Other challenges that are associated with the tendency to build towers with higher hub heights are briefly discussed focusing on limits of tubular towers imposed by the traffic constraints. Finally, an outlook for innovation is shown providing an insight into the on-going research projects.

1 INTRODUCTION

The extraction of mechanical energy from a stream of moving air with the help of a disk-shaped, rotating wind energy converter follows the principle stated by Albert Betz in the 1920's. Betz's Elementary Momentum Theory follows elementary physical laws, that is, the mechanical energy extractable from an air stream passing through a given cross-sectional area is restricted to a certain fixed proportion of the energy or power contained in the air stream. Even with an ideal airflow and lossless conversion, the extractable mechanical work is limited to about 60% of the energy contained in the airflow. When the ideal power coefficient achieves its maximum value c_p = 0,593, the wind velocity in the plane of flow of the converter amounts to two thirds of the undisturbed wind velocity and is reduced to one third behind the converter.

The power that can be extracted by a Wind Energy Converter (WEC) under real conditions is dependent of the characteristics of the converter, e.g. horizontal or vertical turbine, number of blades, a yaw position of the nacelle and a position of the blade pitch. Multi-megawatt wind turbines are currently based on horizontal axis and three blade rotors. The increase of the rotor dimensions and the need for steadier and higher wind speeds requires the increase of the hub height. The electricity output of a converter is roughly proportional to the rotor area. The largest wind turbines today are 5–6 MW units, with a rotor diameter of up to 126 meters. Typical commercial wind converters have a capacity between 1.5 MW and 3 MW, installed on towers about 80–100 m height.

The location where the wind turbine is installed, daily/seasonal variation of the wind speed and the long term variations in wind speed over decades play decisive roles for success of the investments in a wind farm. The last one is not fully understood yet and needs multi-year monitoring to have proper prediction of the electrical energy possible to supply from a wind farm into the grid.

Wind energy facilities, so called a wind farm, consists of hundreds of converters in some cases. Like all power plants, the wind farms are characterized by a capacity factor. The capacity factor of a power plant is the ratio of actual energy output

to the theoretical output had the plant operated at full capacity over a given time period. Although for some wind farms the capacity factors as high as 45% have been reached, the wind energy industry considers capacity factors of at least 25% necessary for economically viable utility-scale facilities.

Tubular steel towers dominate market because of their production, execution and maintenance efficiency. They are transported in segments of about 20 m length and have become the worldwide standard. Costs of such towers and corresponding foundation are about 20% and 10%, of the total investment, respectively. The increase in the hub height raises new questions concerning the design, construction and maintenance costs of the support structures posing significant transportation and execution challenges. Limits of transportation depends on the public road routes, which defines the max diameter often around 4 m.

The main limitation for tubular pre-fabricated towers can be overcome only by extra work on site, comprising the assembly of full diameter sections from smaller pieces. This approach can be used for both concrete and steel towers (Figure 1a, b) using prefabricated modules that are assembled on site.

2 SAFETY CONCEPT AND LOADING

2.1 *Certification and International standards*

Manufacturing and use of wind converters are based on product certification, i.e. all components including support structure are parts of a complete set for which a certification document is issued, usually by insurance companies. Certification companies have developed their own guidelines for certification GL Wind (2010), DNV (2002) based on international IEC 61400-1 (2005), ISO 2394 (1998), ISO 4354 (2009) or national standards DIBt (2012).

Figure 1. a) Siemens polygonal shaped steel tower, b) Modular tower using friction connection developed in HISTWIN projects Veljkovic et al. (2012 & 2014).

Wind Turbine Type Certification requires conformity with regulations and/or guidelines in following items:

- Design safety check
- Safety concept and evaluation of loads
- Evaluation of safety system and design of components (e.g. support structure)
- Type Testing
- Manufacturing Evaluation
- Foundation Design safety check (optional)
- Type Characteristic Measurement (optional)

IEC 61400-1 (2005) outline basic design prerequisites and specifies essential design requirements to ensure the engineering integrity of onshore wind turbines. It is concerned with all subsystems of wind turbines such as control and protection mechanisms, internal electrical systems, mechanical systems and support structures. Compliance with this standard does not relieve from the responsibility of observing other applicable regulations, such as those applied to the supporting structure (tower and foundation) concerning the structural safety, the actions and the relevant design rules. The standard is "not foreseen" to be used in combination with Eurocode however we have combined it by CEN standards, in particular EN1993-* series, as it is explained below.

EN 1990 (2002) describes the principles and requirements for safety, serviceability and durability of the support structures.

EN 1993-1-1, EN 1993-1-6 (2007), EN1993-1-9 (2005) is used in conjunction with IEC 61400-1 (2005) to assess the structural behaviour and reliability of support structures made of steel.

2.2 *External conditions and wind turbine classes*

The external conditions considered for design are dependent on the intended site or site type for a Wind Turbine (WT) installation. In order to be able to pre-qualify WT to be installed in different sites, WT classes are defined in terms of wind speed and turbulence parameters (see Table 1). The reference wind speed v_{ref} is defined as the extreme

Table 1. Wind Turbine Classes according to IEC 61400-1.

	Wind Turbine Class		
	I	II	III
V_{ref} (m/s)	50	42,5	37,5
I_{ref} for type A		0,16	
I_{ref} for type B		0,14	
I_{ref} for type C		0,12	

10 min average wind speed at the hub-height with a 50 year return period and I_{ref} is the reference turbulence intensity.

2.3 *Design criteria for HAWT tower*

The structural design of a wind turbine supporting structure must provide adequate strength and stiffness for following limit state conditions:

- To withstand extreme loads from the highest wind speeds which may occur, Ultimate Limit States (U) concerning strength and stability must be checked.
- To guarantee fatigue strength/life of all components including support structure, Fatigue Strength Limit States (F) must be checked
- To provide adequate dynamic behaviour and control of deflections by avoiding resonance situations between "mechanical" (rotating) part and the structural (fixed) part. This is archived by designing tower stiffness by a certain margin between 1P/3P frequencies and the critical natural frequencies. The calculation of natural frequencies of the tower must include tower head mass and soil-structure interaction.

The vibrational behaviour of a wind turbine can be kept under control only if the stiffness and mass parameters of all its components are carefully considered.

Maximum deflection of blades and tower must be checked so that no contact can occur between the blades and the tower; also, resonance between rotor frequencies and tower eigen-frequencies must be avoided.

The exciting forces of the rotor have basically two sources:

- "mass imbalances" of moving parts, mainly the rotor with blades that develop dynamic loads with frequency of excitation usually called 1*P* (per revolution) and corresponds to the rotor angular speed.
- "aerodynamic imbalances" that result from the asymmetrical air flow against the rotor, mostly the tower shadow effect and the vertical wind shear and result in dynamic loads with higher harmonic frequencies that appear for multi-blade turbines as 2*P,* 3*P, etc*.

The second type of forces is the critical one, since it cannot be avoided neither reduced by improving precision of the manufacturing process.

The tower's first natural bending frequency must not coincide with the critical exciting forces, see Figure 2. Furthermore, care must be taken to ensure that a certain margin from the remaining multiples of the rotor frequency is maintained, depending on structural as well as aerodynamic

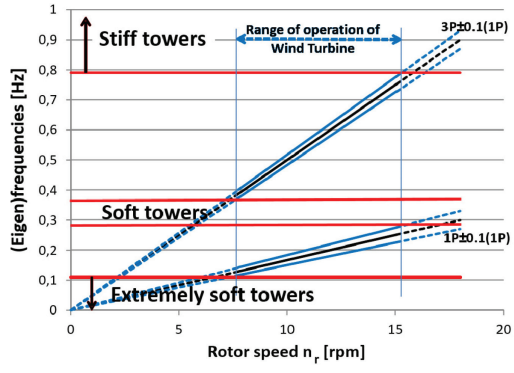

Figure 2. Campbell diagram relating rotor speed and eigen-frequencies of the tower.

damping. A safety margin of about 0,25 *P* from the dominant frequency of excitation and the margin of 0,15 *P* to 0,20 *P* from the less critical frequency is a good guidance for predesign (Hau, 2006). If other values of the first natural frequency is used, this choice should be properly justified. Designation "stiff" or "soft" tower corresponds to the position of the tower's first frequency relative to the dominant excitation frequency of the rotor. Current steel wind turbine towers with heights between 60 and 120 meters belong to soft towers.

2.4 *Wind loading calculation*

The wind loads on the rotor blades during steady and symmetrical flows are determined by the effective wind speed varying from the blade root to the tip and by the geometrical shape of the rotor blades. Pitch controlled rotors limit power capture to the rated power point at about 12 m/s wind speed by changing the angle of the blades. The rotor thrust is maximum at this point dropping off for increasing wind speed.

For design purposes, the life of a wind turbine is represented by a set of design situations covering the most significant conditions that the wind turbine may experience. The load cases are determined from the combination of operational modes or other design situations with the external conditions giving three main design load cases:

- normal operation and appropriate normal or extreme wind conditions
- fault situations and appropriate wind conditions
- transportation, installation and maintenance and appropriate wind conditions

The combination of the design situations with pertinent safety factors is operationalized in IEC 61400-1 (2005) using twenty-two Design Load

Cases (DLC) schematized in Table 2. Fifteen load cases are used for Ultimate Limit State (U) analyses and seven are used for Fatigue Limit State (F) analyses.

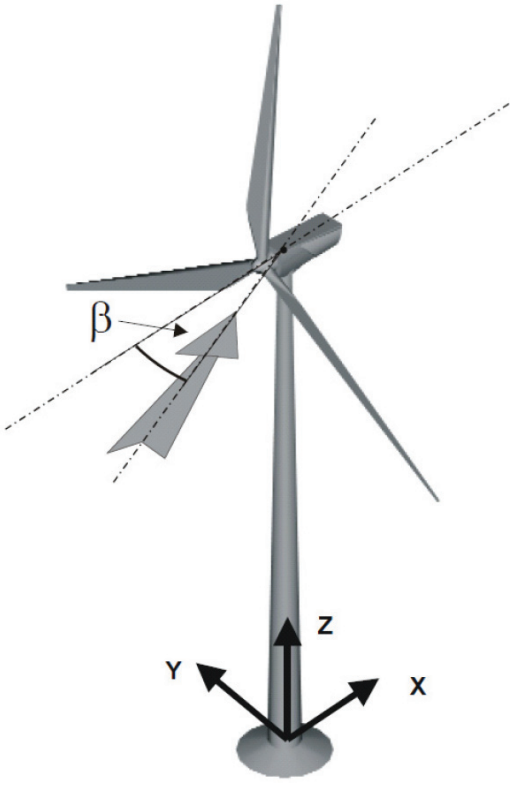

Figure 3. Coordinate system used to define loading and wind direction.

Table 2. Design load cases and type of analysis according to IEC 61400-1 (2005).

DLC	Situation	Type of analysis
1.x	power production	U or F
2.x	power production plus occurrence of fault	U or F
3.x	start-up of wind turbine	U or F
4.x	normal shut down	U or F
5.x	emergency shut-down	U
6.x	parked wind turbine	U or F
7.x	parked wind turbine and fault conditions	U
8.x	transport, assembly, maintenance and repair	U

U–ultimate limit state design. F–fatigue limit state design.

Table 3. Example of extreme loads at tower bottom.

Fx (kN)	Fy (kN)	Fz (kN)	Mx (kNm)	My (kNm)	Mz (kNm)
725.2	958.3	2220.2	64537.7	67796.3	6476.2

Table 4. Example of fatigue damage equivalent loads for $m = 3$ and $N_{ref} = 2.0E+08$ at tower bottom.

ΔFx (kN)	ΔFy (kN)	ΔFz (kN)	ΔMx (kNm)	ΔMy (kNm)	ΔMz (kNm)
102.6	67.8	28.9	4774.0	6204.1	1228.7

Example of the cross section loads used to design the bottom section of a 80 meters high steel tubular tower supporting a 2.1 MW class IIA turbine are given in Table 3 for ultimate limit state analysis and in Table 4 for fatigue limit state analysis. Reference is made to the coordinate system shown in Figure 3.

3 STABILITY OF TOWERS

For most of shell thickness/radius ratios, the shell buckling curves are lower than the column buckling curves, see Figure 4. Therefore, no column-like buckling behaviour has to be checked for shell elements.

Reduced Stress Method is most commonly used according to EN 1993-1-6 (2007) to verify the buckling limit state. Two main input parameters (buckling and squash-load) may be determined either by:

1 a simplified hand-calculation based on analytically solutions (given in the Annex of EN 1993-1-6), or
2 a global FEA in forms of a Materially Non-linear Analysis (MNA) and Linear-elastic Bifurcation Analysis (LBA).

The reduced stress method is based on reduction of design resistance of membrane stress components in the tower shell. Meridional (longitudinal) σ_x, circumferential (tangential) σ_θ and in plane shear stresses $\tau_{x\theta}$, see Figure 5, have to be used in the design check. The safety factor should be taken from relevant application standards or from EN 1993-1-1 (2005). It is worth emphasizing that the partial safety factor to buckling $\gamma_{M1} = 1.1$ is recommended for shell structures in the section 8.5.2. of EN 1993-1-6 (2005).

For the verification of the buckling strength of shells applying the stress design method the following equations have to be checked:

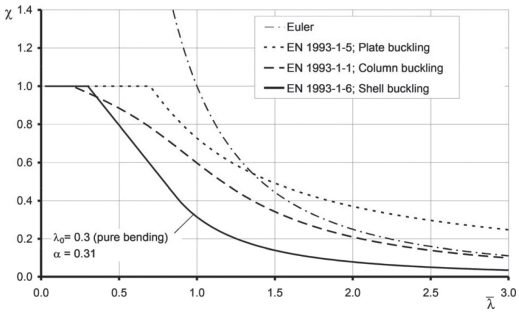

Figure 4. Different buckling curves (BC).

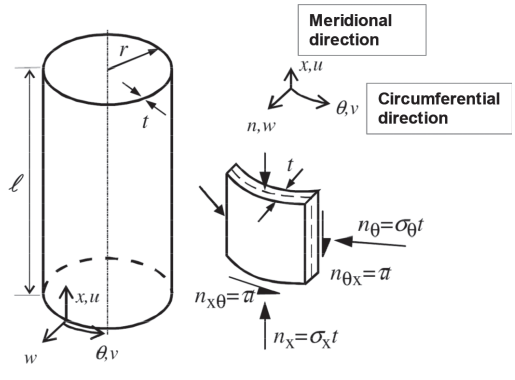

Figure 5. Stress directions in a cylindrical shell according to EN 1993-1-6 (2005).

$$\sigma_{x,Ed} \le \sigma_{x,Rd} = \chi_x \cdot \frac{f_{yk}}{\gamma_{M1}}$$
$$\sigma_{\Theta,Ed} \le \sigma_{\Theta,Rd} = \chi_\Theta \cdot \frac{f_{yk}}{\gamma_{M1}} \quad (1)$$
$$\tau_{x\Theta,Ed} \le \tau_{x\Theta,Rd} = \chi_t \cdot \frac{f_{yk}}{\sqrt{3} \times \gamma_{M1}}$$

If more than one of the three above mentioned buckling-relevant membrane stresses are present, the following interaction check is recommended in EN 1993-1-6 (2007):

$$\left(\frac{\sigma_{x,Ed}}{\sigma_{x,Rd}}\right)^{k_x} - k_i\left(\frac{\sigma_{x,Ed}}{\sigma_{x,Rd}}\right)\left(\frac{\sigma_{\Theta,Ed}}{\sigma_{\Theta,Rd}}\right) + \left(\frac{\sigma_{\Theta,Ed}}{\sigma_{\Theta,Rd}}\right)^{k_\Theta} + \left(\frac{\tau_{x\Theta,Ed}}{\tau_{x\Theta,Rd}}\right)^{k_\tau} \le 1$$

4 FATIGUE

Fatigue calculation methodology is required to assess fatigue damage. Miner's rule for the accumulation of damage is allowed according EN 1993-1-19 (2005) and IEC 61400-1 (2005) standards. There are no substantial difference between these two standards, the limit state is reached when the accumulated damage index equals unity. The format of the design check equation is a bit different because the partial safety factors have different origin and are applied in different way but their impact on the verification of the fatigue strength is marginal. The only difference, relevant for fatigue damage analysis here, is the fact that SN curves used in EN1993-1-9 and IEC 61400–1, are established having 75% confidence level of 95% probability of survival and 97,7% survival probability, respectively.

Fatigue damage calculations shall consider effects of both cyclic range and mean strain (or stress) levels. In case of welded details the major influence on the fatigue strength is due to residual stresses. Classification of details defined by S-N curve has been obtained based on the cyclic loadings.

The partial safety factors defined in standard IEC 61400-1 (2005) in case of fatigue verifications are the following:

- partial safety factor for loads, γ_f = 1.0 for all design situations
- partial safety factor for resistances:
- safe life method: γ_m = 1.10 which assumes that 97,7% survival probability is used as basis for the SN curves.
- if it is possible to detect critical crack development through introduction of a periodic inspection programme, a lower value of γ_m but not lower than 0.9 can be used, i.e. for damage tolerant design $\gamma_m > 0.90$.
- partial safety factor for Component Class 2 is γ_n = 1,15, i.e. failure leads to the failure of a major part of the wind turbine.

To define the partial safety factor for loads in IEC 61400-1 (2005) a consequence of failure factor is defined according to the component classes. This consequence of failure factor, γ_n, is introduced to distinguish between:

- Component class 1: used for "fail-safe" structural components whose failure does not result in the failure of a major part of a wind turbine, for example replaceable bearings with monitoring.
- Component class 2: used for "non fail-safe" structural components whose failures may lead to the failure of a major part of a wind turbine.
- Component class 3: used for "non fail-safe" mechanical components that link actuators and

brakes to main structural components for the purpose of implementing non-redundant wind turbine protection functions

The design of wind turbine towers follows the 'safe life method' and, in the case of steel the fatigue strength is represented by "Wöhler" or "S-N" curves given in EN 1993-1-9 (2005).

The fatigue assessment based on the Palmgren-Miner rule is performed using a linear cumulative damage calculation to obtain the damage index.

Considering the requirement from IEC 61400-1 (2005) that the safety factors should be applied to the load, the limit state relation for fatigue analysis becomes:

$$\sum_{j,k} \frac{n_{j,k}}{N_k(\gamma S_k)} \le 1 \qquad (3)$$

where $\gamma = \gamma_m \gamma_n \gamma_f$.

This Miner's summation uses the number of cycles n_k from the load (effect) fatigue spectrum and the number of cycles $N_{k,}$ from the design fatigue resistance spectrum (see Figure 6). The applied load (effect) ranges S_k should be multiplied by the safety factor for γ and the fatigue strength values S_c should be based on 97,7% survival probability in order to obtain the corresponding number of cycles n_k or N_k for each band in the spectrum.

The number of cycles $N_{ref} = 2 \times 10^6$ is obtained from EN 1993-1-9 (2005), which is also used to choose the curve representing the fatigue detail. Since the tubular tower is manufactured from rolled steel plates using full penetration but welding the representative fatigue detail will be the Detail 71 and therefore the curve $\Delta\sigma_c$ = 71 MPa shall be chosen to compute the damage index.

Figure 7 shows S-N curves obtained from measurements performed in a wind tower (Rebelo et al. 2012a, b), from design curve given by the manufacturer and from the fatigue detail 71 defined in EN 1993-1-9 (2005). The measured stress corresponds to vertical stress component in the shell obtained from strain measurements near the bottom cross section of the tower (Rebelo et al. 2012a, b). The design curve is provided by the manufacturer and the fatigue detail 71 defined according to EN 1993-1-19 (2005) is achieved in the fabrication.

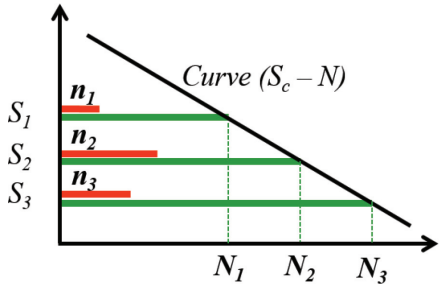

Figure 6. Scheme of the parameters n_i and N_i in the damage index formula $D_i = n_i/N_i$.

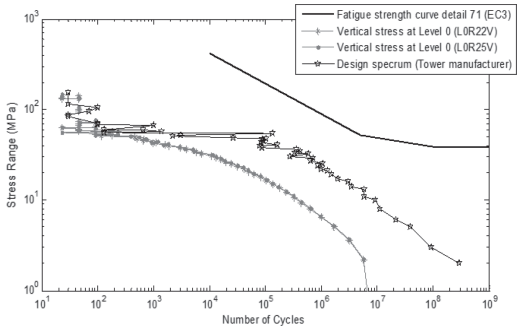

Figure 7. Comparison of S-N curves obtained from measurements in a wind tower (Rebelo et al. 2012a, b), from design curve given by the manufacturer and from the fatigue detail 71 defined in EN 1993-1-19 (2005).

5 CONNECTIONS

The connection between two segments of a steel tubular tower is most commonly realized as a flange connection. However, recent research results offer a competitive alternative: friction connections with long open slotted holes. By their use, the fatigue resistance of the flanges may be overcome as the limiting design criterion. Additionally, the assembly process on site will be accelerated. For design purpose, it is assumed that the resistance of the three dimensional connection detail, which is loaded mostly in bending, can be described by the resistance of a segment with a single bolt and bolt row, respectively. The segment width c is equivalent to the arc length between two bolt holes or bolt rows in the tension zone of the shell, see Figure 8.

Applicability of the segment model has been confirmed by Schaumann & Seidel (2000) and Pavlović et al. (2015). It is shown that the resistance of the circular connection is slightly underestimated by the segment model due to neglecting of the redistribution of the stresses in the cross section of the shell at the ultimate load.

The verification of the flange connection in the Ultimate Limit State (ULS) is usually done according to the plastic hinge theory. Even though bolts in ring-flange connections have to be preloaded, the pre-tensioning load in bolts has not to be considered for the ULS verification. According to

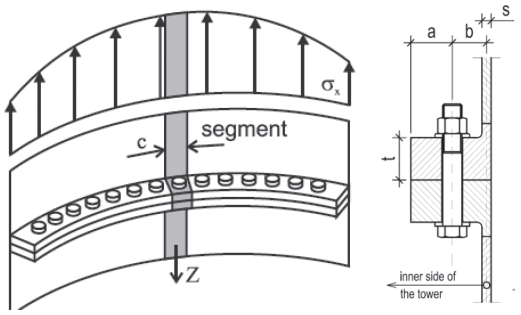

Figure 8. Segment approach for flange connections (Hau 2006).

Petersen (1997) three different failure mechanisms must be checked in L-shaped ring-flange connections, whereas the lowest resistance $Z_{ult,i}$ is governing the design, see Figure 9:

Yielding (failure) of the bolt; this governs failure mechanism if flanges and shells are rather stiff compared to the bolt. The ultimate resistance of the segment then equals to the tensional resistance of the bolt:

$$Z_{ult,1} = F_{t,Rd} \tag{4}$$

1. Yielding (failure) of the bolt and at the same time plastic hinge in shell; the ultimate resistance of this failure mode is given by:

$$Z_{ult,2} = \frac{F_{t,Rd} \cdot a + M_{N,pl,Rd,sh}}{a+b} \tag{5}$$

2. Plastic hinge in shell and flange (failure of connection); the bolt load stays below its tensile resistance ($F_{t,Ed} < F_{t,Rd}$). The ultimate resistance of this failure mode thereby reads:

$$Z_{ult,3} = \frac{M_{N,pl,Rd,sh} + M_{pl,Rd,fl,net}}{b} \tag{6}$$

With:

Z_{ult} = Ultimate tensile resistance force of the segment,

$F_{t,Rd}$ = Design tensile resistance of the bolt,

$M_{N,pl,Rd,sh}$ = Design plastic bending resistance of the shell considering *M*-*N*-interaction:

$M_{pl,Rd,fl,net}$ = Design plastic bending resistance of the flange with deduction of bolt hole,

a = Distance between flange edge and axis of bolt,

b = Distance between axis of bolt and shell.

Seidel (2001) introduced two new failure modes D and E that can be used instead of failure mode

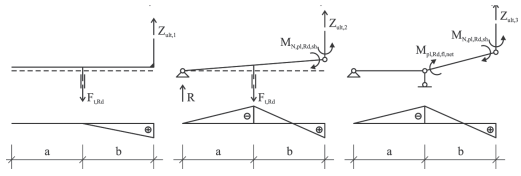

Figure 9. Plastic hinge models for the determination of the ultimate resistance of L-shaped ring-flange connections acc. to Petersen (1997).

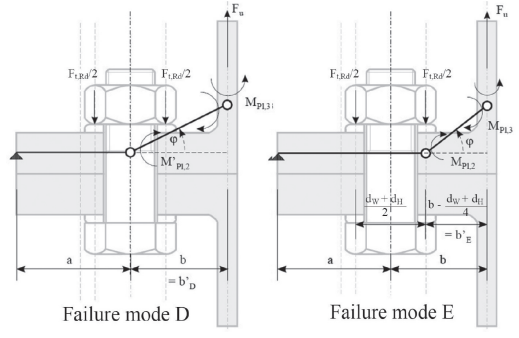

Figure 10. Additional failure modes of L-shaped ring-flange connecitons acc. to Seidel (2001).

C, see Figure 10. Both additional failure modes take into account enhanced bending resistance of the flange due to more realistic transfer of the bolt force through the washer:

1. Failure mode D assumes that the plastic hinge in the flange will develop at the net section in the bolt line but that the failure mechanism is strengthened by the additional bending moment provided by the one half of the bolt force transferred by the side of the washer towards the shell $\Delta M_{pl,2}$:

$$Z_{ult,D} = \frac{M'_{pl,2} + \Delta M_{pl,2} + M_{pl,3}}{b'_D} \tag{7}$$

$$\Delta M_{pl,2} = \frac{F_{t,Rd}}{2} \cdot \frac{d_W + d_H}{4} \tag{8}$$

2. Failure mode E assumes that the plastic hinge in the flange will develop at the gross section of the in the line of the inner side of the washer. In this case the but that the lever arm b is reduced to b'_E, see
3. Figure 10:

$$Z_{ult,E} = \frac{M_{pl,2} + M_{pl,3}}{b'_E} \tag{9}$$

$$b'_E = b - \frac{d_W + d_H}{4} \tag{10}$$

Friction connections with normal clearance holes have been used in structural engineering for decades. Their behaviour has been extensively examined by various researchers and is comprehensively described by Kulak et al. (2001). Slip resistant joints rely on load transfer between the joined elements due to friction, which is ensured by a clamping force provided by preloaded high strength bolts, see Figure 11.

Friction connections are very efficient for cyclic wind loading which varying between tension and compression. Due to preloaded bolts and force transfer by friction, stress concentration does not appear. This structural detail belongs to fatigue class 100 EN 1993-1-9 (2005), which is much above fatigue detail of the L-flange which is between class 36 and 71. In many cases this fatigue criterion of the connection governs the design of the tower. The main innovation of the connection consists of the substitution of the normal clearance holes on the lower tower section with long open slotted holes with the covered plate, Figure 11. The remaining steel parts between the long open slotted holes are with respect to their visual appearance designated as "fingers". The on top opened bolt hole shall ease the assembly process. On the inside of the tower, cover plates shall be mounted to ensure an equal distribution of pressure and to facilitate the assembly process.

The ultimate resistance of the friction connection corresponds to its ultimate slip resistance, Eq. (11). The friction connection with long open slotted holes is a single lap joint, thus providing one friction surface $n = 1$. Recent findings in the HISTWIN2 (Veljkovic et al. 2014) project have shown that the second friction surface is activated after the ultimate limit state is reached. It can be easily determined according to the following hand-calculation procedure:

1. Determination of the ultimate slip design resistance $Z_{s,Rd}$ of one bolt row of the friction joint (segment model):

$$Z_{s,Rd} = \frac{n_r \cdot \mu \cdot k_s \cdot F_{p,C}}{\gamma_{M3}} \tag{11}$$

Where:
n_r = number of bolts per slotted hole,
μ = slip factor,
k_s = reduction factor for long slotted holes,
$F_{p,C}$ = characteristic preload force in bolt,
γ_{M3} = partial safety factor taken as $\gamma_{M3} = 1.25$.

2. Determination of the corresponding maximum stress in shell $\sigma_{x,t}$ due to force Z_{Ed} in segment model, see Figure 8:

$$\begin{aligned} Z_{Ed} &= A_{shell} \cdot \sigma_{mean} \\ &= c \cdot s_{mean} \cdot \sigma_{mean} \cong c \cdot s_{mean} \cdot \sigma_{x,t} \end{aligned} \tag{12}$$

Where:
A_{shell} = area of cross section of segment model,
σ_{mean} = mean of tension/compression stress in segment model,
$\sigma_{x,t}$ = maximum tension/compression stress in shells,
c = segment width = distance between two bolt rows,
s_{mean} = mean shell thickness of the two connected tower segments.

Comparative cost analysis in HISTWIN project (Veljković et al. 2012) showed that up to 80% reduction of the connection costs in a tower can be obtained by using the novel friction connection with long open slotted holes instead of the classical ring-flange connection.

Down-scale experiments of friction connection and ring-flange connection are performed at RWTH Aachen within the HISTWIN project using 4-point

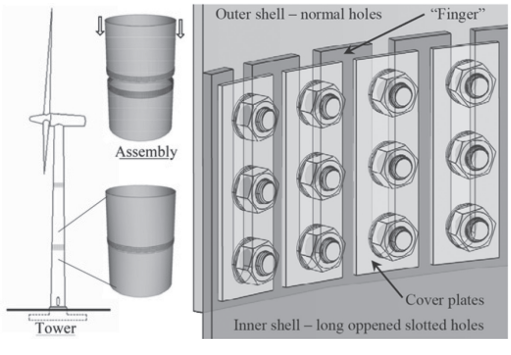

Figure 11. Friction connection with long open slotted holes.

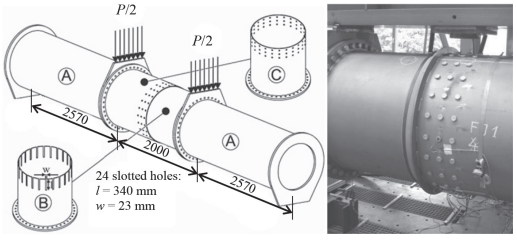

Figure 12. Down-scale experiments of the friction connection and the ring-flange connection bending resistance in 4-point bending set-up at RWTH Aachen (Feldmann et al. 2011).

bending set-up, see Figure 12. Measurements of the bolt forces in both types of the connection showed much less variation of the bolt force in function the external load and therefore their better fatigue endurance in case of the friction connection.

The influence of tower cross-section shape, execution tolerance and length of the friction connection on the bending resistance is thoroughly studied by Heistermann (2014) using FE models validated by down-scale experiments performed at RWTH Aachen. Buckling behaviour of the shell in the vicinity of the friction connection in towers with circular and polygonal cross-sections is analysed in order to check possible advantages of either cross-section. The influence of two types of the execution tolerances on the connection strength is investigated: a parallel gap created by different diameters of the tower segments and inwards bent "fingers", leading to inclined gaps, see Figure 13. Based on validated finite element analyses the design recommendations are proposed regarding the local buckling in the vicinity of the connection and execution tolerance.

6 DOOR OPENING

Openings in the tower shell are made for two reasons: for the door at the lower segment of the tower which is used for maintenance, and for ventilation usually at the lower and top segment of the tower Two possibilities exist for stiffening of the door opening, by adding a stiffener or by increasing the plate thickness in the area around the door opening.

Several failure modes in the ultimate limit state can develop in the area of the opening: buckling of the shell adjacent to the opening due to increased stresses and disturbed boundary conditions, compressive plastic yielding in the areas of stress concentration and tensile rapture due to occurrence of maximum principal stresses mostly above the opening. Resistance of the tower segment is reduced due to presence of the opening. The level of reduction depends on successfulness of the stiffening.

Stress limit approach for the buckling design of the door opening region is approximate and recommendations are limited only for few simple geometry cases. Due to often complicated geometry of the opening and the stiffening approach the design methods relaying on Finite Element Analysis (FEA) are used for design checks. Two approaches, described in EN 1993-1-6 (2007) are used for stability design:

– MNA/LBA—materially nonlinear analysis in conjunction with linear bifurcation analysis, and
– GMNIA—geometrically and materially nonlinear analysis with imperfections included.

Example of analysis by GMNIA of the bottom tower segment with the door opening stiffened by the ring flange is shown in Figure 14.

Tran et al. (2016) investigated buckling resistance of circular and polygonal tower sections made of High Strength Steel (HSS) in down-scale experiments and FEA with the aim to provide necessary information for development of HSS tubular towers for wind converters. A total of 32 specimens were tested under uniaxial compression, with and without opening, thicknesses 4–6 mm, supported by tensile tests of coupon specimens taken from flat, circular and corner parts, see Figure 15. It is concluded that the cold forming to 158° in polygonal sections increases the strength of the corner material 6–11%. Approximately 22% and 26% reduction of the resistance is obtained due to the openings in circular and polygonal specimens, respectively.

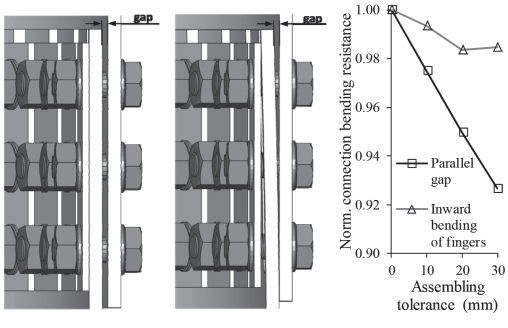

Figure 13. Execution tolerance for the friction connection provided by: a) parallel gap, b) inward bending of the "fingers".

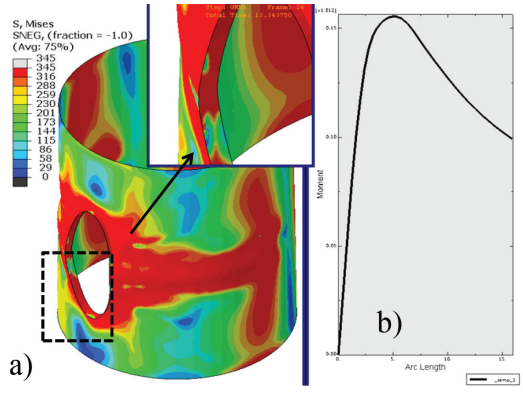

Figure 14. Stability verification of the door opening region by GMNIA: a) post-buckling deformed shape with Von-Mises stresses, b) bending moment at the top of the segment.

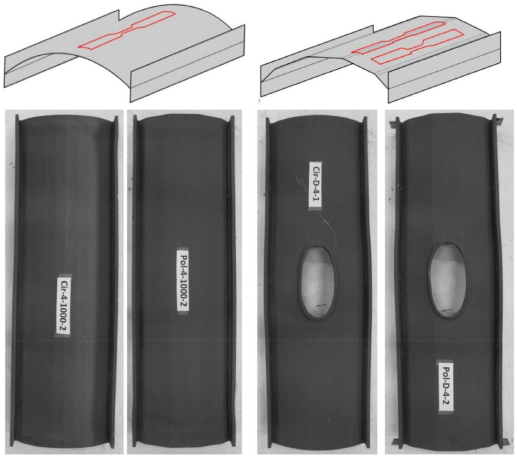

Figure 15. Down-scale experiments by Tran et at. (2016) of the door opening region in circular and polygonal HSS towers.

Initial geometric imperfections obtained by 3D laser scanning turned out to be higher compared to EN 1993–1-6 recommendations.

7 FOUNDATIONS

The onshore foundations of steel wind towers are subjected to strong overturning moments and relatively low vertical forces. Slab foundations consist of circular or rectangular or polygonal footings, which add vertical weight to the tower thus decreasing the eccentricity of the vertical load. The mass and dimensions of the slab are determined so that the weight of the turbine, the tower and the foundation itself are capable of resisting the overturning moment from the horizontal load. Circular slab foundations are considered the most efficient structural solution for the shallow foundations, as the maximum overturning moments are likely to happen in any direction. For construction easiness, in particular to the formwork, a polygonal shape is often preferred for the slab foundation. It is worth noting that an octagonal base, with the same area of the circular foundation, is the most adequate solution.

To optimize the solution, the slab is in general tapered with a pedestal at the centre where the tower base is clamped. Anchoring of the steel tower to the reinforced concrete pedestal by means of preloaded anchors is one of the two most commonly configurations used, the other being the embedment of the lowest course of the tower to the foundation.

New developments in the foundation design using steel micropiles to anchor the slab foundation to the soil can be found in Matos et al. (2015). Life cycle analysis of different solutions for the tubular tower and respective slab foundation can be also found in Rebelo et al. (2014) and Gervasio et al. (2014).

7.1 *Design criteria of slab foundations*

A series of structural and geotechnical design checks are needed in order to ensure that the foundation type, size, and placement are capable of resisting the most unfavourable load combination to design the shallow foundations, which is the most commonly used foundation type for land-based wind turbines. For the design of shallow circular foundations, the following checks should be considered:

- Pressure on the foundation for non-factored loads—in this verification it is estimated the maximum applied stress in the base of the foundation (circular foundation).
- Verification of the compressed area—for characteristics loads, at least 50% of the base area must be compressed which can be fulfilled when $e < 0.59R$. This verification is only applied to the wind action.
- Limit state of equilibrium according to EN 1997-1 (2007)—in this verification it is checked if the resistant bending moment due to the vertical forces is enough to ensure about the equilibrium of the foundation when subjected to the overturning moment.
- Soil bearing capacity according to EN 1997–1 (2007)—in this case it is guaranteed that the maximum applied pressure in the base of the foundation is lower than the bearing capacity of the soil. This verification is considered for three types of combinations according to the EN 1997-1 (ULS-GEO, ULS-STR and accidental combination for seismic loads).
- Soil bearing capacity according to EN 1998-5 (2007) - this part of Eurocode (Annex F) presents a formulation for foundation stability taking into account the soil inertia (kinematic effect). In reference Seismic Assessment and Improvement of building foundations is presented that the drained response is much more sensitive to inertia loading than undrained one.
- Soil bearing capacity according to EN 1998-5 (2007) for extremely eccentric loading—This verification reflects the failure of the soil under the unloaded part of foundation area (Rupture 2).
- Base sliding—it is checked that the friction resistant forces between the base of the foundation and the soil beneath (related to the vertical forces) are higher than the acting horizontal forces on the tower and turbine structures. In

this verification, the torsional contribution of M_z is also considered.

Safety factors are defined in EN 1997–1 (2007). The vertical dead loads (mass and self-weights) and the load cases are usually defined directly from the load cases presented by the technical specifications of the turbine manufacturer. For the safety verifications of the foundation, the loads are reduced to the base of the foundation.

8 FUTURE CHALENGES

Conventional tubular wind towers become less practical and uneconomical at the greater heights. In the near future the goal is to find economical solutions for tall land based towers supporting wind generators. The ongoing research project SHOWTIME (2015), coordinated by Prof. Rebelo, is to develop a new concept for the tower based on a hybrid design, comprising a steel lattice lower part and a steel tubular upper part. The innovative aspects will focus on optimization of the tower erection process, the use of high strength steel in the transition ring between tubular and lattice parts and minimization of in-situ work using newly developed bolted connections. The main idea is to use the lattice part of the tower as a supporting structure to lift up the tubular part of the tower by jacks. The tubular part could have the length of 80–100 m and the latticed part height of the about 30–50 m. Preliminary feasibility studies has shown economic advantages of this concept when erection of the tubular segment including the nacelle is done by the mobile cranes to the heights of about 100 m and launching it from beneath is done by jacks to obtained the total heights of 130–150 m.

9 CONCLUDING REMARKS

Innovation in design and erection technology of steel towers is very important part to maintain competitiveness of steel sector. In addition to innovations mentioned above, there are three additional topics relevant for the steel sector:

a. Advances towards maintenance free bolts will substantially reduce maintenance costs of the towers, Veljkovic et al. (2014).
b. New research efforts to achieve competitive solution of using cable stayed tubular towers is on-going. The idea is not very new but new fabrication technology may increase its competitiveness.
c. Results from the on-going SHOWTIME project will certainly pave the way to additional improvements of sustainable design of lattice towers. Such towers will have positive effect on cost reduction of the foundations which become rather important part of the total investment, estimated costs about 15% of the total investment, which in combination with the tower, accounts of almost one half of the total costs. The above mentioned facts make research in new structural system of towers and foundation as well as in improved efficiency of wind convertors very relevant for further reduction of pay-off time of the investment in the wind energy facilities.

ACKNOWLEDGMENT

The authors are grateful for the financial support of the RFCS (Research Fund for Coal and Steel of the European Community) under the contracts RFSR-CT-2006-00031 "High-Strength Steel Tower for Wind Turbine", RFSR-CT-2010-00031 "High steel tubular towers for wind turbines (HISTWIN2) and RFS2-CT-2014-00023 High-Strength Steel Tower for Wind Turbines (HISTWIN_Plus)". The collaboration of all project partners, Rheinisch-Westfälische Technische Hochschule (Aachen Germany), Germanischer Lloyd Industrial Services GmbH (Hamburg, Deutschland), Aristotle University of Thessaloniki (Thessaloniki, Greece), University of Birmingham (Birmingham, UK), Portugal Equipamentos Eólicos SA (Oliveira de Frades, Portugal), Rautaruukki Oyj (Hämeenlinna, Finnland) is warmly thanked.

REFERENCES

DIBt 2012. *Richtlinie für Windenergieanlagen—Einwirkungen und Standsicherheitsnachweise für Turm Gründung.* Berlin: Deutsches Institut für Bautechnik.
DNV 2002. *Guidelines for Design of Wind Turbines*. Copenhagen: Det Norske Veritas & Wind Energy Department at Risø National Laboratory.
EN 1990: 2002. *Eurocode 0—Basis of structural design*. Brussels: European Committee for Standardization (CEN/TC250).
EN 1993-1-1: 2005. *Eurocode 3—Design of steel structures. Part 1-1: General rules and rules for buildings.* Brussels: European Committee for Standardization (CEN/TC250).
EN 1993-1-6: 2007. *Eurocode 3—Design of steel structures. Part 1-6: Strength and Stability of Shell Structures.* Brussels: European Committee for Standardization (CEN/TC250).
EN 1993-1-9: 2005. *Eurocode 3—Design of steel structures. Part 1–9: Fatigue*. Brussels: European Committee for Standardization (CEN/TC250).
EN 1997-1: 2007. *Eurocode 7—Geotechnical design, Part 1: General rules*. Brussels: European Committee for Standardization (CEN/TC250).

EN 1998-5: 2007. *Eurocode 8—Design of structures for earthquake resistance, Part 5: Foundations, retaining structures and geotechnical aspects*. Brussels: European Committee for Standardization (CEN/TC250).

Feldmann, M. et al. 2011. Zum Last-Verformungsverhalten von Schrauben in vorgespannten Ringflanschverbindungen mit überbrückten Klaffungen im Hinblick auf die Ermüdungsvorhersage. *Stahlbau* 80: 21–29.

Gervásio, H. et al. 2014. Comparative life-cycle assessment of tubular wind towers and foundations. Part 2—Life-cycle analysis. *Engineering Structures* 74: 292–299.

GL Wind 2010. *Guideline for the Certification of Wind Turbines*. Hamburg: Germanischer Lloyd WindEnergie GmbH.

Hau, E. 2006. *Wind Turbines: fundamentals, technologies, application, economics*. Berlin: Springer.

Heistemann, C. 2014. *Resistance of Friction Connections with Open Slotted Holes in Towers for Wind Turbines*. Doctoral thesis. Luleå: Luleå University of Technology.

IEC 61400-1: 2005. *Wind Turbines: Part 1—Design requirements, Third edition*. Geneva: International Electrotechnical Commission.

ISO 2394: 1998. *General principles on reliability for structures*. Geneva: International Organization for Standardization.

ISO 4354: 2009: *Wind actions on structures*. Geneva: International Organization for Standardization.

Kulak, G.L. et al. 2001. *Guide to Design Criteria for Bolted and Riveted Joints, Second Edition*. Chicago: American Institute of Steel Construction.

Matos, R et al. 2015. Improved design of tubular wind tower foundations using steel micropiles. *Journal of Structure and Infrastructure Engineering* (available online September 2015).

Pavlović, M. et al. 2015. Connections in towers for wind converters, Part I: Evaluation of down-scaled experiments. *Journal of Constructional Steel Research* 115: 445–457.

Petersen, C. 1997. *Stahlbau (Steel Construction), Third Edition*. Braunschweig: Vieweg-Verlag.

Rebelo C, et al. 2012a. Structural Monitoring of a Wind Turbine Steel Tower—Part I: system description and calibration. *Wind and Structures* 15(4): 285–299.

Rebelo C, et al. 2012b. Structural Monitoring of a Wind Turbine Steel Tower—Part II: monitoring results, *Wind and Structures* 15(4): 301–311.

Rebelo, C, et al. 2014. Comparative life-cycle assessment of tubular wind towers and foundations. Part 1—Structural design. *Engineering Structures* 74: 283–291

Schaumann, P. & Seidel, M. 2000. Failure analysis of bolted steel flanges. In Zhao, X.L. & Grzebieta, R.H. (ed.). *Proceedings of the 7th International Symposium on Structural Failure and Plasticity (IMPLAST 2000)*. Amsterdam: Elsevier.

Seidel, M. (2001): *Zur Bemessung geschraubter Ringflanschverbindungen von Windenergieanlagen*. Doctoral thesis. Hannover: Universität Hannover, Institut für Stahlbau.

SHOWTIME 2015. *Steel Hybrid Onshore Wind Towers Installed with Minimal Effort*. Research project 2015–2018 (RFSR-CT-2015-00021).

Tran, A.T. et al. 2016. Resistance of cold-formed high strength steel circular and polygonal sections—Part 1: Experimental investigations. *Journal of Constructional Steel Research. Elsevier* (available online 24 October 2015).

Veljkovic M, et al. 2014. *Higher steel tubular towers for wind turbines (HISTWIN2). Final report—RFSR-CT-2010-00031*. Brussels: European Commission (RFCS).

Veljkovic, M. et al. 2012. *High-strenght tower in steel for wind turbines (HISTWIN). Final report—RFSR-CT-2006-00031*. Brussels: European Commission (RFCS).

Cold-formed sections and profiled sheeting

This page intentionally left blank

Recent Progress in Steel and Composite Structures – Giżejowski et al. (Eds)
© 2016 Taylor & Francis Group, London, ISBN 978-1-138-02946-0

Shear strength of trapezoidal and sinusoidal corrugated steel webs

M. Gajdzicki & W. Perlinski
Department of Structural Mechanics, Lodz University of Technology, Lodz, Poland

ABSTRACT: The Eurocode 1993-1-5 gives the guidelines for estimating the shear resistance of beams with sinusoidal or trapezoidal webs. This paper focuses on the comparison of shear strength of steel webs with trapezoidal corrugations and converted to the substitute sinusoidal ones. A parametric numerical study, comprising 60 shell FEA models of corrugated webs under transverse loading, is presented. Numerical results are compared with the corresponding experimental ones with trapezoidal corrugations described in the literature, and summarized with the values obtained on the basis of the Eurocode provisions. Such an analysis allowed the authors to show the geometry of webs with sinusoidal corrugations when the equations for critical shear stress included in the standard give the value on unsafe side.

1 INTRODUCTION

So far the corrugated sheeting was mainly used as a roof and wall covering in industrial buildings. The idea of using them as the webs in plate girder appeared in the 1930's. The corrugated webs allows to reduce the weight of the structure while maintaining comparable strength properties compared to the beams with flat webs. Due to the fact that the corrugations increase stability to the web, the need of transverse stiffeners is eliminated. From all types of corrugates the most advantageous properties characterized the sinusoidal one. A smooth change of curvature allows to easily automate the process of welding. In contrast to the trapezoidal webs, where a system of flat subpanels is sensitive to local instability, in sinusoidal ones there will not appear the interactive shear buckling behavior.

Specific provisions for civil engineering applications in buildings and bridges of such beams can be found in the Eurocode 1993-1-5. Particular attention has been paid to determining the shear resistance, taking into account a local and global shear buckling. While the guidelines for designing beams with sinusoidal webs are more limited, this paper focuses on the comparison of shear strength of steel webs with trapezoidal corrugations and converted to the substitute sinusoidal ones.

Research on the shear buckling behavior of corrugated webs was initiated by Easley & McFarland (1969). Until recently, the solution proposed by the authors was the most commonly used formula for determining the critical value for the transverse loaded orthotropic plates. Afterwards, numerous theoretical and experimental research on the corrugated steel webs strength was performed by Elgaaly et al. (1996, 2006), Abbas et al. (2002) and Sause et al. (2001, 2003). In all these papers the authors focused on clarifying the critical stress values by proposing their own coefficients. Studies have also been conducted in Germany by Lindner et al. (1988) and Pasternak et al. (1999), where interaction between local and global instability and the influence of real boundary conditions on the local stability factor of web plate was investigated. Interactive shear buckling behavior for trapezoidal corrugated webs was also studied by Yi et al. (2008) and Moon et al. (2009). Experimental research using beams with sinusoidal webs under patch load were performed by Kuchta (2004, 2007).

2 SHEAR BUCKLING RESISTANCE— EUROCODE 3-1-5 PROVISIONS

Using the results of previous research, the Eurocode 3-1-5 gives the design rules for determining the shear resistance of I-girders with trapezoidal or sinusoidal corrugated webs. As in the case of plated structural elements with flat webs, the shear resistance is given as:

$$V_{bw,Rd} = \chi_C \frac{f_{yw} t_w h_w}{\gamma_{M1}\sqrt{3}} \tag{1}$$

For corrugated webs, the difference comes down to the reduction factor which is equal to the lesser value of factor for local and global buckling. Local instability can be determined assuming a model of a simply supported isotropic plate of the widest single fold supported by the adjacent folds along its vertical edges and by the flanges along its horizontal edges. A general solution to this case, according to the classical plate buckling theory has the form as below:

$$\tau_{cr} = k_\tau \sigma_e \tag{2}$$

where k_τ = stability factor for simply supported plate subjected to the shear load; σ_e = Euler critical stress for the plate.

If the factor k_τ will be calculated for the infinitely long plate, the local critical shear stress can be obtained from the simple formula:

$$\tau_{cr,l} = 4{,}83E\left[\frac{t_w}{a_{\max}}\right]^2 \tag{3}$$

Based on the numerical studies performed by Pasternak et al. (1999), the Eurocode 3–1-5 also gives the equation to determine the local critical stress for sinusoidal corrugated webs:

$$\tau_{cr,l} = \left(5{,}34 + \frac{a_3 s}{h_w t_w}\right)\frac{\pi^2 E}{12\left(1-\nu^2\right)}\left[\frac{t_w}{s}\right]^2 \tag{4}$$

The reduction factor for global buckling depends on the critical shear stress obtained from the formula:

$$\tau_{cr,g} = \frac{32{,}4}{t_w h_w^2}\sqrt[4]{D_x D_z^3} \tag{5}$$

where:

$$D_x = \frac{E t_w^3}{12\left(1-\nu^2\right)}\frac{w}{s} \tag{6}$$

$$D_z = \frac{E I_z}{w} \tag{7}$$

I_z = second moment of area of one corrugation of length w, see Figure 1.

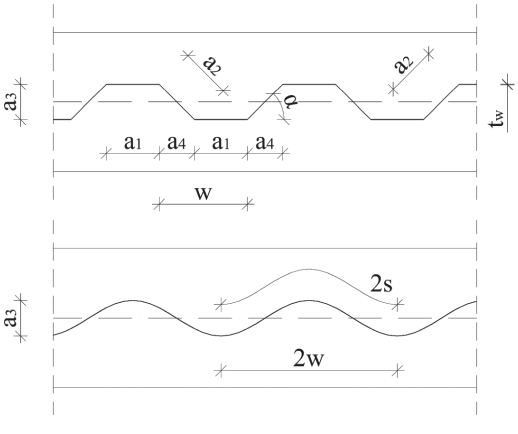

Figure 1. Geometric notations.

In papers (Moon et al. (2009)) and (Yi et al. (2008)), different formulae have been also proposed, to predict interactive buckling strength, which are characteristic for trapezoidal corrugation, but they were not definitively given in the Eurocode 3-1-5.

3 FINITE ELEMENT MODEL DESCRIPTION

To compare the shear resistance of steel webs with trapezoidal and sinusoidal corrugations, the finite element analysis was used. Due to the small number of experiments described in literature with sinusoidal corrugated webs, it was decided to use the results of the research carried out by Elgaaly et al. (1996), where the shear strength of beams with trapezoidal webs was investigated. Using the Abaqus software, 30 models of trapezoidal panels were built with identical geometry as in experiments—Tables 1–2.

Afterwards, another thirty numerical models were defined in which the trapezoidal corrugated webs were converted to the corresponding sinusoidal one, as in Figure 2. Other geometric dimensions of each model have been retained as in the case of trapezoidal webs.

In this research, as well as in previous analytical studies described in the literature, a trapezoidal or sinusoidal web was only modeled (Figure 3), using the general-purpose finite element program. The four-node thin-shell elements with reduced integration (S4R5) were used. The connection with the flange was modeled as simply support boundary conditions as shown in Table 3.

Based on the data contained in Elgaaly et al. (1996), in all models Young's modulus of 199,8 GPa and a Poisson's ratio of 0,3 were used. In order to minimize the computational effort, the influence of the number of elements per each panel on the accuracy of the obtained results were also analyzed. Finally, five elements across each fold of the corrugations were used.

Table 1. Corrugation configuration in beams tested in Elgaaly et al. (1996).

Corrugation	a_1 mm	a_4 mm	a_3 mm	α °	s mm	w mm
UF1X	38,1	25,4	25,4	45,0	148,1	127,0
UFX-36	41,9	23,4	33,3	55,0	165,1	130,6
UF2X	49,8	26,4	50,8	62,5	214,1	152,4

Table 2. Dimension of test specimens.

Model	a mm	h mm	a/h	t mm	Corrugation
1.	304,8	304,8	1:1	0,6629	UF1X
2.	304,8	304,8	1:1	0,6756	UF1X
3.	304,8	457,2	1:1,5	0,6096	UF1X
4.	304,8	457,2	1:1,5	0,7595	UF1X
5.	457,2	457,2	1:1	0,6350	UF1X
6.	457,2	457,2	1:1	0,7366	UF1X
7.	304,8	609,6	1:2	0,6350	UF1X
8.	304,8	609,6	1:2	0,7874	UF1X
9.	304,8	304,8	1:1	0,6299	UFX-36
10.	304,8	304,8	1:1	0,7849	UFX-36
11.	609,6	304,8	2:1	0,6756	UFX-36
12.	609,6	304,8	2:1	0,7823	UFX-36
13.	304,8	457,2	1:1,5	0,6096	UFX-36
14.	304,8	457,2	1:1,5	0,7620	UFX-36
15.	457,2	457,2	1:1	0,6350	UFX-36
16.	457,2	457,2	1:1	0,7366	UFX-36
17.	304,8	609,6	1:2	0,6096	UFX-36
18.	304,8	609,6	1:2	0,7620	UFX-36
19.	304,8	304,8	1:1	0,6401	UF2X
20.	304,8	304,8	1:1	0,7798	UF2X
21.	457,2	304,8	1,5:1	0,6401	UF2X
22.	457,2	304,8	1,5:1	0,9195	UF2X
23.	609,6	304,8	2:1	0,6401	UF2X
24.	609,6	304,8	2:1	0,7772	UF2X
25.	304,8	457,2	1:1,5	0,5969	UF2X
26.	304,8	457,2	1:1,5	0,7493	UF2X
27.	457,2	457,2	1:1	0,6096	UF2X
28.	457,2	457,2	1:1	0,7493	UF2X
29.	304,8	609,6	1:2	0,6223	UF2X
30.	304,8	609,6	1:2	0,7620	UF2X

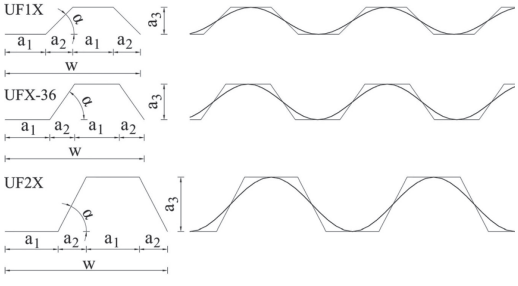

Figure 2. Geometry of corrugated webs.

4 COMPARISON WITH EXPERIMENTAL RESULTS

The ultimate shear capacity from the test (Elgaaly et al. (1996)) and the finite-element analysis for trapezoidal corrugations is given in Table 4.

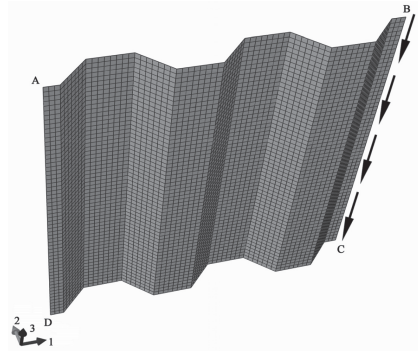

Figure 3. Numerical model.

Table 3. Boundary conditions of the numerical model (F-free, R-restrained).

Boudary	AB	BC	DC	DA
U1	R	R	R	R
U2	R	R	R	R
U3	F	F	F	R
UR1	R	F	R	F
UR2	R	F	R	F
UR3	R	F	R	F

Similar comparison for the sinusoidal webs is given in Table 5.

In general, it can be concluded that, despite the simplifications adopted in the numerical model, they give sufficiently accurate results (an average ratio for all models equal to 0,96) compared with the values obtained from the experiments. However, it can be seen that in the case of corrugations with a smaller depth (UF1X and UFX-36 – see Table 1) the values obtained from the experiments are generally lower than those of the numerical simulation (the corresponding averages ratios are 0,81 and 0,82), and for the geometry UF2X (the deepest corrugation) relationship is reversed—an average ratio of 1,18. Moreover, it can be observed that the proportions of the panel (height to width) do not affect the obtained results in a noticeable way.

As mentioned in Elgaaly et al. (1996), the difference in the results described above could be due to the presence of unavoidable out-of-plane initial geometric imperfections in the test specimens. Even so, the agreement between the analytical and experimental results appears to be satisfactory.

In addition, during the numerical analysis carried out for the purposes of this study, it was observed that the width of the last panels along the AD and BC edge (see Figure 3) affects the

Table 4. Comparison of results from tests and FEM for trapezoidal corrugations.

Model	$N_{cr,EXP,T}$ kN	$N_{cr,FEM,T}$ kN	$N_{cr,EXP,T}/N_{cr,FEM,T}$
1.	50,06	61,49	0,81
2.	87,67	104,62	0,84
3.	93,45	80,14	1,17
4.	119,53	152,31	0,78
5.	74,76	89,49	0,84
6.	96,21	138,17	0,70
7.	75,61	118,83	0,64
8.	133,41	195,51	0,68
9.	46,28	48,27	0,96
10.	72,54	92,59	0,78
11.	43,30	58,66	0,74
12.	61,23	90,50	0,68
13.	61,86	64,91	0,95
14.	97,90	125,78	0,78
15.	56,52	72,56	0,78
16.	93,45	112,65	0,83
17.	77,30	86,21	0,90
18.	126,78	167,06	0,76
19.	41,16	29,04	1,42
20.	61,19	52,35	1,17
21.	34,49	28,70	1,20
22.	53,40	84,53	0,63
23.	31,15	28,59	1,09
24.	48,95	51,03	0,96
25.	51,62	34,64	1,49
26.	80,10	68,31	1,17
27.	52,96	36,44	1,45
28.	78,68	67,48	1,17
29.	69,10	51,95	1,33
30.	101,51	95,12	1,07
		Average ratio:	0,96

Table 5. Comparison of results from tests and FEM for sinusoidal corrugations.

Model	$N_{cr,FEM,T}$ kN	$N_{cr,FEM,S}$ kN	$N_{cr,FEM,T}/N_{cr,FEM,S}$	$N_{cr,EXP}/N_{cr,FEM,S}$
1.	61,49	51,49	1,19	0,97
2.	104,62	77,47	1,35	1,13
3.	80,14	59,18	1,35	1,58
4.	152,31	99,00	1,54	1,21
5.	89,49	62,52	1,43	1,20
6.	138,17	88,47	1,56	1,09
7.	118,83	80,31	1,48	0,94
8.	195,51	135,29	1,45	0,99
9.	48,27	50,34	0,96	0,92
10.	92,59	82,02	1,13	0,88
11.	58,66	57,62	1,02	0,75
12.	90,50	79,57	1,14	0,77
13.	64,91	58,06	1,12	1,07
14.	125,78	97,14	1,30	1,01
15.	72,56	61,72	1,18	0,92
16.	112,65	86,57	1,30	0,88
17.	86,21	69,86	1,23	0,75
18.	167,06	118,32	1,41	0,77
19.	29,04	38,16	0,76	1,07
20.	52,35	61,24	0,86	1,01
21.	28,70	37,81	0,76	0,92
22.	84,53	90,59	0,93	1,08
23.	28,59	37,70	0,76	1,11
24.	51,03	60,26	0,85	1,07
25.	34,64	45,79	0,76	1,08
26.	68,31	78,89	0,87	1,00
27.	36,44	47,28	0,77	0,91
28.	67,48	77,17	0,87	0,59
29.	51,95	61,11	0,85	0,83
30.	95,12	97,78	0,97	0,81
			Average ratio:	1,01

ultimate shear capacity value. Unfortunately, there was no information in Elgaaly et al. (1996) what dimension of that panels had been adopted in the experience. Therefore, in all numerical models the total symmetry of the system was assumed, i.e. the width of the last panels is the same. Slightly different values of ultimate shear capacity were obtained in the case of varying the width of that two panels, while maintaining the overall length of the model.

On this basis the same assumptions in models with sinusoidal corrugated webs were made. The results from another thirty models with sinusoidal webs were summarized in Table 5 and compared first with numerical and later with experimental results for trapezoidal geometry.

Analyzing the results shown in Table 5, it can be concluded that it is reasonable to replace the geometry of the sinusoidal web with an equivalent trapezoidal shape, because their behavior under shear load is similar (Figures 4–9). The comparison of the numerical results for the panels with the sinusoidal web with the experimental ones, which used trapezoidal webs, gives a similar agreement as before (the average ratio of 1,01). The test results were higher than the numerical ones in the case of the geometry with small depth of the corrugation (UFX1) – an average ratio of 1,14. Whereas, in the case of the corrugation with bigger depth (UFX-36 and UFX2) values obtained from the numerical simulation are slightly higher than the experimental ones—respectively for each geometry ratio they are 0,96 and 0,97. However, in the case of the webs with sinusoidal webs it may be noted that models with dimensional proportions of 1:2 (twice higher than wider) give slightly lower results than the average for the group with the same geometry of corrugation.

Comparing the results of the numerical analysis obtained for trapezoidal and sinusoidal webs (Table 5), it can be concluded that the ultimate

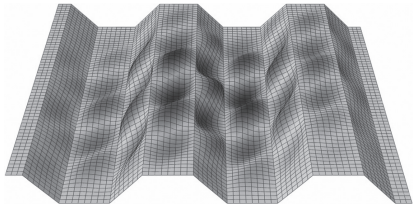

Figure 4. Buckling mode of model 1 – Trapezoidal.

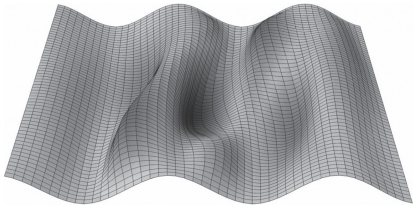

Figure 5. Buckling mode of model 1 – Sinusoidal.

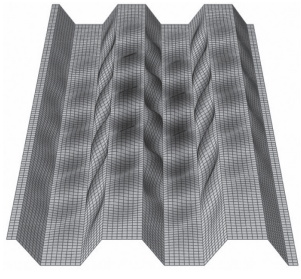

Figure 6. Buckling mode of model 17 – Trapezoidal.

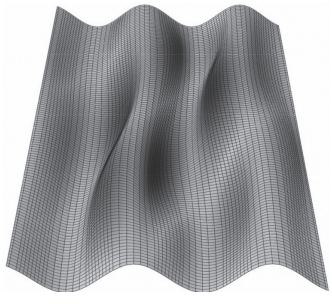

Figure 7. Buckling mode of model 17 – Sinusoidal.

shear capacity is higher for trapezoidal webs with small depths of corrugations. By contrast, the deeper the corrugation is, the more preferable it seems to use beams with sinusoidal webs. For the geometry UFX1 an average ratio was 1,42 in favor of the trapezoidal webs, for UFX-36–1,18, and for the geometry with the biggest depth (UFX2) the ratio was 0,83 in favor of the sinusoidal webs.

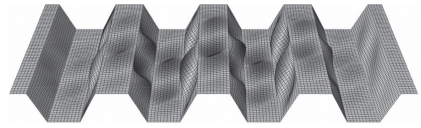

Figure 8. Buckling mode of model 23 – Trapezoidal.

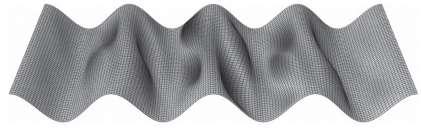

Figure 9. Buckling mode of model 23 – Sinusoidal.

5 COMPARISON WITH RESULTS FROM EUROCODE 3-1-5

Table 6 gives a comparison of the ultimate shear capacity obtained from numerical simulations with the values based on the Eurocode provisions, described in Section 2. It was decided to compare only the numerical values, because as mentioned earlier, they are not affected by deviations resulting from the geometric imperfections. The results shown in Tables 4 and 5, give the reason to conclude that the results are sufficiently accurate and can be used for further analysis.

In all models with trapezoidal webs a form of local buckling decided about shear capacity, except for Model 8, which was sensitive to the global loss of stability. Values obtained from the formula (3) and (5) in all models are lower than the values derived from the numerical simulations (average 0,90), which in engineering practice provides an estimation of capacity on the safe side. Geometric proportions of the model do not affect, in a significant way, the ultimate shear capacity values.

In the case of sinusoidal webs the form of local buckling was decisive in all models, therefore, an ultimate shear capacity was calculated only from the formula (4). However, for this geometry the differences in the assessment of capacity depend on the depth of the corrugation. For the geometry UFX1, with the shallowest corrugation, Eurocode values are lower than the numerical ones, with an average of 0,83. For geometry UFX-36 the average ratio is equal to 0,90, whereas, in the case of deepest corrugation UFX2 values obtained on the basis of the Eurocode are greater than those from numerical models, with an average ratio of 1,16. It should be noted that this is an estimation of the unsafe side.

Furthermore, in the case of sinusoidal webs the influence of the proportion of the panel on the final value of the shear capacity is more noticeable. It can be seen that the Eurocode formula provides a safer estimate for the ratio width to height of 1:2 (model 7, 8 for UFX1 geometry, models

Table 6. Results from numerical analysis and from equation (3), (4) or (5).

Model	$N_{cr,EC3,T}$ kN	$N_{cr,FEM,T}$ kN	$N_{cr,EC3,T}/N_{cr,FEM,T}$	$N_{cr,EC3,S}$ kN	$N_{cr,FEM,S}$ kN	$N_{cr,EC3,S}/N_{cr,FEM,S}$
1.	55,18	61,49	0,90	44,88	51,49	0,87
2.	95,16	104,62	0,91	69,31	77,47	0,89
3.	72,37	80,14	0,90	47,64	59,18	0,81
4.	139,96	152,31	0,92	82,28	99,00	0,83
5.	81,80	89,49	0,91	52,68	62,52	0,84
6.	127,68	138,17	0,92	76,20	88,47	0,86
7.	109,06	118,83	0,92	60,90	80,31	0,76
8.	155,50	195,51	0,80	105,78	135,29	0,78
9.	43,99	48,27	0,91	47,35	50,34	0,94
10.	85,11	92,59	0,92	78,81	82,02	0,96
11.	54,28	58,66	0,93	55,63	57,62	0,97
12.	84,27	90,50	0,93	78,20	79,57	0,98
13.	59,81	64,91	0,92	50,20	58,06	0,86
14.	116,82	125,78	0,93	85,78	97,14	0,88
15.	67,60	72,56	0,93	55,32	61,72	0,90
16.	105,52	112,65	0,94	79,01	86,57	0,91
17.	79,75	86,21	0,93	56,46	69,86	0,81
18.	155,75	167,06	0,93	98,01	118,32	0,83
19.	24,73	29,04	0,85	51,16	38,16	1,34
20.	73,31	52,35	0,85	78,90	61,24	1,29
21.	24,73	28,70	0,86	51,16	37,81	1,35
22.	44,27	84,53	0,87	113,83	90,59	1,26
23.	30,08	28,59	0,87	51,16	37,70	1,36
24.	59,51	51,03	0,87	113,83	60,26	1,30
25.	32,04	34,64	0,87	51,16	45,79	1,04
26.	59,51	68,31	0,87	78,32	78,89	1,01
27.	32,04	36,44	0,88	47,67	47,28	1,06
28.	59,51	67,48	0,88	79,60	77,17	1,03
29.	45,45	51,95	0,87	56,53	61,11	0,93
30.	83,45	95,12	0,88	90,43	97,78	0,92
Average ratio:			0,90			0,99

17, 18 for UFX-36 and models 29 and 30 for the UFX2). When the panels are larger in width than in height—and those are more common in the real construction—the values are overestimated when compared to the average for a given geometry (models 11, 12 for UFX-36 and 23, 24 for UFX2).

6 CONCLUSIONS

The paper presents the values of ultimate shear capacity of panels with the trapezoidal and sinusoidal web obtained from numerical simulation. It compared them with the experimental results described in Elgaaly et al. (1996), where the steel beams with trapezoidal webs of different dimensional proportions were investigated. The numerical values were also compared with the results based on the Eurocode 3–1-5 provisions.

The comparison between the strength calculated by using the finite-element model and that obtained from the tests are very satisfactory. It can be concluded that it is reasonable to replace the geometry of the sinusoidal web with an equivalent trapezoidal shape, because their behavior under shear load is similar.

For trapezoidal webs subjected to shear it was found that the strength can be calculated, to a very good degree of accuracy, by using the buckling stress formulas for flat isotropic or orthotropic plates, given in the Eurocode 3-1-5. Also, in the case of the sinusoidal webs code formulas gave the correct values of capacity, although with a deeper corrugations the obtained values were on the dangerous side. Differences in the overestimation of the ultimate shear capacity are even greater in the case of the panels which are wider than higher, i.e. they have the proportions that occur in real structures.

REFERENCES

Abbas, H.H., Sause, R. & Driver R.G. 2002. Shear strength and stability of high performance steel corrugated web girders. *SSRC conference*: 361–87.

Easley, J.T. & McFarland, D.E. 1969. Buckling of light-gage corrugated metal shear diaphragms. *Journal of the Structural Division ASCE 95*: 1497–516.

Elgaaly, M., Hamilton, R.W. & Seshadri, A. 1996. Shear strength of beam with corrugated webs. *Journal of Structural Engineering ASCE*; 122(4): 390–398.

Ibrahim. S.A., El-Dakhakhni, V.W. & Elgaaly, M. 2006 Behavior of bridge girders with corrugated webs under monotonic and cyclic loading. *Engineering Structures* 28(14): 1941–55.

Kuchta, K.R. 2004. *Nośność i Sztywność Blachownic o Falistych środnikach*, Kraków: Politechnika Krakowska, Kraków.

Kuchta, K.R. 2007. Design of corrugated webs under patch load. *Advanced Steel Construction* 3(4): 737–751.

Lindner, J. 1988. Aschinger R. Grenzschubtragfähigkeit von I-trägern mit trapezförmig profilierten Stegen. *Stahlbau* 57(12): 377–80.

Moon, J., Yi, J. & Choi, B.H. & Lee, H.E. 2009. Shear strength and design of trapezoidally corrugated steel webs. *Journal of Constructional Steel Research* 65(5): 1198–1205.

Pasternak, H. & Brańka, P. 1999. Tragverhalten von Wellstegträgern unter lokaler Lasteinleitung, *Bauingenieur* 5 pp. 219–224.

Sause, R. & Braxtan, T.N. 2011. Shear strength of trapezoidal corrugated steel webs. *Journal of Constructional Steel Research* 67: 223–236.

Sause, R., Abbas, H.H., Wassef, W., Driver, R.G. & Elgaaly, M. 2003. Corrugated web girder shape and strength criteria: work area 1. Pennsylvania innovative high performance steel bridge demonstration project. ATLSS report no. 03–18. Bethlehem (PA): *Advanced Technology for Large Structural Systems. ATLSS.* Center. Lehigh University.

Yi, J. & Gil, & H. Youm, K. & Lee H. 2008. Interactive shear buckling behavior of trapezoidally corrugated steel webs. *Engineering Structures* 30(6): 1659–66.

Recent Progress in Steel and Composite Structures – Giżejowski et al. (Eds)
© 2016 Taylor & Francis Group, London, ISBN 978-1-138-02946-0

Curved cold formed steel roofing: Numerical and experimental analysis

L.C. Prola, T.F.R. Lopes, J.R. Baptista & P.A.L. Fernandes
School of Technology and Management, Polytechnic Institute of Leiria, Leiria, Portugal

ABSTRACT: This work addresses the numerical and experimental analysis of the self-supporting steel roofings produced by the company "Blocotelha—Steel Constructions, SA" in Portugal. The numerical results are presented taking into account geometric and physical non-linearities in order to characterize the structural behavior of cold formed steel roofing and compare them to the performed experimental work. The results were obtained numerically (using the computer program ABAQUS) and experimentally (through tests performed at the Structures and Reinforced Concrete Laboratory in the School of Technology and Management of Leiria) in terms of tables, charts and graphs of the results, such as: (i) stress-strain diagrams, (ii) force-displacement, (iii) force-stress, and (iv) moment-curvature.

1 INTRODUCTION

There are few studies on the curved steel roofing systems, in contrast with its vast uses, mainly in industrial buildings.

The first relevant works on the cold formed steel sheeting have focused on experimental work which in many cases was compared to specifications, especially to the US standard (AISI, 2007). Using this methodology, in the 1970s, Jorgenson & Chern, (1973) performed an experimental study of straight and curved trapezoidal sheeting with small spans which was compared to the results obtained by the AISI standard. Subsequently, in another work, Bergfelt et al. (1975) added to their experimental work the study on the influence of local buckling over the overall strength. Jorgenson & Chowdhury (1982) compared the load capacity of straight and curved sheeting.

Following a similar procedure, Bernard et al. (1993) compared previously conducted tests for trapezoidal sheeting to results obtained under the US (AISI, 2007) and European (*CEN*, 2004) specifications.

For the experimental results of Bernard et al. (1992a,b), Wu et al. (1995) used the specifications given by the AISI standard to the calculations of the Australian (AS 1397 and 650) and North American (ASTM A613-80) steel. The AISI specifications were also used by Papazian et al. (1994) for the comparison with results of experimentally tested trapezoidal sheeting. The same was done by Landolfo & Mazzolani, (1994) in order to perform comparisons with the European specifications.

Fonseca (2000) studied the behavior of cantilever bending steel sheeting, in order to evaluate different types of connections between them. This author compared the results to those theoretical ones obtained by AISI specifications and to a finite element model with linear elastic behavior. Mezzomo (2007) used the finite element to compare critical loads obtained in his experimental work for the same type of sheeting.

Liew et al. (2007) proposed a nonlinear analysis method of corrugated sheeting with and without reinforcement by means the shear first-order deformation theory. The results were compared to simulations performed by ABAQUS software (Simulia Inc., (2008)).

In the work developed by Caramelli et al. (2001) a numerical and experimental study of the sections of cold formed steel sheeting was performed and compared to the results obtained according to the methods recommended by the Italian CNR 10022 standard and the Eurocode 3 (*CEN*, 2004). The numerical analyzes were performed using shell finite elements with ADINA software, in order to verify the applicability of regulatory specifications.

Recently, genetic algorithms for optimization have been applied, as shown by Mezzomo, et al. (2010) applying these algorithms in the geometry of the trapezoidal sections optimization. Mezzomo et al. (2014) analyzed the influence of the boundary conditions and Lu & Mäkeläinen (2006) optimize the sections, using the specifications of EC3.

This paper intends to initiate the study of the profile manufactured by "Blocotelha", a Portuguese company, designated BC900, which presents an Omega-type section and has the ability to cover spans up to 30 meters. The main objective of this study is to characterize the behavior currently used by Blocotelha—Steel Constructions, SA by experimental and numerical analyses.

The structure's experimental analysis is divided into two different approaches: (i) the mechanical characterization of the steel sheet constituent material and (ii) the analysis of two three-profile sets with curved axis and a 12 m span. Experimentally, this intends to (i) obtain the mechanical properties of the steel that constitute the cold formed profile and (ii) analyze the behavior of the roofing system subjected to a mid-span applied load and evaluate its strength capacity.

The numerical analysis is based upon geometrically non-linear numerical modeling of two cases: (i) on the elastic-plastic post-buckling behavior of BC900 omega cold formed profile with straight axis to characterize its phenomena of instability and (ii) the simulation of the experimentally tested 12 m profile, by using, in both situation, the ABAQUS computer program (Simulia Inc., (2008)).

2 EXPERIMENTAL WORK

2.1 *Tension testing*

The tensile strength of the BC900 steel sheet was experimentally determined according to the ISO 6892-1 specification (2009). Twenty specimens (10 type I and 10 type II—the nominal dimensions shown in Table 1) were obtained by cutting a plane steel sheet. The specimens were then measured individually.

The tensile tests were performed using the testing speed rate recommended by the European standard, which were, for the type I and type II, respectively, 0.675 mm/min and 0.8475 mm/min. It is presented the average, maximum and minimum values (with standard deviation) obtained for the mechanical properties related to yield stress and rupture (Table 2) and Young Modulus (Table 3).

The results are represented in Figures 1–2, as well as a summary of all the data collected from tensile tests carried out for a total of 19 specimens (one of the tests was not considered).

Table 1. Dimensions defined for specimens.

Dimensions defined for specimens [mm]				
	b_0	L_0	L_c	
			Paralell length	
Type	Paralel width	Gauge length	Minimum	Recomended
I	12,5 ± 1	45	57	75
II	20 ± 1	55	90	120

According to Table 3, the average yield stress for Type I specimens was approximately 34% superior to its nominal value (250 MPa) and the ultimate stress exceeded by 14% its nominal value (330 MPa). The average ratio of ultimate stress and yield stress, which defines the ductility of the material, was found to be 15% lower than its nominal value (1.32). With regard to the Type II specimens, the results for the same parameters are, respectively, 41% higher, 14% higher and 20% lower.

The Type II specimen's average value for the modulus of elasticity was found to be 11% higher than the Type I's. It is worth noting that the test results for Type I specimens were obtained using an inferior displacement control speed.

2.2 *3-Profile experimental setup*

The cold formed steel roofing system constituted by three profiles linked at the edges by bolts was

Table 2. Yield and Maximum stress of type I and II specimens.

Summary table			
	Yield stress [MPa]	Maximum stress [MPa]	f_u/f_y
Type I Specimen			
$\overline{x}$	**334,86**	**375,03**	**1,12**
σ	14,81	1,52	–
Type II Specimen			
$\overline{x}$	**353,37**	**375,47**	**1,06**
σ	13,15	3,82	–
Max	368,72	381,03	–
Min	335,73	371,28	–

Table 3. Young Modulus of type I and II specimens.

Young modulus	
Type I Specimen	
$\overline{x}$	**175.34 GPa**
σ	1.47
Max	176.90 GPa
Min	173.37 GPa
Type II Specimen	
$\overline{x}$	**194.77 GPa**
σ	3.04
Max	198.17 GPa
Min	190.80 GPa

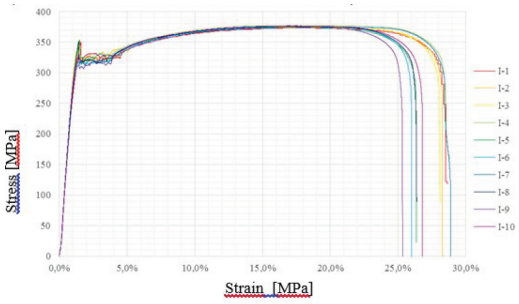

Figure 1. Tensile test—Type I specimens.

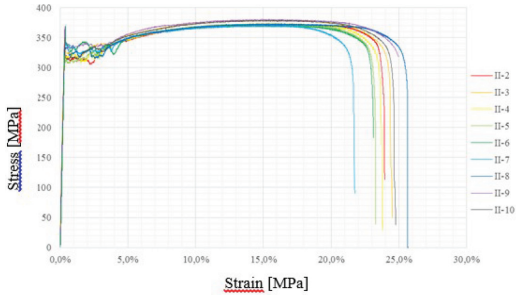

Figure 2. Tensile test—Type II specimens.

installed in a current support the company (Blocotelha) uses. It prevents the displacement in the horizontal and vertical directions, allowing the rotation along the horizontal axis. This support has been assembled on the hot-rolled steel profiles to give a stable basis for the realization of experimental tests in the Structures and Reinforced Concrete Laboratory of Leiria Technology and Management School in Portugal (see Figure 3). The test scheme was composed by fixed and simple support in the opposite ends which were linked by tie bars.

The load was applied through an actuator with 1000 kN of capacity and a load cell, using a hot-rolled profile and sand bags to distribute the load across the width of the section of the assembly, as shown in Figure 4.

The instrumentation of the test sets was performed with 24 strain gauges "Tokyo Sokki Kenkyujo Co., Ltd" PFL-10-11 type and 2 transducers of displacements "Tokyo Sokki Kenkyujo Co., Ltd" SDP-300D, with 300 mm of maximum displacement for each set, half at ½ of span, the other half at ¼. Figure 5 represents the distribution scheme of the strain gauges in each center section on ½ and ¼ lengths, for a total of 22 strain gauges on the steel roofing with two gauges on the tie bars.

In order to measure the vertical deflection, two displacement transducers were linked to the same

a) Set up test

b) Tie bars

Figure 3. Test scheme.

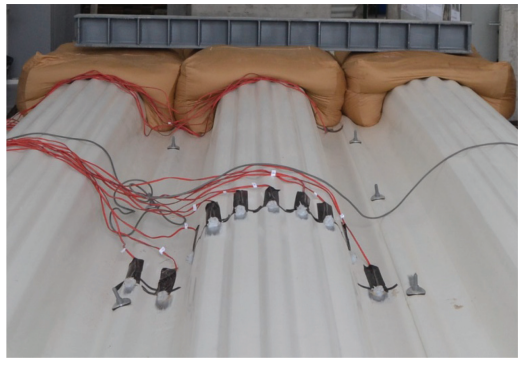

Figure 4. Sand bags and hot-rolled steel supporting beam.

Figure 5. Location of the strain gauges in the transversal section.

sections above mentioned by means two steel filaments, using pulleys to deflect each of the wires and it was fixed to the metal parts by bonding with silicone.

The concentrated load was applied at mid-span with a constant speed of 0.25 mm/min using a

hydraulic actuator resource "Servosis" CH4-100/C300 with a maximum displacement of 300 mm, a loading capacity of 1000 kN and a "Servosis" PCI-200 load cell with 2,000 kN capacity.

While carrying out the first set of tests, there were two cycles of load and unload (because the failure detection configuration was activated in hydraulic actuator control), as shown in the Figure 6.

This figure shows the response of the structure against these cycles, which represents the variation of applied force in the structure with vertical mid span displacement. The weight of sand bags was approximately 8.8 kN, which explains why the curves of the initial part of the curves do not start at the origin. It is observed that, up to 22 kN, the structure behavior is linear elastic and, from that on, there is an elasto-plastic response with loss of rigidity. The curves show a load increase right after the first unload level, where there is a slight increase in resistance, reaching approximately 26.5 kN. The ultimate strength of the structures was found for approximately 27 kN.

The moment-curvature curve represented in Figure 7 shows the behavior of the section at mid span subjected to the applied load. Initially, there is a linear behavior up to approximately 0.026 m^{-1}, from which point it starts to display deformation of the structure until reaching a curvature of 0.042 m^{-1}. It was also observed that the section displays a curve of variation which does not significantly increase from the acting moment up to its collapse.

In order to obtain these moment-curvature curves, the evolution of acting moment in the structure was considered at each moment of loading, taking into account the reaction support, the installed force on the tie bars and the height variation of the structure throughout the test. For the calculation of the curvature, the extensions in two strain gauges were evaluated, one on top and one lower, depending on the distance between them.

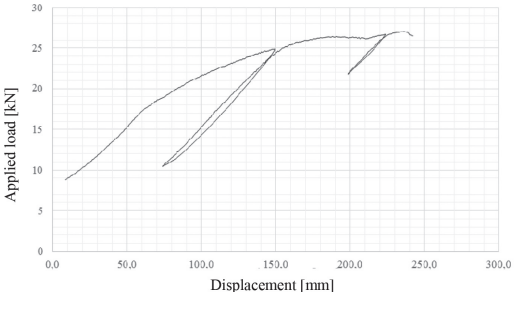

Figure 6. Force-displacement curves for test 1.

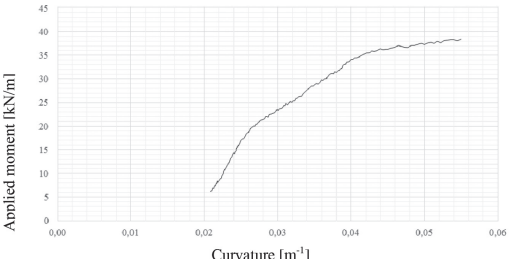

Figure 7. Moment-Curvature of test.

3 NUMERICAL ANALYSIS

3.1 *Elastic-plastic post-buckling behavior*

The numerical modeling of the experimental tests described in the previous section and performed by Baptista (2015) has been carried out by Lopes (2015) as part of his dissertation, using the ABAQUS program (Simulia Inc., 2008). A four node isoparametric shell finite element (S4) was used, taking into account previous tests and simulations, adopting a mesh of elements with 10 mm length in longitudinal direction.

First it was performed a linear stability analysis to (i) determinate the value of critical load, (ii) identify the length associated with the critical buckling modes and (iii) obtain the deformed shape of buckling modes to be used as geometric imperfections into the post-buckling analysis.

Figure 8 presents the values obtained from the linear stability analysis of the pure compression. The depicted curve represents the variation of the critical stress σ_{cr} (the smallest value of the bifurcation stress) with the length (L) (in logarithmic scale). At the bottom of this figure the relevant instability modes are represented.

The buckling curves have three distinct zones, associated with critical modes. The first minimum occurs for L ≈ 100 mm and it is associated to the Local Plate (LP) mode with deformed configuration displaying one wavelength. With increasing the length of the critical mode remains the LP with various half-wave lengths. A second minimum occurs for a length L ≈ 2350 mm and it is associated with a Distortional (D) mode with a half-wave. For L ≈ 4200 mm the mode of instability change from a D mode with two half-waves to a FT mode with one half-wavelength.

The end sections has considered as fixed for transverse displacements and free slopes (simply supported boundary condition). To obtain a uniform state of compression it was applied a set of compression longitudinal force at the end nodal points. The Young's Modulus and Poisson's ratio of the steels are E = 210 GPa and ν = 0.3,

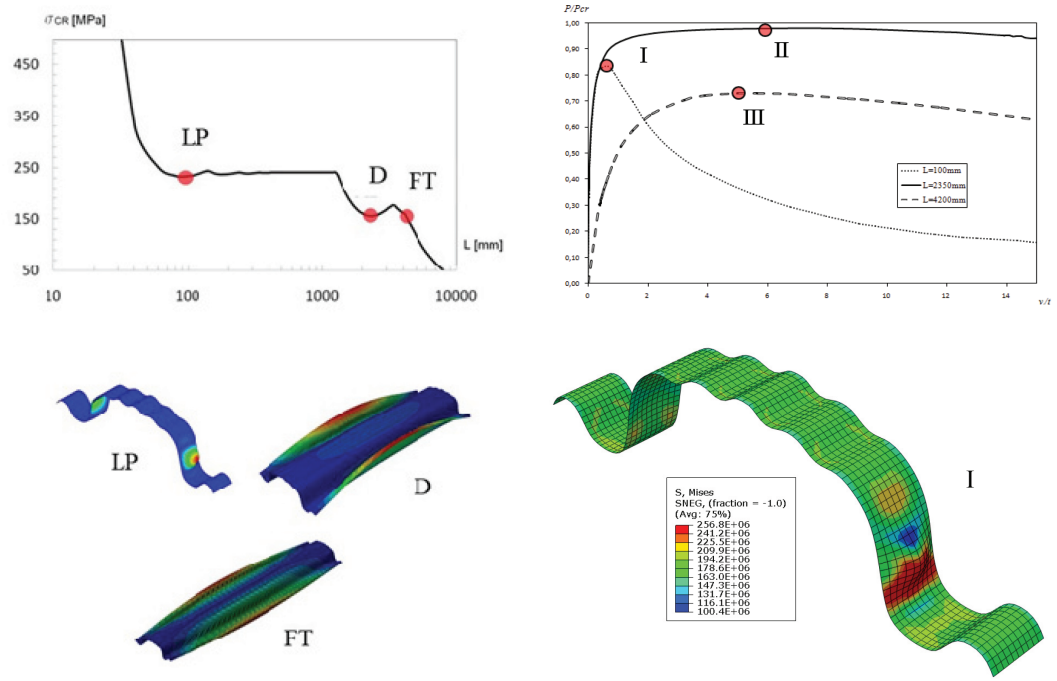

Figure 8. Linear stability analysis.

respectively. It was taken into account the initial geometric imperfections with the magnitude of amplification pure instability modes with 10% of the thickness (t) to local modes LP and distortional D modes and L/1000 for the overall FT mode with configurations shown in Figure 9. In the Figure 9 the elastoplastic equilibrium curves (variation of the load-critical load ratio P/P_{cr} with characteristic displacement/thickness ratio v/t of the associated mode) for the three modes of instability (I-MLP, MD-II and III-MGFT) for a steel with f_y = 250 MPa are presented. The marked points in the curves refer to the maximum stress for the three instability modes. It is observed that the section yielding has strong effects only over de LP mode. In the same figure it is also represented the stress distribution on the profile.

3.2 *Numerical modeling of the experimental tests*

In the Figure 10, the black curve refers to the group behavior modeled of three cold formed steel sections as if they were solidly connected at the longitudinal edges. The curves represented by red and green lines are the results of the two experimental tests of Baptista (2015) reported in section 2 of the present work. The curves of numerical simulations are well correlated to the experimental results, except for the initial deformation caused by the sand bag weight.

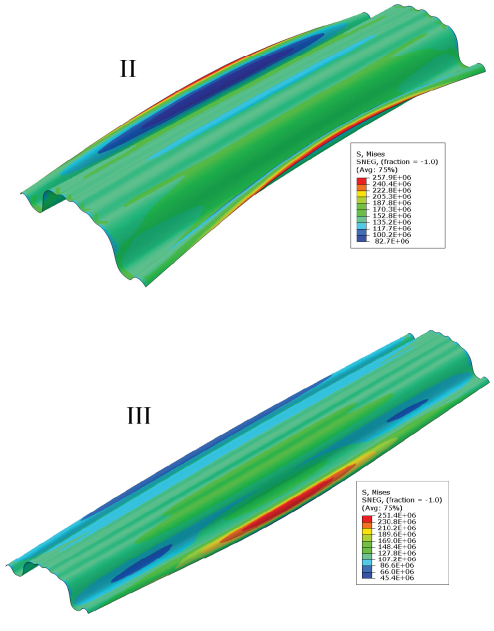

Figure 9. Column elastoplastic behavior for L = 100 mm, L = 2350 mm and L = 4200 mm.

The numerical results of the variation in the longitudinal stress across the (rectified) width of the isolated profile, with fixed displacements at its edges, in order to simulate the condition of

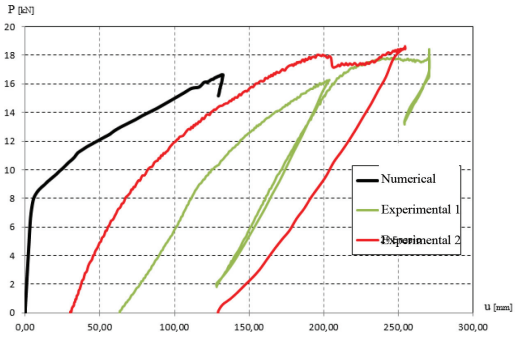

Figure 10. Load/displacement curves without sand bags weight.

continuity for adjacent profiles, in the mid-span section are represented in Figure 11 for three levels of loading: (i) P = 4.21 kN (ii) P = 9.45 kN and (iii) P = 15.72 kN. One observes the development of low tensile stress in the lower flange. The compressive stresses are higher in the central region of the upper flange section (because of the concentrated load) and in the borders of the section (for distortional instability phenomena).

These compressive stresses progressively intensify as the applied load is increased, while the tensioned area becomes gradually less stressed. In other parts of the section, mainly because of the rigidity provided by its folds, no significant stresses were installed. It was not possible to establish comparisons for exactly equal loads because the increases on the numerical procedure were a little different than the experimental procedure ones. Also, the presence of imperfections in the present experimental tests is not considered in the numerical modeling; the distribution of stresses reveals some asymmetries in the experimental results. However, the behavior of the numerical and experimental curves has good correlation (only the positives values obtained experimentally by Baptista (2015), not differentiating tension and compression, are presented in graphics). There is a difference in the stresses of the sections edges that is caused by different boundary conditions applied in testing and modeling numerically. That is because the sections were bolted meter by meter in overlapping zone, while in the numerical modeling the restriction on displacement of these points was imposed, which justifies a higher value of the stresses than the values found in experimental tests.

For a section located at a quarter of the span, Figure 12 shows the same type of numerical results presented to a mid-pan section. The highest compressive stresses are in the vicinity of the lower flange, caused by the distortional instability, while in the upper flange the central section very

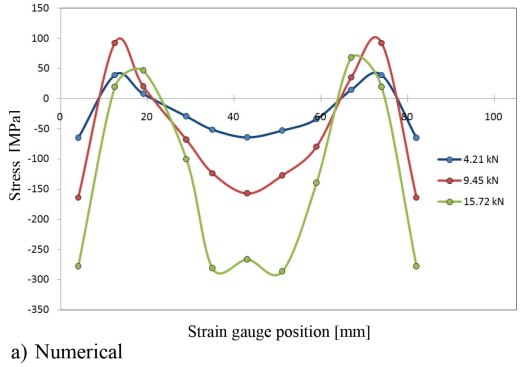

a) Numerical

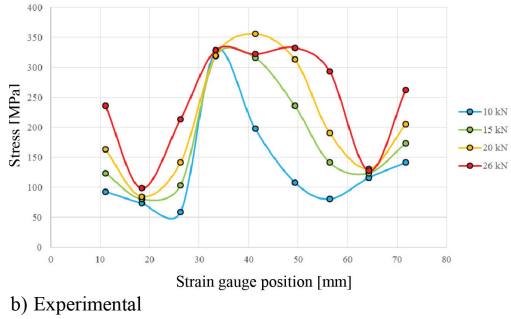

b) Experimental

Figure 11. Stress variation in the transversal section (1/2 span): Numerical and Experimental.

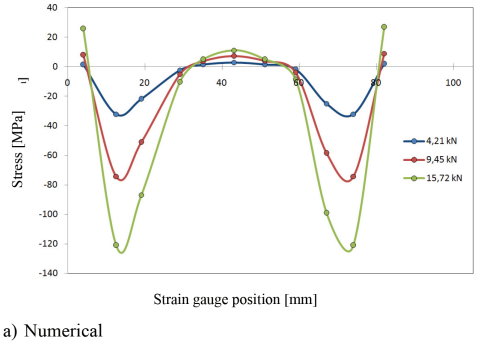

a) Numerical

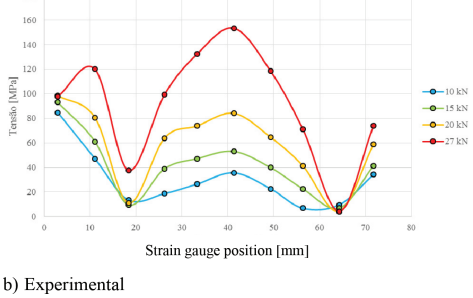

b) Experimental

Figure 12. Stress variation in the transversal section (1/4 span): Numerical and Experimental.

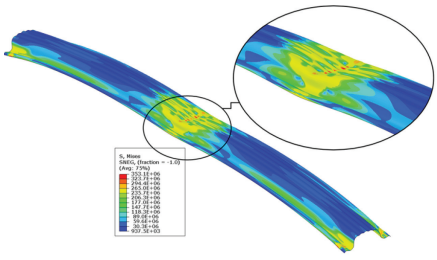

a) Numerical

b) Experimental

Figure 13. Collapse configuration: numerical (Lopes, 2015) and experimental (Baptista, 2015).

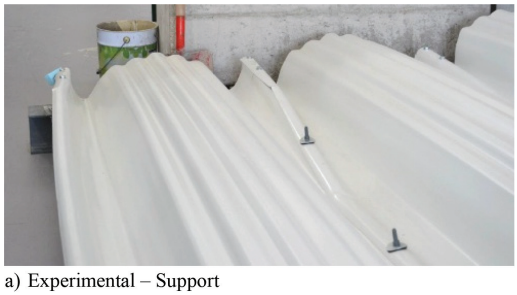

a) Experimental – Support

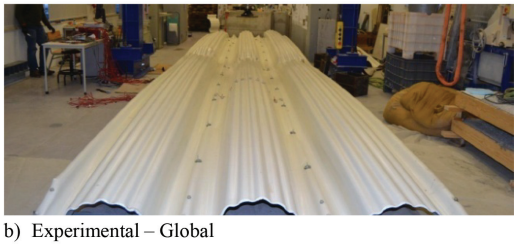

b) Experimental – Global

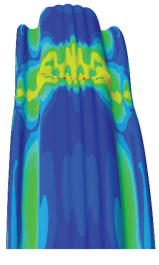

c) Numerical

Figure 14. Experimental and numerical results for the lateral edges deformation.

low stresses develop, since there is no concentrated load applied in this part of section.

Finally it is worth presenting the comparison between the deformed configurations obtained from the numerical simulation performed by Lopes (2015) and the strains obtained in the experiments by Baptista (2015). Figure 13 shows the failure mechanism for the two types of approach (numerical and experimental), where the failure occurs by yielding of the load applied at mid-span zone.

The lateral edges develop distortional deformation caused by the instability of the section—a phenomenon that was observed both in the experimental tests and in the numerical modeling (Figure 14).

4 CONCLUSIONS

In this work numerical simulations performed for curved cold formed steel roofing were compared with the experimental results. This allowed the observation that the numerical analyzes, compared with the experimental results (assuming that the strength experimentally measured is divided by the three sections uniformly), achieve good correlation.

In the stress distribution obtained numerically for mid-span section, the highest compressive stresses are installed in the central region of the upper flange and in the edges, while the tensile stresses develop in the lower flange, and as the load increases, the compressive stresses progressively increase and tensile stresses decrease. Due to the stiffness of the section, significant stresses will not settle in other areas. The experimental results compared with the numerical ones present asymmetries, largely because of the geometric imperfections not considered in numerical modeling. The stresses observed on the longitudinal edges are due to the modeling of boundary conditions, imposing restrictions on the lateral displacement and not taking into account the overlap of the edges in the experiments, which justifies a higher value of the tensions found in numerical model.

Finally, with regard to collapse, the deformed configurations in the numerical model and the experimental tests have very good correlation. The failure mechanism for the two types of approaches was derived from plasticization in the zone of load application and occurrence of distortion of the edges of profile.

REFERENCES

American Iron and Steel Institute (AISI) 2007. North American Specification for the Design of Cold-Formed Steel Structural Members. Washington DC.

Baptista, J. 2015. *Experimental Analysis of Curved Cold Formed Steel Roofing,* MSc. Thesis, Polytechnic Institute of Leiria. (in portuguese).

Bergfelt, A., B., Edlund, and Larsson, H. 1975. Experiments on trapezoidal steel sheets in bending. *Proc. of the Third International Specialty Conference on Cold- Formed Steel Structures*. Missouri: 285–314.

Bernard, E.S.B., Bridge, R.Q. & Hancock, G.J. 1992b. Intermediate Stiffeners in Cold-Formed Profiled Steel Decks". Part 2: "Flat Hat" Shaped Stiffeners. *Research Report n° 658*. Center for Advanced Structural Engineering, School of Civil and Mining Engineering. University of Sydney.

Bernard, E.S.B., R.Q. Bridge, R,Q. & Hancock, G.J. 1992a. Intermediate Stiffeners in Cold-Formed Profiled Steel Decks. Part 1: "V" Shaped Stiffeners. *Research Report n° 653*. Center for Advanced Structural Engineering, School of Civil and Mining Engineering. University of Sydney.

Bernard, E.S.B., R.Q. Bridge, R.Q. & Hancock, G.J. 1993. Design of Decking Panels with Intermediate Stiffeners. *Research Report n° 676*. Center for Advanced Structural Engineering, School of Civil and Mining Engineering. University of Sydney.

Caramelli, Croce, S.P. & Salvatore, W. 2001. Multiple stiffened cold-formed steel profiles for cylindrical vault roofing systems. *Journal of Constructional Steel Research. 57*(8): 831–854.

CEN. 2003. *Design of Steel Structures*, Part 1.3: General Rules (Eurocode 3), Supplementary Rules for Cold Formed Members and Sheeting. ENV 1993-1-3. Brussels.

Fonseca, N.D.R. 2000. Evaluation of theoretical and experimental behavior of cold formed steel roofing subjected to bending. MSc. thesis, UFRGS, Porto Alegre. (in portuguese).

ISO6892-1:2009. 2009. *Metallic materials*—Tensile testing—Part 1: Method of test at room temperature.

Jorgenson, J.L. & Chern., C. 1973. Bending strength of deep corrugated steel panels. *Proc. of the Second Specialty Conference on Cold-Formed Steel Structures. Missouri*: 225–258.

Jorgenson, J.L. and Chowdhury, A. H. 1982. Buckling strength of cold-formed steel curved panels. *Proc. Of Sixth International Specialty Conference on Cold-Formed Steel Structures*, Missouri: 115–132.

Landolfo, R. & Mazzolani, F.M. 1994. Ultimate Behaviour of Trapezoidal Steel Sheets in Bending. *Twelfth International Conference on Cold-Formed Steel Structures*. Missouri: 205–215.

Liew, K.M., Peng, L.X. & Kitipornchai, S. 2007. Nonlinear analysis of corrugated plates using a FSDT and a mesh free method. *Computer Methods in Applied Mechanics and Engineering*, 196(21–24): 2358–2376.

Lopes, T. 2015. *Structural Analysis of Curved Cold Formed Steel Roofing*, MSc. Thesis, Polytechnic Institute of Leiria. (in portuguese).

Lu, W. & Mäkeläinen, P. 2006. Fuzzy optimization of cold-formed steel sheeting using genetic algorithms. *Journal of Constructional Steel Research. 62*(12): 1276–1281.

Mezzomo, G., 2007. Structural analysis of cold formed trapezoidal sheeting. *Master's thesis*. UFRGS, Porto Alegre. (in Portuguese).

Mezzomo, G.P., Iturrioz, I., Grigoletti, G. & Gomes, H.M. 2010. Investigation of the mechanical behavior of trapezoidal roofing sheets using genetic algorithms. *Expert Systems with Applications*. 37(2): 939–948.

Mezzomo, G.P., Iturrioz, I., Grigoletti, G. & Gomes, H.M. 2014. Influence of the fixing type in the optimization of trapezoidal roofing sheets. *Journal of Constructional Steel Research. 96*(0): 26–39.

Papazian, R.P., Schuster, R.M. and Sommerstein, M. 1994. Multiple Stiffened Deck Profiles. *Twelfth International Conference on Cold-Formed Steel Structures*. Missouri: 217–228.

Peng, L.X., Liew, K.M. & S. Kitipornchai, S. 2007. Analysis of stiffened corrugated plates based on the FSDT via the mesh-free method. *International Journal of Mechanical Sciences*, 49(3): 364–378.

Simulia Inc..Abaqus Standard (version 6.7–5), 2008.

Wu, S., Yu, W.W. & LaBoube, R.A. 1995. Strength of flexural members using structural grade 80 of A653 and grade E of A611 steels. *Technical Report: Civil Engineering Study 97-3 Cold-Formed Steel Series*. University of Missouri-Rolla.

Recent Progress in Steel and Composite Structures – Giżejowski et al. (Eds)
© 2016 Taylor & Francis Group, London, ISBN 978-1-138-02946-0

Flexural elastic buckling stress of light gauge built-up member

K. Mitsui & A. Sato
Department of Scientific and Engineering Simulation, Nagoya Institute of Technology, Nagoya, Aichi, Japan

H. Okada
Department of Architecture, Aichi Institute of Technology, Toyota, Aichi, Japan

T. Ono
Nagoya Institute of Technology, Nagoya, Aichi, Japan

ABSTRACT: In Steel Framed House, a built-up member is used for stud. Usually, a stud is composed by two light gauges and interconnected by self-drilling screws. In Japan, flexural buckling strength of the light gauge built-up compression member is evaluated by effective slenderness ratio. The formula is based on Bleich's assumption which was applied for heavy section. From this reason, it is questionable that the formula can be directly applied in light gauge. Firstly, full scale testing were conducted to clarify this issue. Batten type light gauge built-up members were used for specimens in this study. Secondly, the energy equilibrium theory was used to derive flexural elastic buckling strength of the built-up members. Bending moment distribution which were used in this derivation was based on test observation. Moreover, modified effective slenderness ratio was proposed. Finally, supplemental results were obtained from finite element analysis to verify the proposed formula.

1 INTRODUCTION

In Japan, Technical Notification (Ministry of Land, Infrastructure, Transport and Tourism 2001) for Steel Framed House was issued by the Ministry of Land, Infrastructure and Transport in 2001. Light gauge members have become available to the main structure members, and design using light gauge members was enabled. Also, Technical Notification was revised (Japan iron and steel federation 2014), story limit has been extended up to four story and the middle-rise building has become possible to build. Steel Framed House (SFH) model and the detail of shear wall are shown in Figure 1.

The shear wall of SFH is designed as cantilever column, the lowest story shear wall resist against overturning moment from upper stories. The increase of total story increases the axial force of the built-up member of the shear wall. The shear wall of SFH is composed with light gauge frames, a plaster boad and a structural plywood. And the ultimate strength of the shear wall is determined by peeling off panels from the frame. After peeling off panels, there is a possiblity that flexural buckling occurs at the built-up member (vertical frames of the shear wall). The occurrence of the flexural buckling leads to the loss of vertical bearing sharply. In the conventional design for low-rise building, only the safety for the flexural buckling of full web was considered. Therefore, it is necessary to confirm the safety for the flexural buckling of opened web.

In Japan, the buckling stress of built-up compression member is calculated by effective slenderness ratio that is specified in the Design Standard for Steel Structure (AIJ 2005). This formula specified in the Standard is based on Bleich's assumption (Bleich 1952) which was applied for heavy section. Also, Eurocode (ECS

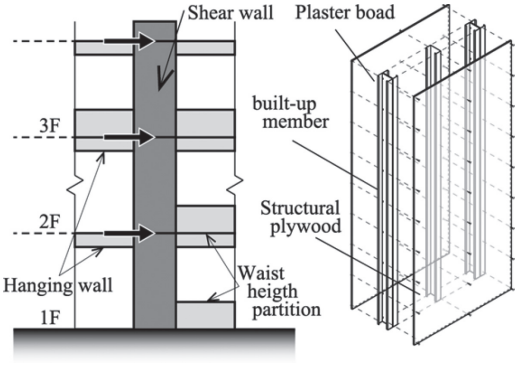

Figure 1. Steel Framed House and shear wall.

2005) follow Bleich's assumption. From this reason, it is quesionable that the formula specified in the Standard can be directly applied in light gauge. Moreover, the bending moment distribution due to flexural buckling was not confirmed by testing.

In this paper, to clarify the buckling strength of light gauge built-up member and the bending moment distribution in the components, full-scale testing of batten type light gauge built-up compression members in elastic range are conducted. The equilibrium theory is applied and modified effective slenderness ratio of light gauge built-up compression members are derived based on the observed bending moment distribution. Finally, to confirm the accuracy of the proposed formula and to supplement test results, the parametric analysis is done by finite element models.

2 TEST PROGRAM

2.1 *Test specimens*

To confirm the flexural buckling of built-up compression member composed two chords are interconnected by batten plates by bolts in elastic range, full-scale testing are conducted. Because the thickness of light gauge used in this test are less than 2.3 mm, the buckling mode in the elasto-plastic range is very complicated. Therefore, to confirm buckling mode clearly, the target specimens are in elastic range in this study. Parameters selected to determine the configuration of the specimens were separation between connectors a, distance between centroids of chords h, and length of the member L. Figure 2 shows the cross section of the test specimens.

As shown in Figure 2, two chords are interconnected by batten plates by pretension bolts. The chord used in this study is C-89 × 40 × 12 mm (called 89 LCN22) and its thickness is 2.2 mm. Figure 3 shows sample test specimens conducted in this study.

Material properties are shown in Table 1, and chord section properties are shown in Table 2.

Geometrical dimensions and mechanical properties of built-up compression members are shown in Table 3. The number in Table 2 refers to the last number of the specimen's name. λ_{ye} is the effectiveslenderness ratio of the built-up compression member in the Design Standard for Steel Structure (AIJ 2005) shall be determined as follow:

$$\lambda_{ye} = \sqrt{\lambda_y^2 + \lambda_1^2} \tag{1}$$

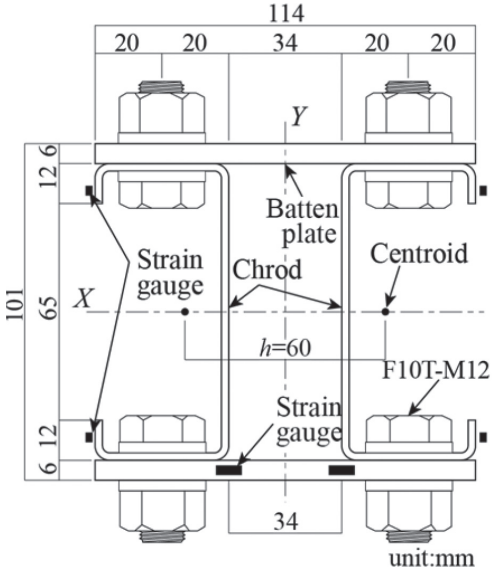

Figure 2. Cross section of test specimens.

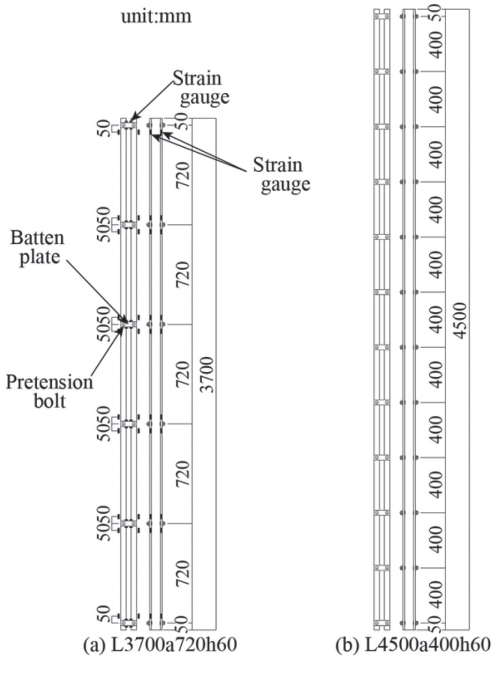

Figure 3. Test specimens.

$$\lambda_y = \frac{L}{i_y} \tag{2}$$

$$\lambda_1 = \frac{a}{i_1} \tag{3}$$

Table 1. Material properties from coupon tests.

Member	Number	E (N/mm^2)	σ_y (N/mm^2)	σ_u (N/mm^2)
Chord	1	201600	306	456
	2	208800	307	461
Batten		213100	309	446

Where: E is Young's modulus; σ_y is yield strength; σ_u is ultimate strength.

Table 2. Chord section properties.

Member	Number	A_1 (mm^2)	I_1 (mm^4)	i_1 (mm)
89 LCN22	1	396	86220	14.20
	2	391	85340	14.77

Where: A_1 is cross sectional area of each individual component; I_1 is moment of inertia of individual components; i_1 is radius of gyration of individual components.

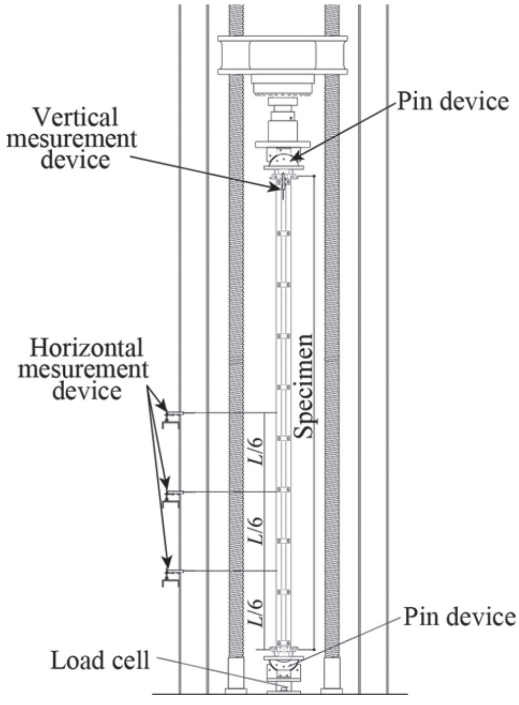

Figure 4. Test setup.

where λ_y is slenderness ratio of built-up member acting on a unit in the buckling direction being considered; λ_1 is slenderness ratio of individual component between connectors.To guaranty the flexural buckling of the built-up member, slenderness ratio of individual component between connectors is smaller than the slenderness ratio of built-up member acting on a unit in the buckling direction being considered. At pretension bolt connections, M12 high strength bolts (F_u = 1000 N/mm^2) are used (See Figure 2).

2.2 *Test setup*

Test setup is shown in Figure 4. Both ends of specimen is supported by pin that is allowed to rotate in buckling direction. Buckling length of specimen is equal to the member length L. The hydraulic jack is used to apply axial force at centroid of the built-up member.

2.3 *Test results*

Table 3 summarizes the test results. Figure 5 shows non-dimensional buckling stress—deformation relations. λ_{ye}, λ_y and λ_1 in Table 3 are evaluated by equations (1)-(3). As seen from Figure 5, the buckling stress of all specimens were determined by flexural elastic buckling. After buckling, with the progress of the flexural deformation, the load declined. As seen from Figure 5(a) and Figure 6(a), with the increase in the distance between connecters (batten plates), the buckling stress decreased. This effect is caused by reduction of the stiffening effect of batten plate. As seen from Figure 5(b) and Figure 6(b), with the increase in the distance between centroids chords (separation), the buckling stress increased. This effect is caused by increasing in the distance between centroids of chords.Figure 7 shows flexural buckling deformations.

Figure 8 shows the bending moment distributions of built-up member at the buckling stress. This distributions at the chords and batten plates were computed from strain gauge reading (See Figures 2 and 3. For gauge location). Because this is a consideration of the bending moment distribution only, the absolute value of the bending moment are not shown. Also, the bending moment distribution of batten plates were smaller than that of chords. The bending moment distribution of batten plates in Figure 8(b) is illustrated by ten times larger. As shown in Figure 8, the bending moment distribution at the chords is mostly single curvature, which is totally different with Bleich's assumption (Bleich 1952).

Table 3. Geometrical dimensions of built-up member and test results.

Name	Symbol	L	a	n	h	I	i_y	$_{exp}P_{max}$	$_{exp}\sigma_{max}$	λ_y	λ_1	λ_{ye}	$_{pro}\lambda_{ye}$
L3700a400h60[1]			400	9	60	95.76	34.9	92.5	117	106	27	109	132
L3700a400h60[2]	×							99.6	127				
								106.5	136				
L3700a720h50[2]	▲		720	5	50	72.69	30.5	65.8	84	122	49	131	167
								66.3	85				
L3700a720h60[1]	△		720	5	60	95.45	34.9	72.9	92	106	49	117	146
L3700a720h60[2]								83.1	106				
		3700						77.2	99				
L3700a1200h50[2]	•		1200	3	50	72.57	30.5	53.4	68	122	49	146	180
								53.9	69				
L3700a1200h60[1]	○		1200	3	60	95.38	34.9	69.1	87	106	81	134	160
L3700a1200h60[2]								72.5	93				
								72.0	92				
L3700a1200h70[2]	○		1200	3	70	121.9	39.5	92.1	118	94	81	124	148
	×							84.4	108				
L4500a400h60[1]	◇		400	11	60	95.67	34.9	89.6	113	129	27	132	157
L4500a400h60[2]								72.5	93				
								62.4	80				
L4500a880h50[2]	■	4500	880	5	50	72.98	30.5	53.0	68	147	60	159	203
								47.5	61				
L4500a880h60[2]	□		880	5	60	95.62	34.9	53.0	68	129	60	142	177
								58.5	75				

Where: L is length of the member (mm); a is the distance between connectors (mm); n is the number of panels; h is the distance between centroids of chords (mm); I is the moment of inertia of built-up member acting on a unit in the buckling direction being considered (cm^4); i_y is radius of gyration of built-up member acting on a unit in the buckling direction being considered (mm); $_{exp}P_{max}$ is the buckling strength (kN); $_{exp}\sigma_{max}$ is the buckling stress (N/mm^2); $_{pro}\lambda_{ye}$ is the modified slenderness ratio.

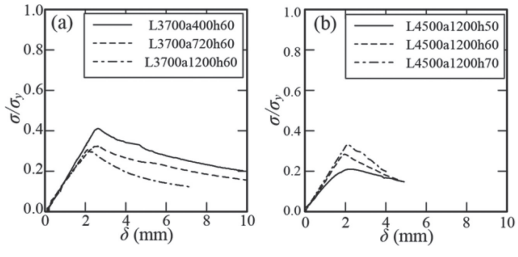

Figure 5. σ/σ_y - δ relations a) $L = 3700$; b) $L = 4500$.

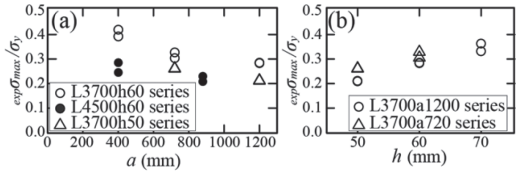

Figure 6. Effect of demension of built-up member on buckling stress a) effect of the distance of connecters; b) effect of the distance between centroid of chords.

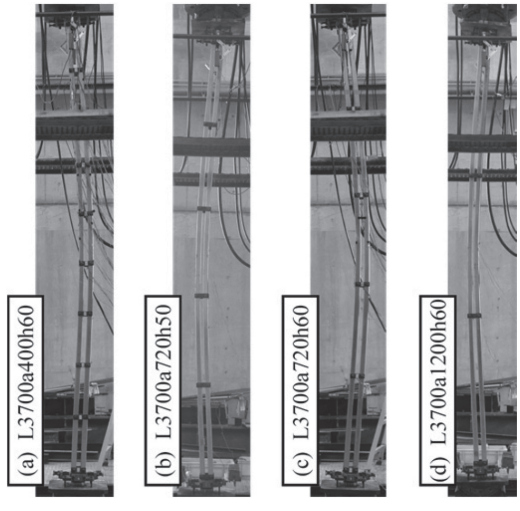

Figure 7. Deformation after testing.

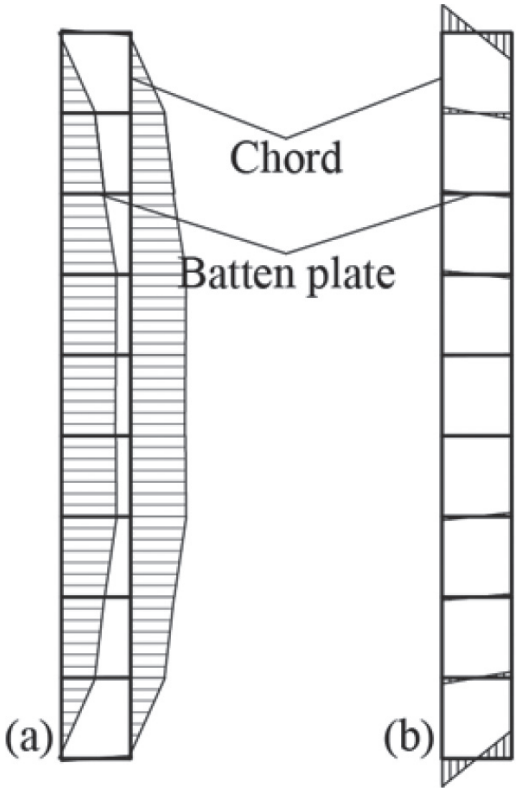

Figure 8. Bending moment distribution of a) chords; b) batten plates.

3 EVALUATION OF EFFECTIVE SLENDERNESS RATIO OF LIGHT GAUGE BUILT-UP COMPRESSION MEMBER

Bleich's bending moment distribution is shown in Figure 9(a). The effective slenderness ratio in the Design Standard for Steel Structures is derived from this moment distribution.

As mentioned in Figure 8, the bending moment distribution due to flexural buckling observed in testing was totally different with Bleich's assumption. Therefore, it can be assumed that difference of the moment distribution lead the un-conservative results. Figure 9(b) shows the bending moment distribution model due to flexural buckling. This model based on test observation. The purpose of this paper is to propose modified slenderness ratio for light gauge based on test observation. In this paper, energy equilibrium theory was used to derive flexural elastic buckling stress of the built-up member.

Modified effective slenderness ratio is derived as follow. Elastic energy of the distorted column consists of axial force F_k (V_1), bending moment at the chords (V_2), and bending moment at the batten (V_3). Additionally, elastic energy due to shear force at chords and battens will be included (V_4,V_5). Therefore, the strain energy is expressed as follow:

$$V = 2V_1 + 2V_2 + V_3 + 2V_4 + V_5 \tag{4}$$

Considering a pin-ended column, the deflected axis of the column assumes the form of a half sin wave:

$$u = f \sin\frac{\pi}{L}x \tag{5}$$

Where u is the deflection curve of the column; f is the maximum amplitude. The work done by the external force P_c is expressed as follow:

$$W = \frac{P_c}{2}\int_0^L \left(\frac{du}{dx}\right)^2 dx = \frac{\pi^2 P_c f^2}{4L} \tag{6}$$

Based on the energy condition, the transition from stable to unstable equilibrium of any elastic system is characterized as follow.

$$V = W \tag{7}$$

The bending moment $M_{all,k}$ at the point $x = (2k\text{-}1)L/(2n)$, corresponding to the middle point of panel k-1, is expressed as follow:

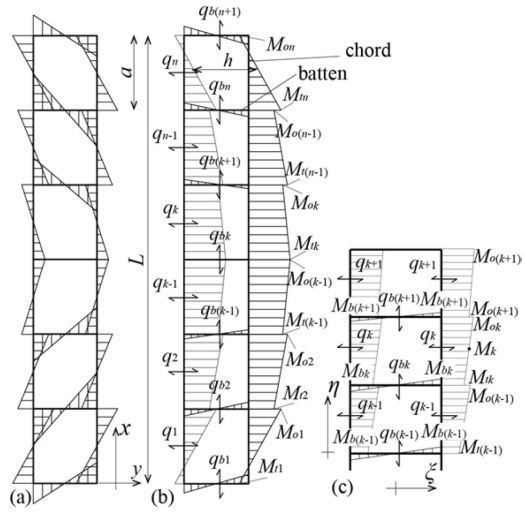

Figure 9. Bending moment distribution of a) Bleich's assumption; b) proposal bending moment distribution: c) cordinate.

$$M_{all,k} = P_c \cdot u = P_c \cdot f \sin\frac{2k-1}{2n}\pi \tag{8}$$

The shear force q_k acting on the chord for the same reference point is expressed as follow:

$$q_k = \frac{1}{2} \cdot \frac{dM_{all,k}}{dx} \tag{9}$$

Also, the longitudinal shear force q_{bk} acting on the batten of joint k is expressed by using coefficient ζ as follow:

$$q_{bk} = P_c f \varsigma \cos\frac{k-1}{n}\pi \tag{10}$$

The bending moment M_{tk} at any joint of the chord member k is expressed as follow:

$$\begin{aligned} M_{tk} &= a\sum_{j=1}^{k-1} q_j - \frac{h}{2}\sum_{j=1}^{k} q_{bj} \\ &= \frac{P_c f}{4\sin\frac{\pi}{2n}}\left(\frac{a\pi}{L}\sin\frac{k-1}{n}\pi - h\varsigma\sin\frac{2k-1}{2n}\pi - h\varsigma\sin\frac{}{2}\right. \end{aligned} \tag{11}$$

Considering the equilibrium of the moments acting on joint from 1 to k, the bending moment M_k at any point of the chord member is expressed as follow:

$$M_k = q_k \eta + M_{tk} \tag{12}$$

As the change of the axial force F_k in the chord between panels points k-1 and k caused by flexure of column in the state of buckling is expressed by $F_k = M_k/h$, the strain energy V_1 is expressed as follow:

$$V_1 = \frac{1}{2}\sum_{k=1}^{n}\int_0^a \frac{{F_k}^2}{EA_1} d\eta = \frac{L{P_c}^2 f^2}{4EA_1 h^2} \tag{13}$$

By similar procedures, the strain energy are given by equations (14), (15), (16) and (17).

$$\begin{aligned} V_2 = \frac{1}{2}\sum_{k=1}^{n}\int_0^a \frac{{M_k}^2}{EI_1} d\eta &= \frac{L{P_c}^2 f^2}{16EI_1}\left[-\frac{\pi^2 a^2}{6L^2}\right. \\ &+ \frac{1}{\pi^2 a}\left\{\frac{h^2}{2a}\left(2L^2+\pi^2 a^2\right)\varsigma^2 - 2\pi Lh\varsigma + \pi^2 \right. \end{aligned} \tag{14}$$

$$V_3 = \frac{1}{2}\sum_{k=1}^{n}\int_{-\frac{h}{2}}^{\frac{h}{2}} \frac{{M_{bk}}^2}{EI_b} d\xi = \frac{{P_c}^2 f^2 h^3 L}{48EI_b a}\varsigma^2 \tag{15}$$

$$V_4 = \frac{1}{2}\sum_{k=1}^{n}\int_0^a \frac{\kappa_1 {q_k}^2}{GA_1} d\eta = \frac{\pi^2 \kappa_1 {P_c}^2 f^2}{16LGA_1} \tag{16}$$

$$V_5 = \frac{1}{2}\sum_{k=1}^{n}\int_{-\frac{h}{2}}^{\frac{h}{2}} \frac{\kappa_b {q_{bk}}^2}{GA_b} d\xi = \frac{\kappa_b {P_c}^2 f^2 hL}{4GA_b a} \tag{17}$$

where I_b is moment of inertia of the batten plates; A_b is area of the batten plates; κ_1 is shear coefficient of individual components; $\kappa_b$is shear coefficient of the batten plates; G is the shear modulus. Using equations (4), (6), (7), (13)-(17), the energy condition is expressed as follow:

$$\begin{aligned} V &= \frac{L{P_c}^2 f^2}{4}\left(\frac{2}{EA_1 h^2} + \frac{1}{2EI_1}\left[-\frac{\pi^2 a^2}{6L^2}\right.\right. \\ &+ \frac{1}{\pi^2 a}\left\{\frac{h^2}{2a}\left(2L^2+\pi^2 a^2\right)\varsigma^2 - 2\pi Lh\varsigma + \pi^2 a\right\}\Bigg] \\ &+ \frac{h^3}{12EI_b a}\varsigma^2 + \frac{\pi^2 \kappa_1}{2L^2 GA_1} + \frac{\kappa_b h}{GA_b a}\varsigma^2\Bigg) \\ &= \frac{L{P_c}^2 f^2}{4EI}\cdot\alpha \end{aligned} \tag{18}$$

$$\begin{aligned} \alpha &= \left(\frac{2I}{A_1 h^2} + \frac{I}{2I_1}\left[-\frac{\pi^2 a^2}{6L^2}\right.\right. \\ &+ \frac{1}{\pi^2 a}\left\{\frac{h^2}{2a}\left(2L^2+\pi^2 a^2\right)\varsigma^2 - 2\pi Lh\varsigma + \pi^2 a\right\}\Bigg] \\ &+ \frac{Ih^3}{12I_b a}\varsigma^2 + \frac{\pi^2 EI\kappa_1}{2L^2 GA_1} + \frac{EI\kappa_b h}{GA_b a}\varsigma^2\Bigg) \end{aligned} \tag{19}$$

Solving for P_c, buckling strength is obtained.

$$P_c = \frac{\pi^2 EI}{L^2}\cdot\frac{1}{\alpha} \tag{20}$$

Besides, by partially differentiating with respect to ζ, coefficient ζ_0 is obtained.

$$\varsigma_0 = \frac{\frac{L}{\pi EI_1}}{\frac{2L^2+\pi^2 a}{2\pi^2 EI_1 a} + \frac{h^2}{6EI_b a} + \frac{2}{GA_b a}} \tag{21}$$

Because the second and the third term of the denominator are very small, these terms can be negligible. Coefficient ζ is expressed as follow:

$$\varsigma = \frac{2\pi La}{h\left(2L^2+\pi^2 a^2\right)} \tag{22}$$

The buckling stress is expressed as follow:

$$\sigma_c = \frac{P_c}{2A_1} = \frac{\pi^2 E}{{}_{pro}\lambda_{ye,0}{}^2} \tag{23}$$

where ${}_{pro}\lambda_{ye,0}$ is the slenderness ratio. The slenderness ratio is expressed as follow:

$${}_{pro}\lambda_{ye,0} = \sqrt{\alpha} \cdot \lambda_y \tag{24}$$

Because the terms of fraction in equation 19 from the third to the last are small compared with the first and second terms of fraction in equation 19, these terms can be negligible. Therefore, using equations (22) and (24), the slenderness ratio is expressed as follow:

$${}_{pro}\lambda_{ye} = \sqrt{\frac{2I}{A_1 h^2} + \frac{\pi^2 I}{24 I_1}\left(\frac{a}{L}\right)^2 \left\{1 + 3\frac{2 - \left(\frac{\pi a}{L}\right)^2}{2 + \left(\frac{\pi a}{L}\right)^2}\right\}} \cdot \lambda_y \tag{25}$$

Modified coefficient by the number of interconnectors which is a part of the second term in equation 25 is expressed as follow:

$$\varphi = 1 + 3\frac{2 - \left(\frac{\pi a}{L}\right)^2}{2 + \left(\frac{\pi a}{L}\right)^2} \tag{26}$$

Moment of inertia of built-up column I_0 is calculated as follow:

$$I_0 = I - 2I_1 = \frac{A_1 h^2}{2} \tag{27}$$

Using equations (25), (26) and (27), modified effective slenderness ratio of batten type light gauge built-up compression member can be obtained as follow:

$${}_{pro}\lambda_{ye} = \sqrt{\frac{I}{I_0}\lambda_y{}^2 + \frac{\pi^2}{12}\varphi\lambda_1{}^2} \tag{28}$$

The effective slenderness ratio derived by Bleich is as follow:

$${}_{Bleich}\lambda_{ye} = \sqrt{\lambda_y{}^2 + \frac{\pi^2}{12}\lambda_1{}^2} \tag{29}$$

The differences between equation 28 and equation 29 are what λ_y is multiplied by the moment of inertia of built-up column I/I_0 and what λ_1 is multiplied by modified coefficient φ.

To guaranty the flexural buckling of the built-up member, following conditionshave to be satisfied. First, the location of the connecters should be greater or equal to three, and it should be distributed in equal distance. Secondly, Design force of the batten plate is 2% of the buckling strength of the member; the batten plate should remain elastic at this force level. This code is based on the Design Standard for Steel Structure (AIJ 2005). Finally, Slenderness ratio of the chord between connectors λ_1 should be smaller than the slenderness ratio of the member λ_y.

4 EVALUATION OF BUCKLING STRESS BASED ON MODIFIED SLENDERNESS RATIO

4.1 *Numerical analysis model*

In order to verify the modified effective slenderness ratio and supplement test results, the parametric analysis is done by finite element models (large deformation, solid, elasto-plastic with strain hardening material). Three dimension model used in the numerical analysis is illustrated in Figure 10(a). The chords used in this analysis is C-89 × 40 × 12 mm (called 89 LCN22) and thickness is 2.2 mm as same as testing. The chord was divided by 12.5 mm in the longitudinal direction. The element division of batten plate is illustrated in Figure 10(a). The batten height is 36 mm and thickness is 6.0 mm. The connectors between chords are divided into 5. The batten plates which remain elastic at the buckling

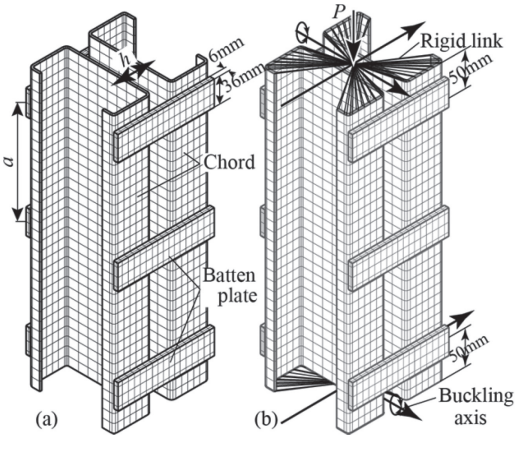

Figure 10. a) Finite element model; b) Boudary condition of finite element model.

Table 4. Geometrical dimensions of built-up member chord and batten plate used in this analysis.

A_b (mm^2)	I_b (mm^4)	A_1 (mm^2)	I_1 (mm^4)	h (mm)	I (mm^4)
432	46660	393	85660	40	485500
				60	878300
				80	1428000

Table 5. Analysis parameters.

h (mm)	λ_{ye}	n	a (mm^2)
40, 60, 80	100–200	3–25	150, 250, 300, 500, 600, 750, 1000

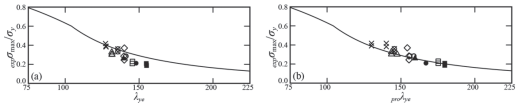

Figure 11. Comparison between column curve and test results of a) evaluated by slenderness ratio λ_{ye}; b) evaluated by modified slenderness ratio $_{pro}\lambda_{ye}$.

strength are as same as testing. Table 4 summarizes the geometrical dimensions of built-up member, chord and the batten plate used in this analysis.

In this analysis, to compare buckling stress by analysis with buckling stress calculated by the effective slenderness ratio λ_{ye} based on the Design Standard for Steel Structure (AIJ 2005) and compare buckling stress with buckling stress calculated by the modified effective slenderness ratio $_{pro}\lambda_{ye}$, analysis parameters were determined. Table 5 summarizes the analysis parameters. According to the Design Standard for Steel Structure (AIJ 2005), the slenderness ratio of individual component between connectors λ_1 is limited up to 50. This limitation was determined to prevent flexural buckling between connectors. In this analysis, the distance between connectors limited by this limitation will be less than 738 mm. However, in order to confirm buckling stress and buckling mode of analysis models exceeding this limitation, the analysis models exceeding this limitation were set. Initial imperfection was given by half sin wave to the direction of buckling and the maximum amount is L/1000 at the middle portion. The boundary condition is same as testing and both side of the model is pin and roller support (See Figure 10(b)). Load is applied at the centroid of the analysis model. Supporting points and both side of the model are connected by rigid link.

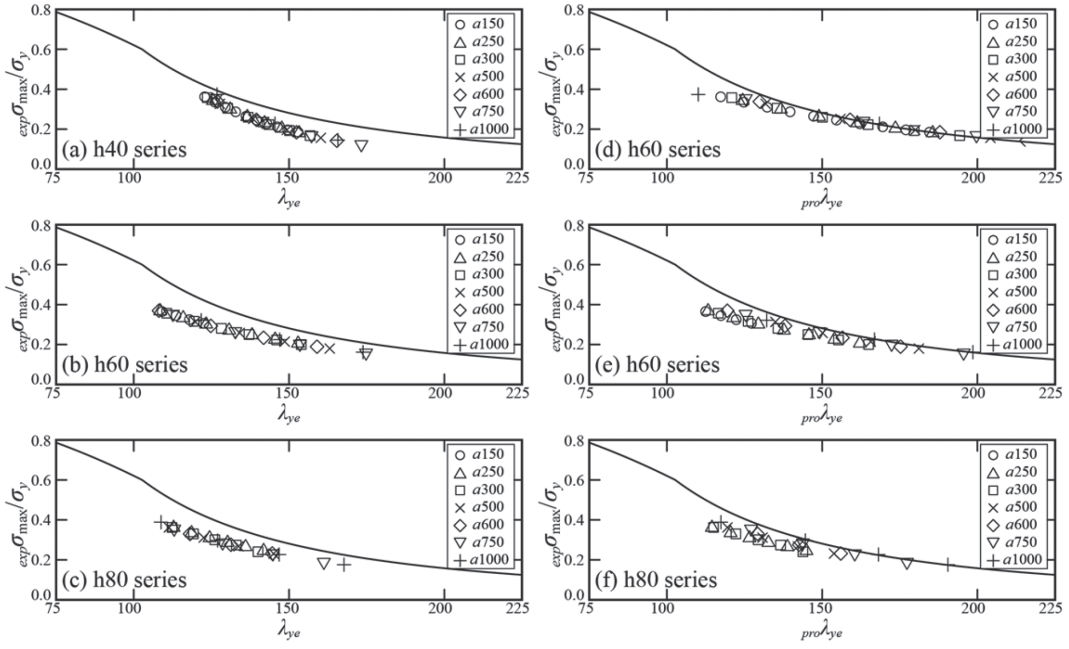

Figure 12. Comparison between column curve and analysis results of a)-c) evaluated by slenderness ratio λ_{ye}; d)-f) evaluated by modified slenderness ratio $_{pro}\lambda_{ye}$.

4.2 *Evaluation of buckling stress*

Comparison between column curve and test results are shown in Figure 11. Comparison between column curve and analysis results are shown in Figure 12. Horizontal axes of Figure 11(a) and 12(a)-(c) are the effective slenderness ratio λ_{ye} based on the Design Standard for Steel Structure (AIJ 2005). Horizontal axes of Figure 11(b) and 12(d)-(f) are evaluated by modified effective slenderness ratio ${}_{pro}\lambda_{ye}$.

As can be seen from Figure 11(a) and 12(a)-(c), evaluating by effective slenderness ratio based on the Design Standard for Steel Structure (AIJ 2005), un-conservative results are observed in test results and all analysis results. Therefore, buckling stress of built-up compression member are overestimated under the current circumstances. On the other hand, as can be seen from Figure 11(b) and 12(d)-(f), test results and all analysis results get close to the column curve. Good agreements were observed from all test results. Additionally, good agreements and improved results were observed from all analysis results. Proposed modified effective slenderness ratio is adequately evaluating the slenderness ratio of built-up compression member composed with light gauge members.

5 CONCLUSION

In this paper, full scale testing and numerical analysis were conducted to clarify the buckling stress of batten type light gauge built-up compression member. Additionally, modified effective slenderness ratio based on test observation was proposed.

From the testing, following results were found.

1. Distance between connectors and separation between chords affected the flexural buckling strength (stress) of the built-up members which have same member length. Flexural elastic buckling strength of the built-up member increased when the distance between connectors gets smaller and separation between chords gets larger.
2. Un-conservative results were observed from all specimens when the flexural elastic buckling strength were evaluated per the Design Standard for Steel Structure (AIJ 2005).
3. Bending moment distribution at the chord that were computed from strain gauge reading differed from Bleich's assumption. Although Bleich was assuming double curvature bending at the chords, single curvature bending was observed from the testing.

From the testing and parametric finite element analysis, following results were obtained.

4. Good agreements were observed from all test specimens when the flexural elastic buckling strength (stress) were evaluated per proposed modified effective slenderness ratio.
5. Compared to the Design Standard for Steel Structure (AIJ 2005), good agreements and improved results were observed from all analysis models when the flexural elastic buckling strength were evaluated per proposed modified effective slenderness ratio.

To guaranty the flexural buckling of the built-up member and obtain good agreements, following conditions have to be satisfied.

1. The location of the connectors should be greater or equal to three, and it should be distributed in equal distance.
2. The design force of the connector is 2% of the buckling strength of the built-up member; the connector should remain in elastic range at this force level.
3. Slenderness ratio of the chord between the connectors should be smaller than the slenderness ratio of the member.

REFERENCES

Architectural Institute of Japan (2005). *Design Standard for Steel Structures – Based o Allowable Stress Concept - fourth edition*.

European Committee for Standardization (2005). *Eurocode 3: Design of steel structures – Part 1.1: General rules – Uniform built-up compression members, EN 1993-1-1*.

Freidrich Bleich (1952). *Buckling strength of metal structures, second Edition*, McGraw-Hill Book Company, inc,.

Japan iron and steel federation (2014). *Design Manual for Light Gauge Structure*.

Ministry of Land, Infrastructure, Transport and Tourism (2001). Ministry of Land, Infrastructure, Transport and Tourism Notification No.1641.

This page intentionally left blank

Recent Progress in Steel and Composite Structures – Giżejowski et al. (Eds)
© 2016 Taylor & Francis Group, London, ISBN 978-1-138-02946-0

FEM model of the steel building roof includes stressed skin diaphragm action effects

M. Gryniewicz & J.K. Szlendak
Faculty of Civil and Environmental Engineering, Technical University of Bialystok, Bialystok, Poland

ABSTRACT: The paper presents new numerical model for pitched roof of steel building covered by metal sheeting. Stressed skin diaphragm action effect is considered as a main subject of the discussion. Structural components of such buildings should be adequately taken into account in analytical models. Various bracings locations or different main frames structure solutions lead to their different global stiffness caused by horizontal forces. Examples of calculations are shown. Presented procedure consists of diaphragms assembly calculations made by using European Recommendations (ECCS) and other data from literature. Representing structural key components are under consideration. Fasteners are replaced by equivalent finite frame elements. Trapezoidal sheeting is substituted by the equivalent orthotropic plate model. Interaction between the frame and sheeting is also considered. Numerical results presented in the paper are verified by full scale tests made by one of the authors and others.

1 INTRODUCTION

Light gauge steel cladding are widely used for buildings, however their including in structural calculations as stressed skin diaphragms, up to now is not common solution. Corrugation of sheets complicate their in plane and out of plane behavior. Moreover, sheets are connected each other and to supporting structure in different configurations. Variety of connector types can be used. Additionally, openings for windows, doors and others can be applied. Analytical studies have to involve many various failure modes e.g. local buckling, global stability loss, connections collapse etc.

Over the past decades design manuals and practical instructions have been prepared. In Europe, research carried out by Baehre with accompany of Bryan & Davies, leads to recommendations provided by European Convention for Constructional Steelwork (1995). General review and the recently state of the art in the stressed skin design of steel structures is given by Davies (2006). The current version of Eurocode 3 for the design of cold-formed members and sheeting is referred to the ECCS Recommendations (ER) (1995). Useful comments and additional practical examples can be found in handbooks e.g. Höglund (2002).

The result of tests and researches in America (e.g. Nilson 1960 and many others), is AISC design manual (Lutrell 2006). Explanations and summary of major changes made in recent editions are presented by Dong Li (2006). Comparison of methods predicting diaphragm behavior are described by Liedtke & Sherman (1982). Additional testing and numerical analyzes are given by Bakhdi et al. (2012).

2 BACKGROUND OF THEORETICAL MODEL

2.1 *Stressed skin design principles*

In ER (1995) formulas and procedures required to calculate bearing capacity and stiffness of shear panels are given for separate cases. There are two general types: sheeting spanning perpendicular to the span of the diaphragm or parallel to it. Depending on using walls bracings, "diaphragm beam" or "cantilever diaphragm" can be recognized. Next step is to describe rest of the structure elements configuration and types (connectors, edge beams, purlins etc.), where design procedures can be recognized into next sub-groups.

As written by Davies (2006) the strength of a diaphragm is defined by the weakest potential failure mode. In case of serviceability conditions, flexibility of the diaphragm is determined by the sum of a series of component flexibilities:

- Sheeting profile distortion: $c_{1.1}$
- Shear strain in the faces of the profile: $c_{1.2}$
- Sheet to support fasteners deformation: $c_{2.1}$
- Seam fasteners deformation: $c_{2.2}$
- Gable connections deformation: $c_{2.3}$
- Axial strain in the edge members: c_3

For each failure mode and each flexibility component simple design expressions are available with the addition of comprehensive examples.

2.2 *FEM analysis of shear diaphragms*

Authors works on numerical approaches and solutions in the context of stressed skin diaphragm action have been inspired by Nilson (1960) and further Atrek & Nilson (1976) investigations. Their methods make greater use of the orthotropic plate conception to describe behavior of trapezoidal sheets. The stress-strain relationship for orthotropic plate in plane stress continuum mechanics problem, can be written as:

$$\begin{Bmatrix} \sigma_x \\ \sigma_y \\ \tau_{xy} \end{Bmatrix} = \frac{1}{1-\nu_{xy}\nu_{yx}} \begin{bmatrix} E_{xx} & \nu_{yx}E_{xx} & 0 \\ \nu_{xy}E_{yy} & E_{yy} & 0 \\ 0 & 0 & \left(1-\nu_{xy}\nu_{yx}\right)G_{xy} \end{bmatrix} \begin{Bmatrix} \varepsilon_x \\ \varepsilon_y \\ \gamma_{xy} \end{Bmatrix} \tag{1}$$

Local coordinate system axis y is perpendicular to cross section plane of folded plate and x is parallel to it. Equivalent elastic modulus expressions are not the same, determined by geometry of corrugations and their physical behavior. It can be estimated, as described by Atrek & Nilson (1976), using two expressions below:

$$E_{xx} = E_s \frac{I_x^0}{I_x} \tag{2}$$

$$E_{yy} = E_s \frac{l_p}{a_p} \tag{3}$$

where E_s = elasticity modulus of base steel material; I_x^0 = equivalent plate moment of inertia about its own plane; I_x = corrugated plate section moment of inertia about its own plane; l_p = the developed width of the corrugation; a_p = width of the shear panel in the direction perpendicular to the corrugations (their pitch in this case).

For the E_{yy} more sophisticated and accurate expressions are exist in recent scientific studies. It is assumed that for described practical method formula (2) is sufficient. The equivalent modulus E_{yy} is simply depend on fact that both sheets (real one and its model) must have the same longitudinal deformation under applied load.

Shear modulus can be determined experimentally or numerically. For described model purposes analytical approach will be used. As seen in Figure 1, expression for G_{xy} can be found using shear strain (4) and stress (5) relationship:

$$\gamma_{xy} = \frac{u}{a_p} = \frac{\tau_{xy}}{G_{xy}} \tag{4}$$

$$\tau_{xy} = \frac{V}{b_p t} \tag{5}$$

where u = diaphragm displacement; V = shear force; b_p = depth of the shear panel in the direction parallel to the corrugations, t = plate thickness.

Diaphragm displacement u can be determined with values described in paragraph 2.1 for sheeting plate flexibility component:

$$u = V(c_{1.1} + c_{1.2}) \tag{6}$$

Applying formulas (4), (5) and (6), shear modulus for corrugated panel is obtained:

$$G_{xy} = \frac{a_p}{b_p t\left(c_{1.1} + c_{1.2}\right)} \tag{7}$$

As a last unknown variable used in orthotropic plate stiffness matrix showed in formula (1), Poisson's ratio ν_{xy} is equal to 0,3 according to EC3. At yx direction this value must be multiplied by the quotient of E_{xx} and E_{yy}.

The connectors model are two perpendicular springs with stiffness k_x and k_y. Those springs connect two nodes having the same coordinates (distance between them equals zero, Figure 2a). One node is a part of sheeting plate while another one is connected with structural element or adjacent

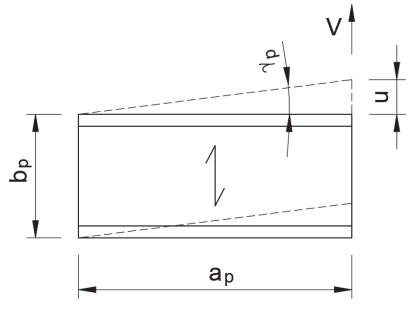

Figure 1. Calculation model for diaphragm shear flexibility.

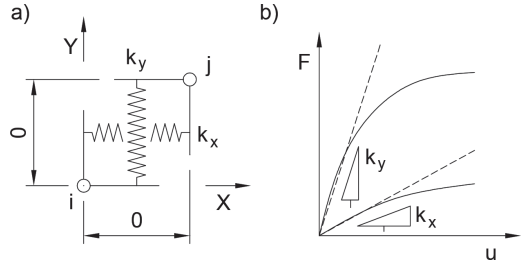

Figure 2. Connection idealization a) theoretical model, b) typical relationship force-displacement for connectors (real behavior and linear approximation).

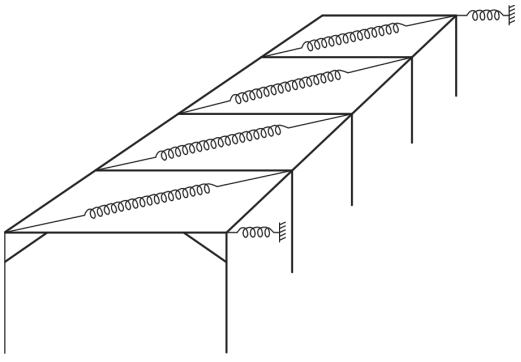

Figure 3. Example reference model for computational calculations method given in ER for flat roof buildings.

sheet. Figure 2b describe typical force-displacement relationship. Generally, linear approximation can be used for practical calculations (Bródka et al. 1999).

2.3 *Diaphragm-frame interaction*

Trapezoidal sheeting as a shear panels is a perfect solution for building structure stabilization. The stiffness of the sheeting is usually greater than the stiffness of the wind trusses which are now common used to stabilize building structures (Höglund 2002).

Stressed skin action effect leads to reduction in the associated forces and bending moments in supporting frames. This depends of the in-plane flexibility of shear diaphragm in relation to the frame flexibility.

ER (1995) give some procedures how to solve this problem, however with some limitations and assumptions. In one of the ER sections, recommendations are given only to single-bay flat roof frames and to symmetrical single-bay pitched roof frames. General assumptions are as follows: all frames in a building has uniform construction, all shear panels are the same and all foundations and other conditions are similar.

For other cases computer analysis methods are allowed. ER gives procedure where sheeting panels are replaced by system of springs (see example in Figure 3). Similar approach with using equivalent diagonal members is proposed e.g. Garncarek & Dziatkowski (2000) and Szlendak (2002).

3 NATURAL SCALE TESTS

3.1 *Prototype steel building*

The steel structure which is the subject of presented analysis is the building with dimensions measured in the axes of the main profiles: 12.0 m (width), 20.0 m (length) and 6.1 m (height of the main frame). It is a single-bay hall composed of five frames spaced at equal distances of 5.0 m (Figure 4). The main structure of the roof is truss (chords made with RHS profiles and diagonals with angles), which are supported by wide flange HEA 160 columns.

Columns bases are designed as hinges. Gable frames are different than main ones and have I-beam member instead of truss.

Gable frame in axis "4" (see Figure 6 for axes localization) is stiffened in its plane by diagonal bracings. Roof and longitudinal walls are also braced between axes "4" and "5". Between "1" and "2" only walls are stiffened. Columns, at the middle of their height, are prevented from out of plane buckling by wall girts.

Roof is covered by trapezoidal sheets T 40 placed in negative position (Figure 5) on purlins made with cold-formed sections Z $200 \times 68 \times 60 \times 1.5$ mm. Sheet profile has height 40.0 mm and thickness 0.7 mm. Pitch of corrugation is equal to 266.0 mm.

3.2 *Tests procedure*

Tests were performed on two stages. First one, where building steel structure was tested without any coverings. In second approach roof was fully covered with TR sheets. At both approaches three frames were under examination: "3", "4" and "5" axis (Figure 6).

Experiments were performed by applying horizontal force at the top joint of the truss (or gable

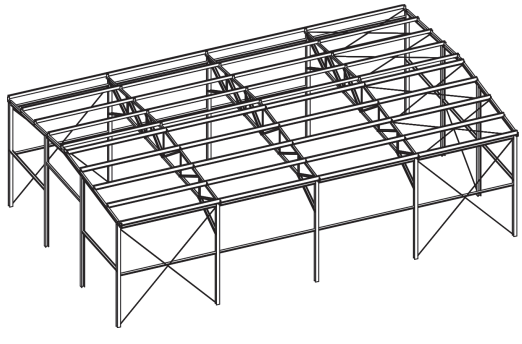

Figure 4. Isometric view of tested steel hall (transverse axes numbers starts from left at "1").

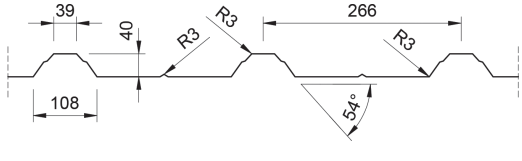

Figure 5. Corrugated plate geometry.

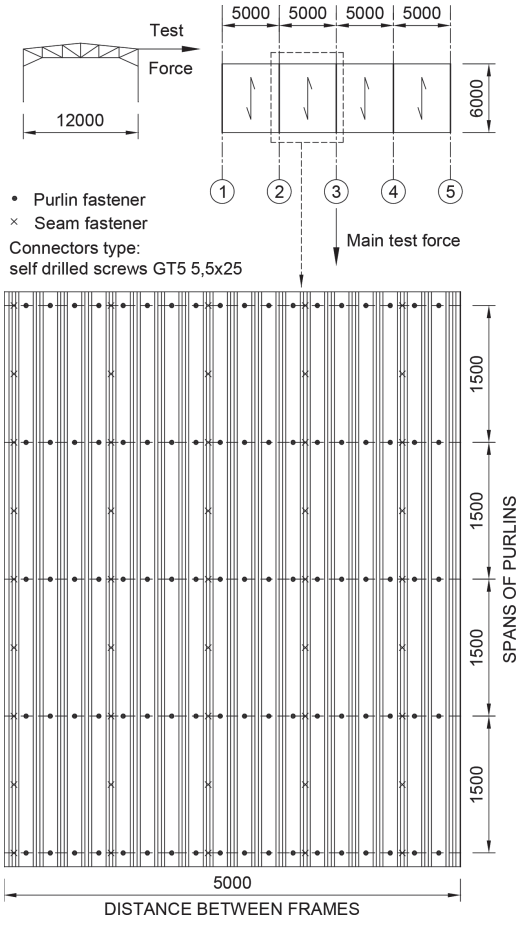

Figure 6. Tested roof diaphragm geometry and fasteners arrangement.

beam) where it is connected to column. Registration of the displacements was carried out at the same node with dial gauge. Range of testing force has been established from 1 kN to 15 kN.

Horizontal displacements values were recorded at every step with 1 kN increment. There were no construction permanent deformations noted. Geometrical imperfection were reduced to minimum by applying initial force.

3.3 *Results and static analysis*

As it was expected, quasi-linear behavior of frames under horizontal point load was registered. At first stage tests were performed to check structure stiffness used for analytical analysis. Second stage was made to define real deformation with stressed skin diaphragm action effect.

Table 1. Main frames theoretical stiffnesses.

Frame type	Axis [–]	Symbol [–]	Stiffness [kN/m]
Gable (unbraced)	1	$k_{f.1}$	116
Middle (main)	2–4	$k_{f.2-4}$	150
Gable (braced)	5	$k_{f.5}$	937

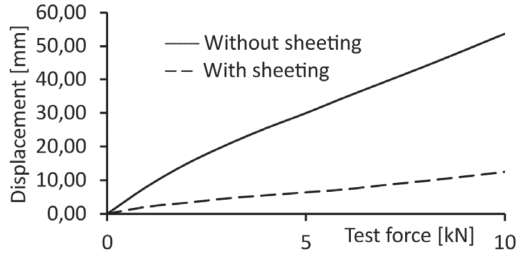

Figure 7. Test results with and without sheeting.

Specific frame in-plane stiffness determination by testing it in complete structure may be difficult. Bracings, wall girts or purlins have also some influence on frame flexibility. In that case, static calculations were made to estimate own theoretical stiffnesses for each type of frames (Table 1).

For comparison purposes, main frame behavior is right to choose since is located in a middle area where only purlins and wall girts are mounted with theoretical pinned joints (relatively minimal influence). Stiffness obtained by test in complete structure was 186 kN/m and by only-frame calculations 150 kN/m. The higher value from test can be caused by interaction of purlins (continuous beams) which involved other frames to act together. Additional dial gauges were applied to every column to check this relationship. Finally, building 3D structure calculation model confirmed this conclusion.

Value 12.5 mm of maximum deflection has been obtained after 10 kN force applying for building with roof sheeting. Deflection of this point in structure without covering (in the first test) has been equal to 53,7 mm (Figure 7). Thus, real displacements reduction caused by application of diaphragm is equals to 78%.

4 CONCEPT OF ANALYTICAL MODEL

Diaphragm-frame interaction procedure could be carried out, e.g. with usage of European Recommendations. As long as every standard requirement given in ER is fulfilled, there should not be any difficulties. Otherwise, the designer have to

use non common and more complicated solutions. Building described in Chapter 3 is an example of such a case, mainly due to its irregular bracings configuration and different frames construction.

Authors propose theoretical model to estimate stressed skin diaphragm action with using ER key principles, previous research and application of Finite Element Method. Every element of diaphragm structure is used in this model to check deflection of the building and compare it with test results.

4.1 *Model components description*

4.1.1 *Corrugated plate*

Formulas given in ER are sufficient and can be used in this approach. First feature to define is sheeting profile distortion:

$$c_{1.1} = \frac{a_p p_f^{2,5} \alpha_1 \alpha_4 K}{E t^{2,5} b_p^2} \tag{8}$$

Second one is shear strain in the faces of the profile:.

$$c_{1.2} = \frac{2a_p \alpha_2 (1+\nu)\left[1+\left(\frac{2h}{p_f}\right)\right]}{E t b_p} \tag{9}$$

In formulas (8) and (9) variables are (except defined before): p_f = pitch of the corrugations; α_1-α_4 = factors to allow for the number of purlins and sheet connectors; K = sheeting constant which is a function of the shape of the cross-section; E = modulus of elasticity of the sheet material; ν = Poisson's ratio of the sheet material; h = height of the sheeting profile.

For analyzed diaphragm $c_{1.1}$ is equal to 0.149 mm/kN and $c_{1.2}$ has value 0.013 mm/kN. Using expressions shown in Chapter 2.2, final form of the stiffness matrix for trapezoidal panel as an equivalent orthotropic plate is given as bellow:.

$$\left[E_{eq}\right] = \begin{bmatrix} 21.5 & 6.5 & 0 \\ 6.5 & 167253.5 & 0 \\ 0 & 0 & 5118.5 \end{bmatrix} \frac{kN}{m} \tag{10}$$

4.1.2 *Connections*

General assumption in case of connections modelling has been explained before (using two springs connected two nodes with zero distance). Authors proposed another solution. Every connector in system will be replaced by equivalent cantilever frame finite element (Gryniewicz & Szlendak, in press).

Needed properties of the equivalent members sections can be determined using ER or other sources and obtained by test or numerical simulations. For connections the most important feature is slip of fasteners and other connectors in diaphragm structure. Theoretical connections flexibilities are shown in Table 2. Slips of fasteners are adopted from ER. Purlin-girder connection is not typical and is tested with numerical simulation as a cantilever plate with different characteristics at both directions.

Representative moment of inertia in specific direction can be calculated with following expression:

$$I_{eq} = \frac{l_{eq}^3}{3sE} \tag{11}$$

where: l_{eq} = chosen length of equivalent finite element member; s = connection slip

Equivalent members for fasteners are described in model as 3D frame finite elements with the same section properties at both directions. In the

Table 2. Equivalent characteristics of diaphragm connections.

Connection type	Element length [mm]	Theoretical slip [mm/kN]	Moment of inertia [10^{-3} mm^4]
Main fasteners	1.0	0.35	4.54
Seam fasteners	2.0	0.25	50.79
Purlin-girder (a)*	10.0	1.40	1133.79
Purlin-girder (b)**	10.0	0.005	317460.32

* out-of-plane direction.
** in-plane direction.

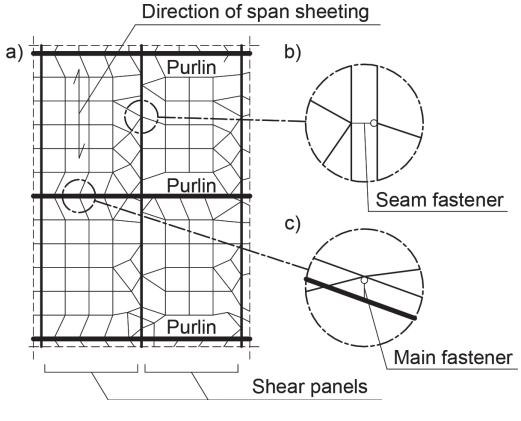

Figure 8. General concept of connectors modeling a) Diaphragm fragment, b) Seam fastener model, c) Main fastener (sheeting-purlin connection) in isometric view.

Figure 8 general approach for connectors modeling is shown, where seam fasteners connects adjacent sheets in their plane. Main connectors are joints between sheets and purlins.

4.1.3 *Building structure members*

Gable walls beams, purlins, bracings etc. are applied as 3D frame finite elements. Bars sections are the same as in the real structure.

In this diaphragm analysis full model of trusses is not necessary, only upper chords are needed to connect purlins (maintain local support flexibility) and create required roof geometry (Figure 9). Each steel frame behavior is carried out by using spring supports with stiffnesses calculated in Chapter 3.3.

Purlins-rafters connections are described using the same method as main sheeting fasteners but with different properties in both directions (see Table 2).

To avoid non-linear calculations only diagonal braces under tension are included into the model as round bars with 12 mm diameter.

4.2 *Diaphragm numerical calculations*

The studied building have pitched roof frames. According to guidelines given in ER the in-plane shear flexibility of a diaphragm could be calculated using expressions given for simple roofs, taking the depth of shear panel as the length of one pitched roof slope. The horizontal shear flexibility is given by:

$$c_h = c \sec^2 \theta \tag{12}$$

where c = flexibility of shear panel calculated as simple roof diaphragm; θ = angle of the rafter to the horizontal line.

Slope of analyzed roof is equal to 5.7°. Thus:

$$\sec^2 5.7° = 1.01 \tag{13}$$

According to fact that roof slope is nearly flat, multiplication factor calculated in (13) is relatively small. It is assumed that obtained in presented model shear flexibility of diaphragm can be calculated as horizontal flexibility.

Figure 9 shows geometry of diaphragm assembly. Every member and connecting methods are described in Chapter 4.1. In natural scale tests, force is applied to frame in axis "3". Range of testing force is from 1 kN to 15 kN. (with 1 kN step). Calculation are made in linear-elastic range.

The behavior of the pitched roof frame can be analyzed as sway and spread structure (Figure 10). Spread is not under consideration in this study. If it will be interesting, ER provide solutions to estimate this effect.

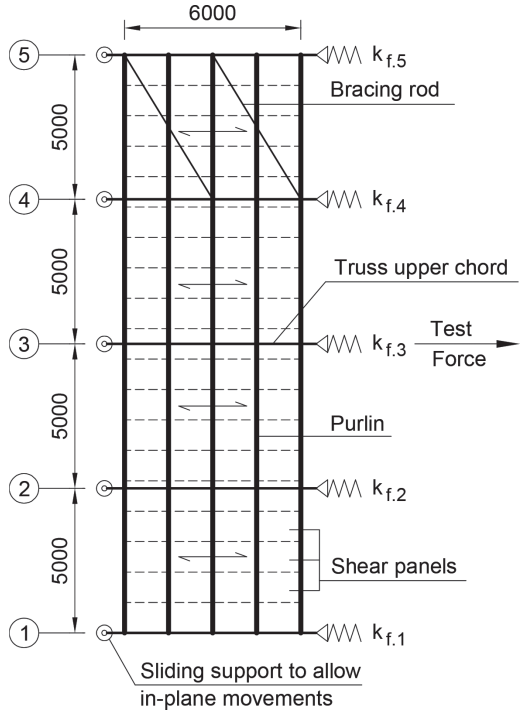

Figure 9. Geometry of diaphragm assembly—calculation model.

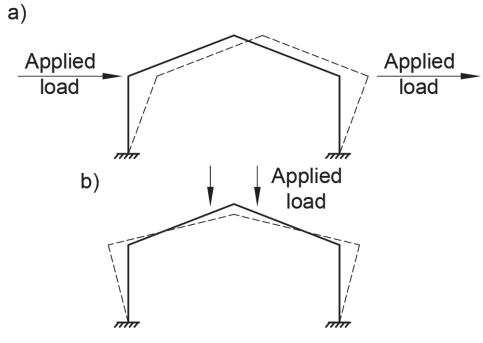

Figure 10. Pitched roof portal frame deformations a) Sway under horizontal load, b) Spread under vertical load.

5 CALCULATIONS RESULTS

Calculations were successfully finished without any warnings about instabilities and convergence alerts. Diaphragm deformation shape is shown in Figure 11. Maximum deflection at node where 15 kN force was applied is 18,80 mm. Relative value obtained in test was 19,70 mm. Accuracy of model prediction is about 95%. Comparison between test and theoretical analysis is presented in Figure 12.

Figure 11 is an original graphic taken from static calculation software without any modification but in enlarged scale relative to construction dimensions. Orientation of drawing is identical to Figure 9, thus both can be qualitatively compared.

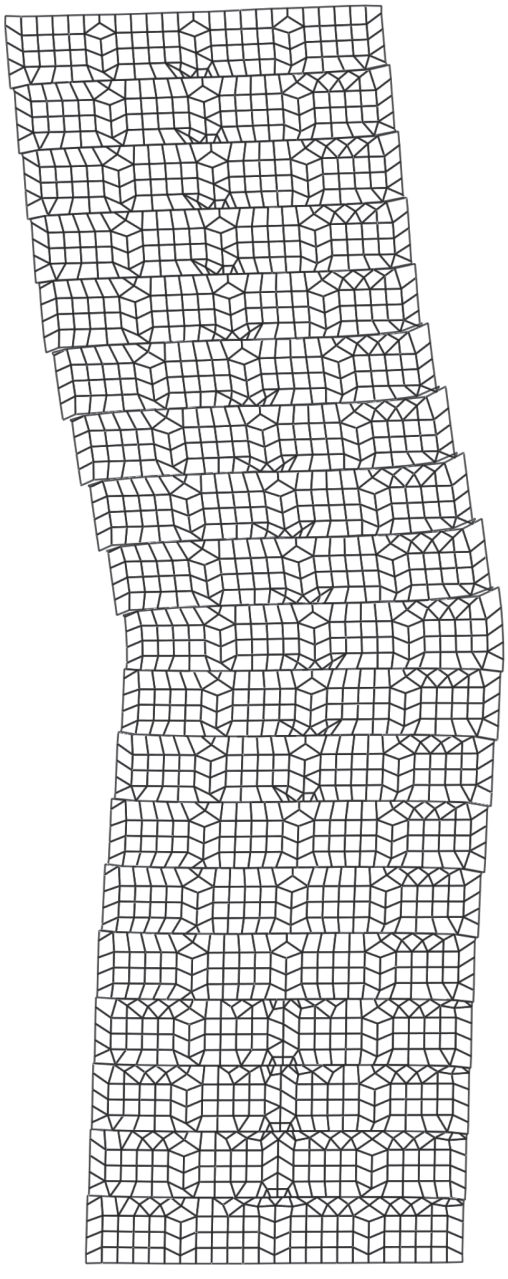

Figure 11. Diaphragm deformation shape under horizontal force—model presented in enlarged scale.

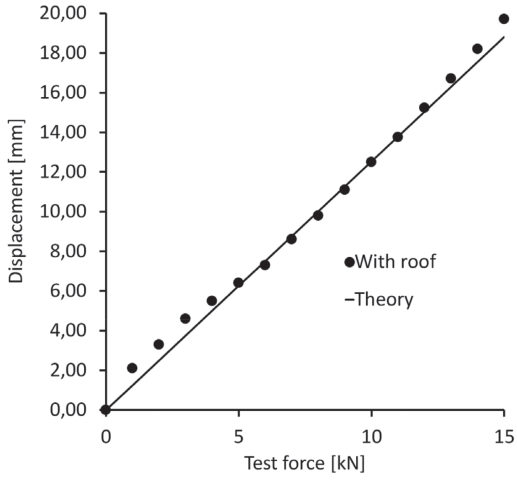

Figure 12. Results of test and theoretical analysis.

It can be easily seen that deflection of frame located in axis "5" (braced gable wall and roof) is substantially less than in axis "1" (opposite, unbraced gable wall and roof). This kind of cantilever-like behavior is due to fact, that braced construction region have higher stiffness than unbraced one. It is important to emphasize that frame "5" is not fully rigid, like it is necessary in standard procedures provided by European Recommendation (1995). Its flexibility is taken into account in this analysis.

Shear panels acting as a separate sheets is also recognized in the diaphragm deformation form. Adjacent sheets are connected only with flexible connectors which is the reason of this effect.

Value of roof real deformation is known. Thus bending moments in columns can be calculated using multiplication factors (different for each frame under consideration), which is obtained from expression:

$$\eta_s = \frac{u_c}{u_b} \tag{14}$$

where u_c = clad frame deflection obtained by numerical analysis; u_b = bare frame deflection.

Finally, bending moment in column in clad frame can be calculated as follows:

$$M_c = M_{ns} + \eta_s \cdot M_s \tag{15}$$

where M_{ns} = no-sway bending moment in bare frame; M_s = sway bending moment in bare frame.

Conception of this approach comes from ER principles, where deflection and bending moment of specific frame with sheeting can be computed

with using the reduction factors η obtained by reading it from tables. It is mainly determined by two variables: relative flexibility (between diaphragm assembly and frame stiffness) and frame position in the system. In presented method it is no necessary to define it in that way.

6 SUMMARY AND CONCLUSIONS

As the reference to calculations results, accuracy of model prediction is near 95%, what is very accurate. This model could find practical use in steel buildings static analysis for structural design or scientific studies.

Carried out experiments, numerical calculations and its result, following conclusions could be listed as follows:

1. Stressed skin diaphragm action effects has significant influence in structure deformation and internal forces. Reduction of sway tested and calculated equals 78% in presented industrial hall with only roof being under consideration.
2. For non-common structures shapes some methods and approaches can be find in literature. Authors propose one solution with emphasis on practical using.
3. Described approach is consistent with European Recommendations (1995), which allow to use Finite Element Method.
4. Linear force-displacements characteristics for connections are used. It is sufficient to analyze structure behavior in elastic range. For more complex solutions non-linear connector model would be used e.g. to include contact deformations with sheeting plate.
5. Analyzed roof has uniform shape (rectangular in plane) and have no openings. Proposed method could be applied in any shapes with various locations of openings.

ACKNOWLEDGEMENTS

Paper was created as part of the statutory work S/WBiIŚ/2/2012.

REFERENCES

Atrek E. & Nilson A.H. 1976. *Non-linear finite element analysis of light gage steel shear diaphragms*. New York: School of Civil and Environmental Engineering at Cornell University.

Bakhdi F., Tremblay R. & Rogers C.A. 2012. Revisiting the SDI and ECCS methods for in-plane shear flexibility of metal roof deck diaphragms using 3D nonlinear finite element analysis. *15th World Conference on Earthquake Engineering* Paper No. 2482. Lisbon.

Bródka J., Garncarek R. & Miłaczewski K. 1999. *Blachy fałdowe w budownictwie stalowym*. Warsaw: Arkady.

Davies J.M. 2006. Developments in stressed skin design. *Thin-Walled Structures* 44 (2006) 1250–1260. Elsevier.

Dong Li 2006, The new SDI diaphragm design manual. *International Specialty Conference on Cold-Formed Steel Structures* Paper 10: 437–452.

ECCS-TWG 7.5. 1995. European Recommendations for the application of metal sheeting acting as a diaphragm. *European Convention for Constructional Steelwork* No. 88.

Garncarek R., Dziatkowski T. 2000. Obliczanie tarcz dachowych z otworami. *Konstrukcji stalowe* 6(43): 45–47.

Gryniewicz M. & Szlendak J.K. In press. Modelowanie numeryczne konstrukcji dachu hali stalowej z uwzględnieniem współpracy poszycia. *61. Konferencja Naukowa KILiW PAN oraz KN PZIiTB Krynica-Bydgoszcz.*

Höglund T. 2002. *Stabilisation by stressed skin diaphragm action* Publication 174. Stockholm: SBI.

Liedtke, P.E. & Sherman D.R. 1982. Comparison of methods predicting diaphragm behavior. *International Specialty Conference on Cold-Formed Steel Structures* Paper 1: 369–389. St. Louis: Department of Civil Engineering University of Missouri – Rolla

Lutrell, L.D. 2006. Steel deck institute diaphragm design manual: third edition. *AISI-Specifications for the Design of Cold-Formed Steel Structural Members* Paper 82.

Nilson, A. 1960. Shear Diaphragms of Light Gage *Steel. Journal of Structural Division*. ASCE 86:11: 111–139.

PN-EN 1993–1-3:2006 Eurokod 3 - Projektowanie konstrukcji stalowych - Część 1–3: Reguły ogólne. Reguły uzupełniające dla konstrukcji z kształtowników i blach profilowanych na zimno.

Szlendak, J.K. 2002. Design concept of pitched portal frame covered by metal sheeting. *Proceedings of the International Colloquium on Stability and Ductility of Steel Structures*, Budapest, 293–300.

Recent Progress in Steel and Composite Structures – Giżejowski et al. (Eds)
© 2016 Taylor & Francis Group, London, ISBN 978-1-138-02946-0

Experimental investigation of the stabilization of the C-section purlins by sandwich panels

R. Studziński & K. Ciesielczyk
Institute of Structural Engineering, Poznan University of Technology, Poznan, Poland

ABSTRACT: The paper describes the experimental investigation of the stabilization of the cold formed thin-walled C-section purlins by sandwich panels. The aim of the paper is the qualitative determination of the interaction between the purlins and the sandwich panels. The purlins, of an asymmetrical channel cross-section, were assumed as simply supported. Two arrangements of sandwich panels with a polyurethane foam core 100 mm in depth were examined. In the first case the sandwich panels were freely placed on the purlins, while in the second case fasteners were used to connect the sandwich panels to the purlins. The purlins connected with the sandwich panels showed a significant improvement in capacity. The laboratory results were compared to the adequate numerical model and the analytical calculations agreed with the EN standards. The stiffness values of the lateral restraint, provided by sandwich panels with and without the use of fasteners, were found. Additionally, the approach (proposed in subject literature), which allows for lateral stabilization of the cold formed purlins by sandwich panels, was verified and discussed.

1 INTRODUCTION

The beams and columns made of cold formed thin-walled steel cross-sections are important elements of many modern steel or steel-concrete structures. The dominant use of these sections is connected with single- or multi-storey steel structures (exhibition halls, sports complexes, factory units or warehouses) where they play the role of secondary elements (purlins and side rails). The typical thin-walled cross-sections used as purlins and side rails are presented in Fig. 1.

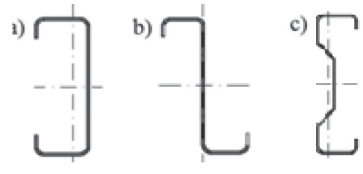

Figure 1. Typical thin-walled cross sections: a) C-section, b) Z-section, c) Σ-section.

The cold formed thin-walled elements are characterized by high capacity coupled with small weight. This feature significantly reduces manufacture, transport and assembly costs. In spite of the mentioned advantages these members are sensitive to local and global instability, boundary conditions and initial geometrical imperfections. Therefore, the stability phenomena are often the key problem in the design of the cold formed thin-walled steel sections (Bazant & Nimeiri 1973, Fang & Pekoz 2001, Garstecki et al. 2002, Timoshenko & Gere 1961).

The secondary elements support cladding systems (sandwich panels, trapezoidal sheeting) and transmit all external loads to the main steel structure. On the other hand, it can be assumed that the cladding system is able to provide the lateral restraint of the thin-walled steel section members. These phenomena were widely discussed in subject literature in the case of the trapezoidal sheeting connected with thin-walled sections (Lucas et al. 1997a, b, Li et al. 2012, Rzeszut & Studziński 2010, Ye et al. 2002, Zhao et al. 2014). Please note that the actual EN 1993-1-3 standard introduced the guidelines for determining lateral and rotational stiffness realized by trapezoidal sheeting. Moreover, the EN 1090 standard distinguished three structural classes associated with failure consequences. For example the structural class II assumes that the cold-formed members and cladding are designed to contribute to the strength and stability of individual structural (secondary) elements.

In the case of sandwich panels the problem with lateral restraint of the hot-rolled elements is widely discussed by Dürr 2008. Sandwich panels are composite elements which consist of two external facings (thin and high strength) and core (thick and soft). Sandwich panels are characterized by: high bending stiffness coupled with small weight,

very good thermal properties, easiness of transport and easiness of erection. Please note that designing sandwich panels requires taking into account several problems, namely: the cooperation of two different materials (facings and core), the number of failure mechanisms and the fact that the structural behaviour strongly depends on the influence of the thermally induced deformations (Studziński et. al. 2015a, b). Dürr 2008 in his PhD dissertation performed the experimental and numerical investigations to obtain shear and torsional restraint provided by sandwich panels. Moreover, the conducted analysis demonstrated that the torsional restraint of sandwich panels with soft core layer can be expressed by a trilinear moment-rotation relationship. Finally, the flexibility of the fasteners was evaluated. The recommendations (Käpplein & Misiek 2011) of the European collaborative project called EASIE include the results obtained in mentioned PhD thesis. Recently, the problem of the stabilisation of Z-purlins by sandwich panels was presented by Georgescu & Ungureanu 2014 and Kujawa & Szymczak 2014.

In the case of sandwich panels, the problem of the lateral restraint of the thin-wall elements still remains an open research problem. The cooperation of the thin-walled beam with the sandwich panel results in a number of problems which affect the effectiveness of the lateral restraint. Four phenomena are distinguished. Firstly, the contact phenomenon between the sandwich panel element and the thin-walled beam element, including the elastic or plastic deformation, the sliding along the contact surfaces and the mechanics of unilateral constraints. Secondly, the phenomenon of the stress concentration and the ovalization of the holes in the vicinity of the fasteners. Thirdly, the problem of the flexural stiffness ratio of the beam element to the plate element. Finally, the problem of the localization and the size of the openings. The scientific description of these problems must take into account the characteristics of the connected and cooperating structural elements, the beam element and the plate element. The present paper describes the experimental investigation of the stabilization of the cold formed thin-walled C-purlins by sandwich panels, which is the first stage to investigate the cooperation phenomena between thin-walled beams and sandwich panels.

2 PROBLEM FORMULATION

2.1 *Description of the test bed*

The aim of the paper is the qualitative determination of the interaction between the thin-walled C cross-section purlins and the sandwich panels with constant flexural stiffness. The C-section members, of an asymmetrical cross-section, were assumed as simply supported. Two arrangements of simply supported sandwich panels were examined. In the first case (case A, two trials) fasteners (eight per one side) were used to connect the sandwich panels to the C-section purlin while in the second case (case B, one trial) the sandwich panels were freely placed on the C-section purlin. The lateral restraint of the C-section purlin was realized along the width of the sandwich panels, i.e. $b = 2.2$ m. The following span lengths were assumed: axial span of the C-section $L_1 = 3.2$ m and axial span of the sandwich panel $L_2 = 2.8$ m. The detailed scheme of the test bed is presented in Fig. 2. Please note that the hinge supports ensure the rotation of the tested C-section elements along the support line. In both approaches the displacements of both C-sections were measured at fourth points: three displacements in the middle of the beam (one vertical and two horizontal) and one horizontal at the end of the beam. Additionally the vertical displacement of the midpoint of the sandwich panel was measured. Please note that because of large displacements of the C-members and the limited range of the displacement transducers the measurements were interrupted at some points.

2.2 *The geometrical and the material properties of the sandwich panel layers and the thin-walled C-members*

The sandwich panels considered in this paper consist of two thin zinc-coated steel faces and a thick and soft polyurethane core.

The geometrical parameters of the layers of the sandwich panel were measured, namely the thickness of the core $d_C = 0.10$ m, the thickness of the external facing $t_{F1} = 0.55 \cdot 10^{-3}$ m and the thickness of the internal facing $t_{F2} = 0.49 \cdot 10^{-3}$ m. The following material properties of the core (subscript C) and the facing (subscript F) layers were obtained: the shear modulus $G_C = 3.2$ MPa, the Poisson ratio $\nu_C = 0.05$, the Young modulus $E_F = 190.0$ GPa, the upper yield point $R_{eHF} = 386.0$ MPa and the Poisson ratio $\nu_F = 0.3$.

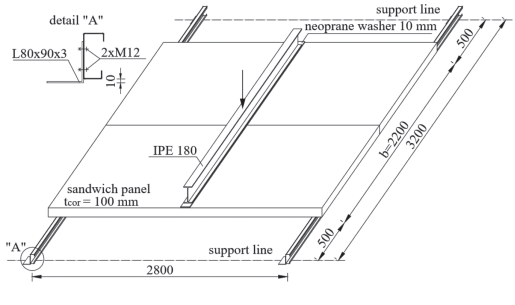

Figure 2. Scheme of the test bed.

In Figures 3a and 3b the linear dimensions of the gross and effective C cross-section are presented.

2.3 *Experimental results*

Table 1 presents the selected results of laboratory trials, where: F_{crit} is the limit force load induced by actuator; q_{crit} is the limit load uniformly distributed per C-purlin corresponding with the limit force load F_{crit} but with added weight of the measurement instruments; u_1 is the vertical displacement of the bottom flange of the C-section of the mid span of a purlin, while u_2 is the vertical displacement of the midpoint of the sandwich panel (under the applied load).

The measurements of the displacements in case B were interrupted (see explanation in section 2.1). The extrapolated value of the maximal displacement u_1 and u_2 for the limit force load equals 43.45 mm and 62.59 mm respectively.

Please note that the load path of the vertical displacements u_1 for both C-purlins overlap (within a framework of a trial). Figure 4 presents the relation between the applied force F and the vertical displacements u_1 and u_2 for all trials. The laboratory trials showed that the C-purlins mechanically connected with sandwich panels (case A) are characterized by a twice larger capacity than those which were freely placed on sandwich panels (case B). Please note that the displacements u_1 of purlins for both cases at the limit force are similar, nevertheless the stiffness of the purlins in case A is twice as large. The obtained deformations of the sandwich

Table 1. The selected results of the laboratory trials.

		F_{crit}	q_{crit}	u_1	u_2
No	Case	kN	kN/m	mm	mm
1	A	11.4	2.8	39.5090	44.6993
2		11.0	2.7	45.1462	48.8778
3	B	5.3	1.4	29.3380*)	43.4502*)

*The measurements were interrupted (see section 2.1).

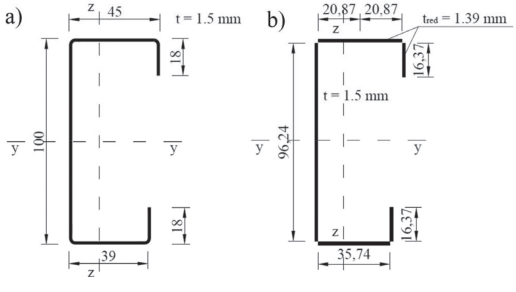

Figure 3. Linear dimensions of the asymmetrical C-section: a) gross cross-section, b) effective cross-section.

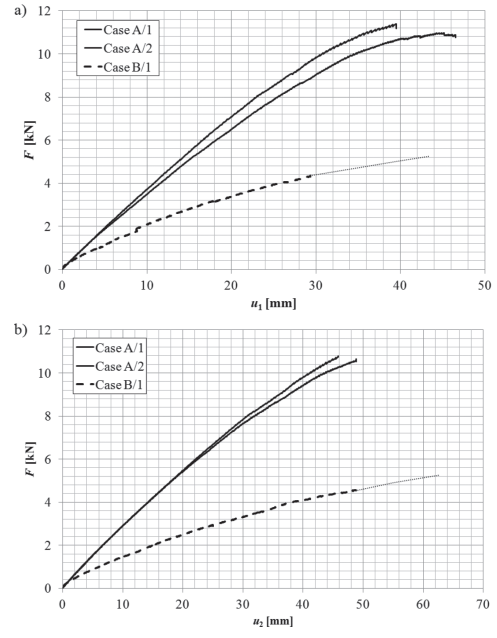

Figure 4. The relation between the applied force F and the vertical displacement: a) displacement of u_1, b) displacement of u_2.

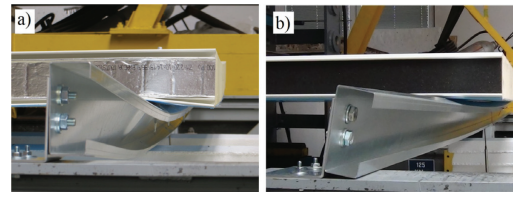

Figure 5. The failure of the purlins: a) the interactive (local and global) buckling failure of the C-purlin mechanically connected with sandwich panel (case A), b) global buckling of the purlins freely placed on sandwich panels (case B).

Table 2. The results of the analytical computations of the unbraced C-section members.

$M_{c,Rd}$	M_{cr}	χ_{LT}	$M_{b,Rd}$	q_{crit}
kNm	kNm	–	kNm	kN/m
3.234	0.905	0.194	0.626	0.542

panels were elastic, therefore after the unloading they returned to their initial configuration.

The failure of the C-purlin in case A was due to local and global interactive buckling. The local buckling of the web was located in the section of the purlin where the extreme fastener was located, see Fig. 5a. The failure of the C-purlin in case B was only due to global buckling, see Fig. 5b.

3 ANALYTICAL APPROACH

3.1 *Capacity of the unbraced C-section members*

In order to determine the buckling resistance of the simply supported unbraced C-section the computations according to EN 1993-1-1 and EN 1993-1-3 standards were performed. The effective cross-section (see Fig. 3b) was obtained. The results of the performed calculations are presented in the Table 2 where $M_{c,Rd}$ is the design resistance for bending; M_{cr} is the elastic critical bending moment determined by the approximate formula for the gross cross-section; χ_{LT} is the reduction factor for lateral-torsional buckling, $M_{b,Rd}$ is the design buckling resistance moment and q_{crit} is the critical value of the uniformly distributed load per purlin.

3.2 *Capacity of the C-section members stabilized by sandwich panels*

The European Recommendations on the Stabilization of Steel Structures by Sandwich Panels describes the simplified method for evaluating stabilization of the purlins by sandwich panels. This method allows to determine whether the sandwich panel provides full resistance of the purlin.

3.2.1 *The required conditions*

It is assumed that the purlin is stabilized by sandwich panel if the following two conditions are met: the Ultimate Limit State (ULS) and Serviceability Limit State (SLS). The ultimate limit state condition is defined by the expression (1)

$$m_{\vartheta A} < m_k, \tag{1}$$

where $m_{\vartheta A}$ and m_k is the stabilization moment and the contact moment, respectively. The stabilization moment is expressed by Eq. 2

$$m_k = q_d\, a, \tag{2}$$

where m_k is the cold-formed cross-section contact moment; q_d is the designing value of the distributed load and a is the width of the flange of the purlin. The contact moment is expressed by Eq. 3

$$m_{\vartheta A} = \frac{1}{C_{\vartheta A}\dfrac{k_c^4 EI_z}{M_{Ed}^2} - 1} C_{\vartheta A}\varphi_0, \tag{3}$$

where $C_{\vartheta A}$ is the torsional spring stiffness of the sandwich panel-purlin connection which is dependent on the type of the purlin cross-section, core material and geometry of external face of the sandwich panel; k_c is the correction factor dependent on the moment distribution; φ_0 is the imperfection parameter. The serviceability limit state is expressed by Eq. 4

$$\varphi = \frac{m_{k,k}}{C_{\vartheta A}} < 0.08 \text{ rad}, \tag{4}$$

where $m_{k,k}$ is cold-formed cross-section contact moment determined for characteristic value of the distributed load.

3.2.2 *The analytical verification of the stabilization criterion of the C-channel by sandwich panel*

In the first computation step the possibility of the stabilization of the considered purlin by sandwich panel for the load q = 0.5 kN/m was verified. The value of the load corresponds to the critical load determined for unbraced C-section. As follows from the computation results presented in the Table. 3 the sandwich panel assumed in experiment provides full stabilization of the purlin for the assumed load level 0.5 kN/m.

In the second computation step the formulas presented in the chapter 3.2.1 were transformed in order to determine the range of the load value needed to provide full resistance of the purlin. It was obtained that the limit value of the load that provides stabilization of the purlin by sandwich panel is equal to 2.70 kN/m. Whereas the limit value of the load due to the serviceability limit load is 1.71 kN/m.

The value of the uniformly distributed limit load which provides stabilization of the purlin in the ultimate limit state corresponds to the critical value of the uniformly distributed load obtained in the experiment (see Table 1) – case A: sandwich panels connected with the purlins by 8 fasteners per one side.

Table 3. The results of the computations.

$C_{\vartheta A}$	φ_0	k	$m_{\vartheta A}$	m_k	φ
Nm/m	–	–	kNm/m	kNm/m	rad
970.78	0.06	0.94	0.002	0.023	0.024

4 NUMERICAL APPROACH

In order to obtain the stiffness of the lateral restraint of the C-purlins numerical analyses were performed. For this purpose 3D shell finite element models were defined using the AxisVM program.

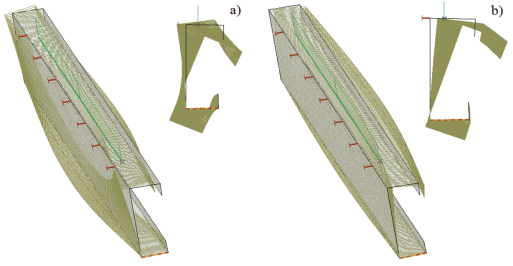

Figure 6. The failure of the purlins: a) the buckling mode shape of C-purlin corresponding to case A, b) the buckling mode shape of C-purlin corresponding to the B.

The 3D model of the C-purlin was simply supported at the ends and laterally restrained along the length of 2.2 m, which corresponded with the laboratory trial. The lateral restraint was realized by 7 horizontal supports. The uniformly distributed load was applied at the top flange of the purlin. Please note that the direction of the load intersected the COG of the C cross-section. The linear buckling analysis of such defined 3D element was performed.

The numerical buckling analysis showed that the lateral restraint of stiffness 161.0 kN/m ensured the q_{crit} = 2.72 kN/m, while the lateral restraint 21.0 kN/m ensured the q_{crit} = 1.39 kN/m. The obtained results corresponded with the laboratory trials presented in Tab. 1 for case A and case B respectively. Figure 6 presents the shape of the lateral torsional deformation obtained numerically.

5 CONCLUSIONS

In the paper the experimental study on thin-walled C cross-section purlins stabilized by sandwich panels was presented. The results from the experimental investigation were compared with the analytical computations performed both for the unbraced and braced C-section purlins. The analytical computations were conducted according to the European designing codes and European Recommendations on the Stabilization of Steel Structures by Sandwich Panels.

The experimental analysis revealed that only freely placing the sandwich panel on the purlin causes two and half-fold increase of C-section purlin capacity (q_{crit} = 1.4 kN/m) compared with analytical value for unbraced purlin (q_{crit} = 0.54 kN/m). Moreover, using the fasteners to connect the purlin with sandwich panel causes next two-fold increase of the value of critical load (q_{crit} = 2.75 kN/m). The value of critical load for C-purlin stabilized by sandwich panel was almost the same both in the experimental study and analytical computations performed according to the European Recommendations.

Based on the performed analysis it can be concluded that purlins can be stabilized by sandwich panels. However, it is worth to mention that described experimental studies have been conducted on a small scale (only three trials) in order to verify the test bed and evaluate feasibility and adverse event of the experiment. For this reasons, the performed studies should only be considered as a pilot study. The next experimental step of investigation of the stabilization of the purlins by sandwich panels will be based on the analysis of the Z cross-section purlins stabilized by sandwich panels. It is planned to analysed the sandwich panels of three different thickness: 60, 80 and 100 mm.

REFERENCES

Bazant Z.P., Nimeiri M., 1973. *Large-Deflection Spatial Buckling of Thin-Walled Beams and Frames*. J. Eng. Mech. (ASCE), 6, 1259–81.

Dürr M., 2008. *Die Stabilisierung biegedrillknickgefährdeter Träger durch Sandwichelemente und Trapezbleche*, PhD dissertation, Karlsruhe.

EN 1090-2: *Technical requirements for the execution of steel structures*, Brussels, 2002.

EN 1993-1: *Design of Steel Structures. Part 1–3: General rules – Supplementary rules for cold-formed members and sheeting*, Brussels, 2001.

European Recommendations on the Stabilization of Steel Structures by Sandwich Panels, International Council for Research and Innovation in Building and Construction, 2013.

Fang Y., Pekoz T., 2001. *Design of cold-formed steel plain channels, School of Civil and Environmental Engineering, Report*, Cornel University, Ithaca.

Garstecki A., Kakol W., Rzeszut K., 2002. *Classification of local-sectional geometric imperfections of steel thin-walled cold-formed sigma members*, Foundations of Civil Environmental Engineering, 45, pp. 87–96.

Georgescu M., Ungureanu V., 2014. *Stabilisation of continuous Z-purlins by sandwich panels: Full scale experimental approach*, Thin-Walled Structures, 81, 242–249.

Käpplein S., Misiek T., 2011. *Connections of sandwich panels, Report No.: D3.3 – part 3*, Ensuring Advancement in Sandwich Construction through Innovation and Exploitation.

Kujawa M., Szymczak Cz., 2014. *Numerical and experimental investigation of rotational stiffness of zed-purlins connection with sandwich panels*, Thin-Walled Structures, 75, pp. 43–52.

Li L., Ren Ch., Yang J., 2012. *Theoretical analysis of partially restrained zed-purlin beams subjected to up-lift loads, Journal of Constructional Steel Research*, 70, 273–279.

Lucas R.M., Al-Bermani F.G.A., Kitipornchai S., 1997. *Modeling of cold-formed purlins – sheeting systems – Part 1. Full model, Thin-walled Structures*, 27(3), pp. 223–243. doi:10.1016/S0263–8231(96)00038–9.

Lucas R.M., Al-Bermani F.G.A., Kitipornchai S., 1997. *Modeling of cold-formed purlins – sheeting systems – Part 2. Simplified model, Thin-walled Structures*, 27(4), pp. 263–286. doi:10.1016/S0263–8231(96)00039–0.

Rzeszut K., Studziński R., 2010. *Stability analyses of thin-walled laterally braced purlins*, The 10th International Conference on Modern Building Materials, Structures and Techniques, Vilnius, pp. 758–762.

Studziński R., Pozorski Z., Błaszczuk J., 2015. *Optimal Support System of Sandwich Panels*, Journal of Engineering Mechanics, 141, 3.

Studziński R., Pozorski Z., Garstecki A., 2015. *Structural behavior of sandwich panels with asymmetrical boundary conditions*, Journal of Constructional Steel Research, 104 (2015) 227–234.

Timoshenko S.P., Gere J.M., 1961. *Theory of elastic stability*. McGraw-Hill, ISBN 0–07-Y85821–7.

Ye Z.M., Kettle R., Li L.Y., Schafer B., 2002. *Buckling behaviour of cold-formed zet-purlins partially restrained by steel sheeting*, Thin-walled Structures, 40, pp. 853–864. doi:10.1016/S0263–8231(02)00029–0.

Zhao C., Yang J., Wang F., Chan H.C., 2014. *Rotational stiffness of cold-formed steel roof purlin–sheeting connections*, Engineering Structures, 59, 284–297.

Recent Progress in Steel and Composite Structures – Giżejowski et al. (Eds)
© 2016 Taylor & Francis Group, London, ISBN 978-1-138-02946-0

Innovative cold-formed GEB section under compression

A. Łukowicz, P. Deniziak, W. Migda, M. Gordziej-Zagórowska & M. Szczepański
Gdańsk University of Technology, Gdańsk, Poland

ABSTRACT: Cold-formed steel sections extensively affect the modern steel construction industry. Not only are they used as secondary elements like purlins or sheeting, but also they can serve as primary load-bearing members in fabricated steel panels and trusses. A new cross-section called shortly a GEB may serve as that member. However, its existence of the metal building structures industry depends on the exact, optimal dimensional parameters which are associated with its production possibility and ultimate and serviceably limit states criteria. According to the European Standard EN 1993-1-3 every new section shape should be tested to assign the cross sectional deformation behavior and capacity. That is why this innovative profile inter alia was tested for axial compression. The paper reports the results of experimental test and also computational analysis in RFEM software e.g. deformation modes and maximum axial load. Simultaneously, values of cross-section capacity were assigned based on Standards.

1 INTRODUCTION

The typical steel structures are usually made of hot rolled sections like I- and C-sections or seamless steel pipes. Unfortunately, these profiles cause high weight of structures, so designers are willing to use the thin cold-formed sections as secondary elements like purlins or sheeting more often, to reduce the weight of structures. These profiles are also used as truss components in typical single-storey structures, but not for primary members. A new GEB section, which was patented three years ago may serve as a primary load-bearing member in fabricated steel frames [Łukowicz A., Urbańska-Galewska E. 2013]. It is an open, trapezoidal cross-section, with a longitudinal assembly gap between the internal folded edges of the member (Fig.1a), where a system connector is located, making it possible to join with other members. This connector is freely located and moves along the length of the member. Additionally, a longitudinal assembly gap is useful to compensate dimensional and assembly deviations (Fig. 1b).

The possibility of free movement of connectors along the gap makes it workable to form structures without additional technological operations (e.g.: cutting, fitting, welding, drilling holes) in order to meet the requirements of individual civil engineering design cases. It may reduce the costs of design and performance of the following stages of the project, as simplifying the erection procedure makes it more effective [Łukowicz A., Urbańska-Galewska E., 2011].

These features of GEB profile will be implemented in a universal design format of a structural system. In this system the profiles are going to be applied not only for secondary elements like purlins or sheeting, but also they may serve as primary load-bearing members in fabricated steel panels, like columns and trusses, which is a novelty in steel structure design. The approved format of a structural system is designed to minimize the total construction costs [Łukowicz A., Urbańska-Galewska E. 2012].

Therefore, dimensional parameters of this section, which are associated with its production possibility and ultimate and serviceability limit states criteria, must be optimal and allows to build the universal design format of a structural system.

According to the European Standard [EN 1993-1-3, 2006] every new section shape should be tested to assign the cross sectional deformation behaviour

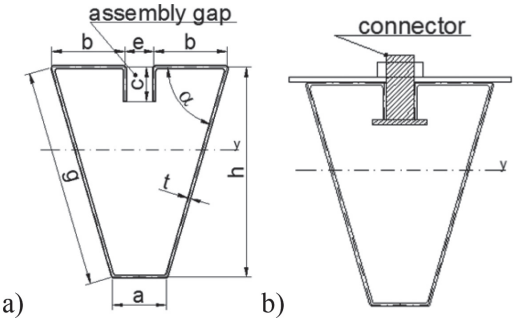

Figure 1. GEB section: a) cross-section dimensions, b) a cross-section with connector in an assembly gap.

and capacity, hence this profile inter alia was tested for axial compression. This experimental investigation and also computational analysis in Dlubal's software RFEM showed deformation behaviour and values of maximum load. Simultaneously, values of cross-section capacity were assigned based on European Standards [EN 1993-1-3, 2006, EN 1993-1-5, 2006].

2 GEB ELEMENT CAPACITY

2.1 *Cross-sectional capacity*

In order to define the GEB elements resistance, both cross-sectional load-carrying capacity and element stability checks have to be made. The cold-formed elements are sensitive to a number of forms of stability loss, e.g.: local buckling of thin walls, distortional and overall buckling. Each of these forms may appear separately but often they appear in interactive form so the relevant limit states have to be checked.

The resistance of the thin-walled cross section is determined on the basis of Winter's theory of supercritical capacity. The thin walls, which are sensitive to local buckling, are analysed incorporating the panel effective width idea. The single element of the cross section is modelled by means of plate panels of specific boundary conditions. When the axial stress are higher than a supercritical stress value some parts of profiles may undergo local buckling. This leads to the introduction of the reduced cross-sectional area (Fig. 2a).

2.2 *Interactive stability*

In the case of compression thin elements of the cross-section the local buckling affects supercritical stress redistribution and occurs only for very small buckling length, comparable to the dimensions of the cross section. What is important, the buckling length means the lengths of the halve-wave by instability deformed section element, part of the section or all the compression member. The small buckling length of the element corresponds to local buckling panel forms, while a large buckling length may lead to overall buckling. There may occur an intermediate length allowing for hybrid, interactive buckling modes.

Typical shapes of cold-formed open steel sections (e.g. bended C- and Z-sections) have been extensively studied in recent years [Schafer B. W. 2002]. Buckling of typical length elements of thin-walled 4 class sections (prone to local buckling) may cause parts of a cross-section to act like plates (local buckling) and the other parts like columns

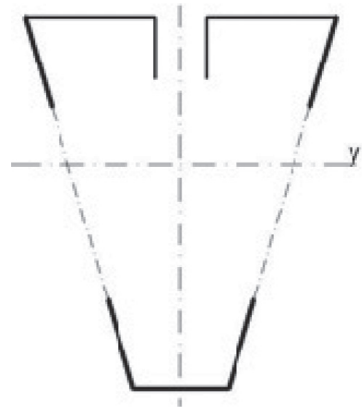

Figure 2. Reduced cross-sectional area under axial compression.

(overall buckling). What is more the nodal points, which not belong to the web, move from their position. This behaviour is referred to as distortional buckling. This loss of stability form is thoroughly described in the European Standard EN-1993-1-3.

The GEB section consists of 5 elements, including 3 internal plate elements (doubly supported) and 2 outstand plate elements with edge stiffeners. To estimate the effective width of every compression element of the cross-section, the edge stiffeners are treated like compression members with continuous partial restraint and spring stiffness depending on the boundary conditions and the flexural stiffness of the adjacent plane elements [EN 1993-1-3, 2006]. In order to use these formulas for various cross-sections, adequate tests are required which are made to assign the cross-sectional deformation behaviour and the form of distortional buckling edge stiffeners resistance. These forms, which arise under the load are very important for cold-formed sections [Crisan A, Ungureanu V, Dubina D., 2012]. Unfortunately, these behaviours are not known for the analysed GEB cross-section, so the adequate strength tests of that sections had to be performed.

2.3 *Initial calculations according code*

Thin elements are analysed according to Winter's theory of supercritical capacity incorporating the panel effective width idea and modelled by means of plate panels of specific boundary conditions. The local buckling of some parts of profiles results from exceeding the critical stress value (by normal stress levels). What is more, the behaviour of the

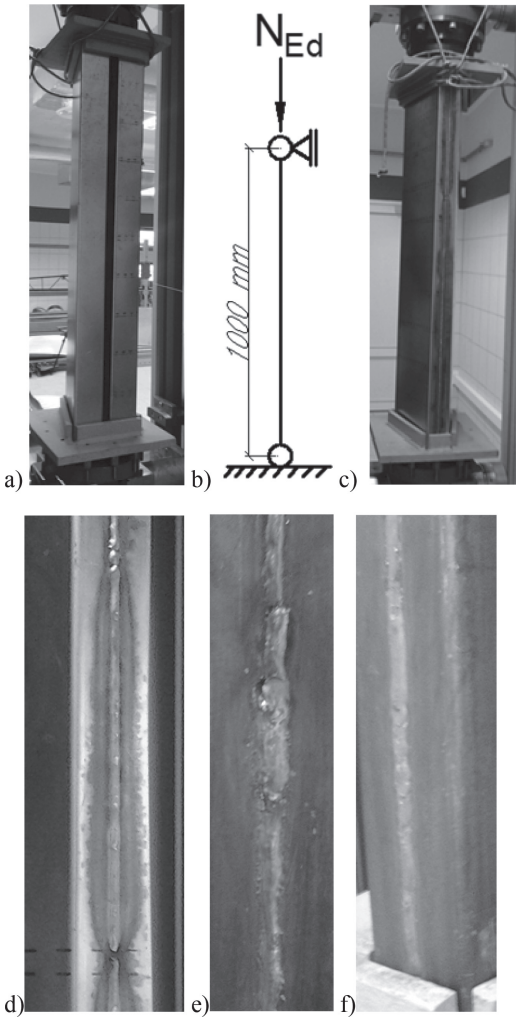

Figure 3. The test stand for axial compression of elements: a) view from the gap side, b) Static diagram; c) View from the spine side, d) e) f) view on the longitudinal butt weld.

Table 1. Values of the resistance for axial compression N_{bRd} and buckling N_{cRd}.

	N_{bRd}	N_{cRd}
Kind of samples	kN	kN
Thickness – 2 mm		
DC04 grade of steel	168.5	168.2
Thickness – 3 mm		
S235 grade of steel	369.1	368.8

plate section elements with edge stiffeners also influence the stability loss and deformation of the section. In Figure 2 shows the reduced cross-sectional area.

Since the GEB section is an open, cold-formed cross-section, thin-walled in class 4 the axial load resistance can be determined based on the relations presented in EN 1993-1-3, using cross-sectional characteristics of effective area according to EN 1993-1-5 as well. To design resistance of such a section the shape of deformation due to the loss of local and distortional stability has to be taken into account. As a result of carried out experimental studies (point 3) it was determined that the form of the deformation of the GEB section is similar to that which exists for the profile types Z and C, so respective, effective cross-sections areas (Fig. 2) were adopted for the studied members. On this basis the values of the cross-section resistance for axial compression and buckling were determined. Computationally static diagram and member length are set according to Figure 3b. All the values are given in Table 1.

3 EXSPERIMENTAL TESTING

3.1 *Axial tensile tests*

The thin-walled cold-formed sections according to EN 1993-1-3 standard are prone to loss of the cross-sectional resistance due to bending moment and axial compression forces. We distinguish: shear force, local transverse forces (for sections with unstiffened webs), local, overall and distortional buckling as well.

For this trapezoidal, open section the distortional buckling criterion is particularly important. It mainly concerns the behaviour of the bracket section members like edge stiffeners. Axial compression tests were provided to find it out which loss of stability mode occurs firstly, causing the sectional deformation. At first the performance of steel were estimated by axial tensile tests and were made of a ZWICK Roell Z400 testing machine. The values of the tensile strength, yield strength

Table 2. Values of the steel performance.

	fu	fy	E-modulus
Kind of samples	MPa	MPa	GPa
Thickness—2 mm			
DC04 grade of steel	293	206	178
Thickness—3 mm			
S235 grade of steel	393	263	210

and E-modulus (which were used to further counting analysis) are given in Table 2.

3.2 *Axial compression*

Eight elements of one-metre-length were used for axial compression resistance testing. A variety of steel grades in members was the result of material accessibility in particular warehouse. Half of members, those 2 mm thick, were performed of DC04 grade steel, and the next four, those 3 mm thick were made out of S235 grade steel.

Members have been manufactured in two stages duo to members complicated cross-section shape. Firstly two steel sheets has been longitudinally bend in three points and then cross-section has been assembled together using longitudinal butt weld (Fig. 3d,e,f).

For the purpose of the test a special handle fixing the strength tester thresholds were designed and applied to simulate the pin-supporting of members. The samples were located sequentially in the thresholds (Fig. 3a,c) and the testing parameters values were input to the software. The compression process of members results in deformation of their elements, these geometry changes were recorded, together with the load imposed, just to create the relevant force-displacement diagram.

The deformation modes of particular elements were observed during the axial compression tests

Figure 4. Deformation of member—spine side: a) 2 mm thick sample, DC04 grade of steel, b) 3 mm thick sample, S235 grade of steel.

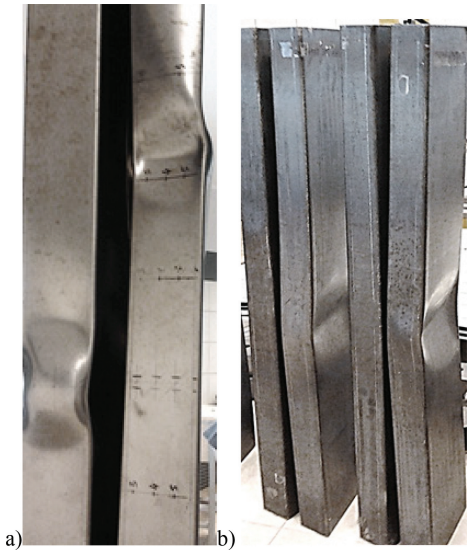

Figure 5. Deformation of member—gap side: a) 2 mm thick sample, DC04 grade of steel, b) 3 mm thick sample, S235 grade of steel.

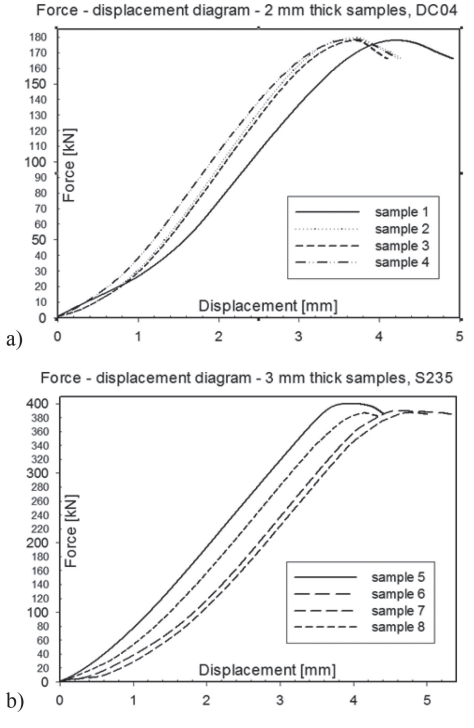

Figure 6. Force-displacement diagram: a) for 2 mm thick samples and DC04 grade of steel, b) for 3 mm thick samples and S235 grade of steel.

(Figs. 4–5) and the value of the maximum load (force value) that causes the destruction of the member was determined on the base of force-displacement diagrams (Fig. 6).

4 FEA CALCULATIONS

4.1 *Finite elements*

Numerical calculations were performed in the RFEM software. Sections were modelled with maximum 10 × 10 mm dimensions finite element quadrangle, used for thin shells. The program has been implemented with basic geometric data such as 2 mm and 3 mm thick elements, and material parameters such as: Poisson ratio of 0.3 and the density of steel equal 7850 kg/m^3. Young's modulus and yield strength of the material determined based on the axial tensile tests are given in Table 2. Also the computer program has been implemented with steel properties like isotropic, elasto-plastic model of material and von Misses yield criterion for nonlinear analysis.

A model of pin supported column with a 1 m length applied for the analysis. The support was modeled as a linear. Upper one as a pin with the possibility of vertical strain along the global "z" axis (Fig. 7a). Further, the lower support modeled as a pin with ability to rotate along the cross-section edge and possibility to separate from the base (Fig. 7b).

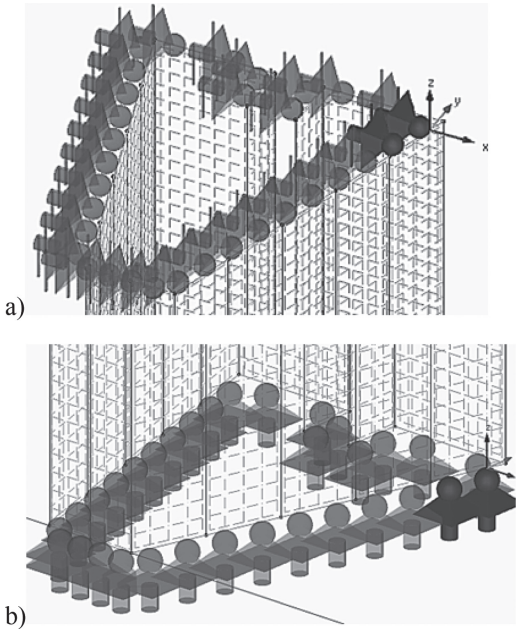

Figure 7. Linear supports model in RFEM: a) upper support, b) lower support.

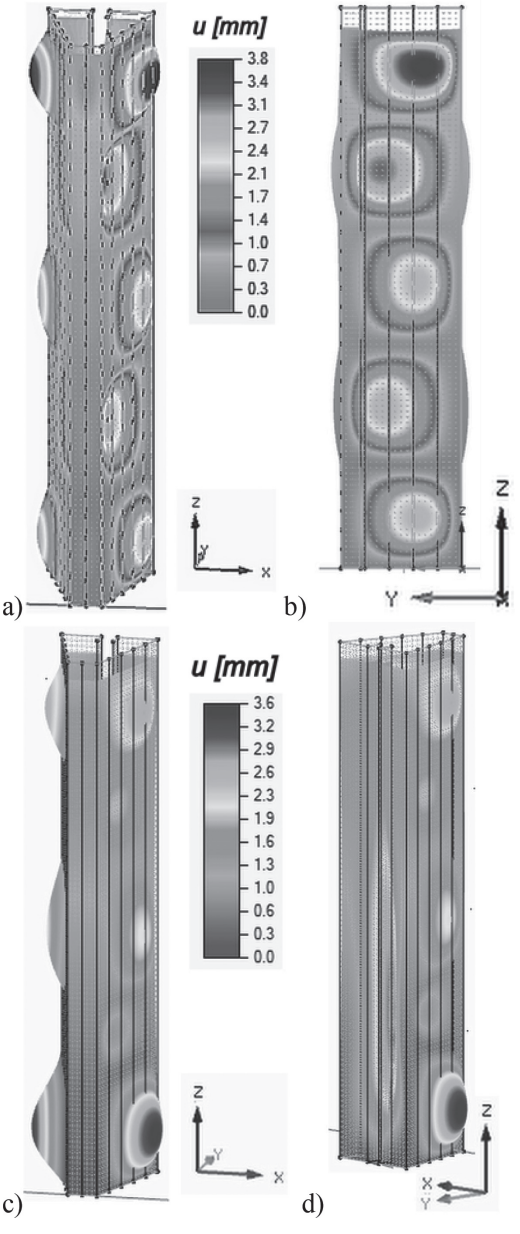

Figure 8. Member deformation: a) 2 mm thick sample, DC04—spin side, b) 2 mm thick sample, DC04—view of the panels, c) 3 mm thick sample, S235—spin side, d) 3 mm thick sample, S235—gap side.

During the test, members were kept from moving by a particular handles which shape was design to block inner elements of the cross-section (those without stiffeners) horizontal movement and make

them fit tight to the support. Further, handles were intentionally shaped to transmit the force axially throughout the plate to whole cross-section perimeter evenly. Therefore, during FEM model creation, the axial compression force was applied as gradual and linear along the edge. Load was implemented with linear increase and the value was respectively 250 kN/m for 2 mm thick section elements and 556 kN/m for 3 mm thickness. Those quantities were chosen according to previous construction, lab tests and calculations based on national standards. Computations imply similar destructive force values. The numeric analysis were conducted by the postcritical Modified Newton-Raphson method.

4.2 *Results*

Maps of displacement resulting from the carried out analysis are presented on Figure 8.

At the same time, according to the RFEM calculations the maximum force value that results in member instability was determined. Those maximum force values were found by iterative application of load which was initially similar to the lab test destructive load monitoring the stiffness matrix. After reaching the instability stress values the stiffness matrix became noninvertible. Results shown in Table 3.

Table 3. Values of the maximum axial compression force N_{Ed} [kN] and corresponding horizontal deformation u_z [mm].

	N_{Ed}	u_z
Kind of samples	kN	mm
Thickness—2 mm		
DC04 grade of steel	180	1.2
Thickness—3 mm		
S235 grade of steel	398	0.9

Table 4. Values of the steel performance.

	Calculations acc. Standards	Experimental tests	FEA
Kind of samples	kN	kN	kN
Thickness—2 mm			
DC04 grade of steel	168.2	178.4	180
Thickness—3 mm			
S235 grade of steel	368.8	390.9	398

5 SUMMARY

5.1 *Buckling capacity*

A comparison of all analyzed results are presented below.

Values of the loading force are similar comparing FEM calculations with those reached at experimental test but slightly higher than the local buckling resistant force according to Standards.

Generally, the aforementioned values vary because the profile geometric wasn't perfect as it was assumed in FEM calculation. Additionally, boundary conditions like pin support and force load weren't exactly the same for those two kind of analysis. Accumulation of those imperfections caused different values of cross section resistance for axial compression. The crucial reason of those differences might be the fact, that the length dimension of the members, were not exactly the same and support were not exactly in axial position.

Furthermore, some local forms of cross sectional deformation, which arose during the experimental study, were the result of numerical calculations (Fig. 8 a, b). While comparing Figs. 4, 5 and 8 it is clearly visible that overall deformation forms are fundamentally different from each other.

5.2 *Deformations*

The deformations behaviour and stability forms of the GEB profile cross-section elements were determined on the basis of testing.

The widest element, i.e. the webs (Fig. 9b,c,f) were deformed firstly in both profile types. Next, bumps and dips occurred on the narrower elements (Fig. 9a,e). At the last stage the bracket elements were deformed at the supports (Figs. 9 g, 10). Thus local buckling was the first and decisive for a stability loss.

Analogical member behaviour was noticed during previous bending resistance tests where local instability was firstly observed in the widest elements (webs) [Łukowicz A., Urbańska-Galewska E., Gordziej-Zagórowska M. 2015].

At the same time, according to the Figs. 4, 5 and 8 differences in overall deformation forms were noticed. Those forms obtained by FEM analysis are the result of modelling perfect section and member geometry. Local instability visualized as hollows and bulges in member elements is arranged in the form of half-waves on each element symmetrically about the vertical cross section. However, previous lab tests gives non-symmetrical deformation form what can be the result of geometrical imperfections in cross-section and lack of member stabilizing handle axial position.

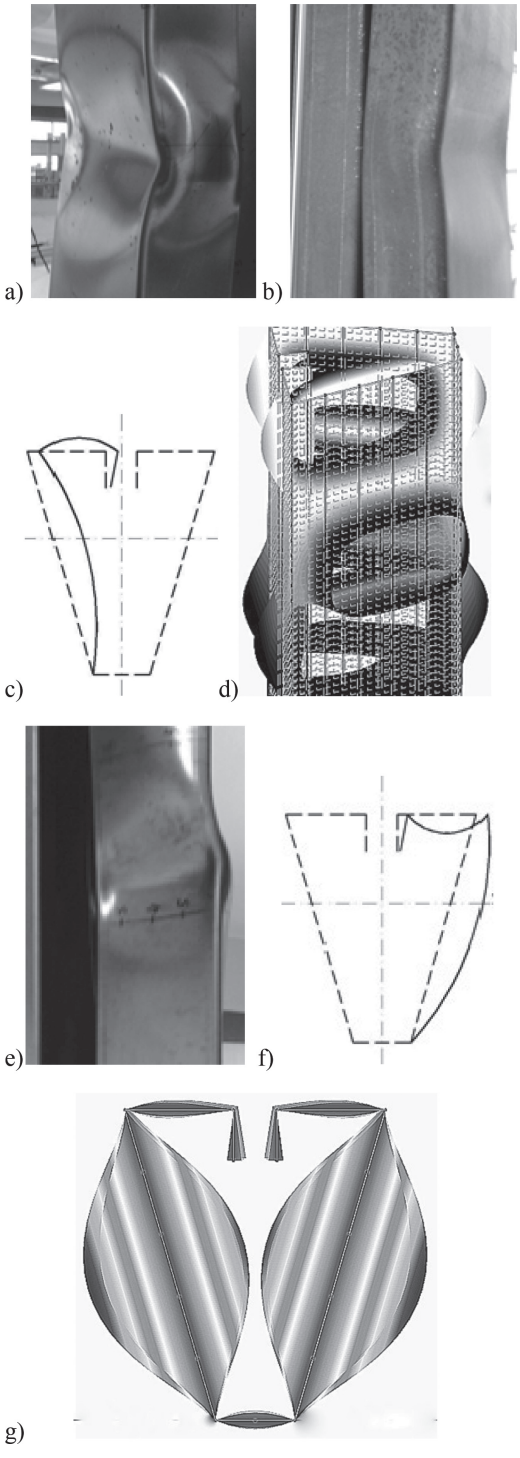

Figure 9. Deformation forms of section elements: a, b, e) photos from test, c, f) theoretical deformation d, g) FEM deformation.

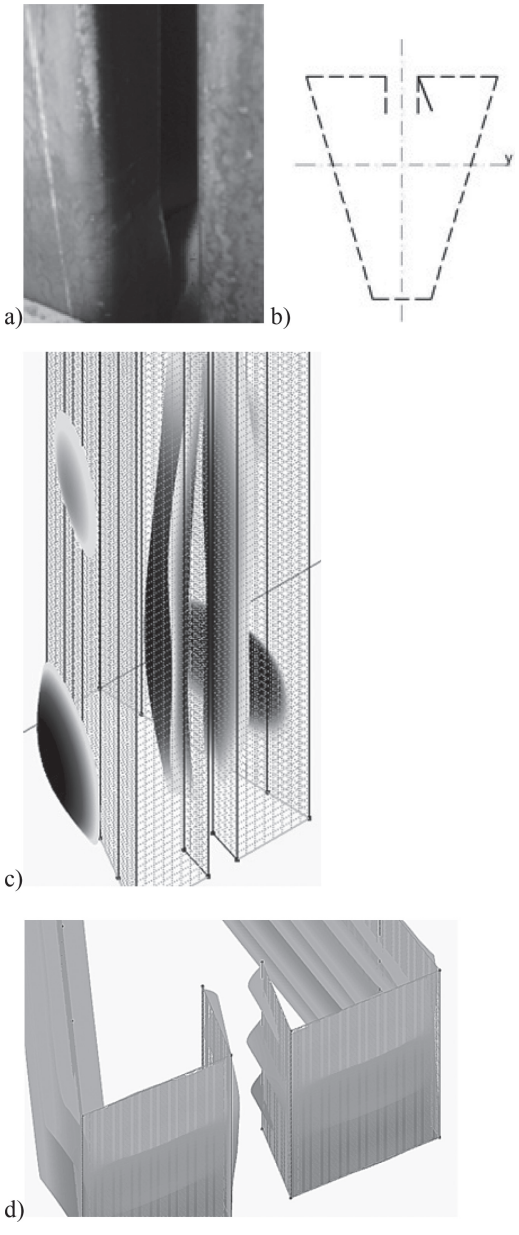

Figure 10. Deformation forms of edge stiffeners: a) photo from test, b) theoretical deformation, c) FEM deformation for 2 mm thick samples, DC04, d) FEM deformation for 3 mm thick samples, S235.

The code formulas can be taken to assess the load-carrying capacity and stability of elements of any given profiles if the experiments confirm that the deformation behaviour of the profiles considered is similar to the results of the profiles already analysed. According to scientific literature,

experimental testing is necessary to investigate for new shapes of cold-formed cross-sections.

The results obtained from the conducted experiments showed that the deformation behaviour of the GEB-section is very similar to those of C-sections and Z-sections. Therefore, the assumptions regarding the designation of the effective cross-sectional area are correct also in the case of the analysed section [Łukowicz A., Urbańska-Galewska E. 2014].

REFERENCES

Crisan A, Ungureanu V, & Dubina D., 2012. *Behaviour of cold-formed steel perforated sections in compression—par2: numerical investigation and design considerations.* Thin-Walled Structures (in this special issue).

Crisan A, Ungureanu V, & Dubina D., 2012. *Behaviour of cold-formed steel perforated sections in compression—part1: experimental investigation.* Thin-Walled Structures (in this special issue).

Dlubal Softwere: RFEM 5.05

EN 10130:2006 *Cold rolled low carbon steel flat products for cold forming. Technical delivery conditions.*

EN 1993-1-3, 2006 Eurocod 3: Design of steel structures" Part 1–3: "*General rules—Supplementary rules for cold-formed members and sheeting*.

EN 1993-1-5, 2006 Eurocod 3: *Design of steel structures" Part 1–5: "General rules - Plated structural elements*.

Schafer B.W., 2002. *Local, Distortional, and Euler Buckling of Thin-Walled Columns*. Journal of structural engineering.

Łukowicz A., & Urbańska-Galewska E. 2014. *Deformations of innovative cold-formed GEB sections*, 7th European Conference on Steel Composite Structures: Eurosteel 2014, Naples.

Łukowicz A., & Urbańska-Galewska E., 2011. *O możliwościach optymalizacji konstrukcji stalowych.* Nowoczesne Hale, ISSN 1899–8224, Vol. 4/11. 26–30.

Łukowicz A., & Urbańska-Galewska E., 2012. *Wpływ ograniczeń technologicznych na dobór parametrów przekroju kształtownika giętego.* Zeszyty Naukowe Politechniki Rzeszowskiej. Budownictwo i Inżynieria Środowiska.

Łukowicz A., & Urbańska-Galewska E., 2013. *Innowacyjna linia technologiczna kształtowników typu GEB.* Logistyka, ISSN 1231–5478, Vol. 4/2013.

Łukowicz A., & Urbańska-Galewska E., Gordziej-Zagórowska M. 2015. *Experimental testing of innovative cold-formed GEB section*. Civil and Environmental Engineering Reports. Rzeszów.

Steel-concrete composite structures

This page intentionally left blank

Recent Progress in Steel and Composite Structures – Giżejowski et al. (Eds)
© 2016 Taylor & Francis Group, London, ISBN 978-1-138-02946-0

Concrete confinement estimation in composite steel-concrete columns

E. Szmigiera, B. Grzeszykowski & M. Szadkowska
Warsaw University of Technology, Warsaw, Poland

ABSTRACT: In this paper two methods of concrete confinement evaluation of composite steel-concrete columns are presented. First method is based on comparison between experimentally obtained ultimate loads with the theoretical bearing capacity of investigated columns computed according to the Eurocode 4. Second method is based on the investigation of the load distribution between concrete and steel parts of columns. Rüsch formula for stress-strain curve for the unconfined concrete and experimentally obtained strains for both steel and concrete are used. I—shaped two chord battened steel-concrete composite columns are investigated. In order to complement the research a numerical analysis in ABAQUS/Standard was conducted to visualize areas of high confinement of column's concrete cores.

1 INTRODUCTION

Reaching critical values of load-bearing capacity in stub steel-concrete columns is accompanied in most cases with cracking and crushing of concrete. Destruction of such kind was noticed in Concrete-Filled-Steel-Sections (CFST) columns made of tubes of relatively thin sidewalls, designed with respect to seismic threats. Similar observations were made in research conducted by the authors of this paper on columns fully encased in concrete, as well as on two-chord battened columns filled with concrete. Hence, analysis of effective load-bearing capacity of concrete in composite columns appears to be an extremely important issue. Consequently, research has been done on possible methods of enhancing the load-bearing capacity of concrete subjected to axial compressive stress in conditions where the risk of lateral buckling was substantially reduced. In the 60ies of the previous century, In (Rüsch & Stöckl (1969)) a relationship between using spiral steel reinforcement and subsequent improvement of confined concrete strength was suggested. Furthermore, in (Mander et al. (1988)) a thorough analysis of a complex character of stress distribution in concrete was provided, taking into account different types of reinforced concrete columns. Similar research has been conducted in recent decades with regard to composite steel-coNCRete columns (El-Tawil (1999)). It is well known that restraining deformation of concrete is related to pressure exerted by lateral reinforcement, a steel tube or steel section. In the effect of confinement, compressive strength of concrete increases. That is conditional on numerous factors, which can be classified as the following:

- type of structure and type of confinement related to it (reinforced concrete or composite column)
- type of composite cross section (e.g. concrete-encased section or concrete filled tube)
- shape of cross section (circular, square, rectangular or other)
- geometry of the cross-section—dimensions and thickness of tube walls.

Many variables that needs to be considered in the design of different types of columns with the concrete confinement phenomenon included enforces testing and analysing each type separately. Experimental research as well as analytical calculations most often aim at assessing quantitative and qualitative influence of the mentioned parameters on the effective concrete strength in different types of composite columns cross sections. In (Cheng & Lin (2006)) a comprehensive analysis of the effect of the shape and layout of steel sections have on stress distribution in concrete and the resultant load capacity of columns was presented. The confinement of concrete in CFST rectangular cross section columns was presented in (Ge & Usami (1994)) and (Cai & He (2006)). Additionally, research has been carried out on CFST rectangular cross sections, with a view to deriving benefits from the complex character of stress distribution in concrete. These can be achieved through seeking solutions at the stage of construction design (Hu et al. (2003)). In (Susantha et al. (2001)) a method of predicting how the stress-strain relationship changes, taking into account the triaxial character of stress in concrete in tubular columns of various cross section shapes was proposed. The effect of concrete confinement has also been studied in

CFST elliptical cross section columns (Yang et al. (2008)), as well as in columns of the FRP type (Yuan et al. (2008)). Analysing the problem of concrete confinement in columns consisting of rectangular steel tubes sections often aims at assessing how to account for the confinement effect in calculating the load-bearing capacity of such columns so as to comply with current standards. For safety reasons, the effect that the complex character of stress distribution in concrete has on enhancement of load-bearing capacity in rectangular tubular columns is most often disregarded, and accounted for only in circular cross sections, as in Eurocode 4. That problem was explored by many researchers. A method of computing load-bearing capacity for rectangular cross section CFST columns was suggested in (Huang et al. (2008)), and the results were compared with computations according to numerous standards. In (Kupina (2015)) the ultimate load of rectangular short CFST columns was analysed and author stated that the increase in compressive strength of concrete due to its confinement is approximately 16%. In case of analysed in this paper two chord steel-concrete columns the confinement effect of concrete is hard to estimate due to the complex non-prismatic geometry of specimens. These types of columns can be analysed either as concrete encased sections or as CFST columns. In (Szmigiera (2012)) the analysis of the stress state of concrete filling the steel cross-section using experimentally obtained horizontal and vertical strains of steel and concrete was conducted. The analysis showed that the concrete fill in this type of columns is in the complex stress state and associated with this fact increase in the ultimate bearing capacity of columns was approximately 8%. In this article two other approaches on estimating concrete confinement was presented. First one is based on the comparison between ultimate load measured experimentally and computed according to the formulated by Emperger (1908) addition law that is placed in the Eurocode 4. Second one is based on the measured in the experiment longitudinal axial strains of steel and concrete.

2 EXPERIMENTAL RESEARCH

The experiment was carried out on 41 natural scale elements with a length of 2500 mm. That length was chosen so that column's slenderness could be disregarded. In order to maintain the transparency of the analysis of concrete confinement authors decided to include in this paper only four types of tested two chord composite columns. The cross sections of the elements consist of two H-shaped S235 grade steel HE160 A sections. The space between flanges and webs of beams are filled with C20/25 or C50/60 concrete grade. Two kinds of batten plates spacing was considered: 240 mm and 780 mm (see Figure 1).

Detailed description of specimens included in this article is presented in Table 1. During the research the following quantities were recorded: axial force, vertical shortening and horizontal deflection of columns, vertical and horizontal strains of concrete and steel parts. Strain gauges measuring vertical strains of steel and concrete were placed in three cross-sections: in the top, middle and bottom of columns (Figs. 2a, b, c). Strain gauges measuring vertical strains of the steel were placed on the surfaces of HE160 A beams. Specific geometry of two-chord steel concrete battened columns allowed placing strain gauges measuring concrete strains on the surface of concrete between the battens, what would be impossible in case of the CFST columns. Further information about the conducted experimental research can be found in (Żółtowski et al. (2006)) or (Szmigiera et al. (2010)).

3 CONCRETE CONFINEMENT ESTIMATION

3.1 *Ultimate load method*

According to the Eurocode 4 the plastic resistance to compression of composite steel-concrete columns without steel reinforcement (with no

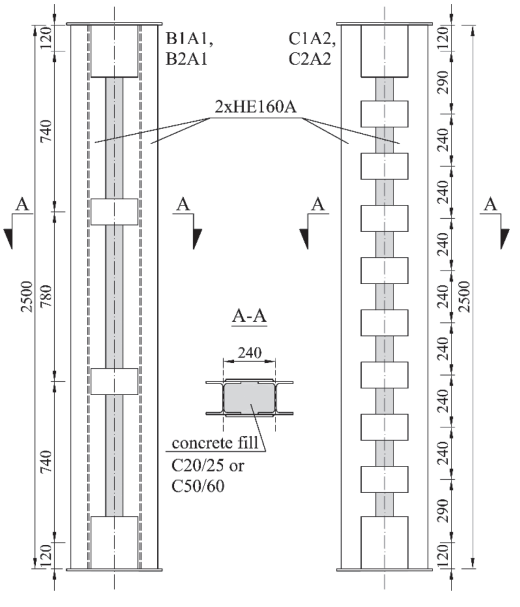

Figure 1. The design schemes for tested columns with 240 mm and 780 mm spacing of battens.

Table 1. Properties of elements including test results.

Notation of series	Spacing of battens mm	Grade of concrete	f_{cm} MPa	f_y MPa	Ultimate load kN
B1 A1	780	C20/25	26.6	301	3200
C1 A2	240	C20/25	26.6	301	3400
B2 A1	780	C50/60	63.6	268	4333
C2 A2	240	C50/60	63.6	268	4377

*Explanation of symbols is under the Equation 1.

buckling effect considered) can be calculated by adding the plastic resistances of the cross-section components:

$$N_{b,Rk} = A_a f_y + A_c k f_{cm} \tag{1}$$

where f_{cm} = mean value of the measured cylinder compressive strength of the concrete; f_y = mean value of the yield strength of structural steel; A_a, A_c = cross-sectional area of the structural steel cross-section and the concrete cross-section respectively.

The k coefficient reduces the compressive strength of concrete and equals to 0.85 for concrete partially encased and fully encased steel sections. For concrete filled sections $k = 1.0$, therefore Equation 1 does not directly take into account any confinement of concrete. For circular CFST columns Eurocode 4 allows to take into account the increase in strength of concrete caused by confinement provided that the relative slenderness of the column and the eccentricity of loading does not exceed given values. In this article authors computed the values of k coefficient using the experimental data. For this purpose authors assumed that the ultimate force computed according to the Equation 1 equals to the ultimate force obtained from the experiment: $N_{b,Rk} = N_U$. Therefore the coefficient k equals to:

$$k = \frac{N_U}{A_c f_{cm}} - \frac{A_a f_y}{A_c f_{cm}} \tag{2}$$

At this point authors think that it may be considered as some kind of averaged over the length of the column concrete confinement coefficient for short columns. Results of the computations are presented on Figure 3, where it can be seen that the k coefficient is greater than 1.0 for every specimen and that indicates that the confinement of concrete occurs with all types of analyzed columns, even with ones with small spacing of battens. Elements with smaller distance between battens (type A2) exhibit greater concrete confinement in relation to

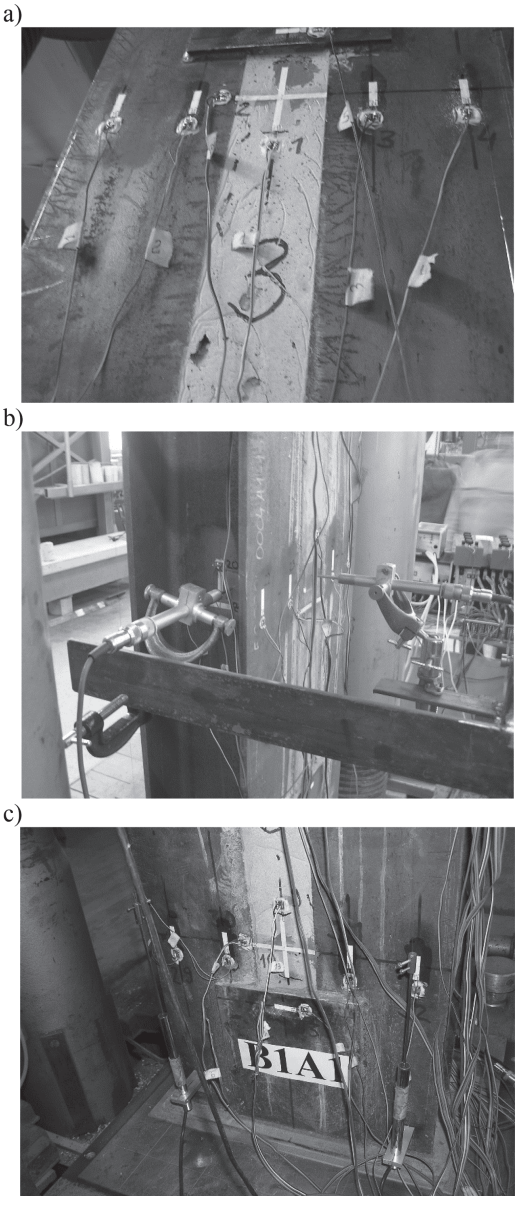

Figure 2. The location of strain gauges on steel and concrete in three cross-sections of the B1 A1 column: a) top, b) middle, c) bottom.

columns with rare batten plates spacing. Depending on the concrete compressive strength the k coefficient for elements filled with C20/25 concrete changes from 1.04 for the A1 column type to 1.28 for the A2 column type which means nearly 20% increase in the confinement of concrete. In case of the columns filled with C50/60 concrete grade the congestion of battens brings only 2% increase

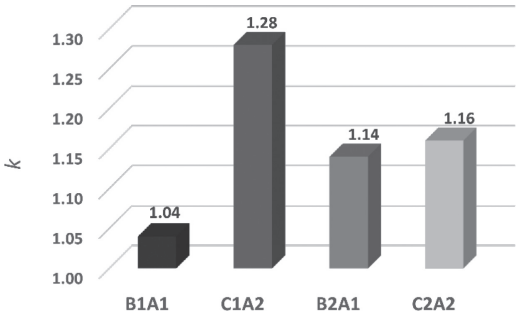

Figure 3. Values of the concrete confinement coefficient k computed for analysed columns.

in the value of the k coefficient from 1.14 to 1.16. That fact indicated that in the case of strong concrete spacing of battens have no apparent effect on the concrete confinement.

3.2 *Load distribution method*

The second method of determining the concrete confinement is also based on the results obtained from the research. The authors analyzed the participation of structural steel and concrete in transferring the acting axial load. The force transferred through the concrete core was computed in two ways. In the first one, it was obtained from the subtraction of the acting force and the force transferred through the steel profiles:

$$N_{ci} = N_i - N_{ai} \tag{3}$$

Second approach was to assume that during the experiment concrete core was in the uniaxial stress state. Measured values of longitudinal strains of concrete were used to calculate the stress-strain relationship according to the constitutive relation for concrete proposed by Rüsch. Dividing obtained in the above manner values, the another concrete confinement coefficient was computed using following equation:

$$\omega_i = \frac{N_i - A_a \sigma_{ai}}{A_c \sigma_{ci}} \tag{4}$$

where ω_i = concrete confinement coefficient; N_i = mean value of the force applied into the column at the given load level; σ_{ai} = compressive stress in the structural steel at the given load level; σ_{ci} = compressive stress in the unconfined concrete core at the given load level determined by the Rüsch formula, known from Eurocode 2, according to Equations 5–8.

$$\alpha_{ci} = f_{cm} \frac{k_R \eta_i - \eta_i^2}{1 + (k_R - 2)\eta_i} \tag{5}$$

$$\eta_i = \frac{\varepsilon_{ci}}{\varepsilon_{c1}} \text{ for } 0 < \varepsilon_{ci} < \varepsilon_{cu1} \tag{6}$$

$$\varepsilon_{c1} = 0.7 f_{cm}^{0.31} \leq 2.8 \tag{7}$$

$$k_R = 1.05 E_{cm} \frac{\varepsilon_{c1}}{f_{cm}} \tag{8}$$

where ε_{ci} = measured mean vertical strains in the concrete core at the given load level; ε_{c1} = compressive strain in the concrete at the peak stress f_{cm}; E_{cm} = secant modulus of elasticity of concrete.

The stress in the steel profiles that were used to determine the value of the force $A_a \sigma_{ai}$, has been defined from elastic-perfectly plastic constitutive relation:

$$\sigma_{ai} = \begin{cases} E_s \varepsilon_{ai} & \text{for } \sigma_{ai} \leq f_y \\ f_y & \text{for } \sigma_{ai} > f_y \end{cases} \tag{9}$$

where ε_{ai} = mean vertical strains of the steel registered for the N_i load level.

The spectrum of the concrete confinement coefficient ω_i, obtained from calculations is presented on Figure 4.

For columns with rare spacing of battens (B1 A1 and B2 A1) values of ω_i coefficients are much about constant and for a wide range of load level are greater than 1. Whereas similar conclusions could not be drawn in case of columns with a dense spacing of battens (C1 A2 and C2 A2). In authors opinion, the reason for this fact was the way of measuring concrete longitudinal strains. The longitudinal strains of concrete taken for calculation in the second method were measured by strain gauges attached to the surface of concrete

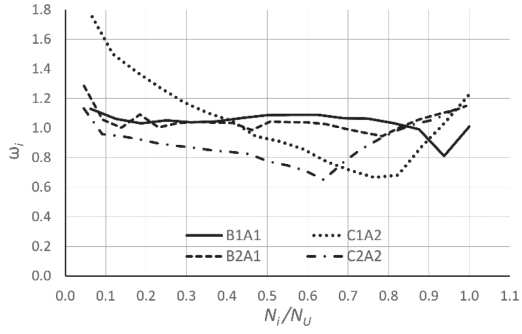

Figure 4. Spectrum of the concrete confinement coefficient ω_i computed for analysed columns.

where, what autors assumed, concrete was close to the uniaxial stress state because there were no steel parts to limit lateral strains of concrete in this area and cause the complex stress state. Nevertheless the distance to the nearest edge of steel sheets was not large and Saint-Venant's principle probably could not be in effect in that areas what could cause some undesirable disturbances in measurements and therefore interfere in the results.

Arguments for which curves from the Figure 4 reach the minimum values corresponds with the load level at which the steel yields. From that moment coefficient ω_i increases for all types of columns. This phenomenon is accompanied by the visible on the Figure 5, which presents the diagram of participation of the steel and concrete in the transfer of the axial load for the C1 A2 column, decrease in the participation of steel in transferring the axial load until the ultimate baring capacity of the column is reached. Moreover it can be seen that the participation of the concrete core in the load transfer, computed with the assumption of the uniaxial stress state, is approximately constant. Therefore a visible increase in the bearing capacity of the concrete core before reaching the ultimate load, which was computed by the subtraction of the acting force and the force transferred through the steel structure, is a result of the fact that the concrete is in the complex stress state.

The ω_i coefficient, besides the material properties, depends on three test variables: the given load level and mean vertical strains in the concrete core and in the steel profiles registered for the given load level: $\omega_i = \omega_i(N_i, \varepsilon_{ci}, \varepsilon_{ai})$. Interesting results were obtained for the ω_i coefficients computed for the maximum load of the anlyzed columns. According to the experimental analysis, in every specimen steel yields before column reaches the maximum load therefore the number of independent variables reduces to only two: $\omega_U = \omega_i(N_U, \varepsilon_{cU})$, what is shown in the following equation, which is derived from the combination of Equations 4–6:

$$\omega_{\mathrm{U}}\left(N_U, \varepsilon_{\mathrm{cU}}\right) = \frac{N_U - A_a f_y}{A_c f_{cm}} \frac{\left(\frac{\varepsilon_{\mathrm{c1}}}{\varepsilon_{\mathrm{cU}}} + k_R - 2\right)}{\left(k_R - \frac{\varepsilon_{\mathrm{cU}}}{\varepsilon_{\mathrm{c1}}}\right)} \tag{10}$$

where ε_{cU} = mean value of the longitudinal strains of the concrete core at the maximum load level N_U.

Values of the ω_U coefficient are presented on Figure 6. Analyzing the data it can be seen that the ω_U coefficient is greater than 1.0 for all types of columns, what confirmes the fact that concrete core is in the complex stress state. The influence of batten plates spacing on concrete confinement of columns filled with C20/25 concrete grade (B1 A1, C1 A2) is significant. While spacing of battens in columns filled with the higher grade of concrete does not have any influence on concrete coefficient ω_U, what confirms results obtained in the paragraph 3.1.

3.3 *Complementary numerical research*

In order to complement the research and visualise the concrete confinement regions in the two-chord test columns the numerical analysis in Abaqus/Standard was conducted for the elements filled with concrete of a lower strength grade (of types B1 A1 and C1 A2). Steel elements of the investigated column (2 × H-beam HE160 A and continuous connecting sheet) were modelled using 4-noded shell elements with appropriate thicknesses. An elastic—plastic material model with von Mises yield criterion and strain hardening was used with the following parameters: density $\rho = 7.85 \cdot 10^{-9}$ *t/mm*^{3}, modulus of elasticity $E = 205$ *GPa*, Poisson ratio

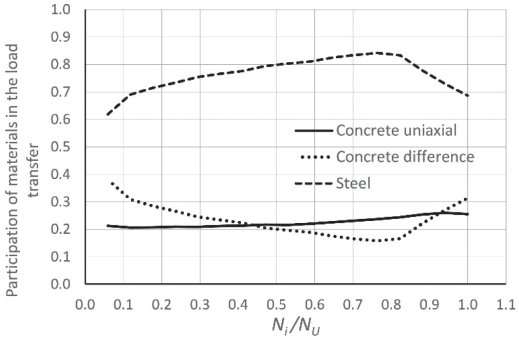

Figure 5. Diagram of participation of the steel and concrete in the transfer of the axial load for the C1 A2 column.

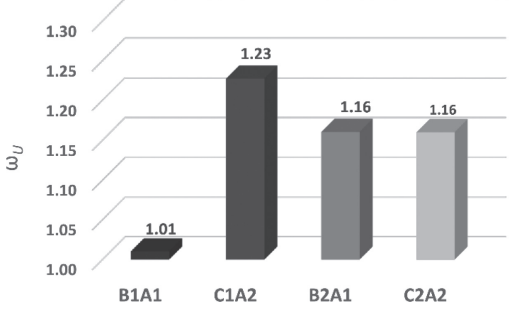

Figure 6. Values of the concrete confinement coefficient ω_U computed for the ultimate bearing capacity $N_i = N_U$ of each column.

ν = 0.3, and strain hardening parameters according to the steel tensile tests. Concrete was modelled using 8-noded brick elements with Concrete Damaged Plasticity material assumed. The default parameters were defined according to the ABAQUS manual and experimental tests of concrete samples. Load was defined as a prescribed motion of a top rigid plate of the column. Imperfections were modelled as a small initial axial load eccentricity. Extensive analysis about the column's imperfections can be found in (Szmigiera et al. (2015)). Further information about the numerical model can be found in (Kwasniewski et al. (2011)).

Figure 7 shows the distribution of compressive stress in the concrete along the height of the columns and the intensity of stress in two directions on the interface between the concrete and the steel surfaces of the sections or battens. It can be seen that the stress state in concrete cores of columns is very complex and is changing along the height of the column. In areas where steel parts cover the concrete the intensity of stress is greater than in areas where concrete is free of the influence of steel sheets. This is undoubtedlly related to the increase in the lateral pressure caused by the steel elements limitating lateral strains of concrete. Using two methods described in the preceding paragraphs one may estimate only average concrete confinement coefficient but what can be seen on Figure 7, this phenomenon is truly complex and hard to be captured in numbers.

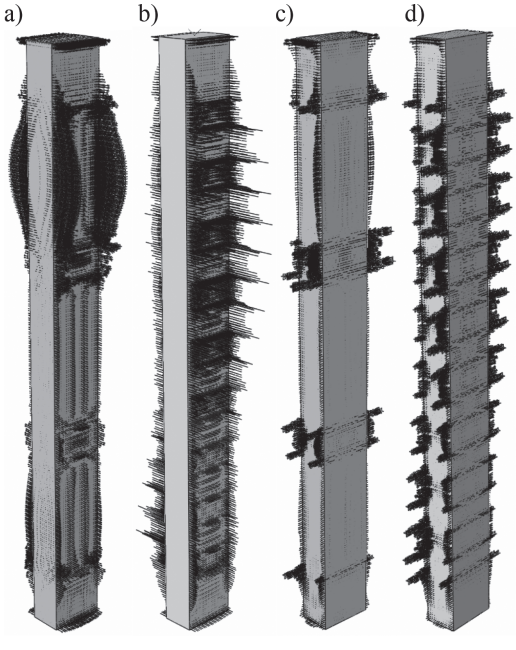

Figure 7. Distribution and intensity of compressive stress on the concrete surfaces in: a), b): perpendicular direction to the battens, c), d): paralell direction to the battens. Figure plotted for column types: a), c): B1 A1 - with 780 mm batten spacing, b), d): B1 A2 - with 240 mm batten plates spacing.

4 CONCLUSIONS

In this paper two approaches of analyzing the concrete confinement phenomenon in two-chord steel-concrete battened columns were presented. Both methods require the experimental data. First one (coefficient k) requires, in addition to the material properties, only the ultimate bearing capacity of columns and the second one (coefficient ω_i) requires also longitudinal strains of the steel profiles and concrete core. Coefficient ω_i allows one to see the spectrum of confinement in concrete along the axial load level. The $\omega_U = \omega_i(N_U)$ is the second concrete confinement coefficient computed for the maximum axial load of columns. Due to the fact that ω_U depends on one additional parameter obtained from the experiment: ε_{cU} and also depends on the Rüsch formula, it can be a good confirmation of the results obtained by the parameter k.

On Figure 8 the comparison between the two concrete confinement coefficients k and ω_U computed using Equations 2 and 10 respectively is presented and as it can be seen the results are very similar.

Both coefficients are greater than 1.0 for every tested specimen. That indicates that the confinement of concrete occurs with all types of analyzed columns, even with ones with small spacing of battens. Elements with smaller distance between battens (type A2) exhibit greater concrete confinement in relation to columns with rare batten plates spacing, but only for columns filled with C20/25 concrete grade. For the columns filled with C50/60 concrete grade the congestion of battens brings only small or none whatsoever increase in the value of the confinement coefficients what indicates, in case of the stronger concrete, that spacing of battens have no apparent effect on the concrete confinement.

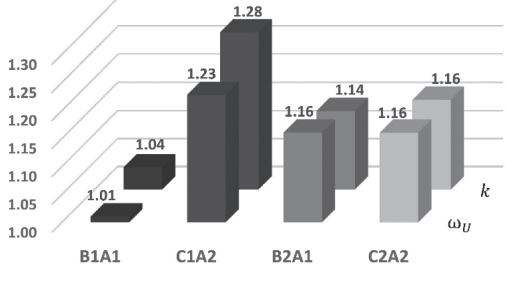

Figure 8. Comparison between the values of the concrete confinement coefficients k and ω_U.

In order to complement the research the numerical computations in Abaqus/Standard were conducted. The FEM analysis allowed authors to specify the distribution of compressive stress in concrete cores along the height of columns. The intensity of stress in two directions on the interface between the concrete and the steel surfaces of the sections or battens was significant, what is the confirmation of the complex stress state in the concrete core in the two chord-steel concrete battened columns. In this type of columns the analysis of the concrete confinement is problematic and hard to be captured in numbers due to the non-prismatic cross-section of elements. Nevertheless, it is possible to estimate this phenomenon by using presented in this article methods.

Reffering to the first method presented in this article authors point out that in the Eurocode 4, for the concrete filled sections the k coefficient in Equation 1 equals to 1.0, while, according to the analysis presented in this paper, for the non-prismatic two-chords steel-concrete battened columns that can not to be considered as concrete filled sections, the value of the k coefficient varies between 1.04 up to 1.28.

Authors intend to extend the analysis of the concrete confinement presented in this article on the other design solutions of the two-chord steel-concrete battened columns. Among other things the influence of the ordinary reinforcement usage as well as other ways of connecting the steel profiles will be investigated.

REFERENCES

ABAQUS. Analysis Theory Manual. ABAQUS, Inc., Version 6.12, USA, 2012.

ABAQUS. Analysis User's Manual. ABAQUS, Inc., Version 6.12, USA, 2012.

ABAQUS. Example Problems Manual. ABAQUS, Inc., Version 6.12, USA, 2012.

Cai, J. & He, Z.Q. 2006. Axial load behaviour of square CFT stub column with binding bars. *J. of Constr. Steel Research* 62: 472–483.

Cheng, C.C. & Lin, N.J. 2006. Analytical model for predicting axial capacity and behaviour of concrete encased steel composite stub columns. *J. Constr. Steel Research* 62: 424–433.

El-Tawil, S. & Deierlein, G.G. 1999. Strength and ductility of concrete encased composite columns. *J. Struct. Eng*. 125(9): 1009–1019.

Emperger, F. 1908. Experiments with reinforced concrete and iron columns filled with concrete in Stuttgart and Vienna. Forscherarbeiten auf dem Gebiete des Eisenbetons. Heft VIII. Berlin: Ernst & Sohn. (in German).

EN 1992-1-1 Eurocode 2: Design of concrete structures. Part1-1: General rules and rules for buildings.

EN 1994-1-1 Eurocode 4: Design of composite steel and concrete structures. Part1–1: General rules and rules for buildings.

Ge, H.B. & Usami, T. 1994. Strength analysis of concrete filled thin-walled steel box columns. *J. Constr. Steel Research* 30: 259–281.

Hu, H.T. & Huang, C.S. & Wu, M.H. & Wu, Y.M. 2003. Nonlinear analysis of axially loaded concrete-filled tube columns with confinement effect. *J. Struct. Eng*. ASCE 129(10): 1322–1329.

Huang, Y.S. & Long, Y.L. & Cai, J. 2008. Ultimate strength of rectangular concrete-filled steel tubular (CFT) stub columns under axial compression. *Steel Comp. Struct*. 8(2): 115–128.

Kupina, M. 2015. Load capacity of axially loaded rectangular steel short columns filled with concrete *PhD Thesis, Faculty of Civil Engineering, Opole University of Technology.* (in Polish).

Kwasniewski, L. & Szmigiera, E. & Siennicki, M. 2011. Finite element modelling of composite concrete-steel columns. *Arch. Civ. Eng.* LVII(4): 373–388.

Mander, J.B. & Priestley, M.J.N. & Park, R. 1988. Theoretical stress-strain model for confined concrete. *J. Struct. Eng.* ASCE, 114(8): 1804–1826.

Rüsch, H. & Stöckl, S. 1969. Behaviour of columns with spiral reinforcement under short-term and long-term axial loading. *Deutscher Ausschuss für Stahlbeton*. Berlin: Ernst&Sohn, 205 (in German).

Susantha, K.A.S. & Ge, H. & Usami, T. 2001. Uniaxial stress-strain relationship of concrete confined by various shaped steel tubes. *Eng. Struct.* 23: 1331–1347.

Szmigiera, E. & Żółtowski, W. & Siennicki, M. 2010. Research on load capacity of concrete filled columns with battened steel sections. *J. of Civ. Eng. and Manag*. 16(3): 313–319.

Szmigiera, E. 2012. Two chord steel-concrete columns. *Printing house of Warsaw University of Technology*. Warsaw (in Polish).

Szmigiera, E & Szadkowska, M & Grzeszykowski, B. 2015. Design of two-chord steel-concrete columns. *Structural review*. 86(1): 40–45 (in Polish).

Yang, H. & Lam, D. & Gardner, L. 2008. Testing and analysis of concrete-filled elliptical hollow sections. *Eng. Struct.* 30: 3771–3781.

Yuan, X. & Xia, S. & Lam, L. & Smith, S.T. 2008. Analysis and behaviour of FRP-confined short concrete columns subjected to eccentric loading. *Journal of Zhejiang University SCIENCE* A 9(1): 38–49.

Żółtowski, W. & Szmigiera, E. & Siennicki, M. 2006. The influence of concrete filling steel columns with two battened chords on their behaviour. *8th Int. Conf. on Steel, Space & Composite Structures*, Kuala Lumpur: Malaysia: 417–423.

This page intentionally left blank

Recent Progress in Steel and Composite Structures – Giżejowski et al. (Eds)
© 2016 Taylor & Francis Group, London, ISBN 978-1-138-02946-0

AAEM method against Volterra integral analysis of composite beam

D. Partov & V. Kantchev
University of Structural Engineering and Architecture, "L. Karavelov", Sofia, Bulgaria

ABSTRACT: The paper presents analysis of the stress-strain behavior due to creep in statically determinate composite steel-concrete beam according to AAEM method of Bažant using the EC2, ACI209-R-92 and Gardner & Lockman provisions for creep of concrete. The analysis is based on the comparing of the results, obtained by numerical solution with Volterra integral equations derived for determining the redistribution of stresses in beam section between concrete plate and steel beam with respect to time "t". On the basis of the theory of the viscoelastic body of Arutyunian–Trost-Bažant it is analyzed the migration of stresses from concrete plate to steel beam using two independent Volterra integral equations of the second kind and two independent algebraic equation according the AAEM method. The comparison between the results obtained by the two methods is demonstrated with an example from the bridge practice.

1 INTRODUCTION

The time-varying behaviour of composite steel-concrete members under sustained service loads drawn the attention of engineers who were dealing with the problems of their design more than 60 years. The solution of structural problems involving creep and shrinkage phenomena in composite steel-concrete beams has been an important task for engineers since the first formulation of the mathematical model of linear viscoelasticity. In general, time-dependent deformation of concrete may severely affect the serviceability, durability and stability of structures (Chiorino).

2 ABOUT SOME METHODS FOR TIME DEPENDENT ANALYSIS WITH ACCENT OF AAEM METHOD

2.1 *Common consideration*

The first works, which give the answer to this problem are based on the Law of Glanville (1933) – Dischinger (1937, 1939) – *theory of aging,* or also called the *rate – of – creep methods*, which first formulated a time-dependent stress-strain differential relationship for concrete. Its refinement is known as the improved "Dischinger theory of aging" was proposed from Rüsch-Jungwirth-Hilsdorf (1973) or rate of flow method proposed from England and Illston (1965). In this theory the compliance function was simplified to a form that allows reducing structural creep problems to ordinary linear differential equations in transformed time, with constant coefficients, one first – order equation for each static or kinematic unknown. Another scientific works which give the answer to this problem used the theory of Maslov (1940) – Arutyunyan (1952) – Prokopovich-(1963) – Aleksandrovskii (1966). This researches used another simplification of $J(t,\tau)$, allowing to reduced the creep problems to ordinary linear first – order differential equations *with time dependent coefficients*. This equations which can be solved analytically in terms of *an incomplete gamma function*. This theory is obviously much more complicated than the "theory of aging", but the theory of aging, is substantially more complicated than the *Effective Modulus Method (EMM)*. This method connected with the name of McMilan (1916) transform the creep solution for time t from the problem of the "*viscoelasticity*" in elastic structural analysis based on the so called effective modulus: $E_{eff} = 1/J(t,\tau) = E(\tau)/1+\varphi(t,\tau)$. For the designers of the composite steel-concrete construction, is better to know that this method is exact only if the loads and stresses in a structure have a single-step history, *which means that they are constant from the moment of first loading*. *This fact is more far from true*, in internally statically indeterminate system with significant stress redistributions induced by creep or shrinkage, as in the case of composite steel-concrete construction. The same problems we met in the statically indeterminate system, where the changes in the structural system during the construction arise, or if the permanent loads are not applied at once. According Bažant & Najjar (1973) the degree of deviation from a single-step history of load and stress governs the error magnitude, which can be very large, especially for

long-time response of structural loaded at a young age. Further development of rheology as a fundamental science and its application to concrete as well as a great number of investigations in the field of creep of concrete have led to new formulations of the time-dependent behavior of concrete. These new formulations giving the relationship between $\sigma_c(t)$ and $\varepsilon_c(t)$ are formulated *by integral equations,* which present the basis of the theory of linear viscoelastic bodies. The integral-type creep law, i.e., the superposition equation for uniaxial prescribed stress history $\sigma(t)$, is expressed by:

$$\varepsilon_c(t,t_0) = \varepsilon^{sh}(t) + \sigma(t_0)J(t,t_0) + \int_{tl}^{t} \frac{d\sigma(\tau)}{d\tau} J(t,\tau)d\tau \quad (1)$$

Since the solutions of structural creep problems with realistic compliance function, such as in ACI209R-92, EC2 and G & L models for creep of concrete provisions cannot be performed analytically and require a deep knowledge in the higher level of mathematics theory(integral equations of Volterra, numerical solutions of such of type equations, using formulae of quadratures—such as: rectangle and trapezoidal rules, Simpson, Chebyshev, Gaus, Euler-Gregory – Macloren, simplified approximate methods have been favoured by designers.

2.2 *Formulation of AAEM*

However, *in order to avoid the mathematical problems* in solving of the integral equations of Volterra for treating the problem connected with the creep of concrete structures, it has been revised the integral relationship into new algebraic stress-strain relationship:

$$\varepsilon_{ct} = \frac{\sigma_{c0}}{E_{c0}}\left[1+\varphi_t\right] + \frac{\sigma_{ct}-\sigma_{c0}}{E_{c0}}\left[1+\rho\varphi_t\right] \quad (2)$$

where ρ is the relaxation coefficient known from Trost-Zerna works. When more extensive test date and data of long duration became available and were systematically analysed from Bažant, it turned out that the afore-mentioned theory leading to differential equations are overall not more accurate than the effective modulus methods (Partov and Kantchev), which leads to algebraic linear equations with respect to time *t*. According Bažant & Jirasek none of them is sufficiently accurate compared to the computer solutions for e realistic (un-simplified) compliance function based on long – time – measurements with a broad range of ages at loading. A remedy that is sufficiently accurate in most basic situations we can found in the age-adjusted effective modulus method, proposed and mathematically proven by Bažant, as a modification and refinement of the relaxation method, semi-empirically developed by Trost. The *Age-Adjusted Effective Modulus (AAEM) method* is formulated for a one-step loading history and is development from Bažant, which stating by brilliant way that the increment of strain over the interval (t_1,t) is equal to the increment of stress divided by the effective modulus plus the initial (elastic) strain multiplied by the creep coefficient, according the next formulae:

$$E''(t,t_1) = \frac{E(t_1) - R(t,t_1)}{\varphi(t,t_1)} \quad (2a)$$

By using algebraic approach a new simpler forms for (1) are obtained from Bažant. His methods are based on the hypothesis that the strain in the concrete fibers can be considered as a linear function of the creep coefficient. This permits transforming (1) in to

$$\varepsilon_c(t-t_1) = \varepsilon^{sh}(t) + \sigma_c(t_0)\left[\frac{1}{E_c(t_0)} + \frac{\varphi_{28}(t,t_0)}{E_{c28}}\right] + [\sigma_c(t) - \sigma_c(t_0)]\left[\frac{1}{E_c(t_0)} + \frac{\chi(t,t_0)\varphi_{28}(t,t_0)}{E_{c28}}\right]; \quad (3)$$

where is the aging coefficient; $\varphi(t,t_0)$ – the creep coefficient; $R(t,t_0)$ – relaxation function, i.e., the stress response to a constant unit strain applied at the time t_0; E_c – the elastic modulus of concrete at 28 days. To avoid a computer solution of the relaxation function $R(t,t_1)$ for a given compliance function

$$\chi(t,t_0) = \frac{E_c(t_0)}{E_c(t_0) - R(t,t_0)} - \frac{E_{c28}}{E_c(t_0)\varphi_{28}(t,t_0)} \quad (3a)$$

$J(t,t_1)$, one may use the following semi-empirical approximate formula with correct asymptotic properties (8).

$$R(t,t_1) = \frac{0,992}{J(t,t_1)} - \frac{0,115}{J(t,t-1)}\left[\frac{J(t-\Delta,t_1)}{J(t,t_1+\Delta)} - 1\right]; \Delta = \frac{t-t_1}{2} \quad (3b)$$

The Age-Adjusted Effective Method (AAEM) directly assumed the expression provided for the aging coefficient. In this case, it is necessary to evaluate previously the relaxation function $R(t,t_0)$. For the computation of the values of the χ aging coefficient at any desired time t and for any desired value of influencing parameters, on the base of prediction models CEB90, GL2000 and B3 a software tool is available at www.polito.it/

creepanalysis/(Chiorino). In the papers of Partov & Kantchev using the mathematical model in Fig. 1, the authors introduce the system of linear Volterra integral equation of second kind and obtain the results from their numerical solutions. The kernels of the integral equations contain the respective creep functions corresponding to the models: EC2, ACI209R-92 and G&L.

2.3 *Basic assumption and constitutive relationship*

The hypotheses in the elastic analysis of composite steel-concrete sections with stiff (rigid) shear connectors are assumed as following:

a. In the range of service ability loads concrete behaves in a way allowing to be treated as a linear viscoelastic body. On the basis of our assumptions for the purpose of structure analysis the total strain for concrete subjected to initial loading at time t_0 with a stress $\sigma(t_0)$ and subjected to subsequent stress variations $\Delta\sigma(t_i)$ at time t_i may be expressed with sufficient accuracy by the integral equations (1) by Bolztmann-Volterra:

$$\varepsilon_c(t) = \frac{\sigma_c(t_0)}{E_c(t_0)}[1+\phi(t-t_0)] + \int_{t_0}^{t} \frac{d\sigma_c(\tau)}{d\tau}\frac{1}{E_c(\tau)}[1+\phi(t-\tau)]d\tau; \tag{4}$$

where according EC2: the creep (compliance) function proposed by the 1990 CEB Model Code ("CEB-FIP" 1991) is given by the relationship:

$$J(t,t_0) = \frac{1}{E_c(t_0)} + \frac{\phi(t,t_0)}{E_c} \tag{4a}$$

where $\varphi(t,t_0)$ = the creep coefficient; and $E_c(t_0)$ and E_c = modulus of elasticity at the age of t_0 and 28 days, respectively.

The creep coefficient is evaluated with the following formula:

$$\varphi(t,t_0) = \varphi_{RH}\beta(f_{cm})\beta(t_0)\beta_c(t-t_0) \tag{4b}$$

where ϕ_{RH} – is a factor to allow for the effect of relative humidity on the notional creep coefficient. RH is the relative humidity of the ambient environment in %. $\beta(f_{cm})$ is a factor to allow for the effect of concrete strength on the notional creep coefficient. $\beta(t_0)$ - is a factor to allow for the effect of concrete age at loading on the notional creep coefficient (for continuous process we consider the function). $\beta(\tau)$ is a function of aging, depending on the age of concrete and it characterizes the process of aging. $\beta_c(t-t_0) = [(t-t_0)/(\beta_H + (t-t_0))]^{0.3}$ is a function to describe the development of creep with time after loading.

$$\beta_H = 150\left[1+(1.2RH/100)^{18}\right]h_0/100 + 250 \le 1{,}500$$

is a coefficient depending on the relative humidity (RH in %) and notional member size (h_0 in mm), where $f_{cm} = f_{ck} + 8 =$ the mean compressive strength of concrete at the age of 28 days (megapascals); and $h_0 = 2A_c/u =$ the notional size of member (millimeters) (A_c = the cross section; and u = the perimeter of member in contact with the atmosphere). Constant Young's modulus is given by $E_c = 10^4(f_{cm})^{1/3}$. Variable Young's modulus is given by: $E_c(t) = \beta_{cc}^{0.5}E_c$, where $E_c = 10^4(f_{cm})^{1/3}$ and $\beta_{cc} = \exp\left[s\left(1-5.3/t^{0.5}\right)\right]$, where $s = 0.25$ for normal and rapid hardening cements.

According ACI209R-92: the creep (compliance) function proposed by the ACI 209R-92 model, that presents the total stress-dependent strain by unit stress is given by the relationship:

$$J(t,t_0) = \frac{1}{E_{cmt0}} + \frac{\phi(t,t_0)}{E_{cmt0}} = \frac{1+\phi(t,t_0)}{E_{cmt0}} \tag{4c}$$

where $\phi(t,t_0)$ is the creep coefficient as the ratio of the creep strain to the elastic strain at the start of loading at the age t_0 (days) and E_{cmt0} is the modulus of elasticity at the time of loading t_0 (MPa), respectively. The creep model proposed by ACI 209R-92 has two components that determine the ultimate asymptotic value and the time development of creep. The predicted parameter is not creep strain, but creep coefficient $\phi(t,t_0)$, (defined as the ratio of the creep strain to the initial elastic strain). The creep coefficient is evaluated with the following formula: $\phi(t,t_0) = \phi_u\beta_c(t-t_0)$, where: $\phi(t,t_0)$ is the creep coefficient at the concrete age t due to a load applied at the age t_0; $(t-t_0)$ is the time since application of load; ϕ_u is the ultimate creep coefficient. For the standard conditions in the absence of specific creep date for local aggregates and conditions, the average value proposed for the ultimate creep coefficient ϕ_u is equal to 2,35. For conditions other than standard conditions the value of the ultimate creep coefficient $\phi_u = 2.35$ needs to be modified by six correction factors, depending on particular conditions. where: $\phi_u = 2.35\gamma_c$; and: $\gamma_c = \gamma_{c,t0}\gamma_{c,RH}\gamma_{c,vs}\gamma_{c,s}\gamma_{c,\psi}\gamma_{c,\alpha}$; $\gamma_{c,t0} = 1.25t_0^{-0.118}$ – corresponds to $\beta(t_0)$ in CEB MC90, is a function of aging, depending on the age of concrete and it characterizes the process of aging; $\gamma_{c,RH} = 1.27 - 0.67h$ for $h \ge 0.40$ is the ambient humidity factor, where the relative humidity h is in decimal -correspond to ϕ_{RH} CEB

MC90; $\gamma_{c,vs} = 0,667.\left(1 + 1.13e^{\{-0.0213(V/S)\}}\right)$ (corresponds to β_H in CEB MC90), where V is the specimen volume in mm^3 and S the specimen surface area in mm^2, allows to consider the size of member in terms of the volume-surface ratio; $\gamma_{c,s} = 0.82 + 0.00624s$ is slump factor, where $s = 75\,mm$ is the slump of fresh concrete; $\gamma_{c,\psi} = 0.88 + 0.0024\,\psi$ is fine aggregate factor, where $\psi = 40$ is the ratio of fine aggregate to total aggregate by weight expressed as percentage; $\gamma_{c,\alpha} = 0.46 + 0.09\alpha \geq 1$ is air content factor, where $\alpha = 2$ is the air content in percentage. $\beta_c(t - t_0) = (t - t_0)^{0.6} / [10 + (t - t_0)^{0.6}]$ – is a function to describe the development of creep with time after loading. The secant modulus of elasticity of concrete E_{cmt0} at any time t_0 of loading is given by $E_{mct0} = 0,043\rho_c^{1,5}\sqrt{f_{cmt0}}$ MPa; where ρ_c is the unit weight of concrete (kg/m^3) and f_{cmt0} is the mean concrete compressive strength at the time of loading (MPa). The general equation for predicting compressive strength at an time t is given by $f_{cm} = t/(a + bt)f_{cm28}$, where f_{cm28} is the concrete mean compressive strength of 28 days in MPa; a (in days) and b are constant and t is the age of the concrete.

The function $\beta_c(t - \tau)$ – (where t is the time interval during which the structure is under observation, τ is the running coordinate of time) – characterizes the process of creeping.

According to Gardner & Lockman: $\phi(t - \tau) = \Phi(t_c)\beta_c(t - \tau)$; is the so called the creep function. The function $\beta_c(t - \tau)$ – (where t is the time interval during which the structure is under observation, τ is the running coordinate of time) – characterizes the process of creeping. The creep (compliance) function proposed by the (Gardner and Lockman 2001), is composed of the elastic and creep strains.The elastic strain is reciprocal of the modulus of elasticity at the age of loading E_{cmto} and the creep strain is the 28 day creep coefficient $\phi_{28}(t,t_0)$ devided by the modulus of elasticity at 28 days E_{cm28}. The creep coefficient $\phi_{28}(t,t_0)$ is the ratio of the creep strain to the elastic strain due to the load applied at the age of 28 days. $J(t,t_0) = 1/E_{cmt0}(t_0) + \phi_{28}(t,t_0)/E_{cm28}$; where: – E_{cmt0} is the modulus of elasticity of concrete at the time of loading t_0; – E_{cm28} – is the mean modulus of elasticity concrete at 28 days (MPa); – $1/E_{cmt0}$ – represents the initial strain per unit stress at loading. $\phi(t,t_0)$ gives the ratio of the creep strain since the start of loading at the age t_0 to the elastic strain due to a constant stress applied at a concrete age of 28 days. The creep of concrete in the service stress range is characterized in currently G & L models in terms of the compliance function. Its use is made possible by the fact that the creep of concrete can be considered as approximately linear with regard to stress, following the principle of superposition. The design codes: EC2, ACI209R-92 and G&L model should specify the compliance function $J(t,\tau)$ rather than creep coefficient: where t. is the current age of concrete, τ is the age of loading. The so called function of aging $\beta(t_0) = \sqrt{7/t_0}$, which characterized the process of the aging is included in the second term of function of creeping $\beta_c(t - \tau)$. $\Phi(t_c)$ is the correction term for the effect of drying before loading. If $t_o = t_c; \Phi(t_c) = 1$; when: $t_0 > t_c$.

$$\Phi(t_c) = \left[1 - \left(\frac{(t_0 - t_c)}{(t_0 - t_c) + 0,12(V/S)^2}\right)^{0,5}\right]^{0,5} \qquad (4d)$$

where: t_o = age of concrete at loading, (days), t_c = age of concrete when drying starts at the end of moist curing, (days). To calculate relaxation, $\Phi(t_c)$ remains constant at the initial value throughout the relaxation period. For creep recovery calculation, $\Phi(t_c)$ remains constant at the value at the age of loading.The constitutive law, represents the stress-strain-time relationship for the concrete slab according(Gardner & Lockman 2000) model is:

$$\varepsilon_c(t) = \frac{\sigma_c(t_0)}{E_c(t_0)}[1 + \Phi(t_c)\beta_c(t - t_0)] + \int_{t_0}^{t} \frac{d\sigma_c(\tau)}{d\tau}\frac{1}{E_c(\tau)}[1 + \Phi(t_c)\beta_c(t - \tau)]d\tau; \qquad (5)$$

$$\beta_c(t - \tau) = 2\frac{(t - \tau)^{0,3}}{(t - \tau)^{0,3} + 14} + \left(\frac{7}{\tau}\right)^{0,5}\left(\frac{(t - \tau)}{(t - \tau) + 14}\right)^{0,5} + 2,5(1 - 1,086h^2)\left(\frac{(t - \tau)}{(t - \tau) + 0,12(V/S)^2}\right)^{0,5} \qquad (5a)$$

where the secant modulus of elasticity of concrete E_{cmt0} is invariant in time t i.e.,but at any time t_0 of loading is given by $E_{cmt} = 3500 + 4300\sqrt{f_{cmt}}$; where the strength development with time can be calculate from the compressive strength using the equation: $f_{cmt} = \beta_e^2 \cdot f_{cm28}$: where $\beta_e = \exp(s(1 - \sqrt{28/t})/2)$ and s = 0,4 is CEB (1993) style strength –development parameter, and β_e relates strength development to cement type. Relationship between specified and mean compressive strength of concrete can be estimated from the equation: $f_{cm28} = 1,1f_c^{/} + 5,0$.

3 BASIC EQUATION OF EQUILIBRIUM

Let us denote both the normal forces and the bending moments in the cross-section of the plate and the girder after the loading in the time t = 0 with

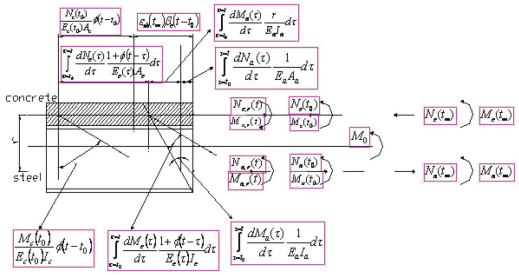

Figure 1. Mechanical-mathematical model.

$N_{c,0}$, $M_{c,0}$, $N_{a,0}$, $M_{a,0}$ and with $N_{c,r}(t)$, $M_{c,r}(t)$, $N_{a,r}(t)$, $M_{a,r}(t)$ a new group of normal forces and bending moments, arising due to creep and shrinkage of concrete. For a composite bridge girder with $J_c = A_c\left(nI_c\right)n/A_sI_s \le 0.2$ according to the suggestion of (Sonntag 1951) we can write the equilibrium conditions in time t as follows:

$$\begin{aligned} &N(t)=0; \quad N_{c,r}(t)=N_{a,r}(t);\\ &\sum M(t)=0; \quad M_{c,r}(t)+N_{c,r}(t)r=M_{a,r}(t). \end{aligned} \tag{5b}$$

Due to the fact that the problem is a twice internally statically indeterminate system, the equilibrium equations are not sufficient to solve it. It is necessary to produce two additional equations in the sense of compatibility of deformations of both steel girder and concrete slab in time t (Fig. 1).

4 DERIVING OF GENERALISED MECHANIC-MATHEMATICAL MODEL USING INTEGRAL EQUATION OF VOLTERRA

4.1 *According EC2*

Using the equation of equilibrium, the geometrical compatibility and constitutive relationship, i.e. an elastic law for the steel part and an integral-type creep law of Boltzmann—Volterra for the concrete part, for assessment of normal forces $N_{c,r}(t)$ and bending moment $M_{c,r}(t)$ used in the analysis of the migration of stresses from concrete plate to steel beam, two independent Volterra integral equations (6 and 7) of the second kind are derived.

$$\begin{aligned} N_{c,r}(t) &= \lambda_N \int_{t_0}^{t} N_{c,r}(\tau)\frac{d}{d\tau}\\ &[1+\varphi\phi_{RH}\beta(f_{cm})\beta(\tau)\beta(t-\tau)]d\tau\\ &+\lambda_N N_{c,0}\varphi\phi_{RH}\beta(f_{cm})\beta(t_0)\beta(t-t_0)\\ &+\lambda_N N_{sh}\beta_c(t-t_0) \end{aligned} \tag{6}$$

$$\begin{aligned} M_{c,r}(t) &= \lambda_M \int_{t_0}^{t} M_{c,r}(\tau)\frac{d}{d\tau}\\ &[1+\varphi\phi_{RH}\beta(f_{cm})\beta(\tau)\beta(t-\tau)]d\tau\\ &+\lambda_M M_{c,0}\varphi\phi_{RH}\beta(f_{cm})\beta(t_0)\beta(t-t_0)\\ &-\lambda_M N_{c,r}\frac{E_cI_c}{E_aI_a}r \end{aligned} \tag{7}$$

where

$$\lambda_M = [1+E_cI_c/(E_aI_a)]^{-1}$$

$$\lambda_N = [1+E_cA_c/(E_aA_a)(1+A_ar^2/I_a)]^{-1}.$$

4.2 *According ACI209-R2*

Using the above mentioned approach, for constant elasticity module of concrete for assessment of normal forces $N_{c,r}(t)$ and bending moment $M_{c,r}(t)$ two linear integral Volterra equations of the second kind are derived.

$$\begin{aligned} N_{c,r}(t) &= \lambda_N \int_{t_0}^{t} N_{c,r}(\tau)\frac{d}{d\tau}\\ &[1+2{,}35\gamma_{c5}\beta(\tau)\beta_c(t-\tau)]d\tau\\ &+\lambda_N N_{c,0}2{,}35\gamma_{c5}\beta(t_0)\beta_c(t-t_0)\\ &+\lambda_N N_{sh}\beta_c(t-t_0) \end{aligned} \tag{8}$$

$$\begin{aligned} M_{c,r}(t) &= \lambda_M \int_{t_0}^{t} M_{c,r}(\tau)\frac{d}{d\tau}\\ &[1+2{,}35\gamma_{c5}\beta(\tau)\beta_c(t-\tau)]d\tau\\ &+\lambda_M M_{c,0}2{,}35\gamma_{c5}\beta(t_0)\beta_c(t-t_0)\\ &-\lambda_M N_{c,r}\frac{E_cI_c}{E_aI_a}r \end{aligned} \tag{9}$$

4.3 *According G & L model:*

Using the above mentioned approach for constant

$$\begin{aligned} N_{c,r}(t) &= \lambda_N \int_{t_0}^{t} N_{c,r}(\tau)\frac{d}{d\tau}[1+\Phi(t_c)\beta_c(t-\tau)]d\tau\\ &+\lambda_N N_{c,0}\Phi(t_c)\beta_c(t-t_0)+\lambda_N N_{sh}\beta_c(t-t_0) \end{aligned} \tag{10}$$

$$\begin{aligned} M_{c,r}(t) &= \lambda_M \int_{t_0}^{t} M_{c,r}(\tau)\frac{d}{d\tau}[1+\Phi(t_c)\beta_c(t-\tau)]d\tau\\ &+\lambda_M M_{c,0}\Phi(t_c)\beta_c(t-t_0)-\lambda_M N_{c,r}\frac{E_cI_c}{E_aI_a}r \end{aligned} \tag{11}$$

elasticity module of concrete for assessment of normal forces $N_{c,r}(t)$ and bending moment

$M_{c,r}(t)$ two linear integral Volterra equations of the second kind are derived.

5 DERIVING OF THE GENERALIZED MECHANIC-MATHEMATICAL MODEL USING ALGEBRIC EQUATIONS ACCORDING AAEM METHOD OF BAŽANT

Using the above mentioned approach, for constant elasticity module of concrete for assessment of normal forces $N_c(t)$ and bending moment $M_c(t)$ two algebraic expressions (12), (13) are derived:

6 NUMERICAL EXAMPLE

6.1 *The following parameters are chosen according EC2 model*

$$N_{c,r}(t) = \frac{N_c(t_0)\varphi(t,t_0)}{\lambda_N^{-1} + \chi(t,\tau)\varphi(t,\tau)} = \frac{N_c(t_0)\varphi(t,t_0)\lambda_N}{1 + \chi(t,\tau)\varphi(t,\tau)\lambda_N} \quad (12)$$

$$M_{c,r}(t) = \frac{M_c(t_0)\varphi(t,t_0)}{\lambda_M^{-1} + \chi(t,\tau)\varphi(t,\tau)} - \frac{N_c(t)r}{\lambda_M^{-1} + \chi(t,\tau)\varphi(t,\tau)} \frac{E_c J_c}{E_a J_a} \quad (13)$$

The two methods presented in the previous paragraph is now applied to a simply supported beam, subjected to a uniform load, whose cross section is shown in Figure 2.

$E_c = 3{,}2.10^4\ MPa, E_a = 2{,}1.10^5\ MPa, A_a = 383.25\,cm^2$
$n = E_a / E_c = 6{,}56$, $I_a = 661500\ cm^4$,
$r_c = 23{,}039\ cm$, $r_a = 80{,}829\ cm$, $r = 103{,}868\ cm$
$A_i = 2453{,}05\ \ cm^2$, $I_i = 4536360{,}758\ cm^4$,
$N_{c,0} = 846{,}60\ kN$, $M_{c,0} = 27{,}56\ kNm$,
$M_{a,0} = 330{,}13\ kNm, M_0 = 1237\ kNm$

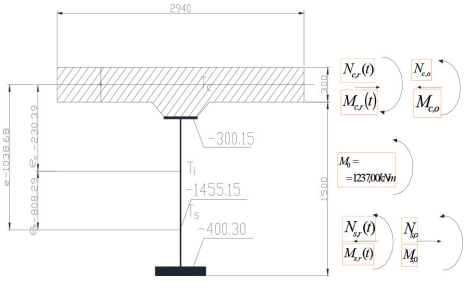

Figure 2. Composite beam.

$A_c = 8820\ cm^2, I_a = 1217963{,}7\ cm^4$
$\lambda_N = 0{,}060545358$, $\lambda_M = 0{,}922950026$

6.2 *According ACE 209R-92 model*

$E_c = 2{,}8178.10^4\ MPa, E_a = 2{,}1.10^5\ MPa, A_c = 8820\,cm^2$
$n = E_a / E_c = 7{,}452$, $I_c = 661500\ cm^4$,
$r_c = 25{,}407\ cm$, $r_a = 78{,}463\ cm$, $r = 103{,}868\ cm$
$A_i = 1566{,}8248\ \ cm^2$, $I_i = 4420140{,}76\ cm^4$,
$N_{c,0} = 837{,}286\ kN$, $M_{c,0} = 24{,}716\ kNm$,
$I_a = 1217963{,}7\ cm^4, M_{a,0} = 338{,}05\ kNm$,
$A_a = 383{,}25\ cm^2, \lambda_N = 0{,}068220902$, $\lambda_M = 0{,}93155$
$M_0 = 1237\ kNm$

6.3 *According Gardner & Lockman model*

$E_c = 2{,}8014.10^4\ MPa$, $E_a = 2{,}1.10^5\ MPa$, $A_c = 8820\,cm^2$
$n = E_a / E_c = 7{,}496$, $I_c = 661500\ cm^4$,
$r_c = 25{,}50\ cm$, $r_a = 78{,}37\ cm$, $r = 103{,}868\ cm$
$A_i = 1560{,}82\ \ cm^2$, $I_i = 4415813{,}859\ cm^4$,
$N_{c,0} = 840{,}5\ kN$, $M_{c,0} = 24{,}72\ kNm$,
$M_{a,0} = 338{,}38\ kNm, I_a = 1217963{,}7\ cm^4$
$A_a = 383{,}25\ cm^2$ $\lambda_N = 0{,}068593645$, $\lambda_M = 0{,}93192$
$M_0 = 1237\ kNm$

7 NUMERICAL SOLUTION USING INTEGRAL EQUATION OF VOLTERRA

In Figures 3–4 it is shown the values of normal forces and bending moments in time *t*. A numerical method for time-dependent analysis of composite steel-concrete sections according EC2, ACI 209R-92 and G & L models is develop using MATLAB code and numerical algorithm which was successfully applied to a simple supported beam. The length of time step of the proposed numerical

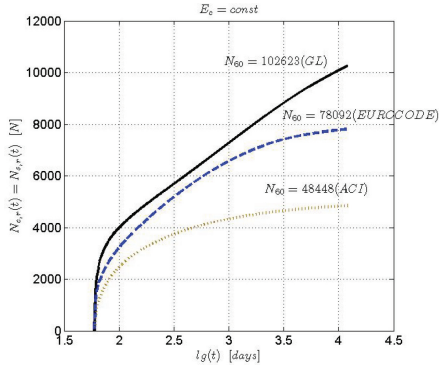

Figure 3. Normal forces $N_{c,r}(t) = N_{a,r}(t)$ in time t = 12060 days.

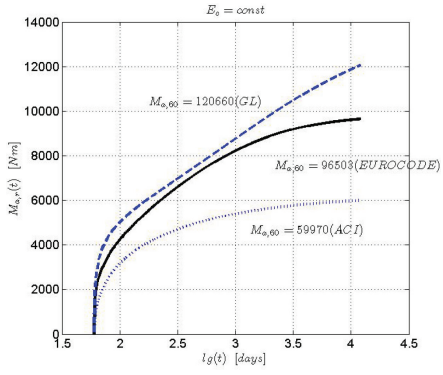

Figure 4. Bending moments $M_{a,r}(t)$ in time t = 12060 days.

algorithm is chosen equal one day. So we conclude that good results can be achieved from practical point of view with one day step. For our purpose we consider a period of about 33–35 years.

8 PREDICTION OF CONCRETE CREEP ACCORDING AAEM

8.1 *Acording to the EC2 provisions*

Let's consider the next following initial data: $t_0 = 60$ days; $t_\infty = 12060$ days; $E_c(t_0) = 32000 MPa$; The creep coefficient:

8.1.1. $\phi(t = 12060, t_0 = 60) = 1,645095488$;
8.1.1.1. $J(t = 12060, t_0 = 60) = 0,0000826059$;
8.1.2. $\varphi(t = 12060, t-1 = 12059) = 0,079087302$;
8.1.2.1. $J(t = 12060, t-1 = 12059) = 0,000033721$;
8.1.3. $\Delta = (t - t_1)/2 = 6000$;
8.1.3.1. $\varphi(t-\Delta, t_1) = \varphi(12060 - 6000, 60) = 1,611666145$;
8.1.3.2. $J(t-\Delta, t_1) = 0,000081614$;
8.1.4. $\phi(t, t_1 + \Delta) = \varphi(t = 12060, t_1 = 6060) = 0,657063792$;
8.1.4.1. $J(t, t_1 + \Delta) = 0,000051783$;
8.1.4.2. Relaxation function: $R(t, t_0) = 10036,495$;
8.1.5. The aging coefficient: $\chi(t, t_0) = 0,84909$;

$$N_c(t) = N_c(t,t_0)\cdot\varphi(t,t_0)\cdot\lambda_N/1 + \chi(t,t_0)\cdot\varphi(t,t_0)\lambda_N = 7774,752314 daN$$

Then:
8.1.6. Calculating: $M_c(t) = 1558,479859$ *daNm.*
8.1.7. Calculating:
$M_a(t) = M_c(t) + N_c(t).r = 9634,112684$ *daNm.*

Comparisons between the results obtained from the numerical solution and AAEM methods are as follows:

$N_c(t)$ = 7774,752 daN (by AAEM) and $N_c(t)$ = 7809,20 daN (by NM); (Δ = 0,44%). $M_c(t)$ = 1558,479 daNm (by AAEM) and $M_c(t)$ = 1538,90 daNm(by NM); (Δ = 1,28%). $M_a(t)$ = 9634,112 daNm (by AAEM) and $M_a(t)$ = 9650,33 daNm (by NM). (Δ = 0,168%).

8.2 *According to the ACI209-R2 provisions*

Let's consider the next following initial data: $t_0 = 60$ days; $t_\infty = 12060$ days; $E_{cm}(t_0) = 28178 MPa$;

8.2.1. The creep coefficient: φ (t = *12060,* $t_0 = 60$) = 0,8899393
8.2.1.1. $J(t = 12060, t_0 = 60) = 0,000067071$;
8.2.2. $\varphi(t = 12060, t-1 = 12059) = 0,04481134$;
8.2.2.1. $J(t = 12060, t-1 = 12059) = 0,000037078$;
8.2.3. $\Delta = (t - t_1)/2 = 6000$;
8.2.3.1. $\varphi(t - \Delta = 6060, t_1 = 60) = 0,874412984$;
8.2.3.2. $J(t-\Delta, t_1) = 0,00006652$;
8.2.4. $\phi(t, t_1 + \Delta) = \varphi(t = 12060, t_1 = 6060) = 0,507232037$;
8.2.4.1. $J(t, t_1 + \Delta) = 0,000053489$;
8.2.4.2. Relaxation function: $R(t, t_0)$ = 14034, 08002;
8.2.5. The aging coefficient: $\chi(t, t_0) = 0,868561999$;
8.2.6. Then:

$$N_c(t) = (N_c(t,t_0).\varphi(t,t_0).\lambda_N) /(1 + \chi(t,t_0).\varphi(t,t_0\lambda_N) = 4828,6772\ daN$$

8.2.7. Calculating: $M_c(t) = 991,6784227$ *daNm*
8.2.8. Calculating: $M_a(t) = M_c(t) + N_c(t).r$ = 6007, 225199 *daNm.*

Comparisons between the results obtained from the numerical solution and AAEM methods are as follows:

$N_c(t)$ = 4828,677 daN (by AAEM) and $N_c(t)$ = 4844,80 daN (by NM); (Δ = 0,332%). $M_c(t)$ = 991,6784 daNm (by AAEM) and $M_c(t)$ = 964,70 daNm (by NM); (Δ = 2,72%). $M_a(t)$ = 6007,225 daNm (by AAEM) and $M_a(t)$ = 5997,00 daNm (by NM); (Δ = 0,166%).

8.3 *According to the G & L provisions*

Let's consider the next following initial data: $t_0 = 60$ days; $t_\infty = 12060$ days; $E_{cmt_0} = 28014 MPa$; where" $t_c = 30$ days, keeping the moisture of the concrete plate.

8.3.1. In our case t_0= 60, we put the sustained load 60 days after concreting.
8.3.2. Then the creep coefficient: $\phi(t_c) = 0,946135$
8.3.3. So the correcting coefficient $\phi(t, t_0)$ is- $\phi(t_c) = 0,946135041$;
8.3.4. The creep coefficient is:
$\phi(t, t_0) = \phi(t = 12060, t_0 = 60) = 2,119418548$.
8.3.5. This value is corrected by $\phi(t_c)$ = 0,946135041. 2,119418548 = 2,005256155;
8.3.6. $J(t, t_0)$ = 0,000107296; $\phi(t$ = 12060, t − 1 = 12059) = 0,04856828647;
8.3.7. $\phi(t_c) = 0,310298413; J(t, t-1)$ $= 0,00003743; \Delta = (t - t_1)/2 = 6000$;

8.3.8. $\phi(t-\Delta=6060,t_1=60)=1{,}85433411$;
$\phi(t_c)=0{,}946135041; J(t-\Delta,t_1)=0{,}0001018$;

8.3.9. $\phi(t=12060,t_1+\Delta=6060)=1{,}652505503$;
$\phi(t_c)=0{,}410978521$;

8.3.10. $J(t,t_1+\Delta)=0{,}000059939$;

8.3.11. Relaxation function: $R(t,t_0)=7095{,}144763$;

8.3.12. The aging coefficient:
$\chi(t,t_0)=0{,}840485213$;

8.3.13. Then:
$N_c(t)=N_c(t,t_0).\varphi(t,t_0).\lambda_N/1$
$+\chi(t,t_0).\varphi(t,t_0)\lambda_N=10607{,}34246\ daN$

8.3.14. Calculating: $M_c(t)=1505{,}96\ daNm$.

8.3.15. Calculating $M_a(t)$ using the formulae:
$M_a(t)=M_c(t)+N_c(t).r=12523{,}80$ daNm.

Comparisons between the results obtained from the numerical solution and AAEM methods are as follows:

$N_c(t)$ = 10607,34246 daN (by AAEM) and $N_c(t)$ = 10262,00 daN (by NM); (Δ = 3,25%). $M_c(t)$ = 1505,96 daNm (by AAEM) and $M_c(t)=1406{,}10$ daNm (by NM); (Δ = 6,63%). $M_a(t)$ = 12523,80 daNm (by AAEM) and $M_a(t)$ = 12066 daNm (by NM); (Δ = 3,65%).

9 CONCLUSIONS

The age-adjusted effective modulus method must to know that is development to be theoretically exact for any creep function deriving in EC2, ACI209R-92 and G & L model. The results obtained by the AAEM method of Bažant are completely comparable with the results based on numerical method, according to the EC2, ACI209R-92 and G&L model provision.

REFERENCES

ACI 209.2R-08. *Guide for Modeling and Calculation of Shrinkage and Creep in Hardened Concrete*. American Concrete Institute, ACI 209.2R-08, ACI, (2008), 48 pp.

Alexandrovskii S.V. 1966. *Analysis of Plain and Reinforced Concrete Structures for Temperature and Moisture Effects (with Account of Creep)*. (in Russian), Stroyizdat, Moscow, (1966), pp. 443.

Arutyunian N. Kh., *Some Problems in the Theory of Creep* (in Russian), Techteroizdat, Moscow, (1952) (French transl., Eyrolles 1957, English transl., Pergamon Press 1966), pp. 319.

Bažant Ž.P., Editor, *Mathematical Modeling of Creep and Shrinkage of Concrete*, John Wiley & Sons, (1988), pp. 459.

Chiorino, M.A., & Carreira, D.J., Factors affecting creep and shrinkage of hardened concrete and guide for modelling, "A state-of-the-art- report on international recommendations and scientific debate", *The Indian Concrete Journal.* December 2012, pp. 11–24.

Chiorino M.A. 2014. Analysis of structural effects of time-dependent behaviour of concrete: an internationally harmonized format, in Proceedings of III All-Russia Int. Conf. "Concrete and Reinforced Concrete - Glance at Future", Moscow, 12–14 May 2014, Russian, pp. 324–337; English, pp. 338–350.:"*Promyshlennoe I grazhdanskoe stroitel'stvo*" (*Industrial and Civil Engineering*) Journal, Moscow, December 2014, pp. 12–20, ISSN0869–7019, УДК (083.75)(100)691.32:539.376.

Dischinger F., Untersuchungen über die Knicksichereit, die Elastische Verformung und das Kriechen des Betons bei Bogenbrücken, *Der Bauingenieur*, Vol.18, (1937), pp. 487–520, 539–52, 595–621.

Dischinger F., Elastische und Plastische Verformungen der Eisenbetontragwerke und Insbesondere der Bogenbrücken, *Der Bauingenieur*, Vol.20, (1939), pp. 53–63, 286–94, 426–37, 563–72.

Jirasek M. & Bažant Z.P. 2002. *Inelastic Analysis of Structures*, J.Wiley & Sons, 734 pp.

Maslov G.N., Thermal Stress States in Concrete Masses, with Account of Concrete Creep (in Russian), *Izvestia* NIIG, 28, (1941), pp.175–188.

Partov, D. & Kantchev, V., "Time-dependent analysis of composite steel-concrete beams using integral equation of volterra, according EUROCODE-4", *Engineering MECHANICS, Vol. 16, 2009, No 5, pp 367–392.*

Partov, D., Kantchev, V., "Level of creep sensitivity in composite s steel-concrete beams, according to ACI 209R-92 model, comparison with EUROCODE-4-(CEB MC90–99)", *Engineering MECHANICS, Vol. 18, 2011, No 2, pp. 91–116.*

Partov, D. & Kantchev V., "Gardner and Lockman model (2000) in Creep analysis of composite steel-concrete section", *ACI Structural Journal*, Vol.111, No. 1(January-February), 2014, pp. 59–69.

Prokopovich I. E. *Fundamental study on application of linear theory of creep*, (In Russian),Vyssha shkola, Kiev, (1978), 143 pp.

Trost, H. (1967), Auswirkungen des Superpositionsprinzips auf Kriech- und Relaxationsprobleme bei Beton und Spannbeton, *Beton-und Stahlbetonbau*, Vol. 62, (1967), No. 10, pp. 230–238; No. 11, pp. 261–269.

Rüsch H. & Jungwirth, D. 1976. *Berücksichtigung der Einflüsse von Kriechen und Schwinden des Betons auf das Verhalten der Tragwerke*, Werner Verlag. Düsseldorf.

Šmerda, Z. & Křistek, V. Creep and Shrinkage of Concrete Elements and Structures, *Elsevier, Amsterdam-Oxford- New York – Tokyo (1988), pp. 296.*

Zerna W. & Trost H.: Rheologische Beschreibung des Werkstoffes Beton, *Beton und Stahlbetonbau*, Vol. 62, H.7, (1967), pp. 165–170.

Recent Progress in Steel and Composite Structures – Giżejowski et al. (Eds)
© 2016 Taylor & Francis Group, London, ISBN 978-1-138-02946-0

Tests of shear connectors used in aluminium-concrete composite structures

Ł. Polus & M. Szumigała
Faculty of Civil and Environmental Engineering, Poznan University of Technology, Poznań, Poland

ABSTRACT: This paper presents the results obtained from laboratory tests of shear connectors used in aluminium-concrete composite structures. Aluminium-concrete structure are a kind of composite structures. The tests were conducted using the standard testing procedure from EN 1994-1-1 modified by the authors of the present article. Three models were tested. Each of them consisted of: two concrete slabs, two steel sheets, eight shear connectors, two reinforcing meshes and an aluminium beam. The connectors were not sheared during tests.

1 INTRODUCTION

Aluminium-concrete structures are a less known kind of composite structures. Szumigała & Polus (2015) recognized them as part of sustainable construction which may be used for building composite bridges, structures situated in inaccessible places and in corrosive or humid environments. An aluminium and concrete beam is presented in Figure 1.

Bruzzese et al. (1989) pointed out that research on aluminium-concrete composite structures did not go beyond the initial stage, although some of them had been applied in bridges. Mazzolani (2003) and Gwóźdź (2007) presented unquestionable advantages which aluminium offers to designers (high resistance to corrosion, lightness, ease of producing any shape). Aluminium has a favourable life-cycle cost and its price has gradually decreased over the years compared to the price of steel. Polus & Szumigała (2014) mentioned that aluminium and concrete structures need a connector which would efficiently join both materials. The authors of this article prepared a steel shear connector which may be used in composite structures where steel sheeting is used as the shuttering of a concrete slab.

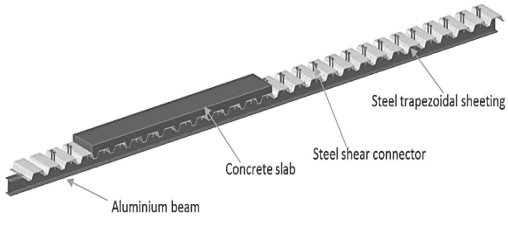

Figure 1. Aluminium and concrete beam.

2 SHEAR CONNECTORS

A steel shear connector consists of the head, shank, flange, thread and nuts (see Fig. 2).

The head facilitates cooperation between the connectors and the concrete. The head, the shank and the flange are embedded in the concrete slab. The flange presses against the steel sheeting, thanks to which the longitudinal slip between the concrete and the steel beam is limited. A prototype of the connector is presented in Figure 3.

The connectors were made of S235 J2 steel. KÖCO SD headed studs, which are easy to obtain, were modified. The modifications included screw cutting and welding the nut to the shank. The nut was meant to serve as a flange.

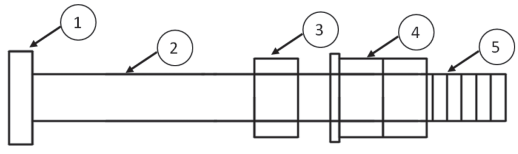

Figure 2. Shear connector: 1–head, 2–shank, 3–flange, 4–nut, 5–thread.

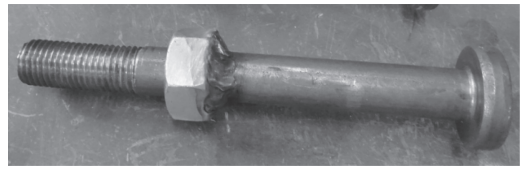

Figure 3. A prototype of the connector.

Table 1. The parameters which were necessary to calculate the design resistance of the shear connector in accordance with EN 1994-1-1.

Parameters	Symbol	Value
Overall height of the stud	h_{sc}	99 mm
Shear connector diameter	d	16 mm
Coefficient	α	1.0
Ultimate tensile strength of the shear connector material	f_u	360 MPa
Characteristic compressive strength of the concrete	f_{ck}	30 MPa
Secant modulus of concrete elasticity	E_{cm}	32 GPa
Partial factor for design shear resistance	γ_v	1.25
Overall depth of the profiled steel sheeting	h_p	55 mm
Width of haunch	b_o	71 mm
Number of connectors in one rib	n_r	2
Reduction factor	k_t	0.51
Design value of the shear resistance of a single connector used with profiled steel sheeting	P_{Rdt}	23.7 kN

3 DESIGN RESISTANCE OF SHEAR CONNECTORS ACCORDING TO EN 1994-1-1

The European Committee for Standardization (2004) prepared a standard which allows to calculate the design resistance of the headed studs used with profiled steel sheeting in buildings. Table 1 presents the parameters which were necessary to calculate the design resistance of the shear connector in accordance with the standard.

The design value of the shear resistance of a single connector used with profiled steel sheeting amounted to 23.7 kN.

4 EXPERIMENTAL INVESTIGATION AND COMPARISON WITH THE STANDARD

4.1 *Models*

The tests were carried out on three models having the same geometric configuration shown in Figure 4. An experimental model consisted of: two concrete slabs made of C30/37 concrete, two steel sheets made of 0.7 mm-thick S320GD steel, eight shear connectors mentioned above, two reinforcing meshes made of 6 mm S235 JRG2 steel round bars and an aluminium beam made of AW-6060 T6 alloy. The concrete slabs were simultaneously casted in the vertical position. The concrete was then cured for 28 days. The tests were performed 70 days after the casting.

4.2 *Test conditions*

The tests were performed using the Instron 8500 Plus test machine. The model was put on a 12 mm-thick OSB board placed on the machine base (Figure 5).

The load was applied cyclically 25 times between 30 kN and 70 kN and subsequently failure load was applied. The longitudinal slip between the concrete slabs and the aluminium beam was measured continuously during loading. Measurements were also performed when the load decreased. The piston velocity was 0.5 mm/min. The location of sensors is presented in Figure 6.

4.3 *Results*

The vertical displacement of the aluminium beam for every model is presented in Figure 7. It is the arithmetic mean of the displacement measured by two sensors. This line chart does not present the stage when the cyclical load was applied.

The failure load was: 180.3 kN for the first model, 196.1 kN for the second model, and 165.8 kN for the last model. The mean value of the maximum load was 180.7 kN. The deviation of any individual test result from the mean value obtained from all three tests did not exceed 10%. Table 2 presents the design resistance of the shear connector determined according to EN 1994–1-1 (2004).

In the tests, the design resistance of a single connector used with profiled steel sheeting was 14.9 kN and it was lower than the resistance calculated based on the standard (23.7 kN). The low design resistance resulted from the form of failure

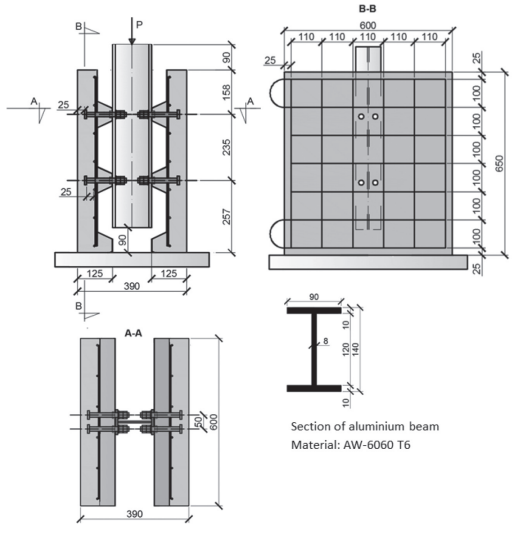

Figure 4. Constructional details of experimental models.

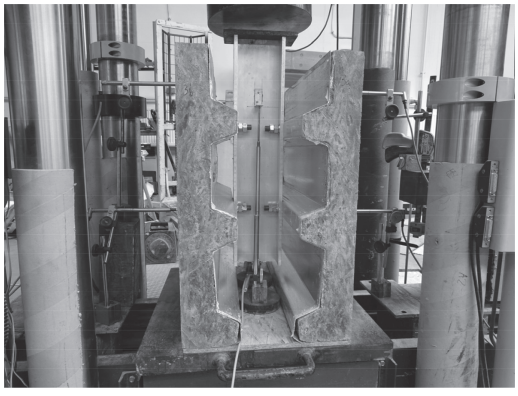

Figure 5. Model placed on the machine base.

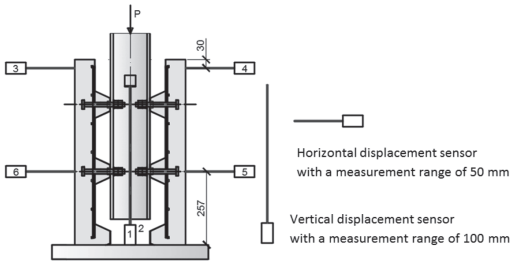

Figure 6. Displacement sensors.

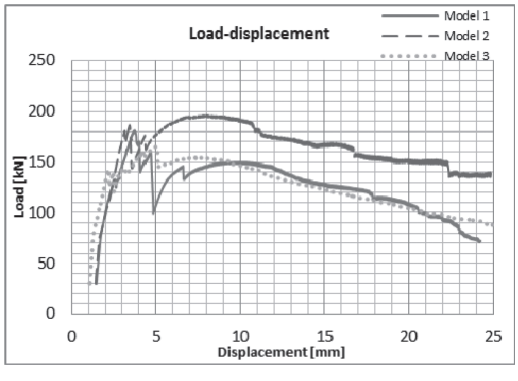

Figure 7. Vertical displacements of the aluminium beam.

of the models. In each model there were cracks in the concrete slabs (Figures 8, 9, 10). Firstly, cracks in the concrete slabs were caused by tension. The concrete slabs bent towards the aluminium beam. The horizontal displacement measured by sensor 3 is presented in Figure 11. The edge of the concrete slab was subjected to tension. The concrete slabs should have been thicker and both slabs should have had two reinforcing meshes. Each crack caused the decrease of load, which was presented as peaks on the line charts in Figure 7. Secondly, cracks in the concrete haunches were caused by shearing. The width of the haunches was small and in model 1 and 3 the haunches were sheared. The connectors were bent, but they were not sheared (Figure 12).

The slip capacity of each specimen was taken as the maximum slip measured at the characteristic load level. The characteristic slip capacity should be taken as the minimum test value of the slip capacity reduced by 10%. The slip capacity for the specimens was: 4.8 mm (model 1), 11.8 mm (model), and 9.5 mm (model 3). The characteristic slip capacity

Table 2. The design resistance of the shear connector according to EN 1994-1-1.

Data	Symbol	Value
Minimum failure load	P	165.8 kN
Number of connectors in one model	n	8
Characteristic resistance of the shear connector	P_{Rk}	18.6 kN
Partial factor for design shear resistance	γ_v	1.25
Design resistance of the shear connector	P_{Rd}	14.9 kN

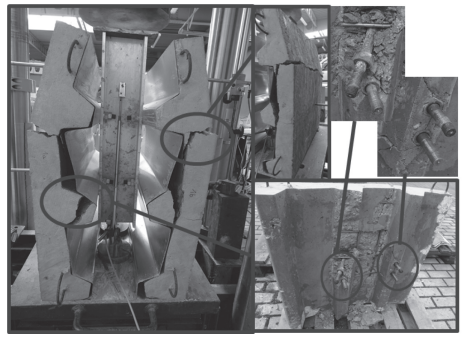

Figure 8. Failure of model 1.

Figure 9. Failure of model 2.

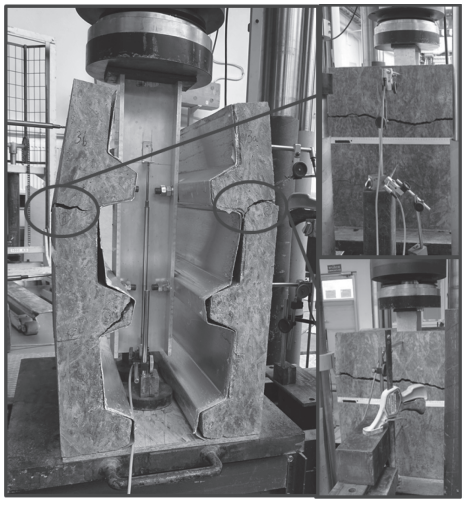

Figure 10. Failure of model 3.

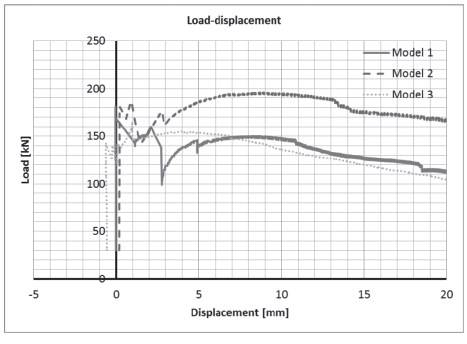

Figure 11. Horizontal displacement measured by sensor 3.

was 4.3 mm. According to EN 1994-1-1 (2004), the tested connector cannot be regarded as ductile because the characteristic slip capacity was less than 6 mm, but this small value of the slip capacity for the first model is connected with the cracks which appeared during the test conducted on model 1. According to the relationship presented in Figure 7, the connector may be regarded as ductile.

5 CONCLUSIONS

The results obtained in the tests prove that an aluminium beam can cooperate and be joined with a concrete slab thanks to the new connectors. However, the resistance of the shear connectors obtained from the tests is lower than the one calculated based on the standard, because connectors were not sheared and failures of models were connected with the cracks in the concrete subjected to tension. The concrete slabs should have been thicker and both slabs should have had two reinforcing meshes. Failures were also connected with the shearing of the haunches. For this reason, it is advisable to use the reduction factor to calculate the design value of the shear resistance of a single connector used with profiled steel sheeting, as it is presented in the standard. The conducted tests may be used to validate numerical calculations. The tests should be repeated with improved concrete slabs.

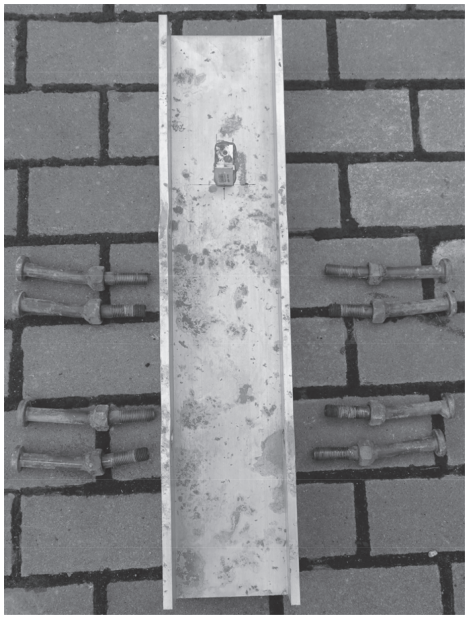

Figure 12. Bent connectors.

REFERENCES

Bruzzese, E. et al. 1989. Experimental investigation on aluminium-concrete beams. *Construzioni Metalliche* 5: 265–282.

European Committee for Standardization 2004. *EN 1994-1-1, Eurocode 4, Design of composite steel and concrete structures—Part 1-1: General rules and rules for buildings*. Brussels.

Gwóźdź, M. 2007. Project problems of contemporary aluminium structures. *Technical Transactions* Z4-A: 281–286.

Mazzolani, F.M. 2003. *Aluminium Structural Design*. Wien: Springer-Verlag GmbH.

Polus, Ł. & Szumigała, M. 2014. A numerical analysis of the resistance and stiffness of the aluminium and concrete composite beam. *CEER* 15 (4): 99–112.

Szumigała, M. & Polus, Ł. 2015. Applications of aluminium and concrete composite structures. In T. Tracz & I. Hager (eds), *Procedia Engineering, Volume 108*: 544–549. Elsevier.

Recent Progress in Steel and Composite Structures – Giżejowski et al. (Eds)
© 2016 Taylor & Francis Group, London, ISBN 978-1-138-02946-0

Innovative solution of transition zone in steel-concrete hybrid beam

P. Kozioł, M. Kożuch, W. Lorenc & S. Rowiński
Faculty of Civil Engineering, Wrocław Univeristy of Technology, Wrocław, Poland

ABSTRACT: The problem of transition zone of structural steel element connected to concrete is discussed in the following paper. This zone may be located for instance in specific bridge composite girder. In such case the composite beam passes smoothly into concrete beam. The main problem is to design the connection with an appropriate load capacity and fatigue resistance, with minimal welding work effort. The authors present innovative solution of transition zone and discuss the first results, with emphasis put on the transition zone structural response in term of bending capacity and failure model. The way of fabrication of the steel-concrete hybrid specimen is presented together with details concerning experimental investigation on the tests. Additionally, linear steel and linear concrete (LsLc) finite element model, as elementary one, aiming to determine the bearing capacity and to study the behavior of a transition zone, was analyzed. The article summarizes the already executed experimental tests and serves as a basis for full scale destructive tests which are in progress.

1 INTRODUCTION

In 2009, within the S5 expressway line, the road bridge WD4 was built with application of innovative technology. The bridge carries both, S5 expressway interchanges, between Stryszek and Białe Błota, and access road over the railway track. The bridge was designed as a frame structure. Prefabricated elements with steel T-section profiles, embedded in concrete plate, were used as external reinforcement of bridge's deck. The key point was the fact that steel sections do not run over the entire bridge span but terminate near zero bending moment zone. The bottom view of WD4 bridge is shown in Figure 1. The continuous shear connection was realized with composited dowels of MCL shape (Berthellemy et al. 2011 a, b, Lorenc et al. 2013). The bridge design and its construction are described in detail in (Seidl et al. 2013).

One of the crucial aspects of construction was the transition zone of steel profiles, which is presented in Figure 2. The construction of the bridge has been widely discussed at different practitioners' and scientists' meetings as well as conferences. Due to many doubts and lack of tests' results the following research which aimed to provide the solution reducing the length of transition zone was conducted. Among different conceptions, the connection with closed holes as analogy to the perfobond rib connectors was chosen (Leonhard et al. 1987). It was decided to situate the perfobond holes in bottom part of steel section web, near the bottom flange. Consequently, the destructive test was planned and beam specimen with testing programmes were developed. The element for test was designed according to the recommendations suggested in EN 1994-1-1 and other approved testing procedures appropriate for composite steel and concrete structures (Lorenc et al. 2012, 2014

Figure 1. Bottom view on the external reinforcement of bridge WD-4 which adapts the force flow.

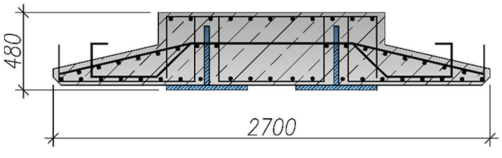

Figure 2. Transition zone in steel beam prepared for fabrication and the cross section of finished prefabricated element.

a, b). The cross-sectional dimensions of the beams correspond to a half-scale of beams applied in constructions.

In particular, the main objective of the destructive test was to estimate flexural carrying capacity of the beam subjected to a positive bending moment. The point of reference, when interpreting the results, was the bending moment capacity of the beam conditioned by failure of transition zone. Load capacity of whole element was compared with load capacity of both composite and concrete sections situated outside the transition zone—in support sections. Another objective to be obtained was to determine the failure mechanism of transition zone. The following paper presents a beam specimens design, the research which has been conducted and the first key test results.

2 DESTRUCTIVE TESTS

2.1 *Specimens for destructive test*

The boundary conditions, such as geometry or materials, and testing procedures were established by analogy to the test of the shear connectors given in Eurocode EN 1994-1-1. The cross section of the beam changes over the length, which means that on the one end of the beam there is a concrete section and on the other side composite one. To be more specific, the cross section shape changes from concrete rectangular shape 650 × 400 mm to composite T-shape section with reinforced concrete slab 650 × 200 mm and reinforced concrete web 200 × 200 mm (Fig. 3a). The steel part was made of welded plates fabricated to simulate half of IPE 500 profile. At the top part of the steel web, the MCL dowels were cut. Estimated dimensions diminish the influence of scale-effect, provide the position of the neutral axis of the composite section in the upper part of the dowels as well as eliminate the problem of the effective width of flanges for shear lag.

The steel element were made of S355 steel grade with nominal tensile yield stress 355 MPa, according to EN 10025. Normal strength concrete of nominal strength C35/45 was used for specimen. The main reinforcement of the concrete part consists of 20 mm in diameter bars from BSt500 steel with nominal yield stress of 500 MPa.

The transition zone was fabricated with 8 connectors, which were the 50 mm diameter holes in steel web spaced 125 mm apart. This connector resist horizontal shear and vertical uplift forces at the steel-concrete interface by using a concrete end-bear zone, concrete dowels, and transverse rebars in the holes. In transition zone, each rebar from bottom reinforcement was folded and perforated the hole.

2.2 *Test layout and instrumentation*

The destructive tests were conducted on a simply supported beam subjected to a 4-point-bending test. On the length of the transition zone, between the concentrated forces, constant bending moment with no shear forces is obtained—connecters do not transmit the longitudinal shear.

The theoretical span of beam was 4,250 mm and total length 4,850 mm (Fig. 3a). Two concentrated forces, with 1,500 mm spacing, were arranged symmetrically at a distance of 1,375 mm from the supports. The vertical monotonic load was applied to the specimen, using a hydraulic jack with a maximum capacity of 6 MN.

While testing the deflection, slips and deformation at key locations on the beam were measured by means of respectively inductive sensors LVDT and strain gauges.

Figure 3 depicts the test layout and the specimen instrumentation. Five vertical displacement transducers LVDTs, labeled V1 ÷ V5, were used to measure the relative deflection of the specimen (Fig. 3b). One LVDT was located at mid-span (V3), one at each quarter point (V2 and V4), and one inside the face of each support (V1 and V5). Three LVDTs, labeled S6 ÷ S8 were used to measure the relative displacement (slip) between steel and

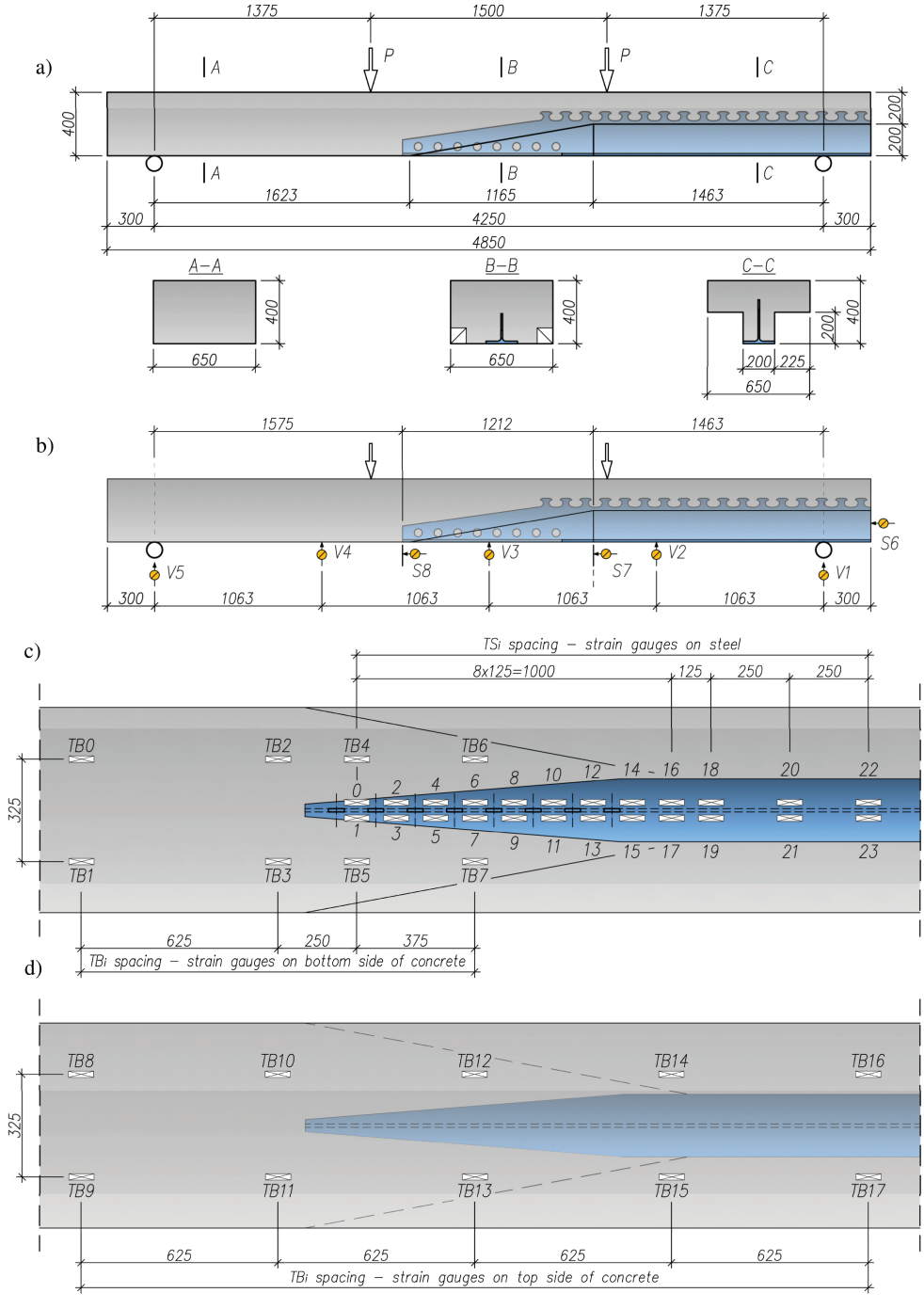

Figure 3. Arrangement of test specimen with instrumentation layout: a) general layout—front view with characteristics cross sections, b) the displacement transducers LVDT layout, c) strain gauges on the bottom side of specimens both on steel and concrete part, d) strain gauges on the top side. The label prefix "*TS*" appropriate for strain gauges on steel was omitted for drawing clarity.

concrete, both in longitudinal and vertical directions. Two of them were mounted in both ends of steel part (S6 and S8) and one LVDT transducer was mounted in the point where T-section starts to change into rectangular shape section (S7).

Strain gauges were also installed. Twenty four strain gauges, labeled TS0 ÷ TS23 were attached to the bottom side of steel flange. Forming 8 pairs of gauges situated under each hole connector (in order to calculate their internal forces) and 4 pairs in next 125 mm and 250 mm. There were also nineteen strain gauges attached to concrete. Labeled TB0 ÷ TB7, at the bottom of the concrete section (Fig. 3c) and labeled TB8 ÷ TB18 at the entire length of the top of the beam (Fig. 3d). The applied load and relative slips were recorded continuously, in order to obtain a bending load versus relative slip curves.

Figure 4. LVDT and strain gauges installed—example of TB3 and S8 sensors attached.

2.3 *Experimental program*

Experimental program involved the testing of one beam specimen as a prototype, first type of transition zone design. The experimental test was performed at the Civil Engineering Research Laboratory in Wrocław University of Technology, Poland.

At the first stage the load was applied in 25 cycles of loading and unloading ranging from 50 kN up to 200 kN (5% up to 25% of the expected failure load) in order to eliminate the adhesive bond between steel and concrete. At this stage the procedure was controlled by an applied load at average rate of 4 kN/s. At the subsequent stage, up to the specimens failure, the load was applied as force-controlled at average rate of 2 kN/s.

2.4 *Test results and failure model*

The first crack was visually detected at the level of 250 kN, at the bottom part of the specimens, near the concentrated force on concrete section.

As the load increases, typical flexural cracks propagate to the top surface of the beam. In the final state, both tensile failure at the bottom and compressive failure at the top occurred. The bottom external reinforcement, was pulled out of the concrete in vertical direction, once the pull-out failure in transition zone occurred (Fig. 5).

The results are shown in Figure 6 however, it present only selected results of destructive tests, especially the load-deflection curve, based on middle-span, relative deflection value V3.

2.5 *Analysis of the test's results*

Due to experiment results, the ultimate bending resistance both of composite and concrete section were sufficient to carry out the destructive test aimed to transition zone failure.

The failure pattern for tested beam is shown in Figure 6. The ultimate load is 854 kN which corresponds to deflection at middle-span of 55 mm, reached due to the high stiffness of the steel element on composite section's side.

According to load-deflection relationship (Fig. 6), the initial displacement response is quasi-linear but the on-set of nonlinearity occurred at relatively low load which is about 60% of resistance. Thus, load value P = 500 kN and corresponding deflection u = 20 mm may be assumed as a limit of elastic range.

Bending resistance of reinforced concrete section and steel-concrete composite section were calculated. For each section characteristic resistance $M_{Rk,i}$ was estimated and compared with the tests results M_{test}. Curve presenting the relationship between maximum bending moment and deflection were obtained and shown in Figure 7. The reference value $M_{Rk,i}$ respectively for $M_{Rk,conc}$, $M_{Rk,comp}$ curve is:

$M_{conc,pl,Rk}$ – plastic, characteristic value of the resistance moment of reinforced concrete section,

$M_{comp,pl,Rk}$ – plastic, characteristic value of the resistance moment of composite section.

The characteristic values were calculated based on both nominal value of the yield strength of steel f_{yk} and characteristic value of the cylinder compressive strength of concrete f_{ck}. The plastic stress distribution for analytical calculation was assumed.

Obtained ultimate resistance of transition zone $M_{test,max}$ = 587 kNm is similar to estimated characteristic value of resistance moment of composite section $M_{comp,pl,Rk}$ = 584 kNm and about 10% higher than estimated characteristic value of resistance

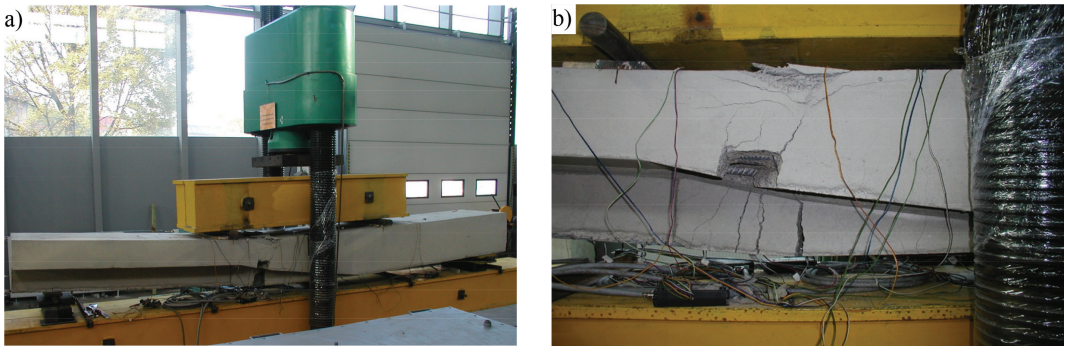

Figure 5. Tests set up with the failure of beam specimens: a) general arrangement of specimen after destructive tests, b) detail of transition zone after experimental tests.

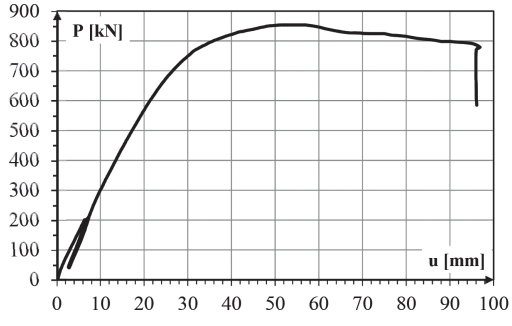

Figure 6. Load-deflection curve obtained from experimental test.

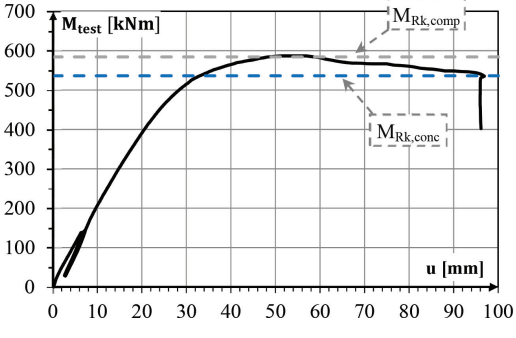

Figure 7. Maximum bending moment—deflection relationship. Additional characteristic values of the resistance moment were presented—description in text.

moment of concrete section $M_{conc,pl,Rk}$ = 536 kNm. The transition zone has sufficient capacity to transfer bending between composite and concrete sections clearly.

3 FEM MODEL

In addition to the experiments, a numerical model is generated and still developed with the objective of analyzing the structural behavior of the transition zone and confirmation of the failure mechanism. Finite Element calculations have been performed using ABAQUS software. The FEM model allows to conduct the parameter studies without any additional experimental effort and to simulate mechanical processes in the interior of the specimen, which are not measurable during the experiments with metrological instruments. To start with, linear steel and linear concrete (LsLc) model, as elementary one aiming to determine the bearing capacity and to study the behavior of a transition zone, was analyzed.

FEM model consists of two major parts: steel and concrete one. Taking advantage of the symmetry of the specimen, only the half of the specimen was modelled. Boundary conditions corresponds to the destructive test described in section 2 and are shown in Figure 8. Vertical force, equal to the experimental tests ultimate load value, is imposed at the top of the analyzed beam.

In the composite connection as well as in internal parts of holes in transition zone, interactions in the direction orthogonal to the surface (in normal direction) prevent the penetration of the steel beam into the concrete slab. Contact interaction property is defined as Hard Contact. In the tangential direction, frictional contact between concrete and steel surface is defined with a coefficient of friction $\mu = 0.3$. The tangential contact condition is modelled using the Penalty Method, which involves compatibility of the kinematic conditions between displacement, velocity and acceleration.

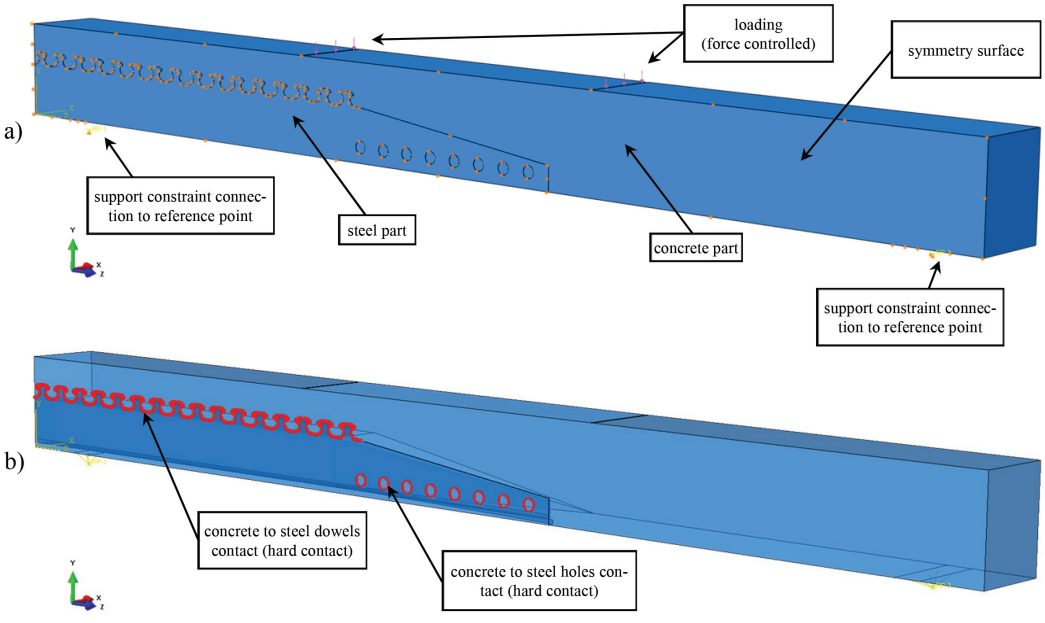

Figure 8. FEM model of transition zone: a) constraints and loading, b) interactions and contact conditions.

Three-dimensional solid, 4-node linear tetrahedral elements C3D4, due to complex beam geometry, were used. An evaluation of the element size was conducted, where a mean element size of 20 mm lead to results with good precision and a reasonable time of analysis.

Detailed description FE analysis' results will be omitted since it is beyond the scope of this study and is still being developed in frame of works for PhD dissertation.

4 CONCLUSION

The newest studies concerning bending capacity of transition zone were presented. Destructive test results confirm that assumed design solutions could be applied in constructions. The relative flexural load bearing capacity is 587 kNm which is sufficient in order to apply the solution in constructions. The expected failure mechanism was obtained and the results indicate an appropriate force redistribution between the holes in the ultimate limit state.

While theoretical analysis with complex FEM models are being performed, preparation for the full scale destructive tests is in progress. The following paper presents an excerpt of PhD dissertation developed by MSc. Piotr Kozioł.

REFERENCES

Berthellemy, J. Lorenc, W. Mensinger, M. Rauscher, S. & Seidl, G. 2011a. *Zum Tragverhalten von Verbunddübeln, Teil 1: Tragverhalten unter statischer Belastung*. Stahlbau 80, Heft 3: 172–184.

Berthellemy, J. Lorenc, W. Mensinger, M. Ndogmo, J. & Seidl, G. 2011b. *Zum Tragverhalten von Verbunddübeln, Teil 2: Ermüdungsverhalten*. Stahlbau 80, Heft 4: 256–267.

Leonhardt, F. Andra, W. Andra, H. P. & Harre, W. 1987. Neues Vorteihaftes Verbundmittel fur Stahlverbund-Tragwerke Mit Hoher Dauerfestigket. In: Betonund Stahlbetonbau Heft 12.

Lorenc, W. Kubica, E. & Kożuch, M. 2012. *Testing procedures in evaluation of resistance of innovative shear connection with composite dowels*. Archives of Civil and Mechanical Engineering 10/2012 No. 3: 51–63.

Lorenc, W. Kożuch, M. & Seidl, G. 2013. *Zur Grenztragfähigkeit von Verbunddübeln mit Klothoidenform*. Stahlbau 82, Heft 3: 196–207.

Lorenc, W. Kożuch, M. & Rowiński, S. 2014a. *The behavior of puzzle-shaped composite dowels—part I: experimental study*. Journal of Constructional Steel Research. 101/2014: 482–499.

Lorenc, W. Kożuch, M. & Rowiński, S. 2014b. *The behavior of puzzle-shaped composite dowels—part II: theoretical investigations*. Journal of Constructional Steel Research. 101/2014: 500–518.

Seidl, G. Stambuk, M. Lorenc, W. Kołakowski, T. & Petzek, E. 2013. *Wirtschaftliche Verbundbauweisen im Brückenbau—Bauweisen mit Verbunddübelleisten*. Stahlbau 82, Heft 7: 510–521.

Recent Progress in Steel and Composite Structures – Giżejowski et al. (Eds)
© 2016 Taylor & Francis Group, London, ISBN 978-1-138-02946-0

Composite structural electric transmission tower

J. Chen & W.L. Jin
Department of Civil Engineering, Zhejiang University, Zhejiang, China

W. Xue
Department of Civil Engineering, Zhejiang University of Science and Technology, Zhejiang, China

ABSTRACT: The landmark structure in the Zhejiang province-Zhoushan electric network project—the tallest electric transmission tower (370 m) in the world was steel-concrete composite structure. In this paper, the key technology of the composite structure tower, namely the concrete-filled steel tubes with lattice angle, as well as the concrete-filled steel tubular connection was summarized.

1 INTRODUCTION

Zhoushanelectric transmission tower, with the height of 370 m, is the tallest electric transmission tower (370 m) in the world, as shown in Fig. 1. It is landmark structure in the Zhejiang province-Zhoushan electric network project, which is one of the most important projects of Zhoushan development program. The structural type of thiselectric transmission tower is composite structure. The four main columns are concrete-filled steel tubes with reinforced lattice angle, as shown in Fig. 2. The braces of the structure are pure steel tubes. Thus the connection between the main column and brace are concrete-filled steel tubular connections, as shown in Fig. 3. Research towards the concrete-filled steel tubes has been widely reported (Geand Usami, 1992, O'Shea, & Bridge, 1997, Uy, 2001, Ellobody, *et al.*, 2006, Han, *et al.*, 2007, Tao, *et al.*, 2007).

Figure 1. 370 m Zhoushan electric transmission tower.

However, the structural members used in this composite structure are different from those reported.Therefore, a series of research programs are conducted.

Figure 2. Main column of concrete-filled steel tube with reinforced lattice angle.

Figure 3. Concrete-filled steel tubular connection.

2 STUDY OF CONCRETE-FILLED STEEL TUBE WITH REINFORCED ANGLE

2.1 *Column test specimens*

A total of 14 concrete-filled steel tube specimens were tested. The measured cross-section dimensions and specimen length for each test specimen are shown in Table 1. The test specimens are labeled such that the type of the specimen, diameter and length of specimen can be identified from the label. The concrete mix was designed for compressive cube strength (f_{cu}) at 28 days ofapproximately 40 MPa.Thecompressive strength (f_{cu}) and elastic modulus (E_c) obtained on 150-mm cubes at 28 days were 47 MPa and 37420 MPa, respectively. The yield strength of steel tube and angle are 298.3 MPa and 263.8 MPa, respectively. The angle size were 30*3 mm and 40*4 mm for 300 mm diameter and 400 mm diameter specimens, respectively (Xu, *et al.*, 2014).

2.2 *Test results*

All L-500 mm column specimens failed in the crush of concrete and crack of the steel tubes, as shown in Fig. 4. There is no local buckling of the steel tubes observed during the test. Failure of specimen CS300-2500 occurred near the bottom end, where the concrete core failed in diagonal cracks. However, the failure mode of specimen CSB300–2500 is overall buckling, as shown in Fig. 5. The lattice angle and concrete core was taken out from the failed specimen CSB300-2500, as shown in Fig. 5. The angle shows overall buckling but there is no single angle element's buckling deformation. The ultimate strengths and failure mode are shown in Table 2.

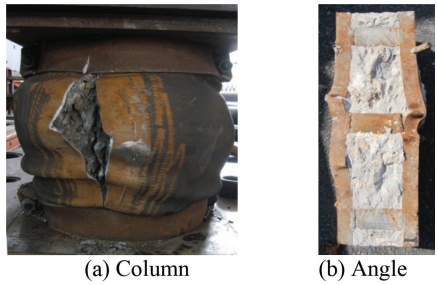

(a) Column (b) Angle

Figure 4. Specimen CSB 500.

(a) Column (b) Angle

Figure 5. Specimen CSB 2500.

Table 1. Dimension of test specimens.

Specimens	*L* (mm)	*D* (mm)	*t* (mm)
CS300-500	500	300	3.98
CSB300-500	500	300	3.97
CS300-1500	1500	300	4.06
CSB300-1500	1500	300	4.00
CS300-2500	2500	300	4.03
CSB300-2500	2500	300	4.00
CS300-3500	3500	300	3.97
CSB300-3500	3500	300	3.98
CS400-500	500	400	3.96
CSB400-500	500	400	3.96
CS400-1500	1500	400	4.00
CSB400-1500	1500	400	4.04
CS400-2500	2500	400	4.02
CSB400-2500	2500	400	3.97

Table 2. Ultimate strengths and failure modes of test specimens.

Specimens	$P_{u\text{-}test}$ (kN)	Failure mode
CS300-500	5680	S & C
CSB300-500	6194	S & C
CS300-1500	3280	SF
CSB300-1500	3626	SF
CS300-2500	2751	OB
CSB300-2500	3150	SF
CS300-3500	2547	OB
CSB300-3500	2751	OB
CS400-500	7711	S & C
CSB400-500	8588	S & C
CS400-1500	4562	SF
CSB400-1500	4696	SF
CS400-2500	4486	SF
CSB400-2500	4614	SF

3 STUDY OF CONCRETE-FILLED STEEL TUBULAR CONNECTIONS

3.1 *Connection test specimens*

The test specimens were fabricated from hot-rolled circular hollow section steel tubes. The concrete was filled in the chord member along its full length for all test specimens. The dimensions and geometric ratios of the connections were given in Table 3. The tests thus covered two different chord wall slenderness ratios (D/t = 75 and 60), which exceed the maximum limitation of 50 for tubular CHS steel connections specified in AISC standard (2010). The designed gap size of K type specimens is 12 mm for gapped K-connections as specified in AISC standard (2010). The compressive strength (f_{cu}) obtained on 150-mm cubes at 28 days were 46.9 MPa. The yield strength of steel chord having nominal thickness of 4 mm and 5 mm are 298 MPa and 267 MPa, respectively (Xu, *et al.*, 2015).

3.2 *Connection test results*

The KT- connections failed by yielding of the brace, and the remaining T-, Y- and K-connections failed by punching shear of chord wall, with the chord ripping at the toe of the weld. There is visible yield-line around the toe of the weld on the chord face (where the chord ripped) when the load reached 85–90% of the ultimate strength. The T-, Y- and K-connections finally showed a sudden failure. Failure modes of test specimens T-300-4, Y-300-4, K-300-4, K-300-5 and KT-300-4 are shown in Fig. 6(a)-(d), respectively. For KT-connections, the MTS actuator reaches its maximum capacity. There is no visible yield-line for KT-connections. However, the reading of axial strain gauges on the loading brace indicates that the brace is yielding (ε = 0.0025).

Table 3. Dimension of test specimens.

	Chord		Brace	
	D	t	D_b	t_b
Specimens	(mm)			
T-300-4	299.84	4.19	132.78	6.08
Y-300-4	300.56	4.18	132.86	6.09
K-300-4	300.24	4.18	132.71	6.08
KT-300-4	300.35	4.17	132.56	6.07
T-300-4R	300.32	4.19	133.12	6.08
Y-300-4R	299.67	4.18	133.32	6.09
K-300-4R	300.11	4.18	133.25	6.08
KT-300-4R	299.52	4.17	133.09	6.07
T-300-5	300.46	5.01	132.66	6.08
Y-300-5	300.48	4.99	132.68	6.10
K-300-5	300.32	5.02	132.98	6.06
KT-300-5	300.28	5.01	133.02	6.09

(a) T connection

(b) Y connection

(c) K connection

(d) KT connection

Figure 6. Failure modes of connections.

Table 4. Comparison of design strengths calculated using proposed equations with test results.

Specimen	Test (kN)	Design (kN)	Design/Test
T-300-4	534.8	59.5	0.11
Y-300-4	620.3	84.2	0.14
K-300-4	785.0	84.2	0.11
T-300-4R	549.1	59.5	0.11
Y-300-4R	699.9	84.2	0.12
K-300-4R	698.9	84.2	0.12
T-300-5	662.4	81.3	0.12
Y-300-5	836.1	114.9	0.14
K-300-5	814.0	114.9	0.14
		Mean	0.12
		COV	0.104

The ultimate strengths of test specimens are shown in Table 4. The small difference between the ultimate strengths of the first and repeated test specimens proved the reliability of test results. Design equation is proposed based on the failure mode. Predictions are compared with test results in Table 4.

$$P_n = 0.6F_y t\pi D_b\left(\frac{1+\sin\theta}{2\sin^2\theta}\right) \quad (1)$$

4 STUDY OF STRESS CONCENTRATION FACTORS OF CONNECTIONS

4.1 *Test specimens*

Experimental investigation was performed to investigate the Hot Spot Stress distribution along the intersection of chord and brace. Five tubular T connection specimens with self compacting concrete filled in the chord were tested. In addition, three hollow steel tubular T connections specimens were also tested for comparison. The measured dimensions of test specimens are shown in Table 5. The test specimens are labeled such that the chord types, outer diameter of chords, outer diameter of braces as well as loading condition could be identified from the label (Chen, *et al.*, 2010).

4.2 *Test program*

A design test rig, as shown in Fig. 7, was used to test these tubular joints subjected to axial loading and in-plane bending, respectively. Stress Concentration Factors (SCFs) were then calculated using the measured strain gauge readings using Eqs (2) and (3).

$$SNCF = \xi_\perp/\xi_n \quad (2)$$

Table 5. Dimension of test specimens.

	Chord		Brace	
Specimens	Diameter (mm)	Thickness (mm)	Diameter (mm)	Thickness (mm)
S-203-133 AX	203	8.40	133	6.79
CS-203-133 AX	203	8.45	133	6.80
CS-203-159 AX	203	8.42	159	6.81
S-203-168IB	203	8.40	168	7.80
S-219-168IB	219	8.42	168	7.81
CS-219-159IB	219	8.42	159	5.60
CS-219-168IB	219	8.43	168	7.82
CS-219-203IB	219	8.42	203	7.79

Note: AX: axial loading, IB: In-plane bending.

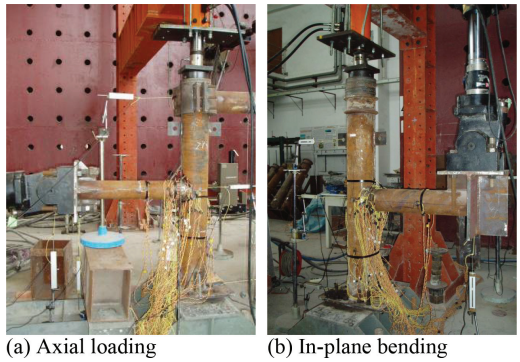

(a) Axial loading (b) In-plane bending

Figure 7. Test setup.

$$SCF = SNCF \times \left(1 + \nu\xi_{\parallel}/\xi_{\perp}\right)\left(1 - \nu^2\right) \quad (3)$$

where $\xi_\perp$ = the hot spot strain; ξ_n = nominal strain obtained from the four midway brace member strain gauges readings; υ = Poisson's ratio.

4.3 *Test results*

The average SCF distributions on the chord and brace of the specimens, subjected to axial loading and in-plane bending are plotted in Figs. 8–9, respectively. It can be seen under the axial load, the SCF distributions on the chord and brace of the hollow steel specimen have a significant difference with those concrete-filled specimens, both the peak SCFs and trends. The peak SCFs of chord and brace of specimen CS-203-133 are 24.0% and 29.4% of those of specimen S-203-133. The peak SCFs on the chord and brace of hollow steel specimens are on the saddles, but those of concrete-filled steel specimens are almost on the crown. This may be caused by the concrete filled in the chord. It also can be seen under

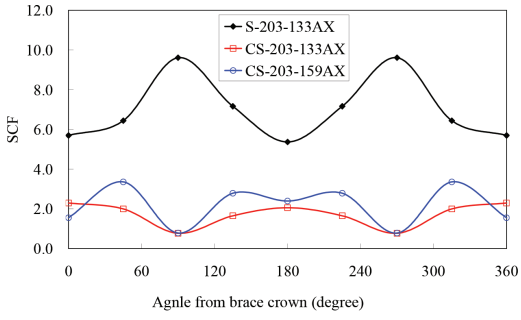

(a) Chord

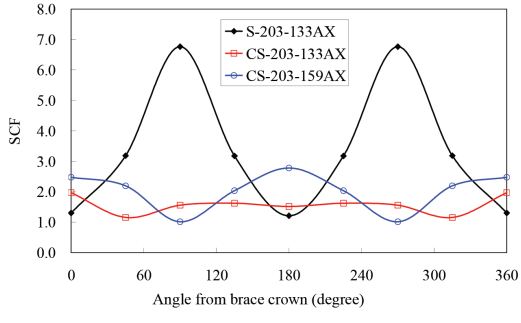

(b) Brace

Figure 8. SCFs of specimens under axial loading.

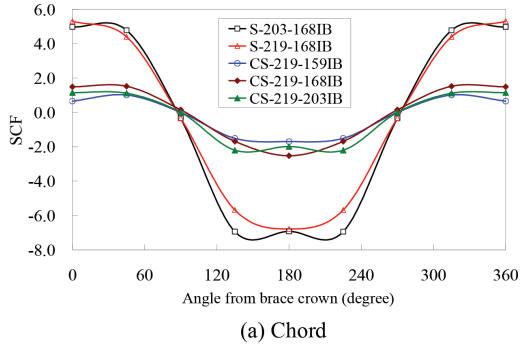

(a) Chord

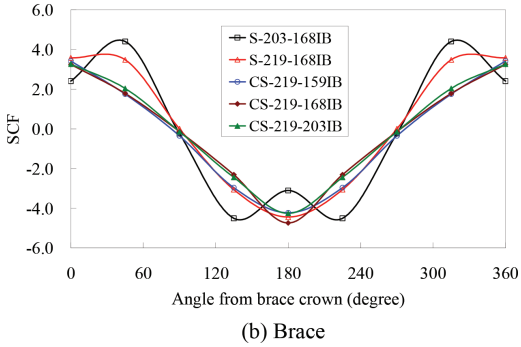

(b) Brace

Figure 9. SCFs of specimens under in-plane bending.

in-plane bending, the SCF distributions on the brace of hollow steel specimens are similar to those concrete-filled specimens. However, the SCF distributions on the chord of hollow steel specimens are different from those concrete-filled specimens. The peak SCFs of chord for concrete-filled specimens are all less than 2.0, while those of hollow steel specimens are 7.2. The trends of the distributions are similar. Generally, the comparison indicate that the filled concrete effectively reduce the peak SCFs under both axial loading and in-plane bending.

5 CONCLUSIONS

The key technology applied in the Zhoushan electronic transmission tower is studied in this paper. The main conclusions are below:

1. The reinforced lattice angle could effectively enhance the strength of concrete-filled steel tubes. It is also shown that the reinforced lattice angle is helpful to the concrete core's resistance to diagonal crack. There is only over buckling for the reinforced lattice angle due to the constraint from the concrete.
2. The concrete inside holds the chord wal1 in their original position and allows the connection to reach bearing capacities of the limit state of punch shear yielding. For tension-loaded concrete-filled tubular T-, Y-, and K- connections, it is recommended that the design strengths be calculated from existing AISC design rules of limit state of punch shear yielding for unfilled tubular CHS connections.
3. The trends of SCFs distributions of hollow steel specimens are different from those of concrete-filled specimens under axial loading. However, trends of SCF distributions of hollow steel specimens and concrete-filled specimens under in-plane bending are similar. It is shown that the filled concrete has minor effect on the SCFs distributions on the brace of specimens under in-plane bending.

ACKNOWLEDGEMENTS

The research work described in this paper was supported by Science and Technology Department of Zhejiang Province (2015C33005).

REFERENCES

AISC. 2010. *Specification for structural steel buildings*. American Institution of Steel Construction (AISC), ANSI/AISC 360–10, Chicago, Illinois, 2010.

Chen, J., Chen, J. & Jin, W.L. 2010. Experiment investigation of stress concentration factor of concrete-filled tubular T joints. *Journal of Constructional Steel Research* 66(12): 1510–1515.

Ellobody, E., Young, B., & Lamc, D. 2006. Behaviour of normal and high strength concrete-filled compact steel tube circular stub columns. *Journal of Constructional Steel Research* 62(8), 706–715.

Ge, H.B. & Usami, T. 1992. Strength of concrete-filled thin-walled steel box columns: experiment. *Journal of Structural Engineering*, ASCE, 118(11), 3006–3054.

Han, L.H., Yao, G.H. & Tao, Z. 2007. Performance of concrete-filled thin-walled steel tubes under pure torsion. *Thin-Walled Structures*, 45(1), 24–36.

O'Shea, M.D. & Bridge, R.Q. 1997. Local buckling of thin-walled circular steel sections with or without internal restraint. *Department of Civil Engineering Research Report No. R740*, The University of Sydney, Sydney, Australia.

Tao, Z., Han, L.H. & Wang, D.Y. 2007. Experimental behaviour of concrete-filled stiffened thin-walled steel tubular columns. *Thin-walled Structures* 45(5), 517–527.

Uy, B. 2001. Strength of short concrete filled high strength steel box columns. *Journal of Constructional Steel Research* 57(2), 113–134.

Xu, F., Chen, J., Jin & WL. 2014. Experimental investigation of thin-walled concrete-filled steel tube columns with reinforced lattice angle. *Thin-Walled Structures* 84: 59–67.

Xu, F., Chen, J. & Jin, WL. 2015. Experimental Investigation and Design of Concrete-Filled SteelTubular CHS Connections. *Journal of Structural Engineer*ing, ASCE, DOI: 10.1061/(ASCE)ST.1943–541X.0001050.

Recent Progress in Steel and Composite Structures – Giżejowski et al. (Eds)
© 2016 Taylor & Francis Group, London, ISBN 978-1-138-02946-0

Prestressing of simply supported composite bridges: A cost-benefit analysis

G. Bertagnoli & D. Gino
DISEG, Politecnico di Torino, Torino, Italy

E. Martinelli
DICiv, University of Salerno, Fisciano (SA), Italy

ABSTRACT: Composite bridges can be prestressed both with internal bonded prestressing in the slabs and with external unbonded prestressing fastened on the steel beams. This technique is generally employed in continuous bridge beams in order to contrast upper slab cracking due to negative bending moments on internal supports. Conversely, this work presents a parametric analysis aimed at understanding if (and to which extent) prestressing can be beneficial in simply supported composite bridges for reducing the profile section and, hence, the demand for ordinary steelwork. Therefore, the effect of both different levels of prestressing action and alternative sequences of construction is taken into account. Moreover, closed-form solutions for Class 3 sections and iterative solutions for Class 4 ones are considered. Finally, a cost-benefit analysis is presented.

1 INTRODUCTION

Composite steel-concrete beams are generally regarded as a rational and sustainable solution for realizing both simply supported and continuous bridges (SETRA, 2010). The concrete slab is generally supported by the longitudinal beams and therefore locally working in transverse direction or supported by transverse beams, with 3÷4 m spacing and working in the longitudinal direction both locally and globally (Jonhson, 2004).

As a matter of fact, prestressing is almost never used in association with these structures as it is generally accepted that steel works fine enough in tension and concrete slab results to be almost completely compressed due to the simply supported scheme. Conversely, this ideal "team-work" achieved by the combined use of the two materials within the simply supported scheme loses its excellent performance when the continuous beam scheme is used (Ryu, 2004). Particularly, in continuous beams the slab is in tension and is often subjected to cracking phenomena developing throughout the zones of negative bending moment, whereas, in the same regions, the bottom flange of steel beams is compressed asking for a massive use of steel (Ryu, 2004).

Continuous beams are nevertheless becoming more attractive as they reduce the number of structural joints, improving the durability of the deck and reducing the maintenance costs. Moreover the use of continuous beams can lead to two clear advantages (Deng, 2012):

1. construction of more slender decks over the same spans (useful to increase clearance especially in case of river crossing), with the same stiffness of simply supported beams;
2. construction of longer spans (useful to avoid piers in river beds) with the same dimensions of simply supported beams;

Prestressing has been therefore sometimes suggested as a possible tool for increasing the performance of composite continuous girders providing crack control of the concrete slab and reduction of steel in the beam bottom flange (Deng & Morcous, 2013a). Both experimental studies (Chen, 2005) and numerical analyses (Deng & Morcous, 2013b) have demonstrated the potential of prestressing in composite steel-concrete bridges.

Unluckily, due to traditional reasons, prestressing is a technology coming from concrete structures designers (Hueste et al., 2012), whereas composite bridges are generally designed by people coming from steel schools and, therefore, not so keen in introducing prestressing in the design (Jonhson, 2004).

This paper focuses on a very common typology of composite bridges: the simply-supported two-girder deck, which is probably the most common solution to cover spans between 40 and 60 m and generally has a width ranging between 10.5 and 12 m.

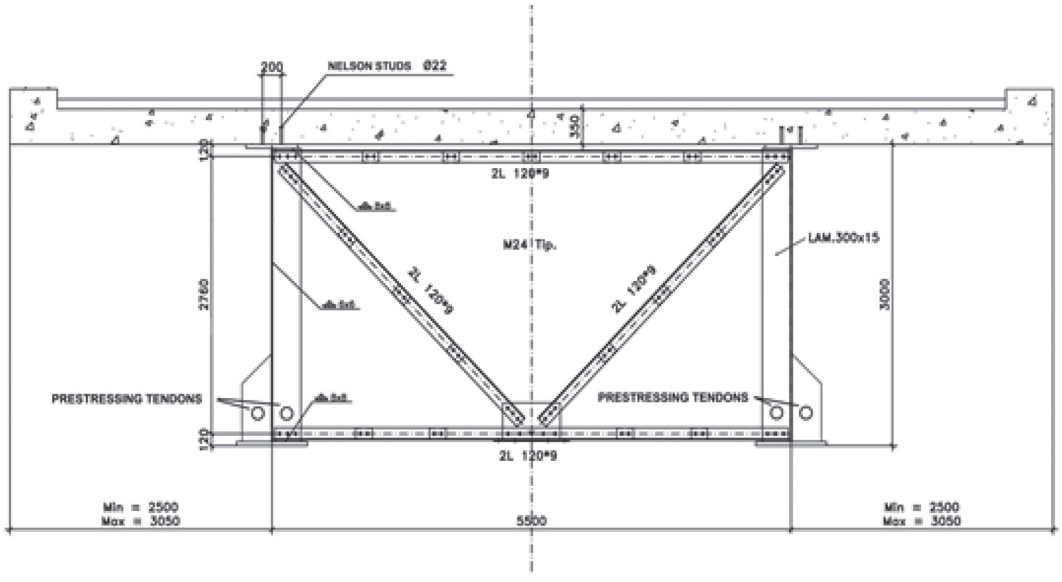

Figure 1. Two girders deck cross section with external prestressing.

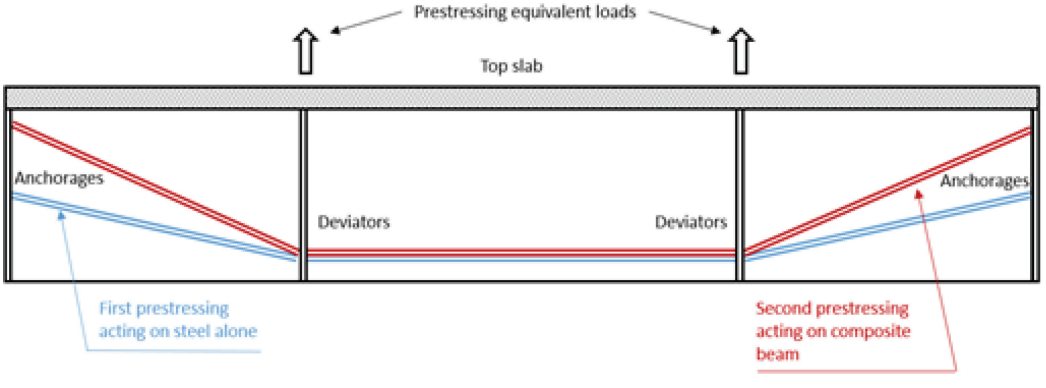

Figure 2. Longitudinal layout of prestressing.

The study aims at investigating the effect of prestressing on the resulting design of the transverse section. Particularly, it proposes a cost-benefit analysis of different solutions based on adopting alternative application sequences of the prestressing action. The cost-benefit analysis is, then intended at determining if and how prestressing can lead to reducing the minimal transverse area of the steel cross section.

The cross section of a typical simply-supported two-girder deck with the introduction of external prestressing tendons within deck depth is depicted in Figure 1.

Longitudinal arrangement of prestressing tendons is shown in Figure 2. The tendons are placed according to a 4 point bending scheme, passing by

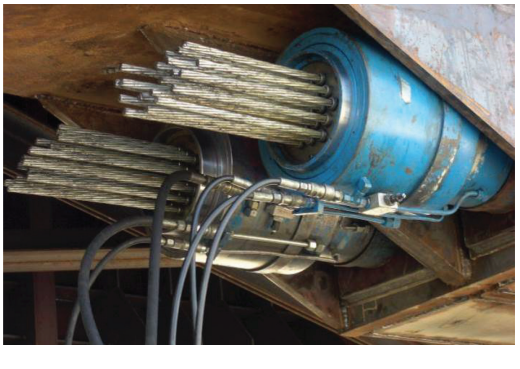

Figure 3. Prestressing jacks acting on steel beam.

centroid of beam at the bearing and reaching a constant maximum eccentricity in the midspan region.

A detail of prestressing anchorage on steel beam during prestressing introduction with jacks is shown in Figure 3.

2 NOTATION

The following symbols will be used hereinafter:

E_c concrete Young modulus
E_s steel Young modulus
$n = E_c/E_s$ homogenization coefficient
γ_c partial safety factor for concrete
γ_{M0} partial safety factor for steel beam
γ_s partial safety factor for prestressing steel
γ_g partial safety factor for permanent actions
γ_q partial safety factor for variable actions
γ_p partial safety factor for prestressing
L bridge girder span
b_c concrete slab width
h_c concrete slab depth
A_{st} steel beam top flange area
A_{sb} steel beam bottom flange area
b_w steel beam web width
h_w steel beam web depth
h_{pb} distance of prestressing tendons centroid from beam intrados
A_{pb} prestressing tendons cross section
σ_{pb} tendons prestress
M_{g2} bending moment due to permanent actions (like pavement, kerbs, barriers)
M_q bending moment due to variable actions (like traffic)

3 CROSS SECTION PROPERTIES

3.1 *Effect of steel web slenderness*

Most of the bridge girders cross sections fall in the Class 4, according to EN1993-1, mainly due to the presence of slender web panels. Nevertheless, some beams can be either included or very close to Class 3.

In the present paper the calculations are done both for Class 3 and Class 4 transverse sections and, then, compared with the aim of assessing the influence of web slenderness on the design output.

It has to be reminded that the analysis for Class 3 sections is linear and, hence, it is much simpler and quicker than the one needed for Class 4, as the latter requires an iterative procedure intended at defining the so-called "effective" section.

3.2 *Class 3 cross section properties*

when the steel girder cross section falls within Class 3 specifications, its geometric properties can be calculated according to the equations summarized in this section. The steel cross section A_s is:

$$A_s = A_{st} + b_w \cdot h_w + A_{sb} \tag{1}$$

Being the thickness of the flanges very small in comparison to the total depth of the steel beam, the simplification of neglecting half of their thickness in calculating the cross section properties is acceptable from an engineering point of view. Therefore, the static moment of the steel section respect to the intrados of the steel beam is:

$$S_s = A_{st} \cdot h_w + b_w \cdot \frac{(h_w)^2}{2} \tag{2}$$

and therefore the centroid distance of the steel section from the intrados of the steel beam (that can actually be confused with the centroid of the bottom flange) is:

$$y_{g,s} = S_S \Big/ A_S . \tag{3}$$

Following the same approach, the steel cross section moment of inertia is:

$$J_S = A_{st} \cdot \left(h_w - y_{g,s}\right)^2 + b_w \cdot \frac{(h_w)^3}{12} + b_w \cdot h_w \cdot \left(\frac{h_w}{2} - y_{g,s}\right)^2 + A_{sb} \cdot y_{g,s}^2 \tag{4}$$

After concrete hardening, cross section properties should be calculated again taking into account the slab contribution through a homogenization of the composite section. Hence, the homogenized cross section area A_0 is defined as follows:

$$A_0 = A_s + n \cdot A_c = A_s + n \cdot b_c \cdot h_c \tag{5}$$

Moreover, the centroid of the composite beam is:

$$y_{g,0} = \frac{n \cdot A_C \cdot \left(h_W + \frac{h_c}{2}\right) + S_s}{A_0} \tag{6}$$

and its moment of inertia is:

$$J_0 = n \cdot \left[b_c \cdot \frac{h_c^3}{12} + A_c \cdot \left(h_W + \frac{h_c}{2} - y_{g,0} \right)^2 \right] + J_s + A_s \cdot \left(y_{g,s} - y_{g,0} \right)^2 . \tag{7}$$

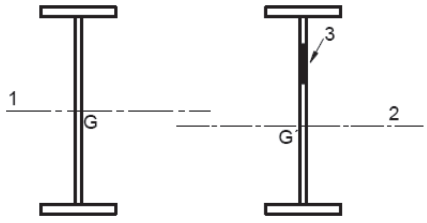

Figure 4. Effect of web buckling.

Stress distribution (compression positive)			Effective[2] width b_{eff}		
σ_1 σ_2 b_{e1} b_{e2} b			$\psi = 1$: $b_{eff} = \rho\ \bar{b}$ $b_{e1} = 0{,}5\ b_{eff}$ $b_{e2} = 0{,}5\ b_{eff}$		
σ_1 σ_2 b_{e1} b_{e2} b			$1 > \psi \geq 0$: $b_{eff} = \rho\ \bar{b}$ $b_{e1} = \frac{2}{5-\psi} b_{eff}$ $b_{e2} = b_{eff} - b_{e1}$		
b_c b_t σ_1 σ_2 b_{e1} b_{e2} b			$\psi < 0$: $b_{eff} = \rho\ b_c = \rho\ \bar{b} / (1-\psi)$ $b_{e1} = 0{,}4\ b_{eff}$ $b_{e2} = 0{,}6\ b_{eff}$		
$\psi = \sigma_2/\sigma_1$	1	$1 > \psi > 0$	0	$0 > \psi > -1$	-1	$-1 > \psi > -3$
Buckling factor k_σ	4,0	$8{,}2 / (1{,}05 + \psi)$	7,81	$7{,}81 - 6{,}29\psi + 9{,}78\psi^2$	23,9	$5{,}98\ (1 - \psi)^2$

Figure 5. EN1993-1 iterative procedure to take into account the effect of web buckling.

In the present paper the effect of concrete creep is simply taken into account by a variation of the modular ratio *n* in time.

3.3 *Class 4 cross section properties*

When a part of the compressed part of the steel webs buckles due to its slenderness (see black area evidenced by number 3 in Fig. 4), it becomes ineffective from the resistance point of view and the neutral axis moves from the elastic position (position 1 in Fig. 2) towards the tensed area of steel (position 2 in Fig. 2). In the present paper the iterative procedure proposed by EN 1993-1-1 (CEN, 2005), and summarized in Figure 5, is followed.

4 CONSTRUCTION PHASES

The midspan section of the girder has been chosen to perform the calculations, but, under the assumption of full shear interaction between slab and profile, the same procedure can be applied to all the other sections. The following simplified construction phases and relative actions have been taken into account for sake of simplicity.

4.1 *Phase 1: assembling of steel girder*

Steel girder self-weight gives rise to bending moment M_{sw} and the following stresses $\sigma_{ph1,t}$ and $\sigma_{ph1,b}$, respectively, at top and bottom face of steel beam.

$$\sigma_{ph1,t} = \frac{M_{sw}}{J_S} \cdot \left(y_{g,s} - h_s \right) \quad \sigma_{ph1,b} = \frac{M_{sw}}{J_S} \cdot y_{g,s} \tag{8}$$

where J_s is given by eq. (3) for class 3 sections or becomes $J_{s,eff}$ for class 4.

4.2 *Phase 2: introduction of first prestressing*

Prestressing can be either introduced in a single stage at this step or split into two contribution, being the first one applied on steel beam and the second one applied on the composite beam after slab hardening. In the present paper, two solutions are explored: the first one considers 100% of prestressing applied on the steel beam, whereas the second one splits 50% of prestressing on steel beam and 50% on composite section.

First phase prestressing gives rise to axial force N_{p1} and bending moment M_{p1} and the following stresses $\sigma_{ph2,t}$ and $\sigma_{ph2,b}$ respectively at top and bottom face of steel beam:

$$\begin{aligned} \sigma_{ph2,t} &= \frac{N_{p1}}{A_S} + \frac{M_{sw} + M_{p1}}{J_S} \cdot \left(y_{g,s} - h_s \right) \\ \sigma_{ph2,b} &= \frac{N_{p1}}{A_S} + \frac{M_{sw} + M_{p1}}{J_S} \cdot y_{g,s} \end{aligned} \tag{9}$$

where A_s and J_s are given by eq.(1) and (3) for class 3 sections or become $A_{s,eff}$ and $J_{s,eff}$ for class 4.

4.3 *Phase 3: concrete slab casting*

In the present work the slab is considered to be cast in a single phase; this assumption can be reasonable for simply supported decks spanning 40 to 60 m, where the volume of the slabs is between 130 and 250 m^3.

Slab self-weight gives rise to bending moment M_c and the following stresses $\sigma_{ph3,t}$ and $\sigma_{ph3,b}$ respectively at top and bottom face of steel beam.

$$\begin{aligned} \sigma_{ph3,t} &= \frac{N_{p1}}{A_S} + \frac{M_{sw} + M_{p1} + M_c}{J_S} \cdot \left(y_{g,s} - h_s \right) \\ \sigma_{ph3,b} &= \frac{N_{p1}}{A_S} + \frac{M_{sw} + M_{p1} + M_c}{J_S} \cdot y_{g,s} \end{aligned} \tag{10}$$

where A_s and J_s are given by eq. (1) and (3) for class 3 sections or become $A_{s,eff}$ and $J_{s,eff}$ for class 4.

4.4 *Phase 4: introduction of second prestressing*

As already said, if prestressing is applied in two phases, the second one takes place after concrete slab hardening. Hence, the second-phase prestressing gives rise to axial force N_{p2} and bending moment M_{p2} and the following stresses $\sigma_{ph4,t}$ and $\sigma_{ph4,b}$ respectively at top and bottom face of steel beam.

$$\sigma_{ph4,t} = \frac{N_{p1}}{A_S} + \frac{N_{p2}}{A_0} + \frac{M_{sw} + M_{p1} + M_c}{J_S} \cdot \left(y_{g,s} - h_s\right) + \frac{M_{p2}}{J_0} \cdot \left(y_{g,0} - h_s\right) \quad \sigma_{ph4,b} = \frac{N_{p1}}{A_S} + \frac{N_{p2}}{A_0} + \frac{M_{sw} + M_{p1} + M_c}{J_S} \cdot y_{g,s} + \frac{M_{p2}}{J_0} \cdot y_{g,0} \tag{11}$$

where A_s and J_s are given by eq. (1) and (3), A_0 and J_0 are given by eq. (5) and (7) for class 3 sections.

For class 4 beams, the values $A_{s,eff}$, $J_{s,eff}$, $A_{0,eff}$ and $J_{0,eff}$ should be calculated considering the same ineffective area of the web in the iterative procedure.

4.5 *Phase 5: introduction of permanent and variable loads*

Permanent and variable loads give rise respectively to bending moments M_{g2} and M_q and the following stresses $\sigma_{ph5,t}$ and $\sigma_{ph5,b}$ respectively at top and bottom face of steel beam.

$$\sigma_{ph5,t} = \frac{N_{p1}}{A_S} + \frac{N_{p2}}{A_0} + \frac{M_{sw} + M_{p1} + M_c}{J_S} \cdot \left(y_{g,s} - h_s\right) + \frac{M_{p2} + M_{g2} + M_q}{J_0} \cdot \left(y_{g,0} - h_s\right) \quad \sigma_{ph5,b} = \frac{N_{p1}}{A_S} + \frac{N_{p2}}{A_0} + \frac{M_{sw} + M_{p1} + M_c}{J_S} \cdot y_{g,s} + \frac{M_{p2} + M_{g2} + M_q}{J_0} \cdot y_{g,0} \tag{12}$$

The same considerations given in paragraph 3.5 apply to A_s, J_s, A_0, J_0 and $A_{s,eff}$, $J_{s,eff}$, $A_{0,eff}$ and $J_{0,eff}$.

5 VERIFICATIONS

Main bending verifications can be grouped into two families: Ultimate Limit State (ULS), where plasticity contributions can be used if available, and Serviceability Limit State (SLS) where in Characteristic combination (the most severe) yielding should NOT be reached in any point of the structure.

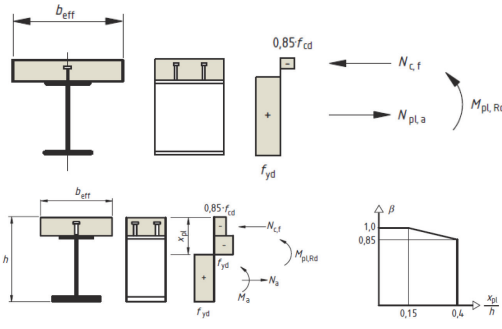

Figure 6. Plastic bending resistance of composite section.

Plastic bending resistance of composite beams at ULS can be calculated according to clause 6.2.1.2 of EN 1994-1-1 (CEN, 2004b) in full shear connection hypothesis (see Fig. 6).

In phases 1, 2 and 3 concrete slab is not present or offers no stiffness contribution, therefore the girder works as a bare steel beam and falls within ductility classes 3 or 4 and, hence, no plasticity can be considered for ULS verification in these phases.

In this situation the introduction of a prestressing force (axial compression) always worsen the steel profile behaviour in class 4.

In phases 4 and 5, the concrete slab is hardened and, then, plasticity can be available at ULS, but elastic verification with composite section in class 3 or 4 should be performed to satisfy SLS Characteristic combination. This verification in phase 5 coincide with the structural check performed on the structure at the end of construction in order to open it to the public.

In addition, it has to be remarked that external prestressing has almost no effect in increasing bending resistance of composite beams at ULS, exactly as happens in externally prestressed concrete beams. In fact, the absence of bond between external tendons and girder does not allow to increase sensibly the stress in the tendon when the section reaches ULS; therefore, the effect of external prestressing can be taken into account only on action side.

6 CASE STUDY

The calculation described in chapter 2 and 3 are applied to a real bridge, that was actually designed and built without prestressing. The bridge was

intended to support a secondary country road (C1 class according to Italian Ministry of Public Works, 1990), whose 9.5 m wide carriageway is presented in Fig. 7.

The deck is 40 m long and 11 m wide, providing 75 cm kerbs on each side to support vehicle restraint systems. The geometry of the midspan cross section is given in Table 1. S355 steel is used for the steel profile (f_{yk} = 355 MPa, E_s = 210 GPa), the slab is realized with f_{ck} = 35 MPa concrete. External prestressing is applied through tendons made of 6" strands (139 mm^2) with E_p = 195 GPa, f_{ptk} = 1860 MPa, f_{p1k} = 1670 MPa and stressed at 1400 MPa at tendon release.

Partial safety factors for materials are taken into account according to EN 1992-1-1 (CEN, 2004a), and EN 1993-1-1 (CEN, 2005), as requested by EN 1994-1-1 (CEN, 2004b): γ_c = 1.5 γ_s = 1.15 and γ_{M0} = 1.0.

Therefore the design yielding stress of the steel profile is f_{yd} = 355 MPa, the design compressive strength of concrete slab is f_{cd} = 23.3 MPa and the design strength of prestressing steel is f_{pd} = 1617 MPa.

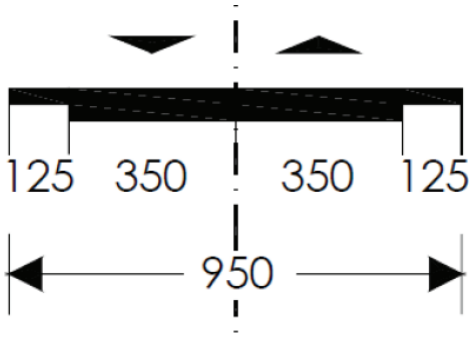

Figure 7. Carriageway type.

Table 1. Geometry of midspan section.

Geometry	Value
	mm
Concrete slab width	5500
Concrete slab depth	350
Transverse inter-axis between longitudinal beams	5500
Top flange width	800
Top flange thickness	25
Steel web width	12
Steel web depth	2960
Bottom flange width	600
Bottom flange thickness	35

The strength ratio between prestressing steel and profile strength is then 1400/355 = 3.94; it could have been 1617/355 = 4.55 in case of bonded prestressing, which is not applicable to this kind of structures. The cost ratio between the same materials in Italy is about 2.50, so replacing one unit of ordinary steel with prestressing one could be cost effective despite the drawbacks outlined in chapter 4.

Two values of the homogenization factor n are considered: n = 1.61E-01 at beginning of service life and n = 6.66E-02 at the end of service life.

Partial safety factors for actions at ULS are taken into account according to EN 1990 (CEN 2002): $\gamma_g = \gamma_q$ = 1.35, γ_p = 1.0.

In this paper local verifications of joints and fatigue verifications are neglected for the sake of simplicity. The contribution to bending resistance of ordinary reinforcement in the concrete slab is also neglected.

Variable loads are applied according to the models described in EN 1991-2 (CEN, 2003). Three notional lanes 3 m wide plus a remaining area of 0.5m are individuated on the carriageway. No pedestrian areas are present on this kind of bridge because of road typology. Only the load combination that leads to the maximum bending moment in midspan is considered in the present work. The total bending moment acting in midspan of the deck due to variable loads is 22230 kNm and 74% of it is supported by the most loaded beam, because of the eccentricities in the transverse position of the notional lanes.

Therefore, the following external actions, derived from the design of the real bridge, are taken into account:

- $M_{sw,k}$ = 1200 kNm
- $M_{c,k}$ = 9625 kNm
- $M_{g2,k}$ = 4400 kNm
- $M_{q,k}$ = 16506 kNm

It can be easily noticed that bending moment acting in midspan of the bridge is almost evenly divided between permanent and variable actions, as generally happens for this bridge typology.

External prestressing is introduced in the model as a concentrated force, corresponding to a couple of tendons (one on the right and one on the left of the web) applied 80 mm above the bottom flange because of external duct encumbrance.

Three different layouts of prestressing are considered in the present work:

1. 100% of prestressing is applied on steel beam in phase 2;
2. 66% of prestressing is applied on steel beam and 33% on composite section;
3. 50% of prestressing is applied on steel beam and 50% on composite section.

These layouts can be obtained both tensioning one part of the tendons in phase 2 and the other

Table 2. N° of strands in each prestressing layout.

Layout 1		Layout 2		Layout 3	
Phase 2	Phase 4	Phase 2	Phase 4	Phase 2	Phase 4
0	0	0	0	0	0
6	0	4	2	3	3
8	0			4	4
10	0	8	4	5	5
12	0			6	6
16	0	12	6	8	8
20	0			10	10
24	0	16	8	12	12
28	0			14	14
32	0	20	10	16	16
36	0	24	12	18	18

one in phase 4, or tensioning all the tendons at a first stress level in phase 2 and then re-tensioning them in phase 4.

Several different amounts of prestressing are taken into account for each layout and are shown in Table 2.

As a conclusion, the verification steps considered in this paper are the following ones:

a. phase 2: ULS of steel profile (class 4): $\gamma_g = \gamma_p = 1.0$;
b. phase 3: ULS of steel profile (class 4): $\gamma_g = 1.35$, $\gamma_p = 1.0$;
c. phase 4: SLS of composite section (class 4), characteristic combination: avoidance of slab cracking due to 2nd prestressing (if applied);
d. phase 5: SLS of composite section (class 4), characteristic combination, beginning of service life (n = 1.61E-01), no yielding should be appreciated in steel, $\sigma_c < 0.6 f_{ck}$ in concrete slab;
e. phase 5: SLS of composite section (class 4), characteristic combination, end of service life (n = 6.66E-02), no yielding should be appreciated in steel, $\sigma_c < 0.6 f_{ck}$ in concrete slab;
f. phase 5: ULS of composite section (plastic calculation according to Fig. 4).

7 RESULTS AND DISCUSSION

7.1 *Results presentation*

The effect of prestressing to the girder is shown in terms of the corresponding reduction in the dimensions of the bottom flange in order to satisfy all the verification (a to f) with the section working at 100% of its bearing capacity in at least one of them, therefore the gain is appreciated in saving of material.

Non dimensional ratios between the stresses in top and bottom flanges of the steel beam, respectively named "S top and S bot" and the yielding stress of steel f_y are calculated and presented in Figures 8–6 as percentages [%].

The non-dimensional ratio between the depth of the ineffective part of the web due to class 4 buckling $h_{non\ eff}$ and the total depth of the web h_w is also calculated and presented in Figures 8–16 as percentages [%].

In every verification step the non-dimensional quantities described above are graphically presented in the following paragraphs in function of the ratio A_p / A_s where A_p is the amount of prestressing area introduced and A_s is the ordinary steel cross section.

The leading verification is "e" (SLS no yielding of bottom flange at end of service life) for small amount of prestressing in all the three different layouts described in chapter 5 but, when a greater amount of prestressing is introduced, it switches to "a" for layout 1 and 2, or to "c" for layout 3, but in any case leads to a non-optimum solution.

Therefore we will focus our attention only on verifications "a", "c", "e" and "f" (ULS).

7.2 *Verification "a"*

Layouts 1 and 2, being the one characterized by the biggest amount of prestressing applied on the steel profile, turn out to be the worst ones for verification "a" as shown in Figures 8 and 9, when $A_p/A_s > 4.85\%$ verification "a" becomes the ruling one for design for layout 1 and when $A_p/A_s > 6.0\%$ in layout 2.

In layout 3 the maximum stress in steel beam reaches only 80% of yielding stress even when total prestressing area is 8% of steel area, because only 50% of prestressing is introduced on steel alone.

It can be also appreciated that without prestressing only 34% of the web is ineffective, whereas about 80% of it becomes ineffective if prestressing is introduced, no matter its intensity or layout.

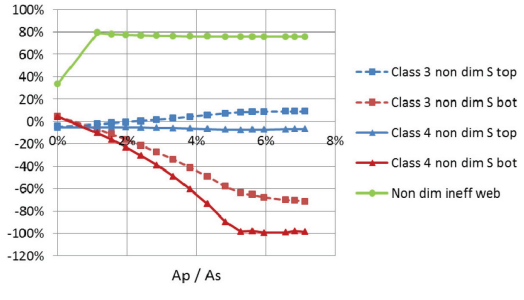

Figure 8. Layout 1: verification "a".

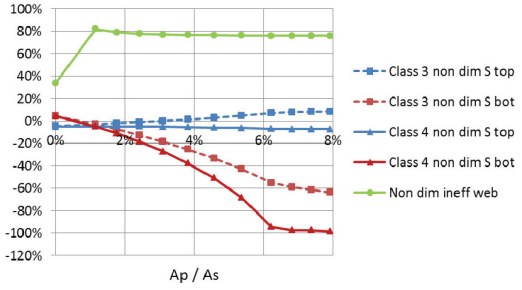

Figure 9. Layout 2: verification "a".

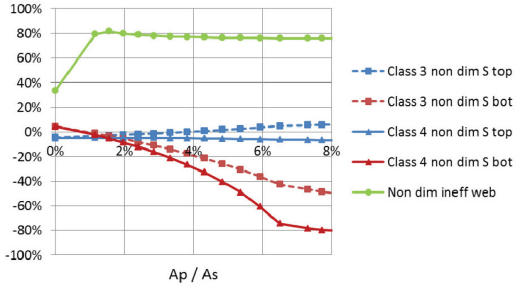

Figure 10. Layout 3: verification "a".

7.3 *Verification "c"*

In phase 3 concrete slab is cast. This phase is never relevant for the verification of the section. In phase 4 second prestressing is introduced and generates tensile stresses in concrete slab.

Non-dimensional ratio between these stresses and concrete mean tensile strength f_{ctm} is calculated, named "S cls", and presented in Figures 11–13 as percentages [%].

Cracking of concrete slab should be avoided in characteristic condition. This verification, called "c" becomes the ruling one in layout 3 for high levels of prestressing when $A_p/A_s > 7\%$.

No tensile stresses are present in phase 4 in layout 1 as nil second prestressing is present.

The results in terms of non dimensional stresses in are plotted in Figures 11 to 13.

7.4 *Verification "e"*

In the proposed cases, because of creep, verification "e" is more severe than verification "d" when related to steel stresses, whereas it is exactly the other way round if we consider compressive stresses in concrete.

All the layouts satisfy the verification $\sigma_c < 0.6 f_{ck}$ in concrete slab and reach $\sigma_s = f_{yd}$ in bottom flange.

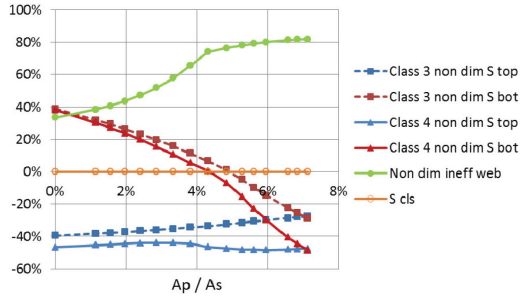

Figure 11. Layout 1: verification "c".

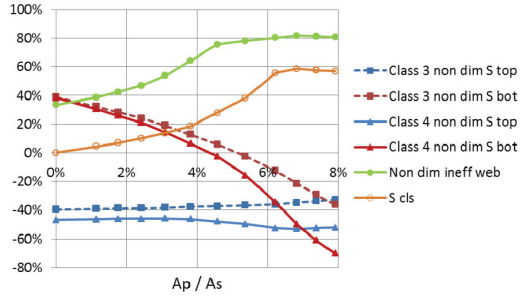

Figure 12. Layout 2: verification "c".

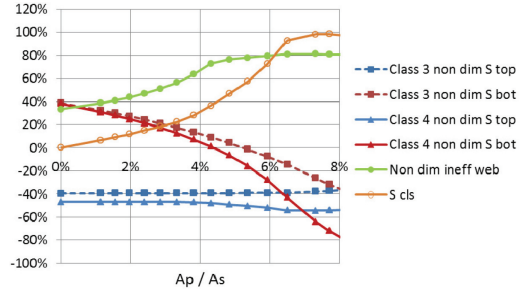

Figure 13. Layout 3: verification "c".

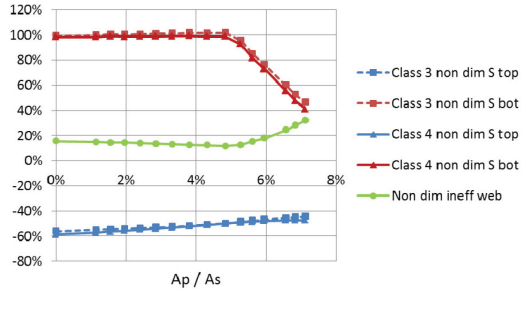

Figure 14. Layout 1: verification "e".

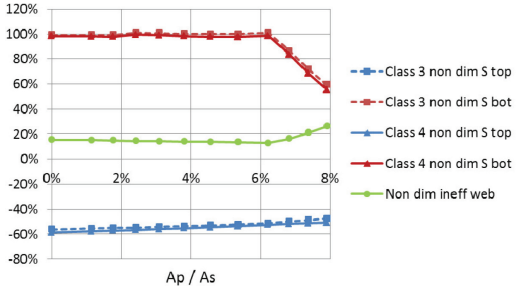

Figure 15. Layout 2: verification "e".

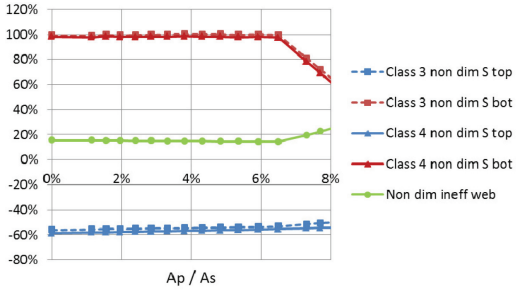

Figure 16. Layout 3: verification "e".

During service life yielding of steel should not be reached in SLS characteristic combination. This verification is thus the leading one for most cases for low and medium levels of prestressing.

Verification "e" leads the design when $A_p/A_s \leq$ 4.85% in layout 1, when $A_p/A_s \leq$ 6.2% in layout 2 and when $A_p/A_s \leq$ 4.85% in layout 3; then verification "a" becomes dominant.

8 COST-BENEFIT ANALYSIS

The cost benefit analysis that follows the results presented above is based on the cost of prestressing steel and ordinary steel given annually by Piemonte Regional Authority for the public civil engineering works. The cost of prestressing is estimated in 9.1 €/kg of tendon whereas ordinary S355 steel is valued 3.7 €/kg; both costs comprehend the complete working process up to opening of the infrastructure to traffic; prestressing cost takes into account the cost of all the devices functional to the use of prestressing technology such as anchoring heads, ducts, grouting, deviators, etc.

Different costs can be obtained in different geographical locations and in function of the quantities purchased, but the ratio between the two costs (about 2.5) is considered by the authors a good standard in Italy.

The economic gain is calculated as the difference between the cost of the prestressed structure and the cost of the non prestressed structure normalized on the cost of the non prestressed one.

The following pictures show, for the three different prestressing layouts, the steel profile cross section reduction and the corresponding economic gain in function of the A_p/A_s ratio, where A_p is the amount of prestressing tendon area and A_s is the ordinary steel cross section.

Both ordinary steel cross section reduction curve and economic gain curve reach a maximum when the leading verification changes in function of the amount of prestressing introduced.

Figure 17 shows that if prestressing is applied completely in phase 2 on steel cross section the maximum gain is 7.4% (17% steel cross section reduction) and can be achieved when A_p/A_s = 4.85%, corresponding to 22 strands. If more prestressing is added the leading verification switches from "e" to "a" as the bottom flange becomes too compressed in phase 2 because of prestressing. Any additional prestressing is, therefore, useless.

Figure 18 shows that if prestressing is applied 66% in phase 2 on steel cross section and 33% in phase 4 on composite cross section, the maximum gain is 9.1% (21% steel cross section reduction) and can be achieved when A_p/A_s = 6.2%, corresponding to 18+9 strands. If more prestressing is added the leading verification switches from "e" to "a" as the bottom flange becomes too compressed in phase 2 because of prestressing. Any additional prestressing is, therefore, useless.

Finally, it can be highlighted that the best results are achieved when prestressing is split 50% in phase 2 and 50% in phase 4, as shown in Figure 19. In this case, the maximum gain is 9.2% (22% steel cross section reduction) and can be achieved when A_p/A_s = 6.5%, corresponding to 14+14 strands.

The bottom flange of the steel beam can be reduced from the original size of 600 × 35 mm^2 (without prestressing) to 220 × 20 mm^2. If more prestressing is added the leading verification

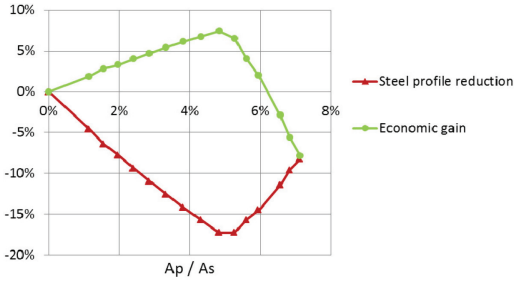

Figure 17. Prestressing applied 100% on steel beam in phase 2.

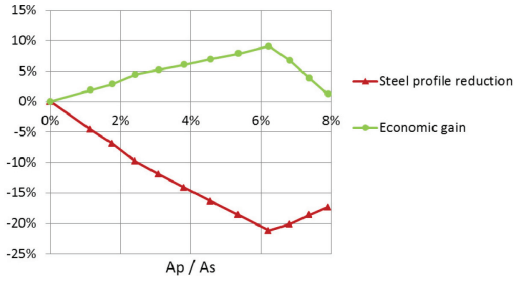

Figure 18. Prestressing applied 66% on steel beam in phase 2 and 33% on composite beam in phase 4.

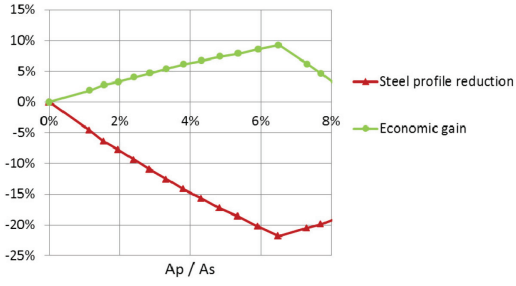

Figure 19. Prestressing applied 50% on steel beam in phase 2 and 50% on composite beam in phase 4.

switches from "e" to "c" as the concrete slab estrados cracks in phase 4 because of prestressing.

9 CONCLUSIONS

The application of external prestressing to simply supported composite bridge beams can be convenient from an economic point of view; in fact the reduction in size the bottom flange of the steel beam is more than sufficient to pay the cost of prestressing and, hence, achieve money saving.

The best solution is achieved when ½ of the prestressing force is introduced on the steel girder before concreting the slab and ½ is introduced after hardening of the concrete slab.

The cost reduction can reach 9% considering the cost of materials estimated for Public Works in Italy.

Grounding on this positive result, a future development of the present research can be the cost benefit evaluation of the introduction of prestressing in continuous decks.

The authors are preparing a new work dealing with crack control of continuous composite bridge girders, where the introduction of prestressing is analyzed as a method to avoid cracking of the slab in negative bending moment zones in combination with a proper scheduling of slab casting sequence.

External prestressing of composite continuous girders can reduce the amount of reinforcing steel placed in the slab and increase the structure's durability avoiding cracks; moreover, it can be used to decrease the amount of ordinary steel as seen in this work.

ACKNOWLEDGMENTS

This work is part of the activity developed by its coauthors within the framework of Task Group T2.6 of the Fédération Internationale du Béton (*fib*).

REFERENCES

CEN (2002), EN 1990. Eurocode—Basis of structural design. Brussels (BE).

CEN (2003), EN 1991-2. Eurocode 1: Actions on structures—Part 2: Traffic loads on bridges. Brussels (BE).

CEN (2004a), EN 1992-1-1. Eurocode 2: Design of concrete structures—Part 1-1: General rules and rules for buildings. Brussels (BE).

CEN (2004b), EN 1994-1-1. Eurocode 4: Design of composite steel and concrete structures—Part 1-1: General rules and rules for buildings. Brussels (BE).

CEN (2005), EN 1993-1-1. Eurocode 3: Design of steel structures—Part 1-1: General rules and rules for buildings. Brussels (BE).

Chen, S. 2005, *Experimental study of prestressed steel–concrete composite beams with external tendons for negative moments*, Journal of Constructional Steel Research, 61, 1613–1630.

Deng, Y. 2012, *Efficient Prestressed Concrete-Steel Composite Girder for Medium-Span Bridges*, Ph.D. Dissertation, University of Nebraska-Lincoln (available online at http://digitalcommons.unl.edu/constructiondiss/9/; accessed on 08/20/15).

Deng, Y. & Morcous G. 2013, *Efficient Prestressed Concrete-Steel Composite Girder for Medium-Span Bridges. II: Finite-Element Analysis and Experimental Investigation*, ASCE Journal of Bridge Engineering, 18(12), 1358–1372.

Deng, Y. & Morcous G. 2013, *Efficient Prestressed Concrete-Steel Composite Girder for Medium-Span Bridges. I: System Description and Design*, ASCE Journal of Bridge Engineering, 18(12), 1347–1357.

Hueste, M.B.D., Mander, J.B, Parkar A.S. 2012, *Continuous prestressed concrete girder bridges—volume 1: literature review and preliminary designs*. Report 0-6651-1, Project 0-6651, Project Title: Continuous Prestressed Concrete Girder Bridges, Texas Transportation Institute, College Station, Texas (available online at http://d2dtl5nnlpfr0r.cloudfront.net/tti.tamu.edu/documents/0-6651-1.pdf, accessed on 08/25/15).

Italian Ministry of Public Works (1990). Update of the technical norms for design, building and testing of road bridges. Ministerial Decree of 4 May 1990. Rome (IT). (*in Italian*).

Buckling and effect of bracings

This page intentionally left blank

Recent Progress in Steel and Composite Structures – Giżejowski et al. (Eds)
© 2016 Taylor & Francis Group, London, ISBN 978-1-138-02946-0

Diagonal bracing members of lattice towers—analytical versus experimental studies

J. Szafran
Department of Structural Mechanics, Chair of Reliability of Structures, Faculty of Civil Engineering, Architecture and Environmental Engineering, Łódź University of Technology, Łódź, Poland

K. Rykaluk
The Faculty of Environmental Engineering and Geodesy, Wrocław University of Environmental and Life Sciences, Wrocław, Poland

ABSTRACT: The main aim of this paper is to present the results of a full-scale experiment performed on a 40 m telecommunication tower under breaking load. The emphasis is on the behaviour of the diagonal bracing members made with using hot rolled angle sections. Analysed lattice structure has the X type bracing system and the theoretical assumptions of the axial forces distribution in bracing elements are presented and compared to the experimental data. Observation of the failure mechanism enriched with stress analysis lead to the conclusion that reliability of the considered tower depends on bearing capacity of the legs.

1 INTRODUCTION

Telecommunication structures (Rykaluk, 2004 & Smith, 2007) are often subjects in many research works, various experimental tests, and highly computerized analyses nowadays. This is caused by the fact that the extension of the existing telecommunication systems, introduction of new services, and construction of new network infrastructure cause the need for fulfilling new, unprecedented requirements. Engineering structures, such as masts and towers of various types, are subjected to complex analyses with the aim of both improving their parameters and making their construction economically viable to mobile network operators. The article includes results collected by the authors during a full-scale experimental test on a lattice telecommunication tower. It is entirely devoted to a behaviour analysis of diagonal bracing members under breaking load. In the analyzed case, the structure's diagonal bracing members were made using angle sections.

Individual steel elements made with hot-rolled L-sections are used in numerous engineering structures (such as plane and space trusses), various telecommunication structures (towers, masts), or transmission towers. Single L-sections are also used as truss elements for multiple struts. They are popular because of easiness of attaching them to other structural members. They are almost always connected eccentrically at their ends. In most practical applications, angles are loaded through one leg only thus introducing eccentricity with respect to the centre of the cross section. At the same time restraining moments at the ends of the member are also present due to the flexural rigidity of the connected elements. In a rational design philosophy, the detrimental effect of the end eccentricity and the advantageous effect on the compression capacity of the end restraint of angle members should be addressed (Galambos, 1998). Taking the above into consideration, it can be stated that designing such steel elements should be based on knowledge regarding their behaviour under breaking load. Parameters like asymmetry of cross sections and eccentric loading along with end restraint should also be taken into account. Galambos in (Galambos, 1998) indicates that end eccentricities cause biaxial flexural deformation of the strut at any given load, therefore the main research challenge for this case is load-deformation response.

The difficulties caused when L-section type elements are used in practical applications brought many research projects devoted to angle steel members. One of the first efforts was one in which an analytical computational approach allowing for determination of elastic capacity of eccentrically connected single angle members (Culver, 1966). In another piece of work (Chan & Cho, 2008), a practical second-order analysis and design method for trusses composed of L-sections were

shown. The authors succeeded at modelling semi–rigid connections (for one or two bolts) with flexible gusset plates as well as member imperfections and load eccentricity. The proposed method was validated by laboratory tests of trusses using single angle members of slenderness ratio of about 150. Finite Element Method analyses were also widely used in works on susceptibility and deformation of L-sections. A paper published by Lee & McClure (Lee & McClure, 2005) constitutes an example of a complex, computational analysis. They have analysed failures of simply supported beam structures of different lengths and slenderness ratios under elastoplastic large deformations. A generalized interpolation scheme for an isoparametric formulation of three-dimensional beam finite elements and a numerical procedure for large deformation were proposed. The work of (Prasad Rao & Kalyanaraman 2001) is fully devoted to non-linear analyses of angle compression members and single panels of angle planar as well as three dimensional lattice frames. The analytical models were calibrated according to the with tests results. Parametric studies were performed to evaluate the forces in the redundants. The results were compared to the standards provisions and recommendations.

Utilization of eccentrically connected angle section members is common for transmission and telecommunication towers. Work of Alberamani et al. (Albermani et al., 2009) wass devoted to creation of a numerical model which allowed for prediction of transmission tower failure. A pushover test of a single, 10 meter transmission tower section consisting of angle beams with typical eccentric connections in order to depict a phenomenon of large deformations was a part of publication of (Lee & McClure, 2007). The numerical assumptions were verified by a comparison with the results obtained during the experiment. Bracing systems of the transmission towers were studied by (Albermani et al., 2004). Experimental studies were taken into account using a tower sub-structure assembly under two types of loading that was strengthened with a variety of diaphragm bracings. Issue of corrosion and its impact on L-section elements is tackled in work (Beaulieu L.V. et al., 2010). The article provided data on the structural behaviour of corroded steel angle members under compressive load. The influence of corrosion on compressive capacity was compared using analytical methods accounting for weight loss.

This paper is fully devoted to presentation of experimental results taken in a full-scale pushover test, elaboration on the obtained data, and formulation of the conclusions. All presented information are dedicated for observation of the behaviour of the L-sections under ultimate load.

2 STANDARD CARRYING CAPACITY OF THE ANGLES SECTIONS

A definition of carrying capacity based on standards (Eurocode 3, 2008) for diagonal bracing members made with L-sections was described in work (Rykaluk, 2015). The verification of buckling resistance of the compressed members in the type X bracing pattern (single, hot-rolled L-section bracings) which are continuous at the intersection locations, is essential for carrying capacity evaluation of such a system. It is commonly known that bearing capacity under tension in elements of this type is greater than buckling resistance. X pattern diagonal bracing system is commonly used in lattice spatial structures due to an assumption that elements under critical load work under tension and compression (interchangeably in one X system).

According to conclusions in point 6.3.1 a of standards (Eurocode 3, 2008), the definition can be carried out using a simplified procedure included in appendices G and H. In case of a bar compressed axially, the buckling resistance should be verified according to standard (Eurocode 3, 2005), that with the equations:

– when the cross section of the member is of class 1, 2, or 3:

$$N_{b,Rd} = \chi \frac{A \cdot f_y}{\gamma_{M1}}, \tag{1}$$

– when the cross section of the member is of class 4:

$$N_{b,Rd} = \chi \frac{A_{eff} f_y}{\gamma_{M1}}, \tag{2}$$

According to remark N23 to the point 6.3.1.4 of standard (Eurokod 3, 2005), in case of elements made with hot rolled angle sections the torsional and torsional-flexural stability can be not verified.

The reduction factor for the relevant buckling mode χ and buckling parameter ϕ are determined with the mentioned simplified procedure based on effective slenderness ratio λ_{eff} calculated in the following equation:

$$\lambda_{eff} = k \cdot \lambda_r, \tag{3}$$

where $\lambda_r = \lambda/\lambda_1$ – non—dimensional slenderness ratio, $\lambda = L_{d,j}/i_j$ - real slenderness ratio in relation to j inertia axis of the cross-section, which should not be greater than 180 (in order to prevent bar's vibrations during wind gusts and bar's damage of local bending caused by human weight), $L_{d,j}$-buckling

length of a member on a surface perpendicular to j axis, $\lambda = 93{,}9\varepsilon$ - comparative slenderness ratio, *k*-effective slenderness factor of diagonal bracing members is defined in table G.2(a) of standard (Eurocode 3, 2008) depending on boundary conditions.

Coefficient *k* takes the same value for type X bracings which are directly connected at each of the ends to a leg using one or two bolts, or by welds. It is calculated according to the formula appropriate for buckling direction as in Table 1.

As already given in explanation regarding formula (3), the buckling length $L_{d,j}$ has to be determined in three possible directions referring the axes: diagonal v-v, perpendicular to the wall y-y, and parallel to the wall z-z. In case of L-sections, the default buckling direction was assumed the one regarding the least inertia axis v-v.

If the layout of the legs is not parallel, the individual wall segments assume a trapezoid shape and the intersection centre F divides every of the bracing members into two parts of lengths $L_{d,1}$ and $L_{d,2}$ as it is presented in Figure 1.

The rules for buckling length determination in the appropriate direction are laid out in point H.3 of the standard (Eurocode 3, 2008). The lengths depend on the static scheme and the secondary bracing (if exists).

Table 1. Definition of the effective slenderness factor k.

Buckling direction perpendicular to L-section axis	Definition of k
v-v	$0{,}7 + 0{,}35/\lambda_{r,v}$
y-y	$0{,}7 + 0{,}40/\lambda_{r,y}$
z-z	$0{,}7 + 0{,}40/\lambda_{r,z}$

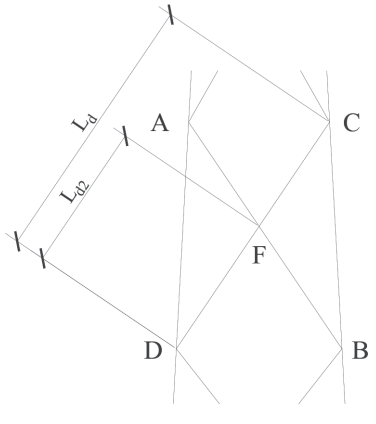

Figure 1. Standard description of the bracing members buckling length.

3 EXPERIMENTAL FULL-SCALE TEST

The experiment was carried out in December, 2014. A controlled destruction of a 40 meter, lattice telecommunication tower was performed taking into consideration several objectives:

– the identification of the failure mechanism of the tower members with particular regard to the diagonal bracing element behaviour,
– the measurements of strains with electric resistance strain gauges placed on diagonal bracing elements of the spatial truss,
– and the comparison of the obtained results against the descriptions and assumptions according to EC3 standard.

3.1 *Structure description*

The tower body was manufactured as a three-dimensional truss of a triangular cross-section and height of 40.0 meters divided into seven sections. Its upper part was of a triangular cross-section and the bottom part (up to 34th meter) formed a pyramid frustum with constant 5% convergence (Fig. 2).

The centreline dimension was 4.90 m at its base and 1.50 m at its top. The leg members in each section consisted of round solid bars, and bracing elements of hot-rolled symmetrical and nonsymmetrical angle sections. Diagonal bracing system of the tower was of type X. The bracing elements were continuous in structure and the joints at their intersections were made with a spacer and a single bolt. Their connections with tower legs were realized with gusset plates and bolts, two for a node (see Fig. 3).

The profiles of particular elements of the tower are presented in Table 2 below:

3.2 *Experimental site, additional elements and equipment*

One of the most important part of the test was proper selection of the experimental site that would fulfil all the specific requirements. Such a place had to be characterized with a set of properties where one of the most important was sufficient area to maintain safe distance between the tested object, electronic equipment, and machinery. Scheme of the test site of the performed experiment is presented in Figure 4. The distance between the tower and the towing truck, the height of placement of the steel diaphragm, as well as points (labelled A, B, and C), which were subjected to geodetic measurements of displacements during the test, are presented.

The basic idea of the experiment was to carry out a pushover test with a steel line attached to the tower at one of its ends (at the height causing

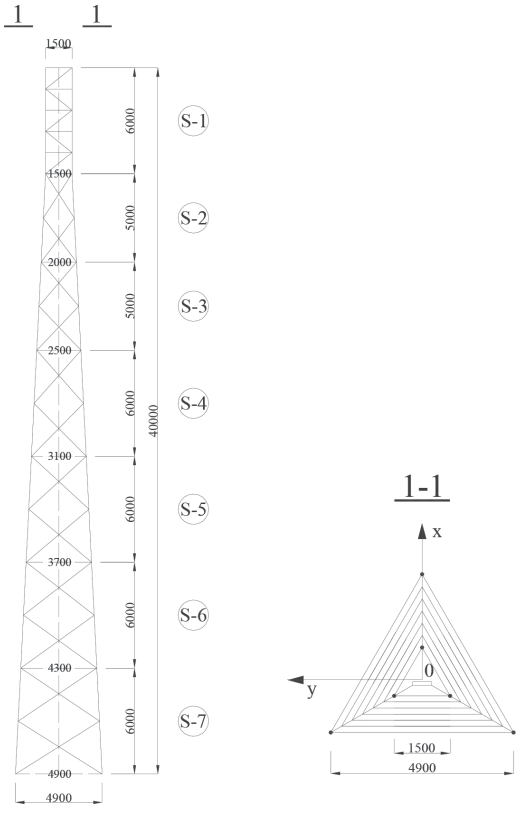

Figure 2. Static scheme of the tower—unit is mm.

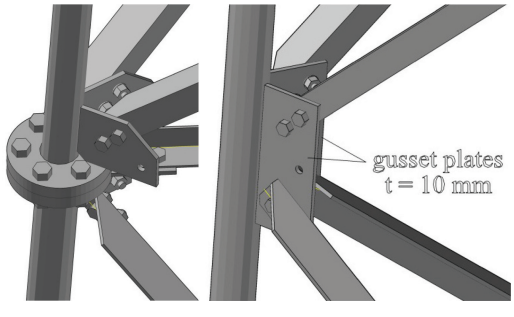

Figure 3. Connections of diagonal bracing members with legs.

maximal axial forces in bottom legs of the tower) pulled by a towing truck. In order to deliver the load to the tower structure provided by the line pulled by a towing machine, an adequate steel diaphragm was produced. The main role of adding that additional element to the structure was creating uniform load at 3 nodes of one cross section of the tower. The diaphragm during experiment is presented in Figure 5.

Table 2. Selected tower element profiles, all dimensions are given in mm.

Section	Legs	Diagonal bracings
S-1	Ø 65	$\llcorner 60 \times 60 \times 5$
S-2	Ø 65	$\llcorner 60 \times 60 \times 5$
S-3	Ø 80	$\llcorner 60 \times 60 \times 6$
S-4	Ø 80	$\llcorner 90 \times 60 \times 8$
S-5	Ø 90	$\llcorner 90 \times 60 \times 8$ $\llcorner 100 \times 75 \times 8$
S-6	Ø 90	$\llcorner 100 \times 75 \times 8$
S-7	Ø 100	$\llcorner 120 \times 80 \times 8$

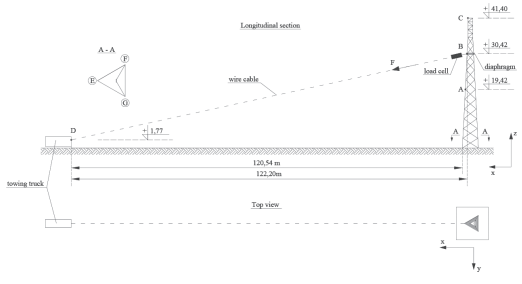

Figure 4. Scheme of the test site of the experiment.

Strain measurements were taken with electric resistance strain gauges and the layout of particular measuring points for the diagonal bracing members of the tower's lowest section is presented in Figure 6.

Every point had four independent strain gauges placed opposite to each other. Their layout of the cross-sections of diagonal bracing members, as well as the location with respect to the acting force, is shown in Figure 7.

Legs of the tower were mounted to the special kind of foundation that was constructed with using steel frame and concrete slabs. The process of design and realization of the part of the structure was performed in such a way-as an intention-that should lead to destruction of the structural members of the tower rather than to stability loss of the foundation. A steel, 9 ton frame constituted the primary foundation element situated on pavement slabs of dimensions $3.0 \times 1.5 \times 0.15$ meters. The slabs, in turn, were placed on a layer of consolidated, compressed sand of thickness of about 0.50 meters. At the level of the frame, the anchoring elements were placed to attach the tower, and then transfer the load from the tower to the frame and subsequently to the foundation slabs, and finally to the ground. The frame was loaded with 54 main slabs (three identical layers) and also additional slabs as it is presented in Figure 8. Summing

Figure 5. Steel welded diaphragm mounted on the tower.

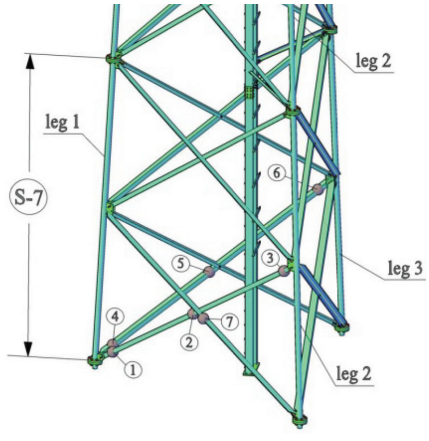

Figure 6. Arrangement of measuring points in section S-7.

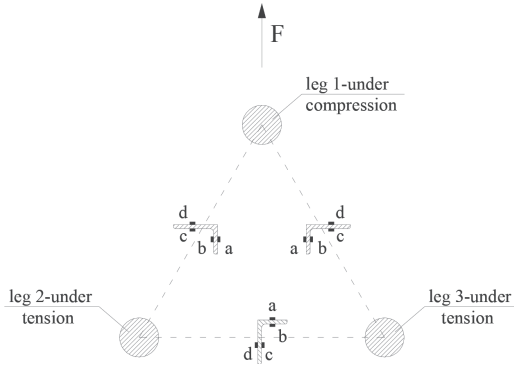

Figure 7. Strain gauges labelling in relation to acting force F.

up, the total mass of the foundation amounted to around 169 tons.

3.3 *Material properties*

In order to determine the mechanical properties of the structural steel, tensile testing of 6 sample L-sections was performed according to standard (EN ISO 6892-1, 2009). Mechanical properties obtained during the laboratory tests are listed in Table 3.

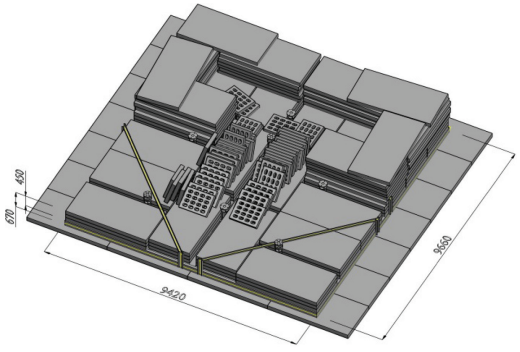

Figure 8. Scheme of the foundation used during the test.

Table 3. Mechanical properties of structural steel.

Mechanical properties	Values
Young's modulus	202,0 GPa
Nominal yield strength	294,2 MPa
Tensile strength	399,8 MPa

4 EXPERIMENTAL RESULTS

4.1 *Failure mechanism and failure models*

One of the goals of the experiment was the observation of failure mechanism of the structure under ultimate external load. In order to attain this goal, the test was recorded with high definition cameras placed within the body of the tower and at various locations over the experimental site. The failure mechanism analysis was assumed to show which of the elements would give in to the destruction first: leg(s) of the tower, bracing member(s), weld(s), tensioned bolts, flanges or gusset plates. The video presenting the failure mechanism is available online and can be accessed via link at https://www.youtube.com/watch?v = FbIGKRy5vEI&feature = youtu.be.

The buckling of the leg in section S-7 (base of the tower) was the first element of the tower to get destroyed. It is worth noting that the buckling of the leg occurred perpendicularly to the loading force. Plastic hinges occurred at the centres of bracing panels: at ¼ and ¾ of section's span. Moreover, the joint connecting sections S-7 and S-6 remained rigid. The leg after buckling with visible plastic deformation is presented in Figure 9.

As a result of the leg buckling at section S-7, joints connecting diagonal bracings with the legs were subjected to vertical displacement towards foundations of the tower. An eccentric connection of gusset plates and angles caused strain at bracing members' ends. It should be highlighted that rupture in the cross-sections around the bolt holes did not take place due to considerable dimensions of L-sections in this segment of the tower ($L120 \times 80 \times 8$). The bolts themselves, $2 \times M16 \times 45$ (8.8), were not damaged either. The greatest deformation could be noticed on gusset plates (thickness 10 mm) at the half of the leg's length. They were twisted by bracing members that were during the buckling of the leg. It is obvious that the method of connection (two screws in a rigid way) also played a part. The deformed shape of the gusset plate is presented in Figure 10 below. During the inventory control of the construction after the experiment, no damage of either bolts or joints was noted.

Figure 9. Buckling of the leg in section S-7 of the tested tower—general (left) and detailed (right).

Figure 10. Deformed gusset plates in middle span of the leg in the lowest section.

4.2 *Stresses in analyzed bracing members*

The selection of bracing members, where strain measurements were taken during the experiment, was made after a static analysis of the tower which incorporated Finite Element Method. An ideal construction layout has been used, that is, one in which impact of actual geometric imperfections, material nonlinearity, slippage of the bolts, and etc., were not taken into account. As the result, the axial forces in bracing members of type X system were obtained. The results of static analysis are presented in a graphical form in Figure 11. Compression axial forces are denoted in blue and tension forces are marked yellow. The load sate was obviously equal to the one during the experiment.

The goal of the experiment was strain determination in the compressed L-section members. Observation of this particular elements was determined due to the fact that compressed elements are the most important one in the X bracing system carrying capacity estimation.

Locations of measurement points on the compressed bracing members were realized in a specific way to observe the change in strains (stresses) as a function of external load. The beginning, ending, and middle (near intersection with the second braicing member, which should be subjected to tension) points of the elements were under the observation.

The results for stresses in measuring points 1, 2, and 3 are presented in Figure 12 as a function of force of the external load.

Only two strain gauge readings were registered in measurement point 1. It can be noticed that some differences in results are apparent for L-section longer panels. Tensile stresses were present in the first panel whereas compression stresses in the second one which definitely indicates the bend-

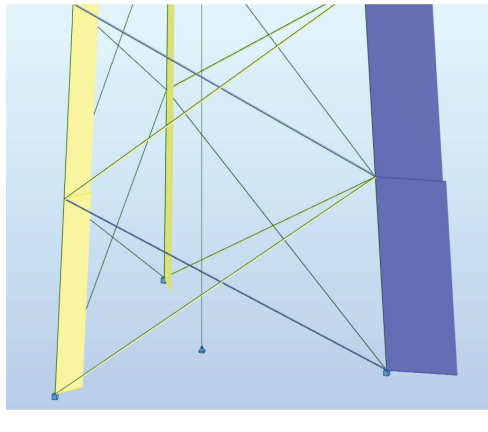

Figure 11. Axial forces distribution in the section S-7 after typical static analysis.

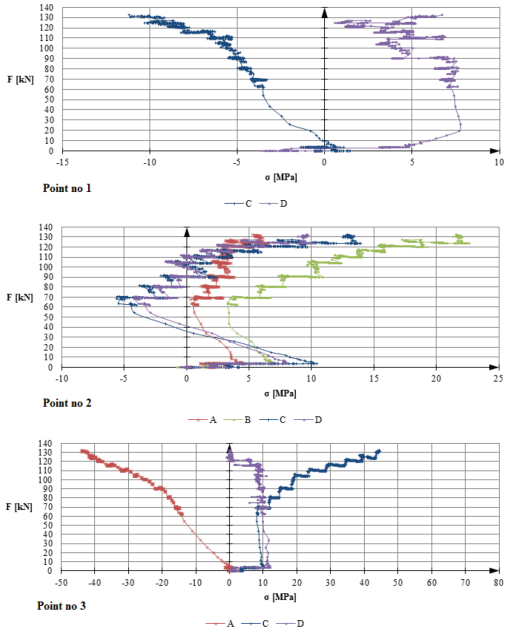

Figure 12. Stresses in measuring points no 1 (top), no 2 (middle) and no 3 (bottom).

ing of the element. It confirms failure mechanism observations and, most of all, the effect of eccentric attachment of the element. Stress values were not equal to the absolute value. In point number 2 (at the middle of the element) they reached about 10 MPa with the value of the external load equal about 5 kN in the first phase of the test. The value of the external load was so small that it could be stated that the stresses was caused by the eccentric connections of the member as well as the micro geometric imperfections. The tension stresses decreased along with the increase in the force in the pulled line until a moment where two strain gauges indicated tensile stresses. After a certain load had been reached, 90 kN in this case, all readings showed tension in this measurement point, what pointed to the fact that the impact of initial geometrical imperfections was essential here. As shown in point 4.1 of this work, ends of the elements got bended with load equal to about 130 kN which could be noticed on the stresses graph for measurement point 3. For the opposing surfaces of angle section panels, the stresses were equal in value but different in sign which further indicates the bending of the cross-section of the memeber.

Stresses in measurement point 7 are presented in Figure 13. The location of the point was analogical to measurement point 2 - on the second element of the bracing X type system. This member was assumed as one that should be under tension. It could be stated that the element in this particular cross-section was entirely under tension and maximum stresses reached about 49 MPa.

Stress graphs presented in Figure 14 for measurement points no 4, 5, and 6. The points were located analogically to points 1, 2, 3: on the element which was assumed under compression. In point no 4 bending could be observed again and the differences between the part under tension and compression increased with an increase in external load value. An analogy to point number 1 is rather obvious especially when the fact that we can observe readings obtained for all four strain gauges for point 4. The compression forces at strain gauges A and B decreased in value considerably when the maximal external load value (132.5 kN in this particular case) was being reached. At the middle of the element (measurement point 5) we

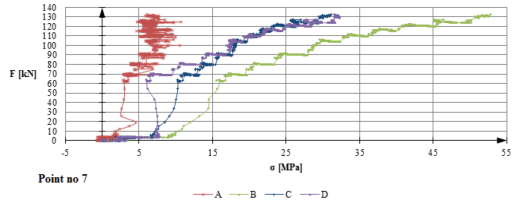

Figure 13. Stresses for measuring point no 7.

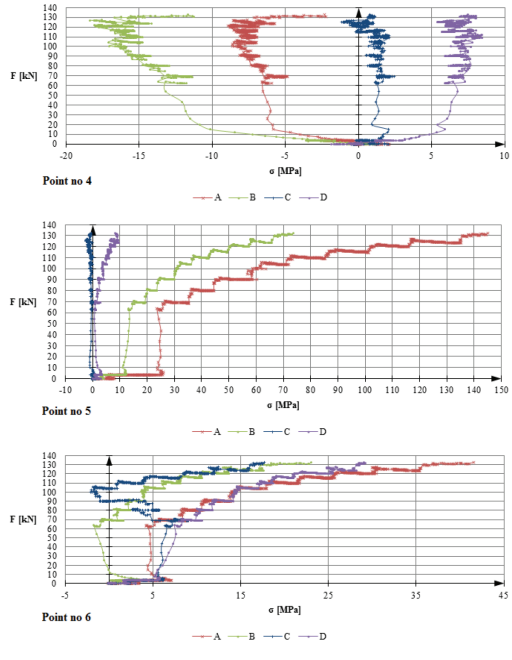

Figure 14. Stresses for measuring points no 4 (top), no 5 (middle) and no 6 (bottom).

have noted tension stresses again but their range was far greater (about 145 MPa). Comparing the results for points 3 and 6, the bending effect is not so visible for measuring point 6.

5 CONCLUSIONS

The results presented in the article allow for drawing the following conclusions:

- It can be stated that the reliability of the tower structure, which was subjected to a pushover test, was without doubt dependent on bearing capacity of its legs. As presented above, the first symptom of failure of the structure was buckling of the leg at a bottom section of the tower.
- The theoretical assumptions for diagonal bracings of X pattern made with angle sections were not justified in the analyzed case. The results of stresses which were registered in the observed elements were tension stresses in most cases. It can be therefore stated that in case of real structural systems, which are characterized with nonlinearities including geometric ones (in both macro and micro scale) as well as material ones, their accumulated effect can considerably influence the results of analyses.
- Eccentric connections of bracing elements to gusset plates utilizing two bolts caused bending at the elements' ends which could also be noticed during the analysis of stresses.
- The research experiment which was carried out does not allow for analysis of diagonal bracing members axial forces. In order to make the analysis possible, a greater number of strain gauges ought to be used for every measurement point. An optimal solution would be observation of strains on the whole perimeter of the element's cross-section.
- Numerical analyses carried out during design process of such structural system made with L-sections should incorporate shell or volume finite elements rather than simple 2 nodded beam elements. As indicated in the article, reflecting the actual work of an element using the simplest numerical model is rather impossible.

ACKNOWLEDGEMENTS

The first author would like to express his deepest gratitude to T-Mobile Poland S.A. whose financial support made this project possible. He would also like to express his gratefulness to Mr. Michał Wójcicki. Acknowledgements should be given to Professor Marcin Kaminski and Jerzy Pakuła, PhD at Lodz University of Technology, Jan Gierczak, PhD at Wrocław University of Technology.

REFERENCES

Albermani, F., Kitipornchai, S., Chan, R.W.K. 2009, "Failure analysis of transmission towers", *Engineering Failure Analysis* 16: 1922–1928.

Albermani, F., Mahedran, M., Kitipornchai, S. 2004, "Upgrading of transmission towers using diaphragm bracing system", *Engineering Structures* 26: 735–744.

Beaulieu, L.V., Legerou, F., Langlois, S. 2010," Compression strength of corroded steel angle members", *Journal of Constructional Steel Research* 66: 1366–1373.

Chan, S.L., Cho, S.H. 2008, "Second—order analysis and design of angle trusses. Part I: Elastic analysis and design", *Engineering Structures* 30: 616–625.

Culver, C.G. 1966, "Exact solution of the biaxial bending equations", *ASCE Journal of Structural Engineering* 92, No. ST2: 63–83.

EN ISO 6892-1 2009, *Metallic materials—Tensile testing—Part 1: Method of test at the room temperature*. European Committee for Standardization, Brussels.

Eurocode 3, 2005, *Design of steel structures—Part 1-1:General rules and rules for buildings*. European Committee for Standardization, Brussels.

Eurocode 3, 2008, *Design of steel structures—Part 3–1:Towers, masts and chimneys—Towers and masts*. European Committee for Standardization, Brussels.

Galambos, T.V. 1998, *Guide to stability design criteria for metal structures*, John Wiley & Son, New York, USA.

Lee, P.S., McClure, G. 2006, "A general three—dimensional L-section beam finite element for elastoplastic large deformation analysis", *Computers and Structures* 84: 215–229.

Lee, P.S., McClure, G. 2007, "Elastoplastic large deformation analysis of lattice tower structure and comparison with full-scale tests", *Journal of Constructional Steel Research* 63: 709–717.

Prasad Rao, N., Kalyanaraman, V. 2001,"Non-linear behavior of lattice panels of angle towers", *Journal of Constructional Steel Research* 63: 709–717.

Rykaluk K. 2004, *Steel structures. Chimneys, towers, masts (in Polish)*. Oficyna Wydawnicza Politechniki Wrocławskiej, Wrocław.

Rykaluk K. 2015, "Długości wyboczeniowe krzyżulca wieży w skratowaniu typu X", *Inżynieria i Budownictwo* 4: 201–204 (in Polish).

Smith, B.W. 2007, *Communication structures*. Thomas Telford Publishing, London.

Recent Progress in Steel and Composite Structures – Giżejowski et al. (Eds)
© 2016 Taylor & Francis Group, London, ISBN 978-1-138-02946-0

A unified resistance verification of beam-columns not susceptible to LT-buckling

M.A. Gizejowski
Division of Metal Structures, Faculty of Civil Engineering, Warsaw University of Technology, Warsaw, Poland

R.B. Szczerba
Faculty of Civil Engineering, Warsaw University of Technology, Warsaw, Poland

M.D. Gajewski
Department of Strength of Materials and Theory of Elasticity and Plasticity, Faculty of Civil Engineering, Warsaw University of Technology, Warsaw, Poland

ABSTRACT: In this paper, a unified verification method of both the design cross-section resistance and the overall stability of steel structural members not susceptible to lateral-torsional buckling is proposed. The case of combined planar bending about one of the section principal axis (y or z) and axial compression is considered. The unified analytical proposal developed herein is verified by the comparison of its results with those of numerical simulations for beam-columns bent about y-y axis. Therefore, geometrically and materially nonlinear analysis with all the second order effects and geometrical imperfections taken into account (GMNIA is the abbreviation used hereafter) is carried out. Numerical analysis is performed with use of ABAQUS/Standard finite element software in which an appropriate shell modeling technique is utilized. Numerical study is carried out for a chosen hot-rolled section and it includes the influence of relative slenderness ratio of beam-column elements on the buckling resistance. Concluding remarks are drawn and directions of future research are outlined.

1 INTRODUCTION

Load transfer by beam-column elements of steel structural frameworks is characterized by two functions, namely that of the beam (transfer of the action components perpendicular to the axis x-x and/or the member end section internal moments resulting from the continuity of the structural system), and secondly—that of the column (transfer of the action components parallel to the axis x-x and/or the member end section axial force resultants existing because of continuity of the structural system). Regarding the behavior difference between structural members of open sections, like hot rolled or welded I or H sections, acting in isolation or as elements of planar frameworks, two major design situations related to the ultimate limit states may be distinguished:

1. in-plane ultimate limit state of one directional bending and flexural buckling in the same plane as bending,
2. out-of-plane ultimate limit state of flexural-torsional buckling and bending existing in the plane of section greater moment of inertia.

The former situation is relevant to two cases of the behavior of perfect beam-columns, namely referred to bending about their:

a. weaker principal axis in which buckling is confined to the plane of bending and as a result the element is subjected to second-order bending only,
b. stronger principal axis but under the condition of being fully laterally and torsionally restrained at which buckling is possible only in the plane of bending, and as a result the element is subjected to second-order bending only.

If the condition stated at b) above is not fulfilled, a perfect beam-column may buckle prematurely out of the plane of second-order in-plane bending and as a result in the postbuckling range it is subjected to lateral and twist deflections.

The Ayrton-Perry computational model is used in steel Eurocodes (EN 1993) for two extreme cases of buckling strength, namely related to geometrically imperfect columns (F- or T-buckling modes) and to geometrically imperfect beams (LT-buckling mode). The Ayrton-Perry approach is summarized by Stachura & Gizejowski (2015), together

with a proposal of redefinition of the resistance partial factors γ_{M0} and γ_{M1}. Using the Ayrton-Perry approach for beam-columns subjected to in-plane buckling (F-buckling) or out-of-plane torsional-flexural buckling (TF-buckling) yields a quite complicated analytical solution, as explained by Simoes da Silva et al. (2010), so that it would be rather difficult to postulate such an approach for codification purposes. The approach adopted in the resistance evaluation in EN 1993-1-1:2005 for nonzero values of both the axial compressive force and bending moments is therefore of different format that it is summarized in the following section.

2 EUROCODE'S APPROACH TO THE RESISTANCE EVALUATION OF BEAM-COLUMN ELEMENTS

The approach of EN 1993-1-1:2005 is of an additive format and of a general nature since the design resistance criteria deal with compression and biaxial bending about the cross section principal axes.

Three terms of two Eurocode's design criteria are related to the following utilization ratio components: n_{yb} of buckling resistance, m_{yb} of lateral-torsional buckling resistance in bending about the major principal axis and m_{zc} of cross section resistance in bending about the minor principal axis. The nonlinearity of complex buckling resistance of imperfect beam-columns is accounted for by specifying the functions of interaction coefficients k_{ij} applied to moment utilization ratio components, where $i = y, z$; $j = y, z$. For beam-columns considered in this paper, dealing with the second-order bending without lateral-torsional instability, and using redefined resistance partial factors as proposed by Stachura & Gizejowski (2015), one can write down the following: $m_{yb} = m_{yc}$ and $k_{ij} = 0$ for $i \neq j$. Thus, the following relationships hold:

– bending and buckling about the stronger principal axis:

$$\frac{N_{Ed}}{N_{yb,Rd}} + k_{yy}\frac{M_{y,Ed}}{M_{yc,Rd}} = n_{yb} + k_{yy}m_{yc} \leq 1, \tag{1}$$

– bending and buckling about the weaker principal axis:

$$\frac{N_{Ed}}{N_{zb,Rd}} + k_{zz}\frac{M_{z,Ed}}{M_{zc,Rd}} = n_{zb} + k_{zz}m_{zc} \leq 1 \tag{2}$$

where N_{Ed}, $M_{y,Ed}$, $M_{z,Ed}$ are the action effects (internal forces) calculated using LA (linear analysis) or GNA (geometrically nonlinear analysis) for the design load combination considered, $N_{yb,Rd}$, $N_{zb,Rd}$ - design buckling resistances about the stronger and weaker principal axes, respectively y-y and z-z:

$$N_{yb,Rd} = \frac{\chi_{y,d}N_{c,Rk}}{\gamma_{M1}} = \frac{\chi_{y,d}N_{c,Rd}}{\frac{\gamma_{M1}}{\gamma_{M0}}}, \tag{3}$$

$$N_{zb,Rd} = \frac{\chi_{z,d}N_{c,Rk}}{\gamma_{M1}} = \frac{\chi_{z,d}N_{c,Rd}}{\frac{\gamma_{M1}}{\gamma_{M0}}} \tag{4}$$

where $\chi_{y,d}$, $\chi_{z,d}$ – buckling resistance reduction factors about the stronger and weaker principal axes, y-y and z-z respectively, in reference to Stachura & Gizejowski (2015), $M_{yc,Rk}$, $M_{zc,Rk}$ – cross section bending resistances about the stronger and weaker principal axes, respectively y-y and z-z:

Table 1. Interaction factors k_{ij} for in-plane behavior of isolated simply supported elements.

k_{ij}	Cross section class	Stocky elements*: $\overline{\lambda} \leq 0{,}2$	Semi-slender elements*: $0{,}2 < \overline{\lambda} \leq 1{,}0$	Slender elements*: $\overline{\lambda} \geq 1{,}0$
k_{yy}	1 or 2	$C_{my}\left[1+\left(\overline{\lambda}_y - 0.2\right)n_c\right]$	$C_{my}\left[1+\left(\overline{\lambda}_y - 0.2\right)n_{yb}\right]$	$C_{my}\left(1+0.8n_{yb}\right)$
	3 or 4	$C_{my}\left(1+0.6\overline{\lambda}_y n_c\right)$	$C_{my}\left(1+0.6\overline{\lambda}_y n_{yb}\right)$	$C_{my}\left(1+0.6n_{yb}\right)$
k_{zz}	1 or 2	$C_{mz}\left[1-2\left(\overline{\lambda}_z - 0.3\right)n_c\right]$	$C_{mz}\left[1+2\left(\overline{\lambda}_z - 0.3\right)n_{zb}\right]$	$C_{mz}\left(1+1.4n_{zb}\right)$
	3 or 4	$C_{mz}\left(1+0.6\overline{\lambda}_z n_c\right)$	$C_{mz}\left(1+0.6\overline{\lambda}_z n_{zb}\right)$	$C_{mz}\left(1+0.6n_{zb}\right)$

*Notation: $n_c = N_{Ed}/N_{c,Rd}$ – cross section resistance utilization ratio in compression; $n_{yb} = N_{Ed}/N_{yb,Rd}$, $n_{zb} = N_{Ed}/N_{zb,Rd}$ – buckling resistance utilization ratio in compression about y-y and z-z axes, respectively; C_{my}, C_{mz} – equivalent uniform moment distribution factors for buckling about y-y and z-z axes, respectively.

$$M_{yc,Rd} = \frac{M_{yc,Rk}}{\gamma_{M0}}, \quad (5)$$

$$M_{zc,Rd} = \frac{M_{zc,Rk}}{\gamma_{M0}}. \quad (6)$$

Other symbols are the same as used in EN-1993-1-1:2005 and ECCS manual (Simoes da Silva et al. 2010).

The interaction factors k_{ij} for $i = j$ are given in Table 1 for the beam-column in-plane behavior about the principal axes *y-y* and *z-z*, and for both I and H sections, when using the so-called Method 2 that is given in EN 1993-1-1:2005 for the respective buckling resistance check. Interaction resistance criteria were evaluated on the basis of a wide range of computer simulations, see Greiner & Lindner (2006). The Eurocode's Method 1 is not referred to in this paper.

Observation of the structure of Equations (1) and (2) developed for the purpose of codification in EN 1993-1-1:2005, and recommended in the National Annex to PN-EN 1993-1-1:2006 in Poland, leads to the following remarks:

- Interaction equations for stocky beam-columns do not coincide with the cross section resistance interaction equations for cross section classes 1 or 2 (see Table 1 for the values of interaction factors k_{ij}).
- In case of the buckling mode that approximately reproduces the shape of member displaced configuration under bending loading, the equivalent uniform bending distribution factors have to be taken as equal to unity (the amplitude of the buckling mode and the maximum bending displacement are close to each other).
- In case of a complex bending moment diagram, when the amplitude of the buckling mode and the maximum bending displacement are at different points of the element *x-x* axis, the factors C_{my} or C_{mz} are less than one, and the buckling resistance verification according to Equations (1) and (2) needs to be accompanied by an additional verification check of the cross section resistance, using criteria given in EN 1993-1-1:2005.

Gizejowski et al. (2015) studied the behavior of perfect beam-column elements and developed a simple method of unified checking of the buckling resistance. The method involves the second-order moments, so that it use for the practical verification requires the application of the second-order analysis and the knowledge of the point along the member length at which there are the maximum values of load effects (the bending moment only in case of uniform compression). In the following, an effort is made in developing alternative relationships for the in-plane behavior of imperfect beam-column elements. Since the application of the method proposed by Gizejowski et al. (2015) requires the search of maximum second-order moment along the member length, it may be considered time consuming, especially in case of class 4 section members. A method of utilizing the first-order load effects is therefore preferred hereafter over the method utilizing the second-order load effects.

3 SCOPE OF INVESTIGATIONS AND FINITE ELEMENT SIMULATIONS OF THE BEAM-COLUMN BUCKLING RESISTANCE

3.1 *Background to analytical formulation*

The starting point for the analytical formulation is the cross section resistance according to Eurocodes. It is postulated that the buckling strength equations format evolves in such a way that for stocky elements it coincides with that of the Eurocode's cross section resistance. Such an approach requires that the cross section utilization ratio in compression is to be replaced by that of the buckling resistance utilization ratio, and the calibration of interaction factors k_{ij} might be performed on the basis of finite element modeling technique for geometrically imperfect elements. The imperfect geometry is to be taken according to the buckling mode corresponding to an appropriate eigenvalue with the amplitude evaluated according the so-called general method of EN 1993-1-1:2005. The unified ultimate strength criteria might be therefore written down as given in Table 2 hereafter.

3.2 *Beam-column elements considered*

Elements subjected to buckling and bending about *y-y* principal axis are considered in the following. Imperfect beam-columns are made of HEB 300 manufactured from steel grade S235, the section of which is of class 1. Beam-columns considered differ with regard to the boundary conditions and loading. The input data for simulations is the same as adopted by Gizejowski et al. (2015) for perfect beam-columns. Three types of support conditions are dealt with: C (cantilever), S (simply supported) and FH (fixed at one end and hinged at the other end). Details are given in Table 3 hereafter together with the coefficient C_{my} for the first-order bending moment that corresponds to the particular loading situation.

3.3 *Finite element modeling and analysis*

Geometrically and Materially Nonlinear with Imperfections Analysis (GMNIA) is performed for

Table 2. Unified stocky elements alike format of the in-plane ultimate state resistance.

Axis	Section class	Range *	Equation *
y-y	1 or 2	$0 \le n_{yb} \le a_y$	$m_{yc} = 1$
		$a_y < n_{yb} \le 1$	$\frac{n_{yb} - a_y}{1 - a_y} + k_{yy} m_{yc} = 1$
	3 or 4	$0 \le n_{yb} \le 1$	$n_{yb} + k_{yy} m_{yc} = 1$
z-z	1 or 2	$0 \le n_{zb} \le a_z$	$m_{zc} = 1$
		$a_z < n_{zb} \le 1$	$\left(\frac{n_{zb} - a_z}{1 - a_z}\right)^2 + k_{zz} m_{zc} = 1$
	3 or 4	$0 \le n_{zb} \le 1$	$n_{zb} + k_{zz} m_{zc} \le 1$

*Notation: For $\overline{\lambda}_i \le 0.2$ ($i = y, z$), $a_y = 0.5a$ and $a_z = a$ where $a = 1–2 \times A_f / A$ but $a \le 0.5$, $A_f = bt_f$ – flange cross section area.

imperfect beam-columns of different relative slenderness ratios $\overline{\lambda}$ from 0.2 to 2.0 (inclusively).

FE models are constructed with use of linear and Rectangular Shell Finite Elements (RSFE) that are available in the ABAQUS/Standard library. The mesh size was gradually decreased to obtain satisfactory solution convergence at acceptable calculation time. Approximate size of elements is 30 mm. Boundary conditions and loads were applied in reference points RP_i (i = 1,2), located at end sections and linked to edges of shell elements with use of *MPC* option available in ABAQUS/Standard. In order to ensure uniaxial bending (to avoid an influence of torsional instabilities) additional boundary conditions at the web-flange junction are applied for all RSFE nodes along the entire member length.

To solve non-linear boundary value problems of buckling, the theory of moderately large deformations implemented in ABAQUS program is used, and available through an option NLGEOM (Jemiolo & Gajewski 2014, Gizejowski, et al. 2015). The σ-ε characteristic of structural steel is described with use of an elastic-plastic model with isotropic hardening. In the elastic range, Young's modulus E equals to 210 GPa is taken into account. The Poisson's ratio is assumed to be equal to 0.3. In the plastic range, the minimum ductility assumption of EN 1993-1-1:2005 is adopted, concerning the ultimate strength $f_u = 1.1 f_y$ and corresponding to the ultimate strain $\varepsilon_u = 0.15$.

Results of finite element simulations using GMNIA are presented in coordinates m_{yc} and n_{yb}, and they are represented by slenderness dependent interaction curves. The buckling resistance

Table 3. Beam-column elements considered.

Support conditions and loading		End moments ratio	Factor
Scheme	Symbol	$\psi = \frac{M_{y,Ed,\mathrm{supp,min}}}{M_{y,Ed,\mathrm{supp,max}}}$	C_{my}
Cantilever	C	1.0	1.0
Simply	S	1.0	1.0
Supported	S	0.0	0.6
	S	–1.0	0.4
Fixed-hinged	F-H	–0.5	0.4

utilization ratio n_{yb} = 1.0 corresponds to numerically obtained buckling strength reduction factor for the column length corresponding to the considered slenderness ratio, i.e. when the cross section resistance ratio in bending m_{yc} yields the zero value. In all the other cases of n_{yb} that take the value between zero and unity, there is a room for the accommodation of bending moments the value of which can be read from the corresponding interaction curve.

The obtained results may be used for the calibration of interaction factors k_{yy} in the analytical formulation presented in Table 2. Following interaction factor calibration equations hold:

– For the range of n_{yb}: $0.5a_y < n_{yb} \le 1$:

$$k_{yy,FEM} = \frac{1}{m_{yc,FEM}} \left(1 - \frac{n_{yb,FEM} - 0{,}5a_y}{1 - 0{,}5a_y}\right) \qquad (7a)$$

– For the range of n_{yb}: $n_{yb} \le 0.5a_y$:

$$k_{yy,FEM} = 1 \tag{7b}$$

where: a_y is the $n_{yb,FEM}$ coordinate for which $m_{yc,FEM} = 1$.

4 RESULTS OF FINITE ELEMENT SIMULATIONS

4.1 *Cantilever beam-columns*

Results of numerical simulations are presented in Figure 1 by solid lines. Figure 1a shows the interaction curves in coordinates m_{yc} and n_{yb} while Figure 1b the interaction factor k_{yy} as a function of n_{yb}. The results are compared with those of EN 1993-1-1:2005 given by dashed lines. Curves of different slenderness ratios are distinguished by colors.

4.2 *Simply supported beam-columns*

Results of numerical simulations for the end moment factor $\psi = 1.0$ are presented in Figure 2, for $\psi = 0.0$ in Figure 3 and for $\psi = -1.0$ in Figure 4. The same notation as used in Figure 1 is used. It is worthy to note that the solid line curve results shown are for geometric imperfections of the lowest buckling mode, i.e. $n_{yb} = n_{yb,1}$.

For comparison, the finite element simulations are repeated for $\psi = -1.0$ but with geometric imperfections of the second lowest bifurcation mode that corresponds to the deflected profile under bending action. The amplitude of the half-wave is taken as $e_{0,y}/2$. The results are shown in Figure 5 by dashed lines. Figure 5a present the results of interaction curves in coordinates m_{yc} and $n_{yb} = n_{yb,1}$. Dashed lines are cut off at the coordinate $n_{yb} = 1.0$ because the buckling strength interaction curves of beam-column with geometric imperfections according to the second lowest eigenvalue mode continue up to the coordinate $n_{yb} = n_{yb,2}$. Figure 5b shows the comparison of Eurocode's buckling curves corresponding to the critical force $N_{cr} = N_{cr,1}$ (solid line for a symmetric buckling mode) and the second lowest bifurcation force $N_{cr,2} = 4N_{cr}$ (dashed line for an anti-symmetric buckling mode). Discrete points of buckling strength curves for both solid and dashed lines represent in Figure 5b the results obtained numerically.

4.3 *Fixed-hinged beam-columns*

Results of numerical simulations for the F-H beam-column are presented in Figure 6. The same notation as used in Figures 1–5 is used also in this case.

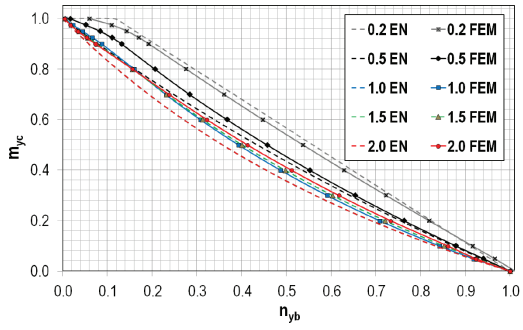

Figure 1. Numerical results for the beam-column C.

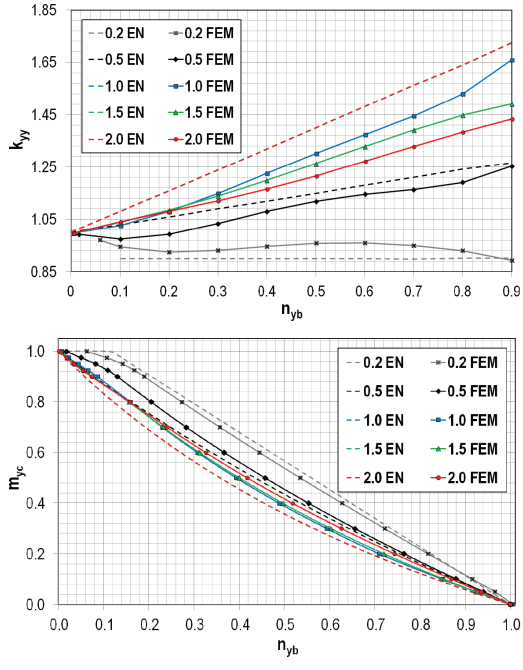

Figure 2. Numerical results for the beam-column S and $\psi = 1.0$.

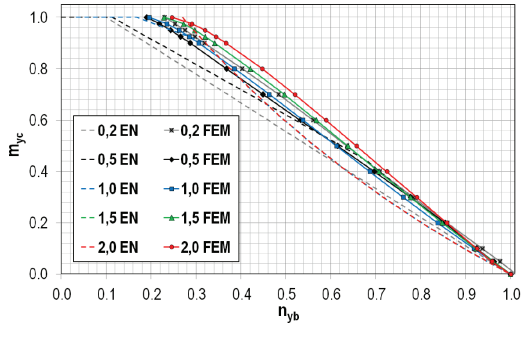

Figure 3. Numerical results for the beam-column S and $\psi = 0.0$.

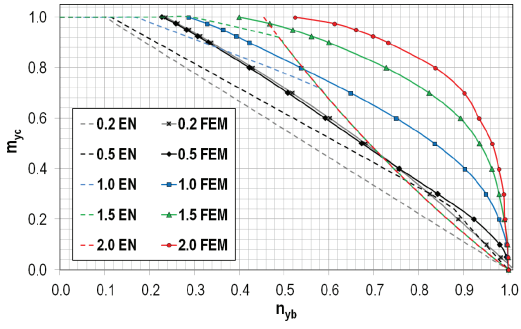

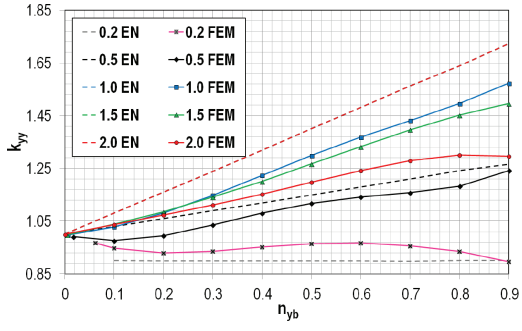

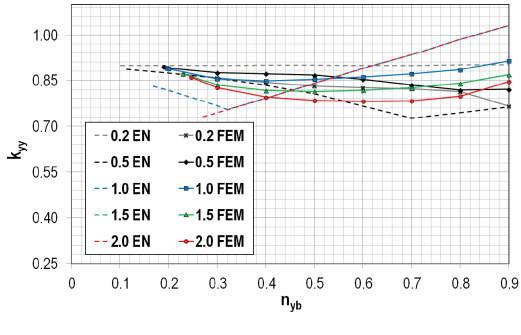

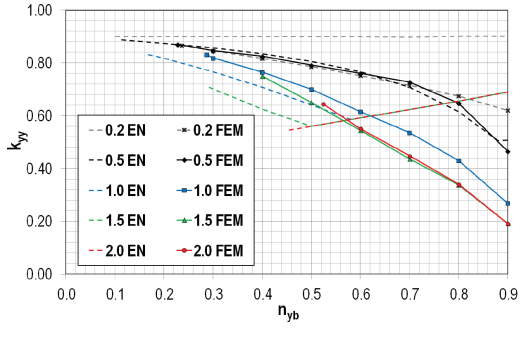

Figure 4. Numerical results for the beam-column S and $\psi = -1.0$ but with geometric imperfection shape corresponding to the lowest eigenvalue (LBM).

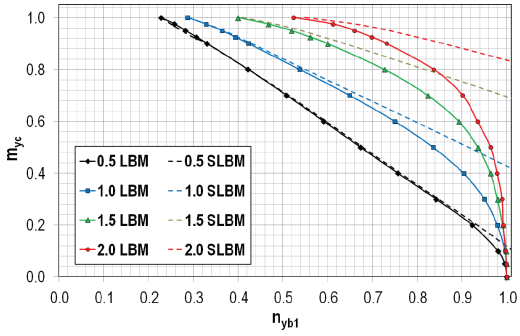

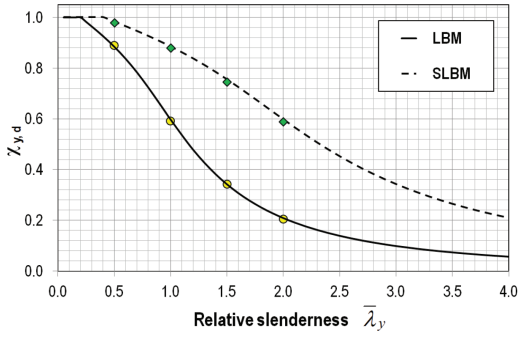

Figure 5. Numerical results for the beam-column S and $\psi = -1.0$ but with geometric imperfection shape corresponding to the second lowest eigenvalue (SLBM).

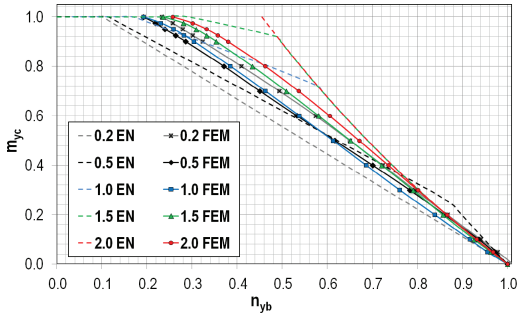

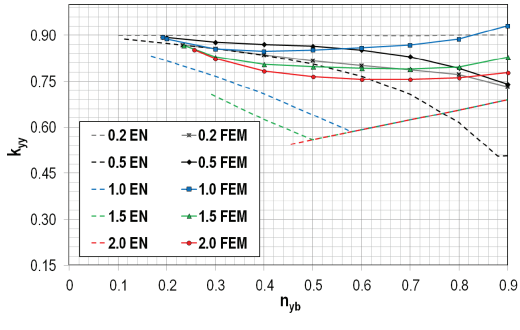

Figure 6. Numerical results for the beam-column F-H.

5 DEVELOPED ANALYTICAL FORMULATION

5.1 *Introductory remarks*

Considering the results of finite element simulations summarized in Section 4, the following observations can be drawn with regards to the interaction curves expressed in the coordinates m_{yc} and n_{yb}:

1. In case of bending moment distribution that produces the displaced configuration being alike the buckling mode of the lowest bifurcation force, the interaction curves in the coordinates m_{yc} and n_{yb} tend to be shifted away from that of the cross section resistance towards the lower values. The interaction curves change from the convex ones (approximated in Eurocode's approach by a bilinear one in case of stocky beam-columns) to concave curves. The lowest curve corresponds to the slenderness around $\overline{\lambda} = 1.0$ where there is the greatest influence of the combined effect of all the imperfections, geometric and material (refer to Figures 1–2).
2. For bending moment distribution that produces the displaced configuration that is different from that of the buckling mode of the lowest bifurcation force, the interaction curves in the coordinates m_{yc} and n_{yb} tend to be shifted away from that of the cross section resistance but towards the higher values. In case of the displaced configuration in bending that is closer to the critical force buckling mode, interaction curves in the coordinates m_{yc} and n_{yb} are the concave ones as the cross section resistance curve is, but closer to it (see Figures 3, 6). Shifting of the interaction curve with the slenderness ratio increase is of a continuous process, hence for a greater slenderness ratio being further away from the beam-column cross section resistance curve.
3. In case of geometric imperfections corresponding to the symmetric buckling mode and the anti-symmetric deflected profile due to bending, trend of the interaction curve shift away from the cross section resistance one is of the same nature like under 2. above but with the greater degree of concavity (see Figure 4). When taking the anti-symmetric buckling mode as the representation of geometric imperfections yields always the higher results (see in Figure 5 dashed lines vs solid lines).

Further observations indicate that the interaction factors k_{yy} evaluated with use of FEM simulations as functions of n_{yb} (see design criteria given in Table 2) need a more complex calibration procedure than that in the domain of coordinates m_{yc} and n_{yb}. The latter calibration procedure is therefore used hereafter.

5.2 *Interpolation functions considered for the buckling resistance interaction curves*

Utilizing the observations stated above, the following unified analytical formulation of the ultimate state of beam-column in-plane failure is suggested:

$$\left(\frac{n_{yb}-a_y}{1-a_y}\right)^{\alpha_n} + \left(m_{yc}\right)^{\alpha_m} = 1 \quad \text{if} \quad a_y < n_{yb} \le 1 \tag{8a}$$

$$m_{yc} = 1 \quad \text{if} \quad 0 \le n_{yb} \le a_y \tag{8b}$$

in which the exponents α_n and α_m as well as the parameter a_y are functions of $\overline{\lambda}$ and need to be calibrated on the basis of results from FEM simulations presented in Section 4. Furthermore, Equations 8 are direct extensions of the Eurocode's cross section resistance criterion for bending and buckling about y-y axis in which $\alpha_n = \alpha_m = 1.0$, and $a_y = 0.5a$ for buckling and bending about y-y axis.

Calibration of model parameters may be done in three Bending Moment Ranges (BMR) dependent upon the condition of the similarity of the buckling mode adopted for the geometric imperfection profile prior to loading and the beam-column deflected profile due to loading. It is referred to the following:

- BMR-1: buckling mode and the beam-column deflected profile under bending moment are alike.
- BMR-2: buckling mode and the beam-column deflected profile under bending moment are not alike but of the same sign displacements.
- BMR-3: buckling mode and the beam-column deflected profile under bending moment are represented by two extreme displacement shapes, e.g. symmetric and anti-symmetric.

In order to establish parameters for the analytical model expressed by Equations 8, the non-linear optimization methods with limits on searched parameters are applied and for final solution the *Mathematica* software is used. On the basis of FEM results presented in Section 4 for all three BMR, the parameters a_y, α_n, α_m are determined and their values presented in the graphical form in the following sections.

5.3 *Model predictions for BMR-1*

In case of BMR-1, the predictions of analytical model are presented in Figure 7 in case of Hinged-Hinged Symmetrical BMD (HHS—green solid lines) and in case of Fixed-FreeEnd (FFE—red solid lines) against results obtained from FEM simulations (black circle markers).

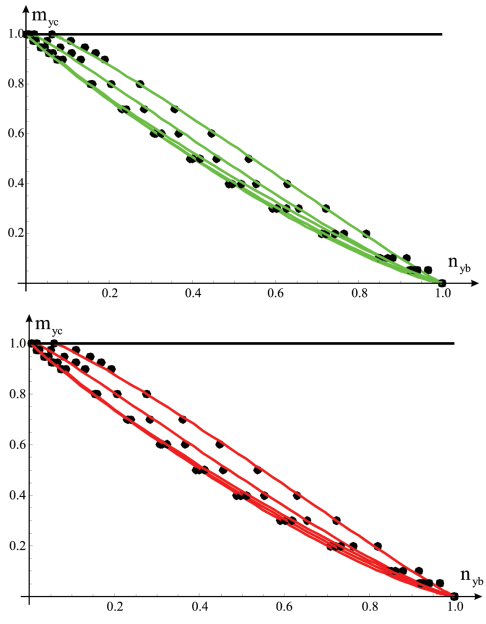

Figure 7. Analytical model approximation of FEM results for HHS BMR-1 (left) and FFE BMR-1 (right).

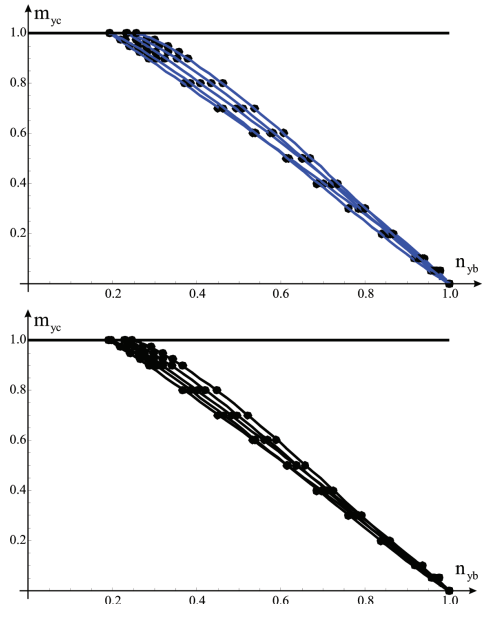

Figure 8. Analytical model approximation of FEM results for FH BMR-2 (left) and HHT BMR-2 (right).

5.4 *Model predictions for BMR-2*

In case of BMR-2, the predictions are presented in Figure 8: blue solid lines in case of Fixed-Hinged (FH) and black solid lines in case of Hinged-Hinged Triangular BMD (HHT).

5.5 *Model predictions for BMR-3*

In case of BMR-3 (Hinged-Hinged Antisymmetrical BMD), the influence of relative slenderness on the shape of function $m_{yc}(n_{yb})$ is very significant. Analytical model predictions are presented in Figure 9.

5.6 *Summary of results for model parameters*

The results of the parameter determination (optimization problem) are presented in a form of functions $a_y(\bar{\lambda})$, $\alpha_n(\bar{\lambda})$ and $\alpha_m(\bar{\lambda})$ graphs in Figures 10–12.

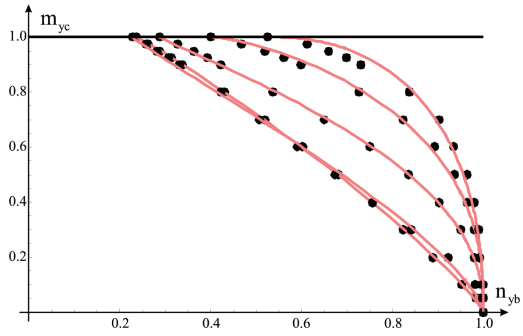

Figure 9. Analytical model approximation of FEM results for HHA BMR-3.

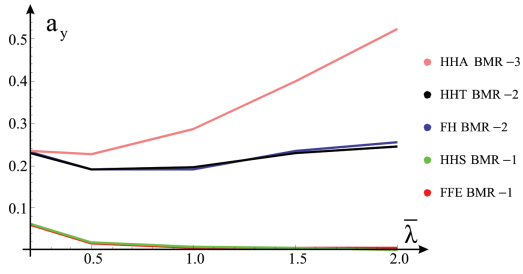

Figure 10. Parameter a_y determined on the basis of non-linear optimization technics as a function of slenderness in case of all three BMR.

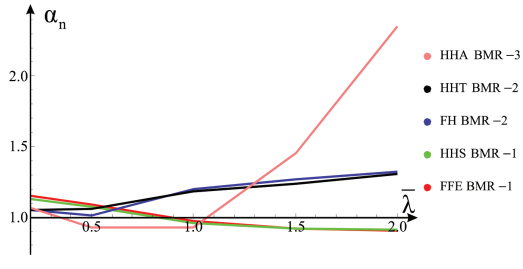

Figure 11. Parameter α_n determined on the basis of non-linear optimization technics as a function of slenderness in case of all three BMR.

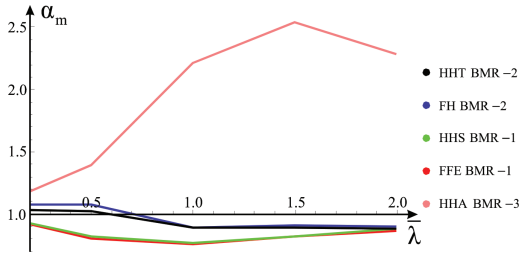

Figure 12. Parameter α_m determined on the basis of non-linear optimization technics as a function of slenderness in case of all three BMR.

6 CONCLUSIONS

i. An alternative verification method of the beam-column resistance to that of Eurocodes is developed herein for planar bending without LT-buckling and is based on Equations 8.
ii. Proposed analytical model allows for a good approximation of FEM results in all three buckling mode ranges with regard to the $m_{yc}(n_{yb})$ function. It is worth underlying that in majority of presented fitting problems the correlation factors R^2 are higher than 0.99.
iii. Results for analytical model parameters shows, that separation of three buckling mode ranges is fully justified from a physical point of view.
iv. In separated buckling ranges, the nature of model parameter functions is quite different, although the effect of boundary conditions is rather negligible.

REFERENCES

ABAQUS *Theory Manual*. 2011. Version 6.11. Dassault Systèmes.

EN 1993-1-1:2005. Eurocode 3: Design of Steel Structures, Part 1–1: General rules and rules for buildings. Brussels: European Committee for Standardization.

Gizejowski, M., Szczerba, R., Gajewski, M. & Stachura, Z. 2015. Beam-column resistance interaction criteria for in-plane bending and compression. *Procedia Engineering*. Special Issue (eds. Jemiolo S., Gajewski, M. & Krzeminski, M.). *Open Access Journal.* Elsevier. Vol. 111: 254–261.

Greiner, R. & Lindner, J. 2006. Interaction formulae for members subjected to bending and axial compression in Eurocode 3—the Method 2 approach. *Journal of Constructional Steel Research* 62: 757–770.

Jemiolo, S. & Gajewski, M. 2014. *Hyper-elasto-plasticity. Publication of the Department of Strength of Materials and Theory of Elasticity and Plasticity*. Vol. 4. Warsaw: OWPW [in Polish].

Simoes da Silva, L., Simoes, R. & Gervasio, H. 2010. *Design of Steel Structures. ECCS Eurocode Design Manual.* Berlin: Ernst & Sohn.

Stachura, Z. & Gizejowski, M. 2015. Partial factors in modeling of steel structures reliability according to Eurocodes. *Civil and Environmental Engineering Reports* 16(1): 195–207. Zielona Gora: University of Zielona Gora Press.

This page intentionally left blank

Recent Progress in Steel and Composite Structures – Giżejowski et al. (Eds)
© 2016 Taylor & Francis Group, London, ISBN 978-1-138-02946-0

Lateral-torsional buckling of steel beams with simultaneously tapered flanges and web

J. Kuś
Technical University of Opole, Opole, Poland

ABSTRACT: A procedure for critical buckling moment of a tapered beam is proposed with the application of potential energy calculations using Ritz method. Respective solution allows to obtain critical moments initiating lateral buckling of the simply supported, modestly tapered steel I-beams. In particular, lateral-torsional buckling of beams with simultaneously tapered flanges and the web are considered. Detailed, numerical, parametric analyses are carried out. Typical engineering, uniformly distributed design loads are considered for three cases of the load, applied to the top flange, shear centre, as well as to the bottom flange. In addition simply supported beam under gradient moments is investigated. The parametric analysis of simultaneously tapered beam flanges and the web, demonstrates that tapering of flanges influences much more the critical moments than tapering of the web.

1 INTRODUCTION

Steel beams or columns tapered along their length or height are commonly applied in civil engineering because of their more optimal capabilities to carry on typical loads. This is particularly true when they are applied for middle size structures like industrial halls, trade malls, small bridges etc.

When properly designed against lateral torsional buckling, the steel beams are very economical in practical applications. However if these beams are not sufficiently resistant against flexural-torsional or lateral buckling their load capacity may substantially be reduced.

Comprehensive publication on the stability of steel beams with tapered webs was presented by Andrade *et al.* in 2007. In their work they applied the Rayleigh—Ritz method to determine the critical load of simply supported beams and cantilevers, for two types of convergence of the web for various spans. A comparison of their results with FEM program ABAQUS showed a good agreement. The extension of the above studies was made by Zhang Lei and Shu Tong Geng (2008).

Recently Asgarian *et al.* (2012) and Benyamina *et al.* (2013) published papers on the stability of tapered beams limiting their research to the problem of tapered web. The paper by Asgarian *et al.* (2012) is devoted to the issue of stability of beams with arbitrary open cross-sections. These authors applied the method of power series to determine the critical lateral-torsional buckling of simply supported beams and cantilevers. They analyzed the same load cases and patterns of convergence as in the paper by Andrade *et al.* (2007), showing good agreement of the results with existing solutions. The second recent paper on the stability of tapered beams was written by Benyamina *et al.* 2013 and was limited to beams with tapered web. They proposed a non-linear formula based on 1D model, which takes into account new kinematic relationships. Web tapered I-beam under uniformly distributed load was investigated for one scheme of convergence. Also simply supported beam with tapered cross-section, under gradient moments at both ends was analyzed. The results were compared with the available previous literature output, demonstrating good agreement.

The purpose of this paper is to apply the Ritz method to obtain the critical lateral-torsional buckling moments for modestly tapered beams. Unlike in the previous papers, this time simultaneous changes of the web height and flange width are considered. This was obtained by defining two separates parameters describing web variations (α_{TP}) and changes in the flanges width (β_{TP}). Respective formula for the critical buckling moment depending on these parameters is derived and applied in detailed parametric study.

2 MODEL OF BISYMMETRIC TAPERED I-BEAM

2.1 *Geometrical properties of tapered cross-section*

Geometrical properties of beams with tapered cross-sections depend on parameters which define their shape. In this paper following two parameters were chosen: α_{TP} to describe the web and β_{TP} for

flanges. This parameters can be change simultaneously in all the calculations. These parameters are described in detail in Fig. 1 together with the initial cross-sectional characteristics defined as follows:

$$A_0 = (2b_{f0}t_f + h_{w0}t_w) \tag{1}$$

$$I_{T0} = \frac{1}{3}\left(2b_{f0}t_f^3 + h_{w0}t_w^3\right) \tag{2}$$

$$I_{z0} = \frac{1}{6}b_{f0}^3 t_f \tag{3}$$

$$I_{\omega 0} = I_{z0}\frac{h_{d0}^2}{4} \tag{4}$$

$$h(x) = h_0\left(1 + \alpha_{TP}\frac{x}{L}\right) \tag{5}$$

$$b(x) = b_{f0}\left(1 + \beta_{TP}\frac{x}{L}\right) \tag{6}$$

$$\alpha_{TP} = \frac{h_m - h_0}{h_0} \tag{7}$$

$$\beta_{TP} = \frac{b_m - b_{f0}}{b_{f0}} \tag{8}$$

Assuming that the thickness of the web and flanges are constant along the length of the beam, the characteristics of any geometrical cross-section varying over the length, can be expressed as follows:

$$A(x) = A_0 + \left(2b_{f0}t_f\beta_{TP} + h_{w0}t_w\alpha_{TP}\right)\left(\frac{x}{L}\right) \tag{9}$$

$$I_T(x) = I_{T0} + \frac{1}{3}\left(2b_{f0}t_f^3\beta_{TP} + h_{w0}t_w^3\alpha_{TP}\right)\left(\frac{x}{L}\right) \tag{10}$$

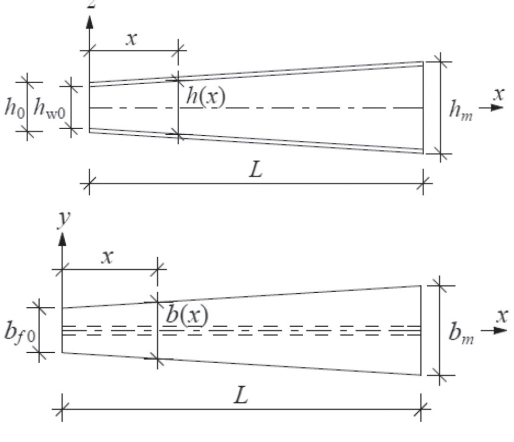

Figure 1. Geometrical properties of beam with tapered web and flanges.

$$I_y(x) = I_{y0}\left(1 + \left(\beta_{TP} + 5\alpha_{TP}\right)\left(\frac{x}{L}\right) + \left(4\alpha_{TP}^2 + 2\alpha_{TP}\beta_{TP}\right)\left(\frac{x}{L}\right)^2 + \left(\alpha_{TP}^3 + \alpha_{TP}^2\beta_{TP}\right)\left(\frac{x}{L}\right)^3\right) \tag{11}$$

$$I_z(x) = I_{z0}\left(1 + 3\beta_{TP}\left(\frac{x}{L}\right) + 3\beta_{TP}^2\left(\frac{x}{L}\right)^2\right) + I_{z0}\beta_{TP}^3\left(\frac{x}{L}\right)^3 \tag{12}$$

$$I_\omega(x) = I_{\omega 0}\left(1 + \left(\beta_{TP} + 2\alpha_{TP}\right)\left(\frac{x}{L}\right) + \left(\alpha_{TP}^2 + 3\beta_{TP}^2 + 6\alpha_{TP}\beta_{TP}\right)\left(\frac{x}{L}\right)^2 + \left(3\alpha_{TP}^2\beta_{TP} + 6\beta_{TP}^2\alpha_{TP} + \beta_{TP}^3\right)\left(\frac{x}{L}\right)^3 + \left(3\beta_{TP}^2\alpha_{TP}^2 + 2\beta_{TP}^3\alpha_{TP}\right)\left(\frac{x}{L}\right)^4\right) + I_{\omega 0}\beta_{TP}^3\alpha_{TP}^2\left(\frac{x}{L}\right)^5 \tag{13}$$

In these equations $A(x)$ is the cross section area, $I_T(x)$ is the torsion constant of the cross-section, $I_y(x)$, $I_z(x)$ are principal moment of inertia about y and z axes, $I\omega(x)$ is the warping constant, h_{w0} is the height of web, t_w is the web thickness, t_f is the flange thickness.

It is assumed that the tapering of the beams analyzed in this paper is limited only to twice the cross-section size at both support. When parameters α_{TP} and β_{TP} equals zero, the beam is prismatic with constant values of dimensions h_0 and b_{f0} along the beam (uniform shape). The maximum tapering takes place when the support cross-section is twice as big as the left support. In this case it is assumed that the taper parameter takes value equal to 1.

2.2 *Total potential energy for beam with tapered cross-section*

In this paper the functional for the total potential energy of the beam, commonly available in the literature (Benyamina *et al.* 2013, Andrade *et al.* 2007, 2010, Bradford and Cuk 1988) was used. In addition, components for total potential energy depending on the strain energy in web and flanges, due to their rotation and displacement during lateral buckling, were included (Bradford and Cuk 1988). Similar derivations of the components of the potential energy functional can be found in

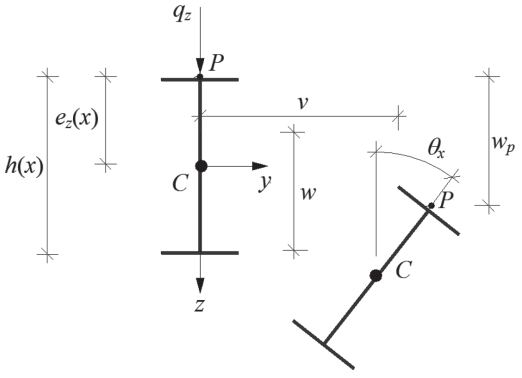

Figure 2. I-section under lateral-torsional buckling.

the papers by Benyamina *et al.* 2013 and Andrade *et al.* (2007, 2010).

Important element of present paper is now an introduction of the parameters defining the tapering of the web α_{TP} and flanges β_{TP} into the integrands of the potential energy.

In Figure 2, u, v, w are the displacement components of the shear centre point in the x, y and z directions, θx is the twist angle.

$$\Pi_{LTB} = \frac{1}{2}\int_L \left(EI_z(x)\left(\frac{\partial^2 v}{\partial x^2}\right)^2 + GI_T(x)\left(\frac{\partial \theta_x}{\partial x}\right)^2 + EI_\omega(x)\left(\frac{\partial^2 \theta_x}{\partial x^2}\right)^2 \right) \mathrm{d}x + \frac{1}{2}\int_L \left(EI_z(x)\left(\left(\frac{\partial h(x)}{\partial x}\right)^2\left(\frac{\partial \theta_x}{\partial x}\right)^2\right)\right) \mathrm{d}x + \frac{1}{2}\int_L \left(\left(h(x)\left(\frac{\partial h(x)}{\partial x}\right)\left(\frac{\partial \theta_x}{\partial x}\right)\left(\frac{\partial^2 \theta_x}{\partial x^2}\right)\right)\right) \mathrm{d}x + \int_L M_y\left(\theta_x\left(\frac{\partial^2 v}{\partial x^2}\right)\right) \mathrm{d}x + \frac{1}{2}\int_L q_z e_z(x)\theta_x^2 \,\mathrm{d}x \tag{14}$$

3 SOLUTION FOR CRITICAL BUCKLING MOMENTS USING RITZ METHOD

Introducing discretization into the integral formulas (14), the problem is brought to systems of algebraic equations with unknowns parameters a_i, assumed for basis shape functions θ_i.

$$\xi_n = \sum_{i=1}^{n} a_i \theta_i \tag{15}$$

When it comes to the state of static equilibrium of the beam, the potential energy takes a minimum value, so the parameters a_i can be determined with following extreme conditions:

$$\frac{\partial \Pi_{LTB}(\xi_n)}{\partial a_i} = 0 \text{ for } i = 1, 2, \ldots, n \tag{16}$$

To solve the stability problems using variational calculus method, proper functions θ_i should be adopted to reflect the appropriate shape of the element axis after lateral buckling. These functions are limited in this paper to the shape characterising for simply supported I-beams. For this model the boundary conditions are defined as follows:

$$\begin{aligned} &v(0) = v(L) = 0,\ \theta_x(0) = \theta_x(L) = 0 \\ &v''(0) = v''(L) = 0,\ \theta_x''(0) = \theta_x''(L) = 0 \end{aligned} \tag{17}$$

Now the Ritz functions can be defined. For this purpose trigonometric functions satisfying the boundary conditions (17) are defined as follows:

$$v = \sum_{i=1}^{n} v_i \sin\left(i\pi\frac{x}{L}\right) \tag{18}$$

$$\theta_x = \sum_{i=1}^{n} \theta_i \sin\left(i\pi\frac{x}{L}\right) \tag{19}$$

Application of a finite number of elements of the sum in the expressions (18–19) leads to formal substitution of a continuous model by the discrete one. In order to obtain the desired level of accuracy of the calculations one must take a sufficiently large number of the elements. For practical, engineering, design calculations of simply supported beams, the critical buckling load can sufficiently be estimated using the first approximation ($i = 1$).

In order to determine the critical buckling load, function of the gradient of the bending moment, depending on the load of the beam

$$m(x) = \frac{M_y}{\overline{M}} \tag{20}$$

should be introduced into the potential energy functional (14). In equation (20) symbol $\underline{M}_y$ stands for the actual bending moment while $\overline{M}$ represents maximum bending moment in static equilibrium, during the state of the loss of stability critical buckling moment.

Finally following form for the potential energy with Ritz functions (18–19) is derived:

$$
\begin{aligned}
\Pi_{LTB} = {} & \frac{1}{2}\int_0^L \left(EI_z(x) \left(\frac{\partial^2}{\partial x^2}\left(\sum_{i=1}^{n} v_i \sin\left(\frac{i\pi x}{L} \right) \right) \right)^2 \right) \mathrm{d}x \\
& + \int_0^L GI_T(x) \left(\frac{\partial}{\partial x}\left(\sum_{i=1}^{n} \theta_i \sin\left(\frac{i\pi x}{L} \right) \right) \right)^2 \mathrm{d}x \\
& + \frac{1}{2}\int_0^L \left(EI_\omega(x) \left(\frac{\partial^2}{\partial x^2}\left(\sum_{i=1}^{n} \theta_i \sin\left(\frac{i\pi x}{L} \right) \right) \right)^2 \right) \mathrm{d}x \\
& + \frac{1}{2}\int_0^L \left(EI_z(x) \left(\left(\frac{\partial h(x)}{\partial x} \right)^2 \left(\frac{\partial}{\partial x}\left(\sum_{i=1}^{n} \theta_i \sin\left(\frac{i\pi x}{L} \right) \right) \right)^2 \right) \right) \mathrm{d}x \\
& + \frac{1}{2}\int_0^L \left(h(x) \left(\frac{\partial h(x)}{\partial x} \right) \left(\frac{\partial}{\partial x}\left(\sum_{i=1}^{n} \theta_i \sin\left(\frac{i\pi x}{L} \right) \right) \right) \right) \mathrm{d}x \\
& + \frac{1}{2}\int_0^L \left(h(x) \left(\frac{\partial h(x)}{\partial x} \right) \left(\frac{\partial}{\partial x} \right) \right) \left(\frac{\partial^2}{\partial x^2}\left(\sum_{i=1}^{n} \theta_i \sin\left(\frac{i\pi x}{L} \right) \right) \right) \\
& + \overline{M}\int_0^L \left(m(x) \left(\sum_{i=1}^{n} \theta_i \sin\left(\frac{i\pi x}{L} \right) \right) \left(\frac{\partial^2}{\partial x^2}\left(\sum_{i=1}^{n} v_i \sin\left(\frac{i\pi x}{L} \right) \right) \right) \right) \mathrm{d}x \\
& + \frac{1}{2}\int_0^L \left(q_z e_z(x) \left(\sum_{i=1}^{n} \theta_i \sin\left(\frac{i\pi x}{L} \right) \right)^2 \right) \mathrm{d}x
\end{aligned}
\tag{21}
$$

Form for the potential energy with Ritz functions (18–19) can be written in a form as follows:

$$
\Pi_{LTB} = \sum_{i=1}^{n} \left(k_{bb(m\ x\ m)} v_i^2 + k_{cc(n\ x\ n)} \theta_i^2 + k_{bc(m\ x\ n)} v_i\ \theta_i \right) \tag{22}
$$

Applying, in accordance with the Ritz method, minimization of the functional of total potential energy (21) using conditions:

$$
\frac{\partial \Pi_{LTB}}{\partial v_i} = 0, \quad i = 1, 2, 3, \ldots, m \tag{23}
$$

$$
\frac{\partial \Pi_{LTB}}{\partial \theta_i} = 0, \quad i = 1, 2, 3, \ldots, n \tag{24}
$$

the following system of homogeneous, algebraic equations is obtained:

$$
\left[\begin{array}{c|c} k_{bb(m\ x\ m)} & k_{bc(m\ x\ n)} \\ \hline sym & k_{cc(n\ x\ n)} \end{array} \right] \left\{ \begin{array}{c} v_{i\ (m\ x\ 1)} \\ \hline \theta_{i\ (n\ x\ 1)} \end{array} \right\} = \left\{ \begin{array}{c} 0 \\ \hline 0 \end{array} \right\} \tag{25}
$$

The determinant of formula (25) equals the smallest, zero value for the critical moment M_{cr} which initiates loss of stability of the beam. The solution of equation (25) takes form of the familiar square polynomial with the unknowns +/–M. Detailed definition of critical moment M_{cr} depends on the external loads and geometrical features of the beam.

4 APPLICATION FOR TAPERED BEAM UNDER DIFFERENT LOAD CASES

The purpose of this chapter is to check the accuracy of solutions obtained by the method proposed in chapter 3, in comparison with the finite element approach as well as to carry on a parametric analysis. Steel beams are assumed to be made of steel with Young's modulus of E = 210 GPa, modulus of Kirchoff G = 81 GPa, i.e., Poisson's ratio = 0.3.

The verifying computations were performed using the ANSYS FEM software system. A rod „BEAM188" finite element was assumed. It is a two-node element with seven degrees of freedom—three translational UX, UY, UZ, three rotary ROTX, ROTY, ROTZ and seventh optional degree of freedom to restrict the freedom of cross-sectional warping. The beam supports were modeled by blocking translational degrees of freedom UY = 0, UZ = 0 and locking the axial rotation degree of freedom ROTX = 0.

4.1 *I-beam with tapered cross-section with uniformly distributed load*

Simply supported beam with uniformly distributed load was adopted.

In this case formula (20) takes following form:

$$m(x) = 4\left(\frac{x}{L} - \frac{x^2}{L^2}\right) \tag{26}$$

while the maximum bending moment in the beam equals

$$M_{\max} = \frac{q_z L^2}{8} \tag{27}$$

and actual bending moment in the beam equals

$$M_y(x) = \frac{q_z L^2}{2}\left(\frac{x}{L} - \frac{x^2}{L^2}\right) \quad \text{for} \quad 0 \le x \le L \tag{28}$$

The components of the matrix (25), taking into account formula (26) and the characteristics of the beam shown in Fig. 1 are:

$$k_{bb} = \frac{1}{2}\int_0^L \left(EI_z(x)\frac{\pi^4 \sin^2\left(\frac{\pi x}{L}\right)}{L^4} \right) dx \tag{29}$$

$$\begin{aligned} k_{cc} = {} & \frac{1}{2}\int_0^L \left(GI_t(x)\frac{\pi^2 \cos^2\left(\frac{\pi x}{L}\right)}{L^2} + EI_\omega(x)\frac{\pi^4 \sin^2\left(\frac{\pi x}{L}\right)}{L^4} \right) \mathrm{d}x \\ & + \frac{1}{2}\int_0^L \left(EI_z(x)\left(\left(\frac{\partial h(x)}{\partial x}\right)^2 \frac{\pi^2 \cos^2\left(\frac{\pi x}{L}\right)}{L^2} \right) \right) \mathrm{d}x \\ & + \frac{1}{2}\int_0^L \left(EI_z(x)\left(h(x)\frac{\partial h(x)}{\partial x}\frac{\pi^3 \sin^2\left(\frac{2\pi x}{L}\right)}{L^3} \right) \right) \mathrm{d}x \\ & + \frac{1}{2}\int_0^L \left(q_z e_z(x) \sin^2\left(\frac{\pi x}{L}\right) \right) \mathrm{d}x \end{aligned} \tag{30}$$

$$k_{bc} = \overline{M}\int_0^L \left(\left(\frac{x}{L} - \frac{x^2}{L^2}\right)\frac{\pi^2 \sin^2\left(\frac{\pi x}{L}\right)}{L^2} \right) \mathrm{d}x \tag{31}$$

Setting the integrand expressions, taking into account the geometric parameters of the tapered beam for various patterns of tapering (Fig. 1), matrix elements (25) were obtained. Finally the particular solution eq. (25) for the simply supported beam under uniformly distributed load equals:

$$\det \begin{bmatrix} k_{bb} & k_{bc} \\ sym & k_{cc} \end{bmatrix} = 0 \tag{32}$$

Solution of equation (32) with respect to moment M, leads to the determination of the critical buckling moments initiating loss of stability.

In the following example, critical buckling moments for simply supported steel I-beam with a cross section which has both tapered flanges and the web are analyzed. Span of the beam is set to 6 m, 9 m and 12 m with properties of cross-section as follows $h_0 = 300$ mm, $b_{f0} = 150$ mm, $t_f = 10{,}7$ mm, $t_w = 7{,}1$ mm.

The tapering parameter of web and flanges changes from $\alpha_{TP} = \beta_{TP} = 0$ (prismatic beam) to $\alpha_{tp} = \beta_{tp} = 1$ ($h_m = 2h_0$, $b_m = 2b_{f0}$).

The values of the critical moments are shown in Figure 3 to 5. The load was applied to the shear centre, as well as to the upper and lower flanges.

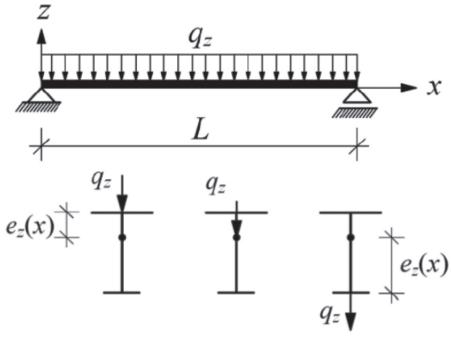

Figure 3. Sketch showing a simply supported beam uniformly distributed load.

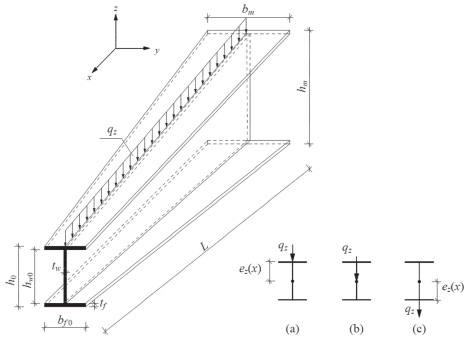

Figure 4. Sketch showing a simply supported beam with simultaneously tapered web and flanges, under distributed load applied to top flange (a), shear centre (b) and the bottom flange (c).

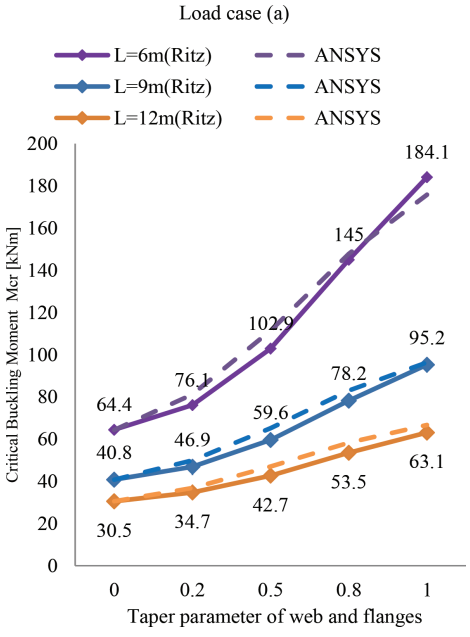

Figure 5. Plot of critical buckling moments for simply supported beam with simultaneously tapered flanges and web under distributed load (Fig. 4a).

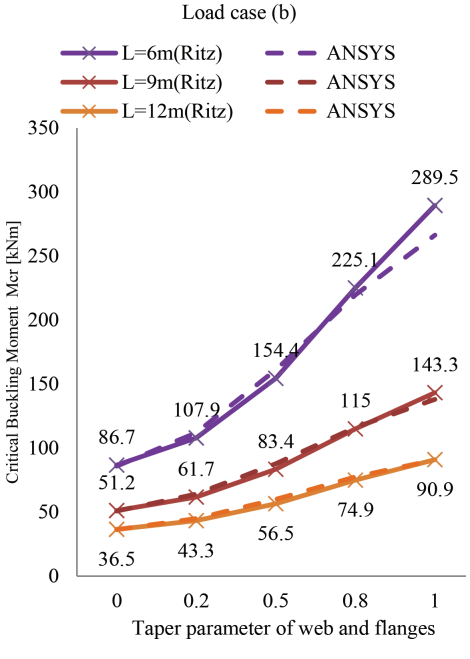

Figure 6. Plot of critical buckling moments for simply supported beam with simultaneously tapered flanges and web under distributed load (Fig. 4b).

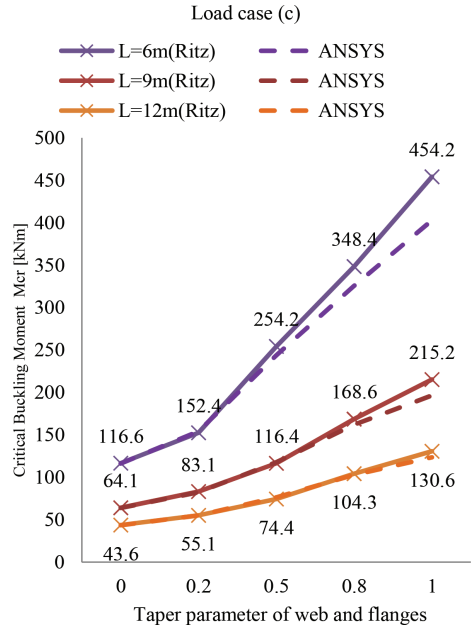

Figure 7. Plot of critical buckling moments for simply supported beam with simultaneously tapered flanges and web under distributed load (Fig. 4c).

First the accuracy of the solutions using formula (32) and the FEM ANSYS model are compared. Again the results using the Ritz method are in sufficient agreement with the results of the FEM analysis. In most cases it is about 0,2%–5% which is enough in practical engineering, design applications. The maximum difference did not exceed 10% (Fig. 7).

As a result of this parametric analysis, it can be concluded that the simultaneous tapering of the flanges and web causes a significant increase of the critical lateral-torsional buckling moments.

Consider for example the results for the beam with the bottom flange loaded. For the tapering parameters $\alpha_{TP} = \beta_{TP} < 0.5$ the increase of critical moments with respect to the prismatic beam assumption equals approx. 24%. For $\alpha_{TP} = \beta_{TP} = 1.0$ the critical moment increases up to 75%.

4.2 *I-beam with tapered cross-section under positive gradient moments*

Simply supported beam under positive gradient moments was considered (Fig. 8).

In this case formula (20) takes following form:

$$M_y(x) = M\left(\psi - \frac{1}{L}(\psi - 1)x\right) \quad \text{for} \quad 0 \le \psi < 1 \tag{33}$$

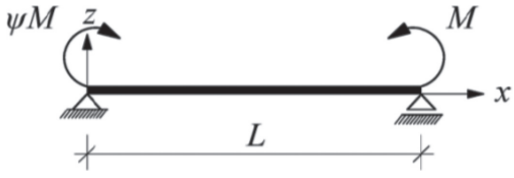

Figure 8. Sketch showing a simply supported beam under gradient moments.

while the maximum bending moment in the beam equals

$$M_{\max} = M \tag{34}$$

and actual bending moment in the beam equals

$$m(x) = \psi - \frac{1}{L}(\psi - 1)x \text{ for } 0 \le \psi < 1 \tag{35}$$

The components of the matrix (25), taking into account formula (35) and the characteristics of the beam shown in Fig. 1 are:

$$k_{bb} = \frac{1}{2}\int_0^L \left(EI_z(x)\frac{\pi^4 \sin^2\left(\frac{\pi x}{L}\right)}{L^4} \right) \mathrm{d}x \tag{36}$$

$$k_{cc} = \frac{1}{2}\int_0^L \left(GI_T(x)\frac{\pi^2 \cos^2\left(\frac{\pi x}{L}\right)}{L^2} + EI_\omega(x)\frac{\pi^4 \sin^2\left(\frac{\pi x}{L}\right)}{L^4} \right) \mathrm{d}x + \frac{1}{2}\int_0^L \left(EI_z(x)\left(\left(\frac{\partial h(x)}{\partial x}\right)^2 \frac{\pi^2 \cos^2\left(\frac{\pi x}{L}\right)}{L^2} \right) \right) \mathrm{d}x + \frac{1}{2}\int_0^L \left(EI_z(x)\left(h(x)\frac{\partial h(x)}{\partial x}\frac{\pi^3 \sin^2\left(\frac{2\pi x}{L}\right)}{L^3} \right) \right) \mathrm{d}x \tag{37}$$

$$k_{bc} = \overline{M}\int_0^L \left(\left(\psi - \frac{1}{L}(\psi - 1)x \right) \frac{\pi^2 \sin^2\left(\frac{\pi x}{L}\right)}{L^2} \right) \mathrm{d}x. \tag{38}$$

Using the same procedure as mentioned in paragraph 4.1 matrix elements (25) were calculated and in next step critical buckling moments for beam under positive moment gradient were computed for cross-section properties of beam with $h_0 = 300$ mm, $b_{f0} = 150$ mm, $t_f = 10{,}7$ mm, $t_w = 7{,}1$ mm (Fig. 9).

Range of gradient moment varies from Ψ = 0,25 to Ψ = 1 (equal gradient moments on both sides). Flange width was changing from $b_{f0} = 150$ mm to $b_m = 300$ mm, height of the beam on right side was changing from $h_0 = 150$ mm ($\alpha_{TP} = 0{,}0$) to $h_m = 300$ mm ($\alpha_{TP} = 1{,}0$). Two types of length are investigated.

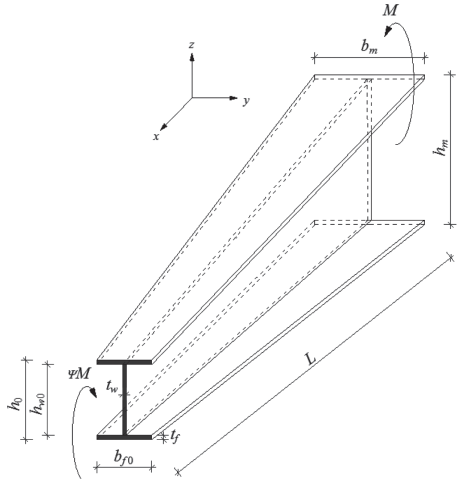

Figure 9. Sketch showing a simply supported beam under gradient moments.

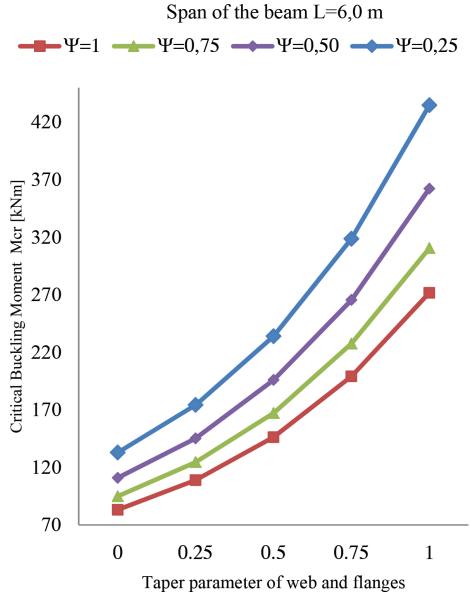

Figure 10. Plot of critical buckling moments for simply supported beam (span = 6,0 m) with simultaneously tapered flanges and web under positive gradient moments.

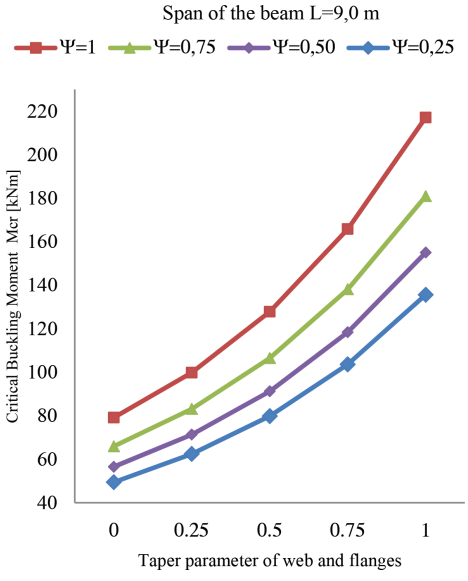

Figure 11. Plot of critical buckling moments for simply supported beam (span = 9,0 m) with simultaneously tapered flanges and web under positive gradient moments.

Critical buckling moments evaluated by the presented method and FE model are in good agreement. Relative differences do not exceed more than 4%. As could be expected highest value of critical load have beams with taper parameter $a_{TP} = \beta_{TP}$ equal 1,0 (Fig. 10 and Fig. 11).

5 SUMMARY AND CONCLUSIONS

Results of the research on lateral torsional buckling problem of beams with simultaneously tapered flanges and webs are reported. A solution of this problem using the Ritz method is developed. It allows to determine the critical lateral-torsional buckling moments for tapered beams.

Bisymmetrical I-beams with linearly equally variable flanges widths and web heights were analysed, considering four load cases: with distributed load applied at the shear centre, at the upper flange and at the lower flange and under gradient moments.

The difference between the values of the critical buckling moments, calculated using the Ritz method, and those of the ANSYS program were determined according to the formula.

$$\Delta = \left| \frac{M_{cr}^{Ritz} - M_{cr}^{Ansys}}{M_{cr}^{Ansys}} \right| \cdot 100\% \tag{39}$$

It was observed that the values of critical buckling moment calculated using the applied implementation of the Ritz method (Eq. 21) and the FEM approach, gave satisfactory agreement from an engineering point of view (mostly below 2% - only in three extreme cases reaching 10%).

For beams with simultaneously tapered flanges widths and web height, the critical buckling moment increased by 70% (α_{TP} = 1,0, β_{TP} = 1,0) compare to the beam with a prismatic cross-section for the same initial values of h_0 and b_{f0} ($\alpha_{TP} = \beta_{TP} = 0$).

It may be concluded that the application of the tapered flanges and web is particularly beneficial since these type of beams are not only lighter but also represent better load capacity with respect to the lateral torsional bucking.

REFERENCES

Abdelrahmane Bekaddour Benyamina, Sid Ahmed Meftah, Foudil Mohri, El Mostafa Daya, 2013. Analytical solutions attempt for lateral torsional buckling of double symmetric web-tapered I-beams. *Engineering Structures*. vol. 56, 1207–1219.

Andrade A., Camotim D., Borges Dinis P. 2007. Lateral-torsional buckling of singly symmetric web-tapered thin-walled I-beams: 1D model vs. Shell FEA. *Computers and Structures*. vol. 85, 1343–1359.

Asgarian B., Soltani M., Mohri F. 2013. Lateral-torsional buckling of tapered thin-walled beams with arbitrary cross-sections. *Thin-walled structures*. vol. 62, 96–108.

Bradford M.A., Cuk P.E., 1988. Elastic buckling of tapered monosymmetric I-beams. *Journal of Structural Engineering*. vol. 114, 977–996.

Kus J. 2013. Stability of beams with tapered cross-sections (in Polish: Analiza stateczności belek ze zbieżnymi przekrojami poprzecznymi). PhD Dissertation. Faculty of Civil Engineering Opole University of Technology. 1–92.

Yeong-Bin Yang, Jong-Dar Yau. 1987. Stability of beams with tapered I-sections. Journal of Engineering Mechanics. vol. 113,.1337–1357.

Zhang Lei, Tong Geng Shu. 2008. Lateral buckling of web-tapered I-beams: A new theory. *Journal of Constructional Steel Research*. vol. 64, 1379–1393.

Recent Progress in Steel and Composite Structures – Giżejowski et al. (Eds)
© 2016 Taylor & Francis Group, London, ISBN 978-1-138-02946-0

Global geometrical imperfections for refined analysis of lateral roof bracing systems

A. Biegus & D. Czepiżak
Department of Civil Engineering, Wrocław University of Technology, Wrocław, Poland

ABSTRACT: In Eurocode 3 the analysis of an equivalent stabilizing forces due to global geometrical imperfections and in consequence the calculation of the lateral bracing systems of the roof girders is given. The forces are assumed to be uniform $N(x) = const$ within the span of restrained member that has an initial bow imperfection e_0. This simplifying assumption is not adequate for the actual non-uniform distribution of forces $N(x) \neq const$ and is considered in Eurocode 3 as slightly conservative. Apart of it the model from Eurocode 3 ignores the geometrical imperfections of the main plane of the restrained truss roof girder, which affect the stress state of purlins and lateral bracing as well. The object of the work is presentation of refined models of calculation of forces due to global, geometrical imperfections of restrained roof rafters, purlins and lateral bracings. Those models incorporate the parabolic distribution of compressive forces in the restrained member $N(x) \neq const$, and its parabolic bow imperfection e_0 in the roof plane. Additionally, the both effect of the lack of verticality described by angle ϕ_0 and entire distorsion of the main plane of the truss rafter (lack of flatness as an effect of the bow e_0 of the compressed upper chord of the truss) are studied. The formulas for an equivalent stabilizing forces assuming the parabolic distribution due to mentioned above global, geometrical imperfections, have been proposed. Obtained results have been discussed and illustrated by an example.

1 INTRODUCTION

The structural, technological and assembly imperfections of the structures diminish their resistance. For this reason in the global analysis of the structure according to Eurocode 3 (EN 1993-1-1:2005) an equivalent geometric imperfection of the members is considered as an initial sway imperfection ϕ_0 or bow imperfection e_0. For convenience, the effects of these imperfections are taken into account in the form of a perfect structure loaded by equivalent stabilizing forces. In this way the geometrical imperfections of the structure are replaced by closed system of equivalent fictions forces. In (EN 1993-1-1:2005), the latter were determined for a member assumed to be uniformly compressed $N(x) = const$ and the effect of the initial bow imperfection of a member is replaced by the equivalent stabilizing load $q_{d1}(x) = const$ uniformly distributed.

Generally, in the analysis of the lateral bracing systems of the restrained roof rafters, that have initial geometrical imperfections, the model with initial bow imperfection e_0 is used (Biegus 2013, Czepiżak 2013, Gardner & Nethercot 2005, EN 1993-1-1:2005, Taylor et al. 1995, Trahair et al. 2008, Timoschenko & Gere 1985). It is assumed (EN 1993-1-1:2005) that the restrained laterally rafter is loaded at the ends by the compressive force N_{Ed} obtained as a maximum force acting uniformly within the span. $N(x) = N_{Ed} = const$, which is not correct owing the real non-uniform distribution of the compressive force. In roof girders (solid or lattice) the force in compressive chord is not constant within its span. For instance in single-span girders free supported at the ends, the compressive force has a quasi-parabolic distribution. For this shape of distribution ($N(x) \neq const$), the non-uniform arrangement of the equivalent stabilizing force within the length of restrained member is adequate – $q_{d2}(x) \neq const$ i.e., variable and with changeable signs. In (Pałkowski & Piątkowski 2014), for an analysis of the non-linear distribution of forces, the equivalent stabilizing force $q_{d2}(x)$ has been revealed in comparison with $q_{d1}(x) = const$, determined according to (EN 1993-1-1:2005).

There is another group of geometrical imperfections of the roof trusses that are ignored in calculation of lateral bracings, like the lack of verticality and distorsion of the main plane of the truss girder.

The lack of verticality of the truss may arise during assemblage. In this case an external, vertical load P acts on inclined truss girder producing additionally horizontal loads H_1 that are taken over by the bracing system increasing its stress level.

The bow imperfection e_0 of the compression truss upper chord (in the roof plane) accompanied by the straightness of the tension in the bottom chord causes a distorsion of the main plane of the truss girder. Also in this situation the external, vertical loads P act on the deformed truss causing additional horizontal loads H_2 transmitted to the bracing. It has been proved (Pałkowski & Piątkowski 2014) that distorsion of the plane of the girder causes a significant increase of stress of the bracing system in comparison with evaluation presented in (EN 1993-1-1:2005).

A refined, generalized models of calculation of equivalent stabilizing forces for restrained roof girders (rafters), purlins and lateral bracings have been proposed in the article. The parabolic distribution of the compressive forces acting in the restrained member $N(x) \neq const$ and its parabolic bow in the roof plane e_0 have been accounted. The effect of the lack of verticality as well as torsion of the main plane of truss girders have been considered as additional sources of the increased stress in purlins and lateral bracing system. The analytic formulas for both equivalent stabilizing forces in case of the parabolic distribution of compressive forces and additional forces caused by geometrical imperfections such as lack of verticality and distorsion of the main plane of the truss have been proposed. The obtained results have been discussed and the approach to the analysis of forces due to geometrical imperfections has been depicted by an example.

2 EQUIVALENT STABILISING FORCE ACTING UNIFORMLY WITHIN THE SPAN OF A MEMBER

The Eurocode 3 (EN 1993-1-1:2005) gives the rules for calculation of the single-span lateral bracing system (Fig. 1). In this case the equivalent stabilizing force has been determined as uniformly distributed q_{d1} caused by initial geometrical imperfections e_0 of the restrained m members (roof girders).

The effect of the initial bow imperfection of compression member of the roof girder (Fig. 1) has been proposed as:

$$e_0 = \frac{L}{500} \tag{1}$$

where: L – the span of restrained member.

The geometrical imperfections of restrained members are not regular and have a random character. Therefore the real force acting on the bracing due to imperfections is smaller from that obtained as a result of a simple adding. This effect is accounted by the reduction factor α_m calculated from:

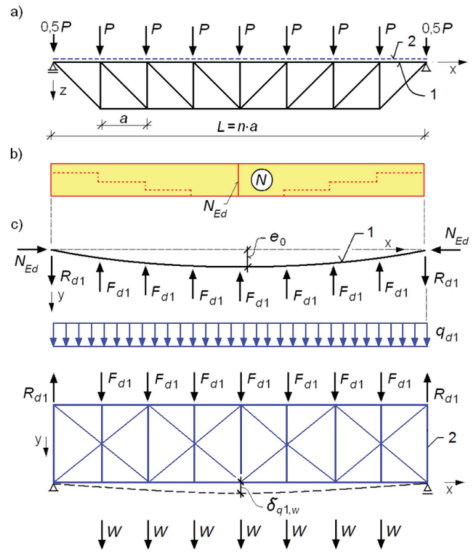

Figure 1. Calculating model of lateral bracing system Eurocode 3: a) scheme of the structure, b) distribution of compressive force in restrained member, c) calculation scheme of lateral bracing system; 1 – restrained member, 2 – lateral bracing system.

$$\alpha_m = \sqrt{0.5\left(1+\frac{1}{m}\right)} \tag{2}$$

where: m – the number of restrained members.

The global effect of actions transmitted by the m restrained members to the lateral bracing is determined as:

$$e = e_0 \alpha_m. \tag{3}$$

For a parabolic bow imperfection e_0 and uniform compressive force $N(x) = const$, acting along the span of the restrained member, the equivalent stabilizing force (Fig. 1c) is:

$$q_{d1} = 8N_{Ed}\frac{e_0}{L^2}, \tag{4}$$

where: N_{Ed} – the maximum compressive force in the restrained member.

The reactions R_{d1} due to loading q_{d1} (Fig. 1c) are:

$$R_{d1} = 0.5q_{d1}L = 4N_{Ed}\frac{e_0}{L}. \tag{5}$$

The total equivalent force $q_{d1,m}$ from m members to be restrained, transmitted to the lateral

bracing (including its deformations) (EN 1993-1-1:2005) is determined from expression:

$$q_{d1,m} = \sum_{i=1}^{m} 8N_{Ed,i} \frac{e + \delta_{q1,w}}{L^2}, \quad (6)$$

where: $N_{Ed,i}$ – the maximum compressive force in the restrained member i; $\delta_{q1,w}$ – in-plane deflection of the lateral bracing system in the mid-span (Fig. 1c) caused by q_{d1} and all other external loads (e.g., wind load w) obtained from first order analysis (it may be assumed $\delta_{q1,w} = 0$ if second order analysis is used).

In the calculation of purlins, which transform the equivalent stabilizing force q_{d1} to the lateral bracing, beside bending (from transverse loads), the additional stress from longitudinal equivalent forces F_{d1} have to be considered. If the restraining truss is constructed from uniform segments of span a, then the force F_{d1} is:

$$F_{d1} = q_{d1}a = 8N_{Ed} \frac{e_0 a}{L^2}, \quad (7)$$

where: a – span of single segment (Fig. 1a).

The highest force $F_{d1,m}$ in the intermediate purlins and its connectors caused by m restrained members, that appears in the roof bay adjacent to the last one, is calculated from expression:

$$F_{d1,m} = \sum_{i=1}^{m} 8N_{Ed,i} a \frac{e + \delta_{q1,w}}{L^2}. \quad (8)$$

The external purlins (eave purlins) are extremely loaded. For them forces $F_{d1,m}(0)$ and $F_{d1,m}(L)$ for m restrained members are:

$$F_{d1,m}(0) = F_{d1,m}(L) = \sum_{i=1}^{m} 4N_{Ed,i} \frac{e + \delta_{q1,w}}{L^2}(L - a) \quad (9)$$

3 EQUIVALENT STABILISING FORCE OF THE MEMBER COMPRESSED BY THE FORCE PARABOLICALLY VARYING WITHIN ITS SPAN

The equivalent stabilizing force of the single-span roof rafter that is free supported, symmetrically loaded, and laterally restrained in the roof plane (Fig. 2) is considered. The distribution of compressive forces $N(x)$ within the length x of its upper chord is quasi-parabolic (Fig. 2b) and described by the relationship:

$$N(x) = 4N_{Ed} \frac{x}{L^2}(L - x). \quad (10)$$

The shape of bow imperfections of the members' axes is random. In work (Goncalves & Camotim 2005) it has been shown that the geometrical imperfection in the shape of second order parabola is extremely disadvantageous for the resistance of individual members. Such an initial parabolic bow of the upper truss chord (EN 1993-1-1:2005) in the roof plane (Fig. 2c) has been adopted in the analysis and expressed as:

$$y(x) = 4e_0 \frac{x}{L^2}(L - x). \quad (11)$$

The bending moment in the restrained member is:

$$M(x) = N(x) \cdot y(x) = 16N_{Ed} \frac{e_0 x^2}{L^4}(L - x)^2. \quad (12)$$

By solving the differential equation of the deflection curve of the member (Trahair et al. 2008) the

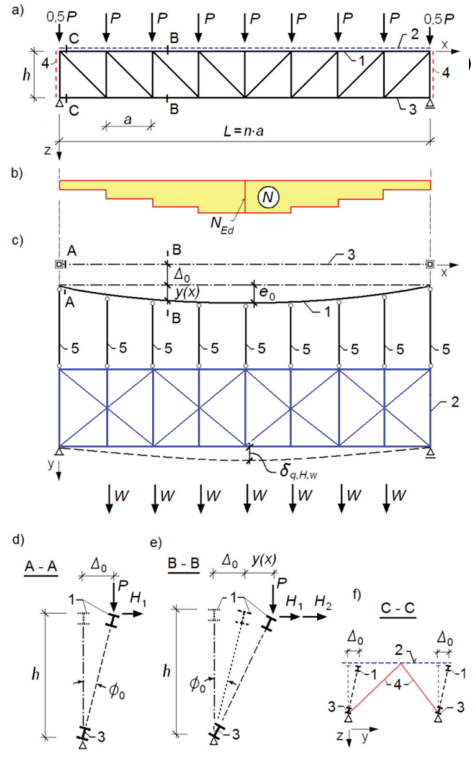

Figure 2. A refined model of calculation of the lateral bracing system: a) scheme of structure, b) distribution of compressive force along the restrained member, c) calculation scheme of the lateral bracing, d), e), f) lack of verticality of the truss: 1 – restrained truss upper chord, 2 – lateral bracing, 3 – truss bottom chord, 4 – longitudinal bracing (between trusses), 5 –purlin.

shear force V_{d2} and the lateral equivalent force q_{d2} can be determined:

$$V_{d2}(x) = \frac{dM}{dx} = 32N_{Ed}\frac{e_0}{L^2}\left(x - 3\frac{x^2}{L} + 2\frac{x^3}{L^2}\right), \quad (13)$$

$$q_{d2}(x) = -\frac{d^2M(x)}{dx^2} = 32N_{Ed}\frac{e_0}{L^2}\left(6\frac{x}{L} - 6\frac{x^2}{L^2} - 1\right). \quad (14)$$

4 EQUIVALENT STABILISING FORCE DUE TO LACK OF VERTICALITY AND THE DISTORSION OF THE TRUSS GIRDER

In currently employed models of calculation of the lateral bracing according to Eurocode 3 (EN 1993-1-1:2005), the equivalent stabilizing forces compensate the bow imperfection of restrained members e_0, that occur in the roof plane. The compression upper chords of the trusses are analyzed as single members isolated from the structure and not connected with bottom chords by the web members. This simplification is not correct, since apart from mentioned above imperfection, there are other significant deformations caused for instance by the lack of verticality and the distorsion of the trusses' main plane lack of flatness. The latter produce equivalent stabilizing horizontal forces H_1 and H_2 as components of the vertical external load P (Fig. 3).

As a result of structural, technological and erection imperfections, the lack of verticality of the main plane of the truss occurs in the form of the angle of rotation ϕ_0 (Fig. 2d, 3a). As it was mentioned before this effect produces horizontal forces H_1 as components of vertical, external loads P, thus:

$$H_1 = \frac{\Delta_0}{h}P = \phi_0 P, \quad (15)$$

where: Δ_0 – basic value of the horizontal translation of the upper chord of the truss measured from the straight line connecting the centroids of supports; ϕ_0 – basic value of the sway imperfection; P – vertical, external loads applied to the upper joints; h – height of the truss.

The horizontal forces H_1, that are transmitted to the lateral bracing increase the stress level in the system. From this point of view the effect of the lack of verticality, expressed by angle ϕ_0, is important particularly for trusses supported at bottom joints (Fig. 3a). Due to the constant value of vertical forces P a suitable constant value of forces H_1 is produced within the length of the lateral bracing.

In the code associated with the execution of steel structures PN-EN 1090-2 (EN 1090-2:2008) the sway imperfection ϕ_0 is not discussed. The value of ϕ_0 may be estimated for the following assumption: $h \approx 0.1L$, $\Delta_0 = L/1000$, as $\phi_0 = 1/100$. Due to the analogy of columns, according to Eurocode 3 (EN 1993-1-1:2005) and taking into account the imperfections provided by EN 1090-2 (EN 1090-2:2008), the value of ϕ_0 to be assumed in calculation is $\phi_0 = \Delta_0 / h = 1/100$.

Apart from the increase of stress in the lateral bracing system due to the lack of verticality, the effect of the initial bow of the compression upper chord in roof plane $y(x)$ (Fig. 2c, e, 3b) is also significant. In Fig. 3b the initial bow imperfection e_0 is indicated for the truss supported at the upper nodes. Another situation is created when the curved, compression upper chord connected with the straight, tension bottom chord by the web members causes a distorsion of the main plane of the truss.

Thus, in presence of vertical forces P, the additional horizontal forces $H_2(x)$ are produced that are transmitted to the lateral bracing (Fig. 2e, 3b) and calculated as:

$$H_2(x) = \frac{y(x)}{h}P. \quad (16)$$

Forces $H_2(x)$ vary within the span of the truss getting the $y(x) = e_0$ maximum at the mid-span where, $x = 0.5L$.

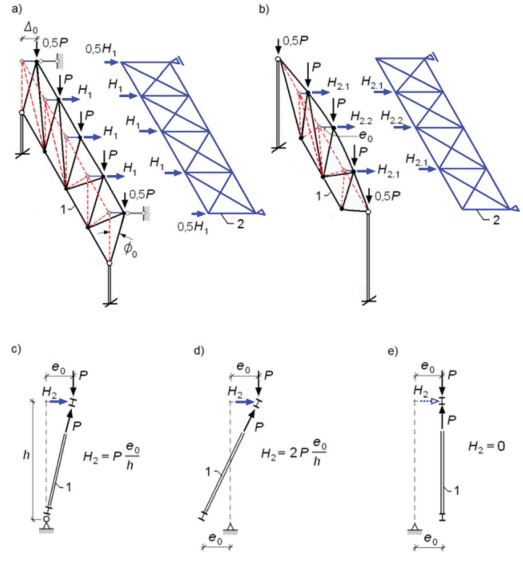

Figure 3. Imperfections: a) lack of verticality of the truss main plane, b) distorsion of the truss main plane (lack of flatness), c) bow of the upper chord, d) changeable signs of bow imperfection of the upper and bottom chord, e) bow of the same curvature of the upper and bottom chord; 1 – truss, 2 – lateral bracing.

Assuming the constant value for vertical forces P and the parabolic bow of the upper chord in the roof plane, according to (11), the forces $H_2(x)$ due to distorsion of the truss applied to the individual upper nodes are:

$$H_2(x) = 4Pe_0 \frac{x}{hL^2}(L-x). \tag{17}$$

The distribution of forces $H_2(x)$ has a parabolic form similar to the assumed shape of the bow $y(x)$ of the restrained upper chord of the truss. The forces $H_2(x)$ are twice larger for the truss in which the upper and bottom chord have an opposite direction of the bow (Fig. 3d). For the same direction of the bow (Fig. 3e) the forces $H_2(x)$ are not present, theoretically. It should be mentioned that the increase of the tension in the chord being under initial bow imperfection causes its straightening and in consequence a decrease of the initial curvature (Fig. 3d, e). Hence, it is proposed to evaluate forces $H_2(x)$ based on the analysis of the scheme shown in Fig. 3c.

5 ANALYSIS OF THE FORCES DUE TO BOW IMPERFECTION, LACK OF THE VERTICALITY AND DISTORSION OF THE TRUSS GIRDER

The longitudinal force $F_{d2}(x)$ due to equivalent stabilizing force $q_{d2}(x)$, transmitted by a single internal purlin to the lateral bracing system is:

$$F_{d2}(x) = \int_{x_i}^{x_i+a} q_{d2}(x)dx. \tag{18}$$

In engineering practice the forces $F_{d2}(x)$ acting in intermediate purlins may be approximated (with acceptable accuracy) from equation:

$$F_{d2}(x) = q_{d2}(x)a. \tag{19}$$

The equivalent stabilizing force $q_{d2}(x)$ is self-sustainable, therefore the located outside reactions are not present in the contrary of the member uniformly compressed where q_{d1} (4) is balanced by reaction R_{d1} (5).

Forces $F_{d2}(0)$ and $F_{d2}(L)$ acting in external purlins due to forces $q_{d2}(x)$ should be determined from equation:

$$F_{d2}(0) = F_{d2}(L) = \int_0^{a/2} q_{d2}(x)dx. \tag{20}$$

Total longitudinal forces $F_m(x)$ in intermediate purlins and its connectors from m restrained members caused by forces q_{d2}, H_1 and H_2 that occur at the bay adjacent to the last one are calculated from equation:

$$F_m(x) = \sum_{i=1}^{m} \left\{ \begin{array}{l} 4\dfrac{e+\delta_{q,H,w}}{L^2} \times \\ \left[8aN_{Ed,i}\left(6\dfrac{x}{L} - 6\dfrac{x^2}{L^2} - 1\right) \right] \\ + \dfrac{P_{Ed,i}}{h}(L-x)x \\ + P_{Ed,i}\dfrac{\Delta + \delta_{q,H,w}}{h}\dfrac{4(L-x)x}{L^2} \end{array} \right\}, \tag{21}$$

where: $\delta_{q,H,w}$ – deflection in the mid-span of lateral bracing (Fig. 2c) from forces q_{d2}, H_1, H_2 and all external loads (such as wind action w) determined from first order analysis ($\delta_{q,H,w}$ may be set to 0 if second order theory is used); Δ – global, horizontal displacement of m restrained trusses to be calculated from equation:

$$\Delta = \Delta_0 \alpha_m. \tag{22}$$

For the vertical force $0.5P$ (Fig. 3) applied to the external nodes of the upper chord of the truss, the longitudinal forces in external purlins $F_m(0)$ and $F_m(L)$ are calculated from the formula:

$$F_m(0) = F_m(L) = \int_0^{a/2} q_{d2}(x)dx + \sum_{i=1}^{m} P_{Ed,i}\frac{\Delta}{2h}. \tag{23}$$

The lack of verticality of the main plane truss, expressed by angle ϕ_0, has no meaning for the stress state of the lateral bracing system ($H_1 = 0$) if the truss girder is supported at its upper nodes (Fig. 1b). In this case the last term of equations (20), (22) may be neglected.

Distribution of equivalent stabilizing force q_{d1} due to the model proposed in Eurocode 3 (EN 1993-1-1:2005), where the compressive force N_{Ed} is constant in the restrained member, is shown in Fig. 4c. This load is acting uniformly and longitudinal forces F_{d1} are transmitted by intermediate purlins to the lateral bracing system are of the same value and direction. Reactions R_{d1} and forces q_{d1} constitute a self-sustainable system (q_{d1} is not transmitted to the bracing between columns).

In Fig. 4e the distribution of an equivalent stabilizing force q_{d2} relevant to the parabolic distribution of compressive force N_{Ed} (Fig. 4d) is shown. Force q_{d2} is non-uniform within the span of the member and changes its sign (13) at the distance of $x \approx 0.2L$ from the supports (Fig. 4e). The intensity of $q_{d2}(x = 0.5L)$ at the mid-span is two times

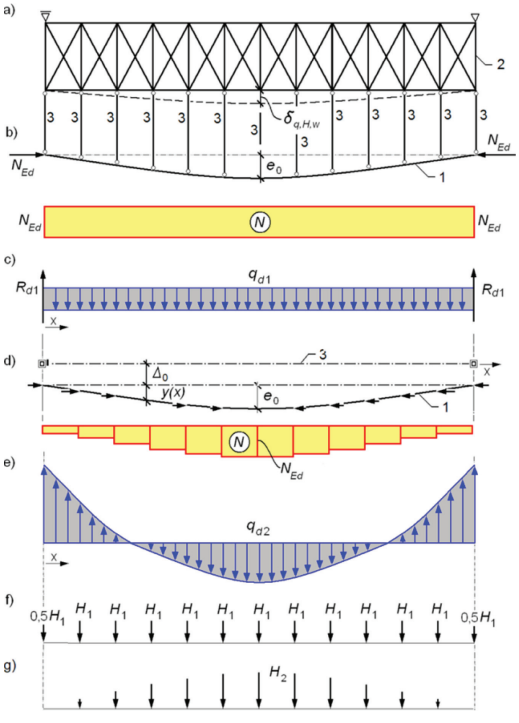

Figure 4. Schemes of: a) lateral bracing system, b) deflected axis of the member and uniform force N_{Ed}, c) uniform distribution of equivalent stabilizing forces, d) deflected axis of the member and parabolic changes of compressive force N_{Ed}, e) non-uniform distribution of equivalent stabilizing forces, f) forces due to the lack of verticality of the truss, g) forces due to the distorsion of the truss; 1 – restrained member, 2 – lateral bracing system, 3 – purlin.

larger from the force q_{d1}. The maximum force q_{d2} is applied to the supporting zone of lateral restraint. Forces $q_{d2}(x=0), q_{d2}(x=L)$ are two times larger from $q_{d2}(x=0.5L)$ and four times larger from q_{d1}. Similarly to the force q_{d1} (4) and reactions R_{d1} (5), the force q_{d2} is self-sustainable.

Concluding, the comparison of equivalent stabilizing forces q_{d1} (according to (EN 1993-1-1:2005)) and q_{d2} regarding the parabolic distribution of the compressive force N_{Ed} in the restrained members reveals deep differences of the qualitative, and first of all the quantitative character. It has an important meaning for an evaluation of the stress state of lateral bracing system and purlins as well.

The force q_{d2} is non-uniform and thus the forces F_{d2} defined earlier are of different values and may have a different sign. If the force q_{d1} is assumed to be uniform then forces F_{d1} (7) have the same value as well.

The action from equivalent stabilizing force q_{d2} transformed by the purlin located at the middle of the span of the lateral bracing may be evaluated from equation:

$$F_{d2}(0.5L) = q_{d2}(0.5L)a - 16N_{Ed}\frac{e_0 a}{L^2}, \tag{24}$$

which is two times larger from F_{d1} (7) determined due q_{d1} (EN 1993-1-1:2005). The maximum forces F_{d2} occur in the eave purlins. These forces are of similar values but of different signs in comparison with forces acting in purlins located in the middle of the lateral bracing. Moreover F_{d2} is smaller from $F_{d1,m}$ (9) if the number of truss segments is not less as 4.

The distribution of internal forces in the members of the lateral bracing is also characteristic for the case whether q_{d1} or q_{d2} is assumed as equivalent stabilizing force. The force q_{d1} produces the maximum stress in the first external diagonals of the bracing, whereas q_{d2} causes the maximum stress in the zone of bracing where the sign of q_{d2} changes.

Both, the forces H_1 (Fig. 4f) and H_2 (Fig. 4g) produce an increase of longitudinal forces in purlins and individual members of the lateral bracing. Consideration of the torsion of the main truss plane (actions H_2) shows an increase of the forces of 50% in the centrally located purlin in comparison with the system loaded purely by q_{d2}, and of 200% for q_{d1}, respectively.

In conclusion, the proposed refined model of analysis and calculation of forces q_{d2}, H_1, H_2 due to analyzed geometrical imperfections reveals a substantial increase of the forces and their distribution that differs from the relevant evaluation given for the force q_{d1} according to (EN 1993-1-1:2005).

6 EXAMPLE

The scheme of analyzed roof structure is shown in Fig. 5 (Pałkowski & Piątkowski 2014) with following data: $L = 24.0$ m, $h = 2.2$ m, $P = 10$ kN, $N_{Ed} = 163.64$ kN. The diagonals of the bracing are taken as flexible members not resisting compressive forces.

1. Case when force N_{Ed} is uniform within the span L of the restrained member. The equivalent stabilizing q_{d1} force (4) is:

$$q_{d1} = 8N_{Ed}e_0\frac{1}{L^2} = 8\cdot 163.64\cdot\frac{24}{500}\cdot\frac{1}{24^2} = 0.109 \text{ kN/m}$$

and the corresponding longitudinal forces F_{d1} (7) transmitted to the lateral bracing by a single intermediate purlin are:

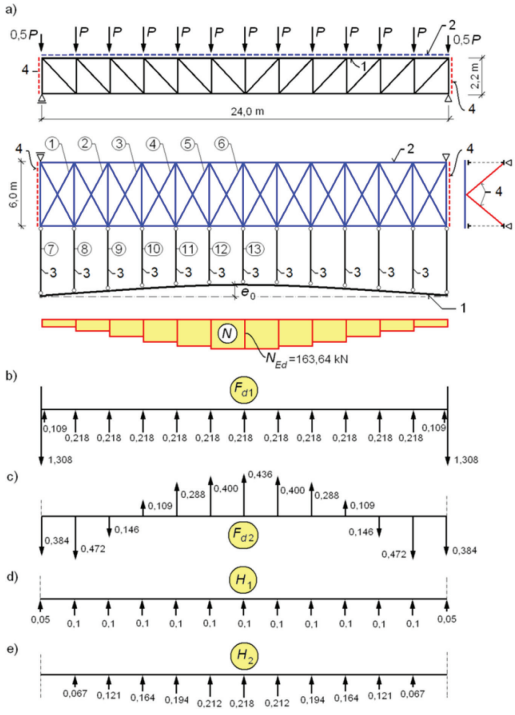

Figure 5. Types of forces applied to the lateral bracing: a) scheme of roof structure, b) forces according to Eurocode 3, c) forces due to parabolic distribution of the compressive force, d) imperfection due to the lack of verticality, g) forces due to the distorsion of the truss; 1 – restrained member, 2 – lateral bracing, 3 – purlins, 4 – longitudinal bracing (between trusses).

$$F_{d1} = q_{d1}a = 0.109 \cdot 2.0 = 0.218 \text{ kN}.$$

Forces F_{d1} transmitted by external purlins are:

$$\begin{aligned} F_{d1}(0) = F_{d1}(L) &= 0.5q_{d1}L - 0.5q_{d1}a \\ &= 0.5 \cdot 0.109 \cdot 24.0 - 0.5 \cdot 0.109 \cdot 2.0 \\ &= 1.308 - 0.109 = 1.199 \text{ kN}. \end{aligned}$$

2. Case for forces N_{Ed} parabolically distributed within the span L in the restrained member. Equivalent stabilising force q_{d2} (13) is:

$$\begin{aligned} q_{d2}(x) &= 32\frac{N_{Ed}e_0}{L^2}\left(6\frac{x}{L} - 6\frac{x^2}{L^2} - 1\right) \\ &= 32\frac{163.64 \cdot \frac{24}{500}}{24^2}\left(6\frac{x}{L} - 6\frac{x^2}{L^2} - 1\right) \\ &= 0.4363\left(6\frac{x}{L} - 6\frac{x^2}{L^2} - 1\right), \end{aligned}$$

$$q_{d2}(0) = 0.4363(-1.0) = -0.4363 \text{ kN/m},$$

$$\begin{aligned} q_{d2}(1.0) &= 0.4363\left(6\frac{1}{24} - 6\frac{1^2}{24^2} - 1\right) \\ &= 0.4363 \cdot (-0.760) = -0.332 \text{ kN/m}, \end{aligned}$$

$$\begin{aligned} q_{d2}(2.0) &= 0.4363\left(6\frac{2}{24} - 6\frac{2^2}{24^2} - 1\right) \\ &= 0.4363 \cdot (-0.542) = -0.236 \text{ kN/m}, \end{aligned}$$

$$\begin{aligned} q_{d2}(4.0) &= 0.4363\left(6\frac{4}{24} - 6\frac{4^2}{24^2} - 1\right) \\ &= 0.4363 \cdot (-0.167) = -0.073 \text{ kN/m}, \end{aligned}$$

$$\begin{aligned} q_{d2}(6.0) &= 0.4363\left(6\frac{6}{24} - 6\frac{6^2}{24^2} - 1\right) \\ &= 0.4363 \cdot 0.125 = 0.0545 \text{ kN/m}, \end{aligned}$$

$$\begin{aligned} q_{d2}(8.0) &= 0.4363\left(6\frac{8}{24} - 6\frac{8^2}{24^2} - 1\right) \\ &= 0.4363 \cdot 0.333 = 0.144 \text{ kN/m}, \end{aligned}$$

$$\begin{aligned} q_{d2}(10.0) &= 0.4363\left(6\frac{10}{24} - 6\frac{10^2}{24^2} - 1\right) \\ &= 0.4363 \cdot 0.458 = 0.200 \text{ kN/m}, \end{aligned}$$

$$\begin{aligned} q_{d2}(12.0) &= 0.4363\left(6\frac{12}{24} - 6\frac{12^2}{24^2} - 1\right) \\ &= 0.4363 \cdot 0.5 = 0.218 \text{ kN/m}. \end{aligned}$$

Longitudinal forces F_{d2} (17), (18) due to imperfections transmitted by purlin to the lateral bracing (Fig. 5c) are:

$$\begin{aligned} F_{d2}(0) &= 0.5 \cdot a \cdot 0.5\left[q_{d2}(0) + q_{d2}(1.0)\right] \\ &= -0.5 \cdot 2.0 \cdot 0.5(0.4363 + 0.332) \\ &= -0.384 \text{ kN}, \end{aligned}$$

$$F_{d2}(2) = q_{d2}(x) \cdot a = -0.236 \cdot 2.0 = -0.472 \text{ kN},$$

$$F_{d,2}(4) = q_{d2}(x) \cdot a = -0.073 \cdot 2.0 = -0.146 \text{ kN},$$

$$F_{d2}(6) = q_{d2}(x) \cdot a = 0.055 \cdot 2.0 = 0.109 \text{ kN},$$

$$F_{d2}(8) = q_{d2}(x) \cdot a = 0.144 \cdot 2.0 = 0.288 \text{ kN},$$

$$F_{d2}(10) = q_{d2}(x) \cdot a = 0.200 \cdot 2.0 = 0.400 \text{ kN},$$

$$F_{d2}(12) = q_{d2}(x) \cdot a = 0.218 \cdot 2.0 = 0.436 \text{ kN}.$$

3. In the analysis of the lateral bracings, the imperfection due to the lack of verticality by the main truss plane is included (Fig. 2d). The value of $\phi_0 = 1/100$ has been assumed. The forces H_1 (14) due to this imperfection (Fig. 5d) exerted by the intermediate and external purlins to the lateral bracing are:

$$H_1 = \phi_0 P = \frac{1}{100}10 = 0.10 \text{ kN},$$

$$0.5H_1 = 0.5 \cdot 0.10 = 0.05 \text{ kN}.$$

4. For the parabolic bow imperfection in the roof plane $e_0 = L/500$, the forces $H_2(x)$ (16) due to the distorsion of the main truss plane (Fig. 5e) are:

$$H_2(x) = 4Pe_0 \frac{x}{hL^2}(L-x)$$
$$= 4 \cdot 10 \cdot \frac{24}{500} \cdot \frac{1}{2.2 \cdot 24^2}[x(L-x)]$$
$$= 0.001515x(L-x),$$

$$H_2(2.0) = 0.001515 \cdot 2(24-2) = 0.067 \text{ kN},$$

$$H_2(4.0) = 0.001515 \cdot 4(24-4) = 0.121 \text{ kN},$$

$$H_2(6.0) = 0.00151 \cdot 6(24-6) = 0.164 \text{ kN},$$

$$H_2(8.0) = 0.001515 \cdot 8(24-8) = 0.194 \text{ kN},$$

$$H_2(10.0) = 0.001515 \cdot 10(24-10) = 0.212 \text{ kN},$$

$$H_2(12.0) = 0.001515 \cdot 12(24-12) = 0.218 \text{ kN}.$$

The internal axial forces in the members of analysed bracing have been calculated for different situation of forces Fig. 5b ÷ e. Forces in the diagonal members have been determined by assuming their resistance to tension only (compression members buckle elastically). The absolute values of the forces in diagonals and purlins for different models of loading are listed in Table 1. In the column 1 the member's number is given according with Fig. 5 and Fig. shown in Table 1. Columns 2 ÷ 5 contain forces calculated for schemes shown in: Fig. 5b (q_{d1}), Fig. 5c (q_{d2}), Fig. 5d (H_1), Fig. 5e (H_2), respectively.

The forces calculated for the sum of loading states $q_{d2} + H_2$ and $q_{d2} + H_1 + H_2$ are given in columns 7 and 8, respectively.

The executed calculations allow to formulate the following conclusions:

1. The assumption of parabolic arrangement of the compression force, that is more close to the real its distribution allows to show, in comparison to the standard model (EN 1993-1-1:2005), the substantial changes, both qualitative and quantitative of the longitudinal forces in purlins and axial forces in the individual members of lateral bracing system.
2. The consideration of the bow parabolic imperfection in the roof plane and the parabolic arrangement of the compression axial force together with the distorsion of the main plane of the truss (column 6 in Table 1; load by forces $q_{d2} + H_2$), reveals in comparison to the standard model (EN 1993-1-1:2005) (column 2 in Table 1; load by forces q_{d1}) the following effects:
   - an increase of forces in the intermediate purlins (excluding the purlin 9),
   - the maximum increase of the forces in the central purlin is of 200%,
   - a decrease of the forces in the eave purlins is of 68%,
   - an increase of axial forces in all diagonals of the bracing of 5% to 200%,
   - maximum force in the diagonal of bracing (member 3) determined for the load from forces $q_{d2} + H_2$ (column 6 in table 1) of 41.5% larger from the maximum force in the diagonal 1 of the bracing under q_{d1} (column 2 table 1),
   - taking into account the effect of torsion of the main plane of the truss shows an increase of forces in the centrally located purlin of 50% in comparison to the load by force q_{d2} and 200% for the load by force q_{d1}.
3. If apart of actions $q_{d2} + H_2$, the action from the lack of verticality is included (column 7 in table 1; loaded by forces $q_{d2} + H_1 + H_2$), then the changes in comparison to the standard model (EN 1993-1-1:2005) (column 2 in table 1; load by force q_{d1}) cover:
   - an increase of forces in all intermediate purlins (excluding the purlin 9),
   - the maximum increase of the forces in the central purlin of 246%,
   - a decrease of the forces in the eave purlins of 64%,
   - an increase of axial forces in all diagonals of the bracing of 51% to 245%,
   - maximum axial force in the diagonal of the bracing (member 2) under forces $q_{d2} + H_1 + H_2$ (column 7 in table 1) is of 76.7% higher in comparison with the maximum axial force occurring in the number 1 calculated for the force q_{d1} (column 2 in table 1),
   - the consideration of the lack of verticality of the main plane of the truss shows an increase of the force in the central purlin of 72.9% in comparison to the load by force q_{d2} and of 245.8% in comparison to the load by force q_{d1}.

The comparison of results of executed analysis of the considered models clearly indicates that there is a substantial discrepancy in the evaluation of the forces acting in both purlins and individual members of the lateral bracing system. Disregarding of the actual distribution of the compression force (EN 1993-1-1:2005) acting along the restrained member and geometrical imperfections due to lack of verticality and distorsion of the main plane of the truss leads to the significant underestimation of the real forces acting in purlins and lateral bracing system. This effect may causes a threat to the safety of the analysed structures.

Table 1. Axial forces in diagonals of the bracing and purlins for different models of load.

Number of the member acc. to Fig. 5	Axial forces in diagonals of bracing and purlins caused by loads [kN]					
	q_{d1}	q_{d2}	H_1	H_2	$q_{d2}+H_2$ (q_{d2+H_2}/q_{d1})	$q_{d2}+H_1+H_2$ ($q_{d2+H_1+H_2}/q_{d1}$)
1	2	3	4	5	6	7
1	**1.264**	0.418	0.580	0.914	1.332 (1.05)	1.912 (1.51)
2	1.034	0.916	0.474	0.843	1.759 (1.70)	**2.234** (2.16)
3	0.804	1.070	0.369	0.716	**1.786** (2.22)	2.155 (2.68)
4	0.574	0.955	0.264	0.543	1.498 (2.61)	1.761 (3.07)
5	0.345	0.651	0.158	0.338	0.990 (2.87)	1.148 (3.33)
6	0.115	0.230	0.053	0.115	0.345 (3.00)	0.397 (3.45)
7	1.199[a)]	0.384[a)]	0.050	0	0.384[a)] (0.32)	0.434[a)] (0.36)
8	0.218	0.472[a)]	0.100	0.067	0.405[a)] (1.86)	0.305[a)] (1.40)
9	0.218	0.146[a)]	0.100	0.121	0.025[a)] (0.11)	0.075 (0.34)
10	0.218	0.109	0.100	0.164	0.273 (1.25)	0.374 (1.72)
11	0.218	0.288	0.100	0.194	0.482 (2.21)	0.582 (2.67)
12	0.218	0.400	0.100	0.212	0.612 (2.81)	0.712 (3.27)
13	0.218	0.436	0.100	0.218	0.654 (3.00)	0.754 (3.46)

Notations: [a)] – the force of the sign opposite to the sign of the other purlins without symbol [a)]

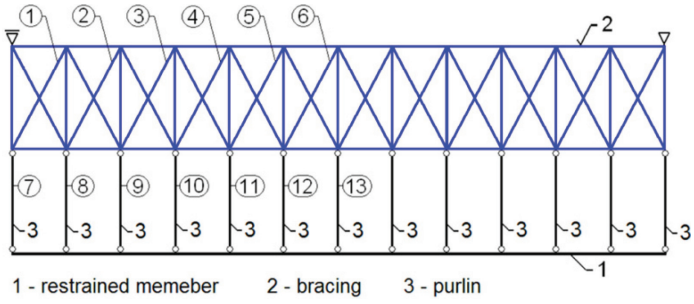

7 REMARKS AND FINAL CONCLUSIONS

The carried out analysis and studies show explicitly that the standard model that has been used for both the evaluation of the equivalent stabilising force q_{d1} (EN 1993-1-1:2005) and the method of calculation of the lateral bracing and purlins (Biegus 2013, Czepiżak 2013, Gardner & Nethercot 2005, Taylor et al. 1995, Trahair et al. 2008) are not adequate (Pałkowski & Piątkowski 2014). This is a result of effects not taken into account in this model such as the actual distribution of the compressive force in the restrained member, the lack of verticality and distorsion of the main plane of truss girders.

In the standard model (EN 1993-1-1:2005), the compression force N_{Ed} and the equivalent stabilising force q_{d1} are assumed to be uniform within the span of restrained member and according to the interpretation given in (EN 1993-1-1:2005) this is slightly conservative. In fact for a parabolic distribution of the force N_{Ed} the equivalent stabilising force q_{d2} has a non-uniform with sign changes character. The value of q_{d2} is substantially larger from q_{d1} (four times at the region of supporting and twice at the mid-span). Thus, apart from the increase of stress, the redistribution of axial forces in purlins and individual members of the lateral bracing is observed in comparison with estimations given in (EN 1993-1-1:2005) (extreme values are higher and occur in different to (EN 1993-1-1:2005) configuration of members).

The lack of verticality of the main plane of truss (analogy to columns in (EN 1993-1-1:2005)) is included for trusses, supported at bottom nodes by the suitable basic inclination ϕ_0. This additionally incorporated geometrical imperfection reveals actions H_1 as horizontal components of the vertical external load P.

The standard model (EN 1993-1-1:2005) takes into account the bow imperfection e_0 in the roof plane for an isolated single member, where in fact the bow e_0 in accompanied by the torsion of the main plane of the truss. This effect produces forces

H_2 as another type of horizontal components of the vertical external load P.

Proposed herein formulas for forces q_{d2}, H_1, H_2 associated with corresponding geometrical imperfections mentioned above, allow to create a more accurate model of analysis of the forces acting on purlins and lateral bracing system. In the general case, the equations (20) and (22) have to be employed. The qualitative and quantitative differences in compression with results obtained due (EN 1993-1-1:2005) are significant (see the analysis and presented example). A special attention needs to be paid to the additionally indicated geometrical imperfections such as the lack of verticality and distorsion of the main plan of truss. Their presence have a significant influence on the increase of axial forces acting in both purlins and members of the lateral bracing system. This effect is taken into account by the presented refined model of analysis that may be proposed in the amendment of the Eurocode 3 (EN 1993-1-1:2005).

REFERENCES

Biegus A. 2013, Calculation of Lateral Bracing for Cantilever and Multispan Girders. *Archives of Civil and Mechanical Engineering*, 13 (2013).

Czepiżak D. 2013, A Simplified Method of Calculating the Transverse Roof Bracing Systems. *Inżynieria i Budownictwo* no 11/2013 [in Polish].

Gardner M., Nethercot D. 2005, Designers Guide to EN 1993-1-1: Eurocode 3 Design of Steel Structures. Part 1-1: General Rules and Rules for Building, (Series ed. H. Gulvanessian). *Thomas Telford Limited*, London 2005.

Goncalves R., Camotim D. 2005, On the Incorporation of Equivalent Member Imperfection in the In-plane Design of Steel Frames, *Journal of Constructional Steel Research* 61 (2005) 1226–1240.

EN 1090-2:2008 *Execution of Steel Structures and Aluminium Structures*. Part 2: Technical Requirements for Steel Structures. CEN, Brussels.

EN 1993-1-1:2005 Eurocode 3: *Design of Steel Structures. Part 1-1: General Rules and Rules for Building*, CEN, Brussels 2005.

Pałkowski Sz., Piątkowski M. 2014, On the Calculation of Lateral Roof Bracing. *Inżynieria i Budownictwo* 4 [in Polish].

Taylor J.C. 1995, et all. Interim Guidance on the Use of Eurocode 3: Eurocode 3 Part 1-1: for European Design of Steel Building Structures, The Steel Construction Institute, Ascot 1995.

Trahair N.S., Bradford M.A., Nethercot D.A., Gardner L. 2008, *The Behavior and Design of Steel Structures to EC3*, Taylor and Francis, London-New York, 2008.

Timoschenko S.P., Gere J.M. 1985, *Theory of Elastic Stability*, Second Edition, McGraw-Hill, New York, 1963, 17th Printing 1985.

Recent Progress in Steel and Composite Structures – Giżejowski et al. (Eds)
© 2016 Taylor & Francis Group, London, ISBN 978-1-138-02946-0

A new method of buckling resistance evaluation of laterally restrained beam-columns

M.A. Gizejowski & Z. Stachura
Division of Metal Structures, Faculty of Civil Engineering, Warsaw University of Technology, Warsaw, Poland

M.D. Gajewski
Department of Strength of Materials and Theory of Elasticity and Plasticity, Faculty of Civil Engineering, Warsaw University of Technology, Warsaw, Poland

R.B. Szczerba
Faculty of Civil Engineering, Warsaw University of Technology, Warsaw, Poland

ABSTRACT: This paper deals with a consistent application of the Ayrton-Perry formulation for the in-plane behavior resulting from flexural buckling and one directional bending of I or H section members. A new analytical model is developed for establishing design criteria. It is based on the decomposition of bending first-order deformations into two components, namely related to the symmetrical loading in case of the first component while the second component is related to the anti-symmetrical loading. The former component is amplified in relation to the lowest bifurcation force amplification factor, while the latter — to the second lowest bifurcation force amplification factor. The results yielding from the developed model are verified using numerical FEM results based on the shell finite element modeling technique. The comparisons of results made available by proposed analytical model and those obtained with use of Eurocode's design criteria are also given. Finally, concluding remarks for future research are also drawn.

1 INTRODUCTION

Codification of design rules introduced in steel Eurocodes for the resistance verification of isolated columns and beams is based on the Ayrton-Perry formulation of a geometrically imperfect element with the crookedness being represented by the buckling mode of the lowest eigenvalue, flexural one for the in-plane behavior or lateral-torsional for the out-of-plane behavior, and by its amplitude that in EN 1993-1-1:2005 is postulated to be of an equivalent value. The obtained analytical expressions are direct solutions of differential equilibrium equations of elements with an initial equivalent crookedness. Its bow amplitude was introduced in order to account not only for geometric imperfections but also for material imperfections that are not explicitly taken care of in the computational model adopted.

Columns and beams represent two extreme cases of beam-columns. The application of Ayrton-Perry analytical formulation for intermediate cases of beam-columns for which the element is subjected to nonzero values of both the axial compressive force and the bending moment, yields a quite complicated analytical solution being not easily implemented in design codes, see Simoes da Silva et al. (2010). As a result, the Eurocode's verification criteria are based on simple interpolation formulas that are a linear combination of the utilization resistance ratio components: (1) buckling resistance utilization ratio, (2) lateral-torsional buckling utilization ratio component for equivalent uniform bending about y-y axis, and finally (3) cross-section utilization ratio component for equivalent uniform bending about z-z axis. The latter two components are additionally multiplied by the interaction coefficients k_{ij} (for $i,j = y,z$) that account for the nonlinear character and complexity of the behavior of steel beam-column elements of real structural systems. These coefficients were calibrated with use of the sensitivity analysis in order to identify the most important parameters affecting the accuracy of the adopted design criteria and the least square error approximation in order to improve the accuracy of adopted analytical equations based on a linear combination of elementary utilization resistance ratios. The verification of accuracy of the linear combination of utilization ratios was made with regard to a rather wide range of finite element simulations.

Recently, research efforts for setting up design criteria of the beam-column resistance are stepping backwards to the Ayrton-Perry approach to stability problems in order to simplify the "exact solutions" yielding from the differential equilibrium state of crooked beam-column elements and to use simplified solutions in the codification of flexural-torsional buckling resistance of beam-columns, e.g. investigations carried out at the University of Coimbra, Tankova et al. (2015). The parallel investigations are also carried out at the Warsaw University of Technology. A simple extension of the Ayrton-Perry formulation developed for columns and beams has already been developed for beam-column elements by Gizejowski & Stachura (2015). It is based on the safety margin ratio evaluation, instead of the utilization ratio evaluation, and in contrast to the former one, it does have a clear graphical interpretation.

This paper deals with a consistent application of the Ayrton-Perry approach based on an approximate second-order formulation of the imperfect member in-plane behavior resulting from flexural buckling and one directional bending of I or H section members as an alternative approach to the proposal presented by Gizejowski et al. (2016). The presentation of developed concept is preceded by some introductory remarks for the redefinition of Eurocode's partial factors application in case of stability problems.

2 CODIFICATION OF BUCKLING RESISTANCE CRITERIA FOR COLUMNS AND BEAMS

Columns and beams represent two extreme cases of beam-columns. The resistance verification of steel column or beam elements may be written down as presented by Stachura & Gizejowski (2015):

$$\frac{S_{Ed}}{S_{b,Rk}} = \frac{S_{Ed}}{\chi_k S_{c,Rk}} \le \frac{1}{\gamma_M} \tag{1}$$

in which $S_{b,Rk}$ is the nominal resistance referred to the buckling stress resultant; S_{Ed}, $S_{c,Rk}$ = nominal cross section resistance; χ_k = nominal buckling reduction factor ($\chi_{LT,k}$ for lateral-torsional buckling); γ_M = resistance partial factor.

The buckling reduction factor is the solution of the Ayrton-Perry equation of a geometrically imperfect element. For the simplest cases of isolated (simply supported) elements, the Ayrton-Perry equation can be expressed in a modified format allowing for the direct derivation of the design buckling resistance reduction factor χ_d as explained by Stachura & Gizejowski (2015):

$$\left(1-\gamma_{M1}\chi_d\overline{\lambda}^2\right)\left(1-\gamma_{M0}\chi_d\right)=\gamma_{M0}\eta\chi_d \tag{2}$$

in which χ_d is the buckling reduction factor for the design buckling resistance; γ_{M0} = cross section resistance partial factor (for stocky elements for which $\overline{\lambda}\le 0.2$); $\overline{\lambda}$ = relative slenderness ratio ($\overline{\lambda}_{LT}$ for lateral-torsional buckling), γ_{M1} = asymptotic member buckling resistance partial factor (for slenderness ratio approaching infinity); η = slenderness dependent Maquoi-Rondal dimensionless amplitude that can be expressed as follows, see Rykaluk (2012):

– for buckling of columns:

$$\eta=\frac{e_0 A}{W}=\alpha\left(\overline{\lambda}-0.2\right)\chi \tag{3}$$

– for lateral-torsional buckling of I or H beams:

$$\begin{aligned}\eta=\eta_{LT}&=\frac{e_{0,z}W_y}{W_w}\left[1+\frac{\theta_{0,x}}{e_{0,z}}\left(\frac{W_w}{W_z}-\frac{GI_T}{M_{cr}}\right)\right]\\&=\alpha_{LT}\left(\overline{\lambda}_{LT}-0.2\right)\end{aligned} \tag{4}$$

but:

$$\frac{\theta_{0,x}}{e_{0,z}}=\frac{N_{cr,z}}{M_{cr}} \tag{5}$$

where e_0 is the amplitude of geometric imperfection corresponding to the lowest in-plane buckling mode ($e_{0,y}$ or $e_{0,z}$ for buckling in compression); ($e_{0,z}$, $\theta_{0,x}$) = the amplitude components (minor axis displacement and twist) of geometric imperfections corresponding to the lowest lateral-torsional buckling mode. The other symbols conform with EN-1993-1-1:2005 and the manual of Simoes da Silva et al. (2010).

The imperfection factors α and α_{LT} of the Maquoi-Rondal amplitude of the equivalent geometric imperfections are associated with the particular buckling curve. The selection of relevant buckling curves for the actual design situation is based on several factors, e.g. the direction of flexural buckling, section geometry and section depth to width ratio, among others.

Using two independent partial factors for the evaluation of the element design buckling resistance, Equation (1) becomes:

$$\frac{S_{Ed}}{S_{b,Rd}}=\frac{S_{Ed}}{\dfrac{\chi_d S_{c,Rk}}{\gamma_{M1}}}=\frac{S_{Ed}}{\chi_d S_{c,Rd}}\frac{\gamma_{M1}}{\gamma_{M0}}\le 1.0. \tag{1a}$$

Equation (1a) is used for the resistance verification of extreme cases of beam-column elements

but not to all other intermediate cases laying between beams and columns, i.e. when there are nonzero values of both the axial compressive force and bending moment. Solving Equation (2) for the reduction factor gives:

$$\chi_d = \frac{1}{\phi_d + \sqrt{\phi_d^2 - \left(\overline{\lambda}\sqrt{\frac{\gamma_{M1}}{\gamma_{M0}}}\right)^2}} \frac{\gamma_{M1}}{\gamma_{M0}} \le \frac{\gamma_{M1}}{\gamma_{M0}}, \quad (6)$$

$$\phi_d = 0.5\left[1 + \alpha(\overline{\lambda} - 0.2) + \left(\overline{\lambda}\sqrt{\frac{\gamma_{M1}}{\gamma_{M0}}}\right)^2\right]. \quad (7)$$

The resistance partial factor γ_M can be now expressed as a function of the slenderness ratio as:

$$\gamma_M = \gamma_{M1}\frac{\chi_k}{\chi_d} \quad (8)$$

where the bucking reduction factor χ_k for the characteristic buckling strength is that calculated with use of Equations (6) and (7) but using the values of partial factors equal to unity, i.e. the ratio $\gamma_{M1} / \gamma_{M0} = 1.0$.

3 CONCEPT OF DESIGN CRITERION FOR THE IN-PLANE BEHAVIOR OF BEAM-COLUMNS

3.1 *Background of analytical formulation*

Let us consider two extreme cases of a simply supported beam-column of class 1 or 2 section, bent about *y-y* axis, that is subjected to a non-uniform bending moment diagram resulting from the application of two different end moments (Fig. 1). S235 steel grade of HEB 300 section is considered.

In the following, the beam-column in-plane behavior in case of a uniform axial force diagram and a complex nonuniform bending moment diagram is dealt with. It is worthy to note that the approach presented on the exemplary end moments bending diagram can be applied to any other nonuniform distribution of the bending moment resulting from the in-span loads only, or in-plane loads and support moments, provided that the complex bending moment diagram is represented by a superposition of two diagrams, the symmetric one and its antisymmetric counterpart.

In case presented in Figure 1, there is a linear change of the first-order moment the distribution of which is characterized by ψ_y-factor:

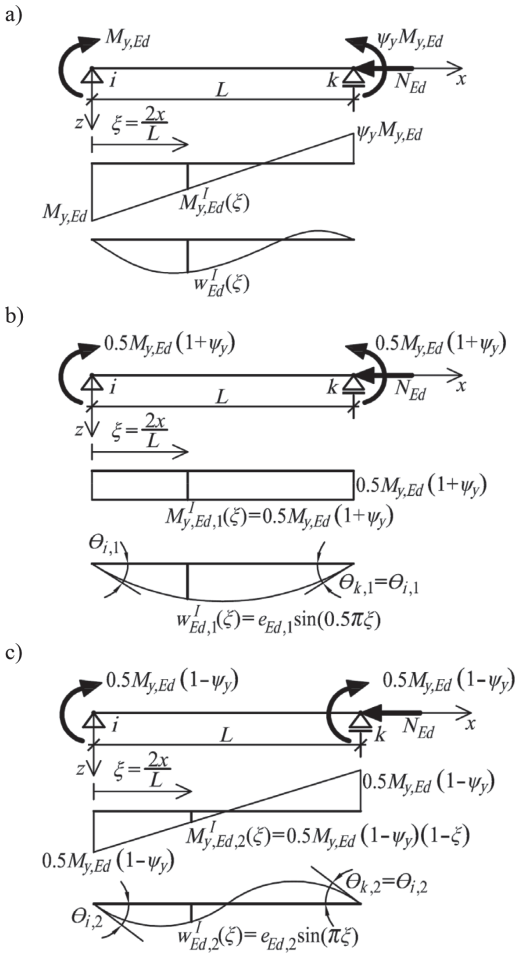

Figure 1. Decomposition of end moment loading case of the beam-column under a constant axial force: a) general loading case; b) symmetrical loading component; c) anti-symmetrical loading component.

$$M^I_{y,Ed}(\xi) = 0.5M^I_{y,Ed}\left[1 + \psi_y + (1-\psi_y)(1-\xi)\right] \quad (9)$$

in where $\xi = 2x / L_{cr}$ is the dimensionless member coordinate (in case of a simply supported member $L_{cr} = L$); $X(\xi)$ = variable being a function of ξ; $M_{y,Ed} = M_{y,Ed,\mathrm{supp,max}}$ = maximum support moment; $\psi_y = M_{y,Ed,\mathrm{supp,min}} / M_{y,Ed,\mathrm{supp,max}}$ = support moments ratio.

For the approximation of second-order displacements of the considered beam-column, an arbitrary distribution of the bending moment may be treated as a linear combination of two extreme bending moment diagram cases, namely the symmetric one and the anti-symmetric one. Furthermore, let us assume that the displacement shapes satisfying the kinematic and static bound-

ary conditions are approximated by sin functions representing the first two buckling modes of a simply supported perfect column. Thus, applying the superposition principle, the following approximate relationship holds for an imperfect beam-column:

$$\begin{aligned} M^{II}_{y,Ed}(\xi) &= \\ &= M^{I}_{y,Ed}(\xi) + w^{I}_{Ed,1}(\xi) N_{Ed} + w^{I}_{Ed,2}(\xi) N_{Ed} \\ &= M^{I}_{y,Ed}(\xi) + \frac{\left(e_{Ed,1} + e_0\right) N_{Ed}}{1 - \dfrac{N_{Ed}}{N_{cr}}} \sin(0.5\pi\xi) \\ &+ \frac{\left(e_{Ed,2} + e_{0,2}\right) N_{Ed}}{1 - \dfrac{N_{Ed}}{4N_{cr}}} \sin(\pi\xi) \end{aligned} \tag{10}$$

in which the last two terms of RHS represent the bending moment due to the so-called *P-δ* effect; N_{cr}, $4N_{cr}$ = represent the bifurcation forces corresponding to the first and the second lowest buckling modes of the simply supported column for which there are the same boundary conditions and the axial force distribution as those of the considered beam-column; e_0 = crookedness specified in EN 1993-1-1:2005 for the lowest bifurcation mode (symmetric); $e_{0,2}$ = crookedness corresponding to the second lowest bifurcation mode (anti-symmetric); $e_{Ed,1}$, $e_{Ed,2}$ = amplitudes of the first-order displacements corresponding to the symmetric and anti-symmetric transverse loading components:

$$e_{Ed,1} = \frac{M_{y,Ed} L^2}{16 EI_y}\left(1 + \psi_y\right), \tag{11a}$$

$$e_{Ed,2} = \frac{M_{y,Ed} L^2}{128 EI_y}\left(1 - \psi_y\right). \tag{11b}$$

Figure 2 presents the approximate deflected profile corresponding to the anti-symmetrical moment diagram. The dashed line is the deflected axis resulting from the adopted superposition principle of the first-order deflections due to symmetric and anti-symmetric cases of end moments. The solid line is the deflected axis predicted only for the anti-symmetric loading case. One can note that there is a shift of the maximum deflection coordinate e_{max} towards the supports if it is compared with the deflected profile corresponding to the anti-symmetric loading case.

Letting the dimensionless variables related to the plastic properties of the section, for the partial factors $\gamma_{M0} = \gamma_{M1} = 1.0$, to be expressed as:

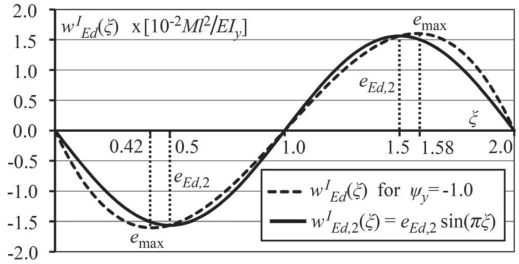

Figure 2. First-order deflected beam-column profile resulting from applied end moments.

$$m^{II}_{y,Ed}(\xi) = \frac{M^{II}_{y,Ed}(\xi)}{M_{y,pl,Rk}}, \tag{12a}$$

$$m^{I}_{y,Ed}(\xi) = \frac{M^{I}_{y,Ed}(\xi)}{M_{y,pl,Rk}}, \; m_{y,Ed} = \frac{M_{y,Ed}}{M_{y,pl,Rk}}, \tag{12b,c}$$

$$n_{Ed}\overline{\lambda}^2_y = \frac{N_{Ed}}{N_{cr}}, \; n_{Ed} = \frac{N_{Ed}}{N_{pl,Rk}}, \tag{12d,e}$$

$$\eta_y = \eta_{y,1} = \frac{N_{pl,k} e_0}{M_{y,pl,Rk}}, \; \eta_{y,2} = \frac{N_{pl,k} e_{0,2}}{M_{y,pl,Rk}}, \tag{12f,g}$$

one can deduce that for the formulation of the second-order resistance criterion it is required to set the magnitude of e_0 and $e_{0,2}$.

3.2 *Selection of bow imperfection amplitudes*

The amplitude component e_0 of the initial deflection profile corresponds to the lowest eigenvalue. The value of this component is taken according to the general method of buckling assessment in EN 1993-1-1:2005 as a function of the member slenderness ratio and plastic class 1 and 2 section resistances:

$$e_0 = \alpha\left(\overline{\lambda}_y - 0{,}2\right)\frac{M_{y,pl,Rk}}{N_{pl,Rk}} \tag{13}$$

so that it allows for defining the quantity $\eta_{y,1}$. Selection of $e_{0,2}$ amplitude component is not so obvious so that one needs to establish a criterion according to which the magnitude of $e_{0,2}$ could be related to e_0. Gizejowski et al. (2016) assumed that the imperfection profile of the second lowest eigenvalue is described by taking the amplitude $e_{0,2} = 0.5e_0$. This assumption corresponds to the situation in which the amplitudes of the successive eigenmodes for $i \geq 2$ yield from the concept of buckling length:

$$\frac{\overline{\lambda}_i}{e_{0,i}} = \frac{\overline{\lambda}}{e_0} \text{ where } \overline{\lambda}_i = \sqrt{\frac{N_{c,Rk}}{i^2 N_{cr}}} = \frac{\overline{\lambda}}{i}. \tag{14}$$

Thus, the following relationship holds:

$$e_{0,i} = \frac{e_0}{i}. \tag{15}$$

Since it is more difficult from the physical point of view to technologically generate the imperfection profile component related to the second buckling mode, it is more credible to postulate that the amplitude of this imperfection profile component is calculated on the basis of energy concept. According to this concept, the amplitudes are related to the elastic strain energy accumulated in the beam element:

$$V_i[w_i(x)] = V_0[w(x)] \tag{16}$$

in which:

$$V_i[w_i(x)] = \frac{1}{2}\int_0^L EI\left[\frac{dw_i(x)}{dx}\right]^2 dx \tag{17}$$

and $V_1[w_1(x)] = V_0$ is the reference elastic strain energy corresponding to the critical force buckling mode. Taking the imperfection profile component for the simply supported column as the i-th buckling mode, given by the following formula:

$$w_i(x) = e_{0,i}\sin\left(\frac{i\pi x}{L}\right) \tag{18}$$

the strain energy component $V_i[w_i(x)]$ is obtained as:

$$V_i = V_i[w_i(x)] = \frac{EIe_{0,i}^2 i^2 \pi^4}{4L^3}. \tag{19}$$

Hence, V_0 can be obtained from (19) by substituting $i = 1$. Finally the application of equality (16) gives:

$$e_{0,i} = \frac{e_0}{i^2}. \tag{20}$$

The amplitudes evaluated for successive eigenmodes describing the imperfection profile are therefore given by: $e_0 = 4e_{0,2}$, $e_0 = 9e_{0,3}$, $e_0 = 16e_{0,4}$, and so on. In the following, for the second lowest eigenmode, the amplitude $e_{0,2} = 0.25e_0$ resulting from Equation (20) is employed. Such an amplitude is half of that resulting from the application of the buckling length concept [see Eqn. (15)]. Figure 3 presents the comparison of the imperfection profile evaluated on the basis of the buckling length concept (dashed line) and the elastic strain energy equivalence concept (solid line).

Using the proposed value of $e_{0,2}$, the quantity $\eta_{y,2}$ can be written down as follows:

$$\eta_{y,2} = \frac{N_{pl,k}e_{0,2}}{M_{y,pl,Rk}} = \frac{N_{pl,k}e_0}{4M_{y,pl,Rk}}. \tag{21}$$

Thus, the following relationship holds for the approximate dimensionless second-order moment equation as a function of the member axis x-x:

$$m_{y,Ed}^{II}(\xi) = m_{y,Ed}^{I} + \frac{\left[\eta_{Ed,1} + \alpha_y\left(\overline{\lambda}_y - 0.2\right)\right]n_{Ed}}{1 - \overline{\lambda}_y^2 n_{Ed}} \times \sin(0.5\pi\xi) + \frac{\left[\eta_{Ed,2} + 0.25\alpha_y\left(\overline{\lambda}_y - 0.2\right)\right]n_{Ed}}{1 - 0.25\overline{\lambda}_y^2 n_{Ed}}\sin(\pi\xi) \tag{22}$$

where $\eta_{Ed,1}$, $\eta_{Ed,2}$ = dimensionless amplitudes of the first-order displacements corresponding to symmetric and anti-symmetric bending moment distributions:

$$\eta_{Ed,1} = \frac{N_{pl,k}e_{Ed,1}}{M_{y,pl,Rk}},\ \eta_{Ed,2} = \frac{N_{pl,k}e_{Ed,2}}{M_{y,pl,Rk}}, \tag{23a,b}$$

and:

$$m_{y,Ed}^{I}(\xi) = 0.5m_{y,Ed}\left[1 + \psi_y + \left(1 - \psi_y\right)(1 - \xi)\right]. \tag{23c}$$

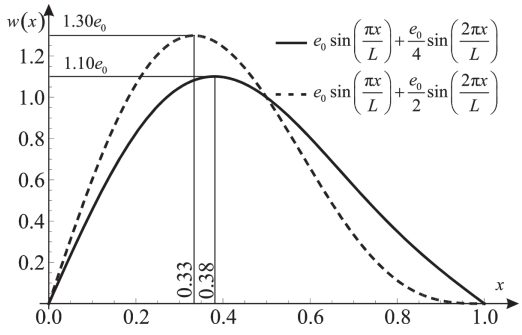

Figure 3. Approximation of the imperfect beam-column profile.

The Ayrton-Perry strength criterion according to the Eurocode's format is therefore of the following format:

$$m_{y,Ed}^{II}(\xi_{\max}) = m_{N,Rd} \tag{24}$$

in which $m_{N,Rd}$ is the dimensionless reduced cross section plastic resistance. Equation (22) leads to the following relationship for calculation of the coordinate $\xi_{\max}$ of the member most stressed section:

$$\begin{aligned} &0.5m_{y,Ed}\left[1+\psi_y+\left(1-\psi_y\right)\left(1-\xi_{\max}\right)\right] \\ &+\frac{\left[\eta_{Ed,1}+\alpha_y\left(\overline{\lambda}_y-0.2\right)\right]n_{Ed}}{1-\overline{\lambda}_y^2 n_{Ed}}\sin\left(0.5\pi\xi_{\max}\right) \\ &+\frac{\left[\eta_{Ed,2}+0.25\alpha_y\left(\overline{\lambda}_y-0.2\right)\right]n_{Ed}}{1-0.25\overline{\lambda}_y^2 n_{Ed}}\sin\left(\pi\xi_{\max}\right) \\ &=\min\left(\frac{1-n_{Ed}}{1-0.5a};1.0\right) \end{aligned} \tag{25}$$

One can realize that for $m_{y,Ed} = \eta_{Ed,1} = \eta_{Ed,2} = 0$ and furthermore, for the LHS terms calculated for $\xi_{\max} = 1.0$ with use of the following approximation of RHS:

$$\min\left(\frac{1-n_{Ed}}{1-0.5a};1.0\right)\approx 1-n_{Ed}. \tag{26}$$

Equation (25) is being reduced to Equation (2) for the characteristic resistance evaluation of imperfect columns in accordance to the original Ayrton-Perry approach. The dimensionless axial force n_{Ed} evaluated for the partial factors $\gamma_{M1} = \gamma_{M0} = 1.0$ becomes the buckling reduction factor $\chi_{y,k}$. One has however to note that in a general case of the imperfect member profile being the combination of two buckling modes, corresponding to the first and the second lowest bifurcation forces, Equation (2) is no longer valid. The calculation procedure of the buckling reduction factor is the same as for a transversally loaded beam-column element.

In Figure 4, the buckling curve "*b*" according to EN 1993-1-1:2005 is drawn and compared with discrete points representing the solution of Equation (25) for the selected beam-column slenderness ratios of 0.5, 1.0, 1.5 and 2.0; note that it is for taking $m_{y,Ed} = 0$. The red circle mark corresponds to the elastic buckling resistance of imperfect beam-column, i.e. when in RHS of Equation (25) the linear interaction curve given by Equation (26) is used. The black diamond mark corresponds to the inelastic buckling resistance evaluated directly from the original Equation (25). From the comparison presented in Figure 4 one can conclude that the developed analytical model yields, for selected slenderness ratios and the linear cross section $m_{y,Ed} - n_{Ed}$ interaction curve, the results laying on the buckling curve. Points representing the results based on the actual nonlinear cross section $m_{y,Ed} - n_{Ed}$ interaction curve are however placed slightly above the Eurocode's buckling curve as one would have expected.

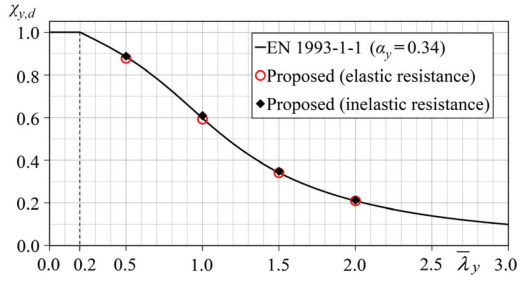

Figure 4. Comparison of buckling reduction factors from developed analytical model and Eurocode's buckling curve.

On the other hand, for $n_{Ed} = 0$ and $\xi_{\max} = 0$, the LHS of Equation (25) reduces to only the first term and becomes the ultimate limit state criterion for in-plane bending of beams.

3.3 *Verification of developed analytical model for nonzero axial force and end moments*

Let us consider different ratios between the dimensionless axial force n_{Ed} and the support dimensionless bending moment $m_{y,Ed}$ of the greater absolute value. Three load cases are considered hereafter that correspond to the lesser dimensionless end moment of the value $\psi_y m_{y,Ed}$ for $\psi_y = 1.0$, 0.0 and –1.0. Solving Equation (25) for three load cases characterized by the considered factor ψ_y and given discrete pairs of n_{Ed} and $m_{y,Ed}$, the dimensionless coordinates $\xi_{\max}$ of the most stressed section may be calculated in order to evaluate the second order dimensionless moment $m^{II}_{y,Ed}$ from Equation (22).

Knowing the coordinate $\xi_{\max}$, the ultimate state interaction curves illustrating the relationship between $m_{y,Ed}$ and n_{Ed} may also be constructed for different ψ_y-factors and slenderness ratios $\overline{\lambda}_y$ .The results are shown in Figures 5 and 6 with use of solid lines. For comparison, finite element interaction curves evaluated for imperfect beam-column elements and presented by Gizejowski et al. (2016) are also given in Figure 5, and marked by the dashed lines. Another comparison is made in Figure 6 with reference to the combined resistance of the cross-section moment resistance reduced due to the axial

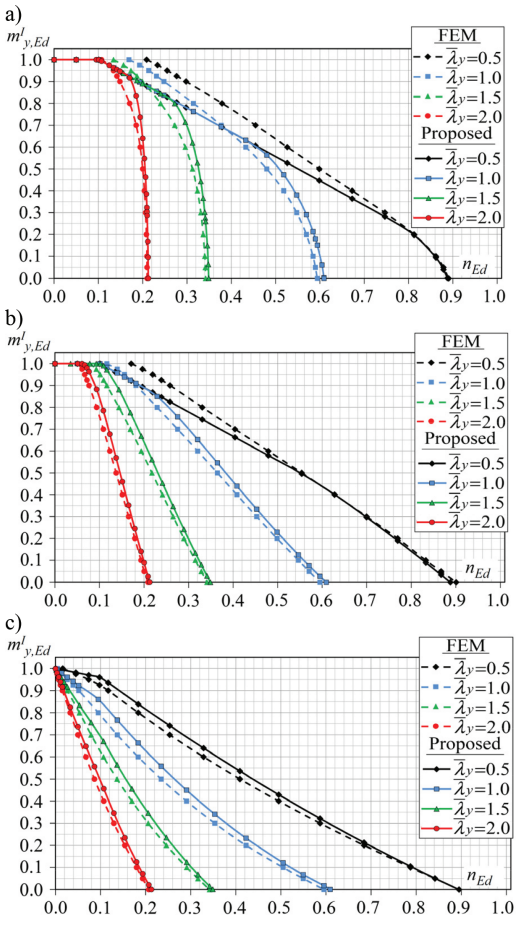

Figure 5. Comparison of interaction ultimate strength curves obtained in this paper with those of predicted by FEM for the slenderness ratios $\bar{\lambda}_y$ = 0.5; 1.0; 1.5; 2.0, and the moment ratios: a) ψ_y = –1.0; b) ψ_y = 0.0; c) ψ_y = 1.0.

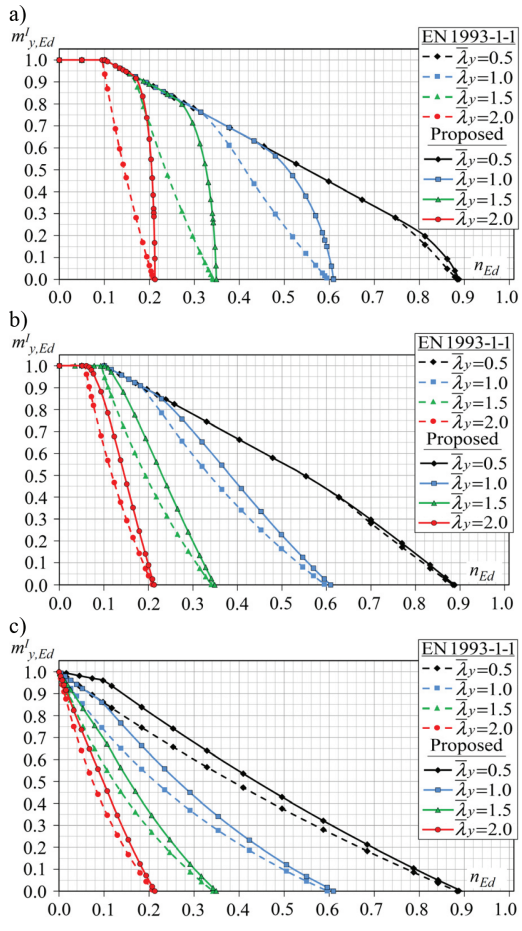

Figure 6. Comparison of interaction ultimate strength curves obtained in this paper with those of EN 1993-1-1:2005 for the slenderness ratios $\bar{\lambda}_y$ = 0.5; 1.0; 1.5; 2.0, and the moment ratios: a) ψ_y = -1.0; b) ψ_y = 0.0; c) ψ_y = 1.0.

force and the buckling resistance in reference to the so-called Method 2 of EN 1993-1-1:2005. Results obtained in this paper are indicated by solid lines, and those of Eurocode by dashed lines.

The results dependent upon the indicator $n_{b,y,Ed} = n_{Ed} / \chi_{y,k}$ are shown in Figure 7 for different slenderness ratios $\bar{\lambda}_y$ = 0.5, 1.0, 1.5 and 2.0. It can be observed that the results for each slenderness ratio constitute a linear relationship between the indicator $n_{b,y,Ed}$ and the second order moment $m^{II}_{y,Ed}(\xi_{\max})$. The dimensionless second order moment reaches the value equal to unity for a dimensionless axial force $n_{Ed} \le a_y$ (a_y is here a new parameter replacing that of $0.5a$ for stocky beam-columns) and for each slenderness ratios there is a different slope of the line.

Since the results shown in Figure 7 are valid for imperfect beam-columns, one can compare these results with those reported for perfect beam-columns by Gizejowski et al. (2015) and evaluated with use of a finite element beam model. Figure 8 recalls the results for perfect elements. It has to be emphasized that the dimensionless buckling resistances in Figures 7 and 8 are normalized with regard to different values of the buckling resistance in case of pure compression. Figure 9 presents a drop in the dimensionless buckling resistance $n_{Ed} = \chi_{y,k}$ in pure compression in case of imperfect elements in comparison of their perfect counterparts, as well as a rise in the dimensionless second-order moment $m^{II}_{y,Ed}$ being the dimensionless moment $m^{II}_{y,Ed}(\xi_{\max})$ for $n_{Ed} = \chi_{y,k}$.

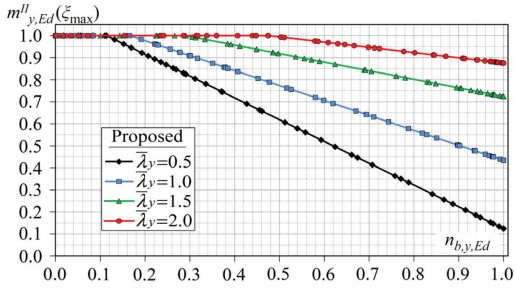

Figure 7. Graphical illustration of the maximum coordinate second-order moment as a function of the indicator $n_{b,y,Ed}$ for all considered moment ratios ψ_y for imperfect beam-columns.

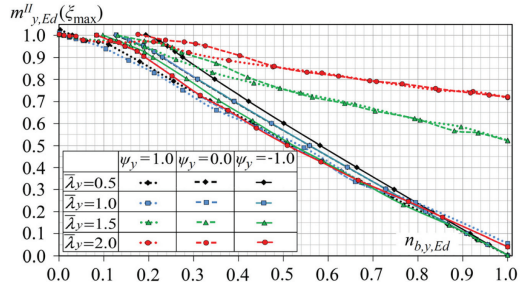

Figure 8. Graphical illustration of the maximum coordinate second-order moment as a function of the indicator $n_{b,y,Ed}$ for all considered moment ratios ψ_y for perfect beam-columns (Gizejowski et al. 2015).

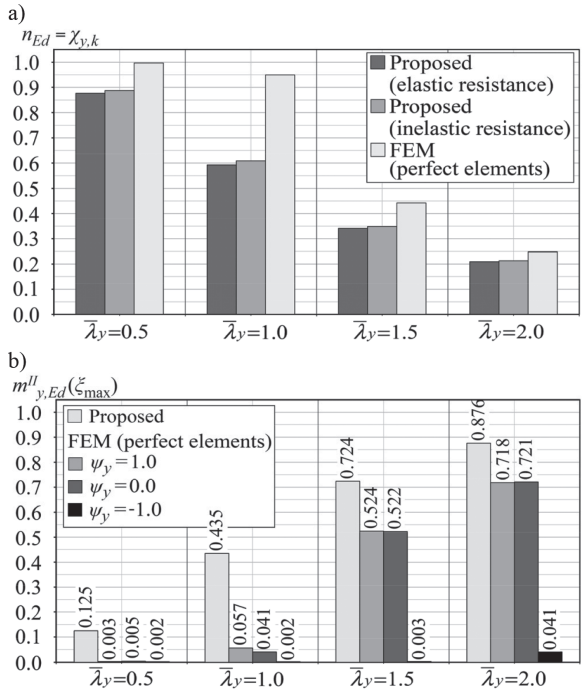

Figure 9. Comparison of the behavior of perfect and imperfect elements: a) dimensionless resistance in pure compression, b) dimensionless moment $m^{II}_{y,Ed}$ being the dimensionless moment $m^{II}_{y,Ed}(\xi_{max})$ for $n_{Ed} = \chi_{y,k}$.

Studying the relationships for both member models one may observe a similarity between results obtained for perfect and imperfect beam-columns. Only the difference is that for imperfect beam-columns the interaction curves are placed above those obtained for perfect beam-columns.

The verification of developed analytical model shows that it represents accurately the in-plane behavior of I or H section beam-columns bent about *y-y* axis provided that they are laterally and torsionally restrained between the supports. Except the beam-columns of low slenderness ratio and end moments producing opposite end rotations, the interaction curves $m_{y,Ed}$ and n_{Ed} from analytical model developed are placed slightly above those obtained numerically with use of FEM and analytically according to Eurocode's interpolation formulas. The accuracy of predictions by the proposed method might be improved by increasing the first order displacement values of $\eta_{Ed,1}$ and $\eta_{Ed,2}$ and multiplying them by a factor greater than one to compensate the error resulting from the fact

that the second order displacements are obtained herein by using the approximate amplification rule. In future it is planned to conduct experimental investigations and the validation exercise, comparing results from the proposed method and test results available from these investigations together with the results existing in literature.

4 CONCLUSIONS

The developed analytical model is a direct extension of the Ayrton-Perry modeling technique applied originally for the imperfect column resistance evaluation, and then also utilized for the evaluation of the buckling resistance of imperfect beams. This model is used herein for the resistance evaluation of beam-columns subjected to in-plane loading without LT-buckling. One can emphasize three important features of the model developed herein for bending and buckling about the major principal axis:

1. Developed model has a clear mechanical interpretation for all the situation of complex bending moment diagrams.
2. It does not need the introduction of the equivalent uniform moment factor to account for the complex distribution of bending moments along the beam-column length.
3. Model developed for major principal axis buckling and bending (about *y*-*y* axis) may be directly employed for minor principal axis buckling and bending (about *z*-*z* axis) provided that the stocky beam-column ultimate strength curve and the column buckling curve representative to this situation are taken into account.

The proposed analytical model for the evaluation of in-plane buckling resistance may be summarized as follows:

1. For the given complex bending moment diagram, obtained for a given beam-column element from relevant structural analysis, decompose it into two simple diagrams that are called SIPB (a symmetric in-plane bending moment diagram) and AIPB (an anti-symmetric in-plane bending moment diagram).
2. Determine the first order amplitudes $e_{Ed,1}$ and $e_{Ed,2}$ (maximum displacements corresponding to load effects relevant to SIPB and AIPB, respectively) using conventional methods of structural mechanics theory, e.g. the unit virtual load method.
3. Amplify the first order amplitudes in order to get their approximate second-order counterparts.
4. Construct Equations (22)–(25) and solve them in order to get the coordinate of an approximate maximum second-order bending moment and corresponding load effects (in case of constant axial force, the second-order bending moment only).
5. Calculate the dimensionless bending moment $m^{II}_{y,Ed}(\xi_{\max})$ corresponding to the actual dimensionless axial force n_{Ed}.

The proposed generalized Ayrton-Perry approach is applied to I and H section beam-columns loaded in the major axis plane, thus producing bending moments acting about the major principal axis, but notifying that it may be used only for structural elements being restrained laterally and torsionally. In case of I or H section beam-columns bent about *y*-*y* axis but unrestrained between the supports, the ultimate state is associated with a failure mode resulting from two-directional bending and warping torsion due to the beam-column out-of-plane behavior. This situation is out of scope of the present paper and it remains to be the subject of forthcoming research stages.

REFERENCES

EN 1993-1-1:2005. Eurocode 3: Design of Steel Structures, Part 1–1: General rules and rules for buildings. Brussels: European Committee for Standardization.

Gizejowski, M. & Stachura, Z. 2015. Resistance partial factors for stability design of steel members according to Eurocodes. *8th International Conference on ADVANCES IN STEEL STRUCTURES, Lisbon, 22–24 July 2015*. Paper 23 on CD: 1–20.

Gizejowski, M., Szczerba, R. & Gajewski, M. 2016. A unified resistance verification of beam-columns not susceptible to LT-buckling. *Proceedings of ICMS'2016* (in press).

Gizejowski, M., Szczerba, R., Gajewski, M. & Stachura, Z. 2015. Beam-column resistance interaction criteria for in-plane bending and compression. *Procedia Engineering*. Special Issue (eds. Jemiolo S., Gajewski, M. & Krzeminski, M.). *Open Access Journal.* Elsevier. Vol. 111: 254–261.

Rykaluk, K. 2012. *Stability problems of metal structures*. Wrocław: Dolnośląskie Wydawnictwo Edukacyjne [in Polish].

Simoes da Silva, L., Simoes, R. & Gervasio, H. 2010. *Design of Steel Structures, Eurocode 3: Design of steel structures, Part 1-1: General rules and rules for buildings. ECCS Eurocode Design Manual*. Berlin: Ernst & Sohn.

Stachura, Z. & Gizejowski, M. 2015. Partial factors in modeling of steel structures reliability according to Eurocodes. *Civil and Environmental Engineering Reports* 16(1): 195–207. Zielona Gora: University of Zielona Gora Press.

Tankova, T., Simoes da Silva, L., Marques, L. & Andrade, A. 2015. Proposal of an Ayrton-Perry design methodology for the verification of flexural and lateral-torsional buckling of prismatic beam-columns. *8th International Conference on ADVANCES IN STEEL STRUCTURES, Lisbon, 22–24 July 2015*. Paper 21 on CD: 1–10.

This page intentionally left blank

Recent Progress in Steel and Composite Structures – Giżejowski et al. (Eds)
© 2016 Taylor & Francis Group, London, ISBN 978-1-138-02946-0

Distortional lateral torsional buckling of open and closed steel cross-sections

R. Studziński & M. Czaja
Institute of Structural Engineering, Poznan University of Technology, Poznan, Poland

ABSTRACT: The paper deals with lateral torsional buckling of open and closed steel cross-sections. The aim of the paper is the verification of the analytical approach of the Vlasov beam theory adopted by the EC3 settlements. This verification was performed by FE simulations. The following design situations were considered: the material model definition (elastic vs. elastic-plastic), the lateral restraint (with or without), the position of the lateral restraint along the height of the cross-section (at the top, in the middle, at the bottom), the ribs (with or without). Additionally, the FE analyses were performed for different slenderness of the cross-sections measured by the height to width ratio. In the case of open cross-sections the distortional lateral torsional buckling was obtained. In the case of closed cross-sections the lateral buckling was not obtained because the plastic deformation of the cross-section walls caused the failure of the beam.

1 INTRODUCTION

Prismatic steel beams are essential elements of many modern steel or steel-concrete structures. They are characterized by high load-bearing capacity and are easy to install, nevertheless their sensitivity to local and/or global instability results in premature failure of the structure. Thus, the stability phenomena are often the key problem in the design of the steel structures since they significantly affect the capacity of steel structures. The present paper deals with the problem of lateral torsional buckling of the open and closed steel cross-sections.

The capacity of the typical steel element in bending consists of the cross-section resistance and the member resistance. The cross-section resistance depends on the geometry of the cross-section and the distribution of the normal stresses along the height of a section. Therefore it consists of the yield stresses and the local buckling phenomenon. In the case of resistance of the member in bending, it depends on the lateral torsional buckling phenomenon. In subject literature the Vlasov beam theory describes the kinematics of the beam in bending, but the simplification makes this description approximate, especially in the case of slender cross-sections (Bazant & Nimeiri 1973, Timoshenko & Gere 1961).

The FE simulations presented in the paper indicate that the deformation of the beams in bending with slender sections usually had to be described by the following modes: longitudinal and transverse displacement, warping, rotation and distortion of the cross-section shape. This phenomenon is called distortional lateral torsional buckling. The warping and the distortion modes cannot be expressed by the conventional beam theory (Vlasov beam theory). The warping mode arises from the influence of shear strain of the middle surface of the walls, while the distortion of the cross-section shape can be eliminated by thickly spaced rigid diaphragms (ribs). Including these deformations of a beam in bending the phenomenon of the distortional lateral torsional buckling can be identified analytically by the General Beam Theory (GBT), the Direct Strength Method or the FEM.

The GBT was developed by Schard (1983) and has been undergoing constant development. Davis (1998) expressed within the framework of the GBT the coupled instability problems. Recently the problem of the distortion modes in thin-walled sections (open and closed) has been investigated by Camotim and Gonçalves. Camotim et al. (2006) and Gonçalves et al. (2009) presented a brief overview of the GBT and an extension of the GBT on: the different cross-section types (branched, closed and closed/branched cross-sections), the elements made of orthotropic and elastic-plastic materials, and the post-buckling behaviours of elastic isotropic and orthotropic members.

The review of the development and actual trends in the Direct Strength Method for cold-formed steel member design was presented by Schafer (2008). Additionally, the author compared the Direct Strength Method with the Effective Width Method. The Direct Strength Method is in fact an

extension of application column curves used for global buckling. Additionally, it makes it possible to determine the local and distortional buckling instabilities including their interactions. The post-buckling reserve is also possible to obtain.

In the case of FEM the simulations usually are very time-consuming and require knowledge and experience in the modeling of the problem. It was observed that the obtained numerical results are very sensitive to the definition of boundary conditions, the mesh size, the type of finite element, the material model, and the way of load implementation.

2 PROBLEM FORMULATION

The simply supported beam with the varied span lengths L under the three-point bending is considered. Within the framework of the parametric numerical research of the distortional lateral torsional buckling the following parameters were assumed as independent variables: type of the cross-section (open, closed); slenderness of the cross-section; material model (elastic, elastic-plastic); support conditions; the presence or absence of diaphragms/ribs and their spacing; the magnitude of the assumed imperfections, the way of load implementation and the position of the out-of-plane restraint, if applicable. The numerical results were compared with an approximate (based on the Vlasov theory) solutions calculated according to the EN Standard formulas.

In Table 1 the considered cross-sections and the information about sections slenderness and classes is presented.

The numerical discretization was conducted using quadrilateral conventional shell elements S4R. The S4R is a four-node element with reduced integration points which makes it possible to avoid shear and membrane locking. Since the application of the load in a single point would cause stress concentration, it was decided to apply the load in another way. In the case of I-beams the load was applied to the reference point which was coupled with ¼ of the height of the web. In the case of the box sections the load was applied to the reference point which was coupled with a section of the web of a length equal to width of the beam, see Fig. 1.

Figure 2 presents the stress concentrations and deformations connected with the way of the application of the load in the FE model with elastic (sections *a* and *b*) and elastic-plastic (sections *c* and *d*) material model definition.

In Figure 2 sections *a* and *c* refer to the suggested (coupled) application of the load (see Fig. 1), while sections *b* and *d* refer to the case when the load is applied in a single point. The deformations and stress concentrations in the latter case are significant and lead to inappropriate results. The suggested way of the application of the load is correct.

The S235 steel grade was assumed. Two material models—linear elastic and nonlinear elastic-plastic—were considered, Table 2.

Table 1. The list of the double-tee (I) and rectangular hollow (RHS) cross-section.

		h	b	h / b	t_f	t_w	class*
Type	Name	mm	mm	–	mm	mm	–
Open	I-120	120	60	2.0	6	4	1
I	I-330	330	160	2.1	11	4	2
	I-450	450	190	2.4	14	4	3
	I-550	550	210	2.7	17	4	4
Closed	120 × 4	120	120	1.0	4	4	1
RHS	180 × 4	180	120	1.5	4	4	1
	240 × 4	240	120	2.0	4	4	1
	300 × 4	300	120	2.5	4	4	2
	360 × 4	360	120	3.0	4	4	3

* class of the cross-section in bending according to EC3.

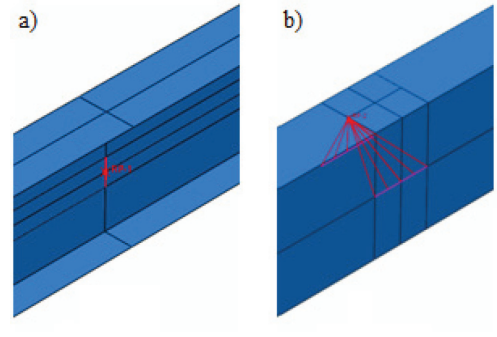

Figure 1. The suggested way of a application of the load in FE model in the case of I (a) and RHS beam (b).

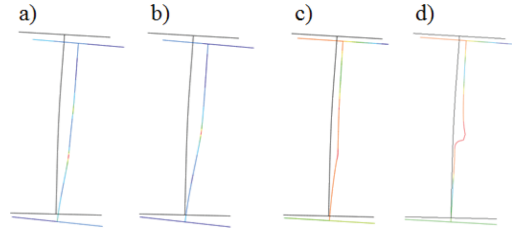

Figure 2. Stress concentrations and deformations of a cross-section provided by two ways of application of load in the FE model (description in text).

Table 2. The physical properties of the material models.

Model	Yield strength f_y MPa	Young modulus E GPa	Poisson ν –	Plastic strain ε –
Linear, elastic	235	210	0.3	–
Non linear, elastic-plastic	235	210	0.3	0.1

The fork simply supported conditions are assumed. They provide lateral restraint at the supports. The two-stage approach was implemented in order to obtain the lateral torsional buckling capacity of the beams in bending. The linear buckling analysis (stage one), and the nonlinear static analysis with implemented geometrical bow imperfection from the first stage (stage two) were introduced.

In the case of linear buckling analysis, the eigenvalue problem is described as follows, Eq. (1)

$$K^{MN} v^M = 0, \tag{1}$$

where K^{MN} is the stiffness matrix of an element, and v^M is the displacement vector. The Eq. (1) can be rewritten, see Eq. (2):

$$\left(K_0^{MN} + \lambda_i K_\Delta^{MN}\right) v_i^M = 0, \tag{2}$$

where K_0^{MN} is the initial stiffness matrix, K_Δ^{MN} is the differential stiffness matrix of the initial stresses and loads due to incremental force Q^N which is defined by the user, λ_i are the eigenvalues, v_i^M are the eigenvalue vectors for the i^{th} buckling mode.

Please note that the assumed shell finite elements (S4R) provide accurate buckling critical loads for membrane states. In the case of lateral torsional buckling of the beam this finite element is not capable of predicting accurate buckling critical loads. Nevertheless, even if the buckling analysis does not give reliable critical loads, it can be used to obtain the shape of the buckling mode which is in general correct. It is often the most useful and desirable result of the buckling analysis, because it makes it possible to predict the likely form of the deformation of the structure. Please note that the provided buckling mode values are not the values of the displacements of the individual points, but are the proportions between them.

After buckling analysis (stage one) the general static analysis (stage two) is performed. In this stage all possible nonlinearities (geometrical, material, boundary) can be taken into account. The calculations were performed using the Newton-Raphson procedure, the mesh size was 5 mm. In this stage the adequate shape of a buckling mode was implemented—the geometrical bow imperfection. The sag of this bow imperfection was in agreement with the code EC3, but the shape was assumed from buckling analysis (stage one) see Table 3.

Table 3. Assumed initial bow imperfection according to EC3.

Type	Name	L m	LT curve –	Bow imperfection e_0 m
Open	I-120	3	c	0.0075
I	I-330	4	d	0.0133
	I-450	6	d	0.0200
	I-550	8	d	0.0267
Closed	120×4	3	d	0.0100
RHS	180×4	4	d	0.0133
	240×4	5	d	0.0167
	300×4	6	d	0.0200
	360×4	7	d	0.0233

3 NUMERICAL ANALYSES

3.1 *Open cross-sections*

The numerical analyses were conducted for all the open cross-sections presented in Table 2. The typical lateral torsional response—which is in agreement with the assumptions of the Vlasov beam theory—was observed only for the section I-120 (section of 1 class). In the case of I-330 (section of 2 class), I-450 (section of 3 class) and I-550 (section of 4 class) the distortional lateral torsional response was observed. Additionally, the section of a 4 class without ribs loses its stability before the limit capacity obtained analytically according to the EC3.

Example equilibrium paths of a I-330 section without ribs for various lateral restraints and for elastic and elastic-plastic material models are depicted in Fig. 3.

The following denotations in Fig. 3 were assumed: the *EC3* refers to the limit load obtained according to EN standard formulas, the *EL* and the *PL* refer to elastic and elastic-plastic material definition (see Table 2), the *NR* stands for beam without lateral restraint, the *Rbf* means one lateral restraint in the middle of a beam applied at the bottom flange (flange in tension) of a section, the *Rmw* means one lateral restraint in the middle of a beam applied at the middle of a web of a section and the *Rtf* means one lateral restraint in the middle of a beam applied at the upper flange (flange in compression) of a section.

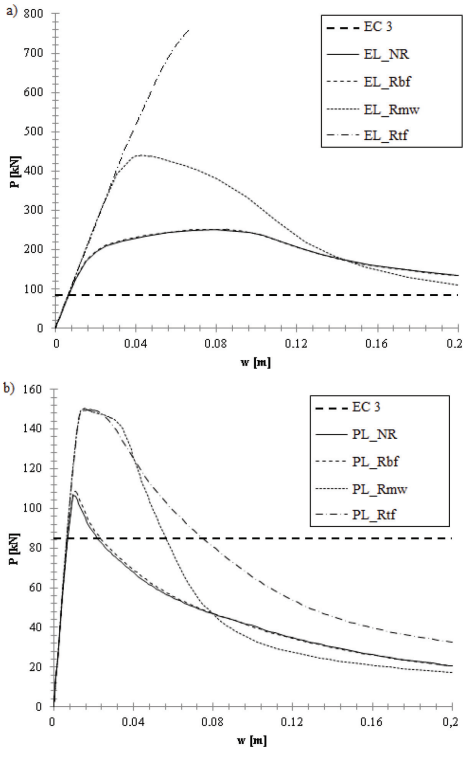

Figure 3. The equilibrium paths of I-330 section without ribs for various lateral restraints for elastic (a) and elastic-plastic (b) material models.

There is a significant difference between the load paths for the elastic and the elastic-plastic material model definition. Under the obtained FE results it can be stated that analysis of a the lateral capacity of an open cross-section with elastic material definition seems to be inappropriate because it gives capacities several times larger than the elastic-plastic model and analytical results.

In the paper the influence of the lateral restraint on the capacity of the I-beam is also presented. Please note that introducing one lateral restraint at the tensioned flange of a beam (case *Rbf*) in fact does not influence the capacity of the considered beam—the load paths of *Rbf* case overlap with the load path of a beam without lateral restraint, see Fig. 3. In the case of the elastic-plastic material definition the lateral restraint attached at the compressed flange of a beam increases the capacity of the beam by about 30%, see Fig. 3b. Please note that the limit points of a beam with elastic-plastic material model are characterized by large sensitivity in respect to the deflection of the beam. The insignificant increase of the deflection leads to significant reduction of the capacity of the beam in bending.

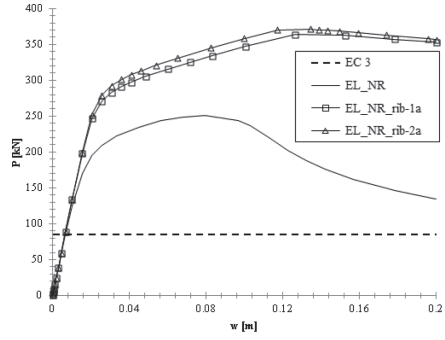

Figure 4. The influence of the ribs on the beam (I-330) in bending with elastic material definition (description in text).

The influence of the ribs on the beams in bending was also considered. The two rib arrangements were analyzed. The results concerning the rib arrangements are presented in Fig. 4.

In Fig. 4 the uniform rib distribution, spaced every double height of the web is represented by the continuous line with squares, while the thickened rib arrangement at the support zone is represented by the continuous line with triangles. The uniform and thickened rib distribution in the case of the section I-330 significantly improves the capacity of the beam in bending, by about 50% and 55%, respectively. The presented results refer to the beam with elastic material definition.

Finally, the shape of the cross-section of the beam in bending was analyzed, see Fig. 5. It was observed that the section, without ribs and regardless of both the way of lateral restraint and the definition of the material, does not preserve the shape of the initial cross-section contour, see Fig. 5*a*, 5*b*, 5*d* – 5*h*. Only in the case of the beam with ribs (Fig. 5*c* and 5*d*) does the cross-section preserve the shape of the contour. Furthermore, the size of the observed distortions is much more pronounced for the elastic-plastic than for elastic material definition. The obtained results are surprising, since it is widely accepted that sections of a class 2 and 3 meet the objectives of the Vlasov beam theory and therefore the use of ribs is not considered necessary. This requirement was only obligatory for the class 4 of the cross-section. In view of the obtained results, this assumption seems to be considered again.

3.2 *Closed cross-sections*

The analyses were conducted for all the closed cross-sections presented in Table 2. The analyzed sections are characterized by different section slenderness expressed by the height to width ratio. The analysis included eight different approaches for each cross-section: the beam without lateral

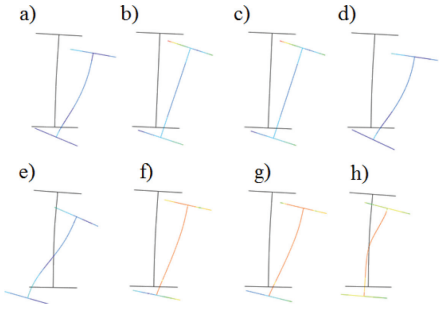

Figure 5. The post-buckling cross-section deformations of a beam I-330: a) elastic model, without ribs and lateral restraint; b) elastic model, ribs, without lateral restraint; c) elastic model, thickened ribs arranged at the support zone, without lateral restraint; d) elastic model, without ribs, lateral restraint at the bottom flange; e) elastic model, without ribs, lateral restraint in the middle of the web; f) elastic-plastic model, without ribs and lateral restraint; g) elastic-plastic model, without ribs, lateral restraint at the bottom flange; h) elastic-plastic model, without ribs, lateral restraint at the middle of a web.

restraint, the beam with one lateral restraint in the middle of the beam but supported at three different points of the section: at the bottom flange (*Rbf*), at the top flange (*Rtf*) and in the middle of the web (*Rmw*), the beam with two different material model definition namely linear elastic (*EL*) and elastic-plastic (*PL*). The analysis with the rib arrangements was not provided.

The results for each cross-section slenderness are in qualitative agreement, therefore only the detailed results for RHS-360 will be presented. The buckling modes of an RHS beam without lateral restraint and RHS beam with lateral restraint applied to the bottom and upper flange of a section (cases *Rbf* and *Rtf*) are local, see Fig. 6 and Fig. 7. The geometry of the locally buckled cross-section shape of these beams is mono-symmetric.

The buckling mode is global and local only in the case of the RHS beam with lateral restraint in the middle of the web of a cross-section, see Fig. 8.

The obtained deformation of this cross-section takes the shape of the letter *S*. In this context it turns out that the *Rmw* case restrains the critical cross-section and allows the global (distortional) mode of the buckling to occur. Both modes (the local and the global) are interactive.

The obtained buckling modes (local and interactive) were introduced as imperfections in the general static analyses. According to the obtained results of the general static analysis of an RHS section it can be stated that introducing the lateral restraint in the considered section does not increase the capacity of the beam in bending for both elastic and elastic-plastic material definition,

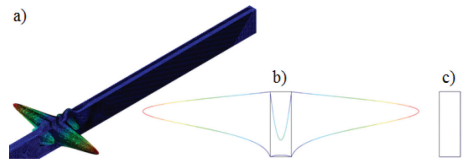

Figure 6. The buckling mode of the RHS-360 beam with lateral restraint at the top flange of the cross-section: a) view, b) shape of the cross-section at the middle of the beam, c) shape of the cross-section at 1/3 length of the beam.

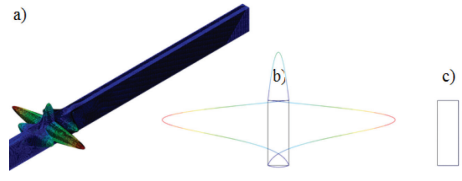

Figure 7. The buckling mode of the RHS-360 beam with lateral restraint at the bottom flange of the cross-section: a) view, b) shape of the cross-section at the middle of the beam, c) shape of the cross-section at 1/3 length of the beam.

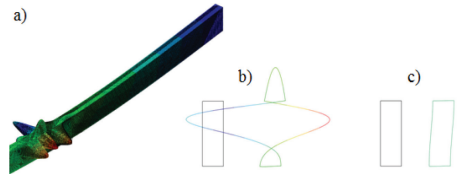

Figure 8. The buckling mode of a RHS-360 beam with lateral restraint at the middle of the web of the cross-section: a) view, b) shape of the cross-section at the middle of the beam, c) shape of the cross-section at 1/3 length of the beam.

see Fig. 9. Next, the capacity obtained for elastic material model seems to be overestimated in comparison with the elastic-plastic model. Please note also that the capacity obtained for elastic-plastic model is much smaller than capacity obtained analytically. It is believed that the analytical results are incorrect.

The shapes of the cross-sections after general static analysis are presented in the Fig. 10. Moreover at the Fig. 10 the assembly of the initial shape of the cross-section with final shape of a cross-section are presented. Unsupported sections, supported at the level of the upper or lower flange have only local deformations. The sections supported laterally at half of the height of the web in accordance with these figures are characterized also by local deformations, nevertheless the small distortional lateral torsional buckling can be also observable.

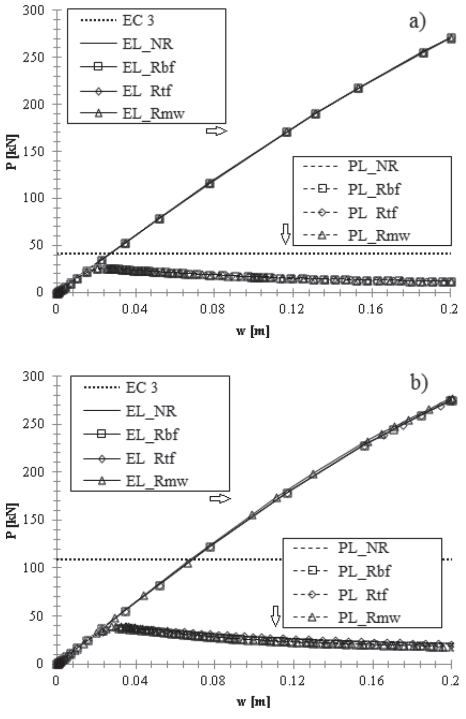

Figure 9. The equilibrium paths of the box cross-sections without ribs for various lateral restraints for elastic and elastic-plastic material models: a) RHS-180, b) RHS-360.

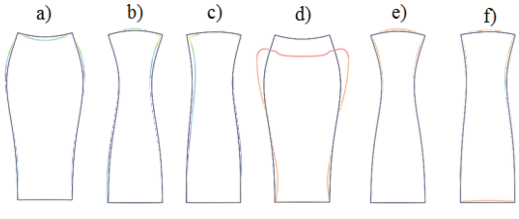

Figure 10. The deformations of a RHS-360 cross-section: a) elastic, restraint at the upper flange of a section, b) elastic, restraint at the bottom flange of a section, c) elastic, restraint at the middle of a web of a section, d) elastic-plastic, restraint at the upper flange of a section, e) elastic-plastic, restraint at the bottom flange of a section, f) elastic-plastic, restraint at the middle of a web of a section.

4 CONCLUSIONS

The performed numerical analyses of the beams with open (I) cross-section show that only sections of the 1 Class fulfill the assumptions of Vlasov beam theory, i.e. the initial cross-section shape retain straight after lateral buckling. The open cross-sections of a 2nd, 3rd and 4th Class do not fulfill the assumptions of the Vlasov beam theory, i.e. the initial cross-section shape is not preserved. These cross-sectional deformations are very important, because significantly reduce the capacity of the beam in bending. The observed phenomenon in subject literature is called the distortional lateral torsional buckling. In the case of the distortional lateral torsional buckling the introduction of ribs leads to an increase in the capacity of the beam in bending.

In the case of the beams in bending with closed (RHS) cross-sections for tested span lengths the lateral and distortional lateral buckling were not obtained. These sections fail due to local plastic deformations of the walls (symmetrical with respect to the vertical axis of a section). The positive effect of the introduced lateral support was observed only for restraint added at the mid-height of the web. However, it has been reported that this restraint results in a insignificant increase in capacity.

For open and closed cross-sections the elastic material definition leads to overestimation of the results, therefore the elastic-plastic material definition should be assumed in the numerical analyses of the beams in bending.

REFERENCES

Bazant Z.P. & Nimeiri M., 1973. Large-Deflection Spatial Buckling of Thin-Walled Beams and Frames. J. Eng. Mech. (ASCE), Vol. 6, pp. 1259–81.

Camotim D., Silvestre N., Gonçalves R. & Dinis P.B., 2006. GBT-based structural analysis of thin-walled members: overview, recent progress and future developments. *Advances in Engineering Structures, Mechanics & Construction Solid Mechanics and Its Applications, Volume 140, p. 187–204.*

Davies J.M., 1998, Generalised beam theory (GBT) for coupled instability problems. Rondal J., editor. *Coupled instabilities in metal structures: theoretical and design aspects (CISM Course no 379)*. Vienna: Springer, p. 151–223.

Eurocode 3. 1993 Design of steel structures—Part 1.1, Part 1.3, Part 1.5.

Gonçalves R., Dinis P.B. & Camotim D., 2009. GBT formulation to analyse the first-order and buckling behaviour of thin-walled members with arbitrary cross-sections. *Thin-Walled Structures,* Elsevier Science Limited, Vol. 47, pp. 583–600.

Schafer B.W. 2008. The Direct Strength Method of cold-formed steel member design, *Journal of Constructional Steel Research, Volume 64, Issues 7–8, July–August 2008, Pages 766–778*.

Schardt R., 1983. The generalized beam theory. Proc. Instability and plastic collapse of steel structures, *M. R. Horne conference. University of Manchester, 1983, p. 469–75.*

Timoshenko S.P. & Gere J.M., 1961. Theory of elastic stability. McGraw-Hill, ISBN 0-07-Y85821-7.

Dynamics, fatigue and seismic analyses

This page intentionally left blank

Recent Progress in Steel and Composite Structures – Giżejowski et al. (Eds)
© 2016 Taylor & Francis Group, London, ISBN 978-1-138-02946-0

Experimental and numerical study on polymer element used for reduction of temporary steel grandstand vibrations

N. Lasowicz & R. Jankowski
Gdańsk University of Technology, Gdańsk, Poland

ABSTRACT: The purpose of the paper is to analyse the effectiveness of a polymer damper in reduction of a temporary steel grandstand vibrations through the experimental and numerical study. The damper considered in the investigation is constructed out of two L-shape steel members bonded with polymer mass of high damping properties. The element has been installed as a diagonal one at the back part of the structure. The method has been compared with the typical solution of strengthening the grandstand with the diagonal stiffener of tubular cross section. Dynamic parameters of a temporary steel grandstand have been determined and behaviour of the structure under crowd load has been obtained. The results of the study clearly show that the response of a temporary steel grandstand equipped with a diagonal damper as well as with the diagonal stiffener is substantially different.

1 INTRODUCTION

There are a number of reasons for vibrations of steel structures. The most common causes include: earthquakes (see, for example, Jankowski 2005; 2007, Mahmoud et al. 2012; 2013), large mechanical vibrating entities, air pressure, vibrations resulting from vehicles/trains using the nearby road/track or movement of people. The last one, if acting on relatively flexible structures, such as temporary steel grandstands, may cause serious problems including severe damages of such structures, their collapses or panic among the spectators (Ellis et al. 2000). For example, the collapse of grandstand in Corsica in 1992 hurt thousands of people and resulted in several deaths. Detailed analysis concerning damages of temporary grandstands has been considered in 2009 (see De Brito & Pimentel 2009). As a main causes, incorrect connections or anchors, quality of material, wrong assembly, inappropriate bracing system, presence of an excessive load (dynamic load) have been mentioned.

Such flexible structures as grandstands are regularly subjected to significant dynamic loads generated by crowd movement. It is necessary to take this effect into account at the design stage, especially when the crowd movement involves rhythmic jumping or dancing (Reynolds et al. 2004). It is a very dangerous situation when crowd provides movement such as jumping. Jumping crowd interacts with the structure while stationary crowd acts only as additional mass. If the synchronized movement excites a natural frequency of the structure, resonant response might occur (Jones et al. 2010).

It is also necessary to pay attention to changes of human perception and comfort level caused by high values of accelerations induced on the structure (Nhleko et al. 2009). To avoid such situations, temporary steel grandstands are commonly strengthened using additional diagonal elements that create bracing systems which is selected depending on the size of the structure, type of the event or acting load, etc. (Crick & Grondin 2008). Such elements are mostly diagonal structural members and their application is crucial in design of such structures.

In this paper, behaviour of a temporary steel grandstand equipped with two different diagonal elements has been analysed through the experimental and numerical study. Typical solution concerning application of a diagonal tubular member has been compared with a element proposed by authors and called polymer damper. It consists out of two L-shape steel members bonded with polymer mass. The polymer mass, applied in it, is a specially designed flexible two-component grout, which is based on polyurethane resin (Falborski et al. 2012; 2013). This kind of material has been already used for filling of cracks in brick walls. Also polymer mass has been applied into the cracks that appear on side runway at Balice Airport in Kraków, Poland.

It has been proven, based on the previous experimental studies, that the material is characterized by very good damping properties (Lasowicz & Jankowski 2014, Lasowicz et al. 2015). During an experimental and numerical study two load cases have been taken into account. One of them

describes an empty structure while the second one consider occupied temporary steel grandstand. It has been proven that mass of the spectators leads to the substantially reduction of natural frequencies of a structure (see Majewska-Lasowicz & Jankowski 2012, Lasowicz & Jankowski 2014).

The aim of the study is to analyse the effectiveness of using additional polymer damper. Dynamic parameters such as modes of free vibrations, corresponding natural frequencies have been obtained through the experimental and numerical analysis. Damping ratios have been determined using half power bandwidth method. A modal analysis has been conducted so as to verify the accuracy of the numerical models created.

2 EXPERIMENTAL STUDY

2.1 *A subject of the research*

A repeatable part of a temporary steel scaffolding grandstand has been considered in this study. The three-storey structure of dimensions: 2.1 (length), 2.7 (width) and 2.42 m (height), consists mostly of tubular steel members of diameter equal to 0.046 m, steel platforms and wooden benches that provide seats for spectators. Typical connections for scaffolding system have been used.

Temporary steel grandstand has been strengthened using two different structural member. The first one considers steel diagonal tubular element that has been commonly used in such structures (Model A). Such typical solution has been presented in Figure 1.

The second solution concerns the application of specially designed element, called polymer damper, that consists of two L-shape steel members (L $50 \times 50 \times 5$ mm) bonded with polymer mass of high damping properties of thickness 5 mm (Model B). A scheme of polymer damper is presented in Figure 2.

A back view of temporary steel scaffolding grandstand equipped with polymer damper is presented in Figure 3.

2.2 *Experimental study*

The aim of the experimental study was to determine and compare dynamic parameters of a temporary steel grandstand equipped with two different diagonal elements. Modes of free vibrations and corresponding natural frequencies have been determined. Based on them, damping ratios have been estimated. Two load cases have been considered during the experimental study. One of them describes an empty structure where only self-weight of the structure has been considered, while the second one takes into account mass of twelve spectators occupying the structure. The presence of people's mass has been simulated by concrete blocks of weight of 8 kg each. The weight of each spectator has been assumed to be equal to 104 kg.

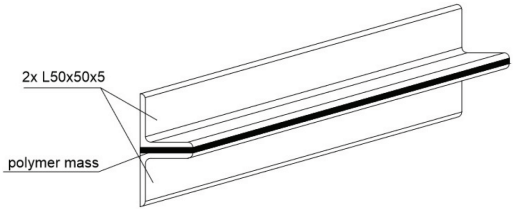

Figure 2. A scheme of polymer damper.

Figure 1. Temporary steel grandstand equipped with typical tubular member (back view).

Figure 3. Temporary steel grandstand equipped with polymer damper (back view).

The mass of twelve spectators has been placed on the structure according to existing standards so as to allow four persons to seat on one bench (see Figure 1).

In the first stage of the experimental study, modes of free vibrations and corresponding natural frequencies have been determined. According to British Standards, horizontal left-to-right (sway) natural frequency is usually the most important one for temporary and retractable grandstands.

Structure has been excited to free vibrations by applying an initial drift at the top of the highest vertical tubular members. The response of the structure has been computed by four accelerometers, placed on each vertical member, till structural damping brought the system to stop. A large number of measurements have been obtained and acceleration time histories describing behaviour of empty and occupied temporary steel grandstand concerning two different types of diagonal elements have been determined.

Acceleration time histories describing first modes of free vibrations and corresponding natural frequencies of an empty temporary steel grandstand with tubular stiffener and polymer element are shown in Figure 4 and Figure 5, respectively.

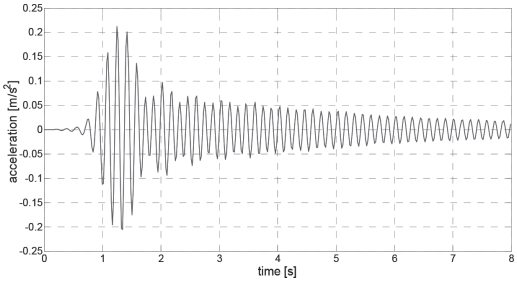

Figure 4. Vibrations determined for an empty temporary steel grandstand with typical tubular element.

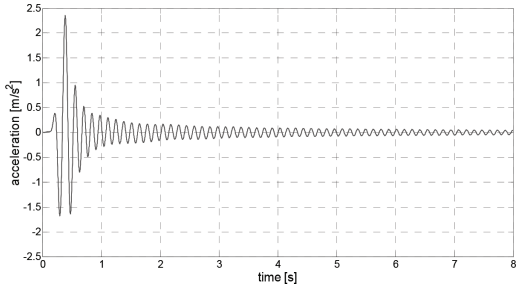

Figure 5. Vibrations determined for an empty temporary steel grandstand with polymer element.

In Figure 6 and Figure 7, acceleration time histories of an occupied temporary steel grandstand with typical steel tubular stiffener member and polymer element are presented.

The values of horizontal natural frequencies estimated from an experimental study for both cases are summarized in Table 1.

It can be seen from Table 1 that value of natural frequency significantly decreases (almost two times) for occupied structure due to increase of the mass. According to the British Standards, acceptable values of natural frequencies in horizontal direction for an empty structure cannot be less than 4 Hz, while, in the case of occupied structure, that value cannot be smaller than 2.5 Hz. For "hard" pop concerts, due to mass of packed spectators, the value might decrease to 2.5 Hz, what may be very dangerous due to the fact of tuning the natural frequency of the structure with the frequency of jumping of crowd. Therefore, in order to predict the behaviour of the temporary steel grandstand under crowd load, the information on dynamic characteristics of an empty structure is valuable. Values of natural frequencies estimated from experimental study for empty and occupied structure are in the safe range.

To assess the effectiveness of application a polymer damper, another dynamic parameters

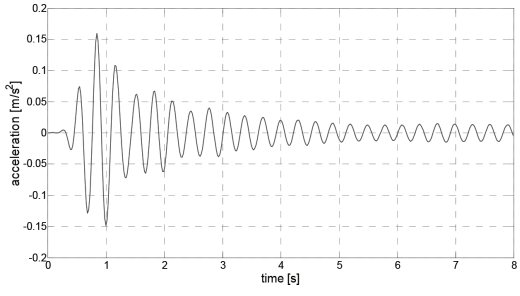

Figure 6. Vibrations determined for an occupied temporary steel grandstand with typical tubular element.

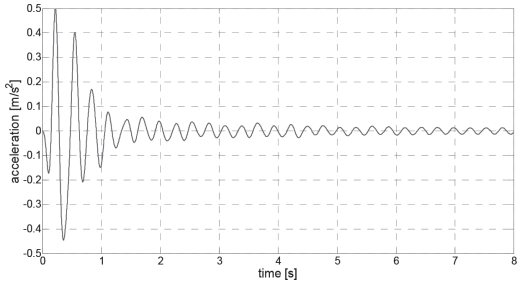

Figure 7. Vibrations determined for an occupied temporary steel grandstand with polymer element.

Table 1. Natural frequencies determined for empty and occupied temporary steel grandstand equipped with different types of diagonal elements.

	Natural frequency	
	Empty structure [Hz]	Occupied structure [Hz]
Model A	5.500	3.120
Model B	5.875	3.375

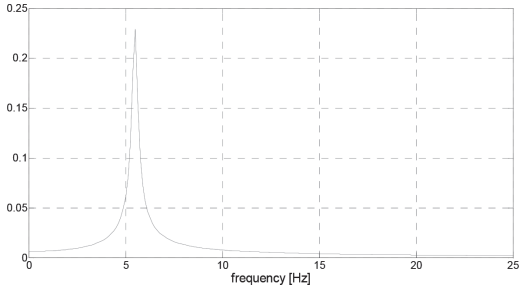

Figure 8. Spectral response of an empty temporary steel grandstand with typical tubular element.

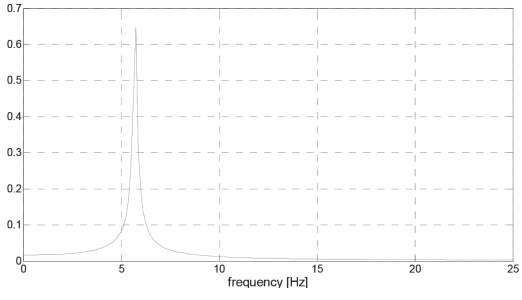

Figure 9. Spectral response of an empty temporary steel grandstand with polymer element.

have been determined. For each model and load cases, damping ratios have been estimated using half power bandwidth method from the frequency domain based on obtained spectral response. Two representative results of spectral response for empty structure with different diagonal elements are shown in Figure 8 and Figure 9.

Spectral response concerning an occupied temporary steel scaffolding grandstand with different diagonal elements are shown in Figure 10 and Figure 11.

Based on half power bandwidth method, damping ratios have been estimated according to the equation:

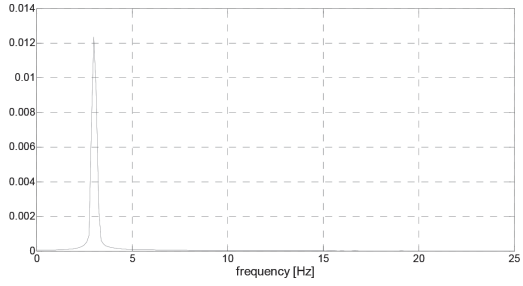

Figure 10. Spectral response of an occupied temporary steel grandstand with typical tubular element.

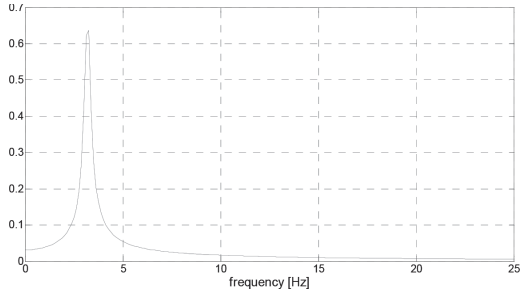

Figure 11. Spectral response of an occupied temporary steel grandstand with polymer element.

Table 2. Damping ratios estimated for empty and occupied temporary steel grandstand equipped with different types of diagonal elements.

	Damping ratio	
	Empty structure [%]	Occupied structure [%]
Model A	0.54	0.98
Model B	1.05	3.05

$$\xi_r = \frac{f_2^2 - f_1^2}{4 f_r} \tag{1}$$

where $f_{1,2}$ are the natural frequencies corresponding to half power points at the mode; f_r is the natural frequency corresponding to the peak in FRF amplitude. The values of damping ratios are summarized in Table 2.

It can be seen from Table 2 that values of damping ratio determined for structure equipped with polymer damper is much more higher (more than three times in the case of occupied structure) than values estimated for temporary steel grandstand

concerning typical tubular stiffener. Based on the results, the method of installation the polymer damper can be considered as a very promising one in reduction of structural vibrations.

3 NUMERICAL ANALYSIS

3.1 *Numerical model*

Four three-dimensional Finite Element (FE) models of a temporary steel grandstand equipped with different types of diagonal elements and concerning two load cases have been generated using commercial programme MSC Marc. Scaffolding system that mainly consists of slender tubular member has been created using two-nodes beam to column elements (six degrees of freedom), steel platforms have been assumed as four-nodes shell elements (six degrees of freedom). In the case of model with polymer damper, eight-nodes solid elements (six degrees of freedom) have been used to generate polymer mass. The base of all models has been considered to be fixed only in translational directions. Steel, as a structural material, has been described by the following values of material properties: E = 210 GPa, v = 0.3, ρ = 7850 kg/m^3.

Numerical models of temporary steel scaffolding grandstand equipped with tubular member (Model A) and polymer element (Model B) are presented in Figure 12 and Figure 13 respectively. The behaviour of polymer has been simulated with the use of the Mooney-Rivlin material model that is the most frequently adopted method for modelling complex mechanical behaviour of elastomers and rubber-like solids. The following material constants

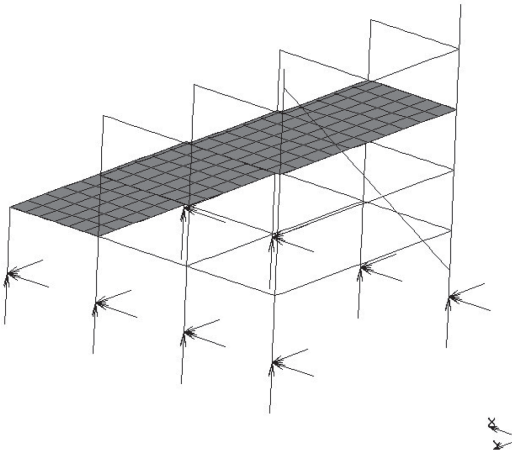

Figure 12. Numerical model of temporary steel grandstand equipped with tubular steel member (Model A).

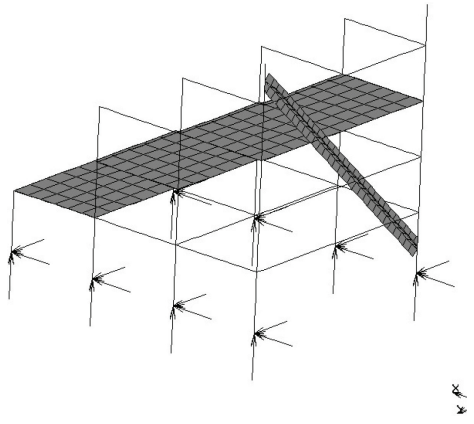

Figure 13. Numerical model of temporary steel grandstand equipped with polymer element (Model B).

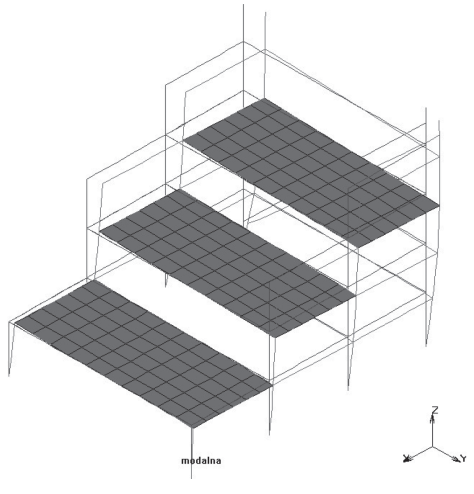

Figure 14. Horizontal mode of free vibrations for an empty temporary steel grandstand with typical tubular element (front view).

for the five-parameter Mooney-Rivlin model have been applied: C10 = 889.490 kPa, C01 = –245.840 kPa, C20 = –155.310 kPa, C11 = 93.786 kPa, C30 = 11.148 kPa. The bulk modulus has been set to be 2.5 GPa, as commonly used for elastomers and rubber-like materials (see Falborski et al. 2012).

3.2 *Modal analysis*

The first part of numerical study has been devoted to modal analysis. A large number of modes of free vibrations and corresponding natural frequencies have been determined as the result of modal analysis. Also modal analysis has been obtain so

as to verify the accuracy of the numerical model generated.

In Figure 14 and Figure 15, horizontal mode of free vibrations (front and back view) for empty temporary steel grandstand with typical tubular member are shown

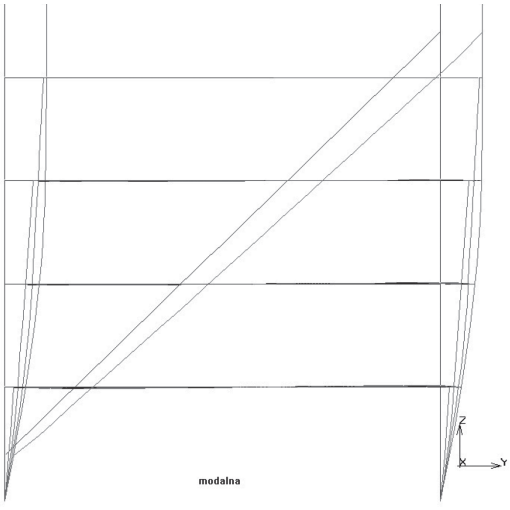

Figure 15. Horizontal mode of free vibrations for an empty temporary steel grandstand with typical tubular element (back view).

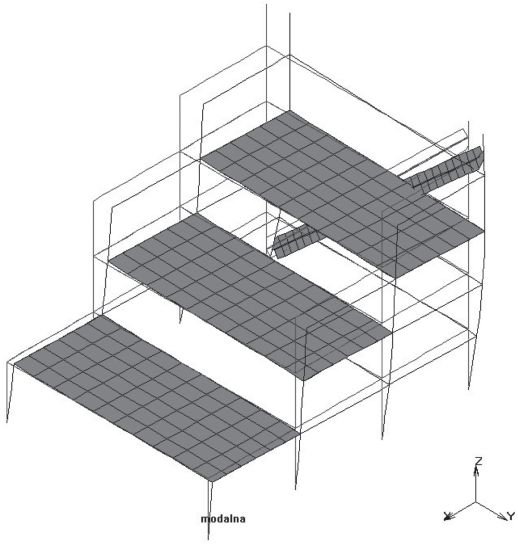

Figure 16. Horizontal mode of free vibrations for an empty temporary steel grandstand with polymer element (front view).

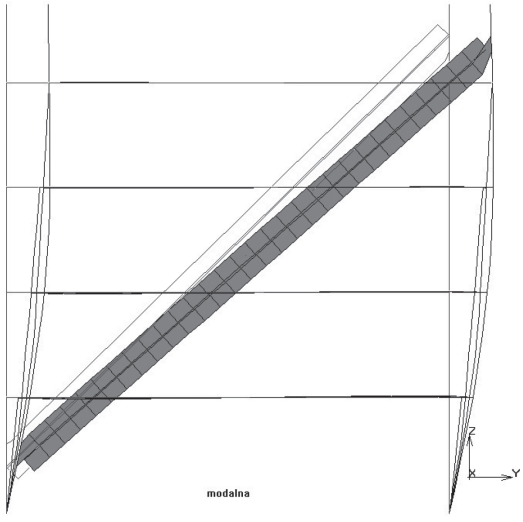

Figure 17. Horizontal mode of free vibrations for an empty temporary steel grandstand with polymer element (back view).

Table 3. Natural frequencies for empty and occupied temporary steel grandstand equipped with different types of diagonal elements.

	Natural frequency	
	Empty structure [Hz]	Occupied structure [Hz]
Model A	5.663	3.354
Model B	5.711	3.465

Horizontal mode of free vibrations (front and back view) for empty temporary steel grandstand with polymer damper are presented in Figure 16 and Figure 17.

The values of natural frequencies corresponding to horizontal modes of free vibrations are summarized in Table 3.

It can be seen from Table 3 that mass of the spectators significantly decreases values of natural frequencies (almost two times). However, there is no major difference between values of natural frequencies of structure equipped with tubular and polymer element.

4 DISSCUSION ABOUT OBTAINED RESULTS

Dynamic parameters, such as modes of free vibrations and corresponding natural frequencies have been determined through the experimental and numerical study. These parameters are crucial

Table 4. Natural frequencies determined for an empty temporary steel grandstand equipped with different types of diagonal elements, as obtained from the experimental and numerical study.

	Natural frequency	
Study	Model A [Hz]	Model B [Hz]
Experimental	5.500	5.875
Numerical	5.663	5.711

Table 5. Natural frequencies determined for an occupied temporary steel grandstand equipped with different types of diagonal elements, as obtained from the experimental and numerical study.

	Natural frequency	
Study	Model A [Hz]	Model B [Hz]
Experimental	3.120	3.375
Numerical	3.374	3.465

in the design of temporary steel grandstand. In Table 4, values estimated from an experimental and numerical study for an empty structure equipped with typical tubular stiffener member and polymer damper are summarized and compared.

Values of natural frequencies presented in Table 4 confirm the accuracy of generated numerical models. The difference between estimated values, in the case of both models, is less than 3%.

The comparison of horizontal natural frequencies for occupied structure from the experimental and numerical study are presented in Table 5. It can be seen from the table that horizontal natural frequencies are quite similar. Bigger difference has been noticed in the case of Model A (almost 8%) concerning structure equipped with typical steel tubular member, while 3% has been observed for Model B. Also, estimated values of natural frequencies for empty and occupied temporary steel grandstands are in the safe range according to British Standards (see paragraph 2.2).

5 CONCLUDING REMARKS

In this paper, effectiveness of a polymer damper in reduction of vibrations of a temporary steel grandstand has been considered based on the results of experimental and numerical study. The analysis described in this paper is a first stage of a wider study. Typical solution of strengthening such structures with diagonal stiffener of tubular cross section have been analysed and compared with the application of damper consisting out of two L-shape steel members bonded with polymer mass of high damping properties. Firstly, the experimental study has been conducted so as to determine modes of free vibrations and corresponding natural frequencies for structure equipped with different types of diagonal elements. Another dynamic parameters such as damping ratio have been determined so as to express effectiveness of application of polymer damper. In the second stage of the study, numerical models of two different temporary steel grandstands have been generated. Modal analysis has been conducted so as to obtain the dynamic parameters.

The results of the study shows that the response of a temporary steel grandstand equipped with a polymer damper as well as with the diagonal stiffener is substantially different.

The application of the polymer damper leads to substantial reduction in the calculated values of damping ratio. Based on the results, the method of installation the polymer damper can be considered as an effective one in reduction of structural vibrations.

Further detailed experimental and numerical study is planned to be conducted so as to determine the behaviour of the steel grandstands under dynamic load induced by spectators due to their jumping so as to verify damping properties which is supposed to be a key issue.

ACKNOWLEDGMENTS

The authors would like to acknowledge the company RUBO-Serwis for renting, transportation and permission to undertake the experimental work on temporary grandstand using scaffolding system. We would also like to thank Mr. Maciej Lasowicz and Mr. Piotr Brzeziński for help in conducting the experimental study as well as Mr. Bogusław Zając for help in preparing the polymer damper.

REFERENCES

Crick D. & Grondin G.Y. 2008. Monitoring and analysis of a temporary grandstand. Structural Engineering Report No.275. Alberta: Department of Civil and Environment Engineering. University of Alberta.

De Brito V. & Pimentel R. 2009. Cases of collapse of demountable grandstands. Journal of Performance of Con-structed Facilities 23: 151–159.

Ellis B.R., Ji T. & Litter J.D. 2000. The response of grandstands to dynamic crowd loads. Proceedings of the Institution of Civil Engineers, Structures and Buildings 140: 355–365.

Falborski, T., Jankowski R. & Kwiecień A. 2012. Experimental study on polymer mass used to repair dam-

aged structures. Key Engineering Materials 488–489: 347–350.
Falborski, T. & Jankowski R. 2013. Polymeric bearings—a new base isolation system to reduce structural damage during earthquakes. Key Engineering Materials 569–570: 143–150.
Jankowski R. 2005. Impact force spectrum for damage assessment of earthquake-induced structural pounding. Key Engineering Materials 293–294: 711–718.
Jankowski R. 2007. Assessment of damage due to earthquake-induced pounding between the main building and the stairway tower. Key Engineering Materials 347: 339–344.
Jones C.A., Reynolds P. & Pavic A. 2010. Vibration serviceability of stadia structures subjected to dynamic crowd loads: A literature review. *Journal of Sound and Vibration* 330: 1531–1566.
Lasowicz N., Kwiecień R. & Jankowski R. 2015. Enhancing the seismic resistance of columns by GFRP confinement using flexible adhesive—experimental study. Key Engineering Materials 624: 478–485.
Lasowicz N. & Jankowski R. 2014. Numerical analysis of a temporary steel grandstand. W. Pietraszkiewicz and J. Górski (ed.), *Proc. of the 10th Conf.: Shell Structures–Theory and Applications*, Gdańsk, Poland 16–18 October 2013. Leiden, Netherlands: CRC/Balkema.
Lasowicz N. & Jankowski R. 2014. The influence of polymer strips in reduction of a steel grandstand vibrations. *Proc. of Eurosteel: 7th European Conf. on Steel and Composite Structure*s, Naples, Italy, 10–12 September 2014.
Mahmoud S., Austrell P-E. & Jankowski R. 2012. Simulation of the response of base-isolated buildings under earthquake excitations considering soil flexibility. Earthquake Engineering and Engineering Vibration 11: 359–374.
Mahmoud S., Abd-Elhamed A. & Jankowski R. 2013. Earthquake-induced pounding between equal height multi-storey buildings considering soil-structure interaction. Bulletin of Earthquake Engineering 11: 1021–1048.
Majewska-Lasowicz N. & Jankowski R. 2012. Modal analysis of a steel grandstand. Technology and Art 3: 94–97.
Nhleko S.P., Williams M.S. & Blakeborough A. 2009. Vibration perception and comfort level for an audience occupying a grandstand with perceivable motion. Proc. of the IMAC-XXVII, Feb. 9–12, 2009, Orlando, Florida USA.
Reynolds P., Pavic A. & Ibrahim Z. 2004. Changes of modal properties of a stadium structure occupied by a crowd. *Proc. of IMAC-XXII: Conference & Exposition on Structural Dynamics*, Dearborn, USA 26–29 January 2004.

Recent Progress in Steel and Composite Structures – Giżejowski et al. (Eds)
© 2016 Taylor & Francis Group, London, ISBN 978-1-138-02946-0

The effect of steel properties on deformation capacity of HSS columns

A. Sato & K. Mitsui
Department of Scientific and Engineering Simulation, Nagoya Institute of Technology, Nagoya, Aichi, Japan

ABSTRACT: In Japan, Hollow Structural Section (HSS) have been widely used as columns of steel structure. Due to development of manufacturing technology, various properties of steel are available to use. SN400B Grade steel is one of the commonly used steel for building; yield strength, ultimate strength and yield ratio are controlled to guarantee ductility. It is known that structural behavior is significantly affected by the properties of the steel; however, the relationships between performance of the members and steel properties are not clearly shown. In Japan, limitation for columns is set for the purpose of ensuring enough plastic deformation. The number of the research which is investigating the relationship between deformation capacity and material properties are limited. The purpose of this study is to clarify these relationships. Numerical simulation is conducted for this purpose. From the analysis result, maximum load and deterioration behavior are significantly affected by steel properties.

1 INTRODUCTION

In Japan, Hollow Structural Section (HSS) have been widely used as columns of steel structures because HSS column have equal rigidity and strength in two directions at orthogonal angles. Seismic load is significant for column design; combined loadings (ie., axial force with bending moment) will be subjected. Therefore, to evaluate seismic performance of columns properly, it is necessary to conform elasto-plastic behaviors of the HSS columns under axial force and bending moment.

Recommendation for Limit State Design of Steel Structures so called LSD (AIJ 2011) have a design limitations, HSS columns that are expected to form plastic hinge at the end of the columns must be satisfy followings;

$$n_y \le 0.75 \tag{1}$$

$$n_y \cdot {\lambda_{c,E}}^2 \le 0.10\left(1 + M_2 / M_1\right) \tag{2}$$

where: n_y is axial compression force ratio of column; λ_{cE} is the bending slenderness ratio $(=1/\pi \cdot \sqrt{\sigma_y / E} \cdot L/i_x)$; σ_y is yieldstress; E is Young's modulus; L is the length of the column; i_x is the radius of gyration of column; M_2/M_1 is the end moment ratio. These limitations are set for the purpose of ensuring enough plastic deformation capacity. However, these limitations are based on test results of H-shaped steel columns, and it is questionable that these limitations can be directly applied in HSS columns. Moreover, test data that will verify the current limitations for HSS columns does not exist.

Also, due to development of manufacturing technology, various properties of steel are available to use for main structures. In LSD, the differences in properties of steel and steel grade are not included enough in the design formula. Therefore, it is necessary to confirm the influence of material properties of steel to the plastic deformation capacity, maximum strength and deformation state.

In this paper, to clarify these relationship, numerical analysis are conducted.

2 STEEL PROPERTIES BASED ON STATISTICS

The relationship between stress and strain that are used in numerical analysis are produced based on a Monte Carlo simulation using the statistics of SN 400B Grade steel. The produced relationship between stress and strain are trilinear-type. Yield stress, ultimate strength and yield ratio satisfies specifications and yield stress is assumed to follow lognormality distribution. Number of stress-strain relationships that are produced are 20,000. Table 1 shows the statistics of SN400B Grade steel and Table 2 shows the specifications of SN400B Grade steel (AIJ 2013).

The coupon tests results were analyzed by linear regression analysis and the correlation between yield ratio and stress are reported to be expressed as follow (AIJ 2013).

$$Y.R = 0.00195 \cdot \sigma_y + 0.102 \tag{3}$$

The correlation coefficient of equation 3 is 0.855. And, strain hardening coefficient κ at each strain level with cyclic loading and stress rising ratio ξ at each strain level are reported to be expressed as follow:

$$\kappa = 0.0812 - 0.0786 \cdot YR \tag{4}$$

$$\xi = 1.0 + \left(\frac{\varepsilon_a}{\varepsilon_y} - 1.0 \right) \kappa \tag{5}$$

The correlation coefficient of equation 4 is 0.934. Average of the uniform elongation ε_u is not shown, however, it is widely known that the average uniform elongation ε_u of SN400B Grade steel is around 17.5% to 25.0%. In this paper, the trilinear-type are adopted to be produce the relationships of stress and strain (herein after referred to as "σ-ε curve"). Therefore, to bring trilinear-type relationship and actual behavior, the average uniform elongation of SN400B is set to 17.5% (See Figure 1). Also, the standard deviation of the uniform elongation is not

Table 1. Statistics of SN400B Grade (The thickness is more than 16 mm and less than 40 mm).

	σ_y (N/mm^2)		σ_u (N/mm^2)		YR (%)	
Steel grade	Mean	SD	Mean	SD	Mean	SD
SN400B	296	23.3	434	16.5	67.9	3.66

Where: σ_y is yield stress; σ_u is ultimate strength; YR is yield ratio; SD is standard deviation.

Table 2. Specifications of SN400B Grade (The thickness is more than 16 mm and less than 40 mm).

	σ_y (N/mm^2)		σ_u (N/mm^2)		YR (%)
Steel grade	Min	Max	Min	Max	Max
SN400B	235	355	400	510	80.0

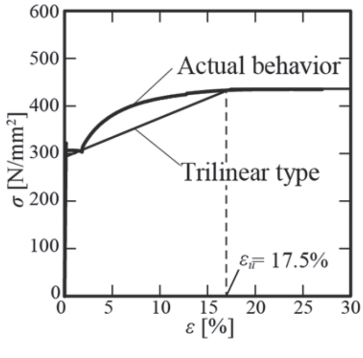

Figure 1. Relationship between stress and strain.

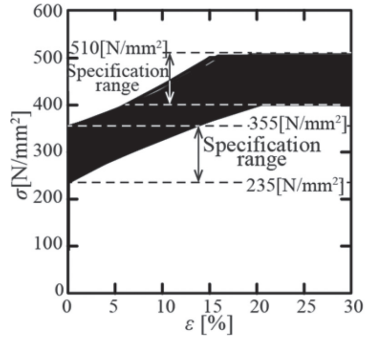

Figure 2. Produced σ-ε curve.

Table 3. Simulation results and selected properties.

	Min	Low	Mean	High	Max
σ_y (N/mm^2)	235.3	249.4	295.6	342.6	354.9
σ_u (N/mm^2)	400.0	403.0	437.0	469.0	508.5

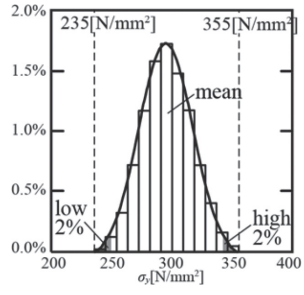

Figure 3. Logarithmic distribution of σ_y.

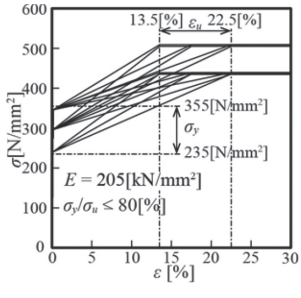

Figure 4. Selected σ-ε curves.

shown in reference 2. However, the coefficient of variation of the elongation can be obtain by calculating equations 4, 5 and that is 6.75×1^{-2}. And, the standard deviation can be obtain by transforming the coefficient of variation into the standard deviation and value of that is 1.18×1^{-2}. Using these element, simulation results (produced σ-ε curves)

Table 4. Properties of selected trilinear-type relationship between stress and strain.

Type	M1	M2	M3	M4	M5	M6	M7	M8	M9	M10	M11	M12	M13	M14	M15
σ_y	240	240	240	296	296	296	296	296	296	346	346	346	346	346	346
YR	55.5	55.5	55.5	58.5	58.5	58.5	67.9	67.9	67.9	68.0	68.0	68.0	78.8	78.8	78.8
ε_u	13.5	17.5	22.5	13.5	17.5	22.5	13.5	17.5	22.5	13.5	17.5	22.5	13.5	17.5	22.5

can be obtain and these are shown in Figure 2. And, these properties are summarized in Table 3. As can be seen from Figure 2 and Table 3, produced σ-ε curves are satisfy specifications.

Relationship between stress and strain which are used for numerical analysis are selected from produced relationship between stress and strain because conducting numerical analysis with all material is time consuming. Figure 3 shows the logarithmic distribution of yield stress as sample.

The 2% of area of the region surrounded by a curve shown in Figure 3 and horizontal axis from both ends are defined "low" and "high" in this paper. Each division and mean are shown in Table 3. The combination satisfies three division (low, mean, high) are selected from simulation results and these are shown in Figure 4 and Table 4. Selected σ-ε curves satisfy manufacturing specification and these curve are used in numerical analysis.

3 NUMERICAL ANALYSIS PROGRAM

In order to confirm elasto-plastic behaviors of the HSS columns under constant axial force and bending moment, the parametric numerical analysis is conducted by finite element analysis (thin walled shell, large deformation, elasto-plastic with strain hardening material). Three dimension model used in the numerical analysis is illustrated in Figure 5 and geometrical dimensions are summarized in Table 5.

Cross section is Box-200 × 200. Analysis parameters are slenderness ratio, axial compression force ratio, width-to-thickness ratio, residual stress and properties of steel. The target range of axial compression force ratio are from 0.10 to 0.50 per 0.05. The target range of slenderness ratio are shown in Figure 6.

Two curves show in Figure 6. The limitation (2) ensures enough plastic deformation. And, another limitation in Figure 6 can be expressed as follow:

$$n_y \cdot \lambda_{c,E}{}^2 \le 0.25\left(1 + M_2 / M_1\right) \tag{6}$$

The range of length of analysis models are from 2000 mm to exceeding limitation (6) per 400 mm. Width-to-thickness ratio are 16.7, 22.2 and 24.0. A width-to-thickness ratio B/t satisfies LSD (AIJ 2013) and it is categorized to compact section which

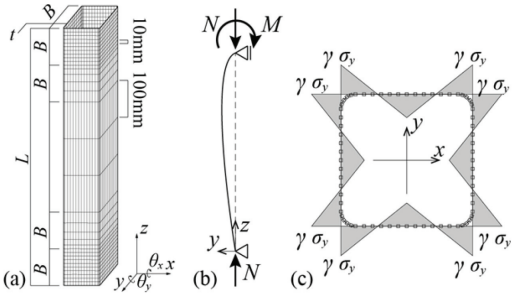

Figure 5. a) Finite element model of HSS column; b) Boundary condition; c) Applied residual stress.

Table 5. Geometrical dimensions of HSS column.

B	*t*		*A*	*I*	*Zp*
(mm)	(mm)	*B*/*t*	(mm^2)	(cm^4)	(cm^3)
200	8.33	24.0	6148	3685	435
	9.00	22.0	6598	3918	465
	12.0	16.7	8530	4859	588

Where: B is the width; t is the thickness; A is the area; I is the moment of inertia; Z_p is the plastic session modulus.

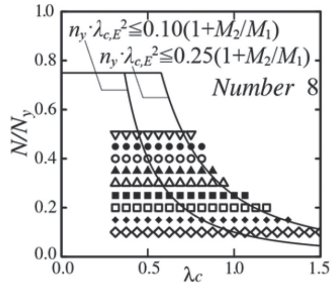

Figure 6. Target range of slenderness ratio.

ensure plastic deformation capacity. Residual stress γ are 0.5 and 1.0 (See Figure 5(c)). Properties of steel shown in Table 4 are used for numerical analysis.

In order to consider bending deformation, initial imperfection was by half sine wave to x and y axis and the maximum amount is L/1000 at the middle portion. Also, in order to consider local buckling, initial imperfection was given by elastic

buckling analysis result. Boundary condition and residual stress are shown in Figure 5(b). Lower end of the column is supported as pin supporting and the upper end of the column is supported as roller supporting. Rotation about z-axis at the both ends are fixed. Bending moment is applied at the upper end to the orthogonal angles after applying constant axial compression force at the centroid of column. Name of analysis model is shown as follow; B200bt24ny050L2000m1. The value of width is shown after B; the value of width-to-thickness ratio is shown after bt; the value of axial compression force ratio is shown after ny; the value of length is shown after L; the number of property of steel used in analysis model is shown after m.

4 ANALYSIS RESULT

4.1 *Effect of the residual stress*

Figure 7 shows relationship between non-dimensional moment and non-dimensional rotation. M_{pc} is full plastic bending moment that is considering the effect of axial compression force N. θ_{pc} is the elastic rotation for full plastic bending moment that is considering the effect of axial force N. Analysis results which residual stress $\gamma = 1.0$ is applied to is represented by the solid line and analysis results which residual stress $\gamma = 0.5$ is applied to is represented by the broken line in Figure 7. As seen from Figure 7, results (maximum moment and initial rigidity) which $\gamma = 1.0$ is applied to are smaller than results which $\gamma = 0.5$ is applied to. This results were caused by increasing stress in the cross section. And, with the increase of the length, the effect of residual stress increases. To evaluate by analysis models which $\gamma = 1.0$ are applied allow to the safety, for the following discussion, analysis results which $\gamma = 1.0$ are applied to are used in this paper.

4.2 *Relationship between non-dimensional moment and non-dimensional rotation*

Figure 8 shows relationship between non-dimensional moment and non-dimensional rotation. These graph show the effect of the properties of steel. B200bt22ny015L3200 series satisfy limitations (2) enough. B200bt22ny015L5200 series and B200bt22 ny045L3200 series set close to limitation (2). B200bt22ny045L5200 series do not satisfy limitation (2). Numbers shown in Figure 8 stand for the numbers of properties of steel. As seen from Figure 8, deterioration behavior after maximum bending moment is influenced by the properties of steel (such as yield stress, yield ratio and uniform elongation) significantly. Especially this tendency is remarkable in analysis models setting close to limitation (2). Compared analysis models having high yield stress with analysis models having low yield stress, the deterioration behavior of analysis models having high yield stress decrease sharply. And, compared analysis models having high yield ratio with analysis models having low yield ratio, the same tendency are conformed. On the other hand, in the range that does not satisfy limitation (2), deterioration behavior after maximum bending moment is only influenced by yield stress. This effect caused by increasing the length of column. Increasing the length lead to increasing P-δ effect. And, in analysis models having high yield stress, this tendency is remarkable. This results caused by increasing axial force with the increase value of yield stress.

4.3 *Stress distribution and deformation*

Figure 9 shows stress distribution in the longitudinal direction. Figure 10 shows deformation at the loading point and the deformation of whole analysis model. These graphs and these photos are taken at the maximum bending moment. Middle line of cross section on the compression side are described by the solid line, and middle line of cross section

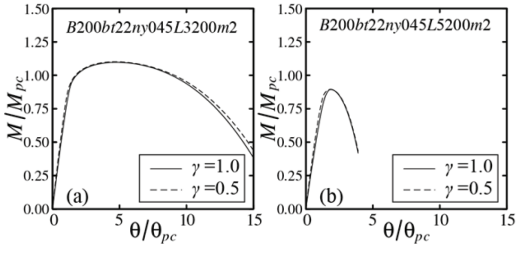

Figure 7. $M/M_{pc} - \theta/\theta_{pc}$ curve.

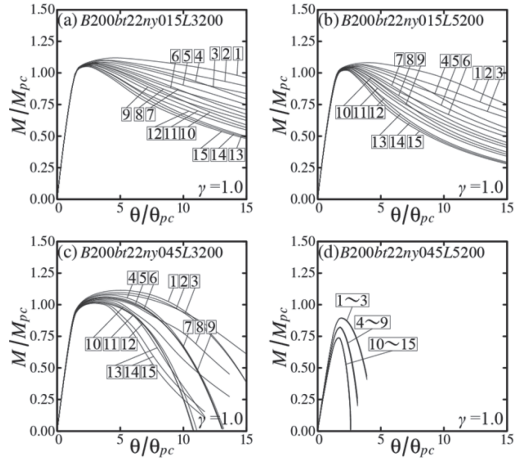

Figure 8. $M/M_{pc} - \theta/\theta_{pc}$ curve.

on the tension side is described by the broken line in Figure 9.

As can be seen from results of B200bt22ny015 L3200m2 which satisfieslamination (2), stress distribution due to local buckling is observed around the loading point (i.e., z/L is around 0.85 to 1.0). Deformation due to local buckling will appear in a narrow region, and compression plate element will deform in a sinusoidal shape that is also corresponding to the stress shape. Similar stress distribution can be observed in B200bt22ny015L5200m2 and B200bt22ny045L3200m2; sinusoidal plate deformation due to local buckling were observed. However, these tendencies are smaller than the result of B200bt22 ny015L3200m2. As seen from the results of B200 bt22ny045L5200m2 which does not satisfy limitation (2), stress distribution in the longitudinal direction are totally different from other results. Increase and decrease stress is not conformed around loading point. From Figure 9 and Figure 10, deformation at the maximum bending moment differ according to the position of the analysis model in the range of limitation (2) and (6) curves. In Figures 10(a–c), the plastic hinge is formed around the loading point. However, the whole deformation of B200bt22ny045L5200m2 is different from other results and whole flexural deformation is observed. This result is caused by $P\delta$ effect with increasing $P\delta$ moment.

Figure 11 shows relationship between rotation at the maximum bending moment and the slenderness bending slenderness ratio. In the range of increasing rotation θ_{max}, the maximum bending moment is determined by local buckling. In the range of decreasing rotation θ_{max}, the maximum bending moment is determined by $P\delta$ effect. And, these range do not vary according to properties of steel.

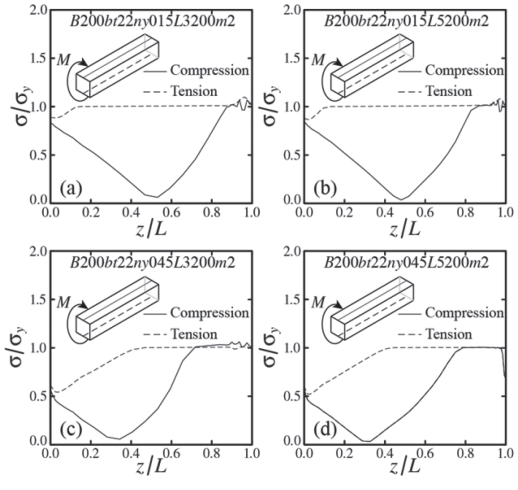

Figure 9. Stress distribution in the longitudinal direction.

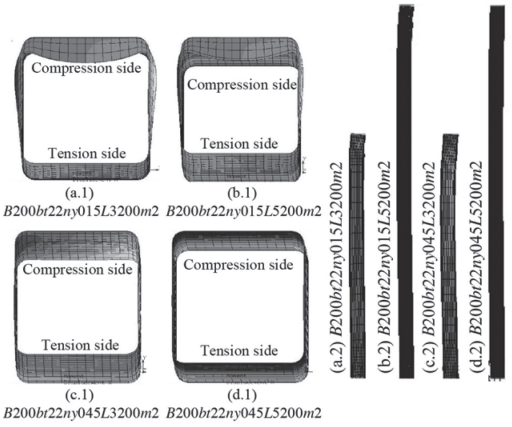

Figure 10. Deformation at the maximum bending moment.

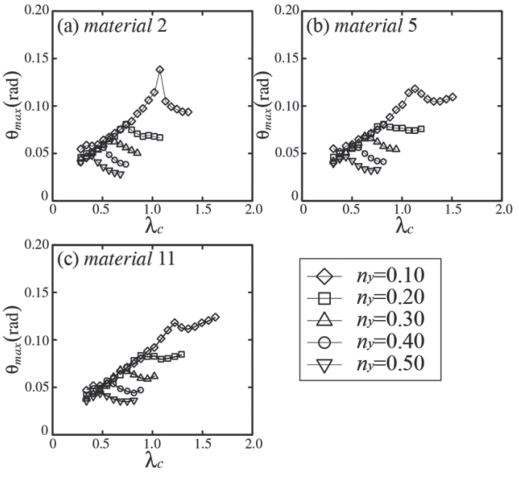

Figure 11. θ_{max}–λ_c curve (B/t = 22.0).

4.4 *Influence on yield bending moment*

Figure 12 shows definition of yield bending moment. In this paper, yield bending moment are defined a point that initial rigidity E_t decreased to one of third value.

Figure 13 shows relationship between non-dimensional yield bending moment and the bending slenderness ratio. As seen from Figure 13, compared analysis models having high yield stress with analysis models having low yield stress, decreasing of the yield bending moment of high yield stress models with increasing the bending slenderness ratio are larger than that of low yield stress models. Compared high axial compression force ratio models with low axial compression force ratio,

decreasing of the yield bending moment of high axial compression force ratio with increasing the bending slenderness ratio are larger than that of low axial compression force ratio. As shown in Figure 13(c), yield bending moment of most analysis models are smaller than all plastic bending moment considered the effect of axial force. On the other hand, the influence of width-to-thickness ratio, uniform elongation and yield ratio on yield bending moment are small.

4.5 *Influence on maximum bending moment*

Figure 14 shows relationship between non-dimensional maximum bending moment and the bending slenderness ratio. As seen from Figure 14, compared analysis models having high yield stress with analysis models having low yield stress, decreasing of the maximum bending moment of high yield stress models with increasing the bending slenderness ratio are larger than that of low yield stress models. This effect caused by increasing axial force. Compared high axial force compression ratio models with low axial compression force ratio, decreasing of the maximum bending moment of high axial compression force ratio with increasing the bending slenderness ratio are larger than that of low axial compression force ratio. Compared width-to-thickness ratio B/t = 16.7 with width-to-thickness ratio B/t = 22.0, maximum bending moment of width-to-thickness ratio B/t = 16.7 for M_{pc} is greater than that of width-to-thickness ratio B/t = 22.0 for M_{pc} in small bending slenderness ratio. On the other hand, the influence of uniform elongation and yield ratio on yield bending moment are small. Compared Figures 14(a–c) with Figures 13(a–c), increments from yield bending moment to maximum bending moment of low yield stress models are greater than that of high yield stress model. This tendency are remarkable in a range of shorter bending slenderness ratio.

Material properties of steel used in this analysis satisfy specification of SN400B Grade. However, even though analysis models satisfy limitation (2), in a part of analysis models, the maximum bending moment do not reach all plastic moment M_{pc}. This tendency is remarkable in analysis model having high yield stress.

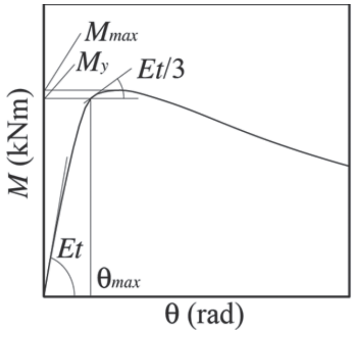

Figure 12. Definition of yield moment M_y.

4.6 *Deformation Capacity*

Figure 15 shows comparison between limitations (2,6) and ductility ratio R of column. Limitation in LSD is specified to have sufficient ductility, i.e., ductility ratio R greater than or equal to three. And, ductility ratio is expressed as follow;

$$R = \theta_u / \theta_{pc} - 1 \tag{7}$$

where θ_u is the rotation that maximum bending moment decreased to 90% (See Figure 12). Lines shown in Figure 15 are the maximum bending slenderness ratio of each properties of steel to satisfy the limitation. As seen from Figure 15(a), all properties of steel that satisfy limitation (2) can ensure ductility ratio R = 3. However, as seen from Figure 15(b), properties of steel having high yield

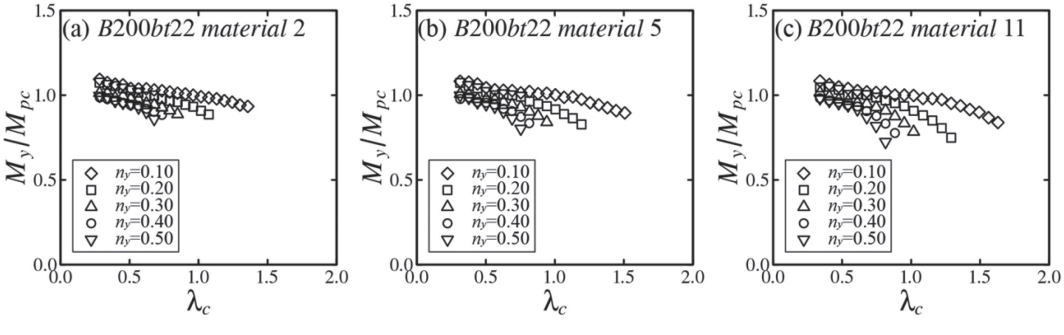

Figure 13. $M_y/M_{pc} - \lambda_c$ relationship (B/t = 22.0).

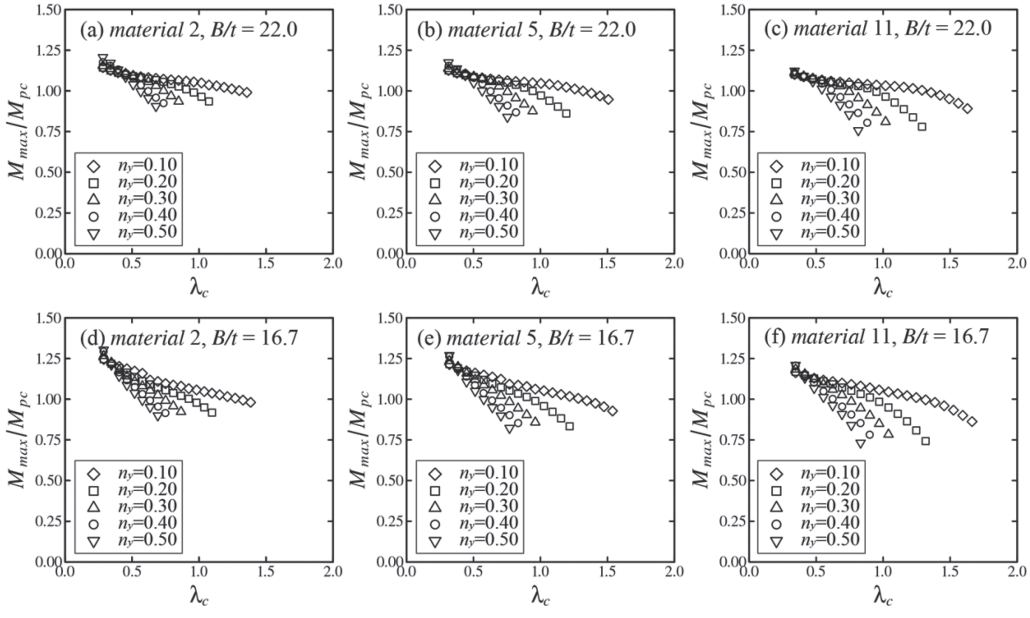

Figure 14. $M_{max}/M_{pc} - \lambda_c$ relationship.

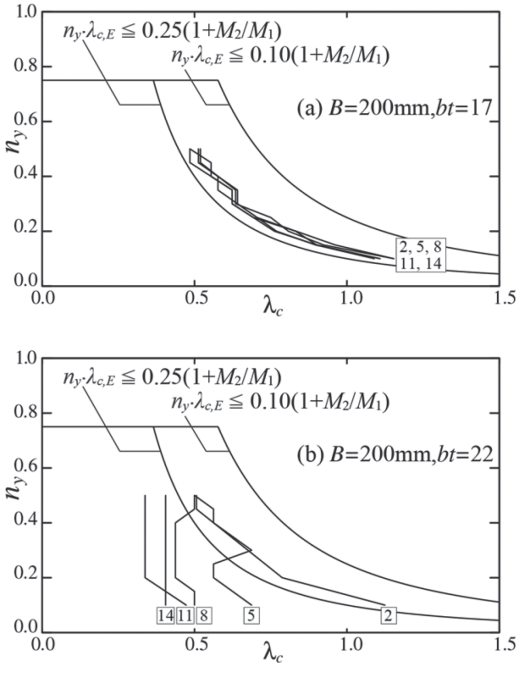

Figure 15. Comparison between limitations and ductility ratio.

stress cannot ensure ductility ratio $R = 3$. Ductility ratio R is depend on properties of steel and width-to-thickness ratio.

5 CONCLUSION

In this paper, in order to conform elasto-plastic behaviors of HSS columns under constant axial force and bending moment, the parametric numerical analysis is done by FEA. From the analysis, following results were found.

1. Compared $\gamma = 1.0$ with $\gamma = 0.5$, maximum moment of $\gamma = 1.0$ and initial rigidity of $\gamma = 1.0$ are smaller than these of $\gamma = 0.5$. And, with the increase of the length, this effect is remarkable.
2. In analysis models setting close to limitation (2), deterioration behavior after maximum bending moment is influenced by the properties of steel (such as yield stress, yield ratio and uniform elongation).

   And, compared analysis models having high yield stress with analysis models having low yield stress, the deterioration behavior of analysis models having high yield stress decrease sharply. And, compared analysis models having high yield ratio with analysis models having low yield ratio, the same tendency are conformed.
3. In the range that does not satisfy limitation (2), deterioration behavior after maximum bending moment is only influenced by yield stress. This effect caused by increasing the length of column and increasing the length of column lead to increasing P-δ effect.
4. Local buckling and increasing or decreasing stress along the local buckling are observed in

the analysis models which set close to limitation (2). Stress distribution in the longitudinal direction of the analysis results which do not satisfy limitation (2) are totally different from the analysis results which satisfy limitation (2).

5. Whole flexural deformations are observed in analysis models which do not satisfy limitation (2).
6. In the range of increasing rotation at the maximum bending moment, the maximum bending moment is determined by local buckling. In the range of increasing rotation at the maximum bending moment, the maximum bending moment is determined by P-δ effect.
7. The range that maximum bending moment is determined by local buckling and the range that maximum bending moment is determined by P-δ effect do not vary according to properties of steel.
8. Compared analysis models having high yield stress with analysis models having low yield stress, decreasing of the yield bending moment of high yield stress models with increasing the bending slenderness ratio are larger than that of low yield stress models. And, the influence of width-to-thickness ratio, uniform elongation and yield ratio on yield bending moment are small.
9. Compared analysis models having high yield stress with analysis models having low yield stress, decreasing of the maximum bending moment of high yield stress models with increasing the bending slenderness ratio are larger than that of low yield stress models.
10. Increments from yield bending moment to maximum bending moment of low yield stress models are greater than that of high yield stress model. This tendency are remarkable in a range of shorter bending slenderness ratio.
11. Even though analysis models satisfy limitation (2), in a part of analysis models, the maximum bending moment do not reach all plastic moment M_{pc}. This tendency is remarkable in analysis model having high yield stress.
12. Ductility of column which is classified by steel material properties were shown. Ductility ratio R is depend on properties of steel and width-to-thickness ratio.

ACKNOWLEDGMENT

Funding for this research was supported by "*The Hibi Science Fundation*".

REFERENCES

Architectural Institute of Japan. 2011. *Recommendation for Limit State Design of Steel Structures*. Japan. Architectural Institute of Japan.

Architectural Institute of Japan. 2013. *Current conditions of the properties of steel for structures and utilization of the same*. Panel discussion material for structural section. pp. 28–37.

Kazuya, M., Atsushi, S. & Tetsuro, O. 2014. *Deformation Capacity of Square Steel Tubular Columns under Constant Axial Force with Bending Moment*.

Recent Progress in Steel and Composite Structures – Giżejowski et al. (Eds)
© 2016 Taylor & Francis Group, London, ISBN 978-1-138-02946-0

Shakedown seismic analysis of composite steel-concrete frame systems

P. Alawdin
Faculty of Civil Engineering, Architecture and Environmental Engineering, University of Zielona Góra, Zielona Góra, Poland

G.V. Bulanov
Research and Experimental Design State Enterprise for Construction "Institute BelNIIS", Minsk, Republic of Belarus

ABSTRACT: The earthquake analysis of buildings and structures can be performed by finding solution of the optimization problem of shakedown analysis, which takes into account the nonlinear properties of materials. Such analysis has several advantages. External actions are introduced as the set of the load cases, that's why we can solve the problem for all direction of seismic load and for every scheme of live load at once. As part of the solution of the optimization problem we can take into account the nonlinear behavior of the elements. This paper presents the solution for shakedown analysis of buildings with elastic-plastic and brittle elements. It is assumed that the load varies randomly within the specified limits. These limits are determined by the possible direction and magnitude of seismic loads. The example of such analysis of system is introduced. Some attention has been paid to the practical application of the proposed mathematical model.

1 INTRODUCTION

The earthquake analysis of buildings and structures is one of the most complicated problems in engineering practice.

Protection of buildings against seismic actions is achieved by equipping them with systems bearing structures of various elements absorbing energy of these actions. As a result, the destruction of the basic structure is prevented. Some elements can be abruptly shut down (brittle elements), and some damaged as a result of plastic flow (elastic-plastic elements). By the way of illustration these may be ties, guys, fascicles, strands, and other elements, which are off in the process of earthquakes.

There are several methods for the earthquake analysis using for design of the buildings (see Skalomenos et al. 2014, Eurocode 8). The nonlinear properties of materials may be taking into account using all of these methods. For example, the nonlinear (plastic) properties of the materials are taking into account by using behavior factor q for elastic analysis based on a response spectrum. Material nonlinearity is taken into account "directly" by inserting plastic hinges in the elements when using push-over analysis. More accurate solution, with taking into account physical and dynamic properties of the materials, can be obtained by using direct integration method of earthquake accelerograms. Shear checks should be performed for the all elements during design by every of these methods, after that all elements will be modified to increase shear resisting and then recalculating of the system will be provided. In the case of a large-scale system with composite elements these checks may require many iterations and therefore calculating time will increase significantly.

The earthquake analysis of buildings and structures can be performed by finding solution of the optimization problem of shakedown analysis, which also takes into account the nonlinear properties of materials (Aliawdin 2005, Atkociunas 2011, Cyras 1983, Fadaee, M. J., et al. 2008, König 1987, Leonetti et al. 2015, Nguyen 2006, Tangaramvong et al. 2013, Weichert and Ponter 2009). Such analysis has several advantages:

External actions are introduced as the set of the load cases, that's why we can solve the problem for all direction of seismic load and for every scheme of live load at once;

As part of the solution of the optimization problem we can take into account the elastic-plastic and brittle behavior of the elements (Zongyuan, Z., et al. 2015).

This paper presents a mathematical model of the shakedown and limit analysis of the buildings with elastic-plastic and brittle elements. It is assumed that the load varies randomly within the specified limits. These limits are determined by the possible direction and magnitude of seismic loads, which can be found from elastic FEA analysis of the system using elas-tic response spectrum.

An illustrative example of composite steel-concrete frames system with the limited plastic redistribution of forces under seismic actions is shown.

2 A MATHEMATICAL MODEL OF STRUCTURES WITH SEISMIC-PROTECTED SYSTEMS

Let us assume the problem of load-bearing capacity of such structures as a generalized dynamic shakedown problem. First we find a solution of the equation of motion for a damped discrete elastic system under load $\boldsymbol{F}(t)$ as a function of time t. This vector belongs to the set $\Omega(\boldsymbol{F}(t), t)$, which generally is nonconvex (Aliawdin and Muzychkin 2011, Dem'anov et al. 1996), but here it is approximated by the convex domain.

The "elastic" solution is used then as basis for analysis of inelastic system with the partial plastic redistribution of forces. Namely the problem of load-bearing capacity of structures made of perfectly elastic-plastic and elastic-brittle elements, under variable loads is formulated as follows. Find a parameter (safety factor) μ for load $\boldsymbol{F}$, as well as the vector of residual forces $S_p^{\ r}$ such, that

$$\mu \to \max \tag{1}$$

$$S^e(t) = f(\mu F(t)) \tag{2}$$

$$AS_p^{\ r} = 0 \tag{3}$$

$$S_p^{\ r} = E_p S^r \tag{4}$$

$$\varphi_{pl}(S^e(t) + S_p^{\ r}, S_{0,\,pl}) \le 0 \tag{5}$$

$$\max_{i \in I_{br}} \varphi_{br}(S^e(t) + S_p^{\ r}, S_{0,\,br})_i \le 0 \tag{6}$$

$$F(t) \in \Omega(F_j(t), t) \tag{7}$$

where $\boldsymbol{S}^e$ = a vector of internal forces; $\boldsymbol{S}_{0,pl}$, $\boldsymbol{S}_{0,br}$ = vectors of limit internal forces in the cross sections of elastic-plastic and elastic-brittle elements accordingly; $\boldsymbol{A}$ = matrix of static compatibility (equilibrium eguations) for residual internal forces $\boldsymbol{S}^r$ in the cross sections of elements; $\boldsymbol{S}^e$, $\boldsymbol{S}^r$ = vectors of elastic and residual internal forces in the cross sections of elements; $\boldsymbol{F}(t)$ = vector of load; $\boldsymbol{I}_{br}$ = set of i-th brittle elements, $\Omega(\bullet)$ = set of loads $\boldsymbol{F}$, t = time.

A matrix $\boldsymbol{E}_p$ assigns a value (true or false) to the residual internal force in elastic-plastic or elastic-brittle elements accordingly (i.e. defines partial plastic redistribution of forces), its concept is as follows:

$$E_p = \mathrm{Diag}\begin{bmatrix} 1 & \text{if plastic element} \\ 0 & \text{if brittle element and } \mathrm{V}_{ed} \ge \mathrm{V}_{rd} \end{bmatrix} \tag{8}$$

where V_{ed} = shear force in the element; V_{rd} = shear resistance of the element.

The subscripts *pl* and *br* relate to the elastic-plastic and elastic-brittle elements, super-scripts *e* and *r* - to the elastic and residual internal forces.

Equations (1)–(8) belong to a problem of nonlinear mathematical programming.

Note, that we analyze here the geometrical linear systems (1st order theory), methods of analysis presented may also be applied to the geometrical nonlinear ones.

3 EXAMPLE OF SHAKEDOWN ANALYSIS OF FRAME

An example of shakedown analysis of plane composite steel-reinforced concrete braced frame with elastic-plastic and elastic-brittle elements (Figure 1) is given below.

Here the rods braces and all elements' cross-sections under shear forces are assumed as brittle. On the contrary, elements' cross-sections under active bending forces we presume as plastic.

There are several methods for the earthquake analysis of structures such as response spectrum analysis, direct integration time history analysis using accelerograms occurred earthquakes or artificial accelerograms and other (Eurocode 8). All of these methods can be applied both in the linear and non-linear formulation. Nonlinear properties of the system under alternating seismic action may be taken into account in the optimization problem of elastic-brittle-plastic analysis.

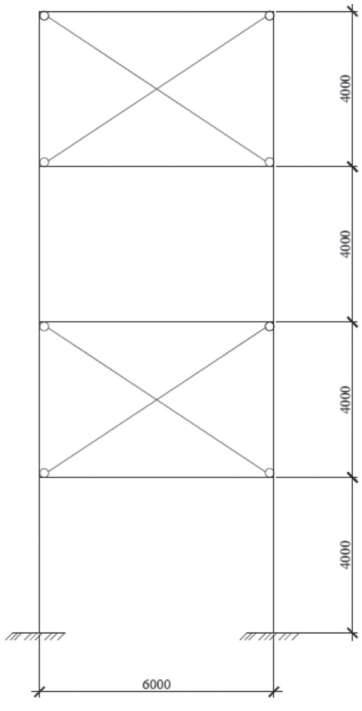

Figure 1. Composite steel-concrete braced frame.

The first step is to define the envelope of internal forces from arising seismic action in elastic stage of work. Seismic action is presented in the form of an elastic response spectrum. For this we use type 1 elastic response spectrum for ground type D, given in Eurocode 8. Peak ground acceleration is equal 10 m/s^2.

The seismic base shear force F_b for each horizontal direction is determined by the following expression (Eurocode 8):

$$F_b = S_d(T_1) \cdot m \tag{9}$$

where m = total mass above the top of basement, T_1 = fundamental period in X and Y direction, $S_d(T_1)$ = the ordinate of the design spectrum at the period T_1.

The horizontal force in i-th joint F_i was determined as follows:

$$F_i = F_b \cdot \frac{z_i \cdot m_i}{\sum z_i \cdot m_i}, \tag{10}$$

where m_i = joint mass above the top of basement, z_i = height of the masses above the basement.

For each critical load cases, the design values of internal forces was determined by combing action for seismic design situation in according with Eurocode 0:

$$Ed = G_{kj,\sup}\left(G_{kj,\inf}\right) + A_{ed} + \psi_{2,i}Q_{k,i} \tag{11}$$

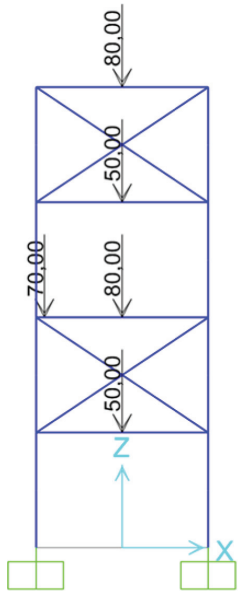

Figure 2. Permanent loads acting on frame, *kN*.

$G_{kj,sup}$ ($G_{kj,inf}$) = unfavourable (favourable) characteristic permanent action (see Figure 2), A_{ed} = design seismic action, $\psi_{2,i}$ = factor by A1.2.2 Eurocode 0, $Q_{k,i}$ = accompanying variable actions.

FEA software SAP2000 is used for structure calculation in elastic stage. Design model with joints and members labels is shown in Figure 3, the cross-sections of the frame elements are exposed in Table 1; strength class for concrete is C35/45.

Design value of material properties for nonlinear analyses was determined according to DIN EN 1992-1-1/NA 5.7 as follows:

$$R_d = R(f_{cR}, f_{yR}, f_{uR})/\gamma_R \tag{12}$$

where γ_R = global safety coefficient is equal 1,3; f_{cR} = 0,85·α·f_{ck}; α = 1; f_{yR} = 1,1·f_{yk}, f_{tR} = 1,08·f_{yR}.

The plastic moment capacity of all composite concrete members was calculated by moment-rotation (curvature) analyses according to Eurocode 4, Skalomenos et al. 2014. The moment-rotation curve can be idealized with an elastic perfectly plastic response to estimate the plastic moment capacity of a member's cross-section (Caltrans Seismic Design Criteria 2013). The elastic portion of the idealized curved should pass through the point marking the first reinforcing bar yield. The idealized plastic moment capacity is obtained by balancing the areas between the actual and the idealized moment-rotation curves beyond the first reinforcing bar yield point, see Figure 4. The idealized moment-curvature curves for members' cross-sections have shown in Table 2.

Transverse reinforcement of all concrete beams is made from bars Ø8 B500B, at 200 mm. Resistance of the concrete beams to vertical shear designed in according with Eurocode 2. Design shear capacity $V_{Rd,s}$ is equal 226.7 *kN*.

Resistance of the composite columns to vertical shear designed in according with Eurocode 4. The distribution of the total vertical shear V_{Ed} into the parts $V_{a,Ed}$ and $V_{c,Ed}$, acting on the steel section and the reinforced concrete core of the composite columns respectively assumed to be in the same ratio as the contributions of the steel section and the reinforced concrete core to the bending resistance $M_{pl,Rd}$ (see Table 3). Envelope diagram of shear forces is shown in Figure 5.

Envelope diagram of elastic bending moments is shown in Figure 6.

To solve the optimization problem first we have to find the residual forces $\boldsymbol{S}^r$ in cross-sections of the elastic-plastic and brittle elements. This frame is 12 times statically indeterminate. Taking in account that brittle ties do not allow plastic redistribution, remain only 4 ties through moments in which the system can adapt to external actions remains. Single i-th unit residual moment diagrams, i = 1, ..., 4, in the system are shown in Figure 8.

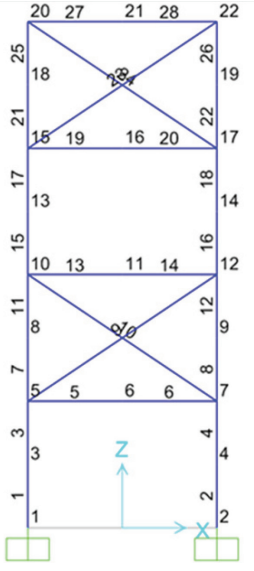

Figure 3. Design model of the frame.

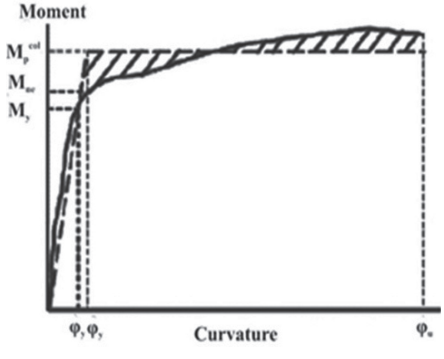

Figure 4. Moment-curvature curve.

Table 1. Sections of frame members.

№	Section	b(D), mm	H, mm	Longitudinal reinforcement, class		Steel section, class
				top	bottom	
1	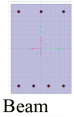 Beam	400	600	3Ø16, B500B	4Ø16, B500B	
2	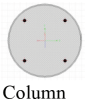 Column	400		4Ø16, B500B		RO 377x6, S235
3	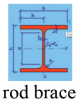 rod brace					HE100 A, S275

Table 2. The plastic moment capacity for members' cross-sections.

Number of cross-section in Table 1 (axial force N, *kN*)	The plastic moment capacity M_p for positive moment, *kN·m*	The plastic moment capacity M_p for negative moment, *kN·m*
1	192	146.5
2 (–574)	284	284
2 (–197)	276	276

Table 3. Shear resistance of composite column.

Part of section	Shear resistance, V_{Rd}, *kN*	Bending resistance $M_{pl,Rd}$, *kN·m*	Shear force (max) V_{Ed}, *kN*
Concrete core	296	102	30.2
Steel tube	630	202	60.4

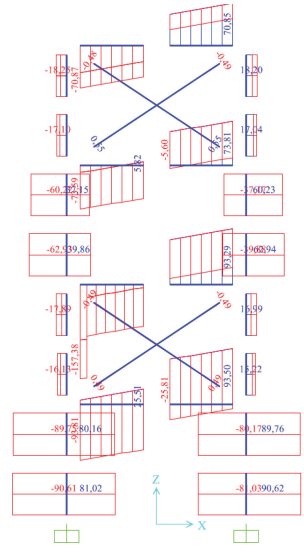

Figure 5. Envelope diagram of shear forces, *kN*.

Solving nonlinear optimization problem using sequence of linear programming tasks, we obtain the solution of optimization problem. Interaction between the moment capacity and the axial force (see Figure 7) was taken into account for the second iteration and the safety factor for load $\mu = 1{,}11$ was obtained for the vector of independent residual forces $\boldsymbol{X} = (-63{,}2;\ -22{,}95;\ 10{,}24;\ 0)$. Envelope diagram of elastic moments with the safety factor for load is shown in Figure 9. Result envelope diagram of moments considering redistribution of internal forces is shown in Figure 10.

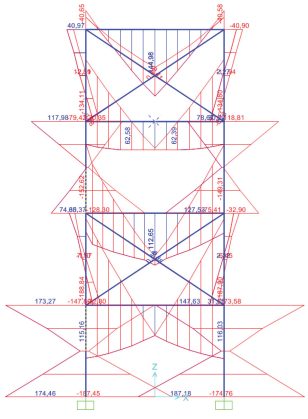

Figure 6. Envelope diagram of "elastic" bending moments, *kN·m.*

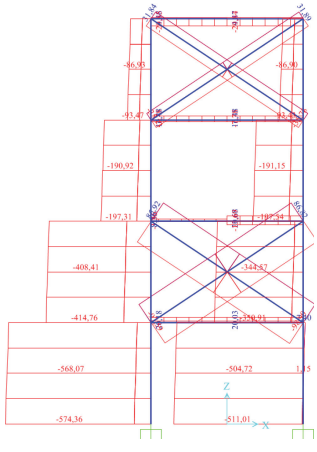

Figure 7. Envelope diagram of axial forces, *kN.*

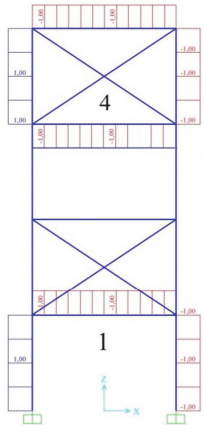

Figure 8. Unit residual *i*-th moment diagrams, $i = 1, ..., 4$.

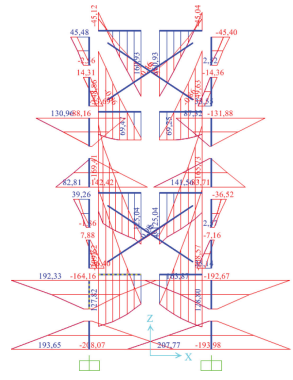

Figure 9. Envelope elastic moments diagram (increased by the safety factor), *kN·m.*

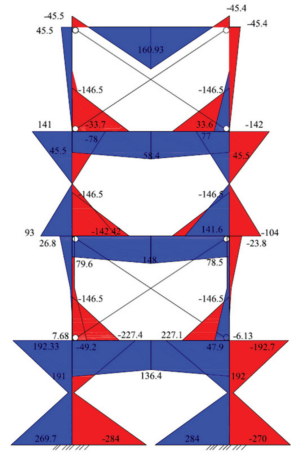

Figure 10. Envelope moments diagram after limited plastic redistribution of forces, *kN·m.*

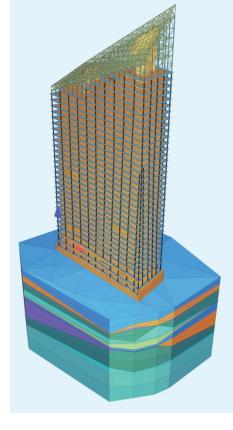

Figure 11. FEA model of high-rise building in Minsk.

Further the proposed mathematical model of the optimization problem of limit shakedown analysis will be used to the design of the high-rise building located in Minsk (see Figure 11), taking into account the construction stages. A numerical FEA model, the existing designing approaches and the experimental data obtained through the monitoring system of the building will help to validate this mathematical model.

4 CONCLUSIONS

In the paper a mathematical model of the optimization problem of shakedown analysis for seismic-protected systems is proposed. This analysis reveals additional reserve of bearing capacity of such structures, due to the ability to limited plastic redistribution of forces in elements, taking into account the plastic and brittle fracture of elements. Identification of reserves of bearing capacity is especially important to accidental design situations such as seismic action. An illustrative example of shakedown analysis for plane composite steel-reinforced concrete braced frame under seismic actions is presented.

REFERENCES

Aliawdin, P.W. 2005. *Limit Analysis of Structures Under Variable Loads*. Minsk: Technoprint. (In Russian).

Aliawdin, P. & Kasabutski, S. 2009. Limit and shakedown analysis of RC rod cross sections. *J. of Civ. Eng. and Manag*. 15(1): 59–66.

Aliawdin, P. & Muzychkin, Y. 2011. Limit analysis of structures with destructible elements under impact loadings. *Engineering Transactions.* 59(3): 139–159.

Alawdin, P. & Bulanov, G. 2014. Shakedown of composite frames taking into account plastic and brittle fracture of elements. *Civ. Environ. Eng. Rep.* 15(4): 5–21.

Alawdin P.W. & Bulanov G.V. 2013. Analysis of RC frames taking in account plastic and brittle fracture of elements, in: *Problems of modern concrete and reinforced concrete. Minsk*: StrojMediaProekt: 13–26. (In Russian).

Alawdin P.W. & Liepa L., 2015. Optimal shakedown analysis of plane reinforced concrete frames according to Eurocodes. *International Journal of Mechanics and Materials in Design*: 1–14.

Atkociunas, J. 2011. Optimal shakedown design of elastic-plastic structures. *Vilnius: Technika.*

Atkociunas, J. & Venskus, A. 2011. Optimal shakedown design of frames under stability conditions according to standards. *Computers & Structures* 89(3–4): 435–443.

Boissonnade, N., Greiner, R., Jaspart, J.P. & Linder, J. 2006. *Rules for member stability in EN 1993-1–1. Background documentation and design guidelines.* Portugal: ECCS Technical Committee 8 - Stability.

Borino, G. 2014. Shakedown Under Thermomechanical Loads. In: Hetnarski R.B. (eds.) *Encyclopedia of Thermal Stresses*. Netherlands: Springer.

Bungale S. Taranath. 2012. *Structural Analysis and Design of Tall Buildings. Steel and Composite Construction*, Boca Raton, Taylor & Francis Group.

Caltrans Seismic Design Criteria, Version 1.7, Caltrans, 2013.

CSI Analysis Reference Manual For SAP2000, 2011. ETABS, SAFE and CSiBridge, USA, Berkley, Computers and Structures, Inc..

Cyras, A. 1983. *Mathematical Models for the Analysis and Optimization of Elastoplastic Structures*. Chichester: Ellis Horwood Limited.

Dem'anov V.F., Stavroulakis G.E., Polyakova L.N. & Panagiotopoulos P.D. 1996. Quasidiffer-entiability and Nonsmooth Modelling in Mechanics, Engineering and Economics / *Non-convex Optimization and Its Applications, (Vol. 10),* Kluwer Academic Publishers, Dordecht/Boston/London.

Eurocode 0: Basis of structural design, Brussels, European Committe for standardizations, 2002.

Eurocode 2: Design of concrete structures. Part 1–1: General rules and rules for buildings, Brussels, European Committe for standardizations, 2004.

Eurocode 4: Design of composite steel and concrete structures for. Part 1–1: General rules and rules for buildings, Brussels, European Committe for standardizations 2005.

Eurocode 8: Design of structures for earthquake resistance. Part 1: General rules, seismic actions and rules for buildings, Brussels, European Committe for standardizations, 2004.

Fadaee, M. J., Saffari, H. & Tabatabaei, R. 2008. Shear effects in shakedown analysis of offshore structures. *Journal of Ocean University of China.* 7(2): 177–183.

König, J.A. 1987. *Shakedown of Elastic-plastic Structures*. Amsterdam: Elsevier.

Leonetti, L., R. Casciaro & G. Garcea. 2015. Effective treatment of complex statical and dynamical load combinations within shakedown analysis of 3D frames. *Comput. & Struct.*, *158*: 124–139.

Narayanan, R. & Roberts, T. M. 1991. *Structures Subjected to Repeated Loading: Stability and Strength*. London and New York: Elsevier.

Nguyen, Q.S. 2006. Min-max duality and shakedown theorems in plasticity. In: Alart, P., Maisonneuve, O., Rockafellar, R.T. (eds.) *Nonsmooth Mechanics and Analysis: Theoretical and Numerical Advances*. US: Springer.

Skalomenos K.A., Hatzigeorgiou G.D. & Beskos D.E. 2014. *Modeling level selection for seismic analysis of concrete-filled steel tube/moment-resisting frames by using fragility curves.* Earthquake Engineering & Structural Dynamics. John Wiley & Sons, Ltd., 44(2): 199–220.

Tangaramvong, S., Tin-Loi, F., Wu, D. & Gao, W. 2013. Mathematical programming approaches for obtaining sharp collapse load bounds in interval limit analysis, *Comput. & Struct. 125*: 114–126.

Weichert, D. & Maier, G. 2002. *Inelastic Behavior of Structures under Variable Repeated Loads*. Wien: Springer-Verlag.

Weichert, D. & Ponter A. 2009. *Limit States of Materials and Structures*. Wien: Springer.

Zongyuan, Z., Baofeng, G., Yinxiao, L., Miao, J. & Shiyan, Z. 2015. Shakedown criterion employing actual residual stress field and its application in numerical shakedown analysis. *Chinese Journal of Mechanical Engineering*. 28(5): 919–927.

Recent Progress in Steel and Composite Structures – Giżejowski et al. (Eds)
© 2016 Taylor & Francis Group, London, ISBN 978-1-138-02946-0

Comparison between behavior of steel and composite Eccentrically Braced Frames with long links

M. Şenilă, A. Şigăuan & I. Petran
Department of Structures, Faculty of Civil Engineering, Technical University of Cluj-Napoca, Cluj-Napoca, Romania

ABSTRACT: Eccentrically Braced Frames (EBF) are used world-wide and represent the alternative to the Concentrically Braced Frames (CBF) and Moment Resisting Frames (MRF). Eccentrically braced frames are characterized by high lateral rigidity, while the dissipation occurs in link elements, by inelastic distortion. The strength and ductility of EBF is directly related to the strength and ductility of the links, development of plastic hinges is designed to be at the extremities of frame elements, preferably in the beams and only at limit states in columns. The seismic energy is dissipated by means of elasto-plastic shear cycles (for the short link), bending cycles (for the long link) and shear and bending cycles (for the intermediate link).

This paper presents the result of numerical studies with the objective to investigate and compare the behaviour of 2D steel and composite eccentrically braced frames under seismic loading with active links which yield in bending.

1 INTRODUCTION

Steel and composite Eccentrically Braced Frames (EBFs) are a very efficient type of structures for structural seismic response. The EBFs combine the advantages of both MRF (moment resistant frames) and CBF (concentrically braced frames), the ductility as the characteristic of moment resisting frames with the lateral stiffness associated with concentrically braced frames (Chao & Goel, 2005).

Considerable research has been undertaken on EBF's since mid- 1970's, beginning with pseudo-static tests on one-third scale three story EBF (Roeder & Popov, 1977), (Manheim, 1982), followed by a five-story one-third scale model tested on shaking table. The tests with short shear yielding links showed that EBFs are very ductile and stable frames for resisting seismic loading. However, the architectural openings available by using short links sometimes are not sufficient. As a consequence, long links with flexural yielding were developed and tests were carried out by Engelhardt and Popov. All the experimental work done to date has demonstrated the superior seismic performance and led EBFs to be among the popular seismic-resistant steel framing systems (Chao & Goel, 2005).

In case of EBF's with composite beams, the current practice recommends a complete detachment between steel beam and concrete slab in the dissipative zones. The lack of connection between the concrete slab and the steel beam in dissipative areas does not lead to a behavior similar with a pure steel beam. The presence of the reinforced concrete slab has an important influence on development of plastic hinges in beams (Ciutina, Danku, & Dubina, 2013).

The distinction between the behaviour of composite beams withand without connectors over the plastic zones hasn't been underlined in almost any of the existing studies.Appears the need to obtain characteristic curves that best describe the phenomena occurring in plastic hinges of composite steel-concretecross-sections under cyclic loads and some specific prescriptions that can be used in current design practice.

For a comparative analysis between the behavior of eccentrically braced frames with steel sections and the ones with composite sections (without connection in dissipative zones), when are subjected to seismic loads, a series of nonlinear static analyses (pushover analyses) and nonlinear dynamic analyses (time-history) were carried out for both types of structures. The structures were modeled as 2D frames with 6 stories. The software SAP2000 was used to create the numerical model.

2 DESCRIPTION OF PUSHOVER, N2 METHOD, TIME-HISTORY AND IDA ANALYSES

The nonlinear static analysis (pushover) is a method used to evaluate the post-elastic capacity of structures. This type of analysis assumes incrementally imposed displacements up to the development of

plastic hinges. As the displacements continue to increase, plastic hinges will be progressively developed until a failure mechanism will be reached (global or local).

The recording of horizontal forces and top displacement of structure generate a graphic called capacity curve of structure or pushover curve. This curve is not associated with any earthquake, being a characteristic of structure. The capacity curve highlights different characteristic bending moments from post-elastic behavior of structure and provides information about the resistance and ductility of structure.

The N2 method implies determination of target displacement using a nonlinear static analysis. The procedure involvesobtaining the base shear force—displacement capacity curve, with the characteristic points marked representing the requirements for displacement according to limit states. The requirements are determined by displacement spectra for inelastic seismic response. General safety condition is: demands ≤ capacity (Fajfar, 2000).

The structures were subsenquently subjected to nonlinear dynamic analysies—time history. Time-history is a type of analysis—step by step (stepping increment) of time that takes into account recording existing data of artificial data (seismograms) of different types of ground motions.

Pushover analyses have as limitation the fact that they do not consider the higher modes of vibration. This could be particulary important for braced frames whose use is beginning to be more advantageous to the detriment of moment resisting frames, as the number of floors increase.

Therefore, actual performance of eccentrically braced frames can be better estimated by nonlinear dynamic analysies made by increasing seismic intensity (called Incremental Dynamix Analysis—IDA). In fact, this kind of analysis (by taking into account the higher modes of vibration and their influence on the formation of global collapse mechanism) provide the best approximation of the seismic response of structures, highlighting requirements for local and global ductility.

The time-history Incremental Dynamic Analyses involded the use of 7 earthquake recordings, all of them recorded from the Vrancea source, but different in magnitude. The recordings were scaled for the design spectrum of Bucharest (a_g = 0.3 g, T_c = 1.6 s).

3 MODELING PARAMETERS FOR THE STRUCTURES

The analysed structure was located in Bucharest, characterized by the following features: a_g = 0,30 g;Tc = 1,6 s; Snow load: $S_{0,k}$ = 2,00 kN/m^2; Live load: Q = 3,0 kN/m^2. Dead load: G = 4,5 kN/m^2.

The structural behavior factor q = 6.0, which represents the energy dissipation capacity of structure is taken from Tab. 6.3 (P100–2013) for a high seismicity area (H): $q = 5\alpha_u/\alpha_1$, where α_u/α_1 = 1.2 for EBF.

The reinforced concrete slab (C25/30, Ø12/15 - PC52) was modeled with steel multi-layered nonlinear type of elements, which can be modeled the concrete in the slab, but also the reinforcement. For both materials a nonlinear behavior has been defined.

Finer mesh was used in the potential plastic zones, where development of plastic hinges is expected. The type of mesh chosen for slab influences the result regarding the needed forces for development of plastic hinges. Different ways of meshing were studied until the optimum one, both in terms of results and analysis time.

The modelling of composite beams is quite challenging. The connection between the concrete slab and steel beam was modeled using link elements—available in software SAP2000. It has been chosen a version with fixed links, where the connection of concrete slab and steel beam is in centroid. A distance of 30 cm between links was chosen taking into consideration different ways for layout of the links.

Initial design was made with modal spectrum analysis (P100–2013), after which nonlinear static analyses—pushovers and nonlinear dynamic analyses—time history were performed, in order to evaluate the development of plastic hinges in dissipative zones and the capacity curve.Two type EBF structures were analyzed: steel structure (S_6) and composite structure (C_6), Figure 1.

For the steel structure—EBF_S_6, the beams of the frame are as follows: HEB360 for the first three levels, HEB340 for levels 4, 5, 6, and HEB280 respectively for the last level.

For EBF_C_6, after performing the pushover analysis using the same sections as for steel structure EBF_S_6, in which was added the contribution of concrete slab, yield mechanism is formed in columns and braces at first level of the central frame.

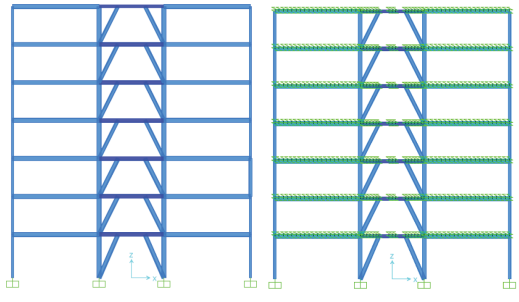

Figure 1. EBF_S_6 (left) and EBF_C_6 (right).

Table 1. Description of the structures P+6E.

Central columns	Marginal columns	Braces	Beams	EBF beam	Type
HEB400	HEB240	HEB340 HEB280	IPE400	HEB360 HEB340 HEB280	S
HEB400	HEB240	HEB340 HEB280	IPE400	HEB320 HEB280	C

For this reason, to assure the development of plastic hinges in the dissipative zones (links) it was necessary a reduction of composite section to HEB320 (exception—beam from the last level, which remain HEB280). In Table 1 are presented the resulted sections for both type of structures.

After performing the pushover analysis, the base shear force—displacement capacity curve (global force—top displacement) was obtained. From capacity curves the target displacements have been determined for both structures.

Next the results obtained in pushover analysis, the results for N2 method and thelocal and global checking for this method are presented.The target displacements for both types of structures (with steel beam and composite beam) were determined for the following limit states: Serviceability Limit State SLS); Ultimate Limit State (ULS); Collapse Prevention Limit State (CPLS).

4 PUSHOVER ANALYSIS RESULTS

The obtained target displacement values for structures with steel beam are: 12.9 cm for SLS, 28.5 cm for ULS, respectively 46.0 cm for CPLS.

For the frame with composite beams are: 7.99 cm for SLS, 18.3 cm for ULS, respectively 32.1 cm for CPLS.

The obtained values are presented in the following graphics (Figs. 2–7):

From the graphics presented above it can be observed that the requirements for target displacements are higher for steel frames than for composite frames (12.9 cm vs, 7.99 cm for SLS, 28.5 cm vs. 18.3 cm for ULS, respectively 46.0 cm vs. 32.1 cm for CPLS).

From those two capacity curves (Fig. 8, Fig. 9) it can be observed that the contribution of concrete slab in case of EBF_C_6 is significant even if the dissipative zones are not provided with shear connectors. The maximum value of the force exceeds the value of 2900 kN for a 38 cm displacement compared with the steel frames, where the maximum value for the force is 2000 kN and the ultimate displacement is approx. 48 cm.

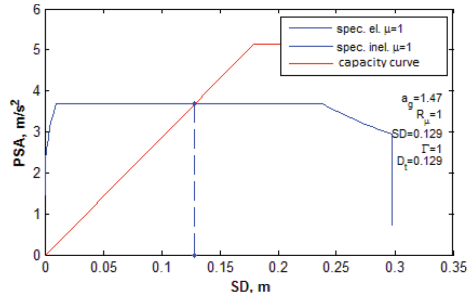

Figure 2. Target displacements SLS-EBF_S_6.

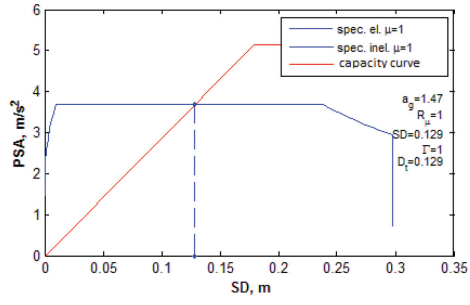

Figure 3. Target displacements SLS-EBF_C_6.

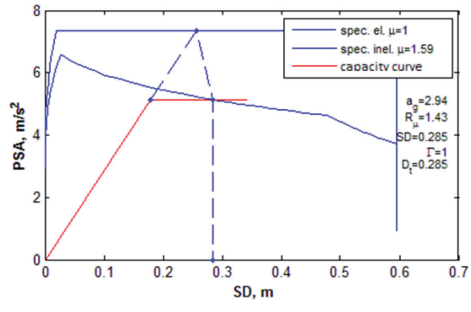

Figure 4. Target displacements ULS-EBF_S_6.

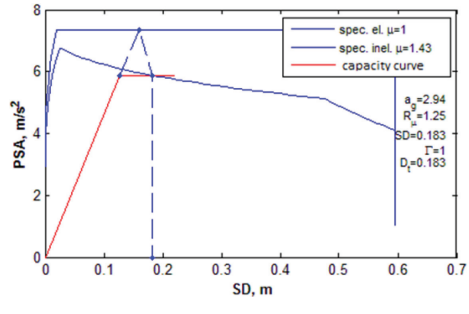

Figure 5. Target displacements ULS-EBF_C_6.

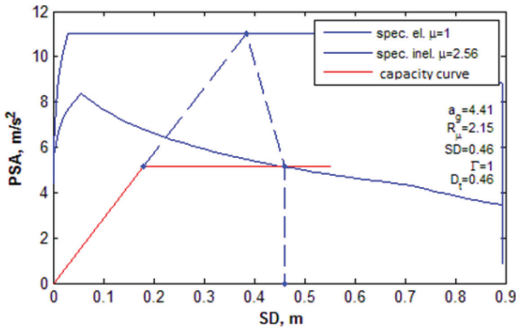

Figure 6. Target displacements CPLS-EBF_S_6.

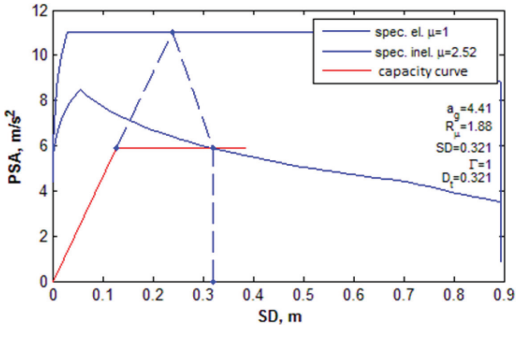

Figure 7. Target displacements CPLS-EBF_C_6.

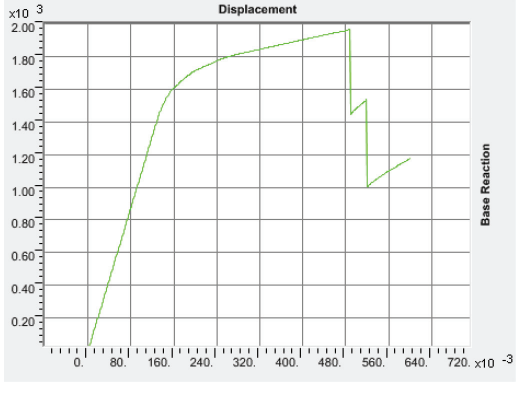

Figure 8. Capacity curve for EBF_S_6.

In Table 2 is presented the development of plastic hinges in the link.It was taken into consideration the following characteristic moments: development of first plastic hinge, the displacement for Ultimate Limit State (ULS) and the formation of failure mechanism.

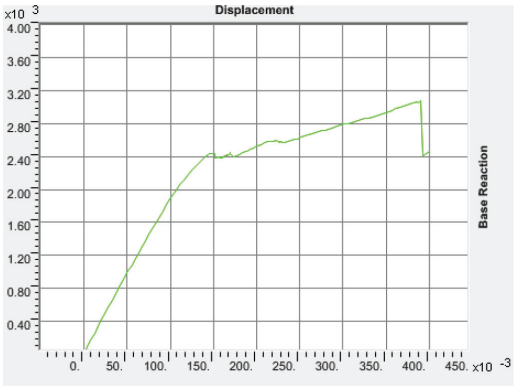

Figure 9. Capacity curve for EBF_C_6.

Table 2. Development of plastic hinges.

Development of first PH	ULS	Collapse
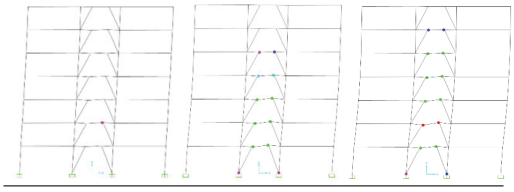		
D_E=12.9cm= D_{TSLS}	D_{ULS}=28.5cm	D_U=48.9cm>D_{TCPLS}
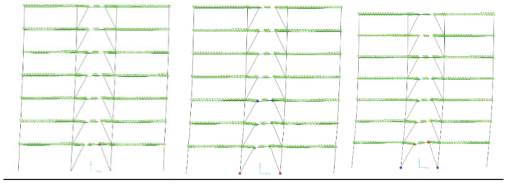		
D_E=9.1cm > D_{TSLS}	D_{ULS}=18.3cm	D_U=39.2cm>>D_{TCPLS}

The requirements for target displacement, calculated by using N2 method for all 3 limit statesare reached for both types of structures (steel and composite).

In case of EBF_S_6 the first plastic hinge is developed approximately in the same time as achieving the requirements for serviceability limit state and plastic hinges are developed in links from the first five levels. For the requirements specific to ultimate state it can be observed that failure mechanism is formed in the link from the second level, by failure of both plastic hinges.The collapse mechanism occurs by failure of dissipative zone from beam of second level.

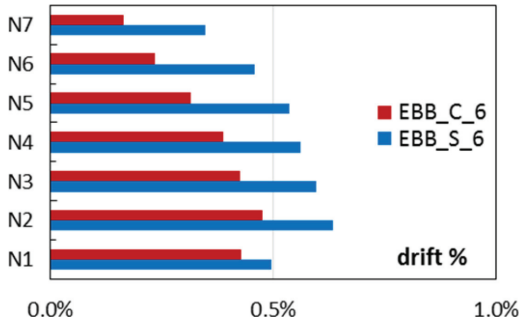

Figure 10. Inter-story drift for EBF_S_6 and EBF_C_6 at SLS.

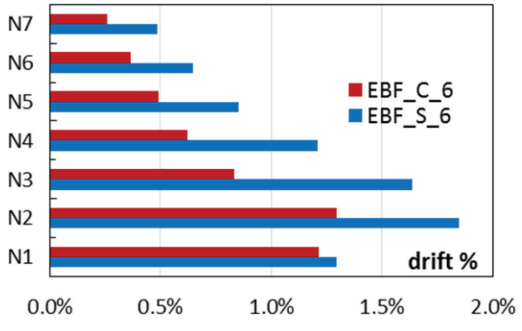

Figure 11. Inter-story drift for EBF_S_6 and EBF_C_6 at ULS.

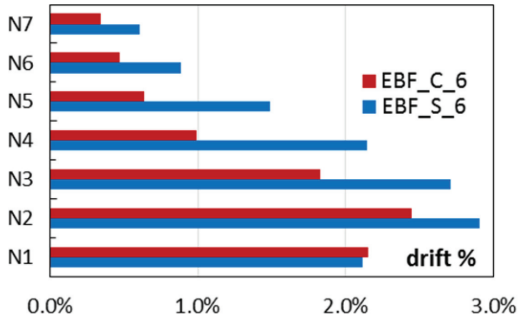

Figure 12. Inter-story drift for EBF_S_6 and EBF_C_6 at CPLS.

In case of composite frame EBF_C_6, the first plastic hinge is formed after reaching the requirements of SLS. For the requirements of ultimate limit state, the plastic hinges are developed in links of the first 3 levels. The collapse mechanism occurs by failure of dissipative zone from beam of the first level.

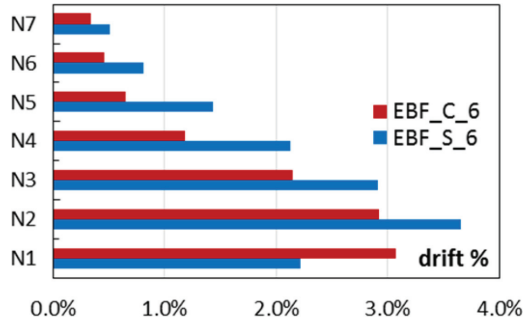

Figure 13. Inter-story drift for EBF_S_6 and EBF_C_6 at collapse.

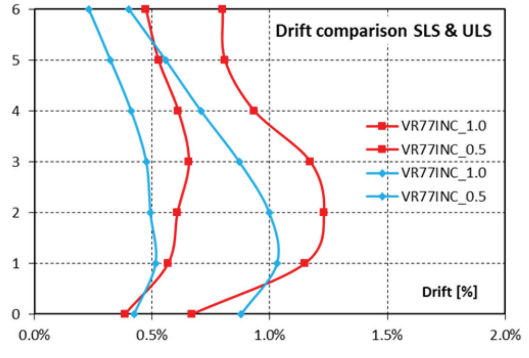

Figure 14. Drift comparison between EBF_S_6 (red) and EBF_C_6 (blue) at SLS and ULS.

The obtained values for inter-story drift are presented in the following graphics (Figs. 10–13).

The values for the drift are within the values specified in the design norms in all the three limit states.

There were taken into account the values from P100–2013, which provides a maximum value for the drift of 0.75% for SLS, 2.5% for ULS and 5% for CPLS provided by the FEMA356 (in P100–2013 does not exist requirements for CPLS).

The maximum value for the inter-story drift is reached to the second level for all the three limit states (SLS, ULS and CPLS).

5 TIME HISTORY ANALYSIS RESULTS

In order to present the difference between the SLS and ULS conditions, the following charts show the values at SLS (smaller seismic intensity, $\lambda = 0.5$) and ULS (seismic intensity, $\lambda = 1.0$), Figure 14. While the ULS results are already known, the SLS

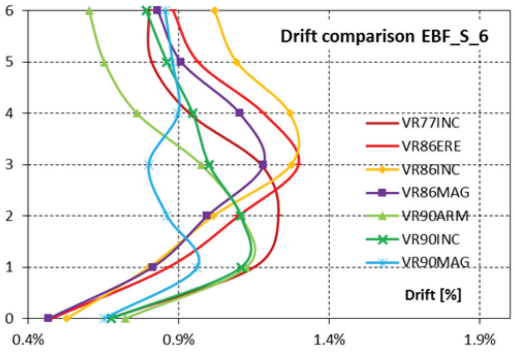

Figure 15. ULS drift comparison EBF_S_6 for all seven accelerograms.

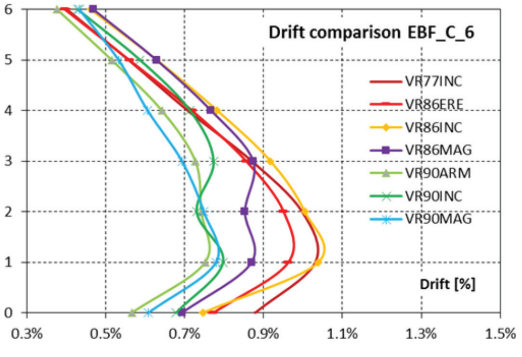

Figure 16. ULS drift comparison EBF_C_6 for all seven accelerograms.

conditions induce very small discrepancies between the steel and composite frames in what concerns the drift values.

In case of steel structure, the values for interstory drift are bigger at second and third level, the result for ULS condition are approximately 50% higher than for SLS. If a comparison between the steel structures and the composite one is made regarding the distribution along the building height, it can be seen a more proportionate distribution in case of steel structure.The values for ULS are almost double that for SLS.

In Figure 15 and Figure 16 are presented the maximum recorded values (envelopes) for drift, for all the seven Vrancea-type accelerograms.

Following the same conclusion as before, when comparing the response of the two structures (steel and composite) at the design ground acceleration (λ = 1.0), at each level, the difference is obvious. However, at ULS conditions the composite structure could be considered safe, with all the required values for drift androtations under the norme limiting values.

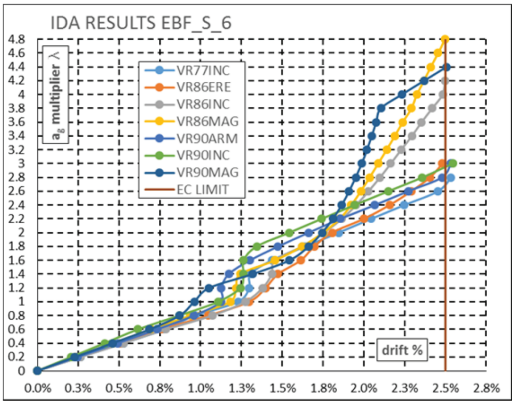

Figure 17. IDA result for EBF_S_6.

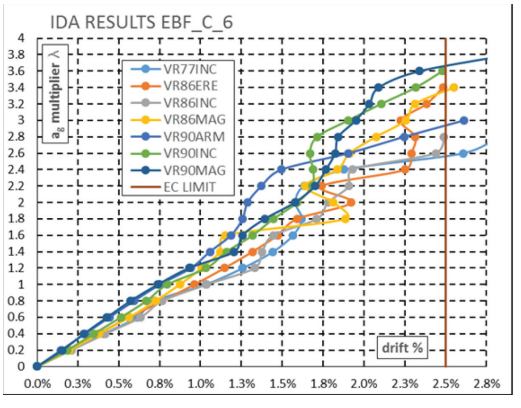

Figure 18. IDA result for EBF_C_6.

The following set of results shows the comparison between the globalresponses of the 7 story structure in the steel and composite beams solution under7 earthquake recordings from Vrancea source (Fig. 17 and Fig. 18). The IDA were performed by step-bystepincrement of the acceleration level and monitoring the top displacementvalue up to the point when a failure criterion was reached.

The maximum value for the interstory drift in case of steel structure is reached at level 4, having a value of 1.3%, which does not exceed the limit value from P100–2013. In case of composite structures, it can be observed a superior behavior, the maximum value for interstory drift is reached at level 2, with a value of 1%, which shows the contribution of the concrete slab in composite structures.

Interstory drift for EBF_S_6 are generally higher with 40–50% that for EBF_C_6 in ULS condition (Table 3). For EBF_S_6, the maximum value for seismic intensity is $\lambda = 4.8$, for the composite structure EBF_C_6, this value is much lower, $\lambda = 3.8$.

Table 3. Results at ULS.

EBF_6	Drift (%)		Rotation (mrad)	
Accelerogram	Steel	Composite	Steel	Composite
VR77INC	1.23%	1.03%	14.24	10.8
VR86ERE	1.30%	0.96%	11.32	8.7
VR86INC	1.27%	1.04%	11.09	13.2
VR86MAG	1.18%	0.87%	8.24	7.4
VR90 ARM	1.12%	0.75%	12.81	3.9
VR90INC	1.11%	0.80%	12.45	6.2
VR90MAG	0.96%	0.78%	9.02	4.5

6 CONCLUSIONS

The difference in behavior between two types of eccentrically braced frames, steel and composite, has been studied. The contribution of the concrete slab is significant in regards to the global behavior of structure, even in the situation when shear connectors are not present in the dissipative zones.

From the pushover analyses it can be observed that the requirements for target displacements are higher for steel frames than for composite frames. The energy dissipation is done through the development of plastic hinges for both types of structures.

The pushover analyses showed that in case of composite beams to lower values of the inter-story drift, plastic hinges are formed later, which leads to a stiffer structure. The values for inter-story drift are within the limit values provided by norms for both types of structures in all the three limit states.

In case of eccentrically braced frames with links that yield in bending, it will be recommend to use the composite beam solution because leads to a better seismic response than the pure steel beams.

The frame with steel beams develops plastic hinges earlier than thecomposite one, while the failure (either by soft story mechanism orattaining maximum rotation in one of the hinges) increment has similarvalues, although the steel structure exhibits higher overstrength.

The drift values are within the code limits, but the composite structure isnoticeably stiffer.All the frames present a safety reserve of at least 20%.

REFERENCES

Chao, S.H. & Goel, S. 2005. *Performance-based seismic design of EBF using target drift and yield mechanism as performance criteria*. Department of Civil and Environmental Engineering, The University of Michigan.

Roeder, C.W. & Popov, E. 1977. Inelastic Behavior of Eccentrically Braced Steel Frames Under Cyclic Loading. *Report No. UCB/EERC-77/18, Earthquake Engineering Research Center*, University of California at Berkeley.

Manheim,D.N. 1982. *On the Design of Eccentrically Braced Frames*, Department of Civil Engineering, University of California at Berkeley.

Ciutina, A., Danku, G. & Dubina, D. 2013. Influence of steel-concrete interaction in dissipative zones of frames: I—Experimental study. *Steel and Composite Structures* 15(3).

Fajfar, P. 2000. A nonlinear analysis method for performance-based seismic design. *Earthquake Spectra 16(3):573–92*.

Senila,M. & Petran, I. 2015. Development of plastic hinges in steel and composite beams of eccentrically braced frames. *Proceedings of Computational Civil Engineering 2015, International Symposium Iasi, Romania, 22 May*.

SR EN1994-1-1:2004. *Design of Composite Steel and Concrete Structures. Part 1.1 - General Rules and Rules for Buildings*. Brussels: CEN, European Committee for Standardisation.

FEMA 356, 2000. *Prestandard And Commentary For The Seismic Rehabilitation Of Buildings*.

SR EN1998–1:2004. *Design of structures for earthquake resistance—Part 1: General rules, seismic actions and rules for buildings*.

This page intentionally left blank

Recent Progress in Steel and Composite Structures – Giżejowski et al. (Eds)
© 2016 Taylor & Francis Group, London, ISBN 978-1-138-02946-0

Collapse behaviour of steel box columns under seismic effect of the combined earthquakes

S. Shimizu
Department of Civil Engineering, Shinshu University, Nagano, Japan

ABSTRACT: When a huge earthquake occurs, occasionally, the quake consists of two or more seismic motions. This combination of the seismic motions is called a combined earthquake. If a structure such as a bridge is subjected combined earthquake, the structure shall suffer the seismic motions successively, with no opportunity to make repair works. This paper describes the numerical results of steel box columns subjected a combined earthquake. The seismic acceleration measured in the great earthquake which hit north-east Japan in 2011 is adopted as the seismic load, and following two cases are compared; (1) the column is subjected to the combined quakes successively, (2) the column is subjected to the quakes, which compose the combined quakes, independently. The numerical results indicate that the column shows different behavior when it suffers the seismic load of case (1) and (2).

1 INTRODUCTION

In the current Japanese seismic design code of steel bridges, bridges must be designed with the "Seismic Performance Level (SPL) 1", "SPL 2" or "SPL 3".

The SPL 1 is the level which brings no significant damage to the bridge, and the bridge members are expected to be in the elastic state after the earthquake. With the SPL 2, the bridge suffers limited damages, and it is expected that it functions after small repair works. In the SPL 3, the bridge cannot be functionable any more, however is prevented from the fatal failure.

The required seismic performances according to the bridge importance and the considered earthquake level are summarized as the performance matrix in Table 1.

Level 1 earthquake in the Table is corresponding with a moderate-scale earthquake which causes the moderate ground motion. This type of earthquake is expected with the high probability, and a bridge may suffer this scale of earthquake one or more times during the bridge is in service. The Level 2 earthquake is an earthquake which occurs with small probability, however, it is estimated to cause the intensive ground motion and may bring the severe damages.

Within these Seismic Performance Levels, SPL2 is a level with which bridges can be opened for the emergency vehicles with the temporary repair work made in immediately after the disaster, and opened with "full-service" for the all traffics after small repair works. That is, the bridges are assumed to be repaired for the service after the disaster by which the bridge suffer the damages, but before the "next" quake.

Table 1. Seismic performance matrix.

Earthquake Level	Normal bridges	Essential bridges
Level 1 Earthquake	SPL 1	SPL 1
Level 2 Earthquake	SPL 3	SPL 2

SPL: Seismic Performance Level.

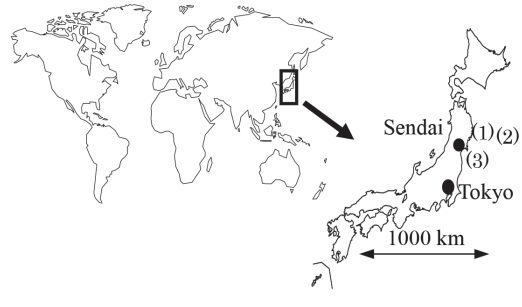

Figure 1. Rupture zones of 2011 Earthquake.

An earthquake is caused by a rupture of a tectonics plate or a movement of a fault. In particular, with a great earthquake, the rupture zone of the tectonics plate shall extends for over 100 km, and once a great earthquake occurs, it may cause the continuous rupture in the adjacent area. This "following" rupture may cause the subsequent quake in the adjacent region. In the results, a

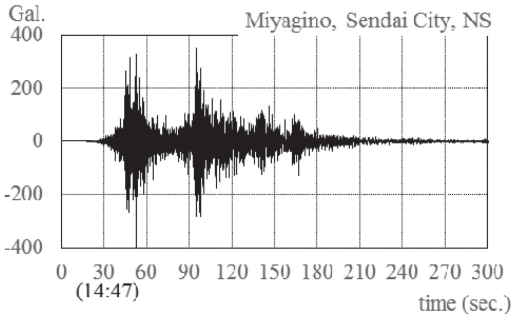

Figure 2. Seismogram of 2011 Japan Earthquake Measured at Sendai City (N-S Component).

huge earthquake, such as the Level 2 quake in the Table 1, sometimes, involves 2 or more ruptures, i.e. a huge earthquake sometimes consists of 2 or more quakes. In the other words, in the huge earthquake disaster, two or more quakes shall arise successively. This type of earthquake is well known as the name of the "combined earthquakes".

The earthquake which hit northeast Japan in 11 March, 2011 is a typical combined earthquakes. Figure 1 is the rough map around Japan with the estimated rupture zones in 2011 quake.

In the 2011 quake, it is reported that the 3 successive and (3) in the Figure 1 with the interval of approximately 1 minute. In this earthquake, it is considered that the first rupture (1) arises at the offshore region of Sendai City, then the second rupture (2) occurs more offshore region in the Pacific Ocean. The third rupture (3) is found at the region of the offshore area between Tokyo and Sendai. This fact means that the 3 large earthquakes occurred with the interval of about 1 minute in the 2011 quake.

Figure 2 shows the seismogram of the 2011 earthquake observed at Sendai City. The horizontal axis of Figure 2 denotes time in seconds from 14:46:30 (2:46:30 PM) of 11 March 2011, and the vertical axis is the measured ground acceleration for the NS (North-South) direction. It is obvious that, in this seismogram, following to the preliminary tremor up to around 14:47, 2 major tremors caused by the ruptures (1) and (2) are found at the time around of 14:47:20 and 14:48:10. In this seismogram, the record of the third rupture (3) is not clear, but the third rupture is observed at around 14:49.

As mentioned above, with the seismic performance level 1 and 2, the structures are to be repaired for the service after they suffered the seismic motion. This is on the premise that we have time to repair after the structure suffers the seismic motion. However, under the combined quake, the second tremor comes immediately after the first tremor, and therefore the structures suffer the successive tremor with no repair works.

With above background, the author made a series of numerical analyses on the behaviour of steel box columns subjected to the seismic motions of the combined earthquakes. In the current study, the practically measured seismic motion of the 2011 Japan Earthquake is used as the seismic load, and the contribution of the subsequent quake is investigated. This paper describes a part of the numerical results on behaviour of steel columns under the combined earthquake.

2 MODEL

2.1 *Observed seismograms and the characteristics of the quake*

In this paper, two seismic motions of the 2011 Japan earthquake are used as the seismic loadings, observed at Ishinomaki City (around 30 km East of Sendai) and at Ofunato City (120 km North-East of Sendai). Figure 3 shows the seismograms

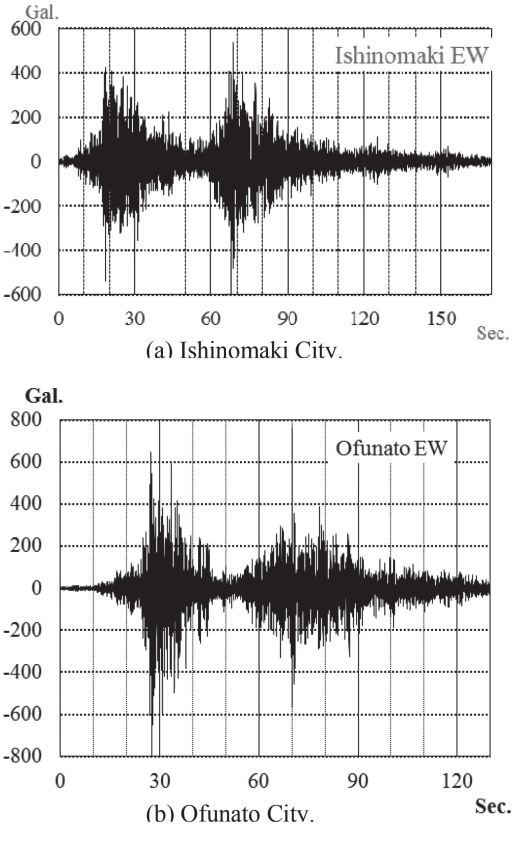

Figure 3. Record of Seismic Motion used for Loadings.

of the EW (East-West) component of these two seismic motions. For the analysis, only the seismic motion after "the time when the preliminary tremor is clearly observed" and until "the time when the amplitude becomes enough smaller" is used, and therefore the portions for 170 seconds (Ishinomaki) or 130 seconds (Ofumato) from the beginnings are used as the seismic loadings. In Figure 3, only the parts of the seismic motions used for the analyses are plotted. It is obvious that these two seismograms has two peaks of the major tremor. Because of the limited room in this paper, seismograms for NS (North-South) and UD (Up-Down) components are not shown, all three components are utilized in the analyses.

In Figure 4, the Fourier spectra of these two seismic motions are plotted. NS, EW and UD in the Figure denote the spectra for North-South, East-West and Up-Down directions respectively. It is found that the spectrum of the tremor of Ishionomaki has the peak value at the period of 0.14 seconds although the peak is found at the period of 0.23 second in the Ofunato tremor.

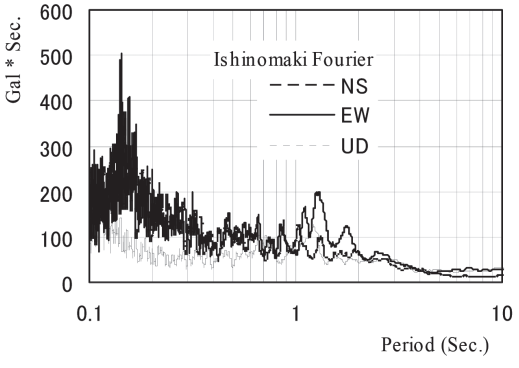

(a) Ishinomaki City.

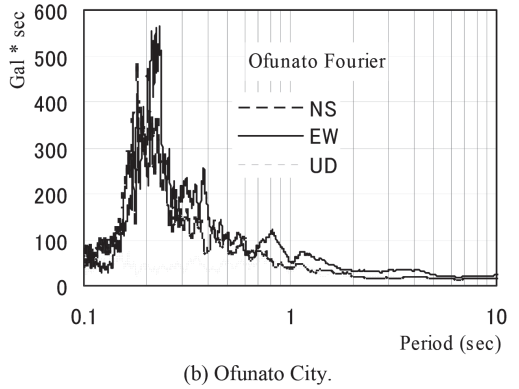

(b) Ofunato City.

Figure 4. Fourier Spectra of Tremors on Ishinomaki & Ofunato.

2.2 *Seismic load*

The aim of this paper is to study the column behavior which is subjected to (1) only the first major tremor, (2) only the second major tremor, and (3) subjected to full of the tremor. Therefore, the seismic motions shown in Figure 3 are divided into 2 parts. For example, the seismic motion of Ishiniomaki City in Figure 3 (a) is divided at the time is 50 seconds as demonstrated in Figure 5. Although the seismic motion of only EW direction is shown in Figure 5, the analyses, the NS and the UD components of the seismic motion are also divided at the time of 50 seconds. That is, on the tremor of Ishonomaki City, the first part the seismic motion is continued for 50 seconds and the second part is for 120 Seconds long.

For the seismic motion of Ofunato City, it is divided at 55 seconds, and therefore length of the second part is 75 seconds.

In this paper, the first part of the seismic motion is denominated as "the Phase 1 loading", the second part as "the Phase 2 loading", and the seismic motion shown in Figure 3 as "the Full loading".

In Figure 6, Fourier spectra of the divided seismic motions are plotted. From this Figure, for example, the Phase 1 loading of the Ishinomali motion involves component of the period of around 0.2 seconds, although the Phase 2 period of 1.1 seconds is conspicuous.

With using these seismic motions, in the analyses of this paper, following three types of loading cases are considered.

1. Seismic motion of Ishinomaki multiplied by 1.5.
2. Seismic motion of Ofunato.
3. Seismic motion of Ofunato multiplied by 2.0.

In the cases (1) and (3), the original (measured) seismic motions are enlarged to clarify the collapse behavior of the column. As mentioned above, each

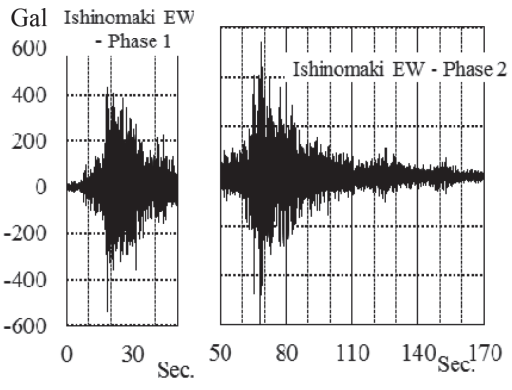

Figure 5. Divided seismic motion.

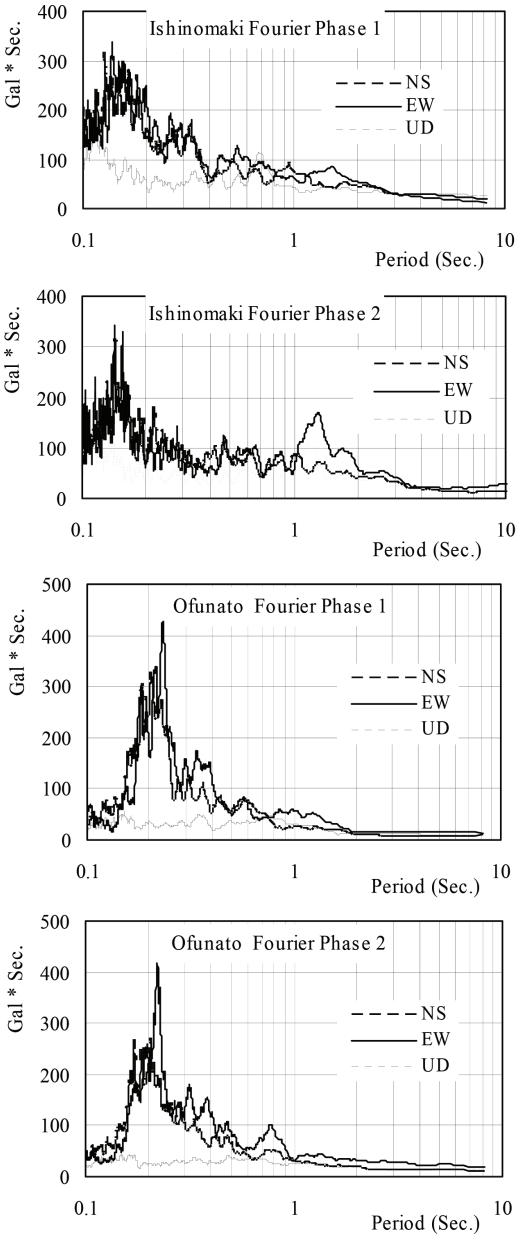

Figure 6. Fourier spectra of divided seismic motions.

case has the three loading patterns such as (a) the Phase 1 loading, (b) only the Phase 2 loading and (c) Full loading. Here, the Phase 1 loading is corresponding with the first part of the Full loading, and the first part of the behaviour under the Full loading is equal to the behaviour of the Phase 1 loading. Therefore, in this study, 6 loading patterns in total are discussed.

2.3 *Numerical models*

The numerical model in this paper is same to the author's previous studies (Shimizu, 2009, 2011, 2012), i.e. the column which is often used for the motorway viaduct. In Figure 7, the layout of the model is illustrated. The model has its height of 10 000 mm and the square section of 3 000 mm. The plate thickness is 20 mm. A practical viaduct column is often filled with concrete in its bottom part to prevent from the collision of vehicles. Therefore, in this study, the concrete filled column is also dealt with. That is, in this study, two types of the models, with or without filled in concrete, are analyzed. The concrete is filled up to 3 000 mm from the bottom a shown in Figure 7.

Material properties of the steel and concrete are summarized in Table 2.

For the steel, bi-linear stress-strain relation is assumed, and beyond the yield stress Young's modulus is set as 0.01% of the value in the Table. For the concrete, the elastic state is assumed throughout the analysis.

The analysis is realized with the software package MSC Marc, and the rectangular shell elements

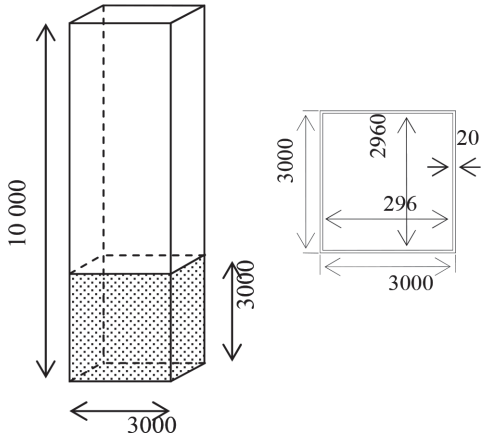

Figure 7. A typical model layout.

Table 2. Material properties.

	Young's Modulus	Poisson's Ratio		Yield Stress
	E		μ	σy
	(GPa)	ν	(Kg/mm^3)	(MPa)
Steel	206	0.3	7.85×10^{-6}	355
Concrete	30	0.167	2.35×10^{-6}	

Table 3. Natural periods and natural frequencies.

	First mode		Second mode	
	Period (sec)	Frequency (rad/sec)	Period (sec)	Frequency (rad/sec)
Filled	0.399	15.741	0.165	38.155
Non filled	0.307	20.492	0.146	43.12

and the 8-nodes solid elements are used for the steel elements and the concrete elements respectively.

At the top of the column, a mass of 700 tons is assumed which is corresponding with the superstructure of the viaduct.

2.4 *Eigenvalue analysis*

To define the dumping factors in the dynamic response analysis in the current study, the natural frequency is required. Therefore, prior to the response analysis, the eigenvalue analysis is carried out to obtain the natural frequency.

In Table 3, the natural frequencies and the natural periods of the models with or without the filled-in concrete are listed.

3 NUMERICAL RESULTS

3.1 *Deformations hysteresis*

In Figure 8 and Figure 9, the displacement hysteresis for EW direction at the top of the column with no filled-in concrete is plotted. Within these Figures, Figure .8 is of the case that the column is subjected to the seismic load Case (1) (the seismic motion of Ishinomaki multiplied by 1.5), and Figure 9 to the load case (3) (the seismic motion of Ofunato multiplied 2.0).

In each Figure, (a) shows the displacement under the Full loading, and (b) is of only the Phase 2 loading. The horizontal axis of these Figures denote time from the beginning of the analyses. It should be noted that the origin of the horizontal axis ($t = 0$ sec.) of Figure 8 (b) is corresponding to $t = 50$ sec. in Figure 8 (a), and $t = 0$ of Figure 9 (b) is $t = 55$ sec. of Figure 9 (a).

It is found in Figure 8 that, under the Full loading of the load Case (1), large displacement is observed at the time of around 19 sec. caused by the loading of Phase 1, and the displacement becomes smaller up to $t = 65$ Sec. Beyond $t = 65$, displacement increases again due to the Phase 2 loading, and the "maximum" displacement for the negative direction (West direction) of −47.6 mm is observed at $t = 70.3$ sec. At this stage, displacement shifts to about −10 mm, and after this stage, the

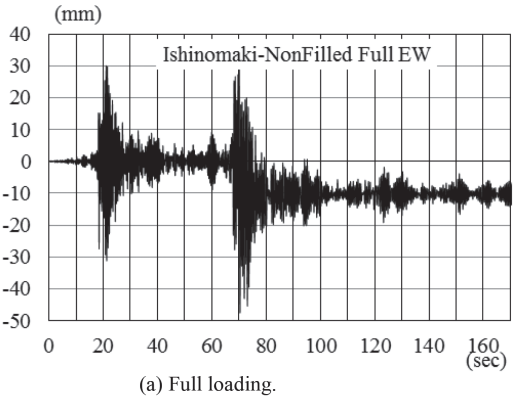

(a) Full loading.

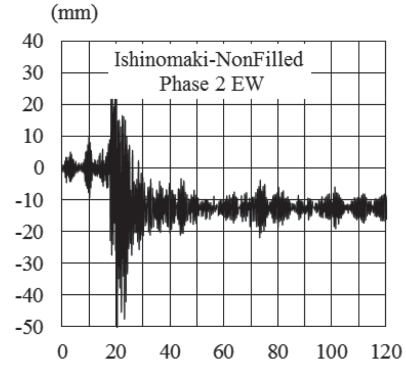

(b) Lone Phase 2 loading.

Figure 8. Displacement hysteresis under Ishinomaki × 1.5.

column shakes around −10 mm. This means that the fatal damage arises at this stage on the column. This displacement dose not restore any more, and the analysis reaches to the final stage with the residual displacement of about −11 mm.

Under the seismic load of only the Phase 2 loading, large displacement is found at $t = 20$ seconds (corresponding to $t = 70$ seconds under the Full load loading), and the displacement shifts to −12 mm.

On the other hand, under the load Case (3) (Ofunato load multiplied by 2.0), shift of the displacement occurs at $t = 28$ seconds under the Phase 1 loading, and after this stage, displacement varies around −35 mm. With only the Phase 2 loading of the load case (3), shift of displacement is not observed.

Thus, it is found that, in the load case (1) (Ishinomaki load), the phase 2 of the seismic motion caused by the second rupture has larger contribution to the column collapse, and in the load case (3), the first part has large influence to the column

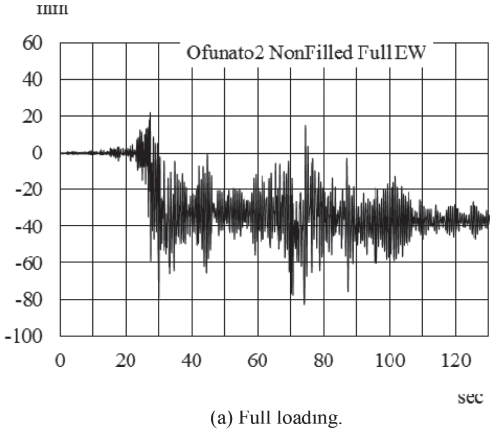

(a) Full loading.

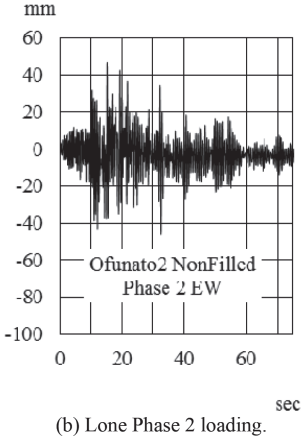

(b) Lone Phase 2 loading.

Figure 9. Displacement hysteresis under Ofunato × 2.0.

behaviour. With the load case (3), slammer out-of-plane deformation arises with the phase 2 load.

3.2 *Residual displacement*

The current Japanese design code for the steel columns defines the damage of the column with, very roughly, the residual displacement at the top of the column, i.e. when the residual displacement at the top of the column exceeds 1% of the column height, it is considered to be collapsed. Therefore, residual displacement of the column is one of the important index for the column strength.

In the Table 4, the residual displacement at the top of the column is summarized for the load cases. "Filled" or "Non Filled" in this table indicate the models with or without the filled-in concrete.

In this table, with the load case (3), the column with no filled-in concrete has the displacement for EW direction of –32.3 mm at the end of the Phase 1, and finally the residual displacement becomes 36.9 mm. However, with only the Phase 2 loading, it is –3.3 mm. That is, with this loading, the column suffers a certain damage within the tremor of the first rupture, and the damage becomes severer with the second tremor.

3.3 *Deformation patterns*

Figure 10 to Figure 15 show the displacement (a) at the end of Phase 1 loading and the displacement of the final stage, and (b) at the end of the lone Phase 2 loading. In these Figures, the deformation patterns are enlarged by 10 times.

In Figure 10 and Figure 15, it is found that the out-of-plane deformation of the final stage is similar to one of the end of Phase 1, and the deformation by the lone Phase 2 loading seems smaller than the Full loading. Figures 12, 13, 14 also shows that the deformation of the lone Phase 2 load seems to be smaller deformation. However, in these Figures, the lone Phase 2 loading brings the out-of-plane deformation for the alternate direction of the Full loading.

In Figure 11, the deformation under the Phase 1 loading is still smaller and finally it becomes larger. The deformation under the lone Phase 2 loading in this Figure is similar to the final state of the

Table 4. Residual displacement.

			Full		Lone Phase 2
Seismic Motion	Concrete		End of Phase 1	Final	Final
		NS	1.14	1.03	2.66
Ishinomaki	Filled	EW	–0.65	–0.47	–2.54
× 1.5		UD	–1.85	–1.88	–1.78
(Case 1)		NS	0.27	4.61	3.64
	No	EW	0.11	–10.40	–12.71
		UD	–1.57	–4.15	–4.56
		NS	–5.67	–4.37	–1.94
	Filled	EW	–11.40	–10.33	–1.27
Ofunato		UD	–6.39	–6.80	–2.61
(Case 2)		NS	–6.48	–6.80	1.51
	No	EW	–0.11	–0.56	1.20
		UD	–2.73	–2.90	–2.06
		NS	–18.88	–16.02	–9.20
Ofunato	Filled	EW	–33.23	–33.37	–33.37
× 2.0		UD	–19.66	–20.83	–20.83
(Case 3)		NS	–21.39	–13.43	–6.97
	No	EW	–32.31	–36.92	–3.28
		UD	–10.03	–11.58	–6.84
					mm

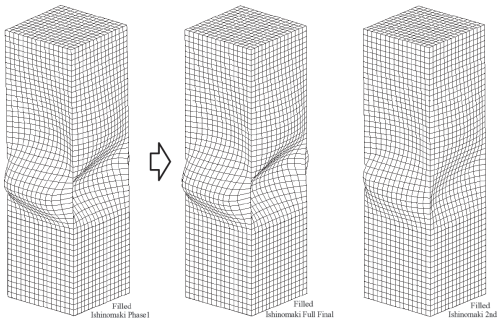

(a) End of Phase 1 & final, Full loading.

(b) Final, lone Phase 2 loading.

Figure 10. Deformation patterns – Seismic load of Ishinomaki × 1.5, with filled-in concrete.

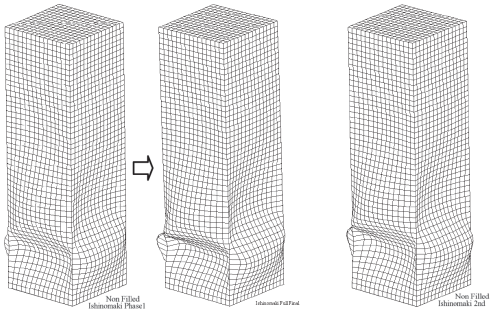

(a) End of Phase 1 & Final, Full loading.

(b) Final, lone Phase 2 loading.

Figure 11. Deformation patterns – Seismic load of Ishinomaki × 1.5, no filled-in concrete.

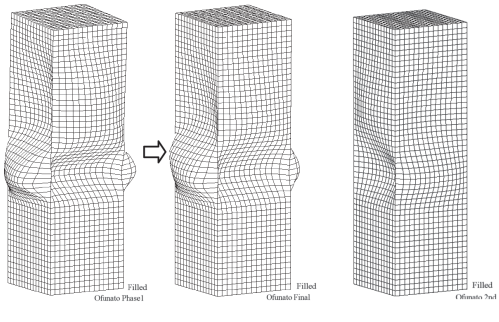

(a) End of Phase 1 & Final, Full loading.

(b) Final, lone Phase 2 loading.

Figure 12. Deformation patterns – Seismic load of Ofunato, with filled-in concrete.

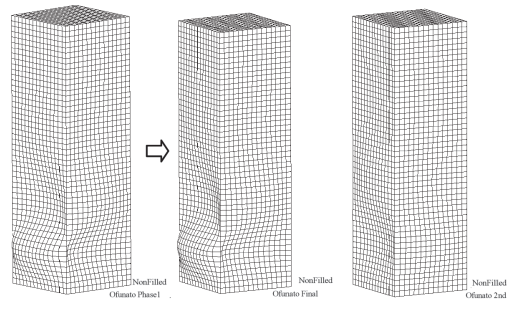

(a) End of Phase 1 & Final, Full loading.

(b) Final, lone Phase 2 loading.

Figure 13. Deformation patterns – Seismic load of Ofunato, no filled-in concrete.

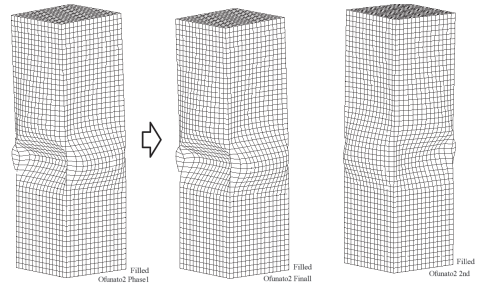

(a) End of Phase 1 & Final, Full loading.

(b) Final, lone Phase 2 loading.

Figure 14. Deformation patterns – Seismic load of Ofunato × 2, with filled-in concrete.

Full loading. Thus, in this case, it is found that the small damage arises within the Phase 1 loading, and column suffers larger damage with the Phase 2 loading.

4 REMARKS

In this paper, behaviour of steel box columns investigated under the seismic load of a so-called combined earthquake. The seismic motion observed in 2011 Japan earthquake which has 2 major tremors is used as the seismic load, and the comparisons are made on column behaviour between the case that the column is subjected to the full of the seismic motion and the case that subjected to only second tremors.

Through the numerical analysis, followings are found;

1. Behaviour of the column subjected to only second part of the seismic load differs in the later part of the column behaviour under the full loading.

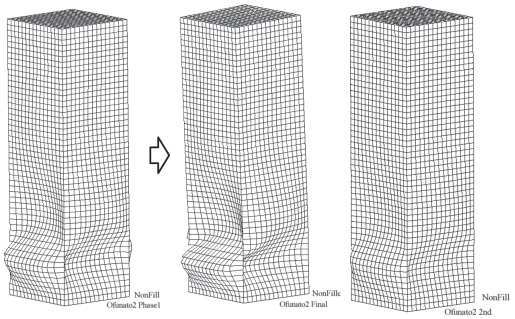

(a) End of Phase 1 & Final, Full loading.

(b) Final, lone Phase 2 loading.

Figure 15. Deformation patterns – Seismic load of Ofunato × 2, no filled-in concrete.

2. In some cases, the column suffers small damage with the first phase of the full seismic load, and the larger damage arises with second major tremor.
3. Unlike to (2), in some cases, significant damage arises with the first tremor, and the damage becomes severer with the second tremor.

With the seismic performance level 2, the structures must be repaired for the service after they suffered the seismic motion. However, in the case (3), the structure suffers the next quake before it is repaired, and the damage becomes larger by the second tremor. In the analysis in a seismic design of a bridge, the single earthquake is often adopted as the loading. However, the current results suggest that it is necessary to consider the seismic motion of a combined earthquake.

5 CONCLUSION

In this paper, only the deformation behavior of the columns are shown because, in the Japanese seismic design code, collapse of a column under an earthquake is defined with the residual deformation. However, to discuss damages of the columns, stress or strain is required.

In this paper, due to the limited room to provide the figures and descriptions of the stress/strain of the columns, yielded zones are found in all models at the bottom part (or a just upper part of the concrete on the case that the column is filled with concrete) at the final stage. With the load case 1 (Ishinomaki × 1.5), the yielded zones develop within the Phase 1 loading, and the yielded zones under the lone Phased 2 loading are smaller than those caused by the full loading.

On the other hand, with the load case 2 (Ofunato), the yielded zone scarcely arises in the Phase 1 within the full loading, and yielding is developed during the Phase 2 loading.

With the load case 3 (Ofunato × 2.0), the yielded zones arise during the Phase 1 loading, and they develop furthermore with the Phase 2 of the full loading. With this load case, yielded zones caused by the lone Phase 2 loading are smaller than those by the full loading.

Thus, with the stress or strain, similar consideration can be made to one with the deformation behavior.

REFERENCES

Ahmed,T. & Shimizu,S. 2012. A study of the seismic effects on a portal frame having a hole at the beam-column connection. *Thin Walled Structures* 52: 53–60.

Iura,M. & Komaki,O. 1997. Local Buckling Analysis of Steel Cylindrical Shell s by Commercial Program. *Proceedings of nonlinear numerical analysis and seismic design of steel bridge piers:* 217–222(in Japanese): JSCE.

Japan Meteorological Agency. 2011. *The 2011 Great East Japan Earthquake -Portal-:* (http://www.jma.go.jp/jma/en/2011_Earthquake/2011_Earthquake.html).

Japan Meteorological Agency. 2011. *The 2011 off the Pacific coast of Tohoku Earthquake* - Source process analysis with local strong motion data: (http://www.jma.go.jp/jma/en/ 2011_Earthquake/chart/2011_Earthquake_SourceProcess.pdf).

Japan Road Association. 2012. *Japanese Specifications for Highway Bridges, V Seismic Design*

National Research Institute for Earth Science and Disaster Prevention, Japan. *Strong Motion Seismograph Network (K-net):* (http://www.kyoshin.bosai.go.jp/).

Sakimoto,T., Watanabe,H., Tomita,S. & Nakashima,K. 1997. Local Buckling Analysis of Steel Cylindrical Shell s by Commercial Program. *Proceedings of nonlinear numerical analysis and seismic design of steel bridge piers*: 111–116 (in Japanese): JSCE.

Sasaki,E., Miki,C, Ichikawa,A. & Takahashi,K. 2004. Behaviour of steel bridge piers during earthquakes. *Journal of Structural Engineering* 50 A: 1467–1477 (in Japanese): JSCE.

Shimizu,S. 2009. Behaviour Of Steel Columns Under 3-D Seismic Load. *Proc. of XII symposium on stability of structures*: Zakopane, Poland.

Shimizu,S. 2011. Behaviour of steel columns under 3-D seismic load. *Thin Walled Structures* 49: 544–553.

Shimizu,S. & Fukasawa,S. 2012. Seismic behaviour of steel box columns connected with a bar element. *Proc. of XIII symposium on stability of structures*, Zakopane, Poland.

Recent Progress in Steel and Composite Structures – Giżejowski et al. (Eds)
© 2016 Taylor & Francis Group, London, ISBN 978-1-138-02946-0

Determination reserve of bearing capacity for steel, with influence of long-term fatigue load, used in structures in case of a fire

K. Pawłowski, R. Świerzko & A. Włóka
Wrocław University of Environmental and Life Sciences, Wrocław, Poland

ABSTRACT: The study contains the results of preliminary tests of steel collected from the steel structure of a railway bridge. The object was constructed in the beginning of the 20th century and it has been in use since then. This resulted in the emergence of high degree of fatigue wear of construction steel. The aim of the conducted research was to determine the relation between steel fatigue resulting from long-term operation of the structure and creep at increased temperatures. Increased temperature occurring in the structure, e.g. as a result of fire, significantly contributes to the deterioration of such mechanical properties of construction steel as yield strength, tensile strength or modulus of elasticity. The aim of the conducted research was to determine the correlation between fatigue-related damages that occur in the structure and being subjected to tempera-tures much higher than those that occur in normal operational conditions. Characteristics of short-term creep of the analysed steel samples were determined for the temperature of 700o degrees Celsius. The results pre-sented in the study are of a preliminary nature. The conducted tests confirmed the existence of the relation be-tween fatigue-related damages, loads caused by temperatures much higher than those that occur in normal conditions of operating the structure, as well as the influence of the above specified loads on the steel creep parameters. Further analyses that will enable us to generalise the obtained results and to propose designing guidelines are currently in progress.

1 INTRODUCTION

1.1 *Introduction*

Structures made from steel are sensitive to a variety of influences, such as fatigue loads, particularly due to the existence of various types of structural notches in such structures. Long-term loads cause the phenomenon of steel creep, as well as fire conditions that lead to the deterioration of such mechanical properties of steel as yield strength, tensile strength or modulus of elasticity. Numerous hypotheses have been formulated over the years in order to enable the determination of fatigue strength for various types of elements (Wyrzykowski & Authors). The methods of calculating the bearing capacity of such points that are particularly prone to fatigue damage are also described in binding reference standards. However, there is insufficient research on the accumulation of various types of damages that may have occurred within a structure that was used for many years.

The main aim of the experiments conducted by the authors was to determine the influence of long-term fatigue load, of a changeable load amplitude that may cause destruction even in the end phase of operation, when the strains are much lower than fatigue strength (the Palmgren-Miner phenomenon) interacting with loads caused by increased temperature, e.g. if such structure is on fire. The study presents the results of tests conducted on samples collected from the steel structure of a railroad bridge that has been in operation for over 100 years. Static tensile testing was conducted, along with the analysis of the chemical composition, in order to determine the type of steel from which the structure was made. Hardness tests were also conducted on samples collected from various elements of the structure, in order to correlate the results with fatigue-related wear of the elements. Characteristics of short-term creep of the analyzed steel samples were determined for the temperature of 700 degrees Celsius. During the tests, samples were subjected to load until strains were obtained equal to 80% of the yield strength at the given temperature, and then they were left under the load until the moment of rupture.

1.2 *Characteristics of the analyzed object*

The study presents the analysis of steel samples collected from the bearing structure of a bridge span. The object, from which samples were collected for analysis, is located on the Łuków-Lublin line, at km 25.414 (Fig. 1). The structure was erected at the end of the 19th century, as part of the Łuków-

Figure 1. A view of the railroad bridge at km 25.414 of line No. 30 Łuków-Lublin.

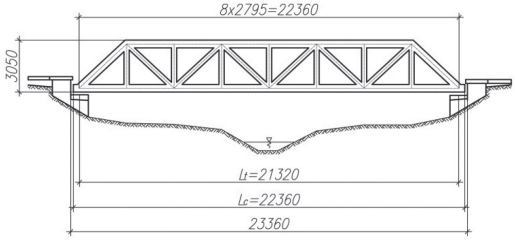

Figure 2. Diagram of the bridge.

Lublin railroad. The purpose of the railroad was to create a supply delivery route for Russian armed forces resisting the German and Austrian attacks along the line of Narew and Vistula Rivers.

The object is a single-span steel structure based on simply supported beam design. The design is shown in Figure 2. The main girders of the object were two trusses of a theoretical span of 22.36 m, with the railroad tracks placed on beams of the bottom chord of the truss. Pratt truss with parallel chords. Crossbars placed at approx. 2.8 m spacing. The height of the trusses was 3.05 m. The spacing between main girders was 5.25 m. Two sidebars with 1.83 m axial spacing were attached to the crossbars, stiffened with a vertical bracing in the middle of the truss span and horizontal bracings on the plane of the top and bottom chords. The main trusses were supported on bridgeheads, on fixed and sliding steel bearings.

In order to determine the influence of fatigue load on the mechanical properties of steel it was necessary to collect samples for tests from the relevant locations on the bridge structure. We succeeded in collecting samples from several elements of the bridge span, including elements of the lower chords of main girders, fragments of crossbars and sidebars, a rod of the main truss and bracing elements. The study presents the results of tests of selected elements only. Samples discussed in the present study were cut out from the plates of the lower chords and the webs of the main girders of the bridge, as well as sidebars. The exact sampling locations of the elements subject to the tests discussed herein are shown in Figure 3.

From the elements shown in Figure 3, samples were cut out for the analysis of tensile strength, creep and chemical composition. The location and designation of the samples obtained from element number 5 is shown in Figure 4, analogical samples were collected from element 3 which is shown in Figure 5. From each element, samples located across and along the plates were collected, to reflect the influence of the direction of steel rolling on the obtained results. Samples for tensile strength and creep tests from element 1 shown in Figure 3 were cut out in an analogical way to that illustrated in Figure 5.

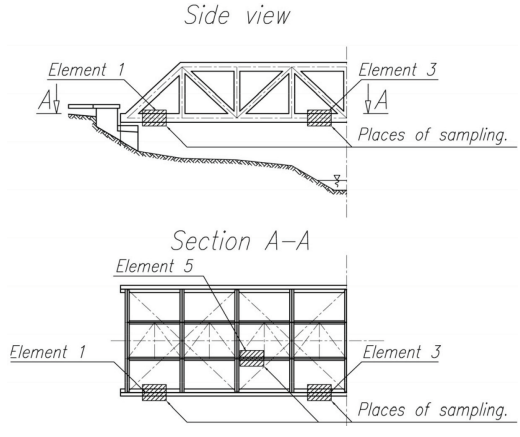

Figure 3. Sampling locations of elements from which samples for analysis were cut out.

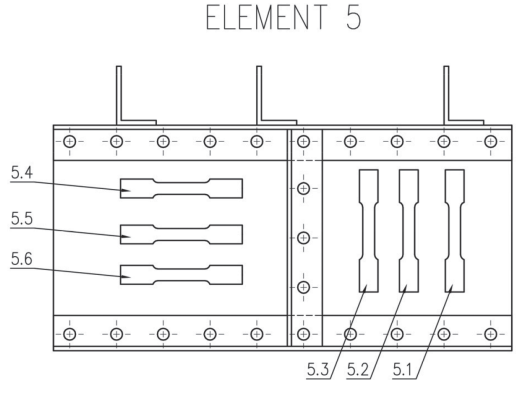

Figure 4. Sampling locations and numbers of series 5 samples.

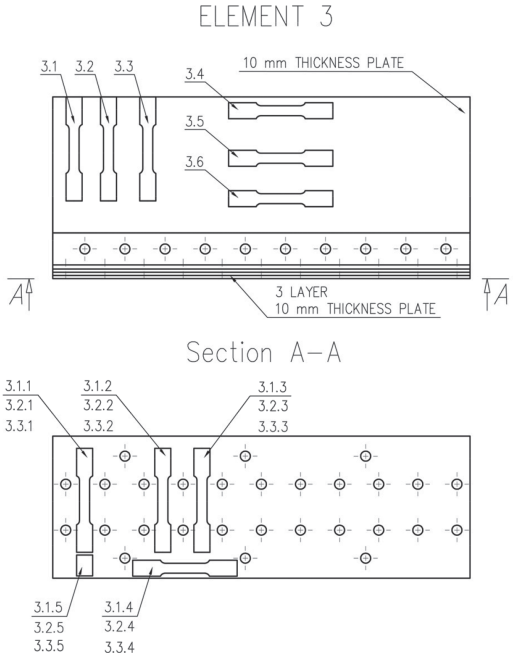

Figure 5. Sampling locations and numbers of series 3 samples.

1.3 *Methodology of the tests*

The study presents the results of tests of chemical composition, hardness, basic mechanical properties and short-term creep at increased temperatures conducted on steel samples collected from selected elements of the railroad bridge structure as illustrated in Figure 3.

Chemical composition analyses were conducted with use of BAIRD-DV4 emission spectrometer on three samples collected from the plates of the lower chord of the main truss girder of the bridge.

Hardness tests were conducted on samples prepared for the determination of basic mechanical properties of steel (Fig. 6) and short-term creep of steel (Fig. 7). Tests were conducted with use of ERNST NR3 DR hardness tester, basing on the Vickers HV100 scale. For each of the analyzed samples, 6 hardness measurements were taken.

Samples for the analysis of basic mechanical properties were prepared in compliance with the guidelines contained in the PN-EN ISO 6892–1:2010 standard (Fig. 6). A total of 11 samples were analyzed, including 6 samples collected from the web of the T-shaped cross-section of the lower chord of the main truss girder and 5 samples collected from the plate of the web of the sidebar of the bridge.

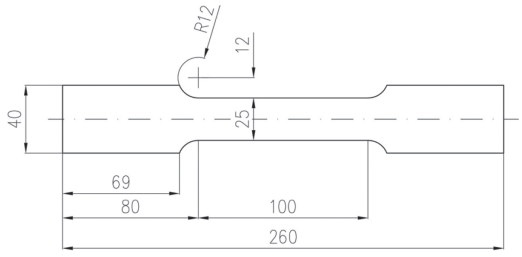

Figure 6. Sample for strength testing, prepared in compliance with the guidelines of the PN-EN ISO 6892-1:2009 standard.

Short-term creep analyses were performed in the universal testing machine Instron/Satec KN 600 equipped with a furnace for high-temperature testing type SF-16 2230 (Fig. 8) that enables testing at temperatures up to 1200°C. Temperature on the sample placed inside the furnace was verified and recorded with use of the compactRIO cRIO-9076 controller, equipped with a module for the connection of NI 9211 and K-type thermocouples. The system of measurement and recording the temperature of the analyzed samples operated in the LabVIEW software environment. During the tests, the samples were heated to the temperature of 700°C and then subjected to a constant load causing a strain of 40 MPa in the cross-section of the sample. Samples were then left under constant load until the moment of rupture, while constantly recording the duration of the test, increase in deformations and the temperature on the surface of samples.

2 RESULTS OF THE TESTS

2.1 *Results of the chemical composition analyses*

Due to the lack of any data indicating the type of steel from which the analyzed structure was made, comprehensive tests were required in order to determine its physical and chemical properties. First of all, the chemical composition analyses were conducted on samples collected from the plates of the lower chord of the truss. The obtained results are listed in Table 1.

The analysis of data contained in the table shows noticeable differences in the content of carbon (nearly 100% between samples 3.1.5 and 3.2.5). The content of phosphorus was also highly differentiated, while the contents of the remaining elements were similar in all analyzed samples. Carbon content has a significant influence on the physical properties of steel. In carbon steel, the percentage share of carbon determines the strength and plasticity. Along with the increase in the content of this

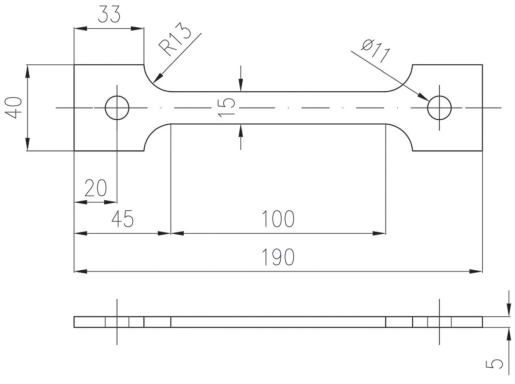

Figure 7. Sample for the analysis of short-term steel creep at increased temperature.

Table 1. Results of the chemical composition analyses.

Sample No.	C	Mn	Si	P	S	Cr
3.1.5	0.043	0.541	0.003	0.05	0.058	0
3.2.5	0.081	0.665	0.005	0.024	0.052	0
3.3.5	0.058	0.592	0.005	0.082	0.056	0
Min	0.043	0.541	0.003	0.024	0.052	0
Max	0.081	0.665	0.005	0.082	0.058	0
Average value	0.061	0.599	0.004	0.052	0.055	0
Sample No.	Ni	Mo	V	Cu	Ti	
3.1.5	0.029	0.005	0.001	0.058	0.003	
3.2.5	0.30	0.007	0.001	0.056	0.003	
3.3.5	0.29	0.005	0.001	0.066	0.003	
Min	0.029	0.005	0.001	0.056	0.003	
Max	0.30	0.007	0.001	0.066	0.003	
Average value	0.206	0.006	0.001	0.060	0.003	

element, the strength increases while the plasticity of the given steel decreases. For contemporary types of steel it is assumed that an increase in the content of carbon by 0.1% may cause an increase in the yield strength by approx. 40÷50 MPa and an increase in the modulus of rupture f_m by approx. 90 MPa. Similar levels of change in the content of other alloying elements result in less significant changes in steel properties. The analysis of Table 1 in the aspect of other elements for samples 3.1.5 and 3.2.5 demonstrates, apart from the increase in carbon content, also an increase in manganese content by approx. 20% and in silicone content by approx. 66%. One may also notice a decrease in the content of phosphorus by nearly 50%. All these aspects influence changes in the properties of steel, which, if used within a single structure, may affect its behavior, e.g. during a fire.

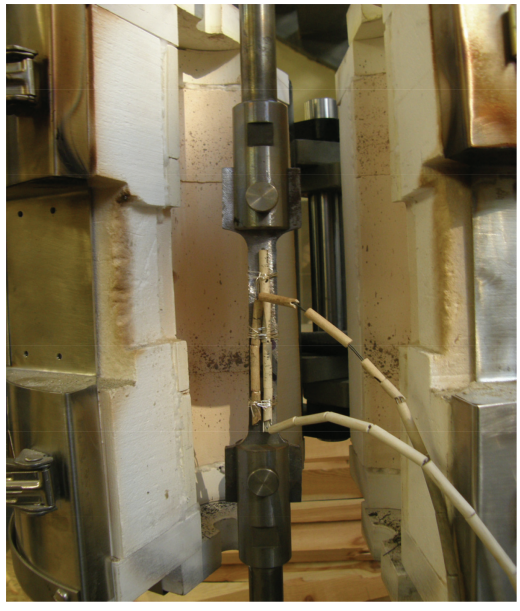

Figure 8. A view of the test site.

2.2 *Results of steel hardness tests*

Hardness tests were conducted on all samples collected from elements of the bridge. The purpose of the hardness tests was to correlate hardness with the results of the static strength test and chemical composition analysis to provide a basis for the determination of the relations between them for steel produced at the beginning of the 20th century that has been in operation for many years. Hardness test with use of the Vickers method as a static test enables to obtain much more accurate results than dynamic methods. It is also possible to convert HV hardness into HB hardness and thus estimate the mechanical properties of the analyzed steel with use of nomograms. Table 2. lists the results of HV100 hardness tests for the analyzed samples.

The above table also demonstrates a difference between the results obtained for elements 3.1.1 to 3.1.4 and those of elements 3.2.1 to 3.2.4. These results are consistent with the outcomes of the chemical composition analysis. The increase of carbon content in steel leads to an increase in hardness, which was demonstrated by analyzing these two series of samples. The comparison of the results of both HV hardness and chemical composition analysis, in particular carbon content in the chemical composition of steel with the nomograms discussed in literature (Gosowski) leads to divergent results related to the relations between these two elements.

Table 2. Results of hardness tests of steel with use of the Vickers method.

Element	Sample No.	Hardness HV100	Average value
Web	3.1	105	
of the lower chord	3.2	107	
of the truss -	3.3	104	104
span	3.4	96	
	3.5	110	
	3.6	103	
Shelf	3.1.1	108	
of the lower chord	3.1.2	108	
of the truss -	3.1.3	117	110
span	3.1.4	109	
Shelf	3.2.1	119	
of the lower chord	3.2.2	111	
of the truss -	3.2.3	124	118
span	3.2.4	120	
Shelf	3.3.1	105	
of the lower chord	3.3.2	117	
of the truss -	3.3.3	108	110
span	3.3.4	110	
Web	1.3	108	114
of the lower chord	1.4	119	
of the truss-			
Pillar			
Web	5.1	112	
of the sidebar	5.2	112	
of the bridge	5.3	108	106
	5.4	96	
	5.5	104	
	5.6	106	

The HB hardness value for samples from the 3.2 series, contained in the nomogram shown in Figure 9 basing on HV hardness is 111. The respective carbon content for this hardness is 0.15%, while the tests show a value of 0.081. which means that the results differ by 46%. For samples from the 3.1 series the HB hardness value is 105. Thus, basing on the nomogram, the carbon content in steel may be estimated at approx. 0.12%, while the actual carbon content listed in Table 1 for this steel is 0.043. which means that the results are nearly three times as high. This may result from the fact that nomograms are prepared for steels produced in the second half of the 20th century. Thus, the application of the same relations for historical types of steel may result in an improper estimation of their properties, in particular, if no comprehensive non-destructive and destructive tests or chemical composition analyses are conducted.

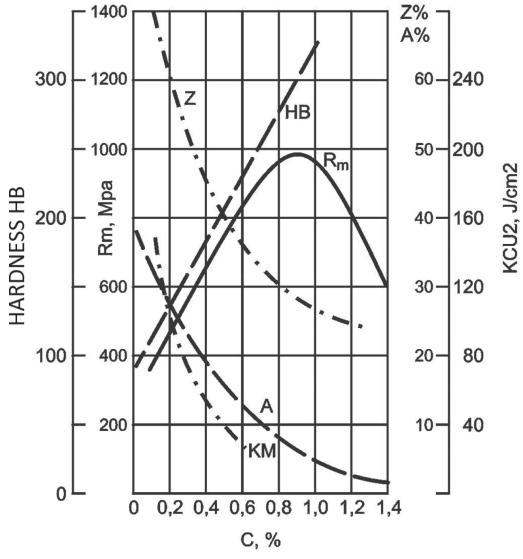

Figure 9. The influence of carbon content on the mechanical properties of carbon steels in raw state.

2.3 *Results of tensile strength tests*

After the hardness tests were conducted, some of the samples were used for the determination of basic mechanical properties of steel and the remaining part for short-term creep tests at the temperature increased to 700 °C. The results of tests of mechanical properties are listed in Table 3. while Figures 10–11 show the course of the strain-deformation curves for all analyzed samples.

Samples collected from the web of the lower chord of the main bearing truss (samples 3.1 – 3.6) were characterized by slightly higher strength parameters than samples collected from the sidebars (samples 5.1–5.5). The diversity of the obtained results was also higher in case of samples collected from the truss element.

2.4 *Results of short-term steel creep tests at increased temperature*

Before starting the short-term steel creep tests at the temperature of 700°C it was necessary to determine the yield strength of the analyzed steel at this temperature, to prevent exceeding it while applying constant load during creep. For this purpose, all results obtained in the course of static tensile test were treated as one series, obtaining the value of specific yield strength of 220 MPa at the temperature of 20°C. The reducing coefficient of yield strength for the temperature of 700°C was assumed pursuant to the PN-EN 1993-1-2 standard, at the value $k_{y\,700} = 0.23$. Thus, the resulting

Table 3. Basic mechanical properties of steel determined in the tests of samples collected from the bridge.

Sample No.	R_m MPa	R_{eL} MPa	R_{eH} MPa	R_z MPa	e_{max} mm/mm
3.1	389	262	282	331	0.328
3.2	429	307	331	371	0.303
3.3	424	303	324	356	0.321
3.4	389	265	291	308	0.317
3.5	388	260	292	311	0.339
3.6	389	264	266	299	0.358
MIN	388	260	266	299	0.303
MAX	429	307	331	371	0.358
Average	401	277	298	329	0.328
Standard deviation	19	22	25	29	0.019
Coefficient of variation	0.049	0.079	0.083	0.087	0.058
Specific value	359	229	243	266	0.286
5.1	333	245	266	281	0.330
5.2	347	263	274	293	0.337
5.3	343	245	273	290	0.329
5.4	336	238	256	254	0.343
5.5	347	243	258	257	0.330
MIN	333	238	256	254	0.329
MAX	347	263	274	293	0.343
Average	341	247	265	275	0.334
Standard deviation	6	9	8	18	0.006
Coefficient of variation	0.019	0.038	0.031	0.067	0.018
Specific value	326	225	246	232	0.320

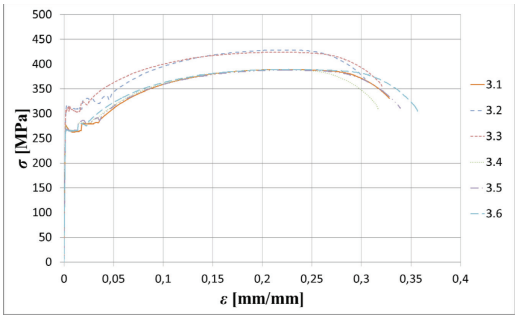

Figure 10. Diagram of the strain-deformation relation for series 3 samples.

calculated value of yield strength at increased temperature was $R_{eL\ 700}$ = 50.6 Pa. For the purposes of the tests a constant load was adopted, causing a strain equivalent to 40 Pa, i.e. approx. 0.8 $R_{eL\ 700}$ in the cross-section.

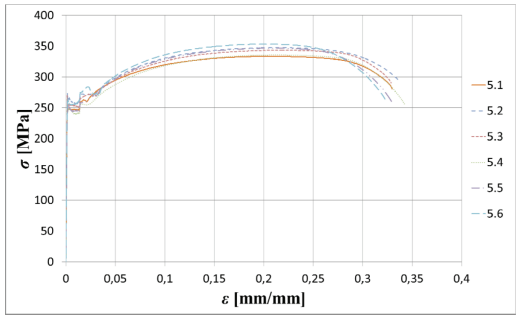

Figure 11. Diagram of the strain-deformation relation for series 5 samples.

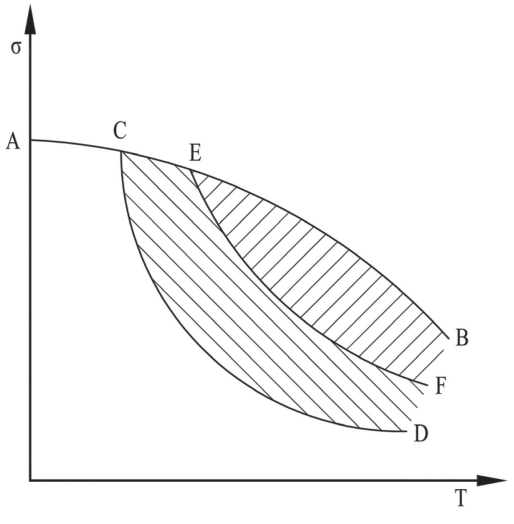

Figure 12. Dependency between strains and temperature (Malinin, Rżysko).

Steel creep at high temperature and exposed to high levels of strain is a short-term creep process, i.e. it lasts only several minutes or even seconds.

Figure 12 shows the dependencies between strain and temperature. Short-term creep will take place in the hatched area (between points BCD) although the first stage of non-determined creep will not occur in the section limited by points BEF (Malinin, Rżysko).

The aim of all tests conducted by authors, both continued tests and those, whose results are presented below is to analyse the phenomenon weakening role of the creep in to fatigue life some details of steel structures (Collins). The tests of creep at increased temperature and at various levels of strain σ conducted by the authors serve to the determination of the k coefficient and the

n exponential in formula 2.1 that determines the value of the minimal deformation pace for the determined creep ξ^c_{min}.

$$\xi^c_{min} = Q(\sigma) = k\sigma^n, \quad (2.1)$$

The creep curves at the temperature of 700°C are presented in Figures 13–16 and the obtained creep times and deformations at the moment of rupture are listed in Table 4.

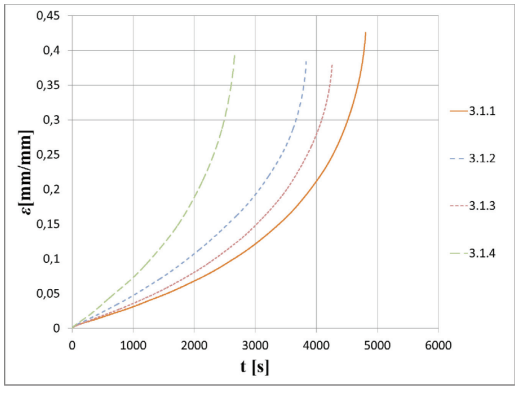

Figure 13. Diagram of the time-deformation relation for series 3.1 samples.

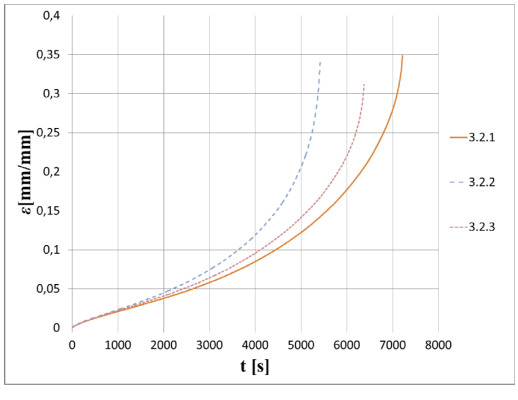

Figure 14. Diagram of the time-deformation relation for series 3.2 samples.

In comparison to room temperature, increased temperature leads to a reduction in the fatigue strength of steel. High temperature influences fatigue processes, also including creep processes (Wyrzykowski & Authors). Three high-temperature ranges may be distinguished: temperatures that do not influence creep, range of increased temperatures in which the rupture of steel is influenced

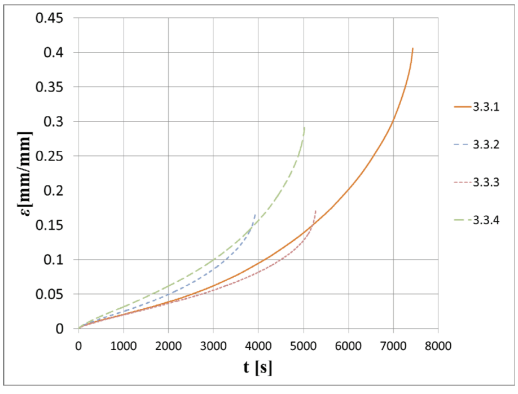

Figure 15. Diagram of the time-deformation relation for series 3.3 samples.

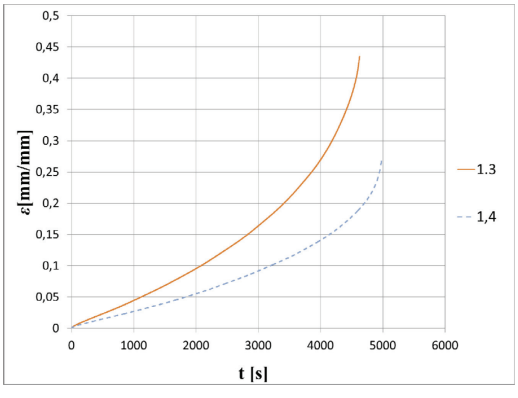

Figure 16. Diagram of the time-deformation relation for series 1 samples.

Table 4. List of the creep test results for samples collected from the structural elements of the bridge.

Sample No.	Time of creep	Time of creep	Average deformation	Average deformation
	s	s	mm/mm	mm/mm
1.3	4624	4804	0.434	0.354
1.5	4983		0.274	
3.1.1	4806	3888	0.426	0.393
3.1.2	3833		0.384	
3.1.3	4256		0.379	
3.1.4	2658		0.393	
3.2.1	7213	6332	0.349	0.334
3.2.2	5411		0.340	
3.2.3	6372		0.312	
3.3.1	7429	5417	0.406	0.263
3.3.2	3936		0.172	

both by fatigue and creep, and very high temperatures, at which the main cause of rupture is creep. The obtained results demonstrate extremely large divergences between creep time for different series of samples. Series 3 samples were collected from a set of 3 plates constituting a shelf of the T-shaped cross-section of the lower chord of the main truss of the bridge. Thus, one should assume that their use with respect to fatigue load during the operation of the bridge was the same for all three plates from which the samples were collected. Basing on this assumption, the divergences in the creep time results at the temperature of 700°C lead to the conclusion that the interaction between creep and increased temperature is much more complex and influenced by a higher number of factors. As it was demonstrated in the previous sections, it is possible that the chemical composition also plays a significant role here. The authors of the present study have also conducted analyses of steel destroyed in a fire (Pawłowski & Włóka 2015). The results have shown that the chemical composition of steel exposed to fire load changes. The temperature at which creep was analyzed is similar to that of a fire, so similar changes may have occurred in the samples. Extremely high variability of the creep time may suggest that it is necessary to conduct numerous tests each time, both of mechanical properties and of chemical composition, in order to evaluate the usability of construction steel, e.g. to determine whether the operation of the given object containing such steel may be continued. Creep time at increased temperatures affects the safety of the structure during fire. It also influences the determination of the fire safety of the structure and the selection of fire protection of the structure.

3 CONCLUSIONS

The conducted tests of both physical properties and chemical composition of the analysed steel allowed us to draw the following conclusions:

- The preliminary results of creep tests of steel collected from the bridge structure show extremely high divergences in the duration of creep time at increased temperature. Further analyses of this phenomenon will enable to present detailed guidelines that may be applied for the purposes of planning the fire protection of historical structures and selecting the appropriate protective means. This issue should be treated with special attention due to the fire protection requirements concerning the time during which the structure should provide safety in fire conditions.
- Depending on the temperature to which the given structure is exposed (e.g. as a result of fire) the interaction between fatigue bearing capacity of the given element and creep at increased temperature may accelerate the destruction process of the element and thus lead to a failure of the whole structure. Creep times for various temperature levels are very changeable. Currently, analyses of these times for other temperatures and material stress of steel. The results will allow for the determination of general correlations and the creation of the relevant nomograms.
- Estimation of mechanical properties of historical steel based only on hardness tests of such steels may result in significant errors. This results from the fact that nomograms available in literature refer to types of steel produced in the second half of the 20th century and cannot be applied to historical types of steel.
- The determination of the bearing capacity of historical structures should take into account the extent of fatigue wear. However, fatigue analyses should be correlated with chemical composition analyses of the steel from which the given element is made. Lack of correlation between these factors may result in improper determination of the strength of the elements and thus of the whole structure.

REFERENCES

Collins J.A., *Failure of Materiale in Mechanical Design 1981*. John Wiley & Sons.

Gosowski, B. & Kubica, E. 2007. *Badania laboratoryjne z konstrukcji metalowych.* Wrocław: Oficyna Wydawnicza Politechniki Wrocławskiej.

Malinin N.N., Rżysko J., Mechanika materiałów, PWN Warszawa 1981.

Pawłowski, K. & Włóka, A. *The impact of the fire load on physical-mechanical properties of steel used in construction of the connector in hotel belvedere Zakopane*. XIV International Scientific Conference Rzeszów 2015 Pages 60–61.

Rykaluk, K. 2000. *Pęknięcia w konstrukcjach stalowych*. Wrocław: DWE.

Wyrzykowski, J.W. & Pelszakow, E. & Sieniawski, J. 1999. *Odkształcenia i pekanie metali.* Warszawa: WNT.

Bridges

This page intentionally left blank

Recent Progress in Steel and Composite Structures – Giżejowski et al. (Eds)
© 2016 Taylor & Francis Group, London, ISBN 978-1-138-02946-0

Atmospheric corrosion tests on weathering steel bridges in the Czech Republic

V. Krivy & V. Urban
VSB-Technical University Ostrava, Ostrava, Czech Republic

K. Kreislova
SVUOM Ltd., Prague, Czech Republic

ABSTRACT: This paper introduces the program of experimental atmospheric corrosion test carried out on weathering steel bridges in the Czech Republic. Attention is paid to study of corrosion processes at different structural elements of supporting structures of bridges. Measurements of corrosion losses and average thicknesses of corrosion products are carried out within this program. The article presents results of corrosion tests after one year of exposure of corrosion specimens. It results from the tests that corrosion losses of weathering steels are conditioned by position and location of exposed surface within the structure. The results indicate the high degree of correlation dependence between measured average thickness of corrosion products and corrosion loss. Protective ability of corrosion products is evaluated using X-ray diffraction analysis.

1 INTRODUCTION

Steels with improved atmospheric corrosion resistance, so-called weathering steels, are the low-alloy steels containing small amount of chromium, copper, nickel, phosphorus and other alloying elements. The content of alloying elements usually doesn't exceed 2 wt%. The balance of individual alloying elements is important, especially the combination of copper, chromium and phosphorus. Protective layer of corrosion products, so-called patina, creates on the surface when suitable atmospheric conditions exist. Corrosion rates of weathering steels are considerably lower when compared with the standard carbon steel (Albrecht & Hall (2003)).

Currently, weathering steels are used mainly in bridge constructions. The use of weathering steel is in many cases economically advantageous. The fabrication and assembly costs of weathering steel structures are typically 2–10% lower when compared with the structures protected with traditional corrosion protection (Fischer (2004), Kogler (2005), Lebet & Lang (2001)). The main economic advantage of using weathering steels is the elimination of costs connected with repairs or restoration of corrosion protection systems. When using weathering steels there is also significantly reduced the amount of ecologically exacting manufacturing operations related to the implementation of coating systems.

The basic specific property of weathering steels is their improved corrosion resistance in atmospheric conditions. Scope of the papers published on the corrosion behaviour of weathering steels in various atmospheric conditions is extensive and includes various characteristics of corrosion layers (Morcillo et al. (2013), Morcillo et al. (2014)). Development of weathering steel has been always accompanied by the implementation of large-scale atmospheric corrosion tests (Copson (1945), Horton (1965)). Long-term exposure of corrosion specimens were realized mainly to study corrosion processes depending on the corrosivity of atmospheres, including evaluation of the specific effects, such as concentration of SO2 and chlorides deposition (Tidblad (2012)). Atmospheric corrosion tests were also carried out to evaluate the different chemical composition of weathering steels (Larrabee & Coburn (1962)).

Results of experimental atmospheric corrosion tests carried out on weathering steel bridges are presented in this paper. In this experimental program, the effects of various design parameters on the corrosion processes are tested. Special attention is paid to study the influence of the position and location of a surface in the structure (typical surfaces are tested—upper and bottom flanges, webs of main girders, orthotropic bridge deck plate, etc.).

Influence of leaking water from failed drainage system is also tested in this experimental program.

Relationship between corrosion losses established in accordance with ISO 8407 (mass loss of the corroded metal specimens is laboratory measured and the corrosion loss is calculated subsequently) and average thicknesses of corrosion products is also presented in this paper. Furthermore, the paper introduces the analysis of corrosion products that can serve as an additional criterion for assessing the patina development on weathering steel bridges.

2 EXPERIMENTAL PART

The program of experimental atmospheric corrosion tests was mainly prepared in order to specify the prediction model for calculation of the design value of corrosion losses of weathering steels. To evaluate the specific local factors affecting the formation of corrosion products (Krivy et al. (2013)), it was necessary to install corrosion specimens on a sufficient number of surfaces of different weathering steel structures. Towards the end of 2014, the corrosion specimens have been installed on 10 weathering steel structures in the Czech Republic (see Table 1).

The corrosion specimens are installed on the structure in such a way to simulate realistic behavior of the investigated structural element surface, see Figure 1. For experimental testing were chosen standard specimens used for atmospheric corrosion tests according to ISO 8407 - test panels 100×150 mm with thickness of 1.5 mm. Testing specimens were made of sheets (steel grade S355J2WP) commonly used for building facades (Helzel 2014, Kreislova & Knotkova 2011). The backside of the specimens, i.e. the side adjacent to the steel structure, is masked to evaluate the corrosion attack only on the exposed side of the specimen.

Corrosion specimens are attached to the steel structure by simple pressure elements made of stainless steel, see Figure 2. This attachment method provides tight contact between corrosion specimen and examined surface of the steel structure. The contact area between the pressure element and the corrosion specimen is minimal, so there is no influence in the development of corrosion products on the exposed surface and specimens copy the thermal inertia of structural elements (Krivy et al. 2015).

Three corrosion specimens have been installed on each of the examined surfaces. Statistical characteristics of corrosion products thickness were ensured during the installation of specimens. Thicknesses of corrosion products were measured with portable thickness gauge based on magnetic induction. For each surface, a total of 30 measurements were recorded. The planned duration of the experimental measurement is 10 years. The thickness of corrosion products on surface of specimens is measured at yearly intervals. Sampling of cor-

Table 1. Structures tested within the program of experimental corrosion tests.

Monitored structures	Year
01 - Road bridge in Frydek-Mistek	1986
02 - Railway bridge in Prague	1981
03 - Road bridge over the railway line in Ostrava	2008
04 - Road bridge over the river Odra in Ostrava	2008
05 - Road bridge over the railway line in Ostrava	2008
06 - Road bridge over the highway D1 in Ostrava	2001
07 - Road bridge over the railway line in Ostrava	1983
08 - Railway bridge in Krnov	1979
09 - Transmission tower Tlusta Hora	1980
10 - Access footbridge in Slusovice	1975

Figure 1. Installation of corrosion specimens on the road bridge over river Odra in Ostrava.

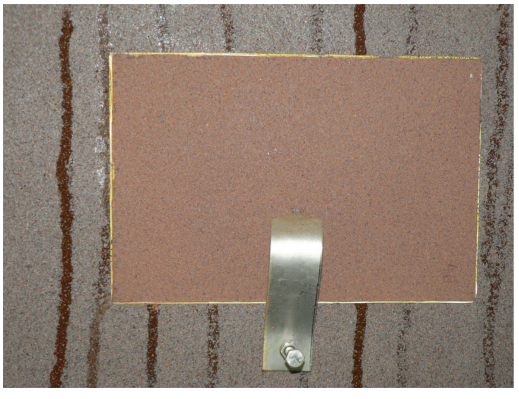

Figure 2. Attachment of corrosion specimen using the pressure element made of stainless steel.

rosion specimens for determination of corrosion losses is planned at 1, 3 and 10 years of exposure.

3 RESULTS OF EXPERIMENTAL TESTING

3.1 *Corrosion processes on typical surfaces of bridge structures*

Bridge structures included in this analysis are designed as steel plate girder bridges. Corrosion specimens are installed on typical surfaces of these bridges. It is necessary to distinguish between external and internal surfaces and also between horizontal and vertical surfaces when evaluating the patina development. Horizontal surfaces are divided into surfaces exposed from above (upper surface of the bottom flanges) and surfaces exposed from the bottom (soffit areas). Average thicknesses of corrosion products and corrosion losses after one year of exposure are given in Table 2. Surfaces listed in Table 2 are not subjected to leakage from expansion joints or failed drainage systems.

Table 2. Results of corrosion tests after one year of exposure.

	Monitored structures (see Table 1)				
Surface*	01	02	03	04	05
Average thicknesses of corrosion products $t_{corr,1}$ (μm)					
S1	46.5	25.4	24.8	32.5	19.4
S2	51.5	29.1	26.0	35.4	–
S3	41.6	23.7	26.6	36.1	10.5
S4	87.5	87.4	76.8	70.4	51.8
S5	66.9	54.1	52.2	77.0	44.2
S6	–	39.4	32.5	36.6	16.9
S7	–	31.0	40.7	36.8	18.0
Corrosion losses $k_{t,1}$ (μm)					
S1	7.8	6.0	4.2	6.4	7.7
S2	7.5	5.7	4.9	6.0	–
S3	5.5	4.5	4.7	7.0	6.0
S4	17.2	19.1	15.3	13.7	17.4
S5	10.7	9.3	9.3	11.9	10.7
S6	–	9.1	5.4	5.6	7.1
S7	–	6.3	5.9	7.2	7.4

*Tested surfaces:
S1 - Outer web of the main girder
S2 - Outer web of the girder 50 mm above the bottom flange
S3 - Inner web of the main girder
S4 - Upper outer surface of bottom flange of the main girder
S5 - Upper inner surface of bottom flange of the main girder
S6 - Soffit area of upper flange of the main girder
S7 - Soffit area of bottom flange of the main girder

The maximum thickness values of corrosion products and corrosion losses were detected on the upper outer surface of the bottom flanges of main girders. The average annual corrosion loss is 2.7 times higher compared to the corrosion loss of the outer web of the main girder (coefficient of variation of the ratio $v = 0.23$). When comparing thicknesses of the corrosion products the values are similar (mean value $m = 2.7$, coefficient of variation $v = 0.22$).

Corrosion losses and thicknesses of the patina on upper surfaces of the inner flanges are smaller compared with external flanges. When compared with the reference outer web of the main girder, the average corrosion losses of internal flanges are 1.7 times higher (coefficient of variation of the ratio $v = 0.21$). Slightly higher ratio has been determined based on the comparison of corrosion products thicknesses (mean value $m = 2.1$, coefficient of variation $v = 0.16$).

It follows from the comparison of corrosion processes on the outer and inner webs of main girders that the annual corrosion losses of the internal webs are average 0.9 multiple of losses on the outer webs (coefficient of variation of the ratio $v = 0.20$). Similar characteristics have been measured also for average thicknesses of corrosion products (mean value $m = 0.9$, coefficient of variation $v = 0.22$).

Annual corrosion losses on the soffit surface of the upper flange 1.2 times exceed corrosion losses on the outer web of the main girder (the coefficient of variation of the ratio $v = 0.23$). Similar values of the ratio are obtained when comparing thicknesses of corrosion products (mean value $m = 1.2$, coefficient of variation $v = 0.21$).

Corrosion losses on soffit areas of bottom flanges are similar to the values that have been measured on soffit areas of upper flanges. Annual corrosion losses are 1.2 times higher in comparison with the outer web of the main girder (coefficient of variation of the ratio $v = 0.16$). Mean value of the multiple $m = 1.2$ and coefficient of variation $v = 0.21$ has been obtained for thicknesses of corrosion products.

Visually different (darker) strip of corrosion products is usually created on outer webs close to the bottom flanges, see Figure 3. This phenomenon occurs only on the outer webs and is caused by different type of wetting in contrast to usual web surfaces of the main girders. On the adjacent bottom flange remains more moisture, deposition, dirt and in winter also snow. The performed measurements show that the corrosion losses on the web close to bottom flanges doesn't differ from the values measured on the usual surface of the web. The requirement for protection of these surfaces using coating systems (Posvarova (2008)) appears to be pointless.

Figure 3. Visually different strip of corrosion products on the outer web of main girder close to the bottom flange.

Figure 4. Road bridge over river Ostravice in Frydek-Mistek.

Figure 5. Road bridge over the railway line on the road II/456 in Ostrava.

Figure 6. Detail of the tested surface with bulky corrosion products (Road bridge over river Ostravice in Frydek-Mistek).

3.2 *Development of corrosion products on surfaces exposed to leaking water*

For a road bridge over the river Ostravice in Frydek-Mistek and road bridge over the railway line on the road II/456 in Ostrava (see Figs. 4–5), corrosion specimens have been also installed on surfaces that are subjected to leakage from failed drainage system.

Surfaces with bulky corrosion products that remain compact and are sufficiently adherent have been selected for this experiment, see Figure 6. Testing of these surfaces is important, because they represent typical failure of bridge structures caused by minor faults in the drainage system of bridges (Yamaguchi (2015)).

It follows from the inspections of bridges that the causes of minor but regular wetting from bridge drainage system are removed with a large time delay. It is therefore important to obtain sufficient experimental data, allowing the prediction of corrosion damage of thus affected surfaces.

To evaluate the adverse effects of leakage from drainage system, the corrosion specimens have been mounted also on the same type surface with favorable patina development. Visual differences in the development of corrosion products on two comparable surfaces after one year of exposure are demonstrated in Figures 7–8.

Experimentally measured data (average thicknesses of corrosion products on structural elements and specimens and corrosion losses after one year of exposure) are shown in Tables 3–5.

It is evident that leakage from failed drainage system negatively affects the development of corrosion processes on affected elements of the load-bearing structure. Significant increase of corrosion losses was identified on all surfaces affected by leakage.

Figure 7. Road bridge in Frydek-Mistek—detail of patina development on inner web influenced by leakage.

Figure 8. Road bridge in Frydek-Mistek—detail of patina development on inner web not influenced by leakage.

Table 3. Influence of leakage from failed drainage system—road bridge in Frydek-Mistek (experimentally measured data on webs of inner load-bearing elements).

	Surface	
Measured quantity*	Inner web of the cross girder with influence of leakage	Inner web of the cross girder without influence of leakage
Q1	439.0 µm	76.9 µm
Q2	62.7 µm	41.6 µm
Q3	10.6 µm	5.5 µm

*Measured quantities:
Q1 - average thickness of corrosion products on the structural element (after 26 years of exposure)
Q2 - average thickness of corrosion products on the corrosion specimen (after 1 year of exposure)
Q3 - corrosion loss after 1 year of exposure

Table 4. Influence of leakage from failed drainage system—road bridge over the railway line in Ostrava (experimentally measured data on upper surfaces of bottom flanges of inner main girders).

	Surface	
Measured quantity*	Inner web of the cross girder with influence of leakage	Inner web of the cross girder without influence of leakage
Q1	190.3 µm	87.6 µm
Q2	102.8 µm	26.6 µm
Q3	22.7 µm	4.7 µm

*Measured quantities:

Q1 - average thickness of corrosion products on the structural element (after 5 years of exposure)

Q2 - average thickness of corrosion products on the corrosion specimen (after 1 year of exposure)

Q3 - corrosion loss after 1 year of exposure

Table 5. Influence of leakage from failed drainage system—road bridge over the railway line in Ostrava (experimentally measured data on upper surfaces of bottom flanges of inner main girders).

	Surface	
Measured quantity*	Inner web of the cross girder with influence of leakage	Inner web of the cross girder without influence of leakage
Q1	204.3 µm	121.1 µm
Q2	98.5 µm	52.2 µm
Q3	26.0 µm	9.3 µm

*Measured quantities:

Q1 - average thickness of corrosion products on the structural element (after 5 years of exposure)

Q2 - average thickness of corrosion products on the corrosion specimen (after 1 year of exposure)

Q3 - corrosion loss after 1 year of exposure

The largest differences in the experimentally measured corrosion characteristics after one year of exposure have been observed at the inner web of the bridge in Ostrava (values of annual corrosion losses on surface affected by leaking are 4.8 times higher when compared with the same type surface with favourable patina development; the average thickness of corrosion products on surface affected by leaking is 3.8 times higher).

The minimum differences were identified on the bridge in Frydek-Mistek where due to leakage from the bridge expansion joint came to a 1.9-fold

increase of annual corrosion losses and a 1.5-fold increase of the average thickness of corrosion products.

Based on the experimentally measured results listed in Tables 3–5 is impossible to make general conclusions about the average expected increase of corrosion losses due to leakage from failed drainage system. The course of corrosion processes on particular surfaces affected by leakage depends on the extent, regularity and kind of wetting from the respective element of the bridge drainage. However, present results do not exclude almost 5-fold increase in corrosion losses after one year of exposure. Relative differences of average thickness of corrosion products after one year of exposure are not as large as the relative differences of corrosion losses.

3.3 *Correlation between thickness of corrosion products and corrosion losses*

Significant correlation was observed between the average thickness of corrosion products ($t_{corr,1}$) and corrosion losses ($k_{t,1}$) after one year exposure of specimens, see Figure 9 – blue points represent the series of observations; the red dotted line represents the linear regression line; the green curve (upper bound) and violet curve (lower bound) define the prediction interval with a probability of 95%; the area between orange lines represents the 95% range of confidence interval. The correlation coefficient between these two quantities is $\rho = 0.88$.

So, from the measured value of the average thickness of the corrosion products after one year of exposure, $t_{corr,1}$, it can be fairly accurately estimated corrosion loss, $k_{t,1}$, according to the equation:

$$k_{t,1} = 0.19 t_{corr,1} + 0.665 \ (\mu m) \qquad (1)$$

The above formula was determined using linear regression analysis. The relation between both quantities can be used for monitoring of patina development. The relation (1) is valid only for the first year of surface exposure. In the longer term there is a stabilization of the thickness of corrosion products, corrosion losses, however, continue to increase.

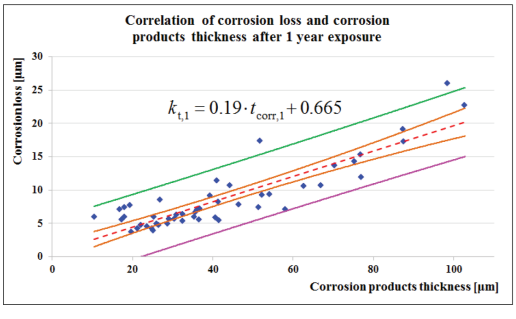

Figure 9. Dependence between the average thickness of the corrosion products and corrosion losses after 1 year of exposure.

Thickness measurements of corrosion products using the portable thickness gauge are easily and quickly feasible and can serve as a simple and relatively fitting procedure to determine real values of the initial corrosion rates of weathering steels. The established dependence between both quantities can thus be used as one of the evaluation criteria of patina development on weathering steel structures.

3.4 *Composition of rust layers*

Composition of patina layers varies depending on time and exposure conditions of the assessed surface (Kreislova & Krivy 2014). Corrosion compounds can occur simultaneously in a crystalline and partially amorphous phases. Transformation of particular phases can occur and the patina composition may vary in thickness of the layer. The main components of steel corrosion products are:

- goethite α-FeOOH–the most stable phase—contributes to protective properties of the surface layer and if present in form of nano-particles, prevents penetration of water, oxygen and chloride ions into the lower rust layers and to steel surface;
- akaganeite β-FeOOH–typical for the environment with chlorides;
- lepidocrocite γ-FeOOH–unstable compound, which transform into magnetite or maghemite γ-Fe_2O_3 in an environment containing oxygen;
- magnetite Fe_3O_4 – typical component of laminated corrosion products formed on surfaces affected by long-term moistening or in crevices;
- amorphous and non-stoichiometric compounds.

The protective ability index (PAI_α) is defined based on comparison of the ratio of the individual compounds in the patina (Kamimura et al. 2006, Hara et al. 2007).

$$PAI_\alpha = \alpha / \gamma^* \qquad (2)$$

where ($\gamma^* = \gamma + \beta + s$) includes mass concentration of α-FeOOH (α), γ-FeOOH (γ), β-FeOOH (β) and Fe_3O_4 (s).

If the ratio $PAI_\alpha > 1.0$, patina layer is protective and corrosion rate is lower than 10 μm.r^{-1}. In case that the ratio $PAI_\alpha < 1.0$, it is necessary to calculate the index PAI_β for determining further criterion of the protective effect of the patina layer ($PAI_\beta < 0.5$ – layer of corrosion products without protective properties or $PAI_\beta > 0.5$ – partially protective patina):

$$PAI_{\beta} = (\beta + s) / \gamma^{*} \quad (3)$$

X-ray diffraction analysis of corrosion products was performed after one year of exposure on selected corrosion specimens installed on the bridges on the road II/456 in Ostrava, *i.e.* road bridge over the railway line and road bridge over the river Odra. Results of the analysis are listed in Tables 6–7.

It results from the analysis that the composition of corrosion products correspond to the initial period of formation of the protective patina (dominant phase is lepidocrocite). The "young" insufficiently developed corrosion layers after one year of exposure doesn't have yet protective character and the values of index PAα are less than 1.0.

The occurrence of akaganeite has been detected on almost all surfaces, in the creation of corrosion products thus participate chlorides. The highest concentration of chlorides in the layer of corrosion products has been detected at the surface (03-E), which is influenced by leakage from failed bridge system. Increased chloride concentration has been also found on the upper surfaces of bottom flanges of main girders.

Table 6. Phase analysis of corrosion products after one year of exposure.

Surface	Phase analysis
03-A	obvious lepidocrocite and goethite
03-B	obvious lepidocrocite, goethite and akaganeite
03-C	obvious lepidocrocite, goethite and akaganeite
03-D	obvious lepidocrocite, goethite and akaganeite
03-E	obvious lepidocrocite, goethite and akaganeite
04-A	obvious lepidocrocite, very poor goethite
04-B	obvious lepidocrocite, very poor goethite, akaganeite
04-C	obvious lepidocrocite, very poor goethite and akaganeite

*Surface notation:

03 - Road bridge over the railway line in Ostrava
- 03-A—soffit outer area of upper flange of the main girder
- 03-B—upper outer surface of bottom flange of the southern main girder
- 03-C—upper inner surface of bottom flange of the main girder
- 03-D—upper outer surface of bottom flange of the northern main girder
- 03-E—inner web of the main girder influenced by leakage from failed drainage system

04 - Road bridge over the river Odra in Ostrava
- 04-A—soffit outer area of upper flange of the main girder
- 04-B—upper outer surface of bottom flange of the southern main girder
- 04-C—outer web of the main girder

Table 7. Analysis of corrosion products—PA indexes and concentration of chlorides after one year of exposure.

Surface	Cl (wt%)	PAI_{α}	PAI_{β}
03-A	0.17	0.58	–
03-B	1.08	0.24	0.69
03-C	0.42	0.36	0.76
03-D	0.55	0.34	0.63
03-E	1.14	0.52	0.84
04-A	0.17	0.15	–
04-B	0.70	0.14	0.67
04-C	0.23	0.16	0.65

4 CONCLUSIONS

The program of experimental atmospheric corrosion tests of weathering steels is designed as a long-term project. Complex results of the program will be first available after 10 years of corrosion specimens' exposure. To create conclusions about the corrosion processes on typical surfaces of steel structures it was necessary to install corrosion specimens on a sufficient number of surfaces. At the end of 2014 corrosion specimens were fixed on 97 surfaces.

The main objective of the program is specification of analytical prediction model for calculation of design values of corrosion losses (Krivy et al. (2013)) on the basis of measured data statistical evaluation. In practice, prediction models for calculation of corrosion losses are used primarily for design of load-bearing structures of buildings. Statically needed value of required corrosion allowances is determined on the basis of predicted corrosion losses (Krivy (2012)). The experimental results can also be used for evaluation of time-dependent structural reliability using probabilistic methods (Damgaard et al. (2009), Czarnecki & Nowak (2008), Kayser & Nowak (1989)).

It is worth mentioning that actual corrosion rates of weathering steels are significantly lower than in the seventies and eighties when some of the bridges were realized. This effect is caused by reduction of SO_2 pollution in the Czech Republic. It was observed that decrease of corrosion aggressiveness of the environment is followed by decrease of corrosion rates practically without time delay.

Simple attachment of specimens on evaluated surfaces of the structure can serve as economically inexpensive approach for evaluation of corrosion processes on weathering steel structures. This method allows quantifying the actual corrosion state. It results from the measurements that corrosion losses of weathering steels are significantly conditioned by location of exposed surfaces within the structure.

An important part of the experimental measurement is an assessment of corrosion processes on the surfaces exposed to leaking water. Results of the experiment can be used in evaluating the impact of corrosion damage on bearing capacity and lifetime of the structure.

Measurement of thicknesses of corrosion products can serve as a tool for apposite estimation of corrosion rates. The measurement is very simple—is carried out using a portable thickness gauge without need anyhow interfere into the structure. Significant correlation dependence between average value of the thickness of corrosion products and corrosion losses after one year of exposure was identified. Equation (1) is determined by linear regression, however, is only valid for the first year of surface exposure. One of expected outcomes of corrosion tests will be the description of dependencies between these two measured quantities for longer exposure. Time course of increase of corrosion products thicknesses and corrosion losses is different for both quantities. It will be important to define the boundary values when this time-dependent processes start to differ.

The analysis of rust layers can serve as a useful additional criterion for assessing of patina development and understanding of corrosion processes during the lifespan of structures. Increased attention is paid to the influence of chloride deposition on corrosion processes on typical surfaces of bridge structures. Local increase of corrosion aggressiveness in the vicinity of roads occurs not only during the use of deicing salts, but due to the secondary dust in other periods of the year.

It results from the analysis of rust layers after one year of exposure that the values of PA indexes aren't influenced by concentrations of sedimented chlorides. The real influencing of rust layers, especially PAI_{β} values, occurs after prolonged exposure (Kreislova & Krivy (2014)).

ACKNOWLEDGEMENT

The works were supported from sources for conceptual development of research, development and innovations and the student research grant competition at the VŠB-Technical University of Ostrava granted by the Ministry of Education, Youths and Sports of the Czech Republic.

REFERENCES

Albrecht, P. & Hall, T.T. 2003. Atmospheric corrosion resistance of structural steels. *Journal of Materials in Engineering* 15: 2–24.

Copson, P.H. 1945. A Theory of the mechanism of Rusting of Low Alloys Steels in the Atmosphere. *Proceedings ASTM* 45: 554–81.

Czarnecki, A.A. & Nowak, A.S. 2008. Time-variant reliability profiles for steel girder bridges. *Structural Safety* 30(1): 49–64.

Damgaard, N. et al. 2009 *Prediction and Prolongation of the Service Life of Weathering Steel Highway Structures*. Waterloo: University of Waterloo.

Fischer, M. 2004. *Merkblatt 434: Wetterfester Baustahl*. Düsseldorf: Stahl-Informations-Zentrum.

Hara, S. et al. 2007. Taxonomy for protective ability of rust layer using its composition formed on weathering steel bridge. *Corrosion Science* 49 (3): 1131–1142.

Helzel, M. 2014. *Dokumentation 585: Fassaden aus wetterfestem Baustahl*. Düsseldorf: Stahl-Informations-Zentrum.

Horton, J.B. 1965. The Rusting of low-alloyed steel in the atmosphere. In *Pittsburgh regional technical meeting of the American Iron and Steel Institute*: 1–24.

Kamimura, T. et al. 2006. Composition and protective ability of rust layer formed on weathering steel exposed to various environments. *Corrosion Science* 48 (9): 2799–2812.

Kayser, J.R. & Nowak, A.S. 1989. Reliability of corroded steel girder bridges. *Structural Safety* 6(1): 53–63.

Kogler, R. 2005. Weathering Steel and Painted Steel: Complementary corrosion protection solutions for Highway Bridges. *Journal of Protective Coatings and Linings* 22(1): 68–73

Kreislova, K. & Knotkova, D. 2011. *Application of weathering steel in architecture* (in Czech), Prague: SVÚOM, Ltd.

Kreislova, K. & Krivy, V. 2014. Evaluation of corrosion resistance of weathering steel with 3% Ni. *Corrosion and Material Protection* 58 (1): 11–18.

Krivy, V. 2012. Design of corrosion allowances on structures from weathering steel. *Procedia Engineering* 40: 235–240.

Krivy, V. et al. 2015. Experimental Corrosion Tests on Weathering Steel Bridges. *Solid State Phenomena* 227(2015): 537–540.

Krivy, V. et al. 2013 Bestimmung der Dickenzuschläge für wetterfesten Stahl im Brückenbau. *Stahlbau* 8(8): 583–588.

Larrabee, C.P. & Coburn, S.K. 1962. The Atmospheric Corrosion of Steels as Influenced by Changes in Chemical Composition. *Proceedings of the First International Congress on Metallic Corrosion*, London.

Lebet, J.P. & Lang, T.P. 2001 *Brücken aus wetterfestem Stahl.* Lausanne: ICOM Construction Métallique.

Morcillo, M. et al. 2013. Atmospheric corrosion data of weathering steels. A review. *Corrosion Science* 77: 6–24.

Morcillo, M. et al. 2014. Weathering steels: From empirical development to scientific design. A review. *Corrosion Science* 83: 6–31.

Posvarova, M. 2008. *Technical conditions TP 197: Bridges and road structures designed from weathering steel* (in Czech). Prague: Ministry of Transportation of the Czech Republic.

Tidblad, J. 2012. Effects of Air Pollution on Materials and Cultural Heritage: ICP Materials Celebrates 25 Years of Research. *International Journal of Corrosion*: 1–16.

Yamaguchi, E. 2015. Maintenance of Weathering Steel Bridge. *Steel Construction Today & Tomorrow* 45: 12–15.

Recent Progress in Steel and Composite Structures – Giżejowski et al. (Eds)
© 2016 Taylor & Francis Group, London, ISBN 978-1-138-02946-0

The history of the first orthotropic bridge in Bulgaria

D. Partov & R. Ivanov
VSU "L. Karavelov", Sofia, Bulgaria

D. Dinev
UACEG, Sofia, Bulgaria

ABSTRACT: The paper presents the rehabilitation project for the movable bridge in Varna, following its failure in 1975. The existing old bridge is designed and built by the "MAN" company in 1939. In 1975 the movable part and one from the stationary parts of the bridge was completely destroyed by a ship accident. The reconstruction included installing new superstructure in two bays, while the original structure in the third bay was kept in place. The bridge is a 3-span steel structure with a total length of 80.34 m. The movable and one stationary parts were designed as simply supported bridge structure with an orthotropic deck. The movable bridge consists of two identical Warren trusses with spans of 31.62 m. The stationary parts were designed as simply supported bridge with an orthotropic deck also. The superstructure consists of two main girders are 2.80 m deep with a distance between them of 8.00 m.

1 INTRODUCTION

It is known that since old times, the water of the Varna Lake feeds the shallow and meandering river passing to the south of the city walls of Varna. Through the years the river had different names; Derza, Vrana, Varna, and is now called Devnja. There is a road of strategic and commercial importance passing through this area, so it could be assumed that there was a bridge over the river for many years now. However, the first conclusive evidence for existence of a bridge comes from the years of the Turkish presence in Bulgaria, and more specifically, from the middle of the 18th century. The bridge was then situated near the city walls, where the present rail cargo terminal is, and was made of stone-block masonry. The name of this bridge was "Tash Kjuprju". According to the Check Skorpil brothers, the bridge suffered a heavy flood in 1758, and was seriously damaged. The texts engraved in the remains of the stone bridge indicate that it was built on top of an older stone or wooden bridge.

In those years Varna was a key city of the Ottoman Empire, laying on the main road from Istanbul to Romania. "Tash Kjuprju", (Figure 1) was thus situated at a bustling location and had its commercial and strategic importance. In 1872, Feliks Kanic, a Hungarian explorer, impressed by the bridge commemorated it in one of his drawings.

After gaining independence from the Ottoman Empire, changes in the urban structure of Varna occurred. The Devnja rives has been gradually dried-up, and "Tash Kjuprju" was eventually demolished in 1907. At about the same time, the digging of a new canal between the sea and the lake began, and was completed in October 1908. Due to the lack of funds for a more substantial structure, a wooden pontoon bridge was erected instead, connecting Varna and the Asparuhovo quarter.

Figure 1. The "Tash Kjuprju" bridge.

The bridge was 50 m long and 5.70 m wide (traffic lanes). At the middle, there were two movable platforms each 11.5 m long (Bascule type), which were lifted-up by a system of pulleys and ropes. The bridge was opened for operation on 22 October 1908.

In time, the traffic demand increased, and both a road and a railroad connection to the Southern industrial quarter became necessary. In May 1937 the construction of a modern movable combined

road-and-railroad bridge began. The bridge was riveted plate girder type, and had total length of 82 m including a movable middle span of 31.62 m. The foundations were laid on sand cushions at 12 m below surface level. The movable part of the bridge (Schercer type) was manufactured by the German company "MAN". This was the first bridge with the name "Asparuhov", and was officially opened for traffic on 28 May 1939 (Figure 2).

However, the passing of ships posed a significant challenge. In order to prevent a collision, RC timber lined columns were installed to better guide ships to the movable span. Even with this precaution taken, a big accident occurred on 28 January 1975. Russian ship "Pavel Postishev" lost control, and hit the lifting machinery of the movable span. As a consequence, the movable part was destroyed and fell in the canal. The two adjacent segments were also seriously damaged. To avoid traffic disruption, two military pontoon bridges were promptly constructed, and on 2 February 1975 the two banks of the canal were connected again. On 15th February 1975, two steel bridge structures taken from the decommissioned railway stations at the villages of Strashimirovo and Trastenik were shipped to the site and installed as a temporary solution. One of the structures was lifted by a crane daily to allow ship passage to the port of Varna. It is under these circumstances that the design of a new combined road-railroad bridge with a movable middle span began.

The design was assigned to Assoc. Prof. B. Bankov, Ph.D., who after a careful survey of the damaged structure proposed that two of the three damaged segments at the Varna side be replaced by new steel structures (Bankov (1958)). The central span which used to be self-raising was now subject to a limitation of a self-weight of 95 t. to allow lifting by a 100 t crane every evening. The movable part was to be permanently fixed on completion of the big Asparuhov Bridge, whose construction was under way at that time. After feasibility studies on several alternative solutions, the final conceptual design included a solid-walled steel structure between the abutment at the Varna side and pier 2, and a steel truss spanning from pier 2 to pier 3 (Bankov (1958)). The rest of the bridge was kept in its original state, i.e., a riveted steel structure between piers 3 and 4 (Figures 3–4).

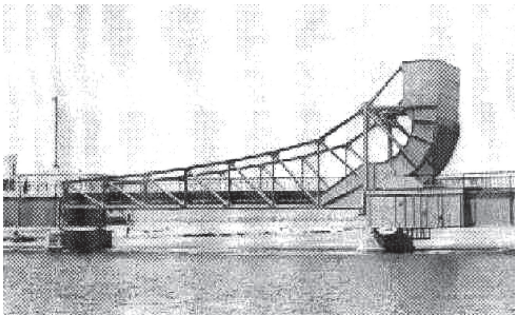

Figure 2. The Schercer type bridge.

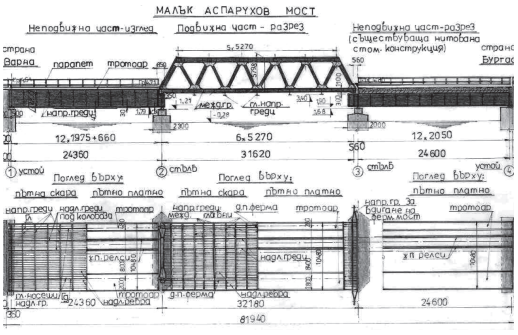

Figure 3. Proposal for the present bridge.

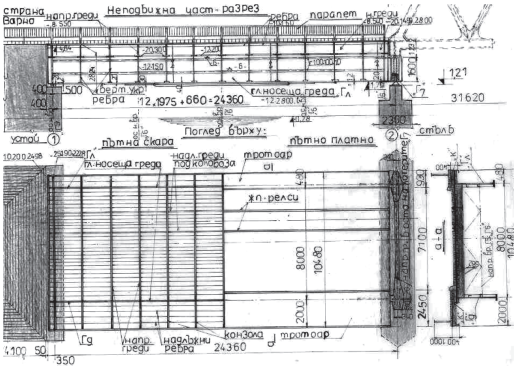

Figure 4. Stationary part of the bridge—longitudinal section and plan.

2 STRUCTURAL SOLUTION FOR THE STATIONARY PART OF THE BRIDGE

The stationary part at the Varna side was designed as a solid-walled simple beam with span 24,360 mm measured between the bearing centres (Figures 4, 6). The cross section shown in Figure 5, is a classical example of a steel bridge with an orthotropic deck. The width of the bridge between the parapets is 10,480 mm, with the two main girders placed at 8,000 mm centres. The main girders are stiffened by cross-girders spaced at 1975 mm. The main girders and a 12 mm thick steel plate fastened to their top flanges form together a channel section. The 12 mm steel plate is stiffened by 10 × 160 mm longitudinal stiffeners at 300 mm centres. The lon-

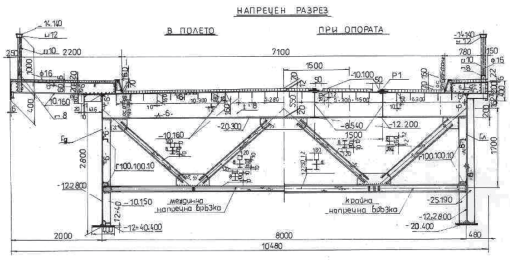

Figure 5. Cross section of the stationary part.

Figure 6. General view of the stationary part.

Figure 7. Details of the stationary part of the bridge.

gitudinal stiffeners are continuous through all the length of the bridge, passing through purpose-made grooves in the webs of the cross girders (Figure 7). With this design the deck becomes an orthotropic slab with different stiffness in the two orthogonal directions. The web of the main girder has 2800 mm depth and 12 mm thickness. The bottom flanges of the main girder have varying thickness, from 12 mm to 40 mm, with constant width of 400 mm, determined by the shape of the bending moment envelope curves. The web of the cross girders is 1550 mm deep and 8 mm thick. The bottom flange has dimensions 20 × 300 mm. The centreline of the railroad is offset from the centreline of the bridge by 1550 mm, and is supported by two longitudinal girders spaced at 1500 mm, having a span of 1975 mm and depth equal to the depth of the cross girders. Their web has dimensions 8 × 540 mm, and the top and bottom flanges dimensions 10 × 100 mm, and 12 × 200 mm respectively. The longitudinal girders also serve as deck stiffeners, and are designed as continuous beams supported by the cross girders (at 1975 mm centres). The webs of the main girder and the cross girders are connected by two 10 mm fillet welds. The bottom flange is welded to the web by two 10 mm fillet welds.

The pedestrian walkways are 2450 mm wide at the right-hand side, and 930 mm wide at the left-hand side. They are designed as orthotropic slabs and are attached to the main structure as cantilevers. The thickness of the walking surface is 6 mm, stiffened by 6 × 60 mm steel strips. The cantilevers are 200 mm deep "I" beams with a bottom flange 10 × 160 mm, a web 8 mm thick, and 1.5% gradient for draining. The parapets are 1100 mm high. The railing is made from 120 mm hot-rolled open channel section, closed by 14 × 140 mm strips. The props of the parapet have a box section formed by two 120 mm hot-rolled open channel sections welded together. The props are spaced at 1606 mm. The fence bars are made by 16 mm reinforcing steel bars. The parapet is welded to the walkway cantilevers, and the walkway cantilevers welded to a longitudinal end girder 400 mm deep. This girder also contributes to pedestrian comfort.

The main girders have been checked for strength and buckling to DIN 4114 (DIN 4114 1961), using the tables and graphical solutions of Prof. Kloeppel (Kloeppel (1968)). Buckling of the web is prevented by two longitudinal stiffeners made by 100 × 100 × 10 mm equal angle sections, and 10 × 150 mm vertical stiffeners spaced at 1975 mm. Both types of stiffeners are placed at the interior side of the web only.

3 STRUCTURAL SOLUTION FOR THE MOVABLE PART OF THE BRIDGE

In order to satisfy the requirements of ship navigation, i.e. the bottom of the structure to be at the same level as that of the bridge before the accident, a truss solution with the road at the bottom chord level was proposed. Both from structural and aesthetic point of view, a simple triangular lattice without vertical members was adopted. In addition, the structure had to weight no more than 95 t, since it would be lifted by a 100 t floating crane during operation. In order to meet the weight requirement, the deck was designed as orthotropic slab, which

includes parts of the bottom chord of the truss. The truss was designed as statically determinate, both internally and externally, with a span of 31, 620 mm. The bottom chord was divided into six members, with node-to-node distance 5270 mm. The deck consists of a 12 mm thick plate stiffened by 10 × 160 mm longitudinal stiffeners at 300 mm centres, main and secondary cross girders at 1757 mm centres, where the main cross girders are spaced at 5270 mm, and are supported by the nodes of the truss. The secondary cross girders are connected to the bottom chord of the truss, between the nodes, at equal intervals, three girders per node-to-node span. The webs of the girders are welded to the bottom chord of the truss by two vertical 7 mm fillet welds. The chords are butt-welded to the node plates.

The dimensions of the longitudinal girders supporting the rail track are 8 × 790, 10 × 200 and 12 × 200 for the web, the top and the bottom flanges respectively. The main cross girders are designed as simply supported beams with span 8.40 m, loaded according to BE, table 6.4.b. The dimensions at mid-span are 10 × 800 mm, 12 × 1250 (effective width) and 20 × 350 for the web, the top and the bottom flanges respectively. The corresponding dimensions at the supports are 12 × 500 mm, 12 × 1250 mm and 20 × 350 mm. In order to alleviate the secondary cross girders, the main cross girders have significant stiffness. In fact, they are designed to independently carry the railroad traffic loads, without resorting to the contribution from the orthotropic deck, i.e. the orthotropic action is considered for the secondary cross girders and the longitudinal stiffeners only. The internal forces are obtained for heavy-vehicle loading HK80, and train loading type A. The secondary cross girders have a constant cross section with dimensions as follows: 8 × 450 mm, 12 × 1550 and 20 × 160 for the web, the top and the bottom flanges respectively. The cross sections of the top and the bottom chords, as well as those of the compressive diagonals are of box type. The tensile diagonals are designed as "I" sections. Various views of the movable part, as well as joint details are shown in Figures 8–11.

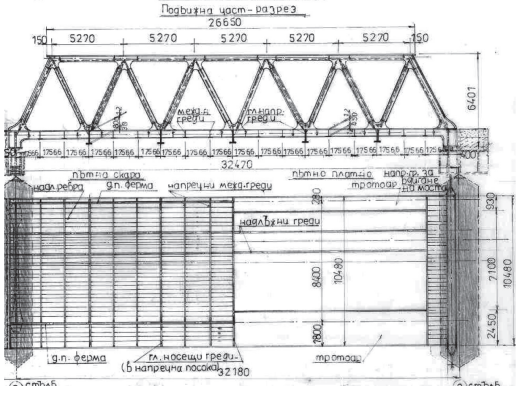

Figure 8. Longitudinal section and plan of the movable part.

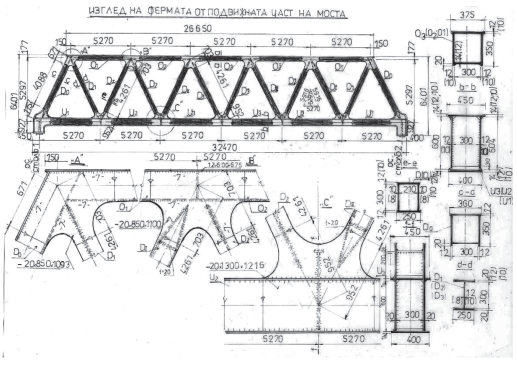

Figure 9. Details of the movable part of the bridge.

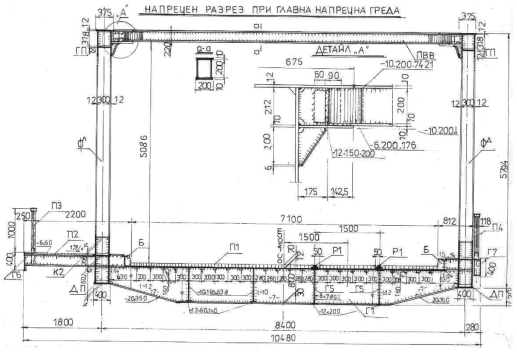

Figure 10. Cross section at a main cross girder of the movable part.

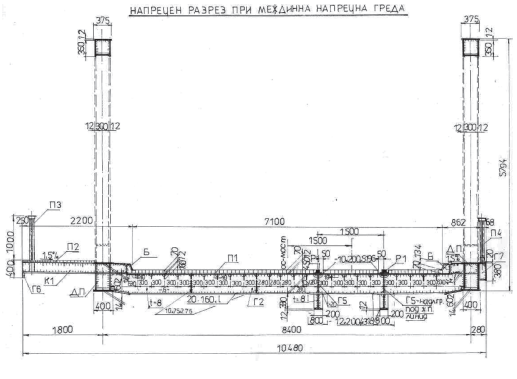

Figure 11. Cross section at a secondary cross girder of the movable part of the bridge.

4 LOADING AND ANALYSIS

The bridge structure was analyzed for the following loading action types:

- Permanent; from self-weight
- Imposed; from traffic, HK 80 and mob 400 kN/m^2 for road bridge; train loading type A for railroad bridge.

The two loading conditions are applied independent from each other and the dimensioning of members was done for the more unfavourable case.

The loads imposed from heavy-vehicle loading HK 80 and train loading type A on cross girders have been determined using influence lines for support reactions and moments for a continuous beam on an infinite number of rigid supports.

HK 80 is represented by four forces 100 kN each, at 1.20 m intervals; and train loading type A is represented by five forces 125 kN each, at 1.6 m intervals imposed on the influence lines of interest.

Since there are not modern Bulgarian codes for the analysis and design of steel bridges, the analysis was done according the well proven in practice German Federal Railways code (DV 804, 1965, DV 848, 1955, DV 805, 1953 and DIN 4114, 1961).

The bending moments in the cross girders and the longitudinal girders under the rail track were initially determined as moments in an orthotropic plate, according to the theories of Cornelius (Cornelius (1952)), Pelikan and Esslinger (Pelikan & Esslinger (1957)), Giencke (Giencke (1955)) and Homberg (Homberg (1951)). Further, a comparison was made by determining the moments according to BE—Table 6.4a. The maxima of the bending moments in the middle of the cross girders, and in the middle of the longitudinal stiffeners along the bridge axis were determined using influence surfaces.

The result of the comparison was that the bending moments due to BE were some 45% higher than those due to orthotropic plate theory. Bearing in mind that the train loading is transferred directly to the longitudinal and the cross girders in both the stationary and the movable parts of the bridge, as well as the large number of welds inducing considerable self-stress, it was decided to adopt the conservative BE results. In this way, a certain amount of reserved capacity was introduced, to provide for the additional forces arising from the spatial action of the structure. Indeed, after further detailed checks were made considering the spatial action of the structure, the difference in the moments determined by the two methods practically vanished, i.e. the loading capacity of the structure was fully utilized.

The stress in the deck was computed as the sum of the stress due to the direct loading on it, and the stress due to its action as a part of the respective flange or chord of a principle structural member (main girder or truss).

The axial forces in the truss lattice were determined using the appropriate influence lines. The stress in the bottom chord of the truss was determined as the sum of the stress resulting from truss action and the stress resulting from bending due to the reactions of the secondary cross girders supported on it. All members of the truss were designed to the strength and stability requirements of DIN 4114, 1961.

According to (DV 804 1965), the design for strength was done in the following order:

1. Determination of the internal forces and support reactions due to main forces, auxiliary forces and extraordinary forces.
2. Dimensioning of the cross sections of the members, and computation of the stress resulting from the forces computed in 1.
3. Performing the following checks:

- Strength check; assuring the stress is less than the yielding or fracture limit;
- Stability check; check to assure buckling does not occur; local and global, warping;
- Fatigue check; proving the safety of a member subjected to repetitive loading and stress fluctuations;
- Overturning check;
- Deflection check; proving that excessive displacements do not occur.

The following auxiliary forces have been considered: lateral pounding, friction at the bearings, vehicle braking forces, mob on the walkways and wind. The walkway cantilever is designed to sustain a UDL 5 kN/m2. The wind loading assumed in the design is 1.50 kN/m2 when acting together with imposed loads and 2.50 kN/m2 when not.

5 SPATIAL BRACING SYSTEM

The purpose of the spatial bracing system is to assure that the simple 2D structural elements—solid-walled and trussed interconnected by it, resist loads in a 3D fashion as a single rigid assembly.

The bracing is resolved in the following manner: In the stationary part of the bridge, a horizontal wind bracing system of K type is installed at the bottom flange level. Its members have box cross sections. In addition, solid-walled framing was installed at both ends of the structure. Vertical wind bracing was also installed at 5925 mm centres. The top chord of the vertical bracing is the cross girder of the bridge. The rest of the members are made by combining "I" sections; 8×150 mm web, and 12×180 mm flanges.

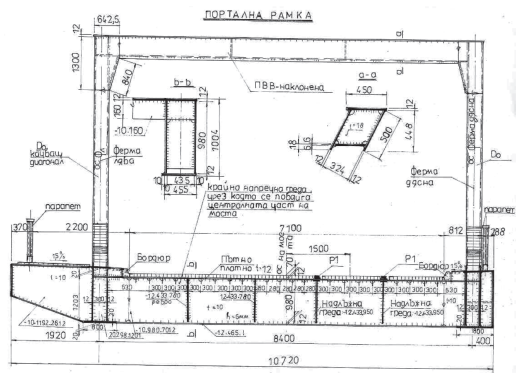

Figure 12. Cross section of the portal frame.

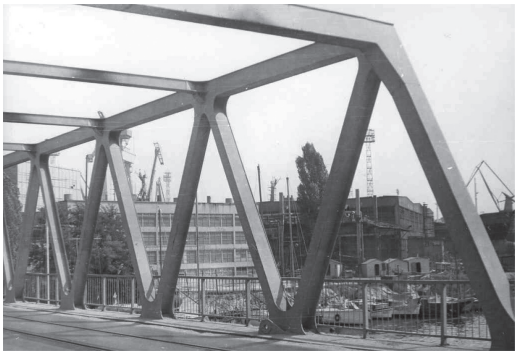

Figure 13. General view of the portal frame.

The trussed part of the bridge is equipped with a moment-resisting box-section frame developed at the top chord level. It assures the transverse stability of the two trusses. The stability of the compressive top chord is secured by developing two portal frames at both ends of the trusses. The pair of diagonals at each end forms the stanchions of each portal frame (Figures 12–13). The asymmetric position of the rail track makes one of the main girders (or main truss) carries 2.13 times the load the other one carries under train loading. The braking forces are transferred to the foundations via the two piers. Since the old structure was supported in the same way, the piers did not require additional checks. The way of support is favourable in terms of thermal expansion, since each movable bearing caters for the expansion in its own span only.

6 MATERIALS, MANUFACTURE AND ASSEMBLY

The road slab and its longitudinal stiffeners, the walkway cantilever and its stiffeners, the longitudinal girders under the rail track, the end longitudinal girder, the bottom chords of the trusses and lattice members D2 and DII, all longitudinal and transverse stiffeners of the solid-walled girders, and all members of the wind bracing are manufactured by steel grade M16C.

The main solid-walled girders, the cross girders, the vertical stiffeners at the supporting points of the girders, the top chord of the trusses and lattice members D0, D1 and DI are made by steel grade 10G2SF.

The manufacture and assembly of the superstructure was commissioned to the ship-maintenance yard “Gocho Ivanov”. All works were completed in high precision and strict compliance to the detailed working drawings submitted to the factory.

The two parts of the bridge were manufactured as independent assembly units. They were shipped to the site by a 100t Gants floating crane and then installed by the same crane (Figure 14).

Neoprene bearings were used for the bridge, with the bearings at the Varna side abutment being movable. To avoid a complicated adjustment of the piers to accommodate new bearings, the movable part of the bridge was seated on top of the old and

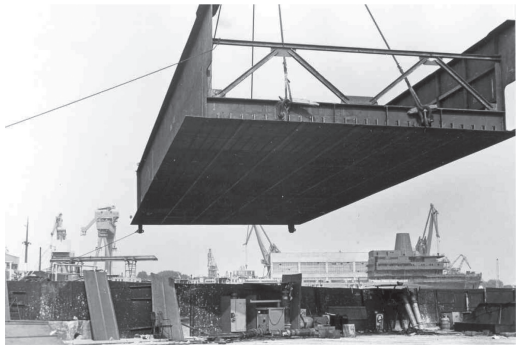

Figure 14. A glimpse of the assembly process.

Figure 15. View of the completed bridge.

Figure 16. View from the fixed part of the bridge.

new solid-walled girders of the stationary part of the bridge. A general view of the completed small Asparuhov Bridge can be seen in Figures 15 and 16.

7 CONCLUSIONS

The design and construction of the small Asparuhov Bridge was executed without interruptions, due to the importance of the project to the national economy. The orthotropic structures were designed to modern standards, and were completely shop-welded at the Varna ship-maintenance yard. The design and construction were executed in parallel, which resulted in a fairly short completion period; just three months. All works and the welds in particular, were subject to strict quality control. All butt welds were X-ray inspected. A defective weld would then be removed, welded and inspected again. The bridge structures were shipped to site by a 100 t Gants floating crane. The final assembly was done by simply placing the assembly units at their design locations. The assembly process went smoothly and was completed in a few days. The total weight of the structures was 81 t for the stationary part and 113 t for the movable part.

REFERENCES

Bankov, B. 1958. *New directions in the development of steel bridges*. Sofia: Tehnika.

Cornelius, W. 1952. Die Berechnung der ebenen Flaechentragwerke mit Hilfe der Theorie der orthogonal—anisotropen Platte. *Der Stahlbau* 21, H2, s. 21–24, H3, s. 43–48, H4, s. 60–64.

DV 804 1965. *Berechnungsgrundlagen fuer staehlerne Eisenbahnbruecken*.

DV 848 1955. *Vorschriften fuer geschweisste Eisenbahnbruecken*.

DV 805 1953. *Grundlagen fuer bauliche Durchbildung staehlerner Eisenbahnbruecken*.

DIN 4114 1961. *Stabilitaetsfaelle*.

Giencke, E. 1955. Die Grundgleichungen fuer die orthotrope Platte mit exzentrischen Steifen, *Der Stahlbau* 24, H.6. s.128–129.

Homberg, H. 1951. Kreuzwerke. Statik der Traegerroste und Platten. *Forschunghefte aus dem Gebiete des Stahlbaues 8, Deutschen Stahlbau-Verband*, Prof. K. Kloeppel (ed). Springer-Verlag, Berlin (Goettingen) Heidelberg.

Kloeppel, K. 1968. *Beulwerte ausgesteifter Rechteckplatten*. W. Ernst, I, II, 8.

Pelikan, W. & Esslinger, M. 1957. *Die Stahlfahrban. Berechnung und Konstruktionen*. Asburg: MAN-Forschungheft 7, K.G. Kieser.

This page intentionally left blank

Recent Progress in Steel and Composite Structures – Giżejowski et al. (Eds)
© 2016 Taylor & Francis Group, London, ISBN 978-1-138-02946-0

Finite element analysis of metal-soil bridge under static loads

D. Beben
Faculty of Civil Engineering, Opole University of Technology, Opole, Poland

ABSTRACT: The paper presents a finite element analysis of the metal-soil bridge under static (dead and live) loads using Abaqus program. The corrugated metal plates are used to bridge shell construction. Maximum displacements were obtained in the bridge crown, and the largest stresses in the haunches. Calculation results were compared with the experimental ones and previous calculations obtained from the Autodesk Robot Structural Analysis program. The shapes of calculated displacements and stresses are similar to those obtained with the experiment, but the absolute values were generally higher than measured ones. The relative differences of maximum calculated and measured values were in the range of 3–28% for displacements, and 4–28% for stresses. Developed calculation model of the metal-soil bridge in the Abaqus program allows to obtain reasonable values of internal forces. Using both calculation programs, the relative differences for displacements were in the range of 25–43%, and 25–56% for stresses in favour of the Abaqus program.

1 INTRODUCTION

Metal-soil bridges are getting widely used as an alternative to traditional steel or concrete bridge structures (Janusz & Madaj (2009)). The well-known advantages which justify the choice of such solution are mainly short period and relatively low cost of construction (Abdel-Sayed et al. (1994)). Numerical analysis of such structures causes many problems such as modelling of corrugated profiles, selection of a soil model and interaction properties (El-Sawy (2003), Elshimi (2011), Machelski (2008)). This is why a reasonable way of numerical analysis of metal-soil bridges has not been elaborated so far. Generally, the calculation results obtained with use of the computational models in comparison with the experimental results are insufficiently satisfactory, therefore further numerical analysis of metal-soil bridges is needed.

Taleb & Moore (1999) executed a two-dimensional (2D) Finite Element (FE) analysis during backfilling process. The results were in the low accuracy level in comparison to experimental tests. El-Sawy (2003) showed the Finite Element Method (FEM) analysis of metal-soil bridge under live loads. FEM and test results indicate large disparities caused by insufficient soil model application. Machelski & Antoniszyn (2004) and Machelski et al. (2006) used 3D and 2D FE analysis of metal-soil bridges, respectively. Kunecki (2006) presented full scale testing and numerical calculations of metal-soil bridge. The calculation results were higher than the ones received from experimental tests. Sargand et al. (2008) presented a metal-soil bridge study which included comparing measured field performance with numerical predictions given by the FE computer program (CANDE). The initial numerical calculations of the metal-soil bridges were also presented by Beben (2009, 2012). 2D FE program (CANDE) and a 3D finite difference program (FLAC) were applied by Yeau et al. (2014) to simulate the behaviour of the small metal-soil bridge. Mellat et al. (2014) showed the 2D and 3D continuum models for dynamic response of the railway metal-soil bridge. Basing on the models, the influence of the Young's modulus of the backfill on the bridge behaviour was also investigated. Beben & Stryczek (2015) present a numerical modelling of an arch metal-soil bridge with Reinforced Concrete (RC) relieving slab. The obtained numerical results are overestimated in comparison to site test results.

The aim of this paper is to propose a numerical analysis of a metal-soil bridge (Figure 1) within

Figure 1. Side view on the analysed metal-soil bridge.

the scope of static (dead + live) loads. A method of numerical analysis of a metal shell with the orthotropic properties has been presented as well as a method of considering a soil-shell structure interaction phenomena. The numerical analysis of the bridge was executed in a 3D space of the Abaqus/CEA 6.11 program (Abaqus 2011). Calculation results (displacements and stresses) were compared to the results of experimental tests as well as to previous numerical calculations in the Autodesk Robot Structural Analysis (ARSA) program (Manko & Beben (2005)). The conclusions mainly consider accuracy of calculation results in comparison to the previous analyses (Manko & Beben (2005)). The underlying reasons of the observed discrepancies were also explained.

2 METAL-SOIL BRIDGE DESCRIPTION

The subject of analysis is metal-soil bridge with effective span of 12.27 m and vertical height of 3.36 m (Figure 2), which was earlier comprehensively tested (Manko & Beben (2005)). The analysed structure in the cross section constitutes a single-span metal box shell structure. The box shell is made of Corrugated Metal Plate (CMP) of thickness $t = 0.007$ m and has a corrugation depth of $a = 0.14$ m with pitch $b = 0.38$ m (detail "A" in Fig. 2). The structure's width is $b_t = 13.60$ m at the top and $b_b = 20.60$ m at the bottom. The individual sheets of corrugated plate are connected together using high strength bolts $\varnothing = 20$ mm using a torque moment of 350–400 Nm. The metal box shell structure was supported, by means of steel uneven-armed channel sections, on two RC strip foundations made from B30 grade concrete. The basic metal shell of the bridge was reinforced in the crown and haunches with using additional corrugated profiles (so-called ribs) with the same plate thickness as in the basic structure.

The load-bearing structure was designed as a shell consisting of corrugated metal plates backfilled with 0.20–0.30 m thick course of permeable soil with 10–32 mm grading, compacted to $I_D = 95\%$ (on the Proctor Normal Density) for the soil being in direct contact with the shell and to $I_D = 98\%$ for the other backfill whereby a pavement could be laid

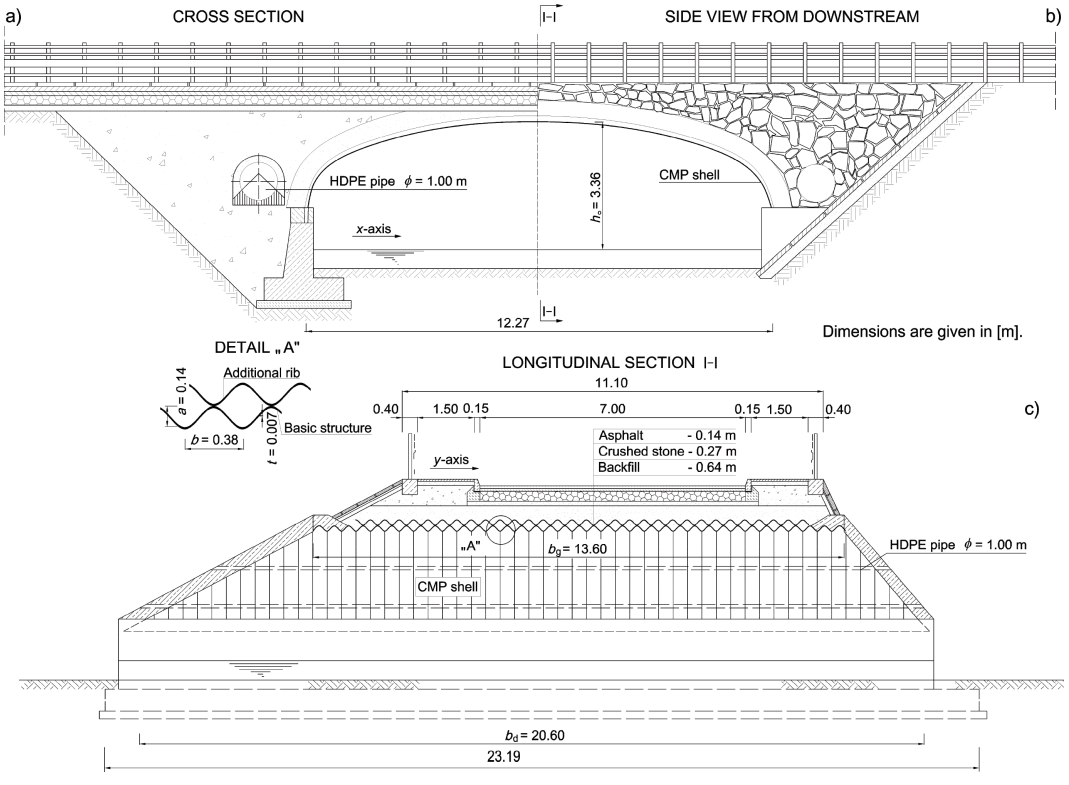

Figure 2. Analysed metal-soil bridge: a) cross section, b) side view form downstream and c) longitudinal section I–I.

on a broken stone subgrade. The backfilling process was conducted step-by-step from both sides of the shell structure. The differences in the soil layer height on both sides did not exceed 2–3 layers, i.e., ca. 0.40–0.60 m. Vibratory plates were used for soil compaction during construction. The cover thickness (backfill, road structure and asphalt) over the CMP crown shell is $hc = 1.05$ m.

Structural steel with strength corresponding to that of Polish steel S315MC (the guaranteed yield strength of the steel used to manufacture corrugated plates was 314 MPa according to PN-EN 10149-2:2014-02 (2014)) was used. Detailed description of the metal-soil bridge and the stages of its construction are presented by Manko & Beben (2005), and the basic geometrical dimensions of the bridge are shown on Figure 2.

3 FINITE ELEMENT MODEL DESCRIPTION

3.1 *General remarks*

For computations of metal-soil bridge, the Abaqus/CEA ver. 6.11 (Abaqus 2011) was used, based on the FEM (Zienkiewicz (1986)). In the numerical model efforts were made to reflect the actual geometry of the analyzed bridge, while not taking into account the secondary elements that may affect the increasing complexity of model and considerably extended time for computation. Therefore, due to the complex shaped structure, a numerical model was slightly simplified, although main parameters of the metal-soil bridge (height and span of metal box shell, top shell length, various radiuses of shell) were maintained. Elements, such as slopes, RC collars reinforcing inlet and outlet of the shell, guardrails and drainage pipes were neglected in the numerical model. These elements should not significantly affect the computational results, because they are located outside the range of active loading, and at the same time represent only additional accessories of the bridge.

Metal-soil bridge calculations were performed in three-dimensional space. Non-linearity in computational model has been addressed by using incremental analysis—the Full Newton method (Abaqus 2011, Skrzat 2010). Bridge model is parts of the 3D space, which are in the dimensions of $16.27 \times 11.10 \times 4.22$ m (Figure 3). Modelling the soils placed at distance greater than 2 m from the metal box shell does not substantially affect the obtained results of computations, while in this case, boundary conditions are rather decisive, which reflect the real structure in quite approximate manner. Hence, the RC foundations, as an element of

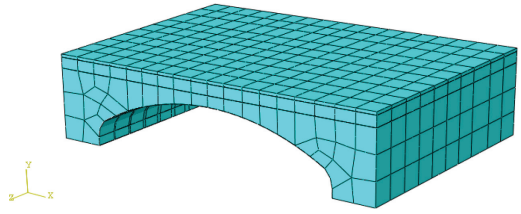

Figure 3. Finite element model of metal-soil bridge.

rigid support for the structure was omitted in modelling process.

In calculation model, nodes have six degrees of freedom (U1, U2, U3 – displacement directions on the axes OX, OY, OZ, and UR1, UR2, UR3 – rotation directions relative to the axis OX, OY, OZ), wherein nodes of elements with their edges laying on external surfaces of the numerical model are blocked at all degrees of freedom—rotations and displacements (total restraint).

3.2 *Materials characteristics*

3D shell tetrahedral elements (S4R) were used to model a metal box shell. The remaining units (soil and roadway layers) are defined as elements with properties of a solid (C3DR8). The material parameters were chosen based on available technical data (the bridge elements and asphalt properties obtained from the producers of such materials and the backfill obtained from the project of this bridge) and material characteristics included in the Abaqus software, that are:

- CMP box shell was modelled as a flat with appropriate parameters of orthotropic shell using the following Equations (1)–(4):
  - equivalent thickness of plate:

$$t_{equ.} = \sqrt{12\frac{I}{A}}, \tag{1}$$

where I = moment of inertia (2.416e-8 m^4/m); A = cross-sectional area (9.81e-6 m^2/m),

  - equivalent elastic modulus of material (Young modulus) in circumferential direction of shell:

$$E_{x\ equ.} = 12\frac{EI}{t_{equ.}^{\ 3}}, \tag{2}$$

where E = a Young modulus of metal structure assumed as 210 GPa,

  - equivalent Young modulus in longitudinal direction of the bridge:

$$E_{y\ equ.} = E\left(\frac{t}{t_{equ.}}\right)^3, \tag{3}$$

where t = a plate thickness (0.007 m),

– shear modulus for the corrugated metal plates is different in different directions. In this paper, an average value for the equivalent shear modulus is used based on the below Equation (4):

$$G_{equ.} = \frac{\sqrt{E_{x\ equ.}\ E_{y\ equ.}}}{2\ (1+v)}, \tag{4}$$

where v = Poisson ratio ($v = 0.3$).

Table 1 presents the equivalent parameters of corrugated plate (basic structure and with the additional ribs) used in the numerical analysis. Plate elements were defined by shell-type elements (SR4) as an elastic-plastic material with a density $\gamma = 78.5$ kN/m^3 and yield strength $\sigma = 314$ MPa. In this case, adopted curvature control accuracy was 0.01 m, due to the complexity of shell itself and its curvilinear shape. The bolt connections between the metal plate elements were omitted during numerical modelling.

- backfill (medium size sand) with thickness of 0.64 m (over the crown shell) was defined as elastic-plastic material (C3DR8 solid-type element) with the hyperbolic Drucker-Prager yield criterion with density $\gamma = 20.5$ kN/m^3, Young's modulus E = 100 MPa, angle of internal friction $\phi = 45°$, dilation angle $\alpha = 5°$, and initial tension equal to 0 MPa. Furthermore, application of the Drucker-Prager model required determining the size of soil reinforcement, due to the fact that the effect of cohesion on the soil behavior was eliminated. For this purpose, a parameter describing the soil reinforcement in compression was used, by fixing its size to 5 MPa.

Table 1. Equivalent orthotropic properties of the CMP box shell structure.

Element	Thickness of plate $t_{equ.}$ (m)	Young modulus in circumferential direction $E_{x\ equ.}$ (GPa)	Young modulus in longitudinal direction $E_{y\ equ.}$ (GPa)	Shear modulus $G_{equ.}$ (GPa)
Basic structure	0.172	11.94	0.0142	0.158
Basic structure + ribs	0.207	16.39	0.000812	0.044

- road structure with thickness of 0.27 m (crushed stone) was defined as elastic-plastic material (solid-type element) with the hyperbolic Drucker-Prager yield criterion with density $\gamma = 18.0$ kN/m^3, Young's modulus E = 60 MPa, angle of internal friction $\phi = 40°$, dilation angle $\alpha = 10°$, and initial tension equal to 0 MPa. As in the case of basic backfill model, Drucker-Prager model-type reinforcement was applied, determining soil reinforcement parameter under compression equal to 5 MPa.
- roadway layer (asphalt with thickness of 0.14 m) was modelled as an elastic material (solid-type element) with density $\gamma = 21.0$ kN/m^3, Young's modulus E = 6.9 MPa and Poisson's ratio $v = 0.41$.
- boundary conditions: total restraint was applied, namely rotations and displacements along each axis of the shell's sides and base were blocked. The metal-soil bridge was modelled as a structure firmly embedded in the environment. This is because, that the lateral earth pressure phenomenon at each direction of displacements and the rigid support of the shell on massive foundations were occurred.
- calculation step was defined as $T = t + \Delta t$, where t is the initial time equal to $t = 0$ s, while Δt is time increment, during which the set static load is applied, according to the three schemas used during experimental tests (Manko & Beben (2005)). Accordingly, Δt equals to the time in which load in applied, and it is usually adopted in the value of 1 s. In calculation step ($T = 1$ s), successive iterations for increments caused by load being applied at that time, and their effect on the metal-soil bridge behavior are computed in the software.

3.3 *Properties of contact zones*

Metal-soil bridge modelling consisting of a three different layers (roadway elements (crushed stone and asphalt), backfill, CMP shell elements) with different physical properties requires determination of their interactions. These interactions shall be determined between all layers, which are in direct contact, even if any of these have similar physical properties (backfill–crushed stone). For modelling interactions between different materials with predefined physical properties, which are incorporated into the metal-soil bridge, contact elements, also called interfaces were used (Abaqus 2011).

Interactions at the interface of materials being interconnected (metal shell–backfill, backfill–crushed stone, crushed stone–asphalt) were modelled as rigid elements of the beam transferring their specific types of interactions from master to slave surfaces. These elements analyze phenomena occurring in the time of interaction between two

materials, that is normal forces (rigidity) and friction forces (friction coefficient). Furthermore, Abaqus software (Abaqus 2011) allows specifying the nature of surface interactions by defining the type of slide between contacting surfaces. Due to the nature of construction and behavior of the entire metal-soil bridge, which transfers loads to the last of its layers, that is corrugated plate, the type of interaction that occurs between the layers (asphalt–crushed stone, crushed stone–backfill) is defined as "finite sliding", which means not sliding. Basic argument for the establishment of this type of interaction is the fact that only in the last contact layer (CMP shell–backfill) small sliding of backfill surrounded by metal plate can occur. In this case, an interaction was adopted in which small sliding is present.

The dependency of master and slave contact surfaces were determined based on the modulus of elasticity of materials being in contact with each other (interaction) and the nature of the metal-soil bridge behavior. Slave was a surface build of the material with lower modulus of elasticity (Young's modulus), and the surface with higher modulus of elasticity was described as master. In numerical model, three types of contact areas (CMP–backfill, backfill–crushed stone and crushed stone–asphalt) were identified. For individual layers, following master–slave dependencies were adopted, that is: (a) CMP shell—backfill → master—slave; (b) backfill—crushed stone → slave—master; (c) crushed stone—asphalt → slave—master.

The type of surface, being in contact with one another was the basis for determining two types of interaction properties specifying friction coefficients between the layers, and surface rigidity formed by these layers. Selecting these two types of interaction properties is the result of specific nature of CMP box shell–backfill interaction, compared with other contact surface properties with relatively similar characteristics (asphalt–crushed stone, crushed stone–backfill). Crucial element, distinguishing this type of interactions from others, is the smooth surface of the shell, which implies lower friction coefficient. Therefore, following friction coefficients were adopted: for CMP box shell–backfill contact surface in the value of 0.3 and for other surfaces of 0.6. However, connection rigidity was established at the level of 2×10^9 kN/m—for CMP box shell–backfill contact surface and 2×10^6 kN/m—for other surfaces.

4 ANALYSIS OF CALCULATION RESULTS

4.1 *General remarks*

In order to compare the results of numerical analysis with measurement results, the same loads as at experimental tests under dead and live loads were used. At the time of experiments two trucks of total mass of 500 kN (Manko & Beben (2005)) were used to bridge loading. To ensure possibility of direct comparison of calculations and measurements results, the forces from the vehicles wheels were nearly identically placed in both the numerical analysis and the experimental tests. An exact description of the three schemes in the scope of static loads is contained within paper (Manko & Beben (2005)). The numerical analysis results of the metal-soil bridge are presented in the form of maps of displacements and stresses.

4.2 *Displacements and stresses*

Selected calculation results of the metal-soil bridge are presented in Figures 4 and 5 in the form of bottom view as well as bridge section along the longitudinal axis of the shell in order to show load distributions in the backfill and shell.

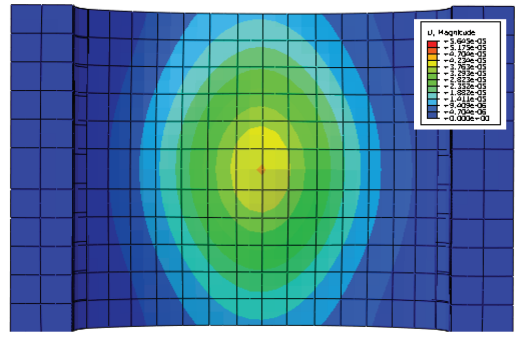

Figure 4. Displacements in the metal shell in bottom view of the bridge from second static load scheme (symmetrical).

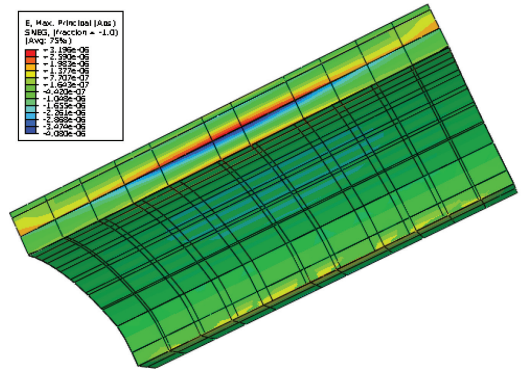

Figure 5. Stresses maps of metal-soil bridge from symmetrical (II) static load schemes.

For the three schemes of static loads under consideration, distribution of displacements in the calculation model indicates that the displacements are not evenly distributed but they are concentrated in the CMP shell crown within the scope of the load impact. The maximum displacements amounting at 2.65 mm were obtained from the scheme of loads I (asymmetric), where the loading vehicles were standing backwards to each other near the curb (Manko and Beben (2005)), from scheme II (1.95 mm) and scheme III (2.35 mm).

A detailed analysis of the results indicates that the impact of loads is manifested as quite considerable local deformations in selected points of the shell (no even distribution of loads over the shell width observed). This is probably a result of a relatively low cover at the shell crown (1.05 m) and a curvilinear shape of the shell. Response of the bridge to the scheme III of load can be considered an exception, where the vehicles are placed side by side, which causes a relatively even distribution of load on the shell width. Moreover, the maps of displacements definitely reflect the impact of the vehicles rear axles on the shell deformations.

Distributions of stresses are presented in Figure 5. Structure behaviour explicitly showed that the loads are transferred onto the metal-soil bridge shell in an indirect way, which results in maximum values at the haunch and at 2/3 of the shell height. In these sections the maximum values amount at 59 MPa from load scheme I and 53 MPa from scheme II and III, respectively. Whereas at the crown the observed stresses are lower (maximum 31 MPa from scheme II—Figure 5). The maps of stresses allow to observe the way a metal-soil structure behaviour. It means, when a quasi-point load is applied (a resultant of loads from the trucks rear wheels), the stresses are moved towards the haunch and the 2/3 of the shell height where the obtained values are the most extreme. Getting the maximum stress values in these sections of the metal-soil bridge confirms necessity to use additional reinforcement there (ribs for example).

4.3 *Discussion of calculation and measured results*

Figures 6–7 show comparison of displacements and stresses obtained from experimental tests (Manko & Beben (2005)) and numerical analysis from the Abaqus and ARSA programs (Manko & Beben (2005)). Numerical modelling in the ARSA program includes the use of isotropic properties for the CMP shell, the elastic, perfectly plastic Mohr-Coulomb model for soil modelling and friction coefficient to reflect interaction between metal-soil bridge elements. As it can be observed from these diagrams, the stresses and displacements obtained from numerical analysis by the Abaqus differ from

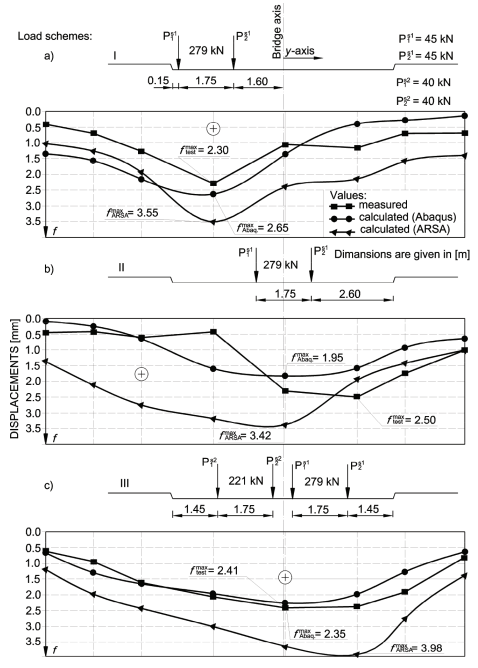

Figure 6. Comparison of maximum displacements of the metal-soil bridge crown obtained with measurements and numerical calculations for three static load schemes: a) I, b) II and c) III.

ones obtained from experiments. However, they are more convergent to measurement results than those obtained from numerical analysis with use of the ARSA program (Manko & Beben (2005))

Comparison of the values obtained from Abaqus and the measurements is shown in Figures 6–7 and explicitly shows that in a real metal-soil bridge some heterogeneities in materials are possible, for example in soil and the metal shell (for example at metal sheet joints), which can hardly be accounted for in numerical analysis. It is manifested in sudden increase in measured displacements and strains (stresses). The displacement and stress courses are similar in shape to the curves representing the actual (measured) values. Relative discrepancies of maximum calculated and measured values were contained within the range of 3–28% for displacements, and 4–28% for stresses. It needs to be underlined that the authors did not know the exact parameters of the backfill. Moreover, the calculation model assumed the same type of soil around the shell and in other parts of the backfill and the shell was modelled as a homogenous flat surface structure (with no corrugations and screw joints between metal sheets). In a real metal-soil bridge some clearances at screw joints can occur. Calculation results show to some extent an idealized behaviour of the analysed metal-soil bridge under

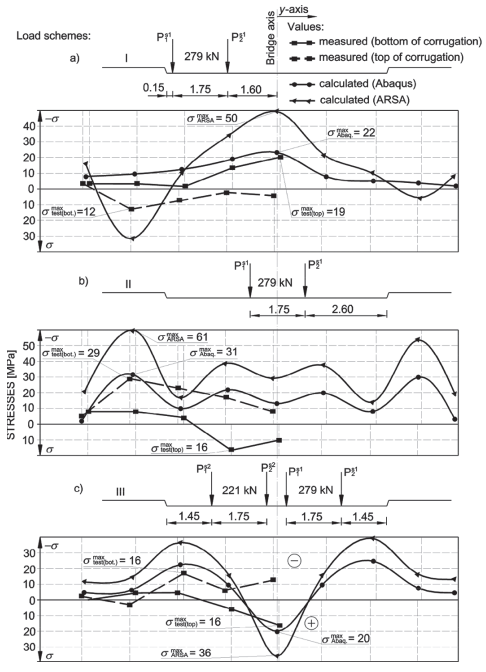

Figure 7. Comparison of maximum stresses of the metal-soil bridge crown obtained with measurements and numerical calculations for three static load schemes.

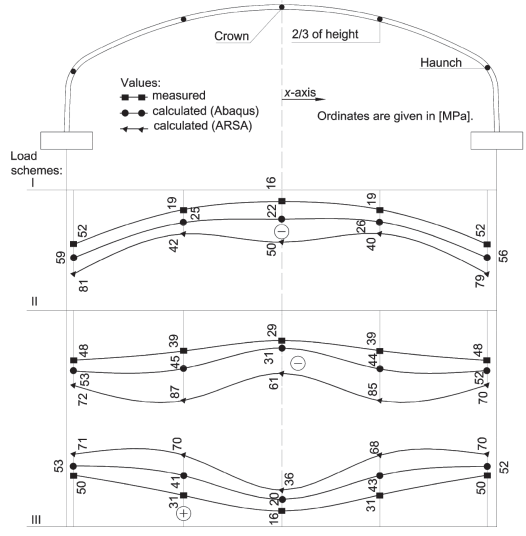

Figure 8. Comparison of maximum stresses in the metal-soil bridge obtained with measurements and numerical calculations for three static load schemes.

static and dead loads. The maximum displacement results obtained from calculations and measurements are located exactly under the point load representing wheels of the vehicles. Whereas in the case of stresses the maximum values are relocated towards the haunch and the 2/3 of the shell height (Figure 8).

Observing, in Figure 7, the stresses course from experiments obtained at the top and at the bottom of corrugation, one can easily notice uneven distribution of loads over the shell width (the neutral axis is not located in the middle of corrugation). Also the diagrams of stresses on the shell circumference (Figure 8) prove the above. As it has already been mentioned, it results in maximum stresses in the haunch and at the 2/3 of the shell height. It should be mentioned that the presented stresses in the numerical analysis were obtained for flat shell structure at the upper fibres.

Apart from that, Figure 8 shows that the two first applied load schemes (I and II) cause maximum compressive stresses in the shell, and the scheme of load III evokes tensile stresses. This is related to the curvilinear shape of the metal shell, the way of the load distribution by soil layers which manifests itself by increased local deformations of the shell, as well as, probably, by the fact that soil pressure is not evenly distributed.

However, when maximum displacements and stresses obtained from calculation models from two types of software, i.e.: Abaqus and ARSA (Manko & Beben (2005)) are compared, it can be stated that the herein presented way of modelling of metal-soil bridge allows to obtain more satisfactory results. When both calculation programs were used, relative discrepancies amounted at 25–43% for displacements and 25–56% for stresses, with advantage to the model worked out by Abaqus. These differences result from the way of modelling in ARSA program, i.e.:

i. the CMP shell is modelled using the isotropic properties,
ii. the soil is modelled with use of the elastic, perfectly plastic model which uses the Mohr-Coulomb yield criteria,
iii. it uses simplified contact elements (friction coefficient only) to reflect interaction between metal-soil bridge elements.

The elaborated calculation model of a metal-soil bridge in Abaqus program makes it possible to obtain reasonable values of displacements and stresses despite the fact that in most cases they exceed the measured values.

5 CONCLUSIONS

As a result of numerical analysis of the metal-soil bridge in the Abaqus program and comparing the results with data from prior experiments and

calculations executed with use of the ARSA program, the following conclusions can be drawn:

a. The most extreme displacements of metal-soil bridge obtained from the Abaqus program were located at the shell crown (2.65 mm) and their courses was uneven (schemes I and II) with quite considerable local deformations. Whereas the maximum stresses amounted at 59 MPa and were observed at the haunch of the shell (scheme II). They approximated the maximum value obtained from experiments (52 MPa).
b. The calculated displacements and stresses exceed the values obtained from experiments. The shape of the displacements and stress curves does not generally differ from the one obtained from experiments. Relative differences between the calculated and measured values ranged from 3 to 28% for displacements, and 4–28% for stresses. However the calculation results are considerably more precise than the ones obtained from the ARSA program (Manko & Beben (2005)). Relative differences were contained within the scope of 25–43% for displacements, and 25–56% for stresses, with advantage to the model elaborated with use the Abaqus. It results from the fact that in the case of Abaqus program, the calculation model assumed a flat shell with orthotropic properties, the soil behaviour was better described (the Drucker-Prager model) and mutual interaction of metal-soil bridge elements was reflected in a more advantageous way.
c. The differences in the obtained test and calculation results may be due to:
   - inexact mapping of the soil in the calculation model (the exact physical and strength parameters were not known). Moreover the numerical analysis should take into consideration the influence of soil consolidation,
   - neglect to take the shell bevel into account in the numerical model, which diminishes the shell surface taking over loads from higher located soil layers,
   - complex geometry of the metal-soil bridge—then numerical model does not constitute an accurate image of the existing structure, numerous details have been omitted or simplified, such as corrugation profile, reinforce concrete reinforcements of the shell at the inlet and the outlet, as well as screw joints between the metal sheets.

REFERENCES

Abaqus. 2011. *Abaqus Theroy Manual. Abaqus 6.11*. Dassault Systèmes Simulia Corp., USA.

Abdel-Sayed, G., Bakht, B. & Jaeger, L.G. 1994. *Soil-steel bridges: design and construction*. New York: McGraw-Hill, Inc.

Beben, D. 2009. Numerical analysis of a soil-steel bridge structure. *Baltic Journal of Road and Bridge Engineering* 4(1): 13–21.

Beben, D. 2012. Numerical study of performance of soil-steel bridge during soil backfilling. *Structural Engineering and Mechanics* 42(4): 571–587.

Beben, D. & Stryczek, A. 2015. Numerical analysis of corrugated steel plate bridge with reinforced concrete relieving slab. *Journal of Civil and Engineering Management*, doi:10.3846/13923730.2014.914092.

El-Sawy, K.M. 2003. Three-dimensional modeling of soil-steel culverts under the effect of truckloads. *Thin-Wall Structure* 41(8): 747–768.

Elshimi, T.M. 2011. *Three-dimensional nonlinear analysis of deep-corrugated steel culverts*. Doctoral dissertation, Queen's Univ Kingston, Ontario, Canada.

Janusz, L. & Madaj, A. 2009. *Engineering structures from corrugated plates: Design and construction*. Warsaw: Transport and Communication Publishers.

Kunecki, B. 2006. Full-scale test of corrugated steel culvert and fem analysis with various static systems. *Studia Geotechica et Mechanica* 28(2–4): 39–54.

Machelski, Cz. 2008. *Modeling of soil-shell bridge structures*. Wroclaw: The Lower Silesian Educational Publishers.

Machelski, Cz. & Antoniszyn, G. 2004. Influence of live loads on the soil–steel bridges. *Studia Geotechica et Mechanica* 26(3–4): 91–119.

Machelski, Cz., Antoniszyn, G. & Michalski, B. 2006. Live load effects on a soil-steel bridge founded on elastic supports. *Studia Geotechnica et Mechanica* 28(2–4): 65–82.

Manko, Z. & Beben, D. 2005. Tests during three stages of construction of a road bridge with a flexible load-carrying structure made of Super Cor type steel corrugated plates interacting with soil. *Journal of Bridge Engineering* 10(5): 570–591.

Mellat, P., Andersson, A., Pettersson, L. & Karoumi, R. 2014. Dynamic behaviour of a short span soil–steel composite bridge for high-speed railways—Field measurements and FE-analysis. *Engineering Structure* 69: 49–61.

PN-EN 10149–2:2014–02. 2014. Flat products hot rolled with steels on high yield strength for cold forming. Part 2: Technical delivery conditions for thermomechanically rolled products. Warsaw: Polish Committee of Standardization.

Sargand, S., Masada, T. & Moreland, A. 2008. Measured field performance and computer analysis of large-diameter multiplate steel pipe culvert installed in Ohio. *Journal of Performance of Constructed Facilities* 22(6): 391–397.

Skrzat, A. 2010. The modelling of linear and nonlinear problems of mechanics of deformable body and heat transfer in the ABAQUS. Rzeszow: Rzeszow University of Technology Publishing House.

Taleb, B. & Moore, I.D. 1999. Metal culvert response to earth loading. Performance of two-dimensional analysis. Transportation Research Record, No. 1656, *Journal of Transportation Research Board*: 25–36.

Yeau, K.Y., Sezen, H. & Fox, P.J. 2014. Simulation of behavior of in-service metal culverts. *Journal of Pipeline Systems and Engineering Practice* 5(2) http://dx.doi.org/10.1061/(ASCE)PS.1949–1204.0000158

Zienkiewicz, O.C. 1986. *Finite element method*. Warsaw: Arkady.

Recent Progress in Steel and Composite Structures – Giżejowski et al. (Eds)
© 2016 Taylor & Francis Group, London, ISBN 978-1-138-02946-0

Effect of endogenous deformations in composite bridges

G. Bertagnoli, D. Gino & G. Mancini
DISEG, Politecnico di Torino, Torino, Italy

ABSTRACT: Early age endogenous deformations due to concrete hydration heat, shrinkage and creep can represent a real cracking risk for composite bridge beams. The phenomenon is very complex and difficult to be taken into account by designers of composite bridges, as it takes place when material properties of concrete are quickly changing in time. Recommendations on this topic in design codes and literature are generally scarce and sometimes ambiguous; for instance, EN 1994-2 and SETRA Guidance book Eurocodes 3 and 4 give contradicting indications. The aim of this work is to perform three sets of non-linear thermo-mechanical analyses on three different bridges: a simply supported one with two-beam girder (50 m span) and two continuous ones, the first with two-beam girder (40 + 50 + 40 m spans), and the second with orthotropic box shaped section (60 + 80 + 60 m spans). The analyses will show the differences between the bridge typologies and will help to understand the relevance of the hyperstatic behaviour in continuous beams.

1 INTRODUCTION

Composite steel-concrete bridges are one of the most used solutions to cross spans between 30 and 80 m.

Their simple construction method, based on the realization in workshop of segments of steel beams, assembling of the steel girder on the ground of the construction site and launching of the steel girder using cranes, leads to short construction time. Furthermore, if the bridge overpasses a road or a railway, it does not require to close traffic in the undergoing line for a long period.

Most of the time composite bridges are designed according to the simply supported scheme in order to use materials in the best way, having steel working in tension and concrete working in compression.

This choice is based on the fact that if the concrete slab undergoes tensile stresses, it can crack reducing its stiffness of several times (sometime 4 to 10 times, depending on reinforcement ratio and stress state). This stiffness reduction changes in a sensible way the cross section properties (homogenized area, inertia and centroid position) of the bridge beam. If the bridge is built using a continuous beam static scheme, this stiffness reduction in cracked zones leads to a redistribution of stresses and to a sensible variation of the internal actions that should be used in design.

A correct evaluation of the cracked zones becomes then essential to achieve a correct design of the bridge. EN 1994-1-1 (CEN, 2004) recommends in clause 5.4.2.3 that appropriate allowance shall be made for the effects of cracking of concrete, stating that in regions where the extreme fiber tensile stress in the concrete due to the envelope of global effects exceeds twice the tensile strength, the stiffness of the section should be reduced neglecting the effect of concrete, both in ultimate and serviceability conditions.

Continuous beams are nevertheless becoming more attractive as they reduce the number of structural joints, improving the durability of the deck and reducing the maintenance costs. Moreover the use of continuous beams can grant two clear advantages:

1. construction of slender decks over the same spans (useful to increase clearance especially in case of river crossing), with the same stiffness of simply supported beams;
2. construction of longer spans (useful to avoid piers in river beds) with the same dimensions of simply supported beams.

Tensile stresses in the concrete slab can be generated by several different causes: direct actions, that is negative bending moment caused by permanent loads or traffic actions, but also indirect actions such as concrete shrinkage, daily or seasonal thermal effect and endogenous deformations related to early age behaviour of concrete.

Whereas direct actions can cause cracking almost only in continuous beams, indirect ones can occur both in continuous and in simply supported schemes.

Moreover, the internal actions (M, N, V) coming from indirect actions depend on the stiffness of the structure in a deeper way than the ones coming from direct actions. A correct evaluation of the actual stiffness of the bridge deck is then fundamental to understand the real effect of them.

Early age endogenous deformations, which occur during concrete hydration and hardening, are difficult to be taken into account during design of composite bridges as they take place just after slab casting, when material properties of concrete are quickly changing in time and creep is very intense.

Recommendations on this topic in design codes and literature (Ducret 1997, Gara & Dezi 2013) are generally poor and sometimes ambiguous. EN 1994-2 (CEN, 2005) states that short term elastic modulus and 20 K temperature difference between concrete slab and steel beam should be used. SETRA Guidance book Eurocodes 3 and 4 (Davaine et al., 2007) reduces the temperature difference to 10 K, but it gives no precise indication on the elastic modulus to be used.

Some researchers (Gara et al., 2013; Kwak et al., 2000a,b; Qiao, 2010) suggested models that take into account hydration heat, endogenous and drying shrinkage, providing a temperature curve for the first days after slab casting and transforming the effect of hydration heat into a kind of equivalent "thermal shrinkage".

These proposed approaches do not come from the research field of early age behaviour of concrete, but from the traditional approach to composite structures.

On the contrary, this paper grounds itself on a work of the same authors (Bertagnoli & Mancini 2015)extending to continuous beams girders the approach there applied to simply supported ones.

The aim of the present work is determining the effect of the static scheme (continuous or simply supported beam) on the crack sensitivity of the girder in the first days after casting.

A set of non-linear thermo-mechanical analyses, grounding on the early age concrete knowledge of the authors (Bertagnoli et al. 2009, Bertagnoli et al. 2011, Bertagnoli & Mancini 2012) is performed on three deck typologies.

The first one is a simply supported two-beam-girder (50 m span); the second is a continuous two-beam girder (40 + 50 + 40 m spans), and the thirdis a continuous orthotropic box shaped section (60 + 80 + 60 m spans).

The analyses will show the differences between the bridge typologies and will help to understand the relevance of the hyperstatic behaviour in continuous beams.

2 PHYSICAL MODEL

2.1 *Concrete hydration model*

The physical model used to describe concrete hydration in the present paper is the same presented by Bertagnoli & Mancini (2015), and will not be explained here in detail.

The slabs of the three decks have been divided, in vertical direction, into seven concrete layers of about 5 cm thickness. Each layer is characterized at a given time t, by the following parameters:

a. an hydration heat based degree of reaction r indicating the progress of the hydration reaction ($r = 0$ when concrete is pumped in the mould and $r = 1$ when hydration reaction is complete);
b. specific mechanical properties (Young modulus and tensile strength) according to the degree of reaction reached;
c. temperature that is function of the heat generation and heat dispersion phenomena;
d. specific shrinkage in function of the distance of the layer from the outer surface of the slab;
e. specific creep functions as a consequence of both the elastic modulus, as given in point b, and the distance of the layer from the outer surface.

2.2 *Shear connection model*

Simulating the cracking phenomena often observed in steel-concrete composite beams should also consider the time evolution of shear connection stiffness and strength. This aspect can be numerically simulated by employing finite element procedures (Zhang & Zhao 2013), but few experimental results are currently available in the scientific literature for validating the results of the aforementioned numerical predictions (Topkaya et al. 2004).

In the present work the authors follow the same approach already presented in 2015 (Bertagnoli et. al. 2015) that is an extension of the well-known Newmark's theory of steel-concrete composite beams in partial interaction (Newmark et al. 1951).

A bilinear approximation is used to model shear connection as can be seen in Figure 1.

The maximum shear force that can be transferred between steel profile and concrete slab, called P_{max}, is calculated according to Ollgard model (Ollgard et al. 1971).

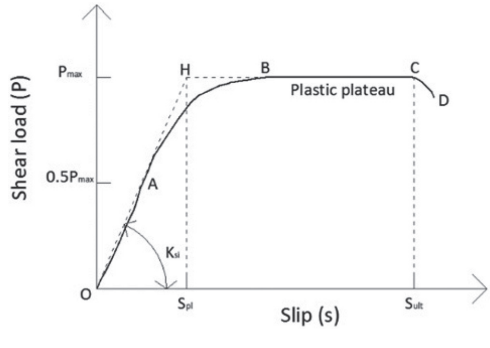

Figure 1. Bilinear model used for connection stiffness.

$$P_{max} = 0.5 A_{sh} \sqrt{f_c E v} \quad (1)$$

where A_{sh} is the cross section of the connection stud, fc is concrete compressive resistance and E_c is concrete Young modulus.

The initial elastic stiffness K_{si} and the ultimate slip S_{ult} can be calculated according to the model proposed by Oehlers (Oehlers & Coughlan 1986) as follows:

$$K_{si} = \frac{P_{max}}{d_{sh}(0.16 - 0.0017 f_c)} \quad (2)$$

$$S_{ult} = (0.48 - 0.0042 f_c) d_{sh} \quad (3)$$

where P_{max} is given by equation (1), d_{sh} is the diameter of the connection stud and fc is concrete compressive resistance.

In the present work, being both f_c and E_c function of time, P_{max}, K_{si} and S_{ult} result to be variable in time because of concrete hardening reaction.

An example of the evolution in time of the shear stiffness of the connection calculated for a C30 normal hardening concrete at 15°C and compared to the value at 28 days proposed by Oehlers is pictured in Figure 2. A fuse of three curves is presented considering an average value (A) and two extreme values, (L) and (F), respectively related to "Lento" and "Fast" development class for Young modulus and compressive strength, as it will be explained in the next paragraph.

2.3 *Parametric analysis*

A parametric study has been done in order to investigate which are the main factors that can control early age cracking in the concrete slab.

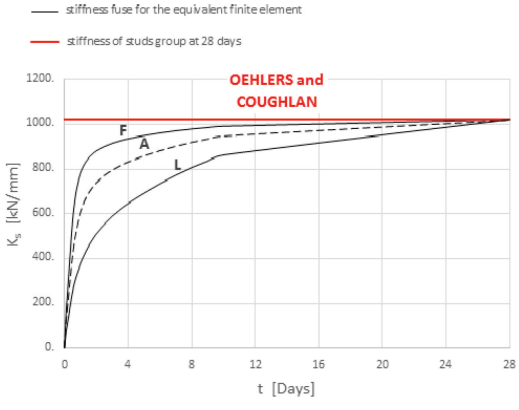

Figure 2. Evolution in time of connection stiffness.

The parameters that have been investigated are resumed in the following list:

1. three different decks;
2. three "hydration speed classes": Slow (S), Normal (N) and Rapid (R). They are respectively associated to the class of cement presented in table 5.1–9 of Model Code 2010 (fib 2013): "Rapid" to 42.5R, 52.5N and 52.5R, "Normal" to 32.5R and 42.5N, "Slow" to 32.5N.
3. three concrete strength classes: C30, C40 e C50. Nominal material strengths at 28 days are assumed according to Model Code 2010 (fib 2013).
4. three ambient temperatures: 5°C, 15°C e 25°C;
5. three "development classes" for tensile strength: Lento (L), Average (A), Fast (F) as described by Bertagnoli & Mancini (2015);
6. three "development classes" for Young modulus: Lento (L), Average (A), Fast (F) as described by Bertagnoli & Mancini (2015);
7. shrinkage and creep are calculated following Model Code 2010 (fib 2013) according to the data chosen for points 2 and 3.

A total of $3^6 = 729$ analyses have been performed.

A tree scheme of the parametric analysis is presented in Figure 3.

It must be underlined that the speed of concrete hydration reaction does not depend only on cement grinding, but also on cement type (Portland, blast-furnace, puzzolanic, composite), cement quantity and water/cement ratio.

As consequence, the association of the terms "Rapid", "Normal", and "Slow" concretes to Model Code 2010 cement classes has to be taken as a general indication. The values of the hydration parameters that are associated to "Rapid", "Normal" and "Slow" concretes in this study are derived from a database of concrete data obtained by the authors in several laboratory tests.

Creep has been modelled by means of a Kelvin-Voigt chain, calibrated on the formulations given by Model Code 2010 (fib 2013).

Shrinkage has been modelled in accordance with Model Code 2010 (fib 2013). Each layer of the slab is subjected to a different shrinkage law in function of his own notional size $2A_c/u$.

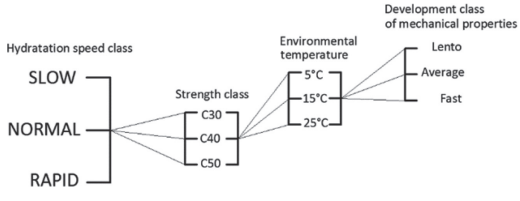

Figure 3. Parametric analysis tree.

The values of the notional sizes of intermediate layers have been calculated assuming a bi-linear variation within the thickness of the slab between the values of the most external and the most internal layer, and forcing the average to be equal to the one calculated for the slab as a whole(see Bertagnoli & Mancini 2015).

2.4 *Crack formation probability*

The probability of crack formation is related to the probabilities associated to the combined occurrence of the "development classes" Lento, Average and Fast (F-F, F-A, F-L; A-F, A-A, A-L; L-F, L-A, L-L) related to evolution in time of tensile strength and modulus of elasticity, where A-A is the most probable, F-L and L-F are of course the less probable.

A probabilistic study of the phenomenon is currently not available, so in the present work the probabilities of each combination is estimated by the authors on the basis of their own knowledge and engineering judgment. Their values are given in Table 1.

Table 1. Probabilities associated to "development class" combinations.

			Young Modulus		
			Slow	Average	Fast
			22.3%	55.3%	22.3%
Tensile strength	Slow	22.3%	5%	12.5%	5%
	Average	55.3%	12.5%	30.5%	12.5%
	Fast	22.3%	5%	12.5%	5%

3 DESCRIPTION OF DECKS' GEOMETRY

All the geometrical data of the three decks analyzed are given in the following paragraphs.

3.1 *Deck n°1: composite simply supported two-beam girder*

Deck n° 1 is a composite simply supported, single span, 50m long, two-beam girder, as shown in Figure 4. The main dimensions of the cross section are listed in Table 2.

3.2 *Deck n°2: composite continuous two-beam girder*

Deck n°2 is a composite continuous two-beam girder, as shown in Figure 3. It is 130 meters long and counts three spans: 40 + 50 + 40 m. The main dimensions of the cross section are listed in Table 3. The transverse inclination has been neglected in the present work, thus the deck is considered perfectly horizontal. Concrete slab depth is variable in transverse direction as shown in Figure 5.

Cross section is kept constant in segments between characteristic sections, whose position is listed in Table 4 (where AB1 is the first abutment, P1 is the first pier). Steelwork dimensions relative to each segment laying between the sections described in Table 4 are presented in Table 5.

3.3 *Deck n°3: composite continuous orthotropic box shaped section*

Deck n° 3 has the orthotropic box shaped section shown in Figure 6. It is 200 meters long and counts

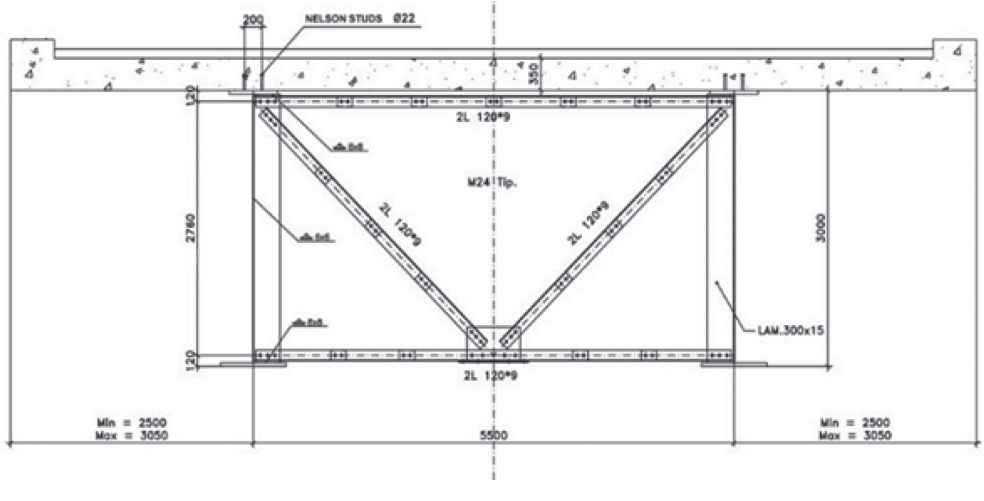

Figure 4. Deck n°1 cross section.

Table 2. Cross section dimensions.

Geometry	Unit	Value
Steel beam depth	m	2920
Top flange width	mm	450
Top flange thickness	mm	40
Web width	mm	2840
Web thickness	mm	12
Bottom flange width	mm	750
Bottom flange thickness	mm	40
Concrete slab width	mm	11
Concrete slab thickness	mm	350

Table 3. Cross section main dimensions.

Geometry	Unit	Value
Concrete slab width	m	12
Steel beam depth	mm	1900
Top flange width	mm	800
Bottom flange width	mm	1000

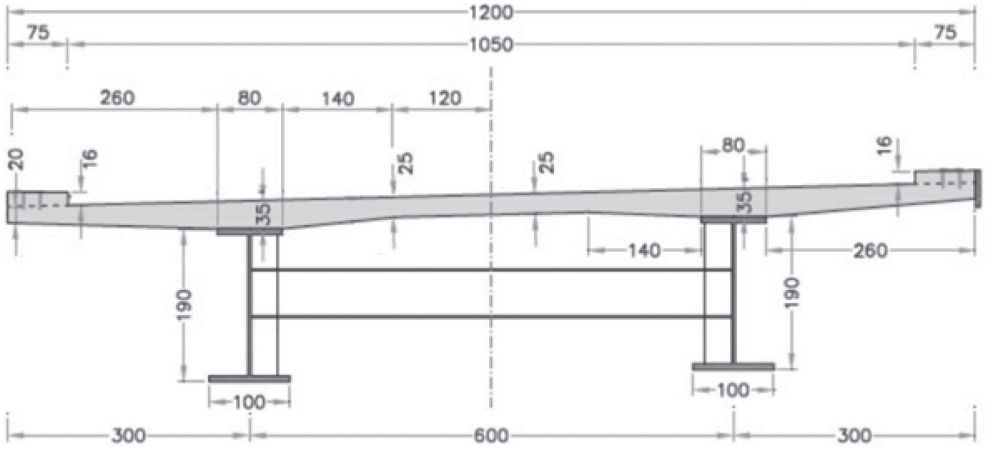

Figure 5. Deck n°2 cross section.

Table 4. Constant steel geometry sections.

Sections	Progressive [m]	Length [m]
AB1	0	–
A	8	8
B	22	14
C	28	6
D	36	8
P1	40	4
E	44	4
F	52	8
G	58	6
S (Symmetry)	65	7

Table 5. Thickness of beam steelwork.

	Thickness [mm]		
Sections	Top flange	Web	Bottom flange
SP1 to A	25	18	35
A to B	25	14	50
B to C	25	16	50
C to D	35	20	50
D to P1	65	24	65
P1 to E	65	24	65
E to F	35	20	50
F to G	25	16	50
G to S	25	14	50

three spans: 60+80+60m. The main dimensions of the cross section are listed in Table 6.

Cross section is kept constant in segments between characteristic sections, whose position is listed in Table 7 (AB1 is the first abutment, P1 is the first pier).

Steelwork dimensions relative to each segment laying between the sections described in Table 7 are presented in Table 8.

Concrete slab depth is variable in transverse direction as shown in Figure 6 and resumed in Table 9.

Table 6. Cross section main dimensions.

Geometry	Unit	Value
Concrete slab width	m	12
Steel box depth	mm	2600
Top flange width	mm	1100
Bottom flange width	mm	5800
Bottom "T" stiffeners	mm	250 × 30

Table 7. Constant steel geometry sections.

Sections	Progressive [m]	Length [m]
AB1	0	–
A	40	40
B	50	10
P1	60	10
C	68	8
D	76	8
E	86	10
S (Symmetry)	100	14

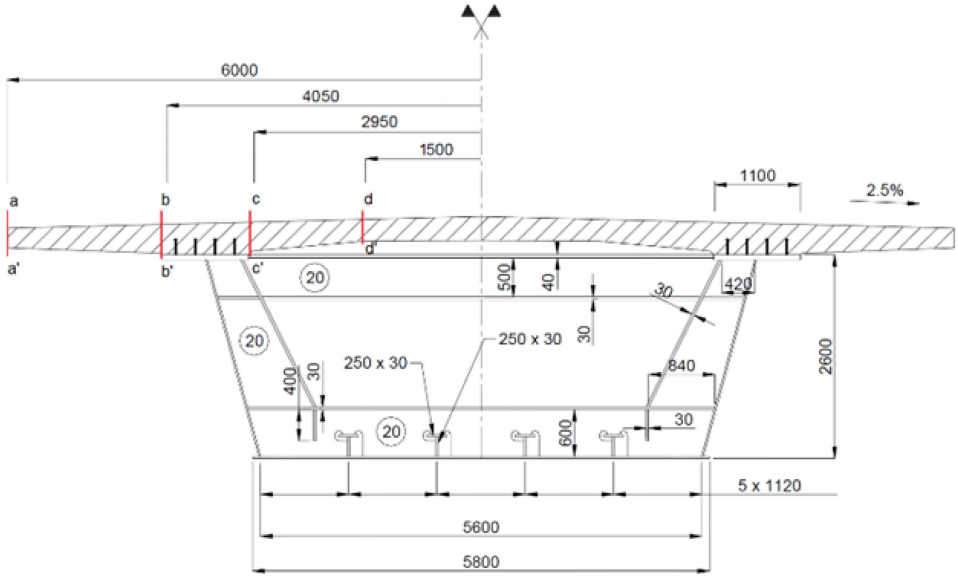

Figure 6. Deck n°3 cross section.

Table 8. Thickness of beam steelwork.

	Thickness [mm]		
Sections	Top flange	Web	Bottom flange
AB1 to A	35	18	20
A to B	65	23	25
B to P1	125	23	40
P1 to C	125	23	40
C to D	70	23	30
D to E	40	18	20
E to S	50	18	25

4 RESULTS

In the following paragraphs a summary of the results of the 729 non-linear analyses performed on the decks is reported.

Table 9. Slab variable thickness.

Sections	Thickness [mm]
a-a'	250
b-b'	389
c-c'	411
d-d'	280
s-s'	310

The results are presented in terms of cracking probability, cracking time range and tensile strength at cracking.

Cracking probability is calculated in relation to: cracking at slab bottom surface "I" (interface with steel beam), cracking at slab top surface "E", and cracking through slab thickness "T".

Cracking time is expressed as a time window in which cracking is likely to occur. The origin of the time axis is the casting time.

4.1 *Deck n° 1: simply supported two-beam girder*

The results in terms of cracking probability, cracking time range and tensile strength at cracking are presented in Tables 10–12.

Figures 7–9 show the evolution of residual stresses and concrete strength into the slab for a C30 – Slow concrete, whereas Figures 10–12 show the same results for a C30 Rapid concrete. All the

Table 10. Deck 1 – Slow concrete.

Class	T [°]	Cracking probability [%] I	E	T	Cracking Time [h]	Tensile Strength [MPa]
C30	5	22%	22%	22%	0÷32	0÷0.1
	15	0%	5%	0%	0÷11	0÷0.1
	25	0%	0%	0%	–	–
C40	5	22%	22%	22%	0÷29	0÷0.1
	15	0%	5%	0%	0÷6	0÷0.1
	25	0%	0%	0%	–	–
C50	5	22%	22%	22%	0÷27	0÷0.1
	15	0%	0%	0%	–	–
	25	0%	0%	0%	–	–

Table 11. Deck 1 - Normal concrete.

Class	T [°]	Cracking probability [%] I	E	T	Cracking Time [h]	Tensile Strength [MPa]
C30	5	0%	0%	0%	–	–
	15	5%	0%	0%	9÷20	0.1÷0.3
	25	17%	0%	0%	4÷16	0.1÷0.5
C40	5	0%	0%	0%	–	–
	15	5%	0%	0%	9÷20	0.1÷0.4
	25	17%	0%	0%	4÷16	0.2÷0.5
C50	5	0%	0%	0%	–	–
	15	5%	0%	0%	9÷20	0.2÷0.4
	25	17%	0%	0%	5÷16	0.2÷0.7

Table 12. Deck 1 – Rapid concrete.

Class	T [°]	Cracking probability [%] I	E	T	Cracking Time [h]	Tensile Strength [MPa]
C30	5	5%	0%	0%	9÷25	0.1÷0.3
	15	17%	5%	5%	4÷22	0.1÷0.4
	25	30%	17%	17%	3÷16	0.1÷1.0
C40	5	5%	0%	0%	9÷25	0.1÷0.3
	15	17%	5%	5%	4÷22	0.1÷0.5
	25	30%	5%	5%	3÷16	0.2÷1.1
C50	5	5%	0%	0%	9÷25	0.1÷0.3
	15	17%	5%	5%	4÷22	0.2÷0.6
	25	17%	5%	5%	3÷13	0.2÷0.9

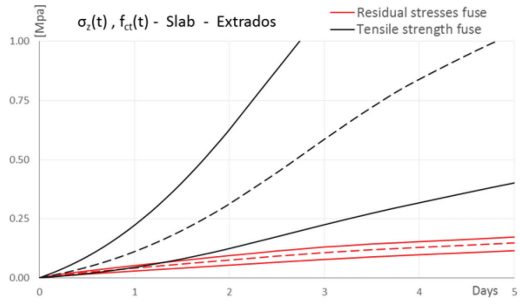

Figure 7. Evolution in time of stress and strength at slab top surface for C30 Slow concrete.

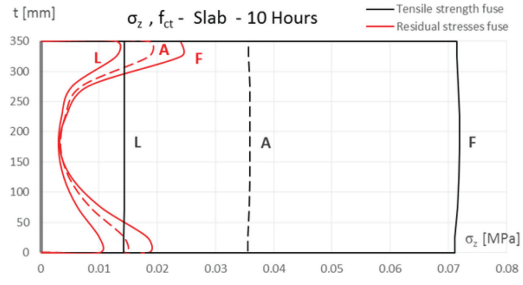

Figure 8. Stress and strength variation through slab depth 10 hours after casting for C30 Slow concrete.

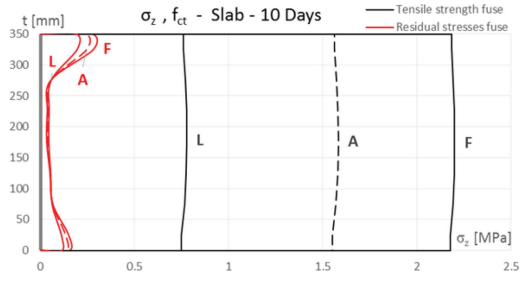

Figure 9. Stress and strength variation through slab depth 10 days after casting for C30 Slow concrete.

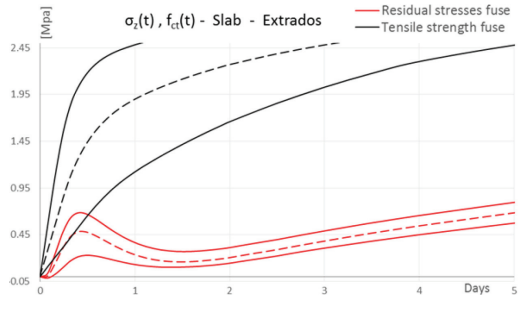

Figure 10. Evolution in time of stress and strength at slab top surface for C30 Rapid concrete.

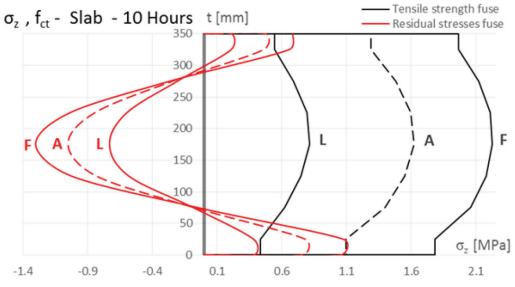

Figure 11. Stress and strength variation through slab depth 10 hours after casting for C30 Rapid concrete.

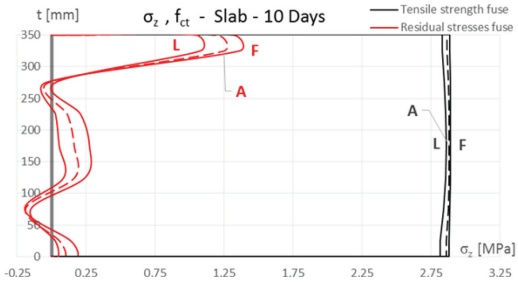

Figure 12. Stress and strength variation through slab depth 10 days after casting for C30 Rapid concrete.

Table 13. Deck 2 – Slow concrete.

Class	T [°]	Cracking probability [%] I	E	T	Cracking Time [h]	Tensile Strength [MPa]
C30	5	22%	35%	22%	0÷36	0÷0.1
	15	5%	5%	5%	0÷9	0÷0.1
	25	0%	0%	0%	–	–
C40	5	22%	35%	22%	0÷29	0÷0.1
	15	5%	17%	5%	0÷6	0÷0.1
	25	0%	0%	0%	–	–
C50	5	22%	22%	22%	0÷27	0÷0.1
	15	5%	17%	5%	0÷10	0÷0.1
	25	0%	0%	0%	–	–

graphs are referred to the middle span cross section of the deck.

The envelope of tensile stresses is plotted in red whereas the envelope of tensile strength is plotted in black. Red and black envelopes, or "fuses", are characterized by two continuous curves and a dashed one. The continuous curves represent the Lento "L" and Fast "F" development classes, whereas the dashed one is used for the Average "A" one.

Table 14. Deck 2 – Normal concrete.

Class	T [°]	Cracking probability [%] I	E	T	Cracking Time [h]	Tensile Strength [MPa]
C3/0	5	0%	0%	0%	–	–
	15	0%	0%	0%	–	–
	25	0%	0%	0%	–	–
C40	5	0%	0%	0%	–	–
	15	0%	0%	0%	–	–
	25	0%	0%	0%	–	–
C50	5	0%	0%	0%	–	–
	15	0%	0%	0%	–	–
	25	0%	0%	0%	–	–

Table 15. Deck 2 – Rapid concrete.

Class	T [°]	Cracking probability [%] I	E	T	Cracking Time [h]	Tensile Strength [MPa]
C30	5	0%	0%	0%	–	–
	15	0%	0%	0%	–	–
	25	5%	17%	17%	8÷10	0.4÷0.5
C40	5	0%	0%	0%	–	–
	15	0%	0%	0%	–	–
	25	5%	0%	0%	7÷11	0.4÷0.6
C50	5	0%	0%	0%	–	–
	15	0%	0%	0%	–	–
	25	5%	0%	0%	7÷11	0.5÷0.7

Table 16. Deck 3 – Slow concrete.

Class	T [°]	Cracking probability [%] I	E	T	Cracking Time [h]	Tensile Strength [MPa]
C30	5	22%	35%	22%	0÷36	0÷0.1
	15	5%	5%	5%	0÷9	0÷0.1
	25	0%	0%	0%	–	–
C40	5	22%	35%	22%	0÷39	0÷0.1
	15	5%	17%	5%	0÷9	0÷0.1
	25	0%	0%	0%	–	–
C50	5	22%	22%	22%	0÷42	0÷0.1
	15	5%	17%	5%	0÷10	0÷0.1
	25	0%	0%	0%	–	–

4.2 *Deck n° 2 and 3: continuous beams*

The results in terms of cracking probability, cracking time range and tensile strength at cracking are respectively presented in Tables 13–15 for deck n° 2, and 16–18 for deck n° 3.

Figures 13–15 show the evolution of residual stresses and concrete strength into the slab for C30 –

Table 17. Deck 3 – Normal concrete.

Class	T [°]	Cracking probability [%] I	E	T	Cracking Time [h]	Tensile Strength [MPa]
C30	5	5%	5%	5%	0÷6	0÷0.1
	15	0%	0%	0%	–	–
	25	0%	0%	0%	–	–
C40	5	5%	5%	5%	0÷7	0÷0.1
	15	0%	0%	0%	–	–
	25	0%	0%	0%	–	–
C50	5	5%	5%	5%	0÷8	0÷0.1
	15	0%	0%	0%	–	–
	25	0%	0%	0%	–	–

Table 18. Deck 3 – Rapid concrete.

Class	T [°]	Cracking probability [%] I	E	T	Cracking Time [d]	Tensile Strength [MPa]
C30	5	0%	5%	0%	2÷5	0.4÷0.9
	15	0%	0%	0%	–	–
	25	0%	0%	0%	–	–
C40	5	0%	5%	0%	2÷4	0.5÷0.8
	15	0%	0%	0%	–	–
	25	0%	0%	0%	–	–
C50	5	0%	0%	0%	–	–
	15	0%	0%	0%	–	–
	25	0%	0%	0%	–	–

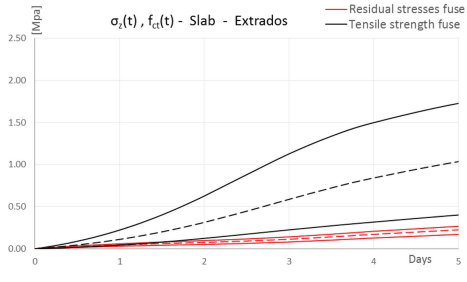

Figure 13. Evolution in time of stress and strength at slab top surface for C30 Slow concrete.

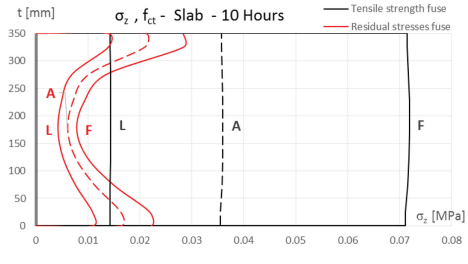

Figure 14. Stress and strength variation through slab depth 10 hours after casting for C30 Slow concrete.

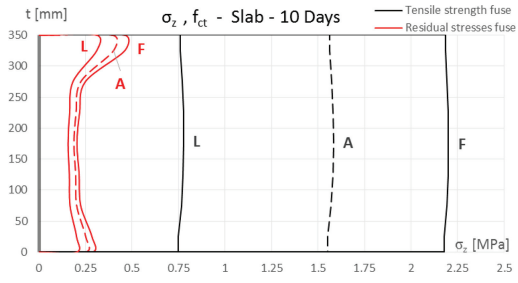

Figure 15. Stress and strength variation through slab depth 10 days after casting for C30 Slow concrete.

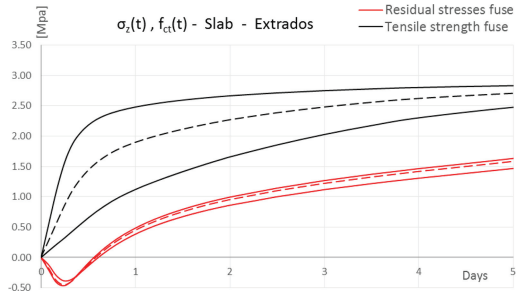

Figure 16. Evolution in time of stress and strength at slab top surface for C30 Rapid concrete.

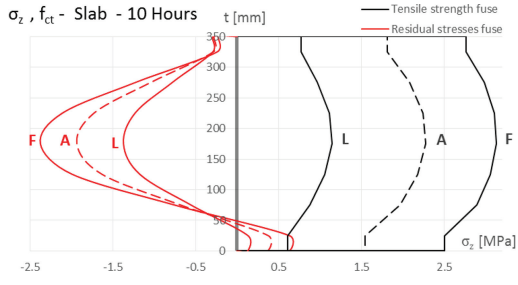

Figure 17. Stress and strength variation through slab depth 10 hours after casting for C30 Rapid concrete.

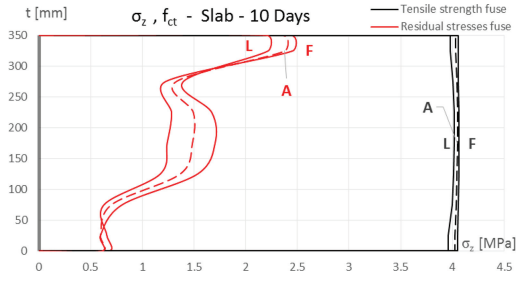

Figure 18. Stress and strength variation through slab depth 10 days after casting for C30 Rapid concrete.

Slow concrete, whereas Figures 16–18 show the same results for a C30 Rapid concrete.

All the graphs are referred to the midspan of the central span of the 2nd deck. Very little differences in this group of results can be appreciated between deck n°2 and deck n°3, so only one set of figures is presented.

5 DISCUSSION

5.1 *Limits of the analysis*

The analyses presented in this work have the following limits:

- the same creep model has been used for all the layers of the slab. For each layer, Young modulus is variable in time according to degree of reaction, but creep has the same formulation;
- no interaction between concrete temperature reached during hydration and creep and shrinkage has been taken into account. Both of them have been calculated referring to ambient temperature;
- no effect of reinforcement in concrete slab has been considered;
- no construction phases have been taken into account. The slab of all three decks is cast in a single phase. This assumption can be reasonable for the first deck (210 m^3 of concrete), but it is not realistic for the second and the third ones (550 m^3 and 840 m^3 respectively);
- no effects of solar radiation or wind are taken into account. Concrete slab is supposed to exchange heat with the surrounding environment in calm air and shadow. A direct exposure to solar radiation may generate a thermal stress in the upper layer of the slab that is much higher than the ones taken into account in the present work.

5.2 *Cold climate behaviour*

Low Heat Concretes (LHC) are almost never used in cold climate, as hydration cannot develop quickly enough to grant proper quality of material.

The results of the present study confirm this use, showing that a high risk of cracking can be undergone in this situation: 22% in simply supported scheme beams, and 35% in continuous ones.

It is important to underline that for the authors of the present work cracking occurs when tensile stresses are higher than the average tensile strength of concrete f_{ctm}. Therefore, undergoing 35% of probability of tensile stresses higher than f_{ctm} means that a high number of cracks can be already found on the real structure, as tensile strength can be lower than f_{ctm} in many different points.

Furthermore, the present study does not deal the problems of deterioration of material properties when hardening takes too much time to complete due to cold.

LHC continuous beam bridges, both n°2 and n°3, seem to suffer from a higher cracking risk than simply supported beams in cold climates.

This phenomenon can be easily explained as LHC in cold climate do not develop enough hydration heat to contrast shrinkage in the first 2 days after casting. A shortening autogenous deformation is then present in the slab as shown in Figure 19.

This imposed deformation causes a positive imposed curvature on the beam as shown in Figure 19.

The hyperstatic answer to this imposed curvature generates a negative bending moment, which increases the tensile stresses in the slab as shown in Figure 20. Hence it is explained the worse behaviour of continuous beams respect to simply supported ones.

5.3 *Mild and hot climate behaviour*

Normal and rapid concretes showed lower cracking risks in mild and hot climates if used in continuous beams (5% crack probability) than if used in simply supported beams (17% cracking probability).

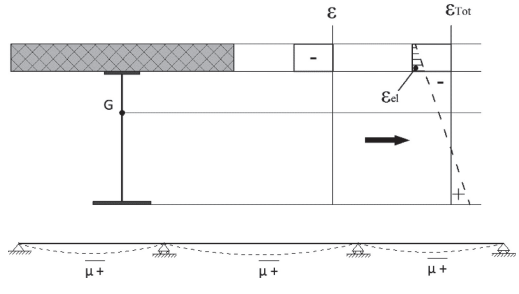

Figure 19. Shortening imposed deformation of LHC in first days after casting.

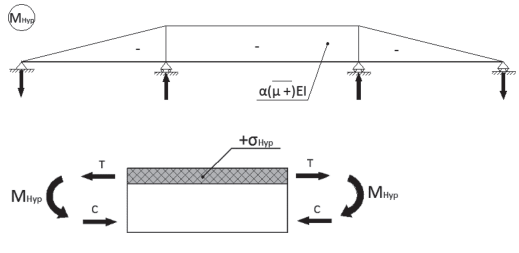

Figure 20. Hyperstatic effect associated to shortening autogenous deformation of the slab.

This result can be easily explained following the same steps seen in the previous paragraph.

In the first 2 days after casting, a swelling autogenous deformation takes place in the slab because of hydration heat, which has a bigger effect than shrinkage as shown in Figure 21. This imposed deformation causes a negative imposed curvature on the beam as shown in Figure 21.

The hyperstatic answer to this imposed curvature generates a positive bending moment, which increases the compressive stresses due to thermal swelling in the slab as shown in Figure 22.

Therefore, as a higher compression is achieved, shrinkage and cooling generate lower tensile stresses and the better behaviour of continuous beams respect to simply supported ones is then explained.

5.4 *Effects of shear connection deformability*

In addition, as a last issue, the effect of the deformability of the shear connection can be discussed.

The amount and the diameter of the studs was more than enough to transfer completely the actions coming from the slab to the steel beam, in each bridge as all the bridges were designed in full interaction scheme.

The magnitude of the forces exchanged between concrete slab and steel beam due to self-restrained autogenous deformation is quite small compared to the ones transferred at ultimate limit state.

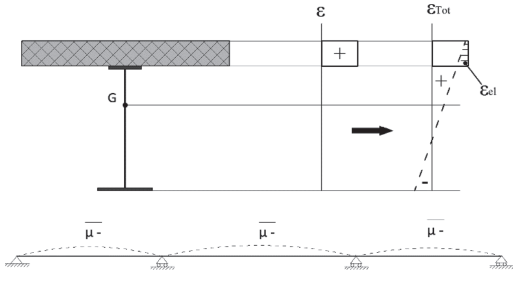

Figure 21. Swelling imposed deformation in first days after casting using normal and rapid concretes.

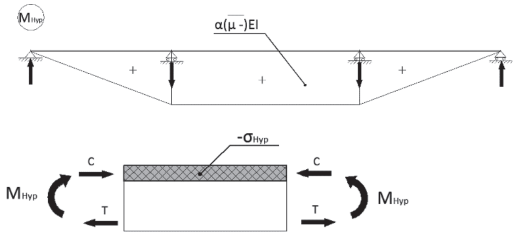

Figure 22. Hyperstatic effect associated to swelling autogenous deformation of the slab.

Therefore the connection remained always in the elastic field (K_{si}) of the bi-linear diagram shown in Figure 1.

On the other hand the stiffness of the connection is variable in time as it starts from a value close to zero just after casting and then reaches the values given in literature after some days.

The magnitude of the stresses in concrete slab calculated taking into account connection stiffness variation in time is about one half of the results obtained using the constant value (at 28days) of the connection stiffness during the whole analysis.

It can be therefore stated that shear connection deformability is a positive factor that works to reduce cracking risk and its contribution is more effective at early age, being the connection weak as concrete is soft, than at complete hardening.

In the studied bridges the deformability of shear connection has, in fact no effects at 28 days, being the connection very rigid, but has a positive effect between 0 and 3 days being much weaker.

6 CONCLUSIONS

A parametric analysis concerning early age endogenous deformations effect in composite steel-concrete bridges has been performed.

Simply supported beam scheme has been compared to continuous one.

The results show quite little differences between the bridge typologies: continuous beam seem to undergo a lightly lower cracking risk than simply supported ones.

The "hyperstatic effect" overall reduces the cracking possibility, except for the use of concrete with slow hydration speed in low ambient temperature conditions.

Concrete strength class (C30-40-50) plays no role in cracking control. All concrete strengths have more or less the same crack sensitivity: higher class means higher tensile strength but also higher elastic modulus.

Environmental temperature plays an important role. Low temperature enhances cracking risk if low heat concretes are used, especially in simply supported beams. Higher temperatures mean quicker hydration of concrete and higher cracking risk if rapid concretes are used in simply supported schemes.

Creep has also a big positive effect in the reduction of cracking risk. Early age creep ($t<3$ days) can be several times bigger than creep at $t>3$ days and reduces tensile stresses due to shrinkage and cooling of concrete.

Moreover the deformability of the shear connection at early age is an additional factor to reduce concrete stresses and therefore cracking risk due to self-restrained deformations.

REFERENCES

Bertagnoli, G., Mancini, G., Tondolo, F. 2009. Numerical modeling of early age concrete hardening. *Magazine of Concrete Research*, Vol. 61, No. 4, 299–307.

Bertagnoli, G., Mancini, G., Tondolo, F. 2011. Early age cracking of massive concrete piers. *Magazine of Concrete research*, Vol. 63, No. 10, 723–736.

Bertagnoli, G., Mancini, G. 2012. Autogenous deformations in massive concrete structures, *RILEM-JCI International Workshop on Crack Control of Mass Concrete and Related Issues concerning Early-Age of Concrete Structures—CONCRACK 3 - Control of Cracking in Concrete Structures 3*, Paris, 15–16 March 2012, 167–180.

Bertagnoli, G., Mancini, G.2015. Effect of Endogenous Deformations in Composite Bridge Beams. *16th European Bridge Conference*, Edimburg: Engineering Technics Press, 1–13.

Bertagnoli, G., Gino, D., Martinelli E. 2015. Predicting Early Age Cracking of Steel-Concrete Composite Beams in Partial Interaction. *XXV Giornate Italiane della Costruzione in Acciaio*, Salerno, 1–3 October 2015.

CEN, Comité Européen de Normalisation. 2004. EN 1994-1-1. Eurocode 4: Design of composite steel and concrete structures—Part 1–1: General rules and rules for buildings.

CEN, Comité Européen de Normalisation. 2005. EN 1994-2. Eurocode 4: Design of composite steel and concrete structures—Part 2: General rules and rules for bridges.

Davaine, L., Raoul, J., Imberty, F. 2007 Guidance book—Eurocodes 3 and 4 - Application to steel-concrete composite road bridges, Published by SETRA's (Service d' Études Techniques des Routes et Autoroutes) Collection, Paris.

Ducret J.M., Lebet J.P., Effects of concrete hydration on composite bridges, IABSE reports, n.999, 1997.

Fédération internationale du béton (fib). 2013. fib Model Code for Concrete Structures 2010, Berlin: Wilhelm Ernst & Sohn.

Gara F., Leoni G., Dezi L., 2013. Slab Cracking Control in Continuous Steel-Concrete Bridge Decks, *ASCE Journal of Bridge Engineering*, 18(12), 1319–1327.

Kwak, H.G., Seo, Y.J., and Jung, C.M. 2000a. Effects of the slab casting sequences and the drying shrinkage of concrete slabs on the short term and long-term behavior of composite steel box girder bridges. Part 1. *Engineering Structures*, Vol. 22, No. 11, 1453–1466.

Kwak H.G., Seo Y.J., and Jung C.M. 2000b. Effects of the slab casting sequences and the drying shrinkage of concrete slabs on the short-term and long-term behavior of composite steel box girder bridges. Part 2. *Engineering Structures*, Vol. 22, No.11, 1467–1480.

Newmark N.M., Siess C.P., Viest I.M. 1951. Tests and analysis of composite beams with incomplete interaction, *Proc. of the Society of Experimental Stress Analysis*, 9(1), 75–92.

Oehlers D.J., Coughlan C.G. 1986. The shear stiffness of stud shear connections in composite beams, *Journal of Constructional Steel Research*, Vol.6, No. 4, 273–284.

OllgardJ.G., Slutter R.G., Fisher J.W., 1971. Shear strength of stud connectors in lightweight and normal weight concrete, *AISC Engineering Journal*, April 1971, 55–64.

Qiao, P., McLean, D., and Zhuang, J. 2010. Mitigation strategies for early-age shrinkage cracking in bridge decks. *Research Rep. WA-RD 747.1*, Washington State Dept. of Transportation, Olympia, WA.

Topkaya C., Yura J.A., Williamson E.B. 2004. Composite Shear Stud Strength at Early Concrete Ages, *ASCE Journal of Structural Engineering*, 130(6), 952–960.

Zhang Y., Li Y., Zhao Z. 2013. Effect of stud connector' s time-dependent shear strength on behavior of steel-concrete composite beams in construction stage, *Journal of Building Structures*, 34(8), 150–157.

Recent Progress in Steel and Composite Structures – Giżejowski et al. (Eds)
© 2016 Taylor & Francis Group, London, ISBN 978-1-138-02946-0

Quality of butt welds in bridges and fatigue classes according to European codes and testing

B. Wichtowski & J. Hołowaty
West Pomeranian University of Technology, Szczecin, Poland

ABSTRACT: The execution class for bridge main members is EXC3/4 and exceptionally EXC2. Quality levels for weld imperfections are qualified according to EN 1090-2 (quality level B+) and EN ISO 5817 (quality levels B, C and D). The latest edition of EN ISO 5817 gives additional requirements for welds subjected to fatigue. According to tests conducted on butt welds in railway bridges, many of them do not fulfill the standard requirements. The fatigue strength of welds with imperfections was assessed on four types of specimens and verified in accordance with the Eurocodes. Substandard welds should be treated individually either for rational repair or for the acceptability of imperfections.

1 INTRODUCTION

For main bridge members, taking into account the appropriate service category (type of actions) and production category (types of execution) as well as failure consequence classes according to EN 1993-1-1:2006/A1:2014 and EN 1090-2+A1:2012, the execution class is EXC3/4 and exceptionally EXC2. Welding such members should be undertaken according to the WPQR (Welding Procedure Qualification Record) and WPS (Welding Procedure Specification) for a given type and weld thickness. All welds should be Visually Tested (VT) throughout their entire length and non-destructive testing NDT of welds should be undertaken in two stages according to the WPS (Wichtowski & Hołowaty 2015).

The acceptance criteria for Weld Imperfections (WI) discovered in NDT tests, shall be taken according to EN 1090–2 (quality level B+) and EN ISO 5817:2014 (quality levels B, C, D). The latest edition of the standard EN ISO 5817 has introduced additional requirements for welds in steel subject to fatigue. Requirements on quality levels in order to meet the fatigue classes (FAT) are given. The value of the FAT fatigue class is the bear-able stress range $\Delta\sigma_C$ at N_C = 2 million cycles established for a 75% confidence level of a 95% probability of survival taking into account the standard deviations, the sample size and residual stress effects (Fig. 1). The so called S-N curves are the most common way to present fatigue test data and design curves. They are adopted in Eurocode 3 at the design stage. They are derived from fatigue test data obtained under constant amplitude loading from welded specimens, by statistical analysis.

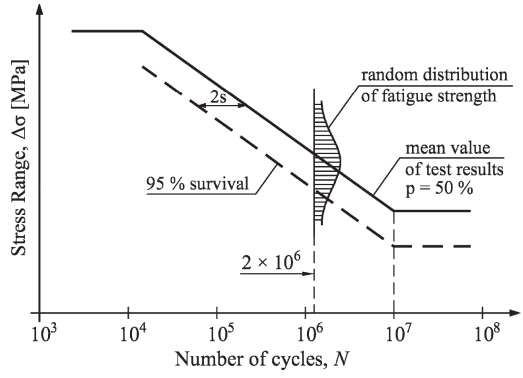

Figure 1. Statistical approach to fatigue strength curves (S-N).

Usually, the design is based on a lower curve, two standard deviation below the mean value (Kozłowski et al. 2009, Macdonald 2011).

For structures subjected to dynamic actions and verified for fatigue the imperfection class of welded joints and values of the FAT fatigue level should be given in the design. Cases of Weld Imperfections (WI) revealed during testing and exceeding the limit value should be assessed individually in order to decide on repair or on tolerance. The aim of the paper is to acquaint designers with published examples of the quantified service category (fatigue) for bridge structures in accordance with the execution class and laboratory tests of welds with substandard service categories. The information may be useful in preparing the Welding Procedure Qualification Record WPQR.

2 FATIGUE REQUIREMENTS FOR BUTT WELDS AND THE CODE DATA

The requirements for welds in structures subjected to fatigue are included in Annex C (informative) in the new edition of EN ISO 5817 published in 2014. Additional requirements are given for quality levels which meet the FAT fatigue class criteria.

With reference to welds with quality C and B, the FAT fatigue class is supplemented. Quality level C63 refers to FAT 63 and lower levels ($\Delta\sigma_C \leq 63$ MPa). Level B90 refers to FAT 90 and lower (63 MPa $< \Delta\sigma_C \leq 90$ MPa), and B125 refers to FAT 125 and lower (90 MPa $< \Delta\sigma_C \leq$ 125 MPa). Levels C63 and B90 include both butt welds and fillet welds, but level B125 only includes butt welds. In the case of levels C63 the additional requirement refers only to an angular misalignment (508), i.e. misalignment between two welded pieces such that their surface planes are not parallel or at the intended angle. Level D is not supplemented.

Limit values for imperfections within classes C63 and B90 given in Annex C to ISO 5817:2014 are taken according to tests and are included in IIW (Hobbacher & Kassner 2010). The FAT fatigue classes for different types of welded joints in IIW are analogous to the values given in EN 1993-1-9:2007 – Table 1 and Nussbaumer et al. 2011.

For a bridge designer, in the initial estimation of FAT fatigue levels for the bridge members the results obtained in the assessment of service categories depend on the level of design actions (Tab. 2) and structural detailing (Tab. 3). The issue is presented according PD 6705–2: 2010.

In Table 2 the static utilization factor k, is the ratio of the Ultimate Limit State (ULS) design action on the member cross-section or joint divided by its design resistance. Where the resistance depends on an interaction formula for more than one stress mode, a pro-rata value of k should be used as the limit. This should apply to all static failure modes at the joint or member. The minimum required value of $\Delta\sigma_C$ is the lowest value for which the damage $D_L \leq 1$ for safe life design (see EN 1993-1-9). The quantified service category depends on the direction of stress fluctuation. The criterion does not apply to $\Delta\tau$. Table 3 gives indicative guidance only, assuming steel grades up to S355. For higher grades the categories are likely to increase proportionately to the steel grade. The actual maximum quantified service categories should be checked for each specified design.

The data included in Tables 2 and 3 allows the designer to approximately assess the quantified fatigue category for the bridge members and prepare guidelines for the welding technology as well as the range of the required testing after execution. It is advisable to include these tables in the planned national annex NA (informative) to the steel bridge design standard PN-EN 1993–2.

3 SERVICE CATEGORIES FOR BUTT WELDS IN TESTS ON FOUR TYPES OF SPECIMENS

Fatigue strength curves, relating to the applied stress range $\Delta\sigma$ and the resulting fatigue life in cycles N, are determined according to the formula:

$$\log N = \log C - m \log(\Delta\sigma) \tag{1}$$

where N = number of cycles of stress range $\Delta\sigma$; m = slope of fatigue strength curve, equal to 3 or 5; log C = constant, connected with slope value and notch category.

Fatigue strength curves (Fig. 1) are derived from experimental test data and take into account such factors as concentration of stress due to weld geometry, size and shape of bearable discontinuity, stress direction, residual stresses and metallurgic conditions. The limit values of weld imperfections in butt welds subject to fatigue for particular quality levels, determined from IIW tests (Hobbacher & Kassner 2010), are given in the EN ISO 5817:2014 and their fatigue strength categories $\Delta\sigma_C$ are shown in Table 1.

Wichtowski (2002) presented the condition of the butt welds in the main girders of 155 existing railway bridges located on Polish Railway lines. The bridges had been constructed between 1936–1975. Overall, 15,875 radiographs were taken. The quality levels C and D for 4123 butt weld sections were assessed, i.e. up to 26% of the joints tested. Cracks were discovered in 34 bridges on 437 radiographs, i.e. on 4.6% of the weld sections tested at these times. Some bridges were tested many times in intervals of 5 to 8 years and no crack changes or formations were observed. To explain this phenomenon, the fatigue strength tests were undertaken on specimens with butt welds. The specimens include imperfections discovered in welds tested in situ. The size and dimensions of the specimens tested are shown in Figure 2.

Four groups of butt welds were prepared for laboratory testing (Fig. 2):

- specimens marked "a" – with welds of quality level higher than D, the total number of specimens is 7 with weld imperfections = 2 × (1011) – longitudinal crack in the weld metal; 1 × (402) – lack of penetration; 4 × (4013) – lack of root fusion, naturally aged for 45 years' service life with infinite life fatigue strength $Z_{rj} = 101$ MPa;
- specimens marked "b" (15 specimens) – with butt welds of quality levels B and C with $Z_{rj} = 125$ MPa;

Table 1. Detail categories $\Delta\sigma_C$ for transverse butt welds.

$\Delta\sigma_C$	Constructional detail *	Transverse butt welds and backing bars in beams
112	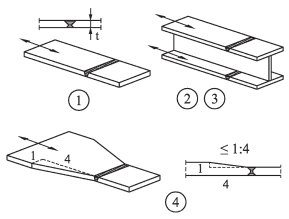	1 - Transverse splices in plates, flats and rolled sections; joints examined in 100 % without micro cracks on their surface. 2 - Plate girders as in 1 before assembly. 3 - Full cross-section butt welds of rolled sections without cope holes. 4 - Transverse splices as in 1 with a slope ≤ 1:4; welded with run-on and run-off pieces, plate edges to be ground flush.
90	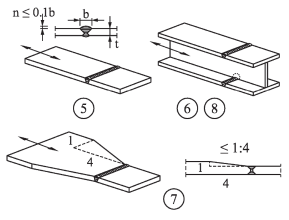	5 - Transverse splices in plates or flats executed in downhand position; height of weld convexity ≤ 10 % of the weld width. 6 - Transverse splices of beams with or without cope holes. 7 - Transverse splices in plates or flats with a slope ≤ 1:4. 8 - As detail 3 but with cope holes
80	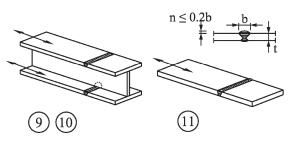	9 - Transverse splices in welded plate girders without cope hole. 10 - Full cross-section butt welds of rolled sections with cope holes. 11 - Transverse splices as in 4; height of weld convexity ≤ 20 % of the weld width.
63	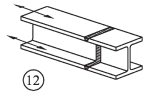	12 - Full cross-section butt welds of rolled sections without cope hole.
71	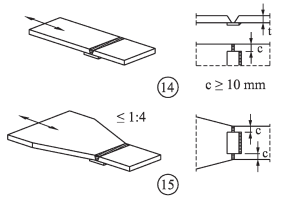	14 - Transverse splices executed with backing strips; fillet welds attaching the backing strip to terminate ≥ 10 mm from the edges of the plate. 15 - Transverse butt weld as in 8 with evenly transition of width and thickness.
50	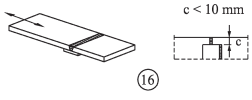	16 - Transverse butt welds as in 8, where backing strips fillet welds end < 10 mm from the plate edge.

*The arrows indicate the direction of the stresses occurring in the base material, in which case the stress range is calculated.

Table 2. Definition of quantified service categories for steel bridges according to PD 6705-2.

Level of service stresses		Quantified service category	Static utilization factor k		Minimum required value of reference fatigue strength $\Delta\sigma_C$
Static	Fatigue				
Reduced	Very low	F36	Tension	$k \le 0.6$	$\Delta\sigma_C \le 36$ MPa
		F36	Shear	$k \le 0.8$	
		F36	Compression	$k \le 0.8$	
Full	Low	F56	–	$k \le 1.0$	$\Delta\sigma_C \le 56$ MPa
Full	Significant	F71	–	$k \le 1.0$	$(56 < \Delta\sigma_C \le 71)$ MPa
		F90	–	$k \le 1.0$	$(71 < \Delta\sigma_C \le 90)$ MPa
		F112	–	$k \le 1.0$	$(90 < \Delta\sigma_C \le 112)$ MPa
		F140	–	$k \le 1.0$	$(112 < \Delta\sigma_C \le 140)$ MPa

Table 3. Typical examples of service categories in steel bridge members according to PD 6705-2.

Quantified service category	Application		
	Pedestrian	Highway	Railway
F56	Most ordinary types	Supporting towers and columns Main girders on medium to long spans Composite bridges with multiple girders	Main girders on medium to long span bridges with heavy ballasted or concrete decks
F71	Special cases where very susceptible to crowd or wind induced oscillation	Cross girders Short span non-composite bridges	Main girders on short span heavy ballasted deck bridges
F90		Steel decks with thin road surfacing	Main girders, cross girders and steel decks on short light weight steel bridges

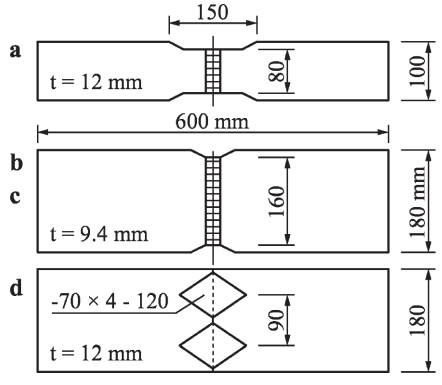

Figure 2. Four types of specimens with butt welds for laboratory testing.

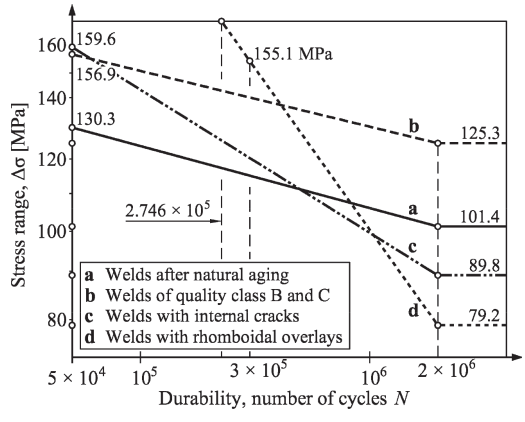

Figure 3. Linear regression for tested welded butt joints.

– specimens "c" (18 specimens) – with welds having longitudinal internal cracks (1011) of length = (14 to 145) mm, with fatigue strength $Z_{rj} = 90$ MPa;
– specimens "d" (16 specimens) – with one-sided cover diamond plates of quality level larger than D because of the weld imperfection (402) with length $l \approx 80$ mm, strength $Z_{rj} = 79$ MPa.

The test results on the welded specimens' linear regression are presented in Figure 3. The equations for the regression lines are calculated by the least square method for four types of butt welds:

– "a": y = 2.43343–0.06779x;
– "b": y = 2.48159–0.06088x;
– "c": y = 2.93535–0.15587x;
– "d": y = 4.12980–0.35407x.

To estimate the service stresses in the main girders of the bridges examined, static calculations were carried out according to Polish bridge standards PN-85/S-10030 (actions) and PN-82/S-10052 (design). In the case of seven plate girder bridges, the stresses under permanent actions, standard live loads and service load (ET21 locomotive) were calculated. Dynamic effects were taken into account. The calculated service stresses are in the range of 42.3 to 74.4 MPa and the stress $\lambda = \sigma_{ser.}/\sigma_{PN}$ in the case of flange joints is in the range of $\lambda = 0.532$ to 0.609, and in the case of web butt joints from $\lambda = 0.618$ to 0.694. The results of static calculation confirm the service stresses are lower than infinite fatigue strength Z_{rj} determined in butt weld joint tests (Fig. 3); they are lower even than the strength value $Z_{rj} = 90$ MPa determined for welds with internal longitudinal cracks in the weld metal (1011).

The fatigue strength values given in Figure 3 for four types of butt welds obtained under pulsing tension (cycle amplitude R = 0.1), are derived for different correlation coefficients: –0.59, –0.76, –0.78 and –0.87 respectively and confidence interval p = (80 to 90)%, by the Student's t-distribution. The question arises as to which detail categories are for the tested butt welds according to the before-mentioned recommendations of Eurocode

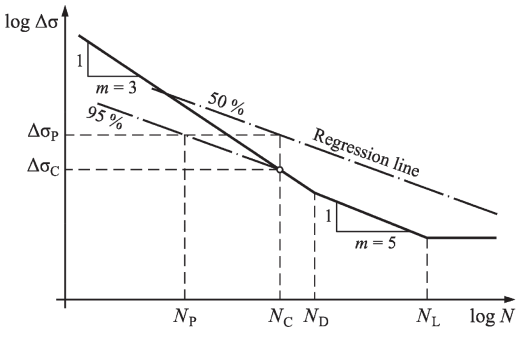

Figure 4. Scheme for determining notch category.

3, i.e. what is their service fatigue strength $\Delta\sigma_C$? Eurocodes 3 refers to EN 1990 for performing and assessment of tests but the standard does not specify how to construct the design S-N curves from tests.

The way to determine the fatigue category of the notch is given in the Czech standard ČSN 731401:1998. The sequence to follow according to Figure 4 is given below:

– the straight regression line is determined for confidence interval with probability p = 50% according to the equation:

$$x = \alpha + \beta y \tag{2}$$

– on the regression line for the number of loading cycles $N_C = 2 \times 10^6$ the stress range $\Delta\sigma_P$ is determined using the equation:

$$\Delta\sigma_P = \left(\frac{2.10^6}{10^\alpha} \right)^{\frac{1}{\beta}} \tag{3}$$

– the regression line of the confidence interval with probability p = 95% is reckoned,
– the number of loading cycles N_P is determined,
– for the number of loading cycles $N_C = 2 \times 10^6$ the notch category is calculated according to the equation:

$$\Delta\sigma_c = \Delta\sigma_P \left(\frac{2.10^6}{N_P} \right)^{\frac{1}{\beta}} \tag{4}$$

According to the above scheme the values given by equations (2), (3) and (4) are calculated and shown in Table 4. The stress range logarithm is considered to be the independent variable for Gaussian distribution, i.e. the fatigue strength

Table 4. Fatigue strength of tested welded joints, in MPa, at $N = 2 \times 10^6$; 5×10^6 and 10^8 loading cycles.

Type of weld	$\Delta\sigma_P$	$\Delta\sigma_C$	Z_{rj}	$\Delta\sigma_D$	$\Delta\sigma_L$
a	77.9	38	101	28.0	15.4
b	103.8	80	125	58.9	32.4
c	68.1	45	90	33.1	18.2
d	65.3	28	79	20.6	11.3

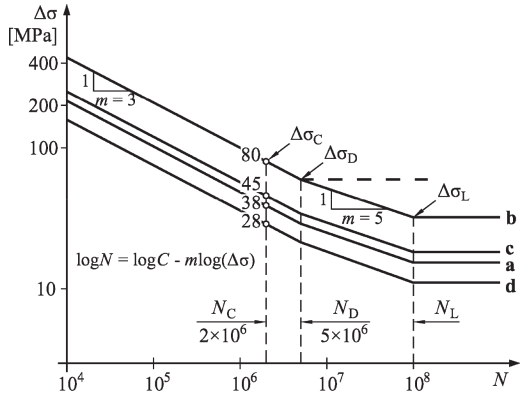

Figure 5. Fatigue strength curves for direct stress range (1) for the four types of tested butt welds (see Tab. 4).

is based on S-N curve which gives relationship between the stress range and the number of cycles at failure. Separate S-N curves are constructed for each detail.

Table 4 shows the stress range $\Delta\sigma_P$, the notch category $\Delta\sigma_C$ and the infinite life fatigue strength from tests Z_{rj}. Using the calculated notch category parameters, fatigue strength curve parameters were established (1), which are shown in Fig. 5, with values of stress ranges for constant amplitude fatigue limit $\Delta\sigma_D$ and cut-off limit $\Delta\sigma_L$ given in Table 4. The equations for the regression lines (2) at p = 50% in Tab. 4 and Figure 5 are equal to:

– "a": $\log N = 16.0921 – 5.1769 \log \Delta\sigma$;
– "b": $\log N = 25.4328 – 9.4889 \log \Delta\sigma$;
– "c": $\log N = 13.4953 – 3.9244 \log \Delta\sigma$;
– "d": $\log N = 10.2072 – 2.1527 \log \Delta\sigma$.

4 CONCLUSIONS

- Before the introduction of Eurocode 3 to metal structures design, the use of Z_{rj} values to determine the infinite life fatigue strength allowed for direct assessment of safe fatigue service conditions for structures.

- Eurocode 3 adopts a uniform system to determine FAT fatigue classes for different butt weld joints, also taking into account technological and metallurgic issues, but this requires a wider subject. The introduction of guidelines DVS 705 in Germany and Published Document PD 6705-2 in Great Britain seem to be right. These guidelines explain fatigue issues in NDT testing. This problem should be also taken into account in the planned National Annex to the Polish bridge standard.
- The determined fatigue categories for the four groups of tested butt welds were analyzed in Wichtowski (2002). But some points should be made:
  - o for welds of quality level B and C the estimated value $\Delta\sigma_C = 80$ MPa is analogous as in IIW tests (detail No 11 in Table 1),
  - o relatively high notch category $\Delta\sigma_C = 45$ MPa for butt welds with internal cracks is rather a surprise (Table 2),
  - o it is right that because of the lower value of notch category $\Delta\sigma_C = 28$ MPa, the butt welds with cover plates are forbidden in dynamically loaded structures.

REFERENCES

ČSN 731401:1998 Design of steel structures. (in Czech).

EN 1090-2+A1:2012 Execution of steel structures and aluminium structures—Part 2: Technical requirements for steel structures.

EN 1993-1-1:2006/A1:2014 Eurocode 3: Design of steel structures—Part 1–1: General rules and rules for buildings.

EN 1993-1-9: 2005 Eurocode 3: Design of steel structures—Part 1–9: Fatigue.

EN ISO 5817:2014 Welding. Fusion-welded joints in steel, nickel, titanium and their alloys (beam welding excluded). Quality levels for imperfections.

Hobbacher, A. & Kassner, M. 2010. On relation between fatigue properties of welded joints, quality criteria and groups in ISO 5817. IIW—document XIII-2323–10.

Kozłowski, A. (ed.) & Bródka, J. et al. 2009. Design and calculation of connections and joints in steel structures, vol. 2. Rzeszów: PWT. (in Polish).

Macdonald, K.A. (ed.) 2011. Fracture and fatigue of welded joints and structures. Cambridge: Woodhead Publishing Limited.

Nussbaumer, A., Borges, L. & Davaine, L. 2011. Fatigue design of steel and composite structures. Berlin: Wiley.

Published document PD 6705–2:2010. Structural use of steel and aluminium. Part 2: Recommendations for the execution of steel bridges to BS EN 1090–2.

Hołowaty, J. & Wichtowski, B. 2015. Testing of welded joints in steel bridges to European standards. 8th International Symposium on: Steel Bridges: Innovation & New Challenges 2015 (SBIC-2015). Istanbul, 14–16 September 2015.

Wichtowski, B. & Hołowaty, J. 2015. Tests of welded joints in steel bridges according to the requirements of PN-EN 1090–2 and PN-EN ISO 5817. Inżynieria i Budownictwo, in press. (in Polish).

Wichtowski, B. 2002. Fatigue strength of welded butt joints in steel railway bridges. PS Scientific Works No. 572, Szczecin. (in Polish).

Recent Progress in Steel and Composite Structures – Giżejowski et al. (Eds)
© 2016 Taylor & Francis Group, London, ISBN 978-1-138-02946-0

Fatigue of structural elements in steel bridges—theory and practice

A. Wysokowski
Road and Bridge Department, University of Zielona Góra, Zielona Góra, Poland

ABSTRACT: It is generally known that due to the nature of the service loads the transport infrastructure facilities are especially due to the phenomenon of fatigue. This concerns mainly steel engineering structures. Fatigue of steel structures is closely related to such important parameters as service safety and durability. In the paper author will discuss service issues related with the phenomenon of fatigue in these objects, and influence of corrosion on the fatigue durability and fatigue load capacity of steel structures specific to the bridge structures. These issues will be discussed, on the analyzes of examples of existing steel bridges in our country. The issues in the presented paper, have been referenced in the previous work of the author in this area including on the multiannual researches described phenomena on tested specimens in laboratory, structures in natural scale and in site.

1 INTRODUCTION

It is well known that due to the nature of the bridge loads they are particularly exposed to the phenomenon of fatigue. Fatigue of steel structures is closely related to such important parameters to them as safety and durability. These issues because of their importance, are the concern of many Research Centers — some of these were, among others, with the author of this paper for example: (Cywiński 1992, Czudek et al. 1980, Czudek & Wysokowski 2004, Czudek & Wysokowski 2005, Rymsza et al. 1994, Wysokowski & Budka 1989, Wysokowski & Ławniczak 1995, Wysokowski et al. 2009, Zobel et al. 2007).

Fatigue phenomenon reveals itself in a critical phase of fatigue cracks in structural steel, or in their joints (Rykaluk 2000, Wichtowski 2000). This leads, in such cases to exclude objects from the service.

The phenomenon of fatigue is intensified by further occurrence of corrosion, which is due to the operating conditions of bridges (including the negative environmental impacts of bad weather conditions) for steel is widespread.

For example, Figure 1 shows the construction of a railway bridge with advanced surface corrosion of main girders. The problem of corrosion fatigue is directly related to the concentration of stresses occur in the area of notches corrosive. Thus, the impact of corrosion on the fatigue life can be expressed by a change of the notch effect, which is the increase of the considered element or type of connection used in the present steel structure. These issues are described in detail by the author in his earlier works and technical research, among others (Czerpak A. et al. 1992, Wysokowski 1998, Wysokowski 2001a, Wysokowski 2001b, Wysokowski 2008).

Figure 1. An example of railway bridge in plan view with advanced surface corrosion of main girder.

It must be realized that the exploitation loads of bridges are random, moreover, there is a general trend of increasing service loads, both for railway and road bridges- vehicles are often overload. There are also a large number of vehicles with oversized load configurations, not included in the design of bridges.

It is also known that in engineering practice we are often faced with design faults, or defects. They are often in the form of geometric imperfections of structural steel elements, or in the form of the most common defects of welding connection joints. Therefore, these aspects should be specifically taken into account in the procedures related

to the determination of a proper assessment of the sustainability of the structure in terms of fatigue.

2 THE PHENOMENON OF FATIGUE IN STEEL BRIDGE ELEMENTS

During the service of steel structures, often appear specific cracks in their structural elements under the action of multiple cyclic loads that cause stresses even much smaller than the maximum durability of the material. This phenomenon is called fatigue, and the final effect of this phenomenon – the fatigue destruction.

Fatigue is reflected adversely on the work of construction, as it restricts to a greater or lesser extent, its durability, and in many cases leads to dangerous failure. There are many known examples of structure disasters caused by fatigue cracks, entail serious economic losses.

In order to detect the causes of the phenomenon of fatigue and quantitative assessment criteria for development, for a long time the test are carried out to minimize the probability of the appearance of fatigue cracks during the service life of bridge construction. The validity of the fatigue problems let by the fact, that in recent years the world has recorded an intimate increase of publications on fatigue issues with this range.

3 INFLUENCE OF THE IMPACT OF THE PHENOMENON OF FATIGUE ON CAPACITY OF STRUCTURES WITH EXECUTIVE IMPERFECTIONS

As generally known transport infrastructure facilities are designed and executed, and also allowed to operate on the basis of the relevant standards and regulations (PN-EN 1990, PN-EN 1090-1, PN-EN 1090–2). Despite the special technological regime for this type of construction is not, after all, to eliminate the imperfections on design, and performing stage, or even at the exploitation stage (Ziółko & Supernak, 2003). In Figures 2 and 3 are examples of imperfection of welds in steel bridges in service.

In order to carry out the analysis of the impact of the imperfections of welded connections, to their fatigue load the author has used the current standardized rules (PN-EN 1993–1, PN-EN 1993–2) as well as the results of earlier work on the subject(Wysokowski 2002).

According to the current standards (deployed and increasingly used in practice) PN-EN 1993–2 from the group of the fatigue assessment of steel bridges the design element for norm "lifetime" should be made on the basis of the following

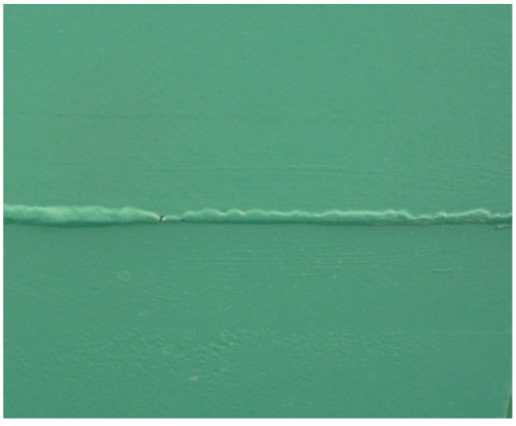

Figure 2. View of weld discontinuities of bottom flange of the main girder at mid-span in road bridge.

Figure 3. An example of the low-quality weld joining the stiffening rib with the bottom flange of the girder.

expressions associated with normal stresses, or shear:

$$\gamma_{Ff}\Delta\sigma_{E_2} \le \Delta\sigma_c / \gamma_{Mf} \tag{1}$$

where:

γ_{Ff} – partial coefficient for the loads, fatigue,

$\Delta\sigma_{E2}$ - equivalent stress amplitude in relation to the 2×106 cycles of changes fixed stress:

$$\Delta\sigma_{E_2} \le \lambda \cdot \Phi_2 \cdot \Delta\sigma_p \tag{2}$$

where:

λ – is the equivalent damage factor (depending on the type of beam, length effect, traffic intensity, the expected life of the bridge, etc.),

Φ_2 - is a dynamic damage equivalent,

$\Delta\sigma_p$ - is the scope of the design stress,

$\Delta\sigma_{(c)}$ - fatigue strength read from tables (fatigue strength curves) for which type of score,

γ_{Mf} - the partial safety factor for fatigue strength.

In order to carry out the appropriate analysis of the fatigue life for the construction of bridges for the purpose of this research in this paper is more convenient to use previously developed method presented by the author in the earlier work (Wysokowski 1989, 1995, 2001a).

This method is based on the same assumptions as terms of fatigue described in norm (PN-EN 1993-2 standard).

The author uses the previously obtained formulas to determine the fatigue life (in years)as following:

$$T = \frac{10^a}{\Delta\sigma_n^m \cdot 365 \cdot N_{\Delta n}^d} \tag{3}$$

where:

T – the durability of bridge fatigue expressed in years

a – fatigue curve parameter (depending on the type of notch) fatigue sensitivity,

$\Delta\sigma_n$ – range of service loadstrains,

$N^{(d)}_{(\Delta)(n)}$ - equivalent substitute cycles of stress in reduced by service load per day,

m - fatigue curves slope coefficient,

By comparing the theoretical norm durability T_n (in technical design) with real life T_1 for weld imperfections of the analyzed we get:

$$\frac{T_1}{T_n} = \frac{(\sigma_1)^m}{(\sigma_n)^m} \tag{4}$$

Using the described method for determining decrease in fatigue life the appropriate calculation was made.

This calculation was performed for several selected most-adverse imperfections of welds in the bridge objects in areas that are the subject of analysis (eg. Figures 2 and 3).

Analyzing the obtained results, it can be concluded very large decreases of fatigue life in relation to those established by the designer. They range for defective welds appears from 48% to 82%. In practice, this means that there is a real danger of fatiguecracks in the welds, even after a period of nearly twenty years of service. It will depend of course on the durability of these structural elements.

Underestimation of this issues according to the author's experience, which sometimes occurs especially with an intense railway loads, can lead to fatigue cracking, and thus the necessary emergency repairs of the bridge objects.

4 INFLUENCE OF CORROSION ON FATIGUE

The load capacity of steel bridge constructions depends not only on the phenomena of fatigue, but also on corrosion of structural steel elements. On the basis of numerous steel bridges inspection (both road and railway bridges), which the author carried out (among others) in the framework of the Bridge Management System on behalf of the General Road Directorate, it follows that the effect of corrosion for these objects is dominant.

Corrosion phenomena in the context of the operational load must be considered in two aspects:

- in terms of loss of capacity as a result of the reduction in cross-section,
- in terms of so far underestimated stress concentration effect by the corrosion notches which reduce the fatigue capacity of structural elements.

The impact of these factors on the fatigue load capacity of structural elements of the bridges are shown in Figure 4.

Contrary to the influence of corrosion on the load capacity, the effect on the fatigue load capacity is a phenomenon relatively little explored. One of the reasons for this is the need to perform lengthy and laborious researches on many variable parameters. It is important at this clear identification of corrosive changes for test samples.

As part of the habilitation work, under the guidance of the author where conducted extensive studies on the impact of corrosion on the fatigue strength of conventional bridge steel (type St3M and 18G2 A). The described phenomenon can be called as **corrosion fatigue**. It is based on creation

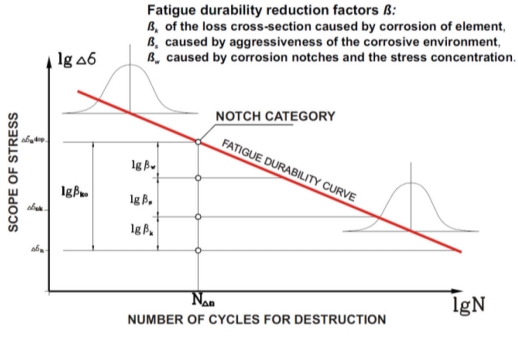

Figure 4. Effect of corrosion on fatigue capacity of structural elements of steel bridges.

of a fatigue crack, having its beginning in the **corrosive notch**, as shown in Fig. 5.

The study whose major results were presented in work (Wysokowski 2001a) showed a significant effect of corrosion phenomena on fatigue, thereby on load capacity of structural bridges. It has been shown by the fact that fatigue increases with the depth of the corrosion notches on the surface of the steel. The results of these studies the author used to support the simulation shown in Example 1 (section 5.2).

For example, below were presented the results of simulations carried out by the author of the occurrence of corrosion defects on the basis of field tests of the bridge located in the main railway line (Figs. 6 and 7).

The analysis allowed to determine the effect of the corrosion degree of individual structural steel elements on modification of geometric characteristics such as the moment of inertia and strength modulus. In particular was determined percentage decrease of the strength modulus on the background of cross-section loss caused by corrosion. The results of the analysis are presented on Figure 8.

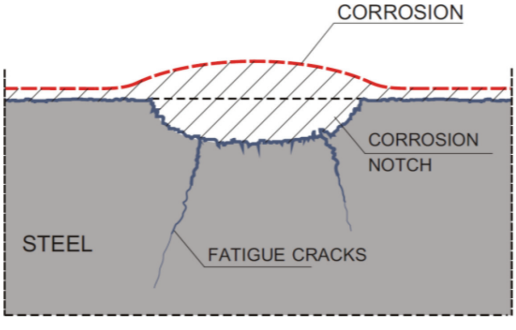

Figure 5. Example of the corrosive notch for the structural elements of steel bridges.

Figure 6. Overall view of the object to be analyzed in the main railway line.

Figure 7. Detail of one of the analyzed structural elements—the upper flange of stringer P5.

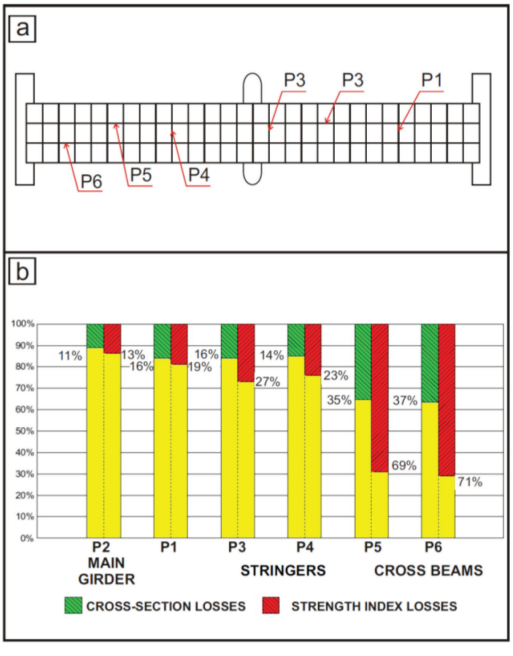

Figure 8. The influence of corrosion degree of structural steel elements in aspect of the modification of geometric characteristics: a) schema of analyzed bridge structural elements, b), the percentage decrease strength modulus of the background loss cross section induced by corrosion.

5 PRACTICAL EXAMPLES FOR DECREASING THE IMPACT OF FATIGUE AND CORROSION ON THE LOAD CAPACITY OF STEEL BRIDGES

5.1 *Introduction*

In the case of operated bridge structures there are many problems connected with the actual fatigue hazard of these structures.

For this reason, the practice of engineering in the field of fatigue issues involves the application of practical technical solutions in order to avoid possible of fatigue cracks. In the case of existing design solutions one of the ways is to reduce the level of strains in the structure elements. The author showed it on two practical examples in the paper below.

The first example shows a clearly beneficial effect uses a complex reinforced concrete slab, which reduces the level of fatigue hazard in old-useful steel girders. In this example, the author has used previously made by impact studies of corrosion on fatigue. These tests was done on corroded samples.

The second example is based on the idea of reducing the stresses for the popular, wide-operated in our country bridge structures with cellular beams. Because of their great fatigue risk was taken different ways to counteract this phenomenon.

5.2 *Example 1: Optimizing concrete slab*

In order to determine the possibility of reduce the impact of fatigue and corrosion on the load capacity service life of steel bridges with the assistance of optimization geometric cross-section including the influence of corrosion of steel girders, the author of the paper conducted an appropriate theoretical analysis. It was based on the tests of steel structure existing road bridge (Wysokowski et al. 2009).

These analysis was made by comparing the concept of two types of steel bridge structure with a reinforced concrete slab:

– Type A – without slant,
– Type B – with slants around the steel main girders.

For further analysis were used diagrams of the impact of corrosion on the fatigue life in a logarithmic scale (ln σ – ln (N f)) developed on the basis of fatigue tests on samples, taking into account varying degrees of corrosion, in the framework of habilitation dissertation of the author (Wysokowski 2001a).

The analyzes also based on modified material factor γ. Due to the expected degree of corrosion occurring in the steel grid according by the tests, for further analysis we assumed fatigue curves for the highest level of corrosion – typek2.

Taking into account the levels of stress for different types of cross-sections was determined fatigue sustainability with the influence of the impact of corrosion and fatigue caused by notches.

The calculated levels of stress on the bottom flange of the main steel girder for both types of bridges lab is shown in Figure 9.

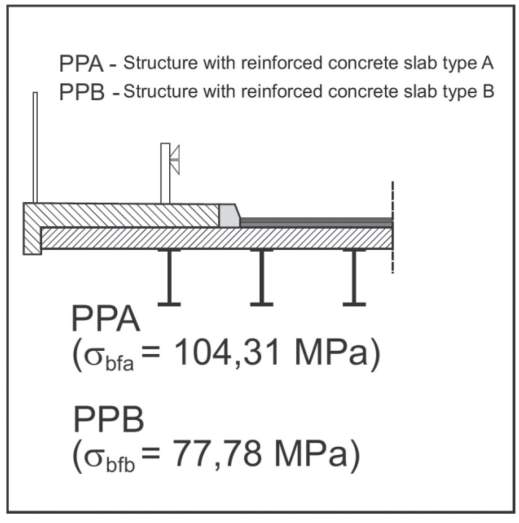

Figure 9. The stresses in the bottom flange of the main steel girder for two types of slab marked as PPA and PPB.

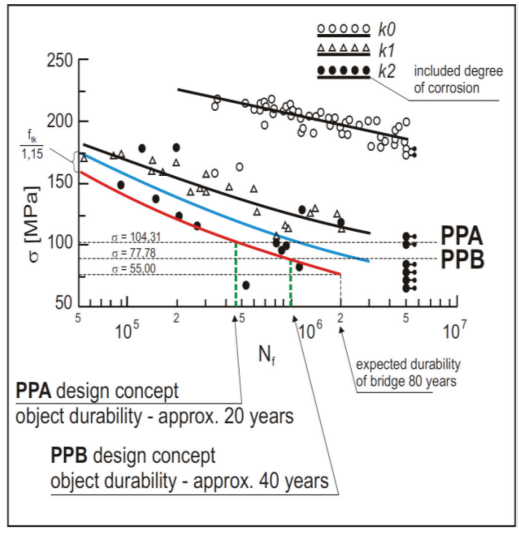

Figure 10. The designation of the fatigue durability of the analyzed bridge with the use of the impact of corrosion on fatiguegrapf for type of PPA and PPB cross-section.

The results of the analysis are presented on Figure 10 as a graph in double logarithmic scale.

On the basis of the analyzes was found that the fatigue life of cross-section with slab slants is twice longer than cross-section without slants.

5.3 *Example 2: Using the technical solutions reducing the stresses in structural elements*

The issue of fatigue mentioned in the paper, is directly related to the concentration of stresses occurring in sensitive areas of structural elements. In Poland, fatigue failures were related to widely used in bridge structures cellular steel beams called "Barzykówki".

These girders in cross-section characterized by a high number of stress concentration areas, and thus susceptible to the phenomenon of fatigue. Therefore, were developed many methods of reinforcing these elements.

In the first phase of reinforcing were used horizontal plates welded to the upper and lower edges of the web (Figure 11).

There after additional steel plates been used as an diagonal stiffener of web. Eventually to reduce the stresses in main girders have been used structural solution by using external pre-stressing of the structure with steel bar. The solution finally solved the problem of fatigue for the construction of this type. An example of the evolution of method reducing the phenomenon of fatigue of road bridge constructed with cellular girders is shown in Figure 12.

Figure 11. Detail of the connection of additional horizontal plates welded to the bottom flange of the girder-witch causes another fatigue area.

Figure 12. An example of the evolution of reducing the phenomenon of fatigue of road bridge constructed with cellular girders.

6 CONCLUSIONS

Due to the successive improvement of the standards of maintenance of transport infrastructure, as well as planned in our country in this field of investment, more and more attention is paid to durability. In the case of steel bridges important determinants of sustainability, is fatigue and corrosion as well as the level of maintenance.

The use of methods taking into account the impact of fatigue on the service life of the elements of bridge structures, whose results are reflected in the relevant standards helps to avoid phenomena of fatigue in the newly designed and operated designs. However, in practice we often deal with old structures and there are many geometrical imperfections and weld defects in their structures.

In addition, we are dealing with a phenomenon, which is negative, so for a loss of capacity, as well as for the phenomenon of corrosion fatigue. According to the research of the author, in this case is important significant decreases the magnitude of the fatigue life with regard to corrosion – in extreme cases even to more than 80% (as shown in the paper).

Under estimation this issue according to the author's experience, which sometimes occurs, especially with an intense railway load, can lead to fatigue cracking, and thus the necessary emergency repairs.

For this reason, the practice of engineering in the field of fatigue issues involves the application of practical technical solutions in order to avoid possible fatigue cracks.

In the case of existing design solutions there are ways to reduce the level of stresses, where the structure is subjected to during service. The author showed it on two practical examples in the second part of the paper. The first example shows an effect of using a reinforced concrete slab design of composite bridge, which reduces the hazard of fatigue in used steel girders. It is obvious that this is from a reduction of the level of stress in the bottom flange.

Underlining the significant size of this effect, which can be successfully used in future solutions to this type of composite structures (steel-concrete).

This is all the more important that, at present, due to the development of transport infrastructure in our country, strengthening and reconstruction shall be

subject to large number of bridges. How to strengthen them for the increased traffic requirements is often performed on existing steel composite structures.

According to the author should be carried out further intensive work on the present topic, because proper construction of objects and their maintenance undoubtedly raises the safety of users and extends the service life of bridge steel structures. Not without importance is the safety of these constructions. This is all the more important that this applies to objects in situated on roads and railways lines.

REFERENCES

Cywiński Z. 1992. Zur Korrosionsrate von Bausthal in alten Brücken. *Bauingenieur* 67/3.

Czerpak A., Czudek H., Pryga A. & Wysokowski A. 2003. Metoda szacowania wpływu korozji na nośność konstrukcji stalowych drogowych obiektów mostowych, Zalecenia GDDKiA. Zmigród: IBDiM. (The recommendations for method of calculating the impact of corrosion on bearing capacity of steel structures of road bridges).

Czudek H. & Pietraszek T. 1980. Trwałość stalowych konstrukcji mostowych przy obciążeniach zmiennych. Warszawa: Wydawnictwa Komunikacji i Łączności. (Durability of bridgesteelstructuresundervariableloads).

Czudek H. & Wysokowski A. 2004. Bezpieczeństwo konstrukcji drogowych mostów stalowych. *Krajowa Narada Mostowa. Kielce.* (The safety of construction of steel road bridges).

Czudek H. & Wysokowski A. 2005. Trwałość mostów drogowych. Warszawa: Wydawnictwa Komunikacji i Łączności. (The durability of roadbridges).

PN-EN 1090-1:2009 Wykonanie konstrukcji stalowych i aluminiowych - Część 1: Zasady oceny zgodności elementów konstrukcyjnych. (Execution of steel and aluminum structures - Part 1: Principles of conformity assessment components).

PN-EN 1090-2:2008 Wykonanie konstrukcji stalowych i aluminiowych - Część 2: Wymagania techniczne dotyczące wykonania konstrukcji stalowych. (Execution of steel and aluminum structures - Part 2: Technical requirements for the implementation of steel structures).

PN-EN 1990:2004 Podstawyprojektowaniakonstrukcji. (Basis of structural design).

PN-EN 1993-1-9:2007 Eurokod 3 – Projektowanie konstrukcji stalowych – Cześć 1–9: Zmęczenie. (Design of steel structures - Part 1–9: Fatigue).

PN-EN 1993-2:2006 Eurokod 3 – Projektowanie konstrukcji stalowych – Cześć 2: Mosty stalowe. (Design of steel structures - Part 2: Steel Bridges).

Rykaluk K. 2000. Pęknięcia w konstrukcjach stalowych. Wrocław: Dolnośląskie Wydawnictwo Edukacyjne. (The cracks in steel structures).

Rymsza J. 1995. Trwałość i model degradacji obiektu mostowego. *Inżynieria i Budownictwo* 10. (Durability and model degradation of the bridge structure).

Wichtowski B. 2000. Wnioski z badań blachownicowych mostów kolejowych z pęknięciami w złączach spawanych. *Inżynieria i Budownictwo* 10. (The conclusions of testing the flatted girder railway bridges with cracks in welded joints).

Wysokowski A &, Budka E. 1989. Ocena skutków zwiększenia obciążeń dróg krajowych na trwałość mostów stalowych. *Konferencja Naukowo – Techniczna pt. Trwałość i przydatność użytkowa konstrukcji mostowych. Poznań*. (The impact of increased loads on national roads on the durability of steel bridges).

Wysokowski A. & Ławniczak M. 1995. Zalecenia dotyczące oceny stanu powłok malarskich i korozji w konstrukcjach stalowych mostów drogowych. *IBDiM. Informacje i instrukcje* 52.Warszawa: IBDiM. (Recommendations for the assessment of the paintwork and corrosion in steel structures of road bridges).

Wysokowski A. 1989. Durability Aspects in the Design of Steel Highway Bridges. *IABSE Symposium "Durability of Structures". Lisbon vol. 51*.

Wysokowski A. 1995. Propozycja sprawdzania trwałości zmęczeniowej w nowelizowanej normie projektowania mostów stalowych PN/S–10052. *Inżynieria i Budownictwo* 7–8. (The proposal of checking the fatigue life of the amended standard design of steel bridges PN/S-10052).

Wysokowski A. 1998. Wpływ korozji na wytrzymałość zmęczeniową przęseł mostów zespolonych. *KonferencjaNaukowo-Techniczna "MostyZespolone". PolitechnikaKrakowska.* (Influence of corrosion on the fatigue strength of the composite bridge spans).

Wysokowski A. 2001a. Trwałość mostów stalowych w funkcji zjawisk zmęczeniowych i korozyjnych. *IBDiM Studia i Materiały* 53. Warszawa: IBDiM. (Durability of steel bridges as a function of fatigue and corrosion phenomena).

Wysokowski A. 2001b. Method of Assessing fatigue hazard to Steel Railway Bridges. *Engineering Transactions* 49(4): 459–483. Warszawa: PAN.

Wysokowski A. 2002. Effect of Fatigue on Durability of Steel Highway Bridges. *Archives of Civil Engineering* 48(1): 59–91. Warszawa: PAN.

Wysokowski A. 2008. Zmęczenie i korozja – wyznacznik trwałości eksploatacyjnej mostów stalowych. *Wrocławskie Dni Mostowe. Mosty stalowe. Projektowanie, technologie budowy, badania, utrzymanie.* Wrocław: Dolnośląskie Wydawnictwo Edukacyjne. (Fatigue and corrosion – the factors of service life of steel bridges).

Wysokowski A. Howis J & Wagner J. 2009. Przykład praktycznego uwzględniania zjawisk korozji i zmęczenia dla zabytkowego mostu zespolonego. *Konferencja Naukowo-Techniczna Zespolone Konstrukcje Mostowe.* Kraków: Wydział Inżynierii Lądowej Politechniki Krakowskiej. (An example of a practical taking into account the effects of corrosion and fatigue for the historic complex bridge).

Ziółko J. & Supernak E. 2003. Damage repair of the double shell tank. *Proceedings of the International Conference Design, Inspection, Maintenance and Operation of Cylindrical Steel Tanks and Pipelines.Prague - Kralupy nad Vitavou, Czech Republic*.

Zobel H., Alkhafaji T. & Wróbel M. 2007. Określanie trwałości mostów drogowych. *Mosty* 2. (Determining the sustainability of road bridges).

This page intentionally left blank

Structural steel, metallurgy and behaviour in fire

This page intentionally left blank

Recent Progress in Steel and Composite Structures – Giżejowski et al. (Eds)
© 2016 Taylor & Francis Group, London, ISBN 978-1-138-02946-0

Redistribution of internal forces generated in a steel frame structure with flexible joints when exposed to a fire

M. Maslak & M. Pazdanowski
Cracow University of Technology, Cracow, Poland

M. Snela
Lublin University of Technology, Lublin, Poland

ABSTRACT: The behaviour of a steel frame load-bearing structure with flexible beam-to-column joints when it is subjected to a fire is analyzed in detail in a current paper. In particular, both the qualitative and the quantitative evaluations are performed of the influence that the statical scheme, and especially the constraints placed upon the fire induced displacements of the considered frame members, exert on the redistribution of internal forces generated in such a structure as a consequence of the constrained thermal expansion. The obtained results clearly indicate that the growing deformation of the load-bearing structure is closely related to the way that this structure is loaded in a manner changing during a fire exposure. This relationship has to be considered, however, with taking into account the increasing flexibility of the heated joints. The identification of the frame failure modes potentially possible to occur under fire conditions as well as the evaluation of the risk of the occurrence of such the modes and also the assessment of their significance for structural safety are the main results of this investigation.

1 INTRODUCTION

The traditional way for evaluating the fire resistance of the steel frame load-bearing structures, based on the conceptual isolation of the particular structural components of the considered frame (such as the beams and the columns), with more or less precisely modeled boundary conditions assigned to these elements, and on the subsequent specification of the sought fire resistance for each of these components separately, usually does not lead to the sufficiently credible estimates. During the analysis of such a type one is incapable of correctly estimating the mutual structural interactions between the components identified beforehand. It is essential that those interactions can often determine the behaviour of the whole structure in fire conditions. This will be shown in a current paper. Thus, it is postulated that, if only possible for problems of the type considered here, the whole structure, or at least structurally and functionally homogeneous subcomponents of it, be analyzed as a whole. For instance the paper (Maślak & Snela 2013) represents an attempt at such, in a sense holistic, approach, in which in order to estimate the fire resistance of a beam in a frame, the action of adjoining columns is taken into account in an indirect manner. This allowed for the verification of the importance of a fire specific risk, consisting of generating in the considered beam at first of an axial compressive force increasing in value with growing steel temperature and thus pushing the columns outwards more and more (*push out effect*). In the later stage, indicated by the increasing beam deflection, this axial force slowly decreases in value, up to changing sign, and thus resulting in pulling action on the adjoining columns, deflecting these columns inwards (*pull in effect*). Such a horizontal force acting across the column axis, and additionally changing its sign during a fire, often determines the capability of the said column to resist the loads when exposed to a fire. Due to this phenomenon, reasonably precise estimation of the magnitude of this axial force plays an important role in a fire safety analysis of the considered load-bearing structure. It was shown in the paper quoted above, that taking into account all the factors affecting the redistribution of internal forces, including the joint flexibility increasing with raising steel temperature, may lead to the forecast axial force value halved in comparison to the axial force value determined by the simplified calculations only. Of course, the decreased value of the axial force immediately translates into the decreased risk of reaching in the considered frame the limit state of a fire resistance. One has to note however, that even the most precise modeling of the analyzed structure, taking into account many factors

affecting the forecast redistribution of internal forces, may not suffice to obtain the fire resistance estimate ensuring the reliability sought by the evaluator. In the formal model submitted for the analysis one has to sufficiently precisely imitate the nonlinear response of the considered structure to a fire exposure. This behaviour is due to the physical nonlinearity prescribing the response of the structural steel to high temperature influence and due to the geometrical nonlinearity induced by the large displacements and thus the large deformations of the structural components are considered. Thus, an attempt to attain a sufficient precision in forecasting of the real fire resistance for the considered frame forces an application of a time consuming iterative computational algorithm. The evaluator has at his hand a plethora of widely known computational approaches. But, as all these approaches are very time consuming, an application of the numerical routines is very convenient. The authors of this paper intend to apply such the routines to verify the independently proposed simplified analytical approaches. Such a verification should allow for the determination of the applicability limits and constraints for the simplified computational models popularly recommended for engineering practice as well as for the quantitative evaluation of the magnitude of an error inherent in the application of such the simplified models. A detailed analysis of the behaviour of a classical substructure in the typical steel frame subjected to a fire, focused on the observation of the process of the redistribution of internal forces induced by a direct fire exposure, constitutes an objective of this paper. The link between this process and the deformation level of the frame components, observed and changing during fire, is of special interest here. The potential risks, which may result in the considered structure reaching the limit state of a fire resistance will be identified as a result of a current work. This in turn will enable the authors to indicate the weak points of the structure threatened by a fire and subjected to the analysis. It has to be underlined here, that such the risks may be hardly distinguishable, if only simplified analytical models are used during calculations.

2 DESCRIPTION OF THE MODEL APPLIED AND OF THE COMPUTATIONAL ALGORITHM

As it was mentioned above, a typical subcomponent of a steel frame dimensioned and loaded as depicted in Fig. 1, was considered in detail. Two variants of the statical scheme, denoted with the symbols A and B, were analyzed separately. These variants differ in the way the column tops are supported. In the variant A (Fig. 1a) the top nodes of both frame columns may move freely in the plane defined by the undeformed structure. Thus both the horizontal translation and the vertical movement of these nodes in this plane are possible, as well as any combination of these displacements. However, these both nodes remain effectively constrained in the perpendicular direction, so as a result of this constraint they can not displace out of the plane defined by the considered structure. Of course, the constraints imposed on the displacements of the nodes only (the nodes both at the top and at the bottom of the columns—in the second case due to the rigid support), will not prevent the potential risk of out of plane buckling of these columns, as well as of other 3D forms of their instability. In the variant B (Fig. 1b) the top nodes of the frame columns may displace only in the vertical direction, while the displacements of these nodes in the horizontal direction are excluded. As in the case A, both nodes remain effectively constrained in the out of plane direction.

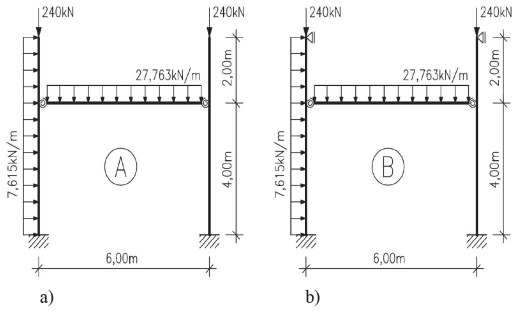

Figure 1. Variants of the steel frame substructure considered here. The column top nodes may displace freely in the in plane directions in the variant A, while in the variant B these nodes may displace only in the vertical direction of the same plane. All the existing supports in the out of plane directions are not denoted in Fig. 1.

In both variants of the steel frame substructure analyzed here, the connections of the beam and the columns are implemented via a flexible end-plate joint having the scheme and dimensions as depicted in Fig. 2. After application of external loads to the structural components, as depicted in Fig. 1, both the columns and the beam are subjected to a direct fire exposure. This exposure is conducted in such a manner, that in any moment of a fire-time the steel temperature in all components of the analyzed structure is equal both along the whole length as well in any cross section of the said components. The steel temperature increases monotonically, following the development of a fire. One has to be aware, that the assumption of a proportional temperature growth in the steel structural elements

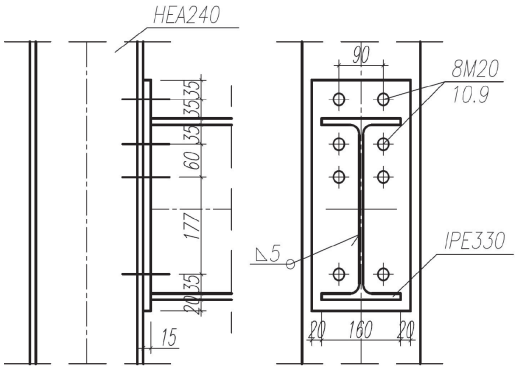

Figure 2. The statical scheme and the dimensions of the end-plate beam-to-column joint used in both variants of the steel frame substructure considered here.

constitutes a significant simplification of the analysis, since in the real fires the beams and the columns get heated with different speed because of having different cross sections. Nevertheless, the general conclusion that in the variant B the degree of the constraint imposed on the potential displacements of the frame components, generated in a fire due to the thermal expansion of structural steel, is substantially larger than in the variant A, seems to be especially important for the following deliberations. This difference in an obvious manner results in the much larger amplitudes of internal forces induced in the considered structure when subjected to a fire.

Numerical analysis was applied to investigate the fire behavior of the substructures depicted in Fig. 1. The analyzed structure was automatically subdivided into the 64025 three-dimensional finite elements (bricks and tetrahedral) without the mid-side nodes. Moreover, the average element size was separately adjusted to the dimensions of each meshed structural component, resulting in the components subdivided into between 300 (in the case of the bolts and the nuts) and 12800 (in the case of the lower part of a right frame column) elements. Regarding the material properties, the thermoplastic model of structural steel was applied to the analysis with basic parameters specified for the S235 low carbon steel and relating to the room temperature equal to 20°C. It was assumed that these steel properties, such as the yield limit, the Young elasticity modulus as well as the coefficient of thermal expansion, change with temperature as prescribed by the curves listed in the standard EN 1993-1-2 (CEN 2005). Due to the expected large deformations during the thermal part of the analysis the total Lagrangian formulation was used for the incremental and the nonlinear computations. The loads were applied to the frame in two steps, i.e. at first the whole static load was applied in the 80 consecutive increments at the reference temperature equal to 20°C, resulting in the initial configuration of the deformed frame, to which the thermal load was applied in the second step, again in the 80 identical increments, ending at evenly distributed steel temperature of the whole structure equal to 500°C. The iteration termination criteria at each load increment, both in the static and in the thermal part of the analysis, were assumed as the displacement only with the threshold value of 0,0005. In order to limit the calculation time, only the connections between the beam endplates and the column flanges were assumed as the contact ones, allowing for the separation and for the relative displacement, while all the remaining connections between the other structural components were assumed as the bonded ones.

3 ANALYSIS OF THE OBTAINED RESULTS

3.1 *Deformations of the structural components, rotations and displacements of the sections near joints*

The behaviour of the analyzed substructures is depicted in Fig. 3. One may observe the deformed configuration of the respective frame after application of the statical loads depicted in Fig 1 only (figures at left of Fig. 3a and Fig. 3b), and the final deformed configuration of the same frame in the steady state after uniform heating of all the structural components to the temperature of 500°C (figures at right of Fig. 3a and Fig. 3b).

In spite of the differences in scaling of the configurations compared, one may easily observe that the fire influence is manifested in distended columns and in raised beam. This is obviously the result of the thermal expansion of the steel components. In both variants the rotation of the column axis in the joint cross section is accompanied by the rotation of the beam axis. Due to the flexibility of the joint itself, the initial right angle between those two axes changes during the loading process.

Let us consider at first the situation before initiation of the fire, i.e. the situation corresponding to the deformed frame configuration depicted in Fig. 3a and in Fig. 3b at left. If only evenly distributed vertical loads were to act on the frame, then the beam would rotate around the bottom edge of the endplate (or around the axis of the bottom flange of the beam, depending on the geometrical properties of the joint components) with respect to the column axis, as a result of the joint flexibility, and the joint would "open" at the top. On the other hand, if only evenly distributed horizontal loads were to act on the column, then the beam would rotate around the top edge of the endplate

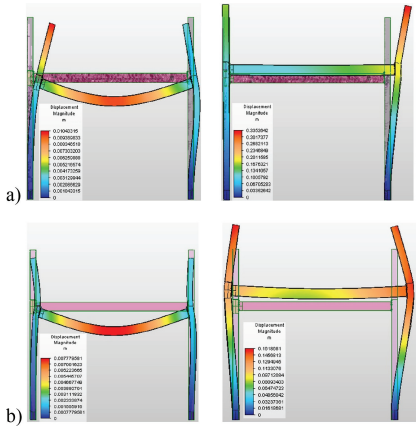

Figure 3. Deformations of the considered substructures. Fig. 3a pertains to the variant A of Fig. 1, while Fig. 3b pertains to the variant B of the same figure. At left—deformations after the application of the statical loads depicted in Fig. 1 only, at right—after the subsequent heating of all the frame components to the uniform steel temperature equal to. 500°C.

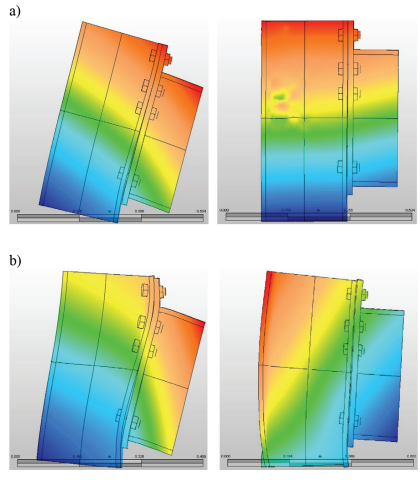

Figure 4. Deformed configuration of the left joint of the considered frame. Fig. 4a pertains to the variant A depicted in Fig. 1, while Fig. 4b pertains to the variant B. The configurations of the node after the application of the statical load depicted in Fig. 1 only are shown at left of Fig. 4a and of Fig. 4b, respectively, while the final configurations after the subsequent heating of all the frame components to the temperature of 500°C are shown at right.

(or around the axis of the top flange of the beam), with the joint "opening" at the bottom. Combination of both loading modes resulted in final rotation depicted in Fig. 4a and in Fig. 4b at left. Let us note that the axis of rotation for both cases is located approximately at the axis of the top flange of the beam. Gradual heating of the frame components resulted in the diminishing rotation of this type, in consequence changing the direction (and the sign). The same deformed joint is depicted in Fig. 4a and in Fig. 4b at right, after additional heating to 500°C. One will immediately notice, that in this case, especially in the variant B, the axis of rotation stabilized at the bottom edge of the end plate (when comparing the pictures indicated above, one should bear in mind, that the deformations are scaled differently, depending on the design scenario considered). The evolution of the direction and of the magnitude of the mutual rotation angle during the heating of the considered frame against the steel temperature is depicted in detail in Fig. 5.

The knowledge of the horizontal displacements of the columns (both the left and the right) in the areas adjacent to the joints is important for the analysis of the redistribution of internal forces in the considered substructure. These displacements increase monotonically with the increasing temperature of the frame components as a result of the thermal expansion of the beam pushing both such the columns outwards. In the following chapter of this paper it will be shown, that the rate of this expansion is high only in the initial stages of

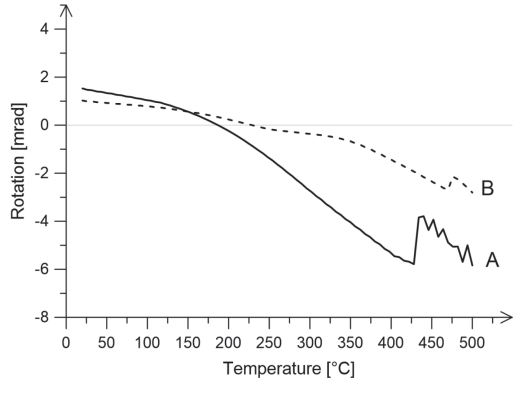

Figure 5. Change in the direction and in the magnitude of the mutual rotation angle at the left joint of the considered frame against the steel temperature in the frame components.

a fire. At higher values of the steel temperature the increase of the pushing out force is much less pronounced. As it was mentioned in the introduction to this paper, at higher temperature levels, the displacements of the beam are so large, that in a certain sense they compensate for this pushing out effect, pulling the joints together. The magnitude of the horizontal displacements in the column at the node determines the magnitude of the bending

moment in such a column. This will be analyzed in detail in the subsequent chapters of this paper. The dependence of the horizontal displacements of the left and of the right column, as measured at the level of the joint, on the temperature of steel in the frame is depicted in Fig. 6. Higher magnitude of the horizontal displacement on the right hand side of the frame is a result of the horizontal load (Fig. 1). Let us note, however, that the horizontal displacement in the variant A of the analyzed frame is in general unconstrained at the level of the beam, resulting in a very large displacement of the right joint accompanied by a very small displacement of the left joint (Fig. 6a). On the other hand, the constraints imposed upon the top ends of both columns in the variant B result in the more evenly distributed displacements at the left and at the right hand sides of the frame (Fig. 6b).

3.2 *Internal forces in the heated components of the frame*

Consideration of the changes occurring during the fire induced redistribution of internal forces in the elements of the structure as a result of the thermal expansion of steel is the key to the analysis presented here. A reasonably precise observation of the initially growing and then slowly diminishing axial force in the beam, pushing the both columns in an outward direction, and accompanied by changes in the shearing force in such the columns, immediately above and below the joint is of special interest. Corresponding changes in the bending moments in the columns and in the beam around the joints follow as a consequence of the variations in shearing and in axial forces. Due to the specifics of the numerical analysis performed in search of the generalized internal forces, three transverse cross sections located respectively:

- for the beam—to the right of the left frame endplate joint,
- for the left bottom column—immediately below the joint,
- for the left top column—immediately above the joint,

are considered. Thus only the results pertaining to the left joint will be presented during the following analysis. Of course, the cross sections indicated above are offset by a small distance (approximately 25 cm) from the theoretical center of the joint (as indicated by the intersection of the beam axis and the column axis) (see Fig. 4), and thus the values of the generalized internal forces obtained in these cross sections may not be used directly to verify the equilibrium of the whole joint.

Analysis of the evolution of internal forces in the components of the considered frame subjected to a fire exposure is begun with the presentation of the relationship between the axial force induced in the beam and the steel temperature. This relationship is depicted in Fig. 7. Please note, that in this figure the negative sign denotes the compressive force.

Due to the obvious reasons, the axial force induced in the beam is substantially higher for the variant B. In this variant the columns of a frame, supported at the top and at the bottom, exhibit much higher flexural rigidity. This in turn means, that the force needed to push them in the outward direction must be much higher. The greater degree

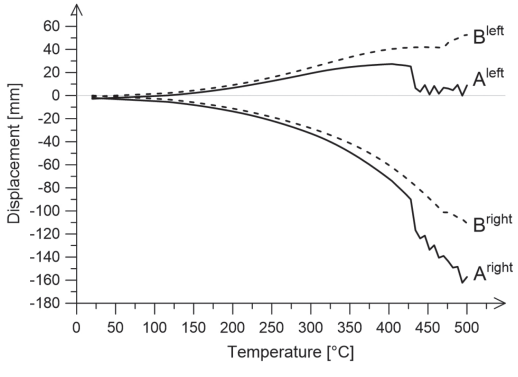

Figure 6. Relationship between the horizontal displacements of the columns at the level of the joints, and the temperature of the whole structure. Results computed for both A and B variants of the frame are depicted for the left and for the right column, respectively. Leftward oriented displacements are considered as positive.

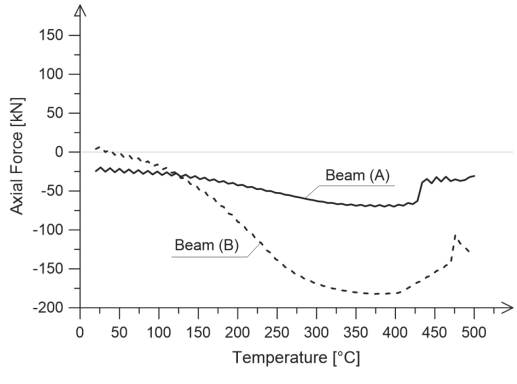

Figure 7. Relationship between the axial force induced in the beam of the considered substructure and the temperature of steel in the frame components. Solutions obtained for the variants A and B of Fig. 1 are shown separately.

of restraint imposed upon the potential displacements of the frame parts subjected to a fire directly affects the magnitude of internal forces induced in those parts. This is hardly a surprise. Let us note, however, that the growth ratio of the compressive force relatively quickly diminishes, and as the temperature nears 400°C this force starts to decrease in magnitude. This phenomenon shall be related to the temperature induced reduction of the yield limit in structural steel (evolution of this value is assumed to follow the piecewise linear approximation of the real curve, as listed in the code EN 1993-1-2 (CEN 2005)). Moreover, the reduction in the flexural rigidity of the beam, which was initiated a bit earlier, is already significantly important and gradually increases with raising temperature. As a result of this reduction, the displacements increase rapidly, and this in turn tends to negate the effect of the axial expansion of the beam initially pushing out columns by pulling the joints inwards (*pull-in-effect*).

The results depicted in Fig. 7 shall be considered in association with the relationship between the shearing force induced during a fire in the cross sections of the left column adjacent to the joint. These relationships are depicted in detail in Fig. 8.

Let us note, that in the variant A differences between the values of the shearing force specified for the upper and for the lower part of the column are very small. This is most probably due to the low magnitude of the axial force induced in the beam and pushing the columns in the outward direction. This conclusion, however, should not be applied to the results of the analysis obtained for the variant B. In this case the relatively large horizontal reaction in the top support of the column adds the influence to the global balance of internal forces. Nevertheless, the general conclusion holds for the both frame variants, stating that the slowing increase rate of the axial force in the beam is accompanied by the slowing increase rate of the shearing force in the both upper and lower parts of the column. Besides that, for the obvious reasons, the shearing force value determined for the variant B is substantially higher than the value of the same force obtained for the variant A. This is a result of more stringently constrained potential thermal displacements of the structural components, induced in a fire by the growing temperature of steel.

The internal force distributions, depicted in Fig. 7 and in Fig. 8, allow for a more unique and more precise interpretation of the bending moment redistribution in the components of the considered frame, occurring as a result of a direct fire exposure. This process is depicted in detail in reference to the increasing steel temperature, in Fig. 9 – for the substructure in the variant A (Fig. 1), and in Fig. 10 – for the substructure in the variant B. The traditional sign convention for the bending moments is applied in such the both figures. Let us recall, that with respect to the bending moments acting on the beam, in these both figures the value of this moment in the cross section adjacent to the joint is depicted, but not this relating to the beam mid-span.

Comparison of the results depicted in Fig. 9 and in Fig. 10 leads to the obvious observation, that in the case of the variant B the values of the bending moment induced in the frame are substantially larger. This is a result of the more stringent limitations enforced upon the potential displacements of the structural components subjected to a fire exposure. However, the conclusion regarding the quantitative differences in the redistribution process of bending moments itself seems to be more interesting. In the substructure in the variant A the upper parts of the columns may displace freely in the plane

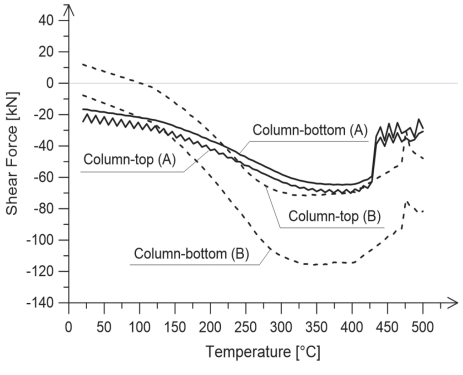

Figure 8. Relationship between the shearing force generated in a fire in the cross sections adjacent to the joint, in the upper and in the lower part of the left frame column, and the temperature of steel. Relationships pertaining to the variant A and to the variant B depicted in Fig. 1 are shown separately.

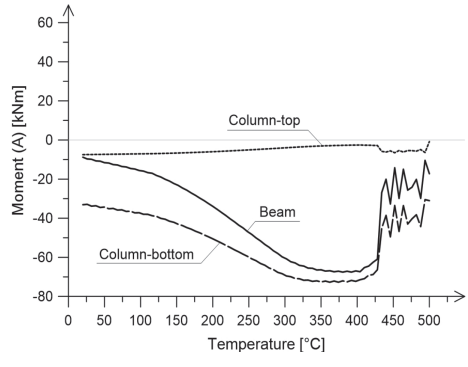

Figure 9. Redistribution of the bending moments in the cross sections adjacent to the joint, specified for the left joint of the substructure in the variant A (Fig. 1).

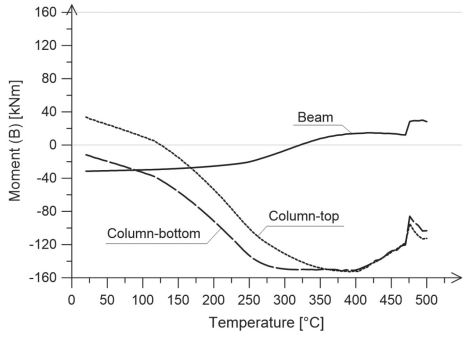

Figure 10. Redistribution of the bending moments in the cross sections adjacent to the joint, specified for the left joint of the substructure in the variant B (Fig. 1).

of the structure during a whole fire. Because of that, the bending moment values generated in these parts of the structure are very small. In addition, they tend to get even smaller when the steel temperature increases. Thus, the bending moment redistribution in the structure of this type results in almost whole bending moment acting on the lower part of the column transferred to the beam. Precisely opposite situation is dealt with in the substructure in the variant B (Fig. 1), where the column upper parts may displace freely only in the vertical direction during a fire. In this case, almost all the bending moment acting on the bottom part of he column is passed on to the upper part of the column. Let us also note the gradual decrease of the bending moments observed in the both variants (A and B) of the considered substructure, after the structure has reached the temperature of approximately 400°C. This phenomenon is a result of a gradual softening of the structural steel, due to the yield limit of steel decreasing in the high and growing temperature. According to the recommendations contained in the standard EN 1993-1-2 (CEN 2005), this phenomenon begins to be quantitatively significant at approximately this value of the steel temperature.

4 SPECIFICATION OF THE OBJECTIVE CHARACTERISTIC DESCRIBING THE JOINT FLEXIBILITY UNDER FIRE CONDITIONS

The joint flexibility, changing with changing steel temperature, plays an important role in the redistribution of internal forces occurring in the load-bearing structure subjected to a fire. The impact of this type is, however, usually neglected in the calculations. The authors of this paper have shown recently, that this simplification may result in the substantial overestimation of the forecast structural fire resistance (Maślak & Snela 2012, 2014). Taking into account both the quantitative and the qualitative influences of the joint rigidity decreasing in a fire as a basis for the objective fire safety analysis results in the need to determine the $M - \phi$ characteristic of such a joint, i.e. the bending moment—the rotation angle characteristic describing the joint behaviour when subjected to the applied load. The characteristic of this type depends on the joint temperature. This was shown experimentally and described in many works (Maślak & Litwin 2010). Thus a set of the analogous relationships is sought. Each of these relationships holds for a predetermined joint temperature. These relationships may be obtained via either the application of the classical component method generalized to the case of a fire (Maślak et al. 2015) or an appropriate correction of the a priori known relationship referring to the persistent design situation i.e. the scenario excluding the influence of a fire (Simões da Silva et al. 2001). These two approaches are not equivalent (Maślak & Snela 2015). In a current paper the relationships between the rotation angle of a flexible joint and the steel temperature, obtained for two variants (A and B) of the considered substructure are shown in Fig. 5. These relationships, however, refer to the preset level of external loads. Thus one may assign a certain value of the bending moment acting on the joint to the given steel temperature. In the analysis of the type mentioned above, a curve describing the relationship between the bending moment and the joint rotation angle for any given steel temperature is sought, instead of putting together the sets of the couples steel temperature—bending moment. Such results may be obtained only after the computational procedure is changed. In the analysis included in a current paper, at first the external loads depicted in Fig. 1 are applied to the appropriate numerical model of a structure, and then the preloaded structure is subjected to a direct fire exposure, resulting in the monotonous temperature increase in the components of the analyzed frame. Change in numerical procedure in this case would result in application of the different values of the steel temperature to an initially load free structure and subsequent determination of the response of this structure to the external loads acting on it (Fig. 1) with growing intensity.

5 CONCLUDING REMARKS

Analysis of the behaviour specifics for the whole structure and for its subcomponents, when subjected to the combined thermal (due to a direct fire exposure) and independently applied statical loads, gains a special importance in the fire related safety analysis of a steel frame structure. Identifi-

cation of the potential risks, resulting in dangerous increase that the structure attaining, globally or locally, the ultimate limit state in fire is the main objective here. The limit state is attained when the structure looses the ability to safely carry the loads applied to it. The second purpose of this analysis is to estimate the potential bearing capacity reserve of the structure subjected to a fully developed fire. This reserve may be due to either the redistribution of internal forces or the fact that the fire itself should be treated as an accidental event, and thus the substantially higher failure probability could be acceptable for the computational procedure attributed to it. The parallel application in the analysis of both those factors, should yield, in the opinion of the authors, the quite reliable estimate of the fire resistance for the considered frame structure. Response of the structure to a fire exposure is very specific, mostly because the classical computational approaches have to be combined with taking into account the simultaneous gradual weakening of structural steel, accompanied by the reduction in flexural rigidity of the frame components and subassemblies. The highly nonlinear character of the relationships between the parameters determining the behaviour of the structure under fire, which has to be accurately replicated in the numerical model, additionally complicates the analysis. Therefore, it is suggested that in the statical analysis pertaining to the fire situation, the analyzed structure should be considered as a whole, if only possible, without isolating of not necessarily functionally or structurally homogenous subassemblies. Thus the development of the more and more reliable numerical models should be especially welcome in this field.

Gaining an insight into the process of the redistribution of internal forces occurring in a typical frame subjected to a fire exposure was the main purpose of the analysis presented in this paper. Many of the phenomena identified above and commented by the authors could not be observed in the analysis conducted in a conventional manner, with the application of only the simplified analytical models. Attempts on the holistic approach to the process of the redistribution of internal forces in the frame structures subjected to a fire exposure, often combining the experimental analysis with the computer modeling, recently became the mainstream research field. Several groups of scientists are active in the domain of a fire safety analysis related to the building structures. The paper (El-Rimawi et al. 1999) may be considered as an example of such the analysis relating to the computer modeling, while the paper (Liu et al. 2014) deals with its application to the design practice and with the interpretation of the experimental research. Undoubtedly all these analyses, performed using the specialized computer programs and based on the evaluation of the results obtained with the appropriately selected numerical models, may and should constitute a basis for the development and further for the verification of the simplified computational algorithms recommended for the conventional design practice. Lack of such the algorithms or, in the case of previously developed ones, their low availability for a common structural engineer, seems to be the main cause of the legal regulations pertaining to the fire safety, currently in force in our country, being in many cases based on insufficiently justified and thus quite often arbitrary arrangements.

REFERENCES

El-Rimawi J.A., Burgess I.W. & Plank R.J. 1999. Studies of the behaviour of steel subframes with semi-rigid connections in fire. *Journal of Constructional Steel Research*, 49: 83–98.

EN 1993–1-2. 2005. Eurocode 3: Design of steel structures. Part 1–2: General rules. Structural fire design.

Liu J, Jána T & Wald F. 2014. Internal forces in the structure during fire test, In: R. Landolfo. & F.M. Mazzolani (eds.) - *Proceedings of the 7th European Conference on Steel and Composite Structures "Eurosteel 2014", Napoli, Italy, 10-12.09.2014*, Published by the European Convention for Constructional Steelwork (ECCS): abstract 801–803, paper—pen-drive 6 p.

Maślak M. & Litwin (Snela) M. 2010. Podatność stalowego węzła belka—słup w temperaturze pożarowej. *Inżynieria i Budownictwo*, 8/2010: 441–445.

Maślak M., Pazdanowski M. & Snela M. 2015. Moment—rotation characteristics for flexible beam-to-column steel joint exposed to fire. *Journal of Civil Engineering and Architecture*, 9: 257–261.

Maślak M. & Snela M. 2012. Influence of increasing joint flexibility on critical temperature of steel frame in fire. *Zbirnik Naukowych Prac Ukrainskogo Institutu Staliewych Konstrukcij imieni W.M. Szimanowskogo*, 9/2012, "Stal" Publishing House, Kijev, Ukraine: 204–217.

Maślak M. & Snela M. 2013. Redystrybucja siły podłużnej w stalowym ryglu o narastającej w pożarze zdolności do wydłużenia. *Journal of Civil Engineering, Environment and Architecture*, vol. XXX, 60(2/13): 189–202.

Maślak M. & Snela M. 2014. Critical temperature of steel frame with joint flexibility increasing in fire—benchmark study prepared for the environment of Autodesk Robot Structural Analysis, In: F. Wald et al. (eds.) – *COST Action TU0904. Integrated Fire Engineering and Response—Benchmark studies. Verification of numerical models in fire engineering*, CTU Publishing House, Czech Technical University in Prague: 281–307.

Maślak M. & Snela M. 2015. Flexibility of a steel endplate beam-to-column joint when exposed to a fire—two different, nonequivalent approaches to evaluate, In: *Proceedings of the Eighth International Conference on Advances in Steel Structures (ICASS 2015), Lisbon, Portugal, July 21–24, 2015*, paper 131, CD + pen-drive, 9 p.

Simões da Silva L., Santiago A. & Vila Real P. 2001. A component model for the behaviour of steel joints at elevated temperatures. *Journal of Constructional Steel Research*, 57: 1169–1195.

Recent Progress in Steel and Composite Structures – Giżejowski et al. (Eds)
© 2016 Taylor & Francis Group, London, ISBN 978-1-138-02946-0

Fire resistance evaluation of a steel sway frame load-bearing structure using the linear programming

M. Maslak & M. Pazdanowski
Cracow University of Technology, Cracow, Poland

A. Tkaczyk
BAUKO Design Company, Kielce, Poland

ABSTRACT: A procedure which may be used to estimate the fire resistance of a steel sway frame load-bearing structure, based on the linear programming method, is presented and discussed in this paper. The approach to the general problem formulation is shown in detail, including the specification of the objective function as well as the basic rules governing the development of the authoritative constraints. Interaction of bending moment and axial force is also taken into account in the recommended computational algorithm. The critical temperature, determined for the whole frame and associated with the occurrence of such potentially possible purely plastic failure mode which corresponds to the lowest activation temperature, constitutes the sought resistance measure.

1 INTRODUCTION

1.1 *The idea of a critical temperature as a measure of a steel frame fire resistance*

Fire resistance of a steel frame load-bearing structure is usually associated with time, during which, in the case of fire, this structure will be capable of safely carrying the loads applied to it. The external loads as well as the internal forces induced in the structure by the restrained potential thermal deformations are to be considered as loads in this case. However, in such situation the estimated resistance may not be interpreted as the objective safety measure uniquely attributed to the analysed frame, since this value depends on the basic characteristics of the fire which may potentially occur in the fire compartment containing the considered structure. More precisely speaking, this safety measure depends not only on the speed with which the temperature of the fire generated gases surrounding steel structural members changes, but also on the extreme value of this temperature and on the effective time of a fire exposure. Consequently, the change in reference fire selected for the analysis results in changed fire resistance. Though, the fire resistance of a steel load-bearing structure may also be associated with the critical temperature estimated especially for this structure. This temperature is then understood as such a value of steel temperature, assigned to the weakest structural member in the sense of reliability, at which the whole structure looses its capability to safely carry the loads applied to it. In other words, the limit state relating to the frame fire resistance is achieved if only the critical temperature value is reached under fire conditions in any frame member. The critical temperature thus can be treated as an objective characteristic of the considered frame, because it depends only on the factors determining its structure and on the load scheme assumed prior the analysis. Let us note that here not only the geometry of the considered frame itself and its statical scheme but also the type of the structural steel used and the applied cross sections are to be counted as the structural components. Moreover, the identification of the external loads must be accompanied by the specification of a potential fire scenario, including in particular its extent. This will allow for, at first, the unique specification of all bearing members heated due to a direct fire exposure, and secondly, the determination of mutual relationships between the steel temperature values in such the members measured at the same, selected time of a fire. Consequently, these particular temperature values shall be evaluated in reference to the one selected value treated in further analysis as the reference temperature. Of course, of all the possible fire scenarios, the fire scenario resulting in the lowest critical temperature will be the critical one for the considered structure. Thus, in the engineering practice such a multiplier for the reference temperature defined above is sought, which at the preset level of external loads will determine the critical temperature value for the whole frame. It is important that the

formal approach of this type is an equivalent to the acceptance of an assumption, that under fire conditions the temperature of structural members will increase in a proportional manner while keeping the predetermined initial relations. Simplicity is an obvious advantage of this method of the analysis, but one has to admit, that usually this assumption is not satisfied. Because of that, the critical temperature values obtained in this way should be treated only as the certain, rather rough estimates of the real values. But, if only the cross sections of the individual structural members are a priori known, then there are no formal obstacles to successful determination of the steel temperature values specified for these members in any given time of a fire exposure. One should note here, that during the whole time of a fire exposure the other relationship does not change at all, this between the so called thermal massiveness coefficients identified for the cross—sections of the considered structural members. Such the coefficients are simply the ratios of an effectively heated girth to heated surface area. Thus, instead of the single reference temperature multiplier applied to the subsequent stages of the analyzed fire scenario, one should apply a certain set of the appropriately corrected multipliers assigned to the particular structural members heated in the fire.

1.2 *Rigid—plastic frame failure model under fire conditions and its application in fire resistance analysis*

The steel structures, as opposed to for instance the reinforced concrete structures and especially the prestressed ones, because of the high material homogeneity and of the very high heat conductivity resulting in the fast equalization of the steel temperature both in the cross section and along the length of the considered structural member, may be counted among such the bearing structures, for which the estimation of the critical temperature is not only computationally possible but also especially efficient. Moreover, in such a case a clear interpretation may be attributed to this temperature value. Recently developed computational algorithms recommended for its determination are usually based on the assumption of a rigidly plastic failure model. In this formal model the plastic deformations are concentrated in the selected cross sections of the considered structural members, i.e. in such the cross sections in which the stress redistribution due to the increasing temperature may result in development of a plastic hinge. Besides, due to the developing rotation capacity in those hinges, additional plastic hinges may emerge, until the kinematically admissible motion mechanism will activate in the structure. Outside of those plastic zones, the behaviour of the structure remains purely elastic. One has to observe, that this type of the failure mode may be authoritative only for a frame effectively braced against its potential out-of-plane buckling (global or local) as well as against the all possible three-dimensional forms of its instability. In practice, the following considerations will be limited to a fire which has reached the flashover point, and thus the temperature of the exhaust gases in the whole fire compartment is uniform, but it did not develop to an extent degrading the bracing system of the structure. It follows that an extension of the classical limit loads algorithms, used to evaluate the ultimate resistance of rigid plastic structures, to the specific case of estimating the critical temperature of those structures under fire conditions seems to be natural. Both the generalised kinematical (Maślak & Tkaczyk (2015)) and the semi-graphical statical (Maślak & Tkaczyk (2014a, 2014b)) approaches may be applied in this field. Presentation of an alternative evaluation approach, based on the linear programming techniques, is the objective of this paper. It seems that for cases important in design practice, pertaining especially to the complex frames of complicated geometry, this approach may prove to be more efficient, though not necessarily less laborious and simpler in application.

2 BASIC ASSUMPTIONS AND LIMITATIONS OF THE PROPOSED METHOD

According to the rules of the linear programming both the objective function and all defined constraints must be expressed in terms of the linear equalities or inequalities (Grabowski (1982)). Due to this fact, it will be convenient to extend to the fire case the classical computational algorithm based on the analysis of potentially possible and kinematically admissible motion mechanisms of the load-bearing structure. These mechanisms may exhibit either local or global character, and activate in the considered frame after a sufficient number of plastic hinges develops, provided that conditions arise for development of unconstrained rotations in those hinges. Those rotations must be correlated, and may not mutually cancel themselves. Appearance, under fire conditions, of any of those mechanisms would mean, that the structure has reached the fire resistance limit state correlated with the critical temperature sought for the whole structure. It has to be noted, that in this formulation the frame resistance correlated to the considered motion mechanism, and thus the critical temperature bound to it, would not depend on the history of changes in the distribution of internal

forces, generated by the fire. It will be only a function of a plastic bearing capacity of those plastic hinges, rotations of which participated in the development of the considered mechanism. It will be shown in the following chapters of this work, that in practice, subject to proper assumptions, it will be a simple function of the steel temperature, treated as the reference temperature. Moreover, in the following considerations our attention will focus on the situation, where both the frame columns and the frame beams are made of the same steel grade and also they are made of the same steel section (in terms of both the shape and the size). Only then the assumption simplifying the analysis, on proportional steel temperature growth in particular members of the load-bearing structure, makes sense. One should also bear in mind, that the critical temperature estimate obtained during calculations would be authoritative only if one could prove that the rigid plastic frame failure mode, associated with the considered motion mechanism be the limiting one in evaluation of a fire resistance. This is to be understood, that one has to formally assure, that the frame would not fail in fire earlier, even before the formation of the first plastic hinge in any cross section, due to the for instance its local or global instability.

The basic idea of the problem solved in this paper may be presented in the following sequence of the statements:

- for any potentially possible and kinematically admissible motion mechanism selected for the analysis the number K as well as the location of each of $k = 1, ..., K$ plastic hinges constituting this mechanism is known in advance,
- the considered motion mechanism will occur only if in each of the K cross sections selected before the plastic hinge will develop, i.e. when:

$$\forall k = 1, \&, K \quad \left| M_{k,\Theta} \right| = M_{pl,\Theta} \tag{1}$$

(the subscript Θ denotes here the dependence on the steel temperature),

- according to the classical statical formulation of the limit loads theory, the bearing capacity of the considered frame would not be reached as long as one can find such a statically admissible and self-equilibrated set of reactions, generating a corresponding distribution of the residual bending moments, which after combining it with the bending moments induced by the remaining loads, and taking into account the rules of the redistribution of all bending moments, would result in safe performance of the whole structure,
- thus one may seek the maximum value of the temperature Θ, here taken as the objective function, which, subject to the constraints resulting from both the equilibrium conditions and the yield limit, will result in breaching the constraint (1),
- the problem formulated above is a typical problem of the linear programming.

3 THE LINEAR EQUILIBRIUM CONDITIONS

The canonical equations of the classical force method are used in this paper to specify the linear equilibrium conditions. Let us consider for the example the statically indeterminate frame depicted in the Figure 1. The hyper-static unknowns in this frame are denoted as x_j, with $j = 1, \ldots, m$ (in the considered example m = 12). Moreover, the symbols P_i, with $i = 1, \&, 11$, are assigned to the loads acting on the frame.

Let us note, that the loads P_i consist of not only the external mechanical concentrated or distributed loads, but also the internal loads generated by the constrained thermal expansion of the frame members. In the analyzed example it was assumed, that the fire was ignited only on the bottom floor of the structure and it did not break through the floor and the walls to the upper floor. Thus, the temperature of the exhaust gases increases monotonically only on the bottom floor of the structure. As the fire has reached the stage of the fully developed fire, this temperature is uniform in the whole seized floor constituting a single fire compartment. Increase in the temperature of the exhaust gases in this compartment results in increasing temperature both of the bottom beams and the bottom

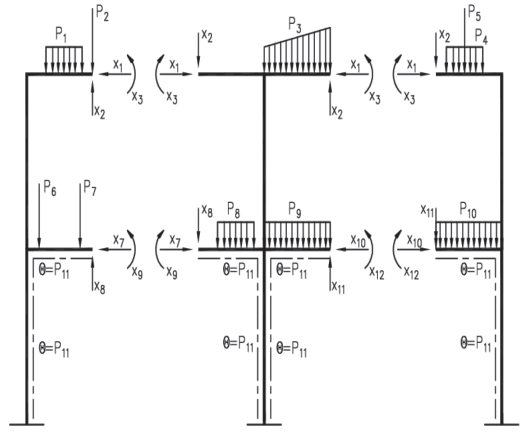

Figure 1. The sample frame with the hyper-static forces as well as with the external loads. The drawing based on (Aribert & Kruppa (1978)) is supplemented with the thermal load induced by the heating of the selected structural members (denoted with the dashed line).

columns of the frame. This is denoted in Figure 1 by the symbol Θ. The steel temperature is in any given time of the fire the same in each of such the above mentioned structural members. This is the consequence of the assumption on identity of the steel shapes applied. Thus the temperature Θ may be treated here as an additional load, subject to the assumption that for $i=11$ is $P_i=\Theta$. Therefore, during the whole time of a fire exposure the loads P_i for $i=1,...,10$ remain constant and do not depend on the steel temperature Θ, while only the load $P_{11}=P_{11,\Theta}$ increases.

According to the formalism of the classical force method the following occurs:

$$\sum_{j=1}^{m}\delta_{kj}x_{j,\Theta}+\sum_{i}\Delta_{ki,\Theta}=0 \tag{2}$$

where δ_{kj} constitute the displacements at the locations k of the basic statically determinate system, when subjected to the hyper-static loads $x_j=1$, while $\Delta_{ki,\Theta}$ represent the analogical displacements of the basic statically determinate system when subject to the loads P_i (or $P_{i,\Theta}$). The relationship (2) is often used to prove the bending moments superposition rule. As a result, the value of the bending moment at the location k in the analyzed frame is determined according to:

$$M_{k,\Theta}=\sum_{j=1}^{m}m_{kj}x_{j,\Theta}+\sum_{i}m_{ki}^{p}P_i \tag{3}$$

where m_{kj} represents the bending moment determined at the location k of the basic statically determinate system for the considered frame, and due to the hyper-static load $x_j=1$, while m_{ki}^{p} is the analogical bending moment determined in the basic statically determinate system, but due to the load $P_i=1$. Of course the load $P_{11,\Theta}$ constitutes one of the loads P_i, but the only one changing with the temperature Θ. This load, however, does not induce any bending moments in the basic statically determinate system for the considered frame, and thus $m_{k,11}^{p}=0$. Per analogy, the longitudinal force at the location k in the frame may be determined by:

$$N_{k,\Theta}=\sum_{j=1}^{m}n_{kj}x_{j,\Theta}+\sum_{i}n_{ki}^{p}P_i \tag{4}$$

while the shearing force via:

$$V_{k,\Theta}=\sum_{j=1}^{m}v_{kj}x_{j,\Theta}+\sum_{i}v_{ki}^{p}P_i \tag{5}$$

where $n_{k,11}^{p}=0$ and $v_{k,11}^{p}=0$. The parameters n_{kj} and v_{kj} as well as n_{kj}^{p} and v_{kj}^{p} have analogical meaning to m_{kj} and m_{kj}^{p}, but pertain to the longitudinal force $N_{k\Theta}$ and shearing force $V_{k,\Theta}$ respectively, instead of the bending moment $M_{k,\Theta}$.

4 THE LINEARIZATION OF THE YIELD CONDITION

By the statical approach of the limit loads theory it follows that if only for the considered structure one could find such a statically admissible distribution of the residual bending moments, generated by the self-equilibrated set of reactions, which after its combination with the distribution of the bending moments induced by the purely elastic deformation regimen of the structure will result in the safe transfer of all applied loads, such distribution would develop during the loading process, and would counter the development of any potential kinematically admissible motion mechanism. In other words, any statically indeterminate structure made of the class 1steel sections, i.e. the sections which after plasticization remain rotation capable, preserves certain additional bearing capacity due to the possible bending moment redistribution. This leads to the statement, that the fire resistance limit state, related to the occurrence of any kinematically admissible motion mechanism, will not be reached as long as one will be able to find a distribution of the residual moments obstructing this motion mechanism. This means, that the critical temperature Θ_{cr} listed for the given motion mechanism will be the highest of the temperature values obtained in the analysis. The yield condition (1), if it is to be located on the safe side of the limit state, should be stated in the form of the following inequality:

$$\forall k=1,\ldots,K \quad \left|M_{k,\Theta}\right|\le M_{pl,\Theta,d} \tag{6}$$

Now one has to determine the relationship between the plastic bearing capacity of the member cross section and the steel temperature, i.e. the function $M_{pl,\Theta,d}=M_{pl,d}(\Theta)$. If the yield limit reduction factor for steel subject to the fire temperature is described by the coefficient $k_{y,\Theta}=f_{y,\Theta}/f_y$ having the values listed in EN 1993-1-2 (CEN (2005)), then under the assumption of the uniform steel temperature distribution both along the length and across the cross section of the heated structural member, the design value of the sought unknown may be determined with the following formula:

$$M_{pl,\Theta,d}=W_{pl}\frac{k_{y,\Theta}f_y}{\gamma_{M,fi}}=k_{y,\Theta}M_{pl,d}\frac{\gamma_{M,fi}}{\gamma_M} \tag{7}$$

where f_y is the nominal value of the yield limit for steel, in the simplified standard regulations usually it is identified with the characteristic value, W_{pl} is the plastic bending modulus, depending only on the geometrical dimensions of the considered cross section, and thus independent of the steel temperature, while the factors γ_M and $\gamma_{M,fi}$ constitute the partial safety factors, both listed for bearing capacity and pertaining to the persistent design situation and to the exceptional fire scenario, respectively. In practical calculations, according to the recommendations of the standard EN 1991-1-2 (CEN (2002), it is assumed, that $\gamma_{M,fi} = \gamma_M = 1{,}0$. This means, that the design plastic resistance of the steel cross section changes with the steel temperature growth following the rules set for thermal changes of the characteristic value of the yield limit for steel subjected to a fire. It is essential that this is a strongly nonlinear relationship. Based on the experimental research, regardless of the high statistical dispersion of determined values, it comes that the relationship:

$$k_{y,\Theta} = \frac{1{,}0087}{\left(e^{\beta}+1\right)^{0{,}2609}} \quad \text{where} \quad \beta = \frac{\Theta - 482}{39{,}19} \tag{8}$$

constitutes a good estimate of the sought function.

The relationship (8) has to be linearized for the purposes of the algorithm proposed in the current paper. Though in the standard EN 1993-1-2 (CEN 2005) this relationship is replaced by the piecewise linear function, the number of component straight line segments is so high, as to prevent practical calculations. However, one may assume, that the resultant critical temperature is very infrequently estimated at the level exceeding 785°C. This limitation allows for acceptance of a simplified relationship proposed previously by the authors (Maślak & Tkaczyk (2012)). This is as follows:

- for $20°C \le \Theta \le 400°C$:

$$k_{y,\Theta} = k_{y,20} = k_{y,400} = 1{,}0 \tag{9}$$

- for $400°C < \Theta \le 785°C$:

$$k_{y,\Theta} = 2{,}04 - 2{,}6 \cdot 10^{-3}\Theta \tag{10}$$

The quality of the approximation of the function listed in the standard EN 1993-1-2 (CEN (2005)) by the lines (9) and (10) is depicted in the Figure 2. One may easily observe, that for the temperature values higher than 785°C the negative values of the coefficient $k_{y,\Theta}$ will be obtained. This does not have any formal justification. Thus, in the proposed approach, this is the limit temperature, above which the anyway very low bearing capacity of the considered structure is disregarded.

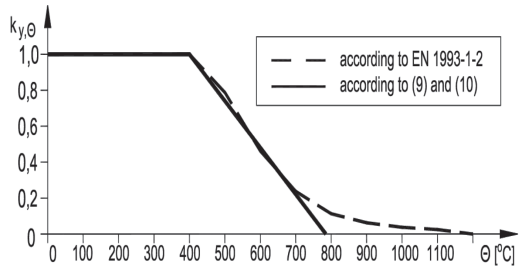

Figure 2. Replacement of the piecewise linear function proposed in the standard EN 1993–1-2 (CEN (2005)) to approximate the formula (8) by the formulae (9) and (10) based on the work (Maślak & Tkaczyk (2012)).

Application of the relationships (9) and (10) makes the linearization of the yield condition possible. Beginning with the form (6) one may state, that:

- for $20°C \le \Theta \le 400°C$:

$$M_{pl,\Theta,d} = M_{pl,d} \tag{11}$$

- for $400°C < \Theta \le 785°C$:

$$M_{pl,\Theta,d} = M_{pl,d}\left(2{,}04 - 2{,}6 \cdot 10^{-3}\Theta\right) \tag{12}$$

It has to be expressly stated here, that there are no formal obstacles to assuming uneven heating of the cross section. For instance, one may consider slightly lower steel temperature of the top flange of an I—beam with respect to the remaining part of the cross section. This, in practical situations usually small difference in temperature, of Θ^l in the bottom flange and in the web of the considered section and $\Theta^u < \Theta^l$ in the top flange, is a result of direct contact between the top flange and the massive reinforced concrete slab acting as heat sink. The parameter α constituting a multiplier of the reference temperature is assigned to the cross section heated in this manner (Aribert & Kruppa (1978)) in the following way:

$$\alpha = \frac{\Theta^l - \Theta^u}{\Theta^l} \tag{13}$$

This means that $\Theta^u = (1-\alpha)\Theta^l$ occurs (see Figure 3). One should also note that the value of the parameter α changes in fire in accordance with the changes of the temperature Θ^l. However, this change is not proportional in any way. The location of the neutral axis changes as well, and this adds

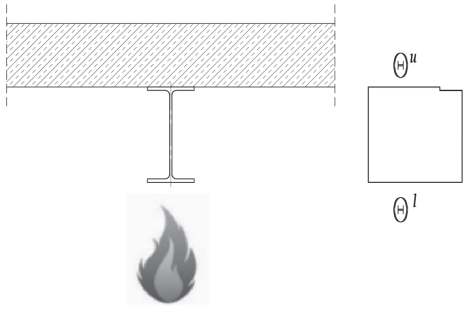

Figure 3. The computational distribution of the steel temperature in the considered cross section of an uninsulated beam of a steel frame, taking into account the influence of the reinforced concrete slab in contact with such the beam.

to the complexity of calculations. The linearization of the yield condition should be then repeated for each assigned value of the steel temperature.

In the case of the multi-storey steel frames taking into account the *M–N* interaction may substantially affect the quality of the obtained Θ_{cr} critical temperature estimate. The yield condition (6) in such case may be stated as follows:

$$\forall k = 1, \ldots, K \quad \left|M_{k,\Theta}\right| \le M_{pl,\Theta,d}\left(1 - \frac{\left|N_{k,\Theta}\right|}{N_{pl,\Theta,d}}\right) \quad (14)$$

As, per analogy to (7), holds:

$$N_{pl,\Theta,d} = A\frac{k_{y,\Theta} f_y}{\gamma_{M,fi}} = k_{y,\Theta} N_{pl,d}\frac{\gamma_{M,fi}}{\gamma_M} \quad (15)$$

where A represents the area of the considered cross section, the condition (14) is reduced to the following form:

$$\forall k = 1, \ldots, K \quad \left|M_{k,\Theta}\right| + \frac{W_{pl}}{A}\left|N_{k,\Theta}\right| \le M_{pl,\Theta,d} \quad (16)$$

being an equivalent to the sequence of the four independent constraints, i.e.:

- if $M_{k,\Theta} \ge 0$ and $N_{k,\Theta} \ge 0$:

$$\forall k = 1, \ldots, K \quad M_{k,\Theta} + \frac{W_{pl}}{A} N_{k,\Theta} \le M_{pl,\Theta,d} \quad (17)$$

- if $M_{k,\Theta} < 0$ and $N_{k,\Theta} < 0$:

$$\forall k = 1, \ldots, K \quad -M_{k,\Theta} - \frac{W_{pl}}{A} N_{k,\Theta} \le M_{pl,\Theta,d} \quad (18)$$

- if $M_{k,\Theta} \ge 0$ and $N_{k,\Theta} < 0$:

$$\forall k = 1, \ldots, K \quad M_{k,\Theta} - \frac{W_{pl}}{A} N_{k,\Theta} \le M_{pl,\Theta,d} \quad (19)$$

- if $M_{k,\Theta} < 0$ and $N_{k,\Theta} \ge 0$:

$$\forall k = 1, \ldots, K \quad -M_{k,\Theta} + \frac{W_{pl}}{A}\left|N_{k,\Theta}\right| \le M_{pl,\Theta,d} \quad (20)$$

5 FORMULATION OF THE LINEAR PROGRAMMING PROBLEM

The linear equilibrium conditions (3), (4) and (5), as well as the linearized yield condition (16) let us formulate the constraints constituting the basis of the linear programming problem. In the beginning, however, one has to assume the initial value of the temperature $\Theta = \Theta_0$, which, in the following calculations will be treated as the reference temperature. Then the critical temperature Θ_{cr} will be determined by the multiplier $\zeta = \zeta_{cr}$, such as:

$$\Theta_{cr} = \zeta_{cr}\Theta_0 \quad (21)$$

In this problem one has to find the maximum value of the multiplier ζ, associated with the objective function, while satisfying at the same time the constraints, linear with respect to the temperature Θ, expressed by the following set of the eight inequalities listed explicitly for each point $k = 1, \ldots, K$ corresponding to the location of plastic hinge in the motion mechanism selected for the analysis:

$$\sum_{j=1}^{m} m_{kj} x_{j\Theta} + \sum_i m_{ki}^P P_i + \frac{W_{pl}}{A}\left(\sum_{j=1}^{m} n_{kj} x_{j\Theta} + \sum_i n_{ki}^P P_i\right) \le W_{pl}\frac{f_y}{\gamma_{M,fi}} \quad (22)$$

$$-\sum_{j=1}^{m} m_{kj} x_{j\Theta} - \sum_i m_{ki}^P P_i + \frac{W_{pl}}{A}\left(-\sum_{j=1}^{m} n_{kj} x_{j\Theta} - \sum_i n_{ki}^P P_i\right) \le W_{pl}\frac{f_y}{\gamma_{M,fi}} \quad (23)$$

$$-\sum_{j=1}^{m} m_{kj} x_{j\Theta} - \sum_i m_{ki}^P P_i + \frac{W_{pl}}{A}\left(\sum_{j=1}^{m} n_{kj} x_{j\Theta} + \sum_i n_{ki}^P P_i\right) \le W_{pl}\frac{f_y}{\gamma_{M,fi}} \quad (24)$$

$$\sum_{j=1}^{m} m_{kj} x_{j\Theta} + \sum_{i} m_{ki}^{P} P_i + \frac{W_{pl}}{A}\left(-\sum_{j=1}^{m} n_{kj} x_{j\Theta} - \sum_{i} n_{ki}^{P} P_i \right) \le W_{pl} \frac{f_y}{\gamma_{M,fi}} \quad (25)$$

$$\sum_{j=1}^{m} m_{kj} x_{j\Theta} + \sum_{i} m_{ki}^{P} P_i + \frac{W_{pl}}{A}\left(\sum_{j=1}^{m} n_{kj} x_{j\Theta} + \sum_{i} n_{ki}^{P} P_i \right) \le W_{pl} \frac{f_y}{\gamma_{M,fi}} \left(2{,}04 - 2{,}6 \cdot 10^{-3} \zeta \Theta_0\right) \quad (26)$$

$$-\sum_{j=1}^{m} m_{kj} x_{j\Theta} - \sum_{i} m_{ki}^{P} P_i + \frac{W_{pl}}{A}\left(-\sum_{j=1}^{m} n_{kj} x_{j\Theta} - \sum_{i} n_{ki}^{P} P_i \right) \le W_{pl} \frac{f_y}{\gamma_{M,fi}} \left(2{,}04 - 2{,}6 \cdot 10^{-3} \zeta \Theta_0\right) \quad (27)$$

$$-\sum_{j=1}^{m} m_{kj} x_{j\Theta} - \sum_{i} m_{ki}^{P} P_i + \frac{W_{pl}}{A}\left(\sum_{j=1}^{m} n_{kj} x_{j\Theta} + \sum_{i} n_{ki}^{P} P_i \right) \le W_{pl} \frac{f_y}{\gamma_{M,fi}} \left(2{,}04 - 2{,}6 \cdot 10^{-3} \zeta \Theta_0\right) \quad (28)$$

$$\sum_{j=1}^{m} m_{kj} x_{j\Theta} + \sum_{i} m_{ki}^{P} P_i + \frac{W_{pl}}{A}\left(-\sum_{j=1}^{m} n_{kj} x_{j\Theta} - \sum_{i} n_{ki}^{P} P_i \right) \le W_{pl} \frac{f_y}{\gamma_{M,fi}} \left(2{,}04 - 2{,}6 \cdot 10^{-3} \zeta \Theta_0\right) \quad (29)$$

The set of constraints is made of the $8 \cdot K$ independent inequalities, where K denotes the number of the plastic hinge locations associated with the motion mechanism selected for the analysis. Let us note, that in this formulation of the problem the relatively insignificant influence of the $M - V$ interaction was disregarded. The solution of the linear programming problem for a given mechanism is expressed as the maximum value of the multiplier ζ, at which all the constraints defined above are satisfied. Of course, in order to estimate the critical temperature authoritative for the whole frame one has to determine the critical temperature values for each of the kinematically admissible failure mechanisms, compare these values and select the lowest one. This will be an equivalent to indicating the authoritative failure mechanism for the assumed rigid plastic frame failure mode.

The constraints (22) to (29), listed for the k-th location of a plastic hinge may be written in the more concise matrix form:

$$\mathbf{A}_{8xj}\mathbf{X}_{jx1} + \mathbf{B}_{8x1} \le \mathbf{C}_{8x1} \quad (30)$$

where:

$$\mathbf{X}_{jx1}^{\mathrm{T}} = [x_1 \ldots x_j] \quad (31)$$

and also:

$$\mathbf{A}_{8xj} = \begin{bmatrix} m_1 + \frac{W_{pl}}{A} n_1 & \ldots & m_j + \frac{W_{pl}}{A} n_j \\ -m_1 - \frac{W_{pl}}{A} n_1 & \ldots & -m_j - \frac{W_{pl}}{A} n_j \\ -m_1 + \frac{W_{pl}}{A} n_1 & \ldots & -m_j + \frac{W_{pl}}{A} n_j \\ m_1 - \frac{W_{pl}}{A} n_1 & \ldots & m_j - \frac{W_{pl}}{A} n_j \\ m_1 + \frac{W_{pl}}{A} n_1 & \ldots & m_j + \frac{W_{pl}}{A} n_j \\ -m_1 - \frac{W_{pl}}{A} n_1 & \ldots & -m_j - \frac{W_{pl}}{A} n_j \\ -m_1 + \frac{W_{pl}}{A} n_1 & \ldots & -m_j + \frac{W_{pl}}{A} n_j \\ m_1 - \frac{W_{pl}}{A} n_1 & \ldots & m_j - \frac{W_{pl}}{A} n_j \end{bmatrix} \quad (32)$$

$$\mathbf{B}_{8x1} = \begin{bmatrix} \sum_i m_i^P P_i + \frac{W_{pl}}{A} \sum_i n_i^P P_i \\ -\sum_i m_i^P P_i - \frac{W_{pl}}{A} \sum_i n_i^P P_i \\ -\sum_i m_i^P P_i + \frac{W_{pl}}{A} \sum_i n_i^P P_i \\ \sum_i m_i^P P_i - \frac{W_{pl}}{A} \sum_i n_i^P P_i \\ \sum_i m_i^P P_i + \frac{W_{pl}}{A} \sum_i n_i^P P_i \\ -\sum_i m_i^P P_i - \frac{W_{pl}}{A} \sum_i n_i^P P_i \\ -\sum_i m_i^P P_i + \frac{W_{pl}}{A} \sum_i n_i^P P_i \\ \sum_i m_i^P P_i - \frac{W_{pl}}{A} \sum_i n_i^P P_i \end{bmatrix} \quad (33)$$

$$\mathbf{C}_{8x1} = \begin{bmatrix} W_{pl}\dfrac{f_y}{\gamma_{M,fi}} \\ W_{pl}\dfrac{f_y}{\gamma_{M,fi}} \\ W_{pl}\dfrac{f_y}{\gamma_{M,fi}} \\ W_{pl}\dfrac{f_y}{\gamma_{M,fi}} \\ W_{pl}\dfrac{f_y}{\gamma_{M,fi}}\left(2{,}04 - 2{,}6\cdot 10^{-3}\zeta\Theta_0\right) \\ W_{pl}\dfrac{f_y}{\gamma_{M,fi}}\left(2{,}04 - 2{,}6\cdot 10^{-3}\zeta\Theta_0\right) \\ W_{pl}\dfrac{f_y}{\gamma_{M,fi}}\left(2{,}04 - 2{,}6\cdot 10^{-3}\zeta\Theta_0\right) \\ W_{pl}\dfrac{f_y}{\gamma_{M,fi}}\left(2{,}04 - 2{,}6\cdot 10^{-3}\zeta\Theta_0\right) \end{bmatrix} \tag{34}$$

It has to be once more repeated here, that the proposed computational algorithm will yield reliable results only if the resultant critical temperature for each considered motion mechanism is lower then the threshold value equal to 785°C (this is an express result of the formula (10) and Figure 2).

6 CONCLUDING REMARKS

If the inventory of the steel load-bearing structure with the sway transversal frames leads to the reliable conclusion, that it is braced sufficiently as to ensure the rigid plastic failure mechanism in the case of a potential fire, the critical temperature estimation method for the whole structure, proposed by the authors in this paper, may be an usable and an efficient tool of the numerical analysis. It should be treated not only as a standard alternative to the classical kinematical and statical approaches generalized to the case of fire, but also as the method which is the complement of both methods mentioned above. On the one hand, the analysis of the particular, kinematically admissible motion mechanisms, based on the virtual work principle, by itself usually leads to the critical temperature estimates located on the unsafe side of the real value. On the other side, the calculations taking into account the bearing capacity reserves due to the redistribution of the bending moments yield results always located on the safe side, but very often substantially underestimated. The algorithm presented above, based on the linear programming technique combines the both approaches. The constraints are developed based on the theorems of the classical statical approach. The maximization rule of the multiplier ζ is also a direct result of this approach. The selection of the authoritative temperature is performed, however, after comparison of all the solutions, each of which pertains to a different kinematically possible motion mechanism. Selection of the lowest temperature out of all the values gathered at the first stage of the calculations represents the formal application of the kinematical approach theorems. According to the authors' opinion the proposed method may be applied mainly to verify the critical temperature estimates obtained with alternative techniques of the analysis, indicated above. Thus it seems that the solutions obtained for the same steel structures and for the same fire scenarios, but using the alternative calculation methods, may be of practical interest.

The preparation and the solution of an example consisting of a steel sway frame subjected to a potential fire exposure with the application of the linear programming method, and next the comparison of the obtained results with the critical temperature estimates for the same steel frame arrived at via the alternative computational approaches, will follow the theoretical deliberations presented here.

REFERENCES

Aribert J.M. & Kruppa J. 1978. Détermination par programation linéaire de champs de temperatures critiques dans des structures soumises a un incendie. *Construction Métallique*, 1/1978: 3–16.

EN 1991–1-2. Eurocode 1: Actions on structures. Part 1–2: General actions—Actions on structures exposed to fire.

EN 1993–1-2. Eurocode 3: Design of steel structures. Part 1-2: General rules—Structural fire design.

Grabowski W. 1982. *Programowanie matematyczne*. Państwowe Wydawnictwa Ekonomiczne, Warszawa, 1982.

Maślak M. & Tkaczyk A. 2012. Oszacowanie nośności granicznej ramy stalowej w pożarze rozwiniętym. *Inżynieria i Budownictwo*, 3/2012: 160–163.

Maślak M. & Tkaczyk A. 2014a. Critical temperature of pitched-roof steel frame. Semi-graphic approach to evaluation for fire conditions, In: R. Landolfo & F.M. Mazzolani (eds.) - *Proceedings of the 7th European Conference on Steel and Composite Structures "Eurosteel 2014", Napoli, Italy, 10–12.09.2014*, Published by European Convention for Constructional Steelwork (ECCS): abstract 821–822, paper—pen-drive 6 p.

Maślak M. & Tkaczyk A. 2014b. A semi-graphic approach to the fire resistance assessment of a gable steel frame. *Czasopismo Techniczne*, 6-B/2014: 67–82.

Maślak M. & Tkaczyk A. 2015. Identyfikacja krytycznego kinematycznego mechanizmu zniszczenia plastycznego ogarniętej pożarem stalowej ramy portalowej. *Inżynieria i Budownictwo*, 2/2015: 103–107.

Recent Progress in Steel and Composite Structures – Giżejowski et al. (Eds)
© 2016 Taylor & Francis Group, London, ISBN 978-1-138-02946-0

Recent developments in heavy plate production for modern steel bridges

T. Lehnert & F. Schröter
Dillinger Hütte, Werkstr, Dillingen, Germany

ABSTRACT: Today's bridge construction is characterized by highest demands on efficiency, quality and sustainability. Facing this, fabricators are longing for developments which can support them to reduce cost, time or environmental impact of a bridge. Even though modern heavy plate production is far developed, quality producer invest consequently to further improve their steels. These smaller developments can nevertheless lead to major advantages in bridge design and construction, e.g. thermomechanically rolling (TM) is a well-known process from the linepipe industry, which due to its superior properties gains increasingly ground in steel construction. With TM-plates even the upcoming challenging demands on weldability of high strength plates can be served. Beyond that, nowadays the maximum plate thickness for TM-plates is increased to 150 mm. Other recent developments are the combination of thermomechanically rolling with weathering properties to overcome the problem of worse weldability for higher strength weathering steel or the so-called longitudinally profiled plates.

1 INTRODUCTION

Being highly cost efficient while maintaining the necessary quality and safety can be considered as the main challenge in modern steel bridge construction. Beside this, nowadays also sustainability gains more and more importance, as often life cycle costs or environmental impact of steel structures are taken into account in evaluating different design concepts. As this ecological aspect is quite new it is addressed by many research groups, e.g. the project SBRI—Sustainable Steel-Composite Bridges in Built Environment (Kuhlmann & Maier 2011). Due to its unlimited recyclability steel as such is already the ideal choice for a sustainable material in construction. This general advantage concerning a sustainable resource input can be furthermore fostered by the cost and energy reduction possibilities modern steel concepts provide in steel construction. Therefore the steel making industry has continuously developed more sophisticated steel grades to meet the arising economic and ecologic requirements (Hever & Schröter 2003, Schröter 2004). Thermomechanically (TM) rolling, for example, is a well-known process used for many years in line-pipe industry. Over the past years such TM-plates have gained more and more ground in the steel construction sector due to their superior processing properties. The following paper will shortly present some new developments in the field of TM rolling (e.g. extended thickness, higher strength weathering steels). Benefits as well as the potential in reducing cost and energy consumption in fabrication, assembly and transportation will be discussed. A second special product for bridge construction are the longitudinally profiled plates, so-called LP-plates. By their uniquely adjustable thickness profile they allow significant weight reductions and fatigue improvements in a bridge construction. New feasibilities can make their application even more efficient.

2 PRODUCTION OF THERMOMECHANICALLY ROLLED PLATES

While classical hot rolling (Process A in Fig. 1) is mainly used to shape and homogenize a heavy plate, thermomechanical rolling (Process D–G in Fig. 1) furthermore leads to an improvement of the mechanical properties of the steel plates by its rolling process. It can be defined as a rolling procedure where the temperature and time course during rolling are precisely controlled and adjusted to the chemical composition of the steel. Thermomechanical rolling basically consists of up to four process steps:

1. Heating of slabs to its predetermined rolling temperature.
2. Rolling: following a given pass list where the last rolling pass takes place in the temperature range of non-recrystallizing austenite or in the two phase region of ferrite and austenite.
3. Cooling: After rolling the steel is cooled down to a definite temperature depending on the targeted steel grade. To do so, different cool-

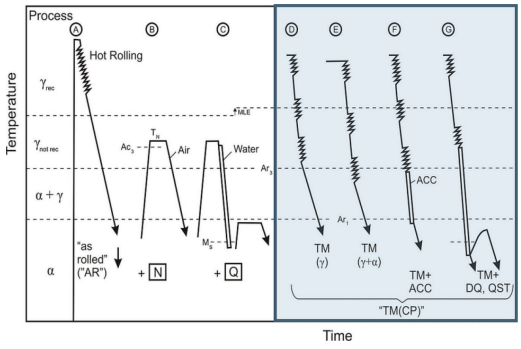

Figure 1. Schematic temperature-time-procedures used in heavy plate production (Schröter 2004).

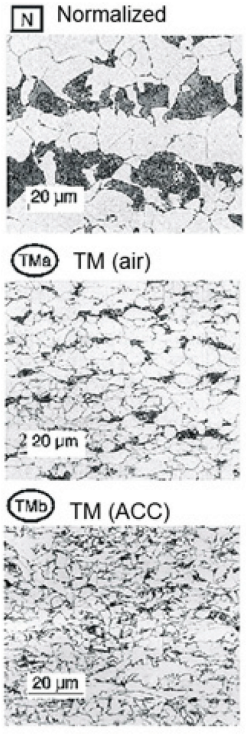

Figure 2. Effect of thermomechanical rolling on the grain size for normalized steel (N), thermomechanically rolled steel cooled on air (TMa), as well as accelerated cooled (TMb).

ing methods can be used: air cooling (D and E in Fig. 1), accelerated cooling (F) or direct quenching (G).

4. If necessary additional heat treatment (Tempering).

All the steps of this complex rolling procedure target an extreme grain refinement in the microstructure of the steel plate. As described by the Hall-Petch relation such a refined grain has a positive influence on strength as well as on toughness of the steel. This structure-related gain in strength obtained by grain refinement allows reducing effectively the carbon and alloy content of a TM-steel compared to a normalized steel of the same grade.

Figure 2 shows the grain refining effect of thermomechanical rolling. Typical steel grades obtained by this rolling method are S355M/ML or S460M/ML according to EN 10025-4 or ASTM A1066 Gr.65.

3 GENERAL BENEFITS OF TM-PLATES ON COST AND SUSTAINABILITY

There are different ways the fabricator as well as the engineer of a steel bridge can profit from using thermomechanically rolled steels:

1. Transition from "normalized" to "thermomechanically rolled" steels in the same strength range (e.g. S355 N ⇨ S355M)
2. Transition to higher strength while maintaining a very good weldability (e.g. S355 N ⇨ S460M)

3.1 *Exchanging N with M in the same strength range*

As already stated thermomechanically rolled plates need less carbon and alloying material compared to its normalized equivalent to achieve the same strength (Fig. 3). Their low alloying contents are therefore the basis for the major advantage of TM-steels, their excellent weldability.

The significantly improved weldability of TM-steels can be verified when comparing the carbon equivalent CET, a common measure of weldability, for a typical normalized S355J2+N with the one of a thermomechanically rolled S355ML (Table 1). CET was computed with Eq. 1 (Uwer & Höhne 1991).

$$CET = C + (Mn + Mo)/10 + (Cr + Cu)/20 + Ni/40 \quad (1)$$

The carbon equivalent CET allows the determination of the necessary preheating temperature Tp for welding, taking into account the avoidance of hydrogen-induced cold-cracking (Uwer & Wegmann 1996). According to EN 1011-2 the preheating temperature Tp is given by: (with hydrogen content in welding consumable HD [ml/100 g], heat input Q [kJ/mm] and plate thickness t [mm]).

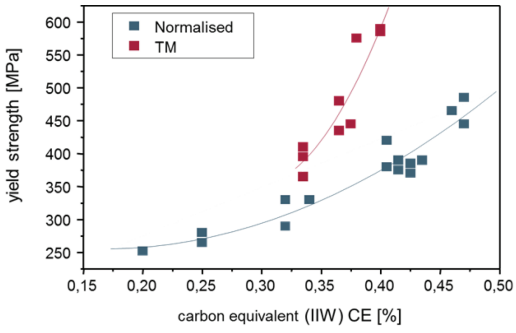

Figure 3. Yield strength as a function of alloying, expressed by the carbon equivalent CE (IIW).

Table 1. Typical carbon equivalent values for typical S355J2+N and S355ML.

Steel grade	CET	CE (IIW)
S355 J2+N	0.30	0.42
S355ML	0.24	0.36

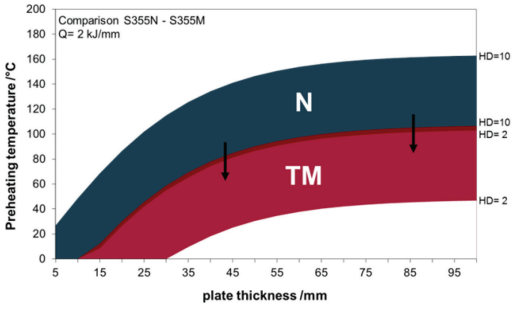

Figure 4. Reduction of recommended preheating temperature for TM-steels.

$$T_p = 697 \times CET + 160 \times \tanh\left(\frac{d}{35}\right) + 62 \times HD^{0.35} + (53 \times CET - 32) \times Q - 328 \quad (2)$$

Due to the considerably reduced CET for TM-steels one can significantly decrease or even omit the preheating by using appropriate welding consumables (with low diffusible hydrogen content) also for higher strength steels and large plate thickness (see Fig. 4).

The achievable savings on the fabrication time (no time for cooling down/heating up, shorter setup times) as well as on the energy consumption during assembly enable a higher cost-effectiveness and improved resource management. An additional benefit of reduced preheating concerns job safety for welders, as it clearly facilitates welding in constricted rooms, e.g. inside box girders (Fig. 5).

Figure 6 gives an example where the fabricator had benefits from the usage of a thermomechanically rolled S355 steel, namely S355M/ML.

Figure 5. The reduction or even elimination of preheating makes working under constricted conditions much easier.

Figure 6. Ennëus-Heerma Bridge in the Netherlands with around 900 t S355M/ML.

3.2 *Transition to higher strength grade*

Even though modern steel production methods enable steel grades with yield strength up to 1300 MPa, in bridge building the usage is mostly limited to steel grades up to 690 MPa (Samuelsson & Schröter 2005). To achieve such "higher" strength steel grades (with yield strength > 355 MPa) different procedures are possible:

1. Alloying: higher carbon equivalents and therefore decreased weldability
2. Thermomechanical rolling: excellent weldability, mainly up to 500 MPa
3. Quenching and Tempering: mostly up to 690 MPa in bridge building

The big advantage of using thermomechanically rolling as a production route for achieving higher strength steel grades is the remaining excellent weldability, while the other processes tend to an increased carbon equivalent and by that to a reduced weldability.

With their increased strength—while simultaneously being sufficiently weldable—these thermomechanically rolled high strength steels allow notable material savings in fabrication and assembly (Willms 2008). If comparing for example the rated values for S355 and S460 (f_y = 315 MPa at 100 mm plate thickness to f_y = 430 MPa at 73 mm plate thickness), the change towards a higher strength steel allows a plate thickness reduction of around 30% (not taking into account fatigue effects which are depending on the exact construction detail) (Fig. 8).

Beside the reduced material amount these reduced cross sections impact the cost and eco-balance of a construction in multiple ways. First, the lower component weight enables bigger assembly units and thereby faster assembly plus optimized transportation. The hence lowered transport energy expenses (for example less truck transport) add a relevant sustainable aspect to the high economic efficiency of high strength steels in bridge building.

Figure 7. Higher strength thermomechanically rolled steel (S460ML) in bridge construction, Øresund Bridge, Danmark.

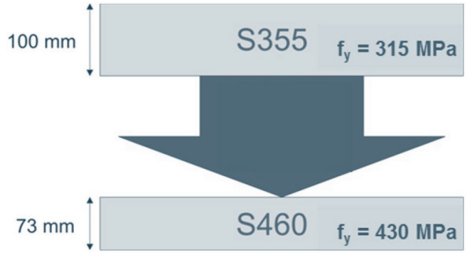

Figure 8. Possible reduction of plate thickness when using higher strength steel leads to savings in material consumption.

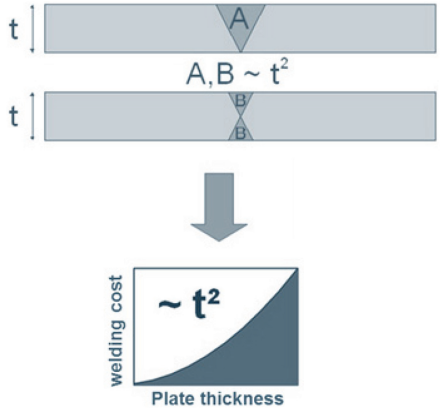

Figure 9. Realizable cost savings in welding dependent on plate thickness.

Furthermore, the thinner steel plates lead to a considerable reduction of weld seam volume. Due to the geometrical situation the weld seam volume is a quadratic function of the plate thickness and therefore the enabled savings in weld material and heating energy are disproportionately high with decreasing plate thickness (Fig. 9).

A reduction of welding time as well as testing time complete the economic advantages associated with high strength thermomechanically rolled steel (e.g. S460ML in Figure 7).

4 NEWEST DEVELOPMENTS IN TM-PLATES

4.1 *TM-Plates up to 150 mm plate thickness*

To achieve the beneficial properties of TM plates a minimum degree of thickness deformation between the slab and the final heavy plate is of cru-

cial importance. Given that, the maximal thickness for TM rolling is mainly limited by the availability of strong rolling forces as well as of semi-finished steel products with appropriate product thickness. Therefore to date the advantages of thermomechanically rolling were only available for plate thickness up to 120 mm. Thus EN 10025-4, as standard for TM plates in steel constructions, has defined such steels also only up to a thickness of 120 mm. Nevertheless, newest developments in steel manufacturing, e.g. very thick slabs from continuous casting, are now able to push this production-driven limit for another 30 mm. Hence, nowadays TM steel plates up to 460 MPa can be produced with plate thickness up to 150 mm. In order to allow maximum usability in bridge constructions these thick TM-plates fulfill the same mechanical requirements as a 120 mm thick plate according to EN 10025-4 (Table 2).

For the S355ML, these so far thickest TM-plates in the world are now also certified by Germanischer Lloyd as well as approved by the German Building Authority (DiBT) up to 140 mm.

Especially the offshore wind industry, which generally needs thick and heavy plates with outstanding weldability to meet the designated efficiency goals by using fast welding processes, will profit from this new development in thermomechanical rolling.

4.2 *Higher strength weathering steel*

The upcoming sustainability discussions in steel constructions, especially in bridge constructions, led to an increased interest in weathering steel solutions in certain parts of Europe.

In order to achieve such weathering properties (e.g. according to ASTM A709 or EN 10025-5) certain amounts of the alloying elements Copper, Chromium and Nickel (the minimum values are given in the respective standards) need to be alloyed to the steel. During first corrosion, these alloying elements form a homogeneous oxidic protection layer (Patina) on the steel surface which significantly decelerates the further atmospheric corrosion of the steel.

Even though these alloying elements lead to higher steel prices at a first glance, the omission of a separate corrosion protection layer can justify its usage economically as wells as environmentally. Especially the reduced maintenance efforts (e.g. no need for regular repainting) positively influence the life cycle costs of a construction with weathering steel. However, the usage of weathering steel in steel construction has certain restrictions and special care in the construction design is necessary, e.g. the construction needs to be designed in a way to prevent standing water on the steel surface. In other words this steel type needs a steady alternation between being wet and completely dried off again.

Several guidelines on how to design with weathering steels are available (e.g. DASt-Ri 007 in Germany).

Nevertheless, weathering steels are today of great interest and a challenging newly upcoming desire from bridge designers is a higher strength weathering steel with yield strength of 460 MPa and a still good weldability. Such a steel grade will combine the benefits of weathering resistance behavior with the ones coming from higher strength steel. But as the minimum content of alloying elements for the corrosion protection itself increases the carbon equivalents, the carbon equivalents of weathering steels are generally higher than the ones of normal constructional steels. The same relation applies for higher strength steels (see Table 3). Therefore a higher strength weathering steel produced by classical routes, e.g. normalizing, suffers from a very high carbon equivalent.

Weather-resistant (S355J2+N → S355J2W+N)
⇨ CET ↑ (Weldability ↓)

Higher Strength (S355J2+N → S460N)
⇨ CET ↑ (Weldability ↓)

Thermomechanically rolling offers therefore an ideal solution to this metallurgical dilemma and somewhat attenuates these disadvantages.

Table 2. Mechanical properties for 150 mm thick S355M/ML.

Plate thickness t [mm]	Min. yield strength R_{eH} [MPa]	Min. tensile strength R_m [MPa]
$t \leq 16$	355	470–630
$16 < t \leq 40$	345	
$40 < t \leq 63$	335	450–610
$63 < t \leq 100$	325	440–600
$100 < t \leq 120$	320	430–590
$120 < t \leq 140$	320	430–590

Table 3. Typical carbon equivalent values for 50 mm thick plates of different steel grades.

Steel grade	CET
S355J2+N	0.30
S355J2W+N (normalized)	0.32
S460N	0.31
S460"W" (TM rolled)	0.28

Figure 10. Higher strength weathering steel (A709M HPS485W) in bridge construction. Haliç Metro Bridge in Istanbul, Turkey.

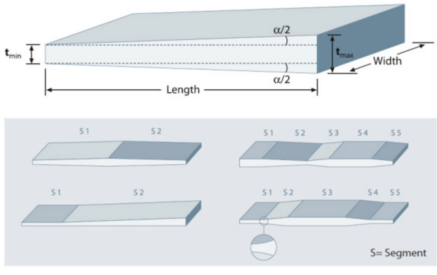

Figure 11. Overview of possible profiles for longitudinally profiled plates (LP plates).

It can significantly enhance the weldability of weathering steels by its facility to allow reduced carbon equivalents. Such a thermomechanically rolled higher strength weathering steel (ASTM A709M HPS485W) was for example successfully used in the Haliç Metro Bridge in Istanbul, Turkey (Fig. 10). Even though the European standard for weathering steel (EN 10025-5) does so far not define a higher strength weathering steel, some heavy plate producers offer already branded steels with this property combination.

5 LONGITUDINALLY PROFILED PLATES

Another interesting product of the steel making industry is the Longitudinally Profiled (LP) plate. By perfect control of the rolling parameters the thickness over the length of the plate can be varied to a certain extent and a thickness profile can be obtained (Richter & Schmackpfeffer 1988). Figure 11 gives an overview of the possible profile types. Newest developments for LP plates allow now slopes of up to 10 mm/m. These new possibilities offer a greater freedom to the engineering in choosing the plate profile desired for various applications, e.g. bridges.

Similar to the high strength steels the economic and ecologic benefit of this special type of steel plates lies mainly in a material weight reduction. The tunable plate thickness gives the opportunity to save excess material in regions where the thickness is not needed from static calculations. Given that the usage of LP plates can offer a cheaper solution by representing less excess material and less welding costs. This consideration implies only the fabrication cost and is not involving the inherent reduction of transportation cost and energy which is associated with such a lower component weight, as already stated before.

6 CONCLUSIONS

The steel making industry can significantly support the economic efficiency of a steel bridge by developing and refining modern steel concepts. Mainly the potential savings are associated with a reduction of fabrication time (faster welding processes, less time for preheating or transportation) or also with reduced energy and material consumption (weight reduction). Therefore positive effects on the environment are immanent. This combination of effects can help the steel fabricators reaching the ambitious goals of high profitability, safety and sustainability in modern bridge construction.

REFERENCES

Kuhlmann U. & Maier P. Sustainability assessment to Steel-Composite Bridges. Proceedings of the International Workshop on Eurocode 4–2, *Composite Bridges*, Stockholm, Sweden, 2011.

Hever M. & Schröter F. Modern steel—High performance material for high performance bridges. *5th International Symposium on Steel Bridges,* Barcelona, Spain, 2003.

Schröter F. Steels for modern steel construction and offshore applications. *10th Nordic Steel Construction Conference*, Copenhagen, Danmark, 2004.

Uwer D & Höhne H. Charakterisierung des Kaltrißverhaltens von Stählen beim Schweißen. *Schweißen und Schneiden 1991; 43 (4):195–199.*

Uwer D & Wegmann H. Anwendung des Kohlenstoffäquivalents CET zur Berechnung von Mindestvorwärmtemperaturen für das kaltrisssichere Schweißen von Baustählen, *DVS-Jahrbuch Schweißtechnik 1996; 96:46-55.*

Samuelsson A & Schröter F. High performance steels in Europe. *Use and Application of High-Performance Steels for Steel Structures*. Structural Engineering Documents, Zurich, 2005.

Willms R. High strength steels in steel construction: Application and processing. *Proceedings of the 5th European Conference on Steel and Composite Structures*, EUROSTEEL 2008, Graz, Austria.

Richter K & Schmackpfeffer H (1988) Herstellung von LP-Blechen und deren Verwendung im Brückenbau. *Stahlbau 1988; 57 (2):33–38.*

Recent Progress in Steel and Composite Structures – Giżejowski et al. (Eds)
© 2016 Taylor & Francis Group, London, ISBN 978-1-138-02946-0

Modelling for the effect of welding process on buckling of built-up high strength steel box column

J. Jiang
School of Civil and Environmental Engineering, Nanyang Technological University, Nanyang, Singapore

C.K. Lee
School of Engineering and Information Technology, The University of New South Wales, Canberra, Australia

S.P. Chiew
Singapore Institute of Technology, Dover Campus, Singapore

ABSTRACT: High strength steel box column are usually fabricated from steel slab by applying welding. The welding process can introduce residual stresses and geometric imperfections into the columns and influence the column strength. In this study, a numerical investigation on the behavior of high strength steel thin-walled box column under the compression force was carried out. The welding processes were firstly simulated with commercial package ABAQUS in this study to find out the residual stress distributions in high strength steel box column. After that, the column behaviors under the compression were modelled with predefined field from the previous step. The effect of the welding process (including FCAW and SAW), heating treatment (including preheating and post-weld heat treatment) and geometrical imperfection on the residual stress field and box column strength was investigated and discussed.

1 INTRODUCTION

Currently, most steel structures are made of mild steel for its satisfactory mechanical property and availability. In existing codes of practice, mild steel is well specified for structural application [1]. However, High Strength Steel (HSS) with yield strength larger than 460 MPa has been an increasing interest in the usage for its merits in economy, aesthetics and safety [2]. The stress-strain behavior of HSS is different from mild steel such that HSS exhibits reduced ductility due to strain hardening after yielding. Furthermore, residual stress due to welding in HSS could be more serious than that in mild steel and might have a negative impact on its structural performance [3]. Uneven cooling of structural steel shapes and plates are the primary result of residual stresses within them. Welded built-up members exhibit tensile residual stresses in excess of the yield stress (in the region of the welded area) of the parent material. Due to the intense heat associated with flame-cutting, the material properties are significantly altered in these areas [4]. The thin HSS plate is likely to buckle locally in compression and therefore of significant importance for designing the thin-walled structures.

The local and overall buckling of columns for mild cold-formed steel structures has been extensively investigated [5–6]. In addition, some studies for the overall buckling of high strength steel can also be found [7–8]. However, only a few studies have been reported on the interaction between the fabrication procedure and the buckling strength for high strength steel. The paper is concerned with a numerical investigation of welding procedure on the buckling strength of thin-walled box column made of high strength steel with yield stress of 690 MPa. A series of box columns with various welding treatments are analyzed.

2 MODELLING FOR WELDING RESIDUAL STRESS

2.1 *Overview*

Thermal cycles in the both of FCAW and SAW processes inherently cause the metal to experience high temperature and to melt and solidify at the weld region, inducing nonlinear mechanical behavior such as residual stress as well as microstructure alternation in the weld region and HAZ. In this study, a coupled thermal-stress analysis is carried out for the both of welding processes with the determination of the resulting residual stress. For FCAW models, the multi-passes of weld will be lumped into two blocks for each corner of the

box to reduce the computation cost. The heat source is applied though the DFLUX subroutine of the Abaqus at two blocks for each corner. Large displacement effects have been considered in the modeling by including the non-linear geometry option, NLGEOM, in the Abaqus. For SAW models, single pass welding for each corner of the box is assumed. The heat input for SAW process is also achieved by the DFLUX subroutine with different setting on the magnitude and coefficient of heat energy with FCAW process. For each welding process, three models corresponding to the specimens with 1) as-welded condition, 2) preheated box column and 3) post-weld heated box column are created. For the as-welded model, a consistent pre-defined temperature field of 30°C is given to the whole model. For the model corresponding to the preheating, 100°C is set for the area within 100 mm from the chord weld toe while 30°C is set for all other parts. It is input into the model as a predefined temperature field. It means that the preheating temperature error is ignored in the modelling and this predefined temperature field is modelled as uniform in the preheated area.

2.2 *Meshing, interaction and boundary condition*

Abaqus includes general purposed linear and second order brick solid elements for heat transfer analysis and stress analysis [9]. In this study, a three-dimensional thermally coupled linear brick element (C3D8T) was used homogeneously throughout the entire model. The C3D8T element consists of a brick with eight nodes, and four degrees of freedom (x, y and z displacements {ux, uy, uz} and temperature) (Fig. 1). This element calculates displacements and temperatures using a linear integration method. As the weld would be added at the four corners of the built-up box column, an improved mesh is applied for the area close to the weldment. To make correctly input the residual stress field into the following column strength analysis model, the same meshing is used in the residual stress simulation and buckling simulation except the element type.

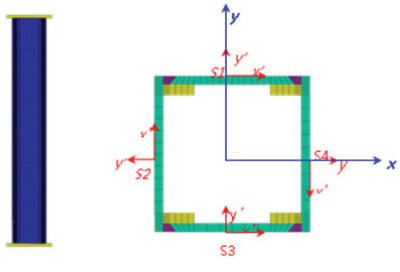

Figure 1. The meshing of the analysis model.

In this analysis, a simplified treatment is assumed for the thermal interaction. All free surfaces (including outside surface, inner surface and two end surfaces) of the boxes are assumed for thermal convection and radiation. It means that all free surfaces from which the heat can dissipate into the air will have thermal convection and radiation for heat dissipation. The convection coefficient h is defined as 15 W/m^2 K and emissivity ε is set as 0.2.

2.3 *The heat source model*

Since that the temperature field driven by the weld heat source is the dominant driving force for residual stress formation during the welding procedure, an accurate analysis of the thermal cycle is required to obtain accurate prediction of residual stress. Furthermore, the heating source is also the driving force for phase transformation, thermal strain and stress, and eventually residual stress formation. For the mathematical modelling of thermal cycles, it can be traced back to in the late 1930 s when Rosenthal [10] firstly applied the Fourier law into moving heat sources. However, the main shortcoming of this solution is the misfit of temperature field near the fusion and heat-affected zones. To accurately capture the temperature near the arc, Pavelic et al. [11] mentioned that the heat source should be distributed and proposed a Gaussion distribution of heat flux deposited on the surface of the work piece. Considering that the temperature gradient in front of the heat source is different from in the rear, a double ellipsoidal model of power density distribution was introduced by Goldak. In the double ellipsoidal model, the front half of the source is the quadrant of one ellipsoidal source and the rear half is the quadrant of another ellipsoid. To define the model, the fractions ff and fr of the heat deposited in the front and rear quadrants are needed such that of ff + fr = 2. It was recommended by Goldak [12] that ff and fr should be set as 0.6 and 1.4, respectively. The power density distributions inside the front quadrant and the rear quadrant can be expressed as:

$$\begin{cases} q_f(x,y,z) = \dfrac{6\sqrt{3} f_f Q}{a_1 \cdot b \cdot c\pi\sqrt{\pi}} e^{\frac{-3x^2}{a_1^2}} e^{\frac{-3y^2}{b^2}} e^{\frac{-3x^2}{c^2}} \\ q_r(x,y,z) = \dfrac{6\sqrt{3} f_r Q}{a_2 \cdot b \cdot c\pi\sqrt{\pi}} e^{\frac{-3x^2}{a_2^2}} e^{\frac{-3y^2}{b^2}} e^{\frac{-3z^2}{c^2}} \end{cases} \quad (1)$$

where, $Q = \eta \cdot U \cdot I$, η is the heat source efficiency, U is the voltage of electric arc, I is the current of electric arc and a_1, a_2, b, c are ellipsoidal parameters.

In this analysis, the double ellipsoidal model is employed to predict the thermal and stress field during the welding. In order to automatically

Table 1. Heat source parameters for two welding processes. Modelling scenario.

Welding process		FCAW [13–14]	SAW
Net power (kW)		4.4	80
Heat coefficient		0.80	0.95
Welding speed (mm/s)		2.6	10.0
Heat source geometrical parameters	a_1	0.010	0.025
	a_2	0.020	0.050
	b	0.010	0.032
	c	0.005	0.016

Table 2. Welding condition and geometry of the model.

			Geometry					
Label	Welding method	Welding condition	*D* mm	*d* mm	*t* mm	*L* mm	λ	λ_0
F-1	FCAW	As-welded	100	76	12	1000	27.58	0.50
F-2		Preheating	100	76	12	1000	27.58	0.50
F-3		PWHT	100	76	12	1000	27.58	0.50
S-1	SAW	As-welded	100	76	12	1000	27.58	0.50
S-2		Preheating	100	76	12	1000	27.58	0.50
S-3		PWHT	100	76	12	1000	27.58	0.50

Note: t: plate thickness, d: inner section width, L: column Length, λ: slenderness of the column, λ_0: non-dimensional slenderness.

renew the weld filler elements as the welding process was carried out, a special FORTRAN program is developed to describe the moving of heat source. In the absence of better data, experience suggests that it is reasonable to take the distance in front of the heat source equal to one half the weld width and the distance behind the heat source equal to twice the width [12]. Table 1 lists the heat model parameters used in both welding processes.

2.4 *Modelling scenario*

2.4.1 *Welding process choice*

There are two welding processes (FCAW and SAW) chosen in this study for the effect of welding methodology on the final residual stress field and column strength. The FCAW offers two distinct advantages over shielded metal arc welding. First, the electrode is continuous to eliminate the built-in starts and stops that are inevitable with shielded metal arc welding. Another advantage is that FCAW increases in deposition rate and productivity.

Submerged Arc Welding (SAW) differs from other arc welding processes in that a layer of fusible granular material called flux is used for shielding the arc and the molten metal. Considering that it is frequently used in cases when welding path is simple and long enough, it is also included in this study to evaluate its extremely high heat input on the residual stress and column behavior. Table 2 gives the modelling scenario of this study.

2.4.2 *Heating treatment effect*

To evaluate the heating effect on the residual stress magnitude and column strength, three models corresponding to 1) as-welded condition, 2) preheating before carrying out the welding and 3) post-weld heat treatment condition are created in this part.

1. *As-welded column*
   To evaluate heat treatment (preheating, post-weld heat treatment) on the residual stress field, the box column welded at ambient temperature without any heat treatment is modelled and analyzed firstly as the benchmark model. It is classified to as-welded specimen, which means there is no preheating before the welding and no subsequent heat treatment operation following the welding.
2. *Preheated column*
   An effective way of preventing the cold cracking and minimize the residual stress is to preheat the weld area to higher temperature to delay the cooling of the welded joint. The minimum preheating temperature is depended on factors including the chemical composition of the base material, the thickness of work piece, the welding process and hydrogen content of the weld metal. There are two methods (Method A: Graphical determination and Method B: Computational determination) provided by EN1011-2:2001 [15]. In this paper, Method B of EN1011-2, computational determination, is used to determine the minimum preheating temperature. The recommended minimum preheating temperatures for joints 12 mm RQT701 steel plate was found to be equal to 85°C. However, in order to make the fabrication procedure easy to handle, a single preheating temperature of 100°C was applied to all preheated joints. It also should be noticed that overheated for Q&T steel may be detrimental in the heat affected zone. Therefore, overheating should be avoided for the joint.
3. *Post-weld heat treated column*
   Post-weld heat treatment is often used to improve the properties of a welded structure. Two most common procedures used for PWHT are post heating and stress relieving [16]. The former one is used to minimize the potential for hydrogen induced cracking, which may happen when the temperature of the component is close to the ambient temperature. In this process, the steel shall not be allowed to cool to room

temperature; instead, it should be immediately heated from the inter-pass temperature to the post heat temperature and held at this temperature for a design time. The latter one is used to reduce the stresses that remain locked in a structure as a consequence of manufacturing processes. Differentiated with post heating process, the component shall be allowed to fully cool down before stress relieving. The stress relieving PWHT will be studied in this paper for its effect on relieving the welding residual stress.

Since that the maximum temperature will not reach Ac1, the temperature at which austenitic transformation begins, PWHT is modelled by incorporating creep with temperature-dependent material properties. The Norton law should be followed during the soaking time for PWHT, which can be expressed as below:

$$\dot{\varepsilon}_{cr} = A\sigma^n \tag{2}$$

where $\dot{\varepsilon}_{cr}$ is the creep strain rate, σ is von Mises equivalent stress, A and n are material constants and equal to $9.016e^{-27}$ and 10.286 respectively in this study, which are according to [17].

2.5 *Modelling results and discuss*

The modelling results for FCAW case are selected for evaluating the heat treatment on the residual stress field in this section. Three models corresponding to as-welded column, preheated column and post-weld heated column are chosen to study the impact of the heat treatment on the residual stress field. The stress along column length direction (S33) and Mises stress are selected for plotting against the local coordinate position (shown in Fig. 1).

1. *As-welded column*
   Fig. 2 and Fig. 3 present the residual stress along column length direction (z direction) and Mises stress respectively, against the distance from the center lines. The figures show four curves, which are respectively representing the stress variation along four outside surface (*S1: topside, S3: bottom, S2: left side, S4: right side, See* Fig. *1*). The curves show that, in the outside surface of the box column, the weld region and its' nearby has a tensile stress with its magnitude much higher than the other position in the base metal. It should be noted that the high tensile stress is only localized in 20 mm from the weld and stress drop quickly to compressive stress for the location outside this distance. Another finding is that the tensile stress is more uneven distributed on the outside surface of the box along S2 and S4 side. This phenomenon should be related to the weld configuration since the heat is transferred to S2 and S4 surface by the connection in the inner surface of the box (similar to "fillet weld" as to S2 and S4), while the heat energy is directly dissipated to S1 and S3 by heat conduction into base metal (similar to "butt weld as to S1 and S3).

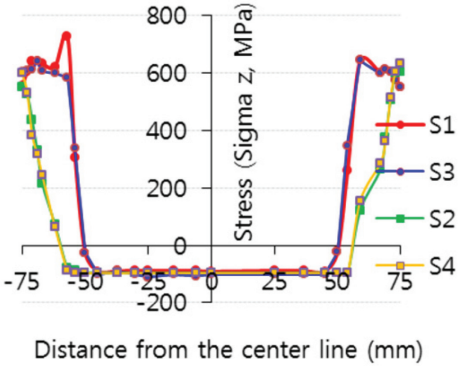

Figure 2. S33 of as-welded column.

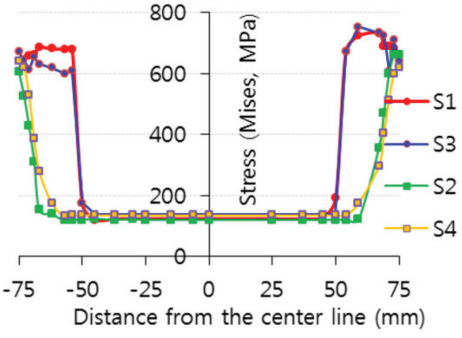

Figure 3. Mises stress of as-welded column.

2. *Preheated column*
   Fig. 4 and Fig. 5 show the welding residual stress along the column length direction (z direction, S33) and Mises stress respectively for preheated column. Similar with stress distribution with as-welded column can be found for preheated column: high tensile stress gathered in the vicinity of the weld and part of those areas is yielded. Compressive residual stress is mostly small in magnitude. By comparing Fig. 4 and Fig. 5 with Fig. 2 and Fig. 3, it can be seen that preheating can reduce the highest tensile residual stress to approximately 13% from their original value (when the preheated temperature is 100°C). Another observed influence of preheating is that it can slightly improve the stress gradient in the vicinity of the weld when comparing with as-welded column.
3. *Post-weld heat treated column*
   Fig. 6 and Fig. 7 show the distribution of residual stresses (S33 and Mises stress) with post-

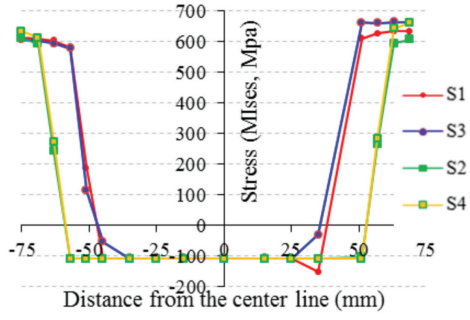

Figure 4. S33 of preheated column.

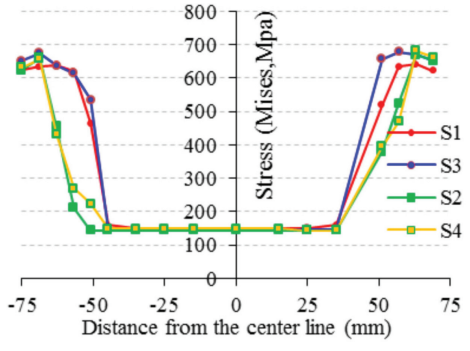

Figure 5. Mises stress of preheated column.

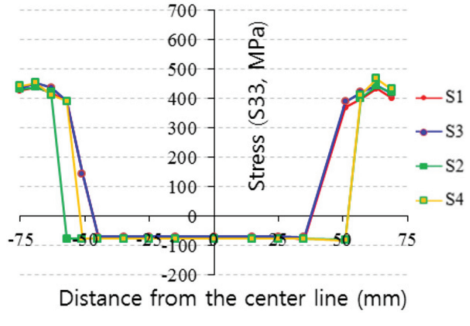

Figure 6. S33 of PWHT column.

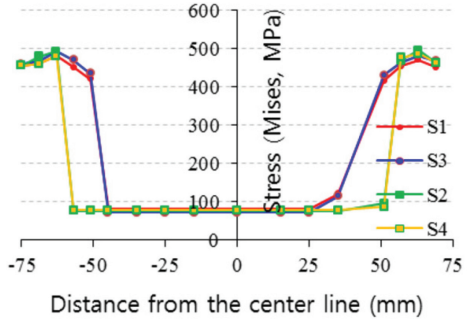

Figure 7. Mises stress of PWHT column.

weld heat treatment. In the PWHT process, the temperature of the box column was heated up to 600°C in the initial 1000 s and hold the temperature for 1.5 hours and then cooled to ambient temperature. It can be found that PWHT reduces nearly one third of the maximum tensile residual stress in the weld and HAZ area when compared with as-welded column. It means that in view of stress relieving effect, PWHT is more effective. The creep deformation during the soaking time can substantially reduce stress magnitude.

4. *Welding process effect*

In this section, a comparative study between the residual stress fields due to FCAW and SAW is carried out. To avoid uncertainty of heating treatment, the as-welded models are selected for the comparison. As shown in Fig. 1, high tensile stress dominantly developed at the four corners of the box column for both welding processes. Owing to the high net power input of the SAW process, the maximum tensile stress (S33, z direction) is around 16% higher than that in FCAW model. Another finding is that the HAZ area in SAW model is wider than that in FCAW model. It means material deterioration is more serious happened in SAW model considering the face that the yielding stress would get a bit worse for Q&T high strength steel after the welding. To make stress state self-balanced, a higher magnitude of compressive stress can be found in the outside surface of the SAW model. This cause the stress gradient in the transition area from HAZ to base metal very high, which would be weaken for its mechanical properties.

3 MODELLING FOR COLUMN BUCKLING

3.1 *Overview*

In this section, the built-up HSS column behavior under the axially loading will be studied. Since the residual stress field obtained from Section 2 would be input into the buckling analysis as predefined field, the same meshing with residual stress simulation is used in this section except the element type is changed to C3D8I, which is an 8-node linear brick element used for stress analysis [9]. To avoid the stress concentration effect for the axial loading in one end of the column, a reference point is created so that the load can be applied in the reference point. A coupling interaction between the reference point and the end plate is added so that the load can be averagely distributed into the end surface. For the reference point, both the translational and rotational degrees of freedoms are free so that load can be exerted directly on the movable end.

3.2 *Geometrical imperfection and residual stress*

The response of some structure depends strongly on the imperfections of the structure geometry, particularly if the buckling modes interact after buckling occurs. Hence, a geometrical imperfection would be assessed and used in the analysis. In this study, the degree of initial imperfection is specified as a percentage of steel plate thickness, which can be expressed as 0.3t (Py/Pcr) 0.5 (Py: yield load, Pcr: the critical buckling load, t: steel plate thickness). In this study, it is modelled by multiplying deformation shape of eigenvalue buckling analysis by the coefficient of $3.6 \times 10–3$. The other method for incorporating geometrical imperfection is to introduce the out-of-plane deflection at mid-length of the column based on the imperfection measurement. It was found that the two ways were not significantly different for stub columns [18]. Meanwhile, a central bow of 1/1000 of the member length covering unintentional load eccentricities is assumed in this study. The approach to define an imperfection in this paper involved two analysis runs with the same model definition: (a) In the first analysis run, an eigenvalue buckling analysis was performed on the "perfect" structure to establish probable collapse modes and to verify that the mesh discretizes those modes accurately. (b) In the second analysis run, an imperfection in the geometry was introduced by adding these buckling modes to the "perfect" geometry. After that, a geometrically nonlinear load displacement analysis of the structure was performed containing the imperfection using the Riks method to perform plastic buckling and post-buckling analyses of the column. The welding-caused residual stress is incorporated in the analysis by importing the residual stress field from Section 3 as the pre-defined field for the buckling analysis.

3.3 *Modelling results*

The six model results are given in Table 3. The differences between modelling results with yielding load are shown in the table. The column deformation after the local buckling is shown as Fig. 8. It is observed that the local buckling load is close to the yielding load for as-welded models when FCAW is applied in the fabrication process. As to the preheating effect, it seems that there is no much improvement on the column strength. However, it should be noticed that PWHT can improve the column strength to some extent for both FCAW and SAW welding processes. Compared with FCAW process, the column strengths of three models corresponding to SAW process are smaller. The influence of the welding residual stress in SAW is more serious (considering that the geometrical imperfections are all the same for the 6 models in the analysis).

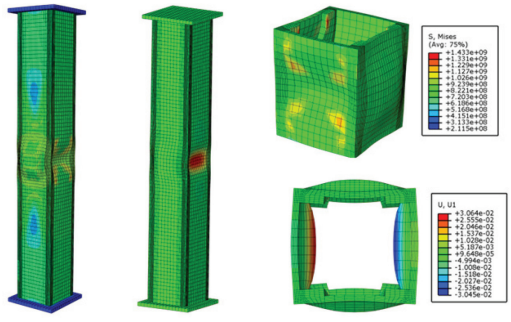

Figure 8. Column deformation after local buckling.

Table 3. Modelling results for the box column.

	FCAW			SAW		
	As welded	Pre-heating	PWHT	As welded	Pre-heating	PWHT
Specimen	F-1	F-2	F-3	S-1	S-2	S-3
Py (kN)	3820	3820	3820	3820	3820	3820
Pn (kN)	3896	3973	4087	3591	3629	4049
Pn/*Py*	1.02	1.04	1.07	0.94	0.95	1.06

4 CONCLUSION

A series of numerical models were carried out in this study to investigate the impact of the welding process and heating treatment on the high strength steel stub box columns. The welding residual stress field for both FCAW and SAW processes were obtained. By importing the residual stress and geometrical imperfections as the pre-defined input for the columns' buckling models, the column strengths with different welding process and heating treatment were obtained. The preliminary findings can be summarized below:

1. High tensile residual stress dominantly developed at the four corners of the box column for both FCAW and SAW welding processes. Owing to the high power input of the SAW process, the maximum tensile stress (S33, z direction) is around 16% higher than that in FCAW model.
2. The HAZ area in SAW model is larger than that in FCAW model. Both preheating and PWHT can reduce the welding residual stress to some extent. However, in term of residual stress-relieving, the PWHT seems have a better effect than the preheating.
3. The local buckling load of the stub high strength steel box column is close to the yielding load. As to the preheating effect, it seems that no much

improvement on the column strength. However, PWHT can improve the column strength to some extent for both FCAW and SAW welding processes.

ACKNOWLEDGEMENT

This research is supported by the Singapore Ministry of National Development (MND) Research Fund on Sustainable Urban Living (Grant No. SUL2013-4).

REFERENCES

[1] EC3, Design of steel structure-Part 1.1: general rules and rules for building, 1993, European Committee for Standardisation (CEN).

[2] Mochuzihi H., Yamashita T., & Fukasawa T. 1995. Application of HT780 high strength steel plate to structural member of super high-rise building: part 1 Development of high strength steel with heavy gauge and welding process. *Proceedings of the 5th East Asia-Pacific Conference on Structural Engineering and Construction, Gold Coast, p.2283–2288*.

[3] Masubuchi K. 1980. Analysis of welded structures: residual stresses, distortion, and their consequences *International Series on Materials Science and Technology:* Pergamon Press.

[4] Pei-Yuan Cheng. 2009. Influence of Residual Stress and Heat Affected Zone on fatigue failure of welded piping joints, Ph.D thesis of North Carolina State University.

[5] Usami T. & Fukumoto Y. 1982. Local and overall buckling of welded box columns, *Journal of the Struatural Division, Proceedings of the American Society of Civil Engineers, Vol,108*, *No. ST3, Page:525–542*.

[6] Richard Liew J.Y., Shanmugam N.E. & Lee S.L. 1989. Local buckling of thin-walled steel box columns, *Thin-Walled Structures, No.8, Page:119–145*.

[7] Ban H.Y., Shi G., Shi Y.J. & Bradford M.A. 2013. Experimental investigation of the overall buckling behaviour of 960 MPa high strength steel columns, *Journal of Construction Steel Research, No.88, Page:256–266*.

[8] Wang Y.B., Li G.Q., Chen S.W. & Sun F.F. 2014. Experimental and numerical study on the behaviour of axially compressed high strength steel box-columns, *Engineering Structures, No.58, Page:79–91*.

[9] ABAQUS user manual. Version 6.13. Hobbit. Karlsson & Sorensen Inc., USA.

[10] Rosenthal D. 1946. The theory of moving sources of heat and its application to metal treatments, *Trans ASME, Volume 68, Page:849–956*.

[11] Pavelic V., Tanbakuchi R., Uyehara O.A. & Myers. 1969. Experimental and computed temperature histories in gas tungsten arc welding of thin plates, *Welding Journal Research Supplement, Volume 48, Page: 295–305*.

[12] Goldak J.A. & Akhlaghi M. 2005. *Computational Welding Mechanics*, Springer.

[13] Lee C.K., Chiew S.P. & Jiang J. 2013. 3D Residual stress modeling of welded high strength steel plate-to-plate joints, *Journal of Constructional Steel Research, 84, Page: 94–104*.

[14] Jiang J., Lee C.K. & Chiew S.P. 2015. Residual stress and stress concentration effect of high strength steel box T-joints, *Journal of Constructional Steel Research, 105, Page: 164–173*.

[15] BS EN 1011–2:2001. Welding-Recommendations for welding of metallic materials. Part 2: Arc welding of ferritic steels, British Standard.

[16] Funderburk R.S. 1998. Key concepts in welding engineering—Post weld heat treatment, *Welding Innovation Volume. XV, No. 2*.

[17] Zhang G, Zhou C & Xue J. 2008. Finite element analysis of high temperature piping creep under inner pressure and welding residual stress, *Acta Metallurgica Sinica, Volume 44, No.10, Page:1271–1276*.

[18] Yang D. & Hancock G.J. 2004. Numerical simulations of high strength steel box-shaped columns, *Research Report No. R 842, the University of Sydney*.

This page intentionally left blank

Recent Progress in Steel and Composite Structures – Giżejowski et al. (Eds)
© 2016 Taylor & Francis Group, London, ISBN 978-1-138-02946-0

Application of Barkhausen method to determine internal stresses in cold-rolled and hot-rolled sheets

A. Łukowicz & D. Kowalski
Gdańsk University of Technology, Gdańsk, Poland

ABSTRACT: The paper presents investigations on internal stress distribution in plane hot—or cold-rolled sheets dedicated for the cold-formed profiles. The motivation of the research is a new profile design whose bending technology, incorporating a longitudinal welded joint and hot-dip galvanization after bending and welding introduces additional internal stresses. In order to identify the entirety of stresses in the process of sheet production and profile forming, in its first stage identification of internal stresses was made, due to sheet rolling, storing and transportation in the form of coils.

1 INTRODUCTION

1.1 *Internal stresses in steel products*

Sheet manufacturing, including the thin-walled elements is a sequence of various technological processes. The major contributing processes are smelting, rolling and workshop treatment.

The first stage of smelting in steel plants brings about significant diversity of chemical contents of pig iron. The traditional, two-stage method of steel smelting, including metallurgic and steel processes, the extent of harmful impurities was controlled by the method of steel deoxidizing. The further non-uniform location of impurities was a result of non-uniform ingot solidification. Segregation zones then emerged of deteriorated plastic parameters and sensitivity to fracture due to cold and hot processing. Continuous steel founding is a modern method to achieve a proper and solid ingot structure, without a zone segregation. The entirety of Huta Katowice steel production is made using this procedure.

The next stage of hot rolling increases material anisotropy, thus changes microstructure and mechanical properties of the material. Due to rolling the primary crystals deflect, in the case of sheets they become tiles. In the rolling direction material hardening occurs. The transverse direction makes material properties deteriorate, to be extremely reduced in the thickness direction, especially for thick sheets. Internal stresses emerge in the final phase of hot rolling. The temperature above 600ºC makes the material deflect freely. Immediate cooling is characteristic for sheet edges, while the middle strips are still hotter. Shrinkage of cooler parts of the sheet is restrained by higher temperature regions. The hotter parts are subjected to yield. After a total cooling parts of the sections cooled first are at compression, the rest is at tension.

Steel properties are affected by rolling temperature. Being too high it causes overheating and reduction of extensibility, too low temperature leads to squeeze, consequently defects and dislocation block.

Especially thin sheets are proceeded by cold rolling to act stronger on mechanical properties than a high cooling velocity after hot rolling. This permanent strain of a material, ranging from 50 to 80%, even exceeding 90% yields plasticity and hardening behaviour [Augustyn J., Śledziewski E., 1974].

Material subjected to cold rolling becomes tougher and stronger, losing its plastic features, especially ductility. Next, sheets usually stored in tapes wound on coils are aligned to plane sheets, prior to further processing. The rectifying methods may employ multi-roll rectifiers or the processes of surface, point, electro-resistant or induction heating. They all act upon plastic parameters of a material [Augustyn J., Śledziewski E., 1981]. In the perspective of further processes of bending and welding their impact on plasticity and resistance of steel must be taken into account. Alignment of elements shape-deformed by welding is an important issue too [Augustyn J., Śledziewski E., 1974], [Garstka T., 2008].

All the above mentioned processes lead to additional material effects, called residual or internal stresses. They occur in an unloaded configuration, their values affected by a stress level due to a cold material squeeze and the final technology used (re-crystalizing annealing, smoothing rolling to produce additional squeeze of 0,5 ÷ 1,5%). Consequently, internal stresses may superimpose with the external load effects, thus causing a joint impact on

load-carrying capacity and stability of particular walls of cross-sections, single structural elements or entire structures.

These stresses may be labeled macrostresses (1st kind) of an equilibrium range comparable to structural dimensions and microstresses (2nd kind) of a grain-scale equilibrium range [Senczyk D., 1998].

1.2 *Advantages and disadvantages of internal stress occurrence*

Internal stresses may act upon the element performance. Thus a tendency arises to reduce them in specified cases, in other situations they are intentionally produced in order to rectify an element, bringing about stresses of a given magnitude and sign.

It is well-known that the increase of compressive stresses on the product surface increases its fatigue resistance. Thus an advantageous internal stress distribution is produced by a surface squeeze by means of e.g. ball peening, finish rolling, shot peening.

While stresses due to external loads cause plasticity at given locations, processing and application of a dedicated technology may introduce additional internal stresses. Summing these stresses up leads to reduction of operational safety of an element.

While external actions occur in an operational stage internal stresses are superimposed to external load effects to possibly reach the yield limit. This leads to non-uniform plastic strain, stability loss, warping, distortion and twist. Internal stresses reduce product resistance at variable and cyclic loads. They also act in the process of corrosion. Sequential corrosive damage of a product surface is controlled by the internal stress level, to increase with the stress increment. It also affects brittle crack and corrosive fatigue.

1.3 *Methods to determine internal stresses in steel*

Due to a high possible impact of internal stresses on structural material performance, numerous methods were worked out for their investigation and determination. The first group requires internal stress vanishing. Relaxation due to strict operational sequence is a cause of strains. Next, stresses may be computed from simple Hooke's law relations. These methods assume that the proper volume change due to deleted internal stresses is independent of the relaxation processing. Thus strains are intended to vary with stresses only.

The second group of internal stress measurement methods is not linked with internal stress vanishing. A material parameter is chosen to vary with the stresses. This allows to determine the surface stress directly. It is linked with calibration —the relation between the measured parameter and stress state. Sensitivity and reliability of the selected parameter to indicate stress level is also of great concern. This group of methods cover:

- toughness measurement method, a destructive one, ma king use of the impact of stresses on toughness,
- radiographic methods (X-ray or neutron radiation), exploring material ability to absorb and reflect radiation,
- vortex current method, exploring electromagnetic induction,
- ultrasonic method, based on partial reflection of sonic wave on the boundary of two media,
- magnetic methods, Barkhausen method exploring magnetic metal properties.

The paper is focused on non-destructive Barkhausen method to determine distributions of internal stresses in flat sheets.

2 BARKHAUSEN METHOD

2.1 *Method description*

The steel material made of ferritic grains, exhibiting internal magnetizing is divided into magnetic domains limited by boundaries. Domains are regions of identical magnetization. Thus the action between atoms makes the neighbouring dipoles unidirectional. The domain layout is acted upon material thickness, external magnetic field and the presence of internal stresses.

Each domain is surrounded by walls, called boundaries. Ferrite identifies boundaries of 180° and 90°, denoting an angle between magnetizing direction in two neighbouring domains. Their thickness ranges hundreds of atoms, which is very low comparing to domain dimensions of several millimetres. Magnetic moments rotate every atom by a small angle, consequently, rotating hundreds of atoms by 90 or 180 degrees.

The domain boundaries are subjected to anchoring, due to material structural defects, e.g. dislocations or internal stresses. Thus internal stresses block the domain boundary translation and rotation. In order to overcome this resistance sufficiently high energy must be delivered, from the magnetic field intensity. Domain dimensions increase of the domains initially magnetized on the direction of the magnetizing field, at the effort of other domains. It happens by means of incorporating atoms neighbouring with the dominating domain. Due to strong magnetic field diversely magnetized domains rotate immediately. This is a Barkhausen effect to exhibit a rapid movement of domain boundaries—unanchoring. Magnetic induction change in a newly magnetized zone

implies a voltage signal inducing in the coil close to material surface. It is a non-invasive procedure, thus applied in non-destructive tests to assess internal stresses.

2.2 *Measurement equipment*

The measurement system consists of electronic equipment—a portable device. It contains module for magnetizing, conditioning and Barkhausen noise parameter detection. Programming application cooperates with the apparatus by means of measurement card in order to perform statistical processing, visualization and measurement result display. The magnetizing module produces electric current of given parameters.

The probe consists of a core with a magnetizing winding and measurement winding, the latter between the pole pieces. Two parameters are measured: voltage signal due to Barkhausen effect and voltage signal controlling the magnetization process. The latter stands for the magnetic flux rate. The former, generated in the probe is a noise of impulses whose number and amplitude are affected by microstructure and investigated stresses.

The role of a measurement module is to filter a background from the noise and to amplify the efficient voltage signal prior to transformation. The basic noise parameters are constant voltage proportional to the RMS Barkhausen effect intensity and the number of Barkhausen impulses in a single magnetizing cycle. The third parameter is the rate of magnetic induction flux, transformed into a DC voltage as a controlling signal. This parameter checks the probe alignment, acting upon measurement accuracy. The idea of measurements lies in comparing one of the parameters: RMS value or the number of steps with a calibration value, expressed in terms of stresses.

2.3 *Experimental procedure*

The experiments involve a measurement box with a display and a connected head with a measurement coil, to induce voltage impulses called magnetic Barkhausen noise (Fig. 2a).

The head includes an electromagnet, a detector of Barkhausen effect voltage signal and a detector of control signal of magnetizing process. Two signals are received: alternating voltage of Barkhausen effect and alternating voltage of control signal. The head layout allows for a single measurement only unidirectional.

Variations of amplification of AC voltage are controlled by decimal switched P1 and P2, the discrimination voltage due to Barkhausen impulse amplitude by a switch P3. Steel name and specimen thickness act on the signal level to reach the RMS voltage V1 = 400 [mV] and discrimination level not less than 100 [ju]. Additionally, the measurement results are debugged and recorded by means of a dedicated software.

3 SHEET INVESTIGATION

3.1 *Scope of the research*

The cold-formed profiles are fabricated form thin sheets, delivered to the plant in coils. Before bending on the rolling mills or bending brakes the sheet is unwound from the colis and straightened. The process of cold bending employs the ability of metal alloys to achieve permanent strains. Plastic permanent strains remain in a profile after removing the shaping load, the material cohesively cannot be affected in any way either by cracks or delamination. While hot bending the plastic strain is accompanied by structural modification of a material, called squeeze. The squeeze zones rise the values of yield and ultimate strength, decreasing the extensibility [Bródka, Giżejowski 2006]. Consequently, material mechanical properties differ in various parts of the section. The results of research on internal stresses in cold-formed profiles was collected in [Dubina 2012]. Modification of steel properties in the cold-forming process is applied in the assessment of load-carrying capacity of structural elements [PN-EN 1993-1-3]. The specific design case directs to apply a minimum yield strength of an original material f_{yb} or the so-called averaged yield strength f_{ya}, due to a profile shaping method, a number of perpendicular bends, design thickness of a steel material before profile shaping and a gross area of a profile. The paper presents research on internal stresses in thin sheets intended for cold-formed profiles. The motivation for the research was a new profile design [Urbańska-Galewska E., Łukowicz A. 2012]. Due to a developed shape of an innovative cross-section a simplified bending technology was considered by means of a longitudinal welded joint and hot-dip galvanizing after bending and welding. It concerns additional internal stresses in the process of welding, bending and hot-dip galvanizing. In order to identify all the stresses in the processes of sheet fabrication and profile manufacturing, identification of internal stresses was made produced by sheet rolling, storage and transportation of the coils.

An innovative profile design of an open shape does not take dedicated research to adjust a distortional buckling mode. The shape of an innovative profile is difficult to fabricate by means of typical bending machinery. It requires an appropriate technology line equipped with a dedicated, unique bending tool. Due to a high cost generated the section

was proposed to split into two parts, easy to bend, next to join them along the entire element length by a butt weld at the symmetry centre of a cross-section. This technology requires internal stress assessment due to bending and rolling and those produced by welding [Dobrociński S., Flis L. 2004]. The sum of post-welding stresses and those already introduced to the material due to initial processing may act strongly on the variability of yield strength of the applied steel [Garstka T. 2008].

3.2 *Preparation for the experiments*

The method compares one of the parameters of magnetic Barkhausen noise: RMS voltage or the number of voltage impulse steps whose amplitude exceeds a given discrimination target in a single magnetizing cycle. The parameter to reflect the number of impulses shows a stronger variation dynamics, being frequently used in this type of research.

The key issue for the measurement accuracy is a proper alignment of measurement head, achieved by tracing the variation of control voltage. The measured values were recorded at a maximum control voltage value, corresponding to the highest magnetization intensity. Head placing is essential for the procedure too. While a head is not perpendicular to the material surface, the air gap increases, to alter the magnetization conditions, consequently, Barkhausen noise level, generating measurement error

The measurements were performed at every point of the mesh, both sides in three directions, as show in Figure 1.

The measurement results, in the form of voltage impulse values or RMS voltage allow to trace the modification of material during the experiment, but not measuring strength parameter variation. Thus investigations for the calibration characteristics were performed.

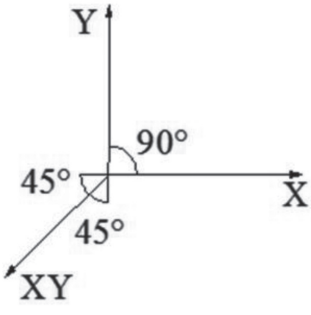

Figure 1. Measuring directions.

3.3 *Calibration characteristics*

Calibration is a check of a measured value to its pattern with a given accuracy. Nonlinear relations require the so-called calibration characteristics, by means of a series of operations to assess a relation between the measurement value and the appropriate physical parameters, defined by a measurement unit pattern. The procedure for such a characteristic is affected by the phenomenon user investigation.

Four calibration samples were taken for the experiments: two of them of dimensions $180 \times 50 \times 2$ mm made of cold-rolled steel DC04 and two $180 \times 50 \times 3$ mm made of S235 hot-rolled steel. They were cut from the same sheets to provide internal stress investigation, prior to making cold-formed profiles. In order to approximate a calibration curve a test stand was built (Fig. 2a). The device allows to fix a material specimen, bolt-fastened in the fastening zone, to provide an appropriate model of a fixed support.

The calibration sample is supported at one side only, thus further analysis employs a bracket static model. At the distance of 24 mm from the free end a bolt M8 was mounted, the thread pitch equal 0,25 mm. The screw in a threaded hole made the upper plate deflect, simulating a point load. This resulted in flexure of an assumed bracket model

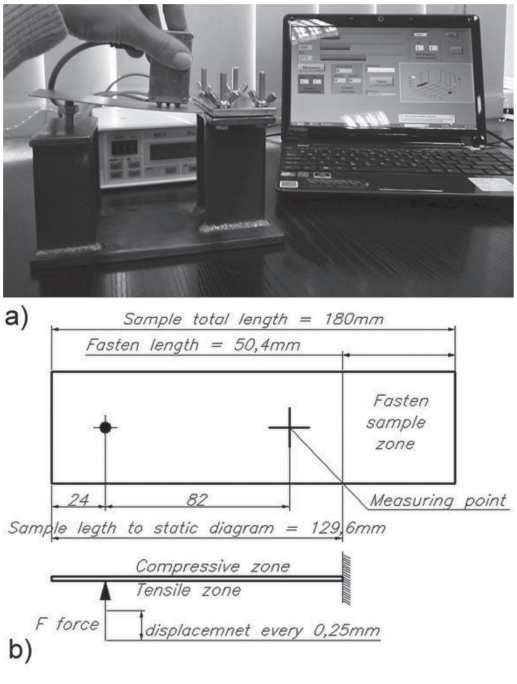

Figure 2. Calibration characteristic: a) test stand and measurement equipment, b) schematic diagram.

and the occurrence of two cross-sectional zones: tensile and compressive (Fig. 2b).

Every sample was subjected to two measurement series, at points signed at both sides of a plate, for the deflections on both tensile and compressed sides. The magnetic Barkhausen noise parameter was taken at the measurement point, 82 mm from the applied load. The value was affected by stress variation due to the shift of a calibration plate. The Barkhausen noise intensity varies with material strain level, so principal directions × and y were fund useful for the problem.

Due to a uni-directional head routine, measurements were taken at every measurement point at three directions: parallel, perpendicular and their bisector, with respect to specimen length. This allows to further compute principal stress directions.

The value of imposed load was not assumed, it was computed on the basis of a given displacement value.

Numerical analysis was conducted by means of ABAQUS software, assuming a flexural bracket model for the element. The FEM model was built 130 mm long, 50 mm wide and 2 mm thick. Proportions of the member made the decision to use shell four-node elastic finite elements. Basic material parameters were used taken from a static tension test. The model was built of 65 finite elements of dimensions 10 × 10 mm. Fixed support conditions were assumed at one of the plate edges. In order to obtain deflections a point force was imposed in the location of a bolt impact on a plate, the force values were 50 N, 30 N and 10 N. The analytical calibration results in the elastic range were as follows:

– displacement values leading to a force—displacement (F-u) quadratic formula,
– bending moment values in the measurement point, 82 mm far from a fixed point,
– normal stress value due to bending, given an elastic cross-section modulus of a sample,
– stress vs voltage impulse function—the so-called calibration curve (Fig. 3).

While making a diagram it was assumed that the measured values of voltage impulses correspond to tensile or compressive stresses.

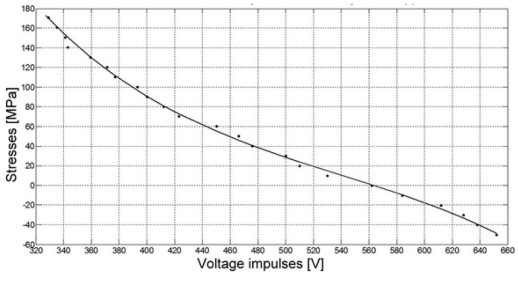

Figure 3. Stress vs voltage impulse diagram.

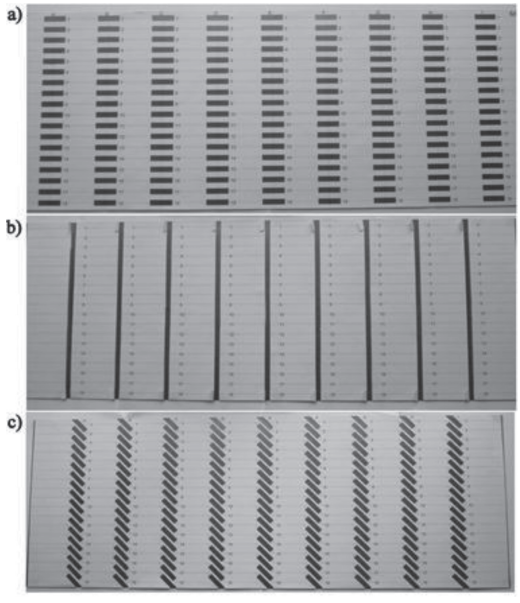

Figure 4. Sheet mesh of the measurement point.

3.4 *Samples for the experiments*

The essential experiments were done on sheets 365 mm wide and 1000 mm long made of DC04 steel grade 2 mm thick and S235 steel grade 3 mm thick. A number of 162 measurement points was assumed on every sheet, in the mesh of dimensions 12 × 100 mm (Fig. 4). Due to a uni-directional head routine, voltage impulses were measured were taken at every measurement point at three directions: parallel, perpendicular and their bisector, with respect to material fibers. Every sheet was examined on both sides, to capture stress variations on surfaces.

4 RESULTS

Internal stress distribution was presented on the surface of representative sheets, due to rolling process:

a. cold-rolled sheets (Fig. 5)
b. hot-rolled sheets (Fig. 6)

5 DISCUSSION AND CONCLUSIONS

In the analysis of surface diagrams (Figs. 5 and 6) of internal stress distribution in the investigated sheets similarities are observed. Both external and internal sides exhibit tensile stresses. Their values for particular sheets were close at both sides.

The results of the Barkhausen method show diversity of internal stresses identified on sheet surfaces. These stresses are remains of technological processes applied for the sheets. The normalization process does not mean a definite homogenization of the material, further operations on the material yield internal stresses. The cold-rolled sheets up to 3.0 cm thickness are frequently manufactured in the form of tapes of a specified width, stored in coils having sheets wound on spools. Such a storage procedure of thin sheets makes the material deform, producing additional stresses. Figure 5 shows single transverse strips on compressive and tension sides, on the left and right sides of a sheet.

The middle part of a diagram shows a uniform zone, detecting approximately constant stress value.

The surface stress diagrams (Fig. 6) show up a repetitive pattern of stress distribution, in the form of longitudinal strips, with a possible information on the direction of sheets in the rolling process.

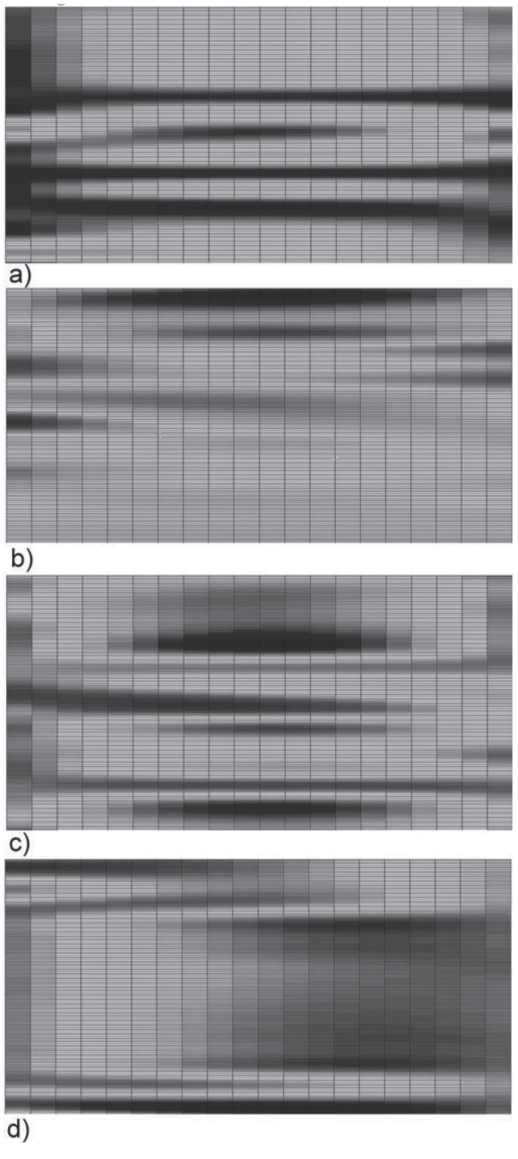

Figure 5. Cold-rolled sheets: a) maximum stress—internal side, b) maximum stress—external side, c) minimum stress—internal side, d) minimum stress—external side.

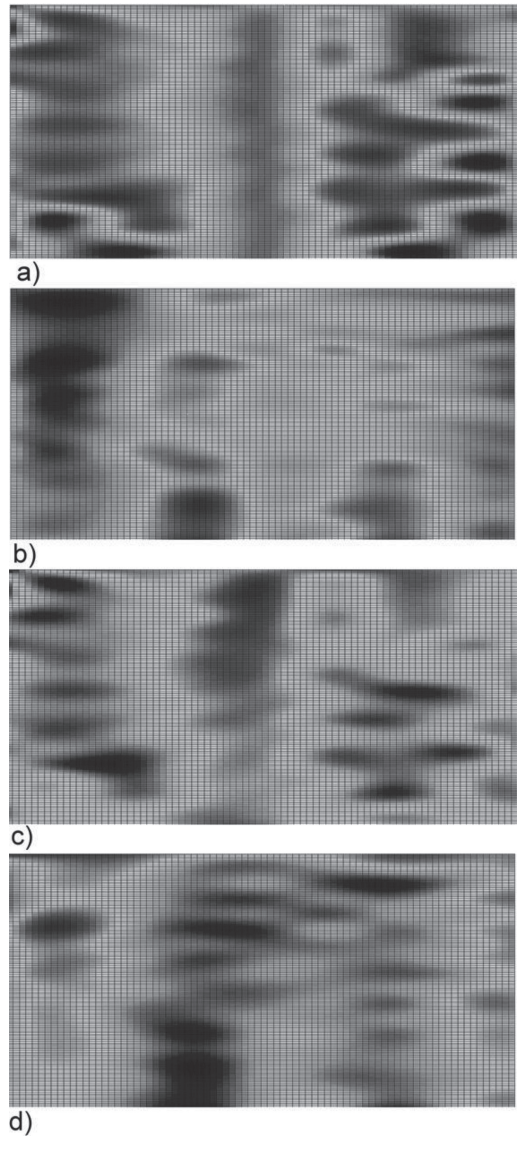

Figure 6. Hot-rolled sheets: a) maximum stress—internal side, b) maximum stress—external side, c) minimum stress—internal side, d) minimum stress—external side.

Additionally, on sheet surfaces distinct points were detected of extreme stresses at every measurement direction. This suggests regions inside the sheets of non-uniform modification of a material structure during processing. This is a key information for the sensitivity analysis of a material to fracture and to diagnose the shape achieving of products due to thermal processes, e.g. hot-dip galvanizing. Further stages of analysis investigate internal stresses in the process of forming elements from the sheets mentioned. Comparing prior and posterior stresses with respect to the bending and welding processes the impact is assessed of technological processes on internal stress values. This percentage results are classified, slight enough to be neglected or significant. It is a key conclusion for industrial fabrication of profiles using mixed bending-welding technology. Slight variations in internal stresses allow to broaden the range of technology applied.

Additionally, the planned research is bound to assess the percentage of internal stresses in the entire cross-sectional stress distribution due to applied load. The thin-walled cold-formed profiles may find stress summation of different production stages strongly deteriorating local or distortional stability.

Meanwhile, the performed experiments and analysis makes it possible to assess the applied Barhausen method. It features a reduced effort, compared to a multitude of measurements. A precise image of stress distribution may be achieved, crucial in the testing of welded joints. It is a non-destructive method, allowing for a couple of measurements at the same location, currently checking the results. It detects a higher mobility compared to the other methods. The only disadvantage is a short period of its use, without a relevant study of diverse actions on its results.

REFERENCES

Augustyn J., Śledziewski E. 1974. Technologiczność stalowych konstrukcji spawanych. Arkady.

Augustyn J., Śledziewski E. 1981. *Technologiczność konstrukcji stalowych*. Arkady.

Augustyniak B. 2003. Zjawiska magnetosprężyste i ich wykorzystanie w nieniszczących badaniach materiałów. Gdańsk.

Bródka J., Broniewicz M., Giżejowski M. 2006 *Kształtowniki gięte*. PWN.

Dubina D., Ungureanu V., Landolfo R. 2012. *Design of Cold-formed Steel Structures*. ECCS Eurocode Design Manuals. Ernst & Sohn.

Dobrociński S., Flis L. 2004. Określenie naprężeń własnych w płycie spawanej. *Zeszyty Naukowe Akademii Marynarki Wojennej*. 3: 158.

EN 1993-1-1, 2006 Eurocode 3: Design of steel structures. Part 1-1: General rules. Supplementary rules for buildings.

EN 1993-1-3, 2006 Eurocode 3: Design of steel structures. Part 1-3: General rules—Supplementary rules for cold-formed members and sheeting.

Garstka T. 2008. System pomiarowy do badań właściwości wyrobów stalowych. *Pomiary Automatyka Robotyka, Rn.* 6: 58–61.

PN-EN ISO 6892-1 Metale. Próba rozciągania. Część 1: Metoda badania w temperaturze pokojowej.

Senczyk D. 1998. Rentgenowskie pomiary tensora naprężenia. WPP.

Urbańska-Galewska E., Łukowicz A. 2011. O możliwościach optymalizacji konstrukcji stalowych. *Nowoczesne Hale* 4: 26–30.

Urbańska-Galewska E., Łukowicz A. 2012. Wpływ ograniczeń technologicznych na dobór parametrów przekroju kształtownika giętego. *Zeszyty Naukowe Politechniki Rzeszowskiej: Budownictwo i Inżynieria Środowiska*. 59 (3): 225–232.

This page intentionally left blank

Recent Progress in Steel and Composite Structures – Giżejowski et al. (Eds)
© 2016 Taylor & Francis Group, London, ISBN 978-1-138-02946-0

Application of Barkhausen effect in the impact assessment of welding to internal stress distribution in steel

D. Kowalski
Gdańsk University of Technology, Gdańsk, Poland

ABSTRACT: The paper presents identification method of internal stresses in plane steel elements in the chase of deliverance and welding assembly. The assessment was made by means of a non-destructive experimental method based on measurements incorporating local external magnetic field and the measurement of induced voltage, including Barkhausen noise. This method allows a degradation assessment due to internal and external actions, causing internal stress variation in a material. Internal stresses combined with the external load effects act on service safety of structural elements. The method allows to assess structural wear, comparing the material after use with the pattern material, leading to non-invasive experiments on ferromagnetic metals, both in qualitative and quantitative meaning.

1 INTRODUCTION

1.1 *Internal stresses in steel products*

Internal stresses in steel products yield from thermal treatment at different stages of steel shaping and processing. It concerns the steelwork production stage of distinct profiles and products, with the steel workshop operations to adjust them to certain applications. Each of these stages of production and processing yields a given internal stress response, cumulating and varying, not vanishing after the process closure. The steel internal stresses come from non-uniform heating and cooling, phase changes of a material due to primary and secondary heating and cooling (cutting, welding, bending), plastic processing (rolling, bending), mechanical treatment of a surface (turning, grinding, milling, shot peening), thermal rectification of elements. Contaminations in steel material, admixtures, modified chemical composition, dislocations of crystal lattice and material structure may produce internal stresses as well. Determination of internal stresses allows for a proper decision-making due to repair of deteriorated elements, conditions of repair, causes of deterioration and damage (Senczyk & Moryksiewicz 2007).

1.2 *Variation of internal stress due to welding*

The welding process makes the joined steel elements heat and structurally transform. The locally concentrated heat source – an electric arc – moving along a weld groove causes non-uniform heating of joined elements. Locally heated steel material is firstly heated to the melting point, next cooled down to the ambient temperature. While steel is a good heat conductor the zones neighbouring with the designed weld are subjected to various heating and cooling. The welding process triggers material expansion and shrinkage. Free deformation is usually restrained by the material not physically treated due to thermal actions. Stresses in materials due to welded joint arise from the following:

a. A locally moving temperature field causes a high temperature gradient in a material. In the movable heat source the temperature is extreme, the case of electric arc detects the magnitude exceeding 3000°C. Non-uniform temperature distribution along a joint length and the non-stationary heat flow cause a diverse thermal and mechanical response.
b. The presence of internal restraints producing system response to thermal strains in a welded material. While a butt weld is used the tensile zone covers it entirely due to shrinkage of a melt material, diverse along the thickness, superimposed with plastic thermal strains. Fillet welds detect a tensile zone inside a weld due to shrinkage of melt material, in the sub-weld region due to plastic strains produced by material heating and cooling.
c. The structural transformations in the coverage of temperature field. The weld region is heated up to the melting point, to shortly sustain and to be cooled down to the ambient temperature. The cooling time is immediate too. Thus phase transformations both in the base metal and the joint are limited in time, which may bring up hardening structures of a material. Due to volumetric changes of structural type after crossing

the critical temperature zone structural stresses emerge. Particular structural steel components vary with specific volume, at increasing order: austenite, perlite, sorbite, bainite, martensite. Austenit detects the lowest while martensite the highest specific volume. Thus austenite transformation is accompanied by volume increase, the highest for austenite-martensite turn, lower while transforming into perlite or bainite forms. Structural volume transformations due to their magnitude and velocity trigger high stresses, exceeding thermal expansion stresses, to become major cause of strains and hardening cracks.

The factors to act upon internal stresses in a welded material are:

- type of a post-welding material cooling agent – the faster colling in the steel martensitic temperature range the higher stresses rise,
- cooling onset temperature, the higher it rises the higher stresses yields,
- chemical composition – inclusion of carbon and alloy admixtures increase the stresses,
- structure and quality of steel – the less homogeneous the higher stresses it causes,
- magnitute of an austenite grain, the greater grains in steel the higher stresses rise,
- shape and magnitude of a joint element – the greater and more developed, the more stressprone.

d. Modification of thermomechanical parameters of a material at heating and cooling. The following parameters are temperature functions: Young's modulus E, Kircchhoff's modulus K, coefficient of thermal expansion, specific heat, heat conductivity.

The post-welding strains are the effect of a joint action of shrinkage of a solidifying metal of a weld and shrinkage due to plastic strains of the material parts close to a weld. Shrinkage acts isotropically, triggering the following strains:

a. lateral, affected by an element thickness, type and dimensions of chamfers, welding method and technique,
b. longitudinal, affected by weld dimensions and the ratio of cross-section and weld areas,
c. angular, produced by nonhomogeneous lateral material shrinkage. It also concerns distortions: bulges, twist, warping,
all varying initial shapes of distinct profiles and entire elements.

1.3 *Magnetic structure of steel*

Civil engineering structural steel is a metallic ferromagnetic material. The magnetic properties of a body are detected by performance of elementary magnetic dipoles in an external magnetic field. Elementary physics says that an arbitrarily dipole-aligned body meets an external magnetic field H, the dipoles are ordered field-wise. A resultant field of induction B arises inside the body (Fig. 1).

Ferromagnetics not subjected to an external field are not polarized at all, this case magnetic domains form closed magnetic circuits in a material. It is an external field to make them approximately aligned and polarized by means of induction. Ferromagnetics are distinguished by a domain structure, due to Weiss hypothesis (Weiss 1907). Domains are micrometer-range zones of uniform magnetization it their amplitude and direction. They are separated by thin layers of magnetic discontinuity, called domain walls or Bloch walls (Bloch 1932) (Fig. 2).

The domain structure of a ferromagnetic material yields its possible modification under external magnetic field or external mechanical stresses. The Barkhausen effect is linked with step variations of local material magnetization.

Re-building of domain structure in the magnetized material is a translation of Bloch walls rotation of magnetic domains.

Translation of domain walls is restrained by inhomogeneity of crystalline structure in the form of shape defects, dislocations, cohesiveness reduc-

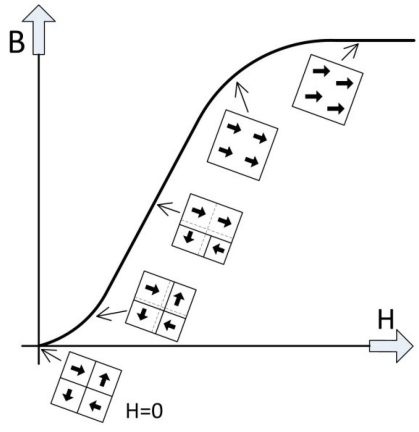

Figure 1. Magnetizing curve and the corresponding domain structure variations of a ferromagnetic material.

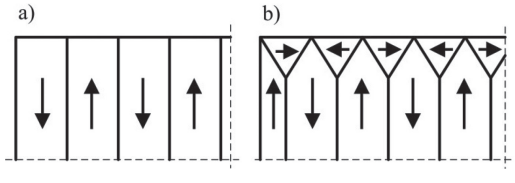

Figure 2. Domain structure of a material: a) the Kittel hypothesis model, b) the Landau – Lifschitz hypothesis model.

tion, inhomogeneity of chemical composition, non-metallic inclusions. Discontinuous modifications of a domain structure act in the surface of a ferromagnetic in the form of induction disturbance, detectable by means of allowable equipment. A signal generated in a measurement system by means of step-wise variation of Barkhausen magnetic induction, thus its name – magnetic Barkhausen noise.

1.4 *Application of Barkhausen noise effect to steel investigations*

The action of external loads produces solid body strains. Plastic strains cause irreversible, permanent deformations due to slip and field, lead to forming zones of high dislocation density. Elastic material strains cause stresses and crystal lattice deformations - atomic distance changes of the ferromagnetic. The latter alter the action between neighbouring atoms, modifying the spin distribution in Romains, thus their magnetic properties. This is the so-called magnetoelastic effect, related to magnetostriction – elastic deformation and mechanical parameter change due to magnetization. Due to magnetoelastic junction external physical actions re-arrange the domain structure of a ferromagnetic, thus change of shape and slope of a magnetization curve. Modifying of a magnetic structure due to loads is conducted by shifting of the Bloch domain walls, especially inclined the Rother way than "180°" type. This motion involves magnetoelastic energy. Considering the energy formula (1):

$$E_m = -1{,}5 \cdot \lambda_s \cdot \sigma \cdot \cos^2 \varphi \tag{1}$$

where: λ_s = magnetostriction constant, φ = inclination angle between direction of a stress σ and a direction of local magnetization J_s.

It may be stated that the stress σ varies the magnetoelastic energy of a ferromagnetic. The impact of external stress-governing load may be related to the equivalent external magnetic field whose intensity is H_σ – formula (2).

$$H_\sigma \approx \frac{1{,}5 \cdot \lambda_s \cdot \sigma}{J} \tag{2}$$

The steel material detects atomic distance variation. In magnetic approach it yields the following result:

a. in compression – increment of domains magnetized perpendicularly to stress direction,
b. at tension – volume increment of domains magnetized stress-wise.

Such variations of a material domain structure lead to area increasing or decreasing of boundaries of "180°" type. Material microstructure and structural lattice defects both form local potential barriers, inhibiting smooth material magnetization by an external magnetic field, translating the domain walls in a material. The next factor to reduce magnetization is local strain of crystal lattice due to internal stresses and external load of a material. Apart from exchange energy and magnetostatic energy, magnetoelastic energy is an important factor, determined by internal stress distribution in a given ferromagnetic specimen.

Introduction of tensile stresses is the action to increase domain volume of a magnetization vector convergent with the stress vector, the magnetization process comes from translation of domain walls of "180°" type (Fig. 3). Compressive stresses introduce anisotropy to the distribution of local magnetization so that magnetizing direction is perpendicular to compressive stress direction (Fig. 4).

The applied external magnetic field yields creation of a "non-180°" type domain walls and volumetric increment of domains magnetized perpendicularly to the compressive stress direction, parallel to the external magnetic field.

The volume increment is conducted mainly translating the "non-180°" type domain boundaries.

The typical Barkhausen effect exhibits step variations of wall displacements of "180°" type. Thus Barkhausen effect intensity arises for tensile stresses (increasing number of "180°" boundaries) and reduces at compression ("non-180°" boundary movements) (Fig. 5).

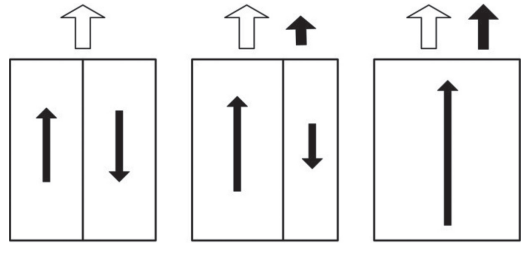

Figure 3. Magnetizing pattern for a material at tension.

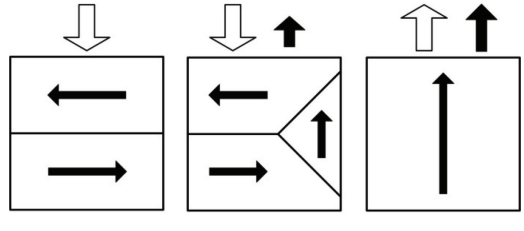

Figure 4. Magnetizing pattern for a material at compression.

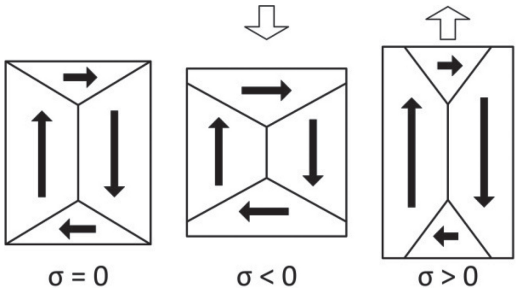

Figure 5. Variation of domain structure with respect to a loaddirection and stress.

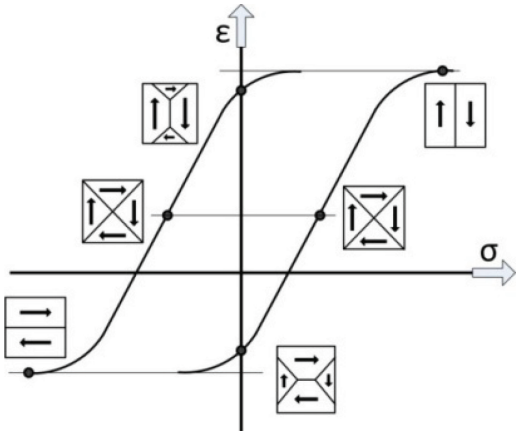

Figure 6. Modifications in the material domain structure in terms of stress and strain variation.

The modifications due to re-building of a material domain structure caused by material stresses, the effect of both internal and external (caused by loads) may be registered by a measurement equipment according to diagram in Figure 6.

2 DESCRIPTION OF AN EXPERIMENT

2.1 *Scope of an experiment*

The experiment detests and identifies internal stresses in steel material for major load-carrying structural elements and the impact of welding processes on the state variation.

2.2 *Experimental procedure*

The steel sheets were subjected to a non-destructive test of the formerly outlined phenomena by means of identification of surface internal stresses estimated on a basis of a Barkhausen effect measure. Two material parts were examined, taken front a single sheet to assure comparable initial data set due to chemical composition, the range of thermal and mechanical processing, squeeze value, surface flatness, smoothness and roughness, surface corrosion development, sort of coating material – mill scale. A key parameter is the absence of loading history and any surface treatment of considered elements. The sheet dimensions were 215 × 478 mm, at mean thickness 4,77 mm. Structural steel of yield strength 355 MPa was applied, it was rolled thermomechanically in the production course. The sheet surfaces were cleaned manually not to act on the signals. A surface part showed a layer of strongly adhesive mill scale at both sides, not removed in order to detect the impact on measurement results. Both sides were attached a mesh of measurement points of 20 × 20 mm resolution (Fig. 7). The mesh pattern is adjusted the designed weld seam to make it smooth and continuous at the joint. All measurement points should be repetitive in both measurement stages.

The experiment was conducted regarding two stages of internal stress assessment. The first, while material at deliverance, to identify internal stresses at the material surface. It is a reference for the second stage measurements. The latter is a re-assessment of internal stresses after completing a welded connection of elements at their longer dimension.

The experiment was conducted using a uniaxial measurement head equipped with a magnetizing coil and a coil to measure induced voltage signal, including Barkhausen noise. Every time the measurements were performed in two orthogonal directions collinear with the measurement mesh and the third, bisector of the major measurement coordinate system.

The voltage signal measurement values for orthogonal directions X and Y on both sides of an investigated sheet are presented in Figures 11–14.

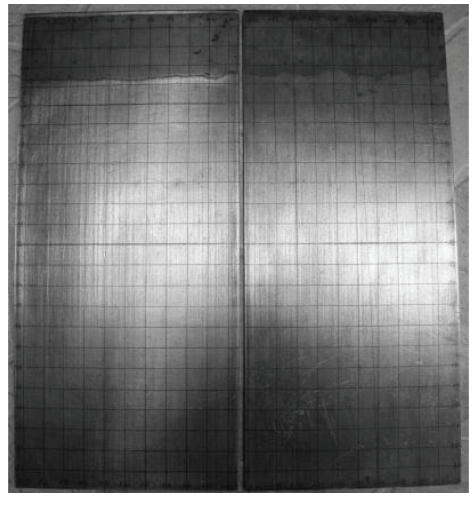

Figure 7. Sheets before internal stress identification.

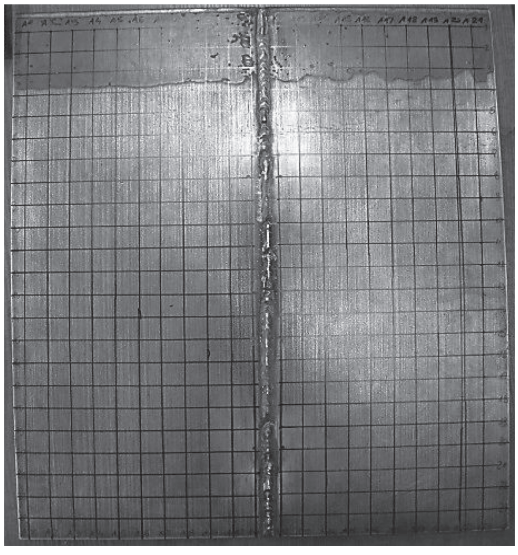

Figure 8. Sheets after performance of the butt weld.

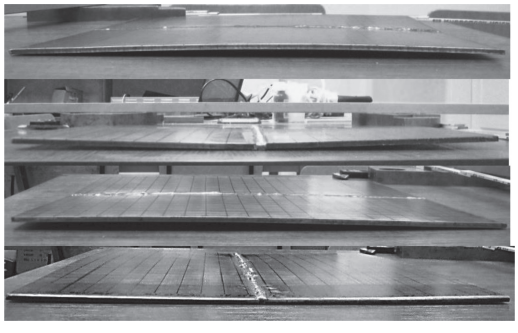

Figure 9. The post-welding deformation sheets.

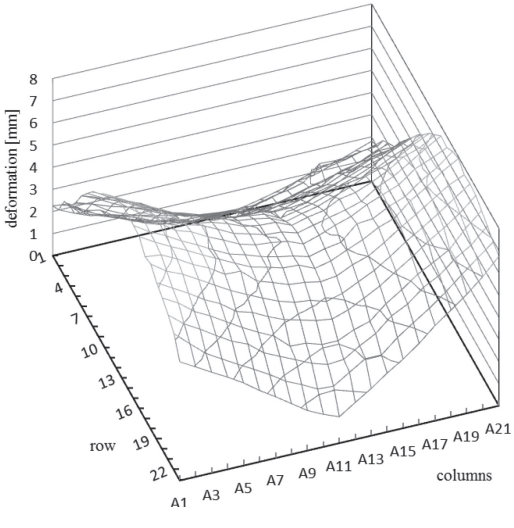

Figure 10. The post-welding deformation map.

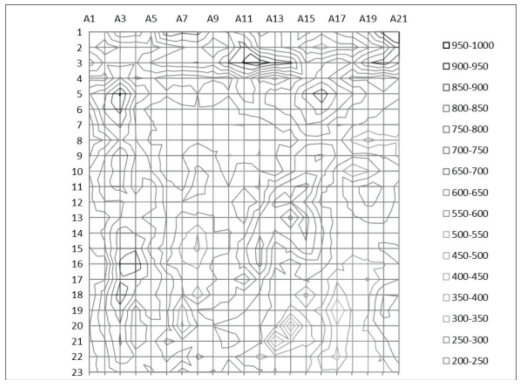

Figure 11. Before welding – side A – direction X.

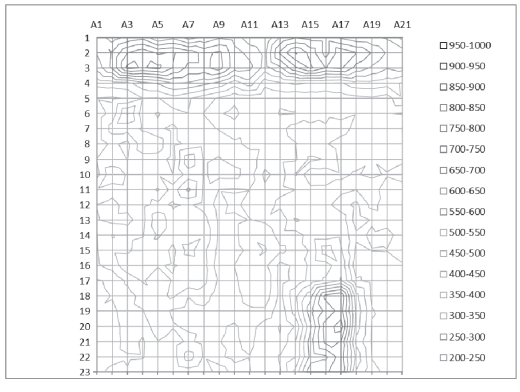

Figure 12. Before welding – side A – direction Y.

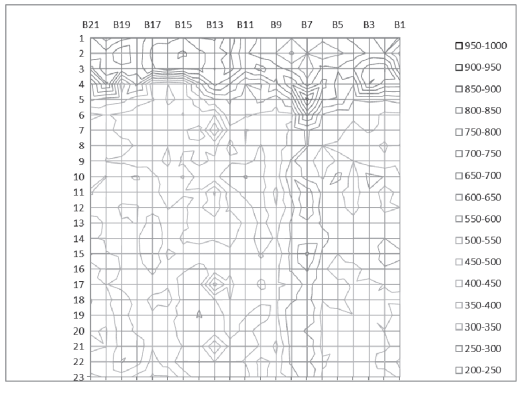

Figure 13. Before welding – side B – direction X.

After the first stage the sheets were united in one element by means of a V-type butt weld, using a Metal Inert Gas (MIG) welding technique. The welding did not involve any elements fixing the sheets alone or fixing sheets with other structural

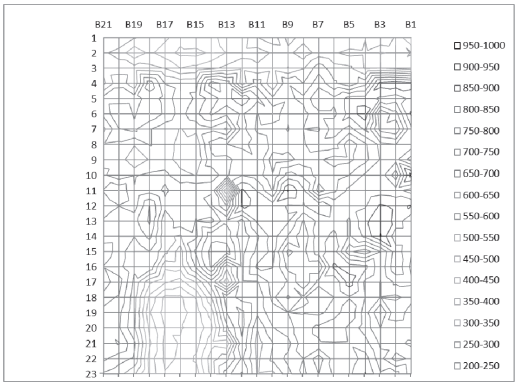

Figure 14. Before welding – side B – direction Y.

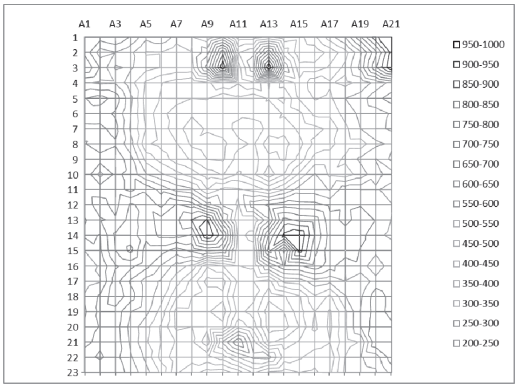

Figure 15. After welding – side A – direction X.

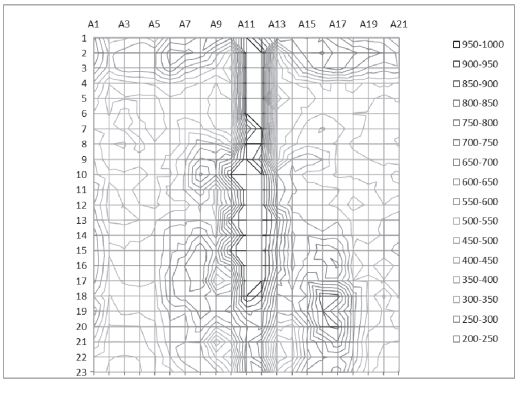

Figure 16. After welding – side A – direction Y.

parts. No precautions were done restraining the final post-welding shape.

After welding (Fig. 8) assessment was done of the weld and identification of geometry variations due to thermal strains at welding, i.e. the processes of heating and cooling.

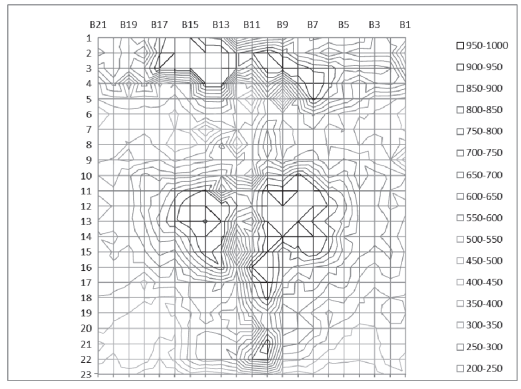

Figure 17. After welding – side B – direction X.

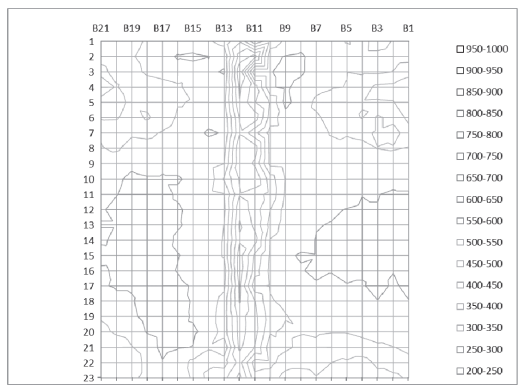

Figure 18. After welding – side B – direction Y.

Initially plane sheets were subjected to deformation due to welding. The deformation modes were shown in the photos (Fig. 8) and presented in the form of measured geometric variation distribution (Fig. 10). The deformation form in the considered element corresponds to a welding seam. Angular strains are seen, typical for one-sided butt weld of V type and bulges, characteristic for non-restrained welding of uniaxial progression.

The research on joint elements was done in the same Framework at measured points. The results were presented by means of maps in Figures 15–18.

3 MEASUREMENT RESULT ANALYSIS

The magnitude of an identified voltage signal in th pre-welded elements, shown in Figures 11–14, detects its relatively uniform surface distribution. Sheet regions may be easily show to raise signal magnitudes, pointing out higher internal stresses there.

Numerical outcomes detect uniquely zones of tensile and compressive stresses, identified by higher or lower signal magnitudes, respectively.

The resolution of the method is affected upon the type of surface contacting with the measurement head. In the upper part of sheets a shell of mill scale was observed at both sides (Figs. 7, 8). The signal measured at this region exceed significantly the results at the other parts of the sheets. A locally increased voltage signal on other surface type proves the research and measurement range of the method, limited to a surface layer of a material. The locally varied surface type of a steel material is a strongly compressed layer of iron oxides. This layer is formed by oxidization of a hot steel surface in contact with air in the rolling process. Thus a mill scale material is highly compressed, much harder than steel, resulting in a modified signal value. The experiments on two sheet parts made of one piece resulted in a continuous voltage signal a their intersection, between the columns 11 and 12. In the contact region of sheets no immediate signal magnitude changes occur.

The next voltage signal maps show a post-welding situation between the considered sheets (Figs. 15–18). First of all, on its A side, Y direction the map shows significant growth of voltage signal, detecting tensile stress increment along a welded joint. This increment comes from longitudinal shrinkage of a chilling weld, translated into tension of a material in the weld vicinity. Additionally, tension at the rest of the surface is amplified by shear strain of the element (Fig. 10) while the A side is at tension.

The B-side of a sheet at Y direction the post-welding signal values also detect the increase of longitudinal stresses at the welded joint, corresponding to shrinkage at the weld root. The values are lower, due to slight heating of that region and a lower shrinkage-prone weld dimension. Other parts of the material show a low voltage signal, essential for strains of the free, unrestrained material.

The X direction on A side of the investigated sheet denotes approximately symmetric zones with respect to a joint, due to both stress increment and decrement. The B side behaviour was similar. The X direction pointed out on both sides of a sheet the signal magnitude change as a featuring effect, resulting from shear strains in a sheet due to its heating and cooling. The signal increment is lower, corresponding to free deformation of elements, not restrained at the perimeter.

On the basis of the analysis of post-welding measurement results, considering deformation mode of investigated sheets, it is suggested that the results tend to the anticipated ones, due to the variation character. The quantitative analysis will be presented in the forthcoming paper.

4 CONCLUSIONS

The Barkhausen effect does not interfere in the material, thus it is useful to examine physical conditions of the outer layer of a ferromagnetic material considered – structural steel. The measured energy signal informs about both surface and volume (through-thickness) operations. The method in general assesses internal stresses, strains and hardness, compares new and processed materials. The method assesses material wear due to operation conditions. It also controls fabrication or design of steel products due to internal stress variation.

After calibration the stress values may be determined directly (in MPa) in terms of voltage induced in the measurement coil.

The magnetic method based on noise analysis (Barkhausen effect) is not codified yet, but applied in mechanical industry to assess materials due to variations in their operation.

Studies of this method are carried out under the terms of the possibility to use it to identify the state of the effort of shell structures with geometrical imperfections (Kowalski 2001, 2004a,b,c, 2014).

REFERENCES

Barkhausen, H. 1919. ZweimitHilfe der neuenVerstaerkerentdeckteErscheinungen. *J.Phys, 2.*

Bloch, F. 1392. Theorie der Wandverschiebungen. *J.Phys*, 74.

Kowalski D. 2001. Stresses in steel tank shell with local deformations of the shell. *Inżynieria i Budownictwo* 6/2001.

Kowalski D. 2004a. Tensometric test of tank shell with imperfection shape. *The study of building materials and construction engineering.*Wroclaw: DWE.

Kowalski D. 2004b. On influence of geometrical imperfections on stress level in cylindrical shell. *Inżynieria i Budownictwo 11/2004.*

Kowalski D. 2004c. Influence of initial imperfections on the vertical tank side stresses. Ph. D. Thesis. Gdansk:Gdansk University of Technology.

Kowalski D. 2014. Influence of geometrical imperfections on stresses in cylindrical shells. *Shell Structures: Theory and Applications, Vol. 3: 527–530.*

Senczyk, D. & Moryksiewicz, S. 2007. Naprężeniawłasne - pojęcia i klasyfikacje. *Non-destructive testings - online services.*

Weiss, P. 1907. Hypothesis of the Molecular Fild and Ferromagnetic Properties. *J. Phys*., 4, 6.

This page intentionally left blank

Strength, stability and postbuckling behaviour

This page intentionally left blank

Recent Progress in Steel and Composite Structures – Giżejowski et al. (Eds)
© 2016 Taylor & Francis Group, London, ISBN 978-1-138-02946-0

Experimental investigations on non-uniform torsion of the two-chord members laced at a single plane

P. Lorkowski & B. Gosowski
Faculty of Civil Engineering, Wrocław University of Technology, Wrocław, Poland

ABSTRACT: The paper presents experimental studies to determine the equivalent second moment of area of the uniform torsion of the two-chord steel built-up members laced at a single central plane. The members are used as poles of railway traction network gates, and steel columns of framed buildings as well. The stiffness of uniform torsion of this kind of columns allows to the determine the critical loads of the spatial stability. The experimental studies have been realized on a single—span members with rotation arrested at their ends, loaded by a torque applied at the mid-span. The relationship between angle of rotation of the considered cross-section and the torque has been determined. Appropriate numerical model was created in the ABAQUS program, based on the finite element method. A very good compatibility has been observed between experimental and numerical studies. The equivalent second moment of area of the uniform torsion for analyzed members has been determined by comparing the experimental and analytical results to those obtained from differential equation of non-uniform torsion, based on Vlasov's theory.

1 INTRODUCTION

The considered herein two-chord members found wide application in the building industry, among others, as individual traction columns in tram net (Gosowski & Lorkowski 2012) or poles of railway traction of network gate (see Figure 1 on the right) (Gosowski 2001). These columns are constructed from two channel chords connected by lacing made of flat bars or angles. Usually in similar way the columns of a industrial buildings are designed (see Figure 1 on the left) (Biegus 2009, Krzyśpiak 1976, Kucharczuk & Labocha 2012). In the buildings equipped by overhead cranes, the upper part of the stepped columns is made of a double-tee members, whereas the lower part is constructed from channels, double-tee or hollow profiles, laced by angles inclined of 45°.

As a part of doctoral thesis (Lorkowski 2014) the experimental investigations in semi-technic scale have been conducted for elements with the construction corresponding to that used for columns in railway traction gates or columns supporting the tram traction network. These results have been compared to the theoretical ones obtained for numerical models created by a program based on finite elements method.

The purpose of the research was to determine the rigidity to torsion of the described above elements, but first of all the second moment of area of uniform torsion $I_{\overline{T}}$ and warping torsion section constant $I_{\overline{\omega}}$. These characteristics are strictly necessary to determine the critical resistance of the elements sensitive to the spatial form of instability namely: in case of elements subjected to unaxial compression—the critical load of flexural-torsional buckling, in case of elements under bending—the critical moment of lateral buckling.

Figure 1. Examples of columns: in industrial building (on the left), intermediate column in railway traction gate (on the right).

2 DESCRIPTION OF TEST PIECES

Four types of members with different lacing have been tested. In all types the chords have been made of hot-rolled channels 80, spaced 221 mm (see Figures 2–5). Lacings have been used in the form of square hollow section RQ 40 × 3 mm or flat bars FB 40 × 5 mm. In the majority of elements the diagonals have been arranged at an angle 45° with the respect to the chords. For comparison, the version of models without diagonals have been executed.

Figure 2. shows the model S-1 with the lacing made of rectangular hollow sections, whereas model S-2 (see Figure 3) has been laced by flat bars.

Elements shown in Figure 4 and Figure 5, denoted as V-1 and V-2have been battened by tubes and flat bars, respectively.

The tests to torsion have been carried out on two models of every type. Models S-1 and S-2 have been investigated once, whereas models V-1 and V-2 twice, wherein before the second tests the models have been modified (see Figure 6) by additional battens 100 × 5 mm welded to the ends of chords—the models V-1P, V-2P.

The chords of all tested elements have been made of the steel grade S355, whereas for lacings and battenings steel S235 have been used.

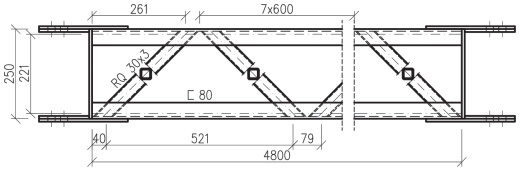

Figure 2. Geometry of the model S-1.

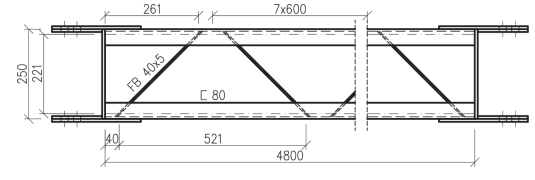

Figure 3. Geometry of the model S-2.

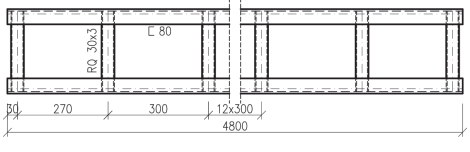

Figure 4. Geometry of the model V-1.

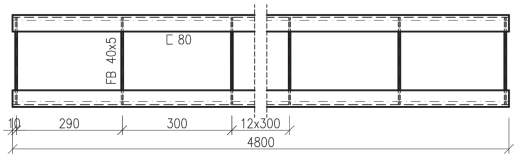

Figure 5. Geometry of the model V-2.

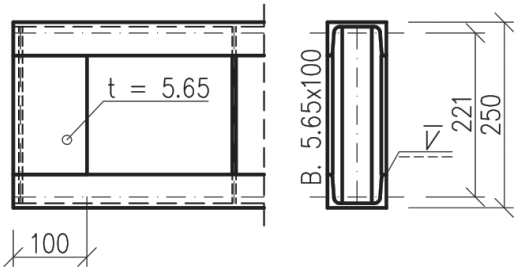

Figure 6. Detail of the battens in models V-1P, V-2P.

3 TEST STAND FOR PHYSICAL MODELS

The models of considered two-chord elements with a scheme shown in Figure 7 have been subjected to the non-uniform torsion on a specially arranged stand (see Figure 8). The load has been exerted by a torque applied in the mid-span. The ends of the member have been arrested due to torsion. Owing to the way of support, the distance between bearings was not constant but differed within the range 4.555 m to 4.670 m.

The torque M_s has been realized by twisting couple of forces P, 310 mm spaced (see Figure 9). The load P has been reached by a hydraulic jack having a maximum load-capacity of 100 kN.

Individual loads P have been recorded by especially constructed and calibrated set of dynamometers based on electro-resisting gauges. The value of P has been recorded electronically every 1 or 3 sec, for models S and V, respectively.

The basic quantity to be measured in the studies was the angle φ of torsion of the mid-span cross-section of a member. This has been accomplished by means of two couples of inductive gauges attached perpendicularly to the main axis, vertically and horizontally, respectively (Figure 11 on the left). In some models (V-1, V-2) the warping effect $\varphi^{(1)}$ has been measured over the support A by four gauges placed perpendicularly to the cross-section at the corners of the channel chords.

Additionally, the rigidity of the support A has been recorded by means of two gauges placed horizontally (Figure 11 on the right).

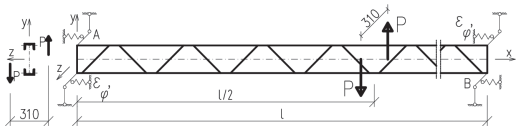

Figure 7. Scheme of the two-chord member under non-uniform torsion.

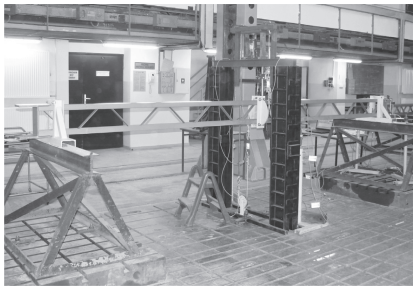

Figure 8. Model of type S on the test stand designed for torsion.

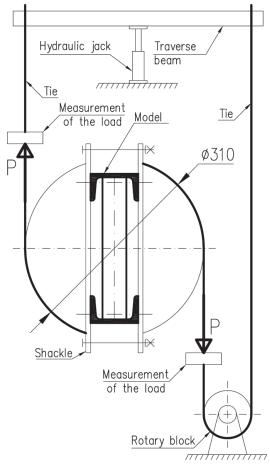

Figure 9. The scheme of realization of the torque.

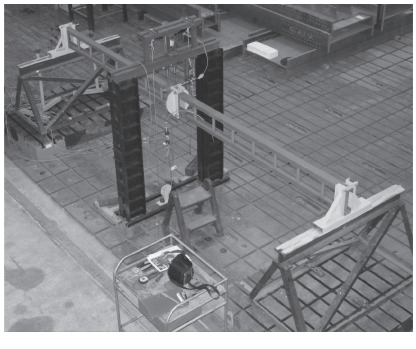

Figure 10. Model of type V on the test stand designed for torsion.

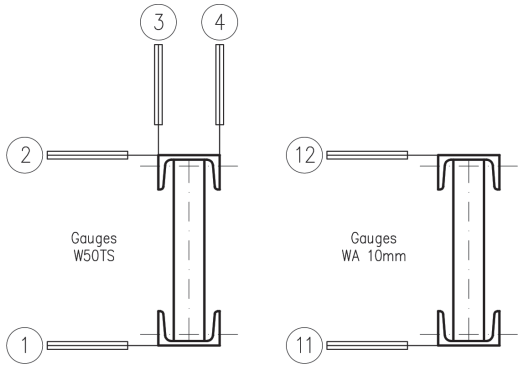

Figure 11. Location of inductive gauges recording the displacements: at the span (on the left), over the support, transversally (on the right).

4 THE COURSE OF EXPERIMENTAL INVESTIGATIONS

All test models have been indicated before the investigations, i.e.: dimensions of the profiles, the gauges (transverse and longitudinal) of the built-up member and its geometrical imperfection. In the first model to be tested, the dimensions have been checked in five random cross-sections, which has been limited to three cross-sections in the rest of models. Since the dimensional deviations from the nominal values have been considered as acceptable by standards (PN-EN 1090-1, PN-EN 1090-2), the further analysis has been based on designing dimensions of elements and nominal dimensions of profiles (ArcelorMittal 2008, Bogucki & Żyburtowicz 2006).

The models have been subjected to torsion in three steps of load-unload cycle with a growing torque. For models of V-type Figure 10 the loads has been limited due to technical conditions, since the excessive displacements (torsion) could have caused a damage of the gauges. The load of S-models have been adjusted to values that are not causing any permanent strains due to the planned further tests.

In Table 1 the test results for a model S-1.1 have been listed. For each cycle the both maximum value of torque M_s, and the permanent strain (remaining angle of torsion) after unloading have been given.

The rest of models have been investigated analogously, but additionally for models of V-type the warping effect has been studied.

The load-displacement relationship has been introduced (Figure 12) for the torque M_s and corresponding angle of torsion φ during the first cycle of the load test. The maximum rigidity to torsion

Table 1. Listed test results of the angle of torsion at the mid-span of the model S-1.1.

				Angle of torsion	
		Cycle	M_s	current	remaining
Model	S-1.1	-	kNm	rad	rad
		1	0.500	0.0247	
			1.000	0.0506	
			1.547	0.0783	0.0008
		2	1.000	0.0509	
			2.000	0.1020	
			2.177	0.1116	0.0017
		3	1.000	0.0525	
			2.000	0.1029	
			2.750	0.1426	
			2.794	0.1455	0.0043

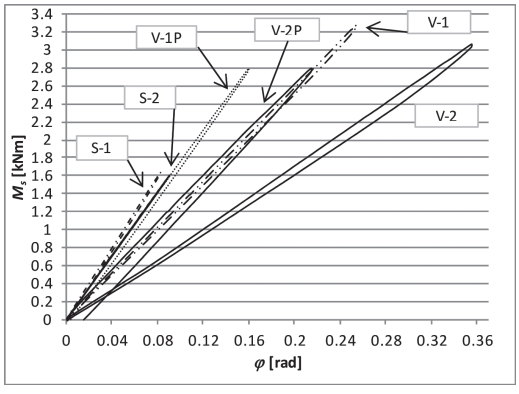

Figure 12. Relationship load-angle of torsion for tested models.

has been presented by the model S-1, whereas the model V-2 exhibits the smallest one.

The application of battens at the ends of the models of V-P type increases their rigidity to the level comparable to the corresponding models of the S-type. The diagram of the relationship load-displacement obtained for a model S-2 overlaps partly the corresponding diagram of a model V-1P.

5 ANALYSIS OF TEST RESULTS OF THE PHYSICAL MODELS

The differential equation of the torsional angles for a member under non-uniform torsion (see Figure 7), that fulfils the condition $0 \le x \le l/2$ is written as (Gosowski 2004, 2007):

$$EI_\omega \cdot \varphi^{(4)}(x) - GI_T \cdot \varphi^{(2)}(x) = 0. \tag{1}$$

The general solution of equation (1) takes a form:

$$\varphi(x) = C_1 + C_2 x + C_3 \frac{1}{k^2}(\cosh kx - 1) + C_4 \frac{1}{k^3}(\sinh kx - kx), \tag{2}$$

where: C_1, C_2, C_3, C_4 – constants of integration, $k = \sqrt{GI_T/(EI_\omega)}$.

For a member having a scheme as shown in Figure 7 the boundary condition take a form:

$$\varphi(0) = \varphi^{(1)}\left(\frac{l}{2}\right) = 0,\ \varphi^{(1)}(0) = \varepsilon_{\varphi'} B_A,\ M\left(\frac{l}{2}\right) = \frac{M_s}{2}, \tag{3}$$

where: B_A – bimoment reaction over A support, $\varepsilon_{\varphi'}$ – batten flexibility coefficient.

From the general solution (2), after determining the constants of integration from the boundary conditions (3), one may obtain a general relationship for the angle of torsion:

$$\varphi(x) = \frac{M_s}{2EI_\omega}\left[\frac{\cosh\frac{kl}{2} - 1}{\varepsilon_{\varphi'} GI_T \cosh\frac{kl}{2} + k\sinh\frac{kl}{2}} \times\left(\varepsilon_{\varphi'} EI_\omega \cdot x + \frac{\cosh kx - 1}{k^2} + \varepsilon_{\varphi'} GI_T \frac{\sinh kx - kx}{k^3}\right) - \frac{\sinh kx - kx}{k^3}\right] \tag{4}$$

and warping:

$$\varphi^{(1)}(x) = \frac{M_s}{2EI_\omega}\left[\frac{\cosh\frac{kl}{2} - 1}{\varepsilon_{\varphi'} GI_T \cosh\frac{kl}{2} + k\sinh\frac{kl}{2}} \times\left(\varepsilon_{\varphi'} EI_\omega + \frac{\sinh kx}{k} + \varepsilon_{\varphi'} GI_T \frac{\cosh kx - 1}{k^2}\right) - \frac{\cosh kx - 1}{k^2}\right]. \tag{5}$$

In the particular case, at the absence of external battens $\varepsilon_{\varphi'} = \infty$, the presented above equations take a simplified form (Gosowski 2004, 2007):
for torsional angle

$$\varphi(x) = \frac{M_s}{2k^3 EI_\omega}\left(kx - \frac{\sinh kx}{\cosh\frac{kl}{2}}\right) \tag{6}$$

for warping

$$\varphi^{(1)}(x) = \frac{M_s}{2k^2 EI_\omega}\left(1 - \frac{\cosh kx}{\sinh \frac{kl}{2}}\right). \tag{7}$$

The equivalent warping torsion section constant of the two-chord member (Rutecki 1966, Lorkowski 2014), built-up of two parallel chords and a single-plane lacing, is determined on the base of geometrical characteristics of the chords:

$$I_{\bar{\omega}} = 2\left(I_{\omega p} + a^2 \cdot I_{yp}\right), \tag{8}$$

where: a – distance between the shear center and the centroid of the built-up cross-section, I_y, $I_{\omega p}$ – second moment of area about y axis, warping torsion section constant of a single chord, respectively (Rutecki 1966, Lorkowski 2014) (in the work of Romanow 1988, in the equation like (8), the distance a is defined incorrectly).

For models V-1, V-2, S-1, S-2, the mean value of the angle of torsion and warping have been calculated for the level of loading by torque M_s equal to: 1.0, 2.0, 2.75 [kNm], where the cycle of loading has been taken into account only as this appearing first. In case of models V-1.1P and V-2.1P the results have been considered analogously, but due to the fact that the model has been made in a single copy, the obtained results are not representing the mean values.

On the basis of received results of the angle of torsion for the elements S-1, S-2, V-1, V-2, having $I_{\bar{\omega}}$ determined from equation (8), the equivalent $I_{\bar{T}}$ has been iteratively searched employing the formula (6). Warping obtained from tests has been compared with the theoretical one calculated from equation (7), where $I_{\bar{T}}$ has been determined by means of the torsion angle. Table 2 presents the results of comparison.

A good agreement between the second moment of area of the uniform torsion (see Table 2) for any level of loading, confirms the correctness of the assumed theoretical model. Discrepancies concerning warping (10÷21%) are resulting from the way of its measurement. The surface of the cross-section to which the gauges have been applied should be polished, due to the small value of displacement.

The models V-1.1P and V-2.1P have got $I_{\bar{T}}$ the same as those obtained for models V-1 and V-2 and the theoretical results (4) and (5) have been compared afterwards to the experimental ones. The coefficient of flexibility has been taken as $\varepsilon_{\varphi'} = 6.681 \times 10^{-5}\left(N \cdot m^3\right)^{-1}$.

Differences between test and theoretical results concerning the angle of torsion, not exceeding 8,13% (see Table 3), confirm practically the correctness of theoretical model that has been assumed for a member restrained at the ends by battens. Lager differences (15 ÷ 47%) are observed in the case of warping. Apart of reasons mentioned in case of models V-1, V-2, an additional effect has been noted for models V-1P and V-2P, where the discrepancies between the test and analytical results have been caused by the battens fixed to the ends of the member. The value of batten flexibility coefficient $\varepsilon_{\varphi'}$ has been calculated with a certain approximation, which causes the differences between theoretical calculation and test recordings obtained for physical models.

Table 2. The list of results for models S-1, S-2, V-1, V-2 and the equivalent second moment of area $I_{\bar{T}}$.

					Warping:	
	l	M_s	φ	$I_{\bar{T}}$	From tests	Calculated
Model	m	kNm	rad	cm^4	rad/m	rad/m
S-1	4.555	1.000	0.0512	19.123	–	–
		2.000	0.1019	19.221	–	–
		2.750	0.1426	18.777	–	–
S-2	4.555	1.000	0.0564	16.786	–	–
		2.000	0.1135	16.667	–	–
		2.750	0.1581	16.359	–	–
V-1	4.670	1.000	0.0779	11.294	0.0364	0.0463
		2.000	0.1558	11.294	0.0835	0.0926
		2.750	0.2151	11.227	0.1114	0.1279
V-2	4.670	1.000	0.1216	5.415	0.0592	0.0749
		2.000	0.2380	5.642	0.1221	0.1464
		2.750	0.3277	5.627	0.1601	0.2016

Table 3. Models V-1P, V-2P – comparisons of results.

				Angle of torsion:		Warping:	
	l	M_s	$I_{\bar{T}}$	From tests	Calculated	From tests	Calculated
Model	m	kNm	cm^4	rad		rad/m	
V-1P	4.670	1.00	11.294	0.0570	0.0543	0.0196	0.0170
		2.00	11.294	0.1139	0.1059	0.0430	0.0332
		2.75	11.227	0.1571	0.1497	0.0606	0.0470
V-2P	4.670	1.00	5.415	0.0738	0.0715	0.0293	0.0224
		2.00	5.642	0.1502	0.1412	0.0624	0.0442
		2.75	5.627	0.2102	0.1944	0.0894	0.0608

6 STUDIES ON NUMERICAL MODELS

Studies on numerical models have been carried out using the computer program ABAQUS (ABAQUS

2012), created on the basis Finite Elements Method (FEM).

The calculations by ABAQUS program have been performed using the resources made available by the Wrocław Centre for Networking and Supercomputing (http://wcss.pl) under the grant No 306.

Models have been generated in the CAE module, while calculations have been executed in the STANDARD module. The models have been divided to 20-nodal solid finite elements (see Figure 13) with a reduced integration (C3D20R), but in some places, where the model's geometry would not allow it, 15-nodal solid elements (C3D15) have been assumed. The solid elements, in the contrary to shell elements, are able to consider the strains throughout the thickness of the cross-section and therefore this shape of elements has been used herein (Gosowski & Niżniowski 2008). The sizes of finite elements have been chosen so that the maximum of them does not exceeded 10 mm in any of thousands (depending of the model's type) of existing elements.

The material characteristics have been assumed like for physical models, and the linear-elastic model has been assumed.

The static scheme and the way of load application have been similar to that taken for physical models. Due to the linear-elastic range of the strength analysis, the load has been applied only one time as a torque $M_s = 1$ kNm, in the contrary to physical models incrementally loaded in three cycles.

The angle of torsion of the mid-span cross-section (see Figure 14) and warping of the model's extreme cross-sections have been examined like in the case of physical models. In the latter the readings of warping have been possible (in contrast to physical models) for all numerical models – also for model S.

In Table 4, the results of calculations of the both angle of rotation in the middle of the span and warping over the support have been summarized. Employing the formula (6) $I_{\overline{T}}$ has been iteratively determined and substituted to the equation (7), Thus, the value of warping has been calculated. Thanks to this, the values of warping obtained straight from numerical calculation and those calculated analytically have been compared.

In case of models of V-type the results of warping are generally consistent-in, case of model of the V-1 type are almost the same, whereas the scale of differences between the calculating warping and the tested one obtained for models S makes

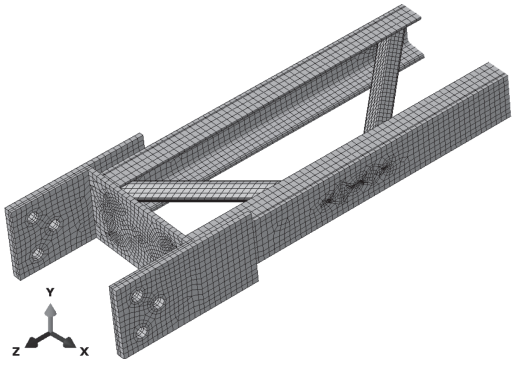

Figure 13. Meshing scheme for model S-1 subjected to torsion.

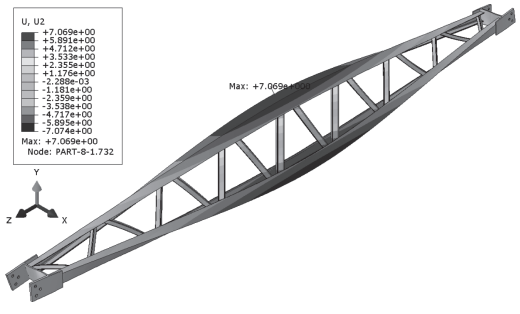

Figure 14. The map of displacements for a model S-1 in Y-direction (enlarged 40 times).

Table 4. Results of analysis of models S and V.

					Warping:	
	L	M_s	φ	$I_{\overline{T}}$	From Numerical ana.	From Analytical cal
Model	m	kNm	rad	cm^4	rad/m	rad/m
S-1	4.555	1.0	0.05655	16.69	0.02507	0.03372
S-2			0.06401	14.09	0.02897	0.03862
V-1	4.8	1.0	0.08128	11.33	0.04610	0.04683
V-2			0.14368	4.33	0.07978	0.08663

Table 5. Comparison of test results for models V-1P and V-2P.

				Angle of torsion		Warping:	
	l	M_s	$I_{\overline{T}}$	From tests	Calcul.	From tests	Calcul.
Model	m	kNm	cm^4	rad		rad/m	
V-1P	4.67	1.00	11.33	0.0612	0.0571	0.0239	0.0172
V-2P	4.67	1.00	4.33	0.0819	0.0808	0.0347	0.0242

that these results can not be considered to be satisfactory. Good agreement of warping in case of models V (see Table 4) results from the lack o restriction of warping at the ends of element. The bearing restraints are applied exactly at the ends of the member. In models of type S discrepancies can be caused by two factors. At the ends of a member the gusset plates are modeled, which in fact they have been planned to attached the model to the another test device. So, the first factor results from those plates and the diaphragm at the end the member that reduce undoubtedly the warping effect at its end. The second factor may result from the fact that the bearing restraints are not applied precisely at the ends of the member but at a certain distance. The cantilever portion of the chord limits adequately the warping effect as well.

To the models V-1P and V-2P, like for physical test models, the $I_{\overline{T}}$ has been assigned respectively from results for models V-1 and V-2 obtained from FEM analysis, and the analytical (see (4) and (5)) and numerical results have been compared in situation when the batten flexibility coefficient is taken as for physical models (see Table 5).

For models with battens welded in at the ends, the torsion angle read out from the ABAQUS program and this calculated from equation (4) show a satisfactory agreement. Whereas, the values of warping, that have been read out, differ significantly from these calculated according to equation (5).

7 COMPARISON OF THE EQUIVALENT SECOND MOMENT OF AREA OF THE UNIFORM TORSION

Table 6 summarizes the both mean values of the equivalent second moment of area obtained from tests of physical models and corresponding results of numerical analysis.

It can be seen (see Table 6) that $I_{\overline{T}}$ determined from physical models is, in the majority of cases, somewhat larger from that obtained for numerical models. The exception is model V-1 (V-1P), in which $I_{\overline{T}}$ determined by FEM is of 0.53% larger from $I_{\overline{T}}$ obtained for a physical model. Owing to the small difference it can be generally considered that the numerical models used here in allow the safe estimation of the angle of torsion of the studied elements.

8 THICKNESS OF THE WEB IN THE EQUIVALENT DOUBLE-TEE MEMBERS

On the basis of obtained moments of area of the uniform torsion (see Table 6), the equivalent, solid double-tee cross-sections have been calculated, in which the discrete lacings has been substituted by a continuous web. A modified expression for the second moment of area of the uniform torsion has been used in which the term due to known I_T of the flange is added:

$$I_{\overline{T}} = 2 \cdot I_{Tp} + \frac{\alpha}{3} \sum_{i=1}^{m} b_i t_i^3 . \tag{9}$$

Transforming this expression we can get a relationship for an equivalent thickness of the web:

$$t_{\overline{w}} = \sqrt[3]{\frac{3\left(I_{\overline{T}} - 2 \cdot I_{Tp}\right)}{\alpha \cdot b_w}} . \tag{10}$$

The results obtained for physical models, assuming coefficient $\alpha = 1.2$ (Lorkowski 2014) are given in Table 7.

Listed above (Table 7) equivalent thickness of webs confirms undoubtedly the high rigdity to torsion of the laced members. These thicknesses are clearly bigger than those used in the engineering practice. It proves the effectiveness of considered binding between chords. At the same time, the equivalent thickness obtained for members with bindings made of flat bars exclusively, in which the diagonals are omitted, shows a very low rigidity of this design solution to torsion.

Table 6. Equivalent second moment of area of the uniform torsion $I_{\overline{T}}$.

	Equivalent moment of area $I_{\overline{T}}$ w cm^4	
Model	Physical models	Numerical models
S-1	19.04	16.69
S-2	16.60	14.09
V-1 (V-1P)	11.27	11.33
V-2 (V-2P)	5.56	4.33

Table 7. Thickness of the web $t_{\overline{w}}$ of double-tee members.

	Equivalent thickness of the web $t_{\overline{w}}$, mm	
Model	Physical models	Numerical models
S-1	11.6	10.9
S-2	10.9	10.1
V-1 (V-1P)	9.0	9.0
V-2 (V-2P)	5.1	1.0

9 GENERAL REMARKS AND CONCLUSIONS

Summarizing the results of studies of the two-chord members laced in a single plane it should be stated as following:

- the bindings of chords designed without diagonal members (battened models V) are substantially less effective from the lacing system (models S),
- the equivalent second moment of area of the uniform torsion of the studied members with no-diagonal bindings (battened) made of square hollow section is about 2 times larger from that constructed of flat bars,
- in both cases of bindings, the more beneficial effect of equivalent second moment of area of the uniform torsion is reached $I_{\overline{T}}$ when the bindings are executed of square tubes,
- the equivalent second moment of area of the analyzed members laced by square tubes is about 15% larger from that laced by flat bars.

The knowledge of geometric characteristics of torsion $I_{\overline{T}}$ i $I_{\overline{\omega}}$ for two-chord members with a single-plane of lacings is important like in case of thin-walled open cross-section, where the spatial instability (lateral-torional buckling, flexural-torsional buckling) causes basic problems. The analyzed members are sensitive to the spatial instability (Lorkowski 2014). These members can be considered as a double-tee objects in which the one-plane lacing is replaced by a solid web. The equivalent double-tee sections are admittedly more rigid to torsion from those fabricated by the industry, but nevertheless, still vulnerable to the spatial forms of buckling, which has to be taken into account during the design process.

REFERENCES

ABAQUS 6.12. 2012 Online Documentation. Dassault Systèmes.

ArcelorMittal. 2008. Kształtowniki i pręty walcowane na gorąco.

Biegus, A. 2009. Stalowe budynki halowe. Warszawa: Arkady.

Bogucki, W. & Żyburtowicz, M. 2006. Tablice do projektowania konstrukcji metalowych. Warszawa: Arkady.

Gosowski, B. 2001. Stalowe konstrukcje wsporcze kolejowej sieci trakcyjnej a problem trwałości. Ochrona przed Korozją. 2: 40–44.

Gosowski, B. & Lorkowski, P. 2012. Ocena stalowych słupów dwugałęziowych tramwajowej sieci trakcyjnej. *Przegląd Budowlany* 83(5): 80–83.

Gosowski, B. 2007. Non-uniform torsion of stiffened open thin-walled members of steel structures. *Journal of Constructional Steel Research* 63(6): 849–865.

Gosowski, B. 2004. Skręcanie i zginanie otwartych. stężonych elementów konstrukcji metalowych. Wrocław: Oficyna Wydawnicza Politechnika Wrocławska.

Gosowski, B. & Niżniowski, P. 2008. Verification of FEM program solutions of stability and torsion problems for I shape steel members. *Archives of Civil Engineering* 54(1): 129–145.

Krzyśpiak, T. 1976. Konstrukcje stalowe hal. Warszawa: Arkady.

Kucharczuk, W. & Labocha, L. 2012. Hale o konstrukcji stalowej. Poradnik projektanta. Rzeszów: Polskie Wydawnictwo Techniczne.

Lorkowski, P. 2014. Nośność krytyczna stalowych elementów dwugałęziwych z pojedynczą płaszczyzną skratowań. Raporty Instytutu Budownictwa Politechniki Wrocławskiej. Seria PRE nr 11 – Rozprawa doktorska.

PN-EN 1090-1+A1: 2012 Wykonanie konstrukcji stalowych i aluminiowych. Część 1: Zasady oceny zgodności elementów konstrukcyjnych.

PN-EN 1090-2+A1: 2012 Wykonanie konstrukcji stalowych i aluminiowych. Część 2: Wymagania techniczne dotyczące konstrukcji stalowych.

Romanów, F. 1988. Wytrzymałość ram i nadwozi pojazdów. Warszawa: Wydawnictwo Komunikacji i Łączności.

Rutecki, J. 1966. Cienkościenne konstrukcje nośne. Obliczenia wytrzymałościowe. Warszawa: PWN.

Recent Progress in Steel and Composite Structures – Giżejowski et al. (Eds)
© 2016 Taylor & Francis Group, London, ISBN 978-1-138-02946-0

Computer FVM-FEM analysis of the large span grid shell roof

J. Szafran & K. Juszczyk
Department of Structural Mechanics, Chair of Reliability of Structures, Faculty of Civil Engineering, Architecture and Environmental Engineering, Łódź University of Technology, Łódź, Poland

M. Kamiński
Department of Structural Mechanics, Head of Chair of Reliability of Structures, Faculty of Civil Engineering, Architecture and Environmental Engineering, Łódź University of Technology, Łódź, Poland

ABSTRACT: The main aim of this paper is presentation of the wind impact analysis results for the structure having complex geometry, where a modular space grid constitutes the roof shell surface. The wind load has been estimated using the pressure coefficients calculated according to the Eurocode standards. The results have been subsequently compared with numerical simulation results obtained by the use of the Computational Fluid Dynamics (CFD) software ANSYS based on the Finite Volume Method (FVM). The internal forces in space grid members have been analyzed in such a dual approach. Numerical results collected demonstrate that the pressure distribution determined according to the standards has more universal character in civil engineering applications, while the distributions resulting from the CFD analysis better fit into the specific shape of the given structure. Internal forces into the structure are determined here with the use of classical engineering package of the Finite Element Method (FEM).

1 INTRODUCTION

Numerous civil engineering structures, because of their functional nature, require designing and manufacturing of the large areas covered by various roofs, which for the sake of serviceability need various supporting structures. Such structures include stadiums, halls, hangars, airports, train stations and some others. They frequently have to comply with rigorous requirements like extremely high performance parameters, e.g. having large spans between supporting structures, being more and more lighter or having enormous strength. One solution to the aforementioned challenges is a roofing system consisting of the modular space grids. It can be the discrete beams system, whose axes constitute a defined, spatial geometric grid. Its smallest dimension like height or thickness differs by at least one order of the magnitude in addition to some other dimensions (Bródka et al., 1985).

Space grid roofing systems have a lot of different advantages; one of them is conservation of long-lasting global stability. Most frequently such a space grids are repeatedly statically indeterminate structures. If a structure of that type gets locally damage, then usually a chain reaction leading to damage expansion and eventual collapse of the entire structure does not occur ensuring the safety of the structure. Moreover, structural roofs make use of geometric mating of particular construction elements. Their high stiffness and relatively small deflection allow them to serve as the roofs for large spans measuring even over 100 m.

All space grid roof systems are made with the basic structural members such as mesh, bars, joints, or spatial elements made with the aforementioned elements (Kurzawa, 2011). Specific locations and construction way of the supporting structures are determined by a type and direction of the dominating loads, by the spans between supporting structures, and also by the geometry of a system.

External loads impacting the whole structure are not gradually transferred, but they rather distributed among numerous beams arranged in different directions. It reduces the internal forces in elements allowing for more economical, usually smaller cross-sections.

The characteristics of such roof systems like large area of the slope and small mass make wind a significant (even dominating) load that has to be taken into consideration; also including dynamical effects like flatter. Therefore, it is of paramount importance to estimate this type of load as accurately as possible, because it directly affects the construction cost.

One of the most preferred ways to analyse an influence of the wind on the structure frequently applied in wind engineering is an application of the CFD software. Computational techniques implemented in such a software, in view of the low costs

of computational analysis itself in comparison to the full scale tests, are used to assess the wind-structure interaction like stresses and deformations of the key structural elements. This has been demonstrated in many scientific works, i. a. Vizotto & Ferreira (2015), Tominaga et al. (2015) or Montazeri & Blocken (2013). Computational Fluid Dynamics are also widely used in numerical simulation of wind environment with building areas. Guo et al. (2015) have used CFD simulation technology of wind environment as a important basis for optimizing the architectural design. Li et al. (2015) compare and validate in their studies turbulent models with measurements of wind tunnel experiments. They have presented useful guidelines and references to choose appropriate turbulent model for numerical wind environment researches and practical application. Zhang et al. (2015) have used CFD to predict wind-induced vibrations of high rise building. They have shown in their researches, that CFD simulations provides predictions of good accuracy and can be considered as a preliminary design tool to evaluate the unsteady wind effects on a tall building. Some issues about using Computational Fluid Dynamics and Experimental Fluid Dynamics in a hybrid management approach in wind engineering and the built environment have been considered by Meroney (2016).

The analysis of the space structural grid, which compares the obtained results using obligatory civil engineering EU standards with the results of an analysis carried out using the CFD software has been presented in this work. The geometry of the object is adequate to the railway station located at the boundary between Hanover and Laatzen in Germany and is a good example of modern architecture.

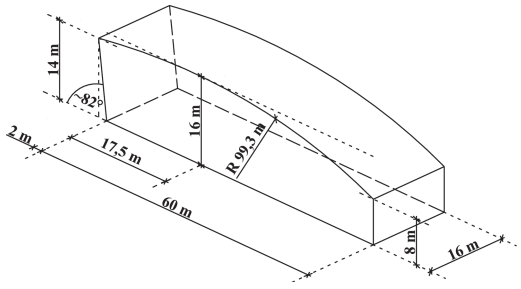

Figure 1. Sketch of the building with basic dimensions of the analyzed object.

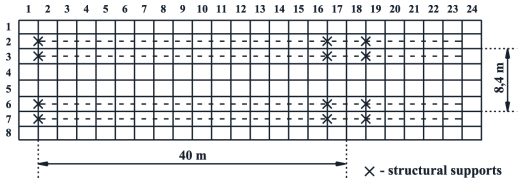

Figure 2. Locations of supporting structures.

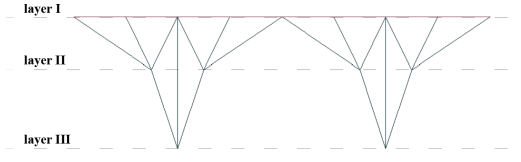

Figure 3. Truss bar system—cross-section.

2 GEOMETRY OF THE OBJECT

The structure subjected to the analysis is a part of a building erected on a rectangular plan with the following characteristic elements: a slant gable wall and the roof designed as a surface of the single curvature, whose generating line is a circular sector. Basic dimensions of the building are shown in Figure 1.

A structure of the roof consists of the three-layer spatial truss, which is entirely manufactured with the circular hot rolled steel pipes. It is supported with four forked columns at two different levels which, in turn, support the strap of the second level of the truss (the arrangement of the supporting columns is illustrated in Figure 2).

The individual layers are parallel surfaces with the distances adopted as 2,0 m between the first and the second layer and 3,0 m between the second and the third. The system roughly reflects a "tree structure" and an analogy to the leaf trees branches may be noticed: bars branch upwards in such a way that the next level is more complex than the lower one (Fig. 3). The first layer is constituted by 9 arcs, which together with the transverse bars create an orthogonal grid (of the mesh size 2,0 m × 2,5 m). These arcs are attached to the bracing members at the joints by welding. The numbers of curved bars of the lower layers are consecutively 4 (in the second layer) and 2 (in the third layer). These arcs of layer two are offset in relation to others by a half of the length of such a mesh.

The layout pattern repeats itself periodically over the entire cross-section—its scheme is presented in Figure 4.

The general view of the structural grid roof structure along with the basic dimensions is presented in Figures 5–6.

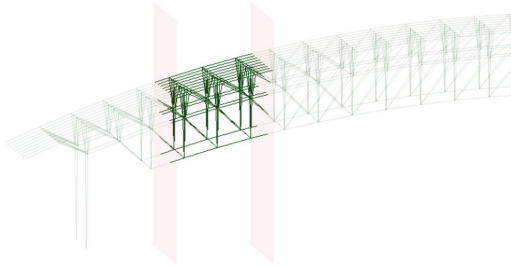

Figure 4. Spatial bar system.

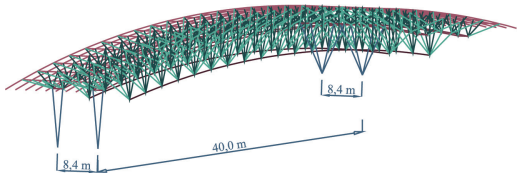

Figure 5. Axonometric view of the analyzed roof structure.

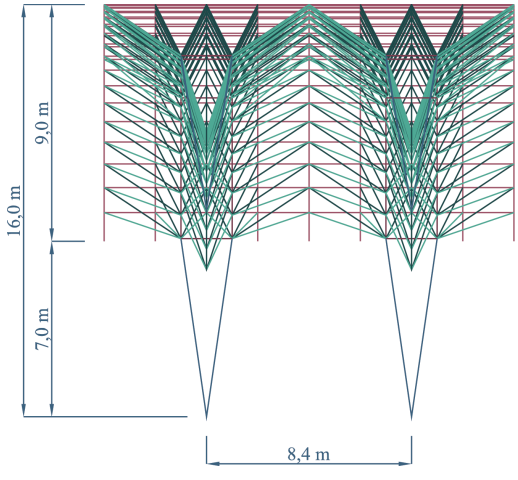

Figure 6. Structural system of the analyzed roof.

3 STRUCTURAL LOADS ANALYSIS

The dead load, the static technological loadings and the impact of wind action, which is essential for the analyzed case, are taken into consideration in this study. The snow load was intentionally postponed, so that a direct impact of the wind on particular values and overall distribution of the internal forces could is discussed. It is additionally assumed that the temperature-induced load is completely transferred by the roof cover, i.e. the layered panels, which fully protects the steel structure.

3.1 *Static load*

It is assumed during the analysis that the technological loading and the dead load altogether acting on the layered panels are equal to q = 0,11 kN/m^2. Technological load in a form of the lighting system suspended to a spatial truss has been inserted by the concentrated forces equal each Q = 1,0 kN, distributed among the set consisting of every second node of the second layer bars.

3.2 *Wind impact*

The wind load has been estimated first using classical engineering method based on the averaged pressure coefficients. However, Eurocode 1 (2008) does not contain detailed guidelines suitable for an estimation of the wind load on a nonstandard object or roof area in particular, similar to the analyzed structure. Therefore, in order to determine the wind load on the building external surfaces we prefer the following two different approaches: (a) estimation of load generated by wind for railway wagon roofs (approach 1) and, independently, (b) for the gable roofs (approach 2). The extreme values obtained according to both approaches were subsequently compared with the results of the wind load simulation for this structure conducted using the software ANSYS 15.0 CFD.

3.2.1 *Wind load estimation from the standards*

The building body has been divided into two parts separately analyzed, whose geometrical dimensions were defined: the heights of walls supporting the arcs, the heights of an arc elevation and also the dimensions of the sidewalls; both parts were treated as separate geometric systems. The division of the entire building and the values used in our calculations are schematically presented in Figure 7.

As the roof cover was considered as the gable roof, the additional simplifications presented in Figure 8 have been applied.

The geometry modification above resulted in the gable roof of slope angles equal to $\alpha_1 = 6^\circ, \alpha_2 = 12^\circ$. The external pressure coefficients were determined using the statements of Eurocode 1 (2008) for both computational approaches and it resulted in the additional pressure maps.

3.2.2 *Wind load simulation for the building carried out by the system ANSYS 15.0 CFD*

The software used in this simulation took advantage of computational fluid mechanics based on the Finite Volume Method (FVM).

A building body has been inserted into a computational domain (Fig. 9), which dimensions were defined based on guidelines (Franke, 2004), though some modifications were applied. The Authors ini-

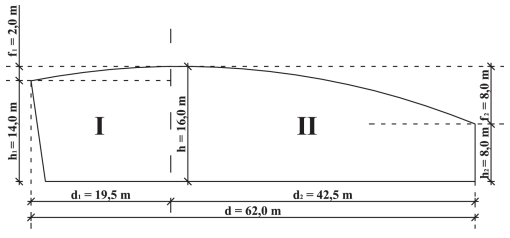

Figure 7. Division of building's body taken for calculations (approach 1).

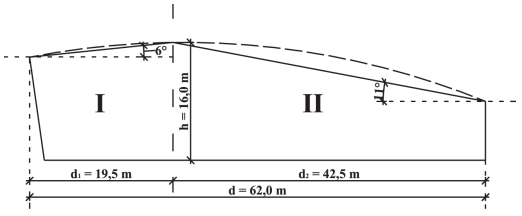

Figure 8. Simplifications of building geometry for the gable roof (approach 2).

tially adopt the rules for proper modeling of space around an analyzed object to ensure that the analysis of impact on a three-dimensional object and surrounding terrain is correct. In the analyzed case, no aerodynamic analysis of wind flow around the structure has been carried out, because its action on the surrounding terrain was insignificant contrary to its action on the building surface.

Computational domain has been subjected to numerical discretization using classical Finite Volume Method. A three-dimensional unstructured grid has been used (Tet/Hybrid—tetrahedral hybrid finite volumes, scale 1:1). By applying local grid creation conditions to the domain sides and the building body, a volumetric grid of pyramids has been generated with the minimum skewness of 0.8 for each pyramid. The density of the FVM grid has been increased for the regions with larger velocity gradients and decreased for ones where velocity increments were small. Computational grid is set in such a way as to capture all essential flow aspects and to avoid numerical discrepancies like local changes of its density or the cells showing improper distortions.

CFD analysis treats the wind flow as turbulent flow of the homogenous, viscous, incompressible Newtonian fluid. The turbulent flow has been analyzed by using of the Reynolds Averaged Navier-Stokes (RANS) equations. The wind is assumed to be incompressible, so that the solution method is also based upon the pressure-based segregated algorithm. The steady-state analysis type and SIMPLE algorithm have been used together with the flow solver using the First Order Accuracy. Numerical simulation of turbulent air flow in near-surface area of an object has been conducted by using of the so-called realizable k-ε model.

In order to obtain an accurate representation of the wind load, five cases corresponding to the five different wind directions named "1", "2", "3", "4" and "5" have considered; they are all schematically shown in Fig. 10.

The roof has been discretized into the bricks (an orthogonal grid of 24×8 areas), whose geometrical dimensions fully correspond to the real layout of the structural rebars. This grid is subsequently applied to recover the gradual changes of the pressure coefficients.

The following rules have been applied during create the maps of coefficients of external pressure:

– an individual grid cell has been assumed to be a surface element, where a single interval of the external pressure coefficient values occurs,
– if one cell has the coefficient value belonging to two different intervals, then more unfavorable values is chosen or the values corresponding to coefficients on larger surface are chosen,

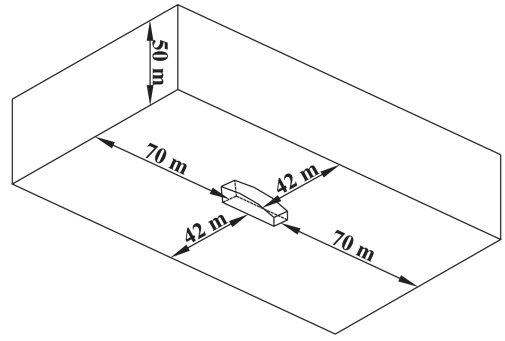

Figure 9. Adopted dimensions of computational domain.

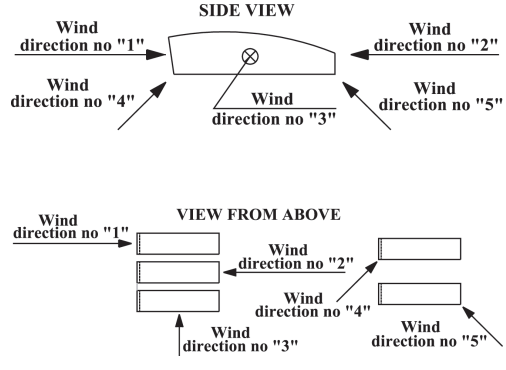

Figure 10. The given wind load cases.

– if coefficients in a given value interval occupy negligible surface, they are rejected as extreme and unreliable,
– the external pressure coefficient value in a given area has been chosen as the least favorable value from its interval.

The 3D image of the wind vortices around the building has been obtained as a result of this simulation. The flow has been observed using velocity vectors, current lines at the wall-boundary layer and the external pressure coefficients on the object surface (Figs. 11–13).

The values of external pressure coefficients on the roof surface (Figs. 14–18) have been used to create the final external pressure coefficient maps.

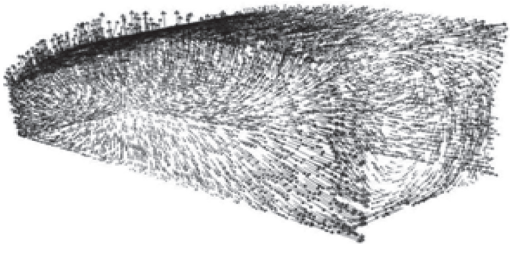

Figure 11. Velocity vectors around analyzed object for the wind in direction “3”.

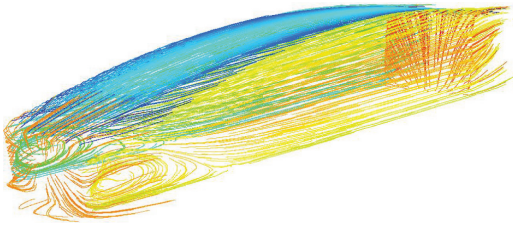

Figure 12. Wind flow around the structure for the direction “2”.

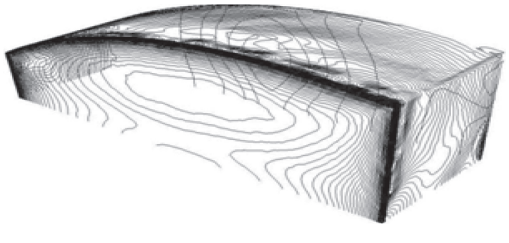

Figure 13. External pressure coefficients for the wind in direction “3”.

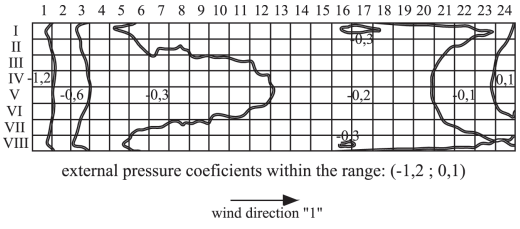

Figure 14. External pressure coefficients for the wind in direction “1”.

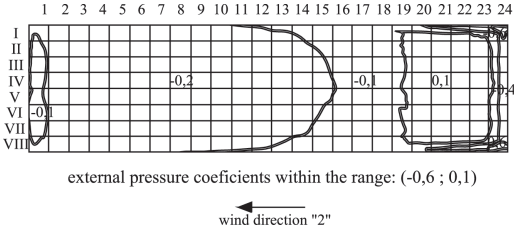

Figure 15. External pressure coefficients for the wind direction “2”.

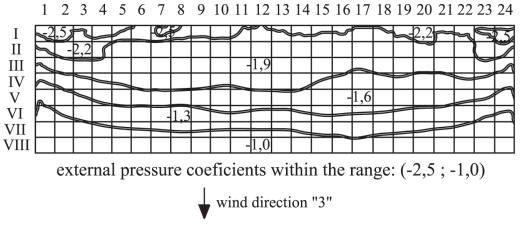

Figure 16. External pressure coefficients for the wind direction “3”.

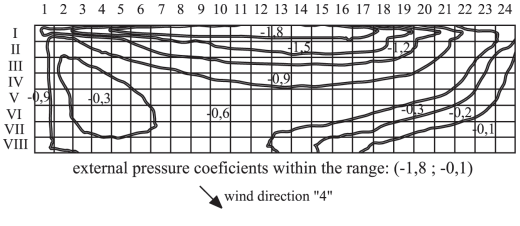

Figure 17. External pressure coefficients for the wind direction “4”.

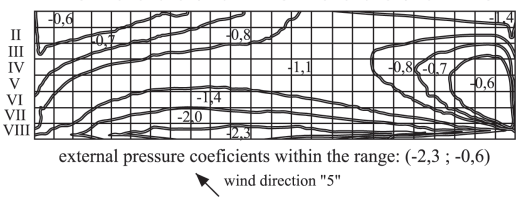

Figure 18. External pressure coefficients for the wind direction “5”.

4 FEM STRUCTURAL ANALYSIS

The Finite Element Method (FEM) model of the representative structural element has been prepared with the use of 359 nodes, 1158 two-noded 3D linear elastic beam elements (6 degrees of freedom in each node) and 192 non-material surface elements, where the external loads taken from the previous analysis have been applied (dead and wind loads). All the environmental loads were combined according to the widely known combination scheme provided by *Eurocode* 0 (2004). The external pressure coefficient maps together with the corresponding internal forces graphs are presented below for two different approaches and the additional wind directions.

4.1 *Wind in direction "1"*

Extreme pressure values were noticed directly at the windward wall of the building, whereas the minimum values occurred at the leeward wall. However, their distribution differs for individual cases: these coefficients are arranged into the vertical lines for approach based on EU standards, while for approach based on CFD analysis pressure coefficients follow the shape of the roof and their distribution was more diversified. In the latter both the lowest values of the external pressure coefficients and the lightest wind load could be found (Fig. 19).

The wind pressure on the structure could be observed at such a part of the roof, which could not be found in other cases. The results obtained based on standards were similar. The maximum wind under pressure values were observed in approach 2, but occurred on negligible surfaces. Therefore, the case, which generated the highest wind load on the structure was approach 1, whose results are also presented on the internal forces diagrams (Fig. 20).

4.2 *Wind in direction "2"*

Correspondingly to the case of wind direction "1", the minimum pressure coefficient values are determined in the CFD analysis. Extreme values (although for small surfaces) are obtained in case, when the roof is treated as the gable, and maximum averaged wind load is generated in case of the approach based on the standards for wagon roof (Fig. 21). It should be mentioned that the differences in the coefficients between CFD simulation and approach based on standards are remarkable (sometimes with the few times).

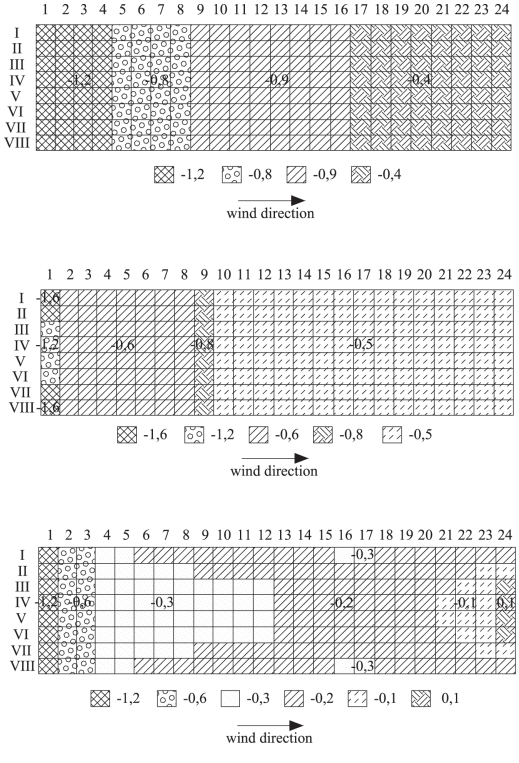

Figure 19. External pressure coefficient maps for EC approach no 1 (top), EC approach no 2 (middle) and CFD simulation (bottom), for the wind direction "1".

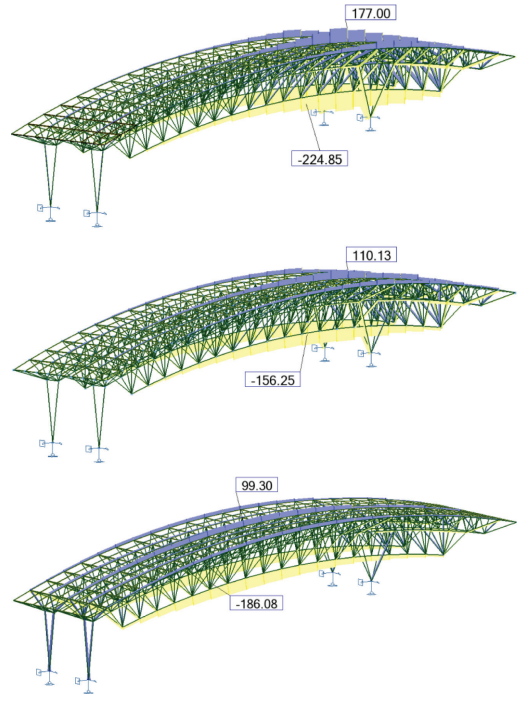

Figure 20. Axial forces in particular structure members for the EC approach 1 (top), EC approach 2 (middle) and CFD simulation (bottom) for the wind direction "1".

However, there were also similar values in-between the distributions in CFD analysis and the gable model: in both cases the maximum values of the coefficients were noticed at the corners of a structure and on the windward wall—with the few times greater than those at other places. Such an analogy has been also observed between the computer simulation and approach 1: wind pressure on the roof slope occurred at frontal part of the roof (closer to the windward wall). The values of coefficients corresponding to the internal forces graphs (Fig. 22): maximum compression and tension is noticed for approach 1 - at the part of the building closer to the windward wall, whereas minimum axial forces values could be observed in CFD analysis. In case of approach 2 and CFD analysis, maximum axial forces values were observed closer to the leeward wall.

4.3 *Wind in direction "3"*

It is essential to be underline that EU civil engineering standards do not contain guidelines for estimating wind load in directions "3", "4" and "5" for approach 1. If the other approaches are

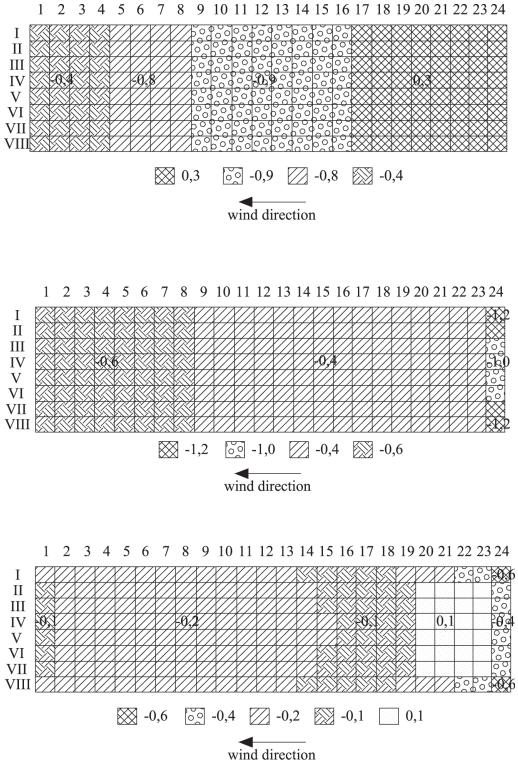

Figure 21. External pressure coefficient maps for the EC approach 1 (top), codified approach 2 (middle) and CFD simulation (bottom) for the wind direction "2".

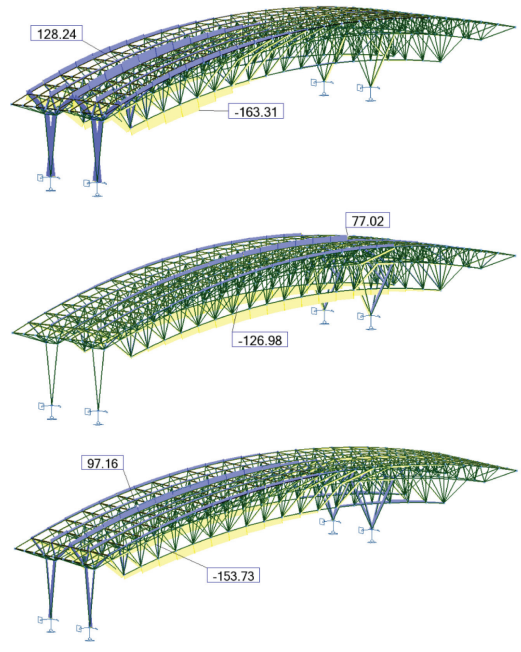

Figure 22. Axial forces in the particular structure members for the EC approach 1 (top), EC approach 2 (middle) and CFD simulation (bottom) for the wind direction "2".

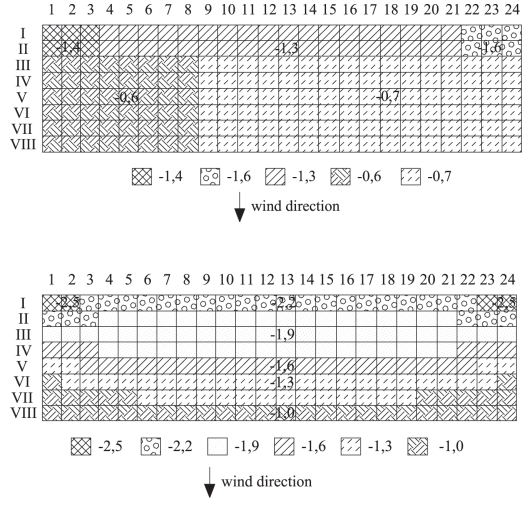

Figure 23. External pressure coefficient maps for codified approach 2 (top) and CFD simulation (bottom), for wind in direction "3".

compared for wind direction "3" it can be noticed that a general character of coefficient distribution is similar for all approaches (Fig. 23). However, the results for the CFD analysis are almost twice as great as these estimated for the gable roofs.

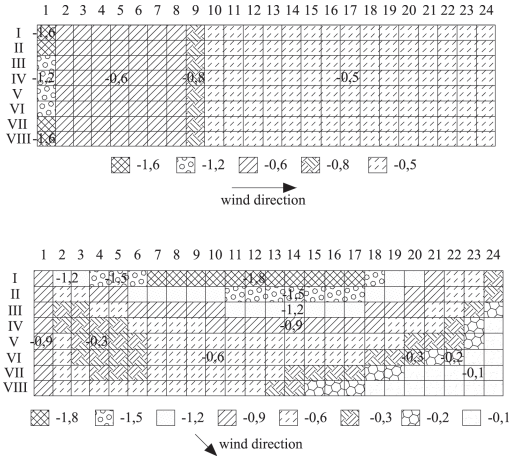

Figure 24. Comparison of external pressure coefficient maps for wind direction "4": approach 2 (top) and CFD simulation (bottom).

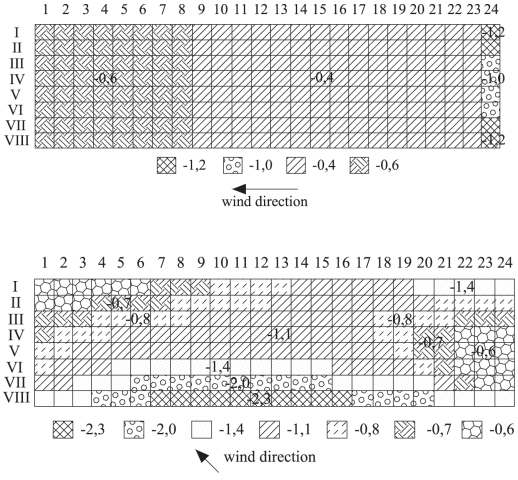

Figure 25. Comparison of external pressure coefficient maps for the wind in direction "5": approach 2 (top) and CFD simulation (bottom).

4.4 *Wind in direction "4"*

The standards permit for treating a wind at the angle of 45º in horizontal projection as perpendicular to the windward wall in case of the gable roofs. Therefore, pressure coefficients obtained in simulation for the wind in direction "4" should be compared with the map prepared according to the standards, as for the wind in direction "1" (Fig. 24). The differences in pressure distribution and their values are noticeable, it is particularly apparent in central part of the roof, where the wind gusting for CFD analysis is several times stronger than in case of the standards.

Table 1. Axial forces for one of the layer I arcs of the roof shell.

		Wind direction "1"	Wind direction "2"
		kN	kN
CFD	Compression	99.3	97.2
	Tension	–8.8	–62.9
Approach	Compression	177.0	128.2
no 1	Tension	–2.7	–11.2
Approach	Compression	110.1	77.0
no 2	Tension	–2.5	–1.5

Table 2. Axial forces for one of the layer III arcs of the roof shell.

		Wind direction "1"	Wind direction "2"
		kN	kN
CFD	Compression	–	51.9
Tension		–186.1	–153.7
Approach	Compression	–	15.7
no 1	Tension	–224.9	–163.3
Approach	Compression	–	–
no 2	Tension	–156.3	–127.0

Table 3. Axial forces for one of the supporting columns of the roof shell.

		Wind direction "1"	Wind direction "2"
		kN	kN
CFD	Compression	40.5	39.2
	Tension-	–	–
Approach	Compression	13.9	85.7
no 1	Tension	–	–
Approach	Compression	10.0	9.1
no 2	Tension	–	–

4.5 *Wind in direction "5"*

In case of the wind in direction "5" the situation is similar to the previous cases: a comparison of the computer simulation results in the wind estimated according to standards, as for gable roofs in direction "2" yields completely different pressure distribution (Fig. 25). The differences of pressure coefficients differ even with the five times.

4.6 *Axial forces comparison*

In order to better present and understand the differences in computational approaches under consideration and their influence on this structure, the values of internal forces have been compared for selected elements (Tables 1–3).

5 CONCLUSIONS

The main goal of the work consisted of an analysis of a spatial grid roof having complex geometry subjected to the wind load. Three various approaches to this problem having different pressure distributions, external load values and structural responses have been compared against each other. The following conclusions have been drawn based on the results obtained above:

- as we can find in the results of axial forces of particular structural members, the CFD analysis allow for more precise evaluation of the forces values, what can directly determine the elements sizing process,
- the analysis of a wind flowing around the object in CFD software, contrary to the standards-based analysis, allowed for showing its impact in any direction; such an analysis not only provides a much more detailed representation of wind load adapted to the actual shape of the building body, but also enables observation of the wind behavior around the structure,
- while Eurocode 1 (2008) gives the pressure distribution representation more general and definitely more universal, the CFD simulation represents real conditions more accurately; EC standards are more efficient in averaging of the wind action, while CFD enables for local pressure fluctuations detection,
- some discrepancies in the values of pressure coefficients of the external pressure are remarkable for especially for the wind directions "4" and "5",
- EU standards give higher pressures for the wind directions "1" and "2", while the CFD approach gives extreme values for the remaining load cases, especially in central part of the roof shell.

According to our computational example it can be stated that the pressure coefficient maps for an external pressure obtained during the wind flow analysis conducted in ANSYS 15.0 Fluid Dynamics software result in great precision in addition to the values proposed by the standards. The program analyzes flow of the air around a specific object model of given dimensions, while the values given in standards can be assigned to surfaces of different sizes and shapes, which make them more universal.

REFERENCES

Bródka, J. et al. 1985. *Przekrycia strukturalne* (in Polish), Warsaw (Poland): Arkady.

Eurocode 0 2004. *Basis of structural design*. Warsaw: PKN.

Eurocode 1 2008. *Actions on structures, Part 1–4: General actions—Wind actions*. Warsaw: PKN.

Franke, J. (edr.) 2004. Recommendations on the Use of CFD in Wind Engineering. Brussels.

Guo, W. et al. 2015. A Case Study on Optimization of Building Design Based on CFD Simulation Technology of Wind Environment, *Procedia Engineering* 121: 225–231.

Kurzawa, Z. 2011. *Stalowe konstrukcje prętowe. Część II: Struktury przestrzenne, przekrycia cięgnowe, maszty i wieże* (in Polish), wyd. 1. Poznań (Poland): Wydawnictwo Politechniki Poznańskiej.

Li, B. et al. 2015. Evaluation of CFD Simulation Using Various Turbulence Models for Wind Pressure on Buildings Based on Wind Tunnel Experiments. *Procedia Engineering* 121: 2209–2216.

Meroney, R.N. 2015. Ten questions concerning hybrid computational/physical model simulation of wind flow in the built environment. *Building and Environment* 96: 12–21.

Montazeri, H. & Blocken, B. 2013. CFD simulation of wind-induced pressure coefficients on buildings with and without balconies: Validation and sensitivity analysis. *Building and Environment* 60: 137–149.

Tominaga, Y. et al. 2015. Air flow around isolated gable-roof buildings with different roof pitches: Wind tunnel experiments and CFD simulations. *Building and Environment* 84: 204–213.

Vizotto, I. & Ferreira, A.M. 2015. Wind force coefficients on hexagonal free form shell. *Engineering Structures* 83: 17–29.

Zhang, Y. et al. 2015. Predicting wind-induced vibrations of high-rise buildings using unsteady CFD and modal analysis. *Journal of Wind Engineering and Industrial Aerodynamics* 136: 165–179.

This page intentionally left blank

Recent Progress in Steel and Composite Structures – Giżejowski et al. (Eds)
© 2016 Taylor & Francis Group, London, ISBN 978-1-138-02946-0

Buckling strength of a steel multi-storey framework according to Eurocode's general method

M.A. Gizejowski & Z. Stachura
Division of Metal Structures, Faculty of Civil Engineering, Warsaw University of Technology, Warsaw, Poland

ABSTRACT: Aspects of design according to EN 1993-1-1:2005 procedures and related to steel semi-continuous frames composed of I-section members are dealt with in relation to the so-called Eurocode's general method. Different problems of design verification criteria of frameworks composed of members subjected to axial compression as well as one directional bending are focused on. An algorithm of the framework resistance verification according to different procedures is presented. The design example of a multi-storey steel framework with non-composite beams restrained against lateral-torsional buckling and columns susceptible to lateral-torsional buckling illustrates simple and more advanced verification procedures of framework resistance verification. Concluding remarks yielding from this example are presented.

1 INTRODUCTION

Eurocode 3 has introduced several options for design procedures of steel frameworks, with some limitations for analysis methods to be used for calculations of load effects (stress resultants). In conventional ones, indirect resistance verification criteria are dealt with. This code introduces also a direct design procedure in which all the stability and imperfection effects are accounted for in one analysis/verification stage that combines an advanced structural analysis and the verification of failure criterion referred to the whole structural system. Such an approach called LRFD using advanced analysis (see Chen & Kim 1997, Trahair & Chan 2003) has been first introduced in the Pan-American region. The global design criterion is referred to an attainment of: (1) the most stressed section resistance as a result of stress resultants distribution (this constitute the so-called *elastic design*), or (2) the limit point on the frame nonlinear load-displacement characteristic as a result of inelastic redistribution of stress resultants between members and joints (this constitutes the so-called *plastic design*), refer to Gizejowski & Stachura (2015a).

The European approach to design using advanced analysis in a general case of the 3D behavior is presented by Bijlaard et al. (2010) as well as by Chladny & Stujberova (2013), among others. Practical implementation of the direct design using advanced analysis is possible when a relevant commercial engineering software is widely available. A method of advanced GNIA-3D calculations based on the second-order theory with equivalent geometric imperfections derived from eigenmode selections is presented by Papp et al. (2014). Presented advanced analysis has employed there a thin-walled beam-column finite element of 14th degrees of freedom allowing to detect all the 2D and 3D global buckling modes within the assumption of no local or distortional buckling of the member cross section walls. The finite element adopted was implemented to the computer software ConSteel, together with a valuable sensitivity analysis indicating the degree of engagement of structural members in reaching the buckling state of the entire framework. Recalled series of their papers has shown the range of software application in different design situations by relevant benchmark problems of steel continuous structures.

Different Eurocode's design procedures are discussed in this paper in relation to semi-continuous non-composite frameworks. The effects of joint in-plane semi-rigidity and strength are taken into account for elastic stability analysis and distribution of stress resultants according to GNIA-3D. For the out-of-plane elastic stability analysis and elastic design, the full continuity is assumed.

2 BENCHMARK FOR SEMI-CONTINUOUS FRAMEWORK DESIGN

Eurocode's resistance verification procedures according to the flow chart presented in Figure 1 are hereafter used for the plane framework design of an office building.

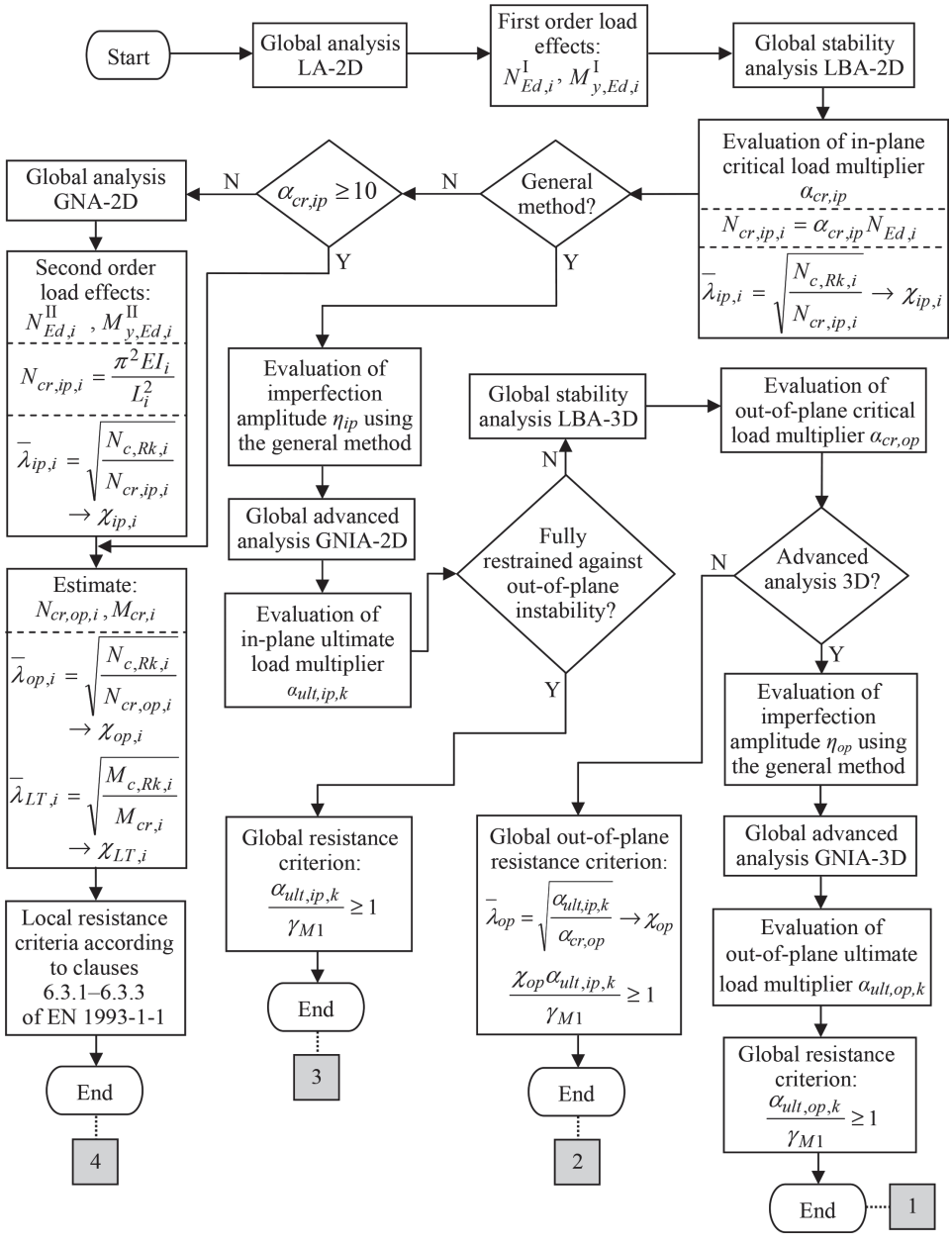

Figure 1. Flow chart of different resistance verification procedures of steel plane frameworks represented by a beam computational model (Stachura & Gizejowski 2015).

The frame was designed using the conventional procedures of Eurocode 3 together with National Annex adopted for the implementation of this code in Poland. In this conventional design, local criteria for the cross section resistance and the member buckling resistance were used together with the stress resultants (load effects) evaluated from LA and the perfect beam computational model, without taking equivalent bow imperfections into consideration. For structural analysis, a 2D model with thick-walled finite elements of 6th degrees of freedom was employed. The commercial software

Robot v. 17.5 was utilized (see Design example IV in Barszcz & Sleczka 2010).

The main structural system of considered office building is a plane 3-storey and 3-bay frame that is spaced at distance of 6 m in the building longer dimension of 30 m. Structural members are made of rolled I- and H-sections of steel grade S235JR. Since beam-to-column joints are end-plate bolted and unstiffened in the column panel, they need to be considered as semi-rigid. Column bases are stiffened and considered as fully rigid joints. Reinforced concrete slabs of 15 cm in thickness are directly laying on frame beams creating rigid slab panels.

The weight of external walls made of aerated concrete blocks is transferred directly onto the structural system as axial loads on the columns. Roof covering and floor layers creating permanent load components are taken as commonly used for office buildings. An additional considered component of loading results from the possibility of suspended services of 0.1 kN/m^2.

Imposed load of category B is taken as 2.0 kN/m^2. In addition, a substitute surface load of 0.5 kN/m^2 is assumed as an equivalent weight of partition walls the weight of which has to be less or equal to 1.0 kN/m (PN-EN 1991-1-1:2004).

Building is located in the snow zone II in Poland (PN-EN 1991-1-3:2005) and the wind zone I (PN-EN 1991-1-4:2008) in the terrain category III. In accordance to wind loading code, two wind directions are considered, namely perpendicular and parallel to the gable wall.

For the purpose of this study, a 3D model with thin-walled elements of 14th degrees of freedom is adopted. The commercial software ConSteel is used that is able to carry out the following analyses: LA-3D, LBA-3D, GNA-3D and advanced GNIA-3D, as well as to perform the resistance verification according to Eurocode's procedures given in Figure 1.

Figure 2 presents the 3D structural model generated by ConSteel with a continuous lateral translation restraints of the beam upper flange. Such boundary conditions result from the safe assumption that one can adopt for any real situation of office buildings construction. It means that the floor slab is not able to fully restrain the frame beams against twist rotation but fully restricts the lateral movement. More realistic modeling of structural systems with monolithic reinforced concrete slabs is that the slab fully restraints the upper beam flange with regard to both the lateral translations and twist rotations. These two modeling options are considered hereafter. In addition, discrete restraints are assumed within the column panels at joints, above and below the beam flange levels, that eliminate the possibility of the panel distortion.

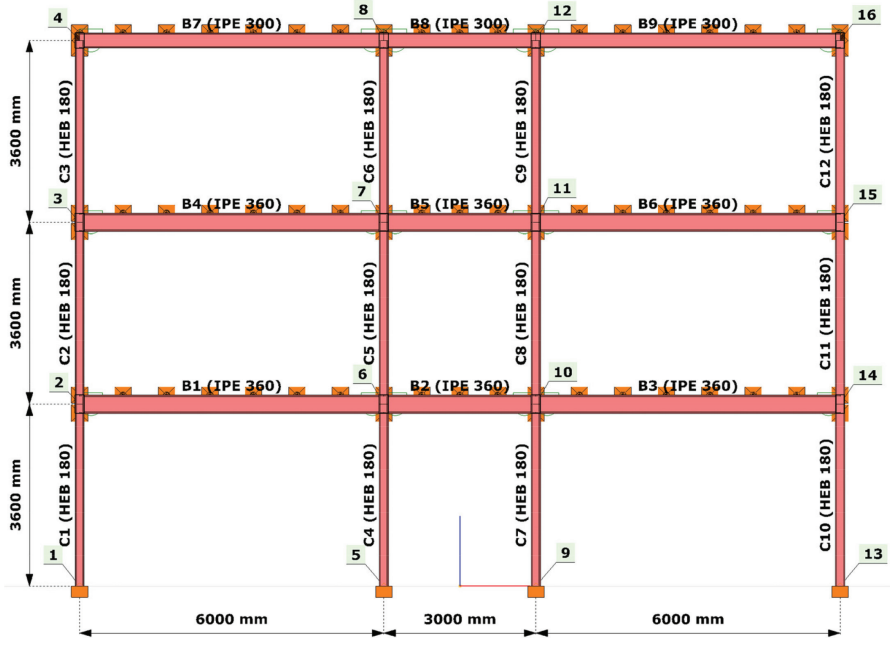

Figure 2. 3D-model of considered plane frame shown together with the location of continuous and discrete out-of-plane restraints generated by ConSteel.

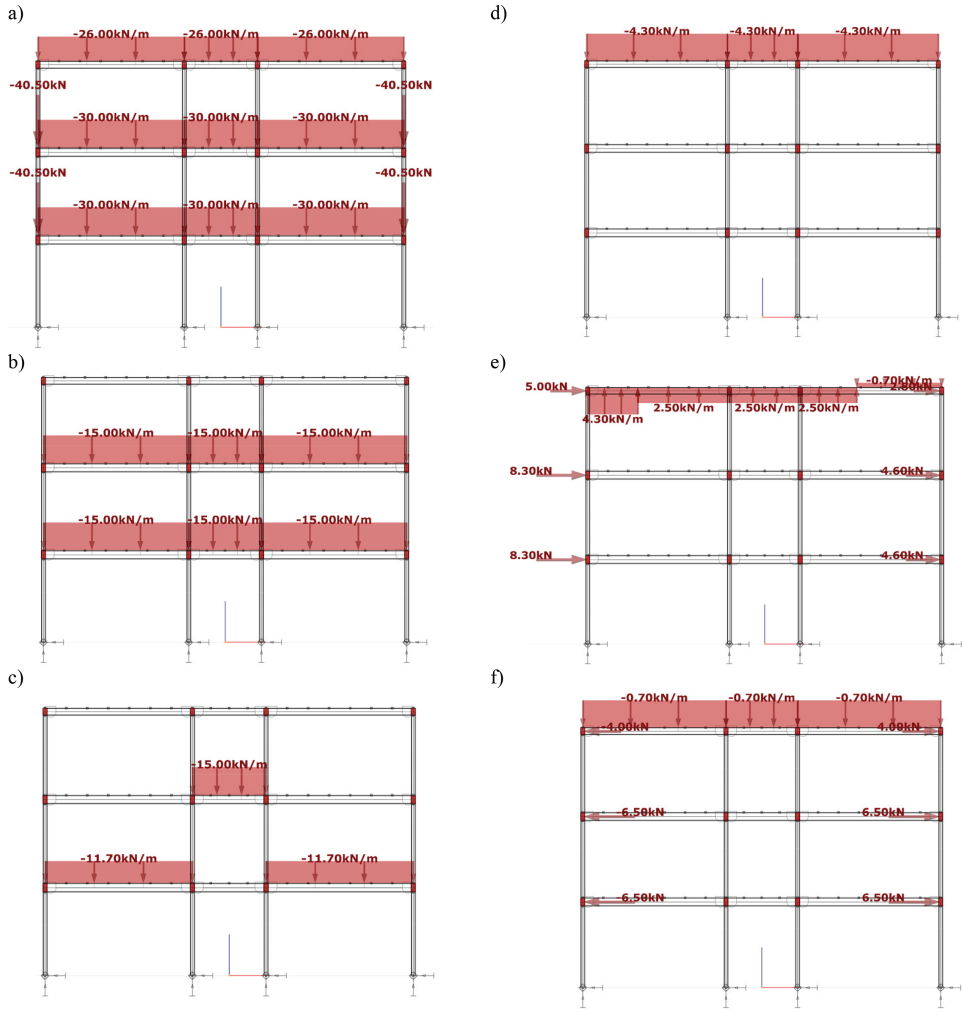

Figure 3. Selected load components: a) distributed and concentrated permanent load components, G; b) imposed load components for the distribution giving the beam maximum support moments and axial loads in columns, Q1a; c) imposed load components for the distribution giving the maximum span moments in beams, Q2b; d) distribution of snow load transferred onto the roof beams, S1; e) distributed and concentrated wind loads acting in parallel to the gable walls and transferred as concentrated loads at storey levels and distributed loads for roof beams, W_e1; f) distributed and concentrated wind loads acting perpendicularly to the gable walls and transferred as concentrated loads at storey levels and distributed loads for roof beams, W_e2.

Figures 3a-f show the load combinations considered in the analysis done with use of ConSteel in accordance to PN-EN 1990:2004 (W_i2 is not given). The combinations being the most decisive are:

COMB1: $1.35G + 1.5{\cdot}0.5S1 + 1.5{\cdot}0.6(W_e2 + W_i2)$

COMB9: $1.35G + 1.5{\cdot}0.7Q2b + 1.5{\cdot}0.5S1 + 1.5{\cdot}0.6(W_e1 + W_i2)$

COMB13: $1.35G + 1.5{\cdot}0.7Q1a + 1.5{\cdot}0.5S1 + 1.5{\cdot}0.6(W_e1 + W_i2)$

COMB19: $1.35{\cdot}0.85G + 1.5(W_e1 + W_i2) + 1.5{\cdot}0.5S1 + 1.5{\cdot}0.7Q1a$

The imposed load distribution according to Figure 3c, namely Q2b, takes into account the allowable reduction factor of $\alpha_A = 0.78$ for beams of category B buildings (beams of 6 m c/c in accordance to theoretical support lines, see PN-EN 1991-1-1:2004).

Beam-to-column joint details are shown in Figure 4a,b (dashed lines correspond to details of the double-sided internal beam-to-column joints while the solid lines represent the single-sided outer column joints). They are modeled in the module

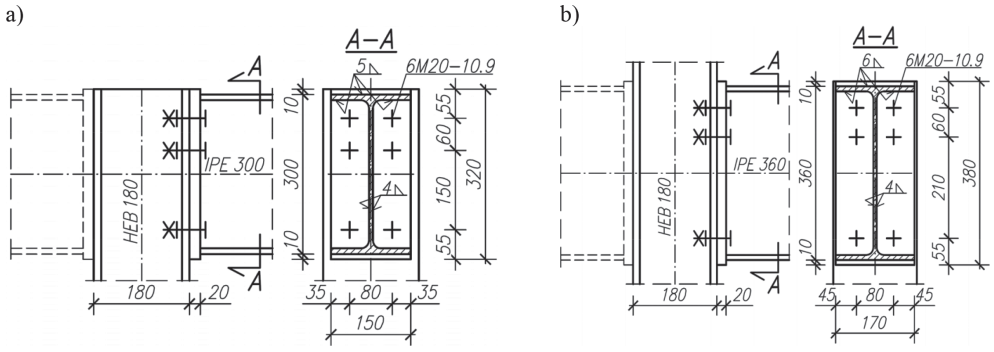

Figure 4. Details for beam-to-column joints; a) roof level, b) floor level.

csJoint of ConSteel and allocated as spring elements in respective places of the structure finite element numerical model. The said module is responsible for the calculation of the joint properties according to PN-EN 1993-1-8:2006, especially the rotational stiffness S_j for the framework global analysis:

$$S_j = S_{j.ini} / \eta \tag{1}$$

in which: $S_{j.ini}$ = joint initial stiffness; η = stiffness modification factor that allows to replace the curvilinear moment-rotation characteristic by its equivalent linear one, and in case of bolted end-plate joints yields $\eta = 2.0$.

2.1 *In-plane analysis and out-of-plane stability*

The joint initial stiffness $S_{j.ini}$ is dependent upon the column panel shear load transfer factor β that is calculated with regard to the beam end section bending moments distribution. Because of interdependence of the load effects distribution and the joint stiffness, global analysis is carried out in an iterative way, as recommended by Simoes da Silva et al. (2010). In the first iteration, in all the considered load combinations specified earlier, the shear load transfer factor is taken as: for all the single-sided joints $\beta = 1.0$ while $\beta = 0.0$ for double-sided ones. Next, in analysis carried out in each load combination separately, the value of parameters β is iteratively being corrected in each iteration with reference to the actual distribution of beam end section bending moments, and the new approximation of the initial joint stiffness $S_{j.ini}$ is calculated. The iteration process is carried out till the convergence of the load effects distribution is reached, i.e. the values of β-factors from two successive iterations remain unchanged with differences within an acceptable degree of accuracy. In ConSteel software this process is carried out automatically and the results concerned with the joint initial stiffness from performed analyses are summarized in Table 1. The convergence is achieved in the 6th iteration.

The joint stiffness that constitutes the boundary between nominally pinned and semi-rigid joint classification criterion is for shorter beams of the considered unbraced (self-stable) framework equal to: 2926 kNm/rad for IPE 300 and 5694 kNm/rad for IPE 360. The joint stiffness that constitutes the boundary between nominally rigid and semi-rigid joint classification criterion is for longer beams equal to: 73150 kNm/rad for IPE 300 and 142362 kNm/rad for IPE 360. Taking into consideration the obtained joint stiffnesses $S_{j.ini}$, see Table 1, the framework is to be considered semi-continuous.

As an initial stage, needed for the evaluation of the imperfect structural model, LBA-3D is carried out for two variants of beam out-of-plane restraining conditions. For all the considered load combinations, the first two buckling modes are in-plane flexural sway modes while the following two are nonsway and related to flexural-torsional buckling of ground floor columns. The lowest value of the critical load multiplier α_{cr} is obtained for the load combination COMB13 and for continuous lateral restraints of beams. Selected buckling modes are given in Figure 5 together with the critical load factor α_{cr}. The most sensitive member with regard to buckling in the first mode is the ground floor internal column C7 that is more stressed than the column C4. Columns of the first and second floors are much less sensitive to buckling (see Fig. 6a). In case of the second sway buckling mode, $\alpha_{cr,ip} = 10.71$, the most sensitive to buckling are columns C8 and C5. In case of the third mode, the most sensitive column is C7 while to for the fourth one, $\alpha_{cr,op} = 12.88$, the most sensitive is column C4. The other structural members of the third

and fourth flexural-torsional buckling modes are practically not sensitive to buckling (see Fig. 6b). It supports the well known consideration that out-of-plane modes are rather localized ones in contrast to in-plane sway modes that engage more structural members for reaching the buckling state.

LBA-3D carried out for the variant of beams with continuous lateral and twist rotation restraints shows that there is practically no effect of additional twist rotation restraints. In conclusion it may be stated that in semi-continuous frameworks the beam end moments are of lower values than those of rigid frameworks, so that the bottom laterally unrestrained beam flanges are subjected to lesser compression. As a result, beams in semi-continuous frameworks that are only supported laterally at the upper flange level are not sensitive to twist rotation buckling.

2.2 *Imperfect geometry profile*

In the following, according to the design path 2 given in Figure 1, the imperfect profile of the system is referred to the first flexural in-plane sway mode. The coordinates of the considered eigenmode are obtained by scaling the amplitude with use of ξ–factor as it has been explained by Gizejowski & Stachura 2015b. For sway buckling modes, involving practically all the structural members, the scaling factors ξ need to be calculated for a group of members most sensitive to buckling, in particular those that are the most stressed in compression, for their highest value to be selected for the evaluation of imperfection profile. The column most sensitive to buckling and most stressed in compression is C7 for the load combination COMB13, so that it is considered for the calculation of ξ–factor according to the following steps:

1. Determination of the major axis rotation of C7 column for considered buckling mode, e.g. using nodal rotation data from software ConSteel LBA-3D and exporting it for further calculations to Microsoft Excel (Fig. 7):

Table 1. Initial stiffness $S_{j.ini}$ of beam-to-column joints.

	Initial stiffness $S_{j.ini}$	[kNm/rad]
Joints	1st iteration	6th iteration
4, 16	14809	14809
8, 12	29113	9930–20665*
2, 3, 14, 15	22464	22464
6, 7, 10, 11	50947	14409–49586*

*Values dependent upon the location, side and load combination.

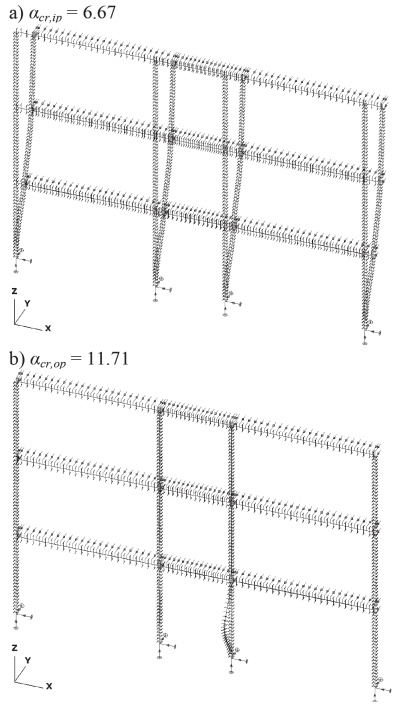

Figure 5. Selected buckling modes from LBA-3D: a) first mode being a sway flexural mode in the framework plan, b) third mode being a nonsway flexural-torsional mode out of the framework plane.

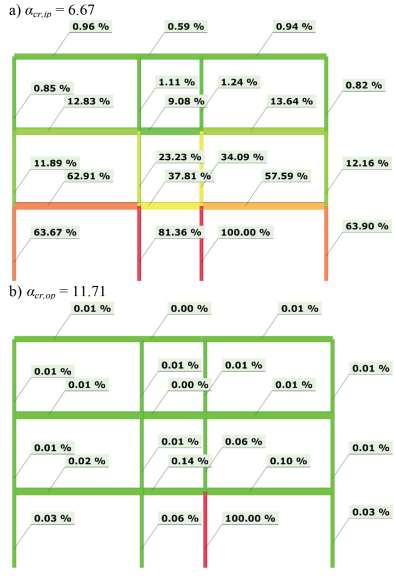

Figure 6. Sensitivity data obtained from ConSteel LBA-3D and corresponding to: a) first mode being a sway flexural mode in the framework plan, b) third mode being a nonsway flexural-torsional mode out of the framework plane.

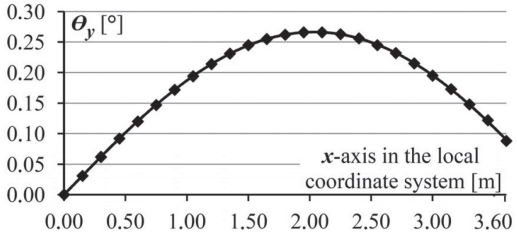

Figure 7. Major axis rotation line corresponding to the sway buckling mode of C7 column.

$$\eta'_{cr}(x) = (2.910\cdot10^{-3}x^4 - 2.444\cdot10^{-2}x^3 + \\ -1.113\cdot10^{-3}x^2 + 2.100\cdot10^{-1}x)\frac{\pi}{180}. \quad (2)$$

2. Calculation of the column C7 curvature as the fist derivative of RHS of Equation (2):

$$\eta''_{cr}(x) = (11.64\cdot10^{-3}x^3 - 7.332\cdot10^{-2}x^2 + \\ -2.226\cdot10^{-3}x + 2.100\cdot10^{-1})\frac{\pi}{180}. \quad (3)$$

3. Determination of the maximum curvature from Equation (3) in reference to the column base coordinate $x = 0.00$ m:

$$\left|\eta''_{cr}(x_{\max})\right|_{\max} = 3.665\cdot10^{-6}\,\mathrm{mm}^{-1}.$$

4. Calculation of the characteristic value of the ultimate state load multiplier $\alpha_{ult,Nk}$:

– design value of the axial force at distance $x = x_{\max}$ from the column C7 base:

$$N_{Ed}(x_{\max}) = N_{Ed}(0.00) = 722\cdot10^3\,\mathrm{N},$$

– characteristic value of the HEB 180 cross section resistance in compression that is of class 1 section:

$$N_{c,Rk}(x_{\max}) = A\cdot f_y = 6525\cdot235 = 1533\cdot10^3\,\mathrm{N},$$

$$\alpha_{ult,Nk} = \frac{N_{c,Rk}(x_{\max})}{N_{Ed}(x_{\max})} = \frac{1533\cdot10^3}{722\cdot10^3} = 2.12.$$

5. Determination of the relative slenderness ratio:

$$\overline{\lambda} = \sqrt{\frac{\alpha_{ult,Nk}}{\alpha_{cr,op}}} = \sqrt{\frac{2.12}{6.67}} = 0.564$$

6. Calculation of the bow amplitude e_0:

– characteristic value of the class 1 cross section resistance in major axis bending at distance $x = x_{\max} = 0.00$ m from the column C7 base:

$$M_{c,Rk}(x_{\max}) = W_{pl,y}f_y = 481\cdot10^3\cdot235 \\ = 113\cdot10^6\,\mathrm{Nmm}.$$

– Maquoi-Rondal imperfection factor for buckling about y-y axis: $\alpha = 0.34$ (curve "b"):

$$e_0 = \alpha\left(\overline{\lambda} - 0.2\right)\frac{M_{c,Rk}(x_{\max})}{N_{c,Rk}(x_{\max})}\xi_{cor} \\ = 0.34(0.564 - 0.2)\frac{113\cdot10^6}{1533\cdot10^3}1.0 = 9.14\,\mathrm{mm}.$$

7. Determination of scaling factor ξ:

– buckling moment associated with the eigenmode η_{cr} considered for the imperfection profile evaluation:

$$EI_y(x_{\max})\left|\eta''_{cr}(x_{\max})\right|_{\max} \\ = 210\cdot10^3\cdot3823\cdot10^4\cdot3.665\cdot10^{-6} \\ = 29.4\cdot10^6\,\mathrm{Nmm},$$

– scaling factor:

$$\xi = e_0\frac{\alpha_{cr,op}N_{Ed}(x_{\max})}{EI_y(x_{\max})\left|\eta''_{cr}(x_{\max})\right|_{\max}} \\ = 9.14\frac{6.67\cdot722\cdot10^3}{29.4\cdot10^6} = 1.50.$$

The value obtained above for C7 column and the first eigenmode for the load combination COMB13 is approximately equal to the amplitude of 36.4 mm calculated directly in the ConSteel software that corresponds to the scaling factor of $\xi = 1.48$. The small difference results from the approximation of the major axis rotation line given by Equation (2). For the other load combinations, the following scaling factors are obtained for the C7 column: COMB1 $\xi = 1.65$, COMB9 $\xi = 1.47$ and COMB19 $\xi = 1.49$. It is worthy to note that for the B9 beam for which the most stressed section reaches the resistance as the first, the scaling factor is $\xi = 0.05$ and is not a decisive factor for the evaluation of the imperfection profile.

2.3 *Advanced analysis and resistance verification*

At this stage, the imperfect computational model is known so that the advanced elastic in-plane

analysis, GNIA-2D, can be performed for the load combination COMB13. The key element the cross section of which reaches the characteristic resistance as the first under increased loads is the beam B9. The cross section utilization ratio according to the linear interaction relationship (conservative for the cross section of class 1) and the corresponding safety margin ratio are given in the following:

$$\frac{N_{Ed}}{N_{c,Rk}} + \frac{M_{y,Ed}}{M_{c,Rk}} = \frac{24.6}{1265} + \frac{121.9}{147.7} = 0.845, \alpha_{ult,ip,k} = 1/0.845 = 1.183.$$

In case of frameworks susceptible to out-of-plane instability, the resistance utilization factor may be conservatively calculated according to path 2 of Figure 1. The reduction factor for out-of-plane buckling might be calculated in a simplified way as proposed by Simoes da Silva et al. (2010). Thus, the slenderness ratio calculated for the beam B9, for the lowest out-of-plane eigenvalue from LBA-3D $\alpha_{cr,op} = 11.71$ and for the in-plane ultimate load multiplier $\alpha_{ult,ip,k} = 1.183$ from GNIA-2D is $\chi_{op} = \min(\chi_z; \chi_{LT}) = \min(0.958; 1.00) = 0.958$. The safety margin ratio evaluated with regard to out-of-plane buckling is therefore given by:

$$\chi_{op}\alpha_{ult,ip,k} / \gamma_{M1} = 0.958 \cdot 1.183/1.0 = 1.133 \geq 1.0.$$

The out-of-plane buckling is in this case rather of a localized character in contrast to the in-plane buckling mode considered earlier. The most stressed section corresponding to the in-plane resistance may not be therefore directly related to the structural element that is the most sensitive to out-of-plane buckling. This situation takes place in case of load combination COMB13 in which the most sensitive to out-of-plane buckling is the column C7, therefore it is not the beam B9. Checking this element, one can obtain:

$$\frac{N_{Ed}}{N_{c,Rk}} + \frac{M_{y,Ed}}{M_{c,Rk}} = \frac{734.8}{1533.4} + \frac{19.3}{113.1} = 0.65, \alpha_{ult,ip,k} = 1/0.65 = 1.538.$$

Thus the safety margin ratio:

$$\chi_{op}\alpha_{ult,ip,k} / \gamma_{M1} = 0.917 \cdot 1.538/1.0 = 1.41 \geq 1.0.$$

It is important to note that the safety margin ratio with regard to out-of-plane buckling should be calculated in each load combination for the decisive element despite of the fact that it may not coincide with the structural element that is the most sensitive one with regard to the system out-of-plane buckling.

Table 2 contains the characteristic safety margin ratios with regard to out-of-plane buckling $\chi_{op}\alpha_{ult,ip,k}$ that are obtained for all selected load combinations and including decisive elements of three groups of structural elements of the same cross section in each group, namely roof beams, floor beams and columns. For each load combination, the out-of-plane critical load factor $\alpha_{cr,op}$ is taken for the lowest out-of-plane eigenvalue of this combination, evaluated from LBA-3D. It may be observed that for each load combination, the decisive element with regard to out-of-plane resistance (for which $\chi_{op}\alpha_{ult,ip,k}$ is of the minimal value) coincides with the structural element that is the decisive one with regard to in-plane resistance (for which $\alpha_{ult,ip,k}$ is of the minimal value).

Table 3 contains the characteristic safety margin ratios with regard to buckling $\chi_{op}\alpha_{ult,ip,k}$ that are obtained for the reduction factor χ_{op} calculated in reference to the critical load factor $\alpha_{cr,op}$ selected for each member on the basis of the lowest out-of-plane buckling mode within the considered load combination in which the given element shows sensitivity to buckling. From Table 3 it can be seen that for the load combinations 9, 13 and 19, the critical load factors to be used for the column resistance verification are higher than those from Table 2 corresponding to the same columns. This results in the higher value of the safety margin ratio (lower value of the resistance utilization ratio). All the beams are practically not sensitive to out-of-plane

Table 2. Safety margin ratios for decisive elements of three element groups the structural elements of which have the same cross section (for the conservative estimation, $\alpha_{cr,op}$ is taken as a constant value within the load combination).

COMB	Elem.	$\alpha_{cr,op}$	χ_{op}	$\alpha_{ult,ip,k}$	$\chi_{op}\alpha_{ult,ip,k}$
1	**B7***	15.17	0.973	1.138	**1.11**
1	B1	15.17	0.949	1.755	1.67
1	C4	15.17	0.923	1.847	1.71
9	B9*	12.93	0.963	1.181	1.14
9	B1	12.93	0.956	1.331	1.27
9	C4	12.93	0.934	1.404	1.31
13	B9*	11.71	0.958	1.183	1.13
13	**B1****	11.71	0.953	1.259	**1.20**
13	C4	11.71	0.932	1.290	1.20
19	B9	12.81	0.955	1.358	1.30
19	B1**	12.81	0.953	1.390	1.33
19	**C4***	12.81	0.943	1.250	**1.18**

*Element decisive for the framework resistance evaluation.
**Element for which the resistance is overestimated since the load combination does not include the floor imposed load reduction factor α_A for the evaluation of actions for beams.

Table 3. Safety margin ratios for decisive elements of three element groups the structural elements of which have the same cross section (for a less conservative estimation, $\alpha_{cr,op}$ is taken a variable value dependent upon the element sensitivity to out-of-plane buckling).

COMB	Elem.	$\alpha_{cr,op}$	χ_{op}	$\alpha_{ult,ip,k}$	$\chi_{op}\alpha_{ult,ip,k}$
1	**B7***	–	1.000	1.138	**1.14**
1	B1	–	1.000	1.755	1.76
1	C4	15.17	0.923	1.847	1.71
9	B9*	–	1.000	1.181	1.18
9	B1	–	1.000	1.331	1.33
9	C4	14.75	0.945	1.404	1.33
13	B9*	–	1.000	1.183	1.18
13	**B1****	–	1.000	1.259	**1.26**
13	C4	12.88	0.942	1.290	1.22
19	B9	–	1.000	1.358	1.36
19	B1**	–	1.000	1.390	1.39
19	**C4***	15.06	0.955	1.250	**1.19**

*Element decisive for the framework resistance evaluation.
**Element for which the resistance is overestimated since the load combination does not include the floor imposed load reduction factor α_A for the evaluation of actions for beams.

buckling (see Fig. 6b) so that the reduction factor $\chi_{op} = 1.0$ may be a priori adopted. As a result, there is a greater resistance estimation of about 5% in case of data from Table 3 in comparison with the resistance evaluation using data from Table 2, i.e. when the critical load factor $\alpha_{cr,op}$ corresponding to the lowest out-of-plane buckling mode for the given load combination is taken as a constant value for verification of the resistance of all the framework members. It can be concluded that for the columns one is not getting much different results when using both approaches but in case of beams the differences are more pronounced. In case when decisive elements are beams in the structural system, more economical design is achieved when the sensitivity analysis is performed and corresponding $\alpha_{cr,op}$ factors from such analysis are used for the resistance verification.

Analyzing the out-of-plane buckling modes and the values of reduction factors χ_{op} listed in Tables 2 and 3, one can conclude that for the frame with continuously restrained beams considered herein, the effect of out-of-plane buckling is rather the phenomenon of localized column modes of buckling. Furthermore, when more exact evaluation of the reduction factor χ_{op} is used as proposed by Tankova et al. (2015) or Gizejowski & Stachura (2015a), among others, the criterion for the inclusion of out-of-plane buckling effect might be set even less conservative. On the other hand, the frame resistance is controlled not by the column flexural-torsional buckling but by the beam resistance that is practically not reduced because of out-of-plane buckling (beams are not sensitive to this form of failure). This observation might be directly linked to the out-of-plane critical load factor values that for all considered load combinations are between 11 and 16. Concluding, one may suggest that conservatively in case of $\alpha_{cr,op} \geq 20$ and the evaluation of reduction factors χ_{op} for columns as adopted in this paper, the effect of out-of-plane buckling can be reckoned as negligible. Thus in this case, one can assume that $\chi_{op} = 1.0$ for all the frame members, hence the design procedure according to path 2 (see the flow chart given in Figure 1) becomes the same as the design procedure according to path 3. One may suggest therefore that the effect of out-of-plane instability may be regarded as meaningless for $\alpha_{cr,op} \geq 20$. This would be a similar criterion as for the in-plane behavior in PN-EN 1993-1-1:2006 but with a different numerical value describing the upper limit for the application of this simplified design procedure.

For comparison, the conventional design procedure according to path 4 in Figure 1 is also applied. Since the in-plane critical load factor $\alpha_{cr,ip} = 6.67 < 10$, then GNA-2D with sway imperfections represented by equivalent horizontal forces has to be performed, as specified in Design example IV in Barszcz & Sleczka (2010). Local ultimate state criteria are checked according to clauses 6.3.1–6.3.3 of PN-EN 1993-1-1:2006. The decisive element with regard to buckling due to compression and LT-buckling due to bending is the column C7 for which the resistance utilization ratio is 0.862 that gives the safety margin ratio of 1/0.862 = 1.16 for the load combination COMB13. The similar value of that ratio holds for the roof beam B7 when neglecting LT-buckling for the load combination COMB1 (note the value of 1.14 in Tab. 3) while for the floor beam B1 the safety margin ratio is 1/0.747 = 1.34 for the load combination COMB9 in comparison to 1.33 from Table 3.

3 CONCLUDING REMARKS

Different aspects of Eurocode's procedures used in the planar steel frames design for estimating the ultimate limit state of frameworks modeled with use of Beam Finite Elements (BFEs) are dealt with in this paper. Application of discussed procedures is illustrated by a sway planar, semi-continuous frame structure constituting the main load bearing structural system of a low-rise office building. All detailed data is provided in order to treat this frame as a benchmark case. A novelty lies in the consideration of both in-plane and out-of-plane buckling modes evaluated from LBA-3D and used in advanced analysis applied to the beam semi-continuous

computational model of the physical framework object. Bolted beam-to-column end-plate joints are modeled as semi-rigid by using spring elements with the in-plane rotational degree of freedom. The effect of joint in-plane semi-rigidity is taken into account with an additional assumption that despite of the framework semi-continuity in its plane, its out-of-plane continuity is maintained.

Two different restraining conditions are assumed for framework beams, namely: (1) continuous lateral restraints and (2) continuous lateral and twist rotation restraints. Both conditions result in the similar buckling behavior in which the first two modes are in-plane sway while the following ones are out-of-plane and being practically localized to the column flexural buckling out of the framework plane.

A flow chart illustrating different Eurocode's design procedures is presented in Figure 1. Application of the so-called general method and the path 2 of this flow chart in which the imperfection profile according to the lowest eigenvalue sway buckling mode is considered, results in the utilization ratio (or the safety margin ratio) of decisive members from the three groups of members of the same cross section being close to the ratios evaluated on the basis of conventional design procedures (according to path 4 in Fig. 1).

The lowest eigenvalue (critical load factor α_{cr}) evaluated from LBA-3D corresponds to the in-plane sway mode, i.e. $\alpha_{cr} = \alpha_{cr,ip}$. The lowest out-of-plane eigenvalue load factor $\alpha_{cr,op}$ is for the mode corresponding to the third lowest eigenvalue that is approximately twice of that obtained for the critical in-plane mode. Verification according to path 1 of the flow chart given in Figure 1 is therefore not applicable in this case. Authors suggest that this path ought to be applied when the lowest eigenvalue (critical load factor) is associated with the out-of-plane buckling, i.e. $\alpha_{cr} = \alpha_{cr,op}$, or the values of factors $\alpha_{cr,op}$ and $\alpha_{cr,ip}$ are close to each other. Real plane frames of structural load bearing systems of typical low-rise buildings are designed as non-sway in the longitudinal direction and featuring: (1) joints to be restrained in this direction against translation and twist rotation, and (2) beams to be continuously restrained by rigid slab panels. The path 1 would therefore be applied rather rarely, because the out-of-plane modes are of higher energy modes, thus having a localized nature and influencing the resistance of selected members but not the behavior of entire frameworks.

It is shown that in case of analyzed frame the member being decisive from the frame resistance point of view depends upon the load combination considered. The resistance utilization ratio of the decisive element of each group of members of the same cross section depends upon the distribution of stress resultants in each load combination, therefore the buckling reduction factor for the frame resistance decisive member might be related to the buckling mode that is not necessarily the critical mode. In the conclusion, the designer has in general to consider in-plane and out-of-plane buckling modes related to all considered load combinations.

In case of the planar frame resistance verified according to path 2 of the flow chart in Figure 1, it is postulated that for each load combination, the resistance evaluation of particular member is done with use of such a buckling mode that gives the out-of-plane critical load factor $\alpha_{cr,op}$ from LBA-3D corresponding to a certain sensitivity of this member to out-of-plane deformations. When the member sensitivity to all the out-of-plane modes of buckling is low, one can use the buckling reduction factor χ_{op} equal to unity for this member. Furthermore, if the lowest eigenvalue $\alpha_{cr,op}$ for all the out-of-plane buckling modes is high, i.e. $\alpha_{cr,op} \geq 20$, the verification procedure may be done according to path 3 of the flow chart in Figure 1, instead of path 2.

In this paper, the ultimate load factor $\alpha_{ult,op}$ from global GNIA-3D is equal to $\alpha_{ult,ip}$ from GNIA-2D noting that $\alpha_{cr} = \alpha_{cr,ip}$ and the imperfection profile being the initial in-plane profile. The value of $\alpha_{ult,ip}$ is assessed in this paper conservatively by using a linear cross section ultimate state interaction relationship between the utilization ratios related to compression and in-plane bending (*elastic* interaction curve). Because frame member cross sections are of class 1, less conservative (more realistic) assessment might be obtained by using the *plastic* interaction curve of PN-EN 1993-1-1:2006. In case of analyzed frame, an increase of the member ultimate load factors is in average of 6% for columns and 2% for beams in comparison to those evaluated with use of the *elastic* interaction curve.

The example of planar frame presented in this paper is rather randomly selected (it is considered in Barszcz & Sleczka 2010) than based on a systematic selection made for the purpose of formulation of more general conclusions related to both rigid and semi-rigid joint frameworks. It is therefore unjustified to formulate more general conclusions than those given above and related to the frame considered in this paper. A wider scope of investigations is planned to better point out the level of generality of conclusions presented in this study and related to the exemplary frame considered herein.

REFERENCES

Barszcz, A. & Sleczka, L. 2010. Design Example IV. *Budownictwo ogólne, tom 5* (eds. M. Gizejowski & J. Ziolko). Warszawa: Arkady [in Polish].

Bijlaard, F., Feldmann, M., Naumes, J. & Sedlacek, G. 2010. The "general method" for assessing the out-of-plane stability of structural members and frames and the comparison with alternative rules in EN 1993 – Eurocode 3 – Part 1-1. *Steel Construction* 3(1): 19–33.

Chen, W.F. & Kim, S.E. 1997. *LRFD Steel Design using Advanced Analysis*. Boca Raton: CRC Press.

Chladny, E. & Stujberova, M. 2013. Frames with unique global and local imperfection in the shape of the elastic buckling mode. *Stahlbau*, Part 1 - 82(8): 609–617, Part 2–82(9): 684–695.

Gizejowski, M. & Stachura, Z. 2015a. Resistance partial factors for stability design of steel members according to Eurocodes. *8th International Conference on ADVANCES IN STEEL STRUCTURES, Lisbon, 22–24 July 2015*. Paper 23 on CD: 1–20.

Gizejowski, M. & Stachura, Z. 2015b. Buckling strength of steel frameworks evaluated in accordance to Eurocode's general method. *Inżynieria i Budownictwo* [in Polish] (in print).

Papp, F., Rubert, A. & Szalai, J. 2014. DIN EN 1993-1-1 based integrated stability analysis of 2D/3D steel structures, *Stahlbau*, Part 1 – 83(1): 1–15; Part 2 - 83(2): 122–141; Part 3 – 83(5): 325–342 [in German].

PN-EN 1990:2004. Eurocode: Basis of Structural Design. Brussels: CEN [in Polish].

PN-EN 1991-1-1:2004. Eurocode 1: Actions on structures, Part 1-1: General actions—Densities, self-weight, imposed loads for buildings. Brussels: CEN [in Polish].

PN-EN 1991-1-3:2005. Eurocode 1: Actions on structures, Part 1-3: General actions—Snow loads. Brussels: CEN [in Polish].

PN-EN 1991-1-4:2008. Eurocode 1: Actions on structures, Part 1–4: General actions—Wind actions. Brussels: CEN [in Polish].

PN-EN 1993-1-1:2006. Eurocode 3: Design of Steel Structures, Part 1-1: General rules and rules for buildings. Brussels: CEN [in Polish].

PN-EN 1993-1-8:2006. Eurocode 3: Design of Steel Structures, Part 1-8: Design of joints. Brussels: CEN [in Polish].

Simoes da Silva, L., Simoes, R. & Gervasio, H. 2010. *Design of Steel Structures, Eurocode 3: Design of steel structures, Part 1-1: General rules and rules for buildings. ECCS Eurocode Design Manual*. Berlin: Ernst & Sohn.

Stachura, Z. & Gizejowski, M. 2015. Eurocode's procedures for buckling resistance evaluation of load bearing capacity of steel planar frames. *Konstrukcje betonowe i metalowe:* 267–276. Bydgoszcz: Wydawnictwa Uczelniane Uniwersytetu Technologiczno-Przyrodniczego [in Polish].

Trahair, N.S. & Chan, S.L. 2003. Out-of-plane advanced analysis of steel structures. *Engineering Structures*, 25(13), 1627–1637.

Tankova, T., Simoes da Silva, L., Marques, L. & Andrade, A. 2015. Proposal of an Ayrton-Perry design methodology for the verification of flexural and lateral-torsional buckling of prismatic beam-columns. *8th International Conference on ADVANCES IN STEEL STRUCTURES, Lisbon, 22–24 July 2015*. Paper 21 on CD: 1–10.

This page intentionally left blank

Recent Progress in Steel and Composite Structures – Giżejowski et al. (Eds)
© 2016 Taylor & Francis Group, London, ISBN 978-1-138-02946-0

Shakedown optimization of the Thin-Wall Metal structures under strength and stiffness constrains

P. Alawdin
Faculty of Civil Engineering, Architecture and Environmental Engineering, University of Zielona Góra, Zielona Góra, Poland

L. Liepa
Department of Structural Mechanics, Faculty of Civil Engineering, Vilnius Gediminas Technical University, Vilnius, Lithuania

ABSTRACT: Up to date, classical optimization problems of metal structures confined mainly with 1st class cross-sections. But in practice it is common to use the cross-sections of higher classes. In this paper, a new mathematical model for described shakedown optimization problem for metal structures, which elements are designed from 1st to 4th class cross-sections, under variable quasi-static loads is presented. The features of limited plastic redistribution of forces in the structure with thin-walled elements there are taken into account. Authors assume the elastic-plastic flexural buckling in one plane without lateral torsional buckling behavior of members. Design formulae for Methods 1 and 2 for members are analyzed. Structures stiffness constrains are also incorporated in order to satisfy the limit serviceability state requirements. With the help of mathematical programming theory and extreme principles the structure optimization algorithm is developed and justified with the numerical experiment for the metal plane frames.

1 INTRODUCTION

The optimization of Thin-Wall Metal (TWM) frames and structures under different load combinations remains important problem today. In reality structures are loaded by the variable repeated quasi-static loads and actions, which are arbitrary varying within known domain. These loads and actions are not prescribed by history in time, but only by their given combinations according to Eurocode or any other standard.

Usually these combinations are assumed as independent, what is true only for linear systems. But relatively few papers take into account the mutual interaction of load combinations for the nonlinear systems such as real TWM ones. For instance, a thin-wall continuous beam with softening behavior under one-path loading was analyzed by Mistakidis & Stavroulakis (1998) taking into account material nonlinearity and local buckling.

The right approach is possible either by laborious analyzing of load history in time without any warranty of accounting for the worst histories of independent load cases, or for the entire class of loading as provided in the theory of shakedown analysis (SDA) (Aliawdin 2005, Atkočiūnas & Norkus 1994, Atkočiūnas 1999, 2011, Borino 2014, Čyras 1983, Čyras & Atkočiūnas 1984, König 1987, Leonetti et al. 2015, Narayanan & Roberts 1991, Nguyen 2006, Venskus et al. 2010, Weichert & Maier 2002, Weichert & Ponter 2009, Zouain 2004). The example of such shakedown approach to the steel frames confined with 1st class cross-sections was published in a paper by Atkočiūnas & Venskus (2011); a shakedown limit analysis of the reinforced concrete frames has been done by Alawdin & Bulanov (2014); an updated mathematical model for optimal shakedown analysis of plane reinforced concrete frames according to Eurocodes has been introduced by Alawdin & Liepa (2015).

The design of elastic-plastic metal frames is performed using the Eurocode 3 (EC3) or other standards, but the algorithms for strength and stiffness evaluation of TWM structures elements are not fully described in these standards. The details of analysis and design of such structures have been given in various works (Boissonnade et al. 2006, Ofner 1997).

In this paper a new mathematical model of SDA and optimization of plane thin-wall metal frames, which elements are designed from 1st to 4th class cross-sections, is proposed for general nonlinear and simplified linearized case. Structures stiffness constrains are also incorporated in order to satisfy the limit serviceability state requirements. The methodology, algorithms and implementation of metal frames weight optimization is presented and illustrated by numerical example.

Optimal results obtained, after solving continuous optimization problem, provided the optimal thin-wall metal cross-sectional area and member sizing. That allowed designing cross-sectional area from the manufacturers' catalogue using mixed-integer nonlinear programs approach.

2 MATHEMATICAL MODELS OF OPTIMIZATION OF THE STRUCTURES

2.1 *General mathematical model and assumptions*

Mathematical model in this paper is based on a hypothesis of small displacements; nonlinear or linear mathematical programing theory and finite elements method are used further. The features of limited plastic redistribution of forces in the structure with thin-walled elements there are taken into account (Aliawdin & Muzychkin 2011). The elastic-plastic flexural buckling in one plane without lateral torsional buckling behavior of members is assumed.

The TWM frames structures are loaded by forces $\boldsymbol{F}$ varying in the certain domain $\Omega(\boldsymbol{F})$. A set of the worst load combinations $\boldsymbol{F}_l, l \in L,$ and corresponded to it a set of the worst inner elastic forces combinations $\mathbf{S}_{ej}, j \in J,$ may be chosen by procedure suggested by Aliawdin (2005).

Distribution of frame element parameters (limit inner forces) is optimized here at shakedown under stiffness and nonlinear strength constraints, when load variation, material parameters and lengths L_k of all k-th elements are known $(k \in K)$.

The general problem of shakedown optimization of TWM frames structures under loads F varying in the certain domain $\Omega(\boldsymbol{F})$ is formulated as follows: find a vector of limit forces $\boldsymbol{S}_0 = (\boldsymbol{S}_{0k}, k \in K)$ of the sections, as well as the vectors of plastic multipliers $\lambda, \lambda_j, j \in J,$ such, that:

$$min\ f_0(\boldsymbol{S}_0), \tag{1}$$

$$\varphi_j(\mathbf{S}_{ej} + \mathbf{G}\mathbf{E}_p\lambda, \Gamma\mathbf{S}_0) \geq \mathbf{0}, \tag{2}$$

$$\boldsymbol{\lambda} = \sum_j \boldsymbol{\lambda}_j, \quad j \in J, \tag{3}$$

$$\boldsymbol{\lambda}_j^T \boldsymbol{\varphi}_j = 0, \quad \boldsymbol{\lambda}_j \geq 0, \tag{4}$$

$$\boldsymbol{A}\boldsymbol{G}\boldsymbol{E}_p\boldsymbol{\lambda} = \mathbf{0}, \tag{5}$$

$$\boldsymbol{S}_0^- \leq \boldsymbol{S}_0 \leq \boldsymbol{S}_0^+, \tag{6}$$

$$u_{min} \leq u_{e,inf} + u_{r,inf}, \quad u_{e,sup} + u_{r,sup} \leq u_{max}. \tag{7}$$

Where $f_0(\boldsymbol{S}_0)$ is criterion of optimization; $\boldsymbol{S}_0^-$ and $\boldsymbol{S}_0^+$ are constraints of limit forces $\boldsymbol{S}_0$ of the sections; $\boldsymbol{\Gamma}$ is configuration matrix of elements limit forces; $\boldsymbol{\varphi}$ is yield or strength function of the sections; $\boldsymbol{G}$ is a influence matrix of residual forces; $\lambda, \lambda_j, j \in J,$ are the vectors of plastic multipliers; $\boldsymbol{u}$ is the vector of displacements; indexes e, r mean elastic and residual ones; *inf*, *sup* – lower and upper bound of displacement variation accordingly; $\boldsymbol{u}_{\min}$, $\boldsymbol{u}_{\max}$ - lower and upper constraints of the vectors of displacements.

A diagonal matrix $\boldsymbol{E}_p$ assigns a value to the residual internal force in every thin-wall element: 1 – if class of element is equal 1 or 2; 0 – if class of element is equal 3 or 4 (i.e. it defines a disposition of the partial plastic redistribution of forces).

A diagonal matrix $\boldsymbol{E}_p$,

$$\mathbf{E}_p = diag\mathbf{E}_{pk}, \quad k \in K, \tag{8}$$

assigns a value to the residual internal force in every k-th thin-wall element cross-section, $k \in K$: 1 – if class of element is equal 1 or 2; 0 – if class of element is equal 3 or 4 (i.e. it defines a disposition of the partial plastic redistribution of forces); K is a number of element cross-sections.

Namely, if a vector $\boldsymbol{S}$ of structure internal forces consists of the subvectors $\boldsymbol{S}_k = (M_k, N_k)$ with the bending moment M_k and normal force N_k in k-th element cross-section, submatrix $\boldsymbol{E}_{pk}$ reads as follows:

$$\boldsymbol{E}_{pk} = \left\{ \begin{array}{l} diag\begin{bmatrix}1\\1\end{bmatrix} \text{for Class (1 or 2)} \\ \text{or} \\ diag\begin{bmatrix}0\\1\end{bmatrix} \text{for Class (3 or 4)} \end{array} \right\}, \quad k \in K. \tag{9}$$

If the problem (1)–(8) will have some active inequalities (2) for one and the same element cross-section at proper loads, such regime of plastic yielding will be named sign-changing. In such case we may calculate this element cross-section as elastic.

Inequalities (2) generally depends on the domain $\Omega(\boldsymbol{F})$ of loading (Aliawdin 2005), checking of this effect may be an actual problem of Code's future variants.

In the formulation of problem (1)–(8) may be included not only the uncertain load, but any other actions, e.g. thermal or kinematic distorsions.

2.2 *Simplified linearized mathematical model*

For the shakedown problem with stiffness and linearized strength constraints a mathematical model will be as follows:

$$min\ f_0(\boldsymbol{S}_0), \tag{10}$$

$$\varphi_j = \Gamma \mathbf{S}_0 - \Phi(\mathbf{S}_{ej} + \mathbf{G}\mathbf{E}_p \lambda) \geq \mathbf{0}, \tag{11}$$

$$\boldsymbol{\lambda} = \sum_j \boldsymbol{\lambda}_j, \quad j \in J, \tag{12}$$

$$\boldsymbol{\lambda}_j^T \boldsymbol{\varphi}_j = 0, \quad \boldsymbol{\lambda}_j \geq 0, \tag{13}$$

$$\boldsymbol{A}\boldsymbol{G}\boldsymbol{E}_p \boldsymbol{\lambda} = \mathbf{0}, \tag{14}$$

$$\boldsymbol{S}_0^- \leq \boldsymbol{S}_0 \leq \boldsymbol{S}_0^+, \tag{15}$$

$$u_{min} \leq u_{e,inf} + u_{r,inf}, \quad u_{e,sup} + u_{r,sup} \leq u_{max}. \tag{16}$$

Here $\boldsymbol{\Phi} = diag\boldsymbol{\Phi}_i$ is a quasi-diagonal matrix of the linear yielding conditions (10), $\boldsymbol{\Phi}_i$ is the matrix of coefficients of the *i*-th section linear yielding conditions.

In this case of linear yield conditions (11), the residual displacements $\mathrm{u}_r = \mathrm{H}\lambda$ and residual internal forces $\mathrm{S}_r = \mathrm{G}\lambda$ can be expressed by influence matrices of residual displacements (17) and forces (18):

$$\mathrm{H} = \left(\left(\mathrm{A}\mathrm{D}^{-1}\mathrm{A}^T \right)^{-1} \mathrm{A}\mathrm{D}^{-1} \right) \boldsymbol{\Phi}, \tag{17}$$

$$\mathrm{G} = \mathrm{D}^{-1}\mathrm{A}^T\mathrm{H} - \mathrm{D}^{-1}\boldsymbol{\Phi}. \tag{18}$$

3 MEMBER STATBILITY CHECK

3.1 *Design formulae for Methods 1 and 2 for members with class 1, 2 and 3, 4 cross-sections*

Two different formats of the interaction formulae are provided in EC3, called Method 1 and Method 2. The main difference between them is the kind of presentation of the different structural effects, either by specific coefficients in Method 1 or by one compact interaction facto in Method 2. This makes Method 1 more adaptable to identifying and accounting for the structural effects, while Method 2 is mainly focused on the direct design of standard cases (Boissonnade et al. 2006).

Both methods deal with the most complex behavior of a single span member subjected to combined bending and axial compression, including all possible interactions and non-linear effects. In Method 1 all the influences of material and geometrical nonlinearities and of interactions between loading components are reflected by separate factors. In contrast, Method 2 uses a reduced number of such factors as a result of globalization of several effects and calibration of the latter on the basis of extensive numerical simulations (Boissonnade et al. 2006).

3.2 *Elastic-plastic flexural buckling without lateral torsional buckling*

It is known, that steel members show linear behavior in the elastic range and non-linear behavior in the plastic range (Boissonnade et al. 2006, BS EN 1993-1-1).

The higher the slenderness, the lower the capacity and the less pronounced is the plastic behavior. This ideal material behavior is significantly affected by the presence of residual stresses in rolled and welded sections, which results in non-linearities even at low load-levels. In this respect a large range of members behave inelastically in principle (Boissonnade et al. 2006).

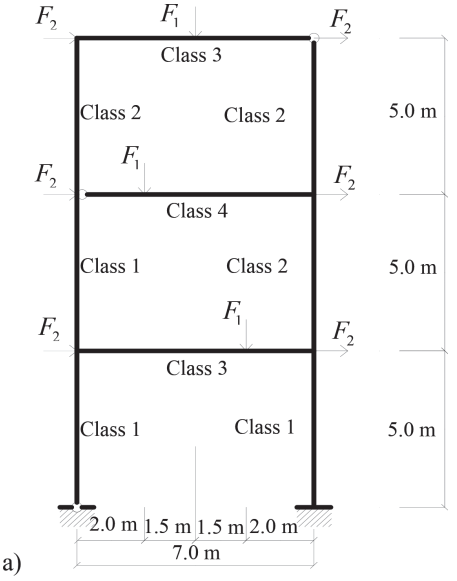

a)

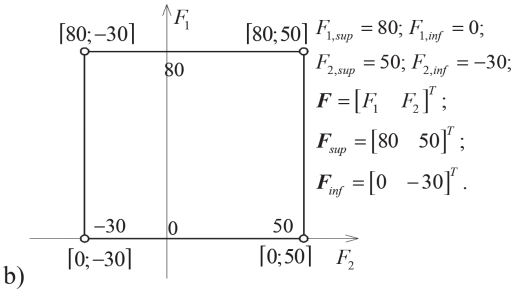

b)

Figure 1. Loading scheme (a), load variation locus (b).

Table 1. Load combinations.

The wind load is from the left.	The wind load is from the right.
Combination 1: $F_{1,sup} + F_{2,sup}$	Combination 2: $F_{1,sup} + F_{2,inf}$
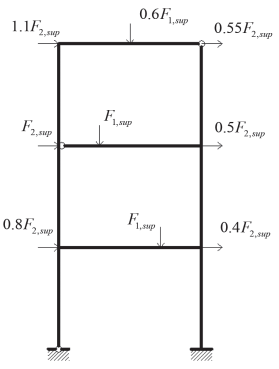	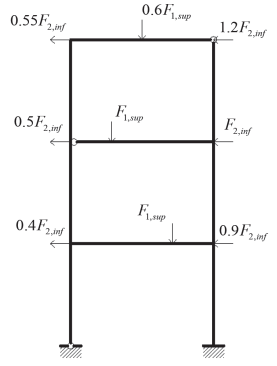
Combination 3: $F_{1,inf} + F_{2,sup}$	Combination 4: $F_{1,inf} + F_{2,inf}$
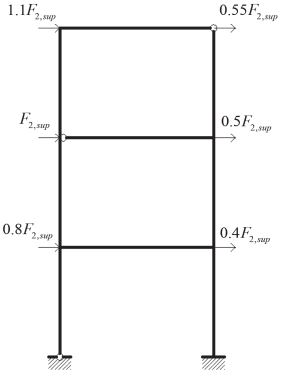	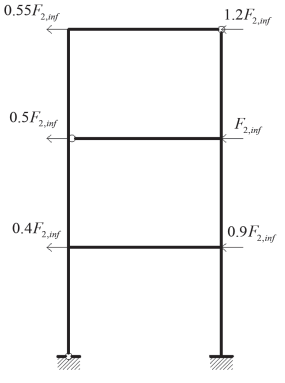

EC3 classifies sections to Class 1 and 2, which are defined as capable of developing a full plastic capacity, and sections of Class 3 and 4, which are defined as elastic. Such classification is often confusing, especially if these definitions are applied to element behavior.

Recent numerical simulations show that Class 3 sections also develop plastic capacity, so that element-behavior presumably is not or is only partially dependent on the class-definition.

For the Class 3 and 4 sections, plastic capacity is not, or is only partly considered. That is why EC3 differentiates between the interaction formulae for "elastic-plastic" Class 1 and 2 sections and "elastic" Class 3 and 4 sections. Because of that, interaction formulae for the Class 3 and 4 section follow the analytically derived equations for flexural buckling.

Members not susceptible to torsional deformation fail in flexural buckling, by in-plane or special deflection. These are closed sections or open sections appropriately restrained against torsional deformations, as frequently fount in building structures (Boissonnade et al. 2006).

3.3 *Axial compression and strong axis bending* $\left(N + M_y\right)$

3.3.1 *Members with class 1 and 2 cross-sections*

Design formulae for the in-plane buckling mode $\left(y-y\right)$ for members with Class 1 and 2 cross-sections is as follows:

$$\frac{N_{Ed}}{\chi_y N_{pl,Rd}} + k_y \frac{C_{my} M_{y,Ed}}{M_{pl,y,Rd}} \le 1.0 \tag{19}$$

where

$$k_y = 1 + \left(\overline{\lambda}_y - 0.2\right) n_y \le 1 + 0.8 n_y \tag{20}$$

is an interaction factor (Eurocode 3), determined on basis of geometrically and materially non-linear

Imperfect Analyses (GMNIA) results provided by Ofner (1997);

$$n_y = \frac{N}{\chi_y N_{pl}} \tag{21}$$

is an axial compression parameter;

$$C_{my} = 0.6 + 0.4\psi \geq 0.4 \tag{22}$$

is an uniform moment factor (Boissonnade et al. 2006), which may differ according to the form of element's moments distribution diagram.

Table 2. Material properties.

Elastic modulus	$E = 210\ GPa$
Characteristic yield strength	$f_y = 235\ MPa$
Partial safety factors	$\gamma_{M0} = 1.0$ $\gamma_{M1} = 1.0$

3.3.2 *Members with Class 3 and 4 cross-sections*
Design formulae for the in-plane buckling mode $(y-y)$ for members with Class 3 cross-sections is as follows:

$$\frac{N_{Ed}}{\chi_y N_{pl,Rd}} + k_y \frac{C_{my} M_{y,Ed}}{M_{el,y,Rd}} \leq 1.0 \tag{23}$$

where

$$k_y = 1 + 0.6\overline{\lambda}_y n_y \leq 1 + 0.6 n_y \tag{24}$$

$$M_{el,y,Rd} = W_y f_y / \gamma_{M1} \tag{25}$$

For Class 4 cross-sections the section properties $N_{pl,Rd}$ and $M_{el,y,Rd}$, need to be replaced by the resistances calculated from the properties of the effective section area of cross-section A_{eff} and W_{eff}, as follows:

$$N_{eff,Rd} = A_{eff} f_y / \gamma_{M1} \tag{26}$$

$$M_{el,y,Rd} = W_{y,eff} f_y / \gamma_{M1} \tag{27}$$

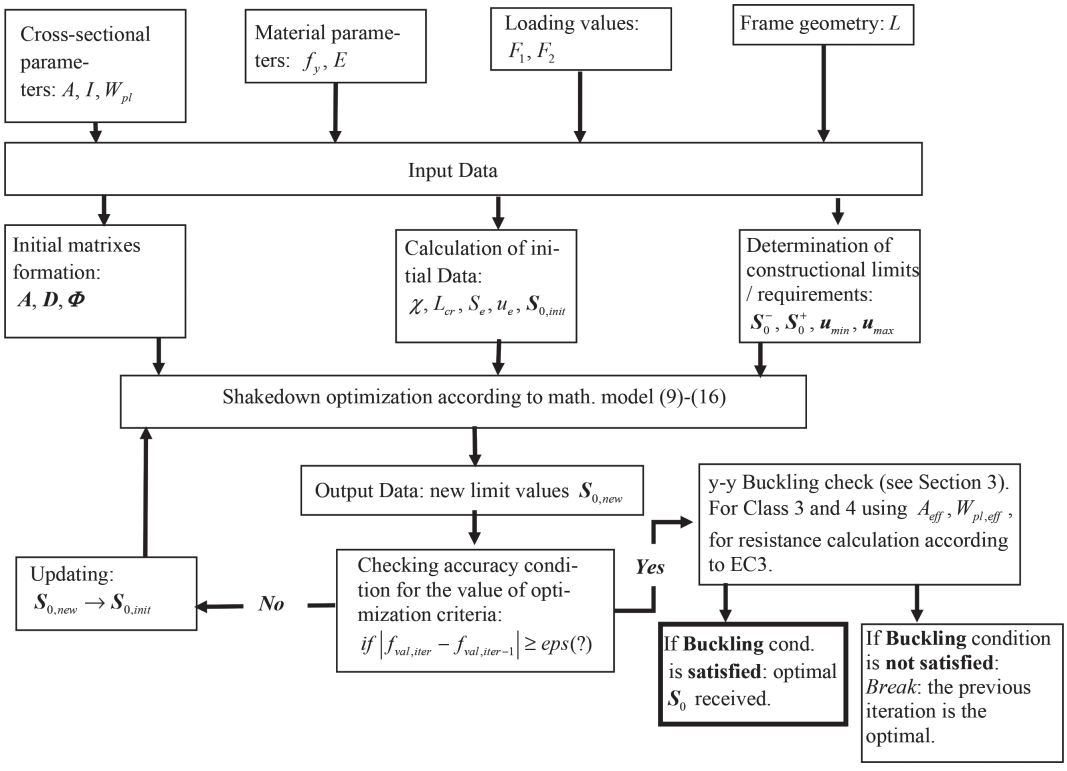

Figure 2. Shakedown optimization principal scheme.

Table 3. Initial and optimal cross-sectional values.

	Class 1	Class 2	Class 3 TWM	Class 4 TWM
Initial cross-sectional properties	HE 300 B $A_1^0 = 149.1\ cm^2$ $I_1^0 = 25170.0\ cm^4$ $W_{pl,1}^0 = 1869.0\ cm^3$ $M_{01}^0 = 261.9\ kNm$	IPE O 400 $A_2^0 = 96.4\ cm^2$ $I_2^0 = 26750.0\ cm^4$ $W_{pl,2}^0 = 1502.0\ cm^3$ $M_{02}^0 = 260.9\ kNm$	IPE 400 $A_3^0 = 84.5\ cm^2$ $I_3^0 = 23130.0\ cm^4$ $W_{pl,3}^0 = 1307.0\ cm^3$ $M_{03}^0 = 521.4\ kNm$	IPE A 360 $A_4^0 = 54.0\ cm^2$ $I_4^0 = 14520.0\ cm^4$ $W_{pl,4}^0 = 907.0\ cm^3$ $M_{04}^0 = 221.2\ kNm$
Optimal cross-sectional properties	HE 500 B $A_1^* = 238.6\ cm^2$ $I_1^* = 107200.0\ cm^4$ $W_{pl,1}^* = 4815.0\ cm^3$ $M_{01}^* = 807.2\ kNm$	IPE O 450 $A_2^* = 118.0\ cm^2$ $I_2^* = 40920.0\ cm^4$ $W_{pl,2}^* = 2046.0\ cm^3$ $M_{02}^* = 283.4\ kNm$	IPE 500 $A_3^* = 116.0\ cm^2$ $I_3^* = 48200.0\ cm^4$ $W_{pl,3}^* = 2194.0\ cm^3$ $M_{03}^* = 615.5\ kNm$	IPE A 550 $A_4^* = 117.0\ cm^2$ $I_4^* = 59980.0\ cm^4$ $W_{pl,4}^* = 2475.0\ cm^3$ $M_{04}^* = 565.7\ kNm$

4 EXAMPLE OF SHAKEDOWN ANALYSIS

4.1 *Design scheme of structure*

A considered three-storey TWM plane frame (Fig. 1a) is subjected to two independent loads: vertical live load F_1 (varying $0\ kN \le F_1 \le 80.0\ kN$) and horizontal wind load F_2 (varying $-30.0\ kN \le F_2 \le 50.0\ kN$), see Figure 1b. Load combinations with an applied load impact coefficients are shown in a Table 1. No load combination coefficients were applied.

Members of the frame structure are designed from standard rolled IPE or HE cross-sections. It is assumed, that members are restrained to prevent both lateral and lateral torsional displacements.

It is being assumed, that structure is designed from members of cross-sectional Classes 1, 2, 3 and 4. For the sake of ease, each frame member has a prescribed Class (Fig. 1a), which remains constant during optimization-design procedure.

Frame members are discretized as beam-column elements subjected to strong axis bending and axial force. Detailed discretization procedure is described in work of Liepa & Karkauskas (2012).

The task is to find an optimal solution of the problem (9)-(16) for determining optimal distribution of limit moments of frame at shakedown.

Lower bound of limit internal force $\boldsymbol{S}_0^-$ is considered as element's limit critical bending moment $M_{0,cr}^{min}$, Karkauskas (2007):

$$M_{0,cr}^{min} = f_y a_3 \left(\frac{L_{cr}^2}{a_1 \lambda_{lim}^2} \right)^{\frac{b_3}{b_1 - 1}}, \qquad (28)$$

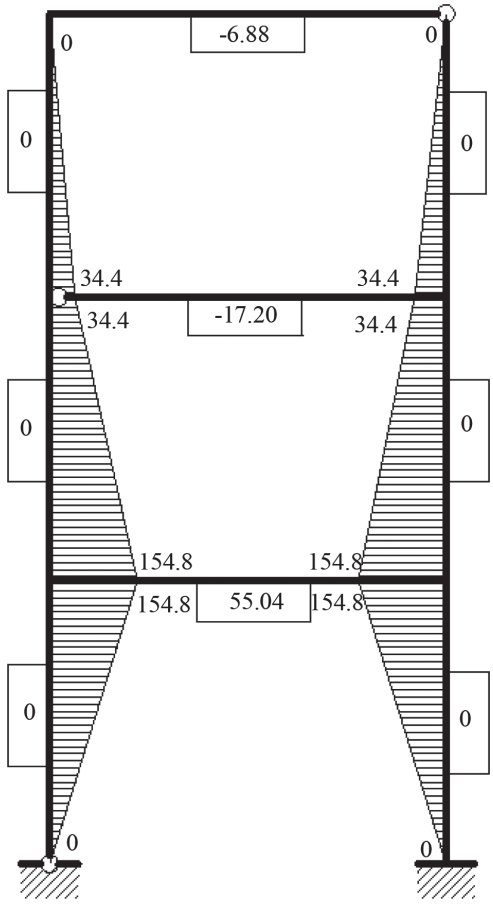

Figure 3. Residual internal forces $\boldsymbol{S}_r$ distribution: moments *kNm*, and axial forces (in squares) *kN*.

here f_y is characteristic yield strength of steel; L_{cr} is the buckling length of the compression member and it is determined according to the algorithm described in work of Liepa (2012); λ_{lim} is limit slenderness of the member, in this paper for all members of the frame it is considered constant $\lambda \le \lambda_{lim} = 120$ (STR 2.05.08:2005); a_1, a_3, b_1, b_3 are relation coefficients of cross-section geometrical characteristics (Atkočiūnas & Karkauskas 2010).

Material properties of steel are described in Table 2.

Detailed design procedure is shown in a Figure 2.

4.2 *Numerical results*

Optimal solution received after seven iterations (Table 3). Optimal limit internal forces distribution obtained when criteria of optimization reached value $f_{val}^{*} = 2.8936e^{4}$.

Optimal residual internal forces $\boldsymbol{S}_r = \left[M_r \; N_r \right]^T$ distribution is shown in a Figure 3.

5 CONCLUSIONS

In this paper a new mathematical model of shakedown and optimization of thin-walled metal plane frames, which elements are from 1st to 4th class cross-sections, under variable repeated uncertain loads, is proposed for general nonlinear and simplified linearized case. Any possible mechanisms of system collapse at shakedown such as plastic yielding and sign-changing ones are analyzed, the partial plastic redistribution of forces in such structures are found. The conditions of elements strength are derived according to the Eurocode 3. The methodology, algorithms and implementation of TWM frames weight optimization is presented and illustrated by numerical example. Results showed, that updated strength conditions could be used in an optimization mathematical model of frames.

Overall structure experienced shakedown, although Class 3 and 4 elements where designed according to thin-wall metal cross-sections design requirements by EC3, preventing any residual actions occurrences by updated mathematical model condition (13).

The optimal solution for the plane frame under variable repeated loading was obtained by solving mixed-integer optimization problem, which requires a choosing of cross-sections from manufacturers' catalogue.

Further investigation needs to be carried out taking into account the effect of shear forces in the frame elements, torsion and bidirectional bending moments for the three dimensional frames at shakedown conditions.

A dependence of elements strength conditions on the domain of loading may be an actual problem for Code's future variants.

In the formulation of problem proposed here might be naturally included not only uncertain loads, but any other actions and environmental influences, material properties and geometrical data.

REFERENCES

Aliawdin, P. 2005. *Limit Analysis of Structures Under Variable Loads*. Minsk: Technoprint. (in Russian).

Aliawdin, P. & Kasabutski, S. 2009. Limit and shakedown analysis of RC rod cross sections. *J. Civ. Eng. Manag.* 15(1), 59–66. doi:10.3846/1392–3730.2009.15.59–66.

Aliawdin, P. & Muzychkin, Y. 2011. Limit analysis of structures with destructible elements under impact loadings. *Engineering Transactions* 59(3), 139–159.

Alawdin, P. & Bulanov, G. 2014. Shakedown of composite frames taking into account plastic and brittle fracture of elements. *Civ. Environ. Eng. Rep.* 15(4), 5–21. doi:10.1515/ceer-2014–0031.

Alawdin, P. & Liepa, L. 2015. Optimal shakedown analysis of plane reinforced concrete frames according to Eurocodes. *Int. J. Mech. Mater. Des.* 1–14. doi:10.1007/s10999–015–9331–0.

Atkočiūnas, J. & Norkus, A. 1994. Method of fictitious system for evaluation of frame shakedown displacements. *Comp. Struct.* 50(4). 563–567. doi:10.1016/0045–7949(94)90027–2.

Atkočiūnas, J. 1999. Mathematical models of optimization problems at shakedown. *Mechanics Research Communications* 26(3). doi:10.1016/S0093–6413(99)00030–0.

Atkočiūnas, J. & Karkauskas, R. 2010. *Optmization of Elastic Plastic Beam Structures.* Vilnius: Technika. (in Lithuanian) doi:10.3846/1137-S.

Atkočiūnas, J. 2011. *Optimal shakedown design of elastic-plastic structures.* Vilnius: Technika. doi:10.3846/1240-S

Atkočiūnas, J. & Venskus, A. 2011. Optimal shakedown design of frames under stability conditions according to standards. *Comput. Struct.* 89(3–4), 435–443. doi:10.1016/j.compstruc.2010.11.014.

Boissonnade, N., Greiner, R., Jaspart, J.P. & Linder J. 2006. *Rules for member stability in EN 1993-1–1. Background documentation and design guidelines.* Portugal: ECCS Technical Committee 8 - Stability.

Castrenze, P. & Borino, G. 2014. Shakedown Under Thermomechanical Loads. In: Hetnarski, R.B. (Ed.) *Encyclopedia of Thermal Stresses.* Netherlands: Springer. doi:10.1007/978–94–007–2739–7_675.

Čyras, A. 1983. *Mathematical Models for the Analysis and Optimization of Elastoplastic Structures.* Chichester: Ellis Horwood Limited.

Čyras, A. & Atkočiūnas, J. 1984. Mathematical model for the analysis of elastic-plastic structures under repeated—variable loading. *Mechanics Research Communications* 11(5), 353–360. doi:10.1016/0093–6413(84)90082-X.

Elishakoff, I., Wang, X., Li, Y., Hu, J. & Qiu, Z. 2013. Regulating the dynamic behavior of a column with uncertain initial imperfections by support-placing. *Int. J. Solids Struct.* 50(2), 396–402. doi:10.1016/j.ijsolstr.2012.10.003.

BS EN 1993–1-1. 2005. *Eurocode 3, Design of steel structures. Part 1-1: General rules and rules for buildings*. CEN, Brussels.

BS EN 1993–1-5. 2006. *Eurocode 3, Design of steel structures. Part 1–5: Plated structural elements.* CEN, Brussels.

Zouain, N. 2004. Shakedown and Safety Assessment. In: Stein, E., de Borst, R., Hughes, T.J.R. (eds.) *Encyclopedia of Computational Mechanics. Volume 2. Solids and Structures.* John Wiley & Sons, Inc. doi: 10.1002/0470091355.

Karkauskas, R. 2007. Optimization of geometrically non-linear elastic-plastic structures in the state prior to plastic collapse. *J. Civ. Eng. Manag.* 8(3), 183–192. doi:10.1080/13923730.2007.9636436.

König, J.A. 1987. *Shakedown of Elastic-plastic Structures.* Amsterdam: Elsevier.

Leonetti, L., Casciaro, R. & Garcea, G. 2015. Effective treatment of complex statical and dynamical load combinations within shakedown analysis of 3D frames. *Comput. & Struct.* 158, 124–139. doi:10.1016/j.compstruc.2015.06.002.

Liepa, L. 2012. *Geometrically Nonlinear Analysis of Elastic-Plastic Frame.* Master Thesis, Faculty of Civil Engineering, Vilnius Gediminas Technical University, Lithuania. (in Lithuanian).

Liepa, L. & Karkauskas, R. 2012. Calculation of Elastic-Plastic Geometrically Nonlinear Frames. *Science – Future of Lithuania* 4(4), 326–324. (in Lithuanian) doi:10.3846/mla.2012.51.

Liepa, L., Gervyte, A., Jarmolajeva, E. & Atkočiūnas, J. 2014. Residual displacements progressive analysis of the multisupported beam. *Science - Future of Lithuania* 6(5), 461–467. (in Lithuanian) doi:10.3846/mla.2014.686.

Mistakidis E.S. & Stavroulakis, G.E. 1998. Nonconvex Optimization in Mechanics: Algorithms, Heuristics and Engineering Applications by the F.E.M. In: Pardalos, P.M. (Ed.) *Nonconvex Optimization and Its Applications*, Vol. 21, US: Springer. doi: 10.1007/978–1-4615–5829–3.

Narayanan, R. & Roberts, T.M. 1991. *Structures Subjected to Repeated Loading: Stability and Strength.* London and New York: Elsevier.

Nguyen, Q.S. 2006. Min-max duality and shakedown theorems in plasticity. In: Alart, P., Maisonneuve, O., Rockafellar, R.T. (Eds.*) Nonsmooth Mechanics and Analysis: Theoretical and Numerical Advances.* US: Springer. doi:10.1007/0–387–29195–4_8.

Ofner R. 1997. *Traglasten Von Staben aus Stahl bei Druck und Biegung.* PhD Thesis, Institut fur Stahlbau, Holzbau und Flaschentragwerke, TU Graz. (in German).

STR 2.05.08:2005. 2005. *Design of steel structures. General rules*, Vilnius.

Venskus, A., Kalanta, S., Atkočiūnas, J. & Ulitinas, T. 2010. Integrated load optimization of elastic-plastic axisymmetric plates at shakedown. *J. Civ. Eng. Manag.* 16(2), 203–208. doi:10.3846/jcem.2010.22.

Weichert, D. & Maier, G. 2002. *Inelastic Behavior of Structures under Variable Repeated Loads.* Wien: Springer-Verlag. doi:10.1007/978–3-7091–2558–8.

Weichert, D. & Ponter, A. 2009. *Limit States of Materials and Structures.* Netherlands: Springer. doi:10.1007/978–1-4020–9634–1.

Recent Progress in Steel and Composite Structures – Giżejowski et al. (Eds)
© 2016 Taylor & Francis Group, London, ISBN 978-1-138-02946-0

Buckling capacity curves for pressurized spherical shells

P. Błażejewski & J. Marcinowski
University of Zielona Góra, Zielona Góra, Poland

ABSTRACT: Existing provisions leading to the assessment of the buckling resistance of pressurised spherical shells were published in the European Design Recommendations (2008). This book comprises rules which refer to the stability of steel shells of different shapes. In the first step of the general procedure they require calculation of two reference quantities: the elastic critical buckling reference p_{Rcr} and the plastic reference resistance p_{Rpl}. These quantities should be determined in the Linear Buckling Analysis (LBA) and in the Materially Nonlinear Analysis (MNA) respectively. Only in the case of spherical shells the existing procedure has exceptional character. It is based on the Geometrically Nonlinear Analysis (GNA) and on the Geometrically and Materially Nonlinear Analysis (GMNA), respectively. From this reason, in this particular case there was a need to change the existing approach. In this paper a new approach is proposed, consistent with other provisions included in European Design Recommendations (EDR) (2008). The closed formulae for p_{Rcr} and p_{Rpl} for spherical shells clamped along their edges are presented. Then three independent parameters of the capacity curve λ_0, α, β were derived for the wide class of spherical shells. As a final result the buckling capacity curves were obtained. These curves were compared with those resulting from existing provisions.

1 INTRODUCTION

Steel, spherical shells subjected to the action of external pressure p are usually very slender and internal forces which are generated within their domain are compressive. For this reason they are exposed to local or global buckling, probably the most important reasons for failures of such shells. An accurate assessment of the buckling resistance, as the maximum pressure p which can be safely sustained, is very important from the engineering point of view. The buckling limit state (LS3 according to EN 1993-1-6) is usually the decisive criterion among all design criteria.

Existing designing provisions define precisely procedures leading to the buckling resistance assessment of steel shells (cf. EN 1993-1-6). The approach based on the MNA analysis and LBA analysis is a commonly accepted approach as far as the plastic reference resistance p_{Rpl} and elastic critical buckling reference p_{Rcr} are concerned. These are two reference quantities on the basis of which buckling capacity curves for particular cases of shells are created. EDR 5th includes provisions which refer to several cases of shells exposed to buckling. In the existing chapter dedicated to spherical shells the different approach was adopted. Reference quantities of the whole procedure p_{Rcr} and p_{Rpl} are determined on the basis of the GNA (geometrically nonlinear analysis) and the GMNA (geometrically and materially nonlinear analysis) respectively and it is a single exception in these recommendations.

In this paper an alternative approach was presented, the approach consistent with the general approach recommended in EN 1993-1-6 and in EDR 5th. All steps of the proposed approach were presented and the final result in a form of buckling capacity curves was obtained. All parameters defining capacity curves were obtained as a result of many numerical analyses carried out for spherical shells of different geometry and different material parameters. Spherical caps of semi-angles φ = 10°, 20°, 30°, 45°, 60°, 90° and of following R/t ratios: R/t = 300, 400, 500, 600, 750, 1000 were considered. Seven different imperfection modes were taken into account and three fabrication quality classes were considered. Only one case of boundary condition was taken into account: the fully clamped basic circle of considered caps (see Figure 1). To obtain the final

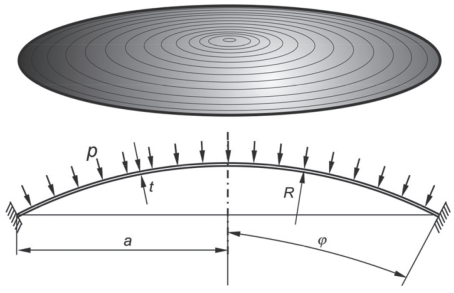

Figure 1. Pressurised, spherical shell.

proposal of buckling capacity curves nearly eight thousand particular cases of spherical cases were analysed numerically.

The presented buckling resistance assessment is simply and user friendly even for budding designers of tanks and pressure vessels.

2 ELASTIC CRITICAL BUCKLING RESISTANCE P_{RCE} AND PLASTIC REFERENCE RESISTANCE P_{RPL}

The elastic critical buckling resistance p_{Rcr} and the plastic reference resistance p_{Rpl} are principal quantities required in the buckling resistance assessment procedure. An attempt of derivation of the simple formulae on p_{Rcr} and p_{Rpl} was undertaken by Authors earlier (2013).

To find this formulae many numerical analyses (LBA – the linear buckling analysis in reference to p_{Rcr} and MNA – the materially nonlinear analysis in a case of p_{Rpl}) were carried out for a huge range of R/t ratios and for a great diversity of semiangles φ defining the rise of spherical shells. Details of this stage of the research were presented in Błażejewski and Marcinowski (2013). As a result the following formulae were obtained:

$$p_{\mathrm{Rcr(LBA)}} = 1.303\,E\left(\frac{t}{R}\right)^2, \tag{1}$$

$$p_{Rpl(MNA)} = 1.986\,f_{yk}\,\frac{t}{R}, \tag{2}$$

in which E – Young's modulus, f_{yk} – characteristic value of the yield stress, both expressed in [MPa].

Formulae (1) and (2) differ slightly from formulae presented in Błażejewski and Marcinowski (2013). They are derived on the basis of the same results of numerical analyses but in the proposed amendments the more accurate best-fit procedures were implemented.

Having both defined above reference quantities, namely p_{Rcr} and p_{Rpl}, one can calculate the dimensionless relative slenderness defined in the standard way:

$$\lambda = \sqrt{p_{Rpl(MNA)} / p_{Rcr(LBA)}} \tag{3}$$

The calculation of relative slenderness is a very easy task due to the fact that all quantities appearing under the square root symbols are described by formulae.

3 MODIFIED CAPACITY CURVES – BUCKLING PARAMETERS

To assess the buckling resistance of a pressurised spherical shell one should know all the buckling parameters λ_0, α, β and η describing the standard capacity curve (cf. EDR 5th and EN 1993-1-6). The dimensionless relative slenderness λ is defined according to eqn. (3) and the buckling strength reduction factor χ is equal to the p_{Rk}/p_{Rpl} ratio, where p_{Rk} is the characteristic value of the buckling resistance.

Values of buckling parameters can be effectively determined by means of the approach proposed by Doerich and Rotter (2011). According to this approach a modified capacity curve should be calculated. This curve is determined for an assumed mode of imperfection and for the adopted amplitude of this imperfection mode. Particular points on this curve are obtained for different values of relative slenderness. This can be achieved by means of artificially changed yield stress and this approach was adopted in this work.

Seven different modes of imperfections were considered. Detailed considerations relating to the selection and generation of these imperfection modes were presented by Błażejewski and Marcinowski (2014).

Similarly as in EDR 5th the amplitudes of imperfections were defined as follows

$$\Delta w_k = \frac{1}{Q}\sqrt{Rt} \tag{4}$$

where Q—is the fabrication quality parameter corresponding to the specified fabrication tolerance quality. For three different fabrication quality classes A, B and C (excellent, high and normal) the quality parameter Q adopts values 40, 25 and 16 respectively.

Figure 1 presents the example of modified capacity curve obtained as a results of many numerical analyses carried out for a particular geometry, for a specific imperfection mode and adopted quality class. On the abscissa of this plot the ratio $p_{R(GMNIA)}/p_{Rcr(LBA)}$ are depicted while the ordinates of this plot present the ratio $p_{R(GMNIA)}/p_{Rpl(MNA)}$. The squash limit relative slenderness is defined by the last point on the horizontal segment of the plot. At this point $p_{R(GMNIA)}$ is equal to $p_{Rpl(MNA)}$ (the ordinate equal to 1,0) and at the same time the ratio $p_{Rpl(MNA)}/p_{Rcr(LBA)}$/ is equal to λ_0^2.

Precise determination of the elastic imperfection reduction factor α is very easy if the modified capacity curve is plotted. For very slender shells $p_{R(GMNIA)}$ can be identified as a product of α and p_{Rcr}. This means that the value of α is determined by the final vertical segment of the plot (see Figure 2).

Transition from the elastic-plastic range into purely elastic range is accomplished at the point at which the vertical segment starts. At this point $\lambda = \lambda p$ and $\chi = 1 - \beta$.

Analysing all obtained results and comparing them with existing proposal for cylindrical, and spherical shells (see EDR 5th) it was assumed that the λ_0 value is constant and equal 0.2. Parameters α and β were determined from all modified capacity curves quite accurately due to the fact that they can be detected very distinctly. Figure 3 presents the "cloud" of calculated alfas for different values of the Δwk/t ratio. Calculation points depicted in Figure 3 were obtained from modified capacity curves determined for spherical shells of different R/t ratios, different semi-angles φ and for different imperfection modes (seven imperfection modes were considered). Amplitudes of imperfections were dependent on Q parameter according to relationship (4).

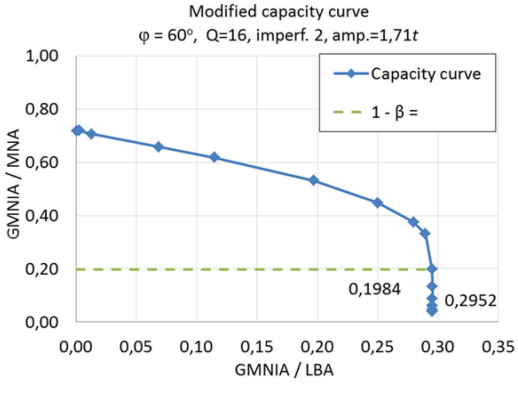

Figure 2. The modified capacity curve.

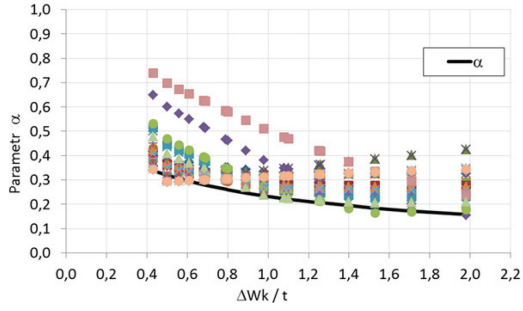

Figure 3. Calculations points defining α as a function of the $\Delta w_k/t$ ratio.

To guarantee the safety in all possible circumstances α was approximated as a lower bound of all points depicted in Figure 3. As a result the following function was obtained:

$$\alpha(\Delta w_k/t) = \frac{0.65}{1+1.8(\Delta w_k/t)^{0.8}} \tag{5}$$

The other parameter describing the final shape of the capacity curve, the β parameter, was determined on the basis of all registered results as a weighted curve approximating points shown in Figure 4. Also in this case particular points were obtained for spherical shells of different R/t ratios, different semi-angles φ and for different imperfection modes (seven imperfection modes were considered). Amplitudes of imperfections were dependent on Q parameter according to relationship (4).

The proposed formula expressing the dependence of the β parameter as a function of the $\Delta w_k/t$ ratio has the following form:

$$\beta(\Delta w_k/t) = 0.87\left(\frac{\Delta w_k}{t}\right)^{0.026} \tag{6}$$

It is worth noting that both determined parameters depend not only on geometrical characteristics R, t, and φ but also on fabrication quality class due to the fact that the $\Delta w_k/t$ ratio is expressed by Q. Figures 5 and 6 shows plots of α and β parameters as functions of w_k/t ratios for different values of the Q parameter. In the same figure proposals of EDR 5th were presented as well.

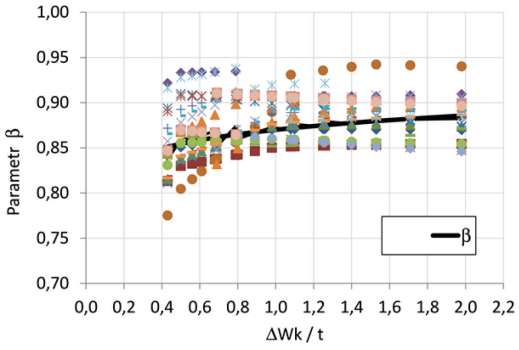

Figure 4. Calculations points defining β as a function of the $\Delta w_k/t$ ratio.

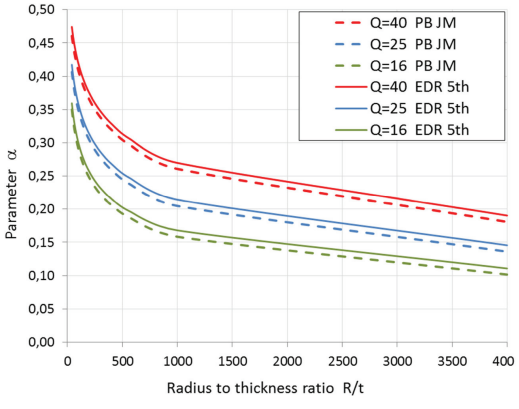

Figure 5. Functions $\alpha(R/t)$ for different values of the Q parameter.

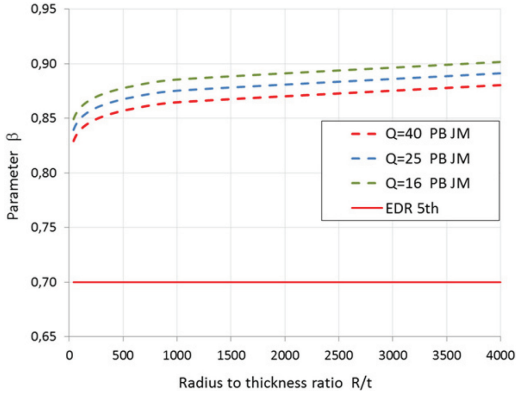

Figure 6. Functions $\beta(R/t)$ for different values of the Q parameter.

The comparison of presented proposals with those proposed in EDR 5th shows that elastic buckling reduction factor α is smaller than its counterpart from EDR 5th. It means that the buckling strength reduction factor χ will be smaller within the elastic interval. On the other hand the greater values of the plastic range factor β mean that the elastic-plastic range will be enlarged in comparison to the previous proposal of EDR 5th.

The knowledge of α and β parameters allows to determine the plastic limit relative slenderness λ_p from the formula

$$\lambda_p = \sqrt{\frac{\alpha}{1-\beta}} \tag{7}$$

4 BUCKLING CAPACITY CURVES

The standard form of the buckling capacity curve consistent with proposals of Schmidt (1991, 1994) and Rotter (2002) was presented in Figure 7a.

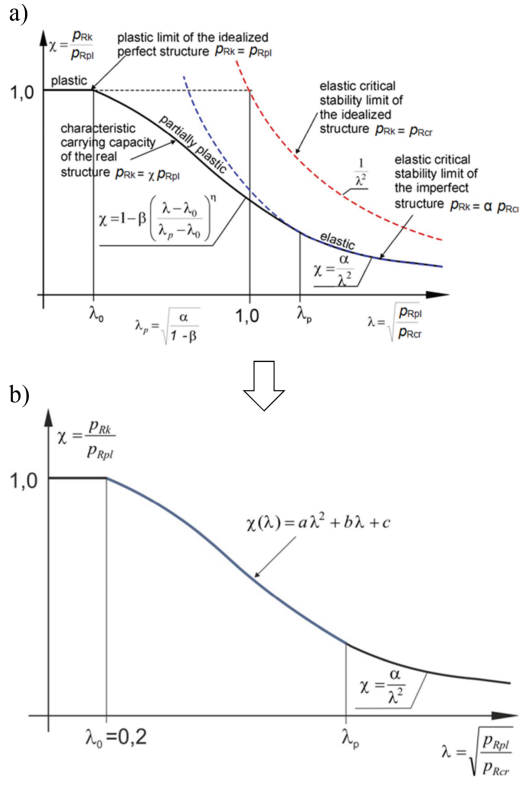

Figure 7. The standard buckling capacity curve a) and modified version of it b).

Due to some significant difficulties arising in the reference to the exact evaluation of the interaction exponent η defining the capacity curve within the elastic-plastic range, Authors have proposed a modification of this standard capacity curve within this range. In place of the function shown in Figure 7a the polynomial of the second order was proposed, and namely

$$\chi(\lambda) = a\lambda^2 + b\lambda + c, \quad \text{for} \quad \lambda_0 \le \lambda \le \lambda_p \tag{8}$$

This function was shown in Figure 7b and its coefficients were determined from continuity conditions at λ_0 and λ_p points. They adopt the following form:

$$a = \frac{\alpha(0.4 - 3\lambda_p) + \lambda_p^3}{\lambda_p^3(0.04 - 0.4\lambda_p + \lambda_p^2)}, \tag{9a}$$

$$b = \frac{-2\lambda_p^4 + \alpha(4\lambda_p^2 - 0.08)}{\lambda_p^3(0.04 - 0.4\lambda_p + \lambda_p^2)}, \tag{9b}$$

$$c = \frac{\alpha(0.12 - 0.8\lambda_p) + \lambda_p^4}{\lambda_p^2(0.04 - 0.4\lambda_p + \lambda_p^2)}. \tag{9c}$$

Using the approach presented above the capacity curves can be generated for the spherical shell of specific geometrical and material characteristics and for three fabrication quality classes. The example of such capacity curves were presented in Figure 8. In this figure the transition from the purely elastic range to the elastic-plastic range was clearly marked.

Figure 9 shows the comparison of the present proposal with existing provisions of EDR 5th. In this case capacity curves are plotted as the function

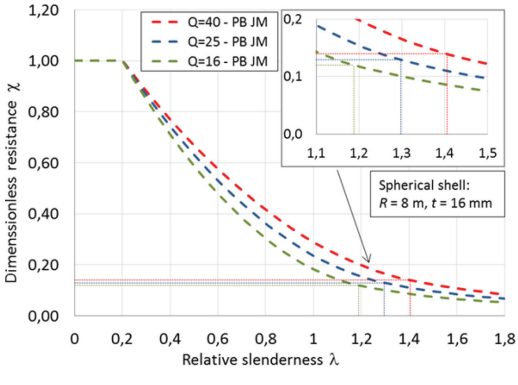

Figure 8. Buckling capacity curves for different values of Q.

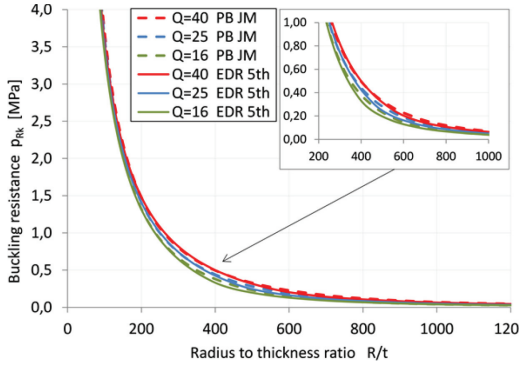

Figure 9. The comparison with existing provisions of EDR 5th.

of the characteristic value of the buckling resistance $p_{Rk}(R/t)$. It is seen that existing provisions provide slightly lower assessment of the buckling resistance, it means that they are more conservative.

5 RECAPITULATION

The buckling resistance assessment of steel spherical shells loaded by the external pressure was the subject of considerations contained in this work. The methodology presented in the paper corresponds to requirements included in EN 1993-1-6 and EDR 5th. Slight modifications refer to the shape of the capacity curve within the elastic-plastic range. The final proposal gives similar results to the existing provisions (see EDR 5th), but contrary to them is fully consistent with standard approach recommended in EN 1993-1-6 and EDR 5th. The complete flow chart of the buckling resistance assessment of pressurised spherical shells was presented in Figure 10. This flow chart can be helpful for designers of tanks, silos and pressure vessels.

The design value of the buckling resistance should be calculated from the formula

$$p_{Rd} = \frac{p_{Rk}}{\gamma_M} \tag{10}$$

in which γ_M is the partial safety factor. In case of tanks and vessels its value is recommended in EN 1993-4-2 and equals $\gamma_M = 1{,}1$.

It is worth noting that the presented buckling resistance assessment method can be applied to segments of steel spherical shells of such geometrical characteristics that $R/t \in <300, 1000>$, the semi-angle $\varphi \in <10, 90>$ degrees, and clamped along their base circles.

Step 1. Adoption of principal design data: E, f_{yk}, R, t

Step 2. Calculation of reference quantities and determination of the dimensionless, relative slenderness λ

$$p_{\mathrm{Rcr(LBA)}} = 1.303 E \left(\frac{t}{R}\right)^2$$

$$p_{\mathrm{Rpl_{(MNA)}}} = 1.986 f_{yk} \frac{t}{R} \quad \Rightarrow \quad \lambda = \sqrt{\frac{p_{\mathrm{Rpl_{(MNA)}}}}{p_{\mathrm{Rcr(LBA)}}}}$$

Step 3. Specification of the fabrication quality class and calculation of the characteristic value of imperfection amplitude.

Klasa A $\rightarrow$ Q = 40
Klasa B $\rightarrow$ Q = 25
Klasa C $\rightarrow$ Q = 16

$$\Rightarrow \quad \Delta w_k = \frac{1}{Q}\sqrt{Rt}$$

Step 4. Determination of buckling parameters α and β. Calculation of the plastic limit relative slenderness λ_p

$$\alpha(\Delta w_k / t) = \frac{0.65}{1 + 1.8(\Delta w_k / t)^{0.8}}$$

$$\beta(\Delta w_k / t) = 0.87 \left(\frac{\Delta w_k}{t}\right)^{0.026} \quad \Rightarrow \quad \lambda_p = \sqrt{\frac{\alpha}{1-\beta}}$$

Step 5. The buckling strength reduction factor χ for different intervals of λ (cf. Figure 7).

$$\chi(\lambda) = 1, \qquad \text{for} \quad \lambda < \lambda_0$$

$$\chi(\lambda) = a\lambda^2 + b\lambda + c, \quad \text{for} \quad \lambda_0 \le \lambda \le \lambda_p \quad , \text{where } \lambda_0 = 0.2$$

$$\chi(\lambda) = \alpha / \lambda^2 \ , \qquad \text{for} \quad \lambda > \lambda_p$$

Step 6. Determination of the polynomial coefficients in the case of elastic-plastic range.

$$a = \frac{\alpha(0.4 - 3\lambda_p) + \lambda_p^3}{\lambda_p^3(0.04 - 0.4\lambda_p + \lambda_p^2)}, \quad b = \frac{-2\lambda_p^4 + \alpha(4\lambda_p^2 - 0.08)}{\lambda_p^3(0.04 - 0.4\lambda_p + \lambda_p^2)}, \quad c = \frac{\alpha(0.12 - 0.8\lambda_p) + \lambda_p^4}{\lambda_p^2(0.04 - 0.4\lambda_p + \lambda_p^2)}.$$

Step 7. Characteristic value of the buckling resistance of the considered spherical shell

$$p_{Rk} = \chi \cdot p_{Rpl}$$

Figure 10. Determination of the buckling resistance - the flow chart.

REFERENCES

Błażejewski, P. & Marcinowski, J. 2012. Buckling resistance of steel spherical roofs subjected to an external pressure. *Proceedings of Stability of Structures: XIII-th symposium*. Zakopane.

Błażejewski, P. & Marcinowski, J. 2013. A new approach to the buckling resistance assessment of pressurized spherical. *SSTA: proceedings of the 10th conference*. Gdańsk, Polska, 2013. London: Taylor & Francis Group. s. 179–182

Błażejewski, P. & Marcinowski, J. 2014. The worst geometrical imperfections of steel spherical shells. *Budownictwo i Architektura.* 2014, Vol. 13, nr 3, s. 219–226.

COSMOS/M. 1999. Finite Element Analysis System, Version 2.5, Structural Research and Analysis Corporation, Los Angeles, California.

Doerich, C. & Rotter, J.M. 2011. Generalised capacity curves for stability and plasticity: Application and limitations. *Thin-Walled Structures 49(9): 1132–1140*.

EN 1993-1-1. Eurocode 3: Design of steel structures. Part 1–1: General rules and rules for buildings.

EN 1993-1-6. Eurocode 3: Design of steel structures. Part 1–6: Strength and stability of shell structures.

EN 1993-4-2. Eurocode 3: Design of steel structures. Part 4–2: Tanks.

Rotter, J.M. 1999. Proposal for generalization of the elastic-plastic buckling interaction rule from Eurocode 3 Part 1.6. ECCS.

Rotter, J.M. 2002 "Shell Buckling and Collapse Analysis for Structural Design: The New Framework of the European Standard", in *New Approaches to Structural Mechanics, Shells and Biological Structures*, eds H.R. Drew and S. Pellegrino, Kluwer Academic Publishers, London, pp. 355–378.

Rotter, J.M. & Schmidt, H. 2008. Buckling of Steel Shells. European Design Recommendations 5th Edition. ECCS.

Schmidt, H. 1991. "The German code DIN 18800 Part 4: Stability of shell-type steel structures, design philosophy and practical applications", *International Colloquium on Buckling of Shell Structures on Land, in the Sea and in the Air, Villeurbanne,* Lyon, France, 17–19 Sept., pp. 265–269.

Schmidt, H. 1994 ."Stability of shells", CEN TC250 SC3 PT 3 (Masts, Chimneys, Pipelines) Report, August, 12 pp.

Recent Progress in Steel and Composite Structures – Giżejowski et al. (Eds)
© 2016 Taylor & Francis Group, London, ISBN 978-1-138-02946-0

An integrated approach for fatigue prevention in Movable Scaffolding System

H. Coelho, A. Torres, C. Moreira, R. Silva, J.M. Soares & D. Pinto
BERD, Portugal

P. Pacheco
Faculty of Engineering of University of Porto, BERD, Porto, Portugal

ABSTRACT: The Movable Scaffolding System (MSS) is a heavy construction equipment used for casting situ of concrete bridge decks. MSSs are often seen as temporary structures, which could apparently justify the adoption of less restrictive design rules. However, in the past decades, MSSs have become increasingly complex and industrialized, enlarging its span ranges, incorporating auxiliary elevation machinery and increasing productivity. The tendency nowadays is for strong reutilization and the notion of MSS as a disposable or temporary structure is somehow reductive. Although fatigue assessment is usually neglected in MSS Design, the main structure of MSSs may be potentially exposed to fatigue, usually characterized by low number of cycles with significant stress amplitude. Fatigue may be prevented through adequate design; judicious selection of materials; demanding quality control and implementation of robust inspection and maintenance plans. The Damage Tolerant Method for fatigue assessment seems to fit particularly well to this type of structure.

1 INTRODUCTION

The Movable Scaffolding System (MSS) is a bridge construction equipment that combines steel structure with heavy hydraulic equipment and it is used for erection of concrete bridge decks.

The MSS supports the bridge deck during the concrete casting process. The concrete casting often occurs in two stages (the bottom slab and the webs casted in the first stage and the top slab casted in a second stage).

The practical case presented herein – M1-90-S — is a structure designed to operate near Ankara, in Turkey. The MSS is not yet in service – the construction beginning is scheduled for 2016.

The main supporting structure is a steel truss girder (Main Girder characterized by having a superior arch (bow-string type), as presented in Figures 1 and 2. Please note that Figure 1 is a picture of a different overhead MSS from the practical case here presented.

The Main Girder supports the Transversal Structures that embrace the deck to support the formwork, as presented in Figure 3. During concreting stage, the Main Girder rests on top of two frames: the Pier Frame and the Rear Concreting Frame.

The formwork is suspended from the superior part of the Transversal Structures by threaded suspension bars, crossing the bridge deck section.

After prestress is applied to the deck, the whole machine is lowered and thus unloaded from deck weight.

The MSS is then self-propelled to the next span.

Before launching, the suspension bars are disassembled and the formwork is separated in halves that slide apart to pass the piers.

The supporting frames are moved before and during MSS launching operation.

MSSs are often faced as temporary structures. Nevertheless, there are several known examples of MSS equipments that have been in service for more

Figure 1. Overhead MSS – M70-S Operating in Jablonov, Slovak Republic.

Figure 2. Overhead MSS – M1-90-S Elevation scheme with identification of Main Girder Diagonal DV.1.

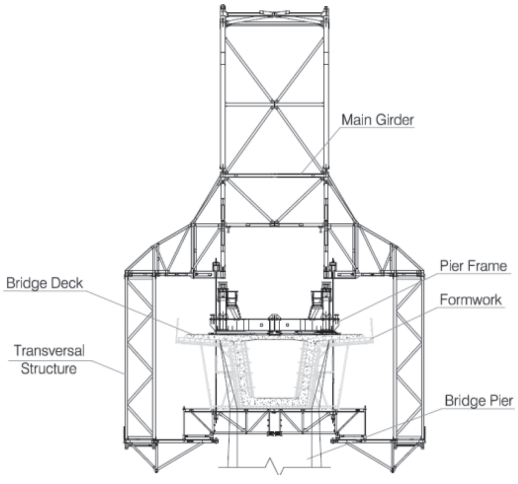

Figure 3. Overhead MSS – Transversal scheme with identification of Main Components.

Figure 4. Underslung MSS equipped with auxiliary tower cranes.

than two decades and that endured successive applications in different environmental conditions, submitted to several assembly and disassembly processes that are often aggressive to structural components. In some cases, the MSS has already operated in different continents, meaning that they went through open sea transportation in severe corrosion environments.

Apart from that, the ongoing tendency for productivity demand in bridge construction results in increasingly complex and industrialized MSS equipments, in many cases incorporating heavy auxiliary machines such as tower cranes or overhead cranes (Fig. 4) (Pacheco 2015).

Given this, the temporary nature of the MSS structures *per se* should not be a reason for decreasing the design safety factors and the steel fabrication requirements.

2 MSS FATIGUE EVALUATION

2.1 *Potential causes of fatigue*

Although fatigue assessment is usually neglected in MSS Design, the main structure of a MSS may be potentially exposed to the following fatigue causes:

– Loading and unloading of the structure followed by launching, causing a significant stress amplitude;
– Action of auxiliary crane machinery such as hoists or overhead cranes (usually, affect auxiliary structures, such as rails);
– Wind effects;
– Contact fatigue in locomotion's rails surface caused by local stresses transmitted by wheels or rollers. This is a particular phenomenon and will not be discussed herein.

2.2 *An integrated approach for fatigue evaluation in MSS structures*

Since there is no specific standard for MSS Design, Annex A of EN 1993-1-9 should be used for fatigue safety evaluation.

1. According to EN 1993-1-9, fatigue assessment should be undertaken using either Damage Tolerant Method or Safe Line Method (Sedlacek 2008).
2. The authors recommend the use of damage tolerant approach for MSS Design, since periodic inspection and maintenance may be easily and efficiently implemented:

– The MSS is delivered with a specific maintenance manual (CNC, 2007);
– Inspections are easy to perform during operation since the MSS is equipped with platforms and stairways and main structural components remain visible and accessible;
– The structure is periodically assembled and disassembled, allowing a strong maintenance and repair actions;

Bolts are usually entirely replaced from application to application;
– Damaged components are frequently replaced;

Table 1. Principles for application of Damage Tolerant Method.

Variable	Description
Cumulative Damage (between inspections)	Dd ≤ 0.25 in order to avoid significant crack initiation between inspections
Safe service period (between main inspections)	5 years or corresponding to 100 working cycles (whichever happens first)
γ_{Mf}	1.15
γ_{Ff}	1.00

– The fatigue loading history is known.

More specifically, in this real case application, the MSS structure is equipped with a monitoring system that allows a frequent assessment of structural response.

The principles indicated in Table 1 are proposed for application of Damage Tolerant Method to MSS structures:

3 PRACTICAL CASE

The DV.1 connection (indicated in Fig. 2) is used in approximately 500 connections of the M1-90-S Main Girder diagonals, being designed to be slip-resistant in service - numerical models indicate that the slipping of connection plates may increase the deflection in about 20%.

The following principles were considered for fatigue assessment:

– Given the absence of an absolutely equivalent detail, the most conservative S-N curve given in EN 1993-1-9 was used ($\Delta s_C = 36$);
– The modified nominal stress was used. The stress concentration factor, k_f, was evaluated through FEM analysis;
– For simplification, the Damage, *Dd,* was evaluated adding the Damage due to the operation cycle loading ($Dd_{,OP}$) with the Damage due to wind loading ($Dd_{,W}$):

$$D_d = D_{d,OP} + D_{d,W} \tag{1}$$

3.1 *Damage due to operation cycle loading*

In each working cycle, the MSS main structure is loaded (concrete casting), unloaded (MSS descending and formwork removal) and then launched.

For a member type, such as main girder diagonal bar (DV.1 in Fig. 2), this loading sequence causes the equivalent to 2 or 3 "fatigue" cycles per operation cycle.

The nominal stress history and the cycle counting in accordance with the reservoir method are given in Figure 5.

A value of 1.4 was considered for k_f in accordance with FEM evaluation.

The stress maps used for evaluation of the stress concentration factor are shown in Figures 6 and 7 (for ULS combination).

The damage due to the operation cycle loading is evaluated applying Annex A of EN 1993-1-9 as follows:

$$D_d = \sum_i^n \frac{n_{Ei}}{N_{Ri}} \tag{2}$$

where n_{Ei} is the number of cycles associated with the stress range $\gamma_{Ff} \cdot \Delta\sigma_i$ for band i in the factored spectrum and N_{Ri} is the endurance obtained from the S-N curve – or Expression (3) – for a stress range of $\gamma_{Ff} \cdot \Delta\sigma_i$.

$$N_R = \frac{(\Delta\sigma_C)^m \cdot 2\times10^6}{(\Delta\sigma_R)^m} \tag{3}$$

The notations used in the previous expressions are the same used in EN 1993-1-9.

Focusing on the practical case, the damage due to operation cycle loading is evaluated as follows:

$$D_{d,OP} = \sum_{i=1}^{2} \frac{n_{Ei}}{N_{Ri}} \tag{4}$$

$$\frac{n_{E1}}{N_{R1}} = 100 / \left[\frac{(36/1.15)^3}{(310\times1.4)^3} \cdot 2\times10^6 \right] \tag{5}$$

$$\frac{n_{E2}}{N_{R2}} = 100 / \left[\frac{(36/1.15)^3}{(150\times1.4)^3} \cdot 2\times10^6 \right] \tag{6}$$

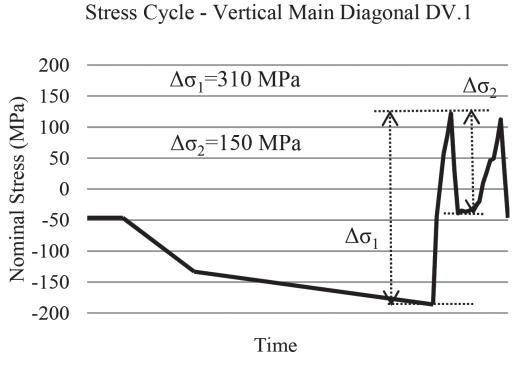

Figure 5. Stress history and cycle counting for DV.1 (for one operation cycle).

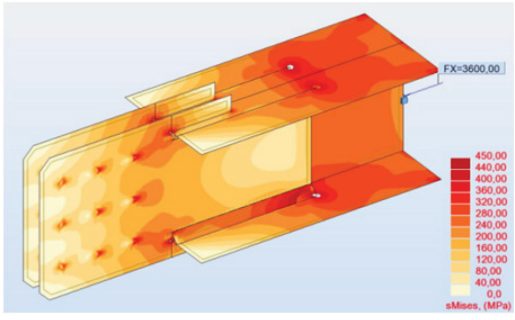

Figure 6. FEM model used for evaluation of k_f factor for DV.1 connection – Von Mises stresses (ULS).

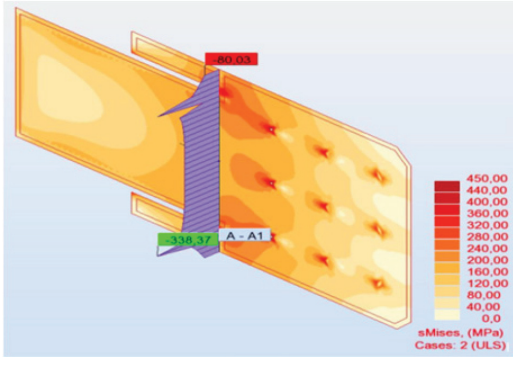

Figure 7. Normal stress map in DV.1 connection plates (ULS).

$D_{d,OP} = 0.148$

In the former expressions, a total of 100 operation cycles is considered (number of cycles between main inspections).

3.2 *Damage due to wind loading*

The standard EN 1993-3-1 gives some guidance for evaluation of fatigue caused by wind in towers and masts. Given the lack of applicable standards, a conservative methodology, with some resemblances with the later was adopted. The principles are defined next:

- Consideration of 3 years of exposition to wind in each safe period of 5 years;
- Consideration of a frequency of 0.2 Hz for wind action (period of 5 s);
- Total number of cycles NT = 3 years/5 seconds (approximately 1.9310^7);
- Drawn up of annual wind speed distribution based on Gaussian distribution, using observed maximum daily wind speeds;
- Calculation of stress amplitude $\Delta\sigma_{Wi}$ corresponding to each wind speed level W_i;
- Calculation of number of cycles n_i corresponding to each wind speed level W_i;
- Application of Damage function discarding the lower speeds (below the cut-off limit).

The Gaussian distribution and the source data used for estimation of the daily maximum wind speed are shown in Figure 8 (Firat 2007, Resende 2015).

The values shown in Figure 8 were registered at a height of 10 m above flat open country terrain. The calculation of the wind speed at a height of 75 m (MSS operation height) may be performed by application of EN 1993-1-4 procedures.

This conservative approach is summarized in Table 2, resulting in a cumulative damage of 0.046,7, for the present detail, caused by the wind fatigue loading.

The joined effect of the damage due to operation cycle ($D_{d,OP}$) and wind loading ($D_{d,W}$) is given by:

$D_d = 0.148 + 0.47 = 0.195 < 0.25$

The result shows that the structure will most likely remain free from significant crack initiation for a period of 5 years or 100 working cycles, by which time the first main inspection must occur.

3.3 *Strain-based approach*

Some doubts may arise regarding the applicability of S-N curves to Low-Cycle fatigue problems. Moreover, the DV.1 detail is not fully equivalent to the fatigue details presented in EN 1993-1-9.

Given this, a complementary strain-based approach, according to a strain-based Coffin-Manson formulation was used and a tri-dimensional FEM simulation model was developed to predict the fatigue life of DV.1, under the action of the operation cycle loading. The stress map is presented in Figure 9.

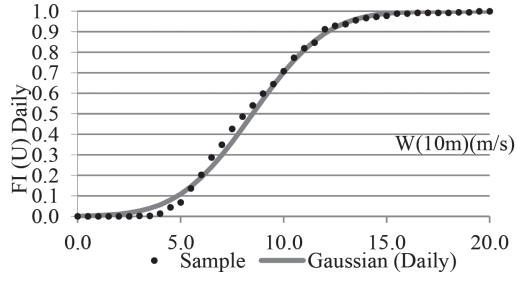

Figure 8. Cumulative Gaussian distribution function for Ankara daily maximum wind speed (10 m height from the ground level).

Table 2. Cumulative damage calculation due to wind fatigue loading (DV.1 detail).

W (10 m)	Wi (75 m)	Δsi	ρ (Wi)	nWi = NT. ρ(Wi)	NR,wi	nWi/NR,wi
m/s	km/h	MPa	%			
36.00	164.27	66.1	0.00	0	212225	0.0000
34,00	155.14	59.0	0.00	0	299046	0.0000
32.00	146.02	52.5	0.00	0	430242	0.0000
30.00	136.89	45.9	0.00	0	633701	0.0000
28.00	127.76	40.0	0.00	0	958659	0.0000
26.00	118.64	34.5	0.00	0	1495451	0.0000
24.00	109.51	29.4	0.00	18	2417379	0.0000
22.00	100.39	24.7	0.00	450	4074517	0.0001
20.00	91.26	20.4	0.00	7103	7218255	0.0010
18.00	82.13	16.5	0.00	69229	13582420	0.0051
16.00	73.01	13.1	0.02	416955	27535457	0.0151
14.00	63.88	10.0	0.08	1554123	61354155	0.0253
12.00	54.76	7.3	0.19	3589001		
10.00	45.63	5.1	0.27	5139001		
8.00	35.50	3.3	0.24	4564782		
6.00	27.38	1.8	0.13	2514675		
4.00	18.25	0.8	0.05	858682		
2.00	9.13	0.2	0.01	181570		
0.00	0.00	0.0	0.00	25760		

Grey Zone: Cut Off Limit.
$D_{d,W}$ = sum(nWi/NR.wi) = 0,0467.

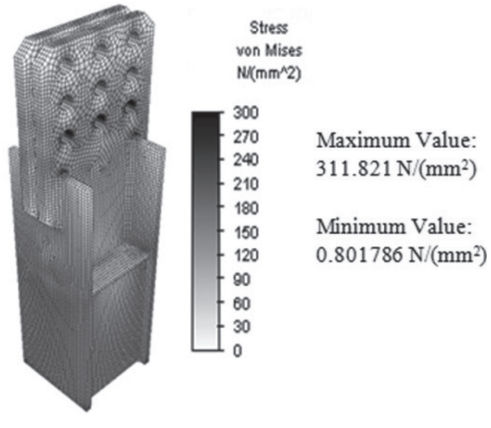

Figure 9. Tri-dimensional FEM simulation model stress map – operation cycle loading.

Given the absence of experimental tests results, the values for estimated low cycle fatigue properties were imported from bibliographic sources that used the same materials (Zhang & Maddox, 2009).

The results have shown a high degree of sensitivity to joint preparation details. Adopting a joint preparation in accordance with EN 1993-1-9 assumptions, a predicted life of 2571 cycles was reached. Making a correlation with S-N approach, the equivalent Δs_C would then be 56 MPa.

4 CHOICE OF MATERIALS

4.1 *Remarks on EN 1993-1-10*

EN 1993-1-10 covers the aspects of material toughness with regard to brittle fracture at low temperatures (so called lower shelf toughness). In this context, toughness means the ability of steel to absorb energy in presence of a crack to avoid the occurrence of a sudden failure due to brittle fracture at low temperatures. Ductility is the ability of steel to absorb energy by plastic deformation which is necessary for energy dissipation during seismic loading or stress redistribution at stress concentration locations.

If the conditions of Table 2.1 of EN 1993-1-10 are fulfilled, the toughness of the selected steel is sufficient to prevent:

– A structural detail with nominal stresses, $s_{Ed;}$
– A defined crack at the critical location to fail due to brittle fracture at a defined reference temperature, T_{Ed}.

The global behavior of the structural component has to be elastic, which is ensured by a limitation of nominal stresses to 75% of the yield strength. However, at the hot spot, the local stresses can be higher (and may be even plastic) due to notch stress concentration and the stress intensity at the crack tip.

Table 3. Evaluation of the reference temperature.

T_{md}	Lowest air temperature	See below
ΔT_r	Temperature adjustment for radiation loss, as in EN 1991-1-5	–5°C *
ΔT_σ	Adjustment for stress and yield strength of material, crack imperfection and member shape and dimensions	0°C
ΔT_R	Safety allowance, if required, to reflect different reliability levels for different applications	0°C
$\Delta T_{\dot{\varepsilon}}$	Adjustment for a strain rate other than the reference strain rate	0°C **
$\Delta T_{\varepsilon cf}$	Adjustment for the degree of cold forming	0°C for non cold-formed elements

*EN 1991-1-5 proposes the relation $T_{e,min} = T_{min} - 3°C$ for Type 1 bridge deck (steel truss or plate girder). The adopted value [–5°C] complies with this restriction and is commonly adopted.
**Although the MSS is a movable machine, the loading may generally be considered as quasi-static in all stages (Soares, 2015).

For the derivation of EN 1993-1-10 all details of EN 1993-1-9 have been investigated in view of brittle fracture, taking into account crack propagation, due to fatigue loading like it is typical in bridge structures. The most critical structural configuration for steel bridges – longitudinal attachments according to Table 8.4 of EN 1993-1-9 – has been selected as reference detail for the evaluation of Table 2.1 of EN 1993-1-10. Therefore, EN 1993-1-10 is only applicable to all structural details given in the fatigue strength categories of EN 1993-1-9. But as the most critical detail was taken for the evaluation, the other details are less critical or, in other words, Table 2.1 of EN 1993-1-10 is conservative for other details with higher fatigue classes than the longitudinal attachments (Feldmann + Weynand Ingenieure, 2015).

4.2 *Application of EN 1993-1-10 to the practical case*

As stated before, the MSS will operate near Ankara, close to the city of Kirikkale, Turkey.

According to EN 1993-1-10, the reference temperature, $T_{Ed,}$ should be determined using the following expression:

$$T_{Ed} = T_{md} + \Delta T_r + \Delta T_\sigma + \Delta T_R + \Delta T_{\dot{\varepsilon}} + \Delta T_{\varepsilon cf} \qquad (7)$$

The application of Expression 7 is detailed in Table 3.

4.3 *Lowest air temperature evaluation*

For evaluation of lowest air temperature, the fundamentals of EN 1991–1-5 are applied, with some adaptations in order to take into account the nature of this type of structures.

The main particularity is that the MSS operation (launching, concrete casting) is ruled by rigid Operational Limits (Maximum Wind Speed, Minimum Temperature). Regarding the Minimum Temperature, the following Operational Limits are applicable:

– It is strictly forbidden to cast concrete if the air temperature is lower than –5°C or if temperatures lower than –10°C are predicted to occur within a period of 72 hours following the concrete casting;
– It is strictly forbidden to launch the MSS if the air temperature is lower than –5°C.

Notice that temperature Operational Limits are more than Manual rules – they are actually physical limits as well, since the MSS hydraulic components are incapacitated for temperatures below Operational Limits. Therefore, two different values for lower air temperature are considered for structural analysis:

T_{md} – Lowest air temperature
$T_{md,OP}$ – Lowest operational air temperature

The two values of temperature are applied according to the following Table 4.

Given the lack of computed statistical data, a record of daily minimum temperatures from Ankara was used. The record covers a period of 20 years, from 1996 to 2015. The record from 1996 and 2015 is incomplete – therefore, those 2 years were not used for extreme value distribution.

The values for minimum temperature are presented in Table 5:

According with EN 1993-1-10, T_{md} is the lowest air temperature for a predefined return period. EN 1991–1-5 defines T_{min} as being minimum shade air temperature with an annual probability of being exceeded of 0.02 (equivalent to a mean return period of 50 years). For the present case, it was assumed that the definition of T_{min} and T_{md} are equivalent.

Since the sample is significantly short, the following procedure was applied:

– Induction of Apparent Return Period for different values of temperature, based on attempts;
– For each attempt, calculation of corresponding T_{min} applying the Expression 8 (from EN 1991–1-5):

$$T_{\min,p} = T_{\min}\left\{k_3 + k_4 \cdot \ln\left[-\ln(1-p)\right]\right\} \qquad (8)$$

– Evaluation of consistency between attempts.

The above described procedure is synthesized in Table 6.

Table 4. Lowest air temperature.

Situation	Lowest temperature	σ_{Ed} (EN 1993-1-10)
MSS in operation	T_{md}	Maximum service stress. Limited to 75% of the yield strength.
Extreme weather (MSS immobilized)	$T_{md,OP}$	Moderate stress. Limited to 50% of the yield strength.

Table 5. Registered minimum annual temperature (Ankara).

Year	Minimum temperature ºC	
1997	–20.6	
1998	–17.2	
1999	–9.4	
2000	–22.8	year
2001	–14.4	
2002	–18.9	
2003	–14.4	
2004	–20.6	
2005	–16.1	
2006	–23.9	year + 6
2007	–14.4	
2008	–20.6	
2009	–17.2	
2010	–13.3	
2011	–14.4	
2012	–23.9	year + 6 × 2
2013	–16.1	
2014	–9.4	

(Weather Underground 2015).

Table 6. Evaluation of lowest air temperature.

				Tmin (EN 1991–1-5)	
Tmin, p	n	p = n/N*	Apparent Return Period	A_1**	A_2***
ºC					
–23.9	3	0.17	6	–31.8	–36.3
–22.8	4	0.22	4.5	–31.9	–37.5
–20.6	6	0.33	3	–31.2	–38.6
–18.9	7	0.39	2.57	–29.6	–37.5
–17.2	9	0.50	2	–28.7	-38.2

*N = 18 (total number of observations).
**Approach 1: Application of EN 1991-1-5 expression with k3 and k4 deriving from the sample.
***Approach 2: Application of EN 1991-1-5 expression with default k3 = 0.393 and k4 = –0.156 deriving from the sample.

The application of Expression 8 using default k3 and k4 parameters leads to a conservative estimation. Even though the sample is reduced, Approach 1 was adopted. Since the consistency between attempts was found to be reasonable, a temperature value of –32°C was adopted for T_{md}.

Applying Expression 7, a value of –37°C is reached for the reference temperature in extreme conditions.

For Operational Limits, an approach using Type I extreme value distribution is not recommended. In Extreme Situations, the MSS is deactivated – therefore the structure will remain unloaded. Even though there are limits defined in the MSS Operations

Manual, a probabilistic approach is always recommended with the following purpose: if the Operational Limit is too restrictive, there is a strong probability of disobedience by the MSS operator. Therefore, design Operational Limits must be based on daily observations of minimum temperature.

The Gaussian distribution often gives good results for evaluation of daily minimum, mean and maximum temperatures. In case of significantly skewed sample distributions and bimodal sample distribution, the approach must be used with some reserve. In order to mitigate the bimodality resulting from the seasonal effects (winter versus summer), the Gaussian distribution was drawn using only the colder months (from December to March). The results are presented in Figures 10 and 11.

The skewness of the sample distribution is moderate and bimodality was solved using the cooler months. The lowest operational air temperature is defined as a characteristic value, with a probability of being out-limited of 98%.

Based on Figure 11 cumulative distribution function, a value of –14.4°C was calculated for the lowest operational air temperature for this practical case.

Applying Expression 7, a value of –19.4°C is reached for the reference temperature in operation conditions.

4.4 *Material selection according to the thickness*

The stress level limit for operation conditions and extreme weather conditions are presented in Table 4 (75% of the yield strength and 50% of the yield strength, respectively).

In this particular case, the following materials were specified:

Plates and profiles
t ≤ 20 mm, S355 JR;
20 mm < t ≤ 50 mm, S355 J2+N;
t > 50 mm (defined case by case).

Applying Table 2.1 of EN 1993-1-10 for plates and profiles to the specified material, the following limits for the reference temperature are defined:

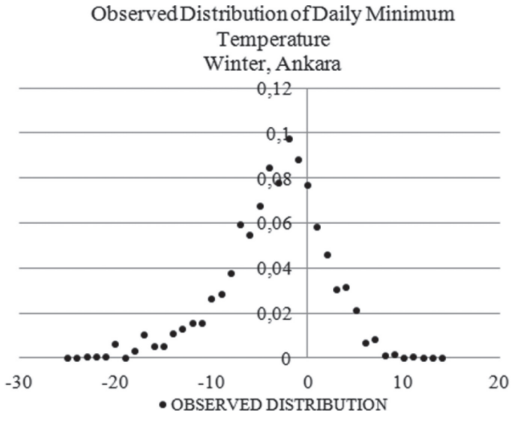

Figure 10. Observed distribution for Ankara minimum daily temperature in winter season.

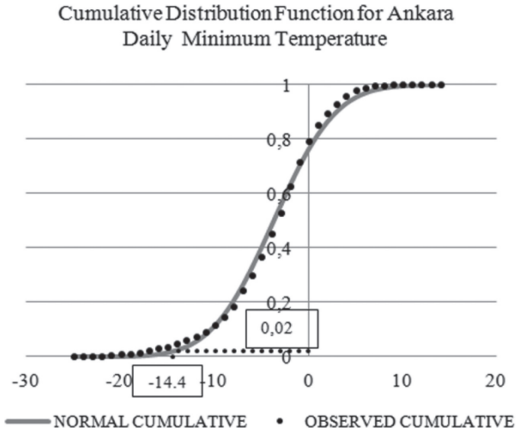

Figure 11. Cumulative distribution function for Ankara daily minimum temperature (winter season level).

Table 7. Limit reference temperature for the specified material.

t for plates and profiles	Minimum allowable temperature	
	MSS in Operation	MSS immobilized
mm	ºC	ºC
t ≤ 20	–20	–50
20 < t ≤ 50	–20	–45

The values in Table 7 show that MSS operation scenarios condition the choice of steel. This scenario governed the choice of material and maximum thickness for each material.

5 FATIGUE PREVENTION DURING MANUFACTURING AND OPERATION

The fatigue prevention is not just a question of design and must be complemented by adequate fabrication control and maintenance procedures.

As a first approach, the following measures are re-commended for MSS structures fabrication:

- Main structural components should be manufactured in accordance with EN 1090-2 EXC3 execution class requirements. Regarding weld examination, the following acceptance levels are recommended: Level B in accordance with ISO 5817 and Level 2 in accordance with ISO 11666;
- All materials should be delivered with inspection certificates 3.1 or 3.2 according to EN 10204;
- All materials should be delivered with Charpy-V notch tests so that the applicability of Table 2.1 of EN 1993-1-10 may be accessed;
- The materials should be specified with adequate trough-thickness properties and specific measures must be implemented to avoid lamellar tearing during welding;
- The welding starts and stops are often prone to imperfections – the use of adequate run-on and run-off plates is recommended;
- All welds must be accessible for inspection, not only in service but also throughout manufacturing. In some cases, it is not possible to perform ultrasonic testing, UT, or radiographic testing, RT. In such situations, the change of details or application of alternative non-destructive testing, NDT, should be considered.
- All welds that remain hidden after fabrication should be submitted to photographic registry, complementing the NDT report;
- The NDT must be performed in the welds extension more prone to crack growth. This should be expressed in the execution drawings or fabrication specifications;
- The joint preparation should be validated before welding. The poor access for welding or the need for demanding welding positions often result in defective welds.

Complementarily, during service life of MSS structures, the following measures are recommended:

- Elaboration of a Maintenance plan which must include an inspection plan, clearly identifying the critical details, the extension of inspection and its periodicity;
- Performance of operational Maintenance, carried out periodically during MSS operation;
- Performance of deep maintenance, carried out after MSS disassembly and before each new application. Structural components with

evidence of crack initiation must be retrofitted or replaced between consecutive applications;
– Detailed registry of all MSS applications, enabling the reproduction of the structure loading history and cycle counting;
– Structural monitoring is highly recommendable. Any abnormal structural behavior should trigger a consistent diagnosis. Some recent MSS equipment also incorporate active control systems, which may have a significant impact in limiting the stress range (Pacheco, 2007);
– The choice for non-slip bolted connections is recommended. Besides improving fatigue performance of bolts and connection plates, non-slip connections enable a better control of force redistribution and stress reversal (Harridge, 2011);
– All bolts should be replaced between two consecutive applications. This should be mandatory for HSFG bolts.

6 CONCLUSIONS

MSS structures are often seen as temporary structures. Given the on growing longevity and complexity of this type of equipment, its temporary nature must be considered with reserve while stablishing the design and fabrication criteria.

One of the design issues that must be carefully considered is the fatigue assessment of MSS structures, which is often neglected. The Damage Tolerant Method seems to be an adequate approach fatigue evaluation in MSS structures, given its specific nature.

The fatigue design must be necessarily complemented by adequate fabrication control and by application of a consistent maintenance plan.

REFERENCES

Confederación Nacional de La Construcción (CNC) 2007, Manual de Cimbras Autolanzables, 1ª ed., CNC, Madrid.

Feldmann + Wynand Ingenieure 2015, Low temperature on steel structure of a movable scaffolding system. Available from: Feldmann + Weynand Ingenieure 2015. [13 April 2015].

Firat, F.K. 2007. Development of Load and Resistance Factors for Reinforced Concrete Structures in Turkey. Ph.D Thesis, Middle East Technical University Ankara.

Harridge, S. 2011, Launching Gantries for Building Precast Segmental Balanced Cantilever Bridges. Structural Engineering *International Journal of IABSE* 21(4): 406–412.

Pacheco, P. 2007. A Scaffolding System strengthened with Organic Prestressing. *Structural Engineering International Journal of IABSE* 17(4): 314–321.

Pacheco, P. 2015. High Productivity in Bridge Construction – the OPS effect. *Multi-Span Large Bridges conference*, pp. 243–244.

Resende, A. & Coelho, H. 2015. Preliminary assessment of wind actions in large span MSS. *Multi-Span Large Bridges conference*, pp. 267–268.

Sedlacek, G. et al. 2008. Commentary and worked examples to EN 1993-1-10 "Material toughness and through thickness properties" and other toughness oriented rules in EN 1993, JRC Scientific and Technical Report.

Soares, J.M. 2015. 16519.1 Choice of steel grades – Effect of low temperatures – Basis for Stage 2 Analysis. Available from: BERD [March 2015].

Weather Underground 2015, Available from: <http://www.wunderground.com/history> [March 2015].

Zhang, Y. & Maddox S. 2009. Fatigue life prediction for toe ground welded joints. *International Journal of Fatigue*, Vol.31, Issue 7, pp. 1124–1136.

This page intentionally left blank

Recent Progress in Steel and Composite Structures – Giżejowski et al. (Eds)
© 2016 Taylor & Francis Group, London, ISBN 978-1-138-02946-0

Stability of a truss under upward wind loading

M. Krajewski & P. Iwicki
Faculty of Civil and Environmental Engineering, Gdańsk University of Technology, Gdańsk, Poland

ABSTRACT: The present paper is devoted to the numerical investigations of stability of a truss under upward wind load. The truss is braced at the upper cord. A case with lateral braces, or lateral and torsional braces is considered. In the research the linear buckling and non-linear static analysis of the truss shell and beam model with geometric and material non-linearity are presented. The initial imperfections were assumed in the form of arch curvature of the compressed bottom chord due to EC3 requirements. As a results the truss buckling and limit load was found related to the truss bracing stiffness and the threshold bracing condition was obtained necessary to provide maximum buckling resistance of the truss.

1 INTRODUCTION

The problem of bracing requirements necessary to provide lateral stability of compressed members is present in design codes PN (1990) or EC3 (2006). Out-of-plane buckling of trusses was studied in the numerical research by Iwicki (2010), or experimental and numerical analysis conducted by Kołodziej & Jankowska-Sandberg (2013) and Iwicki & Krajewski (2013, 2014, 2015). The basic problem was devoted to the investigation of the required bracing stiffness to ensure that the out-of the truss plane buckling occurs between braces, or is prevented, so buckling occurs in the truss plane. The full bracing condition was defined as the bracing stiffness that causes the maximum buckling load of the truss, or when an increase in bracing stiffness does not result in a further increase in the buckling load.

In the case of light weight structures the influence of upward wind loading may be quite significant and may cause compression in the truss bottom chord. However, the truss bottom chord is, in general, not designed for such loading and therefore is not always stabilized by bracing. The force needed to stabilize the bottom truss chord is not anticipated in codes either. There is no information about a required bracing stiffness and an effective buckling length of the bottom truss chord. The buckling length is often assumed by the designers and it is different from calculated by linear buckling analysis. The all of above mentioned problems cause difficulties in the design. An observed failure of truss purlins under wind load (Hotała et al. 2007) is presented in Figure 1. The damage under upward wind loading was reported and confirms that the problem exists.

In order to prevent the bottom truss chord from out-of-plane buckling a additional braces connecting the truss bottom chord and the roof trapezoidal sheeting or purlins may be applied. In a real structure these stiffnesses are interrelated and difficult to determine.

The calculation models for assessment of the lateral supporting of the bottom truss chords as the flexible restraint in the roof trapezoidal sheets were given by Biegus (2014). Furthermore the procedures of the assessment resistance due to out-plane buckling of the bottom truss chord braced by roof sheeting were presented.

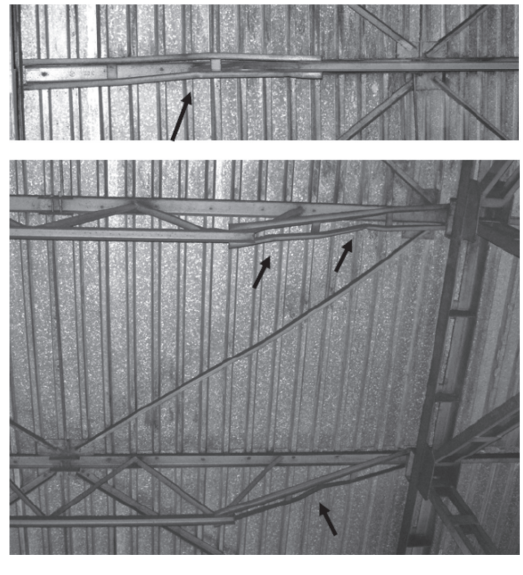

Figure 1. Failure of truss purlins caused by wind load (Hotała et al. 2007).

Similar problem exists in the truss top chord in opened bridges. The polish standard PN-82/S-10052 recommends a verification of stability of compressive truss chords which are not prevented from buckling out of their planes through determining a stiffness of a so-called half-frame. It is created by diagonals and other elements of the half-frame. When the stiffness of the elastic foundation is determined the buckling load may be calculated according theoretical formulas of a buckling of column resting on elastic foundation (Pałkowski & Kołodziej 1995).

In the present paper the truss previously analysed by Biegus (2014) is considered. The truss is braced at the top chord by elastic supports. The linear buckling analysis and non-linear analysis with both geometric and material non-linearity was performed. The results obtained by the stability analysis of the truss modelled by beam elements were compared to the similar analysis of the truss modeled by shell elements and program FEMAP with NX NASTRAN (2009). Some conclusions regarding safety margins were discussed.

2 DESCRIPTION OF THE TRUSS

In the present research the model of steel truss described by Biegus (2014) was taken into consideration. It was assumed that structure is braced by several elastic supports placed at the top chord. The translational (k_t [kN/m]) and rotational (k_{rot} kNm/deg]) brace stiffness was taken into account (Fig. 2). The truss length was $L_t = 15.0$ m, the depth was $h_t = 0.7$ m. The distance between side horizontal braces was equal to 1.5 m. The RHS $120 \times 100 \times 4.0$ hot-rolled tube profile was used as the top chord cross-section and RHS $100 \times 100 \times 4.0$ for the bottom chord. The diagonals cross-section was RHS $50 \times 50 \times 3$. The yield strength of the truss steel was $f_y = 275$ MPa. In the numerical analysis of the 3D models it was assumed that the truss was pinned at the marginal supports and the twisting was blocked. On one of these supports the translational stiffness was neglected (free translation along the truss length). The load corresponding to the wind suction was applied in the form of concentrated forces at nine top chord joints.

The truss was modeled by beam and shell elements and program Femap with NX Nastran (2009) (Figs. 3, 4).

In the shell model about 35 000 QUAD4 elements (with six degree of freedom at node) were used and the elastic supports at the top chord were modeled by means of DOF-spring elements. The walls of the chords cross-section were modeled by 4 or 5 shell elements and the walls of the diagonals by 3 elements. RIGID links between the adjacent parts were modeled as a connections between the truss members.

In the beam model about 400 elements with six degree of freedom at node were used. Each member of the structure was divided on 10 parts. It was assumed that connections between chords and diagonals are rigid. The offsets between separate members were neglected. Braces were modeled by means of DOF-spring elements with translational and rotational stiffness only.

On the basis of results presented by Biegus (2014) the truss purlin was prevented from out of plane buckling by rigid side-supports and the rotational stiffness of braces k_{rot} [kNm/deg] can be determined from equation

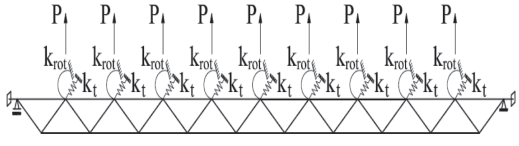

Figure 2. Model of the truss with horizontal elastic braces at the top chord.

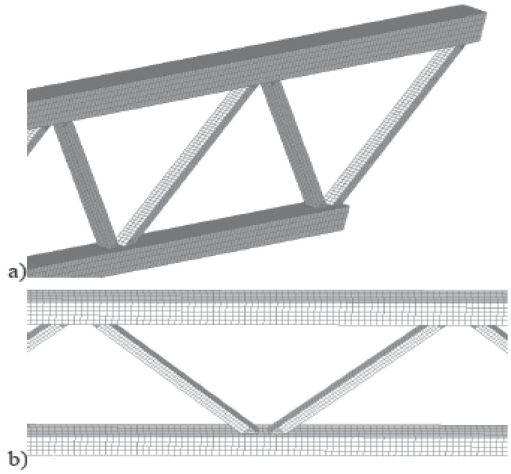

Figure 3. Model of the truss: a),b) shell model details.

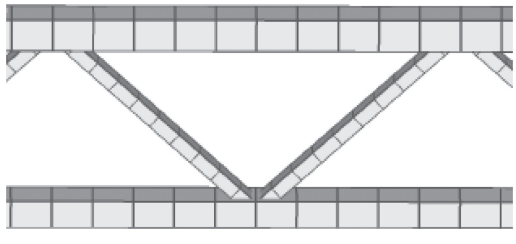

Figure 4. Model of the truss—beam model detail.

$$\frac{1}{k_{rot}} = \frac{1}{k_{roof}} + \frac{1}{k_{con}} \tag{1}$$

where k_{roof} – flexural stiffness of the roof elements such as purlins with sandwich panels or trapezoidal sheet gathered at one node, k_{con} – flexural stiffness of the roof elements to upper chord connection.

In the present research it was assumed that braces perpendicular to the truss plane (k_t [kN/m] and k_{rot} [kNm/deg]) are not rigid and the minimum magnitude of that stiffnesses was found necessary to provide maximum buckling load and limit load for the structure.

3 RESULTS OF NUMERICAL ANALYSIS

3.1 *Linear buckling analysis*

For the truss braced at the top chord buckling load was depended on brace translational stiffness (Fig. 5). For the structure with rigid lateral supports the influence of added supports with rotational stiffness on magnitude of buckling load was presented on Fig. 6.

The buckling load for the structure with braces of stiffness k_t = 10000 [kN/m] (k_{rot} = 0 [kNm/deg]) was about 5% lower than for the truss with supports of stiffness equal to $k_t = 10^6$ [kN/m] (k_{rot} = 0 [kNm/deg]). The threshold condition for rotational brace stiffness can be described as k_{rot} = 150 kNm/deg. That magnitude of brace stiffness ensures that buckling load is only about 5% lower than for the structure with rigid supports.

The results obtained from LBA analysis showed that buckling load rises with rise of rotational stiffness of braces. The magnitude of buckling load was higher up to 12% for the models

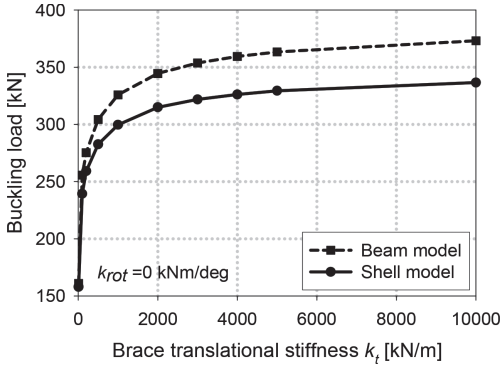

Figure 5. The comparison between the first buckling load for shell and beam model of the truss with respect to the braces translational stiffness.

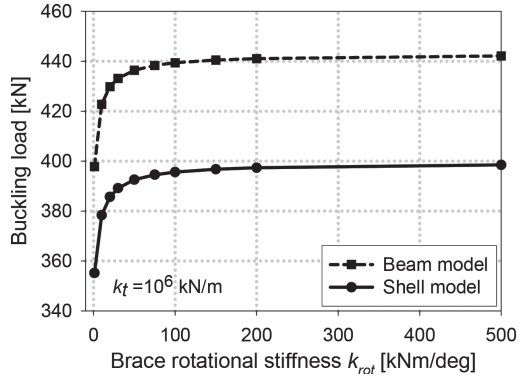

Figure 6. The comparison between the first buckling load for shell and beam model of the truss with respect to the braces rotational stiffness.

with rigid rotational supports in comparison to the models with braces of translational stiffness only.

The magnitude of buckling load for the rigid lateral supports was about 10% lower for the shell model in comparison with beam model. The possible reason for this discrepancies may be different performance of the elastic braces. In the beam model each top chord member, diagonals and elastic support are joined at one node. In the shell model braces were combined only with the several nodes on the perimeter of the top chord cross-section.

The buckled shape of the truss (Figs. 7, 8) changes form one half-wave to three half-waves (bottom chord) depending on the brace translational stiffness.

The increase of rotational braces stiffness (Figs. 9, 10) caused the reduction of the top chord twisting. In this case for the beam model of the truss buckled mode appears in the form of four half-waves.

3.2 *Non-linear analysis*

For the beam and shell model of the structure a non-linear static analysis was carried out (GMNIA). In the analysis the bi-linear perfectly elastic-plastic body model was assumed (f_y = 275 MPa). The initial geometric imperfections presented in Figure 11 were implemented to the models. The truss bottom chord had initial arch curvature with magnitude $\Delta = L_t/500$ according to the code EC3 (2006) requirements. The full Newton-Raphson method was used to solve the equilibrium equations. The loading was applied by means of arc-length method (Femap with NX Nastran – 2009).

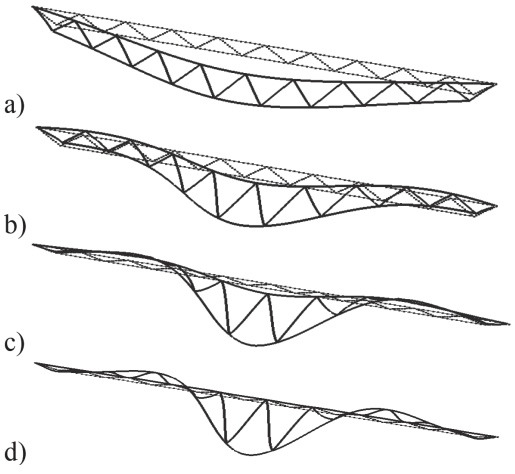

Figure 7. Buckled shape of the truss (beam model) with translational braces (k_{rot} = 0 kNm/rad) of stiffness k_t: a) 10 kN/m, b) 100 kN/m, c) 1000 kN/m, d) 10^6 kN/m.

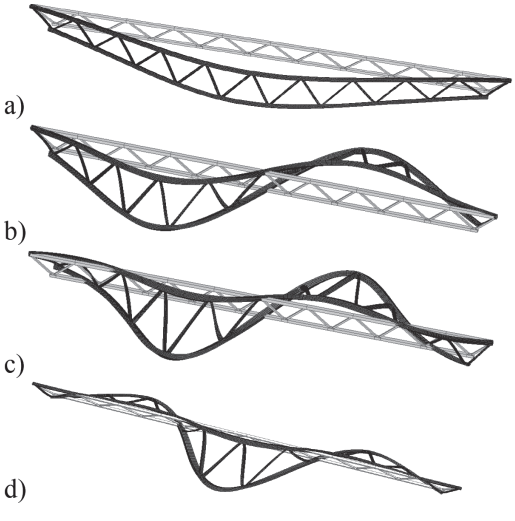

Figure 8. Buckled shape of the truss (shell model) with translational braces (k_{rot} = 0 kNm/rad) of stiffness k_t: a) 10 kN/m, b) 100 kN/m, c) 1000 kN/m, d) 10^6 kN/m.

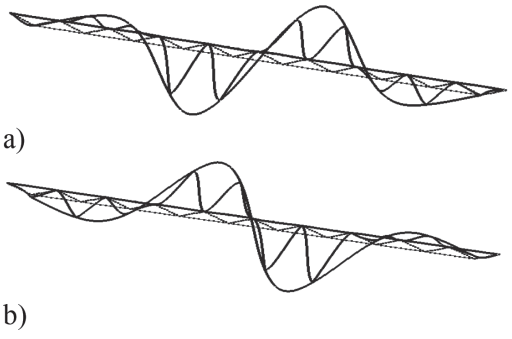

Figure 9. Buckled shape of the truss (beam model) with translational and rotational braces stiffness: a) $k_t = 10^6$ kN/m, k_{rot} = 10 kNm/deg b) $k_t = 10^6$ kN/m, $k_{rot} = 10^6$ kNm/deg.

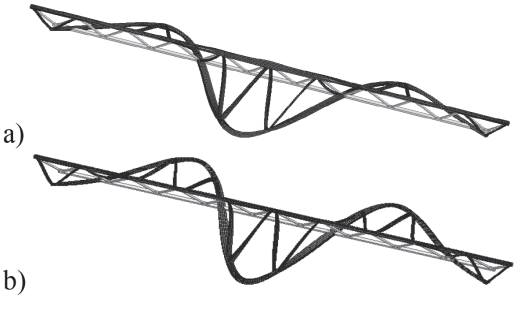

Figure 10. Buckled shape of the truss (shell model) with translational and rotational braces stiffness: a) $k_t = 10^6$ kN/m, k_{rot} = 10 kNm/deg b) $k_t = 10^6$ kN/m, $k_{rot} = 10^6$ kNm/deg.

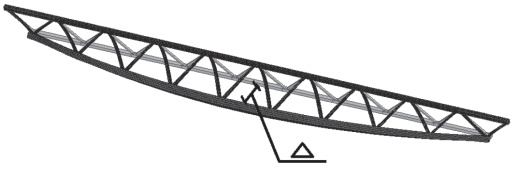

Figure 11. Initial geometric imperfection of the truss: $\Delta = L_t/500$.

For the truss braced by lateral braces of stiffness k_t [kN/m] (k_{rot} = 0 [kNm/deg]) the relation between loading (sum of all concentrated forces at the top chord) and vertical displacements for different stiffness of braces is presented in Figure 12 – beam model and Figure 13 – shell model. Limit load for the imperfect truss models raised with increase of brace stiffness.

On the basis of results presented in Figure 14 the threshold bracing conditions can be described as k_t = 750 kN/m (k_{rot} = 0 [kNm/deg] – beam and shell model). As it is shown the differences between the magnitudes of maximum loading for beam and shell model are about 2%. The possible explanation of the above described discrepancies may be the different number of finite elements which are used along separate members of the truss in the beam and shell model.

The non-linear analysis results for the structure with braces of translational and rotational stiffness are presented in Figure 15. In this case ($k_t = 10^6$ kN/m) the leading displacement of the truss were observed in the truss plane and therefore the

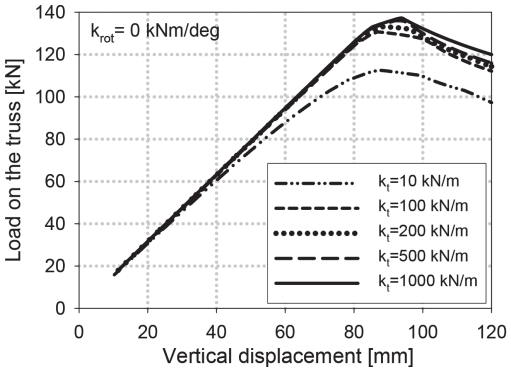

Figure 12. Truss loading vs. vertical displacement (at the middle of the span—bottom chord) for different sliding stiffnesses of braces—beam model.

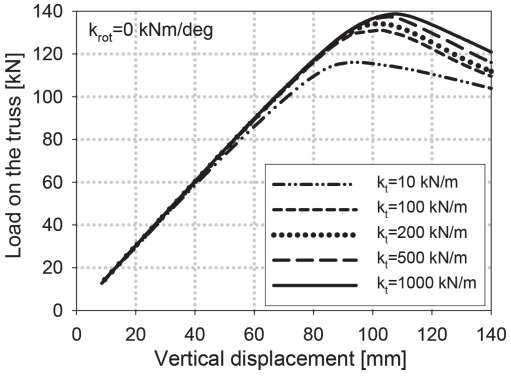

Figure 13. Truss loading vs. vertical displacement (at the middle of the span—bottom chord) for different sliding stiffnesses of braces—shell model.

rotational stiffness of braces had no influence on the limit load magnitudes neither for the beam model nor for the shell model. There was no differences in truss deformation for structure with braces of stiffness $k_t = 10^6$ kN/m, $k_{rot} = 0$ [kNm/deg] or $k_t = 10^6$. kN/m, $k_{rot} = 10^6$ [kNm/deg] (Fig. 16c and Fig. 17c)

The deformation of the structure (after limit state) is presented in Figure. 16 and Figure 17. The shape of deformation was depended on brace translational stiffness and it was comparable for beam and shell models. The significant influence on the shape of the deformed structure might also have the initial geometric imperfection shape and magnitude (Iwicki & Krajewski 2013, 2014).

The details of the structure deformation (plate top HMH stress state) are presented in Figure 18. The pasticity regions appeared at the top and bottom chord of the structure. The range of plasticity at the bottom chord depended on brace stiffness and it was equal to about 7,5 m for $k_t = 10$ kN/m and about 4,5 m for $k_t = 10^6$ kN/m.

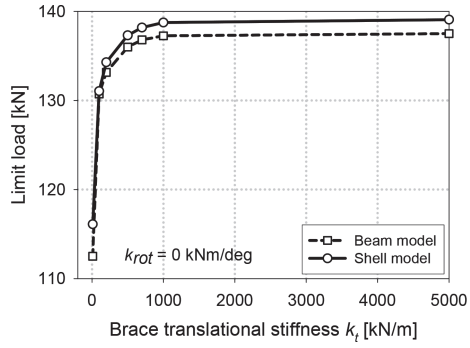

Figure 14. Truss limit load with respect to the sliding brace stiffness for beam and shell model.

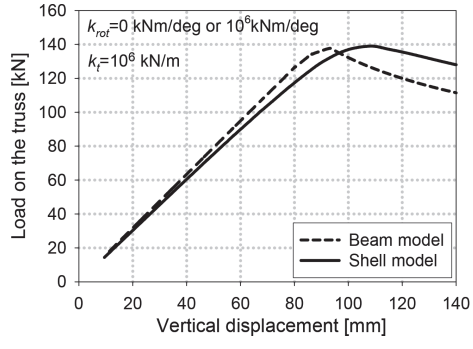

Figure 15. Truss loading vs. vertical displacement (at the middle of the span—bottom chord, shell and beam model) for different rotational stiffnesses of braces (with rigid horizontal braces).

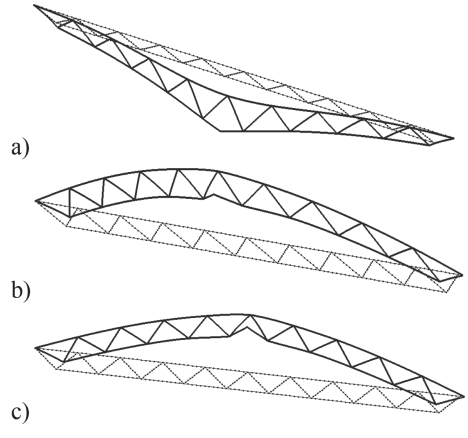

Figure 16. Post-buckling deformation of the truss (at displacement equal to 0,12 m—beam model) with braces of translational stiffness: a) k_t = 10 kN/m, b) k_t = 1000 kN/m, c) $k_t = 10^6$ kN/m.

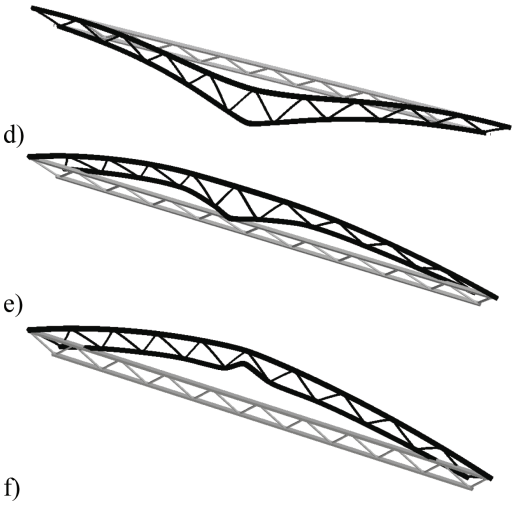

Figure 17. Post-buckling deformation of the truss (at displacement equal to 0,12 m—shell model) with braces of translational stiffness: a) k_t = 10 kN/m, b) k_t = 1000 kN/m, c) $k_t = 10^6$ kN/m.

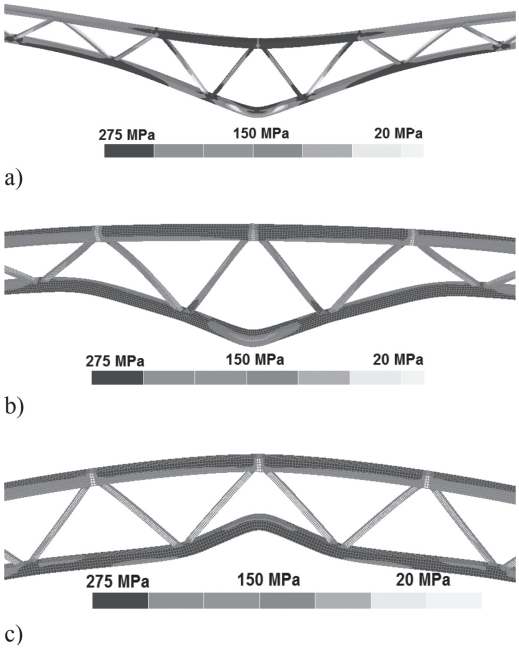

Figure 18. The plastification range due to post-buckling deformation of the truss (at displacement equal to 0,12 m—shell model) with braces of translational stiffness: a) k_t = 10 kN/m, b) k_t = 1000 kN/m, c) $k_t = 10^6$ kN/m.

4 TRUSS BEARING CAPACITY ACCORDING TO EC3

For the structure loaded by unit concentrated forces at nine top chord joints the distribution of the normal force at the bottom chord was obtained (linear static analysis). The results are presented in Figure 19. It was assumed that critical normal force at the bottom chord refers to the middle of the span (maximum magnitude of normal force) and therefore the non-dimensional slenderness was determined from equation

$$\lambda = \sqrt{\frac{Af_y}{N^*_{cr}}} \tag{2}$$

where: A = 14,95 cm^2 – cross section area, yield strength f_y = 275 MPa, N_{cr}^* – critical normal force at the bottom chord (referred to the middle of the span) for the load equal to P_{cr} – first critical load (obtained from LBA).

The relation between non-dimensional slenderness referred to the bottom chord of the truss and brace translational stiffness is presented in Figure 20. The influence of rotational brace stiffness on magnitudes of the slenderness is presented in Figure 21.

On the basis of calculated slenderness the magnitudes of bearing capacity N_{brd} (EC3 2006) were

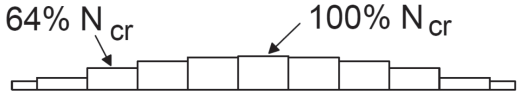

Figure 19. The distribution of the normal force at the bottom chord of the truss.

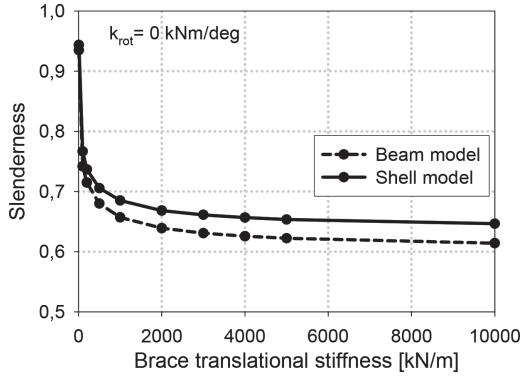

Figure 20. The comparison between slenderness (bottom chord—middle of the span) for shell and beam model of the truss with respect to the braces translational stiffness.

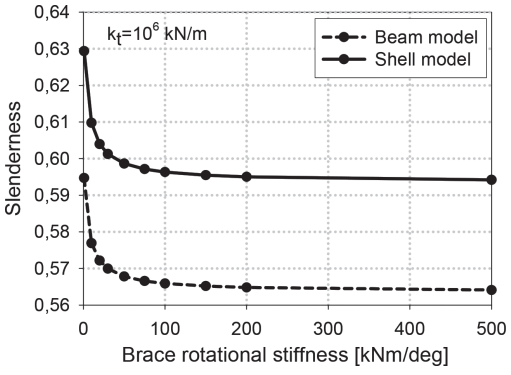

Figure 21. The comparison between slenderness (bottom chord—middle of the span) for shell and beam model of the truss with respect to the braces rotational stiffness.

Table 1. Truss bearing capacity according to EC3 with respect to the brace translational stiffness, beam model, $k_{rot} = 0$ kNm/deg.

k_t	P_{cr}	N_{brd}	P_{max}
kN/m	kN	kN	kN
10	161.0	292.2	100
100	255.6	340.1	116.4
200	275.3	345.6	118.3
500	304.3	352.3	120.6
1000	325.9	356.5	122.0
5000	363.3	362.4	124.0
10000	373.1	363.6	124.4
10^6	386.1	365.3	125.0

Table 2. Truss bearing capacity according to EC3 with respect to the brace rotational stiffness, beam model, $k_t = 10^6$ kN/m.

k_{rot}	P_{cr}	N_{brd}	P_{max}
kNm/deg	kN	kN	kN
1	397.8	366.7	125.5
10	422.7	369.4	126.4
20	429.8	370.1	126.7
50	436.4	370.8	126.9
100	439.3	371.0	127.0
200	441.0	371.2	127.0
500	442.1	371.3	127.1
10^6	442.9	371.4	127.1

obtained (referred to the middle of the truss span). The results for the beam models are presented in Tab. 1 and Tab. 2 and for the shell models in Tab. 3 and Tab. 4. The magnitude of maximum truss loading P_{max} (sum of all concentrated forces at the top chord referred to N_{brd}) were also determined.

Table 3. Truss bearing capacity according to EC3 with respect to the brace translational stiffness, shell model, $k_{rot} = 0$ kNm/deg.

k_t	P_{cr}	N_{brd}	P_{max}
kN/m	kN	kN	kN
10	158.0	289.7	99.1
100	239.4	334.8	114.6
200	259.2	341.2	116.7
500	282.6	347.4	118.9
1000	299.7	351.4	120.2
5000	329.4	357.1	122.2
10000	336.6	358.3	122.6
10^6	347.4	360.0	123.2

Table 4. Truss bearing capacity according to EC3 with respect to the brace rotational stiffness, shell model, $k_t = 10^6$ kN/m.

k_{rot}	P_{cr}	N_{brd}	P_{max}
kNm/deg	kN	kN	kN
1	355.2	361.2	123.6
10	378.4	364.4	124.7
20	385.7	365.3	125.0
50	392.6	366.1	125.3
100	395.6	366.5	125.4
200	397.3	366.7	125.5
500	398.5	366.8	125.5
10^6	399.2	366.9	125.6

The truss loading raised with increase of brace translational and rotational stiffness. For the structure with braces of rotational stiffness equal to $k_{rot} = 0$ [kNm/deg] the magnitudes of P_{max} raised about 25% due to increase of translational brace stiffness. For the truss with rigid lateral supports ($k_t = 10^6$ [kN/m]) the magnitudes of P_{max} raised about 2% due to increase of rotational brace stiffness.

The magnitudes of P_{max} referred to EC3 requirements were about 8% lower than the magnitudes of limit load obtained from GMNIA for the beam model and about 10% lower than the magnitudes of limit load for the shell model.

5 CONCLUSIONS

The Linear Buckling Analysis (LBA) results conducted for the truss under upward loading confirmed that the buckling load depended on the stiffness of elastic braces situated at the top chord. For the structure with rigid side braces ($k_t = 10^6$ [kN/m]) the increase of the rotational brace stiffness can provide to 12% increase of the buckling load.

The limit load obtained from non-linear static analysis (GMNIA) for the imperfect truss model (beam and shell model) depended on brace translational stiffness. The rotational stiffness of braces added to models with rigid lateral braces ($k_t = 10^6$ [kN/m]) had no influence on the magnitude of limit load.

The magnitudes of the truss maximum loading (referred to the bottom chord—middle of the span) calculated due to EC3 (2006) requirements were up to 10% lower in comparison to the results obtained from GMNIA.

The next research step is to propose bottom chord of the truss on elastic foundation as a simplified model of the structure braced by elastic supports at the top chord.

REFERENCES

Biegus, A. 2014. Trapezoidal sheet as a bracing preventing flat trusses from out-of-plane buckling, *Archives of Civil and Mechanical Engineering*, http://dx.doi.org/10.1016/j.acme.2014.08.007.

Biegus, A. & Wojczyszyn, D. 2011. Studies on buckling lengths of chords for out-of-plane instability, *Archives of Civil and Mechanical Engineering*, Vol. XI, No. 3:507–517.

Femap with NX Nastran 2009. Version 10.1.1. Siemens Product Lifecyde Management Software Inc.

Hotała, E. Hotała, P. & Bambrowicz, M. 2007. Bezpieczeństwo płatwi kratowych podczas obciążenia wiatrem lub śniegiem, *Problemy naukowo-badawcze budownictwa, Konstrukcje budowlane i inżynierskie*, pr. zbior. pod red. M. Broniewicza, J. A. Prusiel), Wydawnictwo Politechniki Białostockiej, 2: 241–248.

Iwicki, P. 2010. Sensitivity analysis of critical forces of trusses with side bracing. *Journal of Constructional Steel Research* 66: 923–930.

Iwicki, P. & Krajewski, M. 2013. 3D buckling analysis of a truss with horizontal braces, *Mechanics and Mechanical Engineering*, Vol. 17, No. 1: 49–58.

Jankowska-Sandberg, J. & Kołodziej, J. 2013. Experimental study of steel truss lateral-torsional buckling. *Engineering Structures* 46: 165–172.

Krajewski, M. & Iwicki. P. 2014. Stability and load bearing capacity of a truss with elastic braces, *Recent Advances in Computational Mechanics*, CRC Press Balkema, Taylor & Francis, London: 17–22.

Krajewski, M. & Iwicki. P. 2014. Stability analysis of a truss with sloping elastic braces, *Proceedings of EUROSTEEL: 7th European Conference on Steel and Composites Structures*, Book of abstracts and electronic version, Neapol: 150–152.

Krajewski, M. & Iwicki. P. 2015. Analiza wrażliwości siły krytycznej i badania nośności kratownicy ze sprężystymi stężeniami, *XI Konferencja Nowe Kierunki Rozwoju Mechaniki*, Wydawnictwo Uczelniane Politechniki Koszalińskiej: 53–54.

Pałkowski, Sz. & Kołodziej. J. 1995. Wybrane zagadnienia stateczności ustrojów sprężyście podpartych, *Zeszyty Naukowe Politechniki* Gdańskie, No. 522: 295–309.

PN-82/S-10052 — Obiekty mostowe. Konstrukcje stalowe. Projektowanie.

PN-90 B-03200. Konstrukcje stalowe. Obliczenia statyczne i projektowanie.

PN-EN 1993-1-1 2006. Eurocode 3: Projektowanie konstrukcji stalowych. Część 1–1: Reguły ogólne i reguły dla budynków.

Recent Progress in Steel and Composite Structures – Giżejowski et al. (Eds)
© 2016 Taylor & Francis Group, London, ISBN 978-1-138-02946-0

Preliminary experimental research on stability of truss' joint with positive eccentricity

M. Gordziej-Zagórowska, E. Urbańska-Galewska, Ł. Pyrzowski, P. Deniziak & A. Łukowicz
Gdańsk University of Technology, Gdańsk, Poland

ABSTRACT: Recently, a very large interest in lightweight steel structures made from cold-formed sections has been noticeable. In the design practice, a large emphasis is put on rational shaping of both the thin-walled elements and constructions designed on them. The aim of this paper is to present the methodology for preparation of experimental research that model the behaviour of members in trusses made of cold-formed sections with positive eccentricity in the joint and presentation of these research results. The research problem concerning the real load-carrying capacity of the compressed and bent chord of the lattice girder has been presented in the paper. The laboratory stand for experimental research is described and methodology of the tests presented. Results of the tests which gave the basis for the verification of the research model's and stand's project are presented.

1 INTRODUCTION

1.1 *General*

Recently, a very large interest in lightweight steel structures made from cold-formed sections has been noticeable (Garstecki et al. 2003), (Szychowski, 2008), (Szychowski, 2015), (Rzeszut & Garstecki, 2006), (Mądry, 2006). In the design practice, a large emphasis is put on rational shaping of both the thin-walled members cross-sections and constructions designed on them. Despite the fact, that new research is conducted in this domain, resulting in elaboration of new standards, some aspects of work in this type of constructions remain unresearched and unknown. Therefore, many issues still require detailed numerical analysis and experimental research. The aim of this paper is to present the methodology for preparation of experimental research that model the behavior of members in trusses made of cold-formed sections with positive eccentricity in the joint and presentation of these research results.

1.2 *Research problem*

This paper mainly focuses on system solutions for steel single storey buildings, in which the main support systems are made of frames with truss stiffeners made of cold-formed open cross-sections. In the construction of a typical, mono-pitch, trapezium lattice girder, assuming a fixed spacing between the nods, the angle for brace member inclination changes. The larger the angle, the greater positive eccentricity, and therefore the value of shear force. The area where greatest positive eccentricities occur, is located around the ridge. In accordance with the current state of knowledge presented in the standard (PN-EN 1993-1-8, 2006), when dimensioning the lattice girder's chord, one should take into consideration the eccentricity that leads to the necessity for local increase in the chord's section in the joint area. Practically, this is realized by strengthening the chords though the use of channel-section covers, as shown in Figure 1.

Considering the above, the following research hypothesis was assumed: the load-carrying capacity of the compressed and bent chord of the lattice girder made of cold-formed open cross-sections is

Figure 1. Joint with strengthening covers: A–truss' chord, B–strengthening cover (two-sided) made of channel-section, C–truss' members.

greater that it has been known from hitherto methods of steel construction dimensioning, due to local support conditions for the hat-section member's walls occurring in the truss' joint area.

In order to verify the above hypothesis, experimental research was conducted. Prior to launching the research, a numerical model of the construction designed for research purposes was created. The aim of the preliminary analysis was to verify both the geometry and the static research model, as well as to confirm the research assumptions.

2 PRELIMINARY NUMERICAL ANALYSIS

2.1 *Research model*

The research on stability of the compressed member, additionally loaded with a local bending momentum was planned in a 1:1 scale, on models of lattice girder with the following dimensions: 2000 × 1315 mm (Fig. 2).

The research model was designed from thin-walled cold-formed open cross-sections. The chords design from the hat-section H 39/117/106/117/39 × 2, and the brace members from channel-sections C 17/75/100/75/17 × 2. The assumed sections were made of galvanized steel S350GD with zinc surface Z275MA. All the connections within the truss' joints were designed as screw connections made with six M12 kl. 8.8 screws, placed in the construction in accordance with Figure 2a. Due to a large angle of brace members –60°, which is characteristic for this type of girders, positive eccentricities occur in the chords' joints. For the purpose of the analysis, the joint marked in the Figure 2a located on the compressed chord was considered.

The research model was loaded with two concentrated forces (Fig. 2b). Force *H* results in pressure on the lower chord, while force *P* causes, through natural distribution of force in the joint subjected to eccentricity, local bending of the lower chord in the joint area.

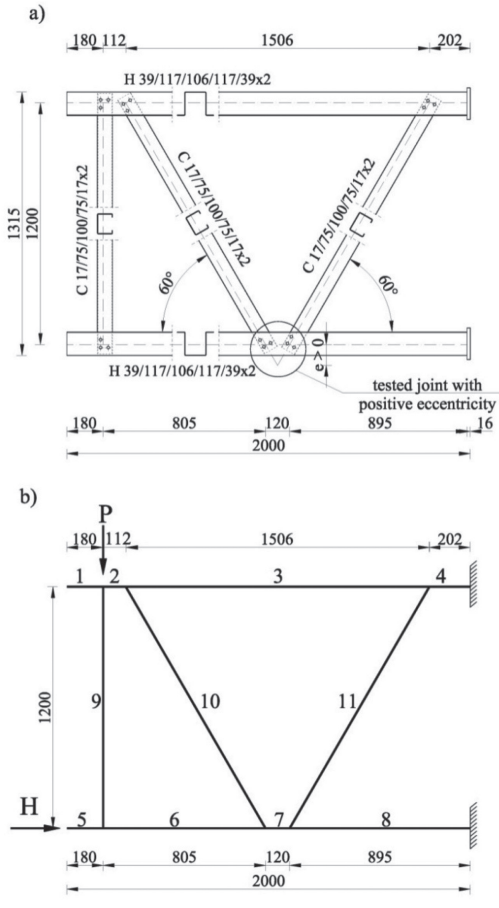

Figure 2. Research model: a) view of the construction, b) static scheme.

2.2 *Preliminary numeric model*

The purpose of a preliminary numerical analysis was to determine the following parameters: a detailed selection of the members cross-sections shapes, the proper static scheme and sequence of construction loads. The parameters had to be selected so as to restore the stress state in a real truss with the eccentric joint. Establishing of this data was necessary to design an appropriate experimental station.

The preliminary numerical analysis was conducted with the use of Marc Mentat—MSC Software. For computational modeling of the research model, shell elements were used. Discretization of the model was performed with the use of 4-node 'thin shell' elements, shaped as close to a square as possible. The construction and meshing of the computational model was performed in the AutoCAD program, with the use of 3D shell elements. Later, a ready, meshed model was imported into the Marc Mentat program, where geometric shapes were mapped with specific finite elements and material features. Supports and loading was also defined at this step. Figure 3 presents geometry of the preliminary numerical model uploaded into the Marc—Mentat program.

In the preliminary analysis it was assumed that the members in the joints will be connected with welds for which a model was made with the use of (3 and 4-node) shell elements of great stiffness, in such a way, as to make them a good substitute for unbuckled joints which will not be deformed under load pressure.

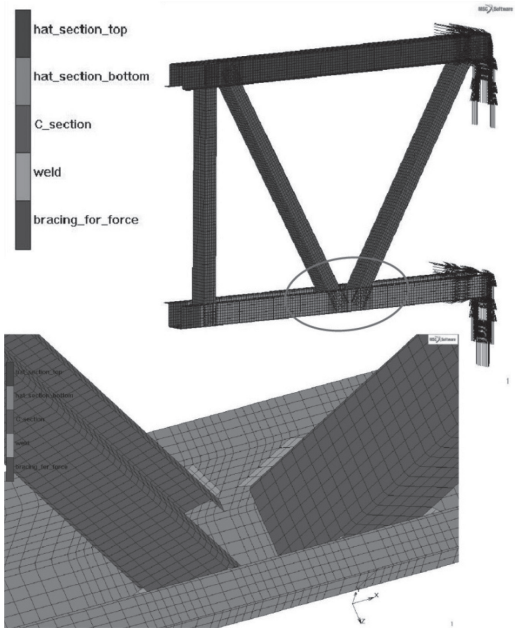

Figure 3. Preliminary numeric model.

It was found that at this stage the rigid joints model is at a sufficient level of accuracy to achieve the objectives set out at the beginning. A complex issue of flexibility of such bolted connections in this type of joints will be taken into consideration during further stages of conducted numerical analysis with the use of relations established (Zaharia & Dubina, 2006) and (Słowiński et al. 2010).

Preliminary numerical analysis was conducted for two types of truss' models with varied thickness of members' walls. The first type of model was created from 5 mm thick shell elements (members) and 6 mm thick (chords), thereby creating sections insensitive to local instability (class 1 in accordance to the standard (PN-EN 1993-1-1, 2006). The second model was created in two variants from elements of the following thickness:

– brace members 2 mm, chords 2 mm (further referred to as "2/2" model),
– brace members 2 mm, chords 3 mm (further referred to as "2/3" model),

which, according to the standard (PN-EN 1993-1-1, 2006) classifies these sections to the fourth class (sections sensitive to local instability).

Both types of truss' models (insensitive and sensitive to local instability) were subjected to three types of analysis: Mechanically Nonlinear Analysis (MNA), Geometrically Nonlinear Analysis (GNA) and Geometrically and Mechanically Nonlinear Analysis (GMNA).

At the stage of preliminary numerical model, two material models were assumed, namely: a model made of a perfectly elastic-plastic material in which the border value for plasticity is 350 MPa and an elastic-plastic model with strengthen, with the slope in the plastic state at $\beta = 2.866°$ (Fig. 4). The value of elasticity in the module equals $E=tg\alpha$ and was established on the basis of mono-axis straining research described in point 3.2.

2.3 *Results of the preliminary numeric model*

Detailed research results for the preliminary numerical analysis were presented by the author in (Gordziej-Zagórowska et al. 2014). This paper only includes main conclusions resulting from the conducted analyses that influenced the project of the work station and the conduct of experimental research.

The analysis of the insensitive model on loss of stability was conducted on the model made of sections with 5 mm thick members' walls and 6 mm thick chords' walls. With the use of the physically non-linear analysis, both in case of model made of perfectly elastic-plastic material and model made of elastic-plastic material with strengthen, a creation of a plastic hinge was observed in the area of the top support joint. However, this joint is not representative for the analyzed case, as it constitutes a model support, and is not a support for the real construction. In all three types of analysis (MNA, GNA and GMNA) a distortional form of instability in brace members was also observed. This was caused by free buckling of the channel-section webs without edge stiffeners. Elevated values of shear stress in the bend and sheared joint were also observed.

The MNA and GMNA analysis for the truss' model made of members with walls sensitive to local instability were performed only for the elastic-plastic material with strengthen. The "2/2" model was subjected to all three types of analysis (MNA, GNA and GMNA), observing large deformations of the compressed hat-section chord (Fig. 5).

However, the analysis performed on the "2/3"model has shown that the weakest element of the construction is the compressed brace member.

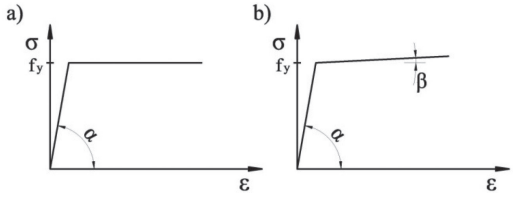

Figure 4. Used material models: a) perfectly elastic-plastic model, b) elastic-plastic model with strengthen.

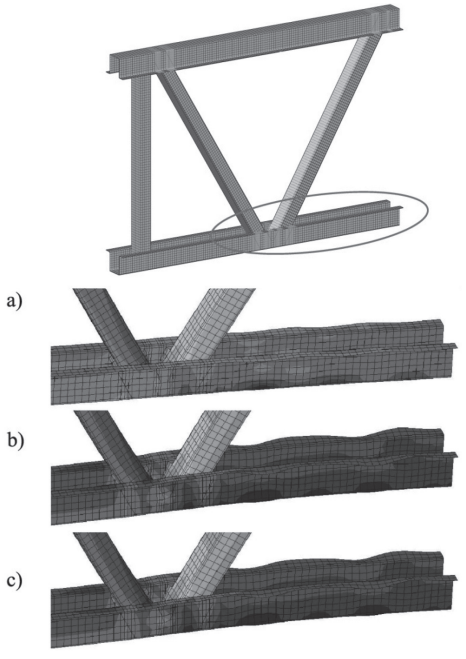

Figure 5. Results of preliminary numerical analysis: a) GNA, b) MNA, c) GMNA.

Local instability of the channel-section's walls that the brace member was made of was also observed.

Conducted research on the preliminary numerical model with stiff joints indicates to the correctness of the assumed research hypothesis, as none of the observed mechanisms of instability occurred in the compressed and bend area of the hat-section (in the joint). Furthermore, no additional material effort was observed.

Therefore, on the basis of the preliminary numeric analysis, it has been stated that the assumed geometry and the static scheme of the research model are adequate for performance of experimental research. As a representative construction for research, a model with walls sensitive to instability and chords made of 2 mm thick hat-sections with members made of channel-sections, also 2 mm thick, was chosen. The approximate maximum value of compression force H and bending force P, which are needed for destructive testing models, were established.

3 EXPERIMENTAL RESEARCH

3.1 *Research station*

The research was conducted in the one of the Gdańsk University of Technology laboratories. The aim of the experimental research was to determine the types of deformations of the hat-section's walls in the area of the analysed joint. The assumed goal is to perform research on 6 models. This paper presents the results of research performed on the first model.

The dimensions of the research model are presented on Figure 2. Due to the limitations of the measurement equipment and technical possibilities within the laboratory, at the stage of designing the research stand, it has been decided to turn the research model by 90° during experimental phase (assuming dead load of the construction as negligible). Figure 6 presents the design of the research stand. Due to thickness of walls of the sections that model is made of (2 mm), it was necessary to appropriately strengthen both the supporting joint and the places where the concentrated forces were applied.

In order to assure a free movement of the C joint under the bending force P, it was not possible to introduce the compressing force through an actuator, as this would result in the change of the static scheme of the research model that was anchored as an cantilever. Such a solution could limit the free displacement of the truss in the C joint. Therefore it has been decided to introduce the compression force H by means of compression. In order to achieve this, a special compressing head was designed (presented on Figure 7). This head was connected to the foundation with two symmetrically located straining elements made of two flat bars and a turnbuckle each. The straining elements were fixed to anchoring beams, which were fixed to special anchoring rails in the laboratory's floor plate. Through this solutions, it was possible to apply the compression force H to the analysed hat-section of the truss' chord while allowing the C joint to move freely.

During the research, the following measurement equipment was used. Three inductive sensors with measuring range of ±100 mm were used and located on the construction in accordance with the scheme presented in Figure 8. The X and Y inductive sensors measured the movements of the research model in the banding axis, while the Z sensor measured the movements of the bending axis. For measurement of the deformations, linear electrical resistance strain gauges LY11-6/120A were used for four measurement cross-sections. Three cross-sections were located accordingly on the compressed hat-section chord: 1–1 above the researched joint, 2–2 in the axis of the joint and one additional section 4–4 on the compressed brace member. The placement of strain gauges was presented in Figure 8. In total 16 strain gauges, including one compensational strain gauge, were used.

During the research, the concentrated forces P and H were applied to the construction be means of an expansion bolt and two turnbuckles (Figs. 6, 7). The value of the bending force P was registered by

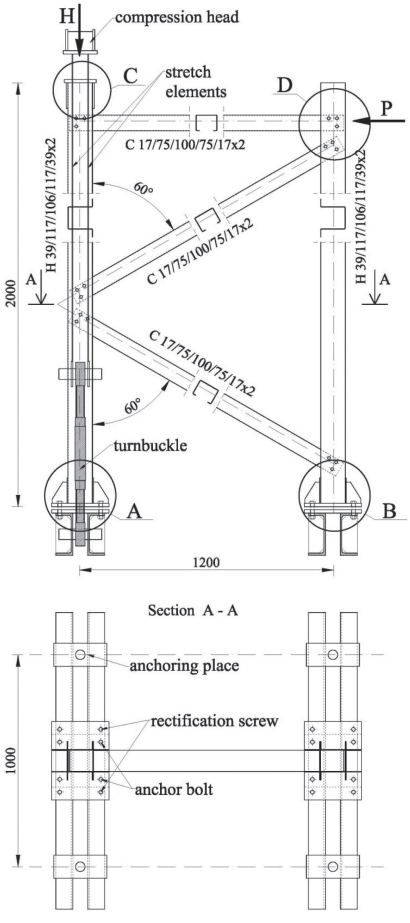

Figure 6. Design of the research station.

means of a dynamometer N.B.C. Elettronica, with a nominal range of ±100 kN, located between the expansion bolt that was causing the bending force *P* and the compressed chord of the construction (Figs. 7, 8). Whereas the value of the compressing force *H* was measured with a dynamometer CZAH CT-25 with nominal range of –250 kN, located between the compressing head and the compressed chord of the research model (Figs. 7, 8).

3.2 *Results of preparatory experimental research*

Prior to conduct of research, a static test was performed for mono-axis strain of steel on a ZWICK / ROELL Z400 machine with 50 kN head. Three samples were taken from both the hat-section and the channel-section for all six models designated for the destructive tests. On the basis of this research, the following average values for material constants were achieved:

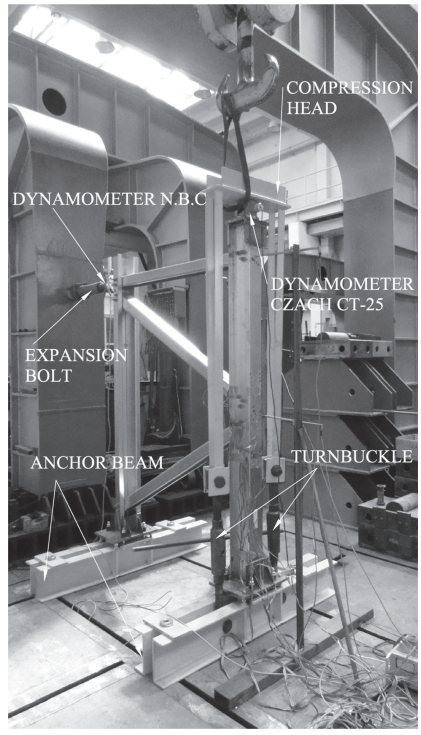

Figure 7. View of the research station.

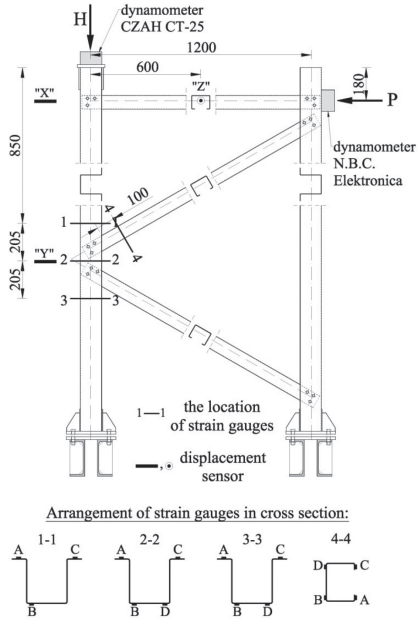

Figure 8. Placement of strain gauges and inductive sensors on the research model.

– hat section $E = 204$ GPa, $f_y = 400$ MPa,
– channel section $E = 185$ GPa, $f_y = 370$ MPa.

The above indicates that the steel used for the production of sections came from various batches.

The research was started by measuring the compliance of the research model with the project. The length of all truss' members was checked together with the joints space with accuracy up to ±1,0 mm. The slopes of the truss' members against the chords was measured with accuracy of up to ±1,0°. The dimensions of the cross-sections were also checked. It has been stated that the accuracy of production complies with the standard (PN-EN 1090-2+A1:2012, 2012).

Application of load to the construction begun with the compressing force H, gradually increasing its value. Introduction of the compressing force ended after reaching the value equivalent to the value of the H force, that is 115 kN (Fig. 9). The value of the compressive force H have not been changed since this moment, as the research model task only was to achieve a certain level of normal stresses in the analyzed cross-section. Further control of the force H was not possible due to the instrumentation used, and maintaining it at a constant level was not important as the purpose of the study was to achieve an eventual destruction of compression chord under bending moment in the area of analyzed joint. Next, the introduction of the bending force P begun. The introduction of the forces in time was presented in Figure 9.

It is noticeable that the increase in the value of the bending force P causes simultaneous decrease in the value of the compressing force H. The value of the force H decreased as the result of the tested truss member displacements under the influence of the force P.

While applying the compressing force H to the construction, no deformations were observed in the members of the research model. Local form of instability was observed only after application of the bending force P has begun. Upon reaching the value of the bending force equal to $P = 22.55$ kN and adequate compressing force $H = 83.3$ kN, local instability occurred in the hat-section around the analysed joint, as presented in Figure 10.

Figure 11 shows the normal strains in time, defined in measuring cross-sections 1–1, 2–2 and

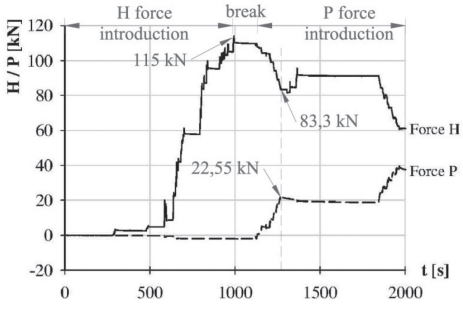

Figure 9. The process of introduction of forces in time (condensed forces H and P).

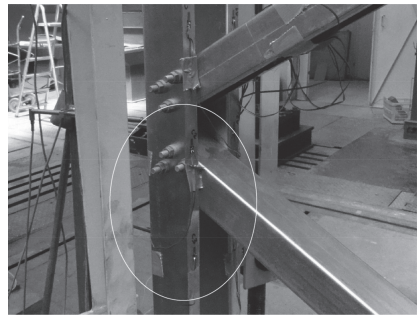

Figure 10. Local instability in the chord.

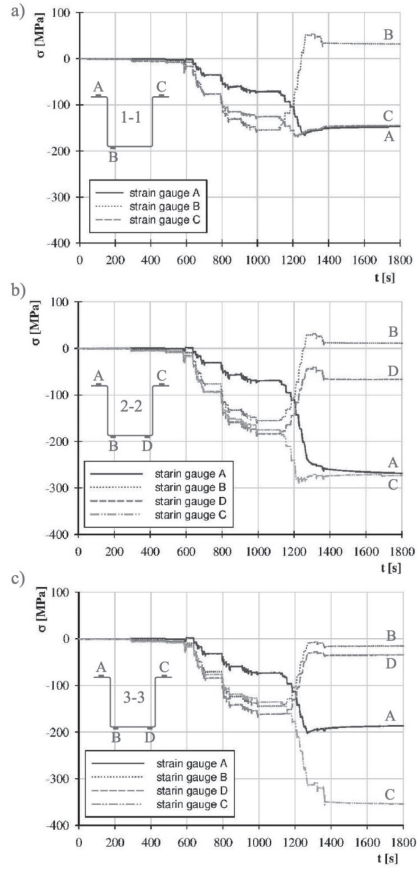

Figure 11. Normal stresses in time defined on the basis of measured displacements in cross-sections: a) 1–1, b) 2–2, c) 3–3.

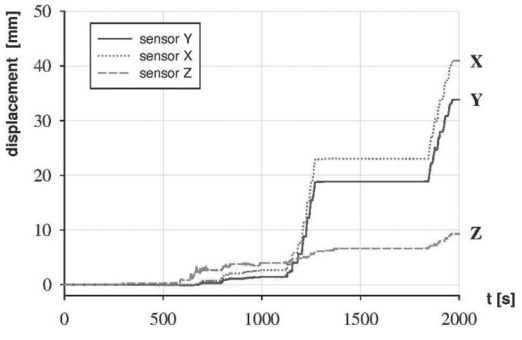

Figure 12. Model displacements in measuring points X, Y and Z (see Fig. 8).

3–3 on the basis of measured displacement. It has been observed that introduction of the compressing force *H* caused (unintentional) twisting of the compressed chord in the research model, as presented on the results from the strain gauge "A". This appeared throughout all three measurement sections. Introduction of the bending force *P* caused further differentiation of strains in separate measurement sections, causing reduction or increase of compression strains, depending on the bending moment.

The displacement control conducted during straining has shown that the researched model has displaced from the axis of compressing and bending (Fig. 12, gauge Z) already at the moment of application of the compressing force *H*. This was a consequence of uneven introduction of the compressing force *H*, which could contribute to the twisting of the section.

4 COMPARISING THE PREPARATORY RESULTS OF EXPERIMENTAL AND NUMERICAL RESEARCH

To compare experimental results with the results of numerical analysis, FEM model was modified with the following parameters: introduction of the experimentally determined average value of the members material constants; the history of the load used in accordance with experimental research (Fig. 9) and changing of the welded joints into the bolted joints.

The model of a bolted connection was performed in the Marc Mentat program by two-node beam elements inserted in places where bolts really occurred.

As we did not achieve the ideal bending only in the plane of the truss, so to compare the results, the strain gauges B, D and A, C readings were calculated as mean values what allow compensating the effects of inadvertent bending. Comparison of stresses in sections 2–2 and 3–3 is shown in Figure 13. Based on a comparison graphs derived from experimental research (Fig. 13) and numerical analysis performed with a new model with bolted connections in the joints (Fig. 14), we stated sufficient compatibility of the tests results.

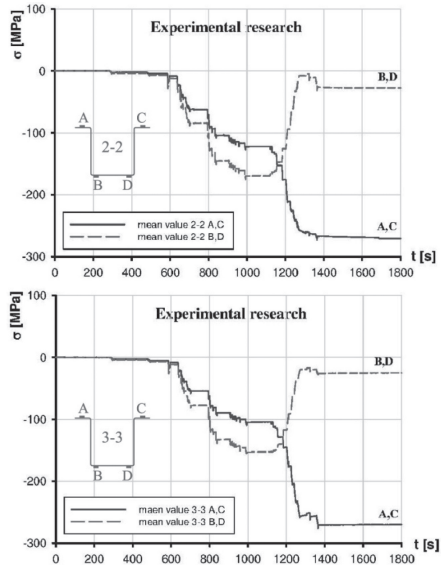

Figure 13. Normal stresses in time in the sections 2–2 and 3-3 identified on the basis of experimental research.

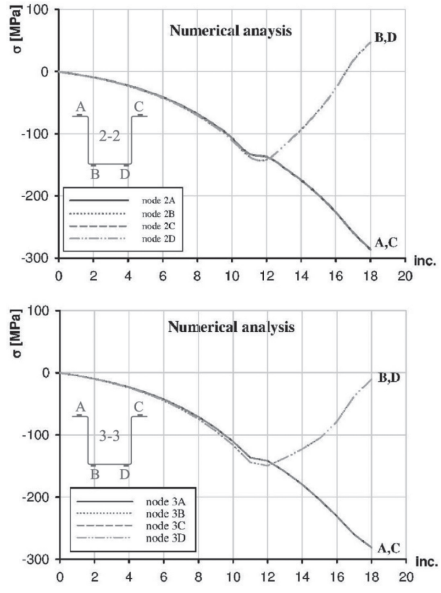

Figure 14. Normal stresses in time in the sections 2–2 and 3–3 identified on the basis of numerical analyses.

5 SUMMARY

The conducted research and its results allow us to achieve all the objectives established at the beginning. It was: to verify both geometry and static model, to design the station and to confirm the research assumptions. It has been concluded that the experimental model itself does not require introduction of changes. However, it is essential to introduce changes to the construction of the research stand. Prior to the research phase on the next research models, elimination of the model side displacements should be ensure. The compressing head should also be redesigned as to assure that no random twisting can appear in the compressed truss' chord.

The results gained after introduction of changes to the research stand and conduct of the final tests on 5 models will constitute solid ground for validation of the numerical model of the analysed joint and will enable full verification of the research hypothesis, which will be presented in the next publication.

REFERENCES

Garstecki, A., Kąkol, W., & Rzeszut, K. 2000. Analysis of thin-walled bars with open and closed-open cross-sections. *Engineering Transaction* (48): 345–355.

Garstecki, A., Kąkol, W., & Rzeszut, K. 2003. Global and local stability analysis of thin-walled beams. *Metal Structures: Design, Fabrication, Economy*: 61–66.

Gordziej-Zagórowska, M., Urbańska-Galewska, E., & Jankowski, R. 2014. Modeling of truss with cold-formed section and positive eccentricity in the node. *Structure and Evironment* (4/2014): 24–34.

Mądry, D. 2006. Niestateczność miejscowa trapezowego przekroju zginanego z uwzględnieniem sprężystego utwierdzenia ścinek. *Inżynieria i Budownictwo* (1/2006): 55–58.

PN-EN 1090-2+A1:2012. 2012. *Wykonanie konstrukcji stalowych i aluminiowych. Część 2: Wymagania techniczne dotyczące konstrukcji stalowych*.

PN-EN 1993-1-1. 2006. *Eurokod 3: Projektowanie konstrukcji stalowych. Część 1-1: Reguły ogólne i reguły dla budynków*.

PN-EN 1993-1-8. 2006. *Eurokod 3: Projektowanie konstrukcji stalowych. Część 1–8: Projektowanie węzłów*.

Rzeszut, K., & Garstecki, A. 2006. Zagadnienia niestateczności prętów z kształtowników giętych. *Inżynieria i Budownictwo* (3/2006): 166–169.

Słowiński, K., Swierczyna, S., Wuwer, W., & Zamorowski, J. 2010. Podatność połączeń zakładkowych w konstrukcjach stalowych z kształtowników giętych. *Inżynieria i Budownictwo* (5-6/2010): 327–331.

Szychowski, A. 2008. The stability of eccentrically compressed thin plates with o longitudinal free edge and with stress variation in the longitudinal direction. *Thin-Walled Structures 46*(5): 494–505.

Szychowski, A. 2015. Stability of cantilever walls of steel thin-walled bars with open cross-section. *Thin-Walled Structures* (*94):* 348–358.

Zaharia, R., & Dubina, D. 2006. Stiffness of joints in bolted connected cold-formed steel trusses. *Journal of Constructional Steel Research*, *62*(3): 240–249.

Joints and connections

This page intentionally left blank

Recent Progress in Steel and Composite Structures – Giżejowski et al. (Eds)
© 2016 Taylor & Francis Group, London, ISBN 978-1-138-02946-0

Durability assessment of connections between sandwich panels and purlins

M. Górski & A. Kozłowski
Rzeszów University of Technology, Rzeszów, Poland

ABSTRACT: Results of experimental research of the durability of single connection between sandwich panels and purlins subjected to repeatedly variable loads has been presented. Subsequently the influence of this factor on the change of ability to stabilization of steel purlins by sandwich panels in time has been analyzed using GMNIA. The values of variable loads acting on fasteners has been determined using numerical analysis including fluid mechanics. Wind and snow actions on the roofs of structures has been derived from climatic data obtained from Polish Institute of Meteorology and Water Management.

1 INTRODUCTION

The lateral-torsional buckling is a kind of the loss of global stability of bended element and depend on buckling of compressed part (e.g. flange) of element with simultaneous twisting of section (Timoshenko & Gere 1961, Pałkowski 2013). This phenomena can lead to significant decrease of element resistance in comparison to resistance of its cross-section. Therefore actions in order to eliminate this instability are desirable. It can be achieved mostly by lateral supports of compressed parts of elements. In case of purlins stabilization, the sheeting acting as diaphragm can be used. As far as purlins stabilization by corrugated sheet has been enough studied (ECCS 1995, Bródka et al. 1999) and is widely used in practice, the cooperation with sandwich panels still raises doubts among designers. The main worries relate to insufficient durability of connections due to small thickness of face sheets (Gosowski 2008) which do not exceed 0.5 mm. This paper shows the results of research about the durability of single connection.

The studies of sandwich panels ability to laterally support the purlins started in 90s of XX century with the prevalence of using self-drilling screws as a fasteners in connections between these elements (Fig. 1). The results of numerous investigations (Baehre & Ladwein 1994, Dürr et al. 2007, Misiek et al. 2010, Dürr et al. 2011, Käpplein & Misiek 2011, Georgescu & Ungureanu 2012) proved that despite of difference in comparison to corrugated sheets way of connecting elements and forces distributions, the sheeting made of sandwich panels has sufficient resistance and stiffness to stabilize purlins, at least initially. However taking advantage of sandwich panels as stabilizing elements in designing structure in Structural Class II (EN 1993-1-3) is still rare.

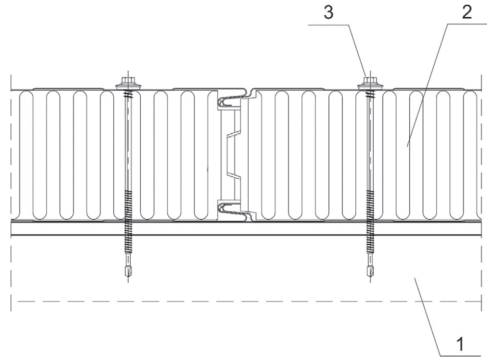

Figure 1. Connection between purlin (1) and sandwich panel (2) with use of self-drilling screw (3).

2 STABILIZATION OF PURLINS BY SANDWICH PANELS

The use of long fasteners as well as flexible core of sandwich panels result in negligible stiffness of connections between stabilized elements and external sheets. Consequently total load in sheeting plane has to be transferred by the internal sheets only. It is worth to mention that they are not connected with each other by seam fasteners. Therefore including cooperation between purlins and covering made of sandwich panels in calculations should be based on the assumption of independent action of each panel (Fig. 2).

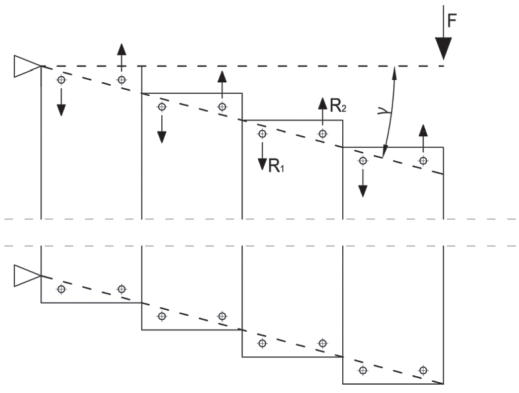

Figure 2. Assumption of transferring load F acting in sheeting plane by sandwich panels.

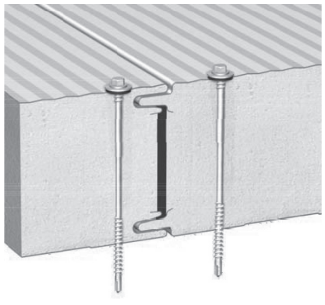

Figure 3. Correct connection between sandwich panels and purlins to designing in II Structural Class.

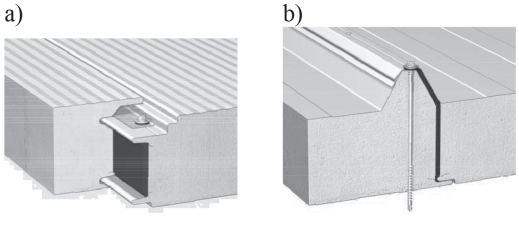

Figure 4. Incorrect connections between sandwich panels and purlins to designing in II Structural Class. a) – the hidden fastener, b) – connection on the top of the fold.

The stabilization moment induced by the pair of forces R_1–R_2 arisen in fasteners of each panel balances the external moment caused by a shear force acting relative to the center of the gravity of that panel (ECCS 2013). It follows that sandwich panels may be used as stabilization only if at least two fasteners are used to connect each panel's internal sheet with purlin (Fig. 3). Meanwhile solutions recommended by producers of sandwich panels often preclude using them to design in II Structural Class (Fig. 4) what is not correct.

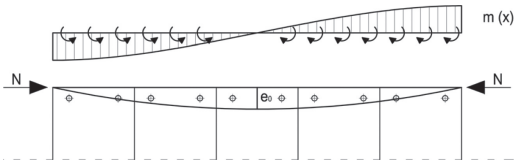

Figure 5. Stabilization moment distribution along the purlin induced by bow imperfection of compressed flange.

Assuming initial imperfection of compressed flange of purlin as a sinusoidal half-wave, the maximum stabilization moment occurs at the supports, where the angle between axis of ideal and deflected element is the biggest (Fig. 5).

3 INFLUENCE OF GAPS IN CONNECTIONS ON PURLINS RESISTANCE

The FEM analysis of exemplary purlin has been conducted to visualize the influence of possible gaps in connections on resistance of purlin stabilized by sandwich panels (Górski 2015). The cold-formed Z-section purlin with static schema and dimensions shown in Fig. 6 has been considered in Autodesk Simulation Mechanical software.

Additional truss elements in top flange's plane representing the behavior of sandwich panels as stabilizing elements has been assumed in model (Fig. 7). Their properties were determined on tests. Furthermore, the possibility of initial gaps (Δ_0) due to ovalisations of holes for fasteners has been included in range 0–5 mm (Fig. 8).

The initial imperfection consisted of combination of global, local and distortion instability of purlin (Fig. 9) with suitable amplitudes based on EN 1993-1-1, EN 1993-1-3, EN 1993-1-5 and EN 1993-1-6 has been assumed in GMNIA analysis (Fig. 10).

The results show significant decrease of purlin's resistance due to gaps appearance (Fig. 11). Moreover, the failure mode depends on value of the gaps (Fig. 12).

In all cases the connections between sandwich panels and purlin ran out of resistance before the purlin was destroyed.

4 INVESTIGATION OF GAPS IN CONNECTIONS BETWEEN SANDWICH PANELS AND PURLINS

4.1 *Calculations of forces in connections*

According to ECCS 2013, stabilization forces in the most strenuous fasteners in case of two fasteners per panel can be calculated from formula (1):

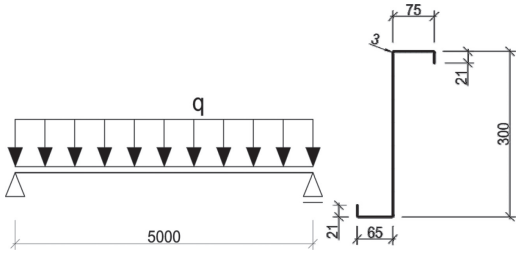

Figure 6. Static schema and dimensions of analyzed purlin.

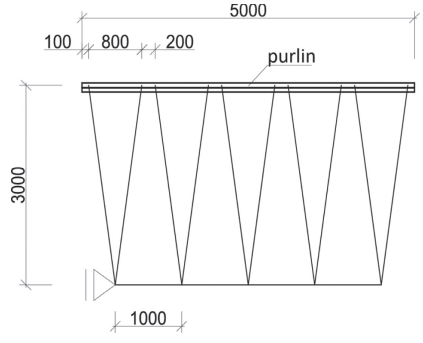

Figure 7. Additional truss elements representing behavior of sandwich panels.

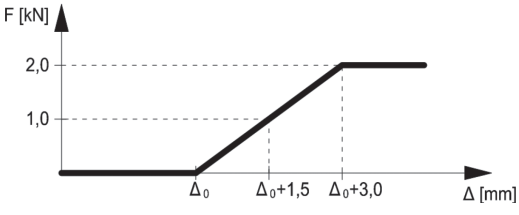

Figure 8. Force-displacement curve of each truss element.

$$V_{s,\max}^{M} = \frac{M_{s,\max}}{c} \tag{1}$$

where:

$$M_{s,\max} = m_{i,\max} \cdot B = F_i \cdot \frac{\pi}{L} \cdot e_0 \cdot \alpha \cdot B \tag{2}$$

- α – amplification factor including effect of 2nd order theory
- c – distance between two fasteners
- B – width of the panel
- F_i – axial force in compression flange of stabilized element

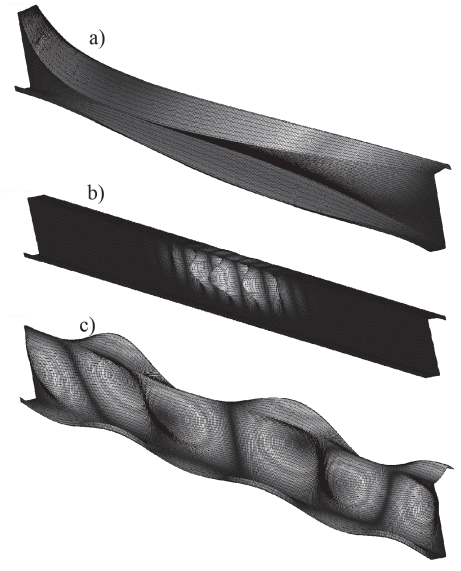

Figure 9. Forms of global (a), local (b) and distortion (c) instability of purlin.

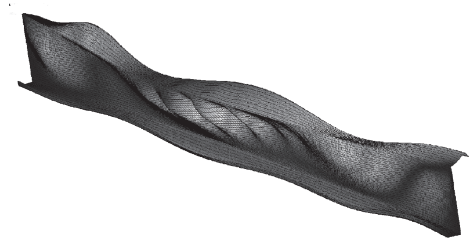

Figure 10. Initial imperfection of model.

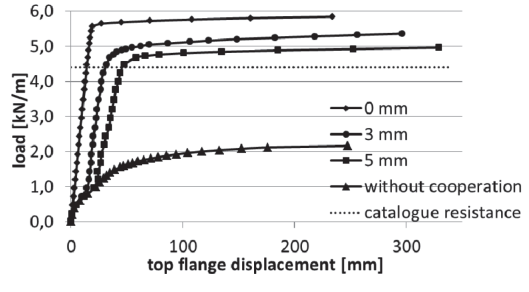

Figure 11. Load-displacement curve of top flange of purlin for various values of gaps.

$$F_i = \frac{M_k}{h} \tag{3}$$

- h – height of stabilized element
- M_k – bending moment in stabilized element
- L – span of stabilized element

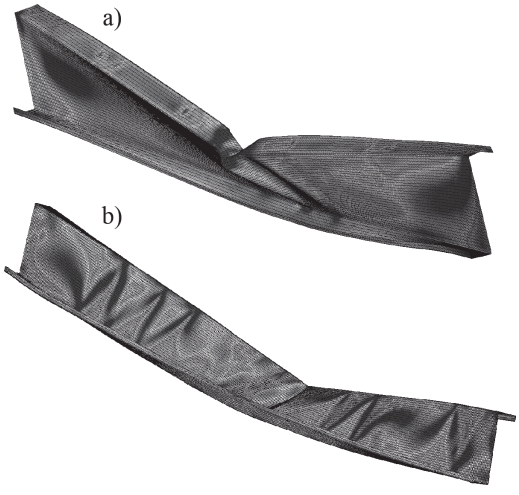

Figure 12. Failure modes for purlin with no gaps (a) and 5 mm gaps (b) in connections with sandwich panels.

e_0 – value of initial imperfection
S_i – stiffness of sandwich panel

therefore:

$$V_{s,\max}^{M} = \frac{M_k \cdot \pi \cdot e_0 \cdot \alpha \cdot B}{c \cdot L \cdot h} \tag{4}$$

assuming:
e_0 = L/500 for sections assigned to LTB buckling curve a,
$M_k = ql^2/8$ for static schema as a simple beam,
B = 1 m as an average width of a panel, the final formula takes the form (5):

$$V_{s,\max}^{M} = \frac{q \cdot L^2 \cdot \pi \cdot \alpha}{4000 \cdot c \cdot h} \tag{5}$$

For example, the forces in connections of purlin analyzed in Section 3, assuming design load from catalogue $q = 4.4$ kN would have follow value:

$$V_{s,\max}^{M} = \frac{4.4 \cdot 5^2 \cdot 3.14 \cdot 2}{4000 \cdot 0.9 \cdot 0.3} = 0.64 \text{ kN}$$

The forces in fasteners resulting from stabilization of the supporting structure depends mainly on the load acting on the stabilized elements, the span and height of these elements, the 2nd order theory effect and the distance between fasteners. These variables usually vary in the following limits:

– length: L = 4 ÷ 8 m,
– height: h = 0.2 ÷ 0.4 m,
– distance between fasteners: c = 0.7 ÷ 0.95 m,
– 2nd order theory effect: $\alpha = 1 \div 4$.
– q can be assumed as the average repeatable load acting on a purlin in [kN/m]. It depends on spacing between elements (usually 2 ÷ 4 m) and value of surface load from snow and wind.

Data from Polish Institute of Meteorology and Water Management (PIMWM) for selected places in Poland were used to estimate the average repeatable load acting per square meter of roof sheeting.

Based on values of the snow cover thickness in last 10 years, the average repeatable load has been initially assumed in the range 50–100 N/m^2. More accurate analysis of snow load will be the aim of further investigations.

The wind load is much more complex to determine. It depends not only on wind speed and direction (Figure 13), which constantly changing in time (see Table 1), but also on the location of considered element in the structure. Moreover, the wind velocity obtained from PIMWM is the value averaged over 10 min, whereas real wind gust are much shorter and usually do not exceed 3 seconds. Dependency between measurement time and average wind velocity is known as The Durst Curve (Figure 14).

Based on data derived from Polish Institute of Meteorology and Water Management and including additional factors mentioned above, the average wind velocity has been assumed in the range 3–8 m/s. To determine the wind pressure acting on each part of building covering, numerical model of typical hall has been created and analyzed in Autodesk Robot Structural Analysis Professional 2015 (Fig. 15). Robot 2015 has been equipped with a tool using fluid mechanics analysis called Wind Load Simulations. It allows to generate the pressures maps from wind blowing on a structure from

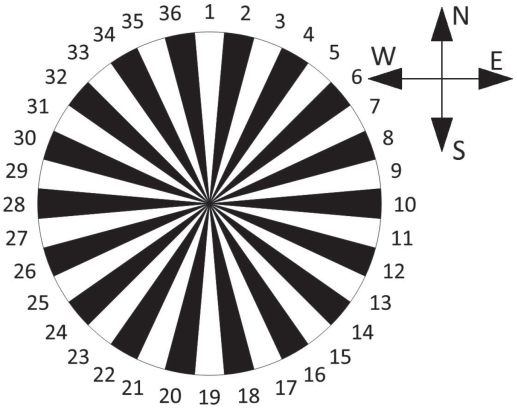

Figure 13. Designations of wind directions used in Table.1.

Table 1. Exemplary of wind data derived from PIMWM for Rzeszów.

Month	Day	Hour	Wind	
–	–	–	Speed [m/s]	Direction –
6	27	14	1	15
6	27	15	2	10
6	27	16	3	10
6	27	17	4	10
6	27	18	5	10
6	27	19	5	11
6	27	20	5	11
6	27	21	6	12
6	27	22	6	16
6	27	23	6	19
6	28	0	7	23
6	28	1	6	23
6	28	2	5	24
6	28	3	5	24
6	28	4	4	24
6	28	5	4	25
6	28	6	4	25
6	28	7	4	25
6	28	8	4	24
6	28	9	5	24
6	28	10	4	24
6	28	11	4	23
6	28	12	4	23
6	28	13	3	23
6	28	14	3	23
6	28	15	3	23
6	28	16	2	23
6	28	17	2	23
6	28	18	2	23
6	28	19	1	23
6	28	20	1	23
6	28	21	1	23
6	28	22	1	23
6	28	23	1	23
6	29	0	1	23
6	29	1	1	24
6	29	2	2	24
6	29	3	3	25
6	29	4	3	25
6	29	5	3	26
6	29	6	3	26
6	29	7	2	28
6	29	8	2	31
6	29	9	2	33
6	29	10	2	31
6	29	11	3	29

8 directions around building with various wind parameters.

Sample results derived from this analysis are shown on Fig. 16.

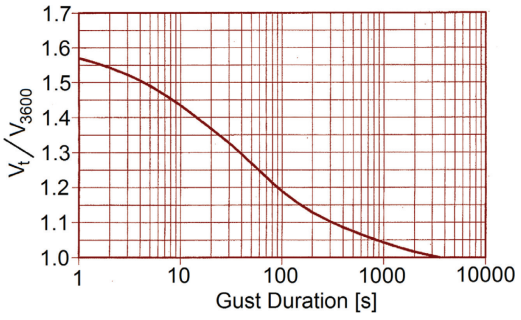

Figure 14. The Durst Curve (Durst 1960).

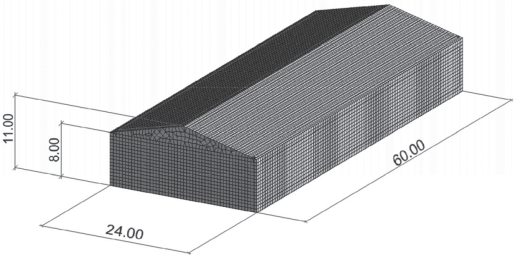

Figure 15. Hall model analyzed using Wind Load Simulations.

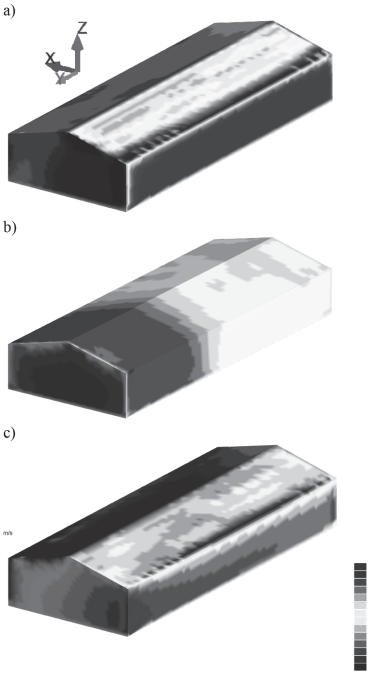

Figure 16. Pressures map for wind blowing with velocity 5 m/s. a) wind blowing on longitudinal wall (X direction) b) wind blowing on front wall (Y direction) c) wind blowing on XY direction.

Finally the values of average wind pressure acting on roof covering ranged from –120 to 90 N/m^2, depending on assumed wind velocity, direction and location of analyzed part of sheeting.

Summarizing, total load q acting on stabilizing element has been assumed in the range 10–400 N/m which results in values of force in single fastener from formula (5) not exceeded 200 N. Nevertheless value of 500 N in 10,000 cycles has been assumed in experimental research.

4.2 *Test standing*

The piece of sandwich panel with dimensions 50 × 60 cm has been fixed in supporting structure consisted of four angle members bolted with I-beams and with each other (Fig. 17). The piece of cold-formed channel section represented purlin has been connected with sandwich panel by single fastener. The repeatable force has been applied to one end of purlin by actuator Schenck 40 kN, and the displacement between sandwich panel and channel section has been measured by inductive displacement sensors (Fig. 18).

9 samples (PW-1–PW-9) of sandwich panels Balextherm PU-W-ST with polyurethane core thickness 100 mm and cladding thickness 0.5 mm

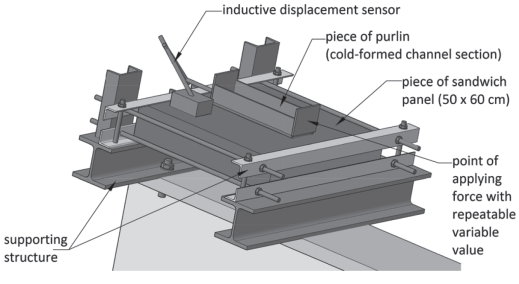

Figure 17. Scheme of test standing.

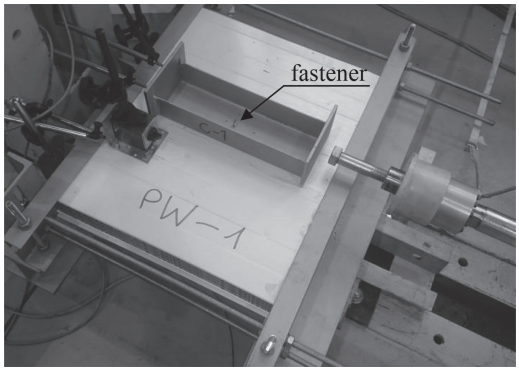

Figure 18. Picture of test standing.

has been tested. 125 mm self-drilled screws 6.3/5.5 with EPDM gasket has been used as fasteners. The purlin has been represented by cold-formed section U80 with 3 mm wall thickness.

At the beginning, the resistance of connection has been tested (sample PW-1). Then, the forces has been applied with values changing 10,000 times from 50 to 500 N in 3 different ways (Fig. 19):

a. sinusoidal with frequency 3 Hz (PW-2),
b. sinusoidal with frequency 0.2 Hz (PW-3),
c. trapezoidal, where duration of applying maximum force (500 N) equals 5 s, min. force (50 N) 1 s and force changed during 2 s in each direction (PW-4).

Additionally, tests with 2000 cycles of forces applied in the trapezoidal way with maximum values 600 N (PW-5), 700 N (PW-6) and 800 N (PW-7), as well as 1000 cycles of 900 N (PW-8) and 1000 N (PW-9) instead of 500 N has been conducted.

4.3 *Results*

Results of the tests in the form of force—displacement relationship has been presented in Fig. 20. The resistance of single connection equals 1.6 kN when permanent displacements occurs. It is noticeably higher value than $F_{b,Rd} = 0.82$ kN derived from EN 1993-1-1. Failure mode of internal sheet is presented in Fig. 21 and of external sheet in Fig. 22.

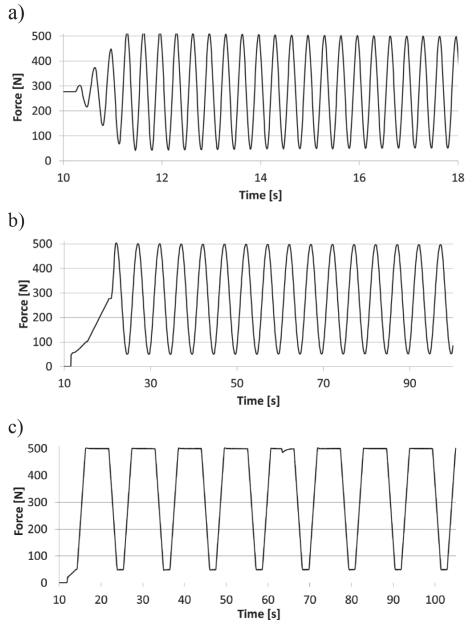

Figure 19. The initial portions of load spectrums during tests (description in text).

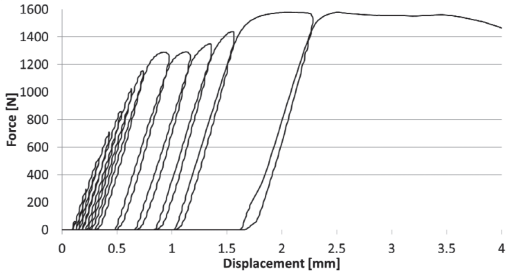

Figure 20. Dependence between force and displacement derived from resistance test of single connection.

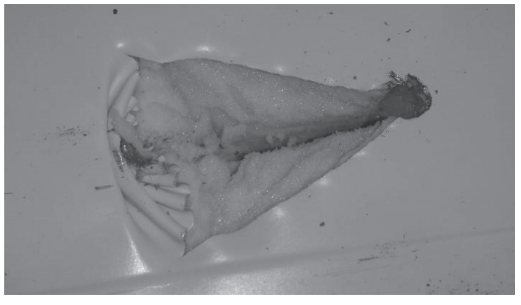

Figure 21. Failure mode of connection (internal sheet).

Figure 22. Failure mode of connection (external sheet).

Dependency between sandwich panel—purlin displacement versus time with different ways of applying force are shown on Figs. 23–24.

The conducted research revealed, that regardless of adopted way of applying force 500 N, no permanent displacement occurs after 10,000 cycles. Moreover increasing value of force to 700 N also did not affect in permanent displacement. For 800 and 900 N a slight growth of displacement in time was observed, but it did not exceed 0,1 mm during 1000 cycles. In case of force value 1000 N, pronounced increasement of displacement at the beginning was observed, but finally it stabilized on about 1 mm. It was probably caused by growth of connection stiffness due to formed corrugation of internal sheet (Fig. 25).

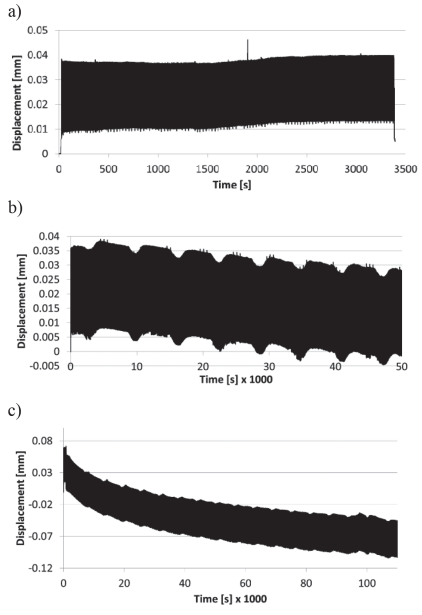

Figure 23. Dependence displacement—time for: a) sinusoidal with frequency 3 Hz; b) sinusoidal with frequency 0,2 Hz; c) trapezoidal way of load applying and maximum force 500 N.

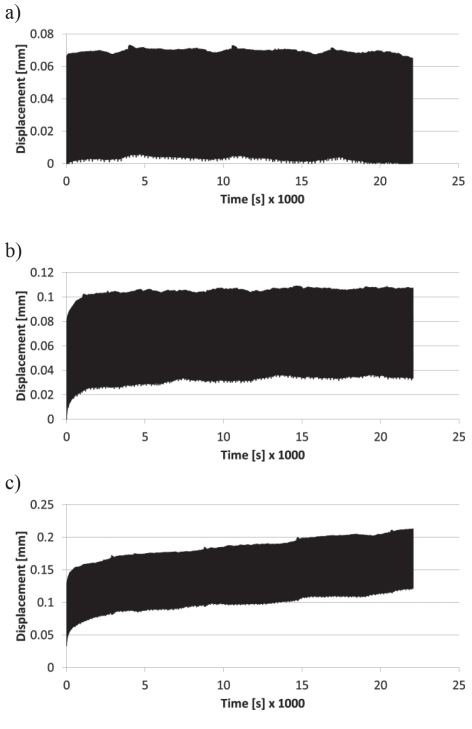

Figure 24. *Continued.*

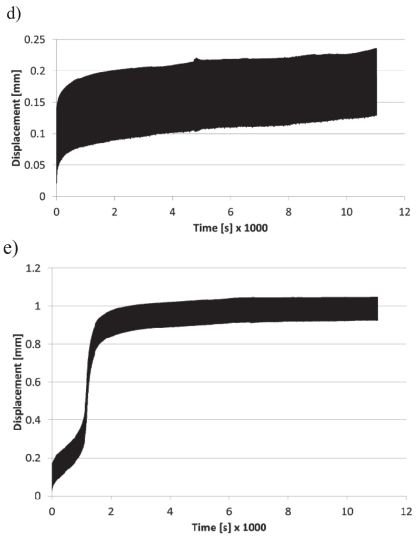

Figure 24. Dependence displacement—time for trapezoidal way of load applying and maximum force: a) 600 N; b) 700 N; c) 800 N; d) 900 N; e) 1000 N.

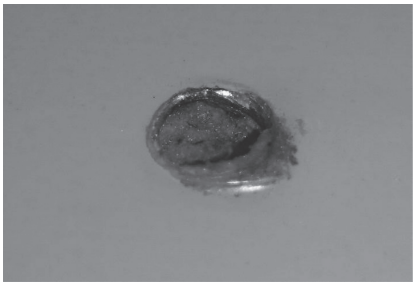

Figure 25. Slightly ovalized hole for fastener in internal cladding with visible corrugation of sheet.

5 CONCLUSIONS

Despite of extremely small thickness of sheets, connections between sandwich panels and purlins have enough durability to ensure the safe cooperation between these elements when are designed in II Structural Class. Results of tests show, that connections handle not only with forces induced by mean and repeatable climatic loads. Also values near the design resistance of connections and elements do not result in permanent strain, that could cause the gaps and reduce the resistance of stabilized element. Based on results of analysis using Finite Element Method, the potential gaps in connections are proved to induce noticeable decrease of purlins resistance, but only if theirs values reached at least few millimeters, whereas the maximum achieved permanent displacement in experimental research did not exceed 1 mm while applied force (1000 N) surpassed the designing resistance of connection (820 N). Nevertheless, the Ultimate Limit States of each connection between sandwich panels and purlins has to be proven before designing in II Structural Class according to EN 1993-1-3.

REFERENCES

Baehre, R. & Ladwein, Th. 1994. Diaphragm action of sandwich panels. *Journal of Constructional Steel Research 31*: 305–316.

Bródka J., Garncarek R., & Miłaczewski K. 1999. *Corrugated sheets in steel building (in Polish)*. Warszawa: Arkady.

Dürr, M., Podleschny, R. & Saal, H. 2007. Investigation of the torsional restraint of sandwich panels against lateral torsional buckling of beams). *Stahlbau* 76: 401–407.

Dürr, M., Misiek, Th. & Saal, H. 2011. The torsional restraint of sandwich panels to resist the lateral torsional buckling of beams. *Steel Construction—design and research* 4: 251–258.

Durst, C.S. 1960. Wind Speed Over Short Peri-ods of Time. *Meteorological Magazine* 89: 181–187.

ECCS 1995. *European Recommendations for the Application of Metal Sheeting acting as a Diaphragm—Stressed Skin Design*.

ECCS 2009. *Preliminary European Recommendations for the Testing and Design of Fastenings for Sandwich Panels.*

ECCS 2013. *European Recommendations On The Stabilization Of Steel Structures By Sandwich Panels*.

EN 1993-1-1 Eurocode 3: Design of steel structures—Part 1–1: General rules and rules for buildings.

EN 1993-1-3 Eurocode 3: Design of steel structures—Part 1–3: General rules—Supplementary rules for cold-formed members and sheeting.

EN 1993-1-5 Eurocode 3: Design of steel structures—Part 1–5: General rules—Plated structural elements.

EN 1993-1-6 Eurocode 3: Design of steel structures—Part 1–6: Strength and stability of shell structures.

Georgescu M. & Ungureanu V. 2012. Stabilisation of continous Z-purlins by sandwich panels: Full scale experimental approach. *The 6th International Conference on Coupled Instabilities in Metal Structures*, Glasgow.

Gosowski B. & Behr O. 2008. Testing of screw connections between sandwich panels and cold-formed channel purlins (in Polish). *Civil and Environmental Engineering* 50/2008: 73–82.

Górski M. 2015. Stabilization of Z-purlin by sandwich panels including ovalisation of holes for fasteners (in Polish). *Concrete and metal structures.* Bydgoszcz: Wydawnictwa Uczelnianie Uniwersystetu Technologiczno-Przyrodniczego w Bydgoszczy.

Käpplein, S. & Misiek, Th. 2011. Stabilisation of beams by sandwich panels. *EASIE report D3.3* – part 1,2 and 3.

Misiek, Th., Käpplein, S., Dürr, M. & Saal, H. 2010. Stabilisation of purlins by sandwich panels—new regulations and recent research results. *Proceedings of 18th CIB World Congress*, Salford.

Pałkowski Sz. 2013. *Steel structures (in Polish)*. Warszawa: Wydawnictwo Nakowe PWN.

Timoshenko S. & Gere J.M. 1961. *Theory of Elastic Stability.* International Student Editions, McGraw-Hill.

www.balex.com.pl.

www.autodesk.com/products/simulation/overview.

Recent Progress in Steel and Composite Structures – Giżejowski et al. (Eds)
© 2016 Taylor & Francis Group, London, ISBN 978-1-138-02946-0

FEM analysis of the extended end-plate splice of welded I-girders with multiple bolt rows and bolts per row

P. Kawecki & J. Łaguna
Design Office Mostostal, Warszawa, Poland

A. Kozłowski
Rzeszów University of Technology, Rzeszów, Poland

ABSTRACT: The aim of the paper is to present results of the FEM analysis by Abaqus software of three numerical models of the splice of welded girders of section 1500-12-470-18, with M24 grade 10.9 bolts. Extended end-plate 24 × 500 × 1600 mm of steel grade S355 with two, four and six bolts in the row close to tension flange were analyzed. Remaining, internal rows with only two bolts per row were placed every 120 mm. Analyzed by FEM connections are also calculated by component method of EN-1993-1-8 to assess ability of this method to design such joints. Comparison shows that moment resistances of analyzed joints calculated by component method are significantly bigger (22–86%) than obtained by FEA. Application of additional stiffeners leeds to increase participation in moment resistance bolts adjacent to stiffeners, but also to decrease participation of bolt rows above top flange and under stiffeners, what in results do not increase moment resistance of the joint.

1 INTRODUCTION

European code EN-1993-1-8 contains design procedures to calculate the design moment resistance $M_{j,Rd}$, and initial stiffness $S_{j,ini}$ of the bolted end-plate beam-to-column connection and beam splices. These procedures are addressed mainly to joints of rolled I section, and to connection with two bolts in each row. EC3 provisions are confirmed by many experimental tests. However extension of these design procedures to connections of welded sections beam with large height (≥ 1000 mm) can lead to wrong results. There is also only a few experimental tests of such beam splices, (SEI 1984, Morrison et al. 1986, Borgsmiller et al. (1995), Ryan (1999), Sumner (2003), Katula et al. (2009)). Reason of this is very high cost of these tests and difficulties with relevant laboratory equipment. Table 1 contains collection of tested splices of beam of height ≥ 1000 mm and with more than one bolt row between flanges. All these experiments, but (Katula et al. (2009)), were conducted in USA and concerns connections with no more than three bolt internal rows, located in tension zone between beam flanges. So results of these tests do not include information needed to assessment of internal forces distribution in connection with multi bolt rows placed on the whole beam height.

Table 1. Collection of the experimental investigations of beam splices h ≥ 1000 mm with multiply bolt rows.

Pos.	Autors	H[1] [mm]	ne/ni[2]	min hi/h[3]
1	SEI	1570	1/3	0,85
2	Morrison et al. 1986	750	1/3	0,72
		1170	1/3	0,81
		1570	1/3	0,77
3	Borgsmiller et al. 1995	1620	1/3	0,84
4	Ryan 1999	600	1/1	0,90
		1400	1/1, 1/3	0,83
5	Sumner 2003	1560	1/1, 1/2	0,88
		750	1/2	0,80
6	Katula et al. 2009	1000	1/2	0,78
			2/2	

[1]Beam height,
[2]Number of external/internal bolt rows,
[3]Range of zone without tensioned internal bolt rows.

In case of the need to transmit big bending moment in the joint designers very often apply connection with four or even six bolts in selected rows (Figure 1). EN-1993-1-8 do not cover such cases. There is few publication on how to extend EC3 rules to such cases (Schmidt (2008), Kozłowski &

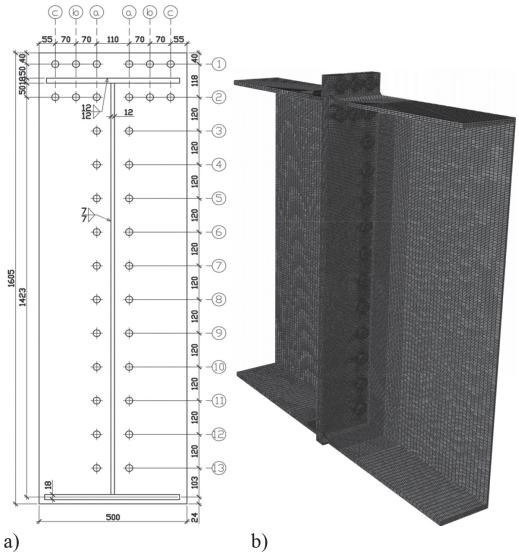

Figure 1. a) Scheme and b) FEM symmetric model as ½ of investigated beam splice. Beam section 1500-12-470–18 mm with end-plate 24 × 500 × 1600 mm.

Pisarek (2008), Demonceau et al. (2010), Weynand et al. (2012), Prinz et al. (2014)), but they are not confirmed by experiments.

The aim of the paper is to present results of the FEM analysis of three numerical models of the splice of welded girders of section 1500-12-470–18 mm, with M24 grade 10.9 bolts. Extended end-plate 24 × 500 × 1600 mm of steel grade S355 with two, four and six bolts in the row close to tension flange were analyzed. Remaining, internal rows with only two bolts were placed every 120 mm.

Analyzed by FEM connections are also calculated by component method of EN-1993-1-8 to assess ability of this method to design such joints. Ultimate moment resistance of joints was calculated using assumption that limit state is reached when average stress in one of the bolts exceeds $0{,}9f_{ub.}$ In the model with two bolt rows also effectiveness of the horizontal and vertical stiffeners used by designers to increase joint resistance has been checked.

Conventional design of simple and the most often used in Europe (covered by catalogue) joints of tall beams was based on the assumption that the whole bending moment is transmitted by bolt rows directly close to tension beam flange. The same assumption is also adapted in design practice of welded girders connection. According to USA regulations (Flush end Extended Multiple-Row Moment End-Plate Connections AISC (2002)) no more than two internal bolt rows in flush end plate (0/2) and no more than three (1/3) in extended end plate can be used in the calculation of design moment resistance of end-plate joints.

Traditionally, connections with multi bolt rows and with relatively thick end plate were calculated according to German publications with the assumption of linear distribution of internal forces and center of rotation of the joint located in the compressed flange of the beam.

According to Eurocode (EN 1993-1-8 and Joints in Steel Constructions. Moment Connections (1995)) design resistance of each bolt row is established by component method, taking into account design resistance of bolts, end-plates and another part of the connections. Prying effects are not directly shown in design procedures. It is allowed to take into account all bolt rows placed between beam flanges, provided that the effective design resistance of each bolt row is not bigger than 1,9 $F_{t,Rd}$ (EN 1993-1-8/6.2.7.2(9)). When one of the previous bolt rows not satisfied this condition, the linear reduction of effective design resistance of all next bolt rows, placed closer to compression flange should be apply. This criterion was recognized as sufficient to assess ability to plastic deformation of each bolt rows, allowing reaching limit resistance of adjoining bolt rows. Practical application of this criterion in case of rigid end plates, leads to linear bolt force distribution, with center of rotation in the compression flange. Results of FEM analysis of beam W760×265×220 splice of configuration (1/8) with two bolt rows (Kozłowski et al. (2013)) show that this criterion can be insufficient. It is worth to mention that additional limitation of number bolt rows taken into account is necessity to balance bolt forces with the resistance of compressed part of the joint $F_{c,fb,Rd}$ (EN 1993-1-8/6.2.6.7(1).

2 FEM ANALYSIS

Analysis were conducted by Abaqus software using 3D numerical models (Figure 1b).

The following non-linearity of steel material and bolts were included in the analysis:

- material, which allows to take into account parametric material characteristics for profiles, end plates, bolts, washers and nuts,
- geometrical, which includes influence of deformation, deflection and bolt prestressing,
- local contacts, area of bearing and friction between particular parts of the joint: end-plate-bolt head, nut-washer, bolt shank-bolt hole.

$\sigma - \varepsilon$ relationship for bolts in prestressed and non-prestressed connections was created on the base of own experimental tests of bolts with f_{ub} = 1040 MPa.

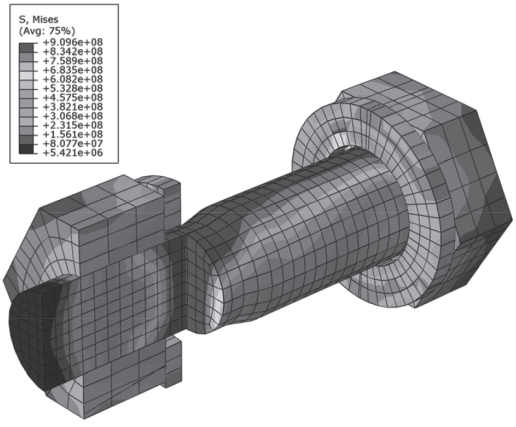

Figure 2. 3D Abaqus bolts model with washers end nuts.

Bolt model was validated by comparison to own experimental tension tests of prestressed and not prestressed one-bolt connections Figure 2.

Bolt model included separately parts of bolts as shank and tread with taking into account bolt bending. Influences of slip and deflection in tread-nut contact and flexibility in bearing zones of nut and head with washers and washer with end plate were included by introducing zone of specific properties.

Bolt preloading force $F_{p,Cd} = 0,7f_{yb}A_s$ was applied by shortening of bolt shank. Loading by bending moment was increased monotonically till reaching ultimate resistance value of one of the bolt.

For material of end-plates, beams and stiffeners stress—strain standard curve with hardening for steel S355 was used. These modelling procedure was verified by comparison to results of experimental tests of welded beam splice (Sumner (2003)).

Analysis allows to determinate following characteristics of analyzed connections in ultimate limit state:

- ultimate bending moment resistance, when force in one of the bolts reaches value $F_{t,b}$ = 318 kN, corresponding to the average stress in the bolt $0,9f_u$,
- value of the forces in particular bolts $F_{t,b}$,
- value of the prying forces in the bolts Q_b,
- value of the effective forces in the bolts (carrying bending moment in the joint) $F_{t,b,eff} = F_{t,b} - Q_b$,
- dimensions and range of the compression bearing stresses between end plates and location of resultant force,
- value of the displacement on the tension flange axis and angle of rotation of the joint.

Models of analyzed beam splices with two, four and six bolts around tension flange were presented in the Figure 3.

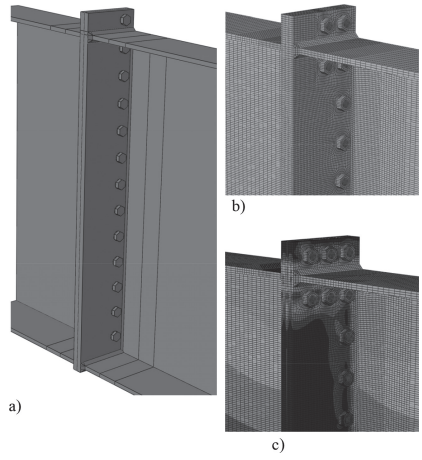

Figure 3. Analyzed multi row joints with a) 2, b) 4 and c) 6 bolts close to tension flange.

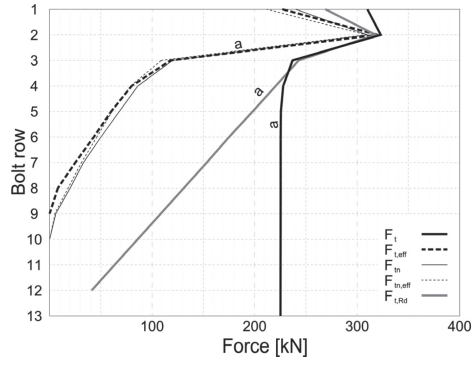

Figure 4. Bolt forces envelopes at the ultimate moment resistance of the splice-2 bolts per row; line marking: – bolt forces in prestressed connection F_t (bold line), in not prestressed connection F_{tn} (thin line), – effective bolt forces in prestressed connection $F_{t,eff}$ (bold dashed line), – effective bolt forces in not prestressed connection $F_{tn,eff}$ (thin dashed line), – effective ultimate bolt row forces acc. to component method $0,5_{FT,Rd}$ (grey bold line).

Results of the FEM analysis are shown in Figures 4–6.

3 RESULTS OF EUROCODE 3 CALCULATION

Analyzed by FEM connections were also calculated according to Eurocode EN-1993-1-8 component method.

Beam section 1500-12-470-18 mm; steel grade S355; t_f = 18 mm; t_w = 12 mm; h_o = 1482 mm;

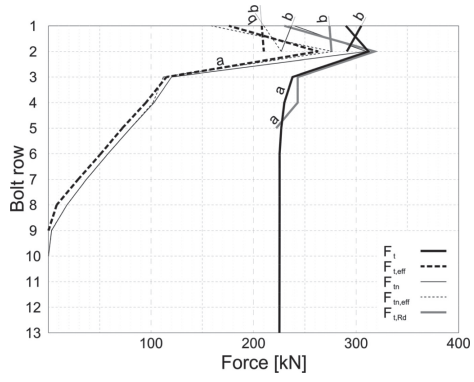

Figure 5. Bolt forces envelopes at the ultimate moment resistance of the splice-4 bolts per row (1 + 2); line marking:
– bolt forces in prestressed connection F_t (bold line), in not prestressed connection F_{tn} (thin line), – effective bolt forces in prestressed connection $F_{t,eff}$ (bold dashed line), – effective bolt forces in not prestressed connection $F_{tn,eff}$ (thin dashed line), – effective ultimate bolt row forces acc. to component method $0{,}5_{FT,Rd}$ (grey bold line); (a), (b) – vertical bolt-rows see Fig. 1.

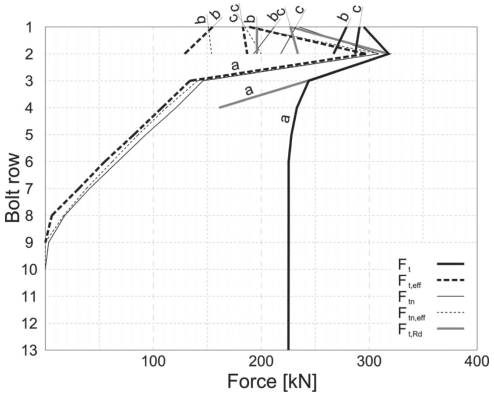

Figure 6. Bolt forces envelopes at the ultimate moment resistance of the splice-6 bolts per row (1 + 2); line marking:
– bolt forces in prestressed connection F_t (bold line), in not prestressed connection F_{tn} (thin line), – effective bolt forces in prestressed connection $F_{t,eff}$ (bold dashed line), – effective bolt forces in not prestressed connection $F_{tn,eff}$ (thin dashed line), – effective ultimate bolt row forces acc. to components method $0{,}5_{FT,Rd}$ (grey bold line); (a), (b), (c) – vertical bolt-rows see Fig. 1.

b_f = 470 mm; f_y = 355 MPa; W_y = 16572 cm^3 M_{Rd} = 5883 kN·m A_{fb} = 84,6 cm^2 $F_{t,fb,Rd}$ = 3003 kN $F_{c,fb,Rd}$ = 16572 · 0,355/1,482 = 3970 kN > 47 · 1,8 · 1,2 · 355 · 10^{-1} = 3604 kN

$c/t_w = 1500 - 2(18 + 12 \cdot 1{,}4)/12 = 127{,}5 > 124 \cdot 0{,}81 = 100$

End-plate 24 × 500 × 1600 mm; steel grade S355;

Bolts M24–10.9: d = 24 mm; $F_{t,Ru}$ = 353 · 0,9 = 318 kN;

Welds—tension flange fillet welds a = 12 mm; web fillet welds a = 7 mm;

Effective ultimate resistance of external bolt row 1 m_x = 50 – 12 · 1,13 = 36,4 mm; $n = e_x$ = 40 mm;

a. 2 bolts per row:
   $Minl_{eff,b}$ = 0,5w+2 m_x +0,625e = 153 mm; $F_{T2,Ru}$ = 538 kN
b. 4 bolts per row:
   – individually bolts $l_{eff\,a}$ = 90 mm, $l_{effb,}$ = 160 mm; $F_{T2,Ru}$ = 1000 kN
   ($F_{t2a,Ru}$ = 274 kN; $F_{t2b,Ru}$ = 226 kN); bolt group (Schmidt 2008) $l_{eff,b}$ = 2 m_x+0,625e+w_1+0,5w_2 = 223 mm; $F_{T2,Ru}$ = 964 kN
c. 6 bolts per row:
   – individually bolts $l_{eff\,a}$ = $l_{eff,c}$ = 90 mm, $l_{effb,}$ = 70 mm; $F_{T2,Ru}$ = 1300 kN ($F_{t2a,Rd}$ = 227 kN; $F_{t1b,Ru}$ = 196 kN; $F_{t2c,Ru}$ = 227 kN);
   bolt group l_{eff} = 250 mm $F_{T2,Ru}$ = 1334 kN

Effective ultimate resistance of internal bolt row 2
m = 49–7·1,13 = 41 mm; n = 41·1,25 = 51 mm;
m_x = 50–12·1,13 = 36,4 mm; n_x = 36,4·1,25 = 46 mm;

a. 2 bolts per row:
   $F_{T3a,Ru}$ = 2·318 = 636 kN > 1,9·318 kN
b. 4 bolts per row:
   $F_{T3a,Ru}$ = 636 kN $l_{effb,}$ = 0,5w+e = 160 mm, $F_{T2,Ru}$ = 1191 kN < 3,8·318 = 1208 kN
   ($F_{t2a,Ru}$ = 318 kN; $F_{t2b,Ru}$ = 276 kN)
c. 6 bolts per row:
   $F_{T2,Ru}$ = 1496 kN< 5,7·318 = 1813 kN
   ($F_{T3a,Ru}$ = 318 kN $F_{T2b,Ru}$ = 196 kN $F_{T2c,Ru}$ = 234 kN)

Ultimate resistance of internal bolt rows 3–13
m = 49–7 · 1,13 = 41 mm; n = 41 · 1,25 = 51 mm;
$l_{effa,}$ = 120 mm;
$F_{T2a,Ru}$ = 486 kN < $F_{tw,Rd}$ = 12·1,2·355·10^{-1} = 511 kN

Ultimate moment resistance of splices

a. 2 bolts per row:
   $M_{j,Ru}$ = 538 · 1,54 + 636 · 1,42 + 486(1,30^2 + 1,18^2 + 1,06^2 + 0,94^2 + 0,82^2 + 0,70^2)/1,30 + 192 × 0,58 = 4180 kN · m
   (see NF EN-1993-1-8/NA)
b. 4 bolts per row:
   $M_{j,Ru}$ = 1000 · 1,54 + 1188 · 1,42 + 486(1,30 + 1,18) + (3604 – 1000 – 1188 – 2 · 486)1,06 = 4902 kN · m

c. 6 bolts per row:
$M_{j,Ru}$ = 1300 · 1,54 + 1496 ·1,42 + 486 · 1,3 + (3604 – 1300 – 1496 – 486)1,18 = 5138 kN · m.

4 COMPARISON OF FEA AND EC3 RESULTS

Value of the forces in particular bolt rows and design moment resistances calculated by component method acc. to EN-1993-1-8 were compared to results of FEM analysis in Tables 2–4, and in the Figures 4–6. Comparison shows that moment resistances of analyzed joints calculated by component method are significantly bigger (22–86%) than obtained by FEA. Reason of this is too big design resistance of bolt rows acc. to component method compared to values of effective forces in bolt rows and assumption of the location of rotation center in the axis of compressed beam flange. The biggest difference was noticed in joints with two bolts in each row, calculated with taking into account all conditions existing in EN 1993-1-8, together with restriction of reduction of forces in bolts acc. to NF-EN-1993-1-8/NA.

Ultimate resistance of bolt-rows closed to tension flange, calculated by component method, consent to effective value from FEM only in row 2 with 2 bolts per row, (Figure 4). In other cases calculated resistance of this bolt-rows is bigger 18–30% than effective row forces obtained by FEM (Figures 5–6). Ultimate moment resistances of splices calculated by component method are bigger than obtained by FEM with 2 bolts per row – 86%, by FEM with 4 bolts per row – 48%, and by FEM with 6 bolts per row – 22%. However, assumption in component method—only three bolt rows for splices with 2 bolts per row and—only two bolt rows for splices with 4 and 6 bolts per row close to tension flange, give consistent results, (see Tables 2–4).

5 ANALYSIS OF CONNECTIONS WITH STIFFENER PLATES

In the splices with two bolts in rows, additional web stiffeners were applied—one horizontal between bolt rows 2 and 3, between rows 2-3-4-5 and 6 and vertical on the both side of end-plates (Figures 7a,b,c).

Application of additional stiffeners leads to increase participation in moment resistance bolts adjacent to stiffeners, but also to decrease participation of bolt rows above top flange and under stiffeners, what in results do not increase moment resistance of the joint.

Bolt forces distribution in connection with stiffener between bolt rows 2-3 is depicted in Fig. 8

Table 2. Comparison results of the FEM with EN calculation for splice-2 bolts per row.

	Bolt-row distance (m)	Bolt row forces (kN)		
			FEM-effective forces $F_{T,mod} = F_{t,b} - Q_b$	
Bolt-row No	$h_{r,d}$[1] $h_{r,mod}$[2]	EN[3] calculation $F_{T,Ru}$ $_{max}F_{t,(a)} = 318$	Prestreesed splice $_{max}F_{t,(a)} = 323$	Not prestressed splice $_{max}F_{t,(a)} = 309$
1	1.54/1.49	2 × 269 = 538	2 × 227 = 454	2 × 212 = 424
2	1.42/1.37	2 × 318 = 636	2 × 323 = 646	2 × 309 = 618
3	1.30/1.25	2 × 243 = 486	2 × 118 = 236	2 × 109 = 218
4	1.18/1.13	2 × 220 = 440	2 × 80 = 160	2 × 79 = 158
5	1.06/1.01	2 × 198 = 396	2 × 60 = 120	2 × 61,5 = 123
6	0.94/0.89	2 × 175 = 350	2 × 43 = 86	2 × 46 = 92
7	0.82/0.77	2 × 153 = 306	2 × 25 = 50	2 × 31 = 62
8	0.70/0.63	2 × 130 = 260	2 × 8 = 16	2 × 18 = 36
9	0.58/0.53	2 × 96 = 192		2 × 5,4 = 10,8
		Σ = 3604		
Ultimate bending capacity (kN · m)		$M_{j,Ru} = 4180$	$M_{j,mod} = 2250$	$M_{j,mod} = 2250$
		Check for rows 1 + 2 + 3 $M_{j,Ru} = 2363$	$M_{j,check} = 2288$	$M_{j,check} = 2217$

[1] $h_{r,d}$–from center of compression flange.
[2] $h_{r,mod}$–from center of compression area in FEM.
[3] $F_{T,Ru}$–bolt-row effective ultimate resistance.

Table 3. Comparison results of the FEM with EN calculation for splice – 4 bolts per row.

	Bolt-row distance (m)	Bolt row forces (kN)		
			FEM-effective forces[4] $F_{T,mod} = F_{t,b} - Q_b$	
Bolt-row No	$h_{r,d}$[1] $h_{r,mod}$[2]	EN[3] calculation $F_{T,Ru}$ $_{max}F_{t,(a)} = 318$	Prestreesed splice $_{max}F_{t,(a)} = 312$	Not prestressed splice $_{max}F_{t,(a)} = 277$
1	1.54/1.49	2(274 + 226) = 1000	2(208 + 176) = 768	2(206 + 159) = 730
2	1.42/1.37	2(276 + 318) = 1188	2(213 + 263) = 952	2(227 + 277) = 1008
3	1.30/1.25	2 · 243 = 486	2 · 115 = 230	2 · 112,5 = 225
4	1.18/1.13	2 · 243 = 486	2 · 95 = 190	2 · 101,8 = 204
5	1.06/1.01	2 · 222 = 444	2 · 72 = 144	2 · 79,4 = 159
6	0.94/0.89		2 · 51 = 102	2 · 58 = 116
7	0.82/0.77		2 · 29 = 58	2 · 37 = 74
8	0.70/0.63		2 · 8 = 16	2 · 18 = 36
		Σ = 3604		
		$M_{j,Ru} = 4902$	$M_{j,mod} = 3300$	$M_{j,mod} = 3300$
Ultimate bending capacity (kN · m)		Check for rows 1 + 2 $M_{j,Ru} = 3231$	$M_{j,check} = 3242$	$M_{j,check} = 3324$

[1]$h_{r,d}$–from center of compression flange.
[2]$h_{r,mod}$–from center of compression area in FEM.
[3]$F_{T,Ru} = 2(F_{t,Ru,(b)} + F_{t,Ru,(a)})$–bolt-row effective ultimate resistance; (a), (b)–vertical bolt-rows see Fig. 1.
[4]$F_{T,mod} = 2(F_{t,mod,(b)} + F_{t,mod,(a)})$–bolt-row effective forces by FEM.

Table 4. Comparison results of the FEM with EN calculation for splice – 6 bolts per row.

	Bolt-row distance (m)	Bolt row forces (kN)		
			FEM-effective forces[4] $F_{T,mod} = F_{t,b} - Q_b$	
Bolt-row No	$h_{r,d}$[1] $h_{r,mod}$[2]	EN[3] calculation $F_{T,Ru}$ $_{max}F_{t,(a)} = 318$	Prestreesed splice $_{max}F_{t,(a)} = 318$	Not prestressed splice $_{max}F_{t,(a)} = 309$
1	1.54/1.49	2(227 + 196 + 227) = 1300	2(183 + 155+189) = 1054	2(185 + 151 + 188) = 1048
2	1.42/1.37	2(234 + 196 + 318) = 1496	2(187 + 129 + 305) = 1242	2(200 + 154 + 309) = 1326
3	1.30/1.25	2 · 243 = 486	2 × 134 = 268	2 × 141 = 282
4	1.18/1.13	2 · 161 = 322	2 × 108 = 216	2 × 112 = 224
5	1.06/1.01		2 × 82 = 164	2 × 86 = 172
6	0.94/0.89		2 × 55 = 110	2 × 62 = 124
7	0.82/0.77		2 × 31 = 62	2 × 38 = 76
8	0.70/0.63			2 × 17 = 34
		Σ = 3604		
		$M_{j,Ru} = 5138$	$M_{j,mod} = 4200$	$M_{j,mod} = 4370$
Ultimate bending capacity (kN · m)		Check for rows 1 + 2 $M_{j,Ru} = 4197$	$M_{j,check} = 4162$	$M_{j,check} = 4348$

[1]$h_{r,d}$–from center of compression flange.
[2]$h_{r,mod}$–from center of compression area in FEM.
[3]$F_{T,Ru} = 2(F_{t,Ru,(b)} + F_{t,Ru,(a)})$–bolt-row effective ultimate resistance; (a), (b), (c)–vertical bolt-rows see Fig. 1.
[4]$F_{T,mod} = 2(F_{t,Ru,(c)} + F_{t,mod,(b)} + F_{t,mod,(a)})$–bolt-row effective forces by FEM.

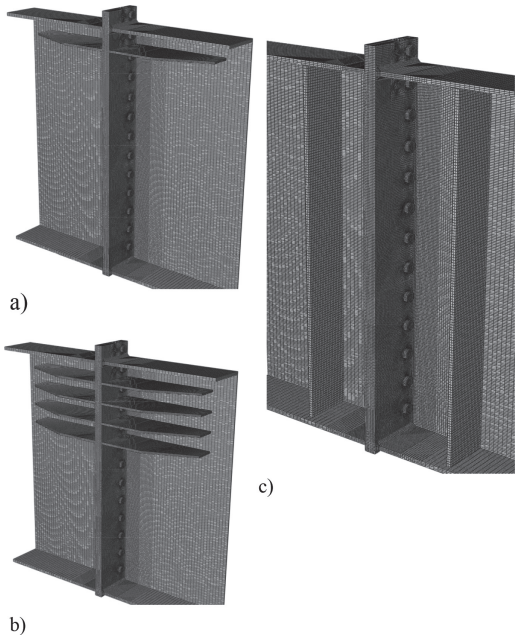

Figure 7. Splices with stiffeners: a) horizontal between bolt rows 2 & 3, b) horizontal between rows 2-3-4-5-6, c) vertical.

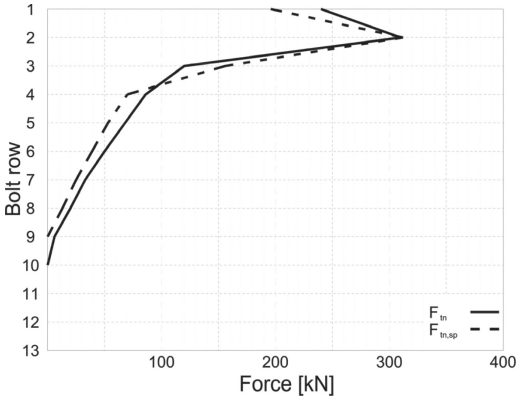

Figure 8. Bolt forces envelopes at the ultimate moment resistance of not prestressed splice-2 bolts per row with and without web stiffener between bolt row 2–3, M_j = 2125 kNm, maxF_t = 312 kN; line marking:
– without stiffener F_{tn} (bold line),
– with stiffener $F_{tn,sp}$ (dashed line).

and with stiffeners between bolt rows 2-3-4-5-6 in Figure 9.

Figure 10 shows bolt forces in splice with vertical stiffener. One horizontal stiffener do not increase ultimate moment resistance of the joint, (see Figure 8). Ultimate moment resistances of

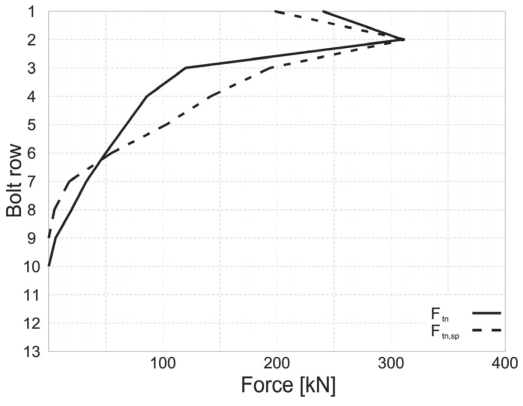

Figure 9. Bolt forces envelopes at the ultimate moment resistance of not prestressed splice-2 bolts per row with and without web stiffeners between bolt rows 2-3-4-5-6, M_j = 2475 kNm, maxF_t = 312 kN; line marking:
– without stiffeners F_{tn} (bold line),
– with stiffeners $F_{tn,sp}$ (dashed line).

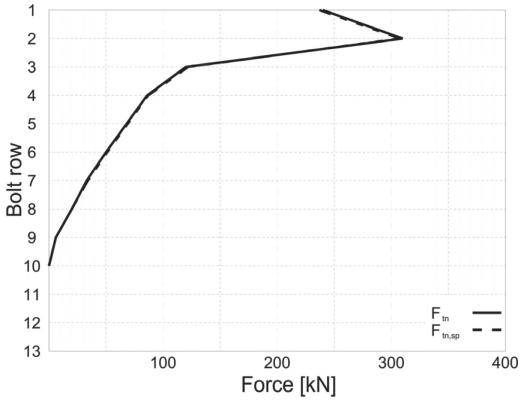

Figure 10. Bolt forces envelopes at the ultimate moment resistance of not prestressed splice-2 bolts per row with and without vertical web stiffeners, M_j = 2475 kNm, maxF_t = 312 kN; line marking:
– without stiffener F_{tn} (bold line),
– with stiffener $F_{tn,sp}$ (dashed line).

splices with four horizontal stiffeners or with vertical stiffeners are 10% greater than without stiffeners, (see Figures 9–10).

6 CONCLUSIONS END DESIGN PROPOSALS

In ultimate moment resistance of welded beam of h = 1500 mm splices with stiff end-plates, location of bearing center is out of the axis of compressed flange (a/h = 0.033). It is a result of small rotation

angle of joint, caused by displacement on the tension flange axis, which are in not prestressed connection $\Delta/h_o = 6{,}7^{-4}$ end in prestressed connection $\Delta/h_o = 3{,}3^{-4}$.

Effective ultimate resistances of bolt rows obtained by component method differ significantly compared to effective forces in bolt rows which participate in moment transmitting (see Figures 4–6).

Component method based on the analysis of T-stubs axially tensioned do not allow to estimate of actual state of stresses in the bolts in ultimate limit state of joints subjected to bending moment. This is because of not taking into account influence of flexibility of particular bolt rows on the internal forces distribution and assumption of the location of center of rotation in the axis of compressed flange.

Condition EN 1993-1-8/6.2.7.2(9) is not satisfied in splices with more than two bolts per row, close to tension flange and shall be limited to the joint with only two bolts in the row.

Assuming in the calculation that location of rotation center is in the axis of compressed flange, reduction of number internal bolt rows to two (for splices with two bolts per row) and to only located around tension flange (for splices with four or six bolts per row close to tension flange) should be applied.

Strain of the bolts in the ultimate limit state in prestressed splices is bigger than in not prestressed ones. Increasing to 5% of moment resistance was observed only in not prestressed splices with multi bolts around tension flange.

Application of horizontal and vertical stiffeners increase participation in moment resistance bolt rows adjacent to stiffeners but do not effectively increase global moment resistance of the joint.

REFERENCES

Borgsmiller J. & Sumner E. & Murray T. 1995. Tests of Extended Moment End-Plate Connections Having Large Inner Pitch Distances. *Research Report CE/VPI-ST-95/01. Department of Civil Engineering.* Virginia Polytechnic Institute and State University. Blacksburg VA.

Demonceau J.F. & Weynand K. & Jaspart J.P. & Muller C. 2010. Application of Eurocode 3 to steel connections with four bolts per horizontal row. SDSS'Rio: 199–206.

EN 1993-1-8 Eurocode 3 Design of Steel Structures Part 1–8 Design of Joints.

Flush and Extended Multiple-Row Moment End-Plate Connections AISC 2002. *Steel Design Guide Series 16*.

Joints in Steel Constructions 1995. Moment Connections. The Steel Construction Institute Publ. No. 207/95.

Katula L. & Dunai L. 2009. Full scale tests on bolted beam-to-beam end-plate connections under bending. *Bauingenieur Band* 84: 132–138.

Kozłowski A. & Łaguna J. & Kawecki P. 2013. Analysis of the moment resistance of I-beam end plate connection with multiple bolt rows. *X Scientific Conference on Steel and Composite Joints. Rzeszów-Bezmiechowa*. (in Polish).

Kozłowski A. & Pisarek Z. 2008. Resistance and stiffness of T-stub with four bolts. *Archives of Civil Engineering.* LIV, 1: 167–191.

Morrison S. & Astaneh-Asl A. & Murray T. 1986. Analytical and Experimental Investigation of the Multiple Row Extended Moment End-Plate Connection with Eight Bolts at the Beam Tension Flange. *Research Report FSEL/MBMA 84–04 Fears Structural Engineering Laboratory*. University of Oklahoma Norman OK.

Prinz G.S. & Nussbaumer A. & Borges L. & Khadka S. 2014. Exprimental testing and simulation of bolted beam-column connections having thick extended end-plates and multiple bolts per row. *Engineering Structures* 59: 434–447.

Ryan J. 1999. Evaluation of Extended End-Plate Moment Connections Under Seismic Loading *Master of Science Civil Engineering Thesis*. Virginia Polytechnic Institute.

Schmidt B. 2008. Zum Tragverhalten von geschraubten momenten-tragfähigen Stirnplattenverbindungen mit 4 Schauben in jeden Schraubenreihe. *Von der Fakultät Bauwesen der Technischen Universität Dortmund genehmigte Dissertation zur Erlangung des Grades Doktor–Ingenieur von Björn Schmidt*.

SEI 1984. Multiple Row Extended End-Plate Connection Tests *Research Report Structural Engineers*. Inc. Norman, OK.

Sumner E. 2003. Unified Design of Extended End-Plate Moment Connections Subject to Cyclic loading. *Dissertation submitted to the Faculty of the Virginia Polytechnic Institute*.

Weynand K. & Oerder R. & Demonceau J.F. 2012. Resistance tables for standardized joints in accordance with EN 1993-1-8. *Connections in Steel Structures* VII.

Recent Progress in Steel and Composite Structures – Giżejowski et al. (Eds)
© 2016 Taylor & Francis Group, London, ISBN 978-1-138-02946-0

Equivalent model of semi-rigid supporting node in the calculations of steel frames

P. Krystosik
Department of Metal Structures, Koszalin University of Technology, Koszalin, Poland

ABSTRACT: In the article a non-linear model of semi-rigid support, replacing two, located close to each other rotational nodes has been presented. Based on the concept of strain energy system and complementary energy, condensation of two nodes to the form of equivalent node has been performed.

A method to define the relation $M - \phi$ for equivalent node has been applied in the cases of flexible members fixed in the supporting nodes, taking into account the flexibility of column bases, as well as the flexible fastening of foundations in soil.

1 INTRODUCTION

A typical supporting node (also called supporting joint or support) of steel frames is composed of two parts (Figure 1):

– column base (stiffness S_1),
– foundation embedded in soil (stiffness S_1).

The first component of a supporting joint is a connection of the column to the foundation. This connection is realized by an un-stiffened, or stiffened base plate and anchor bolts.

The second component of the supporting node—foundation—usually occurs in the form of square or rectangular spread foundations embedded in soil.

Under the action of bending moment M and normal force N on supporting joint, both a column base and foundation—subgrade system are subjected to certain, inevitable deformations. In many real situations these deformations can have a big influence not only to the support behaviour, but also to the displacements and internal forces redistribution in the whole steel frame (Pałkowski & Krystosik, (2011)).

During the calculations of the steel frames with taking the flexibility column base as well as the flexibility of foundation—subgrade into account, it is necessary to model the support using two semi-rigid nodes, represented by S_1 and S_2 stiffness (Figure 2a). Because these two nodes are generally located close to each other and the element connecting these two joints (spread foundation) is practically rigid, it is possible to replace that support by one element (Figure 2b) with the properly selected, equivalent $M - \phi$ characteristic.

For this purpose the characteristic can be designated by using a strain energy U, as well as a complementary energy U^c (Timoshenko, (1966)).

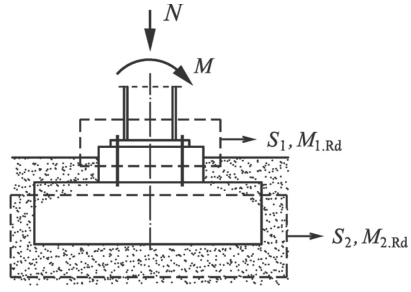

Figure 1. The analyzed supporting joint.

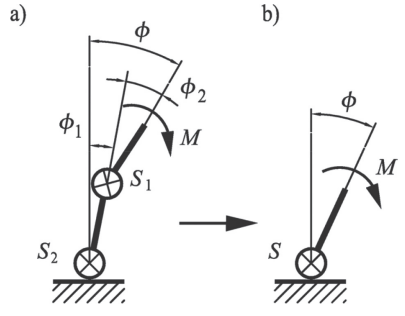

Figure 2. Model of supporting joint: a) model consists of two semi-rigid joints, b) equivalent model.

The value of strain energy stored in the joint can be calculated according to the formula

$$U(\phi) = \int M(\phi) d\phi, \tag{1}$$

while the value of complementary energy associated with the node can be defined with the use of the equation

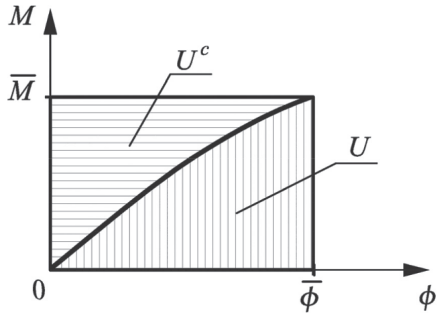

Figure 3. Geometric interpretation of the equations (1) and (2).

$$U^c(M) = \int \phi(M) dM. \tag{2}$$

These expressions can be presented, in the $M - \phi$ coordinates system, as suitable surface areas (Figure 3). It is easy to see that the combination of both areas gives a rectangle of dimensions $\overline{M} \times \overline{\phi}$.

In case of the linear $M - \phi$ relations both areas represent quantities of energies that are equal, which can be written as $U = U^c$.

2 METHOD BASED ON THE STRAIN ENERGY

The first way to determine the equivalent $M - \phi$ characteristic is based on the assumption that the stored strain energy (U_1 and U_2) in two semi-rigid joints and the strain energy U accumulated in the equivalent supporting joint are equal. This assumption can be written in the form of equation

$$U = U_1 + U_2. \tag{3}$$

In case of the adoption of a linear model of joint (Fig. 4a), the formula on the energy stored in the k-th joint takes the form

$$U_k(\phi) = \int M_k(\phi) d\phi = \int S_k \phi d\phi = \frac{1}{2} S_k \phi^2, k = 1, 2 \tag{4}$$

and in the equivalent joint

$$U(\phi) = \int M(\phi) d\phi = \int S\phi \, d\phi = \frac{1}{2} S\phi^2. \tag{5}$$

Assuming that both joints are under the influence of a bending moment M (Figure 4a), based

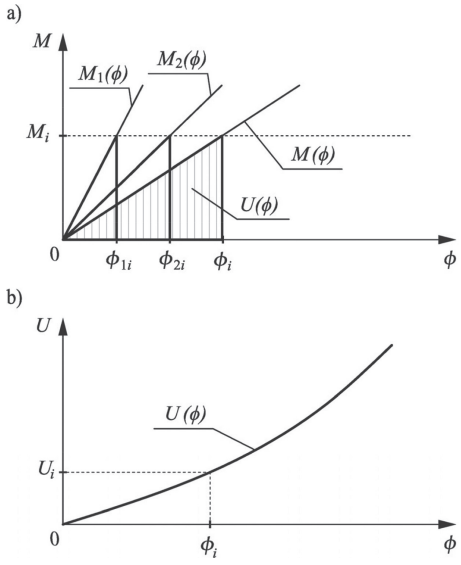

Figure 4. Linear model of semi-rigid joint: a) $M - \phi$ characteristics, b) $U - \phi$ characteristic.

on (3), (4) and (5) the following condition can be formulated

$$S_1\phi_1^2 + S_2\phi_2^2 = S\phi^2. \tag{6}$$

Then, taking into account that

$$\phi_e = \frac{M}{S_e} \quad \text{and} \quad \phi = \frac{M}{S}, \tag{7}$$

from (6) a simple equation on the equivalent stiffness S of joint is obtained in the form of expression

$$\frac{1}{S} = \frac{1}{S_1} + \frac{1}{S_2}. \tag{8}$$

It should be noted that the relation (8) can also be determined using the condition (compare Figure 2)

$$\phi = \phi_1 + \phi_2. \tag{9}$$

In case of nonlinear relationships describing the behaviour of joints (Figure 5a), as a starting point in determining the equivalent $M - \phi$ characteristic of supporting joint, the equation can be assumed in the form

$$M(\phi) = \frac{dU(\phi)}{d\phi}. \tag{10}$$

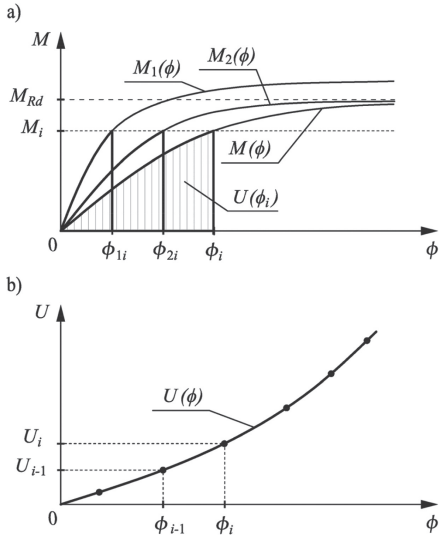

Figure 5. Nonlinear model of semi-rigid joint: a) $M - \phi$ characteristics, b) $U - \phi$ characteristic

In this equation $U(\phi)$ is a function of the stored strain energy in the equivalent model of support (Figure 5b).

In many cases determination of an analytical, equivalent characteristic with the use of expression (10) is impossible, or it can lead to a complex form of searched relations. However, these disadvantages it can be removed through replacing the analytical approach of some approximate solution. This approximation is based on discrete $\mathbf{U} - \boldsymbol{\phi}$ description. For the k-th semi-rigid joint these description can be obtained according to the formula

$$\mathbf{U}_k = \int_0^{\phi} M_k(\phi)\, d\phi, \quad i = 1, 2, ..n. \tag{11}$$

Then, based on equations (3) and (9) the relation between stored strain energy $\mathbf{U}$ and rotation angle $\boldsymbol{\phi}$ of the equivalent supporting joint should be determined (Figure 5b). Thus, obtained discrete form of $\mathbf{U} - \boldsymbol{\phi}$ relation is approximated by a properly selected function $U(\phi)$ with the use, for example, of the least squares method. The result of it is a continuous relationship which, according to the equation (10), can be used to find the nonlinear, equivalent characteristic of supporting joint.

3 METHOD BASED ON THE COMPLEMENTARY ENERGY

The use of the complementary energy in $M - \phi$ characteristic in the calculation of the equivalent supporting joint is an alternative way with reference to the method on the grounds of the strain energy. It is assumed here that the total complementary energy associated with two semi-rigid joints (U_1^c and U_2^c) is the same as complementary energy U^c related to the equivalent supporting joint. This condition can be presented with the use of the formula

$$U_1^c + U_2^c = U^c. \tag{12}$$

It is easy to see that despite of the adoption of a different criterion to find the equivalent $M - \phi$ characteristic of semi-rigid joint, the basis assumption is analogical to the method based on the strain energy. The process of determining the $M - \phi$ relation itself is also very similar. The main difference relates to the functions, which are used in the calculations – $\phi(M), U^c(M)$. These functions are inverses of those that are used in the strain energy method.

A certain disadvantage of the described methods is their use to determine the nonlinear $M - \phi$ characteristic of equivalent joint. The main reason of that is the necessity of approximating a discrete set of points, which describes the $\mathbf{U} - \boldsymbol{\phi}$ characteristic. Obtaining the analytical equivalent model with the use of the least squares method consists of determination of certain constants, for example: a, b and c. For this purpose, it has to use an equation in the form of

$$S(a, b, c) = \sum_{i=1}^{n} \left(F(\phi_i) - F_i\right)^2, \tag{13}$$

where: $F(\phi)$ is an approximating function, F_i and ϕ_i are coordinates of i-th point of the discrete data set. Determination of constants a, b and c of the approximating function comes down to solving, frequently, nonlinear system of equations, which is formulated on the basis of the condition (13).

4 SIMPLIFIED METHOD

Searched $M - \phi$ characteristic of equivalent supporting joint it can be specified only in the area, where both functions $M_1(\phi)$ and $M_2(\phi)$ are defined. Boundaries of this area are: the coordinate origin and the smallest bending moment resistance from resistances of both support components (Fig. 6).

Thus, the upper limit of the common area for both functions can be written by the equation

$$M_{Rd} = \min(M_{1.Rd}, M_{2.Rd}). \tag{14}$$

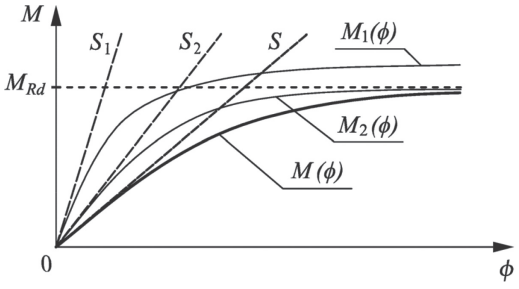

Figure 6. Nonlinear $M - \phi$ characteristics of the complex joint.

The factor that has greatly reduced the effort of determining the equivalent $M - \phi$ relation is also possibility to calculate the initial stiffness of supporting node S from equation (8). Designation of these two important, having a physical sense quantities, i.e. S and M_{Rd}, allows to use the analytical models of joints where these parameters have existed.

5 NUMERICAL EXAMPLE

Based of described methods an equivalent $M - \phi$ relation of a certain supporting joint, composing with two semi-rigid elements: column base and square foundation embedded in soil have been calculated (Figure 7). It was assumed the support is under the influence of the compressing force N equal 400 kN.

Data: steel S235, elastic modulus of steel $E = 210$ GPa, column: HEB 240, foundation concrete: C 16/20, parameters of the soil subgrade: sandy clay: $c' = 10$ kPa, $\varphi' = 23°$, $E_0 = 40$ MPa, $\nu = 0{,}25$.

The discrete $\mathbf{M} - \boldsymbol{\phi}$ relation of column—foundation connection was performed based on presented in (Bajer et al. (2014)) experimental results of the eccentrically loaded, semi-rigid column base (Fig. 7a).

Moment—rotation characteristic of the second component of supporting joint, i.e. foundation—subgrade system (Figure 7b) was performed based on numerical analysis with the use of the boundary element method (MEB). Suitable calculations were done using Sofistik programme (Sofistik, 2011a, b).

Rigid foundation—subgrade system was modelled as a square punch composed of eight-node solid brick elements resting on the boundary surface of the half-space (Figure 8).

In the modelling process of foundation and boundary surface uneven division of the elements was applied. The elements mesh was more dense at

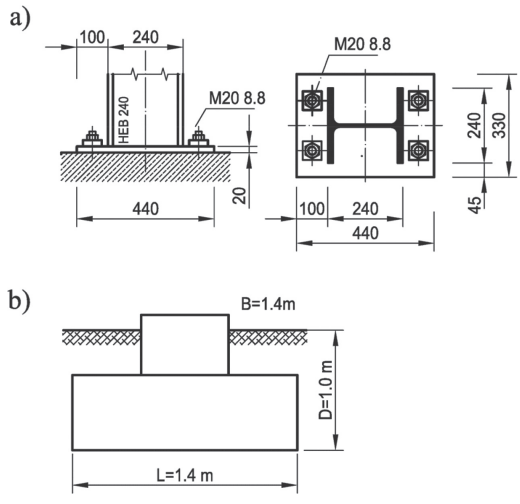

Figure 7. Elements of supporting joint: a) column base, b) spread foundation.

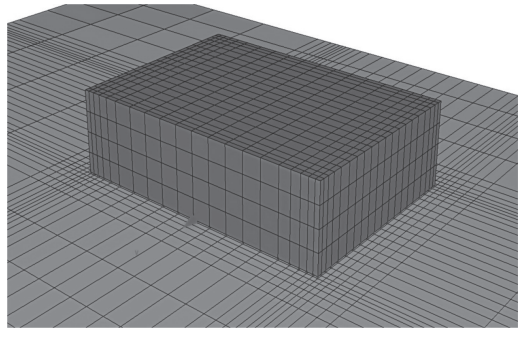

Figure 8. Analysed model of foundation—subgrade system.

the edges as well as corners of the foundation, i.e. in those places where stress is rapidly rising. This allowed to reduce the displacement number of the analysed model that were searched for.

The connection of the nodes between the spread foundation and the half-space surface was accomplished by unilateral constrains that would carry only compression.

The pressing-in and rotating loads of the footing foundation were modelled by surface loads applied to the top foundation surface. The calculations were performed by application of the incremental-iterative method.

In the calculations, elastic-perfectly plastic model of the half-space were used, limiting the compressive stresses under the foundation to the ultimate bearing pressure $q_u = 485$ kPa. This value for the analyzed foundation—soil subgrade system

was determined on the basis of standard PN-EN 1997-1.

The discreet form of **M – ϕ** each component's characteristic of the analysed support was approximated by analytical model of semi-rigid joint in the form of a modified equation (Yee & Melchers, (1986))

$$M(\phi) = M_{Rd}\left(1 - e^{\frac{-S}{M_{Rd}}\phi}\right). \tag{15}$$

The constants in the equation (15) corresponding to the characteristics of the column base and foundation are presented in Table 1. These parameters i.e. M_{Rd} and S were determined by matching the shapes of $M(\phi)$ curves to the discrete **M – ϕ** data of the support components. This process was performed by using the least square method.

The graphical interpretation, both discrete as well as analytical characteristics of components (column base and foundation-subgrade system) are presented in Figure 9.

As it can be seen, stiffness S_2 of the foundation—subgrade system is about twice as big as stiffness S_1 of the semi-rigid column base.

While comparing bending moment resistance M_{Rd} of both components it can be concluded that the connection between column and foundation is characterised by bigger resistance than spread foundation.

It can therefore be noted that the adoption of the footing foundation embedded in soil as rigidly fixed, can be incorrect. The analysed example shows that in many practical cases, the correct determination of the moment—rotation characteristic of the supporting joint should be carried out with taking both components into account.

On the basis of the inverse of equation (15), for adopted values of moment M the rotation angles ϕ and the strain energies U of the components of supporting joint were calculated. The selected values of calculated quantities are presented in Table 2.

The analytical form of the moment—rotation of the equivalent support, in accordance with section 2. was defined by approximation **U – ϕ** relation of the function

$$U(\phi) = M_{Rd}\left(\phi + \frac{M_{Rd}\, e^{\frac{-S}{M_{Rd}}\phi}}{S}\right) - \frac{M_{Rd}^2}{S}. \tag{16}$$

Because of the close relationship between functions $M(\phi)$ and $U(\phi)$, obtained parameters S and M_{Rd}, in order to get the $M - \phi$ characteristic of the whole supporting joint, can be directly used in equation (15).

The approximation of discrete **U – ϕ** joint characteristic was performed using formula

$$F(M_{Rd}, S) = \sum_{i=1}^{n} (U(\phi_i) - U_i)^2. \tag{17}$$

The initial stiffness and bending moment resistance of the equivalent supporting joint, obtained in this manner, are: $S = 1{,}2120$ kN·m/rad and $M_{Rd} =$ 164.9 kN·m. These values were used to determine the analytic form of $M(\phi)$ characteristic of the supporting joint (Figure 10).

Table 1. Parameters of the semi-rigid component of supporting joint.

Column base	Foundation
$M_{1\cdot Rd} = 196$ kN·m	$M_{2\cdot Rd} = 171$ kN · m
$S_1 = 16{,}550$ kN·m/rad	$S_2 = 38{,}350$ kN · m/rad

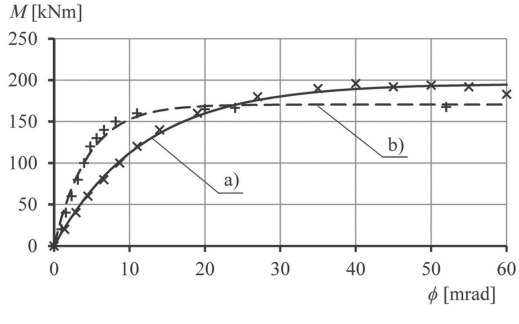

Figure 9. $M - \phi$ characteristic of the components of supporting joint: a) column base, b) foundation.

Table 2. Discrete **U – ϕ** relations of the components of supporting joint.

Moment	Column base		Foundation		Equivalent joint	
M [kNm]	ϕ_1 [mrad]	U_1 [kJ]	ϕ_2 [mrad]	U_2 [kJ]	ϕ [mrad]	U [kJ]
0	0.000	0.000	0.000	0.000	0.000	0.000
25	1.616	0.021	0.705	0.009	2.321	0.030
50	3.488	0.091	1.542	0.032	5.030	0.123
75	5.712	0.231	2.574	0.106	8.286	0.337
100	8.453	0.473	3.919	0.224	12.372	0.697
125	12.026	0.877	5.855	0.444	17.881	1.321
150	17.166	1.588	9.351	0.930	26.517	2.518

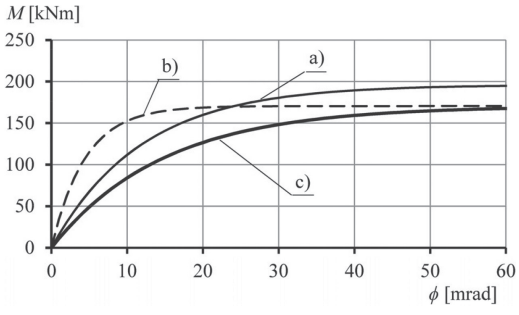

Figure 10. $M - \phi$ characteristics: a) column base, b) foundation, c) equivalent supporting joint.

The similar values of the stiffness and the resistance were also obtained with the use of the complementary energy method—section 3. In this case the constants S and M_{Rd} were determined by approximating the discrete form of $\mathbf{U^c - M}$ relationship using formula $U^C(M)$ – the function formed by integration of the inverse function (15). The initial stiffness S of equivalent joint determined in this way, is equal 1,1570 kN·m/rad, while the bending moment resistance M_{Rd} this joint amounts to 186.7 kN·m.

Determination of the equivalent characteristic of supporting joint were also performed with the use of a simplified method, presented in section 4. The wanted $M - \phi$ relation in the analytical form (15) was obtained through calculations of the parameters S and M_{Rd} using formulas (8) and (14). The values, defined in this way, are respectively: S = 1,1600 kN·m/rad, and M_{Rd} = 171 kN·m. This procedure can be regarded as an accurate, because during calculations there are no errors resulting from the approximation.

6 SUMMARY

The designation of the equivalent moment—rotation characteristics of supporting joints, frees us of having to model complex, composed with two semi-rigid joints, supports. It is allowed to reduce the number of active degrees of freedom in the modelled system.

The estimation of the linear characteristic $M - \phi$ of semi-rigid supporting joint is simple and consists of determination of initial stiffness S. This parameter can be obtained according to the formula (8).

In case of searching the equivalent, nonlinear $M - \phi$ relationship of the whole support is much more difficult, however, there are three possible procedures: strain energy method, complementary energy method and simplified method. Presented in section 2 and 3 methods for determining the equivalent $M - \phi$ relation have a general character and they can be applied with the use of different types of functions. In order to determine the nonlinear characteristics of supporting joints you can use the analytical relations in which the constants are parameters such as, for example: initial stiffness S and bending moment resistance M_{Rd}. To a large degree the process of determining the equivalent characteristics of supporting joint makes this determination easier. The use of e.g. function (15) for this purpose, reduces the number of unknowns which should have to be obtained in the approximation process.

REFERENCES

Bajer M., Vild M., Barnat J.& Holomek J. 2014. *Influence of selected parameters on design optimization of anchor joint.* 2th International Conference on Steel, Space & Composite Structures. Prage. P. 149–158.

Pałkowski Sz, Krystosik P (2011). *Static analysis of steel frames with semi-rigid supporting joints*. XII Internacional Conference on Metal Structures, June 15–17. Wrocław.

PN-EN 1997–1:2008. *Geotechnical design*. Part 1: General rules.

SOFiSTiK (2011). *Halfspace analysis for static soil−structure interaction*.

SOFiSTiK. (2011). HASE. *Half-Space Analysis*. 2011.

Timoshenko S.P. (1966). *History of strength of materials*. Warsaw: Arkady [in Polish]

Yee Y.M., Melchers R.E. (1986). Moment-rotation curves for bolted connections. *Journal of the Structural Engineering*, vol. 112, no. 3/March, 615–635.

Recent Progress in Steel and Composite Structures – Giżejowski et al. (Eds)
© 2016 Taylor & Francis Group, London, ISBN 978-1-138-02946-0

Component-based modelling of beam-to-column joints subjected to variable actions

L. Ślęczka
Rzeszów University of Technology, Rzeszów, Poland

ABSTRACT: The paper presents analytical modelling of steel beam-to-column joints subjected to different histories of variable actions, with control of rotation range. Modelling is based on the component method. Presented approach takes into account material nonlinearity, contact conditions and distinct failure modes. Developed method is able to trace elastic and plastic response of beam-to-column joints under cyclic loading. Such models can be used to assess stiffness degradation and pinching phenomena, which occur in bolted joints in frame structures loaded by variable type of loading. In the paper parametric analysis of flush end plate joint under different types of loading history is also presented.

1 INTRODUCTION

The effects of the behaviour of the joints on the distribution of internal forces within a structure, on the overall deformations and global stability of the structure should generally be taken into account according to Eurocode 3 (EN 1991-1-1 2005). Significant structural properties of joints in frames are moment resistance, rotational stiffness and rotation capacity. They are expressed in the form of moment—rotation characteristics ($M - \phi$) and can be effectively predicted by the component method, (EN 1993-1-8 2005, da Silva 2008).

The component method is based on three steps (Faella et al. 2000). First one is identification of active components, next one is the evaluation of the force-deformation ($F - \Delta$) behaviour of each component, regarding them as elastic-plastic spring, subjected to axial force. Finally, after assembling components into mechanical mechanism, joint moment versus rotation response ($M - \phi$) for complete joint can be produced.

The advantages of this method are versatility and relative simplicity. Other prediction methods for the mechanical behaviour of joints (finite element method, experimental test) can be much more laborious, (Díaz et al. 2011). But predictions coming from "pure" component method are valid only in case of monotonic loading. Nowadays the number of structures subjected to variable and cyclic type loading (coming from conditions of normal use or accidental design situation) is increasing.

Under variable actions (repeated or cyclic) structural properties of joints can deteriorate in terms of strength, stiffness and energy dissipation capacity, and the effects of this deterioration influence the distribution of forces and moments and overall global behaviour of structure.

The paper presents analytical modelling of steel beam-to-column joints subjected to different histories of repeated actions, with control of rotation angle. Modelling is based on the component method. Presented approach takes into account material nonlinearity, contact conditions and different failure modes. Developed method is able to trace elastic and plastic response of beam-to-column joints under cyclic loading. Such models can be used to assess stiffness degradation and pinching phenomena, which occur in bolted joints in frame structures loaded by variable actions.

2 MECHANICAL MODELLING FOR BEAM-TO-COLUMN JOINTS

2.1 *Geometrical properties of the model*

A component-based model for semi-rigid beam-to-column joints was built to investigate its response to repeated and cyclic loading.

First step was identification of the components of the joint that provide significant deformation and failure of the joint. Fig. 1 shows the mechanical model of the flush end-plate beam-to-column joint in case of monotonic loading. Active components are: column web in shear (cws), column web in transverse compression (cwc), beam flange and web in compression (bfc), column web in transverse tension (cwt), column flange in bending (cfb), end-plate in bendig (epb), bolts in tension (bt) and beam web in tension (bwt).

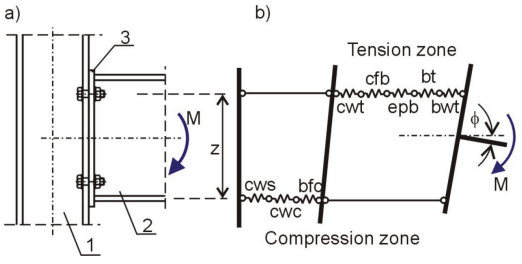

Figure 1. Flush end-plate beam-to-column joint subjected to monotonic loading: a) structural details, b) mechanical model; 1-column, 2- beam, 3- end plate.

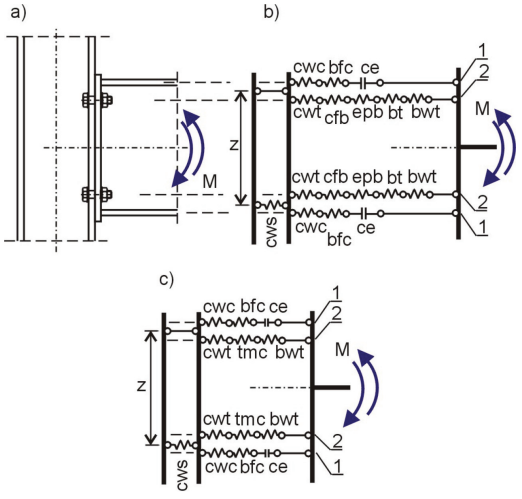

Figure 2. Flush end-plate beam-to-column joint subjected to cyclic loading: a) structural details, b) mechanical model, c) simplified mechanical model; 1 – row transferring compression force; 2 – row transferring tension force.

In any such joint, the components transmitting tension and compression force are situated both the upper and lower part of the joint. In case of monotonic loading only these activated by corresponding sense of bending moment are considered, (Fig. 1). When joint is subjected to bending moment with changing sense, there should be taken into account components transmitting tension and compression in both parts of joint (upper and lower), (Fig. 2).

Location of springs transferring tension force are dependent on location of bolt rows. Components transferring compression force are situated in the levels of beam flanges. A spring corresponding to column web in shear (cws) should have a proper lever arm z, equal to distance from bolt line to the centre of beam flange in compression.

2.2 *Characterisation of the joint components*

In order to guarantee correct behaviour of whole system, every row of components was supplemented by nonlinear spring, transferring only tension or compression force, (Fig. 3). Such elements allow to choose the proper "path" transferring tension or compression force when sense of bending moment is changing.

Nonlinear element transmitting only compression force is build into row of components marked "1" in Figure 2. Nonlinear element allowing for transferring only tension force is taken into account during modelling of bolts in tension (row of elements "2").

In Figure 2b components situated in tension zone like column flange in bending (cfb), endplate in bending (epb) and bolts in tension (bt) are marked independently from each other, while in reality they cooperate and can be modeled as one macro component (T-stub flange), marked as (tmc). This leads to simplification of the whole model, which finally looks like as in Figure 2c.

In case of the cyclic model, force–deformation (F-Δ) behaviour of some components should describe not only constitutive laws in the range of loading, but also in the range of unloading and reloading. The resistance and stiffness under first loading can be predicted using formulas according to Eurocode 3 (EN-1993-1-8 2005). In next semicycles of unloading and reloading the Masing rule can be adopted (the unloading and reloading branches of the steady-state hysteretic response are geometrically similar to the initial-loading curve except for double magnification). Such approach is shown for force–deformation (F – Δ) behaviour of column web in shear (cws) in Figure 4, (Kim & Engelhardt 2002).

One directional characteristics of components are enough only for few components (column web in transverse compression (cwc), beam flange and web in compression (bfc) and bolts in tension (bt)).

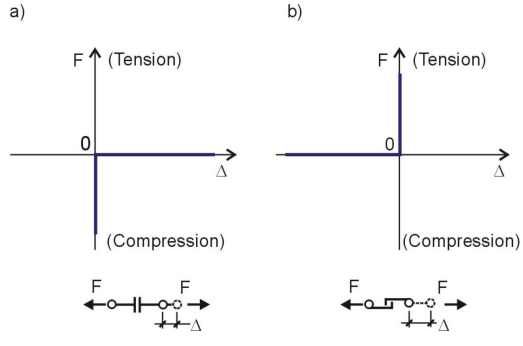

Figure 3. Nonlinear elements: a) transferring only compression force (ce), b) transferring only tension force (te).

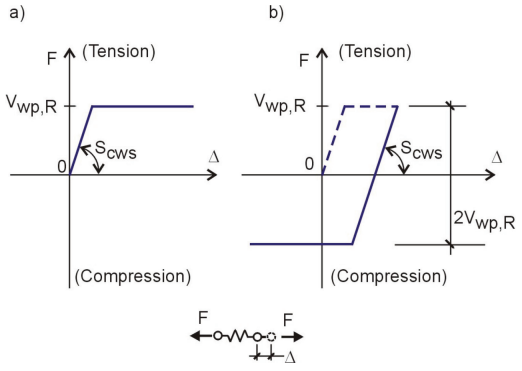

Figure 4. Force-deformation (F-Δ) behavior of column web in shear (cws): a) monotonic response; b) cyclic response.

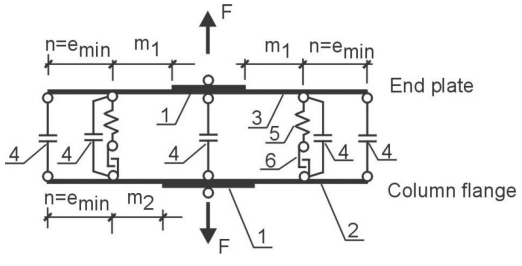

Figure 5. Macro component (tmc) taking into account cooperation between column flange in bending (cfb), end-plate in bending (epb) and bolts in tension (bt).

Macro component (tmc) can be modelled by mechanical system of T-stub, shown in Figure 5. It consists of two beams with elastic-plastic characteristics ("2" and "3"), imitating column flange in bending (cfb) and end plate in bending (epb). Cross sectional area of these beams is rectangular, with dimensions equal to thickness of the column flange or end plate and their effective lengths. In the area where the flange plate and end plate are connected to the web by fillet radius ("1"), the stiffness of beams is properly increased.

To model the bolt, a two truss elements connected in series are utilized ("5" and "6"). First one represents geometric stiffness of a bolt. Its cross section is equal to the tensile area of the bolt. Interaction between bolt and the flange plate (i.e. contact and separation) is modelled by second nonlinear element, which corresponds only to tension behaviour of the bolt (as shown in Figure 3b). Five truss nonlinear elements ("4") transferring only compression are contact elements (as shown in Fig. 3a). The material properties used for the bolt are described by plastic multilinear material model. Macro component was used to verify the behaviour of T-stub under cyclic loads, (Ślęczka 2011). Mechanical model of whole joint (as in Fig. 2c) was built using FE program ADINA.

3 APPLICATION OF THE PROPOSED MODEL

3.1 *Scope of the analysis*

A few flush end plate joints were investigated using the method described above. All joints were one-sided, made of HEM200 (column) and IPE270 (beam). The steel grade S235 was adopted to the analysis. Due to symmetry of joints, lever arms of internal forces were constant, independently of the sense of bending moment. Considered joints and their dimensions are shown in Figure 6. All joints were partial strength. The characteristic resistance of IPE270 for bending about y-y axis is equal to $M_{pl,Rk}$ = 113,7 kNm. Structural properties of analysed joints are summarized in Table 1.

The thickness of end plate, the grade and diameter of bolts were changed in each analysis.

The diameter of the bolts (M16 and M20), the grades of bolts (8.8 and 10.9) and the thickness of end plate were chosen in a such way that moment resistance of the joint was based on different failure modes. Failure mode of F-5 joint was based on formation of plastic hinges in end plate. In case

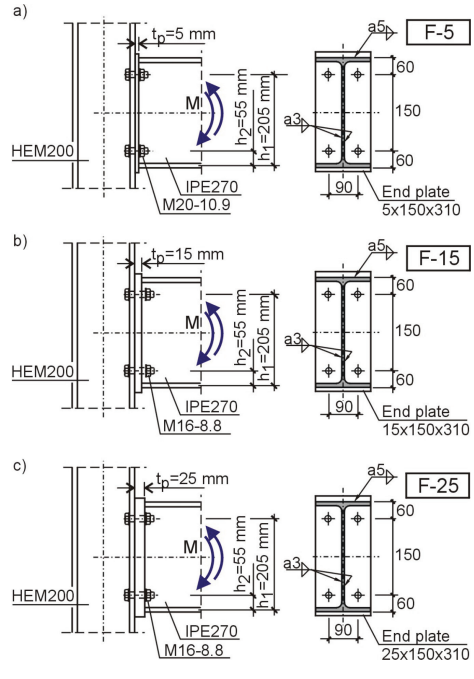

Figure 6. Flush end plate joints: a) end plate t_p = 5 mm, b) end plate t_p = 15 mm, c) end plate t_p = 25 mm.

Table 1. Structural properties of joints.

Joint	The component method $S_{j,ini}$ kNm/rad	The component method $M_{j,Rk}$ kNm	The cyclic model $S_{j,ini}$ kNm/rad	The cyclic model $M_{j,Rk}$ kNm
F-5	3026	7,9	3380	6,7
F-15	14829	45,9	13717	36,1
F-25	15771	56,3	13955	47,8

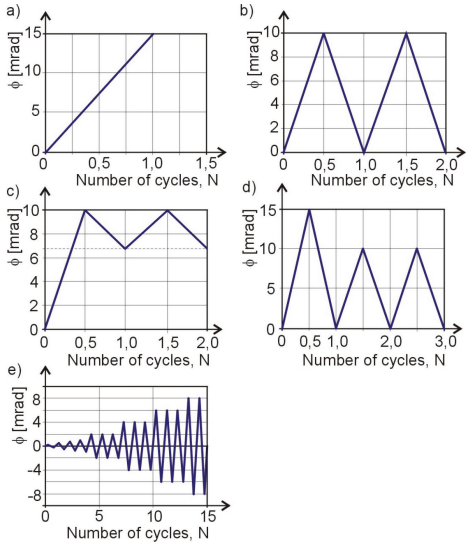

Figure 7. Considered loading histories: a) monotonic loading, b) repeated with constant amplitude, c) variable, d) repeated with overload with first cycle, e) cyclic.

of F-15 failure was characterised by simultaneous bolts failure and yielding of the end plate. Failure in F-25 joints occurred in tensioned bolts.

3.2 *Loading histories*

The M – ϕ behaviour of each joint was investigated under different loading histories, see Figure 7. First, the monotonic loading was applied to each joint (Fig. 7a). Next considered loading patterns had repeated and cyclic character.

The second type is repeated loading with constant amplitude, changing from zero to maximum value. Applied range of the angle rotation was equal to $\Delta\phi = 10$ mrad (Fig. 7b). Such value approximately responds to plastic bending resistance of joints in typical steel frame (Krawinkler 2009).

The third type of loading simulates standard loading pattern, where maximum value of loading comes from a sum of permanent and variable actions. The maximum value of $\phi_{max} = 10$ mrad was adopted. Fluctuating part of the pattern is a result of variable loading. Its proportion to maximum value was found in such a way, that after unloading bending moment was decreased to 1/3 of plastic bending moment of joint $M_{j,R}$. After unloading to such value reloading to ϕ_{max} occurs in two cycles. Such loading protocol refers to the conditions of normal use (persistent design situations).

The fourth loading history imitates overloading situation of the joint, with rotation to 15 mrad. After unloading, two cycles of constant amplitude loading are applied with the range of $\Delta\phi = 10$ mrad. It is a simple simulation of accidental action on the joint and later persistent design situations, (Fig. 7d).

The last loading history (Fig. 7e) has cyclic pattern, according to ECCS recommendations (ECCS, 1986). The history contains few elastic cycles (amplitude is less than 10 mrad) followed by pairs of cycles whose amplitude increases.

The angle of rotation was control parameter in all cases of loading histories applied to the considered joint.

4 RESULTS AND DISCUSSIONS

The moment—rotation curves obtained from analysis are presented in Figures 8–15.

Figure 8 illustrates response of joints under monotonic loading (loading history according

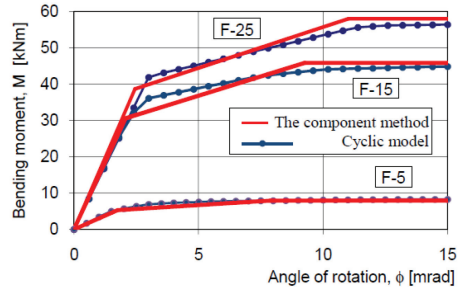

Figure 8. Response of joints under monotonic loading.

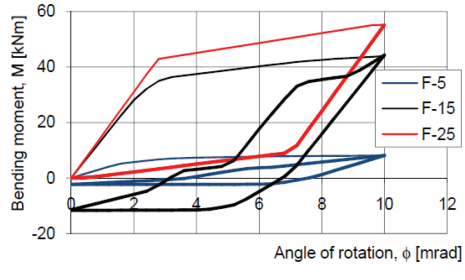

Figure 9. Response of joints under repeated loading with constant amplitude (load pattern according to Figure 7b).

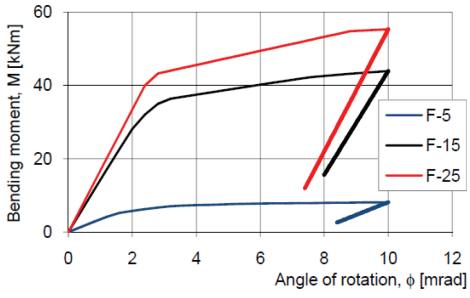

Figure 10. Response of joints under repeated loading (load pattern according to Figure 7c).

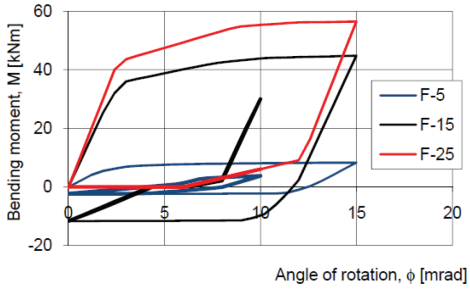

Figure 11. Response of joints under loading simulating overloading situation (load pattern according to Figure 7d).

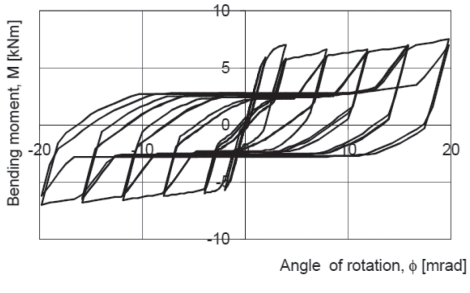

Figure 12. Response of F-5 joints under cyclic loading (load pattern according to Figure 2e).

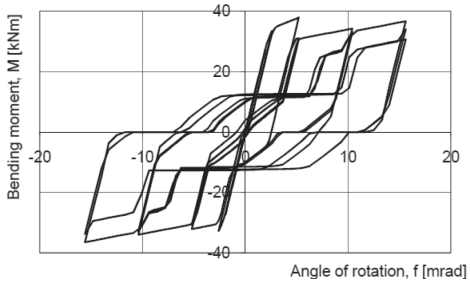

Figure 13. Response of F-15 joints under cyclic loading (load pattern according to Figure 2e).

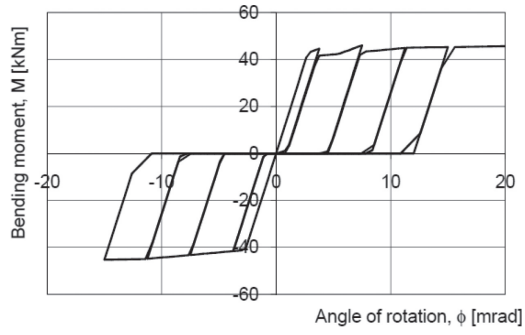

Figure 14. Response of F-25 joints under cyclic loading (load pattern according to Figure 2e).

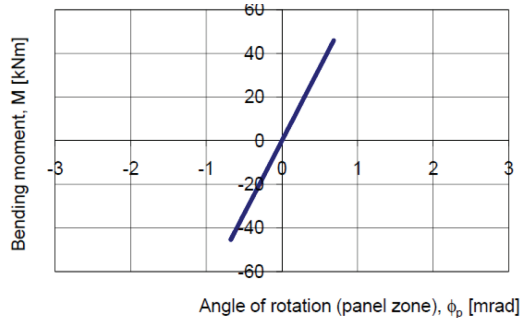

Figure 15. Response of panel zone of F-25 joint under cyclic loading.

to Figure 7a). In comparison with Eurocode 3 (EN 1993-1-8 2005) the proposed mechanical model (cyclic model) slightly underestimates the initial stiffness and the flexural capacity by 3% and 17%, respectively.

The responses of joints under repeated loading with constant amplitude (according to pattern shown in Figure 7b) are changing due to type of failure modes, (Fig. 9). In case of thin end plate (joint F-5), a distinct hysteresis loops are visible. When failure mode depends on bolt failure with yielding of the flange (joint F-15), plastic deformation of bolts influenced reduction of hysteresis loops. In case of failure mode based on failure of bolts only (joint F-25), response of joint, after few cycles of loading, looks like behaviour of a bolted lap joint with initial slip. In Figures 9–11 response of joints to first and second semicyles (loading and unloading) is marked by thin line, while next semicycles of reloading and unloading are marked by thick line.

In case of constant amplitude loading pattern (according to Figure 7b), no joint shows signs of resistance deterioration. Positive bending moment corresponding to maximum value of angle rotation, obtained in next reloading cycles has the same value as in first semi-cycle.

Table 2. Resistance ratio for loading history according to Fig. 7d.

Joint	F-5	F-15	F-25
Resistance ratio ε_{i+}	0,56	0,83	0,13

When joints are loaded by history according to Figure 7c (the conditions of normal use), obtained response is elastic-plastic only in first semi cycle, as for monotonic loading, see Figure 10. In next cycles, (unloading and reloading) behaviour of joints appears as pure elastic (thick line in Fig. 10). No signs of stiffness or resistance degradation phenomena were observed.

Response of joints subjected to simulation of overloading situation and later persistent design situations (loading pattern according to Figure 7d) shows deterioration behaviour in terms of stiffness and resistance, (Fig. 11). The scale of resistance degradation shows resistance ratio—describing proportion of bending moment value corresponding to maximum rotation angle in i-th semi-cycle M_i^+ to the plastic bending resistance in positive moment range M_y^+:

$$\varepsilon_i^+ = \frac{M_i^+}{M_y^+} \tag{1}$$

Values of resistance ratio obtained from analysis are shown in Table 2.

Responses of joints subjected to cyclic loading pattern are shown in Figures 12–15.

Global angle rotation of joints is always sum of rotation of panel zone and connection zone. In case of analysed joints contribution of panel zone is small. Figure 15 shows response of panel zone only in joint F-25 subjected to cyclic loading. As can be seen the response is pure elastic. For the rest of joints, participation of panel zone in total deformability of joints was even smaller.

Obtained results are in line with what was observed by other researches during experimental testing, e.g. (Broderick & Thomson 2002).

5 CONCLUDING REMARKS

Bolted partial strength end plate joints can deteriorate in terms of stiffness and resistance due to variable actions. The main reasons influencing such deterioration are:

– Change of monotonic properties of steel into cyclic ones as a result of cyclic plasticity (cyclic hardening or softening of steel) and as a result of strain rate,
– Material damages starting to exist and develop with a number of load cycles (fatigue cracks, brittle fractures),
– Structural properties of joints (different transferring paths of tension and compression force, one-sided ties (contact conditions), growing plasticity zones and permanent plastic deformations).

The influence of the first two groups is too complex to take into account during the simplified modeling of joints. Also in case of joints, subjected to moderate numbers of load cycles with small amplitude variation, it is usually unnecessary. Presented method enables efficient modeling of deterioration phenomena caused by structural properties of joints.

Described in the paper approach is based on the component method and should be considered as a simplified, but the study showed its effectiveness. Presented analysis is limited to flush end plate joints, but it was also used to extended end plate joints with more bolt rows (Ślęczka 2013).

REFERENCES

Broderick, B.M, Thomson, A.W. 2002. The response of flush end-plate joints under earthquake loading. *Journal of Constructional Steel Research* 58: 1161–1175.

da Silva, L.S. 2008. Towards a consistent design approach for steel joints under generalized loading. *Journal of Constructional Steel Research* 64: 1059–1075.

Díaz, C., Martí, P., Victoria, Querin, M.O. 2011. Review on the modelling of joint behaviour in steel frames. *Journal of Constructional Steel Research* 67: 741–758.

ECCS. 1986. Recommended testing procedure for assessing the behavior of structural steel elements under cyclic loads. European Convention for Constructional Steelworks, Brussels.

EN 1993-1-1. 2005. Eurocode 3: Design of steel structures—Part 1–1: General rules and rules for building. CEN, Brussels.

EN 1993-1-8. 2005. Eurocode 3: Design of steel structures—Part 1–8: Design of joints. CEN, Brussels.

Faella, C., Piluso, V., Rizzano, G. 2000. Structural steel semirigid connections. Theory, Design and Software. CRC Press.

Kim, K.D., Engelhardt, M.D. 2002. Monotonic and cyclic loading models for panel zones in steel moment frames. *Journal of Constructional Steel Research* 58: 605–635.

Krawinkler, H. 2009. Loading histories for cyclic tests in support of performance assessment of structural components. *3rd Int. Conf. on Advances in Experimental Structural Engineering. October 15–16, San Francisco, California*.

Ślęczka, L. 2011. Analytical study on cyclic behaviour of bolted joint component. The 12th International Conference on Metal Structures—ICMS, Wrocław.

Ślęczka, L. 2013. *Shaping and analysis of selected steel frame joints subjected to variable action* (in Polish). Rzeszów: Oficyna Wydawnicza Politechniki Rzeszowskiej.

Recent Progress in Steel and Composite Structures – Giżejowski et al. (Eds)
© 2016 Taylor & Francis Group, London, ISBN 978-1-138-02946-0

Steel column-base solutions for over-roofing of existing buildings: A numerical study

A. Floricel & S. Benzar
Department of Steel Structures and Structural Mechanics, Politehnica University Timisoara, Romania

V. Ungureanu
Department of Steel Structures and Structural Mechanics, Politehnica University Timisoara, Romania
Laboratory of Steel Structures, Romanian Academy, Timisoara Branch, Romania

G. Zagari
Modeling Department, University of Calabria, Italy

ABSTRACT: In today's developing world, in which sustainability has become an essential issue, over-roofing of existing buildings, together with over-cladding form an optimum complete retrofitting solution for the construction sector, instead of demolishing the old structures and building new ones. Moreover, the importance of light, reversible and low-time consuming materials for building these over-roofing systems have made engineers turn to steel-based solutions. In this context, the paper summarizes three types of steel-based over-roofing structural solutions, i.e. a) hot-rolled profiles; b) rectangular hollow sections and; c) cold-formed profiles. The investigation is mainly focused on details concerning the connection of over-roofing to the existing structure. Further on, details of a numerical study on these column-base connections are presented, in both semi-rigid and rigid solutions. Last but not least, for the comfort of building owners, but also for ease in erecting, an option of column-base connection based on chemical anchorage was analysed numerically.

1 INTRODUCTION

Nowadays the process of refurbishment and conversions has become a general phenomenon, as newly built buildings, as green and energy efficient that they can be, do not solve the problem of the already large existing building stock, but only add to the world-wide carbon footprint.

In this context, over-roofing and over-cladding have a considering part to play, as they can form an optimum complete retrofitting solution for the majority of low energetic buildings.

Over-roofing is the general term used to describe the installation of a new roof on an existing building, creating new habitable spaces. However, over-roofing frequently forms part of a more complex modernization scheme which includes over-cladding also, proving the entire concept presented above as a complete retrofitting solution.

The main advantages for over-roofing, in view of RFCS Project RFSR-CT-2007-0043 (Lawson 2008), include: heat reduction by improving thermal insulation, enhancement and modification of the overall building appearance, creation of new space for habitable use or building services, arrestment and overcoming of deterioration of the existing roof and of leakage problems (by a new pitched roof), avoiding disruption that is inevitable in the replacement of an existing roof.

Depending on the size and height of the new structure, it is necessary to recheck the load-bearing capacity of the original structure in order to decide whether or not to take consolidation measures. In seismic countries, as Romania is, this problem can be very serious, and traditional building techniques cannot be always used for this type of restructuring.

The necessity to minimise the weight of the new storey structure added above, makes light materials like steel based structures the most suitable solution (see Figure 1) (Dubina et al. 2001).

For this purpose, steel sections have proven to be the best option due to lightweight components, flexibility in planning, long span capabilities, robustness and durability, with economy and speed of construction on site.

Moreover, over-roofing and over-cladding of existent buildings using these kinds of light weight solutions becomes an optimal retrofitting technique as these small building systems are a prefabricated product that can be easily erected on sight, piece by piece (see Figure 2).

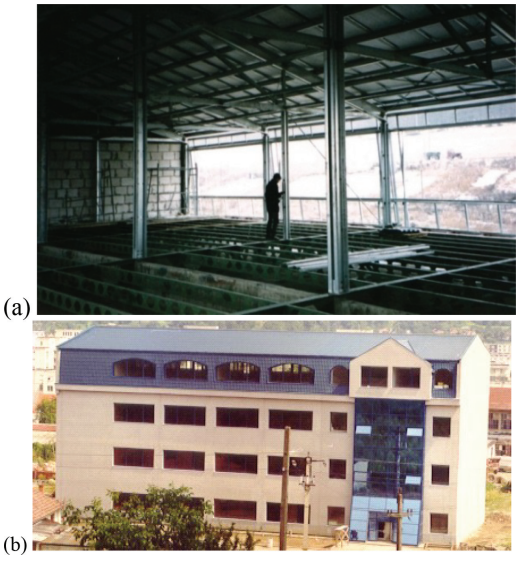

Figure 1. (a) Over-roofing of a single storey industrial building and (b) view of the new building façade.

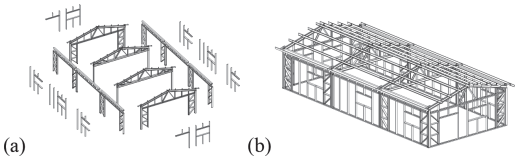

Figure 2. (a) Modular assembly of prefabricated components and (b) view of the small building system module.

Therefore, what was designed initially as a modular hall for industrial purposes can also be transformed in an over-roofing or storey extension of existing buildings.

2 CURRENT SITUATION OF BUILDING STOCK IN ROMANIA

Referring to current building stock in Europe, there are about 196 millions of dwellings corresponding to about 160 millions of buildings, while new buildings represent yearly about 1.5% of the building stock (Norris et al. 2004). However, the measured rate of retrofitting today is still much lower than the one it is foreseen on the long-term future ambitions.

The census conducted in 2002, in Romania, presented that over 71% of existing building stock in urban areas is composed of collective large panel prefabricated houses. These large prefabricated blocks were built in three main periods, i.e.: (a) 1962–1975; (b) 1975–1982; (c) 1982–1989.

Moreover, approximately 95% of Romania's housing stock is owner occupied; so most houses and apartments are occupied by their owners, making retrofitting measures harder to apply at a large scale.

The current major problems of these buildings can be categorized to: problems regarding thermal comfort, ventilation, energy consumption; problems caused by the small inhabitable area and interiors rigid partitions; problems concerning the public space, accessibility, lack of parking areas, elevators, space for social interaction etc. (Botici et al. 2012).

Regarding the envelope of these buildings the majority built between 1960 and 1980, the issue of bad insulation is assumed. Thus, applying retrofitting solutions, like over-roofing together with over-cladding leads also to considerable energy savings improving the carbon footprint of the building.

Taking into account these obvious advantages, however, the renovation of buildings using over-roofing solutions requires good understanding of the building physics requirements in terms of structural performance. Therefore, in present context, there is a large variety of geometries, volumes and aesthetics for the over-roofing and over-claddings even in the boundaries of the same neighbourhood, degrading the overall visual image. Due to this lack of ratified methodology, errors in the execution of these over-roofings are unavoidable and can be divided in two categories: (1) the first regards the bearings and anchorage of the over-roofing system to the existing structure, while (2) the second one is related to the actual and common structural errors.

3 OVER-ROOFING SOLUTIONS BASED ON INTENSIVE USE OF STEEL

The proposed solutions for over-roofing, presented in Figure 3, were considered for the three main block typologies built in Timisoara, Romania in the period 1962–1989.

These are:

- IPCT T744R specific to the period 1962–1975 – hot-rolled profiles (HR) – Figure 3a;
- IPCT 770 specific to the period 1975–1982– cold-formed steel sections (CF) – Figure 3b;
- IPCT 1340 specific to the period 1982–1989– rectangular hollow sections for columns and hot-rolled profiles for beams (RHS) – Figure 3c.

Figure 3 presents the rigid solutions, while Figure 4 the semi-rigid ones.

In the case of semi-rigid connections presented below, in the first case scenario (a), the hot-rolled

profile (HEB 180) is connected to the concrete slab through 2 rectangular steel plates, a smaller one with similar dimensions to the profile, welded over a larger one at the base. The first plate is connected to the base plate by two rows of bolts, placed along the web of the profile, while the second plate anchors the column to the last floor concrete slab through 4 bolts placed in its corners of the as it is shown in Figure 4a. In the third case scenario (see Figure 4b), the columns (two back-to-back lipped channel sections) are also connected to the base concrete slab through a rectangular steel plate, but in this case a steel box was needed to connect webs of the profiles. The second case scenario, i.e. the one using rectangular hollow section, was not presented here because it is similar to the first case scenario. The connection is done by bolts, both for webs as well as at the base. In all three cases, the column-base connection is strengthened by an angle profile placed under the last floor slab and connected to the steel plates above by a row of two bolts, and respectively to the last floor wall also by two bolts (see Figure 4).

The design of the structures subjected to over-roofing is composed of two stages: (i) verification of the current state of the original structure considering the actual codes and (ii) verification of the structure after including the new-added steel structure.

The state of the original structure was done through 3D analyses using ETABS computer code, by using shell finite elements. The thickness of the vertical and horizontal modelled diaphragms was equal to the thickness of the resistance layer.

The buildings were verified according to the actual standards, proving to be resistant to all loading combinations and to some different refurbishment strategies that were considered for enlarging the interior living space, already presented in earlier papers (Botici et al. 2012). The seismic load

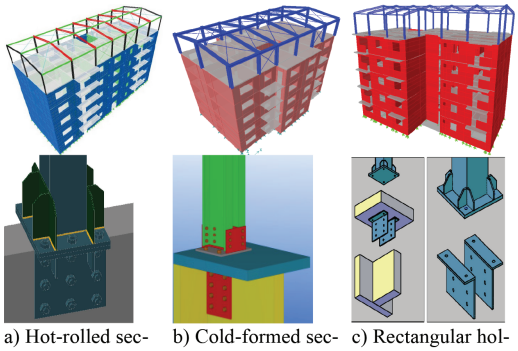

a) Hot-rolled section (HR) b) Cold-formed section (CF) c) Rectangular hollow section (RHS)

Figure 3. Proposed steel over-roofing solutions—rigid case, for block types: a) 744R, b) 770, c) 1340.

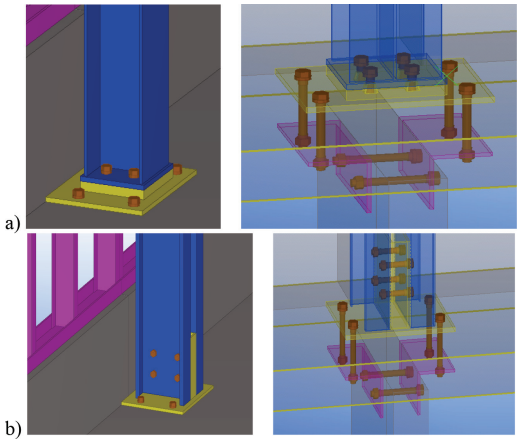

Figure 4. Semi-rigid column-base connection details for case 1 (a) and case 3 (b) respectively.

was accounted through a spectral analysis using the ground acceleration value a_g = 0.20 g and a control period Tc = 0.7 s.

These verifications also showed that, by removing the top thermal insulation layers from the terrace, the adding of a supplementary over-roofing floor would not affect the concrete structure's resistance or stability. Thus, steel was the material chosen for this over-roofing study, due to its lightness, reversibility and clean site.

The over-roofing systems were analysed by including in the already built models in ETABS, the new steel structures as shown in Figure 4. The over-roofing was designed in accordance with the following standards: (1) EN 1990-1-1-2004 "Design code. Basis of structural design"; (2) EN 1991-1-1-2004 "Design code. Evaluation of load actions on structures"; (3) EN 1993-1-1-2004 "Design of steel structures"; (4) EN 1998-1-1-2004 "Design of structures for earthquake resistance". For the seismic analysis of the over-roofing system, a behaviour factor q = 1, specific to non-dissipative structures was chosen.

Three types of solutions for over-roofing based on intensive use of steel were chosen for numerical studies: (a) over-roofing solution based on the use of hot-rolled profiles (IPE beams and HEB columns); (b) over-roofing solution based on the use of rectangular hollow sections for columns and IPE beams; (c) over-roofing solution based on the use of cold-formed sections.

Due to the fact the existing structures are very rigid, i.e. the first period of vibration is 0.1 seconds, no amplification effects will be introduced to the new structure. In these conditions the new structure can be designed independently but, a very important aspect is the connection of over-roofing to the existing structure.

Table 1 presents the main dimensions obtained for the three over-roofing systems presented above.

Therefore, semi-rigid and rigid column-based connections were further investigated (see next paragraph), for all 3 cases, by using numerical analyses, in order to determine the optimum solution for connecting these over-roofing systems (see Figure 5).

Table 1. Main dimensions for the over-roofing systems.

Systems	Cross-section	Type of element
HR	HEB180	Columns in current frames
	IPE220	Beams in current frames
	HEB100	Columns in gable frames
	IPE160	Beams in gable frames
	TV100 × 100 × 4	Longitudinal beams
	ϕ16	Roof bracings
	ϕ24	Wall bracings
RHS	RHS220 × 220 × 8	Columns in current frames
	IPE220	Beams in current frames
	IPE160	Beams in gable frames
	IPE200	Longitudinal beams 1
	RHS100 × 100 × 4	Longitudinal beams 2
	ϕ16	Roof bracings
CF	2C300 × 2	Columns
	2C300 × 2	Beams
	RHS100 × 100 × 4	Longitudinal beams
	ϕ16	Roof bracings
	ϕ24	Wall bracings

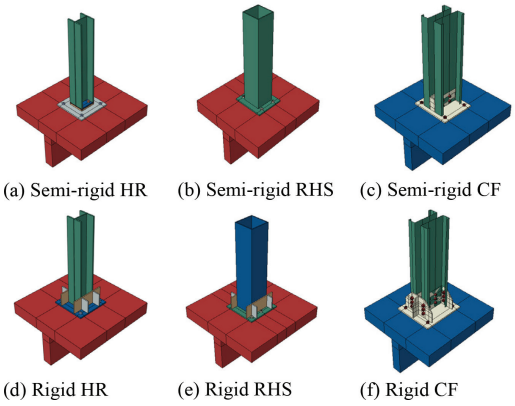

(a) Semi-rigid HR (b) Semi-rigid RHS (c) Semi-rigid CF

(d) Rigid HR (e) Rigid RHS (f) Rigid CF

Figure 5. Semi-rigid and rigid column-base connections.

4 NUMERICAL ANALYSIS

In order to prove the efficiency of the column-base connections chosen for this study, numerical simulations were performed using FE software ABAQUS 6.7. Semi-rigid and rigid base connections using the steel solutions presented above were detailed in the following, as presented in Figure 5.

The first numerical model (see Figure 5a) is a semi-rigid connection with two base plates, connected with two groups of bolts, i.e. M16 and M20. The column is a hot-rolled profile, as shown in Table 1. The first plate is welded on the contour to the base plate connection and the bolts that make the connection with the column are countersunk bolts in this plate. The entire connection is linked to the existing building through a base plate of 390 mm length and a thickness of 25 mm and through angle profiles at the opposite face of the concrete floor. For the rigid connection (see Figure 5d), the detail is simplified by eliminating the intermediate base plates and the countersunk bolts but, supplementary stiffeners of 150 mm height and 10 mm thickness were added.

The second set of numerical models (see Figures 5b and 5e) were also analysed as semi-rigid and rigid connection, but with only one base plate. The column is a rectangular hollow section of 220 × 220 × 8 mm. The dimensions of the base plate are 460 × 420 × 25 mm. The bolts and angle profiles are of the same dimensions as in the previous case, only the bolts' distance being adapted to the new conditions. The rigid connection follows the same pattern as in the previous case.

The third set of numerical models (see Figure 5c and 5f) is also analysed in both cases, as semi-rigid and rigid connection. The column is composed of two back-to-back cold-formed lipped channels of 300 mm height and a 2 mm thickness. Two rows of M16 bolts were used to connect the webs of the profiles via a steel box section of 6 mm thickness of the walls and 150 mm height, placed between the two sections of the column, composing the semi-rigid solution. The geometrical characteristics of the base plate and the angle profiles are the same as for the previous case. For the rigid connection, supplementary stiffeners and bolts were added to connect the flanges of the profiles. Elasto-plastic material models were used for all elements, with the particularity for the M16 bolts class 8.8. For these a correct material model was implemented (Frick 2014), instead of simplified assumption, as can be seen in Figure 6. This was needed in order to obtain a correct strain evaluation and then a faster convergence rate.

SHELL elements of S4R type, with 4 nodes, reduced integration, 6 DOF per node were used for modelling the cold-formed steel sections, while for all other sections, BRICK elements of C3D8R

type, with 8 nodes, reduced integration, 6 DOF per node, were used. Also, the concrete was considered in the analysis as elastic-perfect plastic, as shown in Figure 7 (Korotkov et al. 2004). The option used to simulate concrete plasticity was Concrete Damaged Plasticity.

Concerning the contact between the elements, an initialization strain free step was introduced, which is a preliminary step automatically performed by Abaqus in order to fix initial clearance and geometric interferences introduced by the meshing, for example between bolt-hole and external bolt surface. Secondly, a standard default stabilization property offered by Abaqus was added. Last but not least, the main contact problem concerning the interaction properties of the elements were introduced trough the "All with self" option.

In order to obtain accurate results the Abaqus standard implicit solver was used. Initial convergence problems were issued by a preliminary step of preload and the actual load of 200 mm displacement was imposed trough a Riks step.

The bolt preload was added as a pretension in the bolt axes trough the proper Abaqus option. The step was solved by the standard Newton-Raphson algorithm that needs a small initial time increment, but it performs the full analysis in 8 or

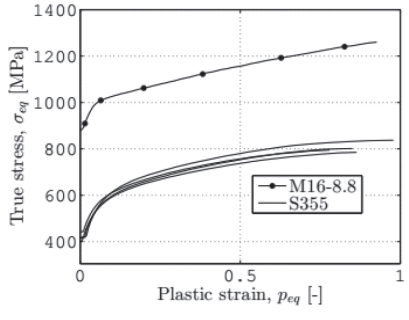

Figure 6. Stress-strain curves considered for M16 bolts class 8.8 (Frick, 2014).

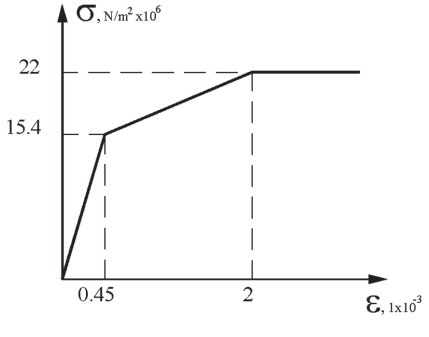

Figure 7. Elastic-plastic model of concrete.

9 time increments; the iterations are due to initial contact setup. These initial pretensions, however, helped the convergence in the following Riks step.

The actual imposed displacement of 200 mm on the column top was performed by Riks step controls. Thus, the automatic time increment schema was used, but in order to prevent huge increments that reduce the convergence rate, a limitation in the maximum increment was assumed equal to 1/50 of the total time (1.0). A relaxed convergence criterion was introduced by incrementing the equilibrium tolerance and accepting the solution. Also, after the maximum number of iterations was reached, it was incremented with respect of the default in order to ensure a suitable convergence.

For the meshing control, fully integrated linear 8 noded elements were needed. In order to obtain correct strains in the plasticity range, fully integration was used with distortion control, C3D8 for brick and S4 for Shell. In the reinforced concrete part, the elastic material and the reduced integration were used. Furthermore, for each part a proper element size was used, each size being optimized by a convergence study. For the plate parts with solid mesh, a minimal number of three elements through the thickness were used in order to improve the plastic strains and the global solution. Also, for the bolts a fine mesh was used. Moreover, for the parts in contact, master-slave types, a finer mesh was used for the slave ones.

The following results were obtained: (1) the first three connections were modelled as semi-rigid but present mostly a pinned behaviour; (2) the performances of the three case scenarios were obtained under lateral loading; (3) after numerical analysis the load transfer mechanism was identified; (4) the weak components were pointed out, which are presumed to yield first; (5) plastic efforts and deformations were obtained; (6) the maximum stresses for the semi-rigid hot-rolled connection was reported in the countersunk bolts; (7) the welded plate of the semi-rigid hot-rolled profile presents a slight plastic deformation (see Figure 8a); (8) the maximum stresses of the rectangular hollow section connection was noticed in the bolts and on the corresponding holes (see Figure 8b); (10) the maximum stresses for the cold-formed connection was reported in the upper flange of the section on the direction of loading, but also around the holes of the web (see Figure 8c); (11) for the third case scenario (rigid solution), the plastic stresses achieve maximum in the web height; moreover, the phenomenon of web crippling occurs in the upper flange (see Figure 8f); (12) the concrete floors did not reach plasticity, not even in full loading conditions; the stresses are still in the elastic range, presenting only local effects at bolt-hole interaction zone, as shown in Figure 9.

The force-displacement curves obtained for each case scenario are presented in Figure 10.

The above force-displacement curves show the following partial conclusions: (1) the curves show no significant results after the threshold of 150 mm, the connections started to fail; thus, the initial load imposed to the columns should be reduced; (2) as expected the maximum capacity was obtained in the second case scenario (column-base connection with rectangular hollow section for the column), for both semi-rigid and rigid solutions (see Figure 10b and 10e); (3) the first and third case scenarios present almost the same capacities, in both semi-rigid and rigid solutions, with the difference that the connection using hot-rolled profile for column presents a higher ductility than the cold-formed section one, especially in the case of rigid solution; (4) the semi-rigid solutions present, as expected, smaller loading capacities, but the intention of using theses solution was to reduce the local effects on the existing structure; (5) the stress level on the existing concrete floors and the additional walls are small and do not introduce supplementary stresses over the existing capacity.

Taking the study further, a chemical anchorage system based on epoxy resin was numerically investigated on the optimum study-resulted solution, the two cold-formed cases, in order to offer a better option for the comfort of the occupants. This solution was chosen for testing as it gives minimum disruption to the last level apartment owners and also for minimum concrete damage.

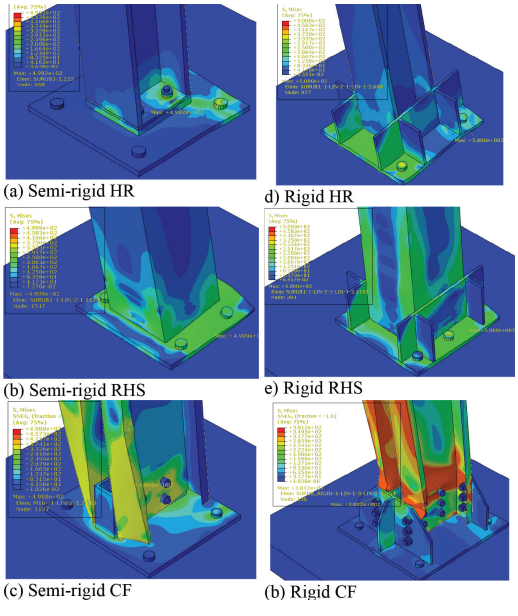

Figure 8. Distribution of stresses in the based connections.

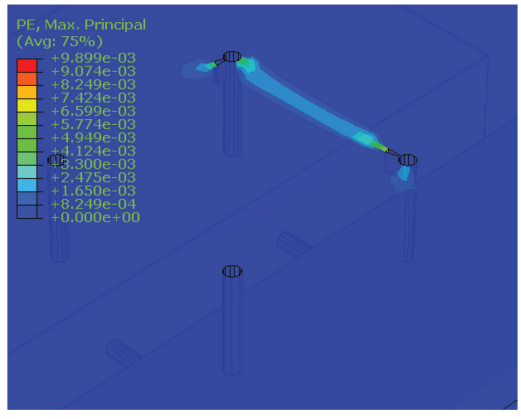

Figure 9. Strains in concrete on bolt hole.

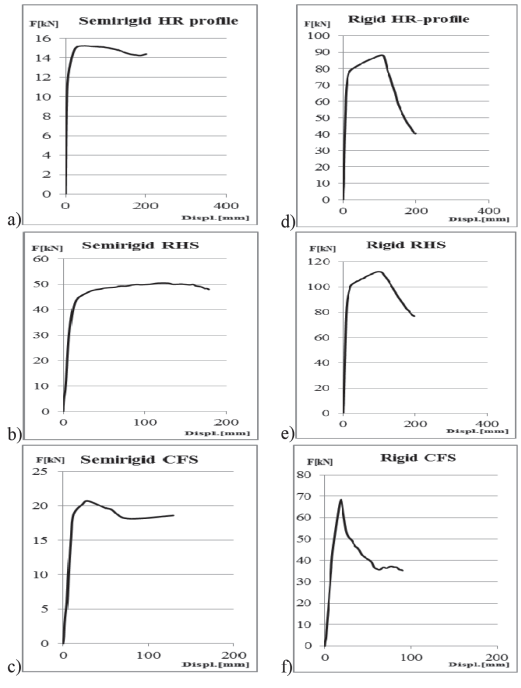

Figure 10. Force-displacement curves for the semi-rigid and rigid steel base connections.

Generally speaking, there is a large variety of chemical anchor types available on the market. As a basic description they are basically a steel screw positioned in a predrilled hole in the concrete material. The connection between the steel screw and concrete is assured by pouring glue-based material (resin). According to most used design methods, at ultimate tensile force of these chemical anchors

the concrete or bond should fail separately. This assumption is also used in certification regulations for steel post-installed anchors for concrete e.g. ETAG.

The two cold-formed models were re-designed in the same finite element software, with chemical anchorage. Most geometrical characteristics were preserved, with a few minor adjustments of bolt distance. However, the steel box section, connecting the two back-to-back cold-formed steel sections, was replaced by a more adequate and practical steel sheet of 6 mm thickness. Nevertheless, the angle profiles were not necessary in this case as the anchors were embedded in concrete (see Figure 11). Also, the same elasto-plastic materials were used in designing the assembly.

Dynamic explicit analysis was used with a lateral displacement force of 200 mm. The initial axial preloading was still necessary for the semi-rigid section in order to simulate real-life loading conditions.

The following results were obtained: (1) the semi-rigid model presents maximum stresses around web bolt-holes and in upper section flanges; moreover at maximum loading conditions the flanges on the direction of loading are crushed; (2) the base-plate of the column presents large deformations in the tension zone (see Figure 12a); (3) for the rigid model, the stiffeners do not allow section rotation, so the flanges are crushed and a phenomenon similar to web crippling appears (see Figure 12b); (4) the concrete floor in both models shows some amount of plasticity at full loading conditions and mostly locally on bolt holes; however, the column sections failed much earlier before concrete reaches its plastic limit (see Figure 13).

The force-displacement curves obtained for each case scenario are presented in Figure 14.

The force-displacement curves show, as expected, the semi-rigid solution has smaller loading capacities than the rigid one, but the intention was to reduce the local effects on the existing structure. The stress level on the existing concrete floors and the additional walls are small and do not introduce supplementary stresses on the existing structure.

The scope of the numerical program is a better understanding of the behaviour of these types of column-base connections and to find the optimum solution for this kind of over-roofing systems, by limiting the stresses to the existing concrete panel building. Based on this numerical study several types of these connections will be experimentally investigated.

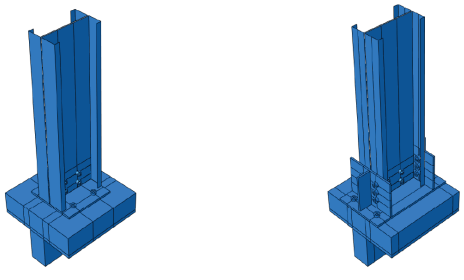

(a) Semi-rigid CF (b) Rigid CF

Figure 11. Cold-formed steel column-base connections with chemical anchorage.

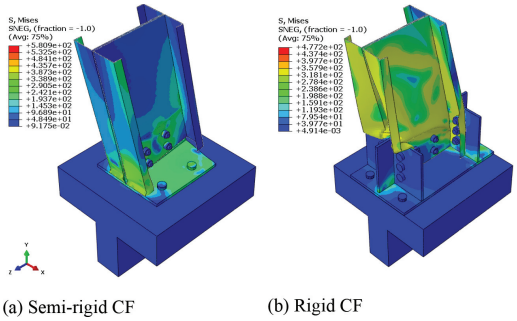

(a) Semi-rigid CF (b) Rigid CF

Figure 12. Distribution of stresses in the column—based connections with chemical anchorage.

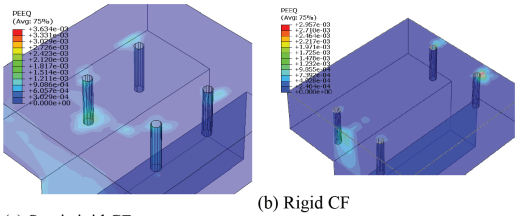

(a) Semi-rigid CF (b) Rigid CF

Figure 13. Distribution of stresses in concrete with chemical anchorage.

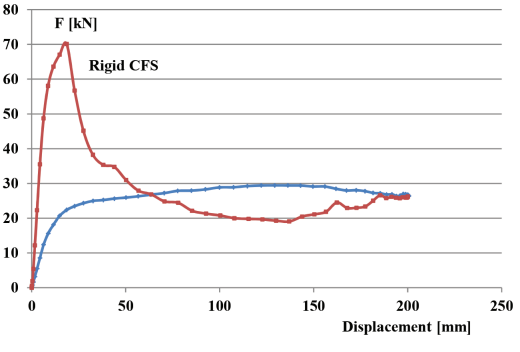

Figure 14. Force-displacement curves for the semi-rigid and rigid cold-formed steel base connections with chemical anchors.

5 CONCLUSIONS

The study presented in this paper shows several possibilities of connecting steel-intensive over-roofing to the existing concrete buildings. The numerical analyses show the following: (1) steel-intensive solutions are ideal systems for over-roofing the existing large precast concrete panel buildings due to their lightness, reversibility and clean sites; also, they can adapt to existing structural systems and several structural typologies can be thought; (2) the numerical program shows that all types of connections presented in semi-rigid and rigid solutions can withstand a considerable amount of loading; (3) however the main concern remains to minimise the structural intervention on the existing concrete structure. Finally, supplementary numerical analyses and experimental tests will be done in order to validate the proposed solutions.

A better solution for the comfort of the occupants seems to be the connection by chemical anchorage. The results show that the column behaviour is mostly the same as for the first solution. Experimental tests will be done in order to validate the proposed solutions.

ACKNOWLEDGEMENT

This work was partially supported by the strategic grant POSDRU/159/1.5/S/134378 (2014) of the Ministry of National Education, Romania, co-financed by the European Social Fund—Investing in People, within the Sectoral Operational Programme Human Resources Development 2007–2013.

REFERENCES

ABAQUS/Standard Version 6.7–1. 2007. Providence, RI: Dassault Systemes, http://www.simulia.com/.

Botici, A.A., Ungureanu, V., Ciutina, A. & Dubina, D. 2012. Sustainable retrofitting solutions for precast concrete residential buildings. *Proc. of the 3rd Int. Symposium on Life-cycle Civil Engineering: Life-Cycle and Sustainability of Civil Infrastructures - IALCCE 2012*. Vienna, Austria (3–6/10): CRC Press: pp. 357 + CD: pp. 1722–1729.

Dubina, D., Ungureanu, V., Georgescu, M. & Fülöp, L. 2001. Innovative Cold-Formed Steel Structure for Restructuring of Existing RC or Masonry Buildings by Vertical Addition of Supplementary Storey. *Proceedings of the 3rd International Conference on Thin-Walled Structures "Advances and Developments"* J. Zaras, K. Kowal-Michalska, J. Rhodes (eds.), Cracow, Poland (5–7 June). Elsevier:187–194.

ETAG 001 2006. Anchoring design methods, *EOTA European Organisation for Technical Approvals,* Avenue des Arts 40, Kunstlaan, 1040 Brussels.

Frick, H. 2014. Beam - Column Connections Subjected to Static and Dynamic Loading. *Master Thesis*, Norwegian University of Science and Technology, Trondheim.

INNSE 2003. The official census regarding population and dwellings made on March 18–27, 2002. The National Institute of Statistics, Romania. http://www.insse.ro/.

Korotkov, V., Poprygin, D., Ilin, K. & Ryzhov, S. 2004. Determination of Dynamic Reaction in Concrete Floors of Civil Structures of Nuclear Power Plant in Accidental Drops of Heavy Objects, *ABAQUS Users' conference*.

Lawson, M., 2008. WP3.1 Review of roof-top extensions using light steel construction", *Renovation of buildings using steel technologies (ROBUST)*, RFCS Project RFSR-CT-2007–0043.

Norris, M., Shiels, P. 2004. Regular National Report on Housing Development in European Countries – Synthesis Report*, The housing unit*, Dublin, Ireland.

Recent Progress in Steel and Composite Structures – Giżejowski et al. (Eds)
© 2016 Taylor & Francis Group, London, ISBN 978-1-138-02946-0

Numerical analysis of stainless steel bolted lap joints

A. Silveira, W. Barbosa, P. Vellasco, A. Silva & L. Lima
Department of Structures and Foundation, State University of Rio de Janeiro, Brazil

ABSTRACT: The use of stainless steel in civil construction has been increasing in recent years due to its inherent high corrosion resistance, aesthetics and environmental appeal. Current procedures to stainless steel joints design are still largely based on analogies to carbon steel despite the fact that stainless steel has significantly different mechanical characteristics and structural performance. The present research work aims to numerically investigate the structural response of lap bolted joint for two stainless steel grades: austenitic and ferritic. The nonlinear numerical analyses carried out using the ANSYS 13 presented a good agreement in terms of the maximum load and failure mode when compared to experimental tests. Moreover, an initial assessment of the structural capacity of these joints has been performed based in the Continuous Strength Method (CSM). The results indicated a good agreement with the ferritic steel grade while significant differences were observed for the austenitic steel grade, possibly due to the adopted conservative deformation limit.

1 INTRODUCTION

1.1 *Stainless steel*

The use of stainless steel in civil construction has been increasing in recent years, mainly due to high corrosion resistance, aesthetics and environmental appeals. Current stainless design codes, for instance EN1993-1-4 (2006), are still largely based on analogies to carbon steel despite the fact that stainless steel has significantly different mechanical characteristics and structural performance. It is common knowledge that the stainless steel presents four nonlinear stress versus strain curves (tension and compression, parallel and perpendicular to the rolling direction). These steels do not present a defined yielding stress while some grades possess a substantial strain hardening region, fact that significantly modifies their global structural response (Santos et al. 2013).

The present research work aims to numerically investigate the structural response of lap bolted joint for two stainless steel grades: austenitic and ferritic. It is recognized that there is substantial difference among these stainless steel types, namely, the constitutive law. The joints have been designed based on the Eurocode EN1993-1-4 (2006). The nonlinear numerical analyses have been carried out using the ANSYS 13.0 (2010).

Moreover, an initial assessment of the structural capacity of these joints has been performed based in the Continuous Strength Method (CSM). The EN1993-1-4 (2006) establishes the procedures for the stainless steel plate design under tensile forces. The structure failure is associated to the smallest tension forces capacity obtained while considering two limit states: gross cross-section yield given by Equation 1, or the ultimate net cross-section tension rupture expressed by Equation 2:

$$N_{pl,Rd} = \frac{A_g \times f_y}{\gamma_{M0}} \tag{1}$$

where, $N_{pl,Rd}$ is the tension plastic capacity, A_g is the gross area, f_y is the steel yield stress and γ_{M0} is the partial safety factor, in this case equal to 1.

$$N_{u,Rd} = \frac{k_r \times A_n \times f_u}{\gamma_{M2}} \tag{2}$$

where,

$$k_r = \left(1 + 3r\left(\frac{d_0}{u} - 0.3\right)\right) \tag{3}$$

where, A_n is the net cross-section area, f_u is the steel tension rupture stress, k_r is obtained from Equation 4 and γ_{M2} is the partial safety factor, in this case equal to 1.25. From Equation 4, r is the ratio between the number of bolts at the cross-section and total number of joint bolts, d_0 is the bolt hole diameter, $u = 2.e_2$ but $u \leq p_2$ where e_2 is the edge distance from the bolt hole center to its adjacent edge, in the direction perpendicular to the applied

load direction and p_2 is the hole center-to-center distance measured perpendicular to the applied load direction.

1.2 *Case studies*

Figure 1 illustrates the investigated joint geometry. These structural dimensions correspond to experiments performed by Santos (2014) involving bolted lap joint made of stainless and carbon steel grades with 24 mm horizontal gaps. The bolted lap joints were made of two 3 mm thick plate and two 15 mm thick carbon steel plates with a 5 mm gap (Figure 1a).

Carbon type steel plates USI 300 and austenitic stainless steel type S304 and ferritic stainless steel grade from line 430 were used in the experiments. The stainless steel yield stress was determined by a straight line parallel to the initial stiffness at a 0.2% stain leading to a value equal to 350 MPa, 352 MPa and 386 MPa for the austenitic, ferritic and carbon steel grades. These yield stresses were obtained from a mean value evaluated from six coupon tests for each steel grade

The bolted lap joint tests were carried out on a 600 kN universal Lousenhausen machine. The data acquisition in terms of strains, displacements and applied loads was performed using the National Instruments system NI-PXI-1050.

1.3 *Numerical models*

The finite element model used in this paper to investigate the load carrying capacity of bolted lap joints was developed with the aid of the ANSYS 13.0 (2010). The numerical model adopted solid elements (SOLID45) defined by eight nodes with three degrees of freedom per node. The adopted mesh was chosen so that the elements had a proportion and size to avoid numerical problems. Figure 2 presents a typical mesh configuration of the complete model. Only half of the model was considered due to symmetry. Contact elements (CONTA173 and TARGE170) present in the ANSYS 13.0 (2010) library were used between the plates and between the holes and the bolt shanks.

The load was applied by means of equivalent displacements (UX), Figure 2. In this figure, it is also possible to observe that the bolt head and nuts were simulated through UZ displacements restraints at the hole adjacent area. The adopted material properties were: Young's modulus of 210 GPa and a 0.3 Poisson's coefficient.

The material modeling was based on stainless steel true stress versus true strain curves with a nonlinear behavior using data from the tensile coupons tests (Santos et al. 2013). In fact, the nominal stress-strain curve obtained from conventional coupon tests does not represent the actual behavior of the material,. Figure 3 depicts the difference between nominal and true stress-strain curves for the austenitic stainless steel grade.

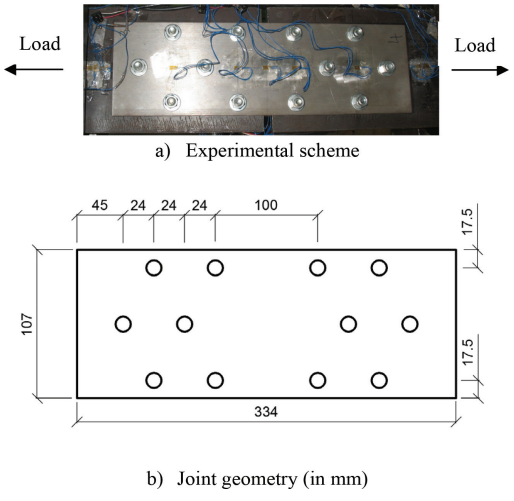

a) Experimental scheme

b) Joint geometry (in mm)

Figure 1. Case studies.

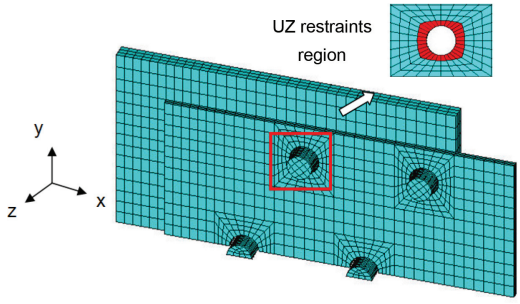

Figure 2. Finite element model.

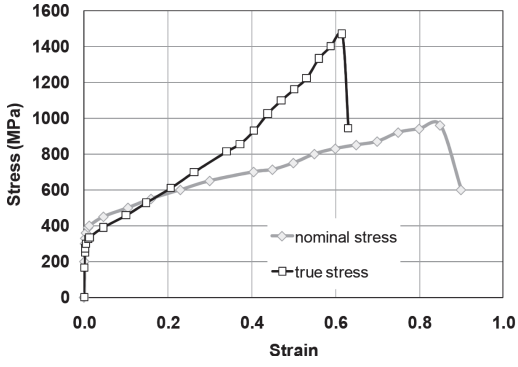

Figure 3. Stress vs. strain curves for the A304 stainless steel.

A full nonlinear analysis was performed for the developed numerical model. The material non-linearity was considered using a Von Mises yield criterion associated to a multi-linear stress-strain relationship and an isotropic hardening response. The geometrical non-linearity was introduced in the model by using an updated Lagrangean formulation. This procedure represents the full structural assessment of the analyzed bolted joints, and may be summarized in several outputs, i.e. stress distribution or the load-displacement curve for any node within the joint.

1.4 *Results*

Figure 4 to Figure 6 present the numerical load-displacement curves for all the performed experiments; highlighted, carbon, ferritic stainless and austenitic stainless steel grades, respectively. The ultimate strength (failure load) in the analysis is assumed to be the maximum load obtained from load-displacement curve. In all the performed simulations, therefore, it was observed that the numerical peak loads were close to experiments collapse loads. On the other hand, the numerical models response showed a higher initial stiffness in comparison with experiments. In fact, this aspect may be attributed to plastic deformations that occur when the bolt shaft touches the hole edge in the initial load stages, due to the inherent difficulties associated to this this contact problem.

Moreover, these figures depict the Von Mises stress and plastic deformation distribution for the three numerical models. The investigated models presented high stresses in the region between the hole and the plate edge being accomplishing by plastic deformation. It is notorious to observe that it was possible to represent the collapse scenario observed in the experiments. The carbon and ferritic stainless steels showed a net cross-section tensile rupture passing through three holes. In contrast, both numerical and experimental cases exhibited

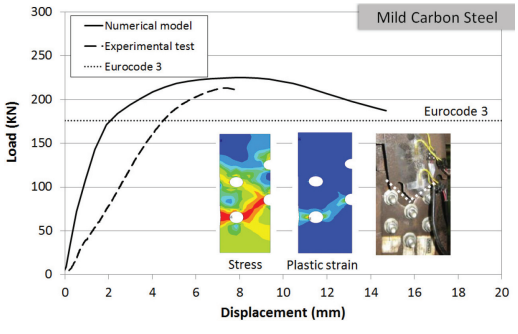

Figure 4. Comparing experimental and numerical response for the ferritic stainless steel grade.

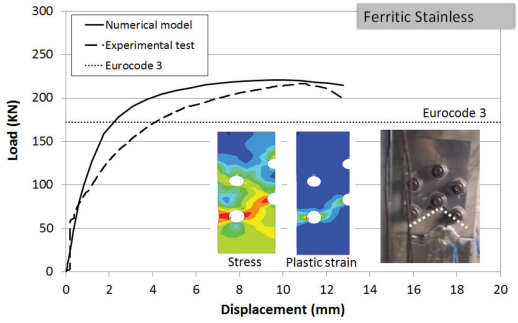

Figure 5. Comparing experimental and numerical response for ferritic stainless steel grade.

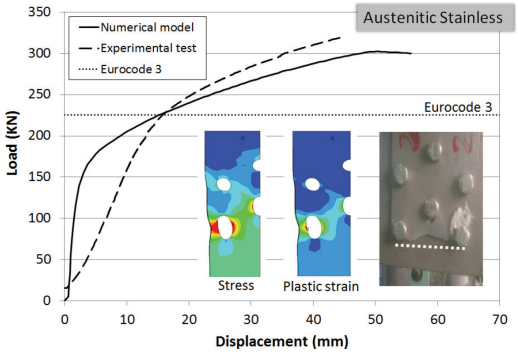

Figure 6. Comparing experimental and numerical response for the austenitic stainless steel grade.

a large stress concentration in area located at the hole edge. In fact, due to adopted austenitic stainless steel constitutive law a more ductile behavior was observed when compared to the response of the carbon steel and ferritic stainless steels. In these last two steel grades there was a change in the collapse scenario now associated to a net cross-section tensile rupture passing through two holes.

Comparing to design strength obtained applying the rules from EN1993-1-4 (2006), it is recognized that strength from both numerical and experimental tests led to values higher than the design code predictions. This is expected due to expected safety level usually adopted in design codes. However, it can be noted that this difference is more significant for the austenitic steels (37%) than in carbon (22%) and ferritic steel (21%) steel grades. According to load-displacement curves, the EN1993-1-4 (2006) considers as design load value a close to end of the elastic range. This assumption makes the code conservative, mainly for the austenitic grades, because this stainless steel have a large deformation capacity and a high load capacity in the plastic range.

In general, the results evidenced a high load capacity of the austenitic stainless steel in comparison to the carbon and ferritic steel grades. In addition, it was possible to observe a similar behavior between the carbon and ferritic steels in terms of both load capacity and ductility. Additionally it is interesting not to forget the extra advantages of the ferritic stainless steel when compared to the carbon steel: low maintenance cost and aesthetic appeal.

2 CONTINUOUS STRENGTH METHOD ASSESSMENT

This section is centred on the assessment of the Continuous Strength Method (CSM) for stainless bolted lap joint design. Thus, a model has been studied based on the numerical response for stainless bolted joint with two roles evaluating both the gross section yield and net section tensile rupture with the CSM provisions.

The CSM was recently developed and is based on deformation limits to enable the design in the plastic range. This is reflected by the incorporation of beneficial strength due to material strain hardening effects while providing an increase of its load carrying capacity. In fact, materials having a high degree of nonlinearity and strain hardening, such as some stainless steel grades are properly designed with the CSM, and it can benefit from use (Afshan & Gardner 2013). An additional advantage of the proposed approach is that the deformability of the structural member is explicitly determined, allowing for a more realist ductility assessment fully utilizing the stainless steels elements.

This method uses a bilinear model to characterize the material behavior (see Figure 7). The first segment corresponds to the material elastic range defined by a straight line parallel to the elastic portion of the curve drawn from at a 0.2% strain. The yield stress (f_y) and strain (ε_y) are determined when this parallel line intercepts the material curve. Equation 4 is used to define the yield strain:

$$\varepsilon_y = \frac{f_y}{E} \tag{4}$$

where, E corresponds to the stainless steel Young modulus and f_y is the evaluated yield stress.

The second segment of curve is determined by the slope of the line passing through the point (f_y,ε_y) and the point corresponding to maximum value for both yield and strain (f_{max}, ε_{max}). The ε_{max} is determined as 0.16 ε_u where ε_u is the ultimate strain corresponding to the coupon test tensile rupture and f_{max} (or f_u) is the ultimate stress related to the coupon test tensile rupture. From these parameters, the plastic material model slope can be determined, Equation 5:

$$E_{sh} = \frac{\left(f_u - f_y\right)}{\left(0.16\varepsilon_u - \varepsilon_y\right)} \tag{5}$$

where, E_{sh} is the plastic material model slope.

The ultimate stress (f_{csm}) can be interpreted as the maximum stress observed at the collapse considering the increased strength of steel due to the strain hardening effect ie.:

$$f_{csm} = f_y + E_{sh}\left(\varepsilon_{csm} - \varepsilon_y\right) \tag{6}$$

The value of the parameter, ε_{csm}, corresponds to the smallest value between $0.1\varepsilon_u$ or $15\varepsilon_y$. Finally the structural member gross section tension capacity based in CSM is defined as:

$$N_{csm} = \frac{A_g \times f_{csm}}{\gamma_{M0}} \tag{7}$$

2.1 *Investigated model*

In order to evaluate the use of CSM in bolted joint submitted to shear, a simply model with two holes has been studied. This model corresponding to the same geometry studied in Kim & Kuwamura (2007). These authors carried out a set experiments using austenitic stainless steel plates. The experimental scheme can be seen in Figure 8a. Both ends of test specimen were fixed to a standard universal

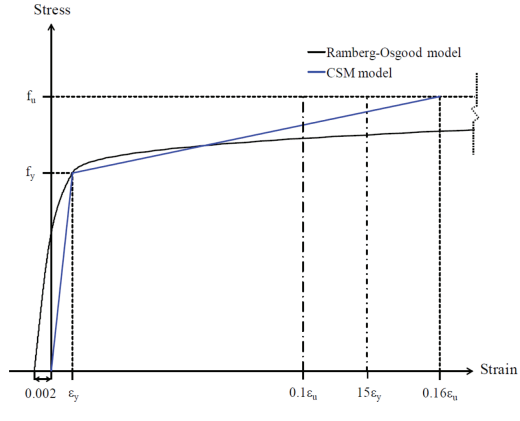

Figure 7. Bilinear curve from the continuous strength method (Afshan & Gardner 2013).

test equipment in which a tensile force was monotonic applied to the test specimen with a displacement control strategy.

The investigated models consist of a 3.0 m thin plate with two hole of 12 mm diameter bolt. Both austenitic and ferritic stainless steel grades have been evaluated. Kim & Kuwamura (2007) only studied the structural behavior of the bolted lap joints using austenitic stainless steel grades—SUS304. However, in the present investigation the ferritic grade with the same constitutive law utilized in the previously analyses was also modelled. The geometry of the investigated models can be seen in Figure 8b.

The numerical model used this section was based on same previous premises. In details, ANSYS 13.0 (2010) was chosen as the finite element program adopting a 3D analyses using solid elements (SOLID45). Moreover, contact elements (CONTA173 and TARGE170) presented in ANSYS 13.0 (2010) were considered between the holes and bolt shanks. The complete model can be observed in Figure 9. Regarding to boundary conditions, they were adopted in order to simulate the actual behavior of the experiments, therefore, in one of the joint ends all the nodes were coupled to a a single node where a displacement was applied to simulate the load. This strategy reduced the analyses computational time.

It is also possible to observe that the bolt head and nuts were simulated through UZ displacements restraints at the hole adjacent area. Furthermore, there is no displacement in X direction. In order to give a level of stability to numerical model, the outplane displacement were restricted in four nodes at the ends.

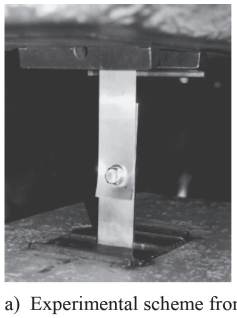

a) Experimental scheme from Kim & Kuwamura (2007)

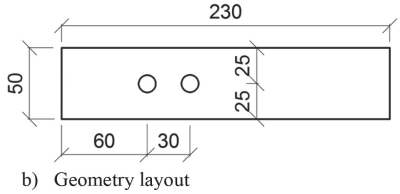

b) Geometry layout

Figure 8. Investigated model.

Concerning to material modelling, the same strategy of using the true stress vs. true strain curves was used. A full nonlinear analysis was performed for the developed numerical model. The material non-linearity was again considered by using a Von Mises yield criterion associated to a multi-linear stress-strain relationship and isotropic hardening response.

2.2 *Results*

Figure 10 depicts the response in terms of load-displacement curve comparing the ferritic with austenitic numerical model. As expected, the model with austenitic constative law led to the higher ultimate strength and associated displacement. In fact, this trend had already been occurred in previous analyzes.

Comparing the ultimate load obtained from numerical model with experiments performed by Kim & Kuwamura (2007), it can be noted that there is a good agreement with numerical and experimental ultimate loads of 84.77 kN and 85.62 kN. This difference correspond to 1% difference. It is again important to stress that these results were associated to the austenitic grade model.

Figure 11 illustrates the Von Mises stress distribution associated to the numerical models ultimate loads. It can be noted that there was a high strength concentration in net section characterizing a tensile fracture for both austenitic and ferritic models. The stresses in these zones exceeded

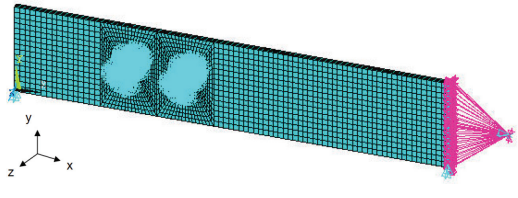

Figure 9. Description of the study case.

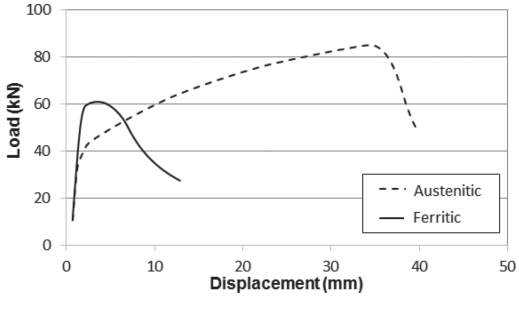

Figure 10. Ferritic & austenitic load vs. displacement curves comparison.

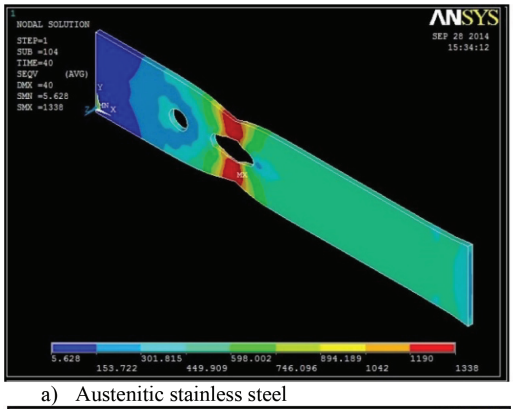

a) Austenitic stainless steel

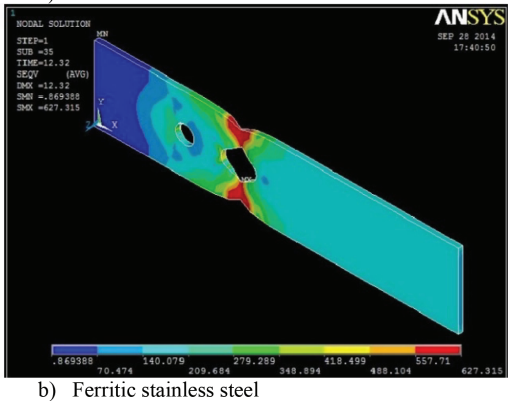

b) Ferritic stainless steel

Figure 11. Von Mises stresses distribution.

the yield stress values of the stress-strain curves. A net section rupture was also observed in experiments for austenitic test.

Table 1 reports the comparison among the numerical, EN1993-1-4 (2006) and CSM responses. As expected, the values recommended by the code are lower than the load carrying capacity observed in numerical model. This fact has already been noted for the cases stated in the previous sections. There was a good agreement between the design predictions associated to the net section ruptures and the numerical model for the ferritic case. On the other hand, the numerical model with austenitic stainless presented a resistance capacity larger than recommended value from EN1993-1-4 (2006) for the two limit states.

As expected, the design resistance predicted by CSM led to a higher values than the Eurocode $N_{pl,Rd}$ due to contribution of the hardening effects. This fact is important when the analysis is made for the austenitic model because the gross section yield governed the structural joint design. Therefore, it confirms the safe predictions from of the EN1993-1-4 (2006) when is used a steel grade with large

Table 1. Assessment of the CSM results and the Eurocode provisions (loads in kN).

Models	FEM	$N_{pl,Rd}$	$N_{u,Rd}$	f_{csm}
Austenitic	84.7	38.3	59.4	61.4
Ferritic	60.6	74.2	61.7	75.9

hardening effects. In the ferritic case, it can be noted that the difference between the CSM and the Eurocode $N_{pl,Rd}$ is lower due to the small contribution of the hardening effects. This fact can be also explained by the limitation of deformations. As had been mentioned, the ε_{csm} is determined for the smaller of two deformations: $0.1\,\varepsilon_u$ or $15\varepsilon_y$. However, the austenitic steel has a deformability higher than that observed in the ferritic steel. Thus, eventually having a limited strength as a matter of deformation. On the other words, the maximum deformation from austenitic model was governed by $15\varepsilon_y$, while for the ferritic case, the value was $0.1\varepsilon_u$.

These results concludes that further research on the applicability of this method should be conducted studying the method based on the limit deformation. In fact, the materials behave differently, therefore could be more interesting to apply a deformation criteria related to the limit of each material. Furthermore, it is important to mention that this proposed was directed to yielding of the gross cross-section, therefore, an additional propose can be address to assessment of the collapse of net cross-section.

3 CONCLUSIONS REMARKS

The present paper aimed to evaluate the structural response of stainless steel lap plate joints with staggered holes. The adopted methodology first considered the available stainless design procedures where the EN1993-1-4 (2006) may be cited. Subsequently, a numerical investigation was made considering three experiments where the material was modified in order to verify the structural behaviour. In detail, three study cases were examined considering a unique geometry for carbon, austenitic stainless and ferritic stainless steel grades.

Comparing the numerical against experimental response, a good agreement in terms of the maximum load and failure mode for three material was observed. On the other hand, the numerical models response presented a larger initial stiffness in comparison to the experiments. In fact, this aspect may be attributed to the occurrence of plastic deformations when the bolt shaft touches the hole edge in the accommodation process, since the phenomena inherent in this process can not be established with

sufficient precision. In addition, it is recognized that strength from both numerical and experimental tests delivered values higher than preconized by code. This is expected due to conservatism that is generally incorporated in the codes. However, it can be noted that this difference is more significant for the austenitic stainless (37%) in comparison to carbon (22%) and ferritic stainless steel grade (21%). In fact, the results evidenced a high load carrying capacity associated to the austenitic stainless steel in comparison to the carbon and ferritic steel grades. This paper aimed to perform an initial study of the applicability of the CSM in which there is a significant strain hardening effect contribution on the stainless steel members structural strength.

The resistance forecasted by CSM is higher than $N_{pl,Rd}$ due to the contribution of the strain hardening effects. This fact is important when the analysis is toward for the austenitic model because the gross section yield governed the structural joint design. Therefore, it confirms the conservatism of the EN1993-1-4 (2006) when is used in a steel grade with high strain hardening effects. Concerning to ferritic case, it can be noted that the difference between the CSM and $N_{pl,Rd}$ is lower when compared to other stainless steel grades due to the smaller strain hardening contribution.

These results indicate that further research on the applicability of CSM should be conducted better defining the stainless steel deformations limits. Furthermore, it is important to mention that the current CSM proposal was directed to the gross section yield, therefore, an additional equation associated to the net section rupture need to be calibrated based on the stainless steel deformation capacity including the strain hardening effects.

ACKNOWLEDGMENTS

The authors would like to thank CAPES, CNPq and FAPERJ by the financial support to develop this research program.

REFERENCES

Afshan, S. & Gardner, L. 2013. *The continuous strength method for structural stainless steel design. Thin-Walled Structures*, v. 68: pp. 42–49.

ANSYS 13.0. 2010. Inc. Theory Reference.

Cochrane, V. 1922. Rules for rivet hole deduction in tension members. *Engineering News-record*, v. 80.

EN1993-1-4. 2006. Design of steel structures—Part 1-4, General rules—Supplementary rules for stainless steel. CEN—European Committee for Standardization, Brussels.

Kim, T. & Kuwamura, H. 2007. *Finite element modeling of bolted connections in thin-walled stainless plastes under static shear. Thin-Walled Structures*, v. 45: pp. 407–421.

Santos, J., Silva, A., Lima, L., Vellasco, P., Andrade, S. & Silva, J. 2013. *Numerical and experimental assessment of stainless and carbon bolted tensioned members with staggered bolts. Revista Escola de Minas*, v. 66(2): pp. 165–172.

Santos, J. 2014. *Comportamento estrutural de elementos em Aço Inoxidável* (in portuguese). PhD Thesis, PUC-Rio, Brazil.

This page intentionally left blank

Recent Progress in Steel and Composite Structures – Giżejowski et al. (Eds)
© 2016 Taylor & Francis Group, London, ISBN 978-1-138-02946-0

FEM based assessment of the rotation capacity of bolted joints

K. Ostrowski
MTA Engineering Ltd., Rzeszow, Poland

A. Kozłowski
Rzeszów University of Technology, Rzeszów, Poland

ABSTRACT: The procedure for rotation capacity determination of end-plate bolted beam-to-column steel connections has been presented in the paper. As an example of application, joints composed of column made from the profile HEB300 and the beam from the profile HEA360 were used. The main variable factors in the analysis are the following: horizontal distance between the fasteners "w" (120÷180 mm), distance from the top surface of upper flange to the axis of bolts "c_{g1}" (50÷90 mm) and end-plate thickness "t_p" (10÷20 mm). The proposed procedure was built on the basis of the Finite Elements Method and numerical simulation with the use of experiment design approach. Material characteristics to FEM models were obtained through the multi-stage hierarchal validation of FEM models. Obtained by regression analysis rotation capacity formula can be used by designers to assess a real joint rotation.

1 INTRODUCTION

Steel structures were usually designed by assuming that the connections are either ideally hinged or fully rigid. Nowadays, this assumption was changed to a semi-rigid joint conception. The most important data for the analysis and design of semi-rigid frames are the M–ϕ curves (moment versus rotation), which represent the joint behavior. Rotation capacity of joints plays a very important role in the advanced analysis of steel frames, especially in the plastic analysis of frame structures with semi-rigid connections.

The design procedures given in Eurocode 3 (EN 1993-1-8) allow to estimate the moment resistance $M_{j,Rd}$ and initial stiffness $S_{j,ini}$ of the bolted joints, but there is not enough information for the calculation of a connection rotation capacity Φ_{cd}. There are only qualitative descriptions of rotation capacity of selected connection types. The previous analysis of rotation capacity was carried out with the use of component method (Kuhlmann, 1997; Silva & Girao, 2001; Beg et al., 2004), probabilistic analysis (Beg & Zupancic, 2004a; Silva et al., 2004) and finite element method (Ostrowski, 2014a; Ostrowski & Kozlowski 2014b), but without a practical suggestion how to apply them in the design process. In the whole world, hundreds of laboratory tests have been conducted, whose results are collected in the databases (Chen & Kishi, 1989; Weynand, 1992). However, those lab tests results very often do not provide the required data. In the laboratory tests the researchers often concentrated on determining only the joint initial stiffness, but not always on the maximum resistance of joints. Because of measuring difficulties, the rotation angle was not always recorded to the end of the test. Furthermore, laboratory tests are very expensive and time-consuming, therefore, they are conducted mainly for scientific reasons.

For the description of joint characteristic mathematical formulas were used in the following forms: linear, bilinear, multi-linear, polynomial (Frey & Morris, 1975), spline functions, power functions and exponential (Yee & Melchers, 1986). Instead of statistical models listed above, mechanical models were used which were the basis for developing component method in the Eurocode 3. There were also attempts to use artificial neural networks. An extensive description and a summary of proposed methods to forecast joint behavior can be found in (Jaspart, 1993; Kozlowski, 1996; Faella et al., 2000; Concepcion et al., 2011). Currently, numerical analyses used for the forecast of joint behavior are generally conducted by means of finite element method (Girao et al., 2006; Ostrowski, 2014a). In the paper the ANSYS software was used for the FEM models calculations.

The main problem connected with FEM modeling of the plastic range of material behavior is an adequate representation of experimental curve. This curve after reaching the maximum moment M_u (Fig. 1), changes into a declining curve, which is usually very difficult to obtain in numerical models.

The paper presents the procedure for obtaining a quantitative estimation of rotation capacity of stiff-

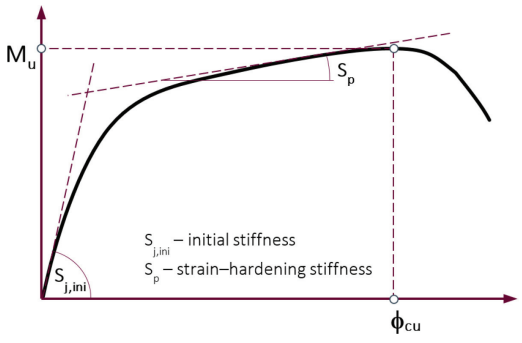

Figure 1. Graphical representation of rotation capacity.

ened beam-to-column end-plate connection with the use of advanced FEM analysis. The authors decided not to use the component method due to the inability to evaluate the changeable behavior of components caused by their mutual interaction.

In the analyzed exemplary joint, column was made from the profile HEB300 and the beam from the profile HEA360. The main variable factors in the analysis are the following: horizontal distance between the fasteners "w" (120÷180 mm), distance from the top surface of upper flange to the axis of bolts "c_{g1}" (50÷90 mm) and end-plate thickness "t_p" (10÷20 mm).

2 DEFINITION OF THE ROTATION CAPACITY

Among many others, the following definition of joint rotation capacity is proposed: this is the rotation angle of joint, which can be achieved without the decrease of joint resistance. This is shown in a graphical representation in Fig. 1. According to this definition, it is possible to determine the maximum available rotation angle of a joint.

3 METHODOLOGY OF ROTATION CAPACITY DETERMINATION

The algorithm of joint rotation capacity determination consists of the following steps:

- The first and the basic stage of this algorithm is to carry out laboratory tests of materials used to make these joints (Girao et al., 2004; Ostrowski & Kozlowski, 2015).The tests are performed on specimen material of beams, columns and end—plates.
- Then, the laboratory tests are performed on bolts sets: bolt-washer—nut (ISO 6892-1, ISO 898-1). In this test, the strains of particular bolt elements were measured.
- The next stage is to carry out a multi-stage, hierarchical validation of the FEM models. This validation consists in a comparison of laboratory tests' results with the results obtained in the FEM analysis. This process enables models' calibration.
- For each type of connection the parametric study is carried out. In this analysis, the variable factors are identified, which have the greatest influence on the rotation capacity.
- Constant factors are established such as: the grade of steel elements, the standard and class of bolts.
- For determination of the approximating function of the maximal rotation angle of joint, the theory of experiment design is adopted to the numerical simulation (Polanski, 1984). In the analysed case, for the three variable factors, Hartley's plan PS/DS-P:Ha_3 based on hypersphere with 11 combinations of variable factors was established.
- The results obtained in the numerical experiment were used for the determination of the available rotation angle function with the use of regression analysis.

4 HIERARCHICAL VALIDATION

4.1 *Introduction*

The results obtained in the Finite Elements Method may be considered as satisfying if the obtained results are comparable with the results of laboratory tests. In order to obtain similar results, the FEM model adjustment is necessary. Adjustment of models is reached by a hierarchical validation method in the comparative analysis of models with different level of complexity with the results of laboratory tests. The main criteria in the validation process is the grade of adjustment of characteristic describing the behavior of the studied object which is analyzed with the use of the Finite Elements Method with the material characteristics received in the laboratory tests.

4.2 *Modeling of curve σ–ε*

According to (EN 1993-1-5), attachment C, the following material models are available:

a. Elastic—plastic model without hardening (Fig. 2a).
b. Elastic—plastic model with minimal hardening (Fig. 2b).
c. Elastic—plastic model with linear hardening (Fig. 2c).

d. Realistic model received as a result of the experimental modification of the stress—strain relation obtained in laboratory tests (Fig. 2d).

The only characteristic which fulfils the requirements of precise representation of deformation of the studied object is the stress—strain characteristic presented in Fig. 2d. The relation stress—strain considered for a small deformation is determined with the use of standard Ramberg—Osgood (Rasmussen, 2003) curve with the following equation:

$$\varepsilon = \frac{\sigma}{E_0} + 0{,}002\left(\frac{\sigma}{\sigma_{0.2}}\right)^n \; for: \sigma \le \sigma_{0.2} \tag{1}$$

Rasmussen has modified the equation (1), which was implemented with small modifications in the EN 1993-1-4 standard (stainless steels).

Depending on the required precision of calculations and the range of deformation the following three approaches (EN 1993-1-4) to material characteristic modeling are mentioned:

a. Stress—strain curve with reinforcement calculated acc. to the formula (2):

$$\varepsilon = \begin{cases} \dfrac{\sigma}{E} + 0{,}002\left(\dfrac{\sigma}{f_y}\right)^n \; for: \sigma < f_{y0{,}002} \\ 0{,}002 + \dfrac{f_y}{E} + \dfrac{\sigma - f_y}{E_y} \\ +\varepsilon_u\left(\dfrac{\sigma - f_y}{f_u - f_y}\right)^m \; for: f_y < \sigma < f_u \end{cases} \tag{2}$$

b. Stress—strain curve calculated as in point a) but on the basis of measured characteristics.

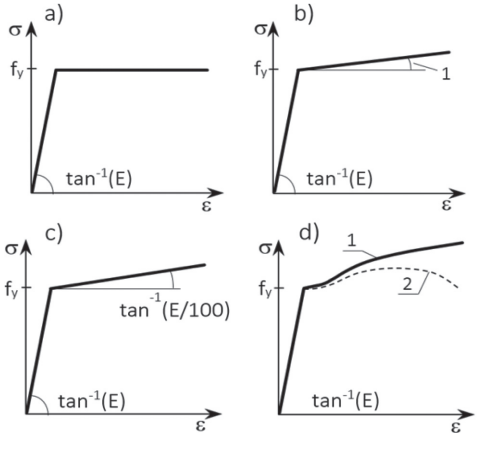

Figure 2. Material models acc. to EN 1993-1-5.

c. Real stress—strain curve calculated on the basis of parameters and relations acc. to formulas (3) and (4):

$$\sigma_{true} = \sigma(1 + \varepsilon) \tag{3}$$

$$\varepsilon_{true} = \ln(1 + \varepsilon) \tag{4}$$

4.3 *The stages of the hierarchical validation*

Validation of material characteristic is considered as effective if the result of its use is as follows: in models with different scale of complexity, the results are comparable with those obtained in laboratory tests. For the need of models' adjustment, 4-stages validation system of FEM models was elaborated. In this method the material characteristic σ–ε as well as other FEM model elements as contacts, supports and the type of used finite elements are assessed.

In the first validation stage, the characteristic σ–ε of the steel specimen and bolt subjected to axial tensile testing is determined (Fig. 3a). Figure 4 shows the results of the first validation stage. On the basis of the obtained results (Fig. 4a, 4b) the compatibility of the response curve σ–ε obtained in FEM analysis in relation to laboratory tests is observed. Material characteristic elaborated on the basis of the realization of the first stage of validation was introduced to FEM model of the next validation stage.

In the second stage the isolated joint elements in the system bolt–washer–nut are tested (Fig. 3b). The FEM analysis in the second stage of validation was performed with the use of two-dimensional (2D—Fig. 5a) and three-dimensional models (3D—Fig. 5b). The comparison of the results obtained in a 2D analysis and a spatial analysis allows for a statement that the results are coincident.

The maximum values of forces obtained in laboratory tests were, for: SAF9 = 261,59 kN, SAF10 = 263,18 kN, SAF11 = 262,81 kN and are very close to obtained in FEM analysis: F_{FEM} = 263,66 kN.

Most of measuring devices which are used for measurements of deformations during the axial tensile test allow for a measurement of a deformation's growth only between two points. Usually, this measurement is the distance between a bolt's head and a bolt's nut. In Fig. 6a the designation of the additional measurement points over the bolts length is presented. Deformations between each measurement points are done with the use of digital image correlation. The use of this method allowed for an observation of deformation of particular bolt's parts. In the Fig. 6b the results of the

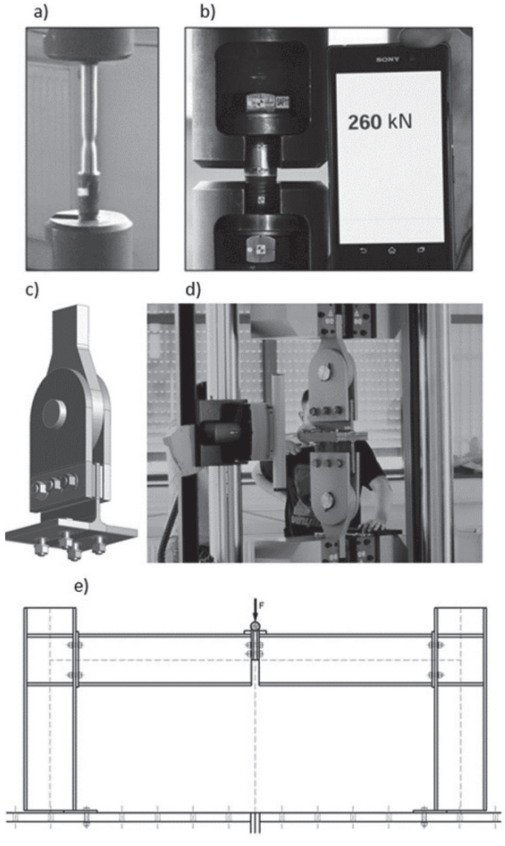

Figure 3. Stages of the hierarchical validation: a) Stage I -axial tensile test of steel specimen b) Stage II –tensile of the bolts in configuration: bolt—washer—nut. c) Stage III–tensile of T- stub (FEM model) d) Stage III – tensile T—stub (laboratory test) e) Stage IV—frame arrangement loaded by concentrated force in the middle of the span.

deformation measured on the sections between points 1–6 and 4–6 are presented. Adequate divisions were introduced into FEM models and the obtained results were coincident with the results of laboratory tests.

In the third stage of validation the following T—stubs were experimentally tested:

- Series H01 – T-stub of profile HEA 240-S235,
- Series B01 – T-stub of profile HEB 240-S355,
- Series SP01 – welded T-stub: end plate 20 mm, S355,
- Series SP02 – welded T-stub: end plate 12 mm, S235.

In numerical models of tested objects geometry projection has been made based on the exact measurement of the elements subjected to tensile test. During the measurement, significant rolling

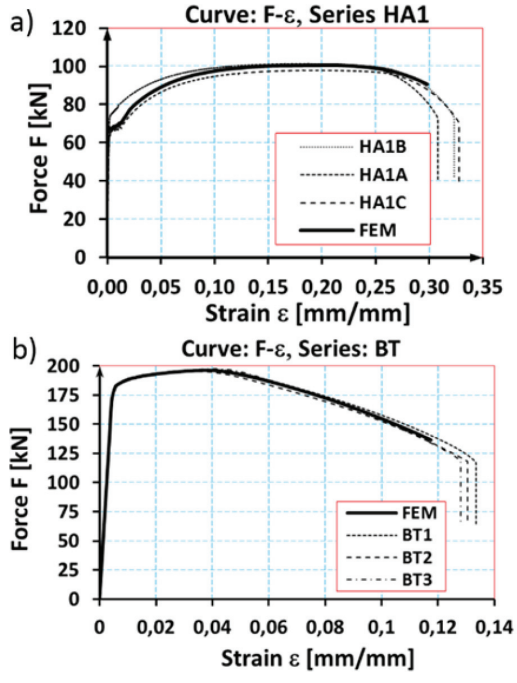

Figure 4. Results of comparison analysis: a) steel specimens S235 (3D analysis), b) Results of comparison analysis for I stage of validation of bolt grade 10.9 (2D analysis).

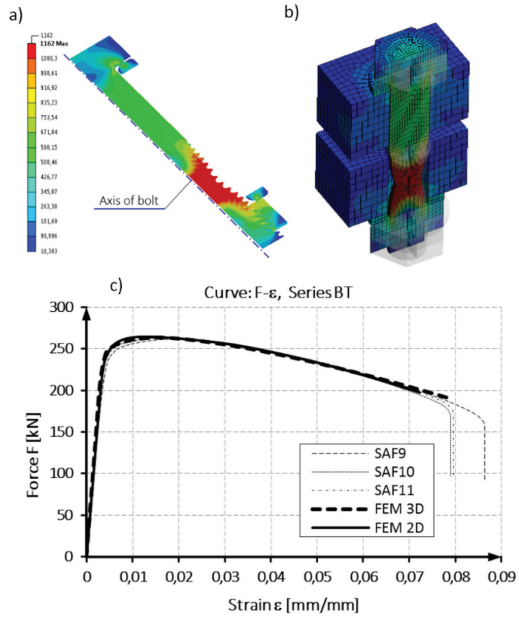

Figure 5. Results of FEM analysis of II stage of validation; a) stress maps in the bolt (2D analysis), b) stress maps in the bolt (2D analysis), c) comparison of FEM results to test results (2D and 3D analysis).

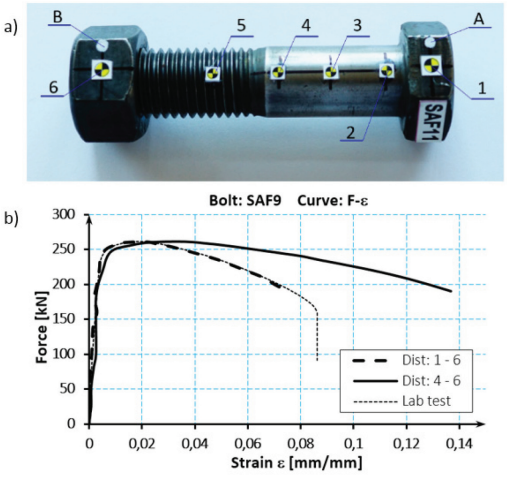

Figure 6. a) Marking measuring points, b) Comparison of laboratory results with the results with the use of digital image correlation.

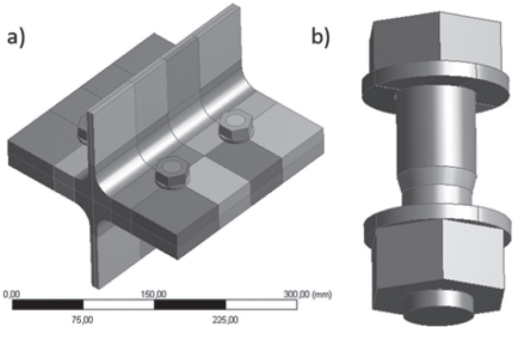

Figure 7. III Stage of hierarchical validation: a) T-stub model, b) Bolt model.

deviations of the profiles have been found. The dispersion of deviations in the thickness of flanges for HEB 240 (series B01) was in the range 16,35 ÷17,84 mm and it was the highest from all tested series. Finally, in the model average value of flange thickness in relation to measurements points in area of section radius was assumed.

The third stage of the validation consists of determination of comparable characteristic F-Δ describing the state of deformation of the end—plate connection defined as tensioned T—stubs (Fig. 3c, 3d).

For each connection type, three axial tensile tests were made. The connections for the laboratory tests were designed in such a way that the first or the second failure modes acc. to EN 1993-1-8 were obtained.

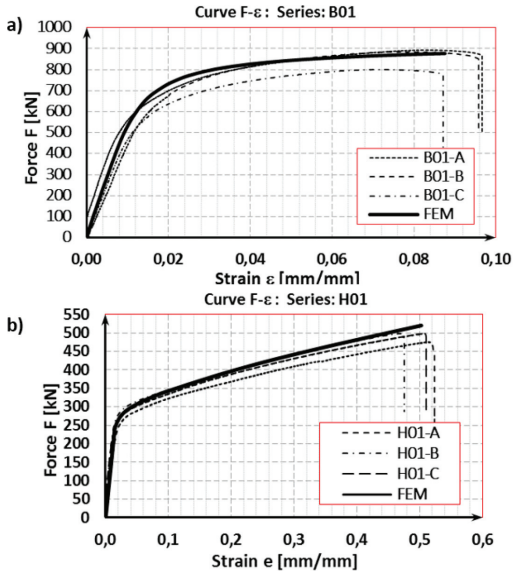

Figure 8. Results from comparative analysis FEM stage III of validation a) Series B01 (HEB 240), b) Series H01 (HEA 240).

A minor discrepancy in the results for tested type B01 has been found, in the area of initial stage of loading the joint. The curve obtained in the tested H01 type (Fig. 8a) is characterized by a relatively good matching of both the initial stage of loading and stage just before destruction.

In the last stage of hierarchical validation a model of beam to column joint is analyzed (Fig. 4e). The proof of validation for this stage is to obtain coincident results of rotation angle acc. to analysis of characteristic M–ϕ.

5 NUMERICAL MODEL

5.1 *Joint components*

The determination of the function describing the rotation angle of a bolted end–plate beam-to-column connection was made on the basis of FEM analysis for an isolated joint, for which the response surface of rotation angle is defined on the basis of the plan of the numerical experiment. The function of the rotation angle was determined in relation to the above mentioned basic variables, whose location is shown in Fig. 9.

For numerical model building the hexagonal, 8–node, cubic finite elements were used. The washers were modelled as separate elements. Bolt's shank was joined with the nut and bolt's head. In the model of washer, 3 layers of finite elements and the division into 48 elements were introduced.

In the area where the thread connects to the nut, mesh density was increased to the size of 1 mm. In end—plate 6 layers of finite elements were introduced and adequately in the column in the area of contact with the plate. In order to increase the efficiency of calculations, the model of a half of the joint was made, with the use of symmetry with respect to a central plane of the system (Fig. 10).

In every joint's component, mesh density of finite elements was introduced in reference to local stresses and strains. The mesh size of finite elements in the initial phase of analysis was created with the use of the adaptation method. For the creation of bolt's model 8-node, cubic elements were also used. The washers were modelled as separate elements (Fig. 11b), a head of bolt and a shank were connected with the nut (Fig. 11a).

5.2 *Modelling of contact surface*

The contacts between particular joint elements were created as nonlinear with the friction factor assumed for the surface in a natural condition with the value of $\mu = 0.2$. Contact surfaces were introduced in the areas of contact between: end plates, washer – end plate, washer – nut, washer – head of the bolt (Fig. 12c).

Additionally, radial surfaces between bolt hole and bolt shank and thread were introduced in the model (Fig. 12a).

The last from mentioned contacts create boundary conditions to support the bolt that rests on the inner surface of the plate's hole caused by a large joint gap. A specific type of contact surface which has been introduced into the FEM model is shown in Fig. 12b.

In the initial stage of joint deformation, the side surface of the washer and the upper surface of the plate have no contact, but with a large gap in the joint they interact between each other, and plate surface is the support for the washer. Introducing such contact surface is dictated by possible occurrence of non-coinciding the FEM model caused by penetrating objects.

5.3 *Methodology of load applying on the model*

In the research plan the FEM model was loaded by introducing of displacement at the end of the cantilever. The values of the displacement were experimentally set in such a way that we obtain the maximal angle, at which the tangent to a curve of response rotation angle has an inclination equal to 0. The displacement was introduced in 50 steps. Bolts' pretensioning was defined as a separate, first step. Due to the prestressing of the fasteners, the thread flexibility was neglected. The bolt prestressing to the force Fp,C = 175 kN was executed by

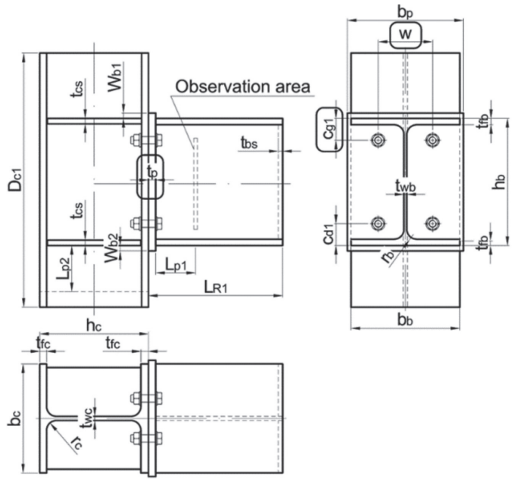

Figure 9. Designation of variable factors: "tp", "cg1" and "w".

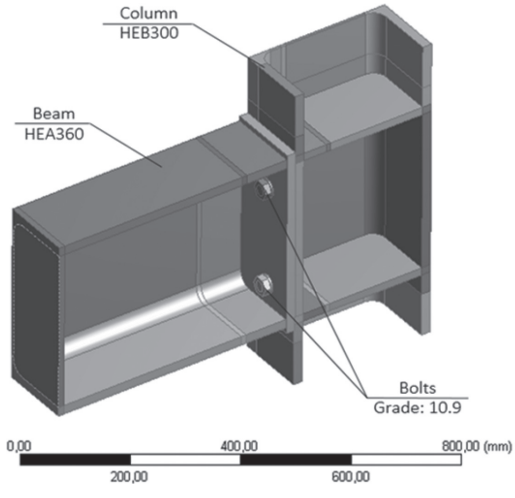

Figure 10. FEM model – 3D view.

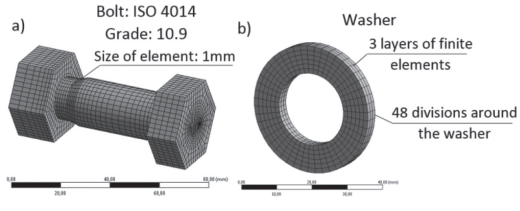

Figure 11. FEM model: a) bolt, b) washer.

the application of the compression force to the lateral surface of the shank. In Fig. 13 the system of support and load location in the FEM model is shown.

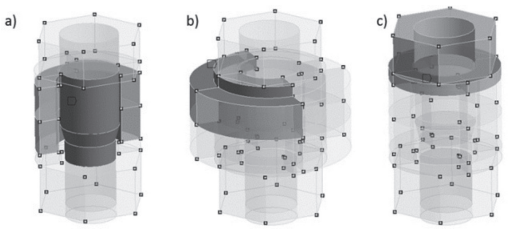

Figure 12. Contact surface: a) radial contact bolt-end plate-column, b) antyslip contact washer-end plate, c) contact washer-bolt head.

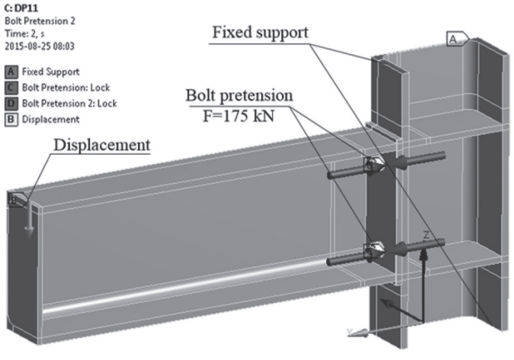

Figure 13. FEM model—location of supports and loads.

6 PLAN OF THE NUMERICAL EXPERIMENT

6.1 *Basis of the thesis*

The mathematical model of the studied object which was made in the process of experimental studies often reflects only the accidental static correlation which is a compilation of geometrical imperfections of joint components and material imperfection. Such a model does not present the real cause and effect relationship. The compromise in such a situation is to create a mathematical model in the form of an approximating function of the tested object, whose relative standard deviation is known and accepted in the whole applicability area. The determination of a proper approximating function on the basis of which it is possible to determine maximal rotation angle, by which the bending moment does not have a downward trend, is made on the basis of the numerical experiment plan.

6.2 *Hartley's plan: PS/DS-P: Ha_3*

For the determination of the response surface of the joint's rotation angle Hartley's plan was applied (Polanski, 1984). The plan is presented in the Table 1. Experiment's plan, built on the 11

Table 1. Plan of experiment (Hartley's plan: PS/DS-P:Ha_3).

	x_k			Rotation angle ϕ_{cu}
	t_p	c_{g1}	W	
D_{p1}	[mm]	[mm]	[mm]	[mrad]
D_{p1}	12.11	58.45	167.32	83.07
D_{p2}	17.89	58.45	132.68	13.98
D_{p3}	12.11	81.55	132.68	106.69
D_{p4}	17.89	81.55	167.32	43,75
D_{p5}	10.00	70.00	150.00	106,84
D_{p6}	20.00	70.00	150.00	15,85
D_{p7}	15.00	50.00	150.00	29,38
D_{p8}	15.00	90.00	150.00	86,58
D_{p9}	15.00	70.00	120.00	45,37
D_{p10}	15.00	70.00	180.00	72,59
D_{p11}	15.00	70.00	150.00	59,81

arrangements, includes the combination of variable factors in the following ranges: t_p = 10÷20 mm, w = 120÷180 mm and c_{g1} = 50÷90 mm. Solving of all plan systems allowed to build the response surface for unknown values of rotation angle based on 11 measuring points. The unknown value of each system is the value of rotation angle at limiting bending moment, at which the joint is in the state of static equilibrium.

6.3 *Approximating function of the studied object*

The function of the maximal rotation angle was defined as a polynomial function as below:

$$\phi_{cu} = t_p^{\alpha} \cdot c_{g1}^{\beta} \cdot w^{\gamma} - A \tag{5}$$

where: α, β, γ – are the coefficients of polynomial,
t_p [mm] – is the thickness of end-plate,
c_{g1} [mm] – is the distance from the top edge of upper flange to the axis of bolt,
w [mm] – is the spacing between the centres of bolts,
A – is the constant of the polynomial.

7 RESULTS ANALYSIS

Solving of all systems of the experiment's plan allowed to elaborate the response surface of the rotation angle. Results of this analysis are presented in Fig. 14.

The coefficients of polynomial which are described by the equation (5) were calculated with the program Statistica 12, with the use of the nonlinear estimation method. Inserting the calculated coefficients (α, β, γ) into equation (5) one can

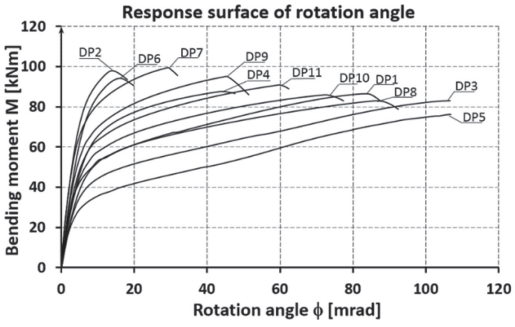

Figure 14. Response surface of rotation angle of experiment plan.

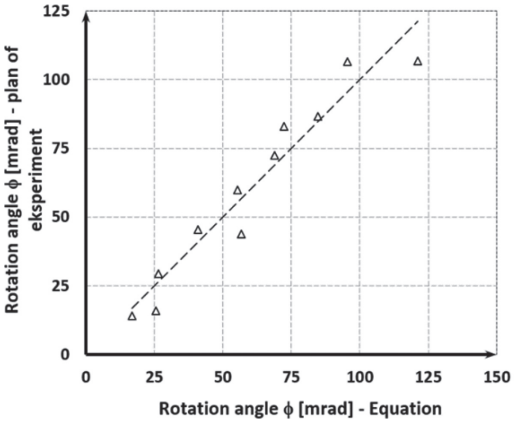

Figure 15. Comparison of the rotation angles results obtained in experiment's plan with rotation angles determined on the basis of the equation (6).

receive the function of available rotation capacity of joint in the following form:

$$\phi_{cu} = t_p^{-1,267} \cdot c_{g1}^{1,044} \cdot w^{0,714} - 42,48 \qquad (6)$$

The values of obtained rotation angles are in the range: ϕ_{cu} = 16,88 ÷ 121,02 [mrad]. In Fig. 15 the comparison of the rotation angles results obtained in the numerical experiment's plan with rotation angles determined on the basis of the equation is presented. The common feature of all analyzed systems is having obtained maximal value of moment of the joint plastic resistance M_u, at the maximal force value, which indicates that achieving of limiting load capacity of joint is caused by decreasing of bolt's load capacity. The maximal value of load capacity in a bolt for the case D_{P1} is $F_{b,max}$ = 277,10 kN and it is comparable with the value obtained in the axial tensile test (F_{bolt} = 263,18 kN) made in the second stage of hierarchical validation. Insignificant differences may be caused by the influence of two-direction bolt bending, caused by end-plate deformation and geometrical and material imperfections.

8 SUMMARY

The introduction of material characteristics into advance FEM analysis as a result of the multi—stages hierarchical validation is the essential condition for obtaining of reliable results of the FEM analysis.

The obtained results of the analysis clearly show the trend of achieving the maximal rotation angle ϕ_{cu} resulted from the decreasing of bolt's load capacity, regardless of the failure modes acc. to EN 1993-1-8 existing in the connection. In connections in which the first failure mode occur the forces are regrouped which results in developing the "membrane" effect. The end—plate along with progressive rigidity degradation goes from a bending state into a membrane state, which does not have its analytical (quantitative) reference.

Proposed in the standard EN 1993-1-8 component method in the area of forecasting rotation capacity has been not fully developed which encourages discovering other, alternative, but possible and reliable methods of estimation of joint rotation capacity in steel structures. Presented procedures will be used in the creation of more general formulas including other beam and column section.

REFERENCES

Beg D. & Zupancic E. 2004a. Statistical evaluation of rotation capacity of moment connections. *Connections in Steel Structures V.*, Amsterdam.

Beg D., Zupancic E. & Vayas I. 2004b. On the rotation capacity of moment connections. *Journal of Constructional Steel Research.* 60: 601–620.

Chen W.F. & Kishi N. 1989. Semirigid Steel Beam-to-Column Connections: Data Base and Modelling. Journal of Structural Engineering. ASCE, Vol. 115, No 1.

Concepcion D., Pascual M., Mariano V. & Osvaldo M.Q. 2011. Review on the modelling of joint behavior in steel frames. *Journal of Constructional Steel Research* 67: 741–758.

EN 1993-1-4. Eurocode 3: Design of steel structures, Part 1.4: General rules, Supplementary Rules for Stainless steels. Brussels: CEN.

EN 1993-1-5. Eurocode 3: Design of steel structures, Part 1.5: Plated structural elements. Brussels: CEN.

EN 1993-1-8. 2005. Eurocode 3: Design of steel structures – Part 1–8: Design of joints. Brussels: CEN.

Faella C., PilusoV. & Rizzano G. 2000. Structural steel semi rigid connections: Theory, design and software. CRC Press, Boca Raton.

Frye M.J. & Morris G.A. 1975. Analysis of Flexibly-Connected Steel Frames. *Canadian Journal of Civil Engineering.* No 2.

Girao A.M., Bijlaard F., Gresnigt N. & Silva L. 2004. Experimental assessment of the behavior of bolted T-stub connections made up of welded plates. *Journal of Constructional Steel Research.* 60: 269–311.

Girao A.M., Silva L. & Bijlaard F. 2006. Finite-Element Modeling of the Nonlinear Behavior of Bolted T-Stubs Connections. *Journal of Structural Engineering.* 132: 918–928.

ISO 6892-1. 2009. (E), Metallic materials — Tensile testing, Part 1: Method of test at room temperature.

ISO 898-1. Mechanical properties of fasteners made of carbon steel and alloy steel, Part 1: Bolts, screws and studs with specified property classes – Coarse thread and fine pitch thread.

Jaspart J.P. 1993. Comparison between Experimental Tests, Numerical Simulations and Available Theoretical Procedures in View of Analytical Prediction of the Semi-Rigid Behavior of Beam-to-Columns Joints with Extended End Plate or Welded Connections. Technical Report No 4. SPRINT CONTRACT 351.

Kozlowski A. 1996. A Review of Models of Semi-Rigid Steel Column-Beam Connections. Archives of Civil Engineering. Vol. XLII, Issue 1.

Kuhlmann U. & Fürch A. 1997. Rotation Capacity of Steel Joints. COST Project C1 Meeting.

Ostrowski K. 2014a. Finite element analysis of the rotation capacity of beam-to-column end-plate bolted joints. Eurosteel 2014, September 10–12, Naples.

Ostrowski K. & Kozlowski A. 2015. Hierarchical validation of FEM models. XIV International Scientific Conference Rzeszow – Lwow – Koszyce. Rzeszow.

Ostrowski K. & Kozlowski A. 2014b. Parametric study on the rotation capacity of stiffened end-plate beam-to-column connection. (In Polish) *Building and Architecture*. Vol. 13(3) 2014. Lublin.

Polanski Z. 1984. Experiment design in technique. (In Polish). PWN. Warsaw.

Rasmussen K.J.R. 2003. Full-range stress–strain curves for stainless steel alloys. *Journal of Constructional Steel Research.* 59: 47–61.

Silva S., Borges L. & Garvasio H. 2004. A probabilistic evaluation of the rotation capacity of end-plate beam-to-column steel joints. *Connections in Steel Structures V.* Amsterdam.

Silva S. & Girao A. 2001. A ductility model for steel connections. *Journal of Constructional Steel Research.* 57: 45–70.

Weynand K. 1992. SERICON - Databank on Joints in Building Frames. COST PROJECT C1. Proc. of the First State of the Art Workshop.

Yee Y.L. & Melchers R.E. 1986. Moment Rotation Curves for Bolted Connections. *Journal of Structural Division.* ASCE. Vol. 112, ST3.

This page intentionally left blank

Recent Progress in Steel and Composite Structures – Giżejowski et al. (Eds)
© 2016 Taylor & Francis Group, London, ISBN 978-1-138-02946-0

Truss design with one-membered elements and N-joints

J. Bródka & M. Broniewicz
Bialystok University of Technology, Bialystok, Poland

ABSTRACT: In the paper the authors present a design method of roof trusses with the verticals made of IPE-sections, the braces made of not battened double angle members and the channel chords. The direct connections of the IPE-section to the web of the chord produce a semi-rigid system which has not been sufficiently explored experimentally, and creates a lot of problems in assessing the capacity of the joint and welded connections. The proposed solution is simple in terms of technology and avoids disadvantages associated with the design of semi-rigid joints between the verticals and the chord. Taking into account the rules for determining the effective lengths of welds in similar T-type joints made of hollow sections, the method of assessing of the resistance of such connections is presented.

1 INTRODUCTION

In a paper devoted to the design of trusses in channel sections according to PN-EN 1993-1-8 rules (Bródka & Broniewicz 2015), the authors gave a proposal to design roof trusses with an average span made of hot-rolled channel sections with K-type joints. The advantages of using such members in the lattice structures also apply to the trusses, where the chords are made of channels as well, but the braces are made of other hot-rolled members (verticals from IPE section and braces from equal or unequal angles).

The currently proposed solution is simpler than that discussed in (Brodka & Broniewicz 2015) in terms of the calculation of connections arranged as fillet welds as well as assessment of the capacity of joints, wherein the ease of implementation of the joints is still an important advantage.

In the traditional approach to designing roof trusses made of hot-rolled angles, the braces are connected at joints using fillet welds (Augustyn 1987), (Stahlbau Verband 1985), (Deutscher Stahlbau Verband 1985), (Kindmann & Stracke 2003), (Łubiński & Filipowicz 2000), (EN 1993-1-8 2006), (EN 1993-1-10 2007). This prevents semi-rigid joints, which are unpopular among designers. In the proposed case the braces having the same width are stacked to the chords. To reduce the expense of the steel, the top chord should be made of S355 or S420 steel and the bottom chord of S235 or S275 steel.

Direct joining of the vertical brace to webs of the chords creates semi-rigid joints, which have not been sufficiently explored experimentally, leading to fears related to the proper assessment of the capacity of connections using fillet or butt welds. Due to these circumstances, in both the literature cited already and in more recent national studies (Bródka & Broniewicz 2013), (Bródka & Juchniewicz 1994), (Giżejowski & Ziółko 2010), there is no information about the design of elements discussed in the present article.

Also, the joints between the verticals made of an IPE-section with the web of the channel chord using butt welds is quite complex. Chamfering of IPE-section walls for execution of V-groove butt welds is difficult because of the different thicknesses of the web and flanges and large deformations of the joint due to the uneven arrangement of layers of weld.

In order to overcome all of the difficulties related with manufacturing and assessing the capacity of the joint, a semicircle shape must be cut in the web of the verticals. Although a semi-rigid joint is then obtained, the assessment of the capacity of the joints can be carried out in accordance with the rules specified in Eurocodes (EN 1993-1-8 2006) using the formulas relating to hollow section joints.

The radius of the notch R is determining as follows:

$$R = 0,5b_i - (t_{wi} - r_{ii}) \tag{1}$$

where b_i = the depth of the IPE-section; t_{wi} = the thickness of the flange of the IPE-section; r_{ii} = the radius between the flange and the web.

Assuming the notch is as described above, the reduced cross-sectional area of the vertical made of the IPE-section can be determined as follows:

$$A_{i,r} = A_i - [b_i - 2(t_{wi} + r_{ii})]b_{ji} \tag{2}$$

where A_i = the cross-section area of the IPE-section; t_{fi} = the thickness of the web.

2 BASES FOR DESIGN

Roof truss structures of this kind are made of steels listed in the standards (EN 10025 2007) according to the rules as indicated in (EN 1993-1-10 2007) and (EN 1090-2 2007). The load capacity and reliability of members and their joints and connections are determined by (EN 1993-1-1 2006) and (EN 1993-1-8 2006).

Such trusses are designed primarily for medium spans (up to about 30 m) and relatively small loads due to the range of channel sections manufactured in Poland (Bogucki & Żyburtowicz 2008) and abroad (ArcelorMittal 2015). The truss in static calculations can be considered as a system of tension or compressed members (diagonals or verticals) that are pin-jointed to the chords. The rigidity of the channels in the plane of the truss is small and the connections of the angles with the chords are treated as pinned.

The layout of the truss members is shown in Fig. 1. Access to the arrangement of layers of welds between the flanges of the chords and flanges of the verticals at the upper chord is large enough. The access to the connections of members at the bottom chord is good from all sides.

3 JOINT'S SHAPES

Figure 2 shows the intermediate joint of the bottom chord welded using fillet welds. The diagonals made of angles are directly welded to the flanges of the chord on both sides. In contrast, the use of fillet welds on the whole perimeter of the vertical raises doubts as to their full effectiveness. Taking into account the rules for determining the effective lengths of similar T-type joints made of hollow sections, only the welds arranged near the flanges of the vertical are fully effective.

Attempts to design verticals made of channel sections with half circles cut at the ends have failed because then the eccentric is formed either within the connection or in the non-reduced cross-section. This always leads to an excessive consumption of steel due to the use of an excessively large cross-section.

Intermediate joints of the upper chord are designed in a manner similar to that shown in Fig. 2. The difference is only due to the angle of inclination of that chord in relation to the bottom chord and the fact that the web is directed in the opposite direction to avoid the formation of trays that will act as containers of dirt and moisture. Such positioning of the chord is also essential for achieving good connecting purlins with a bottom chord. For this reason, the contour of the diagonal should comprise the area of the chord flange.

Figure 3 shows a splice of the bottom chord. Small angles of the diagonals should be placed at a fairly large eccentricity relative to the axis of the bottom chord so that the connection with the flange has no contact with the end plate. The end of the diagonal should be cut perpendicular to the axis of the diagonal. The head plate should have a thickness of 16 to 20 mm, so that their mutual connection using prestressed bolts is very stiff.

The two non-battened angles of the central vertical are welded from one side of that plate. The recommendation that the end plate should have a large thickness enables renovation of the anticorrosion coating of central vertical.

It should be noted that the prestressed bolts of the end plate splice of the bottom tension chord should be symmetrical with respect to the axis y–y and preferably also relative to both axes of the combined section to avoid the formation of an eccentric in the bolt layout. The bolted connection should be designed according to EN 1993-1-8.

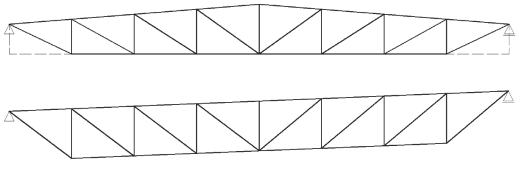

Figure 1. Layout of the truss members.

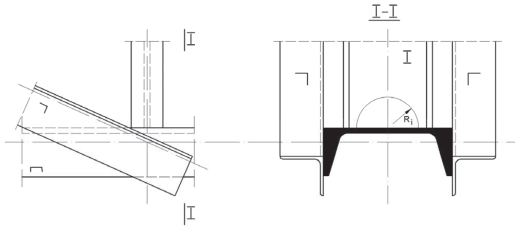

Figure 2. Intermediate joint of the bottom chord.

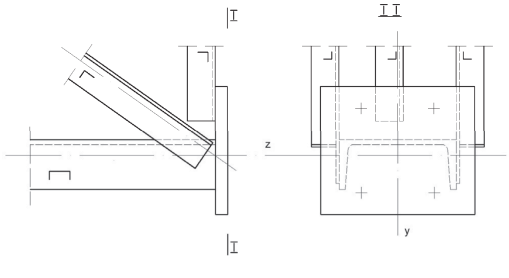

Figure 3. Splice of the bottom chord.

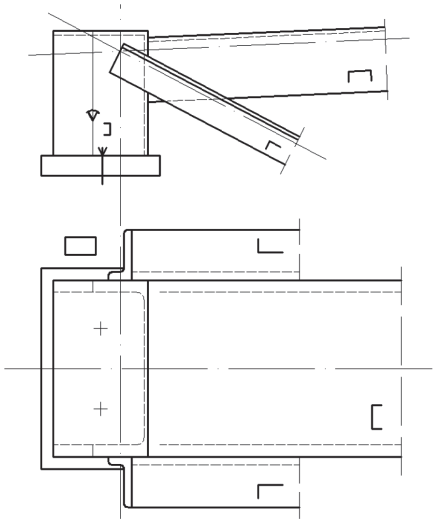

Figure 4. Support joint of the truss.

Figure 4 shows a support joint of the truss in the level of the upper chord. The support is usually designed with the channel member of the same section as that to which the chord member is attached. In order to give it sufficient stiffness, the support is reinforced by vertical plates welded with V-groove butt welds. The connection of the upper channel chord with the web of the support is designed with filled welds and with the flanges of the support with the butt welds. This arrangement of the splice is necessary because of the fact that the diagonals could be joined to the verticals using fillet weld. This is possible if the upper chord channel section has a height of 400, 300, 280, or 260 mm due to the fact that the gradation of hollow and channel sections is compatible only in those cases.

During the application of the hollow section, the flanges of the channel are connected at rounded corners, creating groove welds. The end of the vertical at the top is made by the end plate to obtain a stiffening channel, hermetic closure of the section, and convenient placement of the extreme purlin.

The horizontal base plate of the support has holes for the bolts that are used to connect the truss with the steel or reinforced column or brick walls.

4 THE DESIGN RESISTANCE OF THE MEMBERS

The resistance of the braces is checked during evaluation of the safety of their cross-sections according to the rules of Eurocodes (EN 1993-1-1 2006) and (EN 1993-1-8 2006). Since the diagonal angles are not battened, their resistance is calculated in accordance with the rules of paragraph 4.13 of (EN 1993-1-8 2006), in which the members connected to one arm can be regarded as axially loaded, taking into account the cooperating cross-sectional area. In the case of unequal angles, joined the wider arm or in the case of equal angles as cooperating cross-sectional area can be taken gross cross-sections of the member.

The load capacity of intermediate vertical (except for the support and ridge), designed with IPE-sections, is considered as follows:

a. In the connection with the bottom chord taking into account reduced the cross-section area according to [2]:

$$\frac{N_{Ed}}{N_{Rd}} \leq 1{,}0 \tag{3}$$

where $N_{Ed} = K_i$ the design longitudinal force in the vertical; $N_{Rd} = A_{i,r} f_{yi}$ the compression resistance of the reduced cross-section; f_{yi} = the yield strength of the steel.

b. In the connection with the upper chord, the capacity of the vertical may not be considered, because this member is generally designed with steel that has much higher yield strength than f_{yi}.
c. Outside the joints, the vertical is considered as the compression member with flexural buckling in the plane of the truss according to (EN 1993-1-1 2006).

It should be noted that the diagonal located directly at the central vertical is the compression member. In accordance with paragraph 4.13 of (EN 1993-1-8 2006) its safety can be determined, taking into account the indication about an effective section relating to the tension angles connected by one arm.

The Eurocode (EN 1993 1-1 2006) does not mention clearly how to perform checking the safety of such members. There is no indication which type of buckling we should consider and with respect to which axis assume the value of the imperfections parameter α.

The only indication is a figure presented in Table 6.2 of that standard, which may be interpreted as referring to the angle connected by one arm relative to the axes y-y and z-z and implying the curve "b". But the fact is that in the case of angles of small dimensions this is not important, because in general the calculations using various parameters and relatively small lengths of members show that the value of factor χ is slightly less than 1.0.

The capacity of the bottom chord is determined by reference to a tension channel section when dealing with situations related to its loading:

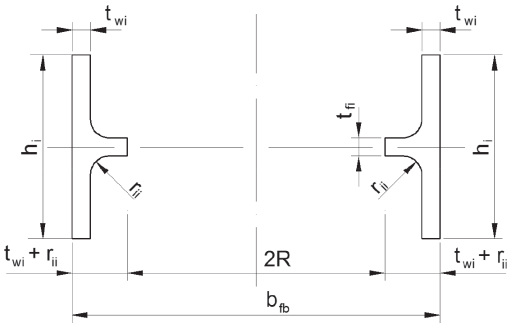

Figure 5. Reduced cross-section of the IPE-section.

a. In the connection of the vertical with the chord, we should take into account the local force K_i applied to the web of chord. This force is transmitted from the vertical through the reduced cross-section of the IPE-section (Fig. 5).
This is the cross-section of the flange of the IPE-section with a part of the section in the rounded area between the flange and the web. The shape of the stiff bearing area can be treated as close to the rectangle $b_i \times t_i$ and the reduced cross-sectional area of the vertical can be taken as a gusset plate. In such a situation, the rule given in Table 7.13 of (EN 1993-1-8 2006) could be taken as a model of the load, referring to the square hollow section loaded with concentrated force, which is passed on to the longitudinally positioned plate.
The expression can be written as follows:

$$N_{r.Rd} = k_m f_{y0} t_{fb}^2 \left[\frac{2h_i}{b_{fb}} + 4\left(1 - \frac{t_{wi}}{b_{fb}}\right)^{0,5} \right] \Big/ \gamma_{M5} \qquad (4)$$

where k_m = 1.0 in the case of tension chord; $k_m = 1.3(1 - n) \geq 1$ in the case of compression chord; f_{y0} = the yield strength of the chord steel; t_{fb} = the thickness of the web of the chord channel; h_i = the width of the flange of the IPE-section; b_{fb} = the height of the web of the chord channel; t_{wi} = the thickness of the flange of the IPE-section; γ_{M5} = 1.0 the partial safety coefficient related to the joint; $n = (\sigma_{0,Ed}/f_{y0})/\gamma_{M0}$; $\sigma_{0,Ed}$ = the design normal stress in the upper chord; γ_{M0} = 1.0 the partial safety coefficient related to the material.
The safety assessment of the joint under local load is determined as:

$$\frac{N_{Ed}}{N_{i \cdot Rd}} \leq 1{,}0 \qquad (5)$$

where N_{Ed} = the deign load of the (= K_i).
The capacity of the compression chord web as a result of the local load in the joint is usually not checked because its yield strength is significantly higher than that of the bottom chord and referred to in this situation the design coefficient k_m has no practical significance.

b. The design capacity of the joints of the bottom or the top chord is determined using the formulas relating to the destruction of the channel section according to the formulas given in Table 7.24 in (EN 1993-1-8 2006) in the case of an N-type joint with a gap. Here there is a joint equivalent of the T-type joint.
c. In general, it is not meaningful to take into account the local loading of the web on the destruction of the chord outside the bearing area, but in case of doubt, the reduced stresses can be determined.
d. If the vertical or the brace is arranged non-axially in the joint in relation to the chord (usually the bottom one), the bending moment is formed. Additional stress is determined as discussed in (Bródka & Broniewicz 2013), (Bródka & Broniewicz 2015), (Bródka et al. 2013).
e. The cross-section of the compression chord is determined by calculating the load capacity of the chord in compression and flexural buckling in the plane of symmetry of the channel section caused by longitudinal force in accordance with the rules specified in (EN 1993-1-1 2006).

5 THE CAPACITY OF WELDED CONNECTIONS

The longitudinal force from the vertical is transferred to the web of the bottom chord axially through the arrangement of two bearing areas as shown in Fig. 5. When the resistance of the reduced cross-section of the vertical is assessed, a simplification is applied by replacing that area by a rectangle $h_i \times t_i$. Similar behaviour appears during the calculation of the stresses in fillet welds arranged around such bearing areas. However, the length of the welds actually arranged in the connection is more than $2h_i$. Apart from sections of welds with wall thicknesses, because in fact they do not participate in the transfer of the load, the actual length is $l_{wr} = 2[h_i + 0{,}5r_{ii}(\pi - 2) - 0{,}5t_{fi}] > 2h_i$.

Taking into account European IPE-sections which can be used for the verticals, the surplus of the length in excess of $2h_i$ is about several percent. If, however, we consider the occurrence of certain non axial transfer of the load from the gross cross-section of the IPE-section on its reduced cross-section, this surplus should compensate for that fact.

The stress in welds that connect the vertical with the chord is determined by the thickness of the weld a_w as:

$$\tau_{\parallel} = \frac{K_i}{4a_w h_i} \le f_{vw.d} \tag{6}$$

where $f_{vw.d}$ = the designed shear resistance of the fillet weld.

In contrast, the stress in the connection of the tension ridge member with the head plate is determined in the following manner taking into consideration the four angles:

$$\tau_{\parallel} = \frac{K_i\left(0{,}5 + e_{zi} / b_i\right)}{4a_w l_w} \le f_{vw.d} \tag{7}$$

where K_i = the design load in the ridge; e_{zi} = the distance of the neutral axis of an angle from its outer edge; b_i = the width of the angle flange.

In such a connection, two sections of welds l_w are arranged on both sides of the angle flange.

It is best to design the connection of a brace with the bottom chord, as shown in Fig. 2, using two weld lengths l_w arranged in parallel on both sides of the angle. Then the stress is determined according to (Bródka et al. 2013) but assuming the number 2 instead of 4 in the denominator, since there are only two members in such joints.

However the connection of the braces with the top chord in all joints and the brace with the bottom chord near the head plate of the assembly joint is performed on fillet welds, arranged around the perimeter of a push contact area. Such connections have quite complicated systems of welds. The centres of gravity of the welds do not coincide with the diagonal axes. Calculating the position of these points is very complicated, and the resulting bending moment must be taking into account to assess the maximum shear stresses. In the former DIN 18800 Part 1, it was permitted to consider such systems in an approximate way. The two most common layouts of welds are shown in Fig. 6. Under this authorization (see Chapter 7 Bródka J. et al. 2013) the design lengths of the welds are determined according to:

Fig. 6a $\quad l_w = l_1 + l_2 + 2b$ (8a)

Fig 6b $\quad l_w = 2\left(l_1 + b\right)$ (8b)

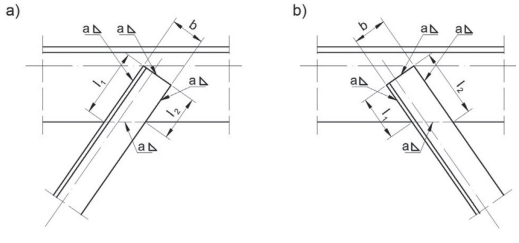

Figure 6. Connection of the braces with the chord.

where l_1, l_2 = the lengths according to Fig. 6; b = the width of the angle flange.

The maximum stress is determined as follows:

$$\max\ \tau_{\parallel} = \frac{K_i}{a_w l_w}. \tag{9}$$

It should also be noted that the ends of the angles should be cut perpendicular to their longitudinal axis.

The layout of the welds as shown in Fig. 3 corresponds to the layout presented in Fig. 6b. However the layout of the welds in the top chord joints is in accordance with Fig. 6a.

The connection on fillet welds placed around the perimeter of the head plates of assembly joints and fillet or groove welds connecting the head plates with the support vertical is calculated by determining the stresses using the directional method, but the layouts of the welds should be analysed according to the rules given in (Bródka & Broniewicz 2015).

6 DESIGN EXAMPLES

6.1 *The intermediate joint of the bottom chord*

The joint (Fig. 2) is loaded with forces: K_i = –240.85 kN, K_j = 585.41 kN, N_0 = 533.9 kN.

It is assumed a vertical is made of IPE 160: A_i = 20.1 cm^2, b_{fi} = 160 mm, h_i = 82 mm, t_{wi} = 7.4 mm, t_{fi} = 5.0 mm, r_{ii} = 9 mm, i_{zi} = 1.84 cm, l = 1750.3 mm. The brace is made of two angles 75 × 75 × 9 mm, A_j = 12.8 cm^2, $e_{yj} = e_{zj}$ = 2.17 cm. The bottom chord will be made of the channel UPE 330: A_0 = 67.8 cm^2, b_{fb} = 330 mm, t_{wb} = 16 mm, t_{fb} = 11 mm, r_{ib} = 18 mm.

In this example all members will be made from steel S235: f_y = 235 MPa, f_u = 360 MPa, $f_{vw.b}$ = 208.1 MPa.

The buckling resistance of the vertical in the plane of the truss:

$$\overline{\lambda}_z = \frac{1750.3}{18.4.93.9} = 1.01,\ \Phi = 1.21,\ \chi = 0.597,$$

$$N_{i.Rd} = 0.597 \cdot 2010 \cdot 235 = 282.0\ \text{kN} > 240.85\ \text{kN}.$$

The effective cross sectional area is calculated according to (2):

$$A_{i.r} = 2010 - \left[160 - 2\left(7.4 + 9\right)\right] \cdot 5{,}0 = 1374\ \text{mm}^2.$$

The capacity of the bottom chord loaded by the vertical force according to (4) – (k_m = 1,0 in case of tension chord):

$$N_{r.Rd.red.} = 1.0 \cdot 235 \cdot 11^2 \left[\frac{2 \cdot 82}{330} + 4\left(1 - \frac{7.4}{330}\right)^{0,5} \right] \Big/ 1{,}0$$
$$= 126{,}6 \text{ kN} > 0.5 \cdot 240.85 \text{ kN} = 120.5 \text{ kN}.$$

The capacity of the bottom chord according to PN-EN 1993-1-8:

$$A_v = 6780 - [330 - 2(16+18)]11 = 3898 \text{ mm}^2,$$

$$N_{i.Rd.} = \frac{235 \cdot 3898}{\sqrt{3} \cdot 1.0} = 529.5 \text{ kN} > 240{,}85 \text{ kN},$$

Or at $V_{pl.Rd} = N_{i.Rd}$

$$N_{0.Rd.} = \left[6780 - 3898 + 3898\left(1 - \frac{240.85}{529.5}\right)^{0,5} \right] \frac{235}{1{,}0}$$
$$= 1354 \text{ kN} > 533.9 \text{ kN}.$$

The capacity of the fillet welds joining the vertical with the bottom chord (a_w = 4.5 mm < $0.7 \cdot 7.4 = 5.2$ mm):

$$\tau_{\parallel} = \frac{0.5 \cdot 240850}{2 \cdot 4.5 \cdot 82} = 163.2 \text{ MPa} > f_{vw.d} = 208.1 \text{ MPa}.$$

Checking the capacity of the brace was made assuming the gross cross-section area of the angle.

$$N_{j.Rd} = 2 \cdot 1280 \cdot 235 = 601{,}6 \cdot 10^3 \text{ N}$$
$$= 601{,}6 \text{ kN} > 584.5 \text{ kN}.$$

The two welds having the thickness of a_w = 6 mm < $0.7 \cdot 9 = 6.3$ mm are designed. The eccentricity of the welds in regard to the axis of the brace is: $e_w = 0.5b_j - e_{zj} = 0.5 \cdot 75 - 21.7 = 15.8$ mm. The lengths of the welds are:

$$l_w = \frac{K_j\left(0.5 + e_w / b_j\right)}{2a_w f_{vw.d}} = \frac{585410\left(0.5 + 15.8/75\right)}{2 \cdot 6 \cdot 208.1}$$
$$= 166.6 \text{ mm}.$$

Hence the length of both welds l_w = 170 mm.

6.2 *The support joint*

The support joint (Fig. 4) is loaded by forces: $N_0 = -535.6$ kN, $K_j = 545.41$ kN, $N_c = 328.4$ kN.

The support vertical is designed from channel UP 330: $A_c = A_0 = 67.8$ cm^2, $b_{fb} = b_{fc} = 330$ mm, $t_{wc} = t_{wi} = 16$ mm, $t_{fc} = t_{fi} = 11$ mm, $r_{ic} = r_{ii} = 18$ mm. The flanges of the channel are reinforced with plates 60 × 16 mm, $e_{zi} = 29.3$ mm.

All members are made from steel S235: $f_y = 235$ MPa, $f_u = 360$ MPa, $f_{vw.d} = 208.1$ MPa.

The position of the neutral axis of the cross-section of the vertical: $e_{zc} = 50.9$ mm. The moment of inertia about the neutral axis $z_c - z_c$: $I_{zc} = 2771$ cm^4. The elastic section modulus: $W_{min} = 242.9$ cm^3, $W_{max} = 544.4$ cm^3.

The support vertical has a small length, so its capacity is determined as the resistance of the reinforced cross-section neglecting flexural buckling according to PN-EN 1993-1-1. Specifying of the class of cross-section:

– the web of the built-up section:

$$\frac{330 - 2(16+18)}{11} = 23.8 < 72 \cdot 0.81 = 58.3,$$

– the reinforced flanges of the channel (assuming $\alpha = 0.7$):

$$\frac{165 - (11+18)}{16} = 8.5 < \frac{9 \cdot 0.81}{0{,}7\sqrt{0{,}7}} = 12.4.$$

The vertical is class 1 cross-section.

The design bending moment in the vertical:

$$M_{Ed} = N_c\left(e_{zc} - e_{zi}\right) = 328.4\left(50.9 - 29.3\right)$$
$$= 7093 \text{ kNmm}.$$

The resistance of the vertical:

$$\frac{N_c}{A_c} \pm \frac{M_{Ed}}{W_{el}} \le f_y.$$

The stress at the edge of the web:

$$\sigma_{x1} = \frac{328400}{6780 + 2 \cdot 60 \cdot 12} + \frac{7093000}{544400}$$
$$= 52.9 \text{ MPa} < f_y = 235 \text{ MPa}$$

The stress at the edge of the reinforcement:

$$\frac{328400}{6780 + 2 \cdot 60 \cdot 12} - \frac{7093000}{242900}$$
$$= 10.8 \text{ MPa} < f_y = 235 \text{ MPa}.$$

The cross-sections of the support vertical is designed primarily because of the good arrangement of the bolts for fixing the base plate to the column of the building.

It remains to consider the impact of the direct attachment of the truss members on each wall of the support vertical.

A normal stress in the cross-section of the upper chord is:

$$\sigma_x = \frac{N_0}{A_0} = \frac{535600}{6780} = 79 \text{ MPa} = 0.34 f_{yc} = 0.14 f_{y0}.$$

The greatest stress in the flanges of the vertical is:

$$\sigma_x = 54.7 \text{ MPa} = 0.34 f_{yc}.$$

With such a small stress it can be taken as sufficient to assess the safety of the walls of the support vertical that the load from the top chord passes directly through the flanges and the web of the top chord.

The flanges of the top chord are joined with the flanges of the support vertical by means of partial penetration butt welds. This thickness is adopted as: $a_w = 0.5t_{wi} = 0.5 \cdot 16 = 8$ mm. The force per flange of the bottom chord will be:

$$N_{0.fi} = h_i t_{fi} \sigma_x = 105 \cdot 16 \cdot 79 = 132.7 \text{ kN}.$$

This force upon non-axial loading of the partial butt weld causes an increase in normal stress in the flange due to the bending moment:

$$\sigma_{x.fi} = \frac{132700}{105 \cdot 16} + \frac{132700 \cdot 0{,}5(16-8)}{105\frac{16^2}{6}} = 197.5 \text{ MPa} < f_y = 235 \text{ MPa}.$$

The same bearing stress occurs in the flange of the support vertical, because the impact of the force $N_{0.fi}$ is analogous. These stresses are almost entirely balanced by the stresses caused by the horizontal component of a tension force in the brace, perpendicular to the support vertical. As a result, such stresses produce the shear force in the flange of the support:

$$\tau_1 = \frac{\sigma_{x.fi} \cdot h_i}{\sqrt{3}\left(h_i + b_r\right)} = \frac{197.5 \cdot 105}{\sqrt{3}(105+60)} = 72.6 \text{ MPa} < f_{vw.d} = 208.1 \text{ MPa}.$$

where $b_r = 60$ mm is the width of the reinforcing plate.

The load passed from the web of the upper chord on a support vertical can be calculated by assuming the fully rigid joint. This load acts by a fillet weld connecting these elements almost directly on the rib closing the channel of the post from the top. It also causes shear force in reinforced flange of the vertical. Without taking into account a small inclination, this load can be determined as:

$$N_{0,fb} = b_{fb} \cdot t_{fb} \cdot \sigma_x = 330 \cdot 11 \cdot 79 = 286.8 \cdot 10^3 \text{ N} = 286.8 \text{ kN}.$$

Thus the shear stress is equal:

$$\tau_2 = \frac{286800}{165 \cdot 16} = 108.6 \text{ MPa} < \frac{235}{\sqrt{3}} = 135.7 \text{ MPa}.$$

The stresses in fillet welds connecting the brace angles with the support vertical are checked in a manner relating to the layout of the welds according to Fig. 6a. The lengths of the welds are: $l_1 = 200$ mm, $l_2 = 75$ mm, $b = 75$ mm, $l_w = 200 + 70 + 2 \cdot 75 = 425$ mm and the width $a_w = 4$ mm $< 0{,}7.9 = 6.3$ mm.

$$\tau_{\parallel} = \frac{585400}{2 \cdot 425 \cdot 4} = 172.2 \text{ MPa} < f_{vw.d} = 208.1 \text{ MPa}.$$

The shear stresses in groove welds connecting the flanges of the top chord with the flanges of the support post at $a_w = 8$ mm are checked by the following formula:

$$\tau_{\parallel} = \frac{N_{0.fi}}{\sqrt{3} h_i a_w} = \frac{132700}{\sqrt{3} \cdot 105 \cdot 8} = 91.2 \text{ MPa} < f_{vw.d} = 208.1 \text{ MPa}.$$

However the load in the web of the top chord is in a support joint transmitted through the two lengths of fillet welds l1 = bfi = 330 mm on the outside of the wall and $l_2 = l_1 - 2(t_{wp} + r_{ii}) = 330 - 2(16 + 18) = 262$ mm on its interior (Fig. 7). The width of the fillet welds $a_{w1} = a_{w2} = 4$ mm $< 0.7 \cdot 11 = 7{,}7$ mm. The force transmitted through the web is equal $N_{0.fb} = 286.8$ kN. The eccentricity of the force in regard to the layout of the welds is equal 4.6 mm. The moment of inertia of such welds $I_{zw} = 13.46$ cm^4.

The bending moment can be determined as:

$$M_k = N_{0.fi} \cdot e_w = 286.8 \cdot 4.6 = 1319 \text{ kNmm}.$$

The distance of the welds from the neutral axis:

$$z_1 = 4.6 + 4 = 8.6 \text{ mm}, \; z_2 = 11 - 4.6 = 6.4 \text{ mm}.$$

The shear stresses are equal:

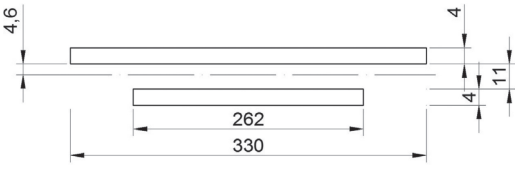

Figure 7. Fillet welds in supporting joint.

$$\tau_{\parallel.1} = \frac{286800}{4(330+262)} - \frac{1319000 \cdot 8.6}{134600}$$

$$= 205.4 \text{ MPa} < f_{vw.d} = 208.1 \text{ MPa},$$

$$\tau_{\parallel.2} = \frac{286800}{4(330+262)} - \frac{1319000 \cdot 6.4}{134600}$$

$$= 58.4 \text{ MPa} < f_{vw.d} = 208.1 \text{ MPa}.$$

REFERENCES

ArcelorMittal. 2015. *Sections and Merchants Bars. Sales Programme*. ArcelorMittal.

Augustyn J. 1987 *Welding connections*. Warsaw. Arkady. (in Polish).

Bogucki W. & Żyburtowicz M. 2008 *Metal structures design tables.* Warsaw. Arkady. (in Polish).

Bródka J. & Broniewicz M. 2002 Design of welded connections of trusses made of hollow sections. *Steel Structures* (4): 29–34. (in Polish).

Bródka J. & Broniewicz M. 2013 *Design of steel structures according to Eurocodes.* Rzeszow. Polish Technical Publisher. (in Polish).

Bródka J. & Broniewicz M. 2015 Design of trusses made of channel sections according to Eurocode rules. *XV International Scientific Conference „Rzeszów–Lviev–Kosice". "Current Issues of Civil and Environmental Engineering and Architecture*". Rzeszow.

Bródka J. et al. 2013 *Design and calculation of connections and joints of steel structures. 2-nd edition*. Rzeszow. Polish Technical Publisher. (in Polish).

Bródka J. & Juchniewicz J. 1994 *Basses of steel structures. Part 2.* Lodz. (in Polish).

Deutscher Stahlbau Verband. Stahlbauhandbuch. Band 2. 1985 Stahlkonstruktionen. 9 Auflage. Stahlbau—Verband. Köln.

EN 1090-2 2007 *Execution of steel structures and aluminium structures. Technical requirements for steel structures*.

EN 1993-1-1 2006 *Eurocode 3: Design of steel structures—Part 1-1: General rules and rules for buildings*.

EN 1993-1-8 2006 Eurocode 3: *Design of steel structures—Part 1-8: Design of joints*.

EN 1993-1-10 2007 Eurocode 3: *Design of steel structures—Part 1-10: Material toughness and through-thickness properties*.

EN 10025 2007 *Hot rolled products of structural steels. Parts 1* to 5.

Giżejowski M. & Ziółko J. (ed.) 2010 General construction. Volume 5. *Steel structures of buildings designed according to the Eurocodes with examples of calculations*. Warsaw. Arkady. (in Polish).

Kindmann R. & Stracke M. 2003 *Verbindungen im Stahl—und Verbundbau*. Berlin. Ernst und Sohn. A Wiley Company. (in German).

Łubiński M. et al. 2000 *Steel Structures. Part 1*. Warsaw. Arkady. (in Polish).

Silos, tanks and vessels

This page intentionally left blank

Recent Progress in Steel and Composite Structures – Giżejowski et al. (Eds)
© 2016 Taylor & Francis Group, London, ISBN 978-1-138-02946-0

Experimental investigations on the resistance of vertical stiffeners of steel silos shells made of corrugated sheets

E. Hotała, Ł. Skotny, M. Kuśnierek & J. Boniecka
Wrocław University of Technology, Wrocław, Poland

ABSTRACT: Cylindrical shells of silos made of corrugated sheets are usually stiffened by columns which transfer practically all vertical loads of this shell. Accurate determination of the resistance of stiffeners in silos made of corrugated sheets is important since many failures of silos are due to the resistances of those stiffeners. Results of experimental investigations of columns in one of the shells made of corrugated sheets show that the code method of calculation of the resistance of these columns given in EN 1993-4-1 is too conservative. Calculated according to the code resistance of columns due to buckling may be even several times smaller than the actual resistance of those stiffeners. In this paper the course of experimental investigations and their results obtained for vertical columns in a cylindrical shell made of corrugated sheets are presented. Authors discuss calculation method for shell's stiffness according to the code procedure of the relevant calculations.

1 INTRODUCTION

1.1 *Ribbed shells from corrugated sheets*

Cylindrical shells made of steel corrugated sheets with vertical stiffeners (often referred to as columns) are relatively common in use as storage structures for grain in agricultural industry. Thin corrugated sheets have horizontal folding, and their resistance in the vertical direction is relatively small and usually omitted in design. In such cases it is assumed usually that the entire vertical loading in cylindrical shell is carried out by vertical stiffeners which are fastened to corrugated sheets by bolts. Said vertical load is mostly produced by material friction to the walls of a silo but also from the weight of roof structure and other loads i.e., loads from transporting equipment or other appliances placed on the silo roof as well.

1.2 *Resistance of ribbed shell from corrugated sheets*

The resistance of vertically ribbed shell of silos can be analyzed as the resistance of an orthotropic shell, but quite commonly an alternative method described in chapter 5.3.4.3.4 of code EN 1993-4-1 is used. In this method two possible approaches are presented. Vertical stiffeners are designed either as a compressed column without any lateral supports or as a compressed beams supported on the shell made of corrugated sheets, treated as elastic foundation. Those stiffeners must carry all of the vertical loads transferred from the shell. According to the code EN 1993-4-1, the resistance of a single stiffener is calculated alternatively as the lower value from results obtained from equations (1) and (2) or, in case of calculating it as a compressed column without lateral supports, equation (3) is used:

$$N_{b,Rd} = 2\frac{\sqrt{EI_y K}}{\gamma_{M1}} \tag{1}$$

$$N_{b,Rd} = \frac{A_{eff} f_y}{\gamma_{M1}} \tag{2}$$

$$N_{b,Rd} = \frac{\chi A_{eff} f_y}{\gamma_{M1}} \tag{3}$$

where K is the rigidity of elastic foundation, EI_y is the rigidity of a stiffener under bending in a vertical plane along the radius of a shell, χ is a buckling coefficient of laterally unsupported compressed element and γ_{M1} is the partial safety factor equal to 1.1. This means that calculations of the stiffener's resistance $N_{b,Rd}$ is reduced to calculations of stability of a stiffener on elastic foundations (1) and the resistance of effective cross-section of a stiffener due to compression (2), or calculating this element as compressed beam without any lateral support (3). The correct estimation of the resistance of vertically ribbed silos made of steel corrugated sheets is critical from the standpoint of a structural safety, because most of collapses of the silos are related to the exceeding of the resistance of a stiffener. (Błażejewski & Marcinowski 2013, Pasternak & Hotała 2002, Iwicki et al. 2011).

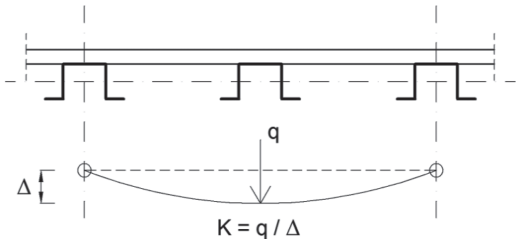

Figure 1. Estimation of rigidity K according to Figure 5.5 in EN 1993-4-1.

Several researchers (Błażejewski & Marcinowski 2013, Iwicki et al. 2011, Sondej et al. 2013) proves that stiffeners' resistance according to (1) is too low in comparison to the real ones, if code (EN 1993-4-1) method accordingly to the Figure 1 is used to estimate the rigidity of elastic support.

1.3 *Experimental investigations*

Authors of this paper carried out quite vast experimental studies of the resistance of vertical stiffeners used in cylindrical shells made of corrugated sheet with horizontal folding. The results of experimental investigations on the resistance of vertical stiffeners are shown herein. Stiffeners attached to the shell made of corrugated sheets with diameter d = 3.8 m and height h = 2.635 m were tested. One of goals in this series of experiments was to verify the code equation (1), in which stiffness K is calculated accordingly to Figure 1. There was no bulk solid in the tested shell, so the stiffness K was dependent only from the rigidity of the shell which means that the rigidity of bulk solid or its horizontal pressure on shell was not taken into account. Currently, the code regulations do not take into account the effect of bulk solid, especially its rigidity, on the resistance of vertical stiffeners of shells discussed herein. It should be noted, that such shells exist in many silos, since silos made of corrugated sheets with diameter of less than 9 m are usually equipped with hopper and supporting skirt. This supporting skirt works in conditions tested in the presented experiments.

2 SHELL MODEL AND THE COURSE OF EXPERIMENTAL INVESTIGATIONS

2.1 *Shell model*

Presented results of experimental investigations are given for a one of few models, represented by relatively short shell (Figures 2, 3) made of corrugated sheets with diameter d = 3.8 m, with 8 vertical stiffeners, made of cold formed "hat" profiles of thickness t = 2 mm and the total length of cross section equal to s = 450 mm (Figure 4a). Models were made of corrugated sheets with thickness t_f = 0.75 mm, wave height d_f = 15.3 mm and wave length l = 102 mm (Figure 4b). Model had 8 stiffeners each with height of h_z = 2.635 m. The top and bottom of the shell were stiffened by octagonal square tube rings pin-jointed to columns.

Stiffeners were attached to each horizontal fold of corrugated sheets by bolts, which spacing was equal to wave length l = 102 mm. Model had 3 continuous stiffeners (Figure 5a), other stiffeners were equipped by variously solved connection in the middle of their height. Two of them of small bending rigidity were classified as hinges (Figure 5b), which is not recommended in the code EN 1993-4-1. Other stiffeners had special connections, which will not be presented in this paper.

Additionally, apart from the complete model, 5 single short specimens with length of 406 mm were made. The resistance due to their compression was also tested in hydraulic press (Figure 10). The presented buckling collapse and the resistance analysis assuming initial imperfections were limited to the stiffeners in the model shown on Figure 2 called in this paper "long stiffeners" in comparison with "short stiffeners" which were tested in hydraulic press (Figure 10). For short stiffeners recognized as almost straight, the test was carried out without the influence of the steel shell. In all stiffeners, short as well as long ones, holes of 10.5 mm diameter were made in accordance to typical solutions used in real silos (Figures 2, 8, 10).

Authors executed also tests on model with a higher diameter d = 8.6 m, where apart from the described here "hat" profiles additional stiffeners made of C-section and flat bars were used. The

Figure 2. General view of a model on the experimental stand. On the right side the hydraulic press.

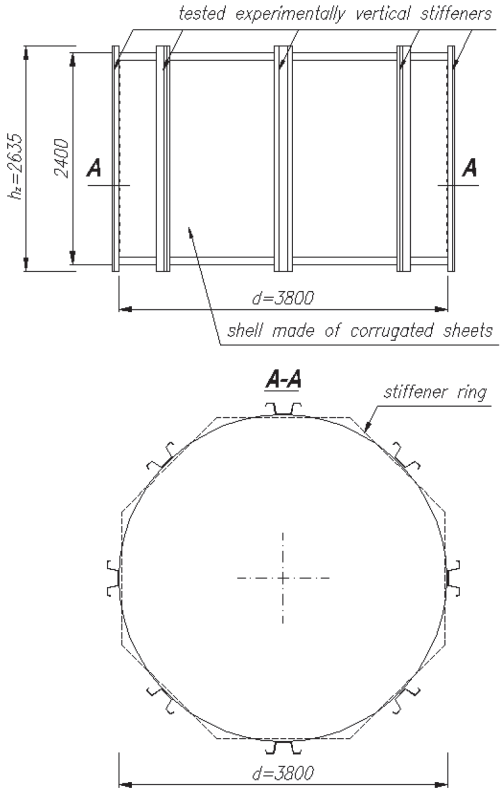

Figure 3. Geometry of shell model with diameter $d = 3.8$ m.

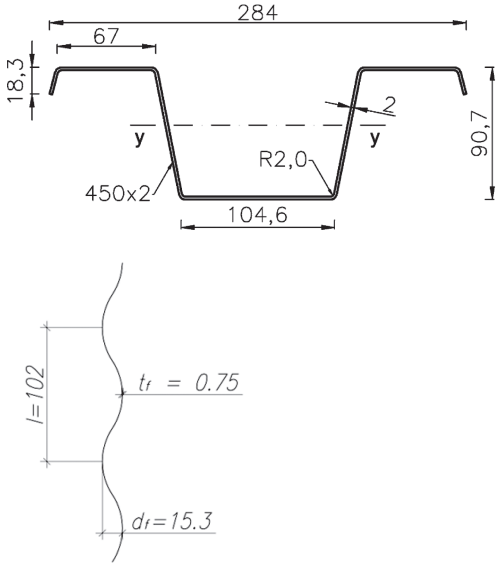

Figure 4. Geometry details a) Cross-section of tested stiffeners, b) wave geometry of corrugated sheet.

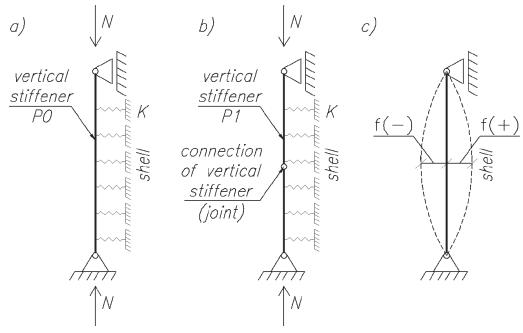

Figure 5. Static scheme of tested continuous stiffeners a) and stiffeners with hinges, b) as well as direction of horizontal deformations, c). Positive value of f means deformation inwards.

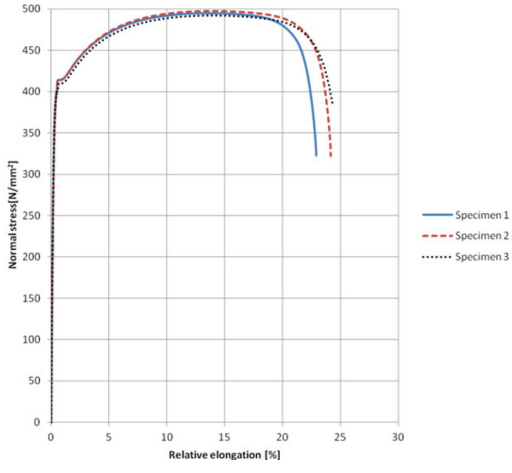

Figure 6. Load-displacement relationship received from static tension tests of specimen cut out from stiffeners.

second model allowed to perform greatly increased number of tests. Different cross sections of stiffeners allowed to obtain different failure mechanisms as local buckling of cross section in class 4 or general buckling failure. Currently authors are working on the outcomes of the tests in this second model, and will publish them in a future. In this paper outcomes for a single stiffener in the second model made of a flat bar with cross section 90×10 mm made of steel grade S355 will be presented. Connection between the stiffener and corrugated sheets is identical as for "hat" profiles.

2.2 *Course of experimental investigations*

Each stiffener in the tested shell was placed one at the time in the hydraulic press (Figure 2) and com-

pressed by force N (Figure 5). During the static process vertical and horizontal deformations of the stiffener were recorded, where the horizontal deformation was denoted as f in Figure 5c. Positive value of horizontal deformation, which was always measured in half-height of the specimen, is treated as a deformation inward, while negative value means deformation outward.

Continuous stiffeners were denoted with P0-x symbol where x is the subsequent number of stiffener having the same geometry. Stiffeners with hinges in the middle of their height are denoted as P1-x, – as previously x is the number of tested stiffener. The stiffeners were bolted at both ends to the octagonal stiffening ring (Figure 2) in a way that did not allow for transferring bending moment. Tested stiffeners were in cross-section of class 4, with the effective cross section area $A_{\text{eff}} = 711$ mm^2, and cross section gross area $A = 900$ mm^2.

Short stiffeners with length of 406 mm were loaded in hydraulic press (Figure 10) by an axial force up to the resistance collapse, which was typical for cross sections in class 4. During tests the shortening of tested stiffener as well as the axial force were measured in a continuous manner.

"Hat" stiffeners were made of steel HX380 (according to EN 10346) with the nominal yield stress f_y = 380 N/mm^2. Within the experimental investigations the Authors carried out tests of static tension on 3 specimen isolated from stiffeners after the main tests were completed. The load-displacement relationships of those tests are given in Figure 6.

From the paths given in Figure 6 a plastic plateau can be observed when normal stress reaches 420 N/mm^2. It should be noted however that before the plateau is reached the relative elongation of specimen is higher than 0.2%, and as such in all tests apparent yield stress was used. For those specimen apparent yield stress was between 389 and 394 N/mm^2 which quite accurately corresponds with the nominal yield stress f_y = 380 N/mm^2.

Test performed on the flat bar in a model with diameter d = 8.6 m was made For a flat bar the nominal yield stress f_y = 355 N/mm^2 was taken. This specimen is marked as FB-1.

2.3 *Column on continuous elastic support*

Deflection of a compressed column during buckling causes a reaction of elastic support given by $q(x) = -K \cdot y(x)$. If we take this fact into consideration in differential equation of the deflection line we will receive:

$$EI\frac{d_y^4}{dx^4} + N\frac{d_y^2}{dx^2} + Ky = 0 \tag{4}$$

where EI –the column bending stiffness, N – the normal force in the column cross-section, K – the foundation stiffness (representing wall sheets) and y – the column horizontal displacement.

For a column with supports free to rotations on both ends the deflection curve given in equation 5 can be assumed as fulfilling all the boundary conditions (y_0 – amplitude, L – column height).

$$y = y_0 \sin\left(\frac{n\pi x}{L}\right) \tag{5}$$

Solution of this differential equation is to find the minimum critical force N_{crit}. With assumed deflection curve and its derivatives one can obtain a equation for critical number of buckling half waves n_{crit}.

$$n_{crit} = \frac{L}{\pi}\sqrt[4]{\frac{K}{EI}} \tag{6}$$

The critical force is given as:

$$N_{crit} = 2\sqrt{EI \cdot K} \tag{7}$$

It should be noted that this equation is valid only if the number of buckling half waves $n_{crit} > 1$.

2.4 *Resistance of stiffeners according to EN 1993-4-1*

Since all experimentally tested stiffeners (in model with diameter d = 3.8 m) have the same cross-section, resistances given in equations (1), (2) and (3) can be calculated once for typical specimen and discussed herein. As mentioned previously the effective cross-section area for the used cross section (Figure 4) is A_{eff} = 711 mm^2. Moment of inertia I_y = 1207819 mm^4 and moment of inertia of effective cross-section is $I_{y,eff}$ = 985094 mm^4. Young modulus for the steel is E = 210 GPa, and corrugated sheet stiffness K = 9.32 kN/m. Buckling coefficient (with h_z = 2635 mm) χ = 0.612.

Thus the resistances of the "hat" stiffener calculated with different equations are as follows: cross-section plastic resistance (equation (2)) $N_{b,Rd}$ = 245.6 kN, resistance for buckling of the stiffener calculated as a axially compressed member without lateral supports (equation (3)) $N_{b,Rd}$ = 150.3 kN. Since $n_{crit} < 1$ for the "hat" profiles (according to equation 6) the equation 1 was omitted for those stiffeners. However for the FB-1 n_{crit} = 1.30, thus the resistance of this specimen was calculated as for column with continuous elastic support $N_{b,Rd}$ = 6.97 kN according to equation 1.

Interesting phenomenon can be observed here. Code EN 1993-4-1 gives two methods of estimating the resistance of compressed stiffeners in the analyzed case. In first method the resistance of the stiffener is calculated as for a compression member not being laterally supported by corrugated sheet according to equation (3). This method should be conservative, since the positive effect of the lateral support is omitted. The latter can be accounted for in the second method by equations (1) and (2).

3 RESULTS OF EXPERIMENTAL INVESTIGATIONS

3.1 *Results for stiffeners in the shell made of corrugated sheets*

Results of experimental investigations for 5 "hat" stiffeners (Figures 2, 3) and flat bar stiffener attached to the cylindrical shell made of corrugated sheets are given in Figure 7. In Table 1 values of received maximum forces before the collapse as well as the initial horizontal imperfections and horizontal deformation f in the middle of a stiffener (after loading) are given together with the maximum axial shortening of the stiffener corresponding to the load-bearing capacity. For "hat" profiles all cases of the resistance collapse were due the destruction of the effective cross section of the stiffener (Figure 8), which can be calculated from equation (2). For every "hat" stiffener higher capacity was obtained that this obtained from equation 3. In the case of a flat bar, the test load-bearing capacity of the stiffener was due to buckling (Figure 9). Capacity obtained for that stiffener is in the contrast with results of equation (1) which gave several times lower value for the stiffener resistance due to buckling collapse. This means that according to designed method the load bearing capacity is significantly underestimated in considered case (comparison between received force from experiments given in Table 1 and value calculated according to equations (1)). Comparison between stiffener capacity $N_{b,Rd}$, calculated from equations (1) or (3) and (2) and those received from experimental tests are given in Table 2. In this table additionally capacity of gross cross section $N_{c,Rd}$ is given calculated according to equation (8), to show the benefits coming from usage of stiffeners with cross sections in class 3 rather than 4 in silo shells.

$$N_{c,Rd} = \frac{Af_y}{\gamma_{M0}} \tag{8}$$

where $\gamma_{M0} = 1.0$.

If eccentricity of the center of gravity e_N between effective cross section A_{eff} and gross cross section A is taken into account as well as resulting bending moment $\Delta M = N_1 \times e_N$, and also bending moment M_y resulting from axial force acting on the eccentricity (due to inward or outward deformation of the stiffener) f then the resistance ratio of analyzed stiffener for its effective cross section is given by equation (9):

$$\frac{N_1}{A_{eff} f_y / \gamma_{M0}} + \frac{M_y + N_1 e_{Ny}}{W_{eff,y,\min} f_y / \gamma_{M0}} = R \tag{9}$$

In which force N_1 is the axial load for which the resistance of the tested stiffener was reached, and the other symbols are given according to EN 1993-1-1 with $\gamma_{M0} = 1.0$. The resistance ratio R calculated according to equation (9) is given in Table 3. It can be seen that the extreme force N_1 received in tests comes from the true stress distributions over the cross sections of the tested stiffeners, not including the flat bar stiffener.

In case of FB-1, the resistance of the stiffener of experimentally tested specimen was calculated according to equation (1) which is the conclusive resistance for this stiffener in the analyzed shell according to EN 1993-4-1. Even if the code method of calculation of stiffeners of the shell K (Figure 1) is treated as an approximate it is still too conservative since the resistances received from the experimental tests – N_1 are at least 12 times higher than those received from the code calculations. This leads to the conclusion that other methods of calculations of shell rigidity K should be proposed. The experimental work on this topic are performed by different researchers (Błażejewski & Marcinowski 2013, Iwicki & Wójcik & Tejchman

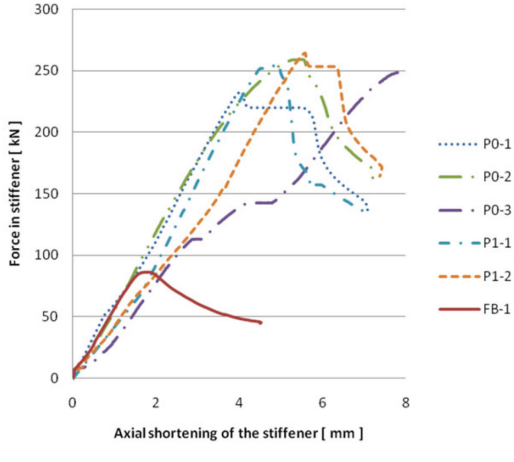

Figure 7. Load- displacement relationship of stiffeners P0 and P1 and FB-1.

Table 1. Basic results from experimental tests.

Stiffener symbol	Maximal axial force N1 [kN]	Axial shortening of the stiffener [mm]	Horizontal imperfection amplitude [mm]	Horizontal deformation at failure f [mm]
P0-1	232.2	4.04	–	–0.51
P0-2	258.9	5.47	–0.64	2.42
P0-3	249.6	6.78	0.36	3.65
P1-1	255.2	4.91	1.82	1.35
P1-2	264.4	5.59	1.71	2.43
FB-1	86.1	1.76	–	8.55

Table 2. Extremal forces N_1 and stiffener capacity according to EN 1993.

Stiffener	Extreme Force N_1 [kN]	Capacity $N_{c,Rd}$ Eq. (8) [kN]	Capacity $N_{b,Rd}$ Eq. (1, 3)* [kN]	Capacity $N_{b,Rd}$ Eq. (2) [kN]	$N_1/N_{b,Rd,min}$ [–]
P0-1	232.2	342.0	150.3	245.6	1.55
P0-2	258.9	342.0	150.3	245.6	1.72
P0-3	249.6	342.0	150.3	245.6	1.66
P1-1	255.2	342.0	150.3	245.6	1.70
P1-2	264.4	342.0	150.3	245.6	1.76
FB-1	86.1	319.5	6.97	–	12.4

*Capacity $N_{b,Rd}$ is calculated according to Eq. (3) for "hat" stiffeners and according to Eq. (1) for flat bar stiffener.

Table 3. Summary of the real forces and resistance ratio R in tested stiffeners.

Stiffener	Force N_1 [kN]	M_y [kNm]	$N_1 * e_N$ [kNm]	$M_{cy,Rd,eff}$ [kNm]	$N_{c,Rd,eff}$ [kN]	R [–]
P0-1	232.2	–0.12	–0.67	6.96	270.2	0.97
P0-2	258.9	0.63	–0.74	6.96	270.2	0.97
P0-3	249.6	0.91	–0.72	6.96	270.2	0.95
P1-1	255.2	0.34	–0.73	6.96	270.2	1.00
P1-2	264.4	0.64	–0.76	6.96	270.2	1.00

* Symbol explained in text.

2011, Sondej & Wójcik & Iwicki & Tejchman 2013) but the real behaviour of the studied members is still not sufficiently recognized.

Authors are currently performing various studies connected with presented tests including FEM modelling for the entire model. Those studies will allow to verify received outcomes as well as to formulate more general conclusions. It should be noted that even at this stage the case of flat bar stiffener clearly shows that the stiffness of the shell made of corrugated sheets is significantly higher than the one calculated according to EN 1993-4-1, this shows that alternative methods of calculating of the stiffness K should be searched.

Symbols in Table 3 are as follows: $M_y = N_1 \times f$, $M_{cy,Rd,eff} = W_{eff,y,min} \times f_y / \gamma_{M0}$ – the effective resistance of the stiffener due to bending in y-y direction, $N_{c,Rd,eff} = A_{eff} \times f_y / \gamma_{M0}$ – the resistance of effective cross section (class 4) of the stiffener due to compression. Horizontal deformation of the stiffener f to the inwards of the shell was marked as positive and gave bending moment M_y that usually was in the opposite direction than moment $N_1 \times e_N$, resulting from the eccentricity of the gravity center in the effective cross section.

The resistance ratio R of the "hat" stiffeners (Table 3) in tested shell, corresponding to the load-bearing capacity in the experimental test is almost equal to 1, which leads to the conclusion that the resistance of the stiffener was calculated precisely. In case of stiffener made of flat bar buckling is decisive in capacity failure, so it was omitted in

Figure 8. Basic form of capacity failure (stiffener P0–2).

Table 3. The value R is however given for cross sections in the middle of the height of a stiffener where maximum values of horizontal deformations f are located. The resistance collapse however took place in a certain distance from the middle section of the stiffener (Figure 8), where horizontal deformations were smaller than in the middle and that leads to much smaller values of bending moment M_y. The imperfections of the calculation model and the yield stress of steel slightly higher than the nominal on should also be taken into account.

3.2 *Results for short stiffeners*

Experimental tests on short stiffeners was carried for 5 short members with the geometry of cross section identical as that of stiffeners in a model with corrugated sheets (Figure 4). Stiffeners were made of steel with nominal yield stress f_y = 380 N/mm^2. Average yield stress of steel was 414 N/mm^2. In most cases the resistance collapse occurred in cross sections weakened by holes (Fig. 10), which were made similarly to holes for bolts in the model with corrugated sheets.

In one case the resistance collapse occurred near hydraulic press. Load—bearing capacities received from the experimental investigations in this series can be seen on Figure 11. It can be noticed that received values of capacity are close to value received from equation (2) 245.6 kN.

3.3 *Alternative method of calculation of stiffness K*

Received outcomes from presented tests, especially for the flat bar shows that the influence of the corrugated sheeting on the stability of stiffeners

Figure 9. Stiffener with flat bar cross-section FB-1. Visible are the beginnings of the buckling collapse.

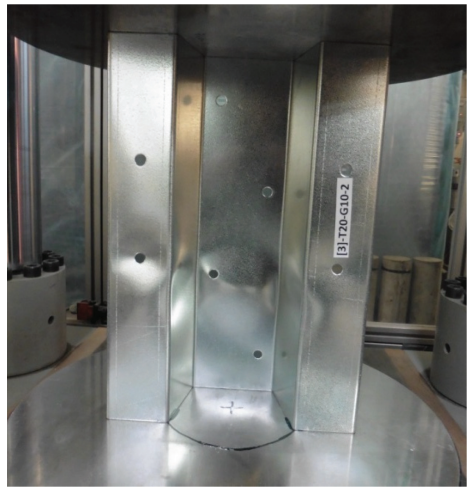

Figure 10. Short stiffener T20-G10-2 in hydraulic press after collapse.

is higher than assumed in EN 1993-4-1. In the method proposed in that code the curvature of the corrugated sheet is being omitted. In authors' opinion this has a significant influence on the outcomes. Basing on the numerical studies of similar shells, the authors propose an alternative method of calculation of the stiffness of the corrugated sheets, which takes into account their curvature.

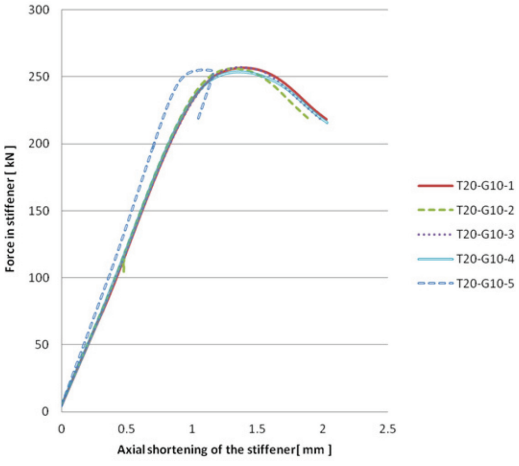

Figure 11. Load- displacement relationship of 5 tested short stiffeners.

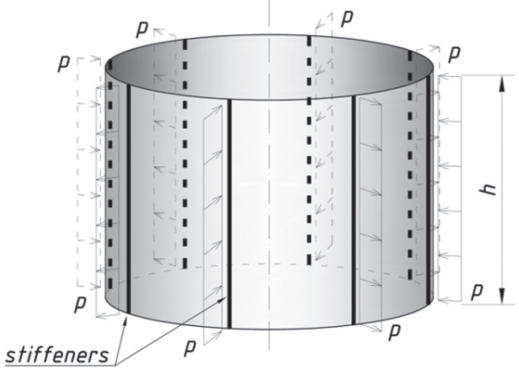

Figure 12. Scheme for an alternative method of calculation of the stiffness K.

In the proposed method a section of the shell is considered with the height h. It is assumed that the stiffeners will buckle alternately to the inside and outside of the shell. This assumption leads to applying forces (on entire length of the stiffener) in the radial direction inwards and outwards as shown on Figure 12. Boundary conditions at the bottom and top of the shell are represented by the restraints only in vertical direction. The rigidity of the corrugated sheets K is defined as the ratio of applied force and maximum radial deformation of the shell similarly as in the method proposed in EN 1993-4-1 shown in Figure 1 of this paper.

Rigidity of analyzed shell calculated according to the proposed method is more than 4 times higher than the one calculated according to EN 1993-4-1.

4 SUMMARY

In the evaluation of the load—bearing capacity of vertical stiffeners in cylindrical shells made of corrugated sheets used often as silos, the equations (1) and (2) given in code EN 1993-4-1 are used, as well as more conservative approach given by equation (3). Estimation of the shell rigidity K according to the method shown in the Figure 1, leads to severe underestimation of the real resistance of stiffeners. This fact was shown in this paper especially in case of stiffener made of flat bar 90 × 10 mm. Alternative method of calculation of shell stiffness which takes into account for shell curvature is proposed. Results obtained for "hat" stiffeners show that usage of stiffeners with cross sections in class 4 is not always rational, since small effective area A_{eff} in obvious way affects the resistance of the compressed element.

In case of axial compression of the stiffener a significant influence of hinged connection (stiffeners P1) in the middle of its height on the overall resistance of the stiffener was not observed. However if the stiffener is bent in the support regions or due to local horizontal loads in shell, then the lack of bending rigidity along its length may lead to overloading of the studied stiffener and in effect its collapse (Hotała et al. 2015).

REFERENCES

Błażejewski P., Marcinowski J. 2013. *Buckling resistance of vertical stiffeners of steel silos for grain storage*. Budownictwo i Architektura12(2), pp. 189–196 (in polish).

Eurocode 3 – Design of steel structures—Part 4–1: Silos. CEN 2009 Brussels.

Hotała E., Skotny Ł., Kuśnierek M., Boniecka J. 2015. *Connections of vertical columns as a weak regions in steel silos made from corrugated sheets*. Materiały Budowlane 9/2015 (in polish).

Iwicki P., Wójcik M., Tejchman J. 2011. *Failure of cylindrical steel silos composed of corrugated sheets and columns and repair method using sensitivity analysis*. Engineering failure Analysis, 18/2011, pp. 2064–2083.

Iwicki P., WójcikM., Tejchman J. 2011. *3D buckling analysis of a cylindrical metal bin composed of corrugated sheets strengthened by vertical stiffeners*, Thin-Walled Structures 49, pp. 947–963.

Pasternak H., Hotała E., Vayas I. 2002. *Schaeden an Stahlsilos - weitere Beispiele*. Bauingenieur Bd 77 Nr 3, s. 108–112.

Sondej M., Wójcik M., Iwicki P., Tejchman J. 2013. *Comparative buckling analysis of cylindrical steel silos with flat or corrugated sheet.* Shell Structures: Theory and Applications, Volume 2. CRC Press, Gdańsk.

Recent Progress in Steel and Composite Structures – Giżejowski et al. (Eds)
© 2016 Taylor & Francis Group, London, ISBN 978-1-138-02946-0

Load-bearing capacity of discretely supported steel silos shells with skirts

Ł. Skotny, E. Hotała & J. Boniecka
Wrocław University of Technology, Wrocław, Poland

ABSTRACT: Local concentrations of meridional compressive stress in the cylindrical shells of steel silos in many cases lead to loss of stability of these shells. Preventing such situations is a fundamental challenge to designers. Standard EN 1993-4-1 allows for inappropriate analysis of the phenomenon of local stability loss in longitudinally compressed cylindrical shell supported discretely through a skirt. To prevent uneven distribution of compressive stress along the circumference of such shells standard EN 1993-4-1 proposes use of a skirt with thickness 20% higher than the thickness of the shell. This proposal is wrong since even this thick skirt cannot provide even distribution of stresses. The paper presents the results of nonlinear numerical analyzes of several cylindrical shells modeled with imperfections (GMNIA). Several solutions of support regions were analyzed. It has been shown that the capacities of analyzed shells are lower than those of uniformly supported shells with the same parameters.

1 INTRODUCTION

1.1 *Preface*

In the code EN 1993-4-1 it is specified, that a skirt (extension of silo shell beyond the contact area with conical hopper) that is 20% thicker than the silo shell provides a uniform support. This should lead to a uniform distribution of compressive meridional pressures over the circumference caused mainly by the stored bulk solid. Obtaining such uniform pressures distribution is however unlikely if not impossible (Hotała & Skotny (2013), Skotny (2011)). When a uniform distribution of meridional compressive pressures is provided, then the shell will buckle in a global shape, which in turn leads to a higher resistance than for the shell supported on a few sectional supports (Hotała (2001), Samuelson & Eggwertz (1992)).

Since code EN 1993-4-1 suggests that the skirt provides such uniform stress distribution, and it was proven previously (Hotała & Skotny (2013)) that this statement is erroneous, efforts were made to calculate several shells to estimate how much the code suggestion overestimates the capacity of the shell, and what practical recommendations can be formulated for the design of shells with skirts.

In this paper, first many computational models are being presented. Authors understand, that providing robust recommendations for such a complex problem requires a vast amount of work which is currently undertaken at The Wrocław University of Technology, and this paper shows first outcomes of said analyses. As such, presented outcomes are limited to certain support solutions with different skirt lengths and thicknesses, and the formulated recommendations will be specific for analyzed models.

1.2 *Assumptions made in the analysis*

This paper focuses on silos with diameter $D = 2R = 6$ m in steel which is one of the most used silo diameters used in various industries. As such it is assumed that the analyzed shell will be supported on 4 discrete supports, which is also a common solution. Shell aspect ratio was $R / t = 600$. A constant thickness of shell was adopted over the entire height of the silo's shell equal to $H = 2D = 12$ m. Skirt thickness t_s varied in several models as it was one of the main parameters as well as the skirt length L_s. It is assumed that the silo will be filled with ash, one of the frequently stored material with parameters taken from EN 1991-4. As shown in Figure 1, the support solution was adapted as suggested in EN 1993-4-1 in drawing 5.6.d with additional vertical stringers used in the area of the local support. This is due to plastic collapse which would obviously occur in the region of discrete support without said stringers. Since such problems appear in all models, it was decided to use stringers with the same cross–section in all models. Those stringers had cross–section of 150×15 mm each. A conical hopper made of steel sheets with 5 mm thickness was inclined (from horizontal direction) by 65 deg.

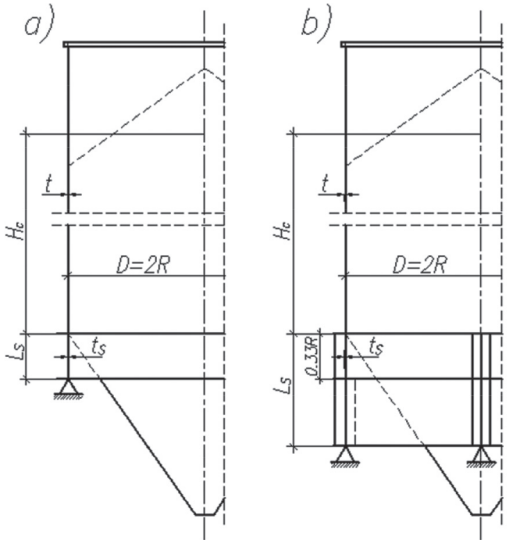

Figure 1. Solution of support adopted in all models; models from series S2 (a) and series S3-S5 (b).

All models were made of steel S235 with corresponding yield stress f_y = 235 MPa, Young's modulus E = 205 GPa and Poisson ratio 0.3.

Calculations were made by commercial finite element program NX Nastran. Since the outcome of numerical analysis is a load-displacement relationship, some of them will be presented in this paper. On all vertical axes the load multiplier from the analysis in reference to the multiplier described in chapter 2.1 will be presented, while on the horizontal axis reference deformations will be shown. By reference in this case Authors understand deformations of a chosen point in the model in the current analysis as divided by deformations of the same point in a LA analysis of the same model.

1.3 *Computational models*

As mentioned previously several computational models were analyzed. Since high bearing stresses in support regions were anticipated, the support solution shown in Figure 1 was used in all model series. Obviously for support on the entire circumference such a support ring in the hopper junction was unnecessary, so the model was simply supported in vertical direction in a hopper junction without triangular ring (so also without the skirt). Difference between the model supported uniformly, and other discretely supported models was produced by the use of a triangular ring as well as stringers which were not used in reference model, due to the absence of high bearing stresses.

Table 1. Computational models symbols.

Symbol	L_S/R	t_S/t
S1	0.0	–
S2 V1	0.333	1.2
S2 V2	0.333	1.6
S2 V3	0.333	2.0
S3 V1	0.833	1.2
S3 V2	0.833	1.6
S3 V3	0.833	2.0
S4 V1	1.333	1.2
S4 V2	1.333	1.6
S4 V3	1.333	2.0
S5 V1	1.833	1.2
S5 V2	1.833	1.6
S5 V3	1.833	2.0

Computational models were divided into 5 groups depending on the skirt length (first group S1 consists only of the reference model supported over the entire circumference), with additional division depending on skirt thickness. Skirt length L_S was measured from the hopper junction and given in reference to the shell radius R = 3000 mm and skirt thickness t_S was given in reference to the shell thickness t = 5 mm. All descriptions of the studied models are presented in Table 1.

Since silos are loaded only by material pressures symmetry of the model was used and each model consists of 90 deg of the actual silo with a discrete column in the middle (symmetry directly through support axis was not used so model was divided in 4 identical parts).

Different kinds of analysis were used for each model (all described in EN 1993-1-6) and material properties sometimes were taken as linear elastic and sometimes as elastic-perfectly plastic. All abbreviations of different types of analysis come from mentioned code and are commonly used so authors did not list them in this paper.

1.4 *Geometry imperfections in models*

Since numerical analysis will be presented there is a need to describe the imperfection distributions used in the analyses that require an imperfect geometry. Amplitudes of the considered imperfections were taken from the code EN 1993-1-6 for quality class A. For all analyses two different sets of imperfections were used: scaled deformation shapes just before stability loss in GNA and just after stability loss (also in GNA analysis). Authors recognize that there are other sets of imperfections (most notably "weld type a" described in Rotter & Teng (1989)) and plan to include them in the future research.

2 RESULTS OF THE NUMERICAL ANALYSIS

2.1 *S1 – Reference model*

As written previously the reference model was used without triangular support ring shown in Figure 1, and was uniformly supported on its circumference. On this model a GNA analysis was performed and stability loss acquired from this analysis is shown in Figure 2.

All other outcomes in this paper will be given in reference to the maximal load multiplier obtained from this analysis. Since imperfections are important in stability design GNIA calculations were also carried out and resulted with the load multiplier $r_{GNIA} = 0.416$ (where $r_{GNA,Ref} = 1.0$ as reference). This shows that introduced imperfections reduce the resistance of the model to only 41.6% of the original resistance of a perfect model. MNA analysis gave a load multiplier equal to $r_{MNA} = 0.769$ (using the well known "Modified Southwell Plot" method described by Doerich & Rotter 2010). Additionally GMNA was performed to verify the plasticity influence on the outcome, and the resulting factor was $r_{GMNA} = 0.505$. Finally the GMNIA calculations were performed, and the load multiplier obtained was $r_{GMNIA} = 0.256$.

2.2 *Results for models in series S2*

This is the most common solution accounting for skirts. Sometimes for technological reasons the skirts are extended beyond the support ring, and such situations will be discussed later, but most commonly in existing silos, the skirts are just parts of the triangular support ring. It should be noted that the geometry of this series of models is identical to the geometry of the reference model with the added triangular ring and 6 vertical stringers as described previously (3 stringers on each side of the shell). In all models the skirt is always at least 20% thicker than the silo's shell. So according to EN 1993-4-1 the said silo should have the same resistance as the reference model. In this case the same analyses were made, starting with GNA, in which the buckling failure had a form shown in Figure 3.

The load multiplier obtained with this analysis was $r_{GNA,S2V1} = 0.229$, which means that it was 77% lower than the resistance of the uniformly supported model. As previously, imperfections were implemented and in GNIA the maximal load multiplier was $r_{GNIA,S2V1} = 0.187$. This shows that discretely supported shells are less affected by introduced imperfections (resistance loss of 18% to the resistance loss of 58% in the reference model). Although the influence of imperfections in this model is smaller, the total resistance of the model with imperfect geometry is more than twice lower than the resistance of the reference model, which clearly shows that the code assumptions are not proper. Plastic capacity was also taken into account and $r_{GMNA,S2V1} = 0.213$ which is also significantly less than in the reference model. If the code requirement of maximal rotation in any node (0.1 rad) should be taken into account then results would be even lower (0.225 for GNA and 0.200 for GMNA). Finally the GMNIA calculations were performed and the resulting multiplier $r_{GMNIA,S2V1} = 0.161$ meant that model's resistance is 36.6% lower than the reference model. Two more models were analyzed in this series and all results are summarized in Table 2 and

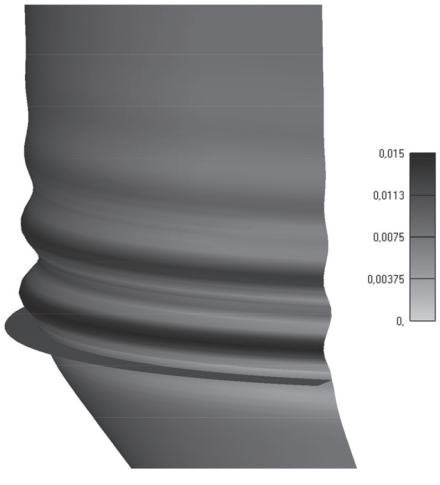

Figure 2. Buckling in the reference model S1 in GNA (deformations in modified scale, results in m).

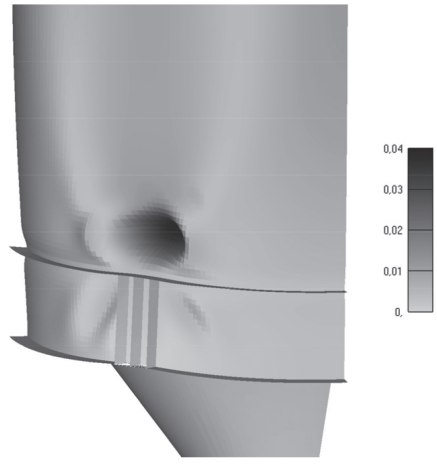

Figure 3. Buckling in model S2 V1 in GNA (deformations in modified scale, results in m).

Table 2. Maximal load multipliers in various analysis of models in seres S2.

Analysis	GNA	MNA	GMNA	GNIA	GMNIA
S2 V1	0.228	0.461	0.200	0.187	0.161
S2 V2	0.262	0.505	0.237	0.206	0.175
S2 V3	0.285	0.532	0.255	0.277	0.231

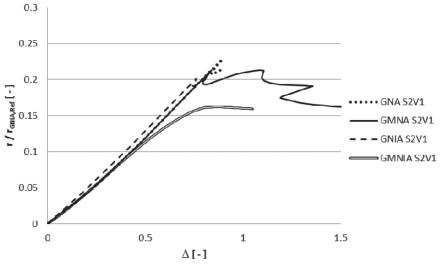

Figure 4. Load-displacement relationship in different analysis of model S2 V1.

obtained load-displacements paths for the model S2 V1 are given in Figure 4.

It should be noted that all GNA outcomes for discretely supported models are significantly lower than the resistance obtained with GNA analysis of the reference model, even for unrealistically thick skirts where t_S / t = 2. Thicker skirts increase the resistance of the shell but in a very small degree. If the shell is thickened instead of the skirt (especially in regions endangered by local instability) the increase of the resistance would be much higher for a similar weight increment of the structure.

2.3 *Results for models in series S3*

In various situations silos are made with longer skirts than the vertical parts of the supporting rings. Mostly an extended skirt is the result of a very steep hopper, that would be in collision with the supporting structure if the skirt was not extended. As such, it should be noted that using extended skirts as a method of increasing the capacity of silos is very ineffective (it is better to thicken other parts of the shell where instability is most likely to occur), but since there are situations where skirts are needed for technological reasons it is important to analyze their influence on the resistance of the shell that is supported by them.

In this series of models the skirt is extended beyond the triangular ring by additional 0.5R (for a total of 0.833R). As in previous models vertical stringers are used over the support up to the hopper junction.

Again different analyses were performed and also this time the maximal load multiplier in GNA ($r_{GNA,S3V1}$ = 0.390) was significantly smaller than in the basic model. However extending the skirt had a big influence on the resistance increase due to buckling of a perfect model. In comparison to model S2V1 (with the same skirt's thickness) in this model the resistance was 70% higher. An interesting phenomenon was observed in the analysis of the S3 models. After an initial buckle was formed, the resistance curve lowered, but then the model stabilized and additional buckles formed with the load multiplier higher than the one obtained for the first buckle. The initial buckle was treated as a buckling failure in GNA analysis. The geometry of the model is shown in Figure 5.

This phenomenon was observed previously by other researchers (Doerich (2007)), and as previously caused some issues during determining of the resistance of the imperfect model. Problem is that, initial imperfections that have the form of first buckle showed in GNA reduction of the resistance greatly, if after the buckle is formed collapse occurs. In this case however after the buckle is formed the post critical part of the load-displacement path is still rising, and while imperfections allow for a smoother resistance curve the first "drop" in the curve is not observed. In such a case GNA and GNIA calculations analyze different forms of the load-bearing capacity as shown in Figure 6 as GNA gives the load multiplier when the first buckle occurs but GNIA gives this value for the situation where the secondary buckles appear as there is no way to determine at which point the first buckle formed (there is no drop on GNIA stability path). This would not be a problem if maximal load multiplier was taken into account in GNA analysis (even if obtained in post-critical part of capacity curve) but that would

Figure 5. Stability loss in model S3 V1 in GNA (deformations in modified scale, results in m).

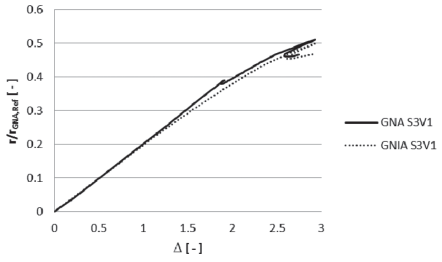

Figure 6. Load-displacement relationship from GNA and GNIA calculations of model S3 V1.

be against regulations that treat the first buckle as the criterion failure (and rightly so in Authors opinion). This is why in code EN 1993-4-1 additional requirements for deformations are being presented (reduced maximal rotation at any node mentioned previously), but such general rule raises considerable doubts. Additional criteria should be proposed and Authors believe that the "deformation criterion" developed by one of the Authors and described in Labocha & Skotny (2014) is a better approach to the problem.

In this approach radial deformations in the center of the forming buckle in GNA are being recorded, with assumption that when in GNIA the same region of shell that buckled in GNA reaches those radial deformations, the shell should be treated as its load—bearing capacity has been reached. Reasoning behind such approach is simple—since certain deformations in GNA analysis were treated as capacity failure, than in GNIA the same deformations can be a limit as well in the analyzed model. In this way one can estimate the moment when this first buckle covers the load-bearing capacity state without the necessity of using very general rules, such as limit of rotation which is constant for all possible models and situations. In this series using different approaches, the several load multipliers can be obtained as a result of GNIA analysis. Those load multipliers are shown in Table 3 where the maximal load multiplier is marked as "maximal", the load multiplier received with code limit to maximal rotation is marked as "Beta", and the load multiplier from described deformation criterion is marked as "Delta". Also in Table 3 GNA outcome is given for the same models for reference.

Comparing the results the most important thing that should be noted is that without additional failure criterion, the imperfections that actually reduce the capacity of the shell give results that may be misleading. In most practical cases, where after the first buckle occurs, the resistance curve reaches higher values of the load multiplier in the post critical part, such imperfections will lead to GNIA giving higher load multipliers than the GNA. When using the code criterion for a node

Table 3. Load multipliers received from GNIA analysis by different approaches—description in text.

Approach	Maximal	Beta	Delta	GNA
S3 V1	0.498	0.378	0.189	0.390
S3 V2	0.577	0.423	0.216	0.440
S3 V3	0.589	0.466	0.234	0.480

Table 4. Maximal reference load multipliers in various analysis of models in series S3.

Analysis	GNA	MNA	GMNA	GNIA	GMNIA
S3 V1	0.390	0.673	0.353	0.189	0.185
S3 V2	0.440	0.720	0.391	0.216	0.212
S3 V3	0.480	0.764	0.409	0.234	0.234

rotation, the received multipliers are almost identical in GNIA and GNA, but in many practical cases the received resistance is still higher in GNIA.

The usage of deformation criteria given here lead to the reduction of the resistance by the ratio that one expects to observe. With this in mind the following results will be given with the deformation criterion where necessary both for GNIA and GMNIA.

The most important information coming from the outcomes given in Table 4 is this, that when comparing maximal load multipliers for GNA analysis of different models (which are obviously unaffected by difficulties with interpretation outcomes from imperfect geometries) even very thick skirt with given length have the resistance ratio more than 50% smaller than uniformly supported shell. One can also observe that the load-bearing capacity of the model is mostly unaffected by yielding, since the buckling failure of the model with imperfections is more than 3 times smaller than the load causing plastic collapse. Also all GNIA outcomes gave the resistance lower than GNA outcomes in corresponding analyses of the studied model.

2.4 *Results for models in series S4*

In series 4 models with skirt length $L_s = 1.333$ R were analyzed. As previously different thicknesses of the skirt were taken into account. Predictably the resistance was higher than in models with shorter skirts. GNA calculations resulted in $r_{GNA,S4V1} = 0.476$ for thinnest of the analyzed skirts and $r_{GNA,S4V3} = 0.685$ for the thickest one (t_s /t = 2). Also outcomes from MNA show that longer skirt have little impact on the capacity due to plastic collapse ($r_{MNA,S4V1} = 0.673$) in the shell portion over the hopper junction. All outcomes received for this series are given in Table 5.

When comparing the results, a sharp increase in capacity in GNA calculations can be seen between models S4 V1 and S4 V2. This is due to the another

Table 5. Maximal load multipliers in various analysis of models in series S4.

Analysis	GNA	MNA	GMNA	GNIA	GMNIA
S4 V1	0.476	0.673	0.419	0.239	0.237
S4 V2*	0.666	0.707	0.439	0.504	0.400
S4 V3*	0.689	0.766	0.460	0.557	0.402

*Models reaching the load-bearing capacity in GNA after secondary buckle appears.

interesting phenomenon—longer and thicker skirts tend to smooth out the load-displacement curve in a similar way as imperfections. In the curves obtained with GNA for various models there is a distinct reduction of the resistance after the first buckling failure before the stability path begins to rise again. For models with shorter skirts (series S2) this resistance drop reaches around 9–10% of maximal load multiplier in the analyzed path and is easily observed in the load-displacement curves presented in Figure 7. For models with longer skirts (series S2), the resistance drop after the first buckle is very small (1–3%) as can be seen in Figure 8.

In series S4 only in model S4 V1 the resistance drop is observed and it is only by 0.5%. In models with thicker or longer skirts this drop, when the first buckle forms, does not appear, and the first drop in the load multiplier is observed after secondary buckles form (Figure 9). Since the single buckle is not treated as capacity failure there is no need to use the deformation criterion because now the resistance is simply the maximal load multiplier received from the analysis. This fact leads to the discussion about the resistance criteria for compressed shells supported discretely by skirts. Since the forming of more general recommendations requires much more models and imperfections to be analyzed it is hard to be firm when it comes to this phenomenon. Some similar criterion based on deformations most likely would be optimal, but since problems appear already in GNA there is no reference deformation state to which one can compare received results. This leads to the conclusion, that a condition should be proposed to limit the allowable radial deformations in compressed shells, and Authors are planning to develop such criteria in the future. In this paper, the received outcomes are given, meaning that the resistance of models S4 V2 and S4 V3 cannot be directly compared to the results received for previously described models. Since given load multipliers are measured after secondary buckles are formed, deformations of model S4 V2, when it reaches its theoretical capacity are given in Figure 9 for reference. To distinguish obtained results they are marked with "*" in Table 5.

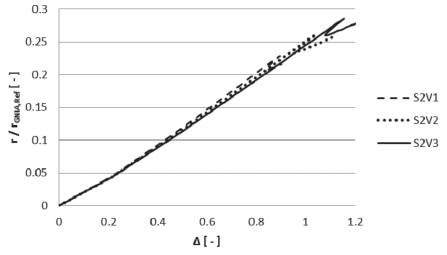

Figure 7. Load-displacement relationship for GNA calculations in models S2.

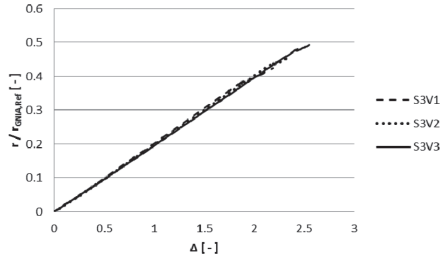

Figure 8. Load-bearing relatioship for GNA calculations in models S3.

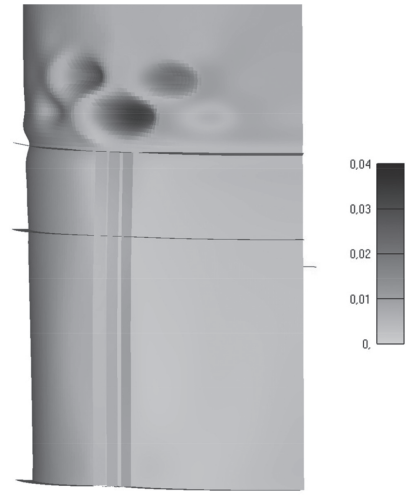

Figure 9. Instability in model S4 V2 in GNA (deformations in modified scale, results in m).

2.5 *Results for models in series S5*

The final series consists of models with very long skirts $L_s / R = 1.833$. As previously different analyzes were performed and a summary of results is given in Table 6. As in case of models S4 V2 and S4 V3 the load multipliers obtained for GNA were taken from the model when secondary buckles were formed. For clarity all models were marked with "*" in anal-

ogy for models in series 4. In this series neither of the models had a drop on the capacity curve where first of the buckles formed (Figure 10), and only after secondary buckles formed (Figure 11) the load multiplier could be obtained as a result of GNA analysis. This means that the obtained outcomes cannot be directly compared to other results given in this paper and are shown mostly for reference.

Since buckling failure in GNA happens after secondary buckles and those outcomes will not be compared it is interesting to note that maximal resistance of the model is more dependent on plastic properties of material than the resistance tied with the first buckle. This is also observed in models in series S4 marked with "*". One should note however that additional imperfection distributions should be considered in such cases.

Currently criteria for stability failure in described cases in this series are not known, as there is no numerical way of interpreting the first buckle appearance in the model.

This leads to the overestimation of the model's resistance due to elastic buckling failure in GNA. It is seen that the obtained resistance, even for models with the longest and thickest of the analyzed skirts does not reach the resistance of the uniformly supported reference model in the geometrically nonlinear analysis.

Table 6. Maximal reference load multipliers in various analysis of models in series S5.

Analysis	GNA	MNA	GMNA	GNIA	GMNIA
S5 V1*	0.662	0.659	0.444	0.516	0.419
S5 V2*	0.705	0.715	0.467	0.528	0.413
S5 V3*	0.735	0.732	0.483	0.563	0.418

*Models reaching capacity in GNA after secondary buckle appears.

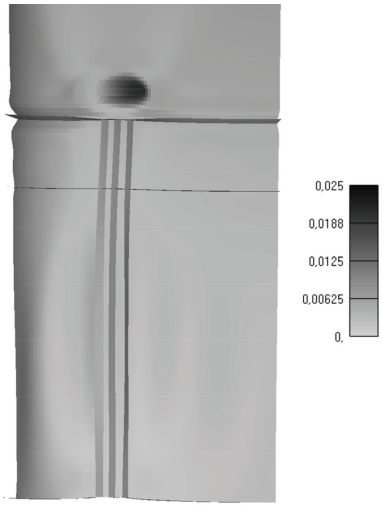

Figure 10. Deformations of model S5 V1 in GNA when first buckle form (deformations in modified scale, results in m).

Figure 11. Instability in model S5 V1 in GNA (deformations in modified scale, results in m).

3 CONCLUSIONS

In this paper numerical analysis of 12 models is presented. Various skirt lengths and thicknesses were analyzed varying from relatively short ($L_S/R = 0.333$) and not very thick ($t_S/t = 1.2$) to very long ($L_s/R = 1.833$) and thick ($t_s/t = 2.0$) all of which were supported on 4 discrete support. For most models that can be seen in practice the global resistance as well as the one due to elastic buckling failure were calculated. All those results were compared with the basic model of a similar geometry, but with a uniform support over the entire circumference. The thicker and longer the skirt the higher is the capacity, it is almost impossible in practically used structures to create a skirt that will guarantee a resistance of the shell above the resistance of the uniformly supported shell. This leads to the conclusion that the statement in code EN 1993-4-1 section 5.4.2(1) stating that the usage of a skirt of 20% thicker than a shell in the case of discrete supports provides working conditions for that shell as if the shell was supported over the entire circumference is erroneous. Additional work is needed to form general rules of calculating the resistance in such cases. Anyhow, the presented analyses allows to form general recommendations.

Firstly, it is important to note, that even the thickest and longest of skirts will not allow for design of discretely supported shell as for the one supported over the entire circumference.

Secondly, the usage of skirts as means of strengthening of the shells is very ineffective. It is much more effective to thicken shell parts endangered with buckling failure (or failure due to plastic collapse), or to use stringers, or stringers with circumferential ring as means of strengthening the shell.

It should be noted however that skirts often are used for technological reasons (mostly collisions between steep hoppers and supporting structure). In such cases the skirt affects the buckling failure resistance. Longer skirts result in higher elastic buckling failure resistance of a perfect model, regardless of skirt thickness as long as it is higher than the thickness of the analyzed shell. The relationships between the GNA resistance and skirt length L_S and thickness t_S are shown in Figure 12 and Figure 13.

Similar comparison can be made for GMNIA analyses, with note that only two sets of imperfections were analyzed in the presented models. Similar relationships between skirt length L_S and thickness t_S are given in Figures 14 and 15. It should be noted that compared results for series S5 and part of series S4 are for the situation where the resistance is reached when secondary buckles form. Currently there are no additional limits to shell resistance calculated in GMNIA, and as such the obtained outcomes are valid. Authors intend to develop additional recommendations to address this problem.

Presented study shows, that even the usage of skirts is not optimal in strengthening the shells. Their influence can be significant in case of lengths greater than $L_S/R = 0.3$. The thickness of the skirt has an influence on the resistance, but considering how much material is needed to create the thicker skirt it seems that the gained resistance is not worth the effort. It is recommended not to use thicker skirts as $t_S/t = 1.2$.

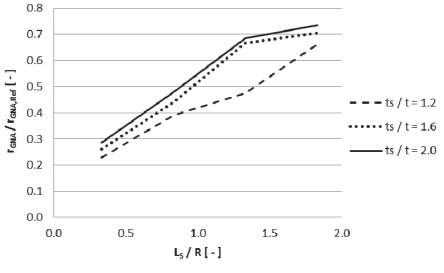

Figure 12. Influence of skirt length L_S on the resistance of silo shell due to buckling failure in GNA.

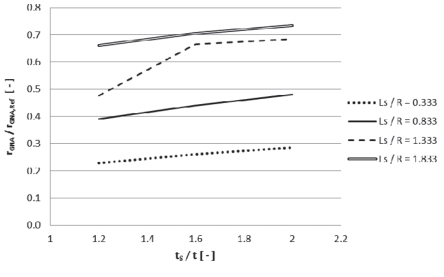

Figure 13. Influence of skirt thickness t_S on the resistance of silo shell due to buckling failure in GNA.

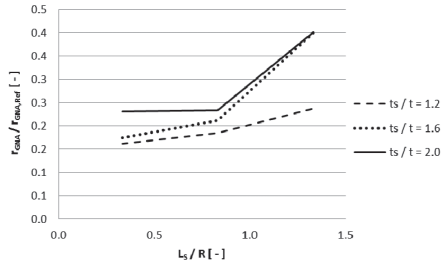

Figure 14. Influence of the skirt length L_S on the resistance of silo shell due to buckling failure in GMNIA.

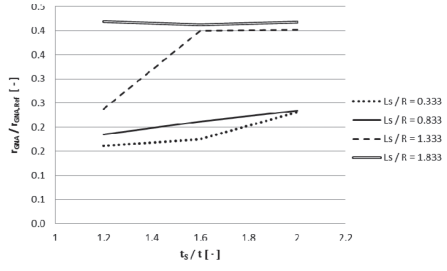

Figure 15. Influence of the skirt thickness t_S on the resistance of silo shell due to buckling failure in GMNIA.

REFERENCES

Doerich, C. 2007. *Strength and Stability of locally supported cylinders*. Edinburgh: The University of Edinburgh, Ph.D. thesis.

Doerich, C., Rotter, J.M. 2010. *Accurate Determination of Plastic Collapse Loads From Finite Element Analyses*. Journal of Pressure Vessel Technology 133 (1). ASME.

Hotała, E. 2001. Buckling of cylindrical steel under local meridional load. *Proc 9th Nordic Steel Construction Conference: 213–220.*

Hotała, E. & Skotny, Ł. 2013. Stress state in axially compressed steel cylindrical shells supported discretely. *Shell structures: theory and applications: proceedings of the 10th SSTA Conference, Gdańsk, Poland,* s. 515–518.

Labocha, S. & Skotny, Ł. 2014. *Linear and non linear analysis in FEM* Wrocław: GM System (in Polish).

Samuelson, L.Å & Eggwertz, S. 1992. *Shell stability handbook*. London: Elsevier.

Rotter, J.M. & Teng, J. 1989. Elastic stability of cylindrical shells with weld depressions. *Journal of Structural Engineering 115 (5). ASCE.*

Skotny, Ł. 2011. *Load-bearing capacity of ribbed cylindrical shells of steel silos in sectional supports areas*. Wrocław: Wroclaw University of Technology, Ph.D. thesis, PRE series report no 2/2011 (in Polish).

Recent Progress in Steel and Composite Structures – Giżejowski et al. (Eds)
© 2016 Taylor & Francis Group, London, ISBN 978-1-138-02946-0

Postbuckling behaviour of open thin-walled shells made of stainless steel

N. Stranghöner & S. Stehr
Institute for Metal and Lightweight Structures, University of Duisburg-Essen, Essen, Germany

ABSTRACT: During construction open thin-walled shells show a very high sensitive regarding buckling due to wind loading. This is often the relevant load case because of the missing stabilization effect of the roof which results into higher wall thicknesses. The consideration of the elastic postbuckling behaviour of open shells might result in an economic advantage. For this reason, investigations have been carried out at the IML at UDE in the frame of the European RFCS research project BiogaSS regarding the postbuckling behaviour of open thin-walled tanks made of austenitic and duplex stainless steels under wind load. Within this contribution, experimental and numerical results are presented and first recommendations regarding the range of possible buckling reduction factors are summarized which might be incorporated in future revisions of EN 1993-1-6 and EN 1993-4-2.

1 INTRODUCTION

Open cylindrical steel tanks are used for permanent storage of various liquids, for example in biogas production. The tank walls are primarily designed for circumferential tensile stresses from hydrostatic internal liquid pressure. As a consequence, this yields rather thin walls and hence radius/thickness-ratios r/t of 2500 up to 5000 in the upper courses are not unusual.

However, open thin-walled tanks show a very high sensitive regarding buckling due to wind loading. Due to the missing stabilization effect of the roof the empty tank is often the relevant load case which results into higher wall thicknesses. In order to obviate global failure of an empty tank under wind load, ring stiffeners at the top of the upper courses are obligatory.

The consideration of the elastic postbuckling behaviour of open shells might result in an economic advantage. Among others Binder (1996) provided a more rational basis for the economic design of open thin-walled cylinders made of carbon steel under wind load. Recently, on this basis investigations have been carried out at the Institute of Metal and Light weight Structures (IML) at the University of Duisburg-Essen (UDE) in the frame of the European RFCS research project BiogaSS regarding the postbuckling behaviour of open thin-walled tanks made of austenitic and duplex stainless steels under wind load which are presented in the following.

2 STATE OF THE ART

2.1 *Design relevant standards*

EN 1993-1-6 and EN 1993-4-2 providethe basis for the design of tank structures. However, the well-known good-natured elastic postbuckling behaviour of end-supported cylindrical tanks under external pressure is not considered. Furthermore, the determination of the buckling reduction factor χ according to EN 1993-1-6 is based on a bilinear material behaviour. Where stainless steels with obvious non-linear behaviour are involved the stress-strain curve should be obtained from EN 1993-1-4 Annex C.

2.2 *Previous research*

The investigations carried out by Binder (1996) and Binder & Schmidt (1997) dealt with the stability and postbuckling behaviour of open, ring stiffened cylindrical shells under uniform external pressure. As a result, recommendations were formulated for determining the characteristic pressure resistance q_{Rk} of thin-walled cylindrical shells initially for radius/thickness-ratios of $r/t \leq 2500$ and length/radius-ratios of $0.3 \leq l/r \leq 1.0$ as follows:

$$q_{Rk} = \alpha^* \cdot q_{cr} \tag{1}$$

with $\alpha^* = 1.71 - 0.71 \cdot \frac{l}{r}$ and $0.65 \leq \alpha^* \leq 1.5$.

Herein, q_{cr} describes the critical buckling pressure according to the former national German standard DIN 18800-4.

Lange & Schmidt (1998) confirmed the conservative simulation of the real wind loading by axisymmetric uniform under pressure from inside by performing comparative studies considering a "wind-like" pressure distribution. Furthermore, their investigations showed that the good-natured postbuckling behaviour of open cylindrical shells could be expanded to radius/thickness-ratios of $1700 \leq r/t < 2500$ with length/radius-ratios of $1.0 < l/r \leq 1.5$.

As these investigations were carried out for the more or less bilinear stress-strain behaviour of mild steels, the aim of the recent studies was to check whether they can be adopted for the nonlinear stress-strain-behaviour of stainless steels or if they have to be adjusted.

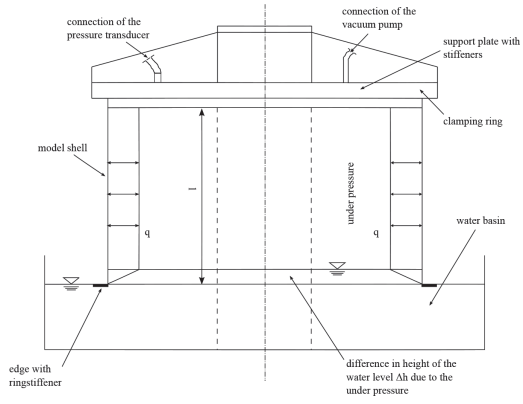

Figure 1. Basic principle of the experimental setup.

3 EXPERIMENTAL SYSTEM

3.1 *General*

The postbuckling tests described below were part of the RFCS research project 'BiogaSS—Innovative and competitive solutions using stainless steel and adhesive bonding in biogas production' funded by the European Research Fund for Coal and Steel.

The experimental test setup was developed and constructed based on the already mentioned previous research. All tests were carried out at the Institute for Metal and Lightweight Structures of the University of Duisburg-Essen.

3.2 *Principle of the test setup*

The basic concept of the experimental test setup already used by Binder and Schmidt for the investigations into the buckling and postbuckling behaviour of open thin-walled cylinders under external pressure was originally based on the idea of M. Esslinger. Herein, the open shell is turned over and dipped into a water basin to seal the cylinder and maintain the boundary conditions. The under pressure is applied by using a vacuum pump. The principle is shown in Figure 1.

Resulting from a difference in the height of the water level Δh, a hydrostatic internal pressure occurs at the bottom of the shell. This may usually be neglected at low vacuum levels, especially if considering that a pressure of $q = 0.1$ mbar corresponds to a difference amounting to $\Delta h = 1.0$ mm. In case of higher pressure (possibly at the end of postbuckling), this effect must be considered with regard to the stabilizing effect.

3.3 *Test setup of current investigations*

For the recent studies a new test setup was designed consisting of four main parts (Jejji (2013)): the water basin steel structure with a supporting structure on which the shell specimens are mounted, the vacuum pump, the pressure control unit and a camera. In order to maintain the under pressure in the shells during testing a vacuum pump was connected. To monitor and record the load steps a pressure control unit was installed as well. Finally, photos for the photo grammetry were taken with a camera and a tripod, see exemplary Figure 2.

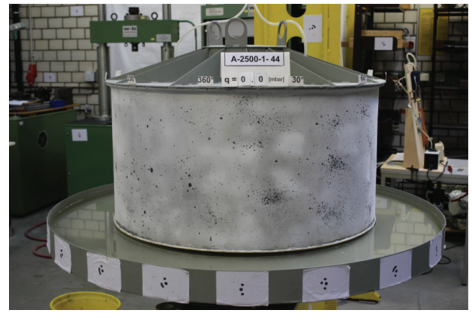

Figure 2. Test setup of specimen A-2500-1-44 (VI).

3.4 *Pressure control*

The measured under pressure was specified as the difference between ambient and internal pressure of the shell. It was applied in appropriate load steps of at least 0.1 mbar, sustained by means of a bypass. The applied under pressure was consistently monitored. Figure 3 shows exemplary pressure curves, which were documented.

3.5 *Principle of measurement*

Due to the thin shell walls, 0.1 to 0.2 mm, a surface measurement by a contact measuring technique was ruled out. Hence, a non-contact surface meas-

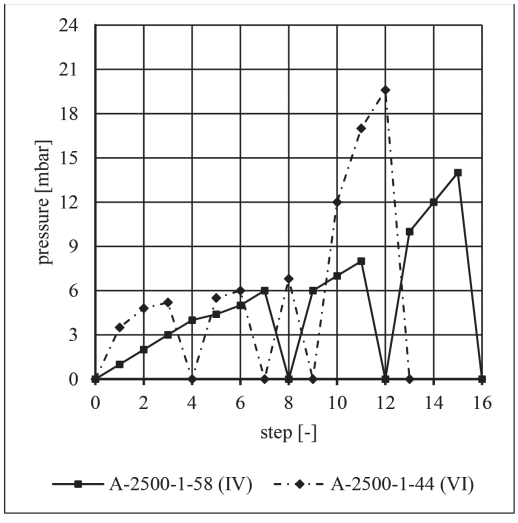

Figure 3. Exemplary pressure curves of specimens A-2500-1-58 (IV) and A-2500-1-44 (VI), see Table 1.

urement of the shell models was carried out by means of photo grammetry. For this reason it was necessary to take photos of the shell over 360° from different height positions at each load and unload step. Based on all photos of one load/unload step a three dimensional model of the specimen by means of point clouds was created with a photogrammetric software. For further editing, the data obtained were output in the form of Cartesian x-, y-, z-coordinates. The advantage of this method is, among others, the rapid feasibility during the tests. However, increased expenses were caused by the post-treatment of the surface of the model shells. Because a bare metal surface shows too strong reflections, the specimens had to be sprayed with a special powder, suitable for this purpose.

The expected measurement accuracy with this photogrammetric technique should be in the range between 0.05 and 0.5 mm. Unfortunately, due to reflections or too monotonous surfaces this accuracies could not be achieved in the presented test series, see also section 6.1.

4 TEST SPECIMENS

4.1 *Materials used*

Stainless steels, and hereby especially austenitic stainless steel, show a highly nonlinear stress-strain behaviour compared to mild carbon steel. For this reason and because of the enhanced use of stainless steel in the construction of biogas tanks, in the frame of the presents test series the shell test specimens were made of austenitic (1.4301, for models I to VII) and austenitic-ferritic (duplex) stainless steel (1.4462, for models VIII and IX) according to EN 10088-2, see Table 1. The top stiffeners of the shells were made of structural steel S235 according to EN 10025-2 except for model I (1.4462accordingtoEN 10088-2).

4.2 *Shell geometry*

Depending on the available material dimensions and taken into account that the diameters of the shells were limited by the geometry of the test setup, the shell models were designed with radius/thickness-ratios r/t of 2500 and 5000. The shells I to VII made of austentic stainless steel had a radius of r = 500 mm and thicknesses t of 0.2 mm and 0.1 mm. The shell models VIII and IX made of duplex stainless steel had a radius of 375 mm and a thickness of 0.15 mm. Length/radius-ratios l/r of about 1.0 and 2.0 were obtained by three different lengths. Specimens I to III had a length l of 960 mm, specimens IV to VII of 480 mm and specimens VIII to IX of 430 mm. The area of the cross sections of the stiffeners are indicated with b_R for the width and t_R for the thickness and varied for the specimens. In Table 1 the geometrical dimensions of the test specimens are summarized. Herein, the designation of the test specimens is defined as follows:

material– r/t-ratio – l/r-ratio – $t_R b_R$.

4.3 *Geometry of the stiffeners*

With regard to preliminary investigations of Binder (1997) a minimum second moment of area min I_{ts} for the stiffeners was defined, which all model shells exceeded:

Table 1. Geometrical dimensions of the test specimens.

	Shell geometries				
Designation	r mm	l mm	t mm	l/r-ratio –	r/t-ratio –
A-2500–2-22 (I)	500	960	0.20	1.92	2500
A-2500–2-58 (II)	500	960	0.20	1.92	2500
A-5000–2-58 (III)	500	960	0.10	1.92	5000
A-2500–1-58 (IV)	500	480	0.20	0.96	2500
A-5000–1-58 (V)	500	480	0.10	0.96	5000
A-2500–1-44 (VI)	500	480	0.20	0.96	2500
A-5000–1-44 (VII)	500	480	0.10	0.96	5000
D-2500–1-44 (VIII)	375	430	0.15	1.15	2500
D-2500–1-33 (IX)	375	430	0.15	1.15	2500

$$\min I_{ts} = 0.05 \cdot t^3 \cdot h \quad (2)$$

The stiffeners consisted of four quarter-circular parts which were soldered on the shell, except for model shell I, here the stiffeners were glued.

During the investigations the area of the cross section of the top stiffener ($t_R \times b_R$) was adjusted three times. The first specimen (I) had a top stiffener with a cross section area of 2 mm × 2 mm. Due to the fact that specimen I showed global buckling failure—instead of expected local buckling failure—this test cannot be counted for further evaluation. For the next tests (II to V) the stiffness was increased up to 5 mm × 8 mm to display a favorable local buckling behaviour. During these tests the under pressure could be increased without global failure occurring so that the rising water in the tank was problematic.

To keep the water at a minimal level, the top stiffener cross section area was reduced again to 4 mm x 4 mm for specimens VI to VIII. At the end of the study the cross section area was reduced again to 3 mm x 3 mm for specimen IX.

5 EXPERIMENTAL PROCEDURE

The aim of this study was to investigate the elastic postbuckling behaviour of open thin-walled, edge stiffened, tanks made of austenitic and duplex stainless steel under wind load. Based on scaled test specimens, the postbuckling behaviour of stainless steel tanks should be examined and documented. The experimental procedure was, in principle, the same for all specimens and was independently observed and reported by three persons.

Before starting of each experiment, the imperfections of the specimens were documented. These data were taken as reference values for the investigations of the deformations and for the classification of the tanks according to EN 1993-1-6. Hence, photos were taken for photogrammetric evaluation in three different heights around the tank. After the initial state was documented, the tank was loaded until the first buckle which was visible. At this stage, the under pressure was kept constant and new photos were taken for the photogrammetry. Afterwards the tank was unloaded and this state was recorded, too, with photos.

In the next step the tank was loaded again up to the pressure which was reached before and then the pressure was further increased stepwise constant to the next stage in which a difference in the buckling was visible. Photos were taken and the tank was unloaded and documented again.

In principle, the same procedure was carried out until the first plastic buckle was visible during an unloaded stage. At this point, the load was increased in larger steps, photos were taken only at selected stages and the tank was unloaded rare until collapse.

At the end, the final state of collapse was documented and the experiment was stopped, see example Figure 3.

6 PHOTOGRAMMETRIC DATA

6.1 *Processing*

The applied photogrammetric method provided irregular '3D point clouds' consisting of Cartesian x-, y- and z-coordinates. The number of points varied on the height and scope.

Firstly, the data were adjusted on the center of an ideal cylinder, so the vertical cylinder axis corresponded to the z-axis. Then the Cartesian coordinates were converted into polar coordinates and a regular point grid was interpolated. Finally, the positions of the x- and y-axes were aligned based on the photo grammetry.

Unfortunately, the desired accuracy of 0.5 mm could not be achieved. Partly, deviations in measure deformations of up to approximately 3.0 mm were observed. For this behaviour, one reason can be found in the surface of the shells which were still partially reflective or too monotonous.

6.2 *Evaluation*

On the basis of the test protocol, each unloading stage can be defined. To specify the first occurrence of plastic buckles, these data were compared with the stages in which the first plastic buckle was visible during testing. After the occurrence of the first plastic buckle, the point of maximum deformation at this level was determined and the height- and the angle-position were documented.

Horizontal sections at the height-position of the plastic buckle were made through the shellmodel, see for example Figures 4, 5 and 6. Thus, the deformations of the shell on different load stages are recognizable. Vertical sections at the angle-position of the considered buckles were made over the total shell height at selected load stages, too, see for example Figures 7, 8, 10. Thereby, the buckles can be localized over the height. In the last step only selected points of the plastic buckle were represented, see for example Figures 10–11. Here, the deformation can be read directly. In principle, the occurrence of the first elastic buckle was specified in the same way. But instead of comparing unloading stages, the first loading stage with deformations was compared with the first unloading stage afterwards.

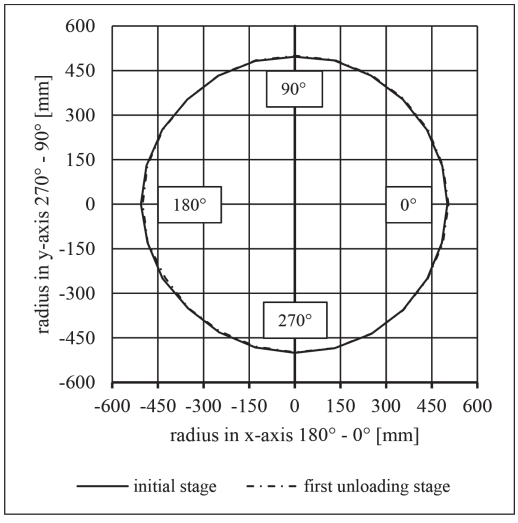

Figure 4. Horizontal section at 221.0 mm height of specimen A-2500-1-44 (VI) for the first unloading stage.

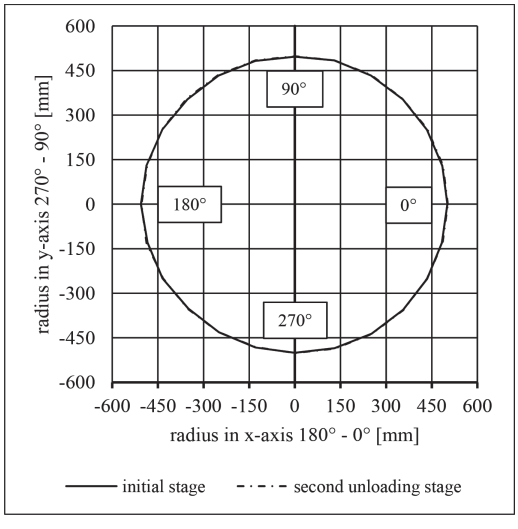

Figure 5. Horizontal section at 221.0 mm height of specimen A-2500-1-44 (VI) for the second unloading stage.

The photogrammetric data were compared with the experimental protocols and could be verified accordingly.

6.3 *Interpretation*

Except for tank number I, all specimens showed local buckling between the top edge stiffener and the clamping during almost the total postbuckling.

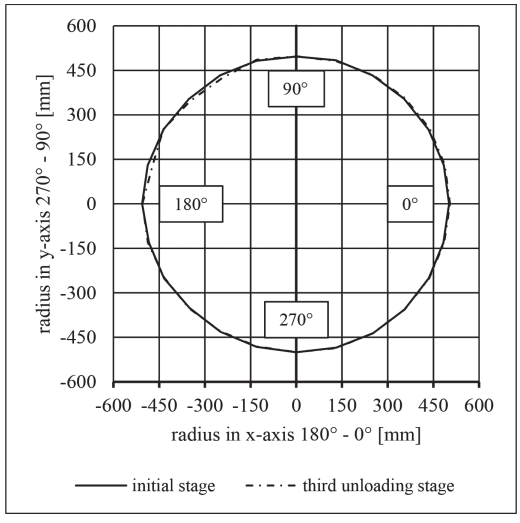

Figure 6. Horizontal section at 221.0 mm height of specimen A-2500-1-44 (VI) for the third unloading stage.

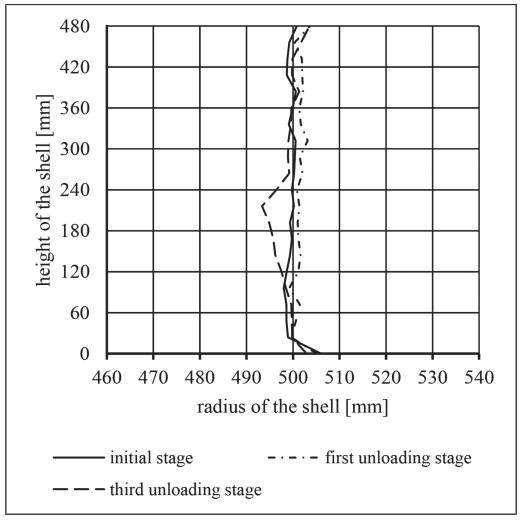

Figure 7. Vertical section at 82° angle of specimen A-2500-1-44 (VI) for the first and the third unloading stage.

At the beginning of the buckling, an elastic behaviour occurred, which is interesting for the structural reserves.

The postbuckling behaviour was illustrated by the example of specimen A-2500-1-44 (VI). Figure 4 shows, that after a previous pressure of 5.2 mbar, there was nearly no deformation remained at the first unloading stage in which no

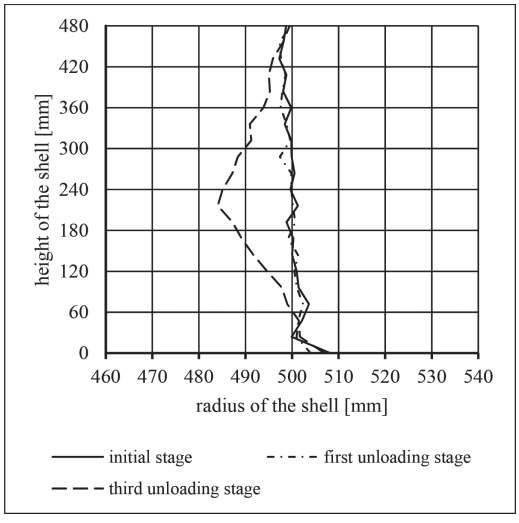

Figure 8. Vertical section at 127°angle of specimen A-2500-1-44 (VI) for the first and the third unloading stage.

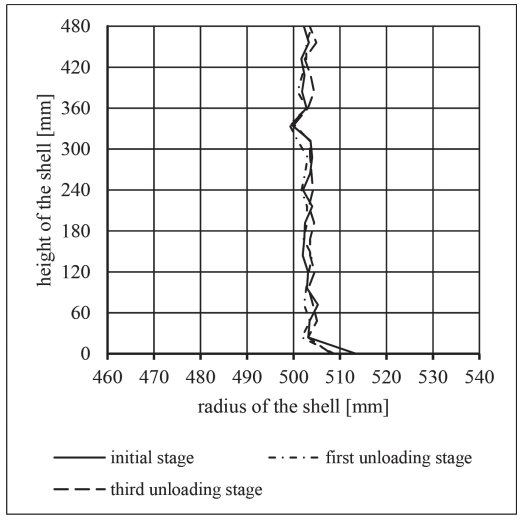

Figure 10. Vertical section at 300° angle of specimen A-2500-1-44 (VI); elastic behaviour.

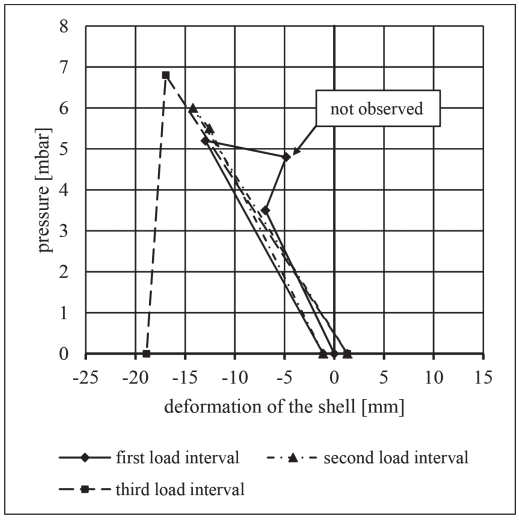

Figure 9. Deformation at 221.0 mm height and 127° angle of specimen A-2500-1-44 (VI).

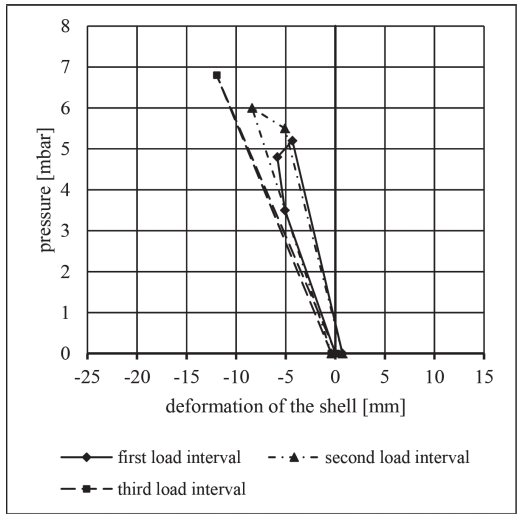

Figure 11. Deformation at 160.0 mm height and 90° angle of specimen A-2500-1-44 (VI); elastic behaviour.

buckles were noticed during testing. Figure 5 shows the same for the second unloading stage, the pressure was at 6.0 mbar at the previous loading stage, and almost no deformations occurred. At the third unloading stage, with a pressure of 6.8 mbar, deformations were visible, see Figure 6. During this test three buckles were noticed between the angles 75° – 90°, 105° – 135° and 150° – 180°, two of these are visible in Figure 6. Figures 7–8 show the buckles between 75° – 90° and 105° – 135° in vertical sections. Figure 9 presents the deformation of the shell at the point of maximum plastic deformation in the third unloading stage at 221 mm height and 127° angle. Here, nearly no plastic deformations occurred after the first and second load interval which corresponds to the observations. The shown deformation during the first loading interval was not observed and has to assumed to be a measur-

ing error. Hence, the third unloading stage was defined as the end of the elastic postbuckling.

As an example, Figure 10 shows a selected section at the angle 300° where no plastic deformation was visible during testing whereas at the angle of 90°, an elastic buckle was visible during testing. Figure 11 shows the deformation at a height of 160 mm. After all three load intervals there were no remaining deformations visible.

In summary, the data confirmed the observations taking into account the existing accuracy. Based on these findings, all tests without test I were evaluated.

7 RESULTS

7.1 *General*

The data of all tests except specimen A-2500-22 (I), which showed global failure, were processed and interpreted. The pressures at the level of the first elastic buckle $q_{b,el}$ and of the first plastic buckle $q_{b,pl}$ were documented, see Table 2.

7.2 *Elastic imperfection reduction factor*

The ideal circumferentially buckling pressure $q_{\theta,Rcr}$ of each specimen was calculated according to EN1993-1-6. The pressure of the elastic buckle $q_{b,el}$ was compared with this value to enable a classification into the fabrication tolerance quality classes according to EN1993-1-6, see Table 3. The minimum circumferential elastic imperfection reduction factor $\alpha_\theta = q_{b,el} / q_{\theta,Rcr}$ for Class C is 0.5 and 0.65 for Class B.

Three specimens (II to IV) showed a calculated circumferential elastic imperfection reduction factor higher than 0.5 but less than 0.65 so they can be assigned to Class C. The other specimens (V to IX) with a factor less than 0.5 cannot be assigned anymore to a fabrication tolerance quality classaccording to EN 1993-1-6.

Table 2. Documented pressures of the first elastic and first plastic buckle of the tested shell models.

	Pressure	
Designation	$q_{b,el}$ mbar	$q_{b,pl}$ mbar
A-2500-2-58 (II)	2.1	3.9
A-5000-2-58 (III)	0.4	1.0
A-2500-1-58 (IV)	4.4	6.0
A-5000-1-58 (V)	0.6	0.8
A-2500-1-44 (VI)	3.5	6.8
A-5000-1-44 (VII)	0.6	0.8
D-2500-1-44 (VIII)	3.2	12.0
D-2500-1-33 (IX)	2.8	11.0

Table 3. Calculated circumferential elastic imperfection reduction factors of the tested shell models.

	Pressure		Ratio (Class)
Designation	$q_{b,el}$ mbar	$q_{\theta,Rcr}$ mbar	$\alpha_\theta = q_{b,el} / q_{\theta,Rcr}$
A-2500-2-58 (II)	2.1	3.8	0.55 (C)
A-5000-2-58 (III)	0.4	0.7	0.61 (C)
A-2500-1-58 (IV)	4.4	7.7	0.57 (C)
A-5000-1-58 (V)	0.6	1.3	0.46 (–)
A-2500-1-44 (VI)	3.5	7.7	0.46 (–)
A-5000-1-44 (VII)	0.6	1.3	0.46 (–)
D-2500-1-44 (VIII)	3.2	6.5	0.49 (–)
D-2500-1-33 (IX)	2.8	6.5	0.43 (–)

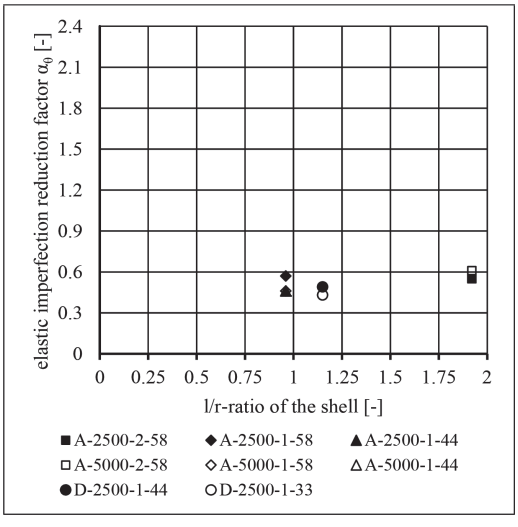

Figure 12. Achieved circumferential elastic imperfection reduction factors for the tested shell models.

Figure 12 shows the calculated circumferential elastic imperfection reduction factors α_θ for the tested shell models. They can at best be assigned to fabrication tolerance quality class C according to EN 1993-1-6.

7.3 *'Plastic imperfection factor'*

To get an advantage of the favourable postbuckling behaviour for the design of tank structures the pressure of the first plastic buckle $q_{b,pl}$ was compared with $q_{\theta,Rcr}$, see Table 4. This ratio corresponds to the α^*_θ value specified by Binder (1996),

Table 4. Calculated 'plastic imperfection factors' of the tested shell models.

Designation	Pressure $q_{b,pl}$ mbar	Pressure $q_{\theta,Rcr}$ mbar	Ratio $\alpha^*_\theta = q_{b,pl} / q_{\theta,Rcr}$
A-2500-2-58 (II)	3.9	3.8	1.02
A-5000-2-58 (III)	1.0	0.7	1.52
A-2500-1-58 (IV)	6.0	7.7	0.78
A-5000-1-58 (V)	0.8	1.3	0.61
A-2500-1-44 (VI)	6.8	7.7	0.88
A-5000-1-44 (VII)	0.8	1.3	0.61
D-2500-1-44 (VIII)	12.0	6.5	1.84
D-2500-1-33 (IX)	11.0	6.5	1.69

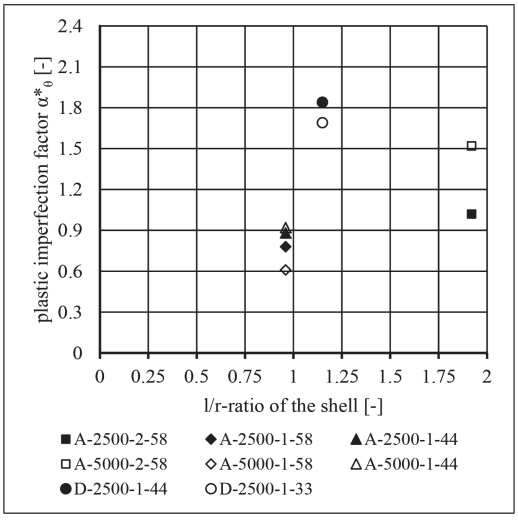

Figure 13. Achieved' plastic imperfection factors' for the tested shell models.

Table 5. Ratios of $\alpha^*_\theta/\alpha_\theta$.

Designation	Values α^*_θ	Values α_θ	Ratio $\alpha^*_\theta/\alpha_\theta$
A-2500–2-58 (II)	1.02	0.55	1.85
A-5000–2-58 (III)	1.52	0.61	2.49
A-2500–1-58 (IV)	0.78	0.57	1.37
A-5000–1-58 (V)	0.61	0.46	1.33
A-2500–1-44 (VI)	0.88	0.46	1.91
A-5000–1-44 (VII)	0.92	0.46	2.00
D-2500–1-44 (VIII)	1.84	0.49	3.76
D-2500–1-33 (IX)	1.69	0.43	3.93

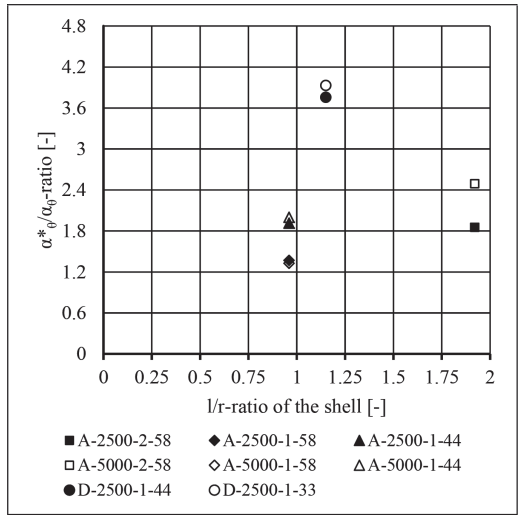

Figure 14. Achieved enhancements compared to the elastic imperfection reduction factors for the tested shell models.

see section 2.2, and is called 'plastic imperfection factor' in this paper.

The two specimens II and III with l/r = 1.92 showed a 'plastic imperfection factor' higher or almost equal than 1.0. Specimen III (A-5000-2-58) with a comparatively smaller wall thickness yields a plastic imperfection factor of almost 1.5.

The 'plastic imperfection factors' of the other four specimens made of austenitic stainless steel with l/r = 0.96 (specimens IV to VII) lie between 0.61 and 0.88. A decisive influence of the top stiffener cannot be recognized. The two specimens VIII and IX made of austenitic-ferritic (duplex) stainless steel which differ only in the dimension of the top stiffener, showed the highest 'plastic imperfection factor' up to 1.84.

Figure 13 shows the achieved 'plastic imperfection factors' α^*_θ for all specimens. The values are consistently higher than the achieved elastic imperfection reduction factors α_θ especially for the shell models made of duplex stainless steel.

The potential advantages which can result in the consideration of an elastic postbuckling behaviour of open thin-walled shells made of stainless steel is summarized in Table 5 and Figure 14. Considering the 'plastic imperfection factors' α^*_θ, the austenitic shell model sachievean enhancement compared to the elastic imperfection reduction factors α_θ of about 1.33 to 2.49. However, the duplex shells achieve an enhancement of up to 3.93. This represents an increase of nearly 400%.

8 CONCLUSIONS

The investigations presented in this paper showed that the consideration of the elastic postbuckling behaviour of open thin-walled shells made of stainless steel might result in an advantage in the design process of thin walled shells.

Further evaluations and numerical parameter studies are currently carried out an the Institute for Metal and Lightweight Structures at University of Duisburg-Essen in order to generate general recommendations which might be incorporated in future revisions of EN 1993-1-6 or EN 1993-4-2 to improve the economical design of tanks.

ACKNOWLEDGEMENTS

The research leading to these results has received funding from the European Union's Research Fund for Coal and Steel (RFCS) research programme under grant agreement n° RFSR-CT-2012-00035 for the research project 'Innovative and competitive solutions using stainless steel and adhesive bonding in biogas' (BiogaSS).

REFERENCES

Binder, B. 1996. *Stabilität einseitig offener, verankerter, aussendruckbelasteter Kreiszylinderschalen unter besonderer Berücksichtigung des Nachbeulverhaltens.* PhD-Thesis, University-GH Essen, Fachbereich 10.

Binder, B. & Schmidt, H. 1997. Experimentelle Untersuchungen zum elastischen Beul- und Nachbeulverhalten extrem dünnwandiger, einseitig offener Kreiszylinderschalen mit und ohne Randversteifung unter konstantem Manteldruck. *Research Report 71*, University-GH Essen, Fachbereich 10.

DASt-Richtlinie 017 Entwurf 1992. *Beulsicherheitsnachweise für Schalen*. Deutscher Ausschuß für Stahlbau, Stahlbau-Verlagsgesellschaft Köln.

DIN 18800-4:2008-11. *Steel structure* - Part 4: Stability - Analysis of safety against buckling of shells.

EN 1993-1-4:2006. Eurocode 3: *Design of steel structures* - Part 1–4: General rules - Supplementary rules for stainless steels.

EN 1993-1-6:2007 + AC:2009. Eurocode 3: *Design of steel structures* - Part 1–6: Strength and stability of shell structures.

EN 1993-4-2:2007 + AC:2009. Eurocode 3: *Design of steel structures* - Part 4–2: Tanks.

EN 10025-2:2004. *Hot rolled products of structural steels* - Part 2: Technical delivery conditions for non-alloy structural steels.

EN 10088-2:2014. *Stainless steels* - Part 2: Technical delivery conditions for sheet/plate and strip of corrosion resisting steels for general purposes.

Franke, A.A. 2015. *Vergleichende experimentelle und numerische Untersuchungen zur Ermittlung von zusätzlichen Faktoren unter der Berücksichtigung des elastischen Nachbeulverhaltens von offenen dünnwandigen Kreiszylinderschalen aus nichtrostendem Stahl unter Windbelastung im Bauzustand*. Master's thesis, Essen, University of Duisburg-Essen, Institute for Metal and Lightweight Structures.

Jejji, A. 2013. *Zum Nachbeulverhalten von zylindrischen Tanks aus nichtrostenden Stählen unter Windbelastung im Bauzustand*. Master's thesis. Essen, University of Duisburg-Essen, Institute for Metal and Lightweight Structures.

Lange, H. & Schmidt, H. 1998. Ergänzende experimentelle Untersuchungen zum Nachbeulverhalten dünnwandiger, einseitig offener, randversteifter Kreiszylinderschalen unter konstantem und windähnlichem Manteldruck. *Research Report 78*, University-GH Essen, Fachbereich 10.

Schmidt, H. 2009. Stabilität stählerner Schalentragwerke. *Stahlbau-Kalender 2009*, edt. Kuhlmann, U., p. 529–612.

Schmidt, H., Binder, B. & Lange, H. 1996a. Postbuckling design of extremely thin walled cylindrical tanks. European Workshop, *Thin-Walled Steel Structures*, Krzyzowa, Poland.

Schmidt, H., Binder, B. & Lange, H. 1996b. Windbuckling design of open thin-walled cylindrical tanks. *Advances in Steel Structures*, ICASS'96.

Schmidt, H., Binder, B. & Lange, H. 1998.Postbuckling strength design of open thin-walled cylindrical tanks under wind load. *Thin-Walled Structures 31 (1998)*, p. 203–220.

Song, Y. 2014. *Vergleichende numerische Untersuchungen zum Einfluss von verschiedenen Ersatzimperfektionen auf das Nachbeulverhalten von offenen dünnwandigen Kreiszylinderschalen aus nichtrostendem Stahl unter Windbelastung im Bauzustand.* Master's thesis, Essen, University of Duisburg-Essen, Institute for Metal and Lightweight Structures.

This page intentionally left blank

Recent Progress in Steel and Composite Structures – Giżejowski et al. (Eds)
© 2016 Taylor & Francis Group, London, ISBN 978-1-138-02946-0

Simplified stability analysis of steel cylindrical silos with corrugated walls and vertical columns

K. Rejowski & P. Iwicki
Faculty of Civil and Environmental Engineering, Gdańsk University of Technology, Gdańsk, Poland

ABSTRACT: In the paper a simplified stability analysis of steel cylindrical silos composed of corrugated walls and vertical open-sectional columns was proposed. The whole 3D silo was modeled as a single column resting on elastic foundation provided by the silo walls. In proposed formula for the calculation of the foundation stiffness the curvature of the silo walls was taken into account. Three different analyses were carried out using commercial FE package ABAQUS: linear buckling, dynamic with the geometric non-linearity and dynamic with the both geometric and material non-linearity. Axisymmetric and non-axisymmetric loads imposed by a bulk solid following Eurocode 1 were considered. The calculated buckling loads were compared with the permissible one given by Eurocode 3 and with results found for the whole silo modeled by shell elements.

1 INTRODUCTION

Silos can be built of thin-walled horizontally corrugated curved sheets strengthened by vertical columns. Silo walls are subjected to pressures and frictional traction from stored bulk solids. The wall sheets carry circumferential tensile forces caused by horizontal wall pressure of a bulk solid and vertical columns carry vertical compressive forces exerted by wall friction from a bulk solid. The silo walls are also an elastic foundation increasing the columns buckling resistance. Silo columns are vulnerable to buckling caused by the wall friction force caused by the interaction between the silo fill and the silo wall, particularly during eccentric discharge, which is usually difficult to avoid with regard to a non-homogeneous character of bulk solids (Rotter 2001).

Currently some papers have dealt with the design of silos with corrugated walls and vertical stiffeners. Wojcik et al. (2011) performed numerous linear and non-linear quasi-static analyses with initial geometric imperfections for a slender silo. The effect of a patch load was investigated analytically by Gallego et al. (2011). Iwicki et al. (2011) dealt with failure of large cylindrical silos and proposed repair methods based on sensitivity analyses. Rotter & Sadowski (2012) presented a bending theory for cylindrical orthotropic shells with normal and shear pressures. The buckling behavior of different corrugated wall silos with vertical stringers was analysed with a dynamic approach by Iwicki et al. (2015).

In the design practice it is necessary to use a simple models instead of analysis of the whole 3D silos. The buckling capacity according Eurocode 3 (2009) uses two alternative methods which depends upon the stiffeners distance d_s. For $d_s<d_{s,max}$ the silo wall is treated as the equivalent orthotropic shell (method 'A') and for $d_s>d_{s,max}$ the stiffener resting on the elastic foundation provided by the silo wall may be taken into account (method 'B'). In a simplified code procedure the silo wall sheets may be assumed as elastic foundation of the columns. Eurocode 3 gives a simplified formula to calculate the buckling strength of vertical silo columns resting on elastic lateral foundation. The 3D FE calculation results presented by Iwicki et al. (2015), Wójcik et al. (2011), Sondej et al. (2015) evidently show that the Eurocode (2009) approach may provide significantly too conservative outcomes for silos with corrugated sheets and columns. Sondej et al. (2014) proposed an improvement of Eurocode 3 buckling formulae for the silo design basing on results of an approximation of numerical finite element (FE) analyses. Iwicki et al. (2015) proposed to apply always formula for orthotropic shell theory with a reduction factor within the range of application of method 'B'. The method 'B' may also be modified in the range $d_s<d_{s,max}$ to obtain better agreement with FE results.

The aim of our present study was to propose a new formula for the calculation of the foundation stiffness. The new stiffness of the silo column elastic foundation provided by corrugated sheets takes into account the circumferential wall curvature.

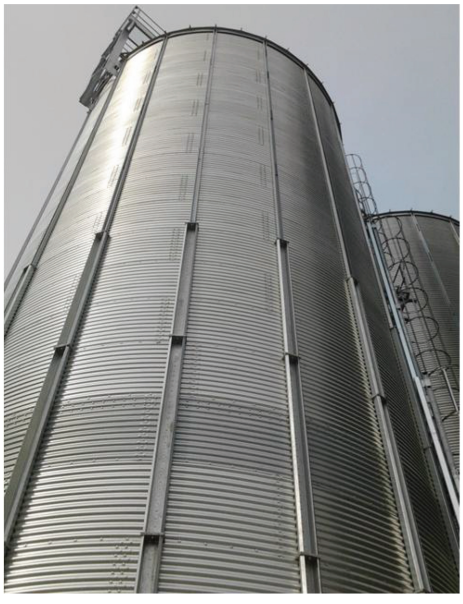

Figure 1. Metal cylindrical silos with corrugated walls and 18 vertical columns at distance of 1.4 m (height H=17.62 m and diameter D=8.02 m).

Stability analysis for the silo modeled as a single column resting on elastic foundation was compared to the results of similar analysis for the whole 3D silo modeled by shell elements presented by Iwicki et al. (2015) and to Eurocode 3 formulas for both present and modified stiffness of the walls. A nonlinear dynamic analysis with geometric (GNA) and material (GMNA) non-linearity by taking into account loads imposed by a bulk solid following Eurocode 1 (2008) was performed. The application of nonlinear dynamic analysis was a computational device used in order to avoid a convergence problem in nonlinear static analysis described by (Iwicki et al. 2014) (Iwicki et al. 2015).

2 SILO DESCRIPTION

The numerical calculations were carried out with a real cylindrical metal silo belonging to a silo battery (Fig. 1). The height of a silo was $H = 17.62$ m and its diameter $D = 8.02$ m ($H/D = 2.2$). The cross-section area was 50.52 m^2 and the perimeter 25.2 m. The silo mantle consisted of 21 horizontally corrugated sheets 890 mm × 2940 mm × 0.75 mm based on a foundation slab. The silo was strengthened by 18 vertical columns composed of open thin-walled profiles with a varying cross-section in the form of the 'C' and 'V' – shape (Table 1) and thickness ($t = 1.5$–4 mm) along the column height uniformly placed along the silo circumference at the constant distance of $d_s = 1.4$ m. The columns were connected to the wall sheets by screws. The corrugation had 76 mm pitch and 18 mm depth. The outflow took place through a hopper separated from the rest of the silo. The silo roof was made from metal sheets inclined under an angle of 25° to the horizontal and stiffened by 36 radial beams. The silo contained corn and was designed for concentric filling and funnel flow emptying with the constant outlet velocity of 50 m^3/h.

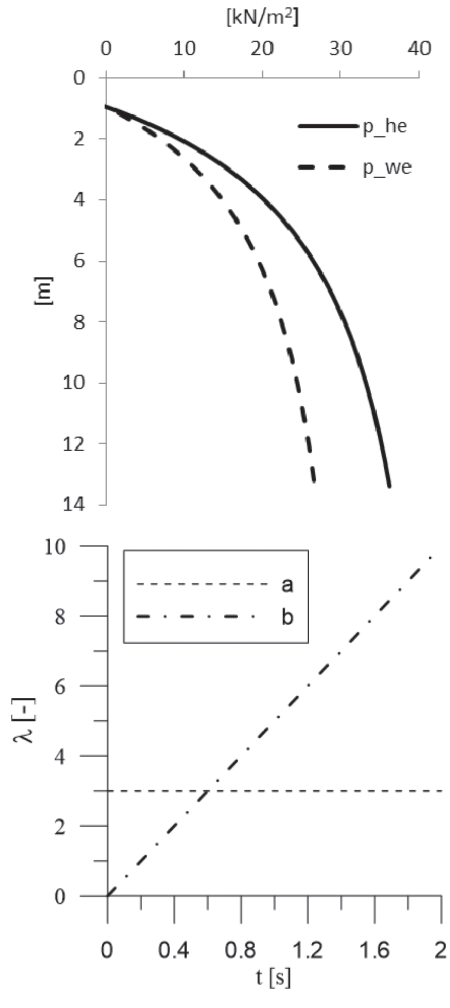

Figure 2. a) Vertical wall frictional traction and horizontal wall pressure in silo during emptying according to Eurocode 1 (2008) (pw – vertical frictional traction, ph – horizontal normal pressure), b) relationship between load and time in dynamic analyses: linear function (line 'a'), and limit load factor for ta=20 s (line 'b').

The silo wall loads induced by maize were calculated according to Eurocode 1 (2008). During axisymmetric emptying, the standard maximum wall normal and shear stress in the bin were p_h=30.52 kPa and p_w=19.38 kPa, respectively. When considering a possible non-symmetric emptying, they increased up to p_h=36.26 kPa and p_w =26.68 kPa (Eurocode 1 2008) (Fig. 2). In numerical analyses it was assumed that the load level according Eurocode 1 (2008) was the reference value, i.e. the load factor λ was always related to the wall shear stress of p_w=26.68 kPa.

In the numerical analysis the fully integrated 4-node quadrilateral S4 shell elements (size: 0.25 m × 0.25 m) were used in the model of the whole silo. The element size in the model was 0.01 m × 0.09 m for the corrugated wall (6 shell elements to describe the curvature of corrugated sheets) and 0.01 m × 0.03 m for the columns. Total number of the S4R elements was 885'000 (Fig. 3).

In the case of model of single silo column resting on elastic foundation simulating corrugated sheets element size was 10×38 mm^2 for the profile C (265 elements along the column height) and for profile V element size was 14.9×38 mm^2 (550 elements along the height). The total amount of finite elements of one column was 5 295. In the case of non-linear analysis (GNA, GMNA) the column stiffness was calculated according Equation 6. The linear buckling analyses were conducted for a different stiffness of elastic foundation in lateral direction. In all cases it was assumed that the column was supported in the torsional direction along its length. At the bottom, the column was fixed (see Figure 4).

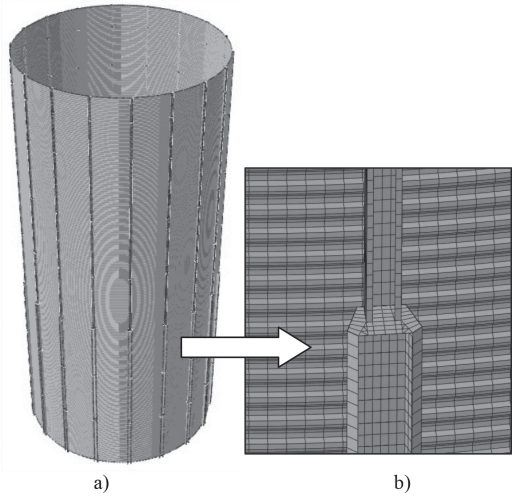

a) b)

Figure 3. FE mesh for silo: a) entire bin and b) columns.

The steel was assumed to be elastic (linear buckling analysis) or elastic-perfect plastic (non-linear analysis) with the following properties: modulus of elasticity E = 210 GPa, Poisson's ratio ν = 0.3 and yield stress fy = 350 MPa.

3 SIMPLIFIED SILO MODEL

3.1 *Eurocode approach*

According to Eurocode 3 (2009), there are two methods for calculating the stability of a cylindrical silo with vertical columns. The applicability of these methods is dependent on the spacing of the columns d_s. The first method named in this paper as the "Method A" is based on an orthotropic shell theory. It is used for spacing column $ds < d_{s,max}$ (Equations 3 and 4) and it gives satisfying results in comparison with 3D FEM analysis (Iwicki et al. 2015) (Sondej et al. 2015). The second method named in this article as "Method B" is based on the solution beams on elastic foundations. For the case of the column distance (d_s>$d_{s,max}$). The characteristic buckling load bearing capacity N of single vertical column in a metal silo with corrugated walls is given by the following formula in Eurocode 3 (2009)

$$N = 2\sqrt{EJ \times K} \tag{1}$$

with

$$K = k_s \frac{D}{d_s^{\,3}} \text{ and } D = 0.13Etd^3 \tag{2}$$

where EJ is the bending stiffness of columns in the plane perpendicular to the wall, the foundation stiffness K denotes the bending stiffness of corrugated sheets between vertical columns, k_s=6 is the coefficient, D denotes the wall sheet bending stiffness, E is the modulus of elasticity, t denote the sheet thickness and d is the sheet height. The following assumptions were met to lay down Equations 1 and 2:

a. the 2D behavior of the column is considered only,
b. the number of buckling half-waves along the circumference is equal to the half of the columns number, if the number of column is a multiple of 4 (buckled silo shape is axially antisymmetric),
c. the column is loaded by vertical forces prescribed at both ends only (horizontal pressure is not considered),
d. the column is supported by elastic springs simulating the presence of corrugated sheets,
e. the column has hinges at its ends.

For the small column distance $d_s<d_{s,max}$, where

$$d_{s,\max} = k_{dx}\left(\frac{r^2 D_y}{C_y}\right)^{0,25} \tag{3}$$

there exists the approach in Eurocode 3 (2009) for the silo buckling based on an orthotropic shell theory. The critical buckling resultant force $n_{x,Rcr}$ per the unit circumference of an orthotropic shell should be evaluated at each appropriate silo level by minimizing Equation 4 with respect to the critical circumference wave number j and the buckling height l_i as

$$n_{x,Rcr} = \min\left(\frac{1}{j^2\omega^2}\left(A_1 + \frac{A_2}{A_3}\right)\right) \tag{4}$$

where: D_y – the flexural rigidity parallel to the corrugation, C_y – the stretching stiffness parallel to the corrugation and r – the cylinder radius and k_{dx} – the coefficient recommended to be taken as 7.4, j – the circumference wave number, ω – the parameter including buckling height l_i and $A_{1,2,3}$ – the parameters including the flexural and stretching stiffness in orthogonal directions of the equivalent orthotropic shell.

The load bearing capacity N of a single vertical column in metal cylindrical silos should be apparently always smaller than the plastic force (Eurocode 3 2009)

$$N_{b,Rk} = A_{eff} f_y, \tag{5}$$

where A_{eff} is the effective cross-sectional area of the column and f_y denotes the yield stress.

Due to the column distance in the silo of Figure 1 d_s=1.4 m > $d_{s,max}$=1.16 m, the appropriate standard formula for the silo buckling strength is described by Equations 1 and 2. Using Equations 1 and 2, the characteristic buckling strength was exceeded in 1 column profile twice for symmetric emptying and in 2 profiles about 2.5 times for non-symmetric emptying (Table 1). The column buckled for the characteristic wall shear stress equal to p_w=10.67 kPa (the limit load factor λ=0.4). In turn, the buckling strength calculated by Equation 6 was almost 7 times higher than this by Equations 1 and 2.

3.2 *Modified stiffness of the silo walls*

There is discontinuity of the Eurocode 3 buckling capacity in function of the number of silo columns (Sondej et al. 2015), (Iwicki et al. 2011) (Fig. 5). As the "Method A" gives satisfying results in comparison with 3D FEM analysis (Iwicki et al. 2015) (Sondej et al. 2015) the discontinuity of relation at Figure 5 may by caused by inaccuracy of the "Method B". Taking into account the circumferential wall curvature, and a component associ-

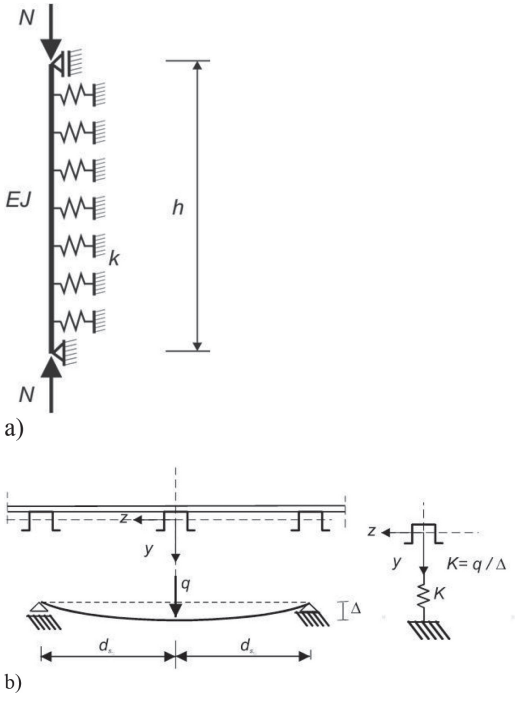

Figure 4. Buckling of silo column (Eurocode 3 2009) (a) vertical beam supported by elastic foundation and loaded by vertical forces at both ends, (b) stiffness determination of wall sheets during column buckling.

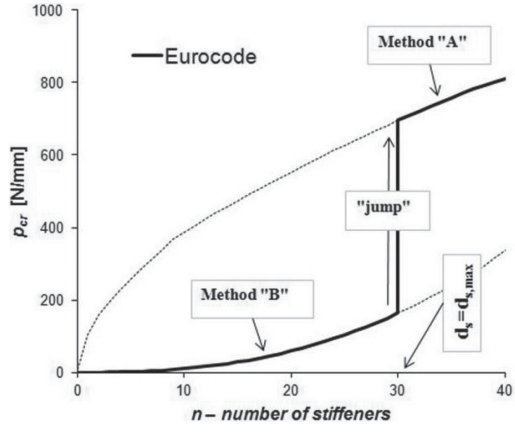

Figure 5. Maximum load factors 1 versus number of columns: according Eurocode 3 (Sondej et al. 2015).

ated with compression the following relation for the equivalent stiffness of the elastic support was derived:

$$K = \frac{8 \cdot D_y}{R^3 \cdot \left(2 \cdot A_1 - 16 \cdot X + 24 \cdot A_1 \cdot X^2 \cdot f^2 + 16 \cdot B_1 \cdot X\right)} + \frac{8 \cdot D_y}{R^2 \cdot \left(-4 \cdot L + 3 \cdot B_1 \cdot L + 16 \cdot X \cdot f - 16 \cdot L \cdot X^2 - 32 \cdot A_1 \cdot X^2 \cdot f\right)} + \frac{8 \cdot D_y}{R^2 \cdot \left(8 \cdot A_1 \cdot L \cdot X - 16 \cdot B_1 \cdot X \cdot f + 4 \cdot B_1 \cdot L \cdot X^2\right)} + \frac{8 \cdot D_y}{R \cdot \left(A_1 \cdot L^2 - 2 \cdot L^2 \cdot X + 16 \cdot L \cdot X^2 \cdot f - 8 \cdot A_1 \cdot L \cdot X \cdot f\right)} \quad (6)$$

where:

$$X = \frac{C_2 + C_3}{C_1} \quad (7)$$

$$C_1 = 4 \cdot L \cdot f + R^2 \cdot \sin\left(2 \cdot A_1\right) + 6 \cdot A_1 \cdot R^2 + 4 \cdot A_1 \cdot f^2 - 4 \cdot L \cdot R - 8 \cdot A_1 \cdot R \cdot f \quad (8)$$

$$C_2 = \frac{R^2 \cdot \cos\left(2 \cdot A_1\right)}{2} + f \cdot \left(2 \cdot R \cdot \cos\left(A_1\right) - 2 \cdot R + A_1 \cdot L\right) \quad (9)$$

$$C_3 = \frac{3 \cdot R^2}{2} - 2 \cdot R^2 \cdot \cos\left(A_1\right) - + A_1 \cdot L \cdot R + L \cdot R \cdot \sin\left(A_1\right) \quad (10)$$

$$A_1 \cdot \arcsin\left(\frac{L}{2 \cdot R}\right) \quad (11)$$

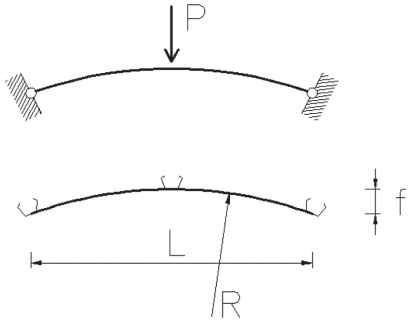

Figure 6. Modification of stiffness determination of wall sheets during column buckling.

$$B_1 = \sqrt{1 - \frac{L^2}{4 \cdot R^2}} \quad (12)$$

where: L – arc length, R – radius of the arc and f – height of the arc (Fig. 6)

Eq. 6 is valid for column distance d_s larger than $d_{s,max}$ (Eq.3) and for the number of columns greater than 4

4 SILO BUCKLING CAPACITY

4.1 *Silo column buckling capacity according to Eurocode 3 and for proposed stiffness k*

Silo column buckling capacity according to Eurocode 3 (2009) during symmetric and non-symmetric emptying. The silo buckling resistance calculated with the method 'A' was 3.8 times higher than required (λ = 3.8) but with the method 'B' (which should be used for this silo with respect to d_s), the buckling load bearing capacity was not sufficient (λ = 0.4). The calculated equivalent stiffness of the silo wall was equal k = 0.631 kN/m^2 and it was 45 times higher than according Eurocode 3 (2009) and the silo buckling load was 6.5 times higher than according to Eurocode 3 (2009) (Table 1).

Table 1. Silo column buckling capacity during non-symmetric emptying for Eurocode 3 and calculated stiffness of foundation.

Silo height level	Profile	Normal load EC1	Normal force	Critical	Load factor λ EC3	Load factor λ For proposed k	Nb,Rk ($A_{eff}f_y$)
m		kN	kN	kN			
0,84	C1.5	0,0	50,4	338,4			
1,67	C1.5	2,5	50,4	338,4	20,1	134,9	43,9
2,51	C1.5	11,0	50,4	338,4	4,6	30,7	10,0
3,34	C2.0	24,1	58,8	394,8	2,4	16,4	6,1
4,18	C2.0	40.6	58.8	394,8	1,4	9,7	3,6
5,02	C2.0	59,9	58,8	394,8	1,0	6,6	2,5
5.85	C3.0	81.4	73,7	494,9	0,9	6,1	2,7
6,69	C3.0	104,7	73,7	494,9	0,7	4,7	2,1
7,52	C3.0	129,6	73,7	494,9	0,6	3,8	1,7
8,36	C4.0	155,7	81,7	548,7	0,5	3,5	1,9
9,20	C4.0	183,0	81,7	548,7	0,4	3,0	1,6
10,03	C4.0	211,2	81,7	548,7	0,4	2,6	1,4
10,87	V04	240,2	163,0	1094,0	0,7	4,6	2,0
11,70	V04	270,0	163,0	1094,0	0,6	4,1	1,8
12,54	V04	300,4	163,0	1094,0	0,5	3,6	1,6
13,38	V04	331,3	163,0	1094,0	0,5	3,3	1,4
14,21	V04	331,3	163,0	1094,0	0,5	3,3	1,4
15,05	V04	331,3	163,0	1094,0	0,5	3,3	1,4
15,88	V05	331,3	184,2	1236,8	0,6	3,7	1,8
16,72	V05	331,3	184,2	1236,8	0,6	3,7	1,8
17,62	V05	331,31	184,2	1236,8	0,6	3,7	1,8

4.2 *Results of numerical analysis*

A simple FE analysis was carried out with single column with a varying cross-section supported by an elastic foundation simulating horizontally corrugated sheets loaded with vertical forces along the column due to wall friction (as in a silo) during non-axisymmetric emptying. Horizontal wall loads were not taken into account as it would be transferred directly into reaction in the elastic foundation. At the bottom, the column was fixed. The Figure 7 presents the first buckling load of a column from a linear elastic buckling analysis with the increasing stiffness of foundation and with supports preventing the cross-section torsion. The increase of foundation stiffness caused non linear rise of the column buckling load. For low lateral foundation stiffness a global buckling of the column occurred, at higher stiffness local, distorsional buckling toke place. For proposed stiffness k = 0.631 N/mm^2 the buckling load factor was 2 times higher than for the stiffness according Eurocode 3. The column buckled forms for stiffenss of foundation according to Eurocode 3 (2009) and for proposed stiffness k are on Figure 8.

For the whole silo modeled by shell elements the calculated buckling load factor from a Linear Buckling Analysis (LBA) for non-symmetric wall shear and normal stresses was $\lambda = 5.5$, i.e. the wall shear stresses at buckling were almost 6 times higher than the non-symmetric wall stresses by Eurocode 1 (2008) ($p_w = 5.5'26.68$ kPa and $p_h = 5.5'36.26$ kPa). The first 200 buckling modes (LBA) indicated solely local buckling of silo column walls. The differences in the results of the silo and one column analysis may be caused be the normal pressure that were taken into account in the silo analysis.

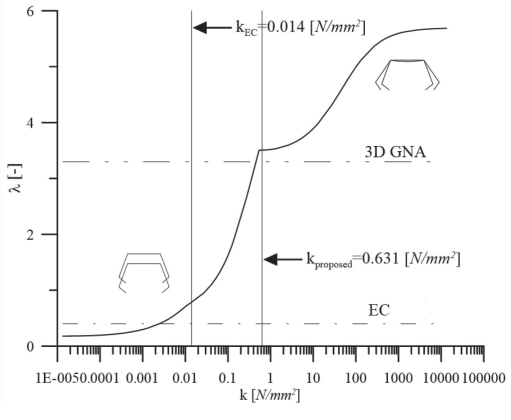

Figure 7. Evolution of column limit and buckling load factor λ against lateral foundation stiffness k.

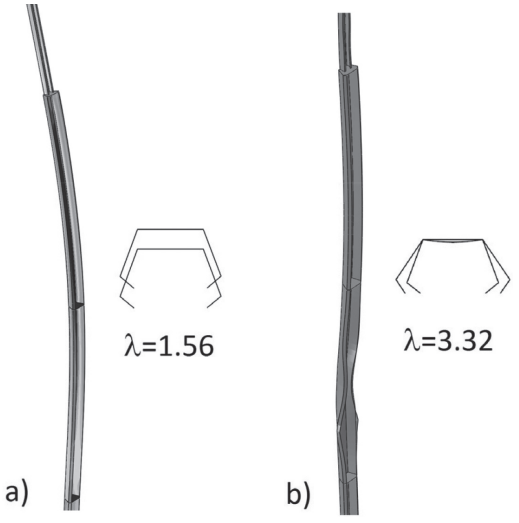

Figure 8. FE analysis: buckled forms for different stiffenss of foundation a) k according EC3 b) proposed k.

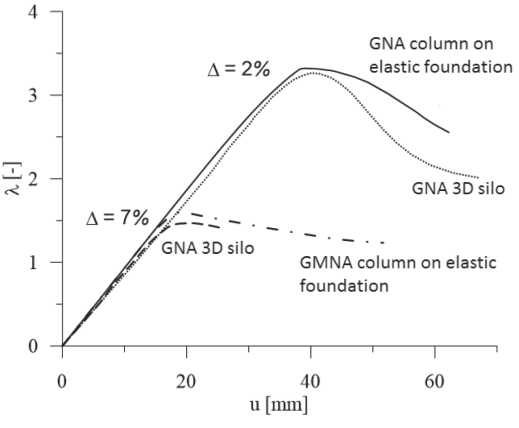

Figure 9. Evolution of vertical load factor λ against vertical displacement u of silo top edge from non-linear dynamic FE analyses of perfect 3D silo and column on elastic foundation.

The limit load factors from non-linear dynamic analyses were: λ = 3.264 (GNA) and λ = 1.47 (GMNA) (Fig. 9).

It was found with the aid of calculations wherein the load increased linearly in time (Fig. 2b) several times faster than the period of natural vibrations (the first-eigen-frequency was $f = 9$ Hz for the silo without the roof and the period of natural vibrations $T = 1/f = 0.11$ s), for the load action time $t_a = 20$ s. The relationship between the load factor and silo top edge vertical displacement was

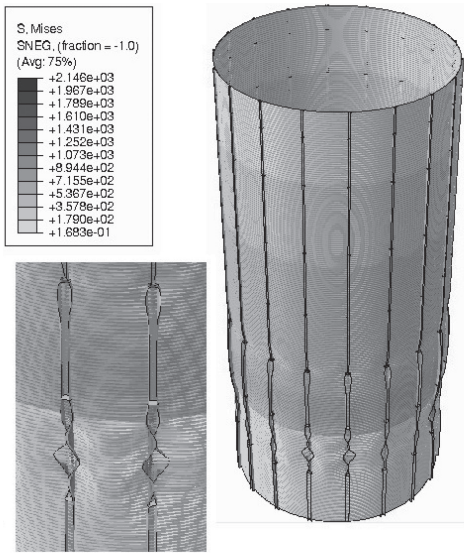

Figure 10. Silo deformation at limit load factor with stresses by von Mises [Pa] and scale factor 6 for GNA.

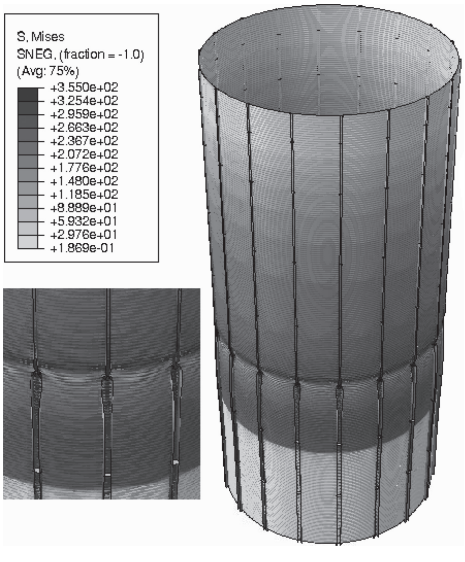

Figure 11. Silo deformation at limit load factor with stresses by von Mises [Pa] and scale factor 6 for GMNA.

approximately linear up to the peak, and after the peak it indicated a pronounced fall for GNA and a mild decrease for GMNA. The decrease of λ in a post-critical regime was caused by the presence of inertial forces (the load factor λ was calculated as the sum of the vertical reactions at the silo column supports).

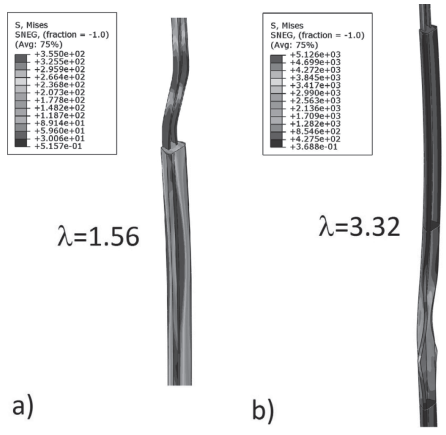

Figure 12. Column on elastic foundation deformation at limit load factor with stresses by von Mises [Pa] and scale factor 6 for a) GMNA, b) GNA.

For the analysis of one silo column resting on elastic foundation with the stiffness calculated according Equation 6 the limit load factors from non-linear dynamic analyses were: λ = 3.32 (GNA) and λ = 1.56 (GMNA), see Figure 12. The difference between simplified one column model and the whole silo was solely 1.8% (GNA) and 7.5% (GMNA).

The failure deformation mechanism for the whole silo and for one column was characterized by a local stability loss of the silo column walls (GNA) (Fig. 10) or by reaching the yield stress at the wall connectors between 2 different column profiles (GMNA) (Fig. 11).

5 CONCLUSIONS

Some conclusions can be derived from our stability FE studies for silos made from corrugated curved sheets strengthened by vertical columns:

- The silo design according to the orthotropic shell theory is in Eurocode more realistic (Equations 3 and 4) than the design based on the method considering the column stability on the elastic foundation (Equations 1 and 2). The latter formulae are largely too conservative as compared to the FE results. The method based on the column stability on the elastic foundation was corrected in the calculation of the foundation stiffness. For proposed stiffness of the foundation the method described by Equations 1 and 2 gives results compared to the FE numerical analysis (differences about 20%) and the silo buckling capacity is 6.5 times higher than for present Eurocode 3 (2008) stiffness foundation.

Table 2. Comparison of the silo buckling capacity for Eurocode 3 (2008) with original and modified stiffness of foundation and for FEM analysis of the whole silo and for single column.

Analysis	3D FEM	Column on Elastic foundation (FEM)	EC
GNA	3,26	3,32	–
GMNA	1,47	1,56	–
EC eq. 1 (K_{EC})	–	–	0,39
EC eq. 1($K_{proposed}$)	–	–	2,56

- Non-linear implicit dynamic analyses were effective to obtain the full load-displacement relationship during the entire buckling process. In non-linear dynamic analyses, the effect of inertial forces was almost negligible for the load action time higher than 20 s.
- The stability strength (GNA) for perfect single column with proposed elastic foundation stiffness was higher by 2% than this calculated for 3D model of the whole silo. For GMNA analysis it was higher by 7% (see Table 2). Larger differences in the non-linear paths were in post buckling region.
- In present research the influence of the geometrical imperfections was not taken into account, but in our previous studies (Iwicki 2015) for geometrically non-linear analyses, the effect of initial imperfections caused a decrease of the maximum limit load by about 20% with respect to perfect silos. The material non-linearity decreased the buckling strength (even by 55%) as compared to geometrically non-linear calculations. For perfect silos (GNA), the maximum limit load was 8 times larger than according to standard Eurocode 3 and 1.27 times for modified stiffness.
- The deformation at the limit state was characterized by local buckling or plastification of columns at connectors depending on the performed analysis (GNA or GMNA).
- Form the LBA analysis of the column on variable elastic foundation it can be concluded that the corrugation pitch depth of wall sheets should be large but at a certain level of corrugation stiffness the local buckling of the column takes place. In order to increase the buckling capacity the columns profiles should be restrained against local buckling by means of additional steel plates, in particular in regions of a cross-section column profile change due to the additional bending.
- Our studied will be continued in order to verify the proposed modification of Eurocode approach to prediction of buckling capacity of other silos. The stiffness of the stored bulk solid will also be taken into account by describing the bulk solid behavior with a hypoplastic constitutive model (Wójcik & Tejchman 2015, Kuczyńska et al. 2015).

ACKNOWLEDGMENT

The financial support of the Polish National Research Centre NCN in the frame of the Grant No 2011/01/B/ST8/07492 "Safety and optimization of cylindrical metal silos containing bulk solids with respect to global stability" and of the Polish National Centre for Research and Development NCBR in the frame of the Grant POIG.01.03.01-00-099/12 "Innovative method of dimensioning and construction of large industrial silos made from corrugated sheets" is gratefully acknowledged. The numerical calculations were performed using the computing resources of CI TASK at Gdańsk University of Technology.

REFERENCES

Abaqus, Theory Manual (2008). Version 6.8. Hibbit, Karlsson & Sorensen Inc.

EN1991–1-4, Eurocode 1: Basis of Design and Action on Structures. Part 4: Actions in Silos and Tanks. (2008). CEN, Brussels.

EN1993–4-1, Eurocode 3: Design of Steel Structures. Part 4–1: Silos, Tanks and Pipelines — Silos.(2009). CEN, Brussels.

Gallego, E., González-Montellano, C., Ramírez, A. & Ayuga, F. 2011. A simplified analytical procedure for assessing the worst patch load location on circular steel silos with corrugatedwalls. *Engineering Structures* 33: 1940–1954.

Iwicki, P. Rejowski, K. & Tejchman, J. 2015. Stability of cylindrical steel silos composed of corrugated sheets and columns based on FE analyses versus Eurocode 3 approach, *Engineering Failure Analysis* 57: 444–469.

Iwicki, P. Tejchman, J. & Chróścielewski, J. 2014. Dynamic FE simulations of buckling process in thin-walled cylindrical metal silos. *Thin-Walled Structures* 84: 344–359.

Iwicki, P. Wójcik, M. & Tejchman, J. 2011. Failure of cylindrical steel silos composed of corrugated sheets and columns and repair methods using a sensitivity analysis. *Engineering Failure Analysis* 18: 2064–2083.

Kuczyńska, N. Wójcik, M. & Tejchman, J. 2015. Effect of bulk solid on strength of cylindrical corrugated silos during filing. *Journal of Constructional Steel Research* December (2015), Pages 1–17.

Rotter, J.M. & Sadowski, A.J. 2012. Cylindrical shell bending theory for orthotropic shells under general axisymmetric pressure distributions. *Engineering Structures* 42: 258–265.

Rotter, J.M. 2001. Guide for the Economic Design of Circular Metal Silos. London: Spon Press.

Sondej, M., Iwicki, P., Tejchman, J. & Wójcik, M. 2015. Critical assessment of Eurocode approach to stability of metal cylindrical silos with corrugated walls and vertical stiffeners. *Thin-Walled Structures* 95: 335–346.

Wójcik, M., Iwicki, P. & Tejchman, J. 2011. 3D buckling analysis of a cylindrical metal bin composed of corrugated sheets strengthened by vertical stiffeners. *Thin-Walled Structures* 49: 947–963.

Wójcik, M. & Tejchman, J. 2015. Simulation of buckling process of cylindrical metal silos with flat sheets containing bulk solids. *Thin-Walled Structures* 93: 122–136.

Recent Progress in Steel and Composite Structures – Giżejowski et al. (Eds)
© 2016 Taylor & Francis Group, London, ISBN 978-1-138-02946-0

Problems of designing tubular shell galleries

J. Dudkiewicz & R. Ignatowicz
Faculty of Civil Engineering, Wroclaw University of Technology, Wroclaw, Poland

ABSTRACT: This paper presents selected problems regarding the design of a specific tubular transport gallery. The transport gallery is a supporting structure for a low-speed conveyor belt over a span of 36.70 m and a height difference of 9.15 m between the supports. The analysed gallery has an internal diameter of 3000 mm. The tubular shell structure is the principal structural element supporting the gallery and also shields the transported material from weather conditions. The technology guidelines, therefore, play a leading role in the design objectives. The authors then present selected static-strength analyses with a particular focus on identifying the magnitude of critical stresses and the impact of the size and spacing of frames on the cross—section's ovalization and stability.

1 INTRODUCTION

In the mining industry, there is a need to continuously move the excavated material from its extraction site directly to its storage location or for further distribution of the raw material. Most often the raw material needs protection from direct effects of the weather. In the case of industrial plants, the technical infrastructure and density of many technological installations prevent transport of the raw material at the ground level. It is often necessary to transfer the raw material at a height of up to 50 m above ground level, which requires designing transport galleries directly between technological buildings; the spans can then reach up to 50 to 70 m. Another important factor is to prevent spillage of the excavated material from accidental sliding of the heap on the conveyor belt. In addition, wind causes the spraying of fine dust fractions onto the objects located under the transport gallery as well as onto people under the gallery. These factors clearly justify the construction of completely enclosed transport galleries. By analysing a completed construction, we present the general issues of designing tube shell galleries. The focus here is on identifying the magnitude of critical stresses and the impact of the size and spacing of frames on the ovalization of the cross-section and stability.

2 STATIC AND ENDURANCE ANALYSES OF THE GALLERY STRUCTURE

The discussed structure of a steel shell gallery (Fig. 1) is located between two technological buildings. The span width in its projection onto a plane is 36.70 m. The gallery's axis is inclined at an angle of 14° to the horizontal. The internal geometry is defined by technological requirements. In the present case, the outer diameter of the gallery is 3000 mm, and the span width in the axes of supports is ~37.82 m. The gallery structure serves as a support structure under the conveyor belt and a bridge for maintenance.

A proper determination of the values and nature of loads (Fig. 2) (Radwańska-Skotniczny 2013) while designing shell structures is an important factor that directly affects the state of effort as well as design solutions.

Variable loads acting on the gallery come from climatic factors (wind [EN 1991-1-4, 2005], snow

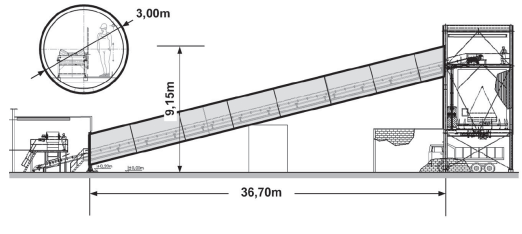

Figure 1. A view and cross-section of the shell gallery.

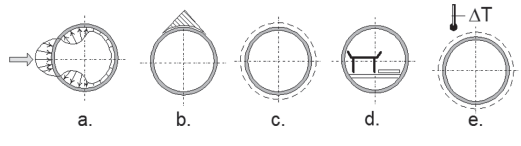

Figure 2. Impacts on the shell gallery: a) wind load, b) snow load, c) ice load, d) technological and dead-weight loads, e) temperature load.

[EN 1991-1-3 2005], ice, temperature), as well as technological factors.

In the balance of loads, special attention should be paid to the prevailing load, which is the wind load. In this paper we mention the problem of an adequate absorption of wind load and the problem of taking the load into account in the analysis of shell stability.

Wind load should be dealt with in two ways: as a result of a global impact and as a result of a local impact, i.e. in relation to a section of the shell between the frames.

Global effects refer to the effect of wind on the gallery as a rod element, and these generate two types of loads: a load acting parallel to the plane of wind action and a load acting perpendicular to the plane of wind action, which is a consequence of spin excitation.

The next step in the design is an appropriate and correct acceptance of a static scheme (Fig. 3).

The commonly utilized software for calculations with the use of the Finite Element Method unfortunately does not include tools particularly useful to calculate steel shell structures.

For this reason, in the first stage of analyses, calculations are usually performed on simple static schemes that guarantee proper 'construction work' (cf. Fig. 4). When creating a static scheme, it should be noted that the main axis of the shell structure gallery does not match the support points.

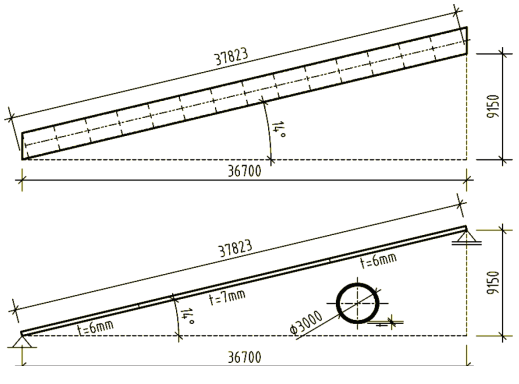

Figure 3. A static diagram of the shell structure gallery.

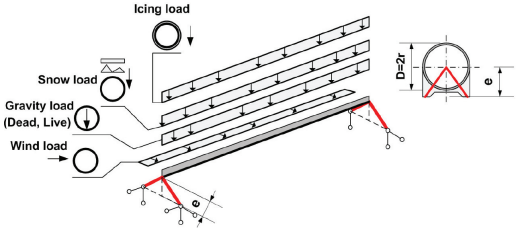

Figure 4. A static diagram of the shell structure gallery.

The result is an eccentric of the radius size, and therefore a beam diagram in the three-dimensional system with suitably shaped support points on a suitable eccentric is more appropriate, as presented in Figure 4. Static calculations enable obtaining the appropriate distribution of internal forces in the gallery.

The methodology of designing steel shell galleries that have been used in Poland was presented comprehensively in the work by Murzewski & Siepak (1978). To date, there has been no description of a method for dimensioning steel shell structures in Polish standards. Some topics can be found in publications by Brzosek (1961), Timoszenko (1955) and in the European Convention for Constructional Steelwork (ECCS) guidelines (Rotter *et al.* 2008). The following researchers dealt with the issues of shell stability at the Wroclaw University of Technology: Bodarski (Pasternak *et al.*, 1998), Rykaluk (2012) and Hotal (2003). In engineering practice, designers often used to utilize the German standard DIN 18800-4 (2008) in which the rules and a method to design shell structures have been provided, particularly with respect to new types of shell galleries. Through publications by Mendera (1993, 2000), it was possible to use the methodology contained in DIN 18800-4 (2008). In this study, we made use of these guidelines and dimensioned this type of structure. Now, the issues of designing shell structures have been included in the Polish standard PN-EN 1993-1-6 (2008), and generally these guidelines are the basis for dimensioning this type of construction. Among the meaningful limit states of steel shells, LS1 (plastic destruction), LS2 (plastic maladaptation), LS3 (instability) and LS4 (fatigue) can be distinguished. In the framework of our paper, the stress approach, considering the state of LS1 and LS3, is described. In this situation, expressions based on the membrane theory, according to Annex A of the standard (PN-EN 1993-1-6 2008), have been utilized.

The gallery structure is provided with lateral stiffenings in the form of internal frames that stiffen the shell contour and at the same time provide a support structure under the crossbars on which the stringers of a technological platform and support beams of the conveyor rest.

The adopted spacing of frames is every 3000 mm, in line with the general recommendations contained in the German guidelines that assume a spacing of frames close to the diameter of the pipe (tube). A design solution allows treatment of the various sections of the gallery as mentally separate shells, to which internal forces can be attributed. The condition for such an assumption is that the frames are of an adequate stiffness (see Fig. 5).

When analysing the mentally separated fragment, a set of internal forces is attributed to it on

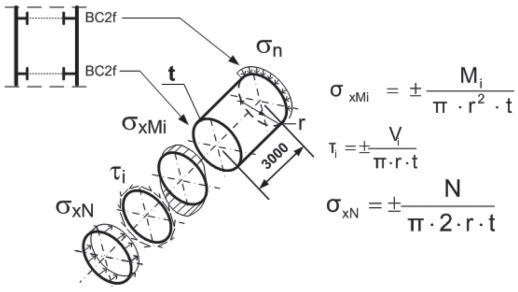

Figure 5. A diagram of the assignment of internal forces for a mentally separated fragment of the shell.

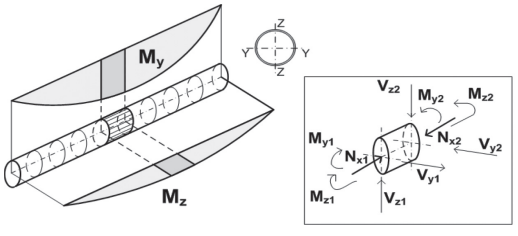

Figure 6. A pattern for calculating stresses in the cross-section of the shell.

the basis of which individual values of membrane stresses in the shell are calculated (Fig. 6).

The LS3 status was verified by checking the conditions (8.18) and (8.19) of the standard (BS EN 1993-1-6 2008). Depending on load conditions and stress state, key values for each membrane stress were checked according to the following formulas: $\sigma_{x,Ed} \le \sigma_{x,Rd}$, $\sigma_{\Theta,Ed} \le \sigma_{\Theta,Rd}$, $\tau_{x\Theta,Ed} \le \tau_{x\Theta,Rd}$, and in the case of a complex stress state, according to the following expression (1):

$$\left(\frac{\sigma_{x,Ed}}{\sigma_{x,Rd}}\right)^{kx} - k_i \cdot \left(\frac{\sigma_{x,Ed}}{\sigma_{x,Rd}}\right) \cdot \left(\frac{\sigma_{\theta,Ed}}{\sigma_{\theta,Rd}}\right) + \left(\frac{\sigma_{\theta,Ed}}{\sigma_{\theta,Rd}}\right)^{k\theta} + \left(\frac{\tau_{\theta,Ed}}{\tau_{\theta,Rd}}\right)^{k\tau} \le 1. \quad (1)$$

Taking into account the analysed shell gallery, it can be seen that stability in the middle of the span length was checked by comparing the highest compressive stresses on the upper edge of the cross-section $\sigma_{x,Ed}$ with computational buckling stresses in the meridional direction $\sigma_{x,Rd}$ set for uniform compression.

Therefore, such a check must be regarded as quite conservative. In the case of the shell galleries, the dominant stresses are stresses derived from bending and shearing. To obtain a result closer to reality, one can take advantage of existing solutions contained in the subject literature that treat the determined values as characteristic ones. Solutions for pure shell bending proposed by Baker (2) or Brazier (3) can be mentioned here:

$$\sigma_{x,Rcr} = 0{,}6 \cdot \gamma_z \cdot \frac{E \cdot t}{r}, \quad (2)$$

$$\sigma_{x,Rcr} = 0{,}34 \cdot \frac{E \cdot t}{r}. \quad (3)$$

In the studies by Grigolyuk & Culkov (1973) and Grigolyuk (1978), estimation of the upper and lower stresses on the basis of a comprehensive comparison of experimental results and theoretical solutions by various researchers has been proposed (Fig. 7).

In order to estimate the critical stresses in the cylindrical shell, we carried out numerical tests consisting of setting static equilibrium paths of a separated fragment of the shell wherein the stress state is generated by pure bending.

The numerical computations were completed in the Finite Elements Method calculation system. Analyses of shells were dealt with in a similar way by Volmir (1963), Volt & Peňáz (2013), Wunderlich & Deml (1997) and Wunderlich & Albertin (2000).

In the first step, an analysis of the shell was carried out, assuming the maintenance of circularities on the ends see Figure 8. In the second stage of the analyses, the deformability of the shell contour on the ends was taken into account. Such an approach makes it possible to observe the impact of the vulnerability of frames on the course of limit equilibrium paths.

Paths of static equilibrium (Figs. 10, 11) were developed taking into account the geometric

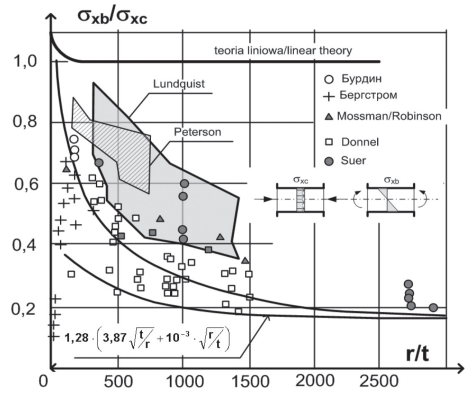

Figure 7. Critical stresses while bending the shell in the r/t function compared to research and proposals by Grigolyuk & Culkov (1973) and Grigoliok (1978).

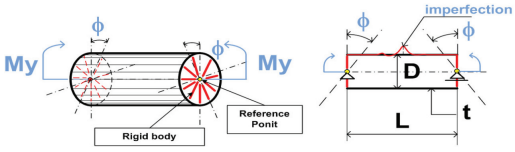

Figure 8. A diagram of the assignment of internal forces for a mentally separated fragment of the shell.

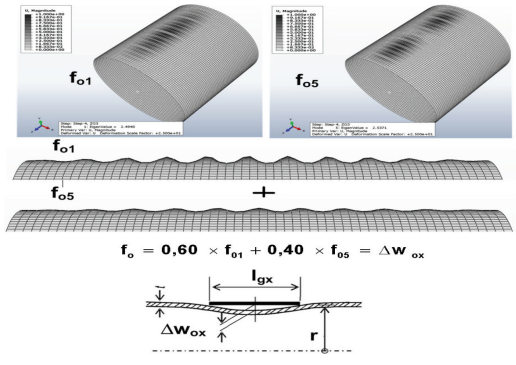

Figure 9. An exemplary chart of the implementation of own forms as geometric imperfections of a cylindrical shell.

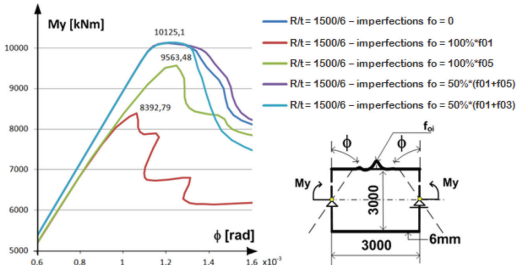

Figure 10. The impact of imperfections on the course of the limit equilibrium path for fo = 0.30t. The steel shell structure R/t = 250.

imperfections along with the plasticity of the material. The sizes of geometric imperfections were determined on the basis of the permissible sizes of local convexities assigned to different classes of workmanship quality according to EN 1993-1-6 2008. Numerical analyses taking into account the imperfections were performed through the implementation of linear combinations of the structure's own forms, which were determined at the beginning (Fig. 9).

To illustrate the effect of different configurations of imperfections, a series of calculations for a 6-mm-thick shell, R/t = 250, L = 3,000 mm were carried out.

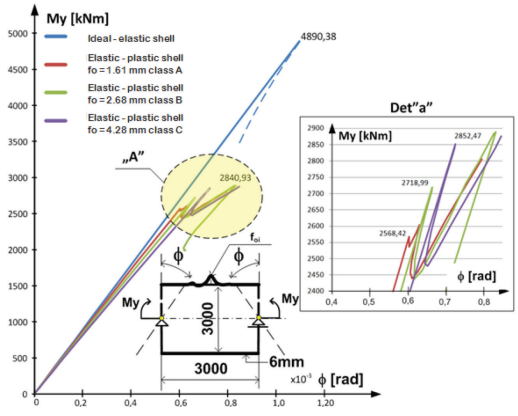

Figure 11. The impact of imperfections on the course of the limit equilibrium path for fo = 0.30t. The steel shell structure R/t = 500.

For a shell with more slender walls but still classified as a medium-length shell ω = 22.3 <0.5 × r/t = 125, the static equilibrium path has local maxima in the places of the jump phenomenon. The size of the initial imperfections has a significant impact on the nature of the path's course as well as on its limit values.

The performed numerical analyses clearly show that the most unfavourable form of geometric imperfections is the first own form. The subject of the analysis is the actual steel shell, which has to be considered as a shell having an average length, where the length parameter of the shell segment is ω = 7.91 < 0.5 × r/t = 125.

Based on the calculations carried out, the shell reaches its limit-bearing capacity within the elastic and plastic range, taking into account the imperfections with a maximum bulging arrow of 0.3 t, which reduces the bearing capacity by 21% in relation to the bearing capacity of an ideal shell. The shape itself and the distribution of imperfections affect the course of the limit equilibrium path. The lowest bearing capacity is achieved in the first own form because the transition to this form of buckling requires the least operation of external forces.

The basis for these calculations was the assumption of non-deformability of the shell's circular contour on the ends of the analysed segment. In real conditions, one has to deal with deformable frames. To estimate the magnitude of the stiffening frames' vulnerability impact, three middle segments of the shell structure gallery were analysed so that the central section was separated with frames (Fig. 12). Reference points were created at the extreme ends of the outer segments, and boundary conditions to preserve the freedom of rotation were assigned to these points.

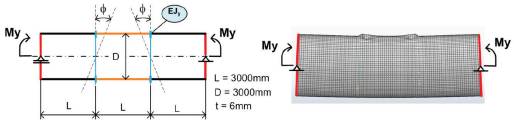

Figure 12. A static diagram of a segment of the shell structure, taking into account the vulnerability of stiffening frames.

The reference points were linked with super elements to the contour of the shell. The numerical model was properly calibrated so that the loss of stability and the mechanism of destruction occurred on the middle segment of the shell. The calculations included imperfections and material nonlinearity. Two extreme cases were analysed: the shell was reinforced with a vertical rib with a thickness of 10 mm and a height of 300 mm, and the shell was stiffened with a rib with a comparable rigidity to that of the transversal stiffness of the shell.

Figure 13 presents the effect of the frame stiffness on the limit-bearing capacity of the shell. The value of the bearing capacity increased by ~4%, but the difference was observed only when compared to the mechanism of a stiffened shell's destruction and a shell devoid of such a stability.

Figure 14 shows the difference in the mechanism of destruction with different stiffnesses of frames. It is clear that the lack of frames with a properly selected stiffness significantly affects the mechanism of destruction—a phenomenon of ovalization. We conducted our analyses only for a shell for the designed gallery; for other proportions of slenderness, other forms of destruction may occur. Therefore, the ovalization of the cross-section, which is a consequence of the inter-strip bending caused by the curvature of the rod, should be considered (Brzoska 1961; Smith 1972). Internal forces in the shell gallery determined on the basis of membrane theory, according to Annex A (EN 1993-1-6 2008), are correct, assuming that the cross-section of the tubular beam is non-deformable.

Therefore, such a phenomenon should be considered.

The value of additional latitudinal stresses can be estimated from the expression (4) by Smith (1972):

$$\sigma_{\varphi} \cong \frac{3 \cdot M_y^2 \cdot r^3}{2 \cdot E \cdot J_y^2 \cdot t}, \tag{4}$$

where My = bending moment, r = radius, Jy = moment of inertia and t = thickness of the shell.

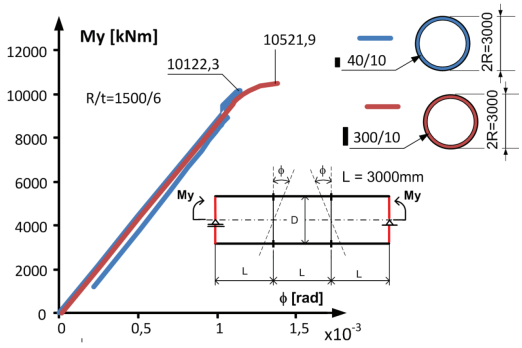

Figure 13. A comparison of the shell's static equilibrium paths for frames of different stiffness.

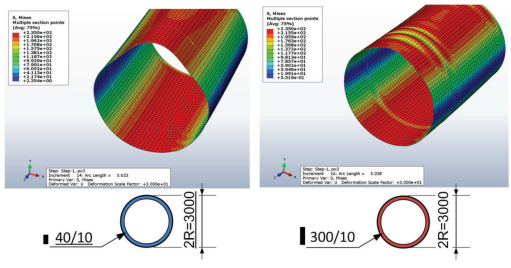

Figure 14. Forms of bearing capacity depletion for a shell stiffened with frames of different stiffness.

Attention should also be paid to the consequence of cross-section ovalization on the rigidity of the structure because the flattening of the cross-section reduces the moment of inertia. To reduce the effect of cross-sectional ovalization, transverse frames are used. In conclusion, the phenomenon of inter-strip bending should be reflected in the procedure for calculating critical stresses from pure bending. A synthetic approach to this phenomenon in relation to the procedure for calculating critical stresses for a shell subjected to pure bending is presented by Samuelson & Eggwertz (1992). The researchers summarized their analyses for design purposes as follows:

– the use of frames in a span equal to the cross-section of the gallery prevents the phenomenon of ovalization, and this can be seen as a rigid cross-section;
– with a spacing of frames equal to 10D, the effect of ovalization is large enough that it cannot be overlooked.

For the case that is the subject of this analysis, ovalization can be omitted. According to Samuelson & Eggwertz (1992), the critical stress of the shell at pure bending can be calculated from equation (5) as follows:

$$\sigma_{xb} = \left(\alpha_2 - 15 \cdot \left(\frac{\Delta w_{ox}}{l_{gx}} - \frac{1}{50}\right)\right) \cdot \left(0.19 + \frac{0.67}{\sqrt{1 + 0.01 \cdot \frac{r}{t}}}\right) \cdot 0.60 \cdot E \frac{t}{r}, \quad (5)$$

where $\alpha_2 = (1/0.70)$ and Δw_{ox} and l_{gx} according to Table 8.3 (PN-EN 1993-1-6 2008) for $r/t \leq 1000$.

In view of these considerations, the characteristic values of critical meridional stresses were calculated and are presented in Figures 15–18.

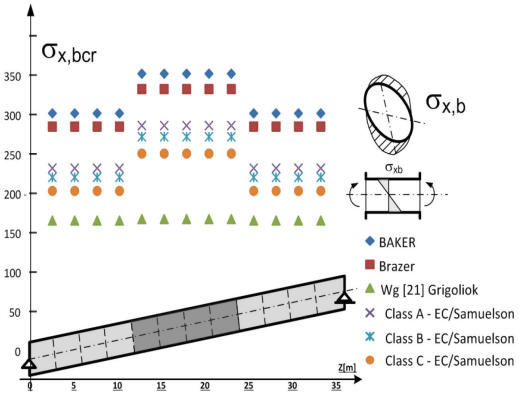

Figure 15. A comparison of critical stresses at pure shell bending according to various authors.

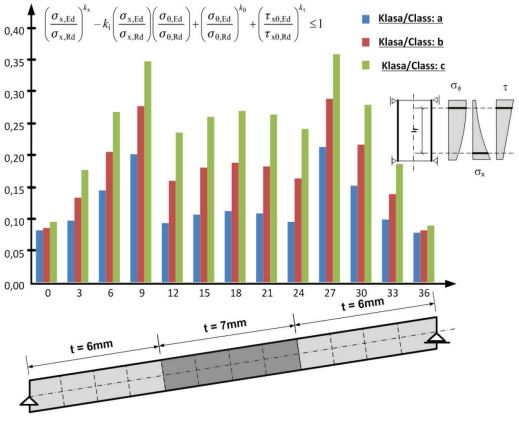

Figure 16. A comparison of calculated meridional stresses to calculated buckling stresses according to EN 1993–1-6 2008.

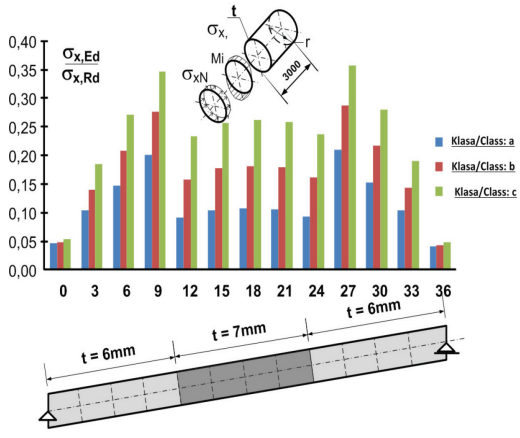

Figure 17. The effort of individual segments of the gallery in the complex state of stress for loads resulting from dead load, technological and snow loads, depending on the class of the steel shell workmanship, according to EN 1993–3-2 (2006).

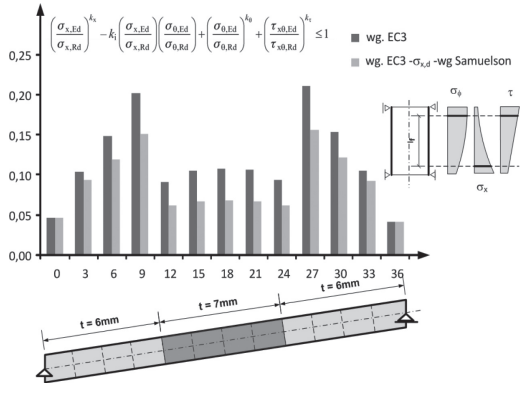

Figure 18. A comparison of effort in a complex state of effort according to EC3 for class A workmanship quality.

3 SUMMARY AND CONCLUSIONS

It is extremely important to design structures that are harmonized with the surrounding environment and at the same time meet all the technological tasks in industrial plants. Such structures include the discussed shell gallery. Economic designing as well as designing related to workmanship necessitates a thorough examination of the dimensioning problems of this type of construction. In this paper the authors have drawn attention to issues that include a correct balance of loads, the adoption of an appropriate static scheme along with the determination of internal forces, and the determination of stresses in the shell using the Finite Element

Method. The authors also have drawn attention to the impact of stiffness and spacing of frames on the ovalization of the cross-section, comparing the paths of limit equilibrium. We also present a method for estimating the value of critical stresses in a cylindrical shell by performing numerical studies consisting of setting static equilibrium paths of a separated fragment of the shell in which the state of stresses is generated by pure bending. The paths of static equilibrium were developed by taking into account geometric imperfections and considering the plasticity of the material.

REFERENCES

Brzoska, Z. 1961. *Statyka i stateczność konstrukcji prętowych i cienkościennych*. Warszawa: PWN.

DIN 18800-4. 2008. Stahlbauten Teil 4: Stabilitätsfälle – Schalenbeulen. NABau im DIN e.V., Beuth-Verlag.

Grigolyuk, E.I. & Culkov, P.P. 1973. *Ustojcivost i kolebanija trehslojnih obolocek*. Moskva: Masinostroenie.

Grigolyuk, E.I. & Kabanov V.V.. 1978. *Stability of Shells. Ustojcivost obolocek [in Russian]*. Moskva: Nauka.

Hotała, E. 2003. *Nośność graniczna nieużebrowanych cylindrycznych płaszczy silosów stalowych*. Wrocław: Oficyna Wydawnicza Politechniki Wrocławskiej.

Kowal, Z. 1972. *Wybrane działy z konstrukcji stalowych cz. II*, Wrocław: Wydawnictwo Politechniki Wrocławskiej.

Mendera, Z. 1993. Interakcyjne kryteria stateczności płyt i powłok metalowych w złożonych stanach naprężenia. *Inżynieria i Budownictwo* 2: 50–53.

Mendera, Z. 2000. Stateczność stalowych powłok walcowych ściskanych podłużnie. *Inżynieria i Budownictwo* 4–5: 240–243.

Murzewski, J. & Siepak J. 1978. *Stalowe belki powłokowe*. Kraków: Politechnika Krakowska.

Pasternak, H., Bodarski, Z., Hotała, E. 1998. Steel Silos – Education by Analysing Failures. *Journal of Constructional Steel Research* 46: 340.

PN-EN 1991-1-3. 2005. *Eurokod 1 – Oddziaływania na konstrukcje – Część 1-3: Oddziaływania ogólne – Obciążenie śniegiem*. Warszawa: Polski Komitet Normalizacyjny.

PN-EN 1991-1-4. 2005. *Eurokod 1 –Oddziaływania na konstrukcje – Część1-4: Oddziaływania ogólne – Oddziaływania wiatru*. Warszawa: Polski Komitet Normalizacyjny.

PN-EN 1993-1-6. 2008. *Projektowanie konstrukcji stalowych. Część 1-6: Wytrzymałość i stateczność konstrukcji powłokowych*. Warszawa: Polski Komitet Normalizacyjny.

PN-EN 1993-3-2. 2006. *Projektowanie konstrukcji stalowych. Wieże maszty, kominy. Kominy*. Warszawa: Polski Komitet Normalizacyjny.

Radwańska-Skotniczny, A. 2013. *Obciążenia budynków i konstrukcji budowlanych wg Eurokodów*, Warszawa: PWN.

Rotter, J.M. & Schmidt, H. (eds). 2008. *Stability of Steel Shells: European Design Recommendations*: 5th Edition, Brussels: ECCS.

Rykaluk, K. 2012. *Zagadnienia stateczności konstrukcji metalowych*. Wrocław: Dolnosląskie Wydawnictwo Edukacyjne.

Samuelson, L. & Eggertz, S. 1992. *Shell stability handbook*. London–New York: Elsevier.

Timoszenko, S.P. 1955. *Ustojczivost' uprugich system*. Moskwa: GITTL.

Volmir, A.C. 1963. *Ustojčivosť uprugich sistěm*. Moskva: Gosudarstvennoe izdastělstvo fiziko-matematiceskoj literatury.

Voltr, O. & Peňáz, J. 2013. Influence of initial imperfections on the laterally loaded cylindrical shell. *Transactions of the VŠB.Mechanical Series* Vol. LIX No. 1. Technical University of Ostrava.

Wunderlich, W. & Albertin, U. 2000. Analysis and load carrying behavior of imperfection sensitive shells. *International journal for numerical methods in engineering* 47: 255–273.

Wunderlich, W. & Deml, M. 1997. Direct evaluation of the worst imperfection shape in shell buckling. *Computer methods in applied mechanics and engineering* 149: 201–222.

This page intentionally left blank

Reliability, masts and towers

This page intentionally left blank

Recent Progress in Steel and Composite Structures – Giżejowski et al. (Eds)
© 2016 Taylor & Francis Group, London, ISBN 978-1-138-02946-0

Searching for significant basic variables of experimentally tested steel, cylindrical shells

J. Kaliszuk & J. Marcinowski
University of Zielona Góra, Zielona Góra, Poland

Z. Waszczyszyn
Cracow University of Technology, Kraków, Poland

ABSTRACT: The paper presents an example of using a numerical model of the existing structure for searching its significant basic variables being an input vector in the probabilistic analysis of its reliability. The paper analyzes a steel cylindrical shell, the FEM model of which was elaborated on the grounds of the experiments carried out earlier (Kaliszuk et al. 2005). Set elements of the shell significant basic variables were selected through an analysis of its sensitivity to a change in the values of given variables. The shell sensitivity was assessed on the grounds of the changes in the value of its ultimate load capacity. The shell ultimate load capacity was determined by means of the numerical, non-linear analysis using FEM –COSMOS/M software.

1 INTRODUCTION

Probabilistic reliability assessment of structures is a very important engineering issue. It should be made both on the design stage of a certain structure as well as on the operational stage of the existing one.

Reliability of structures is determined on the grounds of an analysis carried out following the scheme: INPUT → ANALYSIS → OUTPUT.

The input of the reliability analysis is a set of structure basic variables representing physical quantities which characterise actions and environmental impact, geometrical quantities and material properties (CEN 2002). The output, is the structure reliability expressed in the measure accepted for the analysis. EN1990 distinguishes two basic probabilistic structure reliability measures and they are: survival probability $P_s = (1 - P_f)$, where P_f is the failure probability for the considered failure mode, as well as reliability index β related to P_f relation: $P_f = \Phi(-\beta)$, where $\Phi(\ )$ is the cumulative distribution function of the standardised normal distribution. There are numerous methods of assessing probabilistic reliability of structures, that differ from one another in a degree of exactness of a probabilistic description of a certain issue as well as in the method of computation performance. Taking into account the level of exactness of the probabilistic description of basic variables vector there are two major classes of reliability analysis methods distinguished: first order reliability methods (FORM) – Level II, full probabilistic methods—Level III (CEN 2002, Melchers 1987, Nowak & Collins 2000).

On the other hand, with respect to computation methods applied in analyses, they are divided into analytical and simulation methods. The group of simulation methods comprises Monte Carlo simulation methods (MC).

The classic approach to this method determines an analytical form of the ultimate state of the analyzed structure and then its value for random basic variables is computed. A set of the results obtained for the ultimate state function serves, on the next step, determining reliability index β (Marek 2001).

A weak point of this approach is that the analytical form of the ultimate state function can be determined only with respect to simple structures or to individual elements of complex structures. It means that in case of a complex structure the reliability analysis is limited to the analysis of the selected elements and is not a global analysis of the whole structure. The above mentioned method can be improved by replacing the computation results of the analytical ultimate state function with the results of global analysis of structures performed by FEM.

Unfortunately, this approach is limited significantly by the necessity to generate a huge number of samples needed for the MC simulation. This number increases along with an increase of the expected level of computation accuracy. In case of assessing the probability of a building structure

reliability, the required number of samples is of 10^7–10^8 (Kaliszuk 2011).

Making such number of numerical analysis of a structure by means of the FEM is practically infeasible due to an enormous long time expected for computations (Kaliszuk & Waszczyszyn 2003, Pabisek et al. 2004). The problem presented in the article can, to a great extent, be solved by the so called hybrid approach, in which the FEM analysis results are replaced with the results of the computations made with the Artificial Neuron Network (ANN) (Papadrakakis et al. 1996).

ANN used for the analysis is prepared in the process of designing, teaching and testing. ANN teaching and testing is performed with the use of adequate patterns, prepared in FEM analyzes.

Unfortunately, the minimum number of those patterns increases exponentially with an increase in the number of components of basic variables vector. (Kaliszuk & Waszczyszyn 2003). This is a serious constraint of the Hybrid MC method (HMC).

Therefore, when starting to make a reliability analysis of a structure with the HMC method, it is important to limit as much as possible the number of basic variables by selecting the key ones which have the greatest impact on a change of the analysis result.

Thus, the process of selecting relevant basic variables forming the reliability analysis input is crucial. In order to do this we can make an analysis of a structure sensitivity to a change in the value of the selected basic variables and then select the variables a change in value of which results in significant changes in the results of the structure FEM analysis.

The paper presents a selection process of basic variables for laboratory tested cylindrical shell. The sensitivity analysis was carried out on the shell numerical model elaborated on the grounds of the results of experiments (Kaliszuk et al. 2005).

The sensitivity analysis means making numerous numerical analyses of the shell model by means of FEM COSMOS/M software, and then comparing the influence of changes in the value of particular basic variables on the result of the numerical analysis and on selecting the key variables. The selected basic variables shall in future be used for conducting a reliability analysis of this shell with a HMC method.

2 THE ANALYZED CYLINDRICAL SHELL

The subject of the analysis is a steel cylindrical shell with edges supported by linear hinges and free two other edges, (cf. Fig. 1). In the Figure 1 the following notation was used: 1 – cylindrical shell: $L = 472$ mm, $B = 470$ mm, $t = 5$ mm, $R = 1380$ mm, 2 – steel supporting beam, 3 – clamp beam, 4 –

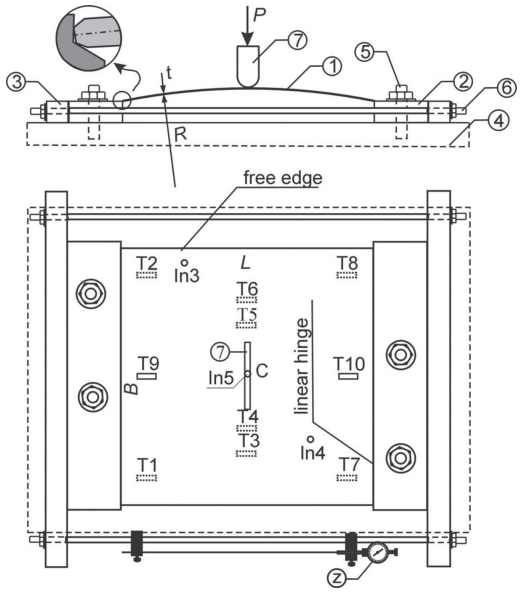

Figure 1. Scheme of the test stand.

lower crosshead plate, 5 – M20 screw of 10.8 class, 6 – tie rod of 8.8 class, 7 – pressing shaft, z—dial gauge, T_i ($i = 1, 2, ..., 8$) – electro-resistance strain gauges on the lower shell surface, T_i ($i = 9, 10$) electro-resistance strain gauges on the upper shell surface. The shell is laterally loaded with a sectional load of constant intensity p. The load is performed with a pressing shaft 7 shown in Figure 1.

It was accepted that a measure of the load capacity of the analysed shell is the value of the failure load at which the elastic-plastic global stability is lost. Three shells were subjected to experiments. The results of the experiments were used for adjusting the numerical shell model necessary for FEM analyses. Numerical shell analyses were made in connection with the sensitivity analysis, designed for selecting significant basic variables.

2.1 *Shell experimental research*

The objective of the experimental research was to obtain data necessary to elaborate a numerical model of the shell, illustrating in the best possible way its real form both in terms of geometry as well as its action effects. Figure 1 presents a scheme of the test stand, whereas Figure 2 shows the picture of the test stand.

For the purpose of the tests 3 shells called A, B, C were prepared. The shells were made of cold rolled steel sheet. Strength parameters of the said sheet were determined in a static tension tests made on 25 samples. On the grounds of the test results the

Figure 2. The test stand.

Table 1. Results of the statistical analysis for the measured: R_{eL}, R_{eH}, R_m, E.

Statistics of tested quantities	μ MPa	σ MPa
R_{eL}	307	10
R_{eH}	319	10
R_m	379	10
E	206,950	20,390

statistics for the lower yield point R_{eL}, upper yield point R_{eH}, tensile strength R_m as well as a longitudinal modulus of elasticity E were determined.

Table 1 presents the mean values for the tested quantities μ as well as the standard deviation values σ.

The next stage of the tests was a detailed measurement of the geometry of the A, B, C shells. The data obtained made it possible to generate nodes of FE grid during numerical test modelling.

The same database was also used for elaborating a functional shape description of midsurfaces of the tested shells. Good approximation was obtained on the basis of cyclometric and trigonometric functions. Three models approximating geometries of midsurfaces of the tested shells were determined and expressed by the formulae 1–3. The accepted models were marked with symbols: AF1, AF2, AF3 respectively.

$$y = \sqrt{R^2 - (d/2 - x)^2} - \sqrt{R^2 - (d/2)^2} \quad \text{where} \quad R = \left(A^2 + (d/2)^2\right)/2A \tag{1}$$

$$y = A_1 \sin(\pi x/d) + A_3 \sin(3\pi x/d) \tag{2}$$

$$y = A_1 \sin(\pi x/d) + A_2 \sin(2\pi x/d) + A_3 \sin(3\pi x/d) \tag{3}$$

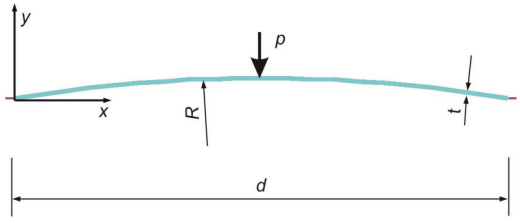

Figure 3. Shell cross-section.

Table 2. Shell approximation parameters and RMSE.

Shell	AF(·)	A mm	A_1 mm	A_2 mm	A_3 mm	RMSE mm
A	AF1	22.30				0.61
	AF2		22.8		0.9	0.41
	AF3		22.8	0.1	0.9	0.41
B	AF1	22.8				0.46
	AF2		23.3		0.6	0.38
	AF3		23.3	–0.0	0.6	0.38
C	AF1	21.52				0.74
	AF2		22.0		0.8	0.73
	AF3		22.0	1.0	0.8	0.34

AF(·) – approximation function.

In the formulae: d – shell width, R – cylinder radius, x, y – coordinates of the midsurface grid nodes, A, A_1, A_2, A_3 – parameters of the approximating functions

Figure 3 shows interpretation of the parameters d, R, t, x, y.

The optimum values of A, A_1, A_2, A_3, for approximation selected functions were determined by the least squares method. The obtained parameter values and the corresponding values of the root of mean square error (RMSE) of approximation are presented in Table 2.

The main stage of the research tests was an experimental analysis of elasto-plastic deformations of the A, B, C shells. The experiment was carried out on the test stand shown in Figure 2 and made as illustrated in Figure 1.

Each of the shells tested was subjected to an increasing, imposed load (the displacement controlled process), resulting in continuing deformations.

During the process the values of the changing in time displacements and deformations of the selected shell points were recorded along with tie rods elongation and the total push force.

The test was finished once the shell load carrying capacity was reached. The measurement database recorded during the experiment was used on the next stage for numerical adjustment of FEM model.

2.2 *Numerical model of the tested shells*

The numerical model of the experimental shells was elaborated with FEM, COSMOS/M program. Its final shape was obtained through a successive adjustment, the objective of which was taking into account successive elements allowing the most real reproduction of the tests made. The basic elements of this model, including boundary conditions and FE mesh, are presented in Figure 4.

The symbols presented in the Figure 4 mean: P—shell with dimensions $d \times l$, thickness $t = 5$ mm and radius R; BP—supporting beams with prevented lateral displacement; PT—family of short bars of a large axial stiffness and a small flexural stiffness performing shell linear hinge support; SC—tie-beams preventing displacement of supports; EO—fictitious bars of perfect rigid—plastic characteristics for modeling static and sliding friction; p—laterally sectional load of constant intensity.

Quality of numerical recording of the course of experiments is illustrated by displacement and deformation equilibrium paths. Figures 5, 6 present equilibrium paths obtained from tests with the corresponding paths from numerical analyses of the elaborated shell model. Figure 5 presents displacement paths and Figure 6 presents deformation paths referring to the selected, central point on the A shell, whereby the values on the vertical axis correspond to total load P.

The presented results confirm a good representation of experiments carried out in FEM analysis of the elaborated shell model. This allows for using the ready model for further shell analysis without the need to construct a real test stand.

On the next stage, the ready numerical shell model was used for the analysis of the shell sensitivity to changes of the values of the selected basic variables.

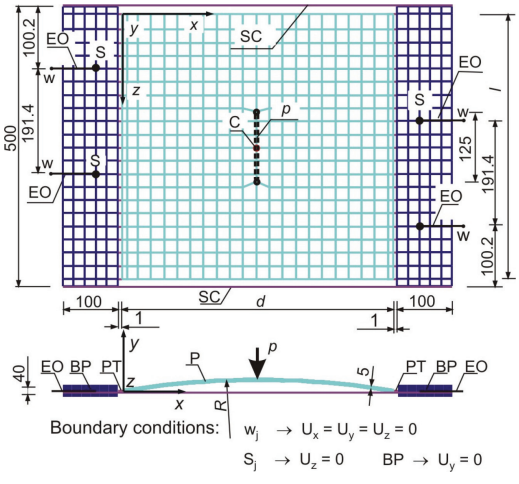

Figure 4. FEM model of experimental shells.

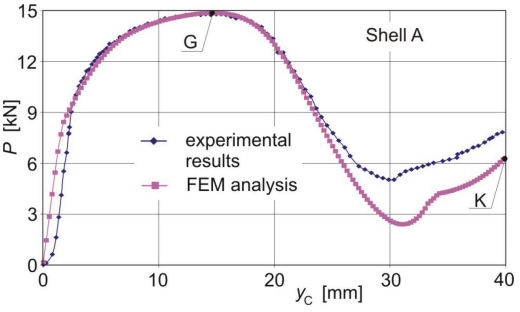

Figure 5. Experimental and numerical load—displacement equilibrium paths.

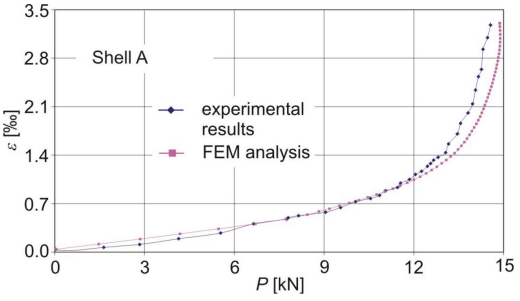

Figure 6. Experimental and numerical deformation paths. ε at bottom surface under point C.

3 SHELL SENSITIVITY ANALYSIS

The conducted experiment led to a detailed analysis of the tested structure behaviour. On the grounds of the observations made a group of parameters deciding about the resistance of the tested system was distinguished. The said parameters comprise: geometrical imperfection parameters, support flexibility parameter, yield point.

In case of similarly made shells, the above mentioned parameters are of a random character and decide about their random resistance. The random resistance of the shell made according to the tested pattern, directly affects its reliability.

Reliability analysis of a structure requires to define basic variables of the tested system. In order to reduce the set of basic variables of the tested shell to the necessary minimum, the sensitivity analysis of the shell was carried out. The sensitivity analysis means to observe changes of the shell ultimate resistance as a result of a change in the values of particular parameters of the tested structure.

The ultimate resistance of the structure is here identified as the maximum load under which the shell loses its global stability.

For completion of the above mentioned sensitivity analysis the elaborated numerical FEM model of the tested shell was used. For every case referring to the established value of the selected basic variable a non-linear analysis of the structure was made.

The analyses, being the numerical simulations of the experiment were carried out by means of FEM—COSMOS/M programme. The comparison of the shell sensitivity was made on the grounds of the obtained in FEM analyses relevant displacement equilibrium paths and the observed ultimate load carrying capacity values P_{ult}.

3.1 *Shell sensitivity to a change of geometrical imperfection parameters*

The analysis of the shell sensitivity to a change in the value of the parameters of its midsurface was preceded by choosing a mathematical model of this surface.

The choice was made by comparing displacement equilibrium paths obtained through numerical analyses, respectively, a shell of a real, measured during tests, surface (R) and shells of surfaces (AF1, AF2, AF3) modeled with functions according to the formulae (1–3). Figure 7 presents the obtained from analyses equilibrium paths for the A shell.

The course of a numerical equilibrium path computed for the shell modeled with the R surface, with real coordinates of the FE nodes practically lines up with the points of the experimental equilibrium path. Thus, the numerical model of the R surface was accepted as the reference model.

The equilibrium paths obtained from numerical analyses, respectively, with models of the midsurfaces of AF1, AF2, AF3 shells line up together, and only slightly differ from the path of the reference model R.

It means that a mathematical model of the real geometry of the tested shell can be a single parameter cylindrical function AF1, described by the formula (1) and this model was accepted for further analysis. In the formula (1) there occur two parameters of d and A. A constant value of the shell width d was assumed along with the random variability of its rise A.

The sensitivity analysis was made on the numerical model corresponding to the tested shell A.

In the FEM analyses performed subsequently various values of the A parameter were taken.

The computation started with the rise $A = A^0 = 22.3$ mm, corresponding to the greatest approximation of the shell surface A. In the following FEM analyses the accepted shell model had the rise: $0.7A^0$, $0.8A^0$, $0.9A^0$, $1.1A^0$, $1.2A^0$, $1.3A^0$ respectively. The displacement equilibrium paths

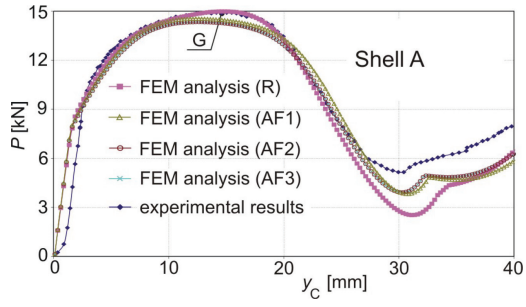

Figure 7. Experimental and numerical displacement equilibrium paths of the A shell.

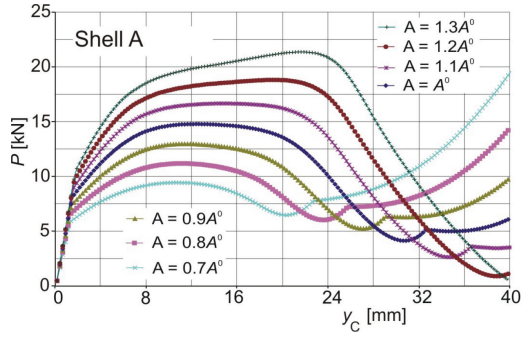

Figure 8. Sensitivity of the shell to geometrical imperfections. Displacement equilibrium paths for various A.

obtained as a result of the computation referring to the central point of the shell are presented in Figure 8.

After analyzing the results obtained it was stated that an increase in the value of the A parameter by 10%, in relation to the input value A^0, results in an increase of the ultimate load P_{ult} by 13.2%. This confirms a great sensitivity of the tested shell to a change of its rise.

3.2 *Sensitivity of the shell to a change in the flexibility of the supports*

Consistently, the sensitivity analysis was carried out on the numerical model of the A shell. It was accepted that the random parameter affecting flexibility of supports is the cross—section field A_T of rods preventing lateral displacement of the shell marked on the model in Figure 4 with the EO symbol.

The A_T parameter value referring to the real shell model A was accepted as the input value $A_T = A_T^0 = 103$ mm^2.

The FEM numerical analyses that followed were made for $0.7A_T^0$, $0.8A_T^0$, $0.9A_T^0$, $1.1A_T^0$, $1.2A_T^0$, $1.3A_T^0$. Furthermore, computations for two edge

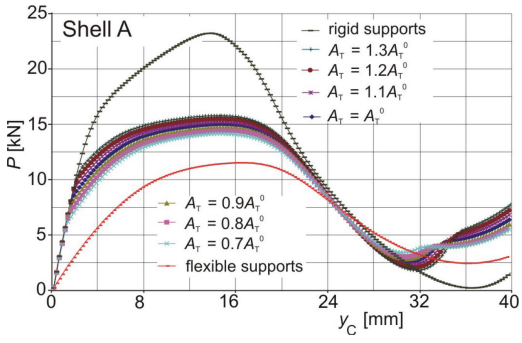

Figure 9. Sensitivity of the shell to a change of the flexibility of supports. Displacement equilibrium paths for various A_T.

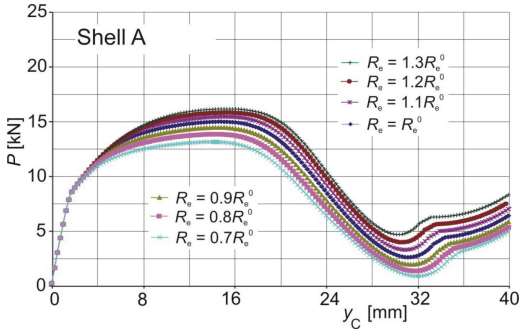

Figure 10. Sensitivity of the shell to a change in yield stress. Displacement equilibrium paths for various R_e.

cases were made, namely, when the supports are not flexible ($A_T = 10^{10}$ mm^2) and with their assumed great flexibility ($A_T = 10^{-4}$ mm^2).

Results of numerical analyses, in a form of the displacement equilibrium paths are shown in Fig. 9.

The analysis of the course of these paths allows for classifying the A_T parameter into a group of factors possessing a strong impact on the ultimate load of the tested shell.

Accepting supports of high stiffness for the numerical experiment, results in a 57% increase in the value of the ultimate load in relation to the value observed during tests. However, 10% fluctuations of the A_T parameter value do not lead to big changes of the ultimate load as was the case of changes in the rise of the A model.

3.3 *Sensitivity of the shell to a change of the yield stress*

The A shell model was subjected to numerical analyses with varying values of the yield stress R_e.

The input value was the mean of the lower yield stress obtained in a tension tests $R_e^0 = \mu(R_{eL})$, see

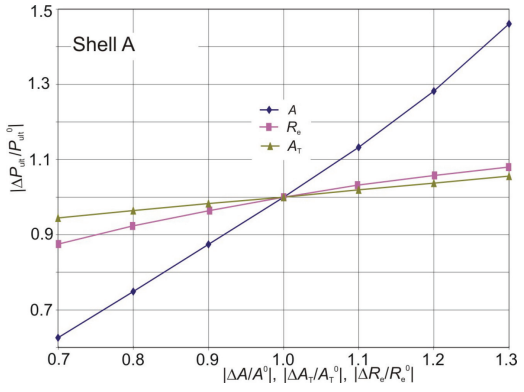

Figure 11. Relative change of the ultimate load P_{ult}.

Table 1. Then, computations for R_e^0, $0.7R_e^0$, $0.8R_e^0$, $0.9R_e^0$, $1.1R_e^0$, $1.2R_e^0$, $1.3R_e^0$ were made.

The results received, in a form of the displacement equilibrium paths are shown in Figure 10. The diagrams compared indicate a monotonic, relatively not big increase in the ultimate load of the shell proportional to the increased value of its yield stress.

4 CONCLUSIONS

The sensitivity analysis made on the numerical model of the experimental shell showed that all the parameters accepted for the analysis and separated through real tests have a significant influence on its ultimate load carrying capacity.

For the analysis a uniform range of the variability of these parameters was accepted, namely, ±30% of the input fixed value with a ±10% increment.

Basing on the results of the analyses, diagrams illustrating the relation between the relative change of the ultimate load carrying capacity and the relative increment of the analyzed parameter were drawn up. The diagrams are shown in Figure 11.

We can see, that within the tested range of the relative variability of parameters an almost linear relation for the two values was obtained, namely for the yield stress R_e and A_T related to flexibility of supports.

Small slope of the graphs related to those variables confirms a small sensitivity of the shell to a change of their values within the accepted, limited range of variability.

The graph obtained for the varying values of the rise of the shell A, significantly differs from the previous ones, it is non-linear and shows great sensitivity to a change of a parameter A value.

Summing up:

1. The shell shows the greatest sensitivity to a change of a parameter related to the geometry of its surface.
2. Another parameter a change of which results in great sensitivity is the material parameter, namely the yield stress.
3. The smallest relative changes of the ultimate load capacity come along with changes of the stiffness of the supports.

It must, however, be remembered that the phenomena observed refer to the accepted for the analysis range of parameter variability identical for each of them. In determining a range of relative variability only a single parameter of real probabilistic distribution of the analyzed random variables was taken into account, that is the mean value.

Making a similar analysis considering additionally a standard deviation when determining boundary values of the variability range of each of the parameters tested, would result in obtaining results that would be more probabilistic.

Nevertheless, the sensitivity analysis presented here allowed to separate a set of significant basic variables, which will be used in other research work on shell reliability.

REFERENCES

CEN 2002. EN 1990: *Eurocode—Basis of structural design*.

Kaliszuk, J. & Waszczyszyn, Z. 2003. Reliability analysis of structures by neural networks. In L. Rutkowski & J. Kacprzyk (eds), *Networks and Soft Computing; Proc. Intern. Conference, Zakopane, 11–15 June 2002*: 754–759. Berlin—Heidelberg: Springer.

Kaliszuk, J., Marcinowski, J. & Waszczyszyn, Z. 2005. Laboratory tests and numerical modelling of large displacements of an elasto—plastic cylindrical shell. In W. Pietraszkiewicz & C. Szymczak (eds), *Shell structures: theory and applications; Proc. Intern. Conference, Jurata, 12–14 October 2005*: 477–480. London: Taylor & Francis.

Kaliszuk, J. 2011. Hybrid Monte Carlo method in the reliability analysis of structures. *Computer Assisted Mechanics and Engineering Sciences* 18 (3): 161–173.

Marek, P., Brozzetti, J. & Gustar, M. 2001. *Probabilistic Assessment of Structures using Monte Carlo Simulation*. Praha: TeReCo.

Melchers, R. E. 1987. *Structural Reliability Analysis and Prediction*. Southampton: Halsted Press.

Nowak, A. & Collins, K. 2000. *Reliability of Structures*. Mc Graw—Hill: Intern. Eition.

Pabisek, E., Kaliszuk, J. & Waszczyszyn, Z. 2004. Neural and finite element analysis of a plane steel frame reliability by the classical Monte Carlo method. In L. Rutkowski, J. Siekmann, R. Tadeusiewicz & L. Zadeh (eds), *Artificial Intelligence and Soft Computing—ICAISC2004*: 1081–1086. Berlin—Heidelberg: Springer.

Papadrakakis, M., Papadopoulos, V. & Lagaros, N. 1996. Structural reliability analysis of elastic—plastic structures using neural Network and Monte Carlo simulation. *Comp. Meth. Appl. Mech. Eng*. 136: 145–163.

This page intentionally left blank

Recent Progress in Steel and Composite Structures – Giżejowski et al. (Eds)
© 2016 Taylor & Francis Group, London, ISBN 978-1-138-02946-0

Reliability level of the buried Main Pipelines Linear Part

S. Pichugin, O. Zyma & P. Vynnykov
Poltava National Technical Yuriy Kondratyk University, Poltava, Ukraine

ABSTRACT: This paper discuss loads and influences, which cause hoop and longitudinal stresses in the walls of the main pipeline linear part. Engineering-geological conditions, where is reasonable account differential settlements and respective longitudinal stresses, are substantiate. Natural and water saturated condition of the loessial loam bilinear models are improved. Stress strain state of the pipeline in the condition of soil local soaking is obtained. Probability density function and other statistics of the input random variables, such as operating pressure, temperature difference, deformation modulus of water saturated soil are developed Probabilistic parameters of the output random variables are obtained with help of Monte Carlo Simulation method. Such output random variables are differential settlements, hoop and longitudinal stresses. Pipeline reliability level is determined in the random variables technique, with help of linearization method.

1 PIPELINE STRENGTH CALCULATION

Hoop σ_h, longitudinal σ_l and radial σ_{rad} stresses make impact in the Main Pipeline Linear Part (MPLP). Radial stresses have relatively small values in the thin-walled high-pressure pipelines, so it used do not take into account (Yong Bai (2001), ASME B31.8-(2003), Eurocode 3 (2007), SNiP 2.05.06-85. (1988)).

Hoop stress are calculated as follow

$$\sigma_h = \frac{nPD_{in}}{2t} \tag{1}$$

where P = internal operating pressure in the pipeline; n = the design (usage) factor for operating pressure (ASME B31.8-2003, Eurocode 3 (2007), SNiP 2.05.06-85. (1988)); D_{in} = pipeline internal diameter; t = pipeline wall thickness.

Calculation of the pipeline wall thickness is almost the same for different codes. The hoop stress σ_h criterion limits the characteristic tensile hoop stress, according to the pipeline steel Specified Minimum Yield Strength ($SMYS$) with accounting of the design (usage) factors, which values are specific for each code.

$$\sigma_h \le \gamma_i SMYS \tag{2}$$

where γ_i = the design (usage) factor specific for each code (ASME B31.8-2003, Eurocode 3 (2007), SNiP 2.05.06-85 (1988)).

Longitudinal stress σ_l value in the MPLP is determined by three main factors: operating pressure P, influence of the temperature deformations and stresses, which caused by MPLP curvature

$$\sigma_l = \mu\sigma_h \pm \alpha E_p \Delta t \pm \sigma_{bend} \tag{3}$$

where μ = Poisson's ratio of the pipe steel; α = linear expansion factor of metal pipes; E_p = pipe steel Young's modulus; Δt = calculating temperature difference, which is extremal difference between MPLP wall temperature during the exploitation and in the moment when pipeline design scheme fixing; σ_{bend} = bending stress in the MPLP.

Bending stress in the MPLP σ_{bend} is composed of stresses caused by elastic bend of the pipeline sections (MPLP follows to the terrain relief) and by stresses caused by differential settlements of the MPLP soil base σ_{dif}

$$\sigma_{bend} = \pm \frac{E_p D_{ex}}{2\rho} \pm \sigma_{dif} \tag{4}$$

where D_{ex} = pipeline external diameter; ρ = pipeline axis curvature radius, which maximal values for each diameter are substantiate in the codes (SNiP 2.05.06-85 1988).

It should be noted, that hoop, temperature and stresses caused by elastic bending are sufficiently analyzed in the Ukrainian and international codes. It has analytical equations and simplified expressions for determination of their values, but stresses caused by differential settlements of the MPLP soil base σ_{dif} haven't such equations. For example, Ukrainian codes proposed to determine efforts from design loads and influences with help

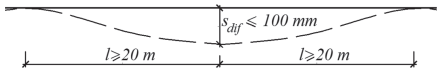

Figure 1. Limit value of the soil basis different settlement according to EUROCODE3–4–3.

of structural mechanics methods for statically indeterminate systems (SNiP 2.05.06-85 (1988)). Also there is recommended to apply software, but there are not specific equations for determining σ_{dif} stresses.

Limit values of the MPLP soil basis different settlements are also not regulated. Instead of Ukrainian and USA, Europe codes (Gresnigt (1986), Eurocode 3 2007) recommend limit value of the soil basis different settlement that is 10 cm on the wavelength 40 m Figure 1.

2 DIFFERENTIAL SETTLEMENTS OF THE PIPELINES OIL BASIS

2.1 *Causes of the pipeline differential settlements*

MPLP soil basis differential settlements lead to additional longitudinal stresses in the pipeline walls, the destruction of anti-corrosion coating, which significantly reduces pipeline durability (Bolotin (1969), Palmer (1972), Gresnigt (1986), Faeli (2010)). In addition, MPLP large deflection may cause violation if the operating condition, which again confirms necessity of the different settlements regulation Figure 1.

It is necessary to understand in such soil conditions impact of the differential settlements significant, and it causes additional longitudinal stresses in the pipes wall. For example, in normal homogeneous soils differential settlements values are very small, and its impact on the MPLP strength and reliability is insignificant (Pichugin (2009)). For pipeline, which basis consist of homogeneous fine sand additional longitudinal stress from different settlements is less than 10 MPa. This is because in normal conditions soil doesn't settling from its own weight, and pipeline weight in most case is less than the weight of excavated soil.

Large values of the MPLP differential settlements is typical for pipeline laying in non-standard soil conditions. Non-standard soil conditions it is when pipeline layer design in areas with the following characteristic features (Zaripov (2000), Palmer (1972), SNiP 2.05.06-85 (1988)): swamp or flooded areas, areas with underground cavities of various nature (mining and mine construction zones, areas with karst cavities, etc.), thawing permafrost areas, landslide territories, seismic zones.

For the Ukraine loessial collapsible soils is one of the most common problem, because such soil occupy 65–70% of the territory. Such problem is especially urgent for the southern region, where loessial layer reaches 45…50 m, and the value of the soil collapse from its own weight may occur 1…2 m (Shokarev (2007)) Figure 2.

Figure 2. Broadening of the loessial soils through the Ukraine territory.

2.2 *Loessial soil collapse effect under the pipeline*

Soil—pipeline interaction in the most cases is modeled by beam on elastic Winkler foundation (Bolotin (1969), Palmer (1972), Pichugin (2009)). In such formulation soil execute function of the space spring supports, which set limits on the MPLP movements. Movement resistance mostly depends on soil deformation modulusE_s. Nevertheless, such formulation is suitable only for standard soil conditions, where pipeline settlements directly proportional to the soil base resistance.

Collapsible soil in natural state is quite well foundation for buildings and structures, but strength and deformation soil characteristics have property to reduce significantly as result of thesoaking. Water saturated soil has a collapse property—soil volume reducing under additional loads or even its own weight. Soil in the natural condition has follow compressive curve Figure 3a. Compressive curve has 3 sections: close to linear section AB—it has small reducing of the porosity ratio (consolidation isn't occur); curve section BD—it corresponds to soil consolidation under pressure that exceeds soil structural strength; section DF—unloading (Zhuk2006).

Saturated loessial soil has typical compressive curve with 4 sections Figure 3b: section AB—settling in the natural state; section BC—soil collapse as result of soaking; section CD—soil settling with broken structural bonds (further consolidation); section DF—unloading. Should be noted that soil collapse occurs only by soil characteristics reducing, without additional load applying.

We propose to limit soil deformation diagram in the second section (point C), if take into account

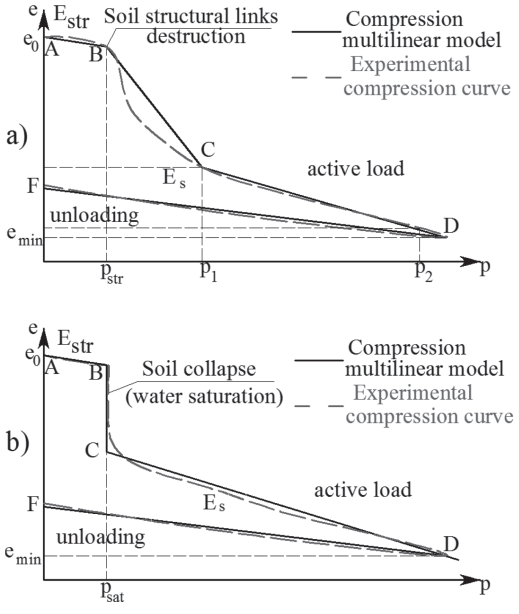

Figure 3. Compression curve of the loessial soilinnatural (a) andwatersaturated (b) condition.

MPLP laying features and soil deformation, which cause longitudinal stresses in the pipeline wall. It is reasonable to consider case when soaking occurs after pipeline laying and additional load is absence. In addition, it is necessary to consider the most adverse soil soaking case, when soaking happen in the some points of the pipeline trace, and it is absent in the other—local soaking.

Complicated soil models using lead to significant complication of calculations, also there is almost impossible to use analytical methods. Taken into account previously experience of pipeline strength calculation, Finite Elements Method (FEM) is reasonable to use in such problems (Seleznev (2002), Faeli (2010)). Problem of the soil base collapse needs accounting of the physical and geometrical nonlinearity, so it is reasonable to use Ansys software.

2.3 *Pipeline stresses caused by soil collapse*

Soil collapse occur as result of local soaking, spot (linear) or square may be respective water sources. Main pipelines usually lay far from cities and countries, so respective water sources is follow: irrigation areas, river overflow places; MPLP crossing with under and over ground communications (sewage collectors, water and irrigation pipelines).

One of the biggest problem during FEM treatment is substantiation of the compressible strata under the pipe. In standard soil conditions, where soil hasn't specific properties, engineering-geological surveys are conduct on the 1 meter deeper than the expect pipeline bottom. But for loessial collapsible soils is necessary to determine the characteristics of all layers that capable forcollapse. Compressible strata is reasonable to limit by layer, where collapsible property is absent Figure 4 (soil 5).

Soil profile typical for Poltavaregion is on the Figure 4. Soil profile consists of soil1– humifiedloam; soil 2 – loessialloam; soil 3 – loessialloam; soil 4 – loam; soil 5 – loam, respective characteristics is in the Table 1.

Should be noted, that collapsible soil characteristics may be different in better or worse, compressible strata may be deeper or it can consist non-collapsible layers. So obtained results from our soil profile is just some estimations for specific geological conditions, but proposed models are advisable to use.

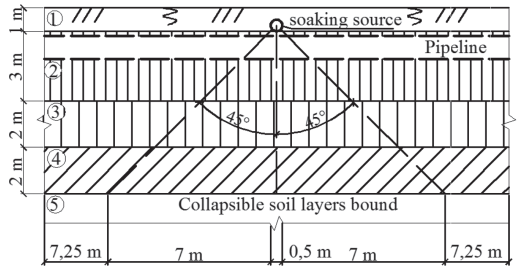

Figure 4. Soil profile typical for Poltava region.

Table 1. Averaged characteristics of loessial collapsible soil of Poltava region.

Soil characteristics		Soil 1	Soil 2	Soil 3	Soil 4	Soil 5
Layer thickness, h, m		1,0	3,0	2,0	2,0	–
Soil density, ρ, kg/m^3		1500	1500	1670	1740	1810
Dry density, ρ_d, kg/m^3		–	1310	1420	1470	1570
Saturated soil density, ρ_{sat}, kg/m^3		–	1770	1840	1870	–
Void ratio, *e*		–	1,05	0,89	0,84	0,69
Relative collapsibility, ε_{sl},%, for pressure, P, MPa	0,05	–	1,4	0,5	0,3	–
	0,10	–	2,5	0,9	0,6	–
	0,20	–	4,4	1,5	1,0	–
	0,30	–	5,5	1,9	1,3	–
Deformation modulus in dry condition, E_s, MPa		–	8	12	14	17
Poisson ratiodry soil, μ		–	0,37	0,36	0,35	–
Poisson ratiowet soil, μ		–	0,45	0,41	0,4	–

On Figure 4 is also shows MPLP crossing with spot water source (irrigation pipelines for example). Soaking area spread from top to bottom in a cone. The angle of the line, which limits the soaking zone in loess loam, is $\beta = 45°–55°$ (Zhuk (2006), Shokarev (2007)). Therefore, MPLP section that is necessary to consider in the calculations can be determinate, in our calculation we accept 30 m section length. We accept 3 m width of the soil strata.

Soil has been modeled in natural and water saturated state. Pressure under the MPLP is almost equal to the pressure in the soil massif from soil own weight. Therefore, in the natural condition soil settlements must follow to 0.If we set dependency diagram "pressure P – relative strain ε" in the linear form, with accounting only soil deformation modulus E_s, settlements from soil own weight will have significant values, it is unacceptable. Therefore, necessary to introduce parameter that eliminates soil settlements from its own weight. We propose to use soil structural strength P_{str} as such parameter for soil in natural (dry) condition. For soil 2 in dry condition structural strength value is $P_{str} = 32$ kPa. When pressure reaches P_{str} value, we propose linear dependence between pressure and settlements, where soil deformation modulus is the main parameter Figure 5.

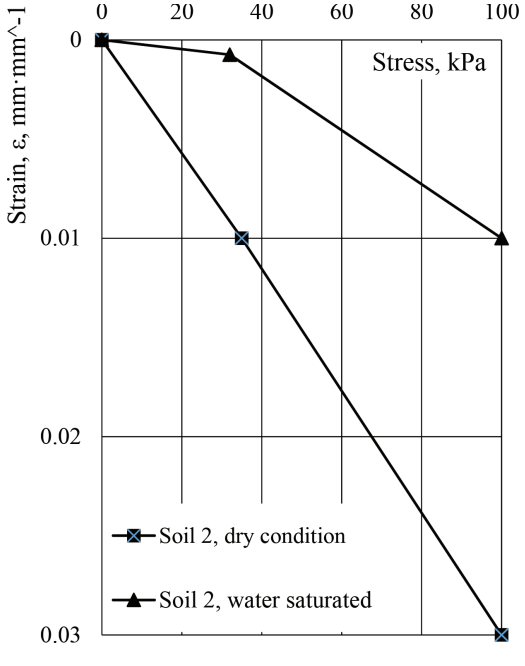

Figure 5. Bilinear dependence diagram "pressure P – relative strain ε" for soil 2 in dry condition (1) and water saturated condition (2) that used in the Ansys calculations.

In Ansys is absent soil direct models, but there are a lot useful models that modeling some required properties, such as elasticity, bilinear or multilinear plasticity, so bilinear hardening model is sufficiently precise, and quite simple in the same time.

Multilinear dependence diagram "pressure P – relative collapsibility strain ε_{sl}" is the most accurate represent collapsible properties of the loessial soil. Such diagram is obtained during soil testing in uniaxial compression device. Multilinear diagram is unuseful for further probabilistic analysis. Therefore, it is advisable to use bilinear depending diagram "pressure P – relative collapsibility strain ε_{sl}". In this case point of diagram fracture is very important, we propose to use average value of the pressure in the each soil layer as such point. That means soil soaking is occur when additional load is absent. For soil 2 in saturated condition diagram fracture point is $P = 35$ kPa.

On Figure 5 is shown that saturated soil has much larger deformations then soil in dry condition. Soil 3 and soil 4 have typical diagram from Figure 5 but with accounting data from Table 1.

In calculations accepted hypothesis that pipeline deformation is equal to the soil basis deformations (Bolotin (1969), Palmer (1972), Zaripov, R. (2000), Seleznev (2002), Pichugin (2009)). Geometrical parameters of the MPLP is follow $D_{ex} = 1020$ mm, wall thickness $t = 9{,}6$ mm. Internal operating pressure $P = 4{,}9$ MPa (Pichugin (2014)). Substantiation of the temperature difference value needs particular attention. We propose to use average monthly maximum temperature of the soil surface $t^{av.max}_{soil} = 42°C$(Kinash 2001) and average pipeline temperature $t_p \approx 8–12°C$, with accounting of the transported product temperature and soil at respective deep (Kinash (2001)). Therefore, temperature difference value is $\Delta t = 32°C$. Pipes are manufactured of steel grade K55, $SMYS = 410$ MPa.

Ansys calculations were made with account of the physical and geometrical nonlinearity, deterministic results are follow Figure 6: soil collapse under the pipeline in the soaking zone is 27,8 mm, pipeline settlements in zones, where soil in natural

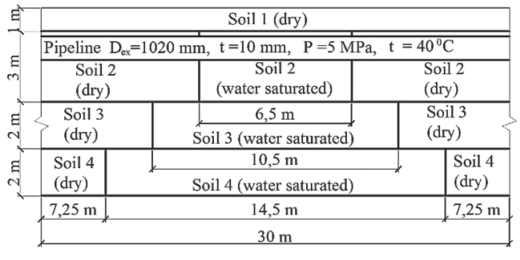

Figure 6. Soil profile division on structural elements for Ansys calculation.

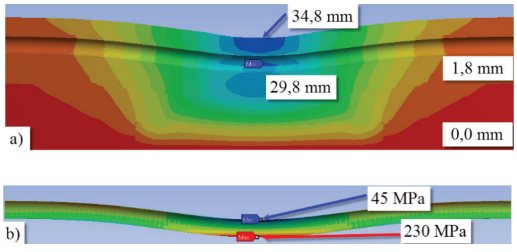

Figure 7. Pipeline local soaking in collapsible soil modelling: soil strata settlements (a), pipeline longitudinal stresses (b).

condition, is about 1,8 mm. Settlements difference is 26 mm Figure 7a. Hoop stresses is 268 MPa, which corresponds exactly to Equation 1, longitudinal stresses is 230,7 MPa. It is easily to obtain value of the longitudinal stresses, which caused by MPLP differential settlements. From Equation 3 such stresses is σ_{dif} = 69 MPa.

Such value of the σ_{dif} is high for relative settlements level, but it is explained by small soaking zone and very high curvature as result. Value of the σ_{dif} in the same soil profile for longer soaking zone (≈ 30–50 m) is about 40 MPa. Despite this, pipeline differential settlements in the collapsible soil cause significant longitudinal stresses. Short area of soaking is especially dangerous, because it leads to the formation of pipeline axis large curvature.

3 PIPELINE RELIABILITY ESTIMATION BY THE HOOP AND LONGITUDINAL STRESSES PARAMETER

The calculation of pipeline streng this usually performed by assumption that its properties and the properties of the soil foundations are deterministic (Gresnigt (1986), Yong Bai (2001), Seleznev (2002)). But this statement is not always true. Firstly, the properties of soil base depend on many factors. Those factors are not exposed directly accounting, and therefore have a random character. Secondly, external loads, material properties and geometrical dimensions of the pipe depend on a number of different, poorly controlled and difficult interacting causes that are also changing randomly (Pichugin (2009), (2014)).

In view of above and the current development of the construction industry, it is actual calculation of MPLP by the probabilistic methods. Stresses and deformations of MPLP laid in a static heterogeneous soil are Random Variables (RV).That fact must be accounting for pipeline strength calculations. Also, reliability levels by the hoop and longitudinal stresses must be obtained.

Firstly, probabilistic approach to calculate MPLP strength was used by Bolotin (Bolotin (1969)). He is focused on the solution of the differential equation of the pipeline curved axis with random parameters. We propose an engineering method for calculating MPLP reliability. It is based on the idea of rational compromise between accuracy and simplicity of probabilistic calculations

Random variables aren't only possible mathematical tools for calculating pipelines strength and reliability. Standard "deterministic" apparatus in which random factors are not taken into account also may use. But it can't be forgotten that it gives approximate schematic description of the system, its some "averaged" values. In-depth study of the system such deviations are necessary to consider using the probabilistic approach.

Main difference between such approaches is given on Figure 8. There is large number of mathematical tools to estimate construction reliability: linearization; Lichov overrun method; random arguments replacement method (numerical integration); Monte Carlo Simulation; Response Surface Method, Point Estimate Method (FO-PEM & A-PEM) and First Order Reliability Method (A-FORM) (Bolotin 1969, Fenton 1997, Avsar 2004, Phoon 2008, Pichugin 2009, 2014, Zotsenko 2011).

Each method is convenient tool for solving a specific problem. Monte Carlo Simulation (MCS), Response Surface Method (RSM) and Point Estimate Method (PEM) are the most universal of them. Such methods use during the investigation of complex nonlinear systems, including problem solution with help of FEM.

Monte Carlo Simulation consist in, that set of variables is organized with help of random number generator according to the specific density functions. Values of the output function are calculated for obtained set of variables. These values add to memory and after sorting in inter-

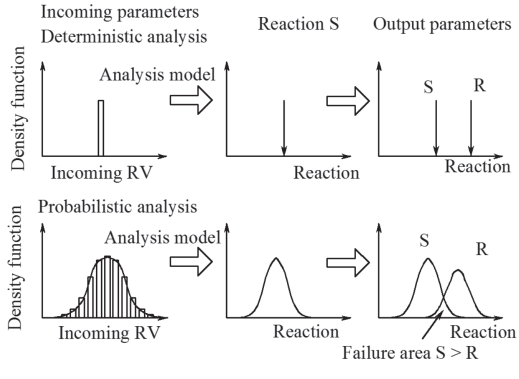

Figure 8. Difference between deterministic and probabilistic calculation method of the building constructions.

val, these values forming experimental histogram. After realization of sufficiently large number of RV output function distribution density is possible to obtained.

To obtain MPLP reliability level by the parameter of hoop and longitudinal stresses is necessary to obtain output function at least from six input arguments, which are RV: operating pressure fluctuation, variations of the average monthly maximum temperature of the soil surface and average pipeline temperature, probabilistic parameters of the collapsible soil deformation characteristics. Obtained output function is extremely complicated, especially if we take into consideration correlation between input RV. But if we know input RV probabilistic parameters, output RV density function and other statistics is possible to obtain, with help of *Monte Carlo Simulation*, which is implemented in Ansys. Hoop and longitudinal stresses output RV is easily to compared with steel yield strength RV.

Internal pressure fluctuation caused by technological factors during normal pipeline operation. Those factors connect with work of the compressor equipment and hydraulic features of the whole pipeline system. Those factors has stochastic nature and cause random overloads of the pipeline construction.

Internal pressure fluctuation is obtained from main pipeline section observations for 3 month. General sampling is 3436 pressure values, which are obtained for 3 month (Pichugin (2014)). Pressure has changed significantly in both upward and downward from nominal pressure value even during stationary pipeline operation.

There had been obtained 11 intervals of the pipeline stationary operation mode during the observation. To improve the reliability of the results more than 20 measuring had to get into interval, and observation period had to be over 12 hours. Observation results is follow: pressure fluctuation has normal density function Table 2. Variation ratio average value from experiment is 6,9% (Pichugin (2014)), which we will use further.

Mostly of the temperature difference RV probabilistic parameters is possible to obtain as result of processing of the meteorological stations long-term climate observations (Kinash 2001) or direct measurements methods. Temperature statistics are in the Table 2.

Existing experience of the geotechnical problems probabilistic study shows that RV of the soil mechanical characteristics even in the natural condition has high variation ratio 20–30%, also it usually has lognormal density function (Fenton (1997), Phoon (2008), Zotsenko (2011)). Soil in saturated condition has even higher variation ratio, because it soaking unevenly. In our research, we apply simplified model of the soil mechanical characteristics RV, Table 2. It is made to simplify calculations and to obtain illustrative representation of results. In future, we will develop soil mechanical characteristics probabilistic model.

Output RV density functions is shown in Figure 9, Table 3. It obtained with help of *Monte Carlo Simulation.*

Obtained density functions for output hoop and longitudinal stresses RV allow estimating pipeline reliability easily in the random variables technique. At this stage, linearization method is reasonable, because final equations is quite simple. All of the input functions has normal density function, respectively output functions has normal density too. Therefore, pipeline reliability is estimating as follow

$$\tilde{Y} = \tilde{R} - \tilde{S} = \tilde{\sigma}_y - \tilde{\sigma}_h(\tilde{\sigma}_l) \geq 0 \qquad (5)$$

where $\tilde{R}$ = pipeline steel strength distribution function; $\tilde{S}$ = hoop (longitudinal) stresses distribution function.

Table 2. Probabilistic characteristics of input random variables—external loads and influences.

Input probabilistic parameters/random variables	Density function	Mathematical expectation	Standard deviation	Variation ratio
Operating pressure, P	Normal	4,9 MPa	0,35 MPa	6,9%
Soil surface temperature, $t^{av.max}_{soil}$	Normal	42 °C	3,1 °C	10,0%
Pipeline temperature operating condition, t_p	Normal	10 °C	1,0 °C	10,0%
Saturated soil 2 initial deformation modulus, E_s	Normal	3,5 MPa	0,875 MPa	25,0%
Saturated soil 3 initial deformation modulus, E_s	Normal	4,5 MPa	1,125 MPa	25,0%
Saturated soil 4 initial deformation modulus, E_s	Normal	8,0 MPa	2,0 MPa	25,0%

Mathematical expectation and standard deviation respectively:

$$\overline{Y} = \overline{R} - \overline{S} = \overline{\sigma}_y - \overline{\sigma}_h(\overline{\sigma}_l) \quad (6)$$

$$\hat{Y} = \hat{R} - \hat{S} = \hat{\sigma}_y - \hat{\sigma}_h(\hat{\sigma}_l) \quad (7)$$

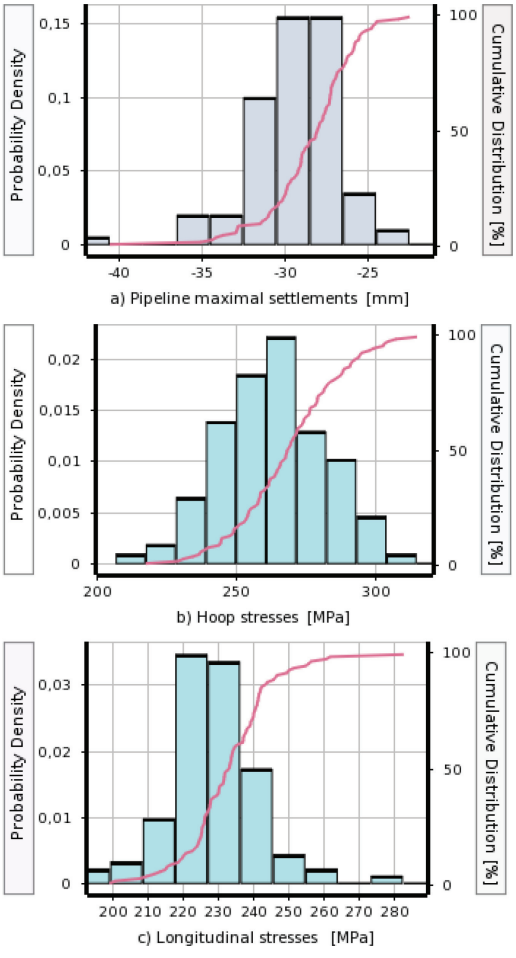

Figure 9. Probability density and cumulative distribution of pipeline reliability output random variables: pipeline maximal settlements (a), hoop (b) and longitudinal stresses.

Safety characteristic:

$$\beta = \frac{\overline{Y}}{\hat{Y}} = \frac{\overline{\sigma}_y - \overline{\sigma}_h(\overline{\sigma}_l)}{\sqrt{\hat{\sigma}_y - \hat{\sigma}_h(\hat{\sigma}_l)}} \quad (8)$$

Reliability level:

$$P(\beta) = 0{,}5 + \Phi(\beta) \quad (9)$$

where $\Phi(\beta)$ = Laplace function safety characteristics respective value β.

Should be noted, that the most important building objects in Ukraine must have failure probability less then $Q = 1 \cdot 10^{-6}$ according to the national codes (DBN V.1.2-14-2009). But if the construction failure leads only to economic losses, there are possible to reduce reliability level based on the conditions to minimize the total cost of manufacture, installation, operation and the elimination of losses from possible failure. Therefore, MPLP has high enough reliability level according to obtained results from Table 4.

As we mentioned, considered soil profile, which is typical for Poltava region, is some average pattern of the possible soil conditions. Compressible strata may be much deeper (Shokarev (2007)), and soil characteristics may change in the wide range. So, soil collapse value may be much higher.

Table 4. Pipeline reliability level by the hoop and longitudinal stresses.

Pipeline reliability parameters	Longitudinal stresses, σ_l	Hoop stresses, σ_h
Mathematical expectation of reliability function, $\overline{Y}$	257,1 MPa	221,5 MPa
Standard deviation of reliability function, $\hat{Y}$	50,6 MPa	52,5 MPa
Safety characteristic, β	5,08	4,2
Failure probability, $Q(\beta)$	$1{,}7 \cdot 10^{-7}$	$1{,}33 \cdot 10^{-5}$
Reliability level, $P(\beta)$	0,9999993	0,9999966

Table 3. Probabilistic characteristics of pipeline reliability output random variables.

Output probabilistic parameters/random variables	Density function	Mathematical expectation	Standard deviation	Variation ratio
Steel yield strength, R	Normal	490	49	10,0%
Pipeline maximal settlements, S, mm	Normal	–28,5 mm	2,7 mm	9,5%
Pipeline hoop stresses, σ_h, MPa	Normal	232,9 MPa	12,6 MPa	5,4%
Pipeline longitudinal stresses, σ_l, MPa	Normal	268,5 MPa	18,8 MPa	7,0%

4 CONCLUSIONS

Pipeline differential settlements and respective longitudinal stresses is reasonable to account only in the non-standard soil condition, especially in the loessial collapsible soils.

Full collapsible strata must be taken into consideration, when differential settlements are calculating. Soil bilinear models is the most appropriate for deterministic and probabilistic differential settlements calculations.

Pipeline differential settlements in the soil profile, which is typical for Poltava region, is 26 mm, and it cause 69 MPa longitudinal stresses. It indicates about significant impact of the differential settlements on the pipeline strength. Short area of soaking is especially dangerous.

Pipeline failure probability by the longitudinal and hoop stresses parameters is $Q(\beta) = 1{,}7 \cdot 10^{-7}$ and $Q(\beta) = 1{,}33 \cdot 10^{-5}$ respectively, which indicates that pipeline high enough reliability level in such soil conditions. Nevertheless, it can be significantly reduce when soil condition is worse.

REFERENCES

ASME B31.8-2003. 2003. New York: American Society of Mechanical Engineers.

Avsar S. 2004. Six sigma quality improvement of compaction at the New Doha International Airport Project. In M. Bakker & G. Bartolomeeusen & J. Vanmechelen. *Terra et Aqua, No. 103*.14–22. The Hague.

Bolotin V.V. 1969. *Statistical methods in structural mechanics*. San Francisco: Holden-Day.

DBNV.1.2-14-2009. 2009. *General principles of reliability and constructive safety of buildings, structures and foundations ensuring*. Kyiv: Мінрегіонбуд.

EN 1993-4-3. 2007. Eurocode 3: Design of steel structures - Part 4-3: Pipelines.

Faeli, Z. 2010. Allowable Differential Settlement of Oil Pipelines. In Ali Fakher & Seyed Reza MaddahSadatieh. *International Journal of Engineering (IJE), Vol. 4: Issue 4*. 308–320.

Fenton, G.A. 1997. *Probabilistic Methods in Geotechnical Engineering*. Utah.

Gresnigt, A.M. 1986. Plastic Design of Buried Pipelines. *HERON, Vol. 31, No. 4*. 113. Delft.

Kinash, R. 2001. *Temperature mode of air and soil in Ukraine*. Lviv: Видавництвонауково-технічноїлітератури.

Palmer, A. 1972. Settlement of a pipeline on thawing permafrost. *Journal of the Transportation Engineering Division, Vol. 98, No.3*. 477–491. New York: American Society of Civil Engineers.

Phoon, K.K. 2008. *Reliability-based design in geotechnical engineering. Computations and applications*. New York: Taylor & Francis.

Pichugin, S.F. 2009. Calculation of the reliability of steel underground pipelines. In A.V. Makhin'ko. Strength *of Materials.– Springer Science,* Vol. 41, No. 5. 541–547. Kyiv.

Pichugin, S.F. 2014. Method for reliability estimation of the main pipeline steelwork structure. In O. Zyma. *Steel constructions, Vol. 20, No.2*. 77–87. Makiyivka.

Seleznev, V. 2002. Implementation of numerical simulations for integrated estimation of main gas pipeline states. In V. Aleshin & G. Klishing. *Papers book of 11th International Colloquium "Reliability of High-pressure Steel Pipelines" (Prague, Czech Republic) 28 February and 1 March (CD version)*. 12 p. Prague: CzPS.

Shokarev, V. 2007. Interaction of the artificial bases with Collapsing Soils. Geotechnical Engineering in Urban Environments: Proc. of 14th European Conf. on Soil Mechanics and Geotechnical Engineering (Madrid, 2007). 481–486. Rotterdam: Millpress Science Publish.

SNiP 2.05.06-85. 1988. *Main pipelines.* Moscow.

Yong Bai. 2001. *Pipelines and risers.* Oxford: Elsevier.

Zaripov, R. 2000 Maintenance of strength of main pipelines in non-standard conditions. In G. Korobov & R. Khasanov & V. Chichelov. *Intellectual service for Oil & Gas industry/Analysis, Solutions, Perspectives*. 247–258. Ufa.

Zhuk, V. 2006. Features of interaction of the frame building with loess collapsible soil base. *XIII Danube-European Conference on Geotechnical Engineering "Active Geotechnical Design in Infrastructure Development"*. 711–714. Ljubljana.

Zotsenko, M. 2011. Evaluation of Failure Probability of Soil Cushions. In Y. Vynnykov & M. Kharchenko. *Geotechnical Safety and Risk: Proc. of the 3rd International Symposium on Geotechnical Safety and Risk (ISGSR 2011)*. 249–257. Munich.

Recent Progress in Steel and Composite Structures – Giżejowski et al. (Eds)
© 2016 Taylor & Francis Group, London, ISBN 978-1-138-02946-0

Influence of the bearing capacity and reliability of connections and nodes on the bearing capacity and reliability of complex bar structures

Z. Kowal
Faculty of Civil Engineering and Architecture, Kielce University of Technology, Kielce, Poland

ABSTRACT: The study presents the quantile method as a means of estimating the influence of the bearing capacity and reliability of connections and nodes on the bearing capacity and reliability of spatial bar structures. It is shown that on the basis of structural reliability analysis performed with the quantile method, in the design process, it is possible to reveal the effect produced by the reliability of nodes and connections, which is a potential source of failures and collapses of complex structures. It is also demonstrated how to increase the bearing capacity and reliability of bar structures by means of coupling bar structures of statically determinate trusses into statically indeterminate complex structures with enhanced bearing capacity and reliability. It is shown that meeting the postulate that the reliability of connections should be greater than that of connected bars is crucial for preventing failures and collapses. Those happen also due to the redistribution of forces caused by bars being excluded from Minimal Critical Sets (MCSs) that occur in Kinematically Admissible Failure Mechanisms (KAFMs) of the structure when connections fail under load.

1 INTRODUCTION

Currently, decisive elements of complex structures are dimensioned on the basis of conventional structural mechanics and materials strength, using conventional algebra. The problem lies in the fact that design capacities N_o of elements and of connections of those are quantiles N_k of bearing capacity distributions $N_k = E(N) - t\,D(N)$ drawn from statistical normal distribution, having the expected reliability index of the order of $t = 3.8$ (Fig. 1). The results of algebraic operations on quantiles differ considerably from the results of operations with the use of conventional algebra. Errors resulting from conventional estimation of the load bearing capacity lead to structural failures and collapses, especially those of prefabricated steel and concrete complex structures. It is possible to estimate, in an objective way, the capacity and reliability of structures composed of many elements by using the quantile method This method can, and should be employed for the analysis of all Kinematically Admissible Failure Mechanisms (KAFMs) in complex building and bridge structures. In the investigations into random bearing capacity of elements of complex structures normal distribution was used (Standard normal table). The advantage of normal distribution in the structural reliability investigations for complex structures concerns good estimation of bearing capacity distribution and lower–bound estimation of the reliability of structural systems. That results from the way the theoretical formula is constructed. In the formula (Fig. 1), the failure rate q of the quantiles of bearing capacity N_k is integrated from $-\infty$ to $+N_k$. This effect can be used in works supervision to detect the lack of bolts, weld flaws, and for repairs of different defects. Normal distribution is especially suitable for monitoring the reliability of complex structural systems, namely to optimize their bearing capacity and reliability. A particular advantage of the normal bearing capacity distribution lies in the fact that it is easy to describe and estimate the trends in bearing capacity and reliability that accompany the adopted geometric topology of the structure.

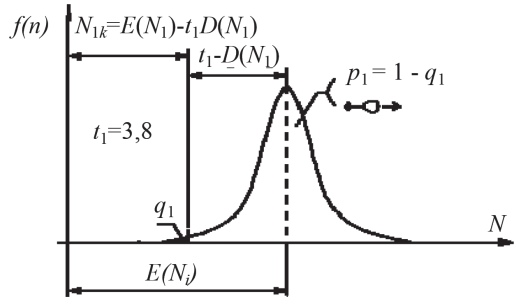

Figure 1. Theoretical distribution of the bearing capacity N and reliability p = (1 – q) of the decisive elements of the structure.

In figures and formulas, the following notation is used, which is in accordance with (Kowal 2014):
$E(N_1)$ – expected (mean) bearing capacity of the decisive element, $v_1 = D(N_1)/E(N_1)$ – coefficient of variation in the bearing capacity of the element,

$D(N_1) = \sqrt{D^2(N_1)}$ – standard deviation of the bearing capacity of the element,
$D^2(N_1)$ – variance of the bearing capacity of the element,
$v = v_1/n^{0,5}$ – coefficient of bearing capacity variation of a coupled bundle (Kowal 2014) of n elements,
$N_k = E(N_1)\,[1 - tv_1]$ – quantile of the bearing capacity of a single element,
$N_k = n\,E(N_1)\,[1 - tv_1/n^{0,5}]$ – quantile of the bearing capacity of a bundle of n stochastically identical elements,
$q_i = 1 - p_i$ – failure rate of the elements of the structure,
$p_i = 1 - q_i$ – reliability of the decisive elements.

In this study, the reliability index is denoted as a letter t, instead of β, to emphasise that it is not the known effect of the structure deterioration level (PN-EN 1990:2002) that is considered, but the influence of the complex structure geometric topology on bearing capacity and reliability.

The term decisive elements is used for bars, connections and nodes. When their random bearing capacity is equal to zero, that leads to the failure of the statically determinate structures, or to the weakening of KAFM in statically indeterminate structures, which leads to failures of different range. The basic principle, termed postulate 1, states that bearing capacity and reliability of connections and nodes must be greater than those of connected bars. However, many connections of two-dimensional and three-dimensional structures, which are commonly used, and some of which have been even patented, do not satisfy postulate 1. Lower extension of connections and nodes is a hidden cause of failures and collapses, especially of bar structures, also the statically indeterminate ones. Meeting postulate 1 is also intended to prevent bar exclusion from KAFM before their bearing capacity is made use of in complex statically indeterminate structures (Kowal, 2013). Bar exclusion from KAFM due to the failure of connections results in the redistribution of cross-sectional forces in bars and is a source of obscurity, which can be an obstacle to revealing causes of failures or collapse of complex structures.

Analysis of the output of technical sciences, reflected in specific standards, justifies making an assumption that bearing capacity of decisive elements dimensioned on the basis of specific standards satisfies the recommendations stated in the general standard (PN-EN 1990:2002). Those concern reliability indexes of structural elements of the classes: RC1-t = β = 3.3; RC2-β = 3.8; RC1-β = 4.3, which refer to 50-year service life of the decisive elements of the structure.

It is possible to adopt an axiom, resulting from the evolution of relevant standards, that decisive elements dimensioned according to currently relevant standards meet the reliability recommended in one of the three reliability classes given in the general standard (PN-EN 1990:2002). That allows estimating the influence of the geometric topology of the structure on the bearing capacity and reliability of structures composed of may decisive elements. That is a good starting point for structure optimisation and for upgrading the existing structures using the methods of reliability engineering (Kowal 2014).

It is of particular importance to remember that lower reliability of connections and nodes when compared with the bearing capacity and reliability of bars integrated with connections produces a hidden impact on structural failures. Disregarding that leads to an error often found in complex structures. The error can be enhanced by automatic dimensioning of connections, which is adjusted to forces determined in computer simulations, and not to finally adopted bar cross-sections.

2 EFECT OF CONNECTIONS ON THE RELIABILITY OF STATICALLY DETERMINATE BAR STRUCTURES

The influence of bearing capacity of connections and nodes on the bearing capacity and reliability of bar structures is shown on the example of gravitationally loaded, statically determinate truss presented in Fig. 2, in which nodes from 1 to 9, and also 10 and 16 are tied by transverse bracings.

Statically determinate truss of RC2 class, acc. the example in Figure 2, is composed of decisive elements, each of which has the reliability index t = 3.8. Decisive elements include 29 bars, 58 bar-to-node connections, and 16 nodes. A failure of an arbitrary decisive element results in the truss failure.

The quantile of bearing capacity N_k expected on the basis of the standard (PN-EN 1990:2002) is estimated from formula (1):

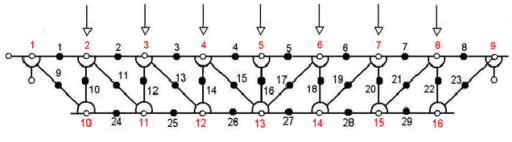

Figure 2. Example of statically determinate truss composed of 29 bars, 58 connections and 16 nodes.

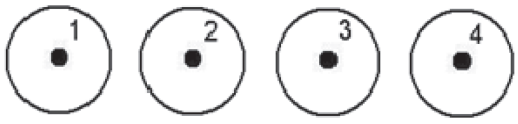

Figure 3. Serial model of the reliability of decisive elements: 1) bars, 2), 3) connections, and 4) nodes.

$$N_k = E(N)[1 - t_2 v] \tag{1}$$

The quantile N_k of the bearing capacity of the elements having the reliability index $t_2 = 3.8$ corresponds to the design bearing capacity estimated according to relevant standards (PN-EN 1993:2006 Eurocode 3).

Bars 1 (Fig. 3) can also be excluded from the structure by the failure of connections 2 o3, or of node 4.

Example 1. Estimate reduction in the bearing capacity of statically determinate truss of RC2 class (Fig. 2). Expected reliability (PN-EN 1990:2002) of each of the decisive elements dimensioned on the basis of the standard (PN-EN 1993:2006 Eurocode 3) is: $p_i = 0.999\,927\,652$. The failure rate of the elements is: $q_2 = 1 - p_2 = 0.000\,072\,348$.

Estimate the reliability p of the truss, in which n = 29 bars + 2 × 29 connections + 16 nodes are found. Those are n = 103 decisive elements altogether, each of which has exemplary variation coefficient of the bearing capacity v = 0.06 and the reliability index (PN-EN 1990:2002) $t_2 = 3.8$. The failure rate q of the truss is: $q = \sum q_i = nq_2 = 103 \times 0.000\,072\,348 = 0.007\,451\,844$. The reliability p of the truss is: p = 1 – q = 0.992,548,151. The reliability index (Standard normal table) of the truss is reduced to: $t_j = 2.434{,}71 < 3.8$.

Conclusion 1. The truss is not compliant with the standard (PN-EN 1990:2002) that recommends the reliability index $t_2 = 3.8$.

A decrease in the truss bearing capacity in relation to the expected one resulting from standard calculations (PN-EN 1993:2006 Eurocode 3) is computed using formula (2) acc. (Kowal 2013):

$$\begin{aligned} s &= [1 - t_2 v_i] : [1 - t_j v_i] \\ s &= [1 - 3.8 \cdot 0.06] : [1 - 2.4347 \cdot 0.06] = 0.904 \end{aligned} \tag{2}$$

Conclusion 2: To maintain the recommended reliability index $t_2 = 3.8$ of the system, it is necessary to increase the bearing capacity and reliability of all decisive elements of the truss.

In study (Kowal 2013), the way of dimensioning decisive bars to maintain the recommended (PN-EN 1990:2002) reliability class of complex structures was given. That was done on the basis of the theorem (Kowal 2013): For a statically determinate structure, composed of n decisive elements, to obtain the reliability p, which is greater than or equal to the standard reliability (PN-EN 1993:2006 Eurocode 3, Standard normal table) it is necessary and it is sufficient that the sum of failure rates $\sum q_i$ of the decisive elements is lower than the admissible failure rate q of the load carrying structure acc. formula (3):

$$\Sigma q_i < q_2 = 1 - p_2 \tag{3}$$

Example 2. Estimate the necessary increase in the bearing capacity of the truss elements acc. Example 1 to obtain the reliability of RC2 class. The reliability of the elements should be as follows:

$p = 1 - q_2$. n = 1 – 0.000,072,348: 103

p = 1 – 0.000,000,702,408 = 0.999,999,297,592.

The necessary reliability index of each of 103 elements is: t = 4.824,32 > 3.8.

Conclusion 3: The design bearing capacity N_0 of truss elements, estimated on the basis of relevant formulas should be increased by means of coefficient s, acc. formula (4):

$$s = [1 - (t_2 = 3.8)v] : (1 - 4.82432v) = 1.086 \tag{4}$$

Due to lower extension of connections when compared with bars, it is better to meet postulate 1. It states that bearing capacity and reliability of connections and nodes in complex trusses should be greater than bearing capacity and reliability of connected decisive bars. The importance of postulate 1 consists in the necessity of preventing premature exclusion of decisive bars from the load bearing structure. The exclusion of decisive bars from the load bearing structure leads to an increase in the probability of collapse of statically determinate structures, or of failure of statically indeterminate ones, in which the redistribution of forces in the bars may also result in a collapse.

Meeting postulate 1 (Kowal 2010, 2014), makes it possible to estimate bearing capacity and reliability of the structure on the basis of the number of decisive elements reduced to the number of bars in the structure. Then, for the estimation of reliability, 29 bars, integrated with connections, considered to be decisive acc. Example 3, can be taken into account.

Example 3. Estimate the reliability of statically determinate truss of RC2 class (Fig. 2), in which the expected reliability of each decisive elements is $p_i = 0.999{,}927{,}652$. The failure rate of the elements is $q_i = 1 - p_i = 0.000{,}072{,}348$. Estimate the reliability p of the truss on the basis of the number of decisive bars only, n = 29, which have the variation coefficient of v = 0.06. The failure rate of the truss is: $q = nq_2$.

$q = 29 \times 0.000\,072\,348 = 0.002\,098\,092$. The reliability of the truss is: p = 1 – q = 0.997,901,908. The reliability index (Standard normal table) of such truss

is: $t_j = 2.863{,}02$. Reduction in the bearing capacity of the truss when compared with expected one, based on standard calculations (PN-EN 1993:2006 Eurocode 3), determined from formula (5) (Kowal 2013), is:

$$s = [1 - t_2 v_i] : [1 - t_j v_i]$$
$$s = [1 - 3.8 \cdot 0.06] : [1 - 2.86302 \cdot 0.06] = 0.932 \qquad (5)$$

Conclusion 1. To maintain the recommended system reliability having the index $t_2 = 3.8$, it is necessary to increase bearing capacity of the bars acc. algorithm shown in Example 1. In the example presented in Fig. 2, the recommended reliability of decisive elements should be: $p = 1 - q_2$: n

$$p = 1 - 0.000{,}072{,}348 : 29 = 1 - 0.000{,}002{,}494{,}759 = 0.999{,}997{,}505{,}241.$$

The necessary reliability index of each of 29 elements is: $t = 4.565{,}23 > 3.8$.

Conclusion 2. The design bearing capacity N_0 of the elements of the statically determinate truss estimated on the basis of the relevant standards should be increased using coefficient s acc. formula (6) (Kowal 2013):

$$s = [1 - (t_2 = 3.8)v] : (1 - 4.56523v) = 1.063 \qquad (6)$$

Coefficients s for increase in the bearing capacity of decisive bars, estimated on the basis of the standards in force, make it possible to maintain the recommended RC2 (PN-EN 1990:2002 Eurocode) reliability class of statically determinate truss structures.

When trusses having the form presented in Figure 2 are used for steel building cover, instead of increasing the bearing capacity of bars (cross-sections), it is possible to increase the bearing capacity of the trusses by means of coupling a larger number of trusses with continuous transverse bracings. Those are capable of carrying transverse loads that result from random differences in loads and bearing capacity of elements.

Chapter 3 presents the way of restoring and increasing the bearing capacity of complex structures by parallel coupling of integrated (Kowal 2013), (Kowal 2014) decisive elements (or segments), where the influence of the reliability of connections and nodes is accounted for.

3 THE EFFECT OF CONNECTIONS AND NODES ON BEARING CAPACITY AND RELIABILITY OF BRACED TRUSSES

Study (Kowal 2014) presented the method of probabilistic optimisation of bearing capacity and reliability of statically indeterminate bar structures. The method is based on the coupling of the elements into kinematically admissible failure mechanisms (KAFMs). Those contain minimal critical sets of elements (MCSs), the characteristic of which is that they satisfy axiom 1: if only one element in the MCS is operational, the whole set is operational, too. Study (Kowal 2010) presented the method for estimating bearing capacity and reliability of connections and nodes so that those should be higher than the bearing capacity of bars. That is intended to prevent bar exclusion from service in MCS due to the failure of connections. Bar exclusion from a statically determinate truss results in a collapse. Bar exclusion from the KAFM of the truss in the statically indeterminate system leads to a local failure or weak spots in the structure.

In Example 1, the reliability of a single truss acc. Figure 2 is estimated. It amounts to: $p = 1 - q$.

$p = 0.992{,}548{,}151$. The reliability index t_2 of the truss is lower than the one prescribed for RC2 class, and it amounts to: $t_j = 2.434{,}71 < 3.8$. Coefficient s for bearing capacity decrease in relation to that recommended for RC2 class, calculated with formula (2) is: $s = 0.904$. In Figure 4, a broken line denotes continuous transverse bracing, which couples m geometrically invariable trusses shown in Example 4.

Estimate increase in bearing capacity of $m = 4$ trusses coupled in parallel, estimated in Example 1, in which 103 decisive elements are found altogether. The possible number of decisive elements that are taken into consideration includes: 29 bars, 58 connections and 16 nodes. Increase in the bearing capacity of m coupled trusses is estimated from formula (7) acc. (Kowal 2014):

$$s_m = [1 - t_j v_i : \sqrt{m}] : [1 - t_j v_i] \qquad (7)$$

From Example 1, the following data are obtained: variation coefficient of bearing capacity $v = 0.06$ and reliability index t_j (Standard normal table) of a single truss: $t_j = 2.434{,}71 < 3.8$.

When $m = 4$ trusses, containing 103 decisive elements, are coupled in parallel, the bearing capacity of the group of 4 trusses increases s_m times acc. (7):
$s_m = [1 - 2.434{,}71 \times 0.06{:}2] : [1 - 2.434{,}71 \times 0.06]$
$s_m = 0.926{,}958{,}7 : 0.853{,}917{,}4 = 1.085{,}537$

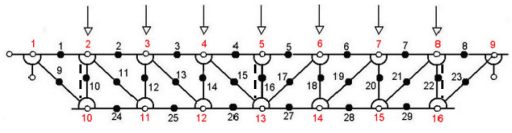

Figure 4. Spacing of transverse bracings that couple m trusses in zones: 2–10, 5–13, 8–16. Top nodes 1 to 9 are held by roof plane bracing.

Conclusion: Increasing bearing capacity by coupling m = 4 trusses does not compensate for the loss of bearing capacity of trusses resulting from the number of n = 103 decisive elements, coupled in series, because the product (8) is smaller than 1:

$$s.s_m = 0.904 \cdot 1.085{,}537 = 0.981 < 1.0 \quad (8)$$

Implementation of postulate 1, which states that the bearing capacity and reliability of connections and nodes must be higher than that of bars, makes it possible to reduce the number of decisive elements in the truss of concern to the necessary number of bars n = 29. For this truss, the weakening coefficient s acc. Example 2 is s = 0.932 and the reliability index (Standard normal table) acc. Example 2 is: $t_j = 2.86302$. In such a design situation, after coupling m = 4 trusses, each containing 29 necessary decisive elements, the bearing capacity of the complex structure increases acc. Example 5.

Example 4. Estimate increase in the bearing capacity of the system formed by coupling m = 4 trusses containing 29 decisive elements (bars), connected in series, dimensioned in accordance with relevant standards. Those are estimated in Example 2, in which 29 decisive elements are found, and in which only bars are considered to be decisive elements.

From example 2, we have: variation coefficient of the bearing capacity v = 0.06. The reliability index t of a single truss is: $t_j = 2.863 < 3.8$.

When m = 4 trusses are coupled in parallel, the bearing capacity of coupled trusses increases acc. formula (7) (Kowal 2014):

$$s_m = [1 - t_j v_i : \sqrt{m}] : [1 - t_j v_i]$$

$$s_m = [1 - 2.863 \times 0.03] : [2.863 \times 0.06] = 0.914 : 0.828$$

$$s_m = 1.1037$$

The product of $s.s_m$ decrease coefficients s = 0.932 of the bearing capacity of the truss consisting of 29 bars, and of bearing capacity increase $s_m = 1.1037$, due to the coupling of 4 trusses, is (9):

$$s.s_m = 0.932 \cdot 1.1037 = 1.029 > 1 \quad (9)$$

Conclusion: after 4 trusses are coupled acc. Example 5, the load bearing capacity meets the reliability recommendation acc. the general standard (PN-EN 1990:2002 Eurocode).

4 SUMMARY, COMMENTS, AND CONCLUSIONS

Currently, decisive elements of complex structures are dimensioned in accordance with conventional structural mechanics and strength of materials using conventional algebra. The problem is that design bearing capacities of elements and their connections are quantiles of the distributions of bearing capacity, having the form of $N_k = E(N) - t\,D(N)$, drawn from statistical normal distribution with the expected reliability index t = 3.8.

The results of algebraic operations on quantiles are significantly different from the results of operations with the use of conventional algebra. Errors in conventional estimation of bearing capacity, especially of the systems with ambiguities in bearing capacity, contribute to failures and collapses. That particularly refers to prefabricated steel and concrete complex structures.

Objective estimation of bearing capacity and reliability of structures composed of many elements can be made using the quantile method. The quantile method can, and should be applied to the analysis of all Kinematically Admissible Failure Mechanisms (KAFMs) of complex building structures and bridges.

It is shown in the examples that coupling of m > 4 elements in KAFM of complex bar structures, which meets postulate 1, leads to a considerable increase in their bearing capacity and reliability, and also to a lower number of failures and collapses, and smaller range of those. It should be noted that collapses of regular spatial structures, in which KAFMs are found containing the number of m higher than 9 elements coupled into MCS, have not been reported.

The quantile of bearing capacity and reliability of elements and complex structures is their eigenvalue, which is associated with the intended use of the object by means of the presented sets of loads of the elements and the structure. This property of the structure should be emphasised because it facilitates the optimisation of its bearing capacity and reliability. In this way it is possible to ensure safe operation of the structure in service and to prevent failures and collapses.

In statically determinate structures, an explicit trend towards a decrease in the bearing capacity and reliability of complex structure is found. The trend is expressed as a function of the number and reliability of decisive elements. The more decisive elements are present, the lower is the bearing capacity and reliability of the system. As regards the number of decisive elements, bar connections to nodes, and nodes must also be included. The defects of those could be a hidden cause of the complex structure failures. Monitoring bearing capacity and reliability of connections and nodes makes it possible to detect faults early, and to reduce the failure rate of the load bearing structure. More than four times reduction in the failure rate q = 1 – p of connections in relation to that of bars should be considered.

Quantile of the bearing capacity of N_k decisive elements of complex bar structures is their eigenvalue related to reliability, having the index $t = \beta$. The index indicates the reliability p of normal distribution acc. the formula: $N_k = E(N) - t\ D(N)$. The mean value E(N) and the standard deviation of bearing capacity D(N) are also eigenvalues.

Quantiles of bearing capacity and reliability complex bar structures are functions of the geometric topology and reliability of decisive elements found in complex structures. Quantiles can, and should be estimated on the basis of the analysis of Kinematically Admissible Failure Mechanisms (KAFMs) of the structure.

When the quantile method is used to estimate the reliability of statically determinate building structures composed of n elements, the properties of numbers close to 0 or 1 should be taken into account. When the notion of failure rate is introduced $_i = 1 - p_i$, we have: $p = \prod p_i = \prod(1 - q_i) = 1 - \sum q_i$. When the expected reliability is the same, namely $q_i = q_1$, the failure rate of the structure $q = 1 - p$ is increased n times $q = nq_1$.

The reliability p of the statically determinate structures composed of the elements having the same reliability can be estimated from the formula $p = 1 - nq_1$. This formula indicates an explicit trend towards a decrease in the bearing capacity and reliability of statically determinate structures as a function of the n number of decisive elements.

In statically indeterminate structures, bearing, capacity and reliability of KAFM increases with an increase in the number of elements coupled in MCS.

The trend towards an increase in the bearing capacity and reliability with an increase in the number m of elements, advantageously coupled into Minimal Critical Sets (MCSs) found in KAFM, is stronger than the trend towards a decrease in the bearing capacity and reliability that occurs in statically determinate structures. Using the quantile method, it is also possible to monitor the necessary increase in bearing capacity and reliability of the existing complex structures by means of coupling the decisive elements. One of the basic instruments of probabilistic optimisation of the bearing capacity and reliability of complex bar structures is putting decisive elements into service in KAFM of the structure.

Another instrument concerns implementing postulate 1 on using greater bearing capacity and reliability of connections to nodes than the bearing capacity of bars, which is intended to prevent bars from being excluded from MCS when the structure is under service load.

When the elements of statically indeterminate building structures cooperate in the conventional mechanics, the synergistic effect of increase in the bearing capacity due to the parallel coupling of the structure elements is also found.

REFERENCES

Baryłka, J. 2009. Collapses of building structures caused by climate phenomena (in Polish). GUNB, Warszawa. *Materiały konferencyjne* /id/8/.

Biegus, A. & Kowal, Z. 1985. Estimation of parameters of random strength limit in bent profiled sheet (in Polish), Kraków - Krynica 1985 conference, vol. 3, pp. 19–24.

Dziubdziela W., Kopociński B. & Kowal Z. 1973. Ultimate bearing capacity of structural systems with minimal critical sets having joint elements in pairs. *Archives of Mechanics* 25 (5): 719–731.

Gwóźdź M. & Machowski A. 2011. *Selected investigations and calculations for building structures using probabilistic methods.* (in Polish). Cracow: Cracow University of Technology publication.

Kopociński, B. 1973. *Outline of the theory of restoration and reliability* (in Polish). Warszawa: PWN.

Kowal, Z. 2010. Dimensioning bar connections in trusses from the standpoint of structural reliability (in Polish), Kielce - Krynica 2010 conference, vol. Problemy Naukowo-badawcze budownictwa, pp. 675–682.

Kowal, Z. 2011. Hazards associated with the load-bearing capacity of bar space structures during assembly and performance. *Promysłowe budiwnyctwo ta inżenerni Sporady* 3: 34–40. Kiev.

Kowal, Z. 2011. The formation of space bar structures supported by the system reliability theory. *Arch. of Civil and Mechanical Engineering*, Vol. XI, No. 1. Polish Ac. of Sciences – Wrocław Branch., Wrocław Univ. of Technology, pp.115–133.

Kowal, Z. 2012. Probabilistic optimisation of the bearing capacity of columns of conventional steel buildings (in Polish). *Rzeszow University of Technology publication*, No. 283, series. 59 (2/2012/II), pp. 185–192.

Kowal, Z. 2013. On Adjusting the Load Bearing Capacity of Decisive Members to Reliability Classes of Statically Determinate Complex Structures. *Archives of Civil Engineering*, LIX, 1, pp.132–142.

Kowal, Z. 2014. Instruments of probabilistic optimisation of load bearing capacity and reliability of statically indeterminate complex structures. Archives of Civil Engineering, LX, 1, 2014, 77–90.

Kowal, Z. 2014. Probabilistic optimisation of bearing capacity and reliability of spatial bar structures (in Polish), KONSTRUKCJE METALOWE ZK 2014 conference, Kielce-Suchedniów 2–4 July 2014, pp. 6–17.

Kowal, Z. 2015. The quantile method versus structural collapses (in Polish), Seminar at the ceremony of awarding Doctor Honoris Causa (DHC) degree at the Zielona Góra University of Technology. 16 June 2015, in press. Murzewski, J. 1989. *Reliability of engineering structures* (in Polish). Warszawa: Arkady.

Kowal Z. & Piotrowski R. 2013. Energy-active expansion segments of steel buildings with structural cover (in Polish). *Budownictwo i Architektura*, Lublin University of Technology publication, Vol. 12(2), pp. 221–228.

PN-EN-1990:2002 Eurocode. Basis of structural design, with Annex B.

PN-EN 1991-1:2005 Eurocode 1. Actions on structures.

PN-EN 1993:2006 Eurocode 3. Design of steel structures.

Standard normal distribution table.

Recent Progress in Steel and Composite Structures – Giżejowski et al. (Eds)
© 2016 Taylor & Francis Group, London, ISBN 978-1-138-02946-0

Deformation of steel lattice towers for overhead lines—case study

M. Just
Cteam Consulting & Anlagenbau GmbH, Siegburg, Germany

ABSTRACT: The transmission of electricity over long distances is usually done with high voltage overhead lines. As supports usually steel lattice masts are used. The design of these masts according to country-specific standards primarily is done as a design in the ultimate limit state. Analyses of the serviceability limit state play a subordinate role, since the masts are not regular subjected to service stress. This results in generally low requirements for the limitation of the deformation. The purpose of this paper is to show on the basis of a case study, that for particular boundary conditions the deformations have to be considered. In the observed case unscheduled deformations occurred, which resulted from a series of unfavourable interacting parameters. These parameters will be described qualitatively and quantitatively in detail. In addition, recommendations will be given, how and to what extent deformations can be limited.

1 INTRODUCTION

The safety concept of DIN EN 1990 (2010), which is valid in Germany, stipulates in the planning and design the analysis of structures in two limit states. In addition to the analysis of the stability in the ultimate limit state, the usability of the structure must be ensured, by also analyzing the serviceability limit state. In the design of typical civil and industrial buildings and bridges this includes strict requirements for the limitation of deformations of the structure, in order for example to avoid damage to adjacent components, as well as to ensure the trafficability and the quality of the optical appearance. In the design of overhead lines the demands on usability are much lower, because the masts are not subject to service load. Deformations must be limited in order to provide the electrical distances between conductor cables and objects next to the line and to ensure the visual appearance. Specific limits are not set for this. Therefore a detailed deformation analysis usually does not take place, often only the elastic deformations are considered and compared to empirical values. The purpose of this case study is to show, that the determination of the expected deformation is required for masts which are particularly vulnerable to deformations. Also it will be shown how to reduce these by taking appropriate measures already in the planning.

2 CASE STUDY OF AN OVERHEAD LINE WITH SEVERELY DEFORMED MASTS

2.1 *Case description*

Basis of the following considerations is a new overhead line, where deformations have been observed at several angle tension and dead-end towers, which are clearly identifiable in their size to the naked eye. The causes are a combination of different parameters which act in this case unfavorably together. These are presented below. In order to assess the causes qualitatively the previously measured deformations and the mast geometry are presented before. The masts belong to a newly developed linkage typ which carries two or three electric systems, including a 380 kV system in the first traverse level and one or two 110 kV systems in the second traverse level. This results in an asymmetric mast design (Fig. 1), the second Traverse was only left-fitted in the case of a single 110 kV system. During assembly, significant deformations have been observed on three masts which exceeded the expected static deformations (see 2.2.1). Measurements of horizontal displacement showed deviations (in relation to the required position) of up to 93 cm at the end of one of the traverses (see Table 1 – data taken from Unseld et al. (2014)). The traverses left and right were horizontally deformed in opposite directions (Fig. 2).

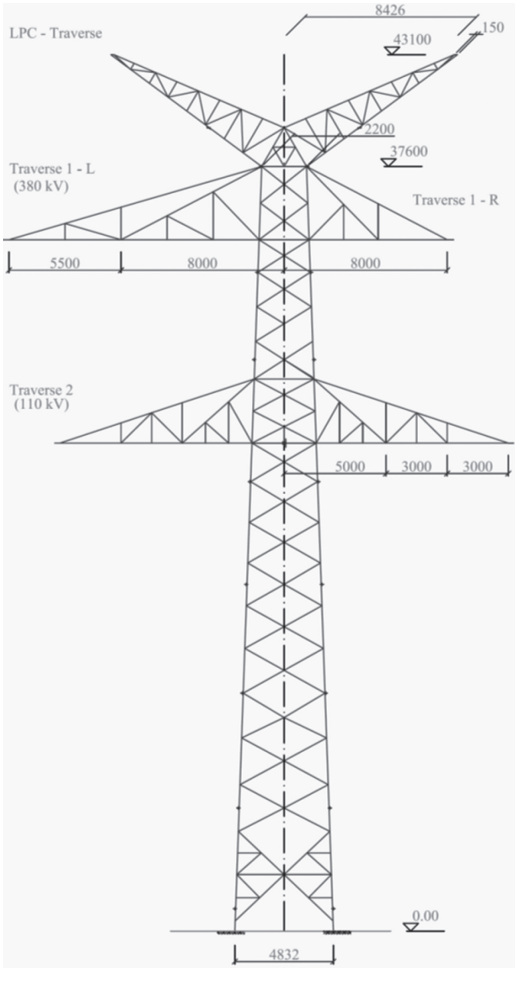

Figure 1. Mast design of a Mast with 3 electric systems.

Table 1. Measured deformations of the traverses.

Traverse	Mast 1 [cm]	Mast 2 [cm]	Mast 3 [cm]
I, left	9	50	93
I, right	18	12	18
II,left	30	10	41
II, right	–	9	16
LPC*, left	18	35	73
LPC*, right	20	5	22

*LPC = lightning protection cable.

The measurements were done with a laser theodolite type "Trimble S6". The measurement points were located over the entire height of the towers on the mast shaft and at the ends of the traverses and measurement of the masts were done from two different directions. As a reference level, the base points were used. The measured deviations therefore relate to the plumb to the base of the mast. So the vertical exaggeration is directly counted out from the measured deformations. The vertical exaggeration is caused by a planned misalignment of the mast foot. This is done to compensate the deformations in the final state from the forces from the conductor cables.

The large deformation of the traverses also can be found in the mast shaft in smaller scale, which has become twisted due to torsion during assembly (see. 2.2.4). In Figure 2 can be seen that the traverse follows the rotation of the mast shaft.

The deformations of the traverses itself is comparatively small, but in consequence of the rotation of the pole shaft and the one-sided loads in the assembly this lead to a misalignment of the lower chord of the traverses, which results in a deformation due to compressive stress within the tension members (Fig. 3). The measured misalignments of lower chord of the traverses were between 1° and 6.4°.

By correspondingly adjusting the conductor cables, the electrical distances could easily be complied with. With respect to the ultimate and serviceability limit states there were no damages resulting from the deformations. On the other hand the visual appearance has been permanently impaired, mainly due to the rotation of the pole shaft.

2.2 *Causes of the observed deformations*

2.2.1 *Static deformations due to first order theory*

A load on a structure always results in a reaction of the same, and thus leads at least to an elastic deformation. In this case, the elastic part alone causes deformations of up to w = 280 mm at the top of the traverse one towards the ideal position in the final state (calculated by finite element software). This is mainly due to the very slender mast shaft. As a measure for the slenderness the average width of the shaft will be used in relation to its height. For the present case there is a slenderness of:

$$\lambda = \left(\frac{H}{\frac{1}{2} \cdot \left(w_o + w_u \right)} \right) = \left(\frac{37600}{\frac{1}{2} \cdot \left(2200 + 4832 \right)} \right) = 10.7 \tag{1}$$

Other typical angle tension and dead-end masts with a similar number of systems have a slenderness of λ = 8 to 9.5. The comparability however is limited because other masts with 380 kV systems almost always have one or more sections at the bottom, which have a significantly larger increase in width (Δ_w) than the rest of the mast shaft. The

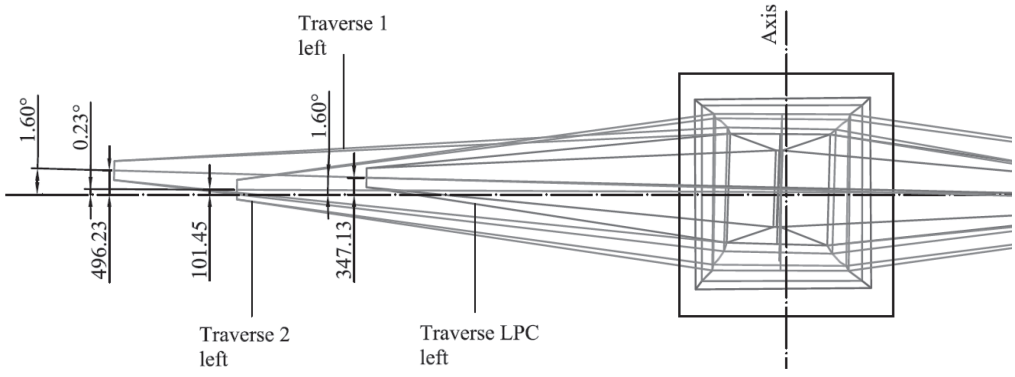

Figure 2. Top view at Mast 2, generated from the measured values, only shaft and left side of the traverses.

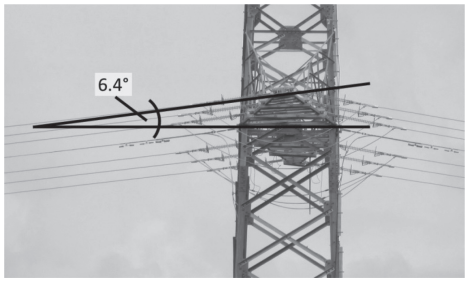

Figure 3. Side view at traverse 2, Mast 3.

above values were calculated by weighting the base of the mast and the rest of the mast shaft with their respective height. Since the greatest moments for towers occur in the lower sections of the shaft and the deformation in these sections have the greatest impact (as pre-curvature) on the deformations of all the top sections the lower sections actually have to be weighted higher than the rest of the mast shaft. Investigations on the degree of weighting are the subject of current research.

Another criterion for comparing the slenderness is the increase in width of the mast shaft itself. Usual angle tension and dead-end towers have values from 80 to 100 mm/m above the kink joint (between lower and upper sections). The lower sections usually have values for the increase in width of 240 to 300 mm/m. In the present case the masts have a width increase of 70 mm/m over the entire height. In Equation 1 there is the increase in width in the variable w_u:

$$\lambda = \left(\frac{H}{\frac{1}{2} \cdot \left(w_o + \left(w_o + H \cdot \Delta_w \right) \right)} \right) \qquad (2)$$

It can be seen, however, that the slenderness will be affected in addition to the increase in width by the height of the mast shaft at the upper end. Although considered masts may have a relatively large width at the upper end of the mast shaft they overall have to be regarded as very slim.

2.2.2 *Deformation due to non-linearity and screws slip*

In addition to the deformations according to first order theory also proportions of non-linear deformations can occur. In the present case, the individual rods of the mast, however, have a low utilization ratio so that there are no additional deformations after second order theory due to plasticization. Even a significant increase in the deformation by increasing the internal forces due to the shift from the ideal position cannot be determined by calculation, the increase in deformations showed a maximum of 5 mm.

However, a further non-linearity is caused by the screw slip. In the design of overhead lines the use of fit bolts and friction couplings is not common. When using raw bolts because of the hole clearance arises a slip of up to 2 mm per screw, which brings a significant contribution for the deformation of steel lattice towers, especially at the joints of the corner legs. Due to the limited space on the mast location during installation only short sections with lengths from 5 to 7 m were installed in the present case, so for a height of 37.6m up to the bottom end of the traverse for the lightning protection cable seven sections were installed. According to Kießling et al. (1989) a slip of $\Delta_s = 4$ mm can be recognized for each joint of the corner legs (summation of the slips of pressure and tension side of the mast), thus resulting in a misalignment of $\alpha_s = \Delta_s/w$, where w is the width of the mast at the joint. For the present case, this results in a mis-

alignment at the top of the mast of (with h distance from the joint to the point of deformation):

$$w_s = \sum_{i=1}^{n} (\tan(\alpha_s) \cdot h) = 202\ mm \quad (3)$$

When calculating the deformation with finite element software, under consideration of the screw slippage at the joints of the corner legs, an enlargement of the horizontal deflection of up to $w_s = 170$ mm compared to the pure elastic deformation occurred. It turns out that the values of the two above calculations have a comparable magnitude.

2.2.3 *Deformation due to assembly tolerance*

For the assembly tolerances DIN EN 50341-1 (2010) references to DIN EN 1090 (2008), which in part 2, Appendix D indicates a permissible deviation for towers of ± 0.05% of the length relate to the ideal vertical (or exaggerated) structural axis. For the present case a permissible deviation of approximately 19 mm can be calculated for a mast with a height of 37600 mm (to bottom end of the traverses of the lightning protection cable).

For the rotation, a maximum permissible deviation of ± 2.0° over the entire structure height is allowed (for structural heights <150 m). Since this is for towers in general and the measured values of the presented case of the rotation are far below, for masts with traverses significantly more stringent requirements should be provided. (For comparison: measured maximum twisting of the mast shaft for the masts 1 and 2 in the final state was ~ 1.85°, while the deformations have exceeded the permitted deviation of ± 0.05%. Mast 4 had a twisting of 3.7° at the final stage—this mast also has the greatest horizontal displacements and exceeds the limits by far).

During the assembly of the mast no exceedances of the allowable positional deviations were observed before the mounting of the conductor cables.

2.2.4 *Deformation due to assembly sequence*

In addition to assembly tolerance also the order of the assembly in the present case has had a decisive influence. Due to an adjacent 110 kV stock line (with 2 electrical systems), which could be dismantled only after adoption of the one of the two electrical systems, the masts had to be built so that at the beginning only on one side of the mast the traverses were installed, otherwise the electrical clearances could not have been guaranteed. Thus the first 110 kV system was suspended and regulated unilaterally. In addition, the conductor cables of the 380 kV system already have been attached to one side. Otherwise these would have had to be installed over the 110 kV line (which then already was under voltage), which is not allowed. Despite the back anchorage of the masts, this led to twist in the mast shaft. Figure 4 shows a photo of the mounting state, including the adjacent stock-line.

Figure 4. Assembly state with unilaterally installed left traverses (View against direction of overhead line).

The deformations registered in this state of assembly could not be appreciably reduced even after complete installation and adjusting of other traverses and conductor cables, which were checked by multiple measurements in various assembly stages and in the final state (Table 1). It is therefore to be assumed that in particular the deformations caused by the screw slip are only partly reversible.

3 NORM SITUATION

In the standards for the design of overhead lines which are valid in Germany, namely DIN EN 50341-1 (2010) and DIN EN 50341-3-4 (2011) only minor demands are made on the usability. It calls for compliance with electrical clearances in the field, as well as the design of the mast by taking into account aesthetic considerations. However, this doesn't result in specific requirements for limits to be observed. Compliance with the electrical distances also can be ensured by a corresponding readjustment of ropes even with comparatively large mast deformations (as done in the observed case, see 2.1).

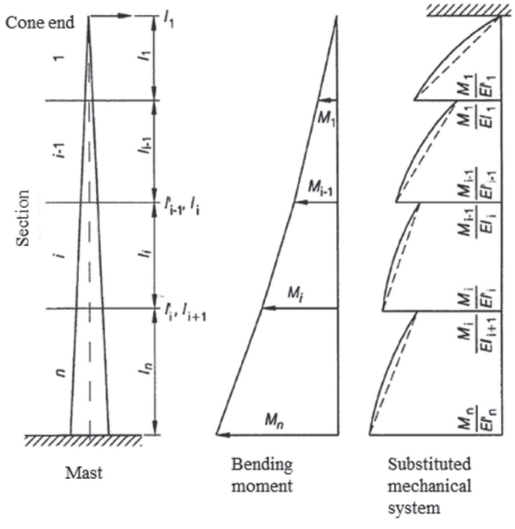

Figure 5. Approximate deformation calculation on substituted system (taken from Kießling et al. (1989)).

4 WAYS OF CALCULATING DEFORMATIONS

As already mentioned in 2.2.1 it is easily possible to calculate the deformations after first order theory with finite element programs. Modern software tools allow to also considering the influence of screw slip and the connection stiffness. This should be considered especially for the joints of the corner legs, as the consideration for the entire mast is too time-consuming.

A simple way of estimating the deformation due to external load is provided by Kießling et al. (1989). In this the moments in the shaft (as one component) get combined with the overall rigidity and the deformations are calculated using a substituted mechanical system (Fig. 5).

The disadvantage of this approach is that the initial curvature of the bottom sections is not considered in the deflection of the top sections, which is why the therefrom determined deformed shape in its curvature differs from the real one. Except for a rough approximate predetermination this method is not recommended. Therefore determining the deformation should be done with finite element software.

5 LIMITATION OF DEFORMATIONS

For fulfilling the serviceability limit state the deformations should be limited. Limits are not imposed by the valid standards, in particular since the electrical distances, the only criterion listed in this limit state, easily are ensured by specifically adjusting the cables. To also take into account the aesthetic aspects limits should be defined, which are to be chosen so that the deformations occurring are not noticeable by non-expert viewers and thus do not impair the appearance negatively.

As shown in section 2.2.3 for the rotation of the mast shaft due to assembly there already are tolerances provided. Unfortunately these are unsuitable for steel lattice masts with traverses, because even when fulfilling the given limit the displacement of the traverses against ideal position would be much too large. In addition to this mounting tolerance the elastic deformation and the deformation of screw slip would add on top. The twist due to mounting tolerance should therefore be limited to ± 0.2°, the twist due to external stress (considering the screws slip) to ± 0.4°. This results in a maximum allowed rotation of ± 0.6° in the final state. The rotation of the bottom flange of the traverse should not exceed ± 1° (with reference to horizontal).

For the deformation of the mast shaft the required straightness after DIN EN 1992-1 (2011) is considered for comparison, as in DIN EN 1993-1 (2010) it is only specified that the limiting values for the horizontal displacement must be agreed with the client. For reinforced concrete components the deflection hast to be limited to H/250, which is required for compliance with the serviceability and acceptable appearance. At cantilever columns (like masts) H can be taken as 2.5 times the height, resulting in a limit for masts of H/100 (where H is the total heigth). This would result in a deflection at the bottom end of the traverse of the lightning protection cable of 376 mm in the present case. This deflection can be assessed as acceptable in terms of the visual appearance, as it is imperceptible for the viewer, as has been demonstrated in several other cases and also in the present case, in which mainly the horizontal deflection of the traverses, as a result of rotation of the mast shaft affects the appearance.

In order to limit the deformations on the above values, a calculation of the deformation can be necessary. Research is ongoing to develop criteria for detecting masts which are particularly vulnerable to deformations. As a first measure, the slenderness of the mast can be used, which should not exceed the value of 9.5. Further criteria are the number of joints of the corner legs, the torsion stiffness of the shaft and the type of linkage. Here, however, yet research is required. If a deformation analysis is required, this should be done in the quasi-permanent design situation according to DIN EN 1990 (2010). This results in significantly lower stresses than in the ultimate limit state:

$$\sum_j G_{k,j} \oplus \sum_i \psi_{2,i} \cdot Q_{k,i} \tag{4}$$

Since the quasi-permanent combination has an exceedance frequency of 50%, the average tensile stress of the conductor cables at an ambient temperature of 10° C should be set. The wind load is to be reduced to 50% (in deviation to DIN EN 1990 (2010), Appendix A the wind should not be combined with $\psi_2 = 0$, but with $\psi_2 = \{0.5 \ldots 1\}$), ice loads are not to be considered (except the assembly takes place in winter months). This calculation is carried out both for the final state as well as for mounting states, insofar the possibility is given that load cases occur in these states, which cause stresses, which do not occur in the final state (for example torsion in the mast shaft due to unilateral cable installation) and may lead to permanent deformation, e.g. due to screw slip. In the calculation, the influence of the screw slip at least has to be considered for the joints of the corner legs. The screw slip in the diagonals can approximately be taken into account with a reduction in stiffness according to Kießling et al. (1989). When using finite element programs, the material stiffness of the diagonals should it be reduced.

If the calculated deformations exceed the above limits, measures must be taken to reduce the deformations. The easiest way to reduce deformations is to increase the stiffness of the mast shaft by increasing the total width and increase in width (Δ_w) over height. If this is not possible, the corner legs should be designed with stiffer cross sections. In order to prevent deformations which affect the rectangularity of the mast shaft, additional horizontal bracings can be installed. If large deformation with big proportions due to screw slip are expected this can be reduced by the use of fitting bolts or friction connections for the joints of the corner legs. In particular if the mast shaft consists of many short sections, this may represent a major part of the deformation.

Special attention should be paid to the assembly sequence. Construction stages where torsion is added to the mast should be avoided or reduced by a correspondingly dimensioned back-anchoring of the mast.

6 SUMMARY

In this paper it was shown that the consideration of deformation of masts in the design of high voltage overhead lines may be relevant when particularly slender masts are planned. Avoiding large deformation is possible in principle; but to take appropriate measures, however, all the influencing factors and the assembly conditions must be taken into account for the calculation of the expected deformations. As a criterion for detecting masts vulnerable to deformations the slenderness of the mast shaft was proposed, however, other factors such as linkage type, rigidity of the corner legs, number of joints and type of cable installation need to be considered as well. For a criterion that considers all these factors a extensive analysis of deformations of different mast types is necessary.

REFERENCES

DIN EN 1990 2010:12. *Grundlagen der Tragwerksplanung.* Berlin: Beuth Verlag GmbH.

DIN EN 50341-1 2010:04. *Freileitungen über AC 45kV—Teil 1: Allgemeine Anforderungen—gemeine Festlegungen*. Berlin: Beuth Verlag GmbH.

DIN EN 1090-2 2008-12. *Ausführungen von Stahltragwerken und Aluminiumtragwerken—Teil 2: Technische Regeln für die Ausführung von Stahltragwerken*. Berlin: Beuth Verlag GmbH.

DIN EN 50341-3-4 2011:01. *Freileitungen über AC 45kV—Teil 3: Nationale Normative Festlegungen (NNA)*. Berlin: Beuth Verlag GmbH.

DIN EN 1992-1 2011:01. *Bemessung und Konstruktion von Stahlbeton—und Spannbetontragwerken—Teil 1-1: Allgemeine Bemessungsregeln und Regeln für den Hochbau*. Berlin: Beuth Verlag GmbH.

DIN EN 1993-1-1 2010:12. *Bemessung und Konstruktion von Stahlbauten—Teil 1-1: Allgemeine Bemessungsregeln und Regeln für den Hochbau*. Berlin: Beuth Verlag GmbH.

Kießling, F., Nefzger, P. & Kaintzyk, U. 2001. *Freileitungen—Planung, Berechnung, Ausführung.* Berlin: Springer-Verlag.

Unseld, H., Hildebrandt, I., Just, M. 2014. *Mastverformung Mast 1b, Mast 1, Mast* 4, Report, unpublished.

Recent Progress in Steel and Composite Structures – Giżejowski et al. (Eds)
© 2016 Taylor & Francis Group, London, ISBN 978-1-138-02946-0

Influence of the initial guy forces on the static computations of mast taking into account the mast shaft buckling form

M. Matuszkiewicz
Faculty of Civil Engineering, Environmental and Geodetic Science, Koszalin University of Technology, Koszalin, Poland

ABSTRACT: The paper pertains to the computations of guyed masts according to the Second Order Theory taking into consideration mast shaft buckling forms. The influence of the adopted initial guy forces on the mast static-strength computations according to the guidelines of the current European Standard EN 1993-3-1 was researched based on an example of a 260 m high mast with 4 levels of guys. The mast shaft with the initial imperfections corresponding to its buckling form at the stage of pre-stress condition was considered in the analyses. To determine the initial curvilinear mast shaft imperfections eigenvectors of the mast shaft stability analysis were used. Due to absence of any standard guidelines, computations were performed with assumption of the maximum buckling values of the mast shaft equal to v_0 = L/1000 (L—span length of the mast), which corresponds with the permissible assembly deviation values as per EN 1993-3-1 standard.

1 INTRODUCTION

Guyed masts belong to the structures in which, due to geometrical non-linearity of the guys, the behaviour of the whole structure is also non-linear, ie. mast shaft displacements are non-linearly dependent on external load. In accordance with EN 1993-3-1 standard the global elastic analysis in mast computations as per the Second Order Theory should be used.

The structures with initial geometrical imperfections should be, therefore, analysed.

However, there is a problem how to take into account the corresponding deformation form of the structures because the guy fixing points in mast shaft cannot be considered like typical supports applied in steel structures. The stiffness of the mast shaft elastic support in the guy fixing points are characterized by wide variation and depend directly on the values of guy forces and the guy chord angles to the horizontal plane. So, it is justified, according to the author, to first determine the corresponding buckling form of the mast shaft for the assumed values of initial guy forces, and then use this form to determine the appropriate mast shaft imperfections. As there are no standard guidelines in this matter, the values of the maximum deflections of the mast shaft spans can be assumed equal to $v_0 = L/1000$, which corresponds with the permissible assembly deviation values as per EN 1993-3-1 standard. It should be noted that the measured values of the mast shaft curvature deflection in many existing mast structures were considerably smaller than these values. In this paper a comparative analysis of a mast for several selected variants of initial guy forces, using the procedure described above, was performed. A substitute, simplified model of the mast shaft in the form of Timoshenko beam was used in the computations. Such a model is often used in practical design of masts. An exact analysis of the mast with the shaft in the form of spatial truss would lead to a very significant extension of computation time and would not affect, according to the author, significant change of conclusions from the presented study.

2 MAST STRUCTURE DESCRIPTION

In this paper analysis of a 260 m high mast with four guy levels at the heights of 55.0, 115.0, 175.0 and 235.0 was performed (Figure 1). The mast shaft was designed as S355 steel in form of tree-walled space truss with side width $a = 2.0$ m. Pipes ∅ 168.3/14.2 mm were used as the leg members, and as mast face lacing—pipes 76.1/4.0 mm. The mast guys were designed of a spiral strand steel ropes 1×61 with featuring strength $R_r = 1570$ MPa and the minimum breaking force 823 kN (∅ 32 mm rope—the guys on level I and II) and 1040 kN (∅ 36 mm rope—the guys on level III and IV). Initially an assumption was made to analyze four different variants of the initial guy forces at various

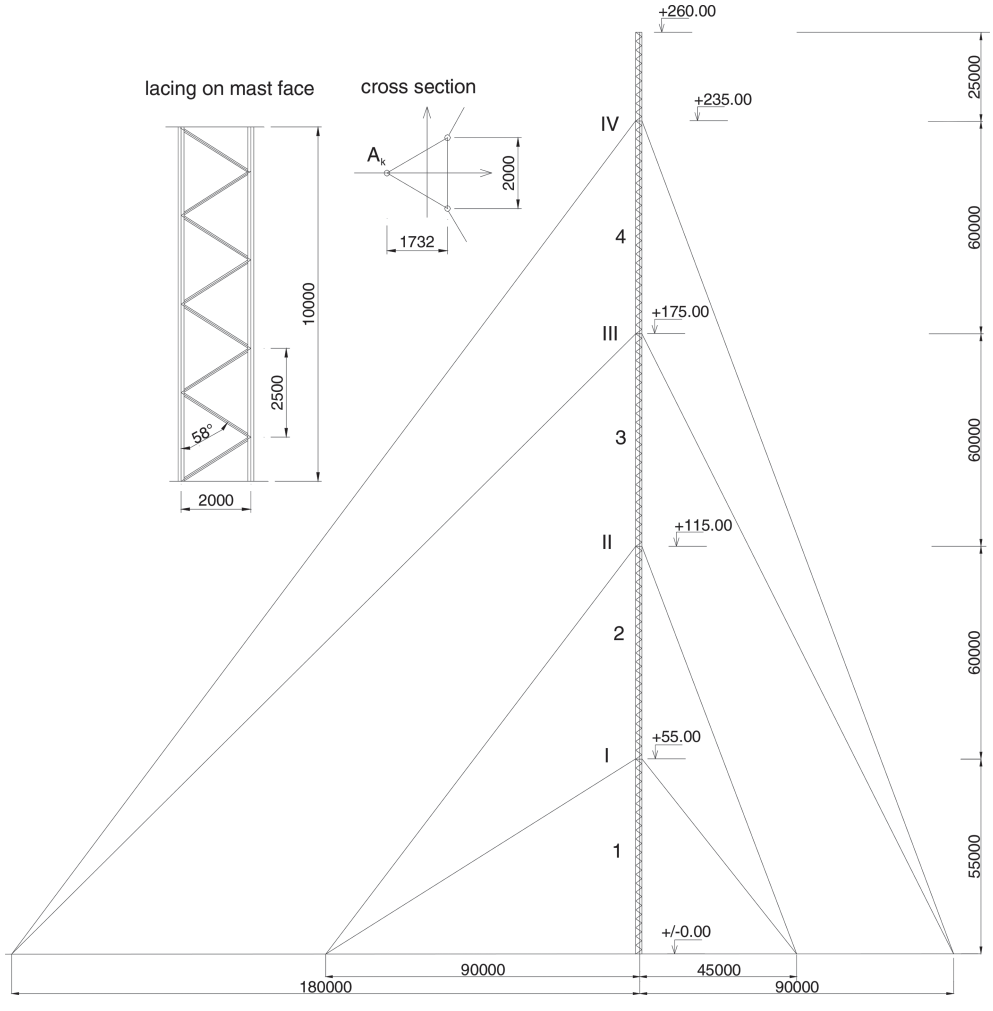

Figure 1. Mast structure diagram.

levels (I to IV): a) 80, 80, 100 and 100 kN, b) 40, 50, 90 and 120 kN, c) 80, 80, 80 and 80 kN, d) 50, 50, 80 and 120 kN.

The mast structure has been qualified to the second reliability class for which the partial factors for permanent loads are equal to 1.1, and 1.4 for variable loads.

3 DESCRIPTION OF THE METHOD OF ANALYSIS

To determine the buckling form of the mast shaft static computations have been performed in a pre-stress condition of the structure for each variant of the initial guy forces. The mast permanent actions and initial guy forces were taken into account in these computations. The static analysis from the Second Order Theory perspective, with consideration of non-linearity of the guys, was performed using Mast1 software described in Pałkowski (2009).

Latticed mast shaft was substituted in computation with a bar featuring proper geometric-strength characteristics taking into account compression, bending, shear and torsional flexibility (Timoshenko beam).

At the next stage, based on the values of normal forces in mast shaft calculated in the pre-stressed conditions and values of forces in stays, mast stability analysis was performed. The computation model adopted to the stability analysis is shown in Figure 2. Values of stiffness in elastic supports of the mast at the guy fixing points were determined from formula (Pałkowski (1994)):

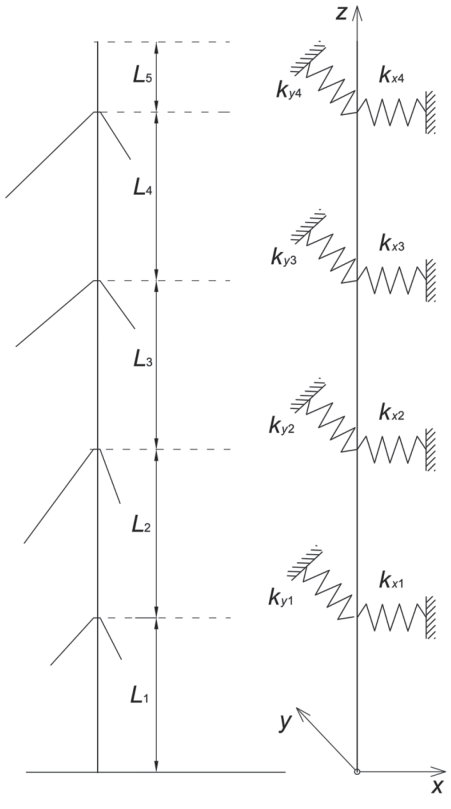

Figure 2. Substitute mast with elastic supports diagram used in stability analysis.

In × axis direction

$$k_x = \sum_{i=1}^{n} k_i \cos^2 \alpha_i, \tag{1}$$

whereas in y axis direction

$$k_y = \sum_{i=1}^{n} k_i \cos^2 \beta_i, \tag{2}$$

where α_i – is the angle between the i-th guy chord and × axis, β_i – is angle between i-th guy chord and y axis, n – number of guys at given level.

Stiffness k_i of a guy in direction of its chord is defined as

$$k_i = \Delta S_i / \Delta L_i, \tag{3}$$

where ΔS_i – change of force in the guy, and ΔL_i – change of the guy chord length, which can be determined from the guy equation indicated e.g. in Pałkowski (2009).

In this research work the author focused only on the first buckling form of the analysed mast shaft. This form was presented, depending on the variant of assumed values of initial guy forces, in Figure 3.

It can be noted that in practically each analysed variant the zero-value points of horizontal displacements are located beyond the guy fixing points. The biggest differences between the mast shaft buckling forms were observed, in the case of the analysed structure, in variants b) and c) and both variants were used in further comparative analysis.

To determine values of initial imperfections of a curvilinear mast shaft, eigenvectors determined in mast shaft stability analysis were used for both variants.

It was assumed that the maximum mast shaft buckling values are equal to $v_0 = L/1000$ (L – mast span length), which is equivalent to the admissible values of mast shaft assembly deviations in accordance with EN 1993-3-1. Form of such created eigenvectors is presented in Figure 4.

At the third stage static computations of a mast during service condition, taking into account initial mast shaft imperfections in accordance with the determined buckling form were performed.

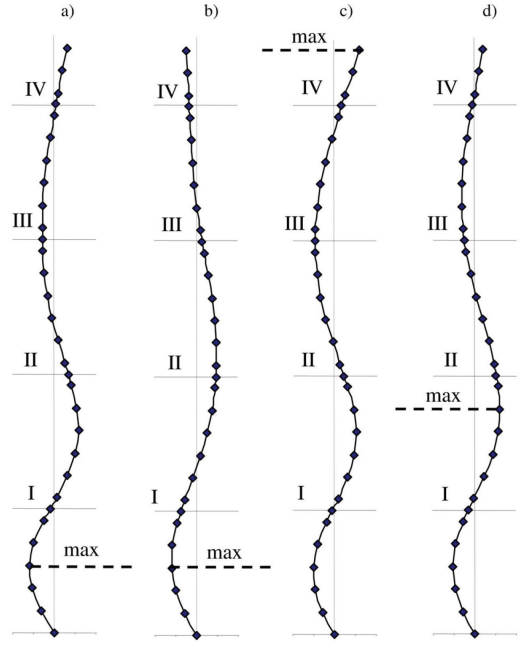

Figure 3. The first buckling form of the mast shaft: a) for the initial guy forces values 80, 80, 100, 100 kN, b) for values 40, 50, 90, 100 kN, c) for values 80, 80, 80, 80 kN, d) for values 50, 50, 80, 120 kN.

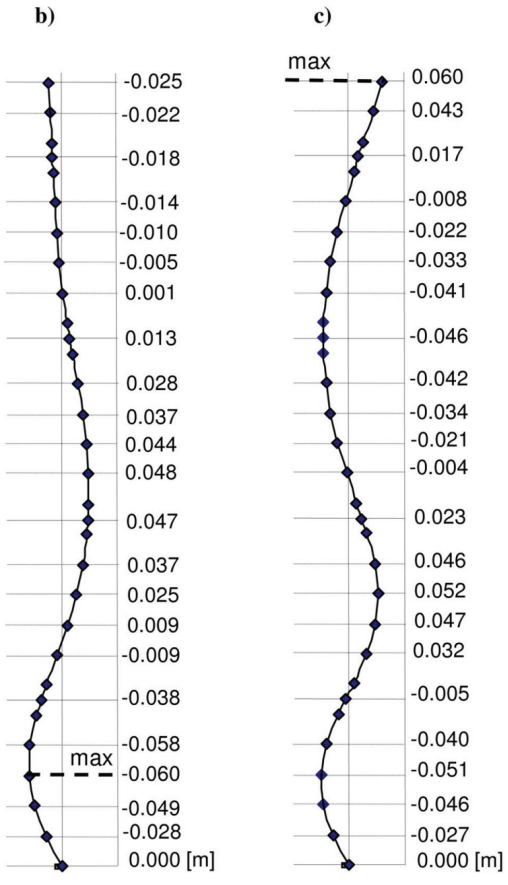

Figure 4. Accepted forms of deformations of the mast shaft for variant b) and c) of initial guy forces.

4 COMPUTATIONS FOR MAST DURING SERVICE

4.1 *Assumptions made for the analysis*

The mast location was assumed in the first wind load zone for the territory of Poland in the Category II area, as per EN 1991-1-4 standard. Diagrams of the mast mean load and patch loads fixed in accordance with EN 1993-3-1 are shown in Figure 5. Self-weight of the structure and a single direction of wind load acting on W1 mast (Figure 5) were used in the static computations.

In accordance with procedure described in EN 1993-3-1 computations of a number of systems of static patch loads in combination with mean wind load were performed; final values of internal forces in mast shaft elements were calculated by addition to (or subtraction from) the mean wind load effect the combined effect of patch loads (comp. Maturszkiewicz (2010)).

For selected values of initial guy forces [b) and c)] computations of the structure in two variants, i.e., with initial mast shaft imperfections and with omission of such imperfection, were performed.

4.2 *Computation results*

Values of internal forces in the mast structure elements obtained from static computations are presented in Tables 1–3. In Table 1 the highest values of forces in guys at particular levels are shown whereas in Table 2–3—maximum values of normal forces and bending moments occurring in the mast shaft are presented.

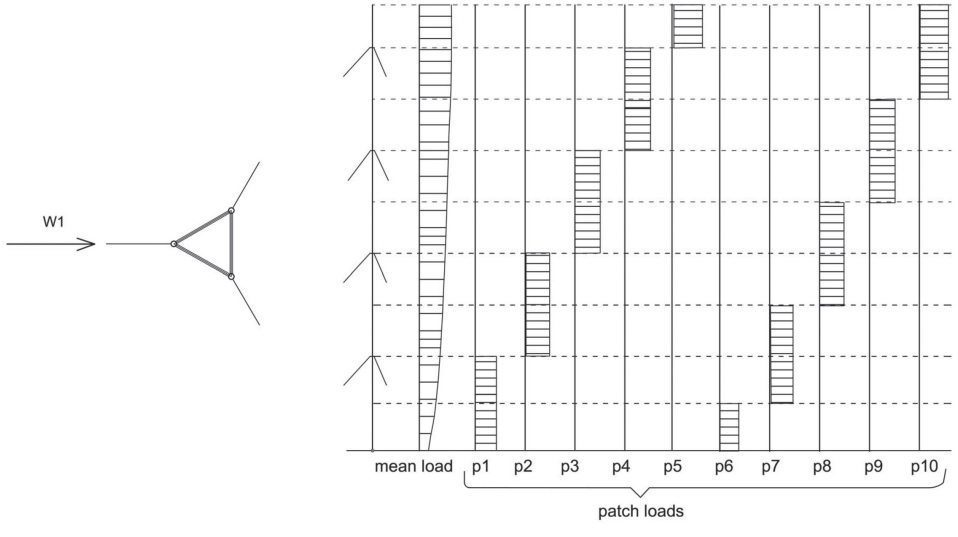

Figure 5. Mast wind load diagrams and directions.

Table 1. The highest values of the forces in mast guys [kN].

	Variant b)		Variant c)	
Guy fixing level	Imperfections $v_0 = 0$	Imperfections $v_0 = L/1000$	Imperfections $v_0 = 0$	Imperfections $v_0 = L/1000$
I	108.4	111.3	136.4	137.0
II	150.9	153.7	172.7	174.5
III	189.7	189.8	180.2	181.5
IV	250.0	250.7	222.5	222.8

Table 2. Maximum values of the normal forces in mast shaft spans [kN].

	Variant b)		Variant c)	
Span	Imperfections $v_0 = 0$	Imperfections $v_0 = L/1000$	Imperfections $v_0 = 0$	Imperfections $v_0 = L/1000$
1	–1512.5	–1512.7	–1520.3	–1520.2
2	–1299.3	–1300.6	–1258.9	–1259.0
3	–973.4	–973.1	–888.6	–888.9
4	–572.0	–572.2	–505.2	–505.6
Cantilever	–48.1	–48.1	–48.1	–48.1

Table 3. Maximum mast shaft bending moments values [kNm].

	Variant b)		Variant c)	
Location	Imperfections $v_0 = 0$	Imperfections $v_0 = L/1000$	Imperfections $v_0 = 0$	Imperfections $v_0 = L/1000$
Span 1	297.0	365.7	268.3	348.6
Support I	–374.5	–379.2	–388.9	–391.4
Span 2	355.9	382.6	281.9	337.3
Support II	–357.7	–369.1	–478.9	–475.0
Span 3	425.8	434.0	379.6	400.9
Support III	–408.9	–417.5	–481.0	–494.2
Span 4	433.3	441.8	428.6	440.5
Support IV	–594.2	–594.4	–594.2	–595.2

It can be noted that irrespectively of the variant of assumed initial mast guy forces usage, in structure computations, of the initial geometrical imperfections had practically no impact on change of values of guy forces and normal forces in the mast shaft compared with computation of the structure without imperfections.

Significant differences have occurred, however, in the computed values of mast shaft bending moments. For variant b) of the initial guy forces, increase of values of bending moments in spans of a mast with imperfections, with relation to the perfect structure computations, was more than 23% for span 1, more than 7% for span 2, and almost 2% for spans 3 and 4.

For variant c) the differences were even bigger—more than 29% for span 1, more than 19% for span 2, more than 5% for span 3 and more than 2% for span 4.

5 REMARKS AND FINAL CONCLUSIONS

Based on the analysis of a selected mast structure one can say that usage in computations of mast shaft initial geometrical imperfections may lead to considerable increase of values of bending moments in spans. The differences, compared with structures without initial imperfections, may vary, depending on the considered form of the curvilinear mast shaft. Due to the fact that this form is, among other, a result of adoption of appropriate values of initial guy forces, which have impact on stiffness of the mast shaft flexible supports, it seems justified to perform such initial structure analysis in order to select in the most advantageous way the values of initial guy forces. In computations performed in line with the Second Order Theory, mast shaft load carrying capacity as per EN 1993-3-1 is determined by load capacity condition for a single leg member taking into account its buckling between the bracing member nodes. Therefore, the most advantageous solution is if for the maximum values of normal forces N the smallest values of bending moments M would occur in the mast shaft spans. In the case of the analysed mast this condition is met in variant c) of initial guy forces.

The computation results presented in this paper pertain to a specific analysed mast structure but those conclusions cannot be generalised with relation to all mast structures, which, as everybody knows, feature very high diversity. The proposed method of analysis that takes into account the form of mast shaft stability loss has, however, a general character and, in author's opinion, can be used in practical design of guyed masts.

REFERENCES

EN 1991-1-4. *Eurocode 1*: Actions on structures. Part 1-4: General actions—Wind actions.

EN 1993-3-1. *Eurocode 3*: Design of steel structures. Part 3-1: Towers, masts and chimneys—Towers and masts.

Matuszkiewicz M. 2010. Computation lattice guyed masts according to PN-EN 1993-3-1. *Inżynieria i Budownictwo.* 4, 194–199. [In Polish].

Pałkowski Sz. 1994. *Cable structures*. Warszawa: WNT. [In Polish].

Pałkowski Sz. 2009. *Steel structures. Some issues of calculating and designing*. Warszawa: PWN [In Polish].

This page intentionally left blank

Recent Progress in Steel and Composite Structures includes papers presented at the XIIIth International Conference on Metal Structures (ICMS 2016, Zielona Góra, Poland, 15-17 June 2016). The contributions focus on the progress made in theoretical, numerical and experimental research, with special attention given to new concepts and algorithmic procedures, and to background knowledge as well as the development and implementation of rules and recommendations for codification worldwide.

The keynote contributions are from: (1) J. Michael Rotter (University of Edinburgh, UK), on advances in the shell buckling phenomenon, which is of particular importance for industrial metal structures such as silos, tanks and vessels; (2) Milan Veljkovic (Lulea University, Sweden), on conceptual and design aspects of supporting structures for wind energy generation, which topic is related to the current worldwide discussion on the benefits of wind power in the light of high vulnerability of modern economies to changes in fuel prices and the imminent shortage of fossil resources; (3) Jiang Qian (Tongji Univeresity, China), on advances in seismic assessment and control of steel-concrete composite high-rise buildings; (4) Johan V. Rietief (University of Stellenbosch, South Africa), international efforts to harmonize and unify reliability-based codification within the area of civil engineering structures. Recent developments in metal and steel-concrete composite structures in Poland are summarized in the 5th and final keynote paper by Tomasz Siwowski (Rzeszów University of Technology, Poland) and Krzysztof Żółtowski (Gdańsk University of Technology, Poland), in which they describe advances in modern structural shaping, material engineering and technology, as well as in computation and design, using examples of recent, spectacular bridges and sporting venues in Poland.

In addition to the five keynote papers the book contains 62 two-page extended abstracts of individual contributions delivered by 164 Authors and Co-authors from 13 countries of four continents. The CD containing all full-length papers is an attachment to the conference book. The individual papers cover a wide variety of topics:

- Cold-formed sections and profiled sheeting
- Steel-concrete composite structures
- Buckling and effect of bracings
- Dynamics, fatigue and seismic analyses
- Bridges, Structural steel, metallurgy and behaviour in fire
- Strength, stability and postbuckling behaviour
- Joints and connections
- Silos, tanks and vessels and
- Reliability, masts and towers

Recent Progress in Steel and Composite Structures is a useful reference source to academics, researchers, graduate students and practicing engineers.

ISBN 978-1-138-02946-0

9 781138 029460

an **informa** business

CRC Press
Taylor & Francis Group
an **informa** business
www.crcpress.com

6000 Broken Sound Parkway, NW
Suite 300, Boca Raton, FL 33487
Schipholweg 107C
2316 XC Leiden, NL
2 Park Square, Milton Park
Abingdon, Oxon OX14 4RN, UK